

# **Defects in Semiconductors**

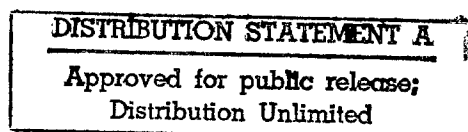
## **ICDS-19**

### **Part 3**



**Editors:**

**Gordon Davies and  
Maria Helena Nazaré**



**ttp** **TRANS TECH PUBLICATIONS**

# Materials Science Forum

ISSN 0255-5476

*As of January 1992 combined with Crystal Properties and Preparation*

---

## Editors:

### G.E. Murch

University of Newcastle  
Department of Mechanical Engineering  
NSW 2308, Australia  
Fax +61 (49) 60 22 28  
e-mail CGGEM@cc.newcastle.edu.au

### Fred H. Wöhlbier

Trans Tech Publications Ltd  
Brandrain 6  
CH-8707 Uetikon-Zuerich, Switzerland  
Fax +41 (1) 922 10 33  
e-mail woehlbier@ttp.ch

---

## Editorial Board:

F. Benière (Rennes), C.R.A. Catlow (London), L.T. Chadderton (Melbourne), M. Doyama (Tokyo), P. Kofstad (Oslo), R. Krishnan (Trombay), C. Moynihan (Troy), J. Nowotny (Lucas Heights), W. Schilling (Jülich), J.B. Wagner (Tempe), H. Wollenberger (Berlin)

---

## Advisory Board:

### Australia

D.P. Dunne (Wollongong)  
P.G. McCormick (Nedlands)  
P.L. Rossiter (Clayton)

### Belgium

J.P. Issi (Louvain-la-Neuve)  
J. van Humbeeck (Heverlee-Leuven)

### Canada

H.W. King (Victoria)  
R.W. Smith (Kingston)

### Czech Republic

P. Lukac (Praha)

### Denmark

M.M. Eldrup (Roskilde)

### Finland

P. Kettunen (Tampere)  
R.M. Nieminen (Espoo)

### France

C. Boulesteix (Marseille)  
A. Charlier (Metz)  
L.P. Kubin (Chatillon)  
V. Pontikis (Palaiseau)  
R. Streiff (Marseille)  
D. Stievenard (Lille)

### Germany

G.H. Bauer (Oldenburg)  
K.-H. Bennemann (Berlin)  
D. Bimberg (Berlin)  
E. Bucher (Konstanz)  
H. Foell (Kiel)  
B. Ilttermann (Marburg)  
U. Köster (Dortmund)  
E. Macherauch (Karlsruhe)  
W. Moench (Duisburg)  
H. Mughrabi (Erlangen)  
H. Neuhäuser (Braunschweig)  
J. Pollmann (Münster)  
H.-E. Schaefer (Stuttgart)  
J.-B. Suck (Chemnitz)  
W. Schüle (Frankfurt/Main)  
H. Zabel (Bochum)

### Hungary

D.L. Beke (Debrecen)  
A. Roos (Miskolc)

### India

D.C. Agrawal (Kanpur)  
H.D. Banerjee (Kharagpur)  
A.K. Bhatnagar (Hyderabad)  
A.H. Chokshi (Bangalore)  
P. C. Jain (Delhi)  
P.C. Mathur (New Delhi)  
D. Pandey (Varanasi)  
I.K. Varma (New Delhi)

### Ireland

M. Buggy (Limerick)

### Israel

A. Voronel (Tel-Aviv)

### Italy

G. Artioli (Modena)  
F. Belluci (Naples)  
E. Bonetti (Bologna)  
R. Cantelli (Roma)  
E. Evangelista (Ancona)  
M. Magini (Roma)

### Japan

M. Miki (Himeji)  
Y. Murakami (Fukuoka-shi)  
S. Nitta (Gifu)  
T. Shimizu (Kanazawa-shi)  
P.H. Shingu (Kyoto)  
H. Tamaki (Niigata)  
K. Yokogawa (Kure-shi)

### Korea

Y.-H. Jeong (Pohang)  
D. Kwon (Seoul)  
J.-S. Lee (Ansan)  
K. Yong Lee (Seoul)  
I.-H. Moon (Seoul)

### Pakistan

Z. Iqbal (Islamabad)

### Poland

J. Jedlinski (Krakow)  
L.B. Magalas (Krakow)  
D. Oleszak (Warszawa)  
H. Stachowiak (Wroclaw)

### Portugal

R.P. Martins (Lisboa)

### Romania

M. Petrescu (Bucharest)

### Slovakia

M. Turna (Bratislava)

### South Africa

P. de V. du Plessis (Johannesburg)

### Spain

F. Agullo-Lopez (Madrid)  
E. Calleja (Madrid)  
N. Clavaguera (Barcelona Catalonia)  
C. Conde (Sevilla)  
R. Navarro Linares (Zaragoza)

### Sweden

H.G. Grimmeiss (Lund)

### Switzerland

R. Car (Geneva)

### The Netherlands

C.A.J. Ammerlaan (Amsterdam)  
J.T. de Hosson (Groningen)  
E.J. Mittemeijer (Delft)

### UK

R.J. Cernik (Warrington)  
R.G. Faulkner (Loughborough)  
C.M. Friend (Swindon)  
G.W. Lorimer (Manchester)  
W.J. Plumbridge (Milton)  
B. Ralph (Uxbridge)  
D.K. Ross (Salford)  
B. Wilshire (Swansea)  
A.S. Wronski (Bradford)

### USA

B.L. Adams (Pittsburgh)  
I. Baker (Hanover)  
R.G. Bautista (Reno)  
G.C. Farrington (Philadelphia)  
T.B. Flanagan (Burlington)  
Y.C. Jean (Kansas City)  
T.G. Langdon (Los Angeles)  
R.B. McLellan (Houston)  
A.K. Mukherjee (Davis)  
G.F. Neumark (New York)  
S. Pearton (Gainesville)  
D.N. Seidman (Evanston)  
G.B. Stingfellow (Salt Lake City)  
W. Yen (Athens)

---

*See back inside cover for scope and subscription information*



# REPORT DOCUMENTATION PAGE

Form Approved OMB No. 0704-0188

Public reporting burden for this collection of information is estimated to average 1 hour per response, including the time for reviewing instructions, searching existing data sources, gathering and maintaining the data needed, and completing and reviewing the collection of information. Send comments regarding this burden estimate or any other aspect of this collection of information, including suggestions for reducing this burden to Washington Headquarters Services, Directorate for Information Operations and Reports, 1215 Jefferson Davis Highway, Suite 1204, Arlington, VA 22202-4302, and to the Office of Management and Budget, Paperwork Reduction Project (0704-0188), Washington, DC 20503.

1. AGENCY USE ONLY (Leave blank)		2. REPORT DATE 23 January 1998		3. REPORT TYPE AND DATES COVERED Conference Proceedings	
4. TITLE AND SUBTITLE Nineteenth International Conference of Defects in Semiconductors				5. FUNDING NUMBERS F6170897W0091	
6. AUTHOR(S) Conference Committee					
7. PERFORMING ORGANIZATION NAME(S) AND ADDRESS(ES) Aveiro University 3810 Aveiro Aveiro Portugal				8. PERFORMING ORGANIZATION REPORT NUMBER N/A	
9. SPONSORING/MONITORING AGENCY NAME(S) AND ADDRESS(ES) EOARD PSC 802 BOX 14 FPO 09499-0200				10. SPONSORING/MONITORING AGENCY REPORT NUMBER CSP 97-1035	
11. SUPPLEMENTARY NOTES Three volumes.					
12a. DISTRIBUTION/AVAILABILITY STATEMENT Approved for public release; distribution is unlimited.				12b. DISTRIBUTION CODE A	
13. ABSTRACT (Maximum 200 words)  The Final Proceedings for International Conference of Defects in Semiconductors, 21 July 1997 - 25 July 1997  Emphasis will be given on the properties of wide-bandgap materials, including quantum enhancement of effective band-gaps, semiconductors (silicon and III-V materials), plus radiation effects on detector materials. Topics will also include: GaN, Nanostructures, Large bandgap materials, defects in Epitaxial growth, self-organizing rare earth, metastable defects, pairs and complexes, defect reactions, radiation effects on detector material.					
14. SUBJECT TERMS Semiconductors, Electronic Devices				15. NUMBER OF PAGES 1864	
				16. PRICE CODE N/A	
17. SECURITY CLASSIFICATION OF REPORT UNCLASSIFIED	18. SECURITY CLASSIFICATION OF THIS PAGE UNCLASSIFIED	19. SECURITY CLASSIFICATION OF ABSTRACT UNCLASSIFIED	20. LIMITATION OF ABSTRACT UL		

NSN 7540-01-280-5500

Standard Form 298 (Rev. 2-89)  
Prescribed by ANSI Std. Z39-18  
298-102

**Defects in Semiconductors**  
**ICDS-19**  
Part 3

# **Defects in Semiconductors ICDS-19**

## **Part 3**

**Proceedings of the 19th International Conference  
on Defects in Semiconductors,  
Aveiro, Portugal, July 1997**

*Editors:*

**Gordon Davies and Maria Helena Nazaré**

**TRANS TECH PUBLICATIONS LTD  
Switzerland • Germany • UK • USA**

19980715 013

**Copyright © 1997 Trans Tech Publications Ltd, Switzerland**

ISBN 0-87849-786-2 (3-Vol. Set)

0-87849-787-0 (Part 1)

0-87849-788-9 (Part 2)

0-87849-789-7 (Part 3)

Volumes 258-263 of  
*Materials Science Forum*  
ISSN 0255-5476

***Distributed in the Americas by***

Trans Tech Publications Ltd  
PO Box 699, May Street  
Enfield, New Hampshire 03748  
USA

Phone: (603) 632-7377

Fax: (603) 632-5611

e-mail: [ttp@ttp.net](mailto:ttp@ttp.net)

Web: <http://www.ttp.net>

*and worldwide by*

Trans Tech Publications Ltd  
Brandrain 6  
CH-8707 Uetikon-Zuerich  
Switzerland

Fax: +41 (1) 922 10 33

e-mail: [ttp@ttp.ch](mailto:ttp@ttp.ch)

Web: <http://www.ttp.ch>

Printed in the United Kingdom  
by Hobbs the Printers Ltd,  
Totton, Hampshire SO40 3WX

## Table of Contents

### PART 3

#### Section 17. Aluminium gallium arsenide

##### Decay kinetics of growth-induced alignment of the first neighbor shell of C<sub>As</sub> in Al<sub>x</sub>Ga<sub>1-x</sub>As

J.A. Zhou, C.Y. Song, J.-F. Zheng, M. Stavola, C.R. Abernathy and S.J. Pearton 1293

##### A plausible evidence of the existence of deep acceptors in Si $\delta$ -doped AlGaAs

K. Takarabe, N. Okada, K. Ohmura and H. Ohkura 1299

##### Magneto-optical and magnetic resonance investigations of intrinsic defects in electron-irradiated n-type Al<sub>x</sub>Ga<sub>1-x</sub>As

K.-H. Wietzke, M.V.B. Pinheiro, F.K. Koschnick, K. Krambrock and J.-M. Spaeth 1303

##### Gallium interstitials in GaAs/AlGaAs heterostructures investigated by optically and electrically detected magnetic resonance

T. Wimbauer, M.S. Brandt, M.W. Bayerl, M. Stutzmann, D.M. Hofmann, Y. Mochizuki and M. Mizuta 1309

##### ODMR investigations of Ge acceptors in p-type Al<sub>0.4</sub>Ga<sub>0.6</sub>As

M.V.B. Pinheiro, K. Krambrock, A.S. Chaves, K.-H. Wietzke, F.K. Koschnick and J.-M. Spaeth 1315

#### Section 18. II-VI compound semiconductors

##### Inverted charge states of anion and cation-site vacancies in zinc blende semiconductors: theory. (Invited)

D.J. Chadi 1321

##### Degradation of II-VI laser diodes. (Invited)

K. Nakano and A. Ishibashi 1329

##### Defect characterization of II-VI compound semiconductors using positron lifetime spectroscopy

G. Tessaro and P. Mascher 1335

##### Defect structures in heavily In-doped II-VI semiconductors

V. Ostheimer, T. Filz, J. Hamann, St. Lauer, D. Weber, H. Wolf and Th. Wichert 1341

<b>The role of cation vacancy in compensation of II-VI compounds by fast diffusors - example of Cu in CdS</b>	
U.V. Desnica, I.D. Desnica-Franković, R. Magerle, A. Burchard and M. Deicher	1347
<b>Experimental evidence for the two-electron nature of In-related DX states in CdTe</b>	
C. Skierbiszewski, P. Wisniewski, A. Wilamowski, W. Jantsch and G. Karczewski	1353
<b>Nature of dislocation-related deep levels in CdS</b>	
A.A. Istratov and O.F. Vyvenko	1359
<b>NMR study of carrier states and trapping complexes in the transparent conductor ZnO: M<sup>III</sup></b>	
W.W. Warren Jr, N. Roberts, R.-P. Wang and W. Sleight	1365
<b>Cathodoluminescence study on the hydrogenation of ZnO luminescence</b>	
T. Sekiguchi, N. Ohashi and Y. Terada	1371
<b>Observation of Frenkel pairs on both sublattices of electron irradiated ZnSe</b>	
H. Zillgen and P. Ehrhart	1377
<b>Interface defects and their effect on the electrical properties of ZnSe/GaAs heterojunctions grown by MBE</b>	
D. Seghier, I.S. Hauksson, H.P. Gislason, K.A. Prior and B.C. Cavenett	1383
<b>Donor doping of ZnSe: lattice location and annealing behaviour of implanted boron</b>	
B. Ittermann, G. Welker, F. Kroll, F. Mai, K. Marbach, H. Ackermann, H.-J. Stöckmann, E. Oldekop and W.-D. Zeitz	1389
<b>Determination of the lattice site of nitrogen after implantation into ZnSe</b>	
K. Marbach, B. Ittermann, M. Füllgrabe, M. Heemeier, F. Kroll, F. Mai, P. Meier, D. Peters, H. Thieß, H. Ackermann, H.-J. Stöckmann, W.-D. Zeitz, H. Wensch, D. Hommel and G. Landwehr	1395
<b>Charge-transfer at Ti ions in ZnTe</b>	
H.R. Selber, P. Peka, H.J. Schulz, U.W. Pohl, J. Kreissl, B. Kaufmann and A. Dörnen	1401
<b>Bistable centers in CdMnTeSe: In crystals studied by light-induced gratings</b>	
B. Koziarska-Glinka, M. Ponder, A. Suchocki, T. Wojtowicz and I. Miotkowski	1407
<b>Deep levels in Cd<sub>0.99</sub>Mn<sub>0.01</sub>Te: Ga</b>	
J. Szatkowski, E. Placzek-Popko, K. Sieranski, P. Fijalkowski, A. Hajdusianek, and B. Bieg	1413

---

**Vacancy-type defects in electron and proton irradiated II-VI compounds**

S. Brunner, W. Puff, P. Mascher, A.G. Balogh and H. Baumann 1419

**UV enhanced and solar blind photodetectors based on large-band-gap materials**

A. Malik and R. Martins 1425

**Section 19. Cadmium fluoride****Lattice relaxation of In donors in CdF<sub>2</sub>**

A. Suchocki, J. Rauluszkiewicz, J.M. Langer, B. Koziarska-Glinka 1431

**Shallow electron centres in CdF<sub>2</sub>:M<sup>3+</sup> and silver halides**

C.-R. Fu and K.S. Song 1437

**EPR investigation of metastable donor states in CdF<sub>2</sub>: In, Ga**

Z. Wilamowski, J. Dmochowski and W. Jantsch 1443

**Photoinduced magnetism in CdF<sub>2</sub> with bistable donors: the clue for negative U ?**

J.M. Langer, A. Suchocki, R. Szymczak and M. Baran 1449

**Section 20. Chalcopyrites and other host lattices****Evidence of metastable deep acceptors in AgGaS<sub>2</sub> from time-resolved emission**

I.-H. Choi and P.Y. Yu 1455

**A positron lifetime study of lattice defects in chalcopyrite semiconductors**

M.S. Al-Kotb, W. Puff and G. Bischof 1461

**Magneto-optical characterisation of CuIn(Ga)Se<sub>2</sub>**

B.K. Meyer, Mt. Wagner, I. Dirnstorfer, D.M. Hofmann and F. Karg 1467

**Defects spectroscopy in  $\beta$ -Ga<sub>2</sub>O<sub>3</sub>**

B.K. Meyer, U. Leib, A. Hofstaetter, C. Krummel and D. Kohl 1473

**Bistability of oxygen vacancy in silicon dioxide**

A. Oshiyama 1479

**Section 21. Erbium****Energy transfer processes at erbium ions in silicon**

J. Michel, J. Palm, T. Chen, X. Duan, E. Oullette, S.H. Ahn, S.F. Nelson and L.C. Kimerling 1485

<b>Energy transfer rate between erbium 4f shell and Si host</b>	
A. Taguchi, K. Takahei, M. Matsuoka and S. Tohno	1491
<b>Photoluminescence study of erbium in silicon with a free-electron laser</b>	
I. Tsimperidis, T. Gregorkiewicz, H.P.Th. Bekman, C.J.G.M. Langerak and C.A.J. Ammerlaan	1497
<b>Direct evidence for stability of tetrahedral interstitial Er in Si up to 900 °C</b>	
U. Wahl, J.G. Correia, G. Langouche, J.G. Marques, A. Vantomme and the ISOLDE collaboration	1503
<b>Photo- and electro-luminescence of erbium-doped silicon</b>	
S. Lanzerstorfer, M. Stepikhova, J. Hartung, C. Skierbiszewski and W. Jantsch	1509
<b>Donor centers in Er-implanted silicon</b>	
V.V. Emtsev, B.A. Andreev, D.S. Poloskin, N.A. Sobolev and E.I. Shek	1515
<b>Structural defects and photoluminescence in dislocation-rich erbium-doped silicon</b>	
V.I. Vdovin, N.A. Sobolev, E.M. Emel'yov, E.I. Shek and T.G. Yugova	1521
<b>Influence of fabrication conditions on properties of Si:Er light-emitting structures</b>	
N.A. Sobolev, A.M. Emel'yanov, Yu.A. Nikolaev, K.F. Shtel'makh, Yu.A. Kudryavstev, V.I. Sakharov, I.T. Serenkov, M.I. Makovijchuk and E.O. Parshin	1527
<b>High temperature luminescence due to Er in porous Si</b>	
M. Strepikhova, W. Jantsch, G. Kosher, M. Schoisswohl, J.P. Cantin and H.J. von Bardeleben	1533
<b>Electron paramagnetic resonance of erbium in bulk silicon carbide crystals</b>	
P.G. Baranov, I.V. Ilyin and E.N. Mokhov	1539
<b>1.54 <math>\mu\text{m}</math> photoluminescence of Er and Er + O implanted 6H SiC</b>	
A. Kozanecki, W. Jantsch, S. Lanzerstorfer, B.J. Sealy and S. Jackson	1545
<b>Erbium-related defects in gallium arsenide. (Invited)</b>	
A.R. Peaker, F. Coppinger, H. Efeoglu, J.H. Evans-Freeman, D.K. Maude, J.-C. Portal, P. Rutter, K.E. Sionger, A. Scholes and A.C. Wright	1551
<b>Electron spin resonance of Er-oxygen complexes in GaAs</b>	
T. Ishiyama, E. Katajama, K. Takahei, A. Taguchi and K. Murakami	1559
<b>Er centers in GaAs: Er, O studied by optical spectroscopy under hydrostatic pressure</b>	
R.A. Hogg, A. Taguchi and K. Takahei	1565



<b>EXAFS measurement on local structure around erbium atoms doped in GaAs with oxygen co-doping</b>	
M. Tabuchi, H. Ofuchi, T. Kubo, K. Takahei and Y. Takeda	1571
<b>Luminescence and annealing studies of Er-implanted GaN with and without oxygen co-doping</b>	
E. Silkowski, Y.K. Yeo, R.L. Hengehold and L.R. Everitt	1577
<b>Er-luminescence in MBE-grown AlGaAs</b>	
O.B. Gusev, E.K. Lindmark, J.P. Prineas, M.S. Bresler, G. Khitrova, H.M. Gibbs, I.N. Yassievich, B.P. Zakharchenya and V.F. Masterov	1583
<b>Crystal-field transitions of Nd<sup>3+</sup> and Er<sup>3+</sup> in Perovskite-type crystals</b>	
M. Dietrich, P. Thurian, I. Loa, S. Gronemeyer, A.P. Litvinchuk and C. Thomsen	1589
<b>Excitation and de-excitation of erbium ions in semiconductor matrices</b>	
I.N. Yassievich, M.S. Bresler, O.B. Gusev and G. Khitrova	1595
<b>Mechanism of generation of f-f radiation in semiconductor heterostructures</b>	
G.G. Zegrya and V.F. Masterov	1601
 <b>Section 22. Low dimensional structures</b>	
<b>Infrared induced emission from silicon quantum wires</b>	
N.T. Bagraev, E.I. Chaikina, W. Gelhoff, L.E. Klyachkin, I.I. Markov and A.M. Malyarenko	1607
<b>Acceptor states in boron doped SiGe quantum wells</b>	
K. Schmalz, M.S. Kagan, I.V. Altukhov, K.A. Korolev, D.V. Orlov, V.P. Sinis, S.G. Tomas, K.L. Wang and I.N. Yassievich	1613
<b>Coulomb interaction between carriers localized in InAs/GaAs quantum dots and on point defects</b>	
M.M. Sobolev, A.R. Kovsh, V.M. Ustinov, A.Yu. Egorov, A.E. Zhukov, M.V. Maximov and N.N. Ledentsov	1619
<b>Influence of the erbium doping on structure and optical properties of the InGaAs/GaAs superlattices</b>	
L.G. Gerchikov, V.F. Masterov, T.R. Stepanova, H.M. Gibbs, G. Khitrova and N.N. Faleev	1625
<b>Defect formation during laser induced intermixing of GaAs/AlGaAs multiple-quantum-well structures</b>	
N.H. Ky	1631
<b>Localized epitaxy for vertical cavity surface emitting laser applications</b>	
M. Erdtmann, S. Kim and M. Razeghi	1637

<b>The long wavelength luminescence observation from the self-organised InGaAs quantum dots grown on (100) GaAs substrate by metalorganic chemical vapor deposition</b>	
K.S. Kim, M. Erdtmann and M. Razeghi	1643
<b>Deep hole traps in Be-doped Al<sub>0.5</sub>Ga<sub>0.5</sub>As MBE layers</b>	
J. Szatkowski, E. Placzek-Popko, K. Sieranski and O.P. Hansen	1653
<b>Nanotubes and pinholes in GaN and their formation mechanism</b>	
Z. Liliental-Weber, Y. Chen, S. Ruminov and J. Washburn	1659
<b>Defect related recombination processes in low-dimensional structures of ZnCdSe/ZnSe, CdTe/CdMnTe and GaAs/AlGaAs</b>	
M. Godlewski, D. Hommel, T. Wojtowicz, G. Karczewski, J. Kossut, K. Reginski, M. Bugajski, J.P. Bergman and B. Monemar	1665
<b>Study of hole traps in p-type ZnSe and ZnSSe epilayers by DLTS and admittance spectroscopy</b>	
I.J. Hauksson, D. Seghier, H.P. Gislason, K.A. Prior and B.C. Cavenett	1671
<b>Auger type nonradiative recombination processes in bulk and quantum well structures of II-VI semiconductors containing transition metal ions</b>	
M. Godlewski, M. Surma, A.J. Zakrewski, T. Wojtowicz, G. Karczewski, J. Kossut, J.P. Bergman and B. Monemar	1677
<b>Spin-dependent processes in self-assembly impurity quantum wires</b>	
N.T. Bagraev, W. Gelhoff, L.E. Klyachkin, A.M. Malyarenko and A. Näser	1683
<b>Comparison between as-grown and annealed quantum dots morphology</b>	
J.C. Ferrer, F. Peiró, A. Cornet, J.R. Morante, T. Utzmeier, G. Armelles and F. Briones	1689
<b>EPR studies of magnetic superlattices</b>	
Z. Wilamowski, V. Svrcek, G. Springhoz and W. Jantsch	1695
<b>Er diffusion and Er-induced Ga-Al interdiffusion in GaAs/AlGaAs quantum structures</b>	
M.S. Bresler, B.Ya. Ber, O.B. Gusev, E.K. Lindmark, J.P. Prineas, H.M. Gibbs, G. Khitrova, V.F. Masterov, I.N. Yassievich and B.P. Zakharchenya	1701
<b>Ground and excited states of D- centres in semiconductor quantum dots</b>	
B. Szafran, J. Adamowski and B. Stébé	1707

---

## Section 23. Surfaces and interfaces

- Electron spin resonance features of the Pb1 interface defect in thermal (100)Si / SiO<sub>2</sub>**  
A. Stesmans and V.V. Afanas'ev 1713
- Silicon surface defects: the roles of passivation and surface contamination**  
A.J. Reddy, T.A. Burr, J.K. Chan, G.J. Norga, J. Michel and L.C. Kimerling 1719
- Heat-treatment induced modifications of porous silicon**  
S. Dannefaer, C. Wiebe and D. Kerr 1725
- Luminescence due to electron-hole condensation in silicon-on-insulator and its application to defect and interface characterization**  
M.Tajima, S. Ibuka and M. Warashina 1731
- Deep electronic states at the inverted AlAs/GaAs interface under different growth modes**  
P. Krispin, R. Hey, H. Kostial and K.H. Ploog 1737
- TEM-study of Frank partial dislocations in ZnSe/GaAs (001) caused by substrate preparation**  
H. Preis, T. Frey, T. Reisinger and W. Gebhardt 1743
- Defect formation and electronic transport at AlGaIn/GaN interfaces**  
L. Hsu, W. Walukiewicz and E.E. Haller 1749
- Characterization of the relaxation by misfit dislocations confined at the interface of GaN/Al<sub>2</sub>O<sub>3</sub>(0001) studied by TEM**  
S. Kaiser, H. Preis, O. Ambacher and W. Gebhardt 1755

## Section 24. Diffusion

- Formation kinetics of the Al-related shallow thermal donors: a probe for oxygen diffusion in silicon**  
P. Kaczor, L. Dobaczewski, T. Gregorkiewicz and C.A.J. Ammerlaan 1761
- Diffusion and precipitation of oxygen in silicon doped with germanium**  
L.I. Khirunenko, V.I. Shakhovtsov and V.V. Shumov 1767
- The influence of isovalent doping on diffusion of interstitial oxygen in silicon**  
L.I. Khirunenko, Yu.V. Pomozev, V.I. Shakhovtsov and V.V. Shumov 1773
- EPR evidence of hydrogen-enhanced diffusion of aluminum in silicon**  
Yu.V. Gorelkinskii, B.N. Mukashev and Kh.A. Abdullin 1777
- Segregation of gold at dislocations confirmed by gold diffusion into highly dislocated silicon**  
H. Bracht, A. Rodriguez Schachtrup and I. Yonenaga 1783

---

<b>Annealing of low-temperature substitutional gold in silicon: ring-diffusion of substitutional gold in silicon</b>	
M. Morooka	1789
<b>Rate limiting mechanism of transition metal gettering in multicrystalline silicon</b>	
S.A. McHugo, A.C. Thompson, M. Imaizumi, H. Hieslmair and E.R. Weber	1795
<b>Intrinsic point defect engineering in silicon high-voltage power device technology</b>	
N.A. Sobolev	1801
<b>Influence of the dislocation loops on the anomalous diffusion of Fe implanted into InP</b>	
C. Frigeri, A. Carnera, B. Fraboni, A. Gasparotto, F. Priolo, A. Camporese and G. Rossetto	1807
<b>Lithium induced vacancy formation and its effect on the diffusivity of lithium in gallium arsenide. (Invited)</b>	
H.P. Gislason, K. Leosson, H. Svavarsson, K. Saarinen and A. Mari	1813
<b>Ab-initio investigations on diffusion of halogen atoms in GaAs</b>	
T. Ohno, T. Sasaki and A. Taguchi	1821
<b>Low temperature intrinsic diffusion coefficient of lithium in GaAs</b>	
K. Leosson and H.P. Gislason	1827
<b>Low temperature impurity diffusion into large-band-gap semiconductors</b>	
N.T. Bagraev, A.A. Gippius, L.E. Klyachkin and A.M. Malyarenko	1833
<b>Background doping effects on Zn diffusion in GaAs/AlGaAs multiple-quantum-well structures</b>	
N.H. Ky	1839
<b>Author Index</b>	1845
<b>Keyword Index</b>	1859

## DECAY KINETICS OF GROWTH-INDUCED ALIGNMENT OF THE FIRST NEIGHBOR SHELL OF $C_{As}$ IN $Al_xGa_{1-x}As$

J. Anna Zhou<sup>1</sup>, C.Y. Song<sup>1,\*</sup>, J.-F. Zheng<sup>1</sup>, Michael Stavola<sup>1</sup>, C.R. Abernathy<sup>2</sup> and S.J. Pearton<sup>2</sup>

<sup>1</sup>Department of Physics, Lehigh University, Bethlehem, PA 18015, USA

<sup>2</sup>Department of Materials Science, University of Florida, Gainesville, FL 32611, USA

**Keywords:** carbon in AlGaAs, growth-induced alignment, carbon diffusion,  $C_{As}$  vibrational modes

### Abstract

It has been recently discovered that the first neighbor shell of the  $C_{As}$  acceptor in  $Al_xGa_{1-x}As$  can be aligned in samples that have been grown by metalorganic molecular beam epitaxy. This alignment gives rise to a strong polarization dependence of the vibrational absorption bands assigned to  $C_{As}$  and also to the  $C_{As}-H$  complexes that are formed when the  $C_{As}$  is passivated by H. Here, results are presented for the decay kinetics of the growth-induced alignment upon thermal annealing. The decay kinetics provide a novel source of information about the diffusion of  $C_{As}$  in  $Al_xGa_{1-x}As$  and permit values of the diffusion coefficient to be determined that are too small to be measured by mass-transport methods.

### Introduction

Carbon occupies an As sublattice site in epitaxial GaAs and  $Al_xGa_{1-x}As$  alloys where it acts as a shallow acceptor. It can be incorporated at concentrations up to  $10^{21} \text{ cm}^{-3}$  from the metalorganic precursors or dopant gases used during growth by metalorganic molecular beam epitaxy (MOMBE) or metalorganic chemical vapor deposition (MOCVD).[1] An attractive feature of  $C_{As}$  as a p-type dopant is the small value of its diffusion coefficient.[2-5] We have recently discovered that the first neighbor shell of  $C_{As}$  can be aligned following growth by MOMBE.[6] In this paper, measurements of the annealing kinetics of this growth-induced alignment are reported. The annealing kinetics can be related to the motion of  $C_{As}$  and provide a means to determine the diffusion coefficient for the small values that occur at low temperatures (500°C to 625°C).

Our probe of the alignment of the first neighbor shell of  $C_{As}$  is the polarization dependence of the vibrational absorption bands due to  $C_{As}$  and  $C_{As}-H$  when the carbon is passivated by H. The vibrational mode of  $C_{As}$  in GaAs at  $582.8 \text{ cm}^{-1}$  has been studied extensively.[7] Isotopic fine structure due to  $^{69}\text{Ga}$  and  $^{71}\text{Ga}$  nearest neighbors has been observed and confirms the mode assignment and site location.[7,8] The situation in  $Al_xGa_{1-x}As$  has been more complicated. Ono and Furuhashi [9] observed seven vibrational bands in the region 570 to  $650 \text{ cm}^{-1}$  that they attributed to the vibrations of  $C_{As}$ . These bands are due to carbon atoms with different possible combinations of Ga and Al first neighbors.[6,10,11] The complicated spectrum of carbon in the alloy has only recently been assigned to the modes of  $C_{As}$  with specific first neighbor configurations.[6]

The H-stretching vibrations of  $C_{As}$  passivated by hydrogen have been used as a probe of  $C_{As}$  acceptors with different combinations of Ga and Al neighbors by Pritchard *et al.*[11] Table I lists the absorption bands attributed to the H-stretching modes of  $C_{As}-H$  complexes in  $Al_xGa_{1-x}As$  epilayers. Pritchard *et al.* [11] noted that the four bands with the highest frequencies have approximately equal separations but that there is then a much larger frequency shift to the fifth band at  $2558 \text{ cm}^{-1}$ . Further, local-density-functional calculations show that the C-Al bond is stronger and shorter than the C-Ga bond.[11,12] Accordingly, Pritchard *et al.* [11] proposed that hydrogen atoms would be

incorporated preferentially between C and Ga atoms, and that hydrogen atoms would only interrupt  $C_{As}$ -Al bonds for  $C_{As}$  atoms with four Al neighbors. Thus the four bands with nearly the same separations in frequency correspond to the  $C_{As}$ -H complexes for which the  $C_{As}$  atom has one or more Ga nearest neighbors. A larger shift to the fifth band at lowest frequency ( $2558\text{ cm}^{-1}$ ) occurs when the H interrupts a  $C_{As}$ -Al bond for configurations with four Al nearest neighbors. The assignments made to first neighbor shell configurations are also given in Table I.

*Table I. The frequencies of  $C_{As}$ -H complexes in  $Al_xGa_{1-x}As$  with different first neighbor shell configurations,  $Al_nGa_{4-n}$ . The successive shifts in the vibrational frequency,  $\Delta\omega$ , as Al atoms are added to the first neighbor shell and the configuration are given. Data and assignments are from Pritchard et al.[11]*

$\omega$ ( $\text{cm}^{-1}$ )	$\Delta\omega$ ( $\text{cm}^{-1}$ )	configuration
2636	0	$Ga_3C-H-Ga$
2626	-10	$AlGa_2C-H-Ga$
2618	-8	$Al_2GaC-H-Ga$
2608	-10	$Al_3C-H-Ga$
2558	-50	$Al_3C-H-Al$

Defect alignments are usually produced by an externally applied stress and have often been used to determine the symmetry and reorientation kinetics of a defect center.[13] Here, a growth-induced alignment will be used similarly to determine defect properties. It has been found previously that a few low symmetry defect complexes are aligned following epitaxial crystal growth.[14-19] The growth-induced alignment to be described here is similar to previous work [17-19] if the  $C_{As}$  impurity in  $Al_xGa_{1-x}As$  and its first neighbor shell are thought of as a low symmetry defect complex. An explanation of the alignment of a defect following epitaxial growth was first proposed by Skolnick *et al.* who had studied a family of luminescence bands observed in epitaxial GaAs grown by MBE.[14] The emitted light was found to be polarized along a particular  $\langle 110 \rangle$  direction for as-grown samples. This was a surprising result because the different  $\langle 110 \rangle$  directions are crystallographically equivalent in the bulk of the crystal. Skolnick *et al.* noted that the equivalence of the  $\langle 110 \rangle$  directions is broken at the growth surface.[14] Consider a (001) As-terminated surface. All of the As-Ga bonds below the surface are along a particular  $\langle 110 \rangle$  direction, say the  $[1\bar{1}0]$ . All of the As-Ga bonds that will be formed above the As terminated surface will be along the perpendicular  $[110]$  direction. This inequivalence of the  $\langle 110 \rangle$  directions is reinforced by reconstruction of the surface and by step growth. To explain the growth-induced alignment it was proposed that a low symmetry defect becomes aligned at the growth surface where the  $\langle 110 \rangle$  directions are inequivalent and that its alignment is maintained as the defect is incorporated into the growing epitaxial layer. We note that the stresses near the surface of the growing epitaxial layer that arise from surface reconstruction might cause the alignment of the  $C_{As}$  atom's first neighbor shell that we have observed because the  $C_{As}$ -Al bonds are shorter than the  $C_{As}$ -Ga bonds.

## Experiment

Carbon-doped  $Al_xGa_{1-x}As$  epitaxial layers were grown by MOMBE on semi-insulating GaAs substrates in a Varian Gas Source Modular Gen II. The Ga and As source gases were trimethylgallium (TMG) and arsine, and the Al source gas was either triethylaluminum (TEAL) or trimethylamine alane (TMAAL). The substrate growth temperature was  $500^\circ\text{C}$  and the carbon was introduced by the TMG. The acceptor concentration was determined from Hall measurements.

Infrared absorption spectra were measured with a Bomem DA3.16 Fourier transform spectrometer operated at a resolution of  $2\text{ cm}^{-1}$ . The spectrometer was equipped with an InSb detector for the spectral region between  $1800$  and  $3200\text{ cm}^{-1}$  and with a Si composite bolometer for

the region between 400 and 750  $\text{cm}^{-1}$ . The incident light was polarized with a wire-grid polarizer. The absorption measurements were made with the samples cooled to liquid He temperature.

To study the decay of the growth-induced alignment, samples were placed face down on a GaAs wafer to prevent As loss and annealed in flowing  $\text{N}_2$ . To introduce hydrogen into samples, they were annealed for 1 hr at 440°C in a sealed ampoule that contained 2/3 atm of  $\text{H}_2$  gas. To insure that the anneals in  $\text{H}_2$  did not affect the defect alignment, a sample was annealed at 450°C in  $\text{H}_2$  for 8 hr as a test. Infrared measurements showed that the growth-induced alignment had not decayed during this anneal in  $\text{H}_2$ .

### Annealing kinetics and the diffusion of $\text{C}_{\text{As}}$

The hydrogen-stretching spectra, measured with light polarized along  $[110]$  and  $[1\bar{1}0]$  directions, are shown in Fig. 1 for a carbon-doped  $\text{Al}_{0.16}\text{Ga}_{0.84}\text{As}$  sample that had been annealed in  $\text{H}_2$  to produce  $\text{C}_{\text{As}}\text{-H}$  complexes. The 2628, 2618, and 2610  $\text{cm}^{-1}$  bands that are observed have been assigned to the  $\text{AlGa}_2\text{C}_{\text{As}}\text{-H-Ga}$ ,  $\text{Al}_2\text{GaC}_{\text{As}}\text{-H-Ga}$ , and  $\text{Al}_3\text{C}_{\text{As}}\text{-H-Ga}$  complexes, respectively.[11] The intensities of the H-stretching bands are polarization dependent. The vibrational bands near 600  $\text{cm}^{-1}$  due to  $\text{C}_{\text{As}}$  have also been studied and show a corresponding polarization dependence.[6,20] (We have found that roughly 5 to 10% of the C is passivated in as-grown  $\text{Al}_x\text{Ga}_{1-x}\text{As}$  samples and that 25 to 30% is passivated in  $\text{H}_2$  treated samples. Thus, the spectra of both  $\text{C}_{\text{As}}$  and  $\text{C}_{\text{As}}\text{-H}$  can be measured for the same sample.) A convenient measure of the polarization dependence of an absorption band is the dichroism  $\mathcal{D}$  defined as,

$$\mathcal{D} = \frac{\alpha_{110} - \alpha_{1\bar{1}0}}{\alpha_{110} + \alpha_{1\bar{1}0}}, \quad (1)$$

where the  $\alpha$ 's are the absorption coefficients for the polarization directions given by the subscripts.

The polarization dependence of the vibrational absorption is explained by  $\text{C}_{\text{As}}$  and  $\text{C}_{\text{As}}\text{-H}$  complexes with first neighbor shells that have been aligned by the epitaxial growth process as is shown in Fig. 2 for the first neighbor configuration with two Al atoms and two Ga atoms. The Ga first neighbors lie preferentially in a specific  $\{110\}$  plane in the as-grown layer and the Al neighbors lie in a perpendicular  $\{110\}$  plane. When the  $\text{C}_{\text{As}}$  is passivated by H, the  $\text{C}_{\text{As}}\text{-H}$  complexes are also aligned because the H preferentially interrupts the  $\text{C}_{\text{As}}\text{-Ga}$  bonds. Here we use the  $\text{C}_{\text{As}}\text{-H}$  modes as a

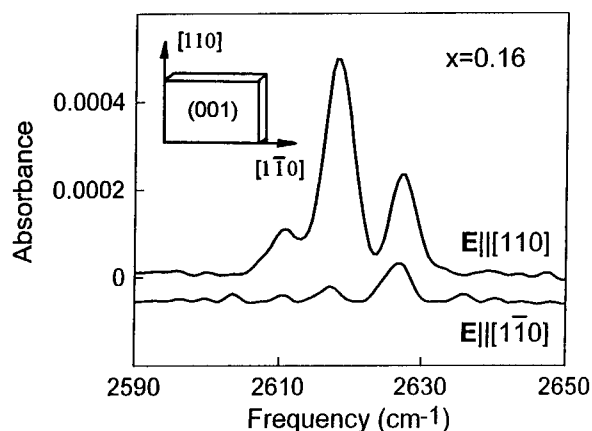


Fig. 1. (a) H-stretching spectra, measured with light polarized along the  $[110]$  and  $[1\bar{1}0]$  directions in the  $(001)$  growth plane for an  $\text{Al}_{0.16}\text{Ga}_{0.84}\text{As}$  epilayer with  $N_A = 1.2 \times 10^{19} \text{ cm}^{-3}$ . The sample was annealed at 450 °C in  $\text{H}_2$  for 60 min to introduce hydrogen. The inset shows the  $(001)$  surface and the polarization directions for the incident light.

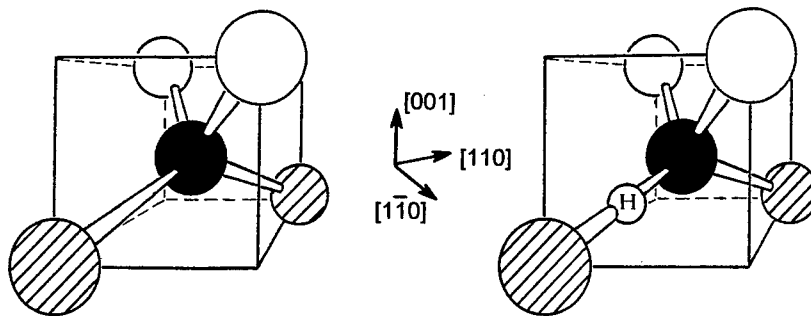


Fig. 2. An aligned  $\text{Al}_2\text{Ga}_2\text{C}_{\text{As}}$  complex (left). The Ga atoms (shaded) lie along the  $[110]$  direction. The Al atoms (unshaded) lie along the  $[1\bar{1}0]$  direction. The  $\text{C}_{\text{As}}$  atom is shown black. When the  $\text{C}_{\text{As}}$  is passivated by hydrogen, the H interrupts a  $\text{C}_{\text{As}}\text{-Ga}$  bond, giving rise to an aligned  $\text{C}_{\text{As}}\text{-H}$  complex (right).

probe of the alignment of the first neighbor shell of  $\text{C}_{\text{As}}$  in our annealing experiments. The vibrational modes of  $\text{C}_{\text{As}}$  give similar results for the annealing of the growth-induced alignment.

The results of isothermal annealing experiments for the dichroism observed for the  $2618\text{ cm}^{-1}$  band assigned to the  $\text{Al}_2\text{Ga}_2\text{C}_{\text{As}}\text{-H}$  complex are shown in Fig. 3. For the annealing temperatures and times used, the concentrations of  $\text{Al}_n\text{Ga}_{4-n}\text{C}_{\text{As}}$  centers are decreased by about 10% while the dichroisms are completely eliminated. The polarization dependence of all of the hydrogen vibrational bands observed in this sample show similar annealing behavior.[20] The data for each temperature gives a time constant for the decay of the growth-induced alignment. A simple model is used to relate this time constant for the decay of alignment to the diffusion coefficient of carbon. It is assumed that the atomic motion by which the alignment is lost is a carbon jump from one As site to another. We consider a carbon atom with a single Al neighbor to which we assume it remains bound during the jump process. For this case, it is straightforward to show that the dichroism obeys the following relationship:

$$\mathcal{D} = \mathcal{D}_0 \exp[-4t/\tau] \quad (2a)$$

where,

$$\tau = \tau_0 \exp(E_A/kT). \quad (2b)$$

Here  $\tau$  is the time constant for a jump from a specific As site adjacent to the Al to another. This simple model explains the loss of alignment that occurs upon annealing while conserving the concentrations of  $\text{Al}_n\text{Ga}_{4-n}\text{C}_{\text{As}}$  defects. If the jump of the carbon from one As site adjacent to the Al to another is taken to be approximately a diffusion jump, then the diffusion coefficient for  $\text{C}_{\text{As}}$  can be written as,

$$D = a^2/\tau, \quad (3)$$

where  $a = 4.00\text{ \AA}$  is the jump distance between neighboring As-sites. It has been proposed that the carbon diffusion jump occurs by an  $\text{As}_i$  kick-out mechanism.[5,21] However, it is not necessary to specify the mechanism for the jump to estimate the diffusion coefficient from our results; only the time constant and distance for the  $\text{C}_{\text{As}}$  jump are required.



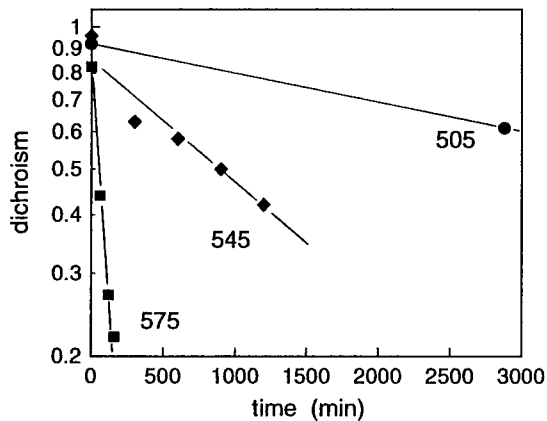


Fig. 3. Isothermal annealing data for the dichroism associated with the  $2618\text{ cm}^{-1}$  band assigned to the  $\text{Al}_2\text{Ga}_2\text{C}_{\text{As}}\text{-H}$  complex. In these experiments, the sample is heat-treated in  $\text{N}_2$  at the temperature shown ( $^{\circ}\text{C}$ ) to eliminate the alignment. Subsequently, hydrogen is added at a lower temperature so that the  $\text{C}_{\text{As}}\text{-H}$  complexes can be used as a probe of the alignment that remains following the anneal in  $\text{N}_2$ .

Values of the diffusion coefficient, determined with Eq. (3) from the annealing data shown in Fig. 3 and from an isochronal annealing experiment performed at  $625^{\circ}\text{C}$  [20], are plotted in Fig. 4. Values of the  $\text{C}_{\text{As}}$  diffusion coefficient determined previously for As-rich conditions by Chiu *et al.* [4] and by You *et al.* [5] are also shown. (Ga-rich conditions give rise to slower  $\text{C}_{\text{As}}$  diffusion.[5]) The values of  $D$  determined here and the values determined previously at higher temperatures are fit well by a single line. This result justifies our initial assumption that the loss of the growth-induced alignment is due to a diffusion jump of the  $\text{C}_{\text{As}}$ . It should also be noted that the diffusion of Al, which might also cause the alignment to decay, has been determined previously [5,22] and is slower than would be consistent with the rate of alignment loss we have measured. The fit to the data shown in Fig. 4 corresponds to the following relationship for the diffusion coefficient of  $\text{C}_{\text{As}}$ :

$$D = 2.6 \times 10^{-3} \exp(-2.87 \text{ eV} / kT) \text{ cm}^2/\text{s}. \quad (4)$$

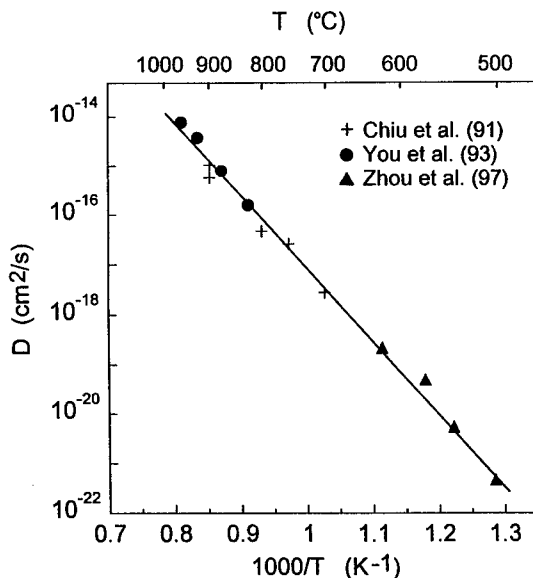


Fig. 4. Diffusion coefficient for  $\text{C}_{\text{As}}$  in  $\text{AlGaAs}$  vs  $T^{-1}$ .

This relationship is in good agreement with previous determinations made from the high temperature data shown in Fig. 4 that gave activation energies of 2.8 eV (ref. 4) and 3.13 eV (ref. 5) for the diffusion coefficient of  $C_{As}$  measured under As-rich conditions.

### Acknowledgements

This work performed at Lehigh University was supported by the U.S. Navy Office of Naval Research under Contract Nos. N00014-94-1-0117 and N00014-93-1-0857.

### References

- \* Permanent address: Institute of Semiconductors, Chinese Academy of Sciences, Beijing 100083, China
- 1. C.R. Abernathy, *State-of-the-Art Program on Compound Semiconductors XXIV*, edited by F. Ren, S.J. Pearton, S.N.G. Chu, R.J. Shul, W. Pletschen and W. Kamijo (Electrochem. Soc., Pennington, 1996), v. **96-2**, p. 1.
- 2. B.T. Cunningham, L.J. Guido, J.E. Baker, J.S. Major, N. Holonyak, and G.E. Stillman, *Appl. Phys. Lett.* **55**, 687 (1989).
- 3. G.E. Höfler, J.N. Baillargeon, K.C. Hsieh, and K.Y. Cheng, *Appl. Phys. Lett.* **60**, 1990 (1992).
- 4. T.H. Chiu, J.E. Cunningham, J.A. Ditzenberger, W.Y. Jan, and S.N.G. Chu, *J. Crystal Growth* **111**, 274 (1991).
- 5. H.M. You, T.Y. Tan, U.M. Gösele, S.-T. Lee, G.E. Höfler, K.C. Hsieh, and N. Holonyak, *J. Appl. Phys.* **74**, 2450 (1993).
- 6. J.-F. Zheng, M. Stavola, C.R. Abernathy, and S.J. Pearton, *Mat. Res. Soc. Symp. Proc.* **442**, 387 (1997).
- 7. R.C. Newman, *Imperfections in III/V Materials*, edited by E. Weber (Academic, Boston, 1993), p. 117.
- 8. W. M. Theis, K.K. Bajaj, C.W. Litton, and W. G. Spitzer, *Appl. Phys. Lett.* **41**, 70 (1982).
- 9. H. Ono and N. Furuhashi, *Appl. Phys. Lett.* **59**, 1881 (1991).
- 10. M.J.L. Sangster, R.C. Newman, G.A. Gledhill, and S.B. Upadhyay, *Semicond. Sci. Technol.* **7**, 1295 (1992).
- 11. R.E. Pritchard, R.C. Newman, J. Wagner, F. Fuchs, R. Jones, S. Öberg, *Phys. Rev. B* **50**, 10628 (1994).
- 12. R. Jones and S. Öberg, *Phys. Rev. B* **49**, 5306 (1994).
- 13. G.D. Watkins, *Early Stages of Oxygen Precipitation in Silicon*, edited by R. Jones (Kluwer, Dordrecht, 1996), p. 1.
- 14. M.S. Skolnick, T.D. Harris, C.W. Tu, T.M. Brennan, and M.D. Sturge, *Appl. Phys. Lett.* **46**, 427 (1985).
- 15. M.S. Skolnick, D.P. Halliday, and C.W. Tu, *Phys. Rev. B* **38**, 4165 (1988), and references therein.
- 16. S. Charbonneau and M.L.W. Thewalt, *Phys. Rev. B* **41**, 8221 (1990), and references therein.
- 17. Y. Cheng, M. Stavola, C.R. Abernathy, S.J. Pearton, and W.S. Hobson, *Phys. Rev. B* **49**, 2469 (1994).
- 18. B.R. Davidson, R.C. Newman, T. Kaneko, and O. Naji, *Phys. Rev. B* **50**, 12250 (1994).
- 19. B.R. Davidson, R.C. Newman, and K.H. Bachem, *Phys. Rev. B* **52**, 5179 (1995).
- 20. J.-F. Zheng, dissertation, January, 1996, Lehigh University.
- 21. B.-H. Cheong and K.J. Chang, *Phys. Rev. B* **49**, 17436 (1994).
- 22. Y. Kim and A. Ourmazd, *Mat. Res. Soc. Symp. Proc.* **184**, 101 (1990).

## PLAUSIBLE EVIDENCE OF EXISTENCE OF DEEP ACCEPTORS IN Si $\delta$ -DOPED AlGaAs

K. Takarabe, N. Okada<sup>1</sup>, K. Ohmura<sup>1</sup>, and H. Ohkura<sup>1</sup>,

Department of Applied Sciences,

<sup>1</sup>Department of Electronic Engineering,

Okayama University of Science,

Ridai, Okayama 700, Japan

**Keywords :** Si  $\delta$ -doped AlGaAs, deep acceptors, photoluminescence.

**Abstract** Three photoluminescence(PL) bands have been observed below the band-gap energy in Si  $\delta$ -doped  $\text{Al}_x\text{Ga}_{1-x}\text{As}$  ( $x=0.35$ ) when excited with an  $\text{Ar}^+$ -ion laser. The PL band at the highest photon energy region can be assigned to a band-to-acceptor(BA) transition(say band I), and the two lower would be donor-acceptor(DA) transitions(band II and III), respectively. The shape of PL band I is well fitted to a transition theory including an alloy effect and an electron confinement effect due to the  $\delta$ -doping. The shapes of band II and III are well fitted to the configuration-coordinate model. After analysis, the Huang-Rhys factors  $S$  are evaluated to be less than 0.6 for two bands. It shows the weak electron-phonon interaction. The temperature dependencies of the peaks of the three bands show similar tendencies as those for the bandgap. A remarkable finding is that thermal quenching energies of three PL bands reveal nearly the same amount, about 90 meV, in the higher temperature range. These two facts imply that the initial states of the three PL bands are commonly from the bottom of the conduction band. The idea is supported by the fact that the energy difference between the L band edge and the  $\Gamma$  band edge is close to 90 meV for this alloy. Accordingly, we may tentatively propose the model of three bands. Namely, the final state of the band I is the  $\text{C}_{\text{Si}}$  acceptor, the  $\text{Si}_{\text{As}}$  acceptor for band II. However, the model of the band III is a deep acceptor that has not been clarified yet.

### 1. Introduction

Silicon(Si) doped into AlGaAs forms various sorts of defects of an electrically active shallow donor, a deep DX center[1] and a shallow acceptor of an anti-site  $\text{Si}_{\text{As}}$  [2], and complicated deep acceptors[3]. Photoluminescence(PL) spectra have been widely studied to characterize these defects. However the consensus of the model of deep PL spectra has not been achieved yet. Henning et al. studied a systematic deep PL of AlGaAs:Si and interpreted their results with DX center physics[4]. In contrast, a lot of experimental reports in the field of crystal growth have discussed deep acceptors as the origin of deep PL in AlGaAs:Si[3]. These spectra appear in a similar range of photon energy. This is our motivation to reinvestigate the deep PL in AlGaAs which appeared about 200 meV below the bandgap energy. In this article, we report the PL spectra measured in a wide range of temperature from 10 to 300K and an analysis based on the band-to-acceptor(BA) theory and the configurational coordinate(cc) model.

## 2. Experiment

Si  $\delta$ -doped samples were grown by molecular beam epitaxy on a semi-insulating [100]-oriented Cr-doped GaAs substrate. The doping-level of the Si  $\delta$ -layer was about  $10^{12} \text{ cm}^{-3}$ . The sample was held in a closed-cycle refrigerator cooling down to 10 K. The sample was excited with an Ar<sup>+</sup>-ion laser operating at 514.5 nm and the PL spectra were dispersed by a JASCO double spectrometer equipped with a cooled photomultiplier.

## 3. Results and discussion

One of the PL spectra at 70 K is shown in Fig.1. Three emission bands are peaked at 1.985 eV, 1.925 eV, 1.835 eV, respectively. They are denoted as bands I, II or III for convenience. The observed spectra are fitted well to suitable forms. We conclude that the band I is a band-to-acceptor(BA) radiative recombination based on the fitting analysis with a theoretical curve of the BA recombination including an alloying effect[4] and an electron confinement effect due to the Si  $\delta$ -doping effect. The alloy broadening of the conduction band(CB) edge is approximated with a Gaussian density of states(DOS) of about 5-meV full width at half maximum(FWHM). The dimensionality of the CB DOS is taken to be 0.01(0.0 for two dimensional DOS). The fit is quite good in both lower and higher energy tails. A discrepancy of the fitting curve, however, is seen below the lower tail, which indicates the existence of another emission band. Actually this discrepancy disappears with increasing temperature. Finally the temperature dependent BA PL spectra were analysed throughout with this fitted curve.

Next, bands II and III are fitted to the cc model using a Gaussian band shape. The best fit is shown in the inset of Fig. 1. A precise analysis shows that both bands consist of zero, one, and two phonon vibronic states, where the zero phonon line dominates the other components. Consistently, as fitting parameters, the Huang-Rhys factor of band II and band III are

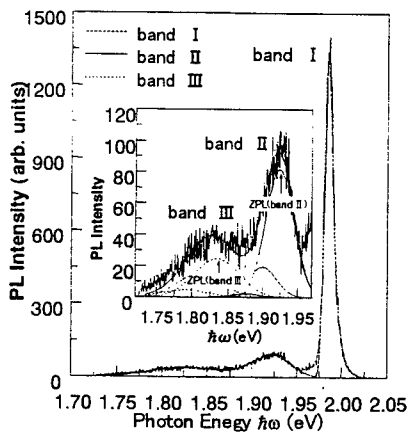


Fig-1. Photoluminescence spectrum at 70 K. Band I is fitted to the modified band-to-acceptor recombination theory(see text) and bands II and III are fitted to the configuration coordinate model. The ZPL in the inset is a zero-phonon line. The other lines are one and two phonon lines(solid line for band II and dotted line for band III).

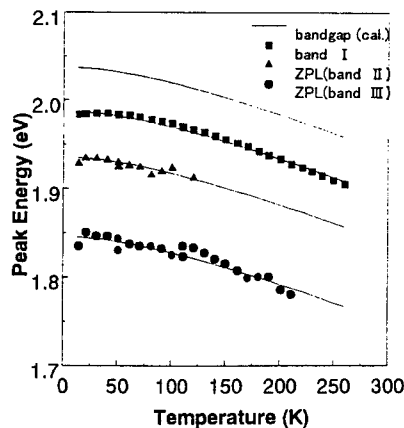


Fig-2. Temperature dependencies of the band-to-acceptor energy and the ZP transition energies the bands II and III, respectively. The top solid line is calculated using Varshni's form for this alloy composition and the other lines are with finite energy difference with each other.

estimated to be 0.24 and 0.6 by using the phonon energy of 24 meV. It is clearly shown that the electron-phonon interaction is weak. The phonon energy involved in this analysis is close to the optical phonon of GaAs of 23 meV at the L edge. The temperature dependence of PL bands II and III were analysed throughout with the same cc model. The width of the zero-phonon(ZP) line starts to increase as the temperature exceeds about 60 K. This result should be analysed in the weak coupling regime[5]. The result of analysis will be reported elsewhere. The effect of spacial distribution between the DA pairs would cause the width of ZP line. With this idea, the alloy broadening DOS of the BA PL is again analysed in the same cc regime. The result shows the Huang-Rhys factor of 0.007 and the same phonon energy of 24 meV.

The band-gap energy calculated and peak energies, analysed in the preceding paragraph, of three PL bands are plotted in Fig.2 as a function of temperature. The former is an empirical plot of Varshni's form[3] arranged for this alloy composition. This result implies that the initial state for three different radiative recombinations is more reasonably related to the CB edge than any other deep donor(DD) levels. If it would be caused by the DD-donor transition, the temperature dependence of its peak energy would be much changed, because of the combination of  $\Gamma$ , L, and X CB edges with finite weight. Thus, we may be convinced that it is due to the bottom of CB.

Figure 3 shows the temperature dependence of integrated intensities for three PL bands. The experimental data fit well to the empirical thermal quenching curves with three activation energies each other. The most prominent feature for three PL emissions at higher temperature region is that the thermal quenching energies are the same of about 90 meV. This is simply understood by the following idea that the electron could be supplied from the same initial state.

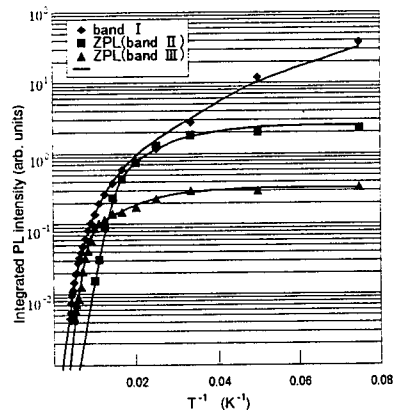


Fig-3. Temperature dependence of integrated PL intensities. The solid lines are calculated by a usual thermal quenching form with three activation energies. Almost the same thermal quenching energy of about 90 meV is obtained at higher temperatures for three PL emissions.

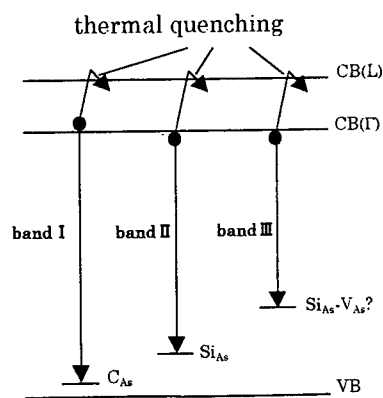


Fig-4. Schematic presentation of a proposed PL mechanism. The thermal quenching at higher temperatures occurs through the non-radiative recombination of the  $\Gamma$  CB electron via the L CB edge. The electron-phonon interaction is weak for bands II and III so that it is removed for simplicity. The chemical species of acceptors are tentative.

It is already known that the BA transition is due to the CB electron, accordingly bands II and III also occur by the CB-associated electron and the final states are reduced to various sorts of acceptors. Most plausible models for these acceptors could be proposed from the comparison of experimental data for acceptors reported previously. Namely, band I(BA) and band II(DA) would be related to the  $C_{As}$ [7] and the  $Si_{As}$  [2] acceptors, respectively. The probable deep acceptor for band III may be the  $Si_{As}-V_{As}$  complex[4]. These are summerized in Fig.4.

#### 4. Conclusion

The three PL bands of the Si  $\delta$ -doped sample were studied in some detail. The initial states of the three radiative recombinations are supposed to lie commonly at the bottom of the conduction-band and the final states are acceptors with weak coupling.

#### References

- [1] P. M. Mooney, J. Appl. Phys. **67**, R1(1990).
- [2] G. Oelgart, G. Lippold, M. Proctor, D. Martin, and F. K. Reinhart, Semicond. Sci. Technol. **6**, 1120(1991).
- [3] A. M. de Paula, G. Medeiros-Ribeiro, and A. G. de Oliveila, J. Appl. Phys. **76**, 8051(1994).
- [4] E. F. Schubert, E. O. Goebel, Y. Horikoshi, K. Ploog, and H. J. Queisser, Phys. Rev. B **3**, 361(1988).
- [5] F. E. Williams and M. H. Hebb, Phys. Rev. **84**, 1181(1951).
- [6] Y. P. Varshni, Physica **84**, 149(1967).
- [7] R. Heilmann and G. Oelgart, Semicond. Sci. Technol. **5**, 1040(1990).

## MAGNETO-OPTICAL AND MAGNETIC RESONANCE INVESTIGATIONS OF INTRINSIC DEFECTS IN ELECTRON-IRRADIATED n-TYPE $\text{Al}_x\text{Ga}_{1-x}\text{As}$

K.H. Wietzke<sup>1</sup>, M.V.B. Pinheiro<sup>1,2</sup>, F.K. Koschnick<sup>1</sup>, K.Krambrock<sup>2</sup> and J.-M. Spaeth<sup>2</sup>

<sup>1</sup> Fachbereich Physik, Universität-GH Paderborn, Warburger Str. 100, 33098,  
Paderborn, Germany

<sup>2</sup> Depto de Física, Universidade Federal de Minas Gerais, CP702, 30161-970,  
Belo Horizonte, MG, Brazil

**Keywords :** intrinsic defects, optically detected EPR, MCDA, AlGaAs, electron-irradiation

**Abstract.** Three intrinsic defects have been observed with magnetic circular dichroism of the absorption (MCDA) and MCDA-detected EPR (MCDA-EPR) in n-type Te-doped  $\text{Al}_{0.16}\text{Ga}_{0.84}\text{As}$  electron-irradiated at low temperatures. Two of them,  $\text{As}_{\text{III}}\text{-III}_{\text{As}}$  (nnn) and  $\text{V}_1$ , are similar to defects created by electron-irradiation in GaAs, the anti-structure pair ( $\text{As}_{\text{Ga}}\text{-Ga}_{\text{As}}$ (nnn)), an As antisite with a Ga antisite in the next nearest neighbour shell, and what is assumed to be a trigonally distorted Ga vacancy-related defect. Although the MCDA-EPR spectra of those two defects,  $\text{As}_{\text{III}}\text{-III}_{\text{As}}$  (nnn) and  $\text{V}_1$ , are very similar to the MCDA-EPR spectra of their analogues in GaAs, their MCDA bands are shifted to higher energies in comparison to the bands in GaAs reflecting the increase of the band gap energy with Al concentration. The third defect,  $\text{V}_2$ , has no analogue in electron-irradiated GaAs and was discriminated from  $\text{V}_1$  with MCDA-EPR experiments involving additional illumination. While its MCDA spectrum is similar to that of  $\text{V}_1$ , its MCDA-EPR spectrum is clearly different. From the annealing behavior of  $\text{V}_1$  and  $\text{V}_2$  monitored by MCDA-EPR it is proposed that  $\text{V}_2$  is also related to a cation vacancy either undistorted or only slightly distorted.

### Introduction

Because of their fundamental role in the compensation of III-V semiconductor compounds, intrinsic defects, being either native or created by radiation damage, have been intensively investigated in the last few years. In the case of electron-irradiated GaAs, mainly defects introduced in the Gallium sublattice were observed, i.e. As-antisites and Ga-vacancies [1-3]. With electron paramagnetic resonance detected via the magnetic circular dichroism of the optical absorption (MCDA, MCDA-EPR), MCDA-detected electron-nuclear double resonance (MCDA-ENDOR) and positron-annihilation spectroscopy (PAS), much information about their microscopic structure has been obtained over the last ten years [3-7]. However, for  $\text{Al}_x\text{Ga}_{1-x}\text{As}$  alloys, the situation is quite different. Recent CV and DLTS measurements performed on proton-irradiated  $\text{Al}_{0.22}\text{Ga}_{0.78}\text{As}$  (1 MeV) showed the existence of vacancy-like defects annealing out in a broad range of temperature above 250 K [8]. Little more is known about irradiation defects in  $\text{Al}_x\text{Ga}_{1-x}\text{As}$ . In this paper we briefly present our most recent results concerning the structural investigation of intrinsic defects created by electron-irradiation in n-type  $\text{Al}_{0.16}\text{Ga}_{0.84}\text{As}$ . In particular, we show that for 16% Al concentration the defects introduced by electron-irradiation are essentially the same as those in semi-insulating and n-type electron-irradiated GaAs. The main difference is that a new Gallium vacancy-like defect has also been created, which is probably not distorted in contrast to the trigonally distorted Ga vacancy-related defect  $\text{V}_{\text{Ga}}$  (trigonal) in GaAs.

### Experiment

The MCDA is the differential absorption of right and left circularly polarized light propagating in a direction parallel to an external magnetic field. It is usually described as a sum of two contributions, the paramagnetic and the diamagnetic parts. The former is proportional to the occupation difference of the Zeeman levels of the ground state of the defect. Its intensity is temperature dependent. By

reducing this occupation difference inducing magnetic dipole transitions, one decreases the intensity of the paramagnetic MCDA signal. This effect is used to detect EPR optically (MCDA-EPR). Its main advantages are the increased sensitivity in comparison to conventional EPR and the possibility of correlating the EPR spectrum of the defect with its optical properties. For further details about this technique see [9].

The MCDA and MCDA-EPR experiments have been performed at 1.5 K in a K-band (24 GHz) spectrometer. A cooled Ge-detector has been used in the spectral range between 0.8 eV and 1.7 eV. Low-pass optical filters have been used to suppress second order effects of the monochromator. For the two-beam experiment, where the sample was exposed to white light additionally to the measurement light, a halogen lamp with a Si filter was used. The experimental setup is described in more details elsewhere [10].

The Te-doped  $\text{Al}_x\text{Ga}_{1-x}\text{As}$  samples were grown with the liquid-phase epitaxy (LPE) technique by Hitachi Cable Co., Ltd. The substrate-free layers were about 200  $\mu\text{m}$  thick. The Te-concentration was approximately  $10^{18} \text{ cm}^{-3}$ . The electron-irradiation took place at 4.5 K in the van de Graaff accelerator ELIAS of the Institut für Festkörperforschung (IFF) in Jülich. After irradiation during transport and transfer into the spectrometer the samples were always kept at temperatures below 77 K. The energy of the incident electrons was 2 MeV, the fluence  $5 \times 10^{17} \text{ cm}^{-2}$ .

## Results and discussion

Since the samples used had a low Al content ( $x=0.16$ ), the group VI donor Te did not form the so-called DX center [11]. This has been verified before [12]. After electron-irradiation, a paramagnetic MCDA, as shown in Figure 1(a), was detected.

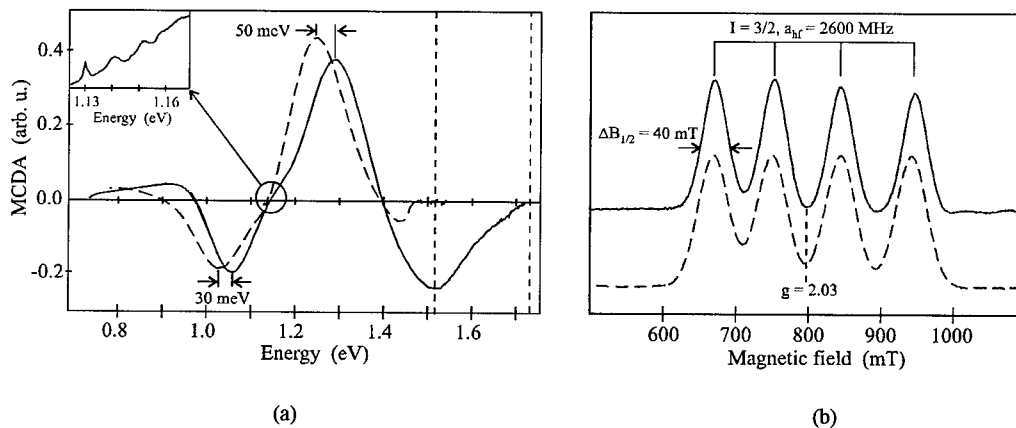


**Fig. 1:** (a) MCDA spectrum of a Te-doped  $\text{Al}_{0.16}\text{Ga}_{0.84}\text{As}$  crystal (solid line), electron-irradiated at 4.5 K and kept below 77 K. For comparison, the spectrum of the anti-structure pair in electron-irradiated n-GaAs (2 T and 1.5 K) is also shown (dashed line). The inset represents the zero phonon line (ZPL) and its replica of the anti-structure pair in GaAs. The two vertical dashed lines at 1.52 eV and 1.76 eV indicate the band edge of GaAs and  $\text{Al}_{0.16}\text{Ga}_{0.84}\text{As}$ , respectively. (b) MCDA-EPR spectra of the anti-structure pairs in  $\text{Al}_{0.16}\text{Ga}_{0.84}\text{As}$  (solid line) and GaAs (dashed line) measured at 1.286 eV and 1.240 eV, respectively (microwave frequency 22 GHz, temperature 1.5 K).

Its line shape is very similar to that of the anti-structure pair defect  $\text{As}_{\text{Ga}}\text{-Ga}_{\text{As}}(\text{nnn})$  in GaAs. This defect had been called  $\text{As}_{\text{Ga}}\text{-X}_1$  before. Meanwhile, the  $\text{X}_1$  in the complex  $\text{As}_{\text{Ga}}\text{-X}_1$  has been identified by MCDA-ENDOR experiments as a  $\text{Ga}_{\text{As}}$  antisite in the second (or next) nearest neighbour shell (nnn) of the  $\text{As}_{\text{Ga}}$  antisite [3]. The MCDA of the anti-structure pair in  $\text{Al}_{0.16}\text{Ga}_{0.84}\text{As}$  is shifted by 30 - 50 meV towards higher energy compared to that in GaAs. The MCDA band in



$\text{Al}_{0.16}\text{Ga}_{0.84}\text{As}$ , however, does not show the zero phonon line (ZPL) that appears in the MCDA spectrum of the  $\text{As}_{\text{Ga}}\text{-Ga}_{\text{As}}(\text{nnn})$  defect in GaAs (at about 1.13 eV) [3]. The MCDA spectrum of electron-irradiated  $\text{Al}_{0.16}\text{Ga}_{0.84}\text{As}$  shows a shoulder at about 0.9 eV which is absent in the spectrum of the anti-structure pair in GaAs. Despite their somewhat different MCDA spectra (fig. 1a), the two defects have undistinguishable MCDA-EPR spectra as to g-factor, hyperfine (hf) splitting and line width ( $g = 2.03 \pm 0.01$ ,  $a_{\text{hf}} = 2600 \pm 70$  MHz and  $\Delta B_{1/2} = 40 \pm 1$  mT) (fig. 1b). The four-line hf-split EPR spectrum with equal intensity and width for each hf-line is a characteristic finger print for one  $^{75}\text{As}$  nucleus having  $I = 3/2$  and 100% abundance. The spin-lattice relaxation time ( $T_{1e}$ ) for the defect in  $\text{Al}_{0.16}\text{Ga}_{0.84}\text{As}$  ( $T_{1e} = 2.4$  s) at 1.5 K is also similar to that of the anti-structure pair in GaAs ( $T_{1e} = 3.9$  s). We conclude that the defect observed in electron-irradiated n-type  $\text{Al}_{0.16}\text{Ga}_{0.84}\text{As}$  is the analogue of the anti-structure pair in GaAs, i.e. an  $\text{As}_{\text{III}}\text{-III}_{\text{As}}(\text{nnn})$  defect where III can be either Al or Ga. For short, we will refer to it as an anti-structure pair. Another similarity between the anti-structure pair in GaAs and  $\text{Al}_x\text{Ga}_{1-x}\text{As}$ , is the fact that with additional illumination the MCDA band of the  $\text{As}_{\text{III}}\text{-III}_{\text{As}}(\text{nnn})$  defect is partially quenchable. The signal intensity decreased by about 33% after illumination. This effect is more pronounced for monochromatic light of photon energies close to 1 eV. As for the  $\text{As}_{\text{Ga}}\text{-Ga}_{\text{As}}(\text{nnn})$  defect in GaAs, this bleaching process is metastable for temperatures below 150 K [13]. We discuss now the two main differences between the spectrum observed in GaAs and the spectrum measured in  $\text{Al}_x\text{Ga}_{1-x}\text{As}$  after electron-irradiation, which are the absence of the ZPL and of its phonon replica of the anti-structure pair and the shoulder at 0.9 eV. According to the interpretation of the MCDA band of the anti-structure pair in GaAs, the absorption transition that causes the ZPL in the MCDA spectrum is a photoionization from the paramagnetic state of the defect,  $(\text{As}_{\text{Ga}}\text{-Ga}_{\text{As}}(\text{nnn}))^+$ , to an L-bound effective-mass type level resonant with the conduction band [3]. A

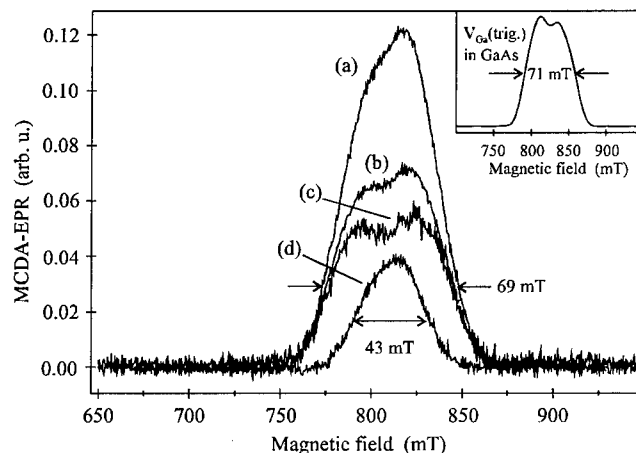


**Fig. 2:** MCDA-EPR spectra measured in Te-doped  $\text{Al}_{0.16}\text{Ga}_{0.84}\text{As}$  after electron-irradiation (1.5 K, 24 GHz and 0.96 eV) (a) with measurement light only, (b) with additional white light. In (c) and (d) the two MCDA-EPR lines, of defects  $V_1$  and  $V_2$ , respectively. The inset shows the MCDA-EPR spectrum of  $V_{\text{Ga}}$  (trigonal) in GaAs.

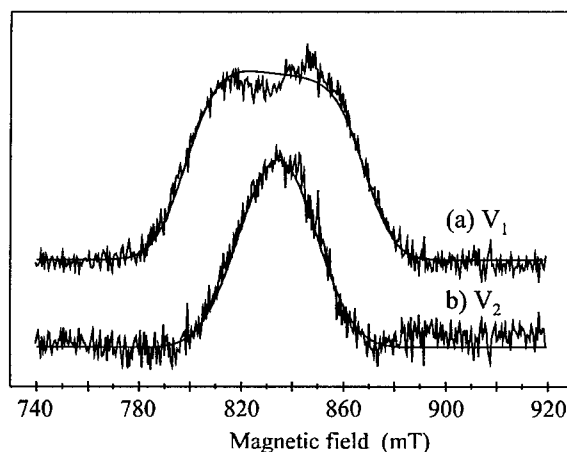


**Fig. 3:** MCDA-EPR spectra of the  $V_1$  and  $V_2$  defects and the simulated spectra. For  $V_1$  a prominent shf interaction of 520 MHz with an As neighbour was assumed (trigonal distortion). For the  $V_2$  defect an undistorted symmetry and a shf interaction of 170 MHz with four equivalent As neighbours was assumed. For further details see text.

ZPL line and its phonon replica would be expected in  $\text{Al}_{0.16}\text{Ga}_{0.84}\text{As}$  near 1.12 - 1.16 eV. However, it was not found there. A reason could be that it is extremely broadened. A probable cause for the broadening could be the presence of random strains in the sample. In fact, random strains have been invoked before to explain the lack of the characteristic ZPL of the  $\text{EL2}^0$  defect in its optical absorption spectrum in GaAs samples grown by molecular beam epitaxy (MBE) at low temperatures [14]. For  $\text{Al}_x\text{Ga}_{1-x}\text{As}$ , such random strains would most probably be caused by alloy disorder.

Another distinct feature in the MCDA spectrum of  $\text{Al}_{0.16}\text{Ga}_{0.84}\text{As}$  is the shoulder at 0.9 eV, which is not seen in the MCDA excitation spectrum of the EPR line of the anti-structure pair in  $\text{Al}_{0.16}\text{Ga}_{0.84}\text{As}$  (for the experimental method see ref. [9]). An additional paramagnetic MCDA band is superimposed to that of the anti-structure pair. At a photon energy of about 0.96 eV, where the MCDA excitation spectrum of the anti-structure pair is zero, a new MCDA-EPR line has been observed (see figure 2, curve (a)). This new MCDA-EPR line has an asymmetric shape. In order to explain the asymmetric line shape of the new MCDA-EPR signal we conclude that it is a superposition of at least two lines. Therefore, we performed a two-beam experiment. In addition to the measurement light parallel to the optical axis of the spectrometer the sample was exposed to a white light beam (halogen lamp and Si filter) perpendicular to the optical axis. The idea was to influence the quasi-Fermi level of the sample with the additional illumination and to change the charge states of defects present in  $\text{Al}_{0.16}\text{Ga}_{0.84}\text{As}$ . In figure 2, curve (b) the MCDA-EPR measured at a photon energy of 0.96 eV with additional illumination of the sample with white light is shown. The shape of the MCDA-EPR signal changed indeed upon additional illumination. The quenching effect of the MCDA-EPR signal accompanying the change of the line shape was reversible. Assuming a linear superposition of spectra, we decomposed the new asymmetric MCDA-EPR signal into two different MCDA-EPR lines from two different defects named  $V_1$  and  $V_2$  (figure 2, curves (c) and (d)).

The MCDA-EPR line of  $V_1$  has a half width of  $\Delta B_{1/2} = 69$  mT and a  $g$  value of  $g = 2.050 \pm 0.005$  for  $B \parallel [100]$ . For  $V_2$  the EPR parameters are  $\Delta B_{1/2} = 43$  mT and  $g = 2.048 \pm 0.005$ . The EPR line of  $V_2$  has a gaussian shape and is isotropic within experimental error, whereas the EPR signal of  $V_1$  shows an unresolved hf structure which could be modeled with the assumption of a prominent hf interaction of  $A_{[100]}/h = 520$  MHz with a single  $^{75}\text{As}$  nucleus (see fig. 3, curve (a)). A line width of 20 mT has been used for a single EPR line in order to take into account unresolved hf interactions with further neighbour nuclei. The depression in the middle of the EPR line of  $V_1$  is probably caused by an enhancement of the wings of the EPR line due to forbidden transitions because of the high microwave power used. This effect was also observed for the trigonally distorted Ga vacancy-related defect ( $V_{\text{Ga}}$  (trigonal)) in GaAs [4]. The line shape of  $V_2$  could be explained well with the assumption of a hf interaction with a tetrahedrally coordinated neighbour shell consisting of 4 equivalent As atoms with a hf interaction of  $A_{[100]}/h = 170$  MHz (see fig. 3, curve (b)). The same width for a single EPR line of 20 mT has been used as for the modeling of the EPR spectrum of  $V_1$ .

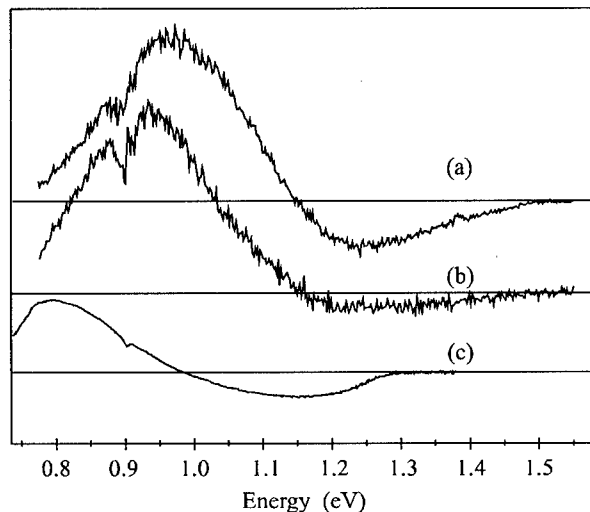


**Fig. 4:** Comparison between the decomposed MCDA excitation spectra of the EPR of  $V_2$  (a) and  $V_1$  (b) defects in electron-irradiated  $\text{Al}_{0.16}\text{Ga}_{0.84}\text{As}$  and that of the trigonally-distorted gallium vacancy in GaAs ( $V_{\text{Ga}}(\text{trig.})$ ) (c). The small depression at approx. 0.9 eV is due to OH<sup>-</sup>-absorption of the fused silica windows of the cryostat.

A small deviation from the tetrahedral coordination of the first neighbour shell of  $V_2$  cannot be ruled out. From our MCDA-EPR investigations, it seems that  $V_2$  has a higher defect symmetry than  $V_1$ .

The spin-lattice relaxation time  $T_1$  was measured to be approx. 0.2 s for both defects. With the measurement of the MCDA excitation spectra of  $V_1$  and  $V_2$  with and without the additional illumination, it was possible to discriminate the MCDA bands of  $V_1$  and  $V_2$  (see figure 4, curve (a) and (b)). The decomposition of the MCDA bands of  $V_1$  and  $V_2$  was performed analogously to the decomposition of the MCDA-EPR spectra (fig. 2 curves (c) and (d)).

Fig. 5 depicts the annealing behavior of the three defects investigated. A

series of isochronal (10 min) annealings from 77 K to 300 K followed by isothermal annealings ( $T = 300$  K) was performed. Curve (a) shows the behavior of the MCDA intensity of the anti-structure pair in  $\text{Al}_{0.16}\text{Ga}_{0.84}\text{As}$ . The intensity of the MCDA-EPR signal of the superposition of  $V_1$  and  $V_2$  is plotted in curve (b).  $V_1$  and  $V_2$  anneal out at room temperature (RT) whereas the MCDA intensity of the anti-structure pair increases. This increase is probably due to a shift of the Fermi level. The annealing behavior of  $V_1$  and  $V_2$  is similar. Also their MCDA bands and the spin lattice relaxation times are similar. Therefore, we conclude, despite of their different EPR spectra, that  $V_1$  and  $V_2$  are defects with a similar nature.

A comparison of the properties of  $V_1$  with those of the  $V_{\text{Ga}}$  (trigonal) in GaAs, a gallium vacancy-related defect which is believed to be trigonally distorted [1,5], shows a close relationship of both defects. The EPR parameters of both defects for  $B \parallel [100]$  are very similar:

-  $V_{\text{Ga}}$  (trigonal) in GaAs:  $g = 2.05$ ,  $\Delta B_{1/2} = 70$  mT, hf structure with a single As nucleus:  
 $A_{[100]}/h = 540$  MHz, defect symmetry  $C_{3v}$

-  $V_1$  in  $\text{Al}_{0.16}\text{Ga}_{0.84}\text{As}$ :  $g = 2.05$ ,  $\Delta B_{1/2} = 69$  mT, hf structure with a single As nucleus:  
 $A_{[100]}/h = 520$  MHz, defect symmetry probably  $C_{3v}$  or  $C_{1h}$

Their annealing behaviors ( $V_{\text{Ga}}$  (trigonal) in GaAs decays at RT as expected for Ga vacancies [7]) and their spin lattice relaxation times are similar, too. Also the MCDA bands of both defects have similar spectral shapes (see fig. 4, curves (b) and (c)). However, the MCDA band of  $V_1$  is shifted to higher energy by approx. 0.22 eV comparable to the shift of the band gap energy with  $x = 0.16$  (0.242 eV at 1.5 K after [15]). From these comparisons, we conclude that  $V_1$  is the analogue defect  $V_{\text{Al,Ga}}$  (trigonal) in  $\text{Al}_{0.16}\text{Ga}_{0.84}\text{As}$  to  $V_{\text{Ga}}$  (trigonal) in GaAs.

Assuming that the MCDA originates from transitions from the  $V_{\text{Al,Ga}}^{2-/3-}$  level to the valence bands [4], the shift of 0.22 eV shows that for  $\text{Al}_{0.16}\text{Ga}_{0.84}\text{As}$ , the level of the distorted vacancy  $V_{\text{Ga,Al}}^{2-/3-}$  is deeper in the gap ( $E_{\text{VB}} + \sim 0.65$  eV) than for the  $V_{\text{Ga}}^{2-/3-}$  in GaAs ( $E_{\text{VB}} + \sim 0.4$  eV) following approximately the conduction band change.

Because of the similar nature of  $V_1$  and  $V_2$ , concluded before, we think that  $V_2$  is a Ga vacancy-related defect, too. The observation of a (nearly) undistorted Ga vacancy-related defect ( $V_1$ ) raises

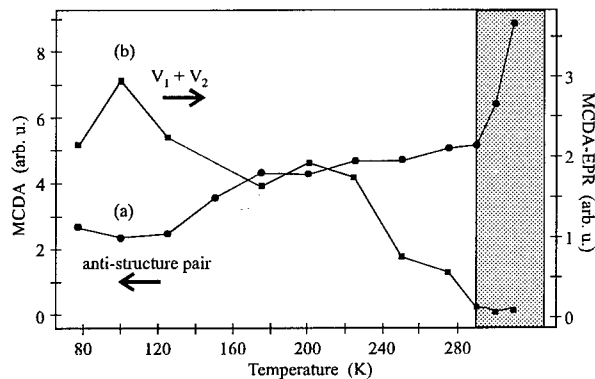


**Fig. 5:** Thermal stability of the electron-irradiation defects in  $\text{Al}_{0.16}\text{Ga}_{0.84}\text{As}$  measured after isochronal annealing (10 min per point) up to 300 K (left part of the graph) followed by isothermal annealing at RT (1 h each point, shaded area). Curve: (a) MCDA intensity of the anti-structure pair at 1.3 eV. Curve (b) total intensity of the superimposed MCDA-EPR line of  $V_1$  and  $V_2$  measured at 0.96 eV (curve (a) in fig. 2).

the question about the microscopic structure of both defects ( $V_1$  and  $V_2$ ). Up to now, we cannot decide whether this new, undistorted defect is special to  $\text{Al}_x\text{Ga}_{1-x}\text{As}$  or if it is the truly isolated vacancy and the trigonal distortion of the other defect is related to an additional component in the defect complex.

### Summary

We conclude that electron-irradiation at low temperatures produces essentially the same defects in n-type  $\text{Al}_x\text{Ga}_{1-x}\text{As}$ , as in n-type and semi-insulating GaAs: the anti-structure pair  $\text{As}_{\text{III}}\text{-III}_{\text{As}}$  (nnn) (where III is Ga or Al) and the trigonally distorted cation vacancy,  $V_{\text{Ga,Al}}$ . While for the latter the optical properties, reflected in the position of their MCDA band, are changed as a consequence of the larger band gap energy of  $\text{Al}_x\text{Ga}_{1-x}\text{As}$ , their microscopic structure has not changed visibly in the alloy. A new cation vacancy related defect  $V_2$  was observed. Unlike the other vacancy  $V_{\text{Ga,Al}}$ ,  $V_2$  seems to show no large distortion.

### Acknowledgments

We are again indebted to Hitachi Cable Co Ltd. for providing the LPE grown Te-doped samples. This work has been financially supported by the following agencies: CNPq (Brazil) and DFG (Germany).

### References

- [1] H. Hausmann, A. Pillukat and P. Ehrhart, Phys. Rev. B **54**, 8527 (1996)
- [2] J.C. Bourgoin, H.J. von Bardeleben and D. Stiévenard, J. Appl. Phys. **64**, R65, (1988)
- [3] J.-M. Spaeth and K. Krambrock. In R. Helbig, Festkörperprobleme / Advances in Solid State Physics **33**, 111-148, Vieweg, Braunschweig (1994)
- [4] K. Krambrock and J.-M. Spaeth, Solid State Commun. **93**, 285 (1995)
- [5] K.-H. Wietzke, F.K. Koschnick and J.-M. Spaeth, Mater. Sci. Forum **196/201**, 1061 (1995)
- [6] C. Corbel, F. Pierre, P. Hautojärvi, K. Saarinen and P. Moser, Phys. Rev.B **41**, 10632 (1990)
- [7] C. Corbel, F. Pierre, K. Saarinen, P. Hautojärvi and P. Moser, Phys. Rev. B **45**, 3386 (1992)
- [8] A. C. Irvine and D. W. Palmer, Phys. Rev.B **49**, 5695 (1994)
- [9] J.-M. Spaeth, J. R. Niklas and R. H. Bartram: in *Structural Analysis of Point Defects in Solids* (Springer Series in Solid-State Science **43** 1992 Berlin)
- [10] F. J. Ahlers, F. Lohse, J.-M. Spaeth and L. F. Mollenauer, Phys. Rev. B **28**, 1249 (1983)
- [11] P. Mooney, J. Appl. Phys. **67**, R1 (1990)
- [12] M. V. B. Pinheiro, M. Linde, H. Ohkura and J.-M. Spaeth, Semicond. Sci. Technol. **11**, 63 (1996)
- [13] M. Hesse, F. K. Koschnick, K. Krambrock and J.-M. Spaeth, Solid State Commun. **92**, 207 (1994)
- [14] K. Krambrock, M. Linde, J.-M. Spaeth, D. C. Look, D. Bliss and W. Walukiewicz, Semicond. Sci. and Technol. **7**, 1037 (1992)
- [15] M. Guzzi and J. L. Staehli, Solid State Phenomena **10**, 25 (1990)

## **GALLIUM INTERSTITIALS IN GaAs/AlGaAs HETEROSTRUCTURES INVESTIGATED BY OPTICALLY AND ELECTRICALLY DETECTED MAGNETIC RESONANCE**

**T. Wimbauer, M. S. Brandt, M. W. Bayerl, M. Stutzmann,  
D. M. Hofmann\*, Y. Mochizuki,\*\* and M. Mizuta\*\***

**Technical University of Munich, Walter Schottky Institute, Am Coulombwall,  
D-85747 Garching, Germany**

**\* I. Physikalisches Institut Justus-Liebig-Universität Gießen, Heinrich-Buff-Ring 16,  
D-35392 Gießen, Germany**

**\*\*Fundamental Research Laboratories, NEC Corporation, 34 Miyukigaoka, Tsukuba,  
Ibaraki 305, Japan**

**Keywords:** GaAs, optically and electrically detected magnetic resonance

**Abstract.** We have performed a comparative optically and electrically detected magnetic resonance study (ODMR and EDMR) on GaAs/AlGaAs heterostructures containing a 50 nm GaAs quantum-well codoped with Si and Be. The donor-acceptor-pair recombination serves as a sensitive detection channel for the ODMR experiments and reveals the presence of Ga interstitials in the GaAs quantum well. The signals observed in EDMR depend sensitively on the chosen experimental conditions. Dependent on the localization of the recombination current in the heterostructure, two cases can be distinguished.  $\text{Cr}^{4+}$  as well as arsenic antisite defects are observed for conditions where the current is dominantly driven through the semiinsulating substrate, whereas Ga interstitials were detected for conditions including a recombination current in the quantum well. These results indicate the large potential of EDMR in view of a selective detection of defects in complicated sample structures.

### **Introduction**

For the identification and analysis of defects in semiconductors electron paramagnetic resonance (EPR) has a long tradition. Despite of the tremendous success of conventional EPR investigations on defects in bulk semiconductors, the method has strong limitations for the application on epitaxial layers or quantum wells. The number of defects present in such structures are in most cases far below the detection limit of  $10^{11}$  spins/G linewidth. Two ways to overcome this drawback have been developed: optically and electrically detected magnetic resonance. Besides a drastically improved sensitivity both magnetic resonance techniques have further advantages in view of defect selectivity. The detection mechanism of ODMR is based on luminescence changes under magnetic resonance conditions so that the location of defects in a multilayer system can be related to the luminescent layer. EDMR on the other hand detects resonant changes in electronic transport properties such as photoconductivity. Therefore, defects detected by EDMR are located in or close to the conductive layers. Furthermore, EDMR is particularly suited to study the influence of paramagnetic defects on the performance of actual electronic devices. While ODMR is a well established technique, EDMR investigations have been reported mainly on elemental semiconductors and devices made of them. Here we present an exploratory investigation on AlGaAs/GaAs heterostructures.

## Experimental

The layer sequence of the AlGaAs/GaAs heterostructure studied is shown in Fig. 1. The 50 nm thick GaAs film is co-doped with Si ( $1 \times 10^{16} \text{ cm}^{-3}$ ) and Be ( $3 \times 10^{16} \text{ cm}^{-3}$ ). The co-doping is used to tailor the radiative lifetime in the layer: In order to perform ODMR measurements, in which one monitors a spin-flip-induced perturbation in the population of radiative species, it is convenient to use a luminescent process with rather small decay rates. In donor-acceptor pair recombination, electron and holes recombine via tunneling from the trapped impurity sites and the small overlap of the carrier wavefunctions yields radiative lifetimes of the order of  $10^{-7}$  s. A single quantum well was also inserted at a deeper location (115 nm from the surface) in order to avoid a high level of carrier injection into the GaAs:D,A layer.

For the EDMR investigations, electrodes were formed by alloying In droplets on top of the GaAs cap layer at 480°C for one minute. In this way, electrical contact to all layers in the structure could be achieved.

The ODMR setup consists of a 4T-superconducting magnet (modified Oxford MD-4) and a 35 GHz-microwave system. During the measurements, the sample as well as the resonator were immersed in pumped liquid helium (1.6 K) and the power was supplied by a GaAs Gunn diode (max. 100 mW). Luminescence was excited by an Ar<sup>+</sup> laser (488 nm, 1 mW/cm<sup>2</sup>) and detected by a Si Photodiode (Hamamatsu Photonics). In order to extract luminescence with a wavelength longer than 810 nm a glass filter was inserted into the optical path. ODMR was measured with lock-in detection by chopping the applied microwave power while the static magnetic field was swept. The typical chopping frequency was 1.2 kHz.

EDMR was performed both at 9 and at 34 GHz. The 9 GHz EDMR spectrometer consists of a standard EPR spectrometer (Bruker ESP 300), equipped with a TE<sub>102</sub> resonator. A Keithley source measure unit 237 was used as a low-noise voltage source together with lock-in detection of the microwave amplitude modulated signal ( $\approx 1$  kHz). The measurement temperature could be varied with a helium flow cryostat (Oxford ESR 900) from 4 to 300 K and the sample was illuminated with a 100 W Tungsten lamp in combination with a KG 3 heat filter. For the EDMR experiments at 34 GHz, a spectrometer consisting of a HP 83640A microwave synthesizer, a microwave power amplifier, and a cylindrical resonator (Bruker ER 5106 QT) immersed in a helium bath cryostat (Oxford CF 935) was employed. Phase sensitive detection of the EDMR signal as well as the illumination of the sample were performed analogously to the 9 GHz EDMR measurements.

GaAs cap	5 nm
Al <sub>0.4</sub> Ga <sub>0.6</sub> As	20 nm
GaAs:Si,Be	50 nm
Al <sub>0.4</sub> Ga <sub>0.6</sub> As	40 nm
GaAs (QW)	
Al <sub>0.4</sub> Ga <sub>0.6</sub> As	800 nm
semiinsulating GaAs substrate	

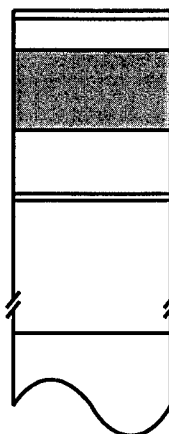


Fig. 1: Layer sequence of the investigated sample.

## Results and Discussion

The characteristic ODMR spectrum obtained previously [1] is shown in Fig. 2. The resonances were detected on the shallow donor-acceptor pair-luminescence originating from the co-doped GaAs

layer. Under magnetic resonance conditions the intensity of the shallow donor-acceptor pair-recombination decreases - the sign of the ODMR is negative. This means that the observed defect provides a shunt path for the radiative process. The spectrum consists of four lines and can be explained by hyperfine interactions with the nuclear spin  $I=3/2$  of the  $^{69}\text{Ga}$  and  $^{71}\text{Ga}$  isotopes having a natural abundance ratio of 61/39. In [1] the corresponding defect was assigned to the Ga interstitial in the co-doped layer.

In EDMR, the observed spin-dependent photoconductivity signals depend sensitively on the experimental conditions. As we already reported in [2], a superposition of resonances from different defects is observed if the sample is illuminated with the unfiltered light of a Tungsten lamp. Then the spectrum is dominated by the  $\text{Cr}^{4+}$  signal. Also, the  $\text{As}_{\text{Ga}}$  resonances are well resolved, but the Ga interstitial resonances can be hardly recognized, as seen in the upper part of Fig. 2.

Since the three defects are localized in two different layers of the sample ( $\text{Cr}^{4+}$  as well as  $\text{As}_{\text{Ga}}$  in the semiinsulating substrate and  $\text{Ga}_i$  in the co-doped GaAs layer) we have tried to separate the resonances by altering the relative photoconductivities of the involved layers via inhomogeneously absorbed light. This was achieved by illuminating the sample with a Tungsten lamp in combination with a heat filter KG 3 ( $h\nu > 1.5\text{eV}$ ). The capacitance in the detection circuit together with the different photoconductivities led to different RC time constants of the substrate and the co-doped layer, so that at a given modulation frequency different phase delays of the signals with respect to the phase of the reference frequency occur. Consequently a proper choice of the phase delay between modulation and detection allowed the observation of the isolated Ga interstitial resonances. The results of the corresponding X-band EDMR investigation performed at a temperature of 5 K is shown in the lower part of Fig. 3.

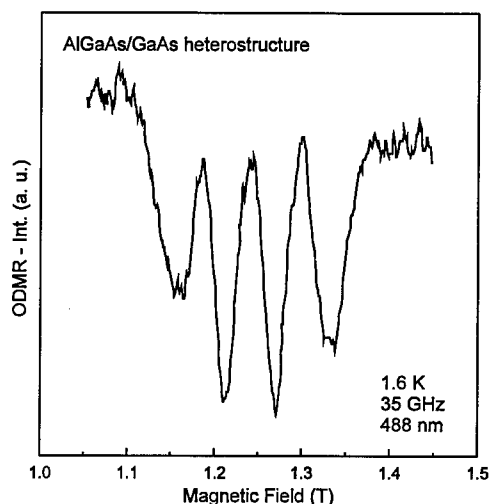


Fig. 2: ODMR spectrum of the Ga interstitial.

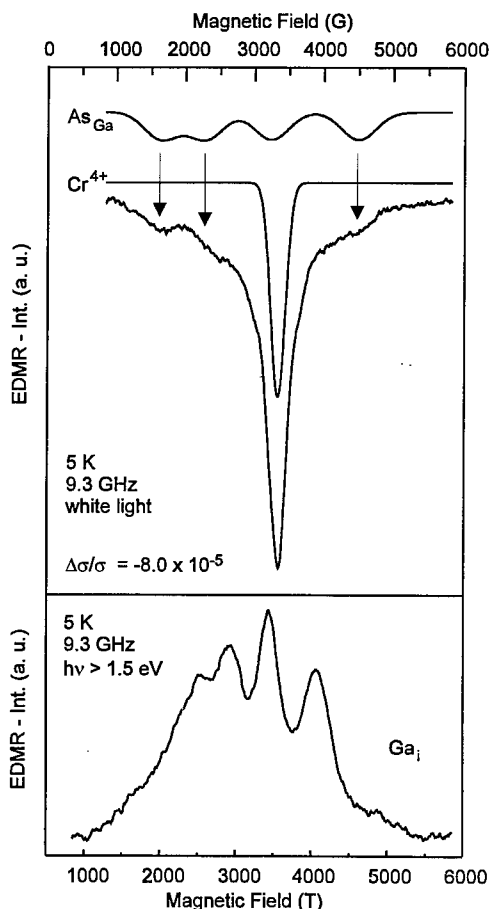


Fig. 3: X-band EDMR spectra - different illumination conditions.

The Ga interstitial resonances caused by hyperfine interactions of the effective spin with the nuclear spin of  $^{69}\text{Ga}$  are described by the Spin-Hamiltonian

$$H = \mu_B \tilde{S} \tilde{g} \tilde{B} + \tilde{S} \tilde{A}_{69} \tilde{I} \quad (1)$$

in which  $\mu_B$  is the Bohr magneton,  $\tilde{S}$  the effective spin,  $\tilde{g}$  the g-tensor,  $\tilde{I}$  the nuclear spin, and  $\tilde{A}_{69}$  the tensor describing the hyperfine interactions between the effective spin and the nuclear spin of  $^{69}\text{Ga}$ . The Spin-Hamiltonian describing the resonances caused by hyperfine interactions with  $^{71}\text{Ga}$  is obtained in an analogous manner with the hyperfine tensor  $\tilde{A}_{71}$ . The Hamiltonian (1) in the basis of  $|m_s m_I\rangle$  functions is a 8x8 matrix because we are dealing with an effective spin  $S=1/2$  and a nuclear spin  $I=3/2$  for both Ga isotopes. Since the resonances shown in Fig. 2 and Fig. 3 are isotropic, some restrictions follow for the tensors describing the Zeeman and hyperfine interactions. The g-tensor can be approximated by a scalar. Hence, if the magnetic field defines the z-axis, only the z-component of the spin operator is important and the matrix describing the Zeeman interaction has diagonal form. In the hyperfine-tensor, only the isotropic Fermi contact term makes a contribution, whereas the anisotropic dipolar term can be neglected. Consequently, the hyperfine-tensor becomes also a scalar. Since the operators for the x- and y-components of the spin and nuclear spin do not commute with the corresponding operators for the z-component, off-diagonal elements appear in the Hamiltonian (1). The Fermi contact interaction is given by the following expression

$$A = \frac{2\mu_0}{3} g \mu_B g_n \mu_n |\Psi(0)|^2 \quad (2)$$

where  $g_n$  and  $\mu_n$  are the nuclear g-factor and the nuclear magneton, respectively.  $|\Psi(0)|^2$  is the probability to find the paramagnetic electron at the core of the atom. The nuclear g-value of  $^{69}\text{Ga}$  is 1.344 and that for  $^{71}\text{Ga}$  1.708. According to equation (2), the ratio of the hyperfine constants is then given by  $A_{71}/A_{69} = g_{n71}/g_{n69} = 1.27$ , assuming that the probability of the paramagnetic electron at the core of the atom is identical for both Ga isotopes. A plot of the eigenvalues of the Hamiltonian (1) over the magnetic field (Breit-Rabi diagram) is shown in Fig. 4. For the calculations a g-value of  $g = 2.000$  and a hyperfine constant for  $^{69}\text{Ga}$  of  $A_{69} = 0.048 \text{ cm}^{-1}$  have been used. Furthermore, the magnetic dipole transitions for microwave frequencies of 9 GHz and 34 GHz are included in the figure. They occur between eigenvalues whose corresponding eigenvectors are dominated by basis vectors  $|m_s m_I\rangle$  with different  $m_s$  ( $\Delta m_s = \pm 1$ ) and identical  $m_I$ .

So far, we have calculated the positions of the Ga interstitial resonances. However, for a complete simulation the intensity ratio of the hyperfine resonances originating from the different Ga isotopes as well as the lineshape of the resonances are necessary. The intensity ratio between the  $^{69}\text{Ga}$  and the

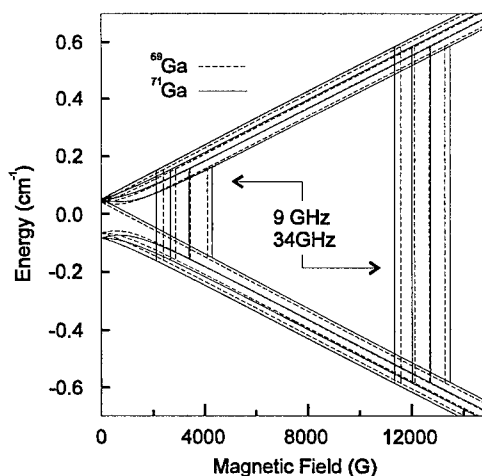


Fig. 4: Breit-Rabi diagram of the Ga interstitial and magnetic dipole transitions for microwave frequencies of 9GHz and 34 GHz.



$^{71}\text{Ga}$  hyperfine lines is determined by the natural abundancies of the Ga isotopes and has a value of 61/39. The resonances were assumed to be inhomogeneously broadened. Therefore gaussians were chosen to approximate the lineshape of the resonances. In Fig. 5 the ODMR measurements at 35 GHz and in Fig. 6 the EDMR measurements at 9 GHz and 34 GHz are compared with simulations using the above mentioned defect parameters. The simulations are in good agreement with the experimental spectra and the defect parameters (g-value and hyperfine constants) are similar to those reported by the Naval Research group [3][4] for AlGaAs and GaAs/AlAs superlattices.

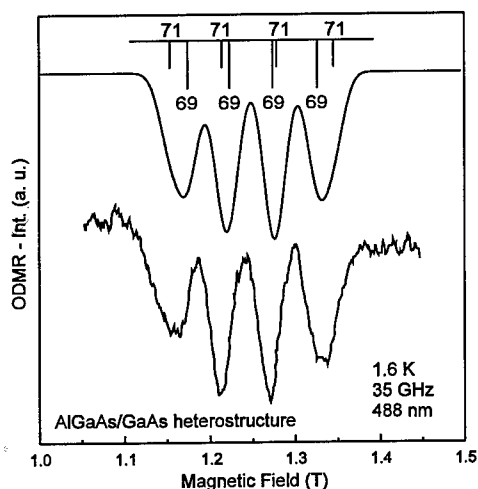


Fig. 5: Experimental and simulated ODMR spectrum of the Ga interstitial at 35 GHz.

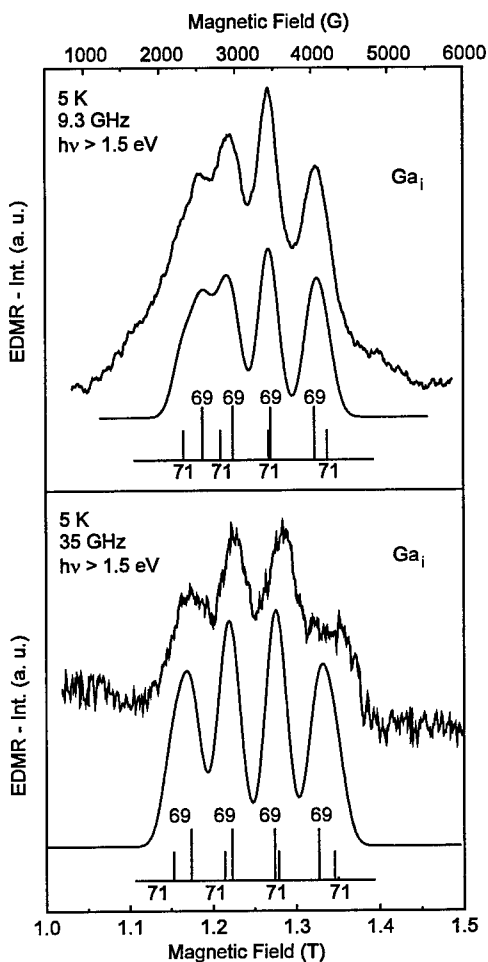


Fig. 6: Experimental and simulated EDMR spectra of the Ga interstitial at 9 GHz and 34 GHz.

### Summary and Conclusions

A comparative EDMR and ODMR study on GaAs/AlGaAs multilayer system was performed. While ODMR is restricted to defects in the luminescent layer, the EDMR results sensitively depend on the experimental conditions. The photoconductivities of the various layers could be influenced by changing the energy of the exciting light. In this way, EDMR signals from defects in different layers could be separated clearly from each other by phase shift analysis.

In EDMR, the arsenic antisite defect  $\text{As}_{\text{Ga}}$  as well as  $\text{Cr}^{4+}$  both located in the GaAs substrate were observed. The Ga interstitial located in a co-doped GaAs quantum well could be detected with both magnetic resonance techniques. The simulated Ga interstitial resonances of the X-band EDMR as well as the Q-band ODMR and EDMR measurements are in good agreement with the experiments.

**Acknowledgements**

The authors would like to thank the Deutsche Forschungsgemeinschaft (SFB348) for financial support.

**References**

- [1] Y. Mochizuki, M. Mizuta and A. Mochizuki, *Mat. Sci. For.* **196 - 201**, 1927 (1995).
- [2] T. Wimbauer, D. M. Hofmann, B. K. Meyer, M. S. Brandt, T. Brandl, M. W. Bayerl, N. M. Reinacher, M. Stutzmann, Y. Mochizuki and M. Mizuta, *Mat. Res. Soc. Symp. Proc.* **442**, 511 (1997).
- [3] T. A. Kennedy, R. Magno and M. G. Spencer, *Phys. Rev. B* **37**, 6325 (1988).
- [4] J. M. Trombetta, T. A. Kennedy, W. Tseng and D. Gammon, *Phys. Rev. B* **43**, 2458 (1991).

## ODMR INVESTIGATIONS OF Ge ACCEPTORS IN p-TYPE $\text{Al}_{0.4}\text{Ga}_{0.6}\text{As}$

M.V.B. Pinheiro<sup>1,2</sup>, K. Krambrock<sup>1</sup>, A.S.Chaves<sup>1</sup>,  
K.-H. Wietzke<sup>2</sup>, F.K.Koschnick<sup>2</sup>, and J.-M. Spaeth<sup>2</sup>

<sup>1</sup> Depto de Física, Universidade Federal de Minas Gerais, CP702, 30161-970,  
Belo Horizonte, MG, Brazil

<sup>2</sup> Fachbereich Physik, Universität-GH Paderborn, Warburgerstr. 100, 33098,  
Paderborn, Germany

**Key words :** Ge, acceptor,  $\text{Al}_x\text{Ga}_{1-x}\text{As}$ , ODMR, persistent photoconductivity

### Abstract

P-type Ge-doped  $\text{Al}_{0.4}\text{Ga}_{0.6}\text{As}$  layers grown by Liquid Phase Epitaxy (LPE) have been studied with near infrared optical absorption and electron paramagnetic resonance detected via the magnetic circular dichroism of the absorption (MCDA-EPR). A broad MCDA band has been observed in the same spectral region as a photoionization absorption band. The MCDA-EPR spectrum revealed an anisotropic and asymmetric line with a g-factor for  $B \parallel [100]$   $g_{[001]} = 2.03 \pm 0.01$ , a half width  $\Delta B_{1/2} = 60$  mT, a spin-lattice relaxation time  $T_1(1.5\text{K}) = 5 \pm 2$  ms and  $S = 1/2$ . The anisotropy of the MCDA-EPR line shows that the symmetry is lower than tetrahedral. In addition, we observed a second weaker EPR line, with a very short  $T_1$  at 1.5 K ( $< 1$  ms) and an anomalously broadened linewidth. For the origin of these two defects we propose a model in which the neutral, paramagnetic Ge-acceptor induces either shallow EMT or deep levels. While the deep acceptor has its symmetry lowered by the alloy disorder, the shallow level is thought to be equivalent to the Ge acceptor in GaAs.

### Introduction

P-type doping in  $\text{Al}_x\text{Ga}_{1-x}\text{As}$  crystals is an essential step for the fabrication of many devices (e.g. solar cells, FETs and optical sources). For liquid phase epitaxy (LPE) grown p-type GaAs and  $\text{Al}_x\text{Ga}_{1-x}\text{As}$  layers, the germanium is an alternative to other acceptor impurities like, for example, Zn and C, since it is easily incorporated on the As sublattice [1-3]. Besides inducing moderately deep non-effective mass-type (non-EMT) acceptors in p-type  $\text{Al}_x\text{Ga}_{1-x}\text{As}$ , whose thermal ionization energy depends strongly on the Al-mole fraction (x) [4], Ge introduces also shallow EMT levels close to the valence band [5]. In the last decade, the Ge-related non-EMT acceptors were intensively studied with photoluminescence spectroscopy resulting in a precise description of their ionization energy deepening with x [4-7]. However, not much is known about their microscopic structure and the reason for the deepening of its ionization level. On the other hand, for the shallower Ge-related levels less is known. In this work, we present recent results of a study of such Ge-related acceptors in an LPE-grown p-type  $\text{Al}_{0.4}\text{Ga}_{0.6}\text{As}$  layer, involving optical absorption, magnetic circular dichroism of the absorption (MCDA) and electron paramagnetic resonance detected via the MCDA (MCDA-EPR).

### Experiment

The MCDA is the differential absorption of right and left circularly polarized light propagating in a direction parallel to an external magnetic field. It consists of two contributions, a paramagnetic and a diamagnetic part. The paramagnetic part of the MCDA is proportional to the occupation difference of the Zeeman levels of the ground state of the defect, being thus a function of both the temperature and the applied magnetic field. By reducing the occupation difference of the Zeeman

sublevels with microwave-induced magnetic dipole transitions, the intensity of the paramagnetic MCDA signal decreases, thus optically detecting EPR. The main advantages of using the MCDA-detection of EPR are the increased sensitivity compared to conventional EPR, if the investigated paramagnetic defect has an appropriate absorption transition, and the possibility of correlating the EPR spectrum of a defect with its optical properties [8]. The MCDA-EPR setup used in this work is described in detail elsewhere [9].

The Ge-doped  $\text{Al}_{0.4}\text{Ga}_{0.6}\text{As}$  samples were grown with the liquid-phase epitaxy (LPE) technique by Hitachi Cable Co., Ltd. The substrate-free layers were about 180  $\mu\text{m}$  thick. The nominal Ge concentration was  $10^{18} \text{ cm}^{-3}$ . The samples were p-type with a hole concentration of approx.  $5 \times 10^{17} \text{ cm}^{-3}$  at room temperature.

## Results

Curve (a) of Fig. 1 shows the spectral shape of the absorption coefficient of the Ge-doped  $\text{Al}_{0.4}\text{Ga}_{0.6}\text{As}$  sample in the photon energy range between 0.7 eV and 2.1 eV. The optical absorption spectrum was numerically corrected for the spectral change of the reflectivity. A procedure similar to the one adopted by Dobrilla and Blakemore for studying the absorption band of the  $\text{EL2}^0$  defect in GaAs has been used [10]. The only difference is that for  $\text{Al}_x\text{Ga}_{1-x}\text{As}$  the refraction index has to be changed to account for the shift of the band-edge with  $x$ . There are two important features in the optical absorption spectrum shown in the curve (a) of Fig. 1. The first is the band-gap edge at 2.08 eV, which is expected for  $\text{Al}_{0.4}\text{Ga}_{0.6}\text{As}$  [11]. The second feature is a near infrared (IR) absorption band tail that increases monotonously towards lower energies. Such a spectral dependence is very similar to what is expected for a deep acceptor with a delta-like impurity potential [12], as described by the Lucovsky photoionization cross-section [13] given in equation (1):

$$\sigma_{Ph}(h\nu) \propto \frac{(h\nu - E_b)^{3/2}}{(h\nu)^3} \quad (1)$$

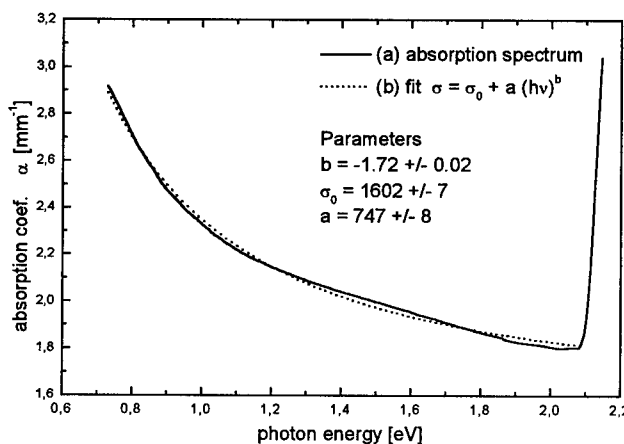


**Fig.1** Curve (a): optical absorption spectrum below the band edge of  $\text{Al}_{0.4}\text{Ga}_{0.6}\text{As}:\text{Ge}$  measured at 1.5 K. Curve (b): best fit for the high energetic tail of the Lucovsky-type photoionization cross section of the non-EMT Ge-acceptor. The fit parameters are  $b = -1.72 \pm 0.02$ ,  $a = 0.747 \pm 7$  and  $\sigma_0 = 1.602 \pm 0.007$ . The cross section is given in relative units for direct comparison with the optical absorption coefficient.

where  $E_b$  is the binding energy of the impurity. For  $h\nu \gg E_b$ , the Lucovsky photoionization band should have a high energetic tail falling off with  $h\nu^{-1.5}$ . The best fit to the spectrum, as shown in Fig. 1 curve (b) has an exponent  $b = -1.72 \pm 0.02$ , which is very close to the coefficient of the non-hydrogenic state described by the Lucovsky cross section ( $b = -1.5$ ). For comparison, a shallow hydrogenic EMT acceptor should have a spectral dependence in the high energy tail of  $(h\nu)^{-7/2}$  [14].

In the same near-IR range, a strong MCDA signal was observed at low temperatures (see Fig. 2 curves (a) and (b) for 1.5 K and 4.2 K, respectively). The total MCDA band belongs to paramagnetic defects since it depends both on the temperature and the magnetic field. Although its line shape is clearly different from the near-IR absorption band shown in Fig. 1, one can still assume that the non-EMT acceptor photoionization transition gives the main contribution to the shape of the MCDA spectrum, since it is, by far, the strongest absorption transition below the band edge.

Fig. 3 shows the MCDA-EPR spectrum, measured at 1 eV and 1.5 K with a microwave frequency of 24.945 GHz. This MCDA-EPR spectrum is composed of two EPR signals, an asymmetric and anisotropic line and a very broad signal, which surprisingly spreads up to 3 T. For  $B \parallel [001]$  an average g-factor of about  $2.03 \pm 0.01$  was estimated for the asymmetric line on the top of the broad signal. The full line width at half maximum ( $\Delta B_{1/2}$ ) of this signal was approximately 60 mT at  $B \parallel [001]$ . The MCDA excitation spectra (MCDA tagged by the EPR [8]), measured at different magnetic fields within the asymmetric EPR line showed that the tagged-MCDA spectrum follows closely the total MCDA band. The defects observed by MCDA-EPR give thus the main contribution to the total paramagnetic MCDA band (see Fig. 2 curve (c)). Therefore, we conclude that the two EPR lines belong to Ge acceptor-related defects.

Using the average g-factor for  $B \parallel [100]$  of the defect with the asymmetric EPR line, it is possible to estimate the spin of this defect with the measurement of the temperature and magnetic field dependence of its paramagnetic MCDA band (for the details of this method see for example [8]). For the asymmetric EPR line of Fig. 3 we obtained an effective spin of  $1/2$ . This value is different from the expected  $J=3/2$  for the ground state of shallow EMT acceptors in GaAs and  $\text{Al}_x\text{Ga}_{1-x}\text{As}$ .

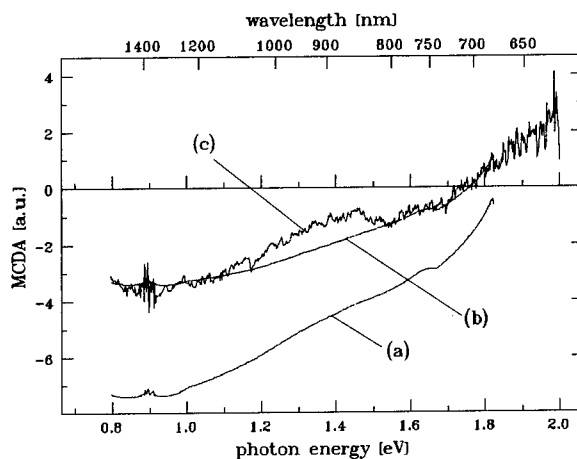


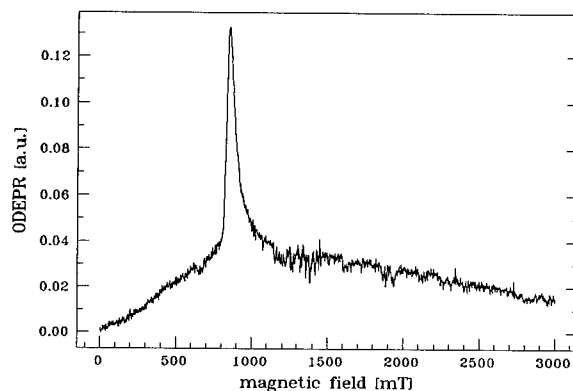
**Fig.2** Spectral shape of the near IR paramagnetic MCDA band observed in the LPE p-type  $\text{Al}_{0.4}\text{Ga}_{0.6}\text{As}:\text{Ge}$  sample measured at 2 T for  $T = 1.5$  K (a) and  $T = 4.2$  K (b). (c) MCDA excitation spectrum measured at 1.5 K, 830 mT and with a microwave frequency of 24.945 GHz.

With the measurement of the transients of the MCDA-EPR signals, the spin-lattice relaxation time  $T_1$  were determined. At 1.5 K the value obtained for  $T_1$  is  $5 \pm 1$  ms for the asymmetric line of the deeper defect ( $B = 847$  mT, and 1.4 eV).

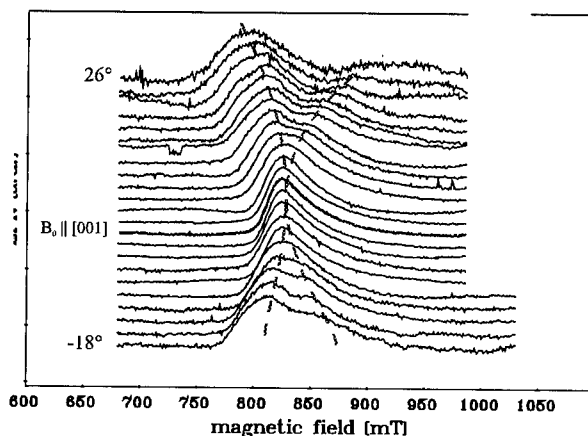
The broad EPR signal has a spin-lattice relaxation which is faster than the time resolution of our time-resolved MCDA-EPR set-up. The spin-lattice relaxation time is less than 1 ms.

Usually, shallow EMT acceptors in III-V compounds are very difficult to observe by EPR mainly because of the dynamic Jahn-Teller effect of their degenerated  $T_2$  ground state causing very small spin-lattice relaxation times and because of the broadening of their EPR lines due to random strains [15,16].

Another important aspect of the asymmetric MCDA-EPR line is the anisotropy. By rotating the magnetic field away from a [001] direction, the EPR line splits into at least two distinct EPR lines which move away from each other (see Fig. 3(b)). This anisotropy is an evidence that the symmetry of the paramagnetic defect is lower than tetrahedral. It is not possible to unambiguously estimate the symmetry of this deep defect from its EPR angular dependence. Presumably, the lowering of its symmetry is also caused by alloy disorder and thus resulting in a "deeper" defect. It is imaginable that the different configurations of the deep Ge acceptor-related defects due to the alloy mixing have different g-tensors reflecting their different symmetry. The probability for different configurations of Ga and Al atoms in the first neighbour shell of the deep Ga acceptor-related defect are listed in table 1. Considering only this first shell consisting of 4 neighbour atoms, two symmetries lower than tetrahedral are possible: trigonal symmetry and orthorhombic symmetry. The g-tensors are expected to be different for all configurations. The alloy mixing can explain the complicated angular dependence and the asymmetric line shape of the EPR of the deep Ge acceptor-related defect resulting from a superposition of various configurations. In comparison, we interpret the broad EPR line to arise from a shallow Ge acceptor with four equivalent atoms in the next neighbour shell.



(a)



(b)

**Fig.3** (a) The MCDA-detected EPR spectrum of the Ge-doped p-Al<sub>0.4</sub>Ga<sub>0.6</sub>As measured at 1 eV, 1.5 K, 24.945 GHz and 0 db (which corresponds to about 100 mW of microwave power inside the cavity). (b) The anisotropy of the asymmetric EPR line. The dashed lines are guides to the eyes.

**Table 1:** Probabilities and defect symmetries for different configurations of a defect on the As sublattice in  $\text{Al}_{0.4}\text{Ga}_{0.6}\text{As}$  considering the alloy disorder only in the first neighbour shell.

Configuration of first neighbour shell	probability	defect symmetry
4 Ga atoms	12.96%	tetrahedral
3 Ga atoms and 1 Al atom	34.56%	trigonal
2 Ga atoms and 2 Al atoms	34.56%	orthorombic
1 Ga atom and 3 Al atoms	15.36%	trigonal
4 Al atoms	2.56%	tetrahedral

## Discussion

From the optical absorption spectrum we can conclude that the strong near IR band is mainly due to the photoionization of the non-hydrogenic  $\text{Ge}_{\text{As}}$  acceptor. However, with MCDA-EPR in the near IR absorption band, two distinct defects have been observed: shallow defects with anomalously broad EPR line and deep defects whose paramagnetic ground states have  $S=1/2$  and an asymmetric and anisotropic EPR spectrum. The asymmetry of the EPR line is thought to arise from slightly different g-tensors for the different configurations of the deep defects due to the alloy mixing. A non-EMT state is more sensitive to the admixture of Al and Ga atoms in its first group III shell due to the higher localization of its bound hole when compared to the case of a hydrogenic acceptor. While some of the Ge acceptors would be stabilized in these new relaxed configurations after capturing a hole, other unrelaxed states would also exist, still inducing shallow levels similar to the  $\text{Ge}_{\text{As}}$  in GaAs.

## Acknowledgements

We are grateful to Hitachi Cable Co. and Prof. H. Ohkura for providing us the LPE Ge-doped samples. This work was supported by the following founding agencies DFG (Germany), CNPq (Brazil) and FAPEMIG (Brazil).

## References

1. W. Schairer and W. Graman, J. Phys. Chem. Solids **30**, 2225 (1969)
2. A.Y. Cho and T. Hayashi, J. Appl. Phys. **42**, 4422 (1971)
3. S.S. Chan, G.T. Marcyk and B.G. Streetmann, J. Electron. Mater. **10**, 213 (1981)
4. G. Oelgart, R. Schwabe, H. Fieseler and B. Jacobs, Semicond. Sci. and Technol. **3**, 943 (1988)
5. A.W. Nelson and P.N. Robson, J. Appl. Phys. **54**, 3965 (1983)
6. V. Swaminathan, J.L. Zilko, W.T. Tsang and W.R. Wagner, J. Appl. Phys. **53**, 5163 (1982)
7. L. Pavesi: in *Properties of Aluminium Gallium Arsenide*, Chap. 2, ed. S. Adachi (1993)
8. J.-M. Spaeth, J.R. Niklas and R.H. Bartram: in *Structural Analysis of Point Defects in Solids* (Springer Series in Solid State Physics Vol **43** Berlin 1992)
9. F.J. Ahlers, F. Lohse, J.-M. Spaeth and L.F. Mollenauer, Phys. Rev. B **28**, 1249 (1983)
10. P. Dobrilla and J.S. Blakemore, J. Appl. Phys. **58**, 208 (1985)
11. M. Guzzi and J.L. Staehli: in *Physics of DX centers in GaAs alloys* (Vaduz: Sci-Tech Publications, Lichtenstein 1990), ed. J. Bourgoin
12. J.C. Bourgoin and M. Lannoo: in *Point defects in semiconductors I - Theoretical Aspects* (Springer Series in Solid State Sciences Vol **22** Berlin 1981)
13. G. Lucovsky, Solid State Commun. **3**, 299 (1965)

14. J.S. Blakemore and S. Rahimi: *in Semiconductors and Semimetals, vol. 20 Semi-Insulating GaAs* (Academic Press, Inc. 1984), ed. R.K. Willardson and AC. Beer
15. T. Morgan, *Phys. Rev. Lett.* **24**, 887 (1970)
16. K. Krambrock and J.-M. Spaeth, *Solid State Commun.* **10**, 667 (1996)



## INVERTED CHARGE STATES OF ANION AND CATION-SITE VACANCIES IN ZINC BLENDE SEMICONDUCTORS: THEORY

D. J. Chadi

NEC Research Institute, 4 Independence Way, Princeton, NJ 08540-6634, USA

**Keywords:** Vacancies; divacancies; native defects; III-V and II-VI semiconductors; compensation, ZnS, ZnSe, ZnTe, CdTe, GaAs, GaN.

**Abstract.** The donor/acceptor character of anion/cation vacancies in III-V and II-VI semiconductors is found to be "invertible" via two different structural modification processes. It is shown that the normally double donor S-site vacancy in ZnS, for example, can be converted into a double acceptor center and, conversely, the normally double acceptor Zn-site vacancy can be transformed into a double donor defect. Additional results from *ab initio* calculations for ZnSe, ZnTe, CdTe, GaAs, and GaN indicate that similar reversals in charge states can be obtained in these compounds. The amphoteric nature of vacancies has important implications for dopant compensation.

### I. Introduction

Vacancies are among the simplest and most important point defects in zinc blende semiconductors and have been extensively studied.<sup>1</sup> They affect diffusion, form complexes with impurities, and play a significant role in determining the electrical properties of many materials. It is well known that anion-site vacancies in III-V and II-VI semiconductors are generally multiple donors whereas cation-site vacancies are multiple acceptors. Depending on Fermi level position, vacancies can exist in different charge states with different atomic configurations and symmetries, consistent with their donorlike or acceptorlike properties.

More than a decade ago, Baraff and Schlüter<sup>2</sup> suggested that the natural donor or acceptorlike property of a vacancy in a zinc blende crystal could be inverted. In particular, they examined the following structural transformations for Ga and As-site vacancies in GaAs:



and,



in which a vacancy on one sublattice is converted into a vacancy on the other sublattice by the motion of a nearest-neighbor atom of the vacancy into the vacancy. An antisite defect is created in each process. The transformation leads to an inversion of the charge state of the defect, changing an acceptorlike vacancy into a donorlike one and vice versa.

In this paper we propose that a reversal in the charge state of anion and cation site vacancies can be achieved without the introduction of antisite defects. The basic feature of the new type of structure suggested here is a strong pairwise dimerization of the four threefold coordinated nearest-neighbor atoms of the vacancy. This leads to structures that are generally lower in energy than those obtained from Eq. (1) for *anion-site* vacancies. For cation-site vacancies, the process in Eq. (2) gives the lowest energy for inverted charge states. However, in most but not all cases, the inverted charge states are stable only over a very limited range of Fermi energies or are even higher in energy than

the normal charge states for all Fermi energies. The accessibility of both negative and positive charge states for vacancies, especially anion-site vacancies, suggests that these defects are intrinsically amphoteric in nature and that vacancies on both sublattices need to be considered when examining dopant compensation phenomena.

Divacancy defects were also studied but will not be discussed much in this paper except to note that they are found to be primarily *double acceptor* defects in both III-V and II-V semiconductors with no states in the band gap after atomic relaxations are taken into account. Surprisingly, the formation energy from two isolated vacancies is *not* always, exothermic (e.g., see results for ZnTe and GaAs). The reason for this is that in *n-type* material, two separated vacancies can compensate *four* electrons whereas a divacancy can only compensate two electrons.

In the following we examine the relative merits of the two routes to charge inversion at vacancies: dimerization versus the transformations in Eqs. (1)-(2). Total-energies were calculated for different charge states, atomic configurations, and symmetries of vacancies in ZnS, ZnSe, ZnTe, CdTe, GaAs, and GaN. An overview of the results is given in Sec. II. The specific results for II-VI and III-V semiconductors are discussed in Secs. III and IV. The method used in the calculations is outlined in Sec. V and the conclusions are summarized in Sec. VI.

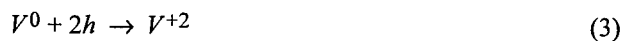
## II. Overview of Results

### A. Anion-site Vacancies

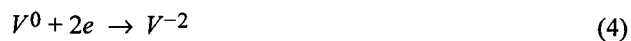
#### 1. II-VI Semiconductors

The "normal" +2 charge state of an anion vacancy has a structure in which the four neighboring cations are displaced radially away from the center of the vacancy by 20-24% of an anion-cation bond-length.<sup>3</sup> The vacancy also has a *neutral* state in which the four cations move *towards* the vacancy by 10-15% of a bond-length. In every case examined, the anion-site vacancy can be transformed into a double acceptorlike defect, either through a transformation like that in Eq. (1) or, alternatively, through a large lattice relaxation leading to a dimerization of the threefold coordinated cations surrounding the vacancy. For anion-site vacancies the dimerization process is found to be energetically most favorable. The lattice relaxation accompanying cation-cation dimerization is very large, with each cation moving by about 35% of a bond-length. The atomic displacements are so large that they lead to a rupture of one anion-cation bond for each cation atom in a dimer. In the optimized geometry, the four cations surrounding the vacancy form two pairs of dimer bonds, and there are four new dangling bonds on *anion* nearest-neighbors of the central cation atoms. It is these new dangling-bond orbitals that are primarily responsible for the reversal of the charge state of the vacancy. These anions also undergo substantial relaxations, moving by about 20% of a bond-length from their ideal crystalline positions. The dimer reconstruction leads to a more extended defect, one in which the new dangling bonds on the anions are 60% further apart than the original ones on the cations in the unrelaxed vacancy and where the open volume becomes split into four smaller portions.

The existence of neutral, +2 and -2 charge states for anion vacancies, each with its own unique structure, makes it necessary to consider the following free carrier compensation reactions:



and,



where a neutral anion vacancy captures either two holes or two electrons. For *p*- and *n*-type materials, the reactions in Eqs. (3) and (4), respectively, are found to be exothermic in all II-VI semiconductors examined. Anion site vacancies in ZnS, ZnSe, ZnTe and CdTe are found to be *positive-U* defects, i.e., two neutral vacancies are stable against a transition to +2 and -2 charge

states.<sup>4</sup> The stability of singly charged states were also examined. The  $-1$  charged states in ZnS and ZnSe have a half-occupied level in the upper half of the band gap and the dimerized structure is very similar to that for the  $-2$  state; however, the reaction  $2V^- \rightarrow V^{-2} + V^0$  is exothermic. In CdTe and ZnTe, the corresponding electronic states for the negatively charged Te vacancy lie below the valence-band-maximum (VBM).

## 2. III-V Semiconductors

An anion site vacancy in III-V semiconductors has  $+1$  and  $+3$  charge states with structures differing in the extent and direction of the relaxations of the four neighboring cations.<sup>5</sup> The  $+3$  state has a large outward relaxation of the four neighboring cations (by 34% of a Ga-As bond-length in GaAs) whereas the  $+1$  state has a smaller *inward* relaxation (by 15% of a bond-length in GaAs). Structurally, therefore, the  $+1$  and  $+3$  states of an anion vacancy in a III-V semiconductor are similar to the neutral and  $+2$  charged states of an anion vacancy in a II-VI semiconductor. The  $+1$  charge state is found to be the most stable state of the anion-site vacancy, even in *p*-type materials. The  $+1$  state has no electronic levels in the band gap. As in the case of II-VI semiconductors, the inverted negatively charge states can be obtained either via dimerization of the cations surrounding the vacancy or through the transformation in Eq. (1). The two possibilities were examined for GaAs and GaN. The dimerization route is found to be, by far, energetically more favorable and it gives rise to an inverted *singly* negative charge state. The lattice relaxation is large but does not lead to anion-cation bond breaking even though some anion-cation bond-lengths become stretched by 8-9%. The possibility of negative-U combinations of charge states was examined. Charge disproportionation of two vacancies in a  $+1$  state to a triply positive and a singly negative charge state is found to be strongly endothermic. In the following, we examine the analog of Eqs. (3) and (4) for anion vacancies in *p*- and *n*-type III-V semiconductors:



and,



## B. Cation-site Vacancies

### 1. II-VI Semiconductors

The normal double negative charged state of a cation vacancy in ZnS, ZnSe, ZnTe, and CdTe has a structure with tetrahedral symmetry and very small lattice relaxations.<sup>3,6</sup> Electronically, there is a highly localized doubly occupied state (originating from the threefold coordinated anions surrounding the vacancy) very close to the VBM. Experimentally an EPR active singly negative charged state has been created via optical excitation of this state in ZnSe.<sup>7-8</sup> As in the case of anion site vacancies the double negative charge state of the cation vacancy can be inverted into a  $+2$  charge state but the inverted states are not very stable, except in ZnS. As before, charge state inversion can be done either by the reaction in Eq. (2) in which the cation vacancy is converted to an anion site vacancy together with an anion site antisite, or alternatively through strongly dimerized anion-anion bonds. Even though for the latter structure, the anion-anion dimer bonds are very strong, particularly in ZnS, in all four compounds examined, the first type of process for charge inversion, i.e., defect transformation according to Eq. (2) is energetically more favorable than the dimerization reaction. For ZnS, the energy difference between the two pathways amounts to 0.76 eV. The inverted charge states are stable only in *p*-type material and even then they are only marginally more stable than the normal charge state. Cation-site vacancies in II-VI semiconductors do not possess a natural neutral charge state.

## 2. III-V Semiconductors

A cation vacancy in a III-V semiconductor such as GaAs is normally a triple acceptor. The vacancy has an inverted +1 charge state. As in the case of II-VI compounds, the +1 inverted charge state obtained from strong anion-anion dimerization is metastable compared to the structure obtained from Eq. (2). The low energy inverted state is 0.4 eV more stable than the normal –3 negatively charged state when the Fermi level is at the VBM. This implies that the normal triple acceptor state is the most stable state when the Fermi energy is more than 0.1 eV above the valence band edge.

## III. Results for ZnS, ZnSe, ZnTe, and CdTe

### A. ZnS: $V_S$

In the normal +2 charged double donor state the neighboring Zn atoms relax away from the vacancy and go into nearly planar  $sp^2$  bonded configurations. The S-vacancy also possesses a neutral charge state with no states in the gap in which the four nearest-neighbor Zn atoms relax inward by 8% of a Zn-S bond length. The inverted –2 negatively charged state occurs when the Zn atoms are allowed to dimerize. In this configuration the defect has a doubly occupied midgap state. The dimerized state is 0.95 eV more stable than  $(V_{Zn} + Zn_{anti})$  obtained via the defect reaction indicated by Eq. (1). The –2 state is 3.2 eV more stable than the +2 state in  $n$ -type ZnS. The S-vacancy is a positive-U defect with a U of nearly 1.45 eV for the reaction  $2V_S^0 \rightarrow V_S^{+2} + V_S^{-2}$ . The hole capture reaction in Eq. (3) is exothermic by 2.3 eV in  $p$ -ZnS while the electron capture reaction in Eq. (4) is exothermic by 0.8 eV in  $n$ -ZnS. The sum of the three calculated energies  $(1.45+2.3+0.8) = 4.55$  eV should be equal to twice the band gap of 3.9 eV in ZnS. However, because of the limitations of the local density approximation used in *ab initio* calculations, the calculated band gap of 2.28 eV is significantly smaller than the experimental value. The same trend can be observed for the other semiconductors examined below.

### B. ZnS: $V_{Zn}$

With only a small lattice relaxation around a Zn-vacancy,  $V_{Zn}$  is a double acceptor defect. As discussed above, the most stable state of the doubly positive charge state of the Zn-vacancy occurs when  $V_{Zn}$  is replaced by  $(V_S + S_{anti})^{+2}$ . The resulting vacancy-antisite complex has an empty electronic state with an energy very close to the conduction-band-minimum and a doubly occupied state close to the VBM. Both states are highly localized on the S-antisite and its neighboring S atoms. The +2 charged defect is expected to be stable only in  $p$ -type ZnS. The calculated energy difference between the normal  $V_{Zn}^{--}$  and the +2 charged states indicates that the +2 state is 1.1 eV more stable than the –2 state in  $p$ -type ZnS. In  $n$ -type samples, the –2 charged state is the most stable state.

In addition to  $(V_S + S_{anti})^{++}$ , the Zn-vacancy has a metastable  $V_{Zn}^{++}$  state in which the neighboring S atoms of the vacancy pair up and form very strong S-S bonds with a S-S bond length very close to twice the covalent bonding radius of S. The relaxation is so large that each of the S atoms breaks a Zn-S bond in the process of dimerization. The dimerized state is 0.76 eV less stable than the antisite-vacancy complex and it has no electronic levels in the band gap of ZnS.

### C. ZnSe: $V_{Se}$

The +2 charge state has tetrahedral symmetry and the four Zn atoms surrounding the vacancy relax away from the vacancy by 0.54 Å. The neutral state also has tetrahedral symmetry with the surrounding Zn atoms moving inwards by 0.39 Å. The stable inverted –2 charge state corresponds to a dimerized structure in which the Zn atoms move by 0.87 Å to form dimers. It has a localized midgap state distributed on the Zn atoms and neighboring Se atoms. The dimerization of the Zn atoms leads to the rupture of one Zn-Se bond per dimerized Zn atom. The resulting threefold coordinated Se atoms undergo a relaxation which makes their hybridization closer to  $s^2p^3$  (i.e., the

angles around the Se atoms are  $97^\circ$ ,  $97^\circ$ , and  $104^\circ$  instead of  $109.5^\circ$ ). The  $-2$  state is 2.5 eV more stable than the  $+2$  state in  $n$ -type ZnSe whereas the  $+2$  state is significantly more stable than the  $-2$  state in  $p$ -ZnSe. The Se-vacancy defect is an amphoteric defect that can easily change its charge state depending on the Fermi level. The negatively charged state has a doubly occupied level at midgap. The neutral state is stable against the reaction  $2V_{Se}^0 \rightarrow V_{Se}^{+2} + V_{Se}^{-2}$  which is endothermic by 1.6 eV; however, the hole capture reaction in Eq. (3) is exothermic by 0.75 eV in  $p$ -ZnSe and electron capture, as in Eq. (4), is exothermic by 0.42 eV in  $n$ -type ZnSe. Recent positron annihilation experiments on N-doped  $ZnS_xSe_{1-x}$  have identified a neutral (or negative) charge state of a Se-site vacancy.<sup>9</sup> The neutral state is likely to occur in a mostly compensated sample with few free holes.

#### D. ZnSe: $V_{Zn}$

The optimized doubly negative charged state has a small lattice relaxation of Se atoms around the vacancy. A band localized on these Se atoms is nearly degenerate with the bulk state at the VBM. The most stable  $+2$  charge state occurs for  $V_{Zn} \rightarrow V_{Se} + Se_{anti}$ . This state has no localized states in the band gap. The three threefold coordinated Zn atoms around  $V_{Se}$  as well as the  $Se_{anti}$  defect are all in planar  $sp^2$  bonded configurations with bond angles very close to  $120^\circ$ . The alternate  $+2$  charge state formed by the dimerization of Se atoms is metastable and is 0.52 eV higher in energy. It has an empty electronic level at  $E_c - 0.19$  eV. The energy of the inverted  $+2$  state is only marginally better than the  $-2$  state; in  $p$ -type ZnSe which should favor the  $+2$  state the most, the total-energy difference is only 0.15 eV. This means that the  $+2$  state is not stable for most values of the Fermi energy.

#### E. ZnTe: $V_{Te}$

The inverted doubly negative  $-2$  charged state of a Te-vacancy is a large 4.2 eV more stable than the double donor  $+2$  state in  $n$ -type ZnTe. The dimerization of Zn atoms for the  $-2$  charged state gives a doubly occupied localized level at about 0.12 eV above the VBM. The fact that both  $V_{Zn}$  and  $V_{Te}$  are most stable in  $-2$  charged states strongly affects the  $n$ -type doping of ZnTe. Since a combination consisting of equal numbers of  $V_{Zn}$  and  $V_{Te}$  constitutes a stoichiometric defect, the absolute formation energy of isolated  $V_{Zn}$  and  $V_{Te}$  centers in  $n$ -type ZnTe can be calculated. The results of such a calculation indicate that in  $n$ -type ZnTe the formation of two such doubly negatively charged vacancies is *exothermic* by 1.24 eV. This energy is much larger in magnitude than  $DX$  formation energies and it suggests that vacancy formation is *the* major cause of the problem in the  $n$ -type doping of ZnTe. The fact that donor electrons are compensated by defects and are not in deep donor levels is supported by the sharp attenuation of persistent-photoconductivity when the Zn concentration in  $Cd_{1-x}Zn_xTe$  alloys is increased beyond 40%. The Te-site vacancy also has a neutral state (with no state in the gap) and is a positive-U defect with  $U = 0.56$  eV for the reaction  $2V_{Te}^0 \rightarrow V_{Te}^{+2} + V_{Te}^{-2}$ . Hole capture by a neutral  $V_{Te}$ , as in Eq. (3), is exothermic by 0.48 eV in  $p$ -ZnTe, while electron capture, as in Eq. (4), is exothermic by a very large 1.8 eV in  $n$ -type ZnTe.

The normally donorlike Te-vacancy, therefore, is far more effective in electron than in hole compensation! Another surprising result for a Te-vacancy in ZnTe is that the analogous reaction to that in Eq. (1) leads to a defect which can passivate *four* electrons and is actually slightly more stable in  $n$ -type ZnTe than the dimerized structure. The defect has a doubly occupied level at 0.75 eV above the VBM and its character is strongly Zn-derived. This type of state was found only for ZnTe. It is important to consider these inverted charge state of the Te-vacancy in the context of problems encountered in the  $n$ -type doping of ZnTe. From the results of our calculations we find that the formation energy of the stoichiometric defect consisting of an isolated Te-site vacancy together with an isolated Zn-site vacancy, each in a  $-2$  charge state, is exothermic by 1.25 eV in  $n$ -type ZnTe. This energy is much larger than any  $DX$  center formation energy<sup>10</sup> and it provides an

explanation for why persistent-photoconductivity decreases sharply in CdZnTe alloys<sup>11</sup> as the Zn content increases. As the Zn content increases, the electrons are no longer in deep donor centers but become compensated by defects such as vacancies. It is interesting to note that in *n*-type ZnTe, *isolated* Zn and Te vacancies, each in a  $-2$  state, are found to be energetically more favorable (by 0.5 eV) than a divacancy. The divacancy can also assume a  $-2$  charge state but it can compensate only 2 electrons as compared to four electrons for two separated vacancies.

#### F. ZnTe: $V_{Zn}$

The inverted  $+2$  state is metastable with respect to the  $-2$  charged state for all values of the Fermi energy. This means that the normal  $-2$  charge state is the most stable state of the Zn-vacancy even in *p*-type ZnTe. The doubly occupied defect level lies below the VBM and Zn-vacancies should lead, therefore, to free hole creation.

#### G. CdTe: $V_{Te}$

The inverted  $-2$  state is found to be stable for Fermi energies above approximately  $E_v + 0.3$  eV where a localized Cd-Cd dimer state occurs. The atomic structure of the  $-2$  state is similar to that of the Zn-vacancy in ZnS and involves strong Cd-Cd dimer bonding which leads to the breaking of a Cd-Te bond for each Cd atom in the dimer (4 Te's are 3-fold and 4 Cd's are threefold). Unlike the case of ZnTe, the formation energy of an equal combination of negatively charged Cd and Te vacancies is strongly endothermic in *n*-type samples. The Te-vacancy has a stable neutral state and it is a positive-U defect with a U of 0.52 eV for  $2V_{Te}^0 \rightarrow V_{Te}^{+2} + V_{Te}^{-2}$ . The hole capture process in Eq. (3) is found to be exothermic by 0.3 eV in *p*-CdTe and electron capture [see Eq. (4)] is exothermic by 0.3 eV in *n*-type CdTe.

#### H. CdTe: $V_{Cd}$

The stable  $+2$  state is of the  $V_{Cd} \rightarrow (V_{Te} + Te_{anti})$  type and it has no defect states in the gap. The  $-2$  state has a highly localized state near the VBM. We find that the most stable state of the Cd-vacancy is always the  $-2$  charged state, independent of Fermi level position.

### IV. Vacancies in GaAs and GaN

#### A. GaAs: $V_{As}$

The As-vacancy in GaAs has positively charged  $+1$  and  $+3$  states, as discussed in Sec. II, with no states in the band gap. The inverted  $-1$  charge state arises from dimerization of the neighboring Ga atoms and has  $C_{2v}$  symmetry. The Ga atoms move by nearly 0.8 Å from their ideal positions to form two sets of dimer bonds. The total-energy is reduced substantially when the symmetry of the relaxation is low such that the two dimers are not equivalent. The dimerized  $-1$  charge state is found to be a very stable defect, more stable than either the  $+1$  or the  $+3$  charged states for Fermi levels above midgap. The reaction in Eq. (5) is found to be 3.9 eV *endothermic* in *p*-GaAs while in *n*-GaAs, the reaction in Eq. (6) is exothermic by 2.6 eV. The singly positive charged state of the As-site vacancy is, therefore, more stable than the triply charged state in *p*-type GaAs.

#### B. GaAs: $V_{Ga}$

The Ga-vacancy is normally a triple acceptor defect and the atomic structure has tetrahedral symmetry. The most favorable structure for the inverted  $+1$  charge state is the one obtained from Eq. (2). The  $+1$  state is 0.4 eV more stable than the triply negatively charged state in *p*-type GaAs. The implication for *n*-doping given that vacancies on both sublattices can act as acceptors was examined. Since isolated Ga and As vacancies form a stoichiometric defect, the absolute formation energy involved in donor passivation can be calculated. We find that under *thermodynamic equilibrium conditions*, the formation of a pair of negatively charged vacancies is *exothermic* by 3 eV in *n*-type GaAs. This is a very large energy and suggests that vacancy formation can be a major

route to carrier deactivation in GaAs. The theoretical results do not suggest that compensation occurs as a result of an equal concentration of Ga and As vacancies but that, on average, the formation energy of a vacancy is exothermic by 1.5 eV. The actual distribution of vacancies over Ga and As sites will depend on growth conditions. Experimental support for vacancies in *n*-type GaAs samples doped to extremely high levels is provided by positron annihilation studies.<sup>12-14</sup> At moderate doping levels (of  $2\text{-}3 \times 10^{19}/\text{cm}^3$ ), *DX* center formation appears to be the dominant mode for dopant compensation. One surprising result is that we find that isolated cation and anion vacancies in *n*-GaAs are 1 eV more stable than a divacancy.

### C. GaN: $V_N$

The *singly* positively charged N-vacancy in GaN is a defect with a small lattice relaxation and no defect levels in the band gap. The hole capture reaction in Eq. (5) is found to be endothermic by 1.1 eV in *p*-type GaN (implying that, as in GaAs, the single positively charged state of the anion-site vacancy is more stable than the triply charged state) while the electron capture reaction in Eq. (6) is found to be barely exothermic by 0.1 eV/electron. The negative charge state has a defect level about 0.63 eV below the bottom of the conduction band.

### D. GaN: $V_{Ga}$

The triple acceptor state of the Ga vacancy has tetrahedral symmetry and practically no lattice relaxation. The displacive reaction in Eq. (2) transforms the vacancy into a single donor center. The +1 state is 1.7 eV more stable than the normal triple acceptor state in *p*-type GaN. The defect levels in the band gap introduced by the donorlike state of the Ga-vacancy explain<sup>15</sup> several defect luminescence lines<sup>16</sup> and deep levels<sup>17</sup> seen experimentally in *p*-type GaN. For *n*-type GaN we find that the formation energy of two vacancies, one on a Ga and the other on a N site, is 1.6 eV *endothermic*; a divacancy in a double acceptor state is only slightly (0.2 eV) exothermic.

## IV. Calculations

The electronic properties of vacancies were examined via *ab initio* pseudopotential calculations using the local density approximation<sup>18</sup> and three dimensionally periodic unit cells containing 32 atoms/cell. Brillouin zone sampling was done using one special point and the zone center point.<sup>19</sup> Kleinman-Bylander<sup>20</sup> type of separable potentials obtained from Troullier-Martins pseudopotentials<sup>21</sup> were used. The fundamental band gaps are underestimated by a factor of nearly two in these types of calculations and this leads to uncertainties in the assignment of defect levels with respect to band edges and in the determination of the magnitude of electron and hole capture energies.

## V. Conclusions

Anion and cation site vacancies are found to be amphoteric native defects in III-V and II-VI semiconductors. They provide a microscopic source for amphoteric native defects that have been postulated to exist in zinc blende semiconductors.<sup>22</sup> Charge inversion from the normal donorlike state of anion vacancies occurs as a result of a strong dimerization of the four cations surrounding the vacancy. In the case of cations, a similar type of dimerization leads to a metastable state. The most favorable atomic structure for the inverted charge state of a cation vacancy involves a nearest-neighbor hop of an anion into the vacancy. The energetics of hole and electron capture by anion site vacancies indicates that the inverted charge states of these defects play a very important role in dopant compensation.

## References

1. G. D. Watkins, in *Deep Centers in Semiconductors*, edited by S. T. Pantelides, Gordon and Breach, New York, pp. 147-183 (1986).
2. G. A. Baraff and M. Schlüter, *Phys. Rev. B* **33**, 7346 (1986).
3. A. García and J. E. Northrup, *Phys. Rev. Lett.* **74**, 1131 (1995).
4. Anion site vacancies are, however, negative-U defects as far as the reaction in which two positively charged vacancies are transformed into a neutral and double positive charge state is concerned (Ref. 3).
5. J. E. Northrup, *Phys. Rev. B* **50**, 4962 (1994); S. B. Zhang and J. E. Northrup, *Phys. Rev. Lett.* **67**, 2339 (1991).
6. D. B. Laks, C. G. Van de Walle, G. F. Neumark, P. E. Blöchl, and S. T. Pantelides, *Phys. Rev. B* **45**, 10965 (1992).
7. G. D. Watkins, in *Radiation Defects in Semiconductors 1976*, Proceedings of the International Conference on Radiation Effects in Semiconductors, edited by N. B. Urli and J. W. Corbett, IOP Conf. Proc. No. 31 (Institute of Physics and Physical Society, London, 1977), p. 95.
8. D. Y. Jeon, H. P. Gislason, and G. D. Watkins, *Phys. Rev. B* **48**, 7872 (1993).
9. K. Saarinen, T. Laine, K. Skog, J. Mäkinen, P. Hautojärvi, K. Rakennus, P. Uusimaa, A. Salokatve, and M. Pessa, *Phys. Rev. Lett.* **77**, 3407 (1996).
10. C. H. Park and D. J. Chadi, *Appl. Phys. Lett.* **66**, 3167 (1995). A new class of orthorhombic symmetry  $DX$  centers is also found to be energetically favorable for Cl dopants in II-VI semiconductors. The structure of these centers is discussed in: C. H. Park and D. J. Chadi, *Phys. Rev. B* **54**, 14 246 (1996).
11. T. Thio, J. W. Bennett, and P. Becla, *Phys. Rev. B* **54**, 1754 (1996).
12. J. Gebauer, R. Krause-Rehberg, C. Domke, P. Ebert, and K. Urban, *Phys. Rev. Lett.* **78**, 3334 (1997).
13. T. Laine, K. Saarinen, J. Mäkinen, P. Hautojärvi, C. Corbel, L. N. Pfeiffer, and P. H. Citrin, *Phys. Rev. B* **54**, 11 050 (1996).
14. A. Polity, F. Rudolf, C. Nagel, S. Eichler, and R. Krause-Rehberg, *Phys. Rev. B* **55**, 10467 (1997).
15. D. J. Chadi (to be published).
16. C. H. Qiu and J. I. Pankove, *Appl. Phys. Lett.* **70**, 1983 (1997).
17. W. Gotz, N. M. Johnson, M. D. Bremser, and R. F. Davis, *Appl. Phys. Lett.* **69**, 2379 (1996).
18. J. Ihm, A. Zunger, and M. L. Cohen, *J. Phys. C* **12**, 4409 (1979).
19. D. J. Chadi and M. L. Cohen, *Phys. Rev. B* **8**, 5747 (1973).
20. L. Kleinman and D. M. Bylander, *Phys. Rev. Lett.* **48**, 1424 (1982).
21. N. Troullier and J. L. Martins, *Phys. Rev. B* **43**, 1993 (1991).
22. W. Walukiewicz, *Phys. Rev. B* **37**, 4760 (1988); *Appl. Phys. Lett.* **54**, 2094 (1989). These papers emphasize the role of amphoteric defects in Fermi level pinning at metal-semiconductor contacts and in semiconductors subjected to high energy irradiation.



## DEGRADATION IN II-VI LASER DIODES

Kazushi Nakano and Akira Ishibashi

Research Center, Sony Corporation, 174 Fujitsuka-cho, Hodogaya-ku,  
Yokohama 240 Japan

**Keywords :** ZnMgSSe, laser diode, degradation, recombination enhanced defect reaction.

**Abstract.** Aging studies of II-VI lasers and light emitting diodes show that these devices degrade not catastrophically, but gradually by recombination-enhanced defect reactions at pre-existing defects. The activation energy and current dependence of the degradation process in devices were examined. ZnMgSSe-based materials are stable under current injection of at least up to 2 kA/cm<sup>2</sup>, about 4 times larger than the current density needed for laser operation. Ways to improve device reliability are also discussed.

### Introduction.

ZnSe-based II-VI materials have been studied intensively because of their potential for applications as blue and green light sources for high-density optical recording systems and full-color displays. Recently Sony has achieved the writing of a 12 GB RAM (random access memory) disk with a diameter of 12 cm, using a ZnMgSSe laser diode (LD) [1]. We have improved device lifetime to 100 hours under room-temperature (RT) continuous-wave (CW) operation [2] and stability for up to 500 A/cm<sup>2</sup> has been proven [3]. Understanding the degradation mechanism is the key to further improvement.

In this paper, we first describe the rapid degradation caused by stacking faults appearing in early II-VI devices and discuss the formation of dislocation networks. We then discuss gradual degradation caused by point defects and present a kinetic model for degradation in II-VI devices.

### Rapid degradation in II-VI devices.

When we achieved the first RT CW operation in 1993, lifetime was just second order [4]. It was found that this rapid degradation was caused by the formation of highly dislocated regions[5,6]. The source of these dislocation networks is stacking faults which begin at the substrate/epilayer interface and are bounded by Frank partial dislocations with Burgers vector  $b = a/3\langle 111 \rangle$ . The dislocations formed were 60° -type with Burgers vector of the types  $a/2\langle 011 \rangle$  inclined at 45° to the (001) junction plane.

The degraded region ( Fig. 1) is thought to be formed as follows. Dangling bonds along dislocation cores are sites of nonradiative recombination. Local thermal stress, created by nonradiative recombination at the dislocation cores, assists, together with built-in stress, the dissociation formation of Frank partial dislocations into 60° -type perfect dislocation dipoles during current injection. After dissociation, dislocation networks expand, enhanced by nonradiative recombination of electron-hole pairs. Elongation along  $\langle 110 \rangle$  is thought to occur through a glide process, since the dipoles lie on {111} slip planes. On the other hand, elongation along  $\langle 120 \rangle$  might be assisted by a climb process. Since dislocation loops were found to have no stacking faults and to be of the extrinsic (interstitial) type, this climb process might occur through recombination-enhanced diffusion of interstitials during operation.

The diffusion of point defects is thought to play a role in this dislocation formation. It is interesting to note that the shape of the dislocation networks is dendritic, which also suggests the

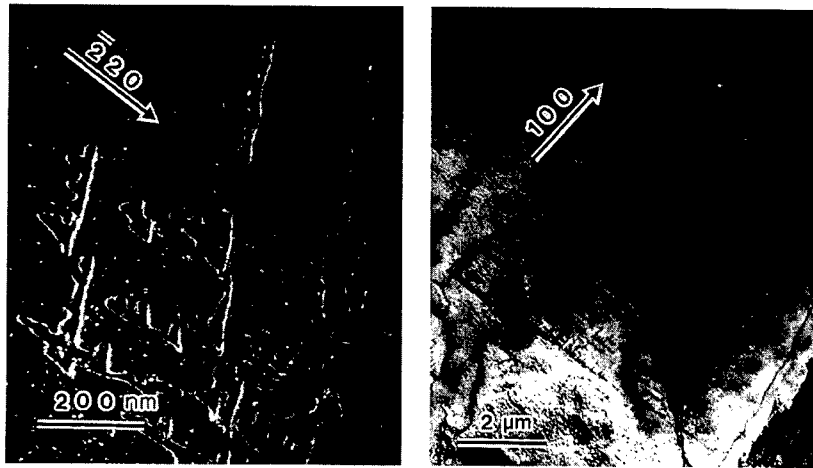


Fig. 1 Plan view TEM images showing the degraded regions.

diffusion process, since the dendritic shape is regarded as a pattern of Diffusion Limited Aggregation (DLA) [7]. From this similarity, the degradation process of dislocation formation could be one example of self-organized criticality [3].

In order to improve device lifetime, it is very important to obtain a high-quality III-V/II-VI interface, since Frank-type stacking faults originate at the substrate/epilayer interface. By introducing GaAs and ZnSe buffer layers and by optimizing growth conditions of the interface, we have achieved a stacking fault density of less than  $3 \times 10^3 \text{ cm}^{-2}$  and a device lifetime exceeding 100 hours under RT CW operation [2]. Comparing defect density and the area of the stripe electrode ( $10 \times 600 \mu\text{m}^2$ ), the 100-hr lifetime appears not to be limited by the formation of defects from stacking faults. We have entered into a stage where the operation of II-VI LDs is limited by point defects. This difference between degradation modes is also confirmed by the difference in temperature dependence of device lifetimes, as discussed later.

#### Gradual degradation process.

In order to analyze the degradation process in II-VI devices, we present a kinetic model [8] for defect generation based on the recombination-enhanced defect reaction (REDR) [9]. In the model, the time dependence of the optical output power can be determined by the following equation

$$\frac{dP}{d\tau} = -2P^2 \left( \frac{1-\eta P}{1+\eta P} \right), \quad (1)$$

where the normalized light output power  $P(t) = Bn(t)p(t)/Bn(0)p(0) = Bn^2(t)/Bn^2(0)$  ( $\therefore$  high current injection), the normalized time  $\tau = gn(0)^2 t$  and the initial radiative quantum efficiency  $\eta = Bn^2(0)/(Jed)$ . Here  $B$  is the radiative recombination coefficient,  $n$  is the carrier concentration,  $g$  is the coupling constant,  $gn(t)^2$  corresponds to the defect generation coefficient,  $J$  is the current density,  $e$  is the electron charge, and  $d$  is the active layer thickness. We assume that electron-hole ( $e-h$ ) recombination enhances the defect generation,

$$\frac{dN_d(t)}{dt} = gn(t)p(t)N_d(t) = gn(t)^2N_d(t), \quad (2)$$

where  $N_d(t)$  is the defect density. This defect-generation process is expressed by the schematic diagram in Fig. 2(a). This model leads to a time dependence of  $t^{-1}$  for the optical power when  $t \rightarrow \infty$ .

If II-VI materials are weak, degradation should behave like a weak-bond-breaking model originally developed for  $\alpha$ -Si [10]. This model corresponds to a process in which the bonds break without pre-existing defects (Fig. 2(b)). In this case, the defect generation rate depends only on the  $np = n^2$  product, namely

$$\frac{dN_d(t)}{dt} = gn(t)^2. \quad (3)$$

This model shows a time dependence of  $t^{-2/3}$  when  $t \rightarrow \infty$ , a relationship not seen in our observation as shown later. The experiments were performed under constant current aging of II-VI devices. The epitaxial layers, including a ZnCdSe/ZnSSe/ZnMgSSe separate-confinement heterostructure (SCH), were grown by molecular beam epitaxy (MBE) on n-GaAs (001) substrates. Two kinds of device structures were fabricated from these wafers. One was a standard gain-guided laser device having a stripe electrode (10- $\mu$ m width, 600- $\mu$ m cavity length). The other was a light emitting diode (LED) with a small electrode (10 x 10 or 10 x 20  $\mu$ m<sup>2</sup>) so as to avoid stacking faults within the electrode [11] and to test under the above threshold current density without lasing. Figure 3 shows aging curves of this small electrode LED at 2 mA (current density = 2 kA/cm<sup>2</sup>), which is higher than the typical threshold current density (500 A/cm<sup>2</sup>). It can be seen clearly that the slope of the decay approaches -1. The similar time dependence was also observed for laser devices. This  $1/t$  dependence is in good agreement with the theoretical curve (solid line). This model also leads to a time dependence of  $t^{-1/2}$  for the defect density  $N_d(t)$ , as  $t \rightarrow \infty$ . From this result, we can expand the stable region; i.e. the current density for which II-VI LDs degrade not catastrophically, but gradually due to REDR, at least up to 2 kA/cm<sup>2</sup>. We have shown that gradual degradation mode can be successfully explained by this model. The proposed kinetic model can be also applied to degradation due to stacking faults [8]. We next discuss the thermally activated process which determines the degradation rate. Laser

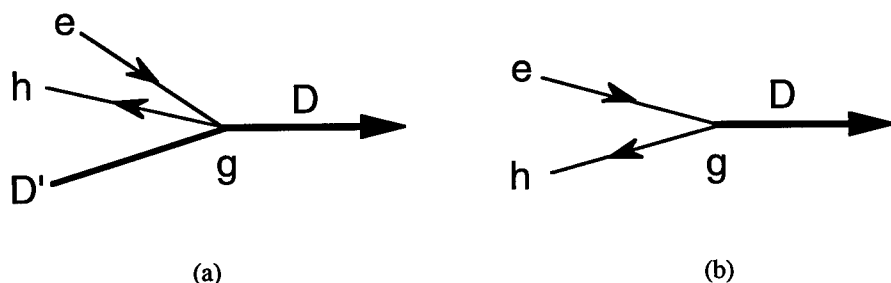


Fig. 2 Diagrams of (a) defect creation by non-radiative e-h recombination at pre-existing defect site and (b) defect generation by nonradiative recombination from the host lattice itself. D and D' are a pre-existing defect and a created defect, respectively.

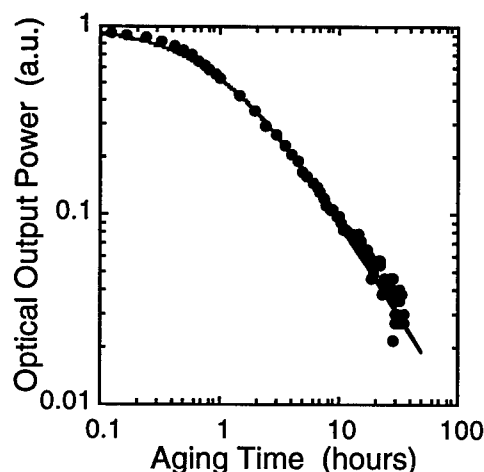


Fig. 3 Optical output power degradation of LED operated at current density of  $2 \text{ kA/cm}^2$ . Output power from a degraded central area is corrected by subtracting output from a current spread outside area. Solid line is calculated.

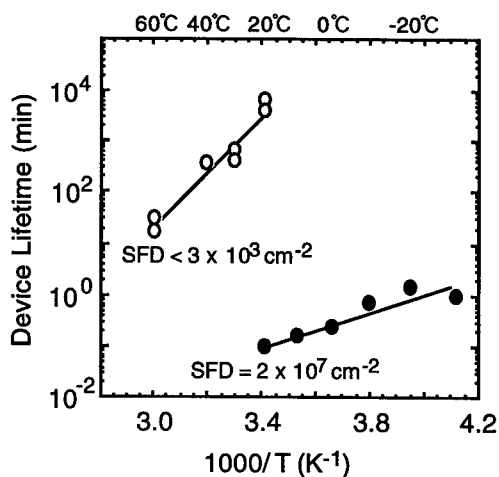


Fig. 4 Device lifetime vs  $1/T$  for samples from wafers with a low stacking fault density ( $\circ$ ) and a high stacking fault density ( $\bullet$ ).

device lifetimes are plotted as a function of reciprocal temperature in Fig. 4. From the slope of the line, the temperature dependence of device lifetime of lasers with a low density of stacking faults can be described by an activation energy of 1 eV. On the other hand, the activation energy for devices with a high stacking fault density was found to be 0.3 eV. These results clearly indicate that the coupling constants  $g$  are different for the cases of  $D' = \text{point defect}$  and  $D' = \text{stacking fault}$  in Fig. 2 (a) and that there are at least two different degradation processes in II-VI devices. These results are further evidence that the present degradation mode is not limited by pre-existing stacking faults. It is important to identify the corresponding thermally activated microscopic processes in the series of degradations in order to understand the whole degradation process. Point-defect diffusion may be involved in both degradation processes. If the same kind of point-defect diffusion is the limiting process in both cases, the activation energy should be the same, contrary to our observation. We have to consider several types of defect diffusion or clustering. Otherwise since the dislocation network formation occurs partly through the recombination-enhanced glide process, the process at 0.3 eV may correspond to this glide process. To conclude that definitely, further

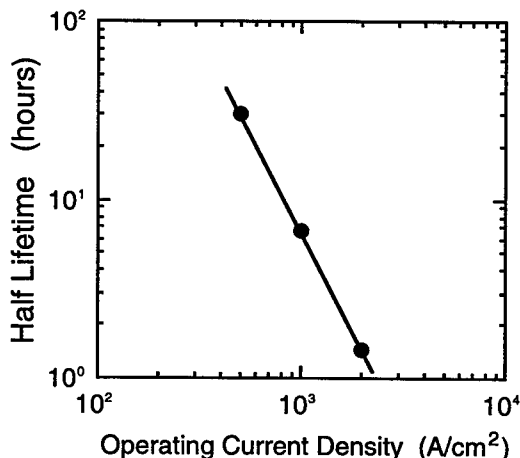


Fig. 5 Half lifetime of small electrode LEDs vs current density ( $80^\circ\text{C}$ ).

investigation is needed.

The degradation rate depends not only on temperature but also on current density. According to the kinetic model, we find that the lifetime is proportional to  $J^m$  ( $m = -0.9 \sim -2$ , which depends on the quantum efficiency). The experimental data shows  $m$  value of -2.2, which is slightly lower than expected (Fig. 5). This deviation could be explained by the effect of heating, since with increasing current, heat generation increases and accelerates the degradation process even though the ambient temperature is kept constant. Note that the degradation even at very high current injection, which is about four times higher than the laser operation current density, is thought to be limited by the same gradual degradation mechanism. This indicates that II-VI materials do not possess fatal instability even under conditions well above laser operation.

From the above discussion, we see that there are three ways to improve device reliability. The first is to lower the operation current density to suppress nonradiative  $e$ - $h$  recombination. It is effective to fabricate the index-guided laser structure so as to reduce the threshold current density  $J_{th}$ . It was found that  $J_{th}$  could be reduced to about 40 %, fabricating a channeled-substrate planar waveguide structure [12]. With this magnitude of current reduction, a several-fold increase of lifetime can be expected. The second is to reduce pre-existing defect density. The optimization of the growth conditions (e.g. growth temperature, growth rate, and II/VI flux ratio) is essential as we did for reducing stacking fault density. Although it is hard to detect point defects directly, time-resolved photoluminescence can yield information about nonradiative recombination centers [13]. Detailed study such as DLTS and ESR, to understand the microscopic structure of defects will improve our analysis of the degradation mechanism. The third is to suppress the generation and propagation of defects. One possible approach is to utilize the alloy-hardening effect. A mixture of materials with different bond lengths results in lattice rigidity. In this respect, BeZnMgSe [14] and ZnCdSSe [15] quaternary alloys are interesting candidates for cladding and active layers.

## Conclusions.

We have identified two kinds of degradation modes of II-VI LDs - the stacking fault-related mode and the point defect-related mode. Their activation energy is different. By the optimization of device structure, we are now at the stage where the operation of devices is only limited by point defects. Experimental and theoretical aging studies revealed that these devices degrade not catastrophically, but gradually by recombination-enhanced defect reactions and ZnMgSSe-based materials are stable up to 2 kA/cm<sup>2</sup>. II-VI materials, when well prepared, have good potential as light-emitting devices. The degradation can be suppressed by controlling the three limiting factors.

## Acknowledgements.

The authors would like to thank Professor S. L. Chuang of University of Illinois at Urbana-Champaign for fruitful discussions. They wish to thank S. Taniguchi, T. Hino for the MBE growth, and S. Tomiya and N. Nakayama for their measurements, and the other BLD project members for their experimental supports and fruitful discussions. They also thank T. Yamada for his encouragement of this work.

## References.

1. Unpublished. However, for 7.7 GB ROM (read only memory) disk system, see N. Eguchi and A. Ishibashi, Conference Digest of 1997 Optical Data Storage Topical Meeting (Tucson,

- 
- Arizona, USA, 1997) p. 79.
2. S. Taniguchi, T. Hino, S. Itoh, K. Nakano, N. Nakayama, A. Ishibashi, and M. Ikeda, *Electron. Lett.* **32**, 552 (1996).
  3. A. Ishibashi, M. Ukita, and S. Tomiya, 23rd International Conference on the Physics of Semiconductors, ed. M. Scheffler and R. Zimmermann (Singapore: World Scientific) pp. 3155-3162 (1996).
  4. N. Nakayama, S. Itoh, T. Ohata, K. Nakano, H. Okuyama, M. Ozawa, A. Ishibashi, M. Ikeda, and Y. Mori, *Electron. Lett.* **29**, 1488 (1993).
  5. S. Guha, J.M. DePuydt, M.A. Haase, J. Qiu, and H. Cheng, *Appl. Phys. Lett.* **63**, 3107 (1993).
  6. K. Nakano, S. Tomiya, M. Ukita, H. Yoshida, S. Itoh, E. Morita, M. Ikeda, and A. Ishibashi, *J. Electron. Mater.* **25**, 213 (1996).
  7. P. Bak, C. Tang, and K. Wiesenfeld, *Phys. Rev. Lett.* **59**, 381 (1987).
  8. S. L. Chuang, A. Ishibashi, S. Kijima, N. Nakayama, M. Ukita, and S. Taniguchi, *IEEE. J. Quantum Electron.* **33**, 970 (1997).
  9. J. D. Weeks, J. C. Tully, and L. C. Kimerling, *Phys. Rev. B* **12**, 3286 (1975).
  10. M. Stutzmann, W. B. Jackson, and C. C. Tsai, *Phys. Rev. B* **32**, 23 (1985).
  11. Y.-K. Song, A. V. Nurmikko, C.-C. Chu, J. Han, T. B. Ng, and R. L. Gunshor, *Electron. Lett.* **32**, 1829 (1996).
  12. T. Kawasumi, N. Nakayama, A. Ishibashi, and Y. Mori, *Electron. Lett.* **31**, 1667 (1995).
  13. K. Nakano, Y. Kishita, S. Itoh, M. Ikeda, A. Ishibashi, and U. Strauss, *Phys. Rev. B* **53**, 4722 (1996).
  14. A. Waag, F. Fischer, H. J. Lugauer, Th. Litz, J. Laubender, U. Lunz, U. Zehnder, W. Ossau, T. Gerhardt, M. Möller, and G. Landwehr, *J. Appl. Phys.* **80**, 792 (1996).
  15. K.-K. Law, P. F. Baude, T. J. Miller, M. A. Haase, G. M. Haugen, and K. Smekalin, *Electron. Lett.* **32**, 345 (1996).

## DEFECT CHARACTERIZATION OF II-VI COMPOUND SEMICONDUCTORS USING POSITRON LIFETIME SPECTROSCOPY

G. Tessaro and P. Mascher  
Department of Engineering Physics  
McMaster University, Hamilton, Ontario, Canada

**Keywords:** CdTe, ZnSe, positron lifetime spectroscopy, point defects

**Abstract.** Positron lifetime spectroscopy was performed on a number of Zn- and Cd-based compound semiconductors. Defects were found to be present in all samples in the mid to high  $10^{16} \text{ cm}^{-3}$  range. The defects in the Zn-based samples were primarily of divacancy type, whereas the Cd-based samples contained either monovacancy or divacancy sized defects. Illumination of the Cd-based samples before the positron measurements indicated that there are no optically active metastable defects in these undoped samples.

### Introduction.

II-VI compound semiconductors are wide, direct band gap materials that are suitable for a wide range of applications in blue-green and near infrared optoelectronic devices. These devices include LEDs and laser diodes, whose shorter wavelengths would result in dramatic improvements for optical data storage systems. For superior device performance, defects in these semiconductors must be thoroughly identified and characterized. Unlike materials such as Si and GaAs, which have been extensively studied, point defects in II-VI materials have been studied considerably less and more work is warranted.

Positron lifetime spectroscopy (PLS) is an ideal technique for studying vacancy-type defects in single crystal semiconductors. Its high sensitivity and non-destructive approach make PLS an appealing defect characterization tool.

In this report we will present the initial results of an investigation of the vacancy type defects in several single crystal Cd and/or Zn based semiconductor samples (CdTe, CdZnTe, CdTeSe, ZnSe, ZnS and ZnO) using a state of the art PLS system. These investigations include measurements at low temperatures and with *in-situ* illumination.

### Experimental Details.

Positron lifetime spectroscopy is an experimental technique used to characterize point defects in solids. It is based on the fact that a thermalized positron in a solid can be trapped at an open volume defect. This occurs due to the lack of the positive core of the atom at the vacancy, which creates an attractive potential. Once the positron is trapped at the defect its annihilation rate decreases due to the lower electron density. The resulting lifetimes and trapping rates are thus related to the size of the defects and their concentrations, respectively.

Positron lifetime spectroscopy was performed using a spectrometer with a resolution of 235 ps (FWHM) and channel widths of approximately 19 ps. An encapsulated  $^{22}\text{NaCl}$  source was used to generate the positrons. To account for annihilations in the Al foil, lifetimes of 155 and 256 ps with absolute intensities of 1.7%

and 4.4% were subtracted from the spectra. The positron lifetime spectra were analyzed using PATFIT88 [1]. Several spectra were measured for each sample and  $7 \times 10^6$  counts were taken in each spectrum to be able to resolve defect related components.

The Cd based bulk samples (CdTe, CdZnTe #1, and CdTeSe) and the bulk ZnSe were grown by II-VI Inc. using the Bridgman technique. Amistar Inc. grew the second CdZnTe #2 sample using the traveling heater method growth technique. Wafer samples of ZnSe and ZnS were grown by CrysTec Inc. All samples were nominally undoped. For the Cd based samples, spectra were measured as a function of temperature in a cryostat system. Temperatures as low as 20 K were attained. Additionally, these samples were measured after illumination with a quartz-halogen light source at low temperatures to investigate if any metastable defects were present in the undoped samples. The system is capable of illuminating with either broad band light or tunable monochromatic light by employing a monochromator.

### Results.

The positron lifetime results of the room temperature measurements are summarized in Table 1.  $\tau_{\text{bulk}}^{\text{TM}}$  is the bulk lifetime of positrons calculated from the fit parameters according to the conventional trapping model [2]. The actual bulk lifetime,  $\tau_{\text{bulk}}$ , is a materials parameter representing the lifetime of positrons in a defect-free lattice. Consistency between  $\tau_{\text{bulk}}^{\text{TM}}$  and  $\tau_{\text{bulk}}$  is used to test the validity of the trapping model. The trapping rate,  $\kappa$ , is directly proportional to the defect concentration. Low temperature measurements on the Cd-based samples were performed in darkness. They indicated no change in the trapping rates or lifetimes for these materials.

**Table 1.** Positron lifetime results for the II-VI compound semiconductors at room temperature. The results are based on the averages of several spectra. All lifetimes are in ps.

SAMPLE	$\tau_{\text{DEFECT}}$	$\tau_{\text{BULK}}^{\text{TM}}$	$\tau_{\text{AVERAGE}}$	$\kappa$ [ $\text{ns}^{-1}$ ]
ZnSe (bulk)	302 $\pm$ 9	233 $\pm$ 1	241 $\pm$ 1	0.39 $\pm$ 0.09
ZnSe (wafer)	305 $\pm$ 9	230 $\pm$ 2	240 $\pm$ 1	0.44 $\pm$ 0.12
ZnS	310 $\pm$ 8	215 $\pm$ 1	227 $\pm$ 1	0.44 $\pm$ 0.07
ZnO	298 $\pm$ 9	183 $\pm$ 1	200 $\pm$ 1	0.59 $\pm$ 0.07
CdTe	332 $\pm$ 11	280 $\pm$ 1	292 $\pm$ 1	0.65 $\pm$ 0.28
Cd <sub>0.96</sub> Zn <sub>0.04</sub> Te #1	326 $\pm$ 8	278 $\pm$ 2	288 $\pm$ 1	0.73 $\pm$ 0.29
Cd <sub>0.96</sub> Zn <sub>0.04</sub> Te #2	367 $\pm$ 17	280 $\pm$ 1	289 $\pm$ 1	0.27 $\pm$ 0.09
CdTe <sub>0.96</sub> Se <sub>0.04</sub>	360 $\pm$ 10	282 $\pm$ 1	289 $\pm$ 1	0.27 $\pm$ 0.06

The Cd -based samples were also measured after being illuminated for 6 hours with a 250W QTH lamp that was filtered to include broadband light from 0.7 to 1.3  $\mu\text{m}$ .



The goal of this experiment was to determine if any metastable defects were present in these samples. No significant change in any of the lifetime parameters was recorded during these measurements. This result was expected given the fact that the samples were undoped.

#### **Discussion.**

##### **Cd-Based Samples**

The bulk and defect lifetimes in CdTe were determined to be  $280 \pm 1$  and  $332 \pm 11$  ps, respectively. This value for the bulk lifetime is in agreement with several other publications and is now well established [3,4,5,6]. The ratio of the defect lifetime to the bulk lifetime is 1.15. This suggests that the defect is approximately the size of a monovacancy. The cadmium vacancy is most likely the defect we are detecting since it can occur in a neutral or negatively charged state which can be detected by PLS [3].

The CdTe low temperature measurements indicated no change or trend in the lifetimes or trapping rates as a function of temperature down to 20 K. This suggests that we are detecting either the neutral Cd vacancy or a Cd vacancy complexed with an impurity that results in a neutral defect. The presence of complexes is likely, given that CdTe contains high levels ( $10^{16}$  to  $10^{17}$  cm<sup>-3</sup>) of residual impurities [7]. This interpretation of a complex is further supported by the expected charge state of the defect. An isolated Cd vacancy is expected to be a double acceptor in CdTe [6]. Thus, for the undoped sample, it would most likely be negatively charged. A negative defect should display changes in the trapping rate as a function of measuring temperature, which was not the case. Stadler et al. obtained similar results when they conducted low temperature measurements on CdTe and recorded no change in the PLS results for undoped CdTe [8]. The trapping rate in CdTe corresponds to a defect concentration of approximately  $7 \times 10^{16}$  cm<sup>-3</sup>.

The results for the first CdZnTe sample (#1) are very similar to those for the CdTe sample. The defect and bulk lifetimes indicate the presence of a monovacancy sized defect with a concentration of approximately  $7 \times 10^{16}$  cm<sup>-3</sup>. The identity of the defect is most likely that of a group II monovacancy. However, the CdZnTe #2 sample from Amistar displayed significantly different results. The defect lifetime of 367 ps in this sample is considerably longer than that in the first CdZnTe sample and is indicative of a divacancy defect. This suggests that the defect profiles in CdZnTe may be very sensitive to the specific growth conditions. The defects in this sample were also neutral, given that no temperature dependencies of the lifetime parameters were measured.

The CdTeSe material's PLS results were noticeably different from the CdTe samples. The addition of 4 % of selenium resulted in the defect lifetime changing to  $359 \pm 10$  ps. This longer lifetime likely originates from a divacancy sized defect. Also, the defect concentration has decreased by a factor of three as compared to the CdTe and CdZnTe samples. These changes may be the result of conglomeration of monovacancies into divacancies due to the presence of Se or to segregation effects. There were no effects detected by low temperature measurements, thus the defects are neutral.

The illumination of the Cd-based sample prior to the positron lifetime measurement indicated no significant change in the PLS results. This suggests the lack of metastable defects in these samples. This finding is expected, given that the models for

metastable defects in CdTe and CdZnTe are associated with a specific substitutional dopant such as Cl or In [9].

### Zn-Based Samples

From Table 1 we see that there is excellent agreement between the bulk and wafer ZnSe samples. The bulk lifetime was found to be  $232 \pm 2$  ps and a defect lifetime of  $\sim 304 \pm 9$  ps was measured. The value of this defect lifetime when compared to the bulk lifetime suggests a divacancy sized defect in the material. From the trapping rates,  $\kappa$ , the concentrations of these defects were determined to be  $\sim 4 \times 10^{16} \text{ cm}^{-3}$ . The agreement between the two samples grown by different manufacturers suggests that the defect profile is not as strongly dependent on the growth technique as in the CdZnTe samples. However, further studies on a wider range of materials will be necessary to prove this.

The ZnS sample yielded a shorter bulk lifetime of  $215 \pm 1$  ps as compared to the ZnSe samples. A long defect lifetime of  $310 \pm 8$  ps was measured with a trapping rate corresponding to a concentration of  $\sim 4 \times 10^{16} \text{ cm}^{-3}$ . As with the ZnSe, this long lifetime is indicative of a larger defect of approximately the size of a divacancy.

The results for the ZnO single crystal indicate that this material's quality is far lower than that of the other Zn-based samples. The defect lifetime of  $298 \pm 9$  ps was dramatically longer than the bulk lifetime of  $183 \pm 1$  ps and is likely an average of several differently sized, small voids in the material. The total concentration of these defects was  $\sim 6 \times 10^{16} \text{ cm}^{-3}$ . This bulk lifetime reported here agrees with several other sources and is now well established [10, 11].

### Conclusion.

Defects were found in all samples in concentrations in the mid to high  $10^{16} \text{ cm}^{-3}$  range. The defects in the Zn-based samples were larger than in the Cd-based samples and were likely divacancy type defects. In the CdTe sample, the defects were neutral monovacancy or divacancy sized defects that are most likely Cd complexes. The addition of Se to CdTe results in a smaller concentration of larger, divacancy size defects. The defect profile of CdZnTe appears to be very dependent on growth conditions given that two samples of the same Zn mole fraction contained dramatically different defect profiles.

The PLS results for the Cd-based samples after illumination indicated that no metastable defects are present in these undoped samples. Investigations of doped samples are underway and will hopefully reveal considerable insight into the nature of such metastable defects.

### Acknowledgment

This work was supported by the Natural Sciences and Engineering Research Council of Canada.

### References.

1. P. Kirkegaard, N. J. Pedersen, M. Eldrup, PATFIT-88: A Data-Processing System for Positron Annihilation Spectra on Mainframe and Personal Computers, Risø National Laboratory, (1989).

2. R. N. West, *Adv. Phys.*, **22**, pp. 263 (1973).
3. C. Corbel, L. Baroux, F. M. Kiessling, C. Gély-Sykes, *Materials Science and Engineering*, **B16**, pp. 134-138 (1993).
4. R. Krause-Rehberg, Th. Drost, A. Polity, *Materials Science Forum*, **143-147**, pp. 429-434 (1994).
5. H. Zimmermann, R. Boyn, P. Rudolph, J. Bollmann, A. Klimakow, *Materials Science and Engineering*, **B16**, pp. 139-144 (1993).
6. B. K. Meyer, W. Stadler, *Journal of Crystal Growth*, **161**, pp. 119-127 (1996).
7. D. M. Hofmann, W. Stadler, P. Christmann, B. K. Meyer, *Nuclear Instruments and Methods in Physics Research*, **A380**, pp. 117-120 (1996).
8. W. Stadler, D. M. Hofmann, B. K. Meyer, R. Krause-Rehberg, A. Polity, Th. Abgarjan, M. Salk, K. W. Benz, M. Azoulay, *Acta Physica Polonica A*, **88**, pp. 921-924 (1995).
9. Y. Y. Shan, K. G. Lynn, Cs. Szeles, P. Asoka-Kumar, T. Thio, J. E. Bennett, C. B. Beling, S. Fung, P. Becla, "Paper from ICPA-11" (1997).
10. J. Zhong, A. H. Kitai, P. Mascher, W. Puff, *J. Electrochem. Soc.*, **140**, pp. 3644-3649 (1993).
11. W. Puff, S. Brunner, P. Mascher, A. G. Balogh, *Mat. Res. Soc. Symp. Proc.*, **378**, pp. 977-982 (1995).

## DEFECT STRUCTURES IN HEAVILY In-DOPED II-VI SEMICONDUCTORS

V. Ostheimer, T. Filz, J. Hamann, St. Lauer, D. Weber, H. Wolf, and Th. Wichert  
*Technische Physik, Universität des Saarlandes, Saarbrücken, Germany*

Keywords: II-VI compounds, donors, Indium, A-centre, compensation, PAC

### Abstract

Dependent on the In-concentration, ranging from  $10^{16} \text{ cm}^{-3}$  to  $10^{20} \text{ cm}^{-3}$ , two different types of In-defect complexes were observed in ZnS, CdS, ZnSe, CdSe, ZnTe, and CdTe. The local atomic configurations of the defects formed with In-donors were investigated by perturbed  $\gamma\gamma$  angular correlation spectroscopy. For ZnS and ZnSe a reversible transition between the two defect structures occurs in the temperature range from 100 K to 300 K. The results are discussed in terms of two structural and electronic configurations of the cation vacancy.

### Introduction

The key issue for the technological application of II-VI semiconductors is the control of their doping properties. For several decades the fabrication of low resistive *p*-type and *n*-type II-VI compounds has been a main topic of semiconductor research. Whereas *p*-type doping turned out to be a severe problem in the case of ZnS, ZnSe, CdS, and CdSe, the *n*-type doping of these compounds can be done by introducing group III elements (Al, In, Ga) or halides (Cl, Br, I). In contrast, ZnTe can be doped *p*-type but it is difficult to achieve *n*-type conductivity [1]. In recent years, there has been significant progress in *p*-doping of e.g. ZnSe, using atomic nitrogen as a dopant source together with ultrapure growth techniques like MBE [2]. Nevertheless, the fundamental physical properties, determining the achievable doping level and the compensation mechanisms for different dopants in the respective compounds are still open questions.

The maximum electron concentration, which has been reached, is about  $n = 10^{19} \text{ cm}^{-3}$  in ZnSe using chlorine [2] and about  $n = 10^{18} \text{ cm}^{-3}$  in the Te-based compounds (with the exception of ZnTe) using indium or iodine as dopants [3]. As mechanisms responsible for the limited efficiency of *n*-doping the formation of intrinsic acceptor like defects, e.g. cation vacancies, the compensation by residual impurities, and the limited solubility of donor atoms are discussed.

The compensation of the donor In, as a representative of the group III donors, is investigated on an atomic scale by applying the locally sensitive perturbed  $\gamma\gamma$  angular correlation (PAC) technique. Using radioactive  $^{111}\text{In}$  as a probe atom, the influence of intrinsic or extrinsic defects, relaxations, or precipitations on the local charge density is detected by their characteristic electric field gradients (EFG).

### Experimental Details

The PAC technique is based on the hyperfine interaction of suitable radioactive nuclei with the EFG caused by the surrounding charge distribution. The decay of the nuclei implies a  $\gamma\gamma$  cascade populating the isomeric level of a daughter nucleus, which is used for the PAC experiment. For the experiments presented here, the probe  $^{111}\text{In}$  is employed, which is a donor on a cation site in II-VI semiconductors. It decays into  $^{111}\text{Cd}$  being isoelectronic or identical to the group II

constituent of the investigated compounds. The interaction between the quadrupole moment  $Q$  of the isomeric  $I = 5/2$  level of  $^{111}\text{Cd}$  and the external EFG yields the three frequencies  $\omega_1$ ,  $\omega_2$ , and  $\omega_3 = \omega_1 + \omega_2$  in the PAC time spectrum  $R(t)$ , which is described by:

$$R(t) = A_2 \left[ f \cdot (S_0 + \sum_{n=1}^3 S_n \cos \omega_n t) + (1-f) \right]. \quad (1)$$

The spectrum is measured by detecting the two  $\gamma$ -rays of the cascade in coincidence. The largest component of the traceless EFG tensor,  $V_{zz}$ , is usually expressed by the quadrupole coupling constant  $\nu_Q = eQV_{zz}/h$ , which is proportional to  $\omega_1$ . The asymmetry parameter  $\eta = (V_{xx} - V_{yy})/V_{zz}$  is deduced from the frequency ratio  $\omega_2/\omega_1$  and satisfies the condition  $0 \leq \eta \leq 1$ . The frequencies  $\omega_n$  can be directly obtained from the Fourier transform  $F(\omega)$  of the time spectrum  $R(t)$ . The coefficients  $S_0$  and  $S_n$  depend on the orientation of the EFG tensor with respect to the detectors. In this way the orientation of the observed defect complex within the host lattice can be determined. The factor  $f$  denotes the relative fraction of  $^{111}\text{In}$  atoms that is associated with this EFG. The factor  $A_2 = -0.14$  describes the spatial anisotropy of the emission of the second  $\gamma$ -quant with respect to the first  $\gamma$ -quant. A detailed description of the PAC spectroscopy is found in [4].

It should be noted that in a PAC experiment the EFG is observed after the radioactive decay at the  $^{111}\text{Cd}$  nucleus within the following 500 ns, whereas the formation of the complex happens at the parent isotope  $^{111}\text{In}$ . The local atomic and electronic configuration is assumed to be adapted to the new local structure within few picoseconds after the radioactive decay. The EFG, therefore, is determined by the charge distribution in the surrounding of the  $^{111}\text{Cd}$  atom. Consequently, the PAC experiments in II-VI semiconductors deliver information about the complex formation at the donor  $^{111}\text{In}$  and about the structure of isolated defects in the neighbourhood of the isoelectronic  $^{111}\text{Cd}$  atom.

The II-VI semiconductors were simultaneously doped by diffusion with radioactive  $^{111}\text{In}$  (about  $5 \cdot 10^{11}$  atoms) and stable In. The temperature was 1070 K, or 900 K in case of CdTe. The diffusion time ranged from 90 min up to 5 days. The In concentration was controlled by adding small amounts of In during the diffusion, which were evaporated as dots onto quartz, each containing  $4 \cdot 10^{15}$  In atoms. For homogenous doping of bulk crystals, pieces of In metal were used instead of the dots. The total number of In atoms, incorporated into the crystals, was determined via the radioactive tracer  $^{111}\text{In}$ . Additionally, CdTe layers *in-situ* doped with radioactive and stable In during metalorganic chemical vapour deposition (MOCVD) were investigated. The layers were grown on GaAs substrates using the precursors dimethylcadmium (DMCd), diisopropyltellurium (DiPTe), and trimethylindium (TMIn).

## Results and Discussion

PAC experiments in II-VI compounds doped exclusively with radioactive  $^{111}\text{In}$  ( $[\text{In}] < 10^{16} \text{ cm}^{-3}$ ) have shown the formation of  $\text{In}_M\text{-V}_M$  pairs as a common phenomenon in all of these semiconductors [5]. These In-defect complexes are subsequently denoted as 'type I'. The observed cation vacancies  $\text{V}_M$  are produced either by thermal treatment or by electron irradiation. The same complexes (A-centres), formed between a donor and a cation vacancy, were observed by EPR e.g. in the case of ZnSe, ZnS [6] and CdTe [7] doped with group III or group VII elements.

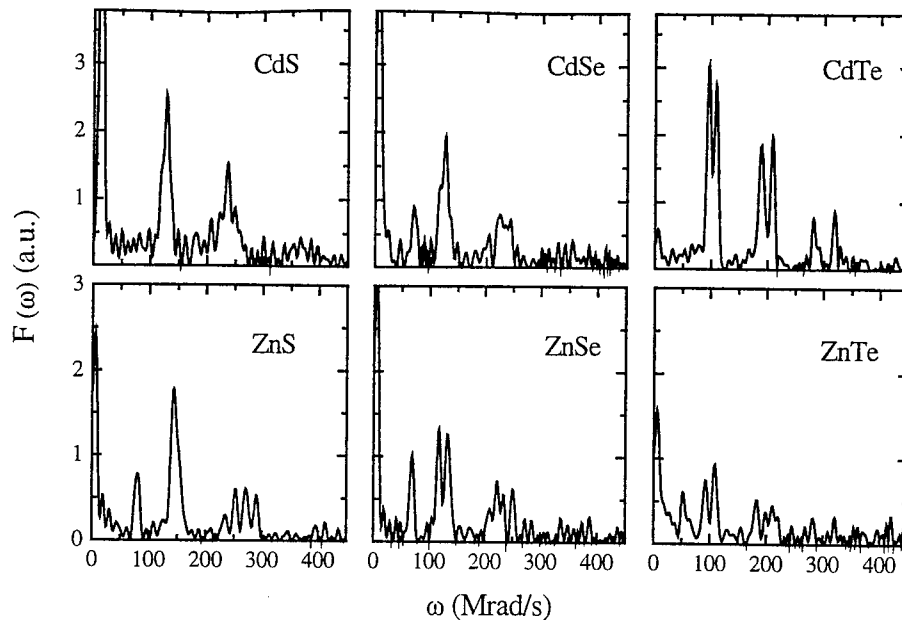


**Fig. 1** Characteristic EFG corresponding to type II complexes that are related to the cation vacancy in highly In-doped II-VI compounds.

Increasing the In-concentration by adding stable In leads to the observation of new EFG when the doping level exceeds about  $[In] = 10^{18} \text{ cm}^{-3}$ . In all II-VI compounds the frequencies  $\nu_Q$  are nearly twice as large as those produced by the known cation vacancies (type I). In addition, the corresponding defects, denoted in the following as type II, are characterised by up to three, slightly different EFG (table I). This feature is common to all investigated II-VI semiconductors. In case of CdS:In and CdTe:In, the same EFG were also reported by Magerle [8] and Wegner [9], respectively.

type II			type I [5]	
compound	$\nu_Q$ (MHz)	$\eta$	$\nu_Q$ (MHz)	$\eta$
CdS	125	0.25	72.5	0.35
			79.0	0.21
CdSe	116	0.15	66.5	0.32
	126	0.2	71.0	0.05
CdTe	100	0.0	60.0	0.10
	103	0.0		
	113	0.18		
ZnS	136	0.3	81.5	0.16
	144	0.2		
	152	0.03		
ZnSe	118	0.18	72.0	0.05
	121	0.0		
	132	0.2		
ZnTe	95	0.0	60.0	0.01
$[In] > 10^{18} \text{ cm}^{-3}$			$[In] < 10^{18} \text{ cm}^{-3}$	

**Table I:** EFG of cation vacancies in II-VI compounds, which were doped by diffusion with different concentrations of In. The EFG ( $T_M = 300 \text{ K}$ ) were measured at the probe  $^{111}\text{In}/^{111}\text{Cd}$ . The relative errors are about 1 % for  $\nu_Q$  and about 10 % for  $\eta$ .

The influence of the growth and doping technique on the formation of the observed type II defect complex was investigated in CdTe layers doped *in-situ* with  $^{111}\text{In}$  atoms and stable In during MOCVD growth. In layers grown at  $T_g = 663\text{ K}$  with a DiPte:DMCd ratio of 3:1, the In-concentration as determined via the radioactive tracer  $^{111}\text{In}$ , was  $5 \cdot 10^{20}\text{ cm}^{-3}$ . The PAC spectra of these CdTe layers show a fraction of about 10 % of the probe atoms to be located within the type II defect structure. Increasing the growth temperature to  $T_g = 693\text{ K}$ , however, the formation of the compound InTe is observed, which is identified by its characteristic EFG of  $\nu_Q = 24\text{ MHz}$ ,  $\eta = 0$  [10]. Since the In-concentration is determined to be more than  $10^{21}\text{ cm}^{-3}$  in this case, a segregation of InTe is plausible. When the DiPte:DMCd ratio is reduced to 1:1 at the same growth temperature, the formation of In-precipitates, characterised by  $\nu_Q = 17.5\text{ MHz}$ ,  $\eta = 0$  [11], is detected.

In CdTe epilayers the degree of compensation of the donor In was also investigated by Hall-effect measurements. In this case, the concentration of stable In was determined with help of SIMS measurements. In as grown layers, the highest conductivity is achieved for  $[\text{In}] = 2 \cdot 10^{18}\text{ cm}^{-3}$ , with a carrier concentration of  $n = 10^{16}\text{ cm}^{-3}$ . Increasing the In-concentration further, the carrier concentration  $n$  decreases again. This result can be correlated with PAC measurements, which yield that most of the In atoms in as grown layers are not located on unperturbed substitutional lattice sites. By annealing these layers at  $T_a = 700\text{ K}$  under Cd-vapour, the carrier density is increased up to  $n = 2 \cdot 10^{18}\text{ cm}^{-3}$ , corresponding to a conversion of almost all of the introduced In atoms into electrically active donors. The same doping limit is reported by Bassani et al. for In-doped CdTe layers grown by MBE using excess Cd [3].

PAC investigations performed at CdTe crystals under annealing conditions similar to those used for the Hall-measurements reveal the formation of type II complexes. After annealing the crystals under Cd-vapour these defects disappear almost completely. Subsequent annealing under Te-vapour again leads to an increase of the defect fractions. This behaviour indicates that the type II defect complex also contains a Cd-vacancy, because it is removed or produced by annealing under Cd- or Te-vapour respectively.

PAC measurements in CdTe show that the orientation of the EFG tensor does not change when the EFG changes from type I to type II. In both cases the orientation of the EFG tensor is almost along the  $\langle 111 \rangle$ -direction of the lattice. The  $\langle 111 \rangle$ -orientation has been explained by the fact that the charge of the cation vacancy is located on the neighbouring Te-atoms [5]. Thus the orientation of the type II defect would be as expected if besides the  $^{111}\text{In}$  probe a single cation vacancy is involved.

For the type II defect complex in CdS, the complex  $^{111}\text{In}_{\text{Cd}}\text{-V}_{\text{Cd}}\text{-In}_{\text{Cd}}$  has been proposed by Magerle et al. [8]. When the high doping level was generated by Ga instead of by In in our experiments, however, the identical EFG are observed in all II-VI compounds. If it is assumed that Ga, which is chemically very similar to In, forms an equivalent complex, a different EFG would be expected for the complex  $^{111}\text{In}_{\text{Cd}}\text{-V}_{\text{Cd}}\text{-Ga}_{\text{Cd}}$  in CdS. It is therefore concluded that the type II defect complex does not correspond to a  $^{111}\text{In}_{\text{Cd}}\text{-V}_{\text{Cd}}\text{-In}_{\text{Cd}}$  complex.

These experimental results indicate, that the type II defect complex consists of a single In-atom and a cation vacancy. Thus a close relation of this defect complex to the A-centre is indicated. The constituents of both defect types are supposed to be the same, whereas the structural and electronic configuration of the observed defects are different.

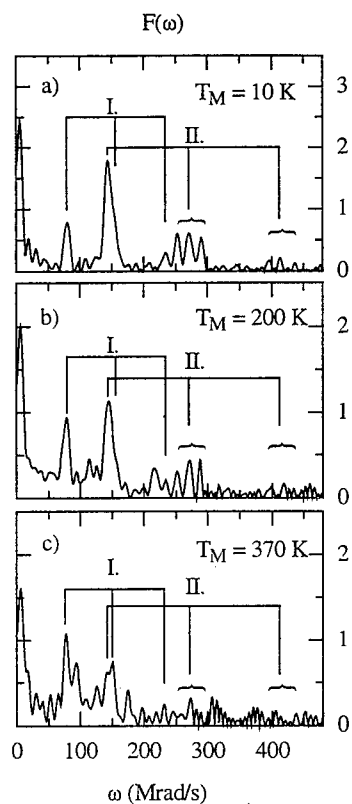


Fig. 2: Fourier transforms of PAC spectra measured at different temperatures in a ZnS crystal containing more than  $10^{18}$  In  $\text{cm}^{-3}$ .

The results of PAC measurements in ZnS as a function of the sample temperature during the measurement confirm the close structural relation of the type II defect complex to the A-centre. ZnS crystals doped moderately with In-donors show the simultaneous formation of the type I and type II defect complexes and a reversible transition between them depending on the sample temperature (fig. 2, fig. 3). Below  $T_M = 100$  K the In atoms are mostly located within the type II defect complex, whereas above up  $T_M = 250$  K the type I defect is preferred. Similar transitions between both defect complexes are observed in ZnSe, ZnTe, and CdSe, whereas in CdTe no such transition between the type I and type II defect has been observed, up to now.

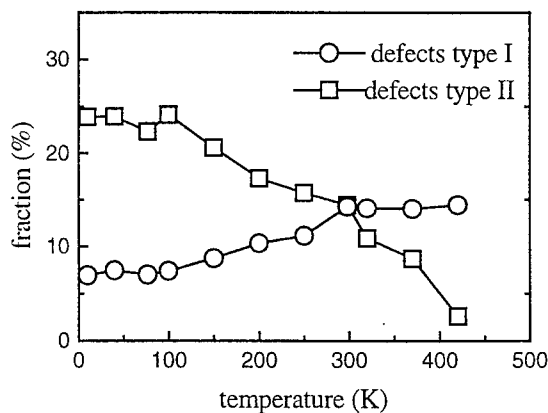


Fig. 3 The relative fraction of defect types I and II in ZnS as a function of the sample temperature.

The reversible transition between the type I and type II complexes upon change of the sample temperature as well as the identity of the EFG measured in In- or Ga-doped crystals clearly show that the type II complex also consists of only one In-atom and one cation vacancy. The magnitude of the EFG corresponding to this  $^{111}\text{Cd}$ -defect complex could be related to two different effects: Firstly, the local arrangement of the atoms surrounding the cation vacancy is changed or, secondly, the electrical charge state of the vacancy is altered due to a different position of the Fermi-level.

It should be recalled that the EFG is always measured at the isoelectronic  $^{111}\text{Cd}$  daughter isotope. Thus the cation vacancies are no longer part of the originally formed  $^{111}\text{In}_M\text{-V}_M$  complex. Provided that the electronic level associated with the  $\text{V}^{-/2-}$  defect is located in the upper half of the bandgap, it is reasonable to assume that the charge state of the vacancy changes under the present experimental conditions: If most of the In-donors are compensated by acceptor-like cation vacancies in weakly In-doped crystals, the Fermi level is located below the  $\text{V}^{-/2-}$ -level, so that the charge state  $\text{V}^-$  is observed. When the donor concentration increases, the Fermi level passes the  $\text{V}^{-/2-}$  level and the doubly charged vacancy  $\text{V}^{2-}$  is observed. For CdTe, the position of the  $\text{V}^{-/2-}$  level has been determined by Marfaing et al. [12] to  $E_V + 0.9$  eV, which is in the upper half of the bandgap and



supports this interpretation. Nevertheless lower values are reported in the literature, e.g. by Emanuelson et al., who determined the level position to  $E_V + 0.47$  eV [13]. Since the crystals were doped by diffusion, the donor-concentration is not homogeneous across the sample. Therefore, it is possible that type I and type II defects are observed simultaneously in one crystal and that the transition between the two defect types occurs over a wide temperature range between 100 K and 300 K. The occurrence of three EFG characterising the new defect structure, however, is not yet fully understood within this model. It may be caused by an additional lattice distortion around the cation vacancy when the charge state is changed.

### Summary and Outlook

It has been shown that in II-VI semiconductors cation vacancies passivate the donor In. Depending on the doping level and the sample temperature, two different configurations of the cation vacancy are observed after the decay of the radioactive probe  $^{111}\text{In}$  into  $^{111}\text{Cd}$ . This effect is common to all investigated II-VI semiconductors and is independent of the nature of the used donor atoms. In a preliminary model it is assumed that the vacancy is singly charged in weakly In-doped crystals and doubly charged in the highly In-doped crystals. In order to investigate the influence of the donor element on the charge state and the configuration of the vacancy more comprehensively, PAC experiments in II-VI compounds doped with group VII elements are in preparation. Additionally, the atomic configurations of the vacancies belonging to the different EFG, will be examined by theoretical calculations of the corresponding EFG.

We would like to thank the Technion Institute in Haifa, Israel, for the performance of SIMS measurements in CdTe and the German Bundesminister für Bildung und Forschung for the support of this work under grant Wi3SAA.

### References

- [1] Y. Fan, J. Han, L. He, R.L. Gunshor, M.S. Brandt, J. Walker, N.M. Johnson, and A.V. Nurmikko *Appl. Phys. Lett.* **65** 1001 (1994)
- [2] K. Ohkawa, A. Ueno, and T. Mitsuyu, *J. Crystal Growth* **117**, 375 (1992)
- [3] F. Bassani; S. Tatarenko, K. Saminadayar; N. Magnea; R. T. Cox; A. Tardot; and C. Grattapain *J. Appl. Phys.* **72** 2927 (1992)
- [4] Th. Wichert, N. Achtziger, H. Metzner, and R. Sielemann in *Hyperfine Interaction of Defects in Semiconductors*, Ed. G. Langouche Elsevier Science Publisher B.V., 1992
- [5] Th. Wichert, Th. Krings, and H. Wolf *Physica B* **185**, 297 (1993)
- [6] J. Schneider, *Mater. Res. Soc. Symp. Proc.* **46**, 13 (1985)
- [7] D. M. Hofmann, P. Omling, H.G. Grimmeiss, B.K. Meyer, K.W. Benz, and D. Sinerius *Phys. Rev. B* **45**, 6247 (1992)
- [8] R. Magerle, M. Deicher, U. Desnica, R. Keller, W. Pfeiffer, F. Pleiter, H. Skudlik, and Th. Wichert, *Appl. Surf. Sci.* **50**, 159 (1991)
- [9] D. Wegner and E.A. Meyer *J. Phys. Condensed Matter* **1**, 5403 (1989)
- [10] M. Frank, F. Gubitz, W. Ittner, W. Kreische, A. Labahn, B. Röseler, G. Weeske *Z. Naturforsch.* **41a** 104 (1986)
- [11] H. Haas, D.A. Shirley, *J. Chem. Phys.* **58** 3339 (1973)
- [12] Y. Marfaing, *Revue de Physique Appliquée* **12**, 211 (1977)
- [13] P.E. Emanuelson, P. Omling, B.K. Meyer, M. Wienecke, and M. Schenk *Phys. Rev. B* **47** 15578 (1993)

## THE ROLE OF CATION VACANCY IN COMPENSATION OF II-VI COMPOUNDS BY FAST DIFFUSORS - EXAMPLE of Cu in CdS

U.V. Desnica, I.D. Desnica-Franković, R. Magerle<sup>1</sup>, A. Burchard<sup>1</sup> and M. Deicher<sup>1</sup>

R. Bošković Institute, Phys. Dept., Bijenička 54, 10000 Zagreb, Croatia

<sup>1</sup>Fakultät für Physik, Universität Konstanz, D-78434, Konstanz, Germany

**Keywords:** CdS, II-VI, Cu, Li, In, cation vacancy, PAC, compensation, fast diffusers

### Abstract

Defects responsible for compensation of CdS doped with fast diffusers were studied using perturbed angular correlation spectroscopy (PAC). Cu was evaporated on CdS containing <sup>111</sup>In probe atoms, and annealed at room temperature (RT). This resulted in gradual increase of pairing between substitutional <sup>111</sup>In atoms and native cadmium vacancies, V<sub>Cd</sub>, up to 100% in cca 7 days period. The model is presented which explains these results as well as electrical compensation of CdS by Cu: The RT in-diffusion of Cu donors into CdS provokes simultaneous in-diffusion of cadmium vacancies, which are double acceptors. Hence Cu compensates CdS crystal indirectly, by bringing into the crystal new V<sub>Cd</sub>, that pair with existing donors causing their electrical compensation. Model explains consistently experimental results on Cu doped CdS and also reconciles two widely accepted but apparently contradictory assumptions: one, that Cu in CdS is a fast diffuser which moves as an interstitial, and hence is a donor, and the other, that Cu compensates donors in CdS and hence effectively acts as an acceptor.

### Introduction

Fast diffusers (Cu, Ag, Au, Li,) are important impurities or dopants in practically all semiconductors. They are characterized by their ease to penetrate into the material[1-10]; often in an uncontrollable way. Particularly, it is well known that Cu dramatically influences electrical, optical and photoelectronic properties (compensation, luminescence, photoconductivity, photosensitivity, carrier lifetime, etc.) of CdS[8,11].

Cu is a very fast diffuser in CdS [1-10], as shown in radio-tracer experiments [4,5], by capacitive technique[7,10], ultrasonic technique[1,2], changes in electrical conductivity[3,9], in photovoltaic properties[8] or photo-acoustic spectroscopy[3]. In all reports the diffusion coefficient was always very high:  $D_{Cu}(T) = 1.2 \times 10^{-2} \exp(-1.05 \text{ (eV)/kT})$ [1]; or  $D_{Cu}(T) = 2.1 \times 10^{-3} \exp(-0.96 \text{ (eV)/kT})$ [7]; or  $D_{Cu}(T) = 1.6 \times 10^{-3} \exp(-0.77 \text{ (eV)/kT})$  [5]. As a consequence, Cu penetrates readily into CdS even at quite low diffusion temperatures[5,6,7,8]. For example, for diffusion temperature of only 250°C the diffusion from the Cu<sub>x</sub>S film into CdS single crystal resulted in Cu penetration of several tenths of microns in only 30 minutes[6], while for the diffusion from the evaporated pure Cu film the penetration of 8 microns in 10 h was reported[7]. Even at room temperature, RT, Cu penetrates considerably: 20 nm in 2 days, 150 nm in 30 days and 200 nm in 120 days[10]. Cu enters easily in both single crystal CdS[1,2,3,6,7,9] and in CdS film[10,12]. Fast in-diffusion of Cu was reported both from pure Cu evaporated on CdS[1,2,3,7,9,10] and from Cu<sub>x</sub>S layer formed on CdS as a copper source[6,10,12]. To explain such an extremely high diffusivity it is generally believed that Cu moves through CdS as an interstitial.

Considering electrical properties, the Cu in-diffusion transforms n-type CdS into a highly compensated material[1,2,5,8,13]. Therefore the effective electrical action of copper in CdS is clearly acceptor-like. Isolated substitutional Cu in CdS is a deep acceptor trap, with an energy level at 1.20 eV above the valence band[11]. Hence when considering defects that can compensate donors and convert n-CdS into electrically compensated, highly resistive material, the substitutional Cu, Cu<sub>Cd</sub>, is a natural choice[1,2,14,15]. This selection is also in accordance with the previous

reports that Cu related compensating defects are deep traps[1,2,6,7]; estimated to be at last 0.3 eV and up to 1.1 eV above the valence band[7].

Heretofore, no plausible explanation has been offered to overcome this apparent contradiction, (Cu as a fast diffusor is a donor in interstitial position, while as a compensating defect Cu is an acceptor in substitutional position) and no conclusive experimental evidences have been reported to explain this problem, particularly not at the atomic level.

In this paper the microscopic mechanism of compensation of donors in CdS by fast diffusor Cu is reported. Along the course of our detailed studies of In doped CdS, we have learned how to introduce In atoms in CdS and position them in a controlled way either exclusively in unperturbed, substitutional  $\text{In}_{\text{Cd}}^+$  sites, or partly in  $\text{In}_{\text{Cd}}^+$  site and partly paired with  $\text{V}_{\text{Cd}}$ , i.e. in  $(\text{In}_{\text{Cd}}^+-\text{V}_{\text{Cd}}^{2-})^-$  complex[16]. The former of these two different In configurations is a donor in CdS while the later is an acceptor. Hence they represent two different types of possible traps for diffusing Cu atoms.  $\text{In}_{\text{Cd}}^+$  could attract and bind by a coulombic attraction Cu atom in any acceptor-like position ( $\text{Cu}_{\text{Cd}}$ , for example), while  $(\text{In}_{\text{Cd}}^+-\text{V}_{\text{Cd}}^{2-})^-$  acceptor can attract and bind Cu atom in any donor-like position ( $\text{Cu}_i$ , for example).  $(\text{In}_{\text{Cd}}^+-\text{V}_{\text{Cd}}^{2-})^-$  also offers a potential recombination site for diffusing Cu atom, which would result in the neutral complex  $(\text{In}_{\text{Cd}}^+-\text{Cu}_{\text{Cd}})$ . Any of these possible new complexes would result in a distinct electric field gradient (EFG) on probe atom  $^{111}\text{In}$ , and in PAC spectra a new frequency would appear, characteristic for this particular defect.

### Experimental procedures

CdS samples were prepared from the commercial, undoped single crystal CdS in several steps: First, approx.  $10^{11}/\text{cm}^2$   $^{111}\text{In}$  atoms were implanted at 350 keV. This small dose is too low to affect the concentration of residual donors in undoped CdS crystal, but inserts enough nuclear probe atoms to enable the use of PAC. Secondly, the samples were annealed under S pressure at 700°C to position  $^{111}\text{In}$  probe partly in a substitutional Cd place,  $\text{In}_{\text{Cd}}^+$ , and partly in complexes  $(\text{In}_{\text{Cd}}^+-\text{V}_{\text{Cd}}^{2-})^-$  [16]. Both sites are characterized in PAC spectra with a characteristic coupling constants (frequencies) 7.4 MHz and 72&79 MHz, respectively. Two close frequencies, 72&79 MHz, arise from small difference in distance between In and  $\text{V}_{\text{Cd}}$  in basal plane and out of it [16]. Then the Cu layer (32 nm thick) was evaporated on the implanted and annealed surface of CdS, to serve as an infinite source of Cu atoms. PAC spectra were measured periodically after Cu evaporation in order to determine the effect of RT annealing on PAC signals.

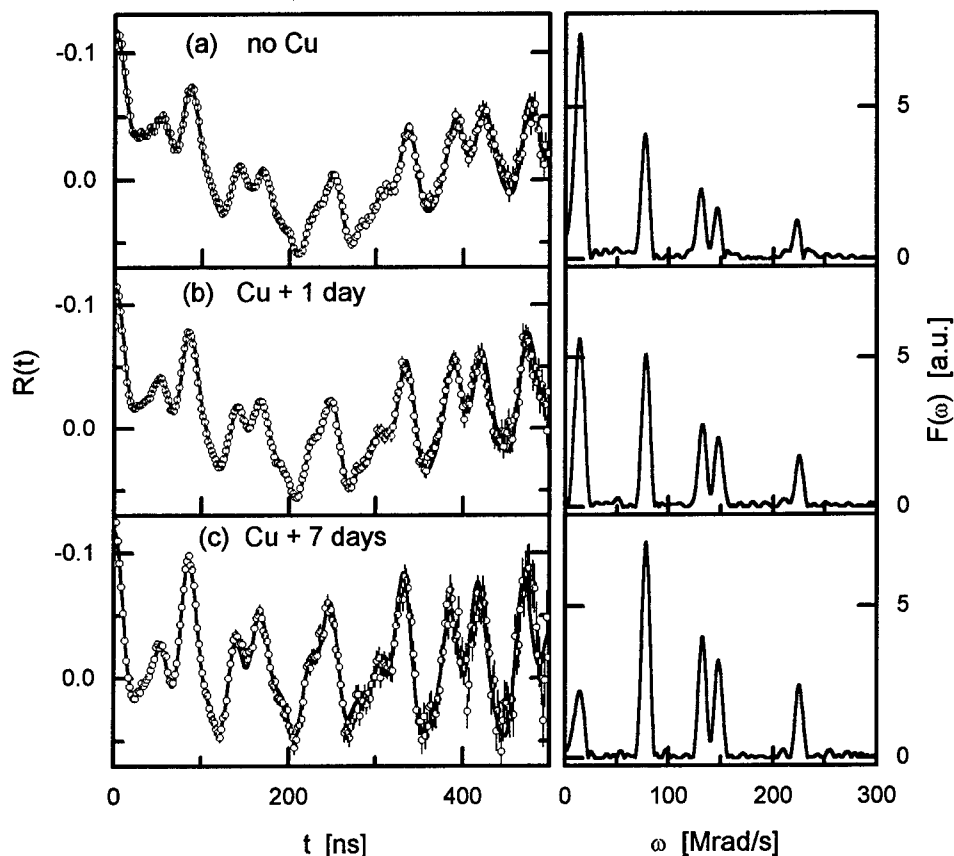
### Results

Figure 1.a shows PAC spectrum and its Fourier transform before Cu evaporation, i.e. after implantation and annealing which positioned  $^{111}\text{In}$  probe atoms in both donor and acceptor sites. The initial fractions of the  $\text{In}_{\text{Cd}}^+$  donors and  $(\text{In}_{\text{Cd}}^+-\text{V}_{\text{Cd}}^{2-})^-$  acceptor pairs were approximately equal. Annealing of the sample at RT for a number of days did not change this ratio. Several hours after Cu evaporation spectrum 1.b was taken. There is no new, Cu related frequency. The only difference in comparison with the initial spectrum is slight increase of  $(\text{In}_{\text{Cd}}^+-\text{V}_{\text{Cd}}^{2-})^-$  pair fraction at the expense of  $\text{In}_{\text{Cd}}^+$  fraction. Spectrum 1.c, taken after one week RT annealing, shows further strong increase of  $(\text{In}_{\text{Cd}}^+-\text{V}_{\text{Cd}})$  pairs, almost to 100%, with practically no  $\text{In}_{\text{Cd}}^+$  atoms remaining unpaired. Again, no new, Cu related frequency was observed.

Figure 2 summarizes the effects of annealing on Cu doped and undoped CdS. As shown in Fig. 1, for Cu doped samples RT is sufficient to provoke an appearance of  $\text{V}_{\text{Cd}}$  and their pairing with In. On the contrary, for undoped CdS samples the annealing temperatures above 400-450°C are needed for  $\text{V}_{\text{Cd}}$  to appear, and even that occurs only under favorable annealing conditions (low chemical potential of cadmium, which was in present experiments obtained via S over-pressure during annealing).

### Discussion

Since fast diffusing Cu interstitial is expected to be a donor, the crucial question arises: how does Cu in CdS effectively acts as an acceptor, as required to explain electrical measurements? Hitherto,



**Figure 1:** PAC time spectra,  $R(t)$ , and their Fourier transforms,  $F(\omega)$ .

a) after implantation of  $^{111}\text{In}$  and annealing under  $S$  pressure at  $700^\circ\text{C}$ , b) 6 hours after  $\text{Cu}$  evaporation, c) 7 days after  $\text{Cu}$  evaporation; annealing at room temperature

the only proposed solution was a  $\text{Cu}_{\text{Cd}}$  acceptor[1,2,14,15]. During  $\text{Cu}$  diffusion in  $\text{CdS}$  the  $\text{Cu}_{\text{Cd}}$  defect can be created in two ways: (i) by filling in an already existing cadmium vacancy, or (ii) by kicking out one  $\text{Cd}$  atom from its substitutional site, and exchanging places. Both explanations have been invoked to account for the effect of electrical compensation but have never been proved by some independent experiment.

(i) The first assumption requires a preexistence of free  $\text{Cd}$  vacancies in the crystal. During indiffusion  $\text{Cu}_i$  would stumble across such a  $\text{V}_{\text{Cd}}$  and would be trapped in it. However, due to thermodynamical requirements the intrinsic, equilibrium concentration of  $\text{V}_{\text{Cd}}$  at RT should be extremely low[13,17]. Furthermore, the isolated  $\text{V}_{\text{Cd}}$  is a double acceptor in  $\text{CdS}$ [13,17-19] and other II-VI's. Hence its concentration has to be lower than the net residual donor concentration, since undoped as-grown  $\text{CdS}$  is always n-type. Besides, the recombination of  $\text{V}_{\text{Cd}}$  with diffusing  $\text{Cu}$  atoms would reduce its negative charge by creating singly ionized acceptors  $\text{Cu}_{\text{Cd}}$ , and  $\text{CdS}$  would become more n-type - not semi-insulating, as observed experimentally[1,2,5,8,13].

An alternative to the single  $\text{V}_{\text{Cd}}$  concept is some  $(\text{D}^+ \cdot \text{V}_{\text{Cd}})^{\cdot-}$  complex, where  $\text{D}$  denotes some unspecified donor. In that case the concentration of  $\text{V}_{\text{Cd}}$  can be considerably higher than its intrinsic value[13,20-23], being essentially determined by these donor concentration. That hypothesis can be checked experimentally at the microscopic level with the PAC method, as demonstrated in this

paper: we created the  $(\text{In}_{\text{Cd}}^+ - \text{V}_{\text{Cd}}^{2-})^-$  trap, offering it to the diffusing Cu interstitials. Should the Cu atom be trapped in such a complex then a new complex,  $(\text{In}_{\text{Cd}} - \text{Cu}_{\text{Cd}})$ , would be formed, which would produce a new and distinctive PAC frequency. However, as shown in Fig. 1 such interaction did not take place.

(ii) The second possibility, the interstitial-substitutional mechanism[2], has also a very serious drawback: The result of kicking out the Cd atom from its lattice site would result, in an acceptor  $\text{Cu}_{\text{Cd}}$ . However, an interstitially placed  $\text{Cd}_i$  would be created as well. This species is known to be (double) donor[13,20,24], and the net result of  $\text{Cu} \leftrightarrow \text{Cd}$  exchange would not lead to electrical compensation of donors, unless these  $\text{Cd}_i$  atoms out-diffuse from the sample (or precipitate somewhere else in the second phase) with the diffusivity larger or at least comparable to that of  $\text{Cu}_i$ . Although diffusion coefficient of  $\text{Cd}_i$  at RT is not known, according to the values at higher T [25,20,21] its RT diffusivity has to be many orders of magnitude lower than that of  $\text{Cu}_i$ . So this mechanism can be also safely ruled out.

Here we propose a new model for the compensation mechanism in CdS by Cu in-diffusion. We are also giving arguments that this model might be more universal and could explain compensation in other II-VI compounds caused by diffusion of other fast-diffusing species as well.

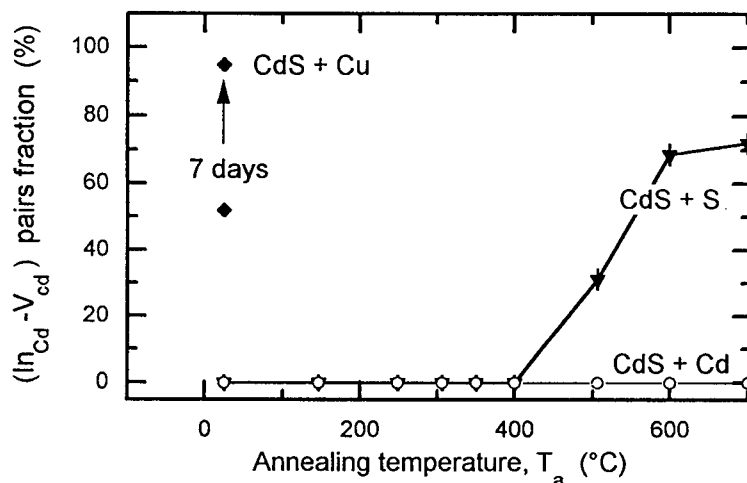


Figure 2: Change of fraction of  $(\text{In}_{\text{Cd}} - \text{V}_{\text{Cd}})$  pairs with annealing:

◆ - CdS with evaporated Cu layer; □ - undoped CdS annealed under S pressure; ○ - undoped CdS annealed under Cd pressure

**Basic assumptions of the diffusion-induced vacancy, DIV, model, for electrical compensation:**

The in-diffusion of Cu donors into CdS provokes simultaneous in-diffusion of  $\text{V}_{\text{Cd}}$  which are (doubly ionized) acceptors in CdS. Along their in-diffusion into the crystal  $\text{V}_{\text{Cd}}$  become trapped by existing donors, compensating them electrically. Hence Cu actually compensates CdS crystal indirectly, by bringing along new Cd vacancies into the CdS. These vacancies pair with free donor atoms, and in fact, do the electrical compensation.

Conceptual arguments for the co-diffusion of  $\text{V}_{\text{Cd}}$  acceptors along with  $\text{Cu}_i$  donors are analogous to those evoked to explain spontaneous self-compensation in doped ionic insulators: In truly ionic, wide band-gap I-VII compounds the presence of II-row-atoms results in spontaneous formation of equal concentration cation vacancies. For example, the presence of each atom of Ca in KCl crystal brings spontaneously one vacancy into cation sub-lattice. Namely, the energy gained by compensation is higher than the energy that is needed to produce a compensating defect. The net result is the lowering of total energy of the crystal, and hence the spontaneous

introduction/formation of such defects is favored[19,26]. Although CdS is a semiconductor and not the ionic crystal it has quite large ionicity of its chemical bonds[27] (ionicity fraction,  $f_i$ , of bonds in CdS is 0.685 by Phillips's definition; or 0.59 by Pauling's, or 0.63 by Coulson's definition), and a quite large band-gap (2.58 eV) as well. Therefore, it should be not surprising but rather expecting that the same minimum-total-energy requirement fulfilled by the formation of self-compensating native defects, so dominant in I-VII ionic crystals, is also the driving force for the spontaneous cation vacancies in-diffusion in CdS during in-diffusion of movable, new donors. Hence, the appearance of fresh  $V_{Cd}^{2-}$  acceptors is a spontaneous reaction to the diffusion of interstitial  $Cu^+$  donors into the crystal. Essentially, high ionicity and large band-gap of CdS are a reason that the minimum total energy requirement is best achieved through the formation of self-compensating defects. The same arguments hold for most of other II-VI compounds, for which the tendency toward electrical self-compensation is generally quite strong[19, 22, 28,26].

The PAC results presented here, give powerful experimental support to the above model. PAC spectra show strong increase of 72&79 MHz signal after Cu evaporation on the CdS crystal. The increase starts already at annealing temperatures as low as RT. As reported earlier, this signal represents  $(In_{Cd}^+-V_{Cd}^{2-})^-$  complex[16,29,30]. The experiment is especially clean since at RT both probe In atoms and these  $V_{Cd}$  which are trapped at  $(In_{Cd}^+-V_{Cd}^{2-})^-$  pairs are immobile[25]. The only mobile specie (besides  $Cu_i$ ) is single  $V_{Cd}$ , having a migration energy of only 1.0 eV [29]. Hence the increase of  $(In_{Cd}^+-V_{Cd}^{2-})^-$  pairs can come only from the in-diffusion of new  $V_{Cd}$ . These Cu-induced cadmium vacancies, are then being trapped at the existing In donors,  $In_{Cd}^+$ , forming additional acceptor-like compensating complexes  $(In_{Cd}^+-V_{Cd}^{2-})^-$ . It seems very probable, that other III-group donors, not seen by PAC, have been neutralized in the same way. This mechanism of compensation is quite efficient since  $(In_{Cd}^+-V_{Cd}^{2-})^-$  acceptor complex does not only neutralize one  $In_{Cd}^+$  donor, but also compensates one  $Cu_i$  donor, or any other shallow donor present in the crystal, as well. Additionally, PAC results show that  $Cu_i$  itself is not in any significant concentration trapped in the vacancy which has already been associated with In donor. Should the Cu be trapped at  $(In_{Cd}^+-V_{Cd}^{2-})^-$  complex, this would influence the 72&79 MHz frequencies, i.e. a new pair of frequencies would appear in the spectra, which obviously did not happen.

The proposed DIV model is compatible with available reports on electrical properties of Cu doped CdS, as well as with the results obtained with a variety of experimental techniques, cited above. In the light of the present model previously reported results on electrical compensation of Cu doped CdS should be re-interpreted: it is  $V_{Cd}$  that does the compensation, not Cu. The compensation does not reflect the extent of in-diffusion of Cu, and formation of  $Cu_{Cd}$  acceptors, but rather the mobility and extent of in-diffusion of  $V_{Cd}^{2-}$  acceptors, although the two are obviously interconnected. It is important to note that neither proposed model nor our experimental results deny (nor confirm) the existence of isolated  $Cu_{Cd}$  species in RT Cu-diffused CdS samples - if present they are invisible to PAC method. The point is that  $Cu_{Cd}$ , according to the proposed model, and also due to arguments given in (i) in (ii), is not the main compensating defect of fast diffusors.

The DIV model reconciles successfully two widely accepted but apparently inconsistent assumptions: one that Cu is an acceptor which compensates donors in CdS, and the other, that Cu in CdS is a fast diffusing interstitial donor. The first step in in-diffusion of Cu into CdS is probably the exchange of Cu atom with Cd atom at the Cu-source/CdS interface. When Cu jumps into interstitial place one  $V_{Cd}$  is created at the CdS surface. Then both Cu and  $V_{Cd}$  start diffusing into CdS, Cu through interstitial and  $V_{Cd}$  by substitutional mechanism. The by-product of the Cu-Cd exchange at the interface would be the presence of Cd atoms in the Cu-source, - which was indeed found in RBS measurements [12]. The proposed model accords nicely with the solely PAC data on fast diffusors reported up to now, where Li, introduced from the metallic phase, also increased significantly the concentration of  $(In-V_{cation})$  pairs in CdS[30], ZnS and ZnTe[31], although at considerably higher temperatures.

Considering similarities between a number of fast diffusors (Ag, Au, Li) with Cu[1,2,11], and relatively high ionicity and large band-gap of most II-VI compounds[27], it seems plausible that the

same or similar mechanism of indirect compensation, by diffusion-induced cation vacancies, can explain compensation effects for other fast diffusors and other II-VI compounds as well.

*Acknowledgments:* This research was supported by the Ministry of Science and Technology of Croatia, and by the Deutsche Forschungsgemeinschaft (SFB 306).

#### References :

1. J.L. Sullivan, J. Phys D: Appl. Phys. 6, 552 (1973)
2. J.L. Sullivan, IEEE SU-32, 71, (1985)
3. K. Shima, Jpn. J. Appl. Phys. 15, 195 (1976)
4. H.H. Woodbory, J. Appl. Phys. 36, 2287 (1965)
5. R.L. Clarke, J. Appl. Phys. 30, 957 (1959)
6. T. Yamagami, Jpn. J. Appl. Phys. 33, 3237 (1994)
7. J. L. Sullivan, Phys. Rev. 184, 796, (1969)
8. T. Lukaszewicz, phys. st. sol. (a), 78, 611, (1982)
9. Yu. A. Zagurulko and B.L. Timan, Sov. Phys. Semicond. 14, 1354 (1980)
10. B. Lepley, P.H. Nguyen, C. Boutrit and S Ravelet., J. Phys. D. Appl. Phys. 12, 1917 (1979)
11. R. Heitz, A. Hoffman, P. Thurian and I. Broser, J. Phys. C.: Condens. Matter 4, 157 (1992)
12. M. Al-Achkar and C.G. Scott, J. Mat. Sci. Lett., 13, 319 (1994)
13. V. Kumar and F.A. Kröger, J. Sol. St. Chem 3, 387 (1971), and F.A. Kröger, *The Chemistry of Imperfect Crystals*, Nort-Holland, Amsterdam, 1964, second edition 1967.
14. P. J. Sebastian and M. Ocampo, J. Appl. Phys. 77, 4548 (1995)
15. P. J. Sebastian, Appl. Phys. Lett. 62, 2956 (1993)
16. R. Magerle, M. Deicher, U. Desnica, R. Keller, W. Pfeiffer, F. Pleiter, H. Skudlik and Th. Wichert, Appl. Surf. Sci. 50, 169 (1991), and U.V. Desnica, I.D. Desnica-Franković, R. Magerle, M. Deicher, and A. Burchard, to be published.
17. D.B Laks, C.G. Van de Walle, G.F. Neumark, P.E. Bloech, and S.T. Pantelides, Phys. Rev. B, 1992, 45, 10965.
18. F.J. Bryant, Prog. Cryst. Growth and Charact. 1983, 6, 191.
19. Y. Marfaing, Prog. Crystal Growth and Charact., 1981, 4, 317-343.
20. H.W. Woodbury, Phys. Rev. 134, A492 (1964) ,
21. E.D. Jones and H. Mykura, J. Phys. Chem. Solids 39, 39 (1978)
22. Y. Marfaing, J. Cryst. Growth, 1996, 161, 205.
23. A. Garcia, and J.E. Northrup, Phys. Rev. Lett. , 1995, 74, 1131.
24. D. Shaw and R.C. Whelan, phys. stat. sol. 36, 705 (1969)
25. S.S. Chern and F. A. Kröger, phys. st. sol (a), 25, 215 (1974)
26. U.V. Desnica, Vacuum, in press. (1997)
27. J. C. Phillips, Bonds and Bands in Semiconductors, Academic Press, London, 1973., or Rev. Modern Phys. 42, 317 (1970)
28. K.A. Prior, J. Cryst. Growth, 1995, 187, 379.
29. Th. Wichert, Th. Krings and H. Wolf, Physica B, 297 (1993)
30. H. Wolf, U. Hornauer, R. Lermen, Y. Endalamov, T. Filz, Th. Krings, St. Lauer, U. Ott, E. Singer, M. Tsige and Th. Wichert, ICDS-17, ed. H. Heinrich and W. Jantsch, Materials Science Forum 143-47, (Zurich: Trans Tech Publications 1994), pp.459
31. H. Wolf, A. Jost, R. Lermen, T. Filz, V. Ostheimer and Th. Wichert, ICDS-18, ed. M. Suezawa, and H. Katayama-Yoshida, Materials Science Forum 196-201 (Zurich: Trans Tech Publications 1995) pp. 321-325

## EXPERIMENTAL EVIDENCE FOR THE TWO-ELECTRON NATURE OF In-RELATED DX STATES IN CdTe

C. Skierbiszewski<sup>1</sup>, P. Wisniewski<sup>1</sup>, Z. Wilamowski<sup>2</sup>, W. Jantsch<sup>3</sup>  
and G. Karczewski<sup>2</sup>

<sup>1</sup> High Pressure Research Center PAS, Sokolowska 29/37, 01-142 Warsaw, Poland

<sup>2</sup> Institute of Physics PAS, Al. Lotnikow 32/46, 02-668 Warsaw, Poland

<sup>3</sup> Institut für Experimentalphysik, Johannes-Kepler-Universität, 4040 Linz, Austria

**Keywords :** DX centers, deep levels

**Abstract.** In this work we investigate electron emission/capture from/to the DX state of indium in CdTe by means of a high pressure freeze-out cycle and by steady-state photo-conductivity experiments. The barriers for electron emission and -capture as well as their pressure dependencies are evaluated. The results indicate that the DX state is occupied by two electrons.

### Introduction

It has been shown recently that the indium donor state in CdTe exhibits metastable behaviour at low temperatures under hydrostatic pressure (HP) above 7 kbars [1]. It was found that the In related state in CdTe is located 110 meV above the conduction band edge at ambient pressure and it has a pressure coefficient of -10 meV/kbar with respect to the conduction band edge [1]. The microscopic structure of this center, however, and its charge state are still not experimentally established. In this work we investigate: (a) the electron emission from the DX state under HP after filling this level by a high pressure freeze-out (HPFO) cycle [2], and (b) electron capture to the DX state under HP in steady-state photo-conductivity experiments. These two types of experiments allow us to estimate the pressure dependencies of the ground state energy of the In- related donor, and the energies of the barriers for electron emission and capture. We obtain agreement on the position of the top of the barrier as seen from emission experiments, on one hand, and capture experiments on the other hand, only, if a two electron process is assumed for the thermal emission from the deep DX state. The results of our experiments show that the DX state is occupied by two electrons and the barrier for electron emission increases with applied pressure.

### Experimental results

We investigate 0.7  $\mu\text{m}$  thick layers of CdTe:In grown by MBE on GaAs substrate with a ZnTe buffer layer, with the doping level in the range of  $5 \cdot 10^{17}$  -  $2 \cdot 10^{18} \text{ cm}^{-3}$  [3].

In Fig. 1 results of Hall measurements vs. temperature are presented for pressures of 0, 3.2 and 5.8 kbar. The electron concentration at 77 K is obtained in an HPFO cycle, i.e., at 300 K a pressure of  $p = 13.5$  kbar was applied. Then the sample was cooled down to 77 K, and the pressure was released to specific values (0, 1.5, 3.2, and 5.8 kbar) in subsequent runs. After achieving a non-equilibrium occupancy of the DX state at 77 K, the sample was heated at a constant rate of 1 K/min. Then characteristic steps are seen in the Hall concentration,  $n_e(T)$ , in Fig. 1 due to thermally activated emission from the DX state. For comparison, the dashed line in Fig. 1 shows the



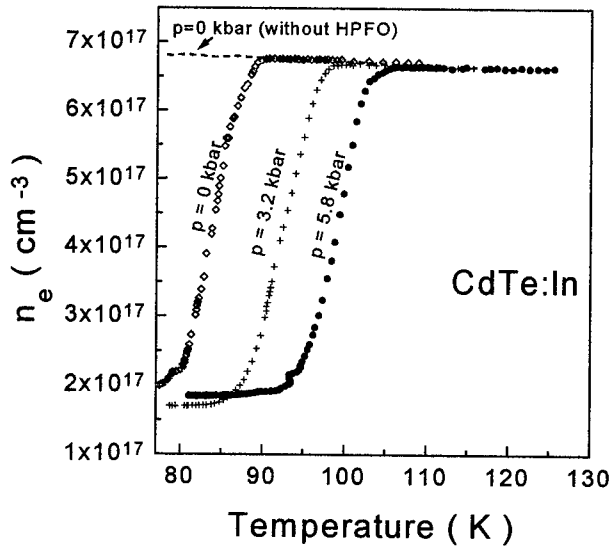


**Fig. 1** Electron concentration as a function of temperature after an HPFO cycle for pressures of 0 kbar (diamonds), 3.2 kbar (crosses) and 5.8 kbar (dots), respectively. The dashed line presents results without HPFO cycle.

The photoconductivity was investigated in the temperature range of 77 - 300 K under HP up to 20 kbar. In these experiments, the sample is illuminated (with controlled intensity) by an infrared light-emitting diode (IR LED) incorporated in the pressure cell and Hall effect- and conductivity are measured. Such a process is described by the following rate equation:

$$n_e \cdot c^{\text{th}} = n_{\text{DX}} \cdot (e^{\text{th}} + \Phi \cdot e^{\text{opt}}) \quad (2)$$

where  $n_{\text{DX}}$  stands for the number of DX states;  $c^{\text{th}}$ ,  $e^{\text{th}}$  are the thermal capture- and emission rates of the DX state;  $e^{\text{opt}}$  the optical emission rate from the DX state and  $\Phi$  the photon flux. Results for  $p = 14$  kbar and for different illumination intensities are presented in Fig. 3. For temperatures higher than 140 K, the barrier for electron capture/emission to/from the DX state is transpar-

behaviour of  $n_e(T)$  without a HPFO cycle, i.e., without applying pressure before cooling. In Fig. 2, the Arrhenius plot for the emission coefficient,  $e^{\text{th}}$ , at different pressures is presented. The analysis of these results was performed assuming that:

$$e^{\text{th}}(T) = e_{\text{th}}^{\infty} \cdot \exp\left(-\frac{E_{\text{em}}}{kT}\right) \quad (1)$$

where the usual factor  $T^2$  before the exponent was omitted (following the arguments presented e.g. in Ref. [4]). This allowed us to determine the energy barrier for emission,  $E_{\text{em}}$ :  $E_{\text{em}}(p) = 255 \text{ meV} + p \cdot 8.4 \text{ meV/kbar}$ ; and:  $e_{\text{th}}^{\infty} = 10^{13} \text{ s}^{-1}$ .

In order to evaluate the barrier for electron capture,  $\epsilon_B$ , the photo-

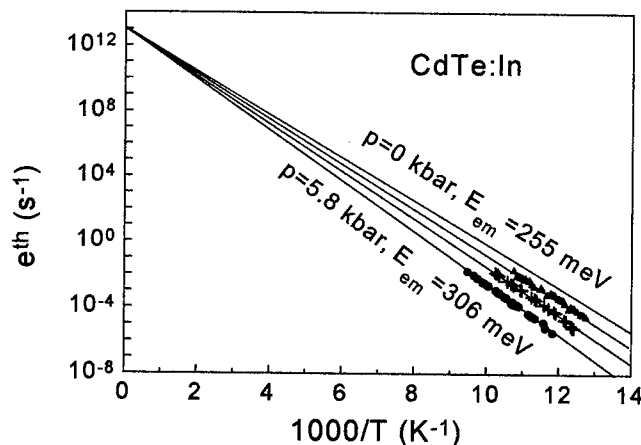


**Fig. 2** Arrhenius plot of the emission rate for 0 kbar (diamonds), 1.5 kbar (triangles), 3.2 kbar (crosses) and 5.8 kbar (dots). Lines: extrapolation of the experimental results for  $1/T \rightarrow 0$ .

ent, and the quasi-Fermi level,  $\epsilon_F^*$ , is pinned to the DX level position,  $\epsilon_{DX} \cdot \epsilon_B$ . (Throughout this paper we denote the one-electron-energies for clarity by  $\epsilon$  plus some index, whereas the total energy changes per event are denoted by  $E$  plus index. For single electron processes,  $\epsilon = E$ ). The pressure dependence of  $\epsilon_{DX}$  is shown by squares in Fig. 4. The dashed line shows the dependence:

$\epsilon_{DX}(p) = 110 \text{ meV} - p \cdot 10 \text{ meV / kbar}$  obtained from pressure experiments in the range 0 - 14 kbar [1].

For  $100 \text{ K} < T < 140 \text{ K}$ ,  $\epsilon_F^*$  is defined by the balance between thermal capture by DX states and optical emission from the DX state. Below 100 K,  $\epsilon_F^*$  saturates because of the limited number of donors which are the source of electrons in this system. As it was presented in [4], under steady-state conditions,  $\epsilon_F^*$  is a linear function of temperature with a slope depending on the illumination of the sample. Extrapolation of  $\epsilon_F^*(T)$  for  $T \rightarrow 0 \text{ K}$  allows to estimate the position of the barrier top  $\epsilon_B$ . For  $p = 14 \text{ kbar}$ ,  $\epsilon_B$  is about 150 meV above the conduction band edge. Fig. 3 shows also that taking experiments with different sample illumination allows to improve the accuracy in the determination of the barrier energy.

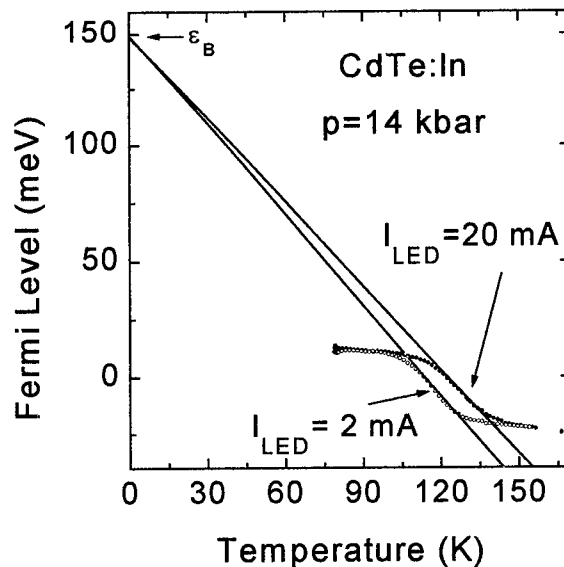


**Fig. 3** Quasi Fermi-level position obtained from Hall concentration in steady-state photoconductivity experiments vs. temperature at 14 kbar for different IR LED currents (dots and circles). The lines represent a linear extrapolation for  $T \rightarrow 0 \text{ K}$ .

## Discussion

### A. Charge of the DX state

For the DX state the following relation should be always fulfilled, no matter whether the DX state holds one or two electrons:

$$E_B - E_{DX} = E_{em} \quad (3)$$

where  $E_B$  is the barrier height for electron capture to the DX state and  $E_{em}$  the activation energy for the emission process from the DX state.

On one side, we obtain from steady photoconductivity experiments the position of the DX state ( $\epsilon_{DX}$ ) and the position of the capture barrier ( $\epsilon_B$ ). Since  $\epsilon_{DX}$  and  $\epsilon_B$  are evaluated from  $\epsilon_F^*$  they are one-electron-energies. On the other side, emission experiments after an HPFO give a characteristic energy,  $E_{em}$  for the emission process. Depending on the nature of the DX level, emission of

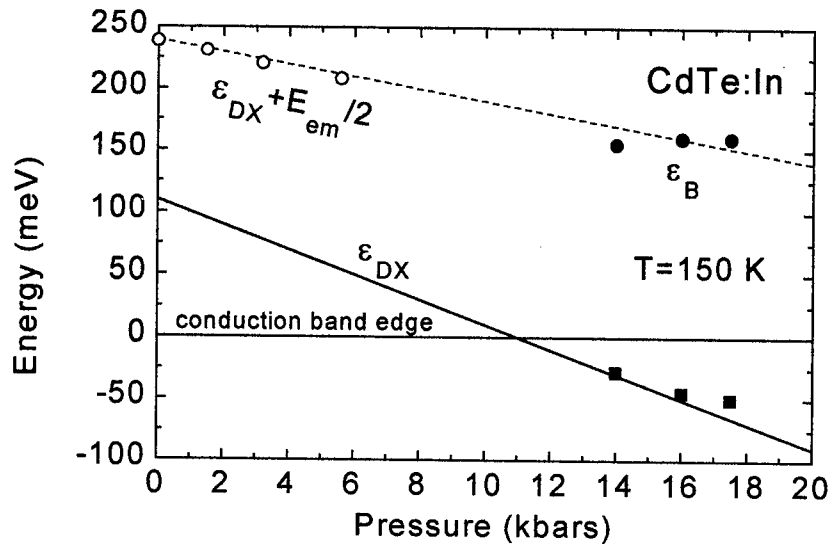


Fig. 4. Pressure dependence of: the position of the DX state  $\epsilon_{DX}$  as obtained in the pressure range up to 14 kbar (lower solid line, after Ref.1), while the results deduced from the position of the Fermi level at  $T = 150$  K from steady-state photoconductivity are shown by squares. The position of the barrier top for the two-electron process (circles) are taken from the emission experiments. The dots stem from steady-state photoconductivity data. The dashed line connecting these points is a guide for the eye.

one or two electrons may occur. For one electron emission:  $\epsilon_B - \epsilon_{DX} = E_{em}$ , but for a two electron process we obtain:  $\epsilon_B - \epsilon_{DX} = E_{em} / 2$ . The results of our experiments presented in the Fig. 4 show that only the latter equation can be fulfilled. It means that the emission process, characterised by the activation energy  $E_{em} \approx 250$  meV at  $p = 0$  kbar, corresponds to the emission of two electrons:  $DX^- + 250 \text{ meV} \rightarrow 2e + D^+$ , i.e., the emission energy per electron is  $\epsilon_{em} = E_{em} / 2$ . Since no intermediate state was found experimentally we also conclude that the emission/capture process consists in the *simultaneous* emission/capture of 2 electrons.

### B. Configuration Coordinate diagram

As shown theoretically [5,6] the mechanism of DX formation in II-VI compounds for group III dopants like In, Ga, Al is essentially the same as for group IV dopants in III-V compounds. The capture of electrons is followed by a large lattice relaxation in one of the four  $\langle 111 \rangle$  directions. For the In-case, the values predicted for the binding energies of the  $DX^-$  state [5,6] are experimentally well confirmed. From our experiments the following informations were obtained:

- the DX state is a two electron state
- the emission energy is pressure dependent
- for low pressures, the In related DX state is metastable ( $\epsilon_{DX} > \epsilon_{d0}$  where  $\epsilon_{d0}$  is binding energy of shallow donor), whereas for pressures higher than 10 kbar, the DX state becomes stable ( $\epsilon_{DX} < \epsilon_{d0}$ ).

In Fig. 5, a configuration coordinate diagram is presented for the In related DX state in CdTe. The solid lines represent the total two electron energy of the DX<sup>-</sup> state. The line marked  $E_{DX}$  corresponds to the relation:  $E_{DX}(Q,p) = k(Q - Q_0)^2 + 2 \cdot \epsilon_{DX}(p)$ , where the configuration coordinate  $Q$  defines a shift of the donor atom away from its substitutional site in one of the four  $\langle 111 \rangle$  directions [5,6], and  $k$  is the elastic constant. The displacement  $Q_0$  of the In atom after capture of 2 electrons was calculated using a first-principle pseudopotential total energy method:  $Q_0$  is found to equal 1.89 Å and it is pressure independent [5,6]. The dash - dotted line shows the energy of 2 electrons plus the elastic energy of the empty D<sup>+</sup> donor:  $E_{D^+}(Q,p) + 2e = k_1 \cdot Q^2 + 2 \cdot \epsilon_F^*$ . In this simple scheme, by choosing the parameters  $k$ ,  $k_1$  and  $Q_0$ , we are able to derive the pressure induced change of the barrier top,  $\epsilon_B$ , from the change of  $\epsilon_{DX}$  (e.g. for  $\epsilon_{DX}(p=0\text{kbar}) - \epsilon_{DX}(p=20\text{kbar}) = 240\text{meV} = \Delta$  - see Figs 4 and 5- the change of the barrier top is:  $\epsilon_B(p=0\text{kbar}) - \epsilon_B(p=20\text{kbar}) = 120\text{meV} = \Delta / 2$ ).

The behaviour of the emission energy under pressure observed for In in CdTe is different than for e.g. for Si in GaAs. For group IV donors in III-V compounds, the maximum of the elastic energy for  $E_{DX}$  occurs before the crossing point with  $E_{D^+}$ , and so the emission energy there is pressure independent [7]. If such a maximum exists for the CdTe:In case it should be located on the left hand side of the crossing points of the curves for  $E_{DX}$  and  $E_{D^+}$ . Our picture then is very similar to the configuration coordinate diagram for group VI donors in III-V compounds [8].

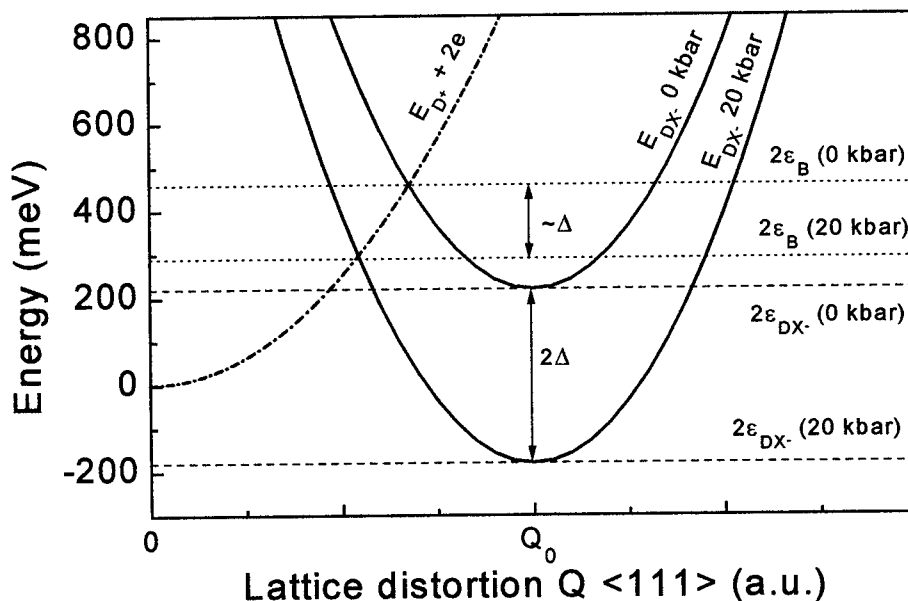


Fig. 5. Configuration coordinate diagram for the In related DX state in CdTe. Solid lines present the total two- electron energy of DX<sup>-</sup>. The dash-dotted line shows the energy of 2 electrons plus the elastic energy of the empty donor. The positions of the barrier top and the energies of the DX state are indicated by dotted and dashed lines, respectively.

## Conclusions

In conclusion, we have shown that: (i) the metastability of the In donor in CdTe originates from strong lattice relaxation connected with the formation of the negatively charged DX center; and (ii) that the emission barrier depends on hydrostatic pressure. We propose a configuration coordinate diagram describing also the pressure behaviour of Indium in CdTe.

## Acknowledgments

Work supported by the *Fonds zur Förderung der Wissenschaftlichen Forschung*, Austria.

## References

1. D. Wasik, J. Przybytek, M. Baj, G. Karczewski, T. Wojtowicz, J. Kossut, *Journal of Cryst. Growth* **159**, 392 (1996)
2. R. Piotrkowski, T. Suski, P. Wisniewski, K. Ploog and J. Knecht, *J. Appl. Phys.* **68**, 3377 (1990)
3. G. Karczewski, A. Zakrzewski, M. Kutrowski, J. Jaroszynski, W. Dobrowolski, E. Grodzicka, E. Janik, T. Wojtowicz, J. Kossut and A. Barcz, *Acta Phys. Polon.* **A87**, 241 (1995)
4. W. Jantsch, Z. Wilamowski, G. Ostermayer, *Semicond. Sci. Technol.* **6**, B47 (1991)
5. C. H. Park and D. J. Chadi, *J. Phys. Chem. Solids*, **56**, 585 (1995)
6. C. H. Park and D. J. Chadi, *Phys. Rev.* **B52**, 11884 (1995)
7. J. Dabrowski and M. Scheffler, *Mat. Sci. Forum* **83-87**, 735 (1992)
8. Z. Wilamowski, W. Jantsch, T. Suski, *Acta Phys. Polon.* **A82**, 561 (1992)

## Nature of dislocation-related deep level defects in CdS

A.A.Istratov and O.F.Vyvenko

Institute of Physics of St.-Petersburg State University, Ulianovskaya 1, St.-Petersburg,  
198904 Russia

**Keywords:** CdS, dislocations, wurtzite lattice, DLTS, cathodoluminescence, DX-center

### Abstract

Dislocation structures around microindentations of differently oriented surfaces of a CdS sample were reconstructed from cathodoluminescent study in scanning electron microscope using subsequential removal of surface layers. Deep levels due to edge prismatic,  $\beta$ -edge and screw dislocations were identified by comparing amplitudes of individual DLTS peak with relative density of each type of dislocations under the schottky-contacts. The main electron trap in plastically deformed CdS was found to be due to DX-level of substitutional donors which became detectable in the vicinity of screw dislocations under the influence of their strain fields.

### Introduction

Theoretical calculations show that the electrical properties of dislocations with different core structures should differ (see for example [1]). However, the experimental data confirming these theoretical predictions are lacking. A few published studies [2,3] have been focused primarily on developing of experimental techniques to separate the  $\alpha$  and  $\beta$ -dislocations in InP and CdTe. This method could be applied only to sphalerite type lattice and could not be used to evaluate the deep levels introduced by screw dislocations.

In this paper, the nature of dislocation-related levels in CdS (a II-VI semiconductor with the wurtzite lattice) is investigated. A new experimental technique for the establishing of the nature of the dislocation-related centers is suggested. The technique is based on the comparison of DLTS spectra, obtained on different dislocation structures, prepared using differently oriented surfaces and successive removal of thin surface layers.

### CL/SEM studies of the dislocation structure

The dislocation structures around microindentations on different surfaces of CdS samples were reconstructed using cathodoluminescence (CL) technique in scanning electron microscope (SEM). There are four different types of dislocations in the wurtzite lattice: screw dislocations and three types of edge dislocations:  $\alpha$  (S-glide),  $\beta$  (Cd-glide) and prismatic.

The contrasts of screw (luminous) and edge (non-luminous) dislocations could be distinguished by means of the spectral-resolved low-temperature cathodoluminescence (LT-CL/SEM) [4] which makes use of near-band-gap luminescence of the cores of screw dislocations in CdS [5]. It was found that the ratio between different types of dislocations in the near-surface layer could be changed, by choosing the orientation of the indented surface and by removing surface layers of increasing thickness. Several of the obtained CL images are presented in Fig.1. The sketches of the dislocation structure are given in Figs.2 and 3, on the right. The dislocation structure on the (0001) surface is formed by six dislocation arms (Fig.1a), parallel to the surface. CL contrasts within these arms consist of edge prismatic dislocations lying perpendicular to the surface, and of screw dislocations, lying parallel to the surface (Fig.1c). The basal glide edge dislocations appear in the near-surface region after re-

removal of a layer of thickness of approximately 5  $\mu\text{m}$  and becomes a dominating type of dislocation after removal of about 10-20  $\mu\text{m}$  (Fig.1b). The type of basal dislocations can not be established from our measurements, but the geometrical considerations imply that they should be mainly  $\alpha$ -dislocations on (0001)S surface and  $\beta$ -dislocations on (0001)Cd surface (see sketches in the Fig.2a,b).

Using the inclined orientation of the surface (see Fig.2c), predominantly edge prismatic and a mixture of screw and edge-type basal dislocations could be obtained on two opposite sides of a microindentation without any surface removal. Since DLTS-spectra, obtained on two different sides of the indentations were consistent with the DLTS data on (0001) surfaces after mechanical and chemical removal of a surface layer, it was concluded that polishing and etching themselves do not influence the dislocation-induced defects in the near-surface region.

The dislocation structure, appearing on the (1210) surface after the microindentation, consists of three dislocation arms. One of them is directed perpendicularly to the surface, the other two at an angle of  $30^\circ$  to the surface. The dominant type of LT-CL contrasts on as-indented

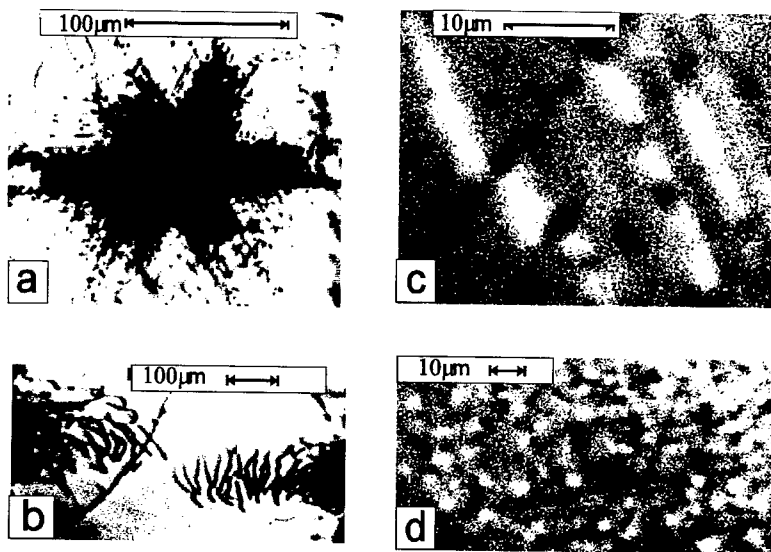


Fig.1.CL/SEM images of dislocations introduced by indentation of basal (a,b,c,) or prismatic (d) surfaces; a,b - room temperature, d - 100K.

a - dislocation rosette obtained on the (0001)S surface after indentation. It consists of the dot-like contrasts due to edge prismatic dislocations and straight-line-like contrasts due to screw dislocations.

b - arms of the dislocation rosette on the (0001)S surface after removal of a surface layer of about 10 micrometers. Most dislocations in the arms are  $\alpha$  (S-glide) basal dislocations. Edge prismatic and screw dislocations are also presented in the peripheral parts of the rosette.

c - CL-images of screw (luminous lines) and edge prismatic (dark dots) dislocations on the indented prismatic surface.

d - CL-images of screw (luminous dots) and edge basal (dark dots) dislocations on the indented basal surface after removal of a surface layer of about 100 mkm.

(1210) surface were luminous dots, formed by the cross-section points of screw dislocations with the surface. On the (1010) surface, the structure consists of four arms; two of them are

(1210) surface were luminous dots, formed by the cross-section points of screw dislocations with the surface. On the (1010) surface, the structure consists of four arms; two of them are parallel to the surface, and two others are aimed into the bulk of the sample under angles of  $60^\circ$ . The structure of these arms is similar to that on the (1210) surface. The dominant type of LT-CL contrasts, originating from the arms parallel to the (1010) surface were dark dots. The density of dots corresponds to a much higher density of cross-points of  $\alpha$  and  $\beta$  dislocation with the surface than on the (1210) surface. After the removal of a surface layer of a thickness of approximately 100  $\mu\text{m}$ , the dislocation structure on both prismatic surfaces consisted of screw and basal edge ( $\alpha$  and  $\beta$ ) dislocations (see Fig. 1d). Sketches in Fig. 3a, 3b depict these two principally different structures: the arms of the dislocation rosette which are parallel to the surface (Fig. 3a), and the arms which are inclined or perpendicular to the surface (Fig. 3b).

In plastically deformed samples, obtained by of uniaxial compression of rectangular samples, the dislocation structure consisted mainly of long straight segments of screw dislocations, ending on low-angle boundaries (see Fig. 3c).

#### DLTS studies

The combination of the sample orientation and the removal of surface layers allowed us to prepare Schottky diodes with 7-8 significantly different dislocation structures in the space-charge region beneath the Schottky-contact. The DLTS spectra are presented on the left hand in Fig. 2 and 3. The reverse bias voltage (3 V) was chosen to obtain the width of space-charge region under the Schottky-diode equal to the penetration depth of the electron beam in the SEM at an accelerating voltage of 10kV. This enabled the direct correlation of the DLTS spectra and the CL images.

In the experiments with successive removal of the surface layers, numerous closely spaced indentations were made and round gold Schottky-diodes of a diameter of 0.5mm were evaporated. In the experiments with the inclined (0001) surface a row of indentations was made between two closely adjacent rectangular Schottky-diodes 0.3x0.6mm. The distance between low-angle boundaries was between 0.2 and 0.6 mm, and it was possible to evaporate a Schottky-diode on virtually boundary-free regions of as-grown and deformed samples.

The spectrum of as-grown samples consisted of a single DLTS peak M1. After plastic deformation, 14 DLTS-peaks were detected [6]. Though the intensity of all peaks depended on the surface orientation and the successive surface removals, only three peaks showed a definite dependence on the relative number of dislocations of a certain type. They could be unambiguously identified as deep levels due to screw, edge prismatic and  $\beta$ -edge dislocations (DLTS-peaks denoted as M5, M7 and M12 in the Fig. 2,3; their parameters are listed in Table 1). The nature of other centers can be attributed only to point defects, either generated or activated by dislocation loops and will be discussed elsewhere.

#### Discussion

To the best of our knowledge no theoretical calculations of dislocation levels in CdS were published, it is interesting to compare our data with the results of calculations for CdTe - a II-VI semiconductor with the sphalerite lattice. It was shown that  $\beta$ -dislocations should have a level slightly above the midgap, whereas  $\alpha$ -dislocations were predicted to have a level in the lower half of the bandgap, close to the valence band [1]. This explains why the level of  $\alpha$ -dislocations could not be detected in our DLTS-measurements.

Surprisingly, it was found that the main electron trap in dislocated CdS is due to screw dislocations which are usually expected to be electrically inactive. Detailed studies of the screw-



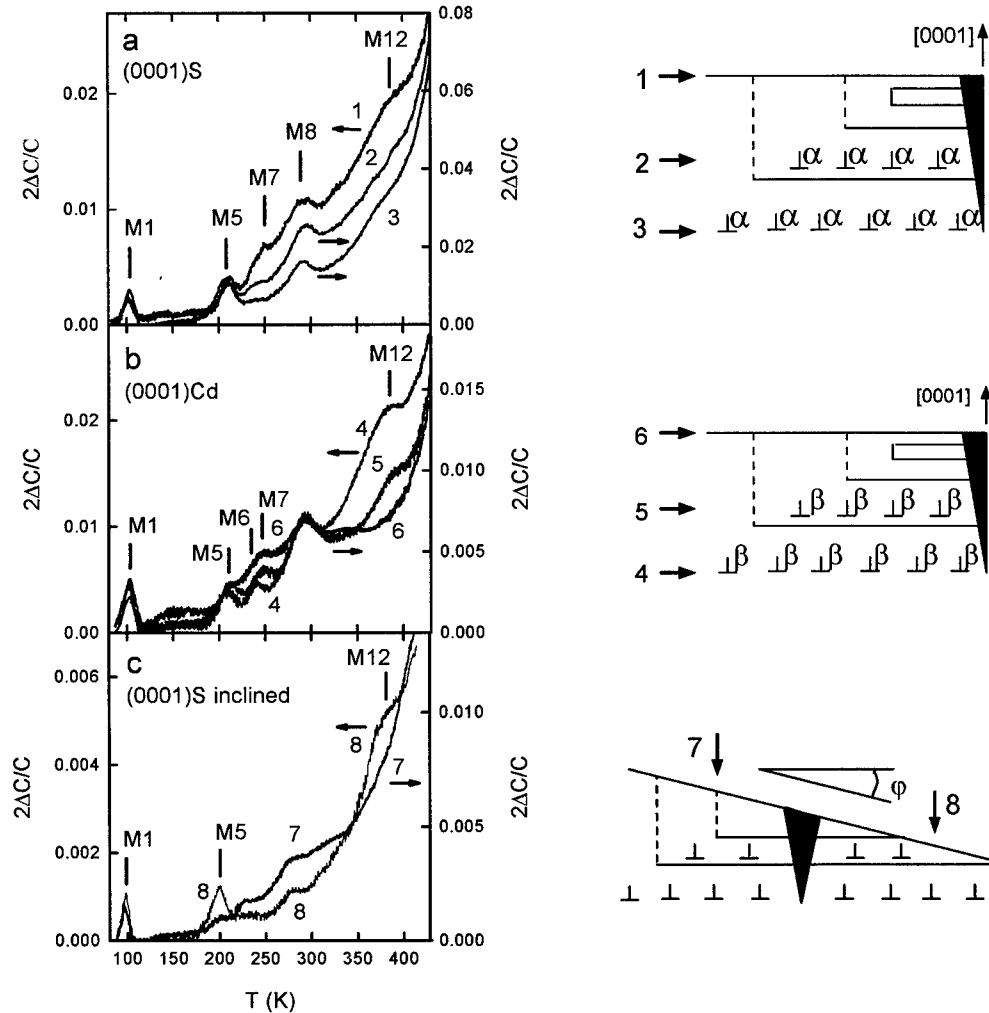


Fig.2. DLTS spectra (on the left) taken on two polar orientations of (0001) surface (Fig.2a and 2b) after the indentation and after removal of the surface layers of the thickness about 10  $\mu\text{m}$  and 20  $\mu\text{m}$ , and on inclined at an angle of about  $5^\circ$  (0001)S surface (Fig.2c). The sketches of dislocation structures are given on the right side. Numeration of curves on the left side and dislocation structures on the right side match. DLTS spectra were taken in the rate window  $0.056 \text{ s}^{-1}$ . Screw dislocations are designated by solid lines, edge prismatic dislocations by dotted lines,  $\alpha$  and  $\beta$  dislocations, perpendicular to the plane of the drawing, are indicated by symbols " $\perp$ ".

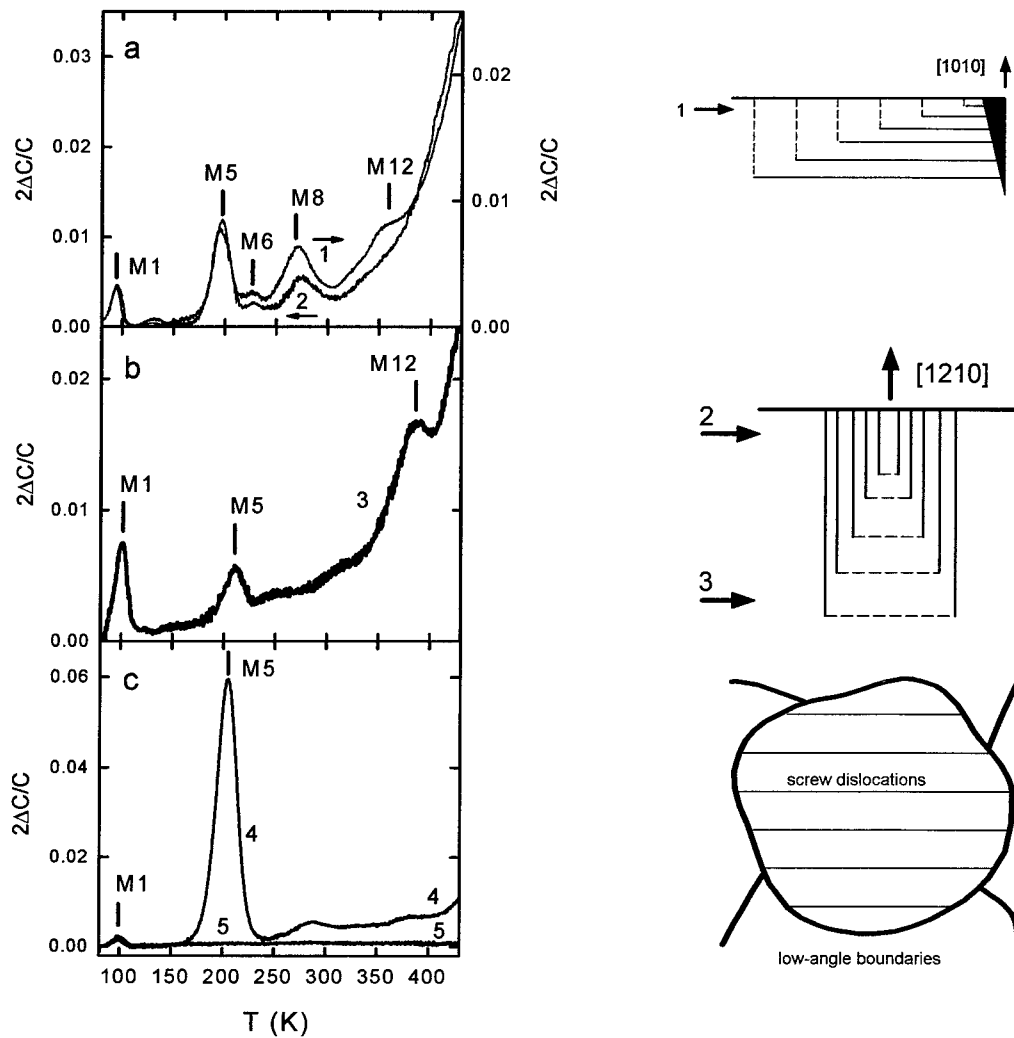


Fig.3. DLTS spectra, taken just after microindentation on (1010) surfaces (Fig.3a, curve 1) and (1210) surfaces (Fig.3a, curve 2) and after removing of a surface layer about 100  $\mu\text{m}$  from the (1210) surface (Fig.3b, curve 3). Spectra in Fig.3a and 3b were taken in different rate-windows, which causes an apparent shift of the peak positions. The DLTS spectrum, obtained on (0001) surface of an uniaxially deformed sample is presented in Fig.3c, curve 4. The Schottky diode was evaporated on the region, free from low-angle boundaries. Curve 5 in Fig. 3c corresponds to the as-grown sample. The drawings on the right illustrate schematically the dislocation structure, corresponding to the DLTS spectra. The numbers of the DLTS spectra and the numbers on drawings match. Screw dislocations are designated by solid lines,  $\alpha$  and  $\beta$  edge dislocations by dashed lines.

Table 1. Parameters of deep levels, identified in this study.

Center	Activation energy, eV	Capture cross-section, cm <sup>2</sup>	nature of the center
M5	0.40±0.01	$5 \times 10^{-15} \exp(-0.33 \text{ eV}/kT)$	screw dislocations
M7	0.63±0.06	$4 \times 10^{-13}$	edge prismatic
M12	0.93±0.05	$5 \times 10^{-14}$	edge $\beta$

dislocation related center were published in a separate paper [7]. Since the emission from these centers was strictly exponential, it was concluded that these centers were point defects surrounding screw dislocations. They exhibited large lattice relaxation upon electron capture, manifesting itself in a large capture barrier and a large difference between thermal and optical ionization energy, i.e. had all essential properties of the DX-centers. The center could be completely filled only using very long filling pulses (about 0.1 s). This led to a significant underestimation of its concentration in previous papers on deep levels in CdS. Though our samples were not intentionally doped, their chemical analysis revealed that they contained sizable concentrations of Al and In, which act as substitutional donors in II-VI semiconductors. A model was suggested, in which the DX level of substitutional donors becomes detectable in the vicinity of screw dislocations under the influence of their strain fields. Numerical estimations of the strain fields in the vicinity of dislocations confirmed the plausibility of the model [7].

The dislocation structure under the indented (0001) surface in CdS is very similar to that reported for the indented (111) surface in sphalerite type InSb and GaAs [8]. The combination of the technique developed in this work (correlation between DLTS spectra and dislocation structures) with the methods [2,3], allows to investigate more precisely the nature of the dislocations-related levels in the materials with sphalerite lattice.

#### References

- [1] H. Teichler, M. Grölich, Bull. Acad. Sci. USSR Phys. Ser. **51** (4), 28 (1987).
- [2] A. Zozime, W. Schröter, Appl. Phys. Lett. **57**, 1326 (1990).
- [3] I. A. Hummelgen, W. Schröter, Appl. Phys. Lett. **62**, 2703 (1993).
- [4] O. Vyvenko, A. Zozime, W. Schröter, Mater. Sci. Engin. **B 24**, 105 (1994).
- [5] V. D. Negrii, J. Appl. Phys. **74**, 7008 (1993).
- [6] A. A. Istratov, O. F. Vyvenko, Semiconductors, **29**, 340 (1995).
- [7] A. A. Istratov, O. F. Vyvenko, J. Appl. Phys. **80**, 4400 (1996).
- [8] M. R. Surowiec, B. K. Tanner, Phil. Mag. **55**, 791 (1987).

## NMR STUDY OF CARRIER STATES AND TRAPPING COMPLEXES IN THE TRANSPARENT CONDUCTOR ZnO:M<sub>III</sub>

W.W. Warren, Jr.<sup>1,3</sup>, N. Roberts<sup>1</sup>, R.-P. Wang<sup>2,4</sup> and A.W. Sleight<sup>2,3</sup>

<sup>1</sup>Department of Physics, Oregon State University, Corvallis, OR 97331-6507, USA

<sup>2</sup>Department of Chemistry, Oregon State University, Corvallis, OR 97331-4003, USA

<sup>3</sup>Center for Advanced Materials Research, Oregon State University, Corvallis, OR, USA

<sup>4</sup>Applied Materials, Inc., Sunnyvale, CA 95054, USA

**Keywords:** II-VI compounds, NMR, group III impurity states, complexes, transparent conductors

**Abstract.** We report <sup>69</sup>Ga and <sup>27</sup>Al impurity, and <sup>67</sup>Zn host species NMR data for heavily-doped ZnO:Ga and ZnO:Al. In stoichiometric samples Zn<sub>1-x</sub>M<sub>x</sub>O (0.03 at. % < x < 3 at. %), a well-defined impurity band emerges from the conduction band for x less than about 0.5 at. %, although the conduction electron spin dynamics retain free electron character to the lowest concentrations. Comparison of the <sup>69</sup>Ga substitutional site quadrupole interaction,  $(e^2qQ/h)^{69} = 3.9 \pm 0.3$  MHz with the host <sup>67</sup>Zn value indicates that the nearly tetrahedral environment of the host Zn<sub>Zn</sub> sites are somewhat further distorted at Ga<sub>Zn</sub>. A second and highly distorted impurity site, decoupled from the carriers, is present with increasing concentration as oxygen content increases in the non-stoichiometric series Zn<sub>0.98</sub>Ga<sub>0.02</sub>O<sub>1+z</sub> (-1.2 at. % < z < +1.0 at. %). We suggest that this is a Ga<sub>2</sub><sup>3+</sup>O<sub>i</sub><sup>2-</sup> trapping complex. The carrier concentration is controlled by the density of remaining substitutional sites.

### Introduction.

The group III metals (Al, Ga, and In) are efficient shallow donors in ZnO which can be doped up to the solubility limits of a few atomic per cent. Although the room temperature conductivities can exceed 1000 (Ω cm)<sup>-1</sup>, the materials remain highly transparent. A 0.5 μm film containing 1 % Al, for example, was recently found[1] to exhibit more than 80 % transmission throughout the visible range, despite a DC electrical conductivity of about 300 (Ω cm)<sup>-1</sup>. There is a long history of work on the electrical and optical properties of ZnO, but there is still little known from the microscopic perspective about the location and local electronic structure of the group III dopants. Another important issue concerns the role of oxygen. The electronic properties of "pure" ZnO vary widely among various samples due, at least in part, to variations in stoichiometry. The conductivity of doped ZnO decreases rapidly with excess oxygen which introduces effective carrier traps.

In this investigation we have exploited the highly local sensitivity of nuclear magnetic resonance (NMR) to probe the environments of gallium, and to a lesser extent, aluminum in ZnO. We report impurity (<sup>69</sup>Ga and <sup>27</sup>Al) and host species (<sup>67</sup>Zn) NMR data for a series of samples with a stoichiometric metal-to-oxygen ratio, i.e. Zn<sub>1-x</sub>M<sub>x</sub>O, and a series of non-stoichiometric samples of composition Zn<sub>0.98</sub>Ga<sub>0.02</sub>O<sub>1+z</sub>. The measurements include resonance shifts, spin-lattice relaxation times, and the shapes and structure of quadrupole-perturbed absorption lines and spin echoes.

### Experimental details.

Powdered samples of gallium- and aluminum-doped ZnO were prepared by high temperature solid-state reaction. One series of gallium-doped samples was prepared by mixing appropriate quantities of reagent grade ZnO and gallium metal (4N) and heating under vacuum in silica tubes to 1200 °C where the samples were held for 10 hours before being cooled at a rate of 300 °C per hour. This preparation is described by the reaction  $x\text{Ga} + \text{ZnO} \rightarrow \text{Zn}_{1-x}\text{Ga}_x\text{O} + x\text{Zn}$ . Under the synthesis conditions, excess elemental zinc is distilled to the cooler part of the preparation tube leaving

„stoichiometric“ material  $\text{Zn}_{1-x}\text{M}_x\text{O}$ . Another series of „non-stoichiometric“ samples was prepared with varying metal-to-oxygen ratios starting with gallium metal,  $\text{Ga}_2\text{O}_3$ , and  $\text{ZnO}$ . All such samples contained 2 at. % gallium relative to the total metal content. We represent such material by the formula  $\text{Zn}_{0.98}\text{Ga}_{0.02}\text{O}_{1+z}$  with  $z$  ranging from -1.2 at. % to +1.0 at. %. Stoichiometric aluminum-doped samples  $\text{Zn}_{1-x}\text{Al}_x\text{O}$  were prepared by dissolving zinc and aluminum powders in 3N nitric acid which was then evaporated and heated at 500 °C for 10 hours to completely decompose the nitrates. The products were subsequently heated for 10 hours at 1200 °C in an evacuated silica tube containing a zirconium foil reducing agent. Details of the preparation and characterization of these samples are presented elsewhere[2].

NMR data were obtained with a Chemagnetics CMX-340 spectrometer in a magnetic field of 8.0 T. Absorption spectra were generated by Fourier transformation of free induction decays or spin echoes. The reference samples for resonance shifts were dilute aqueous solutions of  $\text{AlCl}_3$ ,  $\text{GaCl}_3$ , and  $\text{ZnSO}_4$ , respectively, for  $^{27}\text{Al}$ ,  $^{69}\text{Ga}$ , and  $^{67}\text{Zn}$ . We measured nuclear spin-lattice relaxation times by the inversion-recovery method using  $\pi - \pi/2$  sequences of radio-frequency pulses. Considerable signal-averaging was required to obtain adequate signal-to-noise ratios in the more dilute samples. For a sample containing 0.03 at. % gallium, several tens of thousands of  $^{69}\text{Ga}$  free induction decay or spin echo signals were acquired over 10 - 12 hours to obtain a spectrum.

#### Results and analysis for $\text{ZnO}$ and stoichiometric $\text{Zn}_{1-x}\text{M}_x\text{O}$ .

Absorption lines for the quadrupolar-perturbed  $m = \pm 1/2 \rightarrow m = \mp 1/2$  transition observed at room temperature are reproduced in Fig. 1 for  $^{67}\text{Zn}$  in nominally pure  $\text{ZnO}$  and for  $^{67}\text{Zn}$  and  $^{69}\text{Ga}$  impurities in  $\text{Zn}_{0.9997}\text{Ga}_{0.0003}\text{O}$  ( $1.3 \times 10^{19} \text{ Ga/cm}^3$ ). The spectrum for pure  $\text{ZnO}$  exhibits the characteristic lineshape of a nucleus in an electric field gradient with axial symmetry, reflecting the small axial distortion of the coordinating tetrahedra around  $\text{Zn}_{\text{Zn}}$ . The linewidth yields a quadrupole coupling  $(e^2qQ/h)^{67} = 2.38 \pm 0.02 \text{ MHz}$ , in good agreement with previous values obtained by Bastow and Stuart [3]. In the doped material, the lineshape is distorted and broadened by disorder, but the sharp edges associated with axial symmetry are retained for both  $^{67}\text{Zn}$  and  $^{69}\text{Ga}$ . We consider this strong evidence that the observed  $^{69}\text{Ga}$  nuclei are in substitutional  $\text{Ga}_{\text{Zn}}$  sites. The quadrupolar coupling for  $^{69}\text{Ga}$ ,  $(e^2qQ/h)^{69} = 3.9 \pm 0.3 \text{ MHz}$ , exceeds that of  $^{67}\text{Zn}$  by more than the ratio of the respective nuclear electric quadrupole moments ( $Q^{69}/Q^{67} = 1.19$ ) indicating that the

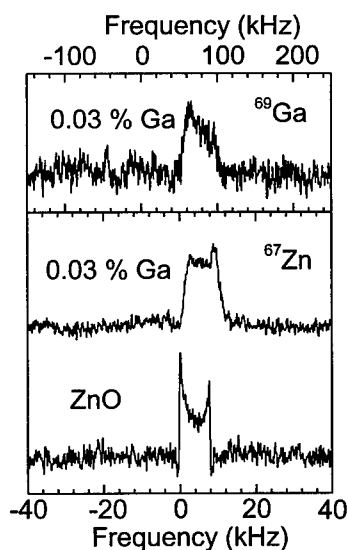


Figure 1. Central ( $m = \pm 1/2 \rightarrow m = \mp 1/2$ ) line of quadrupolar perturbed NMR spectra of  $\text{ZnO}$  and  $\text{Zn}_{0.9997}\text{Ga}_{0.0003}\text{O}$  at room temperature. Upper panel:  $^{69}\text{Ga}$  impurity NMR; lower panel  $^{67}\text{Zn}$  host species NMR.

local electric field gradient at the impurity site is about 40 % larger than that at the pure host sites. X-ray diffraction studies of these samples[2] show that the unit cell *increases* on doping which would tend to *reduce* the EFG at the impurity. These results therefore suggest that expansion of the lattice is also accompanied by a modest increase in the axial distortion at the impurity site.

With increased doping, the  $^{69}\text{Ga}$  impurity resonance rapidly loses the quadrupolar structure without appreciable increase in the overall linewidth. Concomitantly, the resonance frequency decreases slightly, then increases sharply above about 0.5 at. % gallium (Fig. 2). The impurity spin-lattice relaxation rate  $1/T_1$  exhibits similar behavior. The composition range investigated in aluminum-doped material is less extensive, but the  $^{27}\text{Al}$  data presented in Fig. 3 exhibit the same general features as observed for  $^{69}\text{Ga}$ .

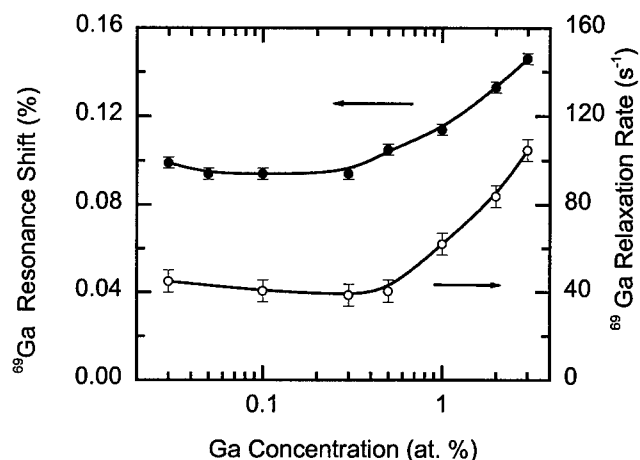


Figure 2.  $^{69}\text{Ga}$  resonance shift (solid points, left-hand scale) and spin-lattice relaxation rate (open points, right-hand scale) versus Ga dopant concentration in stoichiometric  $\text{Zn}_{1-x}\text{Ga}_x\text{O}$ .

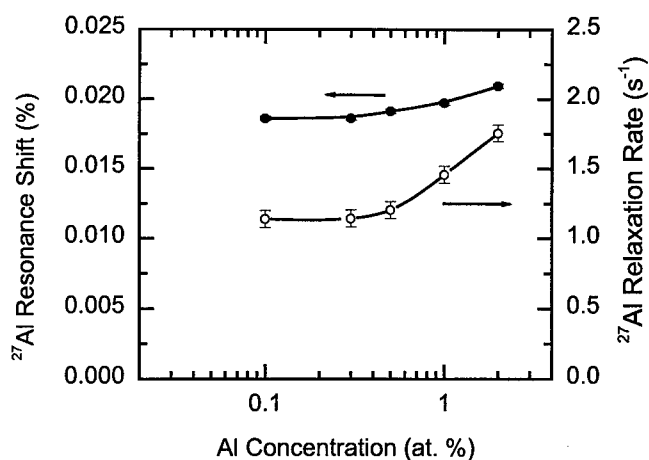


Figure 3.  $^{27}\text{Al}$  resonance shift (solid points, left-hand scale) and spin-lattice relaxation rate (open points, right-hand scale) versus Al dopant concentration in stoichiometric  $\text{Zn}_{1-x}\text{Al}_x\text{O}$ .

In the following, we discuss the composition dependence of the shift and relaxation rates in terms of the local electronic structure at the impurity sites. The most heavily doped samples in the series investigated are essentially poor metals with electron concentrations comparable with the doping level, i.e.  $n \approx 10^{21} \text{ cm}^{-3}$ , Hall mobilities (in films) in the range 20 - 30  $\text{cm}^2/\text{Vs}$ , and DC conductivities of order  $10^3 (\Omega \text{ cm})^{-1}$  [1,2]. In such a case we can expect a substantial contribution to the local field at the probe nuclei from the spin-polarization of the conduction electrons acting

through the magnetic hyperfine interaction. The resulting resonance shift (“Knight shift”) is given by

$$K \equiv \frac{\Delta\nu}{\nu} = \frac{8\pi}{3} \langle |\psi(0)|^2 \rangle_F \chi_{spin} \quad (1)$$

where  $\langle |\psi(0)|^2 \rangle_F$  is the probability density of carriers at the impurity nucleus, averaged over states at the Fermi level, and  $\chi_{spin}$  is the paramagnetic spin susceptibility of the carriers. For degenerate electrons in a parabolic conduction band,  $\chi_{spin}$  is the Pauli susceptibility  $\chi_{spin} = 2\mu_B^2 N(E_F)$ , proportional to the density of states at the Fermi level, i.e.  $K \propto N(E_F) \propto n^{1/3}$ . Detailed analysis of the shift data taking into account the  $^{69}\text{Ga}$  chemical shift[4] shows that the observed shift varies according to  $\Delta\nu/\nu \propto x^{1/3}$  only at the highest concentrations investigated. With decreasing doping, the shift deviates markedly from this dependence, even increasing at the lowest concentrations.  $^{67}\text{Zn}$  host resonance shifts, in contrast, decrease monotonically with decreasing dopant and carrier concentration. Assuming a Pauli susceptibility and conduction band mass  $m^* = 0.38m_0$  [9], the shift observed for the 3 at. % gallium sample and Eq. (1) yield a value  $\langle |\psi(0)|^2 \rangle_F \approx 7 \times 10^{25} \text{ cm}^3$ , roughly twice that obtained from electron spin resonance in ZnS[5].

The concentration dependence of the resonance shift indicates development of an impurity band with sharply enhanced density of states relative to that of the conduction band. We note that our most dilute Ga-doped sample is close to the metal-nonmetal transition predicted by the Mott criterion,  $n^{1/3}a_H^* \approx 0.25$ . For an effective Bohr radius for the donor  $a_H^* = 11.8 \text{ \AA}$ , the transition should occur at  $x = 0.02 \text{ at. \%}$ . The enhanced density of states or effective mass in the impurity band can be expected to shift the plasma edge to longer wavelengths ( $\lambda_{pl} \propto (m^*)^{1/2}$ ), further increasing the optical transparency in the visible, and may also contribute to a decrease in carrier mobility ( $\mu \propto (m^*)^{-1}$ ) observed in thin films at low doping levels[1].

Spin-lattice relaxation in conducting materials is due mainly to fluctuating local hyperfine fields. For degenerate non-interacting electrons, the rate can be expressed in terms of the Knight shift by the Korringa relation[6]

$$1/T_1 = (4\pi k_B T / \hbar) (\gamma_n / \gamma_e)^2 K^2 \quad (2)$$

where  $\gamma_n$  and  $\gamma_e$  are, respectively, the nuclear and electronic gyromagnetic ratios. The temperature dependence of  $1/T_1$  was measured for the more highly doped samples and found to exhibit the linear behavior expected from Eq. (2) for a degenerate system. Comparison of the observed magnitudes of  $1/T_1$  with those calculated from measured shifts ( $K$ ) using Eq. (2) provides a more stringent test of the validity of a free electron model. In practice, this is complicated by the possibility of a significant chemical shift contribution to the observed shift. However, the chemical shift should depend only weakly on composition or temperature, so the Korringa relation can be tested by obtaining the *slope* of a plot  $(1/T_1)^{1/2}$  versus the observed resonance shift  $\Delta\nu/\nu$ . This can be compared with the value given by Eq. (2), i.e.  $(4\pi k_B T / \hbar)^{1/2} (\gamma_n / \gamma_e)$ . We find that the shift and relaxation rate correlate with the Korringa slope *over the full range of dopant concentrations investigated* for both  $^{69}\text{Ga}$  and  $^{27}\text{Al}$  dopant nuclei. This surprising observation, which contrasts sharply with the behavior of  $^{31}\text{P}$  and  $^{11}\text{B}$  dopants in Si[7,8], means that free electron spin dynamics are preserved well into the range of impurity band formation. There is no sign of the strong spin fluctuations and localization effects typically observed near a metal-nonmetal transition.

### Results and analysis for non-stoichiometric $\text{Zn}_{0.98}\text{Ga}_{0.02}\text{O}_{1+z}$

Time-domain  $^{69}\text{Ga}$  spin-echo shapes are shown in Fig. 4 for the series of gallium-doped samples with  $z$  ranging from -1.2 at.% to +1.0 at. %. The echo shapes clearly reveal the existence of two classes of gallium site in all these samples. The broad part of the echo corresponds to a narrow line in the frequency domain and is the component assigned to substitutional  $\text{Ga}_{\text{Zn}}$  in the stoichiometric materials. The sharp, rapidly decaying component is due to a second and highly distorted class of gallium site. We can extract the substitutional fraction of observed sites from the relative intensity of the slowly decaying echo component. These results, displayed in Fig. 5, show that the fraction of  $\text{Ga}_{\text{Zn}}$  sites depends weakly on oxygen content in the range of deficiency, but even a stoichiometric sample  $\text{Zn}_{0.98}\text{Ga}_{0.02}\text{O}$  (not shown in Fig. 4) contained about 10 % gallium in distorted sites. The substitutional fraction decreases rapidly with increasing excess oxygen. As we discuss below, the

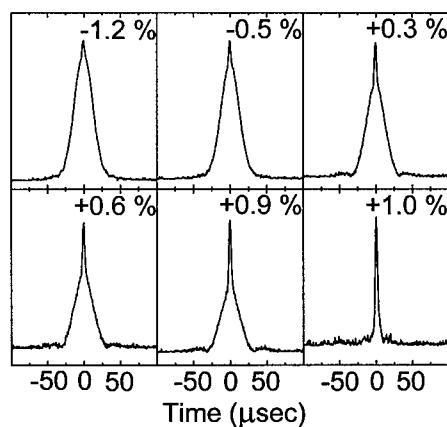


Figure 4.  $^{69}\text{Ga}$  time-domain spin-echo shapes for non-stoichiometric samples  $\text{Zn}_{0.98}\text{Ga}_{0.02}\text{O}_{1+z}$  for various values of  $z$  in at. % oxygen.

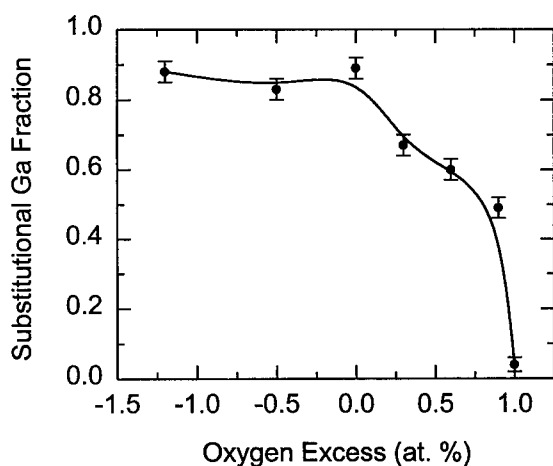


Figure 5. Fraction of substitutional  $\text{Ga}_{\text{Zn}}$  sites determined from slowly varying spin-echo component versus oxygen excess  $z$  (at. %) for non-stoichiometric  $\text{Zn}_{0.98}\text{Ga}_{0.02}\text{O}_{1+z}$ .

resonance shifts and relaxation rates of the substitutional sites correlate strongly with the fraction of substitutional gallium. Because of signal-to-noise limitations, it was not possible to measure accurately the shifts and relaxation rates of the distorted sites in all samples. However, for the most oxygen-rich sample ( $z = +1.0$  at. %), a greatly reduced shift  $\Delta\nu/\nu = 0.035 \pm 0.08$  % was observed; we believe that most of this shift is due to the impurity site chemical shift. The relaxation rate of the distorted site,  $1/T_1 = 1.5 \times 10^{-3} \text{ s}^{-1}$ , is more than three orders of magnitude lower than that of the



substitutional sites. Thus, compared with the substitutional sites, there is virtually no coupling of  $^{69}\text{Ga}$  impurity nuclei to carriers at the distorted sites.

The  $^{69}\text{Ga}$  resonance shifts and relaxation rates are plotted as a function of the substitutional gallium fraction in Fig. 6. Both quantities decrease strongly with the fraction of  $\text{Ga}_{\text{Zn}}$ . This result together

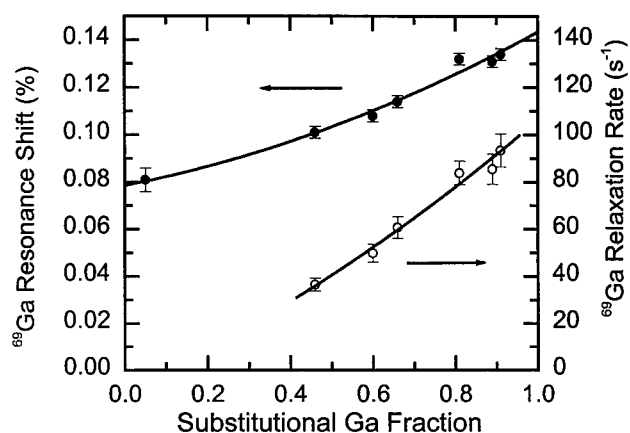


Figure 6.  $^{69}\text{Ga}$  resonance shifts and spin-lattice relaxation rates versus the fraction of substitutional ( $\text{Ga}_{\text{Zn}}$ ) states in non-stoichiometric samples  $\text{Zn}_{0.98}\text{Ga}_{0.02}\text{O}_{1+z}$ .

with the absence of carrier density on the distorted sites suggests strongly that the distorted sites are diamagnetic traps and that the carrier density is controlled by the number of  $\text{Ga}_{\text{Zn}}$  sites – each such site contributing one electron to the conduction band. A likely candidate for the trapping defect is a doubly-charged oxygen interstitial complexed with two  $\text{Ga}^{3+}$  according to the reaction  $2\text{Ga}^{3+} + \text{O} + 2e^- \rightarrow \text{Ga}_2^{3+}\text{O}_i^{2-}$ . An abundance of  $\text{Ga}_2^{3+}\text{O}_i^{2-}$  in oxidized samples is consistent with recent reports[10] of layered  $\text{Ga}_2\text{O}_3$  intergrowth phases in material with higher levels of oxygen excess ( $z > 5$  at. % in our notation). Such  $\text{Ga}_2\text{O}_3$  layers can be viewed as ordered planar arrangements of the  $\text{Ga}_2^{3+}\text{O}_i^{2-}$  defects. It is not clear whether the defects occurring at the lower concentrations characteristic of our samples are isolated or occur in layered clusters. In either case, they would serve as double electron traps. We emphasize that these defects are present at the level of at least a few percent in *all* the 2 at. % gallium-doped samples studied, regardless of oxygen stoichiometry.

#### Acknowledgments.

This work was supported in part by the U.S. National Science Foundation grants DMR-9305780 and DMR-9623299 (W.W.W.) and DMR-9308530 (A.W.S.).

#### References.

1. R. Wang, L.L.H. King, and A.W. Sleight, *J. Mater. Res.* **11**, 1659 (1996).
2. R. Wang, A.W. Sleight, and D. Cleary, *Chem. Mater.* **8**, 433 (1996).
3. T.J. Bastow and S.N. Stuart, *Phys. Stat. Solidi (b)* **145**, 719(1988); T.J. Bastow, *J. Phys.: Condens. Matter* **8**, 11309 (1996).
4. N. Roberts, R.-P. Wang, A.W. Sleight, and W.W. Warren, Jr., unpublished.
5. A. Räuber and J. Schneider, *Phys. Stat. Solidi* **18**, 125 (1966).
6. J. Korringa, *Physica* **16**, 601 (1950).
7. S.E. Fuller, E.M. Meintjes, and W.W. Warren, Jr., *Phys. Rev. Lett.* **76**, 2806 (1996).
8. E.M. Meintjes and W.W. Warren, Jr., unpublished.
9. R.E. Dietz, J.J. Hopfield, and D.G. Thomas, *J. Appl. Phys.* **32**, 2282 (1961).
10. N. Kimizuka, M. Isobe, and M. Nakamura, *J. solid State Chem.* **116**, 170 (1995).

## CATHODOLUMINESCENCE STUDY ON THE HYDROGENATION OF ZnO LUMINESCENCE

T.Sekiguchi, N.Ohashi<sup>1</sup> and Y.Terada<sup>1</sup>

Institute for Materials Research, Tohoku University,  
1-1-2 Katahira, Aoba-ku, Sendai 980, Japan

<sup>1</sup> Department of Inorganic Materials, Tokyo Institute of Technology,  
2-12-1 O-okayama, Meguro-ku, Tokyo 152, Japan

**Keywords :** ZnO, cathodoluminescence, green emission, hydrogen, passivation

**Abstract.** We have studied the luminescence property of ZnO single crystals by means of cathodoluminescence. It was found that hydrogen plasma strongly passivates the green emission and enhances the excitonic luminescence of ZnO. The band edge luminescence shows strong temperature dependence after hydrogenation and its intensity at low temperatures becomes remarkably high. The effect of hydrogenation disappears by an annealing at 700 °C, which indicates hydrogen is rather strongly bound to the centers for green emission. This study indicates that the passivation of deep levels is the key for the application of ZnO crystals for the ultraviolet light source.

### Introduction

ZnO is an unique oxide semiconductor which possesses the tetrahedral symmetry. The most conventional usage of ZnO is phosphor material for the green emission. There have been proposed several candidates for green emission, such as O vacancies, [1,2] Zn interstitials [3], O interstitials [4], and substitutional Cu [5]. Vanheusden et al. [6] observed that the isochronal reduction treatment of ZnO powder under a flow of forming gas [ $N_2:H_2=95:5$  by volume] significantly increased the green emission intensity, while the isochronal oxidation treatment of ZnO:Zn powder decreased the green emission. They correlated this variation with the electron-paramagnetic-resonance (EPR) signal ( $g = 1.96$ ) related to the singly ionized oxygen vacancy or vacancy related defects. Then, they concluded that the green emission results from the recombination of a photogenerated hole with the singly ionized charge state of oxygen vacancy.

Recently, the band edge luminescence of ZnO have attracted much attention for the application of UV lasers [7]. The large exciton binding energy (60 meV) of ZnO is one of the advantage of this materials [8]. Most attempt of UV application, however, was done with ZnO films to avoid the effect of green emission. Thus, if we can suppress the green emission, the bulk ZnO crystal can be applied for UV application.

Annealing of the ZnO powder under the hydrogen ambient is commonly used to enhance the green emission as the reduction treatment. Contrary to such traditional method, we recently have succeeded to passivate the green emission completely by hydrogen plasma. In this paper we describe the effect of hydrogen plasma on the luminescence property of ZnO by means of cathodoluminescence.

### Experiment

ZnO single crystals were grown by a flux method. The mixture of ZnO and  $PbF_2$  powders about 20 : 80 in mole fraction was melted in a platinum crucible at 1040°C for

2 h under the oxygen flow condition and then slowly cooled to 950°C at 5 °C/h. Nominally undoped single crystals about 10x10x0.3 mm<sup>3</sup> in size were obtained. They were annealed at 1000°C for 6 h in an oxygen ambient to improve the uniformity of spatial distribution of deep levels related to oxygen.

Hydrogen plasma treatment was done in a plasma chamber made of high-purity quartz.[9] Hydrogen plasma was excited by a microwave with a frequency of 2.45 GHz. The magnetron power for exciting the plasma was 300 W. The plasma pressure was about 10 Torr. Specimens mounted in the hydrogen plasma was automatically heated up to 400°C and treated about 7 min. The surface of the specimens became cloudy with pale yellow due to hydrogenation. To study the stability of hydrogenation, isochronal annealing was also performed with the hydrogenated specimen for 30 min in an oxygen ambient.

CL measurements were conducted with a scanning electron microscope (TOPCON DS130). The optical system for cathodoluminescence is described in Ref. [10]. A monochromator with a grating of 100 lines/mm (Jobin Yvon HR320) and a charge coupled device (CCD) were used for the detection of spectra. The spectral resolution was set at 1.2 nm in wavelength. The CL spectra were recorded at every 0.8 nm step with 1040 channels. Alternately, another monochromator with a grating of 1200 lines/mm and a conventional photomultiplier (Hamamatsu ; R3310-02) was used for the spectra of high energy resolution.

CL observations were done at temperatures between 30 K and 295 K. The accelerating voltage of the electron beam was 5 kV. The beam current was varied from 60 pA to 1.8 nA. The difference of the beam current in this range did not introduce any changes in the spectral shape except for the absolute intensity.

## Results

### General Feature

Figure 1 (a) shows a typical CL spectrum of as-grown ZnO crystal at room temperature. It consists of a sharp peak at 3.29 eV and a broad peak at 2.2 eV. They are the band edge luminescence and the green emission, respectively. The integrated intensity of the green emission is more than 10 times higher than that of the band edge luminescence. Fig 1 (b) shows the spectrum of ZnO annealed in an oxygen ambient. Although the green emission increases and the peak position shift to 2.1 eV, the spectrum is similar to

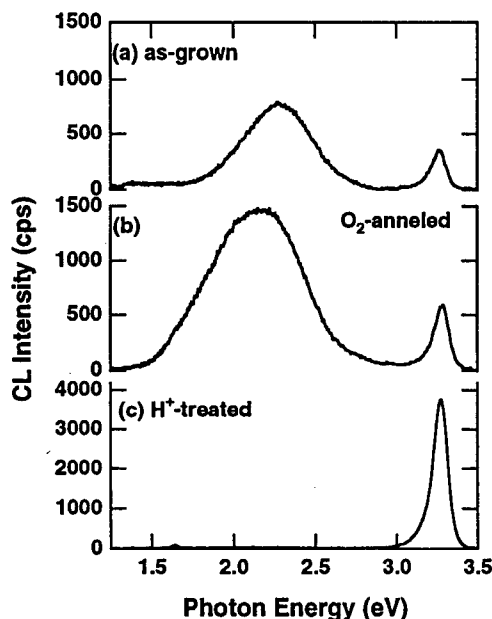


Fig.1 CL spectra of ZnO at R.T.  
(a) as-grown, (b) annealed in O<sub>2</sub>, and (c) hydrogenated.  
5 kV, 1.8 nA

that of as-grown state. Thus, we will refer this specimen as nonhydrogenated ZnO, hereafter. Contrary to these specimens, the hydrogen plasma treatment bring about the significant change on the spectrum as shown in Fig. 1 (c). The green emission is completely passivated and, in turn, the band edge luminescence becomes 8 times higher than that before hydrogenation. It can be explained in terms of the hydrogen passivation of the green emission.

#### Temperature Dependence

Figure 2 shows the CL spectra of nonhydrogenated specimen at various temperatures. The green emission shows rather complicated behavior with temperature. Although the peak at 2.2 eV does not show significant temperature dependence, another peak at 2.0 eV appears about 200K and increases with further cooling. The broad feature of this luminescence, however, makes the detailed analysis difficult. The band edge luminescence, on the other hand, does not show significant temperature dependence. Its peak position shifts to higher energy in accordance with the change of band gap with temperature. The peak intensity at 30 K is only 2 times higher than that at room temperature. This temperature insensitive behavior of the band edge luminescence intensity is peculiar property of bulk ZnO crystals.

Figure 3 shows the CL spectra of hydrogenated specimen at various temperatures. The excitation current is reduced to 1/30 of the former to avoid the saturation of the detector. Since we cannot observe any other luminescence except the band edge luminescence, the band edge region is enlarged to show. Contrary to the former case, the band edge luminescence possesses strong temperature dependence.

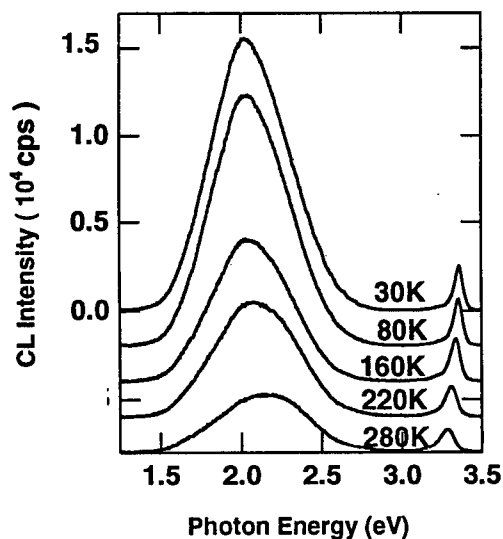


Fig.2. CL spectra of nonhydrogenated ZnO specimen at various temperatures.  
E-beam ; 5kV, 1.8 nA

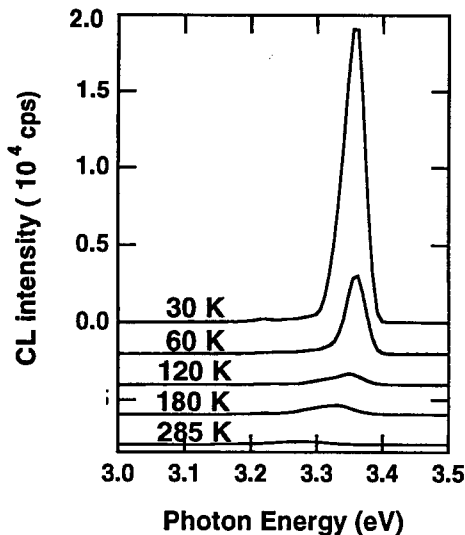


Fig.3. CL spectra of hydrogenated ZnO specimen at various temperatures.  
E-beam ; 5kV, 60 pA

The band edge luminescence increases with the temperature decrease and its intensity at 30 K becomes more than 100 times higher than that at room temperature.

#### Fine Structure of Band Edge Luminescence

Figure 4 shows the logarithmic plot of CL spectra of band edge region of both nonhydrogenated and hydrogenated specimen with high energy resolution. The band edge luminescence of both specimens are composed of only one luminescence peak at 3.3495 eV. It is attributed to the bound excitonic luminescence with a binding energy of 27 meV. The detailed analysis of the spectra indicates that bound excitonic luminescence is dominant below 200 K, while free excitonic luminescence is dominant above 200 K. These data indicates that the hydrogen does not affect the property of band edge luminescence and only increases this luminescence intensity due to the passivation of the green emission.

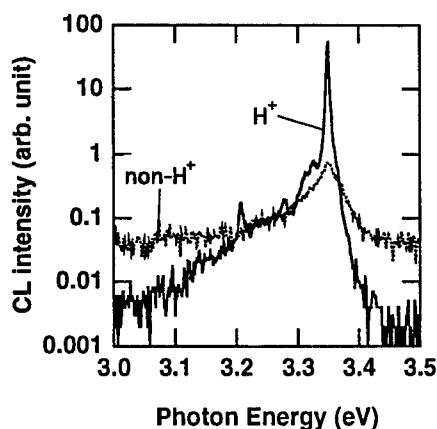


Fig.4 Logarithmic plot of the CL spectra at the band edge region of ZnO. 30K. 5 kV, 1.8 nA.

#### Isochronal Annealing

Figure 5 shows the change of CL spectra of hydrogenated ZnO crystal by isochronal annealing. The CL spectra do not show significant changes after annealing up to 600°C except the decrease of absolute intensity of band edge luminescence. The green emission suddenly appears around 700°C and develops with further annealing.

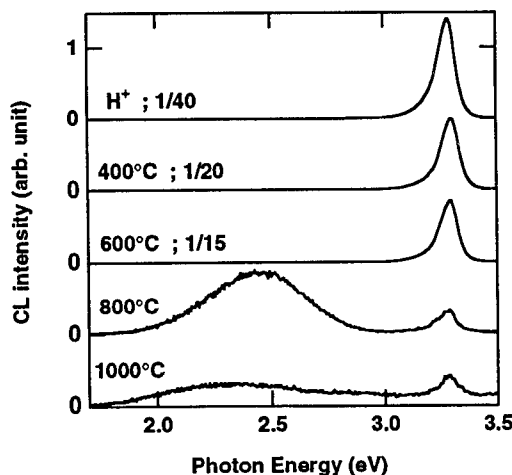


Fig. 5. The effect of isochronal annealing on the CL spectra of hydrogenated ZnO at 295 K.

Accordingly, the band edge luminescence decreases significantly around this temperature so that its intensity of the 800 °C annealed specimen becomes 1/100 of the initial value. Thus, the peak intensity of green emission exceeds that of the band edge luminescence at 800 °C. The intensity of green emission becomes maximum at around 800 °C and decreases with further annealing. The intensities of band edge luminescence and green emission in the specimen annealed at 1000 °C are smaller than those of the specimen before hydrogenation. This discrepancy might have come from the damage induced by hydrogen plasma.

### Discussion

The above result shows that hydrogen plasma treatment only passivates the green emission and does not affect the band edge luminescence. The fine structure of the band edge luminescence is not changed by hydrogenation. Preliminary study of the decay of luminescence also support this idea. The decays of band edge luminescence and green emission is fitted with exponential function. The lifetimes of band edge luminescence of nonhydrogenated and hydrogenated ZnO at room temperature are about 42 ps and 49 ps, respectively, while that of green emission in nonhydrogenated ZnO is longer than 700 ns. The change of lifetime of band edge luminescence due to hydrogenation is negligible. Only small effect has come from the increase of the number of electron hole pairs due to the passivation of green emission.

The temperature insensitive behavior of the band edge luminescence intensity of as-grown or oxygen annealed ZnO may also be attributed to the existence of the green emission. Without the green emission in hydrogenated specimen, the band edge luminescence has come to show the strong temperature dependence. In the nonhydrogenated specimen, most of carriers are captured by deep levels so that the temperature dependence is masked.

The temperature dependence of the peak intensity of band edge luminescence is fitted with the following equation, [11]

$$I(T)/I(0) = 1/[1 + g \cdot T^{3/2} \cdot \exp(-E/kT)] \quad (1)$$

where  $k$ ,  $T$ ,  $E$  are Boltzman constant, temperature, and ionization energy, respectively.  $g \cdot T^{3/2}$  is the effective density of band continuum state. We have got the value of 12 meV for the energy. This value is rather small in comparison with the binding energy of the exciton. We tentatively explained it in terms of the existence of another level which effectively dissociate excitons. [12]

To check the effect of surface damage by plasma, nitrogen or air [ $N_2:O_2=80:20$ ] plasma treatment were also conducted. These plasma treatments, however, did not passivated the green emission, or moreover, they sometimes enhanced the green emission. Thus, we can conclude the hydrogen plays an essential role for the passivation.

The dehydrozation experiment suggests that hydrogen is incorporated in the defect of green emission and it is dissolved from the defects around 700 °C. In the case of silicon, deep levels induced by scratching at room temperature are also passivated by hydrogen plasma. But, this passivation effect is start to be annealed out by heat treatment around 450 °C. [9] Thus, hydrogen is much strongly bounded by deep centers responsible for the green emission of ZnO.

Rough estimation of the integrated intensity of band edge luminescence at 30 K suggests that the number of emitted photons via excitonic luminescence is more than several tenth of electron-hole pairs generated by the electron beam. [12] It indicates that hydrogen plasma treated ZnO is a hopeful candidate of UV light source.

### Conclusion

We found that hydrogen plasma strongly passivates the green emission and enhances the band edge luminescence of ZnO. The band edge luminescence shows strong temperature dependence after hydrogenation and its intensity at 30 K is more than 100 times higher than that at room temperature. Hydrogen is rather strongly incorporated in the deep level responsible for the green emission since the effect of hydrogenation disappears by an annealing over 700 °C. Passivation of deep levels is the key for the application of the band edge luminescence of ZnO.

### References

1. P. H. Kasai, *Phys. Rev.* **130**, 989 (1963)
2. F. A. Kroger and H. J. Vink, *J. Chem. Phys.* **22**, 250 (1954)
3. E. G. Bylander, *J. Appl. Phys.* **49**, 1188 (1978)
4. M. Liu, A. H. Kitai, and P. Mascher, *J. Lumin.* **54**, 35 (1992)
5. C. Solbrig, *Z. Physik* **211**, 429 (1962)
6. K. Vanheusden, W. L. Warren, C. H. Seager, D. R. Tallant, J. A. Voigt, and B. E. Gnade, *J. Appl. Phys.* **79**, 7983 (1996)
7. D. C. Reynolds, D. C. Look, and B. Jogai, *Solid State Commun.* **99**, 873 (1996)
8. E. Tomsig and R. Helbig, *J. Lumin.* **14**, 403 (1976)
9. T. Sekiguchi, V. Kveder, and K. Sumino, *J. Appl. Phys.* **76**, 7882 (1995)
10. T. Sekiguchi and K. Sumino, *Rev. Sci. Instrum.* **66**, 4277 (1995)
11. G. Davis, *Physics Reports*, **176**, 83 (1989)
12. T. Sekiguchi, N. Ohashi, and Y. Terada, *Jpn. J. Appl. Phys.* **36**, L289 (1997)

## OBSERVATION OF FRENKEL PAIRS ON BOTH SUBLATTICES OF ELECTRON IRRADIATED ZnSe

Holger Zillgen and Peter Ehrhart  
IFF, Forschungszentrum Jülich GmbH, D 52425 Jülich, Germany

**Keywords:** ZnSe, vacancies, interstitial atoms, e<sup>-</sup>-irradiation, diffuse X-ray scattering

**Abstract.** ZnSe wafers have been irradiated at 4K with 2.5 MeV electrons up to a highest dose of  $2 \cdot 10^{19}$  e<sup>-</sup>/cm<sup>2</sup>. The irradiation induced defects and their thermally activated reactions have been investigated by measurements of the diffuse X-ray scattering close to different Bragg reflections and of the change of the lattice parameter. As an average over all irradiation defects these measurements yield a defect introduction rate of  $3 \text{ cm}^{-1}$ , a positive relaxation volume for the interstitial atom of  $V_i^{\text{rel}} = 0.4$  atomic volumes and a negative value of  $V_v^{\text{rel}} = -0.25$  atomic volumes for the vacancy. The different annealing behavior allows the identification of different defects. In addition to the well known annealing stage between 100K and 220K, which has been attributed to the recombination of close Frenkel pairs on the Zn-sublattice, we observe a new prominent stage between 20K and 50K. We attribute this defect annealing to the Se-sublattice and conclude that there are similar concentrations of the Frenkel pairs for both sublattices. Final defect annealing is observed along with the beginning of the vacancy migration in the temperature range between 400K and 650K.

### 1. Introduction.

Point defects determine the electric properties of semiconductors and a detailed understanding of the defect properties has become especially important for a better understanding of the technological important doping problems of these compounds and of their behavior under ion implantation. In spite of some decades of research our present knowledge of defects in II-VI compounds is still very limited. ZnSe has become a model compound for the defect investigations and low temperature electron irradiations have been used for some time for the controlled production of Frenkel defects [1,2]. An annealing stage for Frenkel defects around 90K has first been observed by investigation of the luminescence [3]. Most detailed results have been obtained later on from electron paramagnetic resonance (EPR) which identified close Frenkel pairs (FP's) on the Zn-sublattice. The closest pairs have a typical distance of  $5.5 \text{ \AA}$  and recombine within the annealing stage starting at around 60K [4]; more distant pairs anneal at increasingly higher temperatures. Around 250K the free interstitial Zn atom becomes finally mobile. Remaining vacancies become mobile around 400K. In contrast to this detailed knowledge on the metal sublattice there is nearly no direct experimental information on defects on the Se-sublattice except for a recent indication for the formation of  $F^+$  centers after 6MeV electron irradiation at room temperature (RT) [5].

These results indicate that the defects on the Se-sublattice might be characterized by electronic properties which make them invisible to many electrical detection methods. This situation is also characteristic for the interstitial atom (IA) in many other semiconductors. Therefore we tried to investigate ZnSe by diffuse X-ray scattering which is independent of the electronic properties of a defect and which has been successfully applied for GaAs [6], InP [7] as well as Si and Ge [8].

### 2. Experimental.

We used [100]-oriented polished ZnSe wafers from Crystal GmbH with a typical size of  $5 \times 20 \times 0.5 \text{ mm}^3$  for the present investigations. The irradiations were performed with 2.5 MeV electrons at the Jülich irradiation facility [9] using current densities between 5 and  $10 \mu\text{A}/\text{cm}^2$ . The samples were cooled in a stream of liquid He at 4.7K during irradiations and were transferred to the



X-ray diffractometer without warming. Annealing below room temperature was performed in the He atmosphere within the cryostat and in vacuum at temperatures above RT.

The investigations of the diffuse scattering X-ray intensity and of the change of the lattice parameter were performed with  $\text{CuK}\alpha_1$  radiation at a temperature of 6K (for details see e.g. ref.6,7). The theory necessary to deduce the information contained in the measured diffuse scattering cross section,  $S$ , is well documented [10], and we will use the so-called Huang Diffuse Scattering (HDS) which is observed for small deviations,  $\mathbf{q}$ , of the scattering vector,  $\mathbf{k}$ , from a reciprocal lattice vector,  $\mathbf{G}$ . The scattering cross section of the HDS is given by:  $S_H(\mathbf{k}) = c f^2 |\mathbf{G} \cdot \mathbf{s}(\mathbf{q})|^2$ ;  $\mathbf{s}(\mathbf{q})$  is the Fourier transform of the displacement field of an isolated defect,  $c$  is the defect concentration, and  $f$  is the atomic scattering factor. Expressing the strength of the displacement field  $\mathbf{s}(\mathbf{r})$  by the relaxation volume  $V^{\text{rel}}$  of the defect we obtain:

$$S_H \sim c (V^{\text{rel}})^2 G^2/q^2 \quad (1)$$

$S_H$  yields the product  $c(V^{\text{rel}})^2$ , and by combination with measurements of the change of the lattice parameter,  $\Delta a/a \sim c V^{\text{rel}}/3$ , the two unknown numbers  $c$  and  $V^{\text{rel}}$  can both be determined. As we are considering FP's, the experiment yields, however, only average values from contributions of interstitials and vacancies:

$$S_H \sim c ((V_i^{\text{rel}})^2 + (V_v^{\text{rel}})^2) \quad \text{and} \quad \Delta a/a \sim c (V_i^{\text{rel}} + V_v^{\text{rel}}) \quad (2)$$

These equations show that defects with the opposite sign of  $V^{\text{rel}}$  can cancel in  $\Delta a/a$ , however, the diffuse scattering  $S_H$  adds up.

### 3. Results on the defect production and on the defect structure after 4K irradiation.

Fig.1 shows the defect-induced HDS after an irradiation dose of  $\Phi = 2.1 \cdot 10^{19} \text{ e}^-/\text{cm}^2$ . We observe a decrease of  $S_H q^2$  at small values of  $q$ , which characteristically indicates deviations from a random distribution of defects. Combined with additional features of the distribution of the scattering intensity, e.g. the angular distribution of the intensity around the Bragg peak, and especially the asymmetry of the intensity for  $\pm q$  (see ref.5 for a detailed discussion at the example of InP), we can conclude that there is a dominant contribution of close FPs with a typical distance of 1-2 lattice

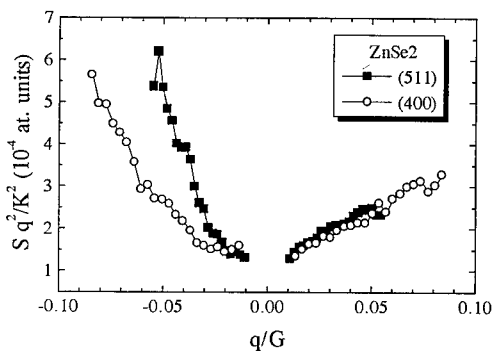


Fig.1: Scattering function of the HDS,  $S_H$ , close to the (511) and (400) reflections of irradiated ZnSe ( $2.1 \times 10^{19} \text{ e}^-/\text{cm}^2$ ).  $S_H$  has been multiplied by  $q^2$ ; for such a plot a constant value is expected for isolated point defects.

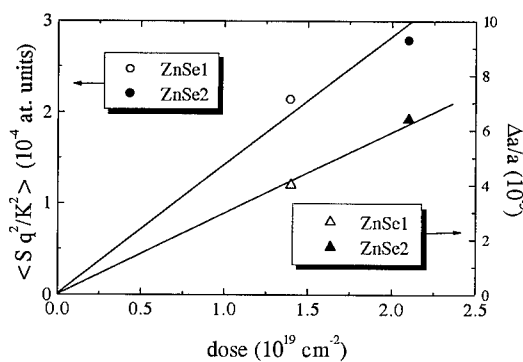


Fig.2: Dose dependence of the average value of the HDS intensity and of the change of the lattice parameter for irradiated ZnSe

constants present after irradiation (see Fig.2 of ref.11). Fig.2 summarizes the average values of  $S_H$  taken close to (511) and (400) reflections and indicates a linear increase of the intensity with the irradiation dose. In addition to the increase of  $S_H$  we observe an increase of the lattice parameter  $a$ , which shows directly that the displacement fields of interstitials and vacancies don't compensate and which yields a specific change  $\eta = (\Delta a/a)/\Phi = (3.0 \pm 0.3) \cdot 10^{-24} \text{ cm}^2$ .

Combining these two results we have no unique solution for  $c$  and  $V_v^{\text{rel}}$  as we have to consider interstitial atoms and vacancies independently (equ.2). As discussed in detail in ref.6 for the case of GaAs we can plot the compatible results using the vacancy relaxation as a parameter (Fig.3). As we have a quadratic equation we get two solutions for one value of  $V_v^{\text{rel}}$ . The positive value of  $\Delta a$  immediately shows that the interstitial atom has a larger and positive value of  $V_i^{\text{rel}}$ . If we neglect the vacancy,  $V_v^{\text{rel}} = 0$ , we obtain  $V_i^{\text{rel}} \approx 1.5 \Omega$  ( $\Omega$  = atomic volume) and an introduction rate  $\Sigma = c/(\Omega\Phi) = 0.26 \text{ cm}^{-1}$ , which is much smaller than the values expected from the threshold energy for defect production of about 8eV [1,4]. In addition the intensity distribution of fig.1 demonstrates immediately that vacancy relaxations can not be neglected. On the other hand the plot shows that only values larger than -0.325 yield non imaginary solutions. Considering all information, i.e. the maximal introduction rate compatible with the given threshold energy ( $\Sigma \approx 6 \text{ cm}^{-1}$  for each sublattice) and theoretical estimates for the defect relaxation volumes, we end up with a most probable set of values for average over all defects:  $V_i^{\text{rel}} \approx 0.4\Omega$ ,  $V_v^{\text{rel}} \approx -0.25\Omega$ , and  $S \approx 3 \text{ cm}^{-1}$ . These values are very similar to the values of those defects in GaAs which are characterized by their annealing around 500K. The high introduction rate shows that high concentrations of defects, i.e. several  $10^{19} \text{ cm}^{-3}$  can be frozen in without annealing or clustering reactions. This scenario is consistent with the deduced structure of close pairs i.e. small defect separation or small recombination- or instability-volumes.

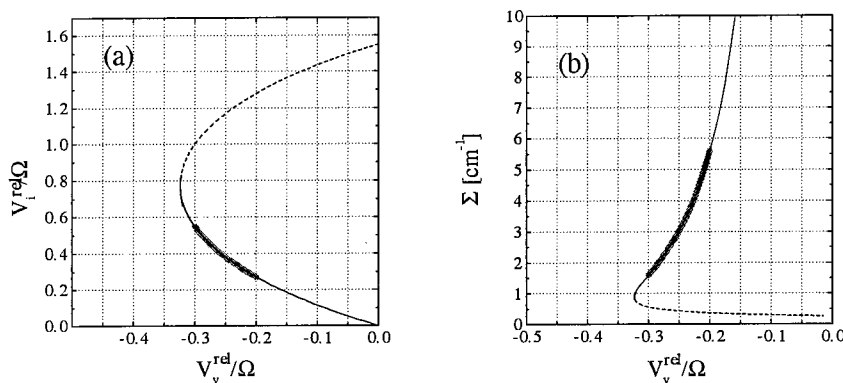


Fig.3: Dependence of the determined value for the relaxation volume of the interstitial atom (a) and of the introduction rate (b) of Frenkel pairs (average over both sublattices) on the assumed value of the relaxation volume of the vacancy. The range of the most probable values is indicated by the hatched line. The dashed part of curves corresponds to high values of the interstitial relaxation volume and to the low introduction rates.

#### 4. Defect annealing.

Some examples for the change of the intensity distribution during defect annealing are shown in Fig.4. The initial curve at 8K represents the symmetrical part of the data of Fig.1 and after annealing at 75K we see a strong annealing at large values of  $q$  and much less annealing at smaller values of  $q$ . Nevertheless there is still an increase of the intensity at larger  $q$  values, i. e. there is some correlation of the FP's left. After annealing at 200K and 300K there is a small but definite increase of the intensity at small  $q$  values. This distribution indicates the formation of small defect clusters along with the thermally activated defect recombination.

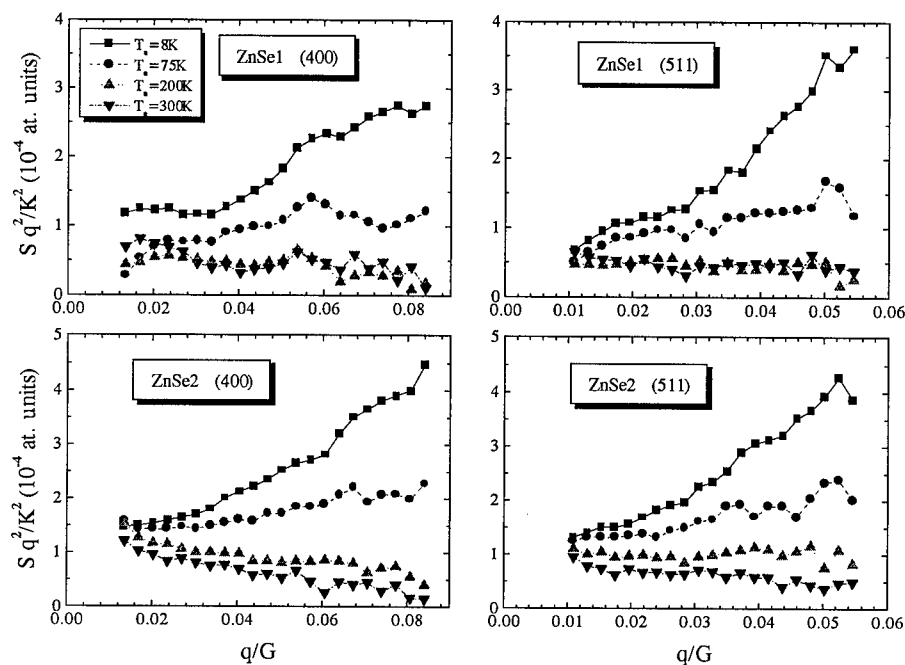


Fig.4: Change of the symmetrical part of the HDS intensity after annealing for 15 min at the indicated temperatures.

The annealing of the diffuse scattering and of the lattice parameter is summarized in Fig.5. The amount of annealing of the HDS depends somewhat on the range of  $q$  values considered in the averaging, however the essential features are independent as demonstrated by the separate averages over the large and small values of  $q$ . We observe essentially a two step annealing of the lattice parameter, :stage I between 30K and 50K and stage II between 100K and 200K. The same stages are seen in the diffuse scattering too, but there is about 30% of the intensity left and final annealing is observed only after annealing at 650K. Only the second stage has been observed so far and has been attributed to differently separated FP's of the Zn sublattice. In addition we observe by the HDS the formation of defect agglomerates which stabilize the defects and reduce the recombination. This observation is in very good agreement with the free migration of interstitials around 200K with an activation energy of 0.6-0.7 eV [2]. Remarkable in addition, there is relaxation during clustering as there is compensation of the lattice parameter at 200K. The vacancies are assumed to be not changed as they are immobile at these temperatures [1].

The first annealing stage which is nearly finished at 50K has not been observed before. Therefore it seems very unlikely that this stage is related to a different less stable FP on the Zn-sublattice and we attribute this stage therefore to defects on the Se-sublattice which have not been observed before. The strong change of the intensity distribution along with the annealing of these FP's (Fig.4) demonstrates that these defects are also characterized by the configuration of close pairs. As the other defects seem to be stable at this temperature we may deduce the more detailed structure of the Se-defects by attributing the difference of the HDS between 8K and 75K to the annealing defect (Fig.6). Assuming further that all the annealing defects are correlated close pairs we may use

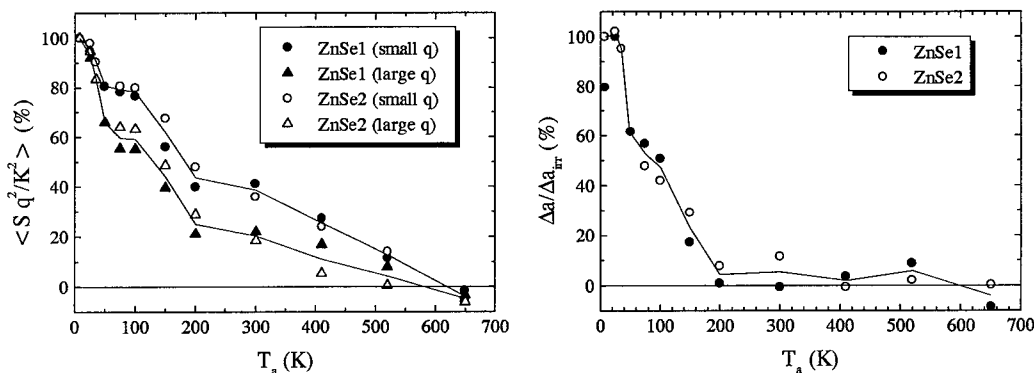


Fig.5: Annealing of the average values of the HDS intensity and of the lattice parameter of electron irradiated ZnSe. Irradiation dose 1:  $1.4 \cdot 10^{19} \text{ cm}^{-3}$  and dose 2:  $2.1 \cdot 10^{19} \text{ cm}^{-3}$ . Averages of the HDS include at (400) reflections : small  $q$ ,  $0.02 \leq q/G \leq 0.45$ , large  $q$ ,  $0.45 \leq q/G \leq 0.74$  ; at (511) reflections: small  $q$ ,  $0.012 \leq q/G \leq 0.038$  and large  $q$ ,  $0.038 \leq q/G \leq 0.052$ .

the value of the HDS obtained by extrapolation to  $q=0$  as an additional information i.e.  $S_{\text{HDS}}(q \rightarrow 0) \sim c (V_i^{\text{rel}} - V_v^{\text{rel}})^2$  and can determine all parameters under these conditions (for details see ref.6):  $\Sigma = 0.5 \text{ cm}^{-1}$ ,  $V_v^{\text{rel}} = 0.6\Omega$ , and  $V_i^{\text{rel}} = -0.25\Omega$ . In spite of the uncertainties of the extrapolation to  $q=0$  this directly deduced values confirm the selection of the branch of solutions of Fig.3 and indicate in addition that the FP's of the Se-sublattice have a somewhat larger relaxation volume than the average over all defects.

As vacancies can be considered as immobile below RT the annealing must be attributed to interstitial mobility. Consistently we attribute the formation of small clusters, which can be deduced from the change of the behavior of the HDS at small values of  $q$  (Fig.4), to the formation of small agglomerates of interstitial type. Due to the small value of  $\Delta a$  remaining at RT, which is within the error bars we can give only a rough estimate with an average size of about 5 atoms.

Final annealing is observed between 400K and 650K and we attribute this annealing to the mobility of the different types of vacancies which eat up the remaining interstitial clusters. Hence this reaction scheme of fast interstitial and slower vacancy mobility compares well also to the III-V compounds GaAs, InP and AlAs [12].

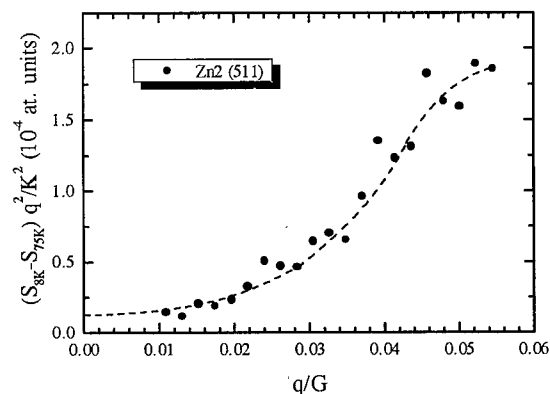


Fig.6: Example of the difference between the scattering intensities after annealing at 8K and 75K which is attributed to the defects which anneal between these two temperatures. The dashed line is a guide to the eye.

### 5. Summary and Conclusion.

[100]-oriented ZnSe wafers have been irradiated at 4K with 2.5 MeV electrons up to a highest dose of  $2 \cdot 10^{19} \text{ e}^-/\text{cm}^2$ . The irradiation induced defects and their thermally activated reactions have been investigated by measurements of the diffuse scattering close to different Bragg reflections and by measurements of the change of the lattice parameter.

Similar to the observations with other semiconductors these measurements yield large defect introduction rates, which are of the order of  $3 \text{ cm}^{-1}$ , and small relaxation volumes of the defects. The distribution of the diffuse scattering intensity indicates the predominance of close Frenkel pairs. In contrast to the observations with the elemental semiconductors there is an increase of the lattice parameter with irradiation dose which indicates, that there is no complete cancellation between the displacement fields due to vacancies and interstitial atoms. Averaging over all defects we obtain a positive relaxation volume for the interstitial of  $V_i^{\text{rel}} = 0.4$  atomic volumes and for the vacancy a negative value of  $V_v^{\text{rel}} = -0.25$  atomic volumes.

We observe two well defined low temperature annealing stages which are located between 20K and 50K and between 100K and 220K respectively, and which account for the annealing of about 40% of the defects each. Only the second stage has been observed so far and has been attributed to the recombination of close Frenkel pairs on the Zn-sublattice/1/. Therefore we attribute the new low temperature stage to the recombination of close Frenkel pairs of the Se-sublattice. Remarkably this first observation of Frenkel pairs on the Se-sublattice yields a similar concentration and size for the Frenkel pairs for both sublattices.

We attribute the annealing up to room temperature to the mobility of the interstitial atoms and observe the formation of small interstitial clusters by those interstitials which escape recombination. Along with the beginning of the vacancy migration we observe total annealing in the temperature range between 400K and 650K.

**Acknowledgements.** We thank Prof. W. Schilling for many helpful discussions and we gratefully acknowledge technical assistance from W. Bergs and U. Dedek and support from Dr. F. Dworschak and B. Schmitz during the irradiations.

### References.

1. G.D. Watkins, in *Electronic Structure and Properties of Semiconductors* (W.Schroeter ed., Vol.4 of Materials Science and Technology, VCH, Weinheim 1992) p.105
2. G. D. Watkins, in *Defect Control in Semiconductors* (K.Sumino ed, Elsevier, 1990) p.933
3. R. M. Detweiler, B. A. Kulp, *Phys.Rev.***146** (1966) 513
4. G.D.Watkins and F.Rong, *Mat.Sci.For.* **10/12** (1986) 827
5. E.S. Volkova, I.A. Gorn, and V.N. Martynov, *Inorganic Materials* **28** (1993) 1973; translated from *Neorganicheskie Materialy* **28** (1992) 2419.
6. A. Pillukat, K. Karsten, and P. Ehrhart, *Phys. Rev.* **B53** (1996) 7823
7. K. Karsten and P. Ehrhart, *Phys.Rev.* **B51** (1995) 10508
8. St. Bausch, H. Zillgen, and P. Ehrhart, *Mat.Sci.For.* 196/201,(1995) 1141
9. J. Hemmerich, W. Sassin, and W. Schilling, *Z.Angew. Phys.*,**29** (1970) 205.
10. P.H. Dederichs, *J.Phys.* **F3** (1973) 471
11. H. Zillgen and P. Ehrhart, this volume
12. A. Gaber, H. Zillgen, P. Ehrhart, P. Partyka, and R.S. Averback, this volume

## INTERFACE DEFECTS AND THEIR EFFECT ON THE ELECTRICAL PROPERTIES OF ZnSe/GaAs HETEROJUNCTIONS GROWN BY MBE

D. Seghier, I.S. Hauksson, H.P. Gislason, K.A. Prior<sup>1</sup> and B.C. Cavenett<sup>1</sup>  
Science Institute, University of Iceland, Dunhagi 3, IS-107 Reykjavík, Iceland  
<sup>1</sup> Department of Physics, Heriot-Watt University, Edinburgh EH14 4AS,  
Great Britain

**Keywords :** ZnSe, GaAs, heterojunction, interface, admittance, hysteresis, capacitance.

**Abstract.** We studied electrical properties of MBE-grown ZnSe/GaAs heterojunctions due to the interface states, by admittance spectroscopy. The capacitance-voltage characteristics show a hysteresis which can be related to an unusually slow capacitance transient. A large frequency dispersion of the capacitance and a broad peak in the conductance spectra are observed at high temperatures. These observations strongly suggest the presence of a continuum of defects in the interface between ZnSe and GaAs. The capacitance versus frequency data was analyzed in terms of Lehocvec's model of an interface state continuum with a single time constant giving a density of interface states about  $4 \times 10^{12} \text{ cm}^{-2} \text{ eV}^{-1}$  for typical both n- and p-type samples. We attribute the long time constant observed in the capacitance transients to slow changes in the electrical charge on the interface states. The presence of interface states may seriously affect the performance of ZnSe/GaAs based devices. The correlation between their behavior and the growth conditions is of prime importance and is presently under study.

### Introduction

Wide-bandgap materials like ZnSe have gained a lot of interest for use in blue-light emitting devices. Due to the lack of high quality ZnSe substrates, it is necessary to grow ZnSe epilayers onto GaAs substrate. The lattice mismatch between ZnSe and GaAs is 0.27 % and is a source of defects created at the heterointerface. The defects are known to affect the mobility [1,2], interface barrier height [3] and other electrical properties such as defect density and degradation phenomena of the related devices. Characterization and control of the ZnSe/GaAs heterointerface are of prime importance in obtaining high-quality ZnSe epilayers on GaAs substrate. Although many reports have been published on the MBE-ZnSe/GaAs interface, it is still a subject of great interest. We here present experimental results obtained by capacitance-voltage (C-V) measurements and admittance spectroscopy which indicate the presence of unusually slow interface states in MBE-grown p- and n-type ZnSe layers on GaAs substrates. These interface states result in a long time constant relaxation in the ZnSe/GaAs heterojunction (HJ) capacitance and thus a hysteresis in the C-V characteristics.

### Experimental

The ZnSe layers with thickness of about 1 to 2  $\mu\text{m}$  were grown by MBE on conductive (100) GaAs substrates. The growth temperature was 300 °C. For p-type doping nitrogen was incorporated by using an Oxford Applied Instruments plasma source. For n-type

doping iodine produced from an electrochemical cell was used. Table I summarizes selected properties of some of our samples.

Different Au/p-ZnSe/p<sup>+</sup>-GaAs and Au/n-ZnSe/n<sup>+</sup>-GaAs structures have been studied. The electrical characteristics of these devices are typical of two diodes connected back-to-back: a ZnSe/GaAs HJ and a Au/ZnSe Schottky diode (SD). Due to the large valence band discontinuity in the HJ and a high doping level in the GaAs substrate the depletion region is only in the ZnSe side. An applied voltage  $V$  will be divided between these two junctions. When the polarity of  $V$  is such that the SD is reverse-biased, most of the bias drops across the SD, and the corresponding depletion region  $x_{SD}$  increases. For the other polarity however,  $x_{SD}$  decreases, until  $x_{SD} = x_{HJ}$ , where  $x_{HJ}$  is the depletion region in ZnSe at the heterojunction. This occurs when  $\phi_{SD} = V + \phi_{HJ}$  where  $\phi$  is the potential barrier. Further increase of  $V$  appears as a reverse bias across the HJ, which at this stage limits the current in the circuit, and therefore  $x_{HJ}$  begins to increase substantially.

### Results and Discussion

Results obtained from the different samples summarized in table 1 were generally similar. Therefore, the curves that will be presented here are obtained from sample # 1 unless otherwise specified.

Figure 1 shows the  $C$ - $V$  plots observed at room temperature. Negative voltages are reverse-bias for the HJ. When the capacitance is measured by scanning the applied voltage from 0 V to a given value of the reverse bias, followed by a scanning in the opposite direction, a large hysteresis is observed. The capacitance is lower in the second scan compared to the first one (Fig. 1). This characteristic is common for GaAs MIS structures, and is interpreted in terms of energy distributed interface states.

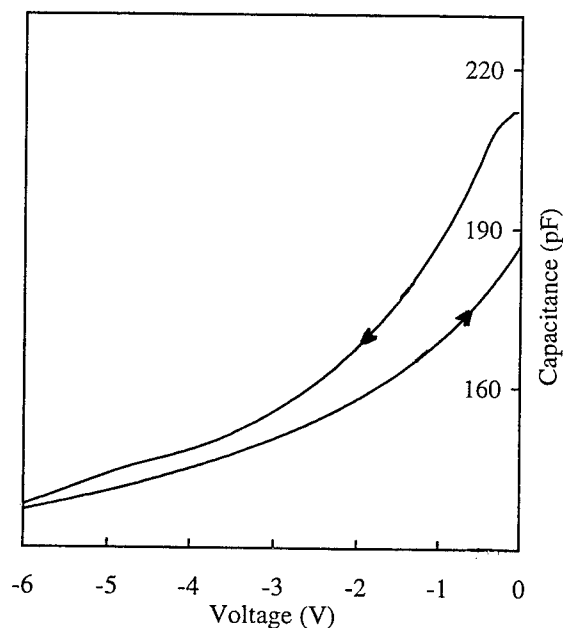


Fig. 1:  $C$ - $V$  characteristics from sample # 1 at 250 K. The arrows indicate the scan directions : from 0 to -6V and from -6 to 0V.

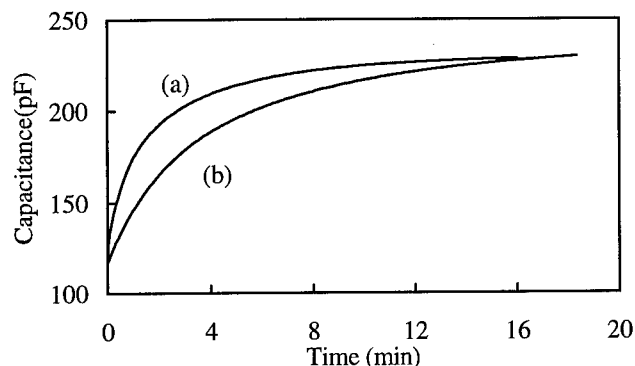


Fig. 2: Capacitance-time transients from sample # 1 for step changes in bias (a) from -4 to 0 V; and (b) from -6 to 0 V, at 250 K.

Capacitance transients ( $C$ - $t$ ) obtained after a change in the reverse bias were measured for a variety of biases and temperatures. Figure 2 shows the  $C$ - $t$  curves for a step change in bias from -4 to 0 V (Fig. 1 a), and from -6 to 0 V (Fig. 1 b) at room temperature. As can be seen, the transients are highly non-exponential, and their shape depends on the initial applied bias. Hence, they are not likely to arise from discrete deep energy levels in the bandgap. Their time constant is unusually long, from a few seconds to minutes at room temperature, depending on samples (Table I), and is longer at lower temperatures. The hysteresis seems to be related only to the slow time constant  $C$ - $t$ . Indeed, when the  $C$ - $V$  characteristics are plotted using a long enough scan delay no hysteresis is observed. Also, at high temperature where the  $C$ - $t$  transients are short, the  $C$ - $V$  does not exhibit a hysteresis irrespective of the scan delay.

We calculated the built-in potential based on the extrapolated voltage intercept  $V_0$  from the  $1/C^2$  versus  $V$  curves. Abnormally high values were measured (8 V in some samples). These observations also suggest the presence of interface states at the heterointerface. In order to check this hypothesis, admittance spectroscopy measurements were performed. Capacitance versus frequency spectra were recorded at a large number of frequencies in the range of  $2 \text{ Hz} < f < 1 \text{ MHz}$ , at different temperatures. Figure 3 shows some typical plots of  $\Delta C$  vs  $\log(f)$  where  $\Delta C$  is the difference:  $C(f) - C(1 \text{ MHz})$ , and  $f$  the frequency. Measurements of the a.c. conductance versus temperature at different frequencies were also performed. Figure 4 shows conductance versus temperature spectra obtained from samples # 1, # 2, and # 3, measured at 10 Hz. At room temperature and below a relatively small difference between low and high frequency HJ capacitance is observed. At high temperature a large frequency dispersion is measured in the junction capacitance of samples # 1 and # 2. Also a broad peak is observed in the conductance-versus-temperature spectra. This peak is quite broad and weakly dependent on the a.c. frequency under analysis. Such behavior is typical for energy distribution of interface states. The high temperature at which the peak is observed suggests a band of interface states deep in the bandgap. At 400 K (our high temperature limit, since higher temperatures may induce irreversible changes in the properties of the sample) the a.c. conductance of samples # 3 and # 4 was still increasing suggesting a peak at higher temperature (Fig. 4). If this is the case, one can infer an interface state band in samples # 3 and # 4 deeper in the bandgap compared to samples # 1 and # 2, which agrees with the longer capacitance transients in the former.



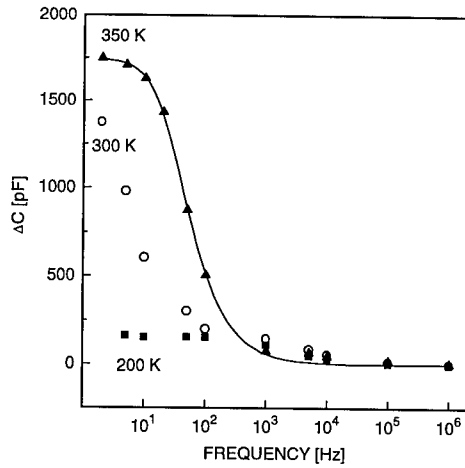


Fig. 3:  $\Delta C$  vs  $\log(f)$  at different temperatures from sample # 1. The discrete points are measured values and the solid curves are the best fits to the experimental data of Eq. (10), for  $T=350\text{K}$ .

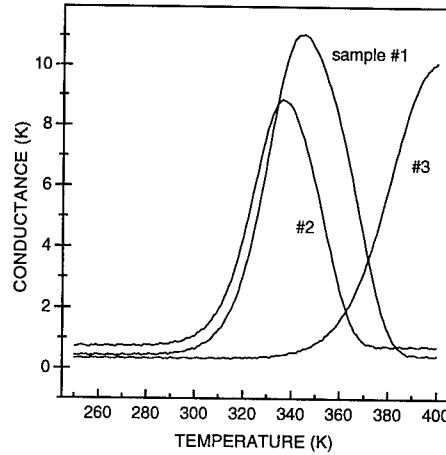


Fig. 4: Conductance versus temperature spectra from sample # 1 and # 2.  $f = 10$  Hz.

We believe that the frequency dispersion of the capacitance and the conductance peak are related to interface states at the heterointerface. The abnormally high values of the built-in potential deduced from the extrapolated voltage intercept confirm this hypothesis. In the literature there is a discrepancy in values of this parameter. A value of 7 V was reported in Ref. 5, while a value of 1.2 V was reported in Ref. 6. Theoretical calculations of the potential barrier of the ZnSe/GaAs HJ gave a value of about 1 V. It is well known, however, that heterojunctions barrier heights strongly depend on the density of interface states [7]. Fonash [8] studied in detail the effect of an interfacial layer on the shape of the  $I/C^2$ -V profiles and the voltage intercept. He showed that in the presence of an interfacial layer,  $V_0$  may be very different from the right barrier value.

In case of a moderately thick interfacial layer, the interface states can readily exchange carriers with the bulk of ZnSe. Assuming : (a) a constant density of interface states; (b) a capture rate for either carrier type which is independent on the surface states energy; and (3) one single time constant; the interface-states-capacitance  $C_p$  is parallel to the depletion-layer-capacitance  $C_d$ . The equivalent circuit is as described in Ref. 10. The interface-states-capacitance  $C_p$  is obtained from :

$$C_p = \Delta C = C - C_d \quad (1)$$

where  $C_d$  is obtained by measuring the capacitance at 1 MHz. As reported by Lehovec [10],  $C_p$  is in this case given by:

$$C_p = q A D_s \arctg(\omega\tau) / \omega\tau \quad (2)$$

where  $A$  is the diode area,  $D_s$  the density of the interface states per unit energy and area,  $\tau$  their relaxation time, and  $\omega$  the angular frequency ( $= 2\pi f$ ).

Sample	Carrier concentration (cm <sup>-3</sup> )	t(s)	Position of the Conductance peak (K)
# 1	p = 1.3×10 <sup>17</sup>	<1	344
# 2	n = 5×10 <sup>17</sup>	<1	335
# 3	p = 5×10 <sup>17</sup>	8	> 400
# 4	p = 2×10 <sup>17</sup>	100	> 400

Table I

*Representative n- and p- type samples studied in this work. t is the approximate time needed to reach the 0 V bias capacitance after the application of 6 V reverse-bias, at 300 K.*

The values of  $C_p$  are deduced from Eq. (1). Typical plots of the experimental values of  $C_p$  vs  $\log(f)$  are shown in Fig. 3. The solid curve represents the best fit of the experimental data (discrete points) to the theoretical formula (2). Fitting to data measured at room temperature and lower temperatures were generally not successful. At these temperatures  $\Delta C$  is mainly due to carrier traps in the bulk. The values of  $D_s$  and  $\tau$  obtained from the fitting procedure for data taken at 350 K are:  $D_s = 4 \times 10^{12} \text{ cm}^2 \text{ eV}^{-1}$ ;  $\tau = 7 \text{ ms}$ , and  $D_s = 3 \times 10^{12} \text{ cm}^2 \text{ eV}^{-1}$ ;  $\tau = 5 \text{ ms}$  for sample # 1 and sample # 2 respectively. As  $D_s$  is significant there is a large contribution  $C_p$  from the interface states in the device capacitance. This high density combined with the slow changes in charge on the interface states give rise to the long transients observed in the HJ capacitance. It is also illuminating to make a correlation between values of the  $C$ - $t$  time constant for different samples with the depth of the interface states continuum in the bandgap. We find that samples which exhibit longer capacitance transients show a conductance peak at higher temperatures than samples with faster capacitance transients.

### Conclusion

In summary, interface properties of MBE-ZnSe/GaAs heterojunctions were investigated. It was found that in response to a change in the applied reverse bias very slow heterojunction capacitance transients are obtained. The time constant of such transients is longer at lower temperatures and may reach a few minutes in some samples. This slow relaxation induces a large hysteresis in the  $C$ - $V$  characteristics of the heterojunction. To understand this behavior admittance spectroscopy measurements were performed. A large frequency dispersion of the capacitance and a broad peak in the conductance spectra were observed at high temperature. This indicates the presence of a density of energy distributed interface states at the heterointerface. Good fitting of calculations by Lehovec[10] to the capacitance versus frequency data were obtained, and the density of interface states was evaluated to about  $4 \times 10^{12} \text{ cm}^{-2} \text{ eV}^{-1}$ . Therefore we attribute the long capacitance transients to slow changes of the charge in the interface states. These results strongly emphasize the

importance of the growth conditions and substrate treatment for growing ZnSe/GaAs based devices.

#### Acknowledgments

This research was supported by the Icelandic Research Council and the University Research Fund.

#### References

1. W. Stutius and F.A. Ponce, J. Appl. Phys. **58**, 1548(1985)
2. K. Morimoto, J. Appl. Phys. **64**, 4951(1988)
3. DJ. Olego, J. Vac. Sci. Technol. B6, 1193(1988)
4. E. Ho, P.A. Fisher, J.L. House, G.S. Petrich, L.A. Kolodziejski, J. Walker, and N.M. Johnson, Appl. Phys. Lett. **66**, 1062 (1995).
5. H. Goto, T. Tanoi, M. Takemura, and T. Ido, Jpn. J. Appl. Phys. **34**, L827(1995).
6. M.A. Haase, H. Cheng, J.M. Depuydt and J.E. Potts, J.Appl.Phys. **67**, 448(1990)
7. A.G. Milnes and D.L. Feucht, *Heterojunctions and Metal-Semiconductor Junctions* (Academic Press, New York, 1972), Chap. 4, p. 98
8. S.J. Fonash, J. Phys. D: Applied Physics **54**, 1966(1983)
9. A. Singh Solid-state Electron. **28**, 223(1985)
10. K. Lehovc, Appl. Phys. Lett. **8**, 48(1966)

## DONOR DOPING OF ZnSe: LATTICE LOCATION AND ANNEALING BEHAVIOR OF IMPLANTED BORON

B. Ittermann, G. Welker, F. Kroll, F. Mai, K. Marbach, H. Ackermann,  
H.-J. Stöckmann, E. Oldekop<sup>1</sup>, W.-D. Zeitz<sup>1</sup>

Universität Marburg, Fachbereich Physik, D-35032 Marburg, Germany

<sup>1</sup>Hahn-Meitner-Institut, Bereich FD, D-14019 Berlin, Germany

**Keywords:** ZnSe, boron, donor doping, ion implantation,  $\beta$ -NMR

**Abstract.** Spin polarized, radioactive  $^{12}\text{B}$  probe nuclei are implanted into nominally undoped ZnSe single crystals at stationary concentrations  $\leq 10^9/\text{cm}^3$ . From temperature and orientation dependent  $\beta$ -radiation detected nuclear magnetic resonance measurements we conclude that at  $T = 800\text{ K}$  about 85% of the implanted B end up as ionized donors at Zn-sites ( $\text{B}_{\text{Zn}}^+$ ) with unperturbed surroundings. The temperature dependence of the  $\text{B}_{\text{Zn}}$  signal intensity yields activation parameters for the population of this site. We obtain  $E_A = 0.61(3)\text{ eV}$  and a value of  $10^{6.0(3)}/\text{s}$  for the pre-exponential factor.  $\text{B}_{\text{Zn}}$  is immobile up to 950 K within the time window of the  $\beta$ -decay lifetime.

### 1. Introduction.

The vast majority of investigations related to doping problems in ZnSe is dealing with p-type doping. This is related to the well known, even though not well understood, compensation effects which up to now prohibit hole concentrations beyond  $10^{18}/\text{cm}^3$  ( see [1,2] for recent reviews). It has to be seen, however, that there are also many open questions concerning n-ZnSe. The highest free-electron concentrations obtained so far are about  $n \leq 10^{19}/\text{cm}^3$  and were achieved using halogens (Cl, I, Br) as donors. While these values are sufficient for most applications it is not clear which microscopic mechanism prevent even higher carrier concentrations. The best suited group-III elements (Al, Ga, In) give only  $n \leq 10^{17-18}/\text{cm}^3$ . We therefore have the same situation as for p-type doping, incorporation of dopants on the Se sublattice apparently gives higher efficiencies. Since the principal mechanisms responsible for the saturation of free carrier concentrations at high doping levels may well be very similar for both, p- and n-type doping, an improved microscopic understanding of these problems is needed for either type of conductivity.

It is another remarkable fact that just for the lightest elements of groups III and VII of the periodic table, B and F, there is virtually no experimental (or theoretical) information available concerning their potential as dopants in ZnSe. The main objective of this study is to rectify this situation for the case of boron by an investigation of its microscopic properties with emphasis on its suitability as a donor in ZnSe. For this purpose we performed  $\beta$ -radiation detected nuclear magnetic resonance ( $\beta$ -NMR) measurements on implanted, radioactive  $^{12}\text{B}$  probe nuclei. Due to the high sensitivity of this 'nuclear technique' we are able to explore, as a first step, the behavior of well isolated probes at stationary concentrations of  $\leq 10^9\text{ B}/\text{cm}^3$ . In a later stage it is intended to look at samples which are pre-implanted with  $\approx 10^{18}/\text{cm}^3$  stable B.

### 2. Experimental.

Details of the  $\beta$ -NMR technique are given in Refs. [3,4] and references contained therein. Essentially,  $\beta$ -active  $^{12}\text{B}$  probe nuclei with a radioactive lifetime  $\tau_\beta = 29.3\text{ ms}$  and a nuclear spin  $I = 1$  were created in the nuclear reaction  $^{11}\text{B}(\text{d,p})^{12}\text{B}$  in a thin boron target foil irradiated with a beam of 1.5-MeV deuterons from an ion accelerator. The recoil ejected  $^{12}\text{B}$  nuclei were spin polarized along an external magnetic field  $B_0$  by selection of a recoil angle of  $45 \pm 8^\circ$  relative to the incident beam and implanted into the ZnSe crystal with broadly distributed energies between 0 and 450 keV. Thus, the concentration profile was rather homogeneous up to a maximum depth of about 1.2  $\mu\text{m}$ . The total

number of  $^{12}\text{B}$  nuclei being simultaneously present in the sample never exceeded  $10^5$ , corresponding to a concentration of  $\leq 10^9/\text{cm}^3$ . Not only the probe nuclei themselves but also their implantation-damage cascades are therefore well isolated from each other. The detected quantity was the  $\beta$ -decay asymmetry  $a$  which is proportional to the nuclear spin polarization  $P$ .

We used nominally undoped bulk crystals ( $\rho > 10^8 \Omega\text{cm}$ ) of  $10 \times 10 \times 2 \text{ mm}^3$ , cut along (100) surfaces. In order to prevent Se effusion at higher temperatures the samples were coated with a  $\sim 20\text{-nm}$   $\text{Si}_3\text{N}_4$  film.

### 3. Results and discussion.

#### 3.1 Lattice locations

There is a checklist of five preconditions that any useful donor element in ZnSe has to fulfill.

- i) The implanted impurities have to occupy the 'right' lattice site, i.e., we need  $\text{B}_{\text{Zn}}$ .
- ii) The full  $T_d$  symmetry of this site has to be maintained. In case of a distortion we would expect a deep rather than a shallow center.
- iii) As a shallow donor  $\text{B}_{\text{Zn}}$  has to be ionized at room temperature ( $\text{B}_{\text{Zn}}^+$ )
- iv) B has to be thermally stable at the Zn-site, a rapidly diffusing dopant is technologically rather useless.
- v) if, as in our case, the incorporation of the impurities is achieved by ion implantation it is mandatory that unperturbed  $\text{B}_{\text{Zn}}$  is formed at convenient temperatures. Any necessity for an annealing step at high temperatures would be a severe obstacle in the case of the temperature sensitive II-VI semiconductors.

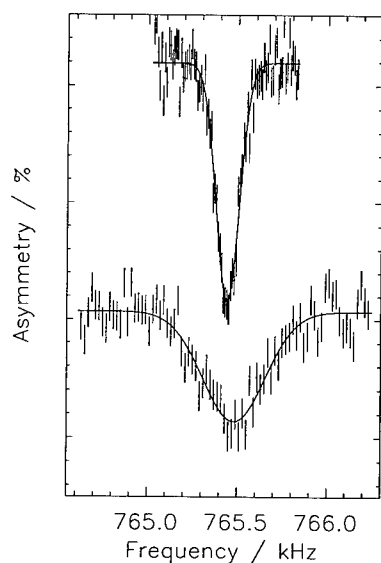


**Fig. 1.**  $\beta$ -NMR spectra of  $^{12}\text{B}$  in ZnSe.  $T = 800 \text{ K}$ ,  $B_0 = 0.1 \text{ T}$ ,  $\langle 100 \rangle \parallel \mathbf{B}_0$  (top) and  $\langle 110 \rangle \parallel \mathbf{B}_0$  (bottom). The strong orientation dependence of the dipolar line widths is used for a determination of the corresponding lattice site

$\beta$ -NMR spectra measured at  $T = 800 \text{ K}$  are shown in Fig. 1 for two different crystal orientations. The resonances occur at the Larmor frequency  $\nu_L$  and so far no further resonances were observed. The existence of a Larmor resonances means that the corresponding B impurities are located at sites with  $T_d$  symmetry and are in their diamagnetic charge state. There are four cubic sites available in the zincblende lattice, two substitutional ones on either sublattice,  $\text{B}_{\text{Zn}}$  and  $\text{B}_{\text{Se}}$ , and two tetrahedral interstitial sites ( $\text{B}_i$ ), surrounded by either four Zn or four Se atoms.

In Fig. 1 an inhomogeneous broadening of the resonances can be seen which depends strongly on the crystal orientation. This broadening  $\Delta \nu_{\text{inh}}$  is due to the dipole-dipole interaction between the nuclear spins of the  $^{12}\text{B}$  probes and neighboring Zn and Se host atoms. The angular dependence of  $\Delta \nu_{\text{inh}}$ , obtained from the measured line widths after proper subtraction of all instrumental contributions, is plotted in Fig. 2 together with a fit curve which obviously gives a reasonable description of the data. The first theoretical description of the dipolar line width was already given by Van Vleck [5] and later extended to the case of isolated impurities in a host lattice by

Hartmann [6].  $\Delta v_{inh}$  can be calculated for any of the lattice positions in question with the local bond lengths as only free parameters. In contrast to homogeneous systems these bond lengths are *a priori* not known since a local lattice relaxation around the impurity atom has to be considered. There are, however, physical constraints in sign and magnitude on this local distances as we will discuss later on.

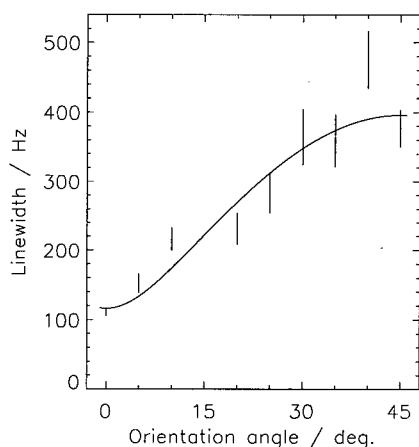


**Fig. 2.** Angular dependence of the dipolar line width.  $\mathbf{B}_0$  is rotated in the  $\{100\}$  plane.  $0^\circ$ :  $\langle 100 \rangle \parallel \mathbf{B}_0$ ,  $45^\circ$ :  $\langle 100 \rangle \perp \mathbf{B}_0$ . The solid line represents a fit which assumes B at Zn sites and a  $\sim 20\%$  lattice contraction around the impurity.

The solid curve in Fig. 2 represents the best fit of the Hartmann-Van Vleck theory to our data. It is based on the assumption of  $B_{Zn}$  and yields a quite strong lattice contraction of the first and second shell of neighboring atoms by  $-21(1)$  and  $-25(2)\%$ , respectively. It has to be stated, however, that also if the  $B_{Se}$  or B sites are assumed we can obtain fits of comparable quality. In any case a strong lattice contraction of about 20% in the first two shells is necessary to obtain acceptable agreement. Especially around interstitial impurities, however, we consider a strong inward relaxation as an unphysical result and therefore discard the possibility of B at tetrahedral interstitial sites. Also, we believe that the assumption of  $B_{Se}$  cannot explain the experimental observations satisfactorily. For  $B_{Se}$  we had to assume the  $B_{Se}^{3-}$  charge state, otherwise the defect would not be diamagnetic or we would expect it to undergo a Jahn-Teller distortion because of its partially filled electronic p-shell (see Ref. [7] for a general discussion of that point). A triply charged defect, on the other hand, should cause a strong local

charge perturbation and therefore large electric field gradients (EFG's) at the neighboring Zn nuclei. The Hartmann-Van Vleck fit requires, however, the impurity induced quadrupole interaction in the first shell to be much smaller than the Zeeman interaction of the  $^{67}Zn$  nuclei (4.1% natural abundance). We determine an upper limit of  $e^2qQ/h(^{67}Zn) \leq 0.5$  MHz for the quadrupole coupling constant. This is such an extraordinarily small value for a mid-sized nucleus with a rather average quadrupole moment of  $Q = 0.150$  b that we also discard the assumption of  $B_{Se}$ .

The only remaining possibility is  $B_{Zn}$  which with all its properties fits well into the experimental picture. In the  $B_{Zn}^+$  charge state the center is i) diamagnetic (as observed) and ii) not prone to Jahn-Teller distortions.  $B_{Zn}^+$  is a very small ion ( $r_{ion} = 0.35$  Å), therefore a local contraction of the surrounding lattice is not surprising. For the impurity induced EFG around  $B_{Zn}$  we get essentially no restriction. This is mainly due to the fact that the first shell of Se neighbors has no quadrupole moments and in the second shell the quadrupole interaction is already very weak anyway.

Our conclusion therefore is that the observed Larmor resonances correspond to  $B_{Zn}$  in the positive charge state and with full  $T_d$  symmetry. Conditions i), ii), and iii) of our check list are therefore fulfilled. The same is true for point iv) of that list. An inhomogeneous broadening of a resonance, as we observed it up to  $T = 950$  K, is always an indication of immobile probe nuclei. If the opposite were true and we had diffusing impurities with jump rates  $w \geq \pi \Delta v_{inh}$ , the well known effect of motional averaging would occur resulting in the same narrow line width for all crystal orientations. From the smallest value of  $\Delta v_{inh} \approx 100$  Hz (for  $\langle 100 \rangle \parallel \mathbf{B}_0$ ) we obtain  $w < 300$  s $^{-1}$  as an upper limit for the possible jump rates of  $B_{Zn}$ .

In the only other investigation of this system that we are aware of Adachi and Machi [8] found a new peak in photoconductivity spectra of ZnSe after high-dose boron implantation and annealing at 400°C for 10 min. This feature was attributed to  $B_{Zn}$  and a donor ionization energy of  $E_D = 0.12$  eV was derived. Our microscopic results, even though obtained under quite different implantation and annealing conditions, confirm this assignment.

### 3.2 Annealing Behavior

The temperature dependence of the  $\beta$ -NMR signal intensity at the Larmor frequency is shown in Fig. 3. According to our discussion in the preceding section, this signal measures the fraction  $f_{Zn}$  of  $^{12}B$  nuclei at unperturbed Zn sites. In previous experiments [9] we found that 100% of Larmor resonant probes give a 10% asymmetry signal. The data of Fig. 3 were measured under somewhat different experimental conditions which cause a different scaling between measured asymmetry and corresponding probe fraction. From reference spectra measured at  $T = 950$  K (not shown) we determine that the saturation value of the asymmetry signal in Fig. 3 corresponds to  $f_{Zn} \approx 85\%$ .

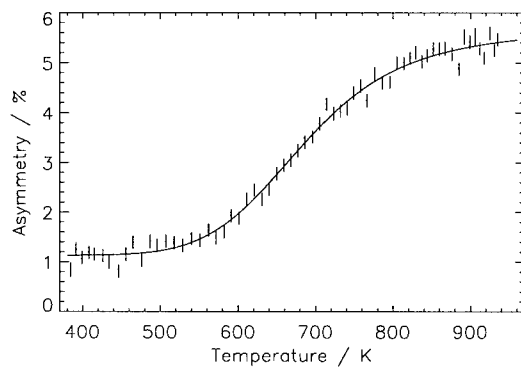


**Fig. 3** Temperature dependence of the  $\beta$ -NMR signal intensity at the Larmor frequency. This signal represents the fraction of implanted B at unperturbed Zn sites. The solid line represents a fit of two-state annealing model.

rising temperature. The quantitative analysis yields  $\mu_0 = 10^{6.0(3)} s^{-1}$  and  $E_A = 0.61(3)$  eV as parameters of the thermally activated conversion. We neglect, in this picture, the possibility that, due to some depolarizing interaction, the *polarization* of  $B_x$  might decay faster than the *fraction* itself. In such a case we had to replace  $\lambda_\beta$  by  $\lambda_x = \lambda_\beta + \lambda_{Pol,x}$ , with a depolarization rate  $\lambda_{Pol,x}$ . Our parameters represent only lower limits for the true conversion rates since we assumed  $\lambda_x = \lambda_\beta$ , i.e., the lowest possible value for  $\lambda_x$ .

One possible picture of in-beam  $\beta$ -NMR is to look at this experiment as an annealing experiment where the annealing temperature  $T_A$  is given by our actual measuring temperature and the annealing time  $t_A$  by  $\tau_\beta$ . At first glance, the temperatures of Fig. 3 may appear quite high, we need unpleasant 875 K in order to have the  $B_x \rightarrow B_{Zn}$  conversion to 90% completed. But if we use the activation parameters  $\mu_0$  and  $E_A$  to convert this temperatures to  $t_A = 1000$  s, the typical time scale of a more conventional experiment, we find that already at  $T_A = 385$  K the conversion process would be to 90% completed. This value is well below the growth temperatures used even in the modern epitaxial techniques and there is certainly little danger to generate intrinsic point defects at  $T < 400$  K. We can conclude, therefore, that for all practical purposes the last remaining point on our 'suitable donor'-check list is satisfied, too.

The fit function included in the figure is based on a two-state trapping model which we already used in previous studies [9,10]. This model assumes that directly after the implantation  $f_{Zn}$  is almost zero. The majority of the implanted B, however, initially forms an unidentified defect center  $B_x$ . We further assume that a thermally activated conversion  $B_x \rightarrow B_{Zn}$  with a rate  $\mu = \mu_0 \cdot \exp(-E_A/k_B T)$  takes place while back conversion is not included ('trapping' at the Zn site). In both configurations,  $B_{Zn}$  and  $B_x$ ,  $^{12}B$  decays with a rate  $\lambda_\beta = 1/\tau_\beta$ . Within this model the observed increase in  $B_{Zn}$  signal intensity now simply reflects the dominance of  $\mu$  over  $\lambda_\beta$  with

Attempts on a more physical interpretation of this annealing parameters, especially the identification of the underlying microscopic process are underway but a completely satisfactory picture has not yet emerged. This topic will certainly be a central issue of our future work on this system.

#### 4. Summary.

We have investigated microscopic properties of implanted B in ZnSe in the temperature range of 300 to 900 K with  $\beta$ -NMR. We conclude that the only detected resonances are due to isolated and unperturbed  $B_{Zn}^+$ , i.e., the regular, ionized donor. The complete ionization already at room temperature indicates a shallow donor in accordance with the ionization energy of 0.12 eV, as found by Adachi and Machi [9]. From the temperature dependence of the  $B_{Zn}$ -signal parameters were derived for the thermally activated population of the Zn site. This, in turn, allowed to calculate the annealing temperatures that would be necessary in conventional experiments not restricted to the short 30 ms time window. We obtain the result that after implantation of stable B an annealing step of 1000 s at 385 K would be sufficient for quantitative formation of  $B_{Zn}$ . The bottom line of our study is that from a microscopic point of view all preconditions for B as a suitable donor in ZnSe are fulfilled.

It has to be emphasized, however, that so far the validity of this result is restricted to the case of infinite dilution, we had only about  $10^5$  probe nuclei simultaneously in the sample. As a next step we intend to pre-implant stable B at concentrations of about  $10^{18}/\text{cm}^3$ , perform an annealing step as described above, and then study the properties of the post-implanted  $\beta$ -NMR probes  $^{12}\text{B}$  under these different conditions.

#### Acknowledgements

We thank Dr. W. Stolz, Marburg, for many helpful discussions and his continuous support with the sample characterization. The experiments were performed at the ISL laboratory of the Hahn-Meitner Institut, Berlin and at the Strahlencentrum Gießen. The hospitality of both institutes and the assistance of their technical staff is gratefully acknowledged. This work was supported by the BMBF (contract no. AC4-MAR).

#### References.

1. Y. Marfaing, J. Crystal Growth **161**, 205 (1996)
2. H. Kukimoto, Mat. Sc. Forum **143-147**, 385 (1994).
3. H. Ackermann, P. Heitjans, H.-J. Stöckmann, in "Hyperfine Interactions of radioactive nuclei", ed. J. Christiansen (Springer, Berlin-Heidelberg-New York) p. 291 (1983).
4. B. Ittermann, H. Ackermann, E. Diehl, B. Fischer, H.-P. Frank and H.-J. Stöckmann, Hyp. Int. **79**, 591 (1993).
5. J. H. Van Vleck, Phys. Rev. **74**, 1168 (1948).
6. O. Hartmann, Phys. Rev. Lett. **39**, 832 (1977).
7. G. D. Watkins, Mat. Sci. Forum **143-147**, 9 (1994).
8. S. Adachi, Y. Machi, Jap. J. Appl. Phys. **17**, 135 (1978).
9. H. Metzner, G. Sulzer, W. Seelinger, B. Ittermann, H.-P. Frank, B. Fischer, K.-H. Ergezinger, R. Dippel, H.-J. Stöckmann and H. Ackermann, Phys. Rev. **B42**, 11419 (1990).
10. E. Diehl, K.-H. Ergezinger, B. Fischer, H.-P. Frank, F. Kroll, F. Mai, K. Marbach, W. Seelinger, S. Weißenmayer, G. Welker, H. Ackermann, H.-J. Stöckmann, Hyp. Int. **C1**, 219 (1996).



## DETERMINATION OF THE LATTICE SITE OF NITROGEN AFTER IMPLANTATION INTO ZnSe

K. Marbach, B. Ittermann, M. Füllgrabe, M. Heemeier, F. Kroll, F. Mai, P. Meier, D. Peters,  
H. Thieß, H. Ackermann, H.-J. Stöckmann, W.-D. Zeitz<sup>1</sup>, H. Wensch<sup>2</sup>, D. Hommel<sup>2</sup>, and  
G. Landwehr<sup>3</sup>

Universität Marburg, Fachbereich Physik, D-35032 Marburg, Germany

<sup>1</sup>Hahn-Meitner-Institut, Bereich FD, D-14109 Berlin, Germany

<sup>2</sup>Universität Bremen, Institut für Festkörperphysik, D-28359 Bremen, Germany

<sup>3</sup>Physikalisches Institut der Universität Würzburg, D-97074 Würzburg, Germany

**Keywords:** ZnSe, nitrogen, acceptor doping, ion implantation

**Abstract.**  $\beta$ -radiation detected nuclear magnetic resonance measurements are reported on the lattice site of  $^{12}\text{N}$  ions implanted into undoped ZnSe. At 800 K a Larmor resonance is observed indicating the existence of diamagnetic N with full  $T_d$  symmetry. From the resonance intensity in ZnSe compared to the reference system  $^{12}\text{N}$  in Cu it is estimated that at 800 K about 40% of the implanted  $^{12}\text{N}$  end up in this highly symmetric site. An unambiguous experimental determination of the precise site is still lacking. Arguments are given, however, that the observed signal corresponds to  $\text{N}_{\text{Se}}^-$ . Searches for quadrupolarly disturbed signals from some of the missing 60% of  $^{12}\text{N}$  in configurations of lower symmetry, e.g., complexes with intrinsic defects, were so far not successful.

### 1. Introduction.

Significant p-type doping in ZnSe has been achieved by doping with atomic N in molecular beam epitaxy (MBE) [1,2]. Up to now the hole concentration is limited by compensation processes to  $10^{18} \text{ cm}^{-3}$  despite incorporation of N at levels as high as  $10^{20} \text{ cm}^{-3}$ . Different mechanisms as compensation by donors, passivation of the N due to formation of complexes or interstitial configurations and a limited solubility of N on Se sites have been discussed to explain this compensation (see, e.g., [3] and references therein). In most of this processes intrinsic defects play an important role either as donors or as partners for the N to build up complexes. Consequently, the reduction of intrinsic defect concentrations is one of the most challenging tasks for the crystal-growth community.

The incorporation of dopant atoms by ion implantation is frequently considered incompatible with high doping efficiencies because of the lattice defects created in the implantation event. In the present study we use just this way to introduce N impurities into ZnSe with a twofold intention. At first we want to investigate experimentally whether implantation doping with N is really impossible. For this purpose we apply  $\beta$ -radiation detected nuclear magnetic resonance ( $\beta$ -NMR). This so-called nuclear technique uses spin-polarized radioactive  $^{12}\text{N}$  probe nuclei but there is no reason to assume any differences in the defect properties of radioactive and stable N. Due to its high sensitivity,  $\beta$ -NMR allows to work with a rather low implantation flux of below  $10^4 \text{ cm}^{-2}\text{s}^{-1}$ . This ensures isolated N impurities and non-overlapping implantation damage cascades, thereby reducing the complications in interpreting the results considerably. Additionally,  $\beta$ -NMR is sensitive only to structural properties of defect centers containing the implanted species  $^{12}\text{N}$ . The latter fact means that even very high background concentrations of other defects in the sample, either native impurities or intrinsic defects created in the implantation process, have virtually no effects on our signals as long as the probes' immediate neighborhood is not affected. Consequently, *passivation* of N acceptors due to complex formation and *compensation* due to distant donors can easily be distinguished.

The second reason to investigate implanted N is the rather high concentration of intrinsic defects created in the vicinity of the impurities. Complex formation of N with intrinsic defects is frequently assumed to be the mechanism responsible for the compensation effects at high N content. For instance, the  $N_{\text{Se}}-V_{\text{Se}}$  center, suggested by Haukson *et al.* [4], is often cited in that context. The  $N_{\text{Se}}-\text{Zn}_i$  pair could be another candidate. It is even favored by Garcia and Northrup [5] on grounds of the high binding energy of 1.2 eV they calculated for the similar  $\text{As}_{\text{Se}}-\text{Zn}_i$  complex. If it is true that these complexes of N with intrinsic defects are responsible for the acceptor compensation at high N concentrations than they should readily be formed. Consequently, there ought to be a good chance that a noticeable fraction of the implanted N gets trapped and can be studied in such configurations.

As a first step we started to investigate the structural properties of implanted  $^{12}\text{N}$  in nominally undoped samples with  $E_F$  close to mid-gap and the first results of these experiments are reported here. In the longer run we will extend the measurements to p-type  $\text{ZnSe:N}$  samples and look for differences caused by the pre-doping.

## 2. Experimental.

$\beta$ -NMR and its applications to point defects in semiconductors are described in more detail in Refs. [6,7], we will present only a brief outline here. The radioactive  $^{12}\text{N}$  probe nuclei have a  $\beta$ -lifetime of  $\tau_\beta = 15.87$  ms, a nuclear spin  $I = 1$ , and decay to  $^{12}\text{C}$ . They are produced in the nuclear reaction  $^{10}\text{B}(^3\text{He},n)^{12}\text{N}$  by irradiation of a  $^{10}\text{B}$  target ( $80 \mu\text{g}/\text{cm}^2$   $^{10}\text{B}$  on a Ta sheet) with a 3.0-MeV  $^3\text{He}$  beam from the ISL accelerator. The recoil emitted  $^{12}\text{N}$  nuclei are spin polarized along an external magnetic field  $B_0$  by recoil angle selection with an angle of  $19 \pm 8^\circ$  relative to the incident beam and then implanted into the ZnSe sample. The broad kinematic spread of the recoil energies from 0 to 1.7 MeV results in a rather homogeneous implantation profile up to a maximum depths of 2.0  $\mu\text{m}$ . In equilibrium we have only 100 probe nuclei simultaneously in the sample corresponding to a stationary N concentration of  $< 10^6 \text{ cm}^{-3}$ . Not only the probe nuclei themselves but also their implantation damage cascades are therefore well isolated from each other. In total,  $\geq 10^7$   $^{12}\text{N}$  nuclei are needed to generate a spectrum. Since especially the target geometry is not yet fully optimized for the production of  $^{12}\text{N}$  probe nuclei we are so far limited to count rates of about 300/s which imposes severe limitations on the statistical quality of the data.

The sample is positioned in an external magnetic field of typically 0.4 T and surrounded by a radio frequency (RF) coil to realize the NMR. At the end of their lifetime the probe's remaining nuclear polarization  $P$  is detected via the asymmetry in the angular distribution of the emitted  $\beta$  particles which is given by

$$W(\alpha) = v/c A P \cos \alpha,$$

where  $v/c$  is the average  $\beta$  velocity relative to the speed of light,  $A$  is the asymmetry coefficient of the particular  $\beta$  decay, and  $\alpha$  is the angle between  $\mathbf{v}$  and  $\mathbf{P}$ . The  $\beta$  asymmetry  $a$  is defined as the normalized difference in the emission probability parallel and anti-parallel to  $\mathbf{P}$  (and  $\mathbf{B}_0$ ),

$$a = [W(0^\circ) - W(180^\circ)] / [W(0^\circ) + W(180^\circ)] = v/c A P.$$

The nuclear polarization can be measured by counting the  $\beta$  particles in a 'north' and a 'south' detector mounted at the pole pieces of the NMR magnet. In a  $\beta$ -NMR spectrum the time-averaged  $\beta$ -asymmetry is monitored as a function of the RF frequency.

The sample in use was grown by MBE on a p-GaAs:Zn substrate and has a size of  $10 \times 10 \text{ mm}^2$ . The 2.9  $\mu\text{m}$  thick ZnSe layer was deposited using a Zn/Se beam equivalent pressure of 0.34 resulting in

an undoped, stoichiometric film with the Fermi level estimated at midgap. The crystal was capped with a 25-nm  $\text{Si}_3\text{N}_4$  layer to prevent outdiffusion of Se at high temperatures. It could be rotated around a  $[100]$  crystal axis to vary the direction of  $B_0$  within the  $(100)$ -implantation surface.

### 3. Results and discussion.

#### 3.1 Larmor resonances.

A  $\beta$ -NMR spectrum of  $^{12}\text{N}$  in ZnSe, measured at  $T = 800$  K and with  $B_0 \parallel \langle 100 \rangle$ , is presented in Fig. 1. Additional scans at the same temperature but different crystal orientations showed no significant differences within the limits of statistics. The fact that the resonances occur right at the

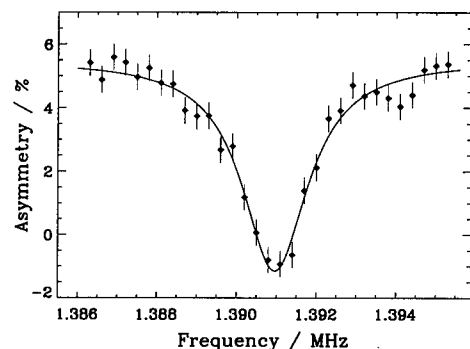


**Fig. 1.**  $\beta$ -NMR spectrum of  $^{12}\text{N}$  in ZnSe,  $T = 800$  K,  $B_0 = 0.4$  T,  $B_0 \parallel \langle 100 \rangle$ . The resonance occurs at the Larmor frequency. The absolute values of the observed asymmetries are determined by instrumental effects and without physical significance.

Larmor frequency, together with the missing orientation dependence, proves the absence of any electric field gradients and hyperfine fields. The corresponding  $^{12}\text{N}$  defects have, therefore, tetrahedral ( $T_d$ ) symmetry and are in their diamagnetic charge state. The possible lattice sites with  $T_d$  symmetry are the Se, the Zn, and two interstitial sites surrounded by four Se ( $T_{\text{Se}}$ ) or Zn ( $T_{\text{Zn}}$ ) atoms. An experimental identification of one of these sites by  $\beta$ -NMR was not yet possible. The cross-relaxation technique, best suited for site determinations in other systems (see, e.g., [8]) is not applicable due to the low abundance of host isotopes with quadrupole moments. The second best experimental choice, a dipolar-line width analysis like in the case of  $^{12}\text{B}$  in ZnSe [9], demands for excellent statistics and instrumental stability and will be attempted if we succeed to improve our  $\beta$ -count rates.

We may, however, discuss the  $^{12}\text{N}$  locations on grounds of our charge state informations, theoretical results, and general models for the properties of point defects in semiconductors. In a simple, but nevertheless very successful, one-electron model proposed by Watkins [10,11] we can picture a defect in  $T_d$  symmetry as having a twofold degenerate  $a_1$  plus a sixfold degenerate  $t_2$  state with the  $a_1$  state typically being lower in energy. Whether or not the level positions fall into the band gap depends on the individual system. These states are consecutively filled according to the number of available electrons. The essential statement of Watkins' empirical rule is that whenever the  $t_2$  level is partially filled a Jahn-Teller distortion will occur reducing the defect symmetry below  $T_d$  (see Ref. [11] for a discussion on exceptions). In adopting this model for our case of N in ZnSe, we see that only the following configurations fulfill both requirements,  $T_d$  symmetry and diamagnetic charge state:  $\text{N}_{\text{Se}}^-$ ,  $\text{N}_{\text{Zn}}^+$ ,  $\text{N}_{\text{Zn}}^{3+}$ ,  $\text{N}_i^{3-}$ , and  $\text{N}_i^{3+}$ , where for  $\text{N}_i$  either of the two tetrahedral sites is possible.

In a variety of theoretical investigations defect properties in ZnSe were calculated with state-of-the-art computational techniques [5,12-15]. For our purposes the study of Kwak *et al.* [15] is particularly interesting since it is the only one with a detailed discussion of N on T sites. The most important conclusions of Ref. [15] in our context are:

- i) The  $T_{\text{Se}}$  site is energetically much less favorable than the  $T_{\text{Zn}}$  site. Since all interstitial sites are equally available there is no reason that N should not prefer the one lowest in energy. We do not consider, therefore,  $\text{N}_i(T_{\text{Se}})$  any further.

- ii) The  $N_{Zn}$  hetero-antisite has a rather low-lying donor level. The calculated value of  $E(+/0) = E_V + 1.0$  eV implies that in our sample, where  $E_F$  is close to midgap,  $N_{Zn}$  should be neutral or even negatively charged, therefore have partially filled  $t_2$  states and undergo a Jahn-Teller distortion. In accordance with Watkins' rule, Kwak *et al.* obtain  $C_{3v}$  symmetry for  $N_{Zn}^0$  and  $N_{Zn}^-$ . Based on these results we discard the assumption of  $N_{Zn}$ , too.
- iii) The  $N_i(T_{Zn})$  acceptor levels are all very close to the valence band. The theoretical result of  $E(2-/3-) = E_V + 0.30$  eV forces us to assume that  $N_i(T_{Zn})$  would be in its triply negative charge state in our sample and therefore have  $T_d$  symmetry. Thus, the assumption of  $N_i(T_{Zn})^{3-}$  would be consistent with the observed Larmor resonance.

For the last remaining alternative,  $N_{Se}^-$ , we don't have to rely on theoretical results. It is a well known fact, of course, that  $N_{Se}^-$  with full  $T_d$  symmetry exists in undoped material and is *the* acceptor in ZnSe.

Tentatively we assign the observed resonances to  $N_{Se}^-$ . The reason to discard the remaining alternative of  $N_i(T_{Zn})^{3-}$  is mainly based on the fact that we observe resonances as shown in Fig. 1 only at high temperatures. If we decrease the sample temperature below 500 K we can still detect a Larmor signal but its intensity drops by a factor of  $\sim 5$ . In an implantation experiment, the low-temperature conditions are always closer to the situation directly after the implantation event, while at higher temperatures we are seeing the effects of subsequent thermally activated processes. Now it is a quite common situation that an implanted probe ion is initially located interstitially or in a low-symmetry environment, and reaches unperturbed substitutional sites only after thermal activation [16-18]. We never observed the opposite case, however, that thermal activation is needed to occupy an interstitial site. In the following we therefore assume that the Larmor resonance reflects  $^{12}N$  located in unperturbed Se sites. We have to keep in mind, however, that the possibility of  $N_i(T_{Zn})^{3-}$ , initially trapped in some complex with an intrinsic defect from the damage cascade, cannot be excluded for certain.

We now turn to the question which fraction of the implanted  $^{12}N$  ends up as unperturbed  $N_{Se}$ , i.e., participates in the Larmor resonance. Such a determination can be done by comparing the signal intensity of the  $^{12}N$  resonance in ZnSe with a measurement in a reference system. Well suited for this purpose is single-crystalline Cu. In  $\beta$ -NMR measurements at  $T = 100$  K the Osaka group found 100% of the implanted  $^{12}N$  at cubic lattice sites [19]. Assuming that the same is still true at higher temperatures,  $T = 100$  K was not accessible for technical reasons, we performed a measurement at  $T = 442$  K which is shown in Fig. 2 together with the ZnSe resonance of Fig. 1. After correcting for the effects of the temperature dependent spin-lattice relaxation in Cu, we obtained a value of  $f(N_{Se}) = 40 \pm 10\%$  for the 800-K resonance of Fig. 1. The given errorbar is mainly due to the estimated systematic errors of this calibration procedure.

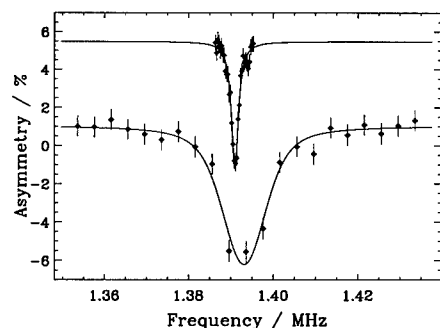


**Fig. 2.** The Larmor resonance of Fig. 1 (top) and a reference spectrum measured in Cu at 442 K. From the smaller integrated area of the ZnSe resonance a  $N_{Se}$  fraction of about 40% is deduced.

### 3.2 Search for $^{12}N$ in low-symmetry sites.

As already mentioned earlier, the implantation process produces a lot of intrinsic defects which could take part in complex formation with the implanted N. Some of these complexes, as the  $N_{Se}-V_{Se}$  center or the  $N_{Se}-Zn$  pair, are widely discussed as compensating donors. The non-cubic symmetry of these complexes would result in an electric field gradient at the  $^{12}N$  lattice site and hence a quadrupole splitting in the  $\beta$ -NMR spectrum. A search scan for

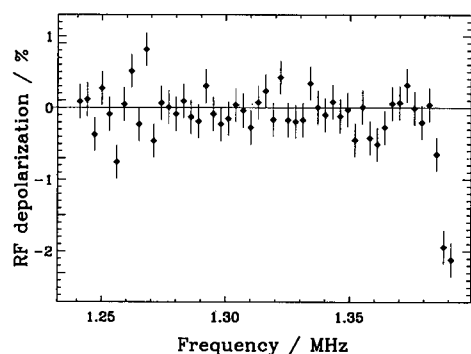


**Fig. 3.** Search scan for quadrupole split signals of  $^{12}\text{N}$  in ZnSe. The solid line represents the true instrumental asymmetry. Two frequencies, symmetrical to the Larmor frequency at 1.391 MHz, were irradiated simultaneously.  $T = 900\text{ K}$ ,  $\mathbf{B}_0 \parallel \langle 110 \rangle$ .

such signals at resonance positions different from the Larmor frequency is shown in Fig. 3. In order to enhance a possible signal two frequencies, symmetrical to the Larmor transition, were irradiated simultaneously. This way the scan covered a frequency span of  $\pm 150\text{ kHz}$ . Evidently, there is no resonance present within this range except from the Larmor line itself. The spectrum of Fig. 3 was measured with  $\mathbf{B}_0 \parallel \langle 110 \rangle$ , a second scan (not shown) with  $\mathbf{B}_0$   $10^\circ$  off  $\langle 100 \rangle$ , i.e. an orientation with much smaller splittings for centers with  $\langle 111 \rangle$ - or  $\langle 110 \rangle$ -defect axes, gave no different results.

We have to conclude, therefore, that our attempts to detect  $^{12}\text{N}$  defects with less than cubic symmetry were so far not successful even though we are still missing about 60% of the total  $^{12}\text{N}$  polarization. There is still hope for the future, however, since for at least two reasons we might

have overlooked a signal. First, a larger than expected electric field gradient would not have been detected because of our limited frequency window. In future experiments we have to extend the search range, therefore. Second, for centers with very low symmetry the total  $\beta$ -NMR-signal intensity would be spread out over many different resonances corresponding to the various defect orientations. These cases will elude detection unless we can considerably improve the statistical accuracy of our data.

#### 4. Summary.

After implantation of  $^{12}\text{N}$  into nominally undoped ZnSe at  $T = 800\text{ K}$  we observed a  $\beta$ -NMR resonance at the Larmor frequency indicating a probe fraction of about 40% at sites with  $T_d$  symmetry. At room temperature the same signal is observed, however with a drastically reduced intensity. From theoretical calculations we concluded that  $N_{\text{Zn}}$  and  $N_i(T_{\text{Se}})$  could not maintain such a high symmetry in a sample with  $E_F$  close to midgap. We tentatively assigned the signal to  $N_{\text{Se}}^-$ , the unperturbed and ionized acceptor. The alternative assumption of  $N_i(T_{\text{Zn}})$  could not definitely be excluded, however. Search scans to detect some of the missing 60%  $^{12}\text{N}$  probes in less symmetric configurations were so far not successful.

#### Acknowledgements

We gratefully acknowledge the hospitality of the Hahn-Meitner-Institut, Berlin, and the assistance of its technical staff. This work was supported by the BMBF under Contract No. 03-AC4MAR.

#### References.

1. R. M. Park, M. B. Troffer, C. M. Rouleau, J. M. DePuydt, M. A. Haase, *Appl. Phys. Lett.* **57**, 2127 (1990).
2. K. Ohkawa, T. Karasawa, T. Mitsuyu, *J. Crystal Growth* **111**, 797 (1991).
3. Y. Mairfang, *J. Crystal Growth* **161**, 205 (1996).
4. I.S. Haukson, J. Simpson, S.Y. Wang, K.A. Prior, B.C. Cavenett, *Appl. Phys. Lett.* **61**, 2208 (1992).
5. A. Garcia and J. E. Northrup, *Phys. Rev. Lett.* **74**, 1131 (1995).

6. H. Ackermann, P. Heitjans, H.-J. Stöckmann, in "Hyperfine Interactions of radioactive nuclei", ed. J. Christiansen (Springer, Berlin) p. 291 (1983).
7. B. Ittermann, H. Ackermann, E. Diehl, B. Fischer, H.-P. Frank, H.-J. Stöckmann, *Hyp. Int.* **79**, 591 (1993).
8. E. Jäger, B. Ittermann, H.-J. Stöckmann, K. Bürkmann, B. Fischer, H.-P. Frank, G. Sulzer, H. Ackermann, P. Heitjans, *Phys. Lett. A* **123**, 39 (1987).
9. B. Ittermann, G. Welker, F. Kroll, F. Mai, K. Marbach, H. Ackermann, H.-J. Stöckmann, E. Oldekop, W.-D. Zeitz, *Proceedings to this conference*.
10. G.D. Watkins, *Mat. Sci. Forum* **143-147**, 9 (1994).
11. G.D. Watkins in "Electronic Structure and Properties of Semiconductors", ed. W. Schroeter, *Materials Science and Technology*, Vol. 4 (VCH Weinheim) p. 105 (1991).
12. D. J. Chadi, *Appl. Phys. Lett.* **59**, 3589 (1991).
13. C. G. Van de Walle D. B. Laks, G. F. Neumark, S. T. Pantelides, *Phys. Rev. B* **47**, 9425 (1993).
14. H. Katayama-Yoshida, T. Sasaki, T. Oguchi, *J. Crystal Growth*, **117**, 625 (1992).
15. K. W. Kwak, D. Vanderbilt, R. D. King-Smith, *Phys. Rev. B* **52**, 11912 (1995).
16. H.-P. Frank, E. Diehl, K.-H. Ergezinger, B. Ittermann, B. Fischer, F. Mai, K. Marbach, S. Weißenmayer, G. Welker, H. Ackermann, H.-J. Stöckmann, *Mat. Sci. Forum* **143-147**, 135 (1993).
17. B. Ittermann, H. Ackermann, H.-J. Stöckmann, K.-H. Ergezinger, M. Heemeier, F. Kroll, F. Mai, K. Marbach, D. Peters, G. Sulzer, *Phys. Rev. Lett.* **77** 4784 (1996).
18. S. G. Jahn, U. Wahl, M. Restle, H. Quintel, H. Hofsäss, M. Wienecke, I. Trojahn, and ISOLDE-Collaboration, *Mat. Sci. Forum* **196-201**, 315 (1996).
19. T. Minamisono, *Hyp. Int.* **35** 979 (1987).

## CHARGE TRANSFER AT Ti IONS IN ZnTe

H. R. Selber<sup>1</sup>, P. Peka<sup>1</sup>, H.-J. Schulz<sup>1</sup>, U. W. Pohl<sup>2</sup>, J. Kreissl<sup>2</sup>, B. Kaufmann<sup>3</sup>,  
A. Dörnen<sup>3</sup>

<sup>1</sup>Fritz-Haber-Institut, Faradayweg 4-6, D-14195 Berlin, Germany

<sup>2</sup>Institut für Festkörperphysik, TU Berlin, Hardenbergstr. 36, D-10623 Berlin

<sup>3</sup>4. Phys. Institut, Universität Stuttgart, Pfaffenwaldring 57, D-70550 Stuttgart

**Keywords:** Transition-Metal Doping, Luminescence, EPR, Zeeman Effect

### Abstract

In low-temperature photoluminescence (PL) of Ti-doped ZnTe crystals, three zero-phonon lines (ZPL) show up at 3903, 4013, and 4103  $\text{cm}^{-1}$ . By Zeeman measurements the line at 3903  $\text{cm}^{-1}$  is identified with the  ${}^2T_2(D) \rightarrow {}^2E(D)$  transition of substitutional  $\text{Ti}^{3+}$  ( $3d^1$ ). The weak  ${}^3T_2(F) \rightarrow {}^3A_2(F)$  band of  $\text{Ti}^{2+}$  ( $3d^2$ ) exhibits a single ZPL at 2855  $\text{cm}^{-1}$ . Magneto-optic spectra display a threefold splitting of the isotropic  $\text{Ti}^{2+}$  line and a further splitting of the  $\text{Ti}^{3+}$  lines. In Ni co-doped crystals the known PL bands of  $\text{Ni}^{2+}$  ( $3d^8$ ) at 3840  $\text{cm}^{-1}$  and  $\text{Ni}^+$  ( $3d^9$ ) at 3095  $\text{cm}^{-1}$  occur in addition. While after cooling these crystals in the dark, only the luminescence of  $\text{Ti}^{3+}$  is observed, the  $\text{Ti}^{2+}$  emission appears after irradiation with light ( $\bar{\nu} > 7000 \text{ cm}^{-1}$ ):  $\text{Ti}^{3+} + h\nu \rightarrow \text{Ti}^{2+} + e_{\text{VB}}^+$ . This charge transfer (CT) is confirmed by electron paramagnetic resonance (EPR) investigations. Under irradiation, the isotropic signal of  $\text{Ti}^{3+}$  at  $g = 1.9139$  present in thermal equilibrium at 4 K, is reduced in favour of the photo-stimulated  $\text{Ti}^{2+}$  signal at  $g = 1.9255$ . Excitation and sensitisation processes are discussed in one-particle models comprising the involved ionisation states of Ti.

## 1 Introduction

In the tetrahedral crystal field of a lattice site in a ZnTe crystal the  ${}^3F$  term of the free  $\text{Ti}^{2+}$  ( $3d^2$ ) ion is split into  ${}^3T_1(F)$ ,  ${}^3T_2(F)$  and  ${}^3A_2(F)$  [ground state (GS)] levels. Similarly, from the  ${}^2D$  term of the free  $\text{Ti}^{3+}$  ( $3d^1$ ) ion  ${}^2T_2(D)$  and  ${}^2E(D)$  (GS) levels emerge.

So far, nothing has been published about Ti in ZnTe. There have been, however, several studies on Ti ions in other host crystals, such as GaP [1], ZnSe [2-5] and CdTe [5-8].

In all these crystals Ti was detected as the isoelectronic  $\text{Ti}^{2+}$  and also as the singly ionised donor  $\text{Ti}^{3+}$ . In ZnSe, the (0,+) donor level of Ti was found at  $E_{\text{CB}} - 8500 \text{ cm}^{-1}$  (1.05 eV) using PL excitation (PLE) [2,3] and photo-EPR [2], and at  $E_{\text{CB}} - 6200 \text{ cm}^{-1}$  (0.77 eV) by isothermal capacitance transient spectroscopy [4]. Using photoconductivity and absorption [5,6] and photo-EPR [7], the donor level of Ti in CdTe was determined at  $E_{\text{CB}} - 7300 \dots 8500 \text{ cm}^{-1}$ . According to the internal reference rule [9] the donor level of Ti in ZnTe should be expected at  $E_{\text{CB}} - 12000 \text{ cm}^{-1}$  (assuming a valence band (VB) offset of 7300  $\text{cm}^{-1}$  with respect to ZnSe) or  $E_{\text{CB}} - 15000 \text{ cm}^{-1}$  (assuming a VB offset of 800  $\text{cm}^{-1}$  with respect to CdTe).

In this work, PLE and PL sensitisation spectra will be used to identify the PL emission bands of  $\text{Ti}^{2+}$  and  $\text{Ti}^{3+}$  and to obtain the donor level of Ti in ZnTe.

## 2 Emission Spectra

The setups for PL and PLE measurements are described elsewhere [10]. In the low- $T$  PL spectrum of a ZnTe:Ti crystal (Fig. 1), broad, featureless bands appear above 4000  $\text{cm}^{-1}$  which

have been previously described [10] as well as the  ${}^5T_2(D) \rightarrow {}^5E(D)$  emission of  $\text{Fe}^{2+}$  below  $2500 \text{ cm}^{-1}$  [11]. The band around  $3500 \text{ cm}^{-1}$  is attributed to the  ${}^2T_2(D) \rightarrow {}^2E(D)$  emission of  $\text{Ti}^{3+}$ . At higher resolution (Fig. 2) it shows three ZPLs at  $4103$ ,  $4013$  and  $3903 \text{ cm}^{-1}$ , each accompanied by a number of distinct phonon replicas in distances of  $50 \text{ cm}^{-1}$  ( $\approx TA(X)$ ) and  $139 \text{ cm}^{-1}$  ( $\approx LA(X)$  or  $LA(L)$ ), and their sum energies. The weak lines at  $4013$  and  $4103 \text{ cm}^{-1}$  probably originate in a disturbed environment of the Ti ion. This conclusion arises because these lines are stronger in crystals with a larger amount of macroscopic defects.

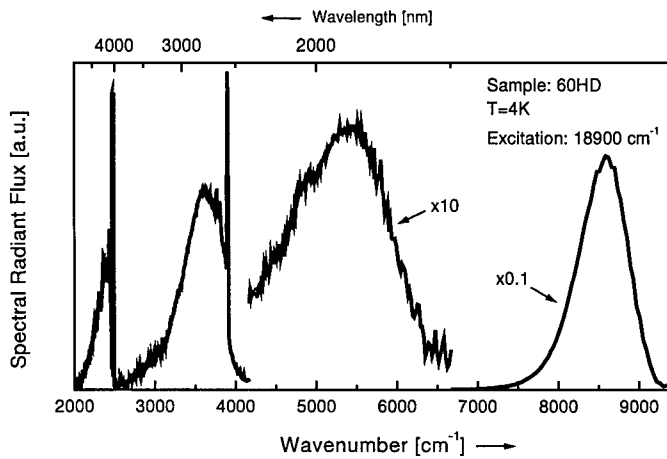


Figure 1: PL spectrum of a Ni-codoped ZnTe:Ti sample under band-to-band excitation.

Between  $2500$  and  $3100 \text{ cm}^{-1}$ , the  ${}^3T_2(F) \rightarrow {}^3T_1(F)$  transition of  $\text{Ti}^{2+}$  and the  ${}^2E(D) \rightarrow {}^2T_2(D)$  transition of  $\text{Ni}^{2+}$  [10] occur with single ZPLs at  $2855$  and  $3095 \text{ cm}^{-1}$ , respectively. Excitation with an energy of  $9400 \text{ cm}^{-1}$  (Fig. 2, dashed line) displays also the  ${}^3T_2(F) \rightarrow {}^3T_1(F)$  band of  $\text{Ni}^{2+}$  [10], which is covered by the luminescence of  $\text{Ti}^{3+}$  at an excitation energy of  $18900 \text{ cm}^{-1}$ .

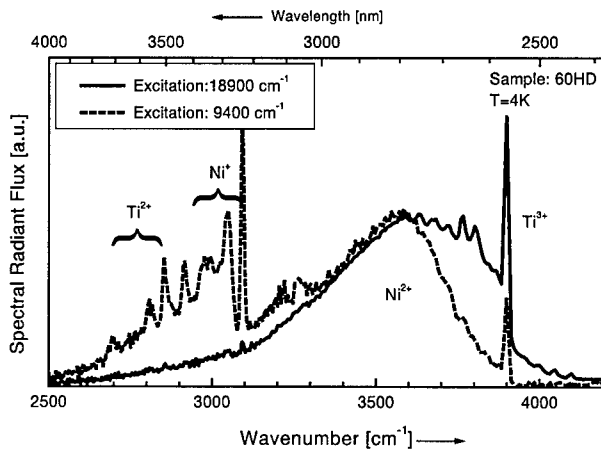


Figure 2: Low-energy region of the spectrum presented in Fig. 1 under two different excitations. With lower excitation energy (dashed line), a superposition of Ni and Ti luminescence is observed. Another band superimposing the  $\text{Ti}^{2+}$  luminescence near  $3250 \text{ cm}^{-1}$  could arise from traces of  $\text{Co}^{2+}$  [12] found with EPR (Fig. 5).

### 3 Zeeman Measurements

Under the influence of a magnetic field, the ZPL of the  ${}^3T_2(F) \rightarrow {}^3A_2(F)$  luminescence of  $\text{Ti}^{2+}$  is split into three lines. The positions ( $2851$ ,  $2854$  and  $2857 \text{ cm}^{-1}$  at  $B = 4 \text{ T}$ ) and intensities of these three lines are isotropic under rotation of the sample in the magnetic field. Since the  ${}^3A_2(F)$  level is threefold spin-degenerate, this finding is an indication for the correct



identification of this luminescence. The  $g$ -factor obtained by Zeeman measurements agrees well with that obtained by EPR.

The ZPL of the luminescence of the  $\text{Ti}^{3+}$  ion at  $3903\text{ cm}^{-1}$  yields several lines in the magnetic field, revealing a second ZPL at zero magnetic field at a distance of  $2.3\text{ cm}^{-1}$  towards higher energies. Both lines split isotropically in the magnetic field. The doublet is assigned to the spin-orbit states  $\Gamma_7$  and  $\Gamma_8$  of  $^2T_2$ . The lines at  $4013$  and  $4103\text{ cm}^{-1}$  remain uninfluenced by the magnetic field, probably owing to a low symmetry of the corresponding center in the sense discussed above. A detailed discussion of the Zeeman effect including numerical calculations of the Zeeman terms of  $\text{Ti}^{3+}$  will be published separately [13].

## 4 Excitation Spectra

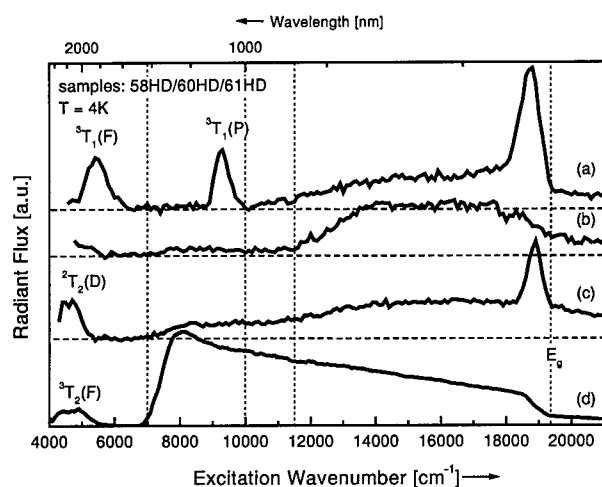


Figure 3: Excitation spectra of  $\text{Ni}^{2+}$ ,  $\text{Ti}^{2+}$  and  $\text{Ti}^{3+}$  in various ZnTe crystals. (a):  $\text{Ti}^{2+}$  (sample # 60HD), (b):  $\text{Ti}^{3+}$  (# 61HD), (c):  $\text{Ti}^{3+} + \text{Ni}^{2+}$  (# 60HD), (d):  $\text{Ni}^{2+}$  (# 58HD). Detection ranges: (a):  $2780\text{--}3330\text{ cm}^{-1}$ , (b,c,d):  $3330\text{--}3850\text{ cm}^{-1}$ . Dotted lines mark the onsets of CT transitions and  $E_g$ .

The excitation spectrum of  $\text{Ti}^{2+}$  (Fig. 3a) exhibits two characteristic internal bands (cf. ref. [2] for ZnSe:Ti) around  $5000$  and  $9000\text{ cm}^{-1}$ , corresponding to the  $^3T_1(F) \leftarrow ^3A_2(F)$  and  $^3T_1(P) \leftarrow ^3A_2(F)$  transitions of the  $\text{Ti}^{2+}$  ion and a broad CT band starting at approximately  $10000\text{ cm}^{-1}$ . In addition, we find a near-band-gap peak at  $18500\text{ cm}^{-1}$ .

The excitation spectrum of the  $\text{Ti}^{3+}$  luminescence attains different shapes for different crystals. In solely Ti-doped crystals, it contains only a CT band with a low-energy onset at  $11500\text{ cm}^{-1}$  (Fig. 3b), similar to GaP [1]. In Ni co-doped crystals, it displays also a CT band starting at  $7000\text{ cm}^{-1}$  (Fig. 3c). This excitation band does not arise from the luminescence of  $\text{Ti}^{3+}$  but from  $\text{Ni}^{2+}$ , since the luminescence of  $\text{Ti}^{3+}$  is almost absent under excitation of  $9400\text{ cm}^{-1}$  (Fig. 2, dashed line). For comparison, Fig. 3d shows an excitation spectrum of the  $\text{Ni}^{2+}$  ion in a ZnTe crystal containing only Ni [10].

## 5 Sensitisation Spectra

Sensitisation spectroscopy is a variation of excitation spectroscopy with two exciting light sources. One of them, the *primary source*, is modulated by a chopper and kept at a fixed wavelength. The *secondary source* is unmodulated and its wavelength is varied. Thus only the influence of the primary source is directly detected by the lock-in amplifier. The influence of the secondary source is detected only indirectly by its effect on the particular combination of primary excitation and the recorded emission.

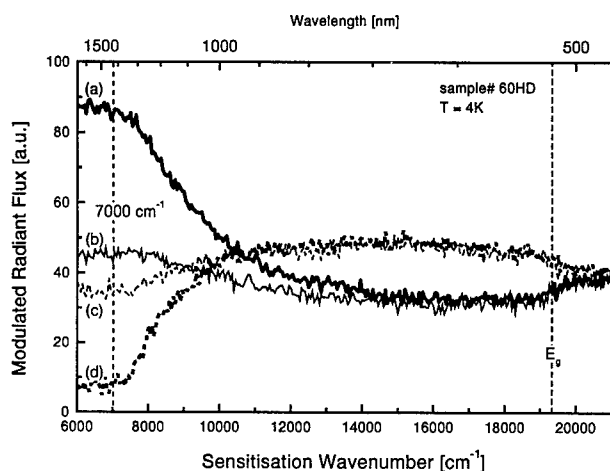


Figure 4: Sensitisation spectra of  $\text{Ti}^{2+}$  and  $\text{Ti}^{3+}$  in ZnTe (crystal # 60HD). a,b: (solid lines)  $\text{Ti}^{3+}$ , detection:  $3330\text{--}3850\text{ cm}^{-1}$ , primary excitation:  $4250\text{--}5400\text{ cm}^{-1}$ . c,d: (dashed lines)  $\text{Ti}^{2+}$ , detection:  $2780\text{--}3330\text{ cm}^{-1}$ , primary excitation:  $5000\text{--}6250\text{ cm}^{-1}$ .

In the purely Ti-doped crystals no influence of auxiliary irradiation on the luminescence of the Ti ions was discernible. In the co-doped crystals, however, an enormous effect is observed. Figure 4 shows sensitisation spectra of the Ni co-doped crystal. The  ${}^3T_1(F) \leftarrow {}^3A_2(F)$  transition of  $\text{Ti}^{2+}$  (cf. Fig. 3a) was chosen for the primary excitation of the dashed curves (c,d). The detection range contains not only the luminescence of  $\text{Ti}^{2+}$ , but also the luminescence of  $\text{Ni}^{2+}$  (cf. Fig. 2). Since the excitation spectrum of  $\text{Ni}^{2+}$  [10] does not display any band below  $10000\text{ cm}^{-1}$ , it can be assumed that only the  $\text{Ti}^{2+}$  luminescence is excited by this primary excitation.

The wavenumber ranges chosen for detection and primary excitation in the sensitisation of  $\text{Ti}^{3+}$  (Fig. 4a,b) correspond to the  ${}^2T_2(D) \leftrightarrow {}^2E(D)$  transitions of  $\text{Ti}^{3+}$  (cf. Fig. 3c). The bold curves (a,d) represent a measurement started directly after cooling the sample before treatment with light. The thin curves (b,c) were recorded directly after the respective bold traces, i. e. after some minutes of irradiation. The scan direction was from low to high wavenumbers.

Without auxiliary irradiation, i. e. at the low-energy starting point of the bold curves, only the  $\text{Ti}^{3+}$  luminescence is observed. The small signal of curve (d) originates from the low-energy tail of the  $\text{Ti}^{3+}$  luminescence (Fig. 2).

When the secondary irradiation crosses a threshold at  $7000\text{ cm}^{-1}$ , the situation changes drastically: The intensity of the  $\text{Ti}^{3+}$  luminescence decreases to one third of its original value; the  $\text{Ti}^{2+}$  luminescence increases in a complementary manner. The intensity scales of both spectra are approximately comparable. Thus the extent at which the  $\text{Ti}^{3+}$  luminescence decreases equals the amount of the increase of the  $\text{Ti}^{2+}$  luminescence.

After the auxiliary irradiation is switched off, the PL signal of  $\text{Ti}^{2+}$  under continuous primary excitation decreases (non-exponentially) with time constants in the range of 1000 s to a level well above the initial state. Similarly, the luminescence of  $\text{Ti}^{3+}$  increases. The initial state is reached again only after warming up the sample to room temperature.

## 6 EPR

By EPR both donor charge states,  $\text{Ti}^{3+}$  ( $3d^1$ ) and  $\text{Ti}^{2+}$  ( $3d^2$ ), have been identified (Fig. 5). Further EPR spectra could be assigned to residual Co, Fe, and Mn contaminations. The positively charged donor state, exclusively observed in the thermal equilibrium at 4 K, shows a low-temperature isotropic EPR line at  $g = 1.9139$  that has been analysed by Ham's theory of a dynamic Jahn-Teller effect (for more details see the analogy given for  $\text{Ti}^{3+}$  ( $3d^1$ ) in II-VI semiconductors [5, 7]). The EPR line at  $g = 1.9139$  has been attributed to the transitions

between the  ${}^3A_2(F)$  ground state components of the  $Ti^{2+}$  ions. The EPR line of the  $Ti^{2+}$  charge state has only been verified after irradiation with light at an energy above the Ge band edge ( $6000\text{ cm}^{-1}$ ). In both cases no deviation from the tetrahedral lattice symmetry was found.

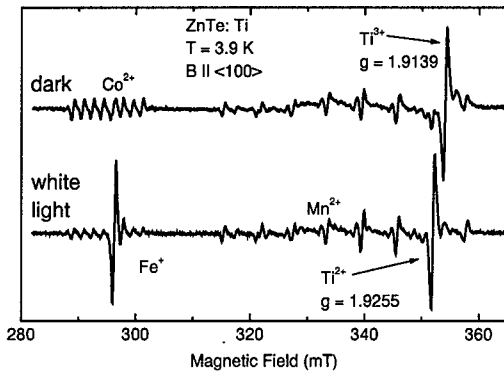


Figure 5: EPR spectra of sample # 60HD. The upper curve was obtained in the dark; the lower curve under optical irradiation (tungsten-halogen lamp).

Additional evidence for a correct assignment of the two spectra to  $Ti^{3+}$  and  $Ti^{2+}$  is given by the saturation behaviour of the respective EPR lines. This observation reflects the very short relaxation time because of a strong lattice coupling as expected for  $Ti^{3+}$  with a vibronic  ${}^2E$  ground state, in contrast to the expected longer relaxation time for the orbital singlet  ${}^3A_2$  ground state of  $Ti^{2+}$ . It should be noted that the CT behaviour measured by EPR fits very well the observations found by the sensitisation studies (Sec. 5).

## 7 Conclusions

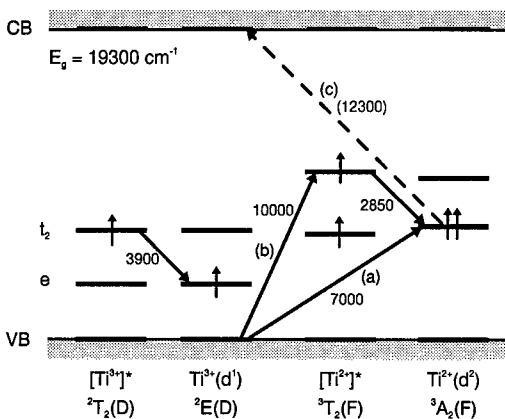


Figure 6: One-particle model of Ti ions in ZnTe crystals. The two-electron states of  $Ti^{2+}$  are displayed roughly as combination of one-electron states  $t_2$  and  $e$ . The numbers indicate the transition energies in  $\text{cm}^{-1}$ . The donor transition (c) is not directly observed, as indicated by a dashed line.

The sensitisation spectra in Fig. 4 show clearly that illumination above a threshold of  $7000\text{ cm}^{-1}$  induces a transition from the GS of  $Ti^{3+}$  to the GS of  $Ti^{2+}$ , because the internally excited luminescence of  $Ti^{2+}$  increases while the equivalent luminescence of  $Ti^{3+}$  decreases in a complementary manner. The same behaviour is observed by EPR. It is not a priori necessary that this threshold represents a transition of the Ti ion. Especially an interaction with the Ni present in the crystal appears feasible. The CT threshold of  $Ni^{2+} + h\nu \rightarrow Ni^+ + e_{VB}^+$ , which is also located at approximately  $7000\text{ cm}^{-1}$  can be ruled out, since this transition generates holes as well. Thus we interpret this transition as  $Ti^{3+} + h\nu \rightarrow Ti^{2+} + e_{VB}^+$ , denoted in Fig. 6 by an arrow labeled (a). Consequently, the donor level of Ti in ZnTe is located  $7000\text{ cm}^{-1}$  ( $0.87\text{ eV}$ )

above the VB, i. e. approximately  $12300\text{ cm}^{-1}$  ( $1.5\text{ eV}$ ) below the conduction band (CB). The corresponding  $(0/+)$  donor transition [Fig. 6(c)] was not observed.

This assignment is further justified considering the CT band in the excitation spectrum of  $\text{Ti}^{2+}$  (Fig. 3a) at  $10000\text{ cm}^{-1}$ . The intensity of this CT band decreases upon irradiation above  $7000\text{ cm}^{-1}$  (not shown) indicating that its initial state is the GS of  $\text{Ti}^{3+}$  whose population is decreasing. Taking the excited  $\text{Ti}^{2+}$  as its final state (since it occurs in the excitation spectrum of  $\text{Ti}^{2+}$ ), the band is identified with transition (b) in Fig. 6.

The position of the  $\text{Ti}^{2+}/\text{Ti}^{3+}$  donor level in ZnTe is in excellent agreement with that in ZnSe according to ref. [9]. The bands of CdTe, however, would have to be shifted upwards by approximately  $2700\text{ cm}^{-1}$  in order to obtain good agreement.

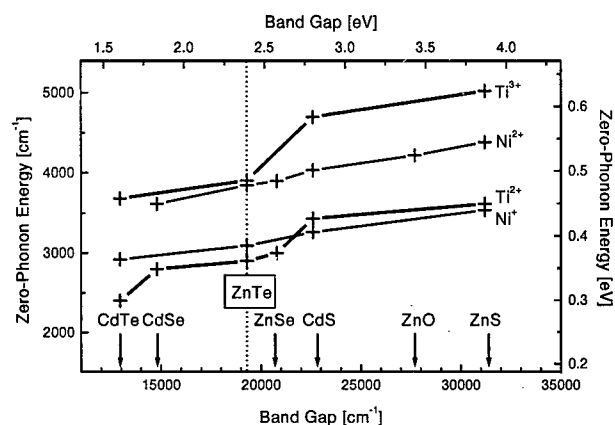


Figure 7: Zero-phonon lines of internal transitions of Ti (bold lines) and Ni (thin lines) ions in various II-VI host crystals as a function of the band gap.

The observed internal transitions of Ti and Ni ions in ZnTe comply with a general trend in the II-VI compounds (Fig. 7). The energies of the internal transitions depend almost linearly on the band gap of the host material. A similar trend has been found for several 3d transition metals in II-VI compounds [10, 14].

## References

- [1] P. Roura, G. Guillot, T. Banyattou, and W. Ulrici: *Semicond. Sci. Technol.* **6**, 36 (1991).
- [2] J. Dziesiaty, P. Peka, M. U. Lehr, H.-J. Schulz, and A. Klimakow: *Phys. Rev. B* **49**, 17011 (1994).
- [3] A. Klimakow, J. Dziesiaty, J. Korostelin, M. U. Lehr, P. Peka, and H.-J. Schulz: *Advanced Materials for Optics and Electronics* **3**, 253 (1994).
- [4] H. Okada: *Appl. Phys. Lett.* **70**, 1587 (1997).
- [5] J. Kreissl and H.-J. Schulz: *J. Crystal Growth* **161**, 239 (1996).
- [6] E. Rzepka, Y. Marfaing, M. Cuniot, and R. Triboulet: *Mat. Sci. Eng.* **B16**, 262 (1993).
- [7] H.-J. Schulz and J. Kreissl: *Optical Mater.* **4**, 202 (1995).
- [8] P. Peka, M. U. Lehr, J. Dziesiaty, S. Müller, J. Kreissl, P. Rudolph, and H.-J. Schulz: *Mater. Sci. Forum* **143-147**, 435 (1994).
- [9] J. M. Langer, C. Delerue, M. Lannoo, and H. Heinrich: *Phys. Rev. B* **38**, 7723 (1988).
- [10] H. R. Selber, H.-J. Schulz, and U. W. Pohl: *Solid State Commun.* **103**, 265 (1997).
- [11] H.-J. Schulz, M. Thiede, U. W. Pohl, J. Rivera-Iratchet, M. A. de Orúe, M. L. Flores, O. Mualin, and E. E. Vogel: *Z. Phys. B* **98**, 215 (1995).
- [12] A. P. Radliński: *J. Lumin.* **18/19**, 147 (1979).
- [13] A. Dörnen, H. R. Selber, B. Kaufmann, and H.-J. Schulz: (to be published 1997).
- [14] P. Peka, H. R. Selber, H.-J. Schulz, R. Schwarz, and K. W. Benz: *Solid State Commun.* **98**, 677 (1996).

## BISTABLE CENTERS IN CdMnTeSe:In AND CdMnTe:Ga CRYSTALS STUDIED BY LIGHT - INDUCED GRATINGS

B. Koziarska-Glinka<sup>(1)</sup>, M. Ponder<sup>(1)</sup>, A. Suchocki<sup>(1)</sup>, T. Wojtowicz<sup>(1)</sup>  
and I. Miotkowski<sup>(2)</sup>

<sup>(1)</sup> -Institute of Physics, Polish Academy of Sciences, 02-668 Warsaw,  
Poland

<sup>(2)</sup> - Purdue University, West Lafayette, Indiana, 46 566, USA

Keywords: DX centers, negative U, II-VI semiconductors, light-induced gratings

### Abstract

Bistable DX centers in CdMnTe and CdMnTeSe crystals, associated with In and Ga impurities, have been studied with the use of the light-induced grating technique. Two bistable centers with different lattice relaxation energies have been detected in CdMnTeSe:In crystals. Both of these centers have negative U character. Only one bistable center has been found in CdMnTe:Ga crystal. Its metastability temperature is higher than those for centers associated with In doping.

### 1. Introduction

Bistable centers in compound semiconductors have been a topic of extensive studies in the past. Several bistable centers have been identified in various semiconductors. The best known are the EL2 defect in GaAs and DX-centers in several A<sup>III</sup>-B<sup>V</sup> semiconductors [1]. The DX (or DX-like) centers have also been found in A<sup>II</sup>-B<sup>VI</sup> semiconducting compounds [2] as well as in unconventional semiconductors as in CdF<sub>2</sub> [3]. Indium and Gallium ions are well known to form bistable DX-like centers in A<sup>II</sup>-B<sup>VI</sup> semiconductors [3,4,5] and also in more ionic hosts as in CdF<sub>2</sub> crystals [3]. Bistability is associated with electron trapping either at localized or delocalized - hydrogen like states. The wavefunction of the former is very compact, while of the latter diffuse, effective mass like. It is associated with the large lattice relaxation (LLR) effect, responsible for the existence of DX centers in A<sup>III</sup>B<sup>V</sup> and very likely in A<sup>II</sup>B<sup>VI</sup> semiconductors. A phototransformation of the center from one state to another must lead to a large change of the local polarizability, and thus large changes of the local refractive index. The refractive index changes in the order of 10<sup>-4</sup> are easily obtainable with the concentration of phototransformed centers about 10<sup>18</sup> cm<sup>-3</sup>. [6] Therefore such centers can be efficiently used in writing volume holographic gratings and this is a reason for new interest in the bistable centers.

Indium ions in Cd<sub>1-x</sub>Mn<sub>x</sub>Te<sub>1-y</sub>Se<sub>y</sub> crystals exhibit the photomemory effect which persists for very long time if samples are kept at liquid helium temperature [4]. This effect has been detected by SQUID measurements. Due to the formation of magnetic polarons (magnetic complexes of ionic spins of Mn<sup>2+</sup> oriented within Bohr radii of localized carriers) during phototransformation of metastable centers from the deep, localized state to the shallow donor state, large changes of magnetization occur, which has been measured with the use of SQUID. The measurements also support the "negative-U" model of bistable In centers in the examined crystals, which assumes a two-electron state ground state of the

In metastable impurity. The same conclusion has been derived from the studies of transients of the carrier concentration upon illumination for the  $\text{Cd}_{1-x}\text{Mn}_x\text{Te:Ga}$  sample [5]. We have used light-induced (holographic) gratings as a spectroscopic tool for studying properties of metastable centers in these compounds.

## II. Experimental

The  $\text{Cd}_{1-x}\text{Mn}_x\text{Te:Ga}$  ( $x = 0.03$ ) and  $\text{Cd}_{1-x}\text{Mn}_x\text{Te}_{1-y}\text{Se}_y\text{:In}$  ( $x = 0.1$  and  $y = 0.08$ ) crystals grown by the Bridgman method were used in our experiments. The room temperature concentration of free electrons was in the order of about  $10^{16} \text{ cm}^{-3}$  and a few times  $10^{16} \text{ cm}^{-3}$  in  $\text{Cd}_{1-x}\text{Mn}_x\text{Te:Ga}$  and in  $\text{Cd}_{1-x}\text{Mn}_x\text{Te}_{1-y}\text{Se}_y\text{:In}$  samples, respectively. The light-induced grating experiment was performed with the use of a Ti:sapphire c.w. ring laser (COHERENT model 899), pumped by an argon-ion (Innova 200) laser. The Ti:sapphire laser was tuned to 935 nm. This wavelength of near-bandgap energy coincides with the photoionization spectrum of localized centers in the crystals. The same wavelength was used for the grating detection. In order to minimize the grating erasure by the read beam its intensity was kept below 10% of the power of the write beams, which created the grating. The scattered beam was detected by a S1 type photomultiplier with the use of a lock-in. The decay kinetics were stored in SR 430 multichannel scaler.

## III. Results and discussion

The temperature dependence of the scattering efficiency of the light-induced gratings in the  $\text{Cd}_{1-x}\text{Mn}_x\text{Te}_{1-y}\text{Se}_y\text{:In}$  crystal is presented in Fig. 1. The dependence has two maxima at

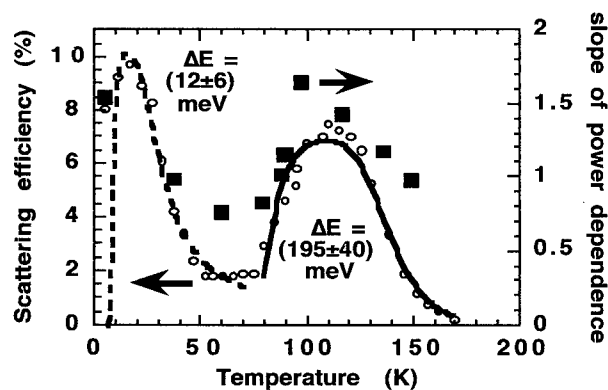


Figure 1. Temperature dependence of the light-induced grating c.w. scattering efficiency in  $\text{CdMnTeSe:In}$  crystal (open points) and the temperature dependence of the slope of the scattering efficiency as function of power of the write beams (full squares). The lines are the theoretical fits of the “negative U” model to the data.

temperatures  $T_1 = 17 \text{ K}$  and  $T_2 = 110 \text{ K}$ . They are associated with two types of bistable centers with different thermal activation energy for electron emission from the metastable state. The scattering efficiency of the light-induced gratings in this material reaches 10%. That means that the local changes of refractive index are mainly responsible for creation of the light induced gratings [7]. The shape of the c.w. scattering efficiency dependence for each of the bistable centers is associated with mechanisms,

which destroy the grating. At higher temperatures thermal recovery from the shallow to the deep state via the energy barrier which separates the states destroys the grating. At low temperatures the grating is being erased by the non-coherent residual stray light, which phototransforms the bistable centers in all illuminated region. Due to high

photorefractive sensitivity of the material this process of grating erasure is very efficient at low temperatures.

For small changes of the refractive index in the material the scattering efficiency is proportional to the square of the difference between refractive indices in peaks and in valleys of the grating [7]. The quantitative description of the process must include the solution of a rate equation, which gives the populations of the shallow delocalized state of the bistable centers in the peaks and in the valleys of the grating. In the most simplified form the concentration,  $n_s$ , of the "negative U" centers (with **two electrons** in the ground state) in the shallow donor state, can be expressed by the relationship:

$$\frac{\Delta n_s}{dt} = -cn_s^2 + I\sigma(N_0 - n_s) \quad (1)$$

where  $c$  is the kinetic parameter,  $I$  is the light intensity,  $\sigma$  is the photoionization cross section of the deep state and  $N_0$  is the total concentration of the dopant ions. The temperature dependence of the kinetics parameter,  $c$ , is given by the following formula:

$$c(T) = c_0 \exp(-\Delta E/k_B T) \quad (2)$$

where  $\Delta E$  is the value of the energy barrier separating shallow and deep states and  $k_B$  is the Boltzman constant. Thus the temperature dependence of the scattering efficiency is proportional to the square of the difference of steady-state ( $dn_s/dt = 0$ ) solutions of the Eq. 1 for peaks and valleys of the grating. It is a result of the temperature dependence of the kinetics constant,  $c$ . The maximum of the scattering efficiency is obtained when the speed of thermal grating destruction is equal to the speed of erasure by scattered non-coherent light. The lines at Fig. 1 are the computer fits of theory described above to the experimental data. The value of energy barrier  $\Delta E$  has been treated as an adjustable parameter. The best fits have been obtained for  $\Delta E_{B1} = (12 \pm 6)$  meV and for  $\Delta E_{B2} = (195 \pm 40)$  meV for the bistable centers associated with the scattering efficiency maxima, which occur at  $T_1 = 17$  K and  $T_2 = 110$  K, respectively. These values are in very good agreement with those obtained from the activation energy of higher temperature slopes of the scattering efficiency vs. temperature dependence (12 and 138 meV, respectively). The value of the energy barrier  $\Delta E_{B2}$  also agrees very well with the activation energy for electron emission obtained from the DLTS measurements [4]. The temperature  $T_2 = 110$  K, at which this peak occurs, is in good agreement with the onset of bistability observed in the temperature dependence of the electrical resistivity [8]. This is a proof that the signal with maximum at  $T_2$  is associated with the same bistable center which has been detected in the DLTS. The other bistable center, associated with the low temperature peak of the scattering efficiency vs. temperature dependence, has not been detected in the DLTS measurements. Thus the light-induced grating technique is complementary to DLTS measurements for detection of metastable centers in semiconductors.

Another important consequence of the assumed form of the rate equation, describing the process of phototransformation from the ground localized to the shallow state of the metastable impurity, is the dependence of the scattering efficiency of the light-induced grating on the power of the write beams at fixed temperatures. In the case of linear rate equation (for "positive U" model of the bistable center) the scattering efficiency is proportional to the square of power of write beams, independent of temperature. The nonlinear rate equation (Eq. 1) results in different behavior. For the high temperature side

of the peak of the temperature dependence of scattering efficiency, the concentration of the shallow donors is expressed by the equation:

$$n_s = \sqrt{\frac{I\sigma}{c}} N_0 \quad (3)$$

In contrast to that, the equation which describes this concentration at the low temperature side of the peak of the temperature dependence of scattering efficiency, has the following form:

$$n_s = N_0 \left( 1 - \frac{cN_0}{I\sigma} \right) \quad (4)$$

Therefore, the light-induced grating signal, which is proportional (for small light intensities) to the square of the difference of populations of shallow centers in peaks and in valleys of the photoinduced gratings should be proportional to the square of the power of the write beams at low temperatures. In contrast to that, at high temperatures it should be linearly dependent on the power of the write beams. Figure 2 presents the power dependence of the scattering efficiency for two temperatures. The power dependence on

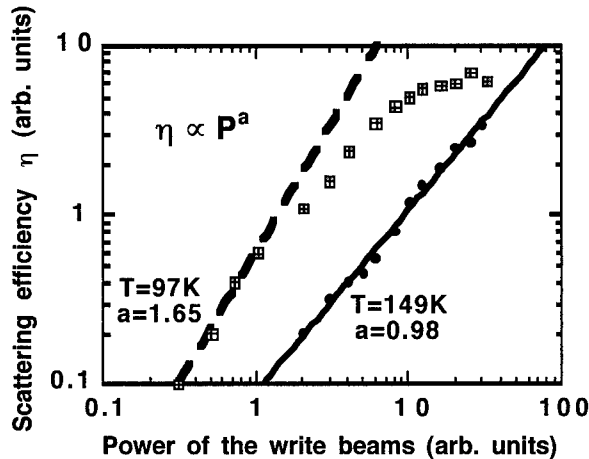


Figure 2. The power dependence of the scattering efficiency for two temperatures: 97 K and 149 K.

the high temperature side ( $T=149K$ ) of the second peak in the temperature dependence of the scattering efficiency is linear. The beginning part of the power dependence in the vicinity of the maximum of the scattering efficiency is much steeper. At higher power, as expected, the saturation occurs at this temperature, that decreases the slope. The slopes of such dependencies for various temperatures are presented in Fig. 1 (full squares). The same behavior as for this centers,

is also observed for the other bistable center with maximum of scattering efficiency at temperature  $T_1=17K$ . In the region between the maxima of the scattering efficiency the power dependencies for two centers affects each other and the results of such analysis are less meaningful.

The decay kinetics of the light induced gratings after switching off the write beams have bimolecular, non-exponential form, expressed by the Eq. 5:

$$\eta(t) = \left( \frac{A}{Act + 1} \right)^2 \quad (5)$$

where  $A^2$  is an initial scattering efficiency at time  $t=0$ . The example of the decay kinetics is presented in Fig. 3. The decay kinetics are well described by the Eq. 5. This is another support for the validity of the assumed model of the phototransformation process. The



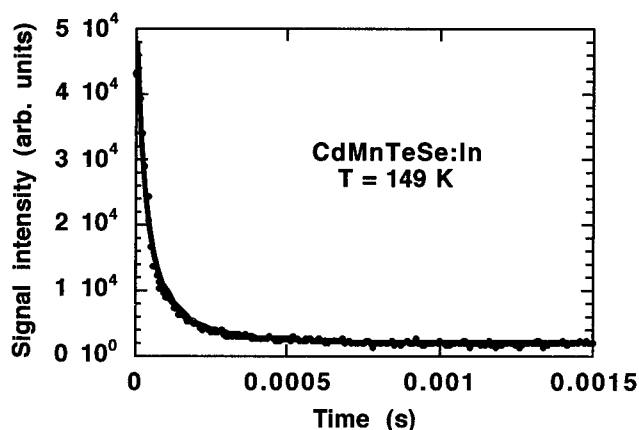


Figure 3. Light-induced grating decay kinetics of CdMnTeSe:In crystal at temperature  $T = 149$  K

partial erasure of the grating by the read beam, which have the same wavelength as the write beams and it is coincident with the photoionization spectrum of deep centers. When the write beams are switched off the read beam considerably contributes to the grating erasure, especially at low temperatures, when the process of thermal erasure is weak. Therefore, a decrease of the activation energy is observed.

The studies of light-induced gratings in semiconductors have been motivated, besides of pure spectroscopic reasons, by the search for new materials for holographic recording. Semiconductors with bistable centers could be very good materials for application in holography since they are very sensitive and have high dynamic range of refractive index. Unfortunately low metastability temperature hinders their practical application. This also applies to CdMnTeSe:In crystal. The metastability temperature of our crystal is relatively low (about 130 - 140 K). On the other hand it has been observed that in CdF<sub>2</sub> Ga dopant has higher metastability temperature than Indium [3, 9]. This effect is

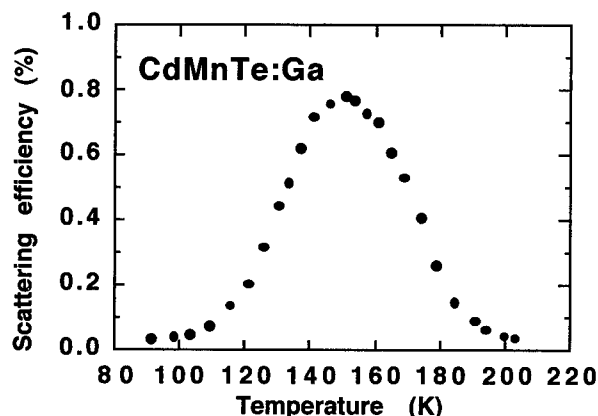


Figure 4. Temperature dependence of the scattering efficiency of light-induced grating in CdMnTe:Ga crystal

temperature dependence of the kinetics constant  $c$  calculated from the light-induced grating decay kinetics should reveal the value of the energy barrier between the shallow and deep state of the examined bistable centers.

The activation energies calculated from the decay kinetics are considerably smaller than those obtained from the scattering efficiency temperature dependence.

This effect is caused by the

associated with larger energy barrier separating shallow and deep states for Ga ion than for Indium. This is associated with smaller ionic radius of Ga dopant as compared with Indium. Moreover, in the DLTS measurements two deep donor centers have been detected in the Cd<sub>1-x</sub>Mn<sub>x</sub>Te:Ga, with activation energy for electron emission of about 240 meV and the about 500 meV, respectively [4]. Driven by this we

performed light-induced grating experiment also in  $\text{Cd}_{1-x}\text{Mn}_x\text{Te:Ga}$  sample. The results of the experiment are presented in Fig. 4.

Only one peak in the temperature dependence of the scattering efficiency has been observed. Its activation energy, calculated from the high temperature slope of the dependence, is equal to about 240 meV, which is in perfect agreement with the DLTS data for main metastable defect detected in the same crystal. At higher temperatures we were not able to detect any signal which could have been assigned to the second centers with higher activation energy for electron emission, as observed in the DLTS. This is probably a result of relatively low concentration or with much smaller lattice relaxation, associated with the photoionization of this center.

#### IV. Conclusions

The light-induced grating experiments, performed on  $\text{Cd}_{1-x}\text{Mn}_x\text{Te}_{1-y}\text{Se}_y\text{:In}$  crystals, show that behavior of both metastable centers detected in this crystal are in good agreement with the large lattice relaxation model which also assumes “negative U” character of these centers. The light-induced grating technique is complementary to the DLTS experiment, which allowed us to detect the second metastable centers in this crystal, not detected in the DLTS. On the other hand, only one metastable center was found in the  $\text{Cd}_{1-x}\text{Mn}_x\text{Te:Ga}$  crystal. Although the metastability temperature of this center is higher than for In doped crystals, it is still much below room temperature, which is desired for application in holographic storage.

#### Acknowledgments

The authors kindly acknowledge stimulating discussions with J.M. Langer on the problem of power dependence of the light-induced gratings scattering efficiency. This work has been partially supported by the grants no. 2 P03B 152 12 and 2 P03B 087 09 of Polish State Research Committee.

#### References:

1. K.J. Malloy and K. Khachaturyan, *Semiconductors and Semimetals* **38**, 235 (1993).
2. D.J. Chadi and C.H. Park, *Material Science Forum* **196-201**, 285 (1995).
3. U. Piekara, J. M. Langer and B. Krukowska-Fulde, *Solid State Commun.* **23**, 583 (1977); J. E. Dmochowski, J. M. Langer, Z. Kaliński, and W. Jantsch, *Phys. Rev. Lett.*, **56**, 1735 (1986)
4. T. Wojtowicz, G. Karczewski, N.G. Semaltianos, S. Kolesnik, I. Miotkowski, M. Dobrowolska and J.K. Furdyna, *Proc. of International Conference on Defects in Semiconductors, Gmunden 1993*, *Material Science Forum*, **143-147**, 1203 (1994); T. Wojtowicz, S. Kolesnik, I. Miotkowski and J.K. Furdyna, *Phys. Rev. Lett.* **70**, 2317 (1993)
5. N.G. Semaltianos, G. Karczewski, T. Wojtowicz and J.K. Furdyna, *Phys. Rev. B* **47**, 12 540 (1993)
6. A. I. Ryskin, A. S. Shcheulin, B. Koziarska, J. M. Langer, A. Suchocki, I. I. Buczinskaya, P. P. Fedorov, and B. P. Sobolev, *Appl. Phys. Lett.* **67**, 31 (1995); B. Koziarska, J. M. Langer, A. Suchocki, A. I. Ryskin, and A. S. Shcheulin, *Acta Phys. Polon. A* **88**, 1010 (1995)
7. H. Kogelnik, *Bell System Technical Journal* **40**, 2909 (1969).
8. T. Wojtowicz, unpublished results
9. A. Suchocki, B. Koziarska, T. Langer and J.M. Langer, *Appl. Phys. Lett.* **70**, 2934 (1997).

## DEEP LEVELS IN $\text{Cd}_{0.99}\text{Mn}_{0.01}\text{Te} : \text{Ga}$ .

J.SZATKOWSKI, E.PLACZEK-POPKO, K.SIERANSKI, P.FIALKOWSKI,  
A.HAJDUSIANEK, B.BIEG<sup>1</sup>

Institute of Physics, Technical University of Wrocław, Poland  
Wybrzeże Wyspiańskiego 27, 50-370 Wrocław

<sup>1</sup>Institute of Physics, Maritime Academy, Waly Chrobrego 1, 70-500 Szczecin, Poland

**Keywords :** CdMnTe, defect centers, DLTS.

**Abstract:** In this paper we present the results of our investigation of deep level defects in bulk Ga doped  $\text{Cd}_{0.99}\text{Mn}_{0.01}\text{Te}$  mixed crystal by Deep Level Transient Spectroscopy (DLTS) method. Schottky diodes were used for the investigations. In the material with higher donor concentration four electron traps have been found with activation energies obtained from Arrhenius plots equal to  $E_{T2} = 0.24\text{eV}$  and  $E_{T3} = 0.36\text{eV}$ . Electric field enhanced electron emission from the levels E1 and E4 has been observed and described in terms of Frenkel-Poole mechanism. In the as-grown samples with lower concentration only one dominant level with energy activation  $E_{T5} = 0.63\text{eV}$  has been observed in DLTS measurements. The capture process of electrons from the trap E2 and E5 is thermally activated with a capture barrier of 0.20 eV and 0.21 eV, respectively. This yields the true energetic distance of the trap levels E2 and E5 from the bottom of conduction band as 0.04 eV and 0.42 eV, respectively.

### RESULTS

Deep level transient spectroscopy, DLTS, is one of the widely used techniques to study defects in semiconductors. With the help of this method the most important parameters which characterise a deep level such as its thermal ionisation energy, concentration of the deep centers and their capture cross sections may be easily obtained.

Semiconducting compound CdMnTe is often used as a substrate for p-n junctions working as infrared photovoltaic detectors. So far several papers have reported on deep levels in CdMnTe [1-4]. In this paper we summarise the results of our deep level studies on 1% manganese content n-type Ga doped CdMnTe. Two types of samples were studied by us: type A of shallow donor concentration  $N_D = (1-5) \times 10^{16} \text{cm}^{-3}$  and type B of lower concentration of  $N_D$  of the order of  $10^{15} \text{cm}^{-3}$ . The material comes from prof. W.Giriat from IVIC Venezuela.

The Schottky contact was prepared by vacuum evaporation of gold  $1\text{mm}^2$  layer on chemically cleaned surface of CdMnTe sample. Indium soldered served as an ohmic contact.

For the samples A of higher donor concentration the DLTS signal temperature scans were taken within 80-420K temperature range. Temperature range for the samples of lower  $N_D$  concentration was limited to 180-420K due to the strong carrier freezing out of electrons from a donor level. The DLTS measurements performed on our samples revealed the presence of several deep levels, marked by us from E1 to E5. Exemplary DLTS signal for both types of samples within 80K-300K is shown in Fig.1.

In the case of the DLS-82E system at the temperature corresponding to DLTS signal peak following relation is valid [5] for thermal emission rate  $e_n$  from a trap :

$$e_n = 2.17 f \quad (1)$$

where  $f$  is the lock-in frequency.

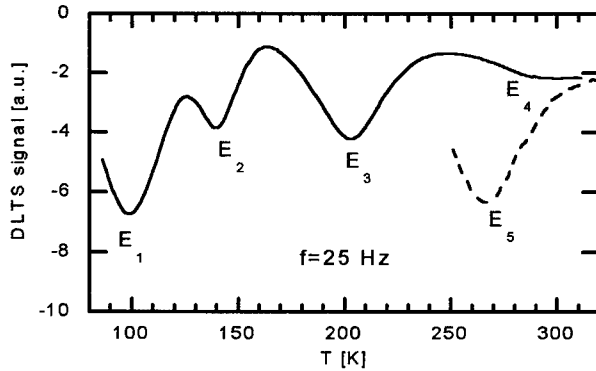


Fig.1. Exemplary DLTS signal for both types of  $\text{Cd}_{0.99}\text{Mn}_{0.01}\text{Te} : \text{Ga}$  samples : A- type-solid line, B- type dashed line. The same measurement conditions. Filling pulse width 1 ms.

On the other hand the electron emission rate  $e_n$  can be obtained from the detailed balance equation :

$$e_n = \sigma_n v_{th} N_C \exp [ - E_T / kT ] \quad (2)$$

where  $\sigma_n$  is capture cross section for electrons,  $v_{th}$  is the thermal velocity of electrons,  $N_C$  is the effective density of states at the bottom of conduction band and  $E_T$  is energy activation of the trap. The electron emission rate  $e_n$  obtained from DLTS data divided by temperature square  $T^2$  (in order to take into account the  $T^2$  dependence of  $N_C v_{th}$  product) plotted as a function of reciprocal temperature - which is the so called Arrhenius plot - provides the value of energy activation of the trap  $E_T$  and its capture cross section  $\sigma_n$  according to Eq.(2). Arrhenius plots corresponding to the DLTS signal peaks from Fig.1 are shown in Fig.2.

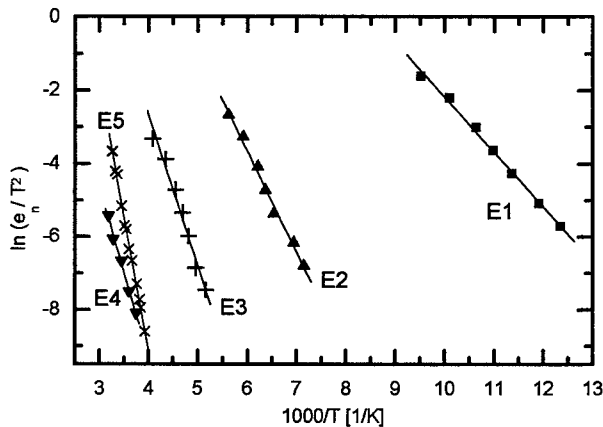


Fig.2. Arrhenius plots corresponding to the traps E1-E5. The plots for the traps E1 and E4 are at high electric field  $1.2 \times 10^5 \text{ V/cm}$ .

From the Arrhenius plots we calculated  $E_T$  and  $\sigma_n$  by the least-squares method. The results are summarised in Table I.

Level	Energy activation [ eV ]	Capture cross section [ cm <sup>2</sup> ]
E2	0.24	1 10 <sup>-15</sup>
E3	0.36	5.5 10 <sup>-15</sup>
E5	0.63	2.0 10 <sup>-12</sup>

**Table 1**  
Energy of activation  
and capture cross  
sections obtained  
from Arrhenius plots

### ELECTRIC FIELD DEPENDENCE

The DLTS measurements were taken for different values of reverse bias and depolarisation pulse heights. In that manner different values of electric field were realised. Detailed description of the isothermal differential DLTS (DDLTS) mode of operation of our DLS-82E system used for this study is given in [6].  $E_T$  and  $\sigma_n$  in the Table 1 are given only for the traps for which there was no (or very weak) influence of electric field on emission rate. Three of the traps: E1, E3 and E4 have shown electric field enhanced emission rate. Arrhenius plots are given also for them yielding trap energies  $E_{T1} = 0.13$  eV and  $E_{T4} = 0.4$  eV at the high electric field equal to  $1.2 \times 10^5$  V/cm.

Usually the influence of electric field on emission rate can be explained in the terms of Frenkel-Poole effect [7]. Brief explanation of this effect is following. Due to the electric field superimposed on a defect potential a lowering of effective emission barrier occurs. The thermionic electron emission from the trap is easier now but it is possible only if a defect center acquires a net charge upon carrier emission which means that the trap has to be donor-like (neutral when occupied and positively charged when empty) in n-type material and acceptor like in p-type material. Emission rate in the presence of electric field of intensity  $F$  in the terms of the Frenkel-Pool effect is given by following equation:

$$e_n = \sigma_n v_{th} N_C \exp [ - (E_{T0} - \Delta E_{PF}) / kT ] \quad (3)$$

where  $\Delta E_{PF}$  is the lowering of effective emission barrier and is equal to :

$$\Delta E_{PF} = \alpha (F)^{1/2} \quad (4)$$

and  $\alpha$  :

$$\alpha = e (Ze/\pi/\epsilon/\epsilon_0)^{1/2} \quad (5)$$

where  $e$  is electron charge,  $\epsilon$  is a semiconductor dielectric constant,  $\epsilon_0$  is the free-space permittivity and  $Z$  is the charge state of the defect after electron emission. According to Eq. (3) to Eq.(5) the semilogarithmic plot of emission rate  $e_n$  versus square root of electric field divided by  $kT$  product should give a straight line of slope  $\alpha$ . The theoretical value of  $\alpha$  for the  $\text{Cd}_{0.99}\text{Mn}_{0.01}\text{Te}$  material should be equal to  $2.2 \times 10^{-4} ((\text{eV})^2 \text{cm/V})^{1/2}$ . In Fig. 3 to Fig.5 the  $\ln e_n = f(F/(kT))^{1/2}$  for the traps E1, E3 and E4 are shown for several temperatures. From the figures one can see that the slope of the lines for each of the traps is temperature independent. However only in the case of the trap E4 the experimental value is close to the theoretical one:  $\alpha_4 = (3-3.5) \times 10^{-4} ((\text{eV})^2 \text{cm/V})^{1/2}$ . Energy activation extrapolated to zero-electric field intensity is therefore according to Eq.(3) to Eq.(5)  $E_{T40} = (0.51 \pm 0.01)$  eV.

For the trap E3,  $\alpha_3$  is around  $1 \times 10^{-4} ((\text{eV})^2 \text{cm/V})^{1/2}$  which is twice less than the theoretical value. Too low  $\alpha_3$  for the trap E3 can be attributed to higher localisation of impurity potential for this trap. Due to the weak electric field dependence of emission rate we assume the trap E3 activation energy to be constant and put the data together with corresponding capture cross section into Table I.

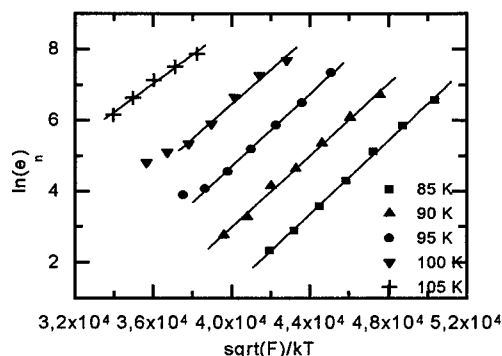


Fig.3. Emission rate as a function of electric field for the trap E1 at several temperatures. Solid lines were calculated by the least-squares method. Slopes of the lines:  $\alpha_1 = (4 - 5) \times 10^{-4} ((\text{eV})^2 \text{cm/V})^{1/2}$ .

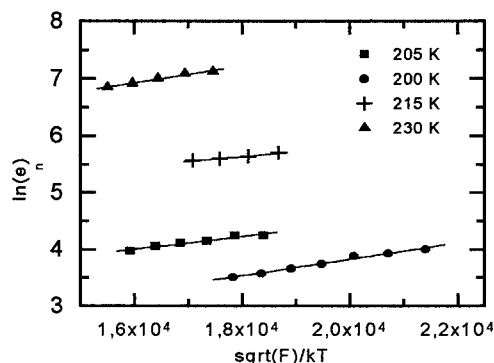


Fig.4. Emission rate as a function of electric field for the trap E3 at several temperatures. Solid lines were calculated by the least-squares method. Slopes of the lines  $\alpha_3 = (0.8-1.5) \times 10^{-4} ((\text{eV})^2 \text{cm/V})^{1/2}$ .

Too high value of  $\alpha_1 = (4-5) \times 10^{-4} ((\text{eV})^2 \text{cm/V})^{1/2}$  can be explained either by contribution of phonons in emission process or by multiply charged defect center resulting according to Eq. (5) in higher value of  $\alpha$ . Energy activation extrapolated to zero-electric field intensity is therefore according to Eq.(3) to Eq.(5)  $E_{T10} = (0.28 \pm 0.02) \text{ eV}$ .

#### CAPTURE CROSS SECTION

The DLTS measurements were taken also for different time duration of filling pulses. In that way different level of filling of the traps was realised. No influence of the trap filling degree on electron emission from the trap has been observed because the value of energy activation determined at different time width of filling pulse remained constant. We could assume therefore that we deal with point defects. However for the traps E2 and E5 strong temperature dependence of capture cross section has been observed.

In order to study the capture cross section for the levels E2 and E5 we applied the method proposed by Lang [8]. From the experimental data one gets the DLTS peak height versus filling pulse time  $A(t_p)$  dependence. Usually in the case of point defects the amplitude of DLTS peak height is exponential function of filling pulse duration  $t_p$ . However we observed also nonexponential contribution in  $A(t_p)$  dependence. According to Pons[9] this nonexponential contribution comes from the capture in Debay tail and the total  $A(t_p)$  is the sum of both terms:

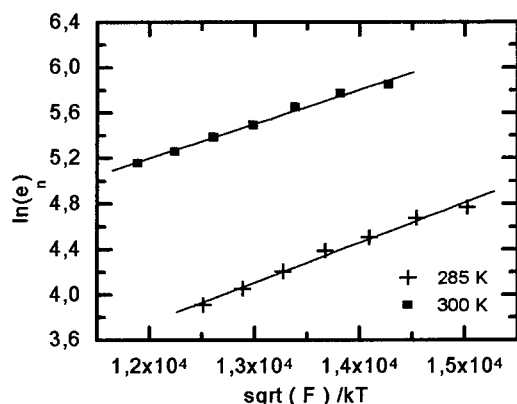


Fig.5. Emission rate as a function of electric field for the trap E4 at several temperatures. Solid lines were calculated by the least-squares method. Slopes of the lines:  $\alpha_4 = (3-3.5) \times 10^{-4} ((\text{eV})^2 \text{cm/V})^{1/2}$ .

$$A(t_p) = C_1(1 - \exp(t_p / t_c)) + C_2 \ln(t_p / C_3) \quad (6)$$

where  $C_1$ ,  $C_2$ ,  $C_3$  and  $t_c$  are fitting parameters. The inverse of  $t_c$ :

$$1/t_c = c_n = n v_{th} \sigma_n \quad (7)$$

where  $c_n$  is a capture probability and  $t_c$  is the time interval for a trap to capture a carrier,  $n$  is the electrons concentration, equal to the net donor concentration  $N_D$ . Fitting Eq. (6) to the experimental data we determined the value of capture cross section at the temperature corresponding to the DLTS peak. Repeating this procedure for different lock-in frequencies, which means different temperature of DLTS peak, the temperature dependence of capture cross section was achieved. We have used such procedure for the levels E5 and E2. With the help of equation (7) we calculated capture cross section  $\sigma_n$  at given temperature. Resulting capture cross sections as a function of inverse temperature are plotted in Fig. 6 and Fig. 7. For both traps capture cross section is exponentially decreasing function of  $1/T$  and

obeys relation:

$$\sigma_n = \sigma_\infty \exp(-E_B / kT) \quad (8)$$

where  $\sigma_\infty$  is the high-temperature cross section and  $E_B$  is the thermal energy barrier for capture of electrons. The solid lines in Fig. 6 and Fig. 7 present the best theoretical fitting of Eq. (8) to the experimental data. The values of  $E_B$  yielded with the help of the fitting procedure were equal to 0.20 eV for E2 and 0.21 eV for E5.

Such a temperature dependent capture cross section may be the evidence that there is strong electron-phonon coupling for the states E2 and E5. In that case the energy activation  $E_B$  is understood as an energetic barrier for the carriers to be captured at the trap level.

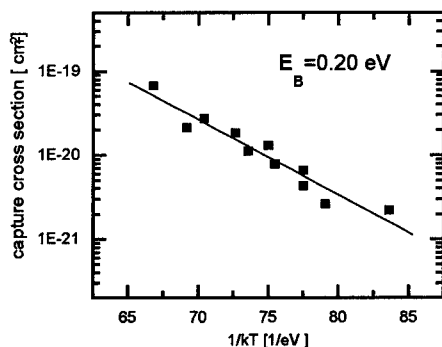


Fig.6 Capture cross section of the trap E2 vs inverse temperature. The solid line represents the best fitting of Eq.(8) to experimental data;  $\sigma_\infty = 6e^{14} \text{cm}^2$ .

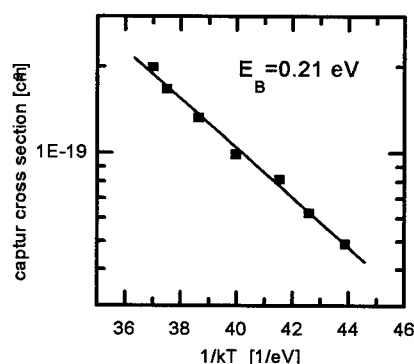


Fig.7 Capture cross section of the trap E5 vs inverse temperature. The solid line represents the experimental data fitting to equation (8);  $\sigma_{\infty} = 1.5 \cdot 10^{-12} \text{ cm}^2$ .

Taking into account the height of barrier energy for capture  $E_B = 0.20 \text{ eV}$  for E2 and  $0.21 \text{ eV}$  for E5 we obtain the true energetic distance of the trap levels E2 and E5 from the bottom of conduction band as  $0.04 \text{ eV}$  and  $0.42 \text{ eV}$ , respectively.

Presence of defect centers with such energetic barrier for carrier capture is well known in III-V compounds [10]. The shallow-deep metastability of these defects is explained in the terms of the so-called large relaxation model (LLR). Energetic barriers of the type were also observed in CdTe [11] and related CdZnTe [12] and CdMnTe [1-4] compounds. In indium doped CdTe [11] the level labelled as ET2a of energy  $0.34 \text{ eV}$  with energy barrier for capture equal to  $0.28 \text{ eV}$  results in true distance of the level from

the bottom of conduction band as  $0.06 \text{ eV}$ . In [3,4] the level of energy  $0.25 \text{ eV}$  with thermal energy barrier for capture equal  $0.11 \text{ eV}$  was found in gallium doped  $\text{Cd}_{0.97}\text{Mn}_{0.03}\text{Te}$ . These data are close to the data obtained by us for the level E2. As for the level E5 its activation energy is also close to the value observed in [3,4]. As regards the levels E1 and E4 it is difficult to compare them with the data given in [11] as those were from Arrhenius plots and the influence of electric field was not analysed. The level E3 of energy activation  $0.36 \text{ eV}$ , almost electric field independent is also impossible to compare with other data [11] as its capture cross section is different from the one given for candidates to do so (cf. levels EB2 and EB3 in [11]).

## References.

1. I. Terry, T. Penney, S. v. Molnar, J.M. Rigotty, P. Becla, Solid State Communications **84**, 235 (1992).
2. N.G. Semaltianos, G. Karczewski, T. Wojtowicz, J.K. Furdyna Phys. Rev. B **47**, 12540 (1993).
3. T. Wojtowicz, G. Karczewski, N.G. Semaltianos, S. Kolesnik, I. Miotkowski, M. Dobrowolska, J.K. Furdyna Mat. Sci. Forum **143-147**, 1203 (1994).
4. N.G. Semaltianos, G. Karczewski, B. Hu, T. Wojtowicz, J.K. Furdyna Phys. Rev. B **51**, 17499 (1995).
5. G. Ferenczi, P. Horvath, F. Toth, J. Boda U.S. Patent No 4437060 (1984).
6. J. Szatkowski, E. Placzek-Popko, K. Sierański, O.P. Hansen, present Conference paper entitled „Deep hole traps in Be-doped AlGaAs MBE layers”.
7. J. Frenkel, Phys. Rev. **54**, 647 (1938).
8. C.H. Henry, D.V. Lang Phys. Rev. B **15**, 989 (1977).
9. D. Pons, J. Appl. Phys. **55**, 3644 (1984).
10. L. Dobaczewski, A.R. Peaker, J.M. Langer in Properties of Aluminium Gallium Arsenide edited by S. Adachi (EMIS Datareview Series No. 7, INSPEC 1993) p.278 (1993).
11. G.M. Khattak, C.G. Scott J. Phys.: Condens. Matter **3**, 8619 (1991).
12. 8. K. Khachatryan, M. Kamińska, E.R. Weber, P. Becla, R.A. Street Phys. Rev. B **40**, 6304 (1989).



## VACANCY-TYPE DEFECTS IN ELECTRON AND PROTON IRRADIATED II-VI COMPOUNDS

S. Brunner<sup>1</sup>, W. Puff<sup>1</sup>, P. Mascher<sup>2</sup>, A.G. Balogh<sup>3</sup>, H. Baumann<sup>4</sup>

<sup>1</sup>Institut für Technische Physik, Technische Universität Graz, A-8010 Graz, Austria,  
brunner@ifk.tu-graz.ac.at

<sup>2</sup>Centre for Electrophotonic Materials and Devices, Department of Engineering Physics,  
McMaster University, Hamilton, Ontario L8S 4L7, Canada

<sup>3</sup>Department of Materials Science, Technische Hochschule Darmstadt, Darmstadt,  
Germany

<sup>4</sup>Institut für Kernphysik, J.W. Goethe Universität Frankfurt, Frankfurt/Main,  
Germany

**Keywords:** II-VI compounds, positron annihilation, point defects, electron and proton irradiation

**Abstract.** Positron lifetime and Doppler-broadening measurements have been performed on the wide-bandgap compound semiconductors ZnO, ZnS, ZnSe, and ZnTe to investigate the basic properties of intrinsic and radiation induced defects. The samples were irradiated either with 3 MeV protons at 223 K to a fluence of  $1.2 \times 10^{18}$  p/cm<sup>2</sup> or 1 MeV electrons at 4 K to a fluence of  $1 \times 10^{18}$  e/cm<sup>2</sup>. The isochronal annealing was done in an Ar atmosphere. It was found that both electron and proton irradiation caused significant changes in the positron annihilation characteristics and several annealing stages were observed, related to the annealing of variously sized vacancy complexes.

### Introduction

ZnO, ZnS, ZnSe and ZnTe are wide band gap, II-VI compound semiconductors and, therefore, of prime interest for opto-electronic applications in the visible spectrum. The knowledge of the defect structure is not only of fundamental but also of technological interest because native defects appear to control the optical and electrical properties. A frequently used method to investigate the intrinsic defect structure in materials is the irradiation with energetic particles such as electrons or protons and to study the annealing behaviour of the induced defects. Electron irradiation mainly introduces isolated Frenkel-pairs, proton irradiation, on the other hand creates essentially isolated defects of monovacancy-type and collisions cascades which might produce bigger defect complexes. Most of the isolated defects are not stable at room temperature and rearrange. Before these defects recombine they can be trapped by other defects and might form more stable configurations. However, the interpretation of experimental results is complicated by the fact that in compound semiconductors native defects may exist in both sublattices and in different charge states. Magnetic resonance studies [1-7] have given some basic understanding of intrinsic point defects in II-VI compounds. The positron annihilation technique has shown to be able to give additional information on open volume defects and their interactions in semiconductors.

### Experimental Details

The ZnO samples used in the present study are as-grown single crystals (ZnO-SX). The ZnS-CVD samples are polycrystals grown by chemical vapour deposition (CVD), supplied from II-VI Inc., Saxonburg. The samples ZnS-SX, ZnSe-SX and ZnTe-SX obtained from CrysTec, Berlin, are single crystals (SX) grown by the Markov vapour phase transport method. For investigations of irradiation induced defects a pair of the respective samples were irradiated either with 3 MeV protons at 223 K to a fluence of  $1.2 \times 10^{18}$  p/cm<sup>2</sup> or with 1 MeV electrons at 4 K to a fluence of  $1 \times 10^{18}$  e/cm<sup>2</sup>. The positron lifetime and Doppler-broadening measurements were performed at room temperature. A conventional fast-fast coincidence system having a time resolution of 192 ps full width at half

maximum (FWHM) was used for positron-lifetime measurements. As positron source, 30  $\mu\text{Ci}$  of  $^{22}\text{NaCl}$  was enclosed in a 1.35 mg/cm Al foil and then sandwiched by two samples. To guarantee good statistics in the numerical analyses at least  $5 \times 10^6$  counts were collected for each lifetime spectrum. Up to three spectra were measured per data point. The numerical analyses of the spectra were performed using the computer program PFPOSFIT [8]. Details of the analysis procedure and the physical background can be found in [9]. The Doppler-broadening of the 511 keV annihilation line was measured using an intrinsic Ge detector with a resolution (FWHM) of 1.18 keV at 497 keV. During the measurement the annihilation peak was digitally stabilised. Each measurement, with a total area of about  $2 \times 10^6$  counts, was repeated at least 5 times. To characterise the spectra, the usual S-parameter, the ratio of the counts in the central portion and the total counts of the spectrum, were used.

## Results and Discussion

In Table 1 the positron lifetimes and intensities together with the values of the Doppler-broadening line shape parameter, S, for the respective samples in the as-received state and after proton or electron irradiation are shown. Also shown are the mean lifetime,  $\tau_m$ , and the bulk lifetime,  $\tau_b$ , as calculated by the positron two-state-trapping model [10]. The bulk lifetime represents the annihilations from the "perfect" crystal and hence is very important as a material constant.

**Tab.1:** Observed positron lifetimes, intensities, and S-parameter values, together with calculated values for  $\tau_m$  and  $\tau_b$  ( $\pm 2$  ps) before and after irradiation with 1 MeV electrons or 3 MeV protons. Typical uncertainties in the short lifetime are  $\pm 2$  ps, in the second lifetime  $\pm 10$  ps and in the intensities  $\pm 5$  %. The error in the S-parameter is  $\pm 0.0004$ .

Sample	Treatment	$\tau_1$ [ps]	$I_1$ [%]	$\tau_2$ [ps]	$I_2$ [%]	$\tau_m$ [ps]	$\tau_b$ [ps]	S
<b>ZnO-SX</b>	as-res.	160	66	253	34	192	183	0.4260
	ann.	180	100	-	-	180	180	0.4201
	p-irr.	168	53	317	47	238	216	0.4338
<b>ZnS-SX</b>	as-res.	219	94	304	6	224	223	0.4785
	e-irr.	154	18	250	82	233	225	0.4811
	after ann.	221	100	-	-	221	221	0.4781
<b>ZnSe-SX</b>	as-res.	233	100	-	-	234	234	0.4899
	p-irr.	183	22	308	78	268	281	0.5012
	e-irr.	156	18	272	82	251	239	0.4929
<b>ZnTe-SX</b>	as-res.	254	100	-	-	254	254	0.5078
	p-irr.	181	20	336	80	305	287	0.5234
	e-irr.	214	46	306	54	264	255	0.5091
<b>ZnS-CVD</b>	as-res.	178	38	305	62	257	240	0.4854
	p-irr.	175	32	297	68	258	243	0.4869
	after ann.	224	100	-	-	224	224	0.4772

In the following the results of the respective samples will be discussed.

## ZnO-SX

In comparison to earlier investigations [11-15] the observed mean lifetime,  $\tau_m = 192$  ps, is rather high. Moreover, the second lifetime component,  $\tau_d = 253$  ps with an intensity of 34 % (see Tab.1), which has to be attributed to annihilations from a defect state, are indications that the our single crystal was not defect free. After annealing at a temperature of 1150 °C for 2 hours followed by a cooling down in 100 hours to room temperature we obtained only one lifetime component, with a value of  $\tau = 180$  ps, indicating that no positron sensitive defects exist any more.

Irradiation with protons causes a large increase of the mean lifetime,  $\tau_m$ , from 180 ps to 236 ps, showing that positrons annihilate in vacancy type defects introduced by the irradiation. A two term fit gives an additional lifetime component of 317 ps. The ratio of the defect lifetime component and the bulk lifetime,  $\tau_d/\tau_b$ , can be used to characterise the defect. For divacancies this ratio should be around 1.4 – 1.5 [16]. In our case, this ratio amounts to 1.76, indicating that this defect component is a superposition of at least two components, one stemming from divacancies and the other from even larger complexes. A more detailed analysis reveals indeed two defect components, one with  $(261 \pm 10)$  ps and  $(54 \pm 7)$  % and the other with  $(440 \pm 70)$  ps and  $(10 \pm 5)$  %. The first one has to be attributed to divacancies and the second one comes from larger three-dimensional vacancy cluster.

The dependence of the mean lifetime and the S-parameter as a function of isochronal annealing are shown in Figs.1 and 2. We observe 3 annealing stages, one at around 200 °C, the second at 500 °C and the third one at around 850 °C. After annealing at 1250 °C the mean lifetime as well as the S-parameter reaches the well annealed value before irradiation, indicating that all defects have annealed out. A more detailed analysis of this annealing will be published elsewhere.

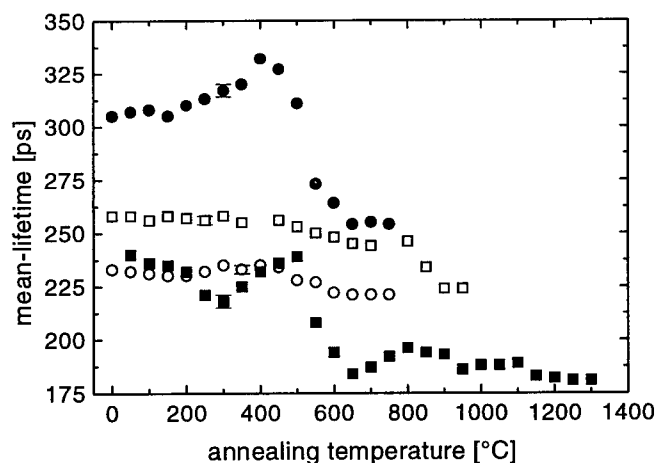


**Fig.1:** Mean lifetime of proton irradiated ZnO-SX (■), ZnS-CVD (□), ZnTe-SX (●) and electron irradiated ZnS-SX (○) as a function of isochronal annealing.

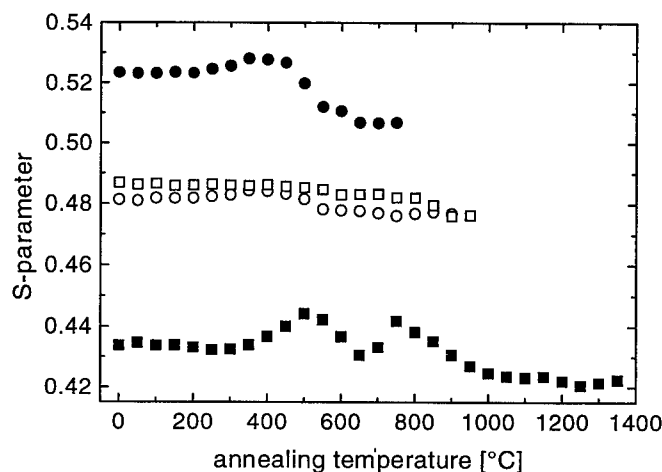


**Fig.2:** S-parameter of proton irradiated ZnO-SX (■), ZnS-CVD (□), ZnTe-SX (●) and electron irradiated ZnS-SX (○) as a function of isochronal annealing. The uncertainties are within the size of the symbols.

### ZnS-SX and ZnS-CVD

The positron lifetimes and intensities before electron irradiation show that the sample was nearly defect free (see Table 1). The calculated bulk lifetime has a value of  $\tau_b = 223$  ps, in good agreement with the theoretical predicted values of  $(219 \pm 2)$  ps [17, 18]. The increased mean lifetime after irradiation gives clear evidence for positron trapping at vacancy-type defects. Detailed analysis [19] revealed a defect lifetime of  $\tau_d = 250$  ps. The calculated bulk lifetime after irradiation ( $\tau_b = 225$  ps) proves that the trapping model is applicable. Hence, the trapping rate, which is proportional to the defect concentration, can be calculated,  $\kappa = I_2/I_1(\lambda_b - \lambda_2)$ . According to [20] a trapping rate of  $\approx 1 \text{ ns}^{-1}$  corresponds to a concentration of  $10^{17} \text{ cm}^{-3}$  neutral defects. Therefore, we can estimate that irradiation with 1 MeV electron to a fluence of  $1 \times 10^{18} \text{ e/cm}^2$  introduce about  $2 \times 10^{17}$  defects per  $\text{cm}^3$ . The mean lifetime is nearly constant during annealing up to (see Fig.1). Detailed analysis reveal that the defect lifetime is still observable at 250 °C. Since Frenkel-pairs which are the main defects introduced by electron irradiation should have annealed at this temperature [7, 21], we attribute these defects to monovacancies which are stabilized in small complexes such as vacancy-impurity pairs.

At 250 °C, both, the mean lifetime and the S-parameter increases (Fig.1 and Fig.2), indicating the agglomeration of the defects to divacancies, with a lifetime of 295 ps [19]. These defects are not stable at temperatures above 500 °C.

In Fig. 1 also the mean lifetime of a polycrystalline ZnS-CVD sample, irradiated with protons as a function of isochronal annealing is shown. Due to the high concentration of grown in defects with a lifetime of 305 ps, proton irradiation does not change the defect distribution in a significant manner. Isochronal annealing of the irradiated ZnS-CVD in an argon atmosphere up to 900 °C improves the properties of the samples in two annealing stages between 450-500 °C and 800-900 °C nearly to the single crystal quality. More details are given in [19].

### ZnSe-SX

For the as-grown single crystal the analysis of the lifetime spectra reveal only one lifetime component, indicating that no positron sensitive defects exists. The observed lifetime  $\tau_b = 234$  ps is, therefore, the bulk lifetime. Theoretical work using the local-density approximation (LDA) predicts a positron bulk lifetimes of  $\tau_b = 233$  ps [17, 18] in excellent agreement with our experimental value. The recently published value of 240 ps [22] and 255 ps [23] seems rather too high.

After irradiation with 3 MeV protons a discoloration from yellow to brown was observable. This

might be due to vacancies in the anion lattice, the well known F-centre, introduced by irradiation with protons [1]. The irradiation also causes a strong increase in the mean lifetime from 236 ps to 286 ps, indicating that additional vacancy type defects has been introduced. The analysis reveals two lifetime components with  $\tau_1 = 183$  ps (22 %) and  $\tau_2 = 308$  ps (78 %). In this sample, we again observe complete positron trapping after proton irradiation. The shorter lifetime component must, therefore, be a composition of a defect component and the bulk component. From the theoretically predicted values for the monovacancies,  $\tau_d = 245$  ps ( $V_{Zn}$ ) and  $\tau_d = 252$  ps ( $V_{Se}$ ) [17, 18] it is clear that this lifetime can't be separated in the analysis procedure, since it is too close to the bulk value. The second lifetime component comes from divacancies ( $\tau_d/\tau_b \approx 1.3$ ). Again, the measured lifetime of  $\tau_d = 308$  ps agrees very well with the theoretical value for nearest-neighbour divacancies,  $V_{Zn}V_{Se}$ , of 310 ps [17, 18].

After irradiation with electrons we observe a defect component with 272 ps. In the sight of the theoretical calculations the induced defect might be a monovacancy or a small complex containing a vacancy. The trapping model gives for the concentration of these defects  $\approx 3 \times 10^{17}$  per  $\text{cm}^3$ .

### ZnTe-SX

From the results of the lifetime measurements (see Tab.1) it can be seen that the as grown ZnTe-SX was defect free. The obtained bulk lifetime,  $\tau_b = 254$  ps, is in good agreement with theoretical calculations [17, 18] and significantly shorter than that obtained by *de la Cruz et al.* [15].

Irradiation with 3 MeV protons introduces defects as can be seen in the increased mean lifetime from  $\tau_m = 254$  ps to  $\tau_m = 305$  ps. Detailed analysis in [24] reveals a defect related lifetime of  $\tau_d = 336$  ps (see Tab.1). From the lifetime ratio  $\tau_d/\tau_b = 1.3$  we identify this defect in accordance with theoretical calculations [17, 18] as divacancies, most probably  $V_{Zn}V_{Te}$ . The short positron lifetime component might again be a composition of a defect component with the bulk component, which can not be separated.

The behaviour of the mean lifetime,  $\tau_m$ , and the S-parameter during isochronal annealing up to 750 °C is also shown in Figs.1 and 2. As one can see the mean lifetime is essentially constant up to a temperature of 150 °C. A detailed analysis of the spectra [24] reveals that the second lifetime component, starts steadily to increase at a temperature of 200 °C and reaches the maximal value of about 409 ps at 500 °C, indicating some defect agglomeration. At about 500 °C a distinct annealing stage in the mean lifetime as well the S-parameter can be observed. At a temperature of 650 °C the mean lifetime of the as-grown state is reached and no second lifetime component could be separated, showing that all irradiation induced defects are now annealed out.

As expected, the situation after 1 MeV electron irradiation to a fluence of  $1 \times 10^{18}$  e/cm<sup>2</sup> is quite different. After irradiation an additional lifetime component with 306 ps is observable. A comparison with the calculated vacancy lifetimes,  $V_{Zn}$  (261 ps) and  $V_{Te}$  (291 ps) [17, 18], suggest to ascribe this lifetime to annihilations in Te vacancies, in agreement that isolated Zn vacancies do not exist [7], or complexes containing vacancies. The trapping model is applicable and yields a defect concentration of about  $8 \times 10^{16} \text{ cm}^{-3}$ . Low temperature measurements are planned to study the respective charge states of the defects.

### Acknowledgements

The electron irradiation was performed at the Institut für Festkörperforschung, Forschungszentrum Jülich. The authors wish to thank Dr. F. Dworschak for carrying out the irradiation. In Canada his work has been supported by the Natural Science and Engineering Research Council of Canada.

## References

1. J. Schneider and A. Räuber, *Solid State Commun.* **5**, 779 (1967).
2. M.J. Smith and W.E. Vehse, *Phys. Letters* **A31**, 147 (1970).
3. A.L. Taylor, G.Filipovich and G.K. Lindeberg, *Solid State Commun.* **8**, 1359 (1970).
4. G.D. Watkins in "Proc. International Conference on Radiation Effects in Semiconductors" (Bristol: Inst. of Phys. Conf. Ser. 31 ,IOP) pp. 95 (1977).
5. D. Galland and A. Herve, *Solid State Commun.* **14**, 953 (1974).
6. G.D. Watkins, *Phys. Rev. Lett.* **33** 223 (1974).
7. G.D. Watkins, *J. Crys. Growth* **159**, 159 (1996).
8. W. Puff, *Comput. Phys. Commun.* **13**, 371 (1983).
9. W. Puff and X.-T. Meng, *J. Appl. Phys.* **73**, 648 (1993).
10. R.N. West, *Adv. Phys.* **22**, 66 (1973).
11. W. Puff, S. Brunner and P. Mascher in "The Physics of Semiconductors" ed. D.J. Lockwood (Singapore: World Scientific Publ.) pp. 2439 (1995).
12. W. Puff, S. Brunner, P. Mascher and A.G. Balogh, *Mat. Res. Soc. Symp. Proc.* **378**, 977 (1995).
13. W. Puff, S. Brunner, P. Mascher and A.G. Balogh, *Materials Sci. Forum* **196-201**, 333 (1995).
14. J. Zhong, H.A. Kitai, P. Mascher and W. Puff, *J. Electrochem. Soc.* **140**, 3644 (1993).
15. R.M. de la Cruz, R. Pareja, R. Gonzalez, L.A. Boatner and Y. Chen, *Phys. Rev.* **B45**, 6581 (1992).
16. S. Dannefaer in "Defect Control in Semiconductors" ed. K. Sumino (North-Holland:Elsevier Science Publishers B.V.) pp. 1571 (1990).
17. F. Plazaola, A.P. Seitsonen and M.J. Puska, *J. Phys.: Condens. Matter* **6**, 8809 (1994).
18. F. Plazaola, A.P. Seitsonen and M.J. Puska, *Materials Sci. Forum* **175-178**, 469 (1995).
19. S. Brunner, W. Puff, P. Mascher, A.G. Balogh and H. Baumann, *Mat. Res. Soc. Symp. Proc.* **438**, 235 (1997).
20. P. Mascher, S. Dannefaer and D. Kerr, *Phys. Rev.* **B40**, 11764 (1989).
21. B.K. Meyer and W. Stadler, *J. Cryst. Growth* **161**, 119 (1996).
22. R. Pareja, R.M. de la Cruz and P. Moser, *J. Phys.: Condens. Matter* **4**, 7153 (1992).
23. K. Terashima, E. Tokizaki, A. Uedono and S. Tanigawa, *Jpn. J. Appl. Phys.* **32**, 736 (1993).
24. S. Brunner, W. Puff, P. Mascher, A.G. Balogh and H. Baumann, *Materials Sci. Forum* (in print).

## UV ENHANCED AND SOLAR BLIND PHOTODETECTORS BASED ON LARGE-BAND-GAP MATERIALS

A. Malik and R. Martins

CEMOP/UNINOVA, Quinta da Torre, 2825 Monte de Caparica, Portugal

**Keywords :** UV photodetectors, heterojunctions, zinc sulphide, tin oxide films, fluorine doping.

### Abstract

High quantum efficiency, UV-enhanced monocrystalline zinc sulphide optical sensors for precise radiometric and spectroscopic measurements have been developed by spray deposition of heavy fluorine-doped tin oxide thin films with carrier concentration near  $10^{21} \text{ cm}^{-3}$  onto the surface of zinc sulphide monocrystals as an alternative to the UV-enhanced silicon photodetectors as well as to new detectors based on SiC and GaN. The fabricated sensors have an unbiased internal quantum efficiency that was nearly 100% from 250 to 320 nm, and the typical sensitivity at 290 nm is 0.15 A/W. The sensors were insensitive to solar radiation in earth's conditions and can be used as solar blind photodetectors for precision UV-measurements under direct solar illumination, both terrestrial and space applications.

### Introduction

Traditionally, the photomultiplier tubes and the silicon photodiodes with shallow *p-n* junction have been applied to registration and measurements of ultraviolet (UV) radiation. Disadvantages of silicon UV-enhanced photodiodes include the facts that silicon has indirect bandgap of 1.12 eV and peak sensitivity is around 700-900 nm, so that external filtering is needed to block out the visible and infrared radiation. This adding both to the expense and volume of the detector assembly [1].

The large-band gap materials, such as silicon carbide (SiC) and gallium nitride (GaN) are more perspective for applications where it is desirable to detect UV in an infra-red (IR) background. Several aerospace, medical, biological, spectroscopic, astronomy and radiometry measurement applications require optical semiconductor sensors with high ultra-violet (UV) sensitivity, insensitive to direct solar radiation, for wavelengths higher than 350 nm and long term stability. These are the so-called solar blind photodetectors. Monocrystalline [2] or thin-film photodiodes [3] developed based on an indirect bandgap SiC material are not really solar blind sensors due to their some sensitivity to solar irradiation. Compared to SiC, another wide band semiconductor candidate, GaN presents direct gap materials with the cut-off wavelength near 360 nm [4]. However, UV detectors based on these perspective semiconductor materials are in their infancy and a significant progress in device fabrications can be expected over the next few years [5].

The zinc sulphide (ZnS) with the direct bandgap of 3.6 eV is also a perspective candidate for fabrication of the solar blind detectors. However, ZnS presents an ionic compound and a doping problem causes difficulties in the formation of *p-n* junction-based devices. Other methods for devices fabrication such as, for example, formation of the Schottky barrier by deposition of semitransparent metallic films on ZnS surface, were also used [6]. However, a strong absorption in the metallic electrode limits the detector's quantum efficiency. This limitation can be overcome by using transparent and conductive metal oxide films. So, a low resistive tin-doped indium oxide films (ITO) were applied to fabricate UV photodetectors based on gallium phosphide (GaP) [7] and GaN [8]. Since the ITO films have a significant UV absorption, the quantum efficiency at wavelengths less than 300 nm was highly reduced.

Among all known transparent conductive metal oxide films, the heavy fluorine-doped tin oxide films (FTO) have the highest bandgap value ( $\sim 4.4 \text{ eV}$  at carrier concentrations of  $4.6 \times 10^{20} \text{ cm}^{-3}$  [9]) and are the more suitable for applications in UV-enhanced surface-barrier photodetectors. In the present paper we report an improved version of the surface-barrier ZnS optical sensors, which

presents an enhanced UV-sensitivity using a transparent electrode based on a heavy doped FTO film deposited by spray pyrolysis technique.

#### Spray deposition process and device's fabrication.

FTO films have been deposited at 450 °C on heated substrates by spray technique [10], at atmospheric pressure, under air conditions. A schematic diagram of the spray pyrolysis system used to deposit the metal oxide thin films is shown in Figure 1.

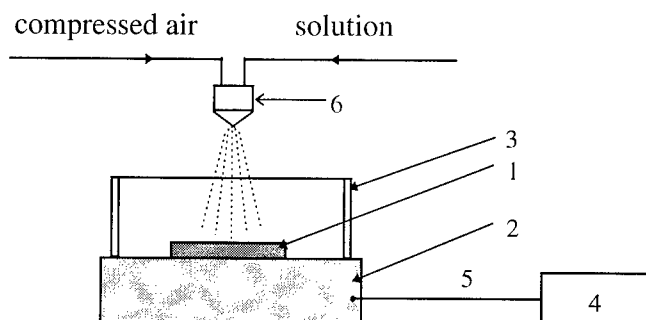


Fig. 1 -Spray equipment used to prepare the metal oxide films studied in this work

The substrate (1) is placed onto a heater (2) with a temperature screen (3). The temperature is controlled by a temperature controller (4) connected to a thermocouple (5) which is inserted into a small hole, in the surface of the heater. Prior to the deposition, the heater temperature was maintained to within  $\pm 1$  °C, at temperature of 430 °C. All depositions have been carried out using compressed air as the carrier gas for spraying the solution onto the surface of the substrate by means of a special designed glass atomiser (6), typically at a pressure of about 0.5 kgf cm<sup>-2</sup>.

The solution was prepared based on SnCl<sub>4</sub>·5H<sub>2</sub>O precursor, to deposit the FTO films. The precursor have been dissolved to concentrations of 0.6 M in alcohol. Adding in the solution HF or NH<sub>4</sub>F was used to dope the films. The deposition rate was near 100 nm/min. The films deposited on glass and sapphire substrates were used for structural, electrical and optical characterisation of the films.

The device's design was similarly to ITO/ZnS heterostructures described elsewhere [8]. N-type ZnS monocrystalline wafers, with carrier concentration of 10<sup>15</sup> -10<sup>16</sup> cm<sup>-3</sup> were used to produce the detectors. The photo-active area of the detectors produced were in the range from 10 to 100 mm<sup>2</sup>.

#### Measurement tools for films and device characterisations.

The film's thickness was measured by a Sloan Dektak IIA profilometer and their crystalline structure was determined by X-ray diffraction measurements using a Siemens diffractometer equipped with a Cu rotating anode. The Van der Pauw's technique was employed to measure the electrical resistivity and Hall coefficient of the films, under vacuum conditions, using a cryostat specially designed (HL5500PC - Biorad Microscience). The optical specular transmittance and reflectance spectra, in the wavelength range from 0.3-2.5 μm, were obtained using a Shimadzu double-beam UV-VIS-NIR scanning spectrophotometer. The transmittance of the thin FTO films (100 nm) in UV region as well as the devices sensitivity were measured in low light scattering conditions by means of a double-monochromator DMR-4 equipped with a deuterium lamp as light source. The electrical parameters of devices were measured with an electrometer VK2-16 and a capacity bridge, by standard techniques [11].

#### Results and discussion.

The growth mechanism of the FTO films deposited by spray pyrolysis depends on many technological parameters such as the size of droplets, the type of chemical precursors, the substrate temperature, the solution spray rate and the distance between the atomiser and the substrate [10].



The structure of all FTO films are polycrystalline and present a single phase. Their structure depends on the fluorine content used in the gas phase during the deposition process. The X-ray data (Figure 2) of as-deposited heavy doped FTO (40 at.% F in solution) films on glass substrates with thicknesses near  $0.4\ \mu\text{m}$  show a strong preferred grain orientation in (200) direction.

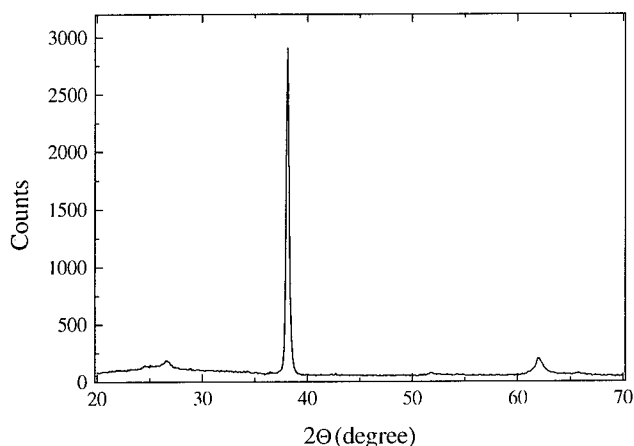


Fig. 2 -X-Ray diffraction spectra of as-deposited on glass substrate the FTO films.

The mean size of the columnar grains was determined from the full width at half maximum (FWHM) of the X-ray peak using the classical Debye-Scherrer formula, leading to values between 40 nm and 50 nm.

The F/Sn ratio in the solution of 40 at.% was optimal for the deposition of the FTO films with excellent electrical parameters. So, at this condition we fabricated films with carrier concentration and mobility of  $10^{21}\ \text{cm}^{-3}$  and  $20\ \text{cm}^2/\text{V-s}$ , respectively. The optimised films present a sheet resistance of  $10\ \Omega/\text{sq}$ . This behaviour is explained by the way how the F atoms substitute the anion oxygen in the crystalline lattice, do not giving place to the formation of the scattering centres, as it happens with the Sn-doped  $\text{In}_2\text{O}_3$  films.

The specular transmission (measured with respect to air) in the wavelength ranges from  $0.3\ \mu\text{m}$  to  $2.5\ \mu\text{m}$  of the as-deposited optimised FTO films is shown in Figure 3 in comparison with the low resistive ( $5.5\ \Omega/\text{sq}$ ) ITO films. The value of the optical energy gap in ITO and FTO films depends on the carrier concentration, as it is shown in Figure 4.

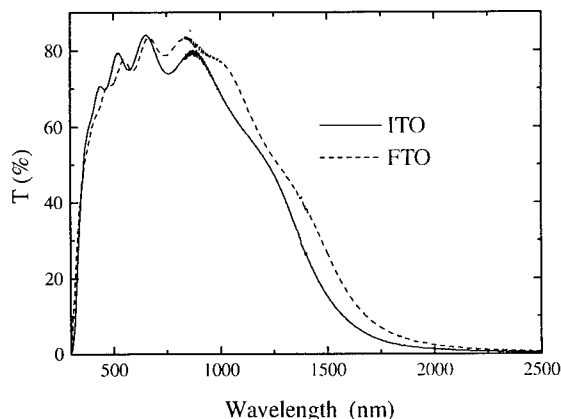


Fig. 3 -The specular transmission in the wavelength ranges from  $0.3\ \mu\text{m}$  to  $2.5\ \mu\text{m}$  of the as-deposited FTO and ITO films with sheet resistance 5.5 and  $10\ \Omega/\text{sq}$ . and thicknesses of  $0.4\ \mu\text{m}$ .

The data show that the films with carrier concentration's near  $10^{21} \text{ cm}^{-3}$  are more suitable as electrode in UV surface-barrier devices than ITO films. In order to decrease the optical losses in the UV region, the thickness of the FTO films used was less than 100 nm.

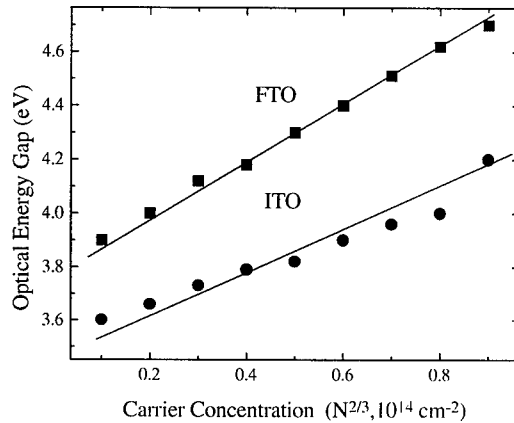


Fig. 4 -Optical energy gap vs. carrier concentration in ITO and FTO spray deposited films.

The rectification coefficient of the FTO/ZnS sensors at applied voltages of 1.5 is near  $10^5$ . The exponentially dependence of the dark current at a fixed small bias voltage on the temperature suggests the presence of a temperature activated carrier transport mechanism, such as multistep tunnelling through the potential barrier [12], similar to what is obtained in the ITO/ZnS photodiodes, as referred elsewhere [8]. At high forward bias, the Schotky model based on the thermoionic emission of carriers through the potential barrier is valid to explain the current-voltage characteristics. The level of the leakage current detected at reverse bias depends on the quality of the substrates used.

For devices working at zero bias voltage, the shunt resistance ( $R_{sh}$ ) which determines the noise equivalent power (NEP) was determined at  $\pm 10 \text{ mV}$  bias voltage. The values recorded for  $R_{sh}$  and NEP in the best detectors with an area of  $1 \text{ cm}^2$  are  $10^7 \Omega$  and  $10\text{-}12 \text{ W/Hz}^{1/2}$ , respectively.

Figure 5 shows the spectral response of the FTO-ZnO photodetectors as well as the one of a ITO/ZnS photodiode developed elsewhere [8], for comparison purpose. In contrast to ITO-ZnS, the maximum spectral sensitivity of detector produced in this work is shifted from 330 to 290 nm, due to the widen of the optical energy bandgap of the FTO layer, when compared to the ITO layer.

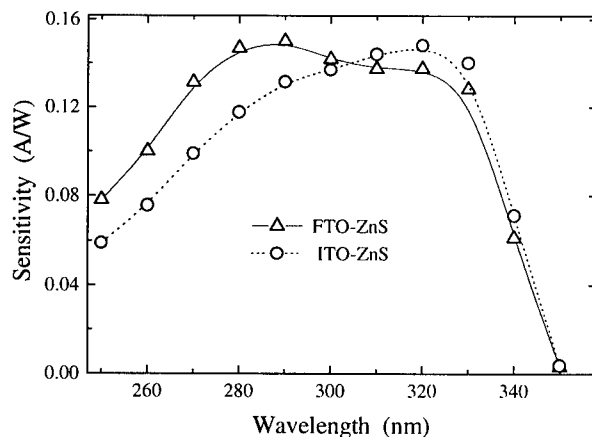


Fig. 5. -The spectral response of the FTO/ZnS and the ITO/ZnS optical sensors.

In Fig. 6 we present the dependence of the photocurrent on the light intensity used, for the detector developed. The data show a linear dependence in the range from  $10^{-8}$  to  $10^{-3}$  W.

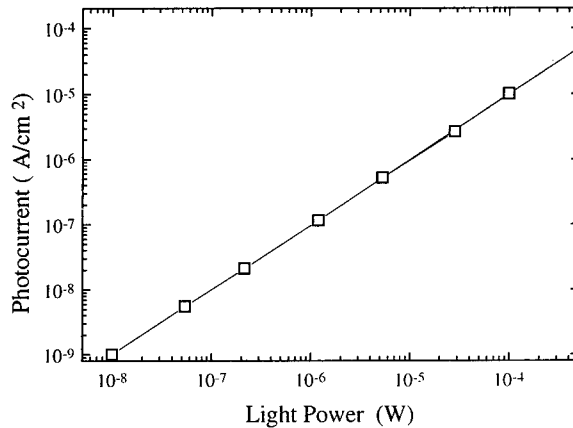


Fig. 6. -The dependence of photocurrent on light power for FTO/ZnS sensors.

Taking now into account the value of the measured refractive coefficient and the transmittance of the FTO electrode (Fig. 4), we estimate an internal quantum efficiency of about 100%, in the UV range for FTO-ZnS sensors. Hence, the recombination losses of the photogenerated carriers in the depletion region are negligible. For an ideal solar blind photodetector the value of the photocurrent under solar illumination is zero. The utilisation coefficient ( $k_u$ ) of solar radiation serves as the figure of merit to compare different solar blind photodetectors [8]. This coefficient can be determined for a detector with a known spectral sensitivity ( $S_\lambda$ ) as being the ratio between the device's effective radiation flow ( $\Phi_{eff}$ ) and the full solar radiation flow ( $\Phi$ ), according to equation (1):

$$k_u = \frac{\Phi_{eff}}{\Phi} = \frac{\int_0^\infty E_\lambda S_\lambda d\lambda}{\int_0^\infty E_\lambda d\lambda}, \quad (1)$$

where  $E_\lambda$  is the spectral distribution of the solar irradiation. Using as  $E_\lambda$  the solar spectrum in AM1 conditions [13] and the measured  $S_\lambda$  data (Fig. 5), the calculated value of  $k_u$  was estimated as 0.1%.

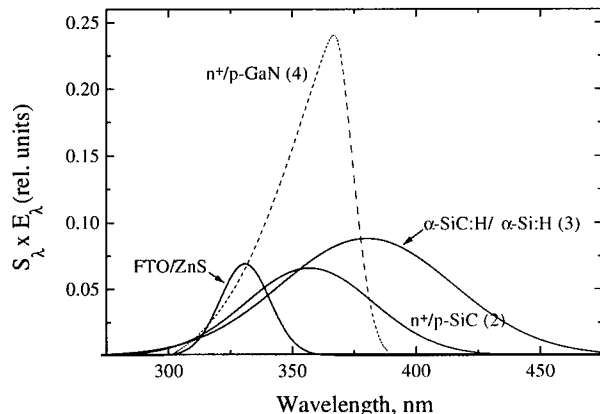


Fig. 7 -The calculated spectral values of the ( $E_\lambda \times S_\lambda$ ) in formula (1) for FTO/ZnS (a), SiC (b) [2],  $\alpha$ -SiC:H/ $\alpha$ -Si:H (c) [3], and GaN (d) [4] UV photodetectors.

In Figure 7 we compare the spectral values of the in formula (1) calculated for the detector developed in this work with the values recorded in SiC [2,3] and GaN [4] photodetectors. As the integral of the  $(E_\lambda \times S_\lambda)$  product in formula (1) directly determines  $k_{in}$ , we conclude that the photodetectors developed in this work are more suitable for UV measurements with solar background than the ones based on the conventional SiC or GaN photodetectors.

### Conclusions

A new type of UV enhanced optical sensor with a high UV quantum efficiency, linearity within a broad range of light intensity and insensitivity to direct solar radiation in terrestrial conditions has been fabricated and tested. Such detectors are of great interest for aerospace, medical, biological, spectroscopic, astronomy and radiometric measurement applications, since present a sensitivity to the UV light higher than the available devices.

### Acknowledgements

We are grateful to Dr. V. Machnii for ZnS monocrystalline substrates. Dr. Alexander Malik would like to thank NATO Scientific Programme and JNICT for the possibility to finish these investigations in Portugal.

### References

1. C.L. Joseph, *Proceedings of SPIE*, **2999**, 244 (1997).
2. D.M. Brown, E.T. Downey, M. Ghezzi, J.W. Kretchmer, R.J. Saia, Y.S. Liu, J.A. Edmond, G. Gati, J.M. Pimbley, and W.E. Schneider, *IEEE Trans. Electron. Devices*, **40**, 32 (1993).
3. D. Caputo, G. de Cezare, F. Irrera, and F. Palma, *IEEE Trans. Electron Devices*, **43**, 1351 (1966).
4. M.A. Khan, J.N. Kuznia, D.T. Olson, M. Blasingame, and A.R. Bhattarai, *Appl. Phys. Lett.* **63**, 2455 (1993).
5. M. Razeghi, A. Rogalski, AlGaIn ultraviolet detectors, *Proceedings of SPIE*, **2999**, 275 (1997).
6. J.R. Richardson, R.D. Baertsch, *Sol. St. Electron.*, **12**, 393 (1969).
7. A.I. Malik, and G.G. Grushka, *Sov. Phys. Semicond.*, **25**, 1017 (1991).
8. V. Machnii, A.I. Malik, and N. Melnik, *Sov. J. Techn. Physics (in Russian)*, **60**, 146 (1990).
9. E. Snanthi, A. Banerjee, V. Dutta, and K.L. Chopra, *J. Appl. Phys.*, **53**, 1615 (1982).
10. A.I. Malik, PhD Thesis, Chernovtsy University, Chernovtsy, USSR (1980).
11. S.M. Sze in "Physics of Semiconductor Devices" (Singapore: J. Wiley & Sons) pp. 279-293 (1981).
12. S.S. Fonash, in "Solar Cell Device Physics" ed. J. Denton (London: Academic Press ) p.118 (1981).
13. M.M. Koltun, in "Solar Cells" (Moscow: Nauka) p.185 (1987) (in Russian).

## LATTICE RELAXATION OF In DONORS IN CdF<sub>2</sub>

A. Suchocki, J. Rauluszkiewicz, J. M. Langer, B. Koziarska-Glinka,  
Institute of Physics, Polish Academy of Sciences, Al. Lotników 32/46, 02-666 Warsaw, Poland

**Keywords:** bistable donors, CdF<sub>2</sub>:In, photostriction, large lattice relaxation

**Abstract.** Contraction of CdF<sub>2</sub> crystals during phototransformation of In bistable centres has been measured with use of scanning tunnelling microscope. The observed change of the lattice constant ( $-1.8 \times 10^{-6}$ ) is metastable at liquid helium temperature. This result confirms that the large lattice relaxation is responsible for the metastability of In dopant in CdF<sub>2</sub>.

### Introduction

Defects related rearrangement of the crystal lattice has been seen in various physical processes. Many theoretical and experimental methods of studying these phenomena were developed. The process of lattice rearrangement is a very complicated issue, since it involves many ions, sometimes located quite far away from the defect itself. Additionally, it can be influenced by the other phenomena. Good example is photogeneration of band carriers during ionisation of defects. Their presence affects the lattice dynamics, and thus influences such macroscopic parameter as the lattice constant. Macroscopic changes of the crystal dimension cannot be universally predicted for a given defect process. Sometimes it is even difficult to predict sign of the lattice dilatation [1].

Lattice distortion is especially important for metastable defects in semiconductors. It has been already well established that the large lattice relaxation (LLR) is a major mechanism responsible for defect metastability in these materials [2,3]. In more covalent hosts ( $A_{III}-B_V$  and very likely  $A_{II}-B_{VI}$  semiconductors) relaxation is due to a change of the atomic site (interstitial - substitutional transition). This mechanism leads to the formation of the DX states and there exists ample amount of data testifying its validity [3]. In case of more ionic hosts one should consider a simpler lattice distortion, which leaves the symmetry of the point defect unaffected, namely a symmetric collapse (or expansion) of the lattice around defect during its phototransformation [2,4]. The expected lattice relaxation for the breathing mode is fairly close to the difference ionic radii of the impurity in the two charge states. The total relaxation energy is large and is well above 1 eV.

Experimental studies of the lattice distortion upon phototransformation of defects have been carried out using different techniques. Photoionization cross sections of the non-relaxed states are broadened by the strong impurity - lattice coupling. Changes of absorption spectra under the influence of hydrostatic or uniaxial pressure can reveal details of the defect phototransformation processes, such as the changes of local symmetry. Additional information can often be obtained with help of the electron paramagnetic resonance. EXAFS studies reveal changes in local bonds around the defect. Recently, the Mossbauer effect and positron annihilation was also applied in the studies of metastable defect phototransformation. Macroscopic changes of the lattice constant have been studied mostly by X-ray diffraction techniques. All above-mentioned techniques have different sensitivities. Sensitivity of X-ray diffractometers can be as high as  $10^{-6}$ , sensitivity of capacitance dilatometer can reach even  $10^{-8}$ . However, in practice these values are not attained. Additionally, these techniques suffer from severe drawbacks. For example, X-rays may transform metastable centres also interpretation of results of positron annihilation or EXAFS is not so straightforward. This communication is aimed to presentation of a novel approach to measure global changes in crystals with bistable defects. It is the use of the scanning tunnelling microscope (STM) as a precise dilatometer. Process of the lattice relaxation is studied in bulk CdF<sub>2</sub> crystals doped with In bistable donors.

Indium dopants in CdF<sub>2</sub> crystals are well-characterised bistable centres in semiconductors. Its bistable properties have been studied since the end of seventies (see Ref.2 for review of the past

results). The renewed interest in this material is driven by the possible application in holographic recording [5]. At low temperatures (below 80 K), illumination transforms all deep localised In donors into hydrogenic states with a Bohr radius of about 0.7 nm. It has been well established that large broadening of the photoionization spectra of deep localised state comes from the strong impurity-lattice coupling. In the original model of bistability [2,6] it has been suggested that the non-relaxed state is a neutral  $\text{In}^{2+}$  localised state and the charged  $\text{In}^{3+}$  forms the relaxed metastable state with electron bound to it at hydrogenic orbit. Strong Coulomb attraction between the central  $\text{In}^{3+}$  and eight surrounding fluorine F<sup>-</sup> ions in the metastable state causes symmetric lattice contraction. Although various experiments support a general validity of the model and the role of lattice relaxation in the defect bistability, the lattice relaxation itself has not been detected directly yet.

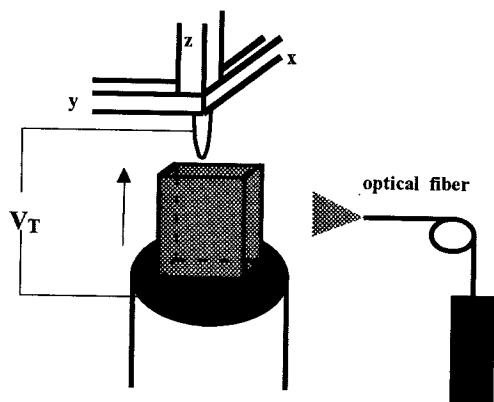


Figure 1. STM in dilatometer mode

necessary for proper operation of STM. The device was immersed in liquid helium for measurements at 4.2 K temperature. The samples were cooled in darkness and afterwards illuminated uniformly through an optical fibre by the light from the argon-ion laser (multiline: mainly 488 nm and 514.5 nm, coinciding with the absorption of deep donor state). The vertical movements of the sample surface, induced by the illumination, scanned by the STM tip, were reflected in the voltage signal and recorded by a computer. Piezodrives of our STM dilatometer were calibrated with known pattern. The scheme of the experimental set-up is shown in Fig.1.

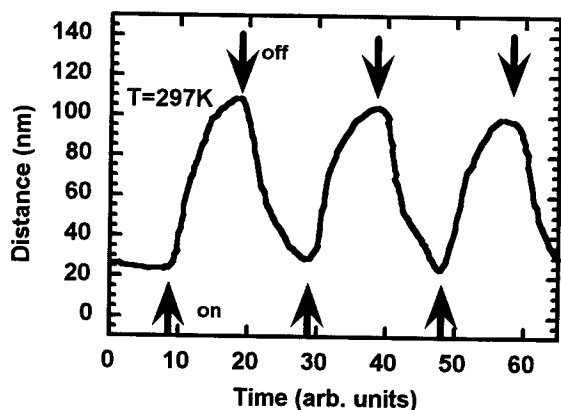


Figure 2. Dilatation of  $\text{CdF}_2:\text{In}$  crystal upon illumination by argon-ion laser at room temperature. Arrows denote sequence of the illumination

### Experimental method and results

Traditional methods of measuring the dilatation as X-ray diffractometry, capacitance dilatometer and also stress sensors turned out to be inadequate for our measurements. The experimentally observed changes of crystal dimensions were smaller than the detection limit at low temperatures. Therefore a custom-made scanning tunnelling microscope (STM), capable of working at liquid helium was used as a dilatometer. The STM was working in a constant current regime with very minute lateral scanning, only about 0.2 nm, in order to assure proper operation of the device. Samples were partially covered by evaporated gold layer in order to assure good electrical conductivity

necessary for proper operation of STM. The device was immersed in liquid helium for measurements at 4.2 K temperature. The samples were cooled in darkness and afterwards illuminated uniformly through an optical fibre by the light from the argon-ion laser (multiline: mainly 488 nm and 514.5 nm, coinciding with the absorption of deep donor state). The vertical movements of the sample surface, induced by the illumination, scanned by the STM tip, were reflected in the voltage signal and recorded by a computer. Piezodrives of our STM dilatometer were calibrated with known pattern. The scheme of the experimental set-up is shown in Fig.1.

The  $\text{CdF}_2:\text{In}$  crystals used in our experiment were parallelepipeds with dimensions of  $5 \times 3 \times 2 \text{ mm}^3$ . They were not crystallographically oriented. Two samples have been studied: one having small concentration of In donors (below  $10^{17} \text{ cm}^{-3}$ ) and the second one with much higher concentration of shallow donors. The problem of determining exact concentration of shallow donors in the  $\text{CdF}_2$  crystal is not a simple task. Concentration of shallow donors was estimated from the Hall effect measurement and the strength of the

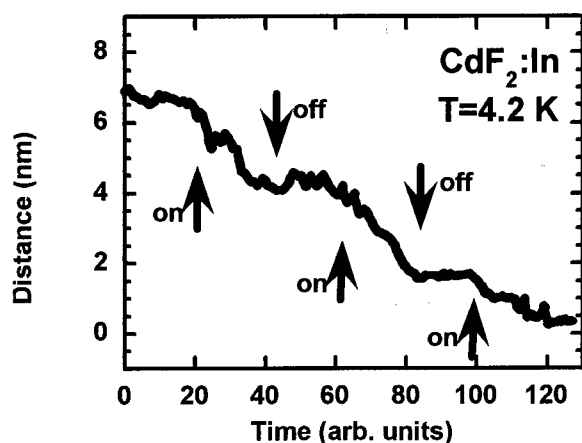


Figure 3. Contraction of the  $\text{CdF}_2:\text{In}$  crystal upon illumination by argon-ion laser light at 4.2 K, measured by STM

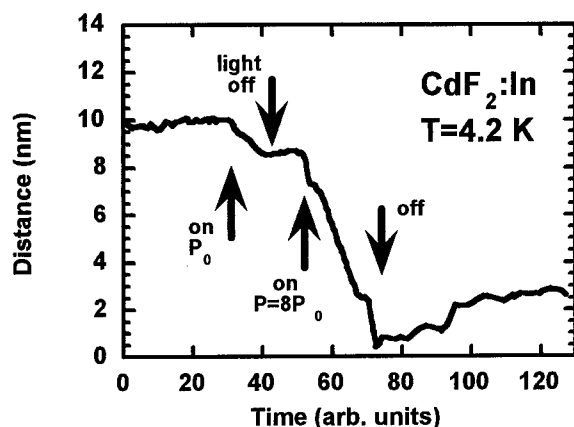


Figure 4. Photostriction of the  $\text{CdF}_2:\text{In}$  crystal upon illumination by light of different intensity

performed in liquid helium. Now the crystals contract when illuminated by light, as expected. Moreover, when laser is switched off, the crystal size remains unchanged, which is a direct proof of metastability of the effect. This is illustrated in Fig. 3. Figure 4 shows that the effect depends on the accumulated photon dose. The crystal was first illuminated with small light intensity and it contracted by about 1.5 nm. The process of contraction was much faster and larger when the 8 times stronger illumination was used. Finally this strong illumination saturated the effect. Maximum changes of the crystal length upon prolonged illumination did not exceed 9 nm which corresponds to the linear dilatation of  $-1.8 \times 10^{-6}$ .

Measurements of the second sample with smaller concentration of bistable donors reveals much weaker effect. Total contraction of this crystal was about 1 nm, which is close to the resolution of our system.

shallow donor photoionization spectrum. Unfortunately, both of these techniques are not very reliable for  $\text{CdF}_2$  crystals, although they give results consistent with each other and equal  $8 \times 10^{18} \text{ cm}^{-3}$ . Relatively small mobility of free carriers in the material (below  $10 \text{ cm}^2/\text{Vs}$  at room temperature) allows us only to estimate the carrier absolute concentration with poor accuracy. The scaling of absorption was done in the past for much smaller concentration of shallow donors [6]. Therefore we believed that much more accurate results are obtained from magnetisation measurements [7]. Concentration of shallow donors in the more concentrated sample, estimated from this measurement equals  $2.3 \times 10^{18} \text{ cm}^{-3}$ . We use this value in further analysis.

Figure 2 shows the results of experiment performed at room temperature. Crystal expands upon illumination by the laser beam and restores former length rapidly after the illumination is turned off with no metastability or hysteresis. The effect is due just to thermal heating of the crystal by intense laser beam. From the value of the thermal expansion coefficient, we estimate that the observed crystal expansion is caused by the increase of the crystal temperature by about 1 K.

Dramatically different behaviour is observed when the experiment is

### Discussion

The effective local relaxation  $\Delta a/a_0$  can be estimated from the macroscopic changes of the crystal by using the formula:

$$(\Delta l/l)_{size} = (\Delta a/a_0)(N_{In}^*/N_{cation}), \quad (1)$$

where  $(N_{In}^*/N_{cation})$  is the ratio of concentration of ionised centres to the total concentration of cations. Substitution of the measured global contraction of  $\Delta l/l = -1.8 \times 10^{-6}$  and the shallow donor concentration of  $N_{In}^* = 2.3 \times 10^{18} \text{ cm}^{-3}$  yields the effective local lattice relaxation around ionised In ions of about 2.3% only. This value is about 3 times smaller than obtained either from early empirical estimation of Langer et al. [2,8] or from recent calculations made by Cai and Song [9]. According to their results, the symmetric lattice relaxation around the In is equal to 7.9 %.

Situation is even worse, since the recent results indicate that In is, in fact, a negative-U system [7,10]. Since there are 2 electrons in the ground state, the effective local lattice relaxation equals 4.6%. Relaxation based upon the known difference in ionic radii between  $\text{In}^+$  and  $\text{In}^{3+}$  would be about 20%, therefore a symmetric relaxation in this case is most unlikely.

Proper description of the bulk crystal relaxation must however include an opposite contribution coming from the local weakening of local bonds after photopopulation of the hydrogen-like In metastable states. The effect is roughly the same as the lattice expansion by the presence of the free carriers [11-14]. For n-type of semiconductors the effects is described by the formula:

$$(\Delta l/l)_{el} = (-D_n/3B) n, \quad (2)$$

where  $D_n$  is the deformation potential,  $B$  is the bulk modulus and  $n$  is the concentration of electrons. In our case  $n$  should be replaced by the concentration of shallow donors, as the concentration of free electrons in  $\text{CdF}_2$  at low temperatures is negligible. It is safe to assume that the deformation potential of the shallow donor level in  $\text{CdF}_2$  is the same as the deformation potential of the  $\Gamma$  - type conduction band minimum. Unfortunately, we are not aware of any accurate estimation of the deformation potential of the bottom of the conduction band in  $\text{CdF}_2$ . It is actually very complicated problem both theoretically and experimentally [15], and very often we have only rough estimation of its value. Therefore we decided to estimate the deformation potential for  $\text{CdF}_2$  from our data of lattice dilatation, assuming that total dilatation of the crystal  $(\Delta l/l)_{tot}$  is a sum of size  $(\Delta l/l)_{size}$  and electronic  $(\Delta l/l)_{el}$  effects.

$$(\Delta l/l)_{tot} = (\Delta l/l)_{size} + (\Delta l/l)_{el} \quad (3)$$

The first term has been estimated from Eq. (1) and substituting  $\Delta a/a_0$  either from the Cai and Song theory for  $U > 0$  or from the difference in ionic radii for the  $U < 0$  model. Substituting the known values of the elastic constants of  $\text{CdF}_2$  [16], we get for the value of deformation potential of the shallow donor level in  $\text{CdF}_2$  values of  $D_n^{U>0} = -4.6 \text{ eV}$  and of  $D_n^{U<0} = -10 \text{ eV}$ , depending on the adopted model of deep-shallow donor phototransformation, classical ( $\text{In}^{2+} \Rightarrow \text{In}^{3+} + e$ ) or negative U ( $\text{In}^{1+} + \text{In}^{3+} \Rightarrow 2(\text{In}^{2+} + e)$ ), respectively. These values may be taken as some guideline, as a more accurate procedure must take into account the extended character of the local lattice dilatation (not only the nearest neighbour movement, especially when the defect becomes charged [17], as it is in the case there). For the negative U case, a more realistic model of relaxation is needed.

### Acknowledgements

This work was supported in part by the contract no 8 T11B 017 09 from the Polish State Research Committee. We would like to acknowledge comments by J. Adamowski, M. Baj, K. S. Song and A.M. Stoneham on the problem.



---

References

1. A. M. Stoneham, J. Phys. C.: Solid State Phys. **16**, L925 (1983).
2. J. M. Langer in *Lecture Notes in Physics* (Springer, New York), **122**, 123 (1980); J. Phys. Soc. Jpn. Suppl. **49A**, 207 (1980); Radiat. Effects **72**, 55 (1983).
3. P. Mooney, J. Appl. Phys. **67**, R1 (1990).
4. A. M. Stoneham, *Theory of Defects in Solids* (Clarendon Press, Oxford, 1975);
5. A.L. Ryskin, A. S. Scheulin, B. Koziarska, J. M. Langer, A. Suchocki, I.I. Buczinskaya, P.P.Fedorov and B. P. Sobolev, Appl. Phys. Lett. **67**, 31 (1995); A. Suchocki, B. Koziarska, J. M. Langer, T. Langer, Appl. Phys. Lett **70**, 2934 (1997).
6. U. Piekara, J. M. Langer and B. Krukowska-Fulde, Solid State Commun. **23**, 583 (1977); J. E. Dmochowski, J. M. Langer, Z. Kalinski, and W. Jantsch, Phys. Rev. Lett., **56**, 1735 (1986)
7. J.M. Langer, A. Suchocki, R. Szymczak, M. Baran, this volume
8. J.M. Langer, U. Ogonowska and B. Iller, in *Proc. 14th Inst Conf. Semicond*, Inst. Phys. Conf. Ser. **43**, 277 (1979).
9. Y. Cai and K.S.Song, J. Phys.: Condens. Matter **7**, 2275 (1995)
10. A.S. Scheulin, A.I. Ryskin, K.Swiatek and J.M. Langer, Phys. Lett. A **222**, 107 (1996); S.A. Kazanskii, A.I. Ryskin and V.V. Romanov, Appl. Phys. Lett. **70**, 1272 (1997).
11. M. Leszczynski, J. Bak-Misiuk, J. Domagala, J. Muszalski, M. Kaniewska and J. Marczewski, Appl. Phys. Lett. **67**, 539 (1995).
12. T. Figielski, phys. stat. sol. **1**, 306 (1961).
13. R. W. Keyes, Solid State Physics **20**, 37 (1967).
14. J. A. Van Vechten and J.C. Phillips, Phys. Rev. B **2**, 2160 (1970).
15. D.D. Nolte, W. Walukiewicz and E.E. Haller, Phys. Rev. Lett **59**, 501 (1987); M. Cardona and N.E. Christensen, Phys. Rev. B **35**, 6182 (1987).
16. *Crystals with the Fluorite Structure*, edited by W. Hayes, (Clarendon Press, Oxford 1974).
17. S. Bednarek, J. Adamowski, Proc. 22<sup>nd</sup> Int. Conf. Sermiconductors, Berlin (World, Scientific, Singapore, 1996)

## SHALLOW ELECTRON CENTRES IN $\text{CdF}_2\text{:M}^{3+}$ AND SILVER HALIDES

Chun-rong Fu and K.S. Song

Physics Dept., University of Ottawa, Ottawa Canada K1N 6N5

**Keywords:** excited electron centres,  $\text{CdF}_2\text{:M}^{3+}$ , silver halides

**Abstract.** Shallow electron centres are associated with interesting properties in  $\text{CdF}_2\text{:M}^{3+}$  ( $\text{M}=\text{Ga}, \text{In}$ ) and silver halides. The trivalent centres in  $\text{CdF}_2$  exhibit shallow-deep bistability and have potentials for optical data storage. The shallow electrons associated with certain impurities or interstitial silver in  $\text{AgBr}$  and  $\text{AgCl}$  are believed to play key roles in some of the photo-induced processes. We have studied these systems using a method developed earlier for excited electron centers in insulators. In  $\text{CdF}_2$  we found that the deep level (compact state) is separated from the shallow level (diffuse state) by a small potential barrier and the estimated changes of the optical refractive index between the deep and shallow states are in qualitative agreement with experiment. We also report on our preliminary work of the shallow electron centres in silver chloride. The topics considered are the electron state trapped at an interstitial silver, and the role of the excited electron in the diffusion of the interstitial silver toward the silver vacancy. Possible mechanisms for the recently observed anomalous heat generation in photo-excited silver halides are discussed.

### Introduction.

The study of the bistable defect system in semiconducting  $\text{CdF}_2$  crystals doped with In and Ga impurities has drawn considerable attention recently[1][2]. Most of the trivalent metals in  $\text{CdF}_2$  produce stable (or metastable) hydrogenic donor state. The dopants In and Ga have on the other hand shown unusual bistable behavior, i.e., the electrons can be trapped by the impurity either in a highly localized orbit or a delocalized one separated by a vibronic barrier. At low temperature (below 70K), a 200 meV barrier prevents the recovery to the ground state from the shallow hydrogenic state in  $\text{CdF}_2\text{:In}^{3+}$ . The photoionization of the two In states occurs in different spectral regions. At room temperature, two strongly asymmetric bands are seen[1]. The absorption band in the visible range ( $\lambda < 650\text{nm}$ ) is caused by the photoionization of the localized  $\text{In}^{2+}$  ground state, while the IR band, peaking at  $\lambda \approx 8\mu\text{m}$ , is due to the photoionization of hydrogenic, diffuse state of  $\text{In}^{3+}$ . The localized ground state is only 0.1 eV thermally deeper than the hydrogenic state, but it exhibits an enormous 2 eV Stokes shift. The shift is caused by a large lattice relaxation around the impurity during photoionization. The resulting lattice collapse in the diffuse state is responsible for the 0.2 eV vibronic barrier separating the two In states and hence, for the defect metastability. The absorption spectra of  $\text{CdF}_2\text{:Ga}$  has similar asymmetric bands peaked at 4 eV and 0.17 eV[2], respectively.

In silver halides, there are well-known shallow electron centers associated with  $\text{Cd}^{2+}$  and other divalent ions[3], or with interstitial silver ions[4]. As the clustering of interstitial silver ions in the formation of latent image is mediated by conduction electrons, the role of shallow electron

traps is very important. The defect or impurity-trapped electrons are generally considered to be in shallow state, often described by the effective mass approaches[3][4]. Recent work by Kondo et al[5] has shown that in silver chloride and bromide crystals, anomalous amount of heat is generated after a photo-excitation, and the effect lasts ten hours after the bandgap excitation has been terminated. They attributed it to the silver interstitial migration toward the cation vacancies assisted by excited electrons. In another word, the excited electron assists the recombination of Frenkel defect pairs in the cation sublattice with a high efficiency. In this report we present a brief account of our recent works on the two topics described above which are examples of atomic processes in solids induced by excited electrons. The method we used is the same as those developed earlier[6] in the studies of the self-trapped excitons in rare gas solids and ionic halides. A few electrons (usually the excited electron) are treated in the Hartree-Fock approximation and the lattice and polarisation are treated by respectively the classical pair potentials and point polarizable dipole approaches. In evaluating the electronic energies of the diffuse state, the contribution of a large number of ions (about 2000) is taken into account. A limited number of atoms, typically in the range of about 60 are explicitly relaxed to new equilibrium position one at a time by evaluating the gradient of the total energy of the system. Details of the method are given in[6][7]. The process is repeated until the total energy converged to the minimum within a predetermined threshold value. This is similar to the approach used in the recent molecular dynamics studies of excited ionic halide clusters[8].

## Results and discussion.

### Bistable systems $\text{CdF}_2:\text{M}^{3+}$ .

The results obtained by Cai and Song[7] for the trivalent atoms In and Ga, and by Fu and Song for Al[9] are shown in Fig.1. A simple configuration coordinate (c.c.) model is adopted in which the c.c. represents the distance between the trivalent atom and the first fluorine atom shell. As expected the theoretical calculations show a strongly relaxed lattice environment associated with the shallow level (diffuse electron wavefunction), and an almost undistorted lattice environment for the deep level (compact-state). There is clear evidence of bistable levels separated by a moderate potential barrier between the two states. The results for In and Ga are in reasonable agreement with the experimental data of reference[1]. The absence of a deep level in Y and Sc centres was also predicted, and is in agreement with experimental observation. It is attributed to the short range intra-atomic potential difference of the two atoms compared with those of In and Ga[7].

It has been suggested that Al impurity may lead to a similar bistable behavior to that of Ga and In. In this case the deep atomic core contains only 1s electrons, and the radius of the  $\text{Al}^{3+}$  is much smaller than those of the other trivalent metals. Therefore, the short-range interaction between  $\text{Al}^{3+}$  and  $\text{F}^-$  is expected to be much weaker. Our calculation found that Al behaves very differently from In and Ga mainly due to its small size of the atomic core[9]. As a result, the compact state is found at a higher energy than the diffuse state in sharp contrast to the situation found in In and Ga.

Recently, Ryskin et al[10] and Koziarska et al[11] reported on a successful holographic recording based on the bistable defect centers in  $\text{CdF}_2$ . They reported that a saturation value of about  $-1.3 \times 10^{-4}$  was achieved in the refractive index change in the  $\text{CdF}_2:\text{In}$  at about 120K, while the maximum of the diffraction efficiency occurs at about 280K for Ga. Therefore,  $\text{CdF}_2:\text{Ga}$

crystals are apparently suitable for room temperature recording. This trend toward higher operating temperature has led to the anticipated interest in the Al-doped cadmium fluoride.

We evaluated the optical parameters connecting the ground states to the p-like excited states, and estimated the refractive index changes. The calculated oscillator strengths and the refractive index changes are presented in Table 1. Generally speaking, theoretical determination of the ionization limit is more complex. We therefore considered the first p-like excited state. The transition energies are compared with the experimental values of the ionization energies in Table 1. A two-oscillator model has been employed to estimate the maximum change of the refractive index as has been proposed in Ref.[10]. The calculated results for the oscillator strengths and the refractive index changes  $\delta n$  are in reasonable agreement with the experiment. The oscillator strengths for the IR are larger than one for Ga and Al when theoretical transition energies are used. This is due to our calculated transition energies being too large by comparison with the experimental values. The optical process taking place in holographic recording is briefly as follows: At temperature low enough that the defects are at their stable state (e.g. the deep compact state for  $\text{CdF}_2:\text{In}$ , Ga) the ionization with about 3 eV photons takes the electrons successively to the compact ionized state, then to the diffuse ionized state via non-radiative transitions and finally to the metastable shallow donor state. This cycle induces the refractive index change which we have evaluated. Below about 100K and 260K respectively for  $\text{In}^{3+}$  and  $\text{Ga}^{3+}$  centers, the metastable shallow state can be preserved, thereby storing the optical data.

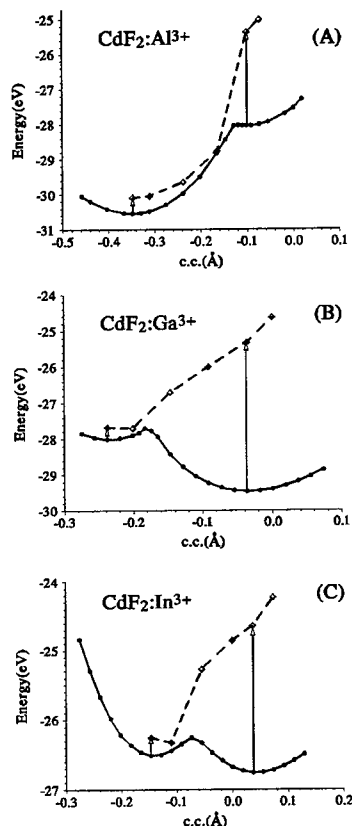


Figure 1. The APES of  $\text{CdF}_2:\text{Al}^{3+}, \text{Ga}^{3+}, \text{In}^{3+}$ . Solid lines denote the ground states; Dashed lines for excited p-like states.

Table 1 Characteristic data of transition energies,  $f_{IR}$ ,  $f_{vis}$ , and  $-\Delta n$

	$\Delta E_{diffuse}$ (eV)		$\Delta E_{compact}$ (eV)		$f_{IR}$		$f_{vis}$		$-\Delta n$	
	theor.	exp.	theor.	exp.	theor.	based on exp*.	theor.	based on exp*.	theor.	based on exp*.
In	0.26	0.14	2.11	1.90	0.65	0.35	0.43	0.38	$0.70 \times 10^{-4}$	$0.46 \times 10^{-4}$
Ga	0.34	<0.17	4.14	3.00	1.36	0.75	0.19	0.14	$1.10 \times 10^{-4}$	$0.60 \times 10^{-4}$
Al	0.45	—	2.45	—	1.27	0.40	0.28	0.20	$1.10 \times 10^{-4}$	$0.40 \times 10^{-4}$

\* This indicates that the evaluated numbers are obtained using the experimental values of optical transition energies.

#### Shallow electron states in silver halides.

The recent observation[5] according to which crystals of AgCl and AgBr photoexcited at low

temperature generate an anomalously large amount of heat is the subject of this second part. According to Kondo et al, between ten and hundred times more energy is released than the energy absorbed. Also, this process continues for more than ten hours after the band to band excitation has been turned off. They attributed this to the repeated non-radiative recombination of the interstitial-vacancy pairs in the silver halide crystals which is mediated by the excited electron until the electron is annihilated eventually. We have made some preliminary studies. The method used is the same as in the bistable defects presented above. The pair interatomic potential used is that reported in [12]. Because of the importance of the polarisation energy in the determination of the relaxed system in silver halides, we scaled the polarisation energy by a constant factor (0.65) so that the calculated Frenkel pair formation energy agreed with experimental data (1.2 eV[12]). The number of atoms which are allowed to relax explicitly is 82 in results reported here. The number of atoms which interact directly with the excited electron through various short range terms and those atoms which contribute to the polarization energy are respectively taken to be 2301 and 1000. The large number of ions used in evaluating the electronic energy reflects the diffuse character of the electron.

We considered the diffusion of interstitial silver ion in the absence and in the presence of an excited electron. In the following are given the results obtained for AgCl. We found a relatively monotonous change in the system total energy as a function of the vacancy-interstitial separation, as shown in Table 2. There is, however, a potential barrier between the adjacent sites. We found that the activation energy for the interstitial diffusion via the *interstitial mechanism* is clearly larger than that via the *interstitialcy mechanism*. In an *interstitialcy mechanism* there are collinear and non-collinear diffusion paths. Our calculation showed that the non-collinear path offers smaller potential barrier than a collinear one. In the non-collinear case, the diffusion from the fourth to the third nearest neighbour site is found to be about 0.6 eV, compared to about 0.9 eV in the case of the collinear diffusion. Experimentally, the activation energy of interstitial silver diffusion is 0.01-0.04 eV[13]. This shows that our evaluation is one order of magnitude or more too large. This problem has been discussed earlier in Ref.[14], in which the importance of an elliptical deformation of  $(Ag^+)_i$  has been noted.

**Table 2 Frenkel pair energy as a function of vacancy-interstitial separation ( $X_{vi}$  in units of the shortest anion-cation distance)**

$X_{vi}$	0.5	1.5	2.5	3.5	4.5	5.5	6.5	7.5	infinite
$\Delta E(\text{eV})$	.692	.476	.483	.534	.605	.677	.757	.825	1.2

At this stage it is not our aim to get numerically acceptable activation energies of this magnitude, but to understand the role of the excited electron. To this end a pair of gaussians with  $\alpha=0.01$  (in atomic units) is placed on the pair of silver atoms which is either the old or the new interstitial atoms. When the silver interstitial is accompanied by an excited electron the activation energy for the non-collinear diffusion is found to drop to about 0.3 eV, which is quite a large change from the value obtained without electron. On comparing the various energy terms as well as the atomic displacements at the barrier peak obtained with and without the excited electron, it was found that a substantially larger outward distortion of the nearby anions is obtained when the electron is present, and results in a lower activation energy.

We now consider the final step of interstitial atom-vacancy recombination after the pair is brought within the same cell. Our preliminary results are as follows. There is virtually no

potential barrier on the path to recombination (only about 0.04 eV according to our calculation). For the same path a much larger barrier is encountered, about 0.6 eV, when an excited electron is centered on the diffusing silver ion from the midpoint of the unit cell to the vacancy. This seems to indicate that the last step of interstitial silver-vacancy recombination takes place without the accompanying electron. In other words, the electron which assisted in the diffusion of the interstitial silver upto this point abandons the silver ion and becomes free. It is also interesting to note from **Table 2** that an energy package of about 0.7 eV is released to the lattice when a silver interstitial travels to the second neighbor position from infinite separation. The electron wavefunction we used is more compact than that generally considered for the shallow centers, about 4.2 Å compared with 12 Å[3][4]. It is our impression that a truly shallow electron may have too extended wavefunction to interact efficiently with the diffusing silver atom. Finally, how the electron becomes available to start another cycle of silver interstitial transport is one of the most interesting subjects. It seems that the electron wavefunction should undergo a cyclic change as it is bound (deep level) and then freed (shallow or extended state) from a silver ion. Perhaps the electron undergoes repeated cycles between the two states as has been proposed by Kanzaki and Tadakuma[15] as a mechanism of latent image formation in silver halides. We may say that the excited electron is in a bistable system and converts back and forth between a shallow and a deep level, similar to what has been described for the impurity centers in cadmium fluoride above.

This work is still in its exploratory stage and we intend to investigate further. The seemingly poor agreement with experiment regarding the activation energy of the interstitial silver diffusion reflects not only the nature of the approximations we have used, but also on the extremely small activation energy involved. Our future work would include non-spherical deformation of the interstitial silver ion to lower the activation energy as has been proposed in Ref.[14]. In this work our principal interest was in understanding the role played by the excited electron in the process. In this regard the so-called split-interstitial[16] might be of interest. We found that two silver ions form a molecule in the presence of an excited electron (optimized  $\alpha=0.02$ ) at a bondlength of about 2.4 Å. Such species could diffuse through a sequence of bond switching process in the lattice in a manner similar to that of the self-trapped hole, or a  $V_k$  center, in alkali halide crystals. It is hoped that understanding these steps may contribute in clarifying the broader photographic processes.

## References.

1. U. Piekara, J.M. Langer and B. Krukowska-Fulde, Solid State Commun. 23, 583 (1977) ; J.E. Dmochowski, J.M. Langer, Z. Kalinski and W. Jantsch, Phys. Rev. Lett.**56**, 1735 (1986)
2. J.E. Dmochowski, W. Jantsch, D. Dobosz and J.M. Langer, Acta. Phys. Polon. **73**, 247 (1988)
3. S. Sakuragi, H. Kanzaki, Phys. Rev. Lett.**38**, 1302 (1977)
4. M.T. Bennebroek, O.G. Poluektov, A.J. Zakrewski, P.G. Baranov, J. Schmidt, Phys. Rev. Lett. **74**, 442 (1995)
5. Y. Kondo, I. Goto, N. Sakaida, Phys. Rev. **B55**, 9534 (1997)
6. K.S. Song and R.T. Williams, "Self-Trapped Excitons" 2nd ed. (Berlin: Springer, 1996)
7. Yang Cai and K.S. Song, J.Phys.:Condens.Matter **7**, 2275 (1995)

8. G. Rajagopal, R.N. Barnett, U. Landman, *Phys. Rev. Lett.* **67**, 727 (1991)
9. Chun-Rong Fu, K.S. Song, *J. Phys.-Condens. Matter* **9**, 3575 (1997)
10. A. L. Ryskin, A.S. Shcheulin, B. Koziarska, J.M. Langer, A. Suchocki, I.I. Buczinskaya, P.P. Fedorov and B.P. Sobolev, *Appl. Phys. Lett.* **67**, 31 (1995)
11. B. Koziarska, J.M. Langer, A.I. Ryskin, A.S. Shcheulin, A. Suchocki, *Acta. Phys. Polon.* **88**, 1010 (1995)
12. C. R. A. Catlow, J. Corish, P. W. M. Jacobs, *J. Phys.* **C12**, 3433 (1979)
13. R. Friauf, "The Physics of Latent Image Formation in Silver Halides" (Singapore: World Scientific, 1984)
14. P. W. M. Jacobs, J. Corish, C. R. A. Catlow, *J. Phys.* **C13**, 1977 (1980)
15. H. Kanzaki, Y. Tadakuma, *J. Phys. Chem. Solids* **55**, 631 (1994)
16. R.C. Baetzold, R.S. Eachus, *J. Phys.-Condens. Matter* **7**, 3991 (1995)

## EPR INVESTIGATION OF METASTABLE DONOR STATES IN CdF<sub>2</sub>:In, Ga

Z. Wilamowski<sup>1,2</sup>, J. Dmochowski<sup>1</sup> and W. Jantsch<sup>2</sup>

<sup>1</sup>Institute of Physics of the PAS, Al. Lotnikow 32/46, PL 02-668 Warsaw, POLAND

<sup>2</sup>Institut für Halbleiterphysik, Johannes Kepler Universität, A-4040 Linz, AUSTRIA

**Key words:** Donor - metastability, negative-U, sp-d coupling, spin relaxation

**Abstract.** We present results of photo-EPR on CdF<sub>2</sub> doped intentionally by either Y, Ga or In, but containing also unintentionally incorporated Mn. We observe the resonances of both the shallow donors and that of Mn. The shallow donor signal of Ga or In are metastably enhanced below a characteristic temperature after illumination ( $h\nu > 2\text{eV}$ ) but no deep donor resonance is observed in agreement with the negative-U model. The Mn spectra are strongly affected by the excitation of the metastable donor state: those lines which coincide with the shallow donor resonance are strongly enhanced by desaturation: their spin-lattice relaxation time is reduced by a resonant cross-relaxation mechanism. We explain the peculiar saturation curves quantitatively assuming s-d coupling of the Mn and the shallow donor states.

### Introduction.

The large gap semiconductor CdF<sub>2</sub> ( $>8\text{ eV}$ ) received considerable attention in the past because of the metastable character of some donors in this material [1-5]. Both In and Ga were shown to act as shallow donors below some metastability temperature,  $T_M$ , after illumination ( $h\nu > 2\text{eV}$ ), whereas Y acts allways as a shallow donor under normal conditions [1,2]. After cooling in darkness, however, In and Ga behave rather like deep donors with much higher activation energy: there is strong freeze-out of the carrier concentration. After their conversion by light they remain shallow until the sample is heated above  $T_M$ . Apart from this persistent photo-conductivity such samples exhibit also other persistent effects like an illumination induced infrared absorption which is accompanied by a bleaching of the excitation band centered at 3 eV [5]. Obviously, there are two different states of these donors, and a barrier in between. The observed huge Frank-Condon shift shows that this barrier separates two strongly different equilibrium positions in the host lattice. There is a „strong lattice relaxation“ accompanying the transition from the shallow to the deep state.

All effects observed are very similar to those seen for n-type Al<sub>x</sub>Ga<sub>1-x</sub>As with  $x > 0.14$  doped with group IV or VI elements. There it was shown first theoretically [6] and then also by experiment [7,8] that the ground state of the donor, for historical reasons called DX center, is a two-electron state. The effective Hubbard correlation energy,  $U$ , is therefore negative: the donor can lower its energy by breaking one bond, thus moving towards an interstitial site and by binding an extra electron [6].

The renewed interest in these effects in CdF<sub>2</sub> results from their applicability for optical memories as pointed out by Ryskin *et al.* [3]. In the case of Ga, the metastability barrier is effective nearly up to room temperature and therefore the metastable infrared absorption induced by short wavelength ( $h\nu > 2\text{eV}$ ) illumination can be used to store illumination patterns, *e.g.*, in 3D holograms. The underlying principles of the donor metastability are not as well established, however, as in the case of the III-V compounds.

More recently, the magnetic susceptibility of CdF<sub>2</sub>:Mn, Ga was investigated and strong support was found for a diamagnetic ground state of the Ga donor in agreement with the negative  $U$



model [4]. The magnetic susceptibility is an integral quantity, however, it detects all contributions due to any paramagnetic ions in addition to the diamagnetic background. Moreover, the presence of Mn impurities with a large spin,  $S=5/2$ , and a possible coupling between the two spin subsystems may impair the conclusion about the diamagnetic ground state. Therefore, in this paper we use electron paramagnetic resonance (EPR) which allows to separate the different contributions to the magnetic susceptibility and to study coupling between both subsystems. In agreement with the susceptibility investigations we do not observe any trace of a paramagnetic deep donor state. After photoexcitation to the metastable state, we observe the resonance of the shallow donor and another effect connected with it: those parts of the saturated Mn resonance spectrum are strongly enhanced which coincide with the shallow donor resonance, even under conditions when the latter is practically invisible. We explain this effect by cross relaxation: the spin lattice relaxation time of Mn is shortened for those transitions which are in resonance with the shallow donor Zeeman splitting. Therefore these transitions are “desaturated” and the resonance becomes stronger again. Finally, we present a quantitative model for this effect considering the s-d exchange coupling between shallow donors and the Mn.

### Experimental.

Bridgman grown samples of  $\text{CdF}_2$  were doped with Y, Ga or In during growth with resulting donor concentrations in the range of  $0.2..3 \cdot 10^{18} \text{ cm}^{-3}$ . The concentration of residual Mn varies in the range of  $1..5 \cdot 10^{18} \text{ cm}^{-3}$  as estimated from the EPR amplitude. To achieve conductivity, the donors were activated according to well known thermal treatment in Cd vapour [1].

The EPR measurements are performed with the help of a standard Bruker X-band spectrometer with an available maximum microwave power of 200 mW. In all samples we observe at least at temperatures close to 300 K a single line with a g-factor close to 2 in addition to the well resolved fine, hyperfine (HF) and superhyperfine (SHF) structures of the Mn spectrum. We identify the single line as that of the shallow donor on behalf of the observed motional narrowing of its linewidth: with increasing temperature above 140 K, the linewidth decreases. The narrowing shows activated behaviour and its activation energy is close to the shallow donor energy [1]. This behaviour can be explained by hopping of the effective mass electrons between different donor sites [9]. This effect is easy to observe for the Y donor which does not show a deep state, in contrast to Ga or In doped samples where capturing of electrons on the deep ground state reduces the number of shallow donors and thus their EPR signal is weak.

**Tab.1: g-factors of donors in  $\text{CdF}_2$**

Donor:	g-factor	Metastability Temp. $T_M$ [K]
Y	$1.956 \pm 0.002$	-
Ga	$1.952 \pm 0.005$	270
In	$1.967 \pm 0.005$	70

There is no other signal observed which could be attributed to the deep state of the donors before photoexcitation. Assuming a paramagnetic deep state this fact is not understandable since deep states have a narrower line width than shallow, more delocalized states (without motional

narrowing). Moreover, the relaxation rates and the resonance linewidth in large gap materials with pure *s*-bands are generally low. Therefore the sensitivity for these states should be higher than for shallow states at low temperature, since the concentration of the deep states before illumination is the same as that of the shallow ones after complete excitation. Since the latter are clearly detected here, we conclude that the donor ground state is diamagnetic and we have the same situation as for DX centers in III-V - and II-VI - compounds, namely a spontaneous disproportionation of charge within the donor system: half of the donors are empty (*i.e.*, positively charged) and the other half is negatively charged (neglecting compensation just for simplifying the discussion), and both are diamagnetic.

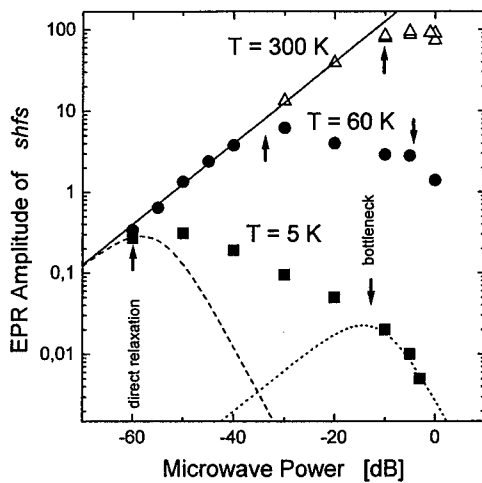


Fig.1: EPR amplitude of one super-hyperfine line of Mn as a function of microwave power at 5 K (squares), 60 K (circles) and 300 K (triangles).

Fig.2 shows the temperature dependence of the amplitude of one of the hyperfine lines of the Mn EPR with a resonance field corresponding to  $g=2$  measured at constant microwave power with and without illumination. The influence of illumination is dramatic at low temperatures: there the amplitude increases by two orders of magnitude and it remains constant after illumination for arbitrary long time until the sample is heated above  $T_M$ . This effect is less pronounced for small microwave power (s. Fig.3) demonstrating that it is caused by different saturation behaviour induced by light: obviously illumination causes a substantial shortening of the spin-lattice relaxation time for this particular transition. From the dependence of this effect on temperature and illumina-

The  $Mn^{2+}$  EPR spectrum dominates at low temperatures where the shallow donor spectrum is rather wide and the shallow donor resonance is not directly seen. The Mn spectrum is characterized by its strong tendency for saturation at low temperature. In Fig.1 the amplitude of one of the SHF lines due coupling to the 8 F - neighbours is given as a function of the microwave power,  $P$ , for 300 K, 60 K and 5 K. At room temperature, the amplitude shows the usual increase according to a  $P^{1/2}$  law and a maximum at higher microwave power. At low temperature, the maximum signal occurs already at very low microwave power. For higher  $P$ , the EPR signal decreases but at lower rate, which indicates an inhomogeneous broadening due to a distribution of spin-lattice relaxation times [10].

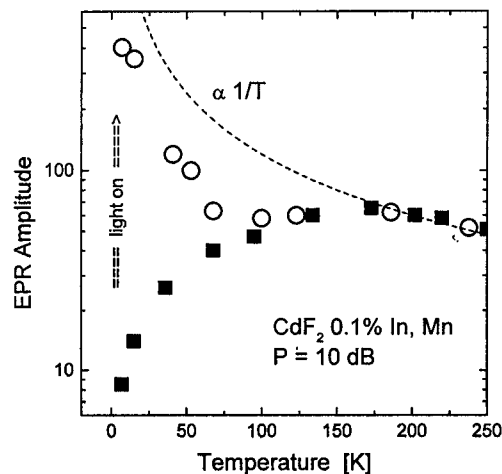


Fig.2: EPR amplitude of the  $I=3/2 \rightarrow -1/2$  HF transition of Mn as a function of temperature in darkness (squares) and during white light illumination (circles). Dashed line: unsaturated line.

tion it is evident that this shortening is caused by the persistent excitation of the donors to the metastable state.

The mechanism for the shortening becomes more clear by the fact, that the effect is much weaker for the outer HF lines of Mn. Actually the shortening of the spin-lattice relaxation time and the resulting desaturation due to the shallow donor state occurs strongest for those lines of Mn for which the EPR absorption of the shallow donor is strongest. This is illustrated in Fig.3 where we have plotted the normalized amplitudes of the 6 Mn HF line intensities vs. their resonance positions for different microwave power. The envelope curves are centered exactly at the shallow donor resonance.

This demonstrates that there is obviously a cross relaxation of magnetic moments between the Mn- and the shallow donor subsystem which is effective only for transitions with the same Zeeman splitting- a resonant energy transfer between the Mn and the shallow donor. For small microwave power the overall effect is much smaller since the Mn is not as strongly saturated and therefore the decrease in the spin lattice relaxation time has a smaller effect.

### Discussion.

It is natural to attribute the observed cross relaxation effect to the exchange interaction between the Mn 3d states and the s-like shallow donor states. The sign of the interaction cannot be evaluated from the EPR data but the recently observed increase in susceptibility at low fields and the early saturation of this effect demonstrate ferromagnetic interaction [4].

A modeling of the effect of cross relaxation is somewhat complicated by the effect of the random arrangement of donors and Mn ions in the crystal lattice. Since exchange interaction and thus the longitudinal relaxation rate of the Mn will depend on the number and the distances of donors in the neighbourhood of the Mn ion, there will be a wide distribution of relaxation rates which narrows as the concentration of Mn and the donors is increased. In order to model this situation, we generate a random distribution of substitutional Mn and of donors and we calculate the exchange integral for each Mn-donor pair in the generated distribution. The exchange constant for such pair is obtained from:

$$J_D = \alpha \left| \psi_D(r_{Mn}) \right|^2 = \{N_o \alpha\} V_o \left| \psi_D(r_{Mn}) \right|^2 \quad (1)$$

where the product  $\{N_o \alpha\}$  parameterises the *s-d* coupling and  $V_o = 1/N_o$  is the volume of the elementary cell.

The integral relaxation rate of each Mn ion is obtained by summing up the cross-relaxation rates to all donors:

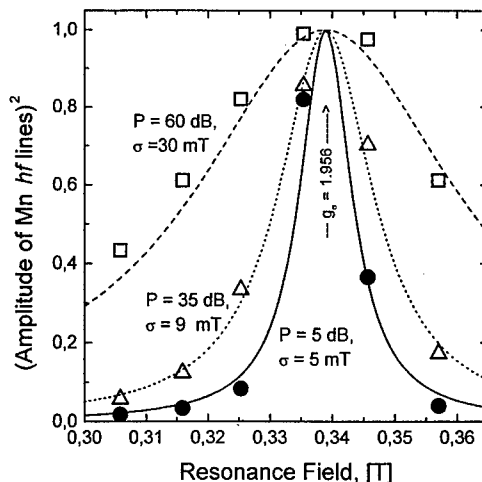


Fig.3: Amplitudes of the 6 Mn HF lines at their resonance positions for different microwave power, as indicated.

$$\frac{1}{T} \propto \frac{2\pi}{\hbar} f(\omega_{Mn} - \omega_D) \sum_D J_D^2 \quad (2)$$

Finally we obtain the distribution function of relaxation rates. An example is given in Fig.4.

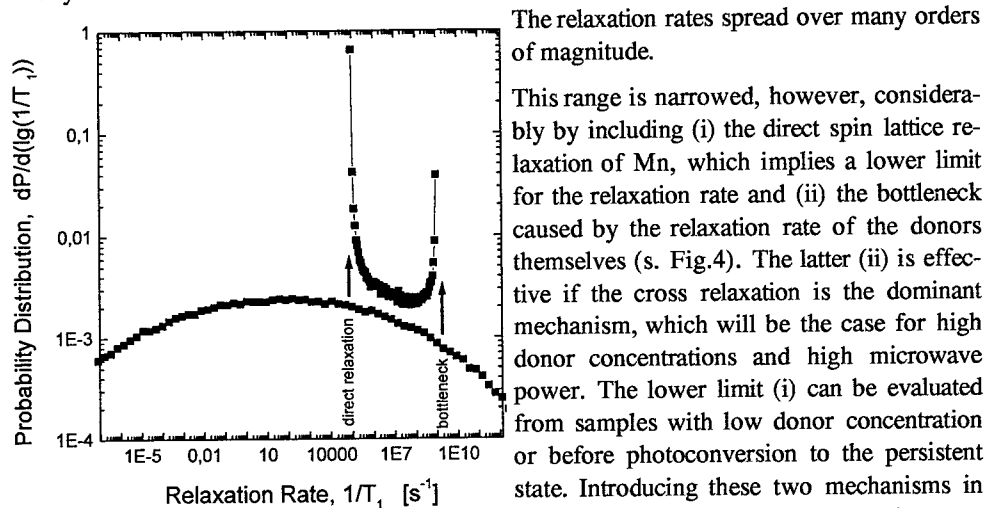


Fig.4: Distribution function of the longitudinal relaxation rate of Mn due to cross relaxation via shallow donors (broad curve). The range is narrowed strongly by including direct relaxation and the bottleneck due to the finite donor relaxation rate.

The relaxation rates spread over many orders of magnitude.

This range is narrowed, however, considerably by including (i) the direct spin lattice relaxation of Mn, which implies a lower limit for the relaxation rate and (ii) the bottleneck caused by the relaxation rate of the donors themselves (s. Fig.4). The latter (ii) is effective if the cross relaxation is the dominant mechanism, which will be the case for high donor concentrations and high microwave power. The lower limit (i) can be evaluated from samples with low donor concentration or before photoconversion to the persistent state. Introducing these two mechanisms in the model, the distribution of relaxation rates becomes much narrower and simpler at that, it has two peaks at the lower (i) and the upper (ii) limit as indicated by arrows in Fig. 4.

Finally, knowing the distribution of relaxation rates, we can evaluate the power dependence of the microwave resonance absorption, *i.e.*, the saturation behaviour. The quantitative analysis of the power dependence allows to estimate the direct relaxation rates of the Mn and the donors. For Mn we obtain a value of  $10^5 \text{ s}^{-1}$  at 4.2 K. This value increases by 5 orders of magnitude as the temperature increases to 300 K. The bottleneck due to the finite donor relaxation limits the Mn relaxation rate to  $10^9 \text{ s}^{-1}$  at 4.2 K. Since the concentrations of the shallow donors and of Mn are similar for the sample considered here, we can conclude that this is also the order of magnitude of the longitudinal relaxation rate of the shallow donors. With increasing temperature it increases but because of the limited power of our experimental setup we were not able to follow its dependence to higher temperatures.

The s-d exchange interaction dominates the spin relaxation of Mn over a broad range of experimental conditions. Nevertheless, because of the peculiar probability distribution of the exchange constants and the relaxation rates, a precise evaluation is difficult at present. For the evaluation we use a value of  $N_0 \cdot \alpha \approx 50 \text{ meV}$  which gives good agreement of model and experimental data.

### Conclusion.

We observed the EPR signals of Mn and those of the shallow donor states of Y, In and Ga in  $\text{CdF}_2$ . Gallium and In show the metastable, persistent population of the shallow donor states after illumination. We do not observe any indication of a paramagnetic deep ground state of Ga and In although the sensitivity should be sufficient. The EPR results thus support the negative U model for these donors in  $\text{CdF}_2$ .

The observed effect of a cross relaxation of Mn by s-d coupling to the shallow donor states shows up a new possibility to detect the EPR of the latter indirectly with high sensitivity in a regime where the direct observation is not possible because of too large broadening. From a detailed analysis of the Mn EPR we are able to determine the spin relaxation behaviour of the two components and their coupling. The modeling of the power dependence of the EPR absorption is rather complex conceptually but the appearance of the two limiting cases permits relatively simple access to the spin relaxation times of the two interacting impurities. The arrows given in Figs. 1 & 4 indicate the onset of saturation due to the direct relaxation of Mn and the bottleneck due to the limited shallow donor relaxation rate. They define the plateau in the power dependence in Fig.1 and the present calculation shows that they can be evaluated simply from the positions of the maxima of saturation curves for a single relaxation rate (dashed and dotted curve in Fig.1) fitted to the low- and the high power limits, respectively.

As compared to other semimagnetic semiconductors (II-VI and IV-VI compounds plus transition metal or lanthanide doping) a most peculiar property of the  $\text{CdF}_2\text{:Mn}$  in this context is the very small Bohr radius ( $7\text{\AA}$  according to effective mass theory) of the shallow donor state, a consequence of the large energy gap. Therefore, the exchange field acting on the Mn spins in the immediate neighbourhood of a donor is relatively high, since it is proportional to the inverse Bohr volume,  $r_B^{-3}$ . We obtain thus for the used value of  $(N_0 \cdot \alpha) = 50 \text{ meV}$  an exchange constant of  $J = 1.2 \text{ meV}$ . These values result in an effective field of 10 T which is strong enough to allow for the formation of a strong magnetic polaron at sufficiently high Mn concentration [11].

**Acknowledgments.** We would like to thank J. Langer, A. Suchocki and A. Ryskin for communicating their recent results to us prior to publication. Work supported by the *Committee for Scientific Research*, Poland, grant 2 P03B 191 08 and by the *Fonds zur Förderung der Wissenschaftlichen Forschung*, and the *Österreichischer Akademischer Austauschdienst*, Austria.

#### References.

- [1] U.Piekara, J.M. Langer and B. Krukowska-Fulde, *Solid State Comm.* **23**, 583 (1977)
- [2] J.E. Dmochowski, W. Jantsch, D. Dobosz and J.M. Langer, *Acta Phys. Polon.*, **A73**, 247 (1988)
- [3] A.I. Ryskin, A.S. Shcheulin, B. Koziarska, J.M. Langer, A. Suchocki, I.I. Buczinskaya, P.P. Fedorov, and B.P. Sobolev, *Appl. Phys. Lett.* **67**, 31 (1995).
- [4] A. Suchocki, B. Koziarska, T. Langer, and J.M. Langer, *Appl. Phys. Lett.* **70**, (1997), *to be published*.
- [5] J.E. Dmochowski, J.M. Langer, Z. Kalinski, and W. Jantsch, *Phys. Rev. Lett.*, **56**, 1735 (1986)
- [6] D.J. Chadi and K.J. Chang, *Phys. Rev. Lett.* **61**, 873 (1988)
- [7] W. Jantsch, Z. Wilamowski and G. Ostermayer, *Semicond.Sci.Technol.* **6**, B47 (1991)
- [8] V. Mosser, S. Contreras, J.L. Robert, R. Piotrkowski, W. Zawadzki, and J.F. Rochette, *Phys. Rev. Lett.* **66**, 1737 (1991)
- [9] M. Potemski and Z. Wilamowski, *Acta Phys. Polon.*, **A71**, 369 (1987)
- [10] Z. Wilamowski, H. Przybylinska, W. Jantsch, *J. Magn. Magn. Mat.* **140-144**, 1733 (1995)
- [11] Z. Wilamowski, W. Jantsch, and W. Faschinger, *J. Magn. Magn. Mat.*, **140-144**, 1697 (1995)

## PHOTOINDUCED MAGNETISM IN $\text{CdF}_2$ WITH BISTABLE DONORS: THE CLUE FOR THE NEGATIVE U?

J. M. Langer, A. Suchocki, R. Szymczak and M. Baran,  
Institute of Physics, Polish Academy of Sciences, Al. Lotników 32/46, 02-668 Warsaw, Poland

**Keywords:**  $\text{CdF}_2\text{:In}$ ,  $\text{CdF}_2\text{:Ga}$ , bistable centres, negative U, photomagnetism

**Abstract.** We report measurements of photoinduced magnetisation of  $\text{CdF}_2$  bulk crystals doped with In or Ga. At temperatures at which metastable photo transformation of donors occurs, magnetic susceptibility increases and it follows a Curie law. Low magnetic field data are dominated by spin-spin ferromagnetic coupling of  $d^5$  electrons of Mn codopants with donor electrons of In or Ga metastably phototransferred from a localised to the hydrogenic shallow donor state. Enhancement of magnetisation is due to effective spin increase resulting from this coupling. At high magnetic fields (above 2 T) and temperatures below 5K, saturation of the photoinduced magnetisation is observed. This provides first direct proof of a negative-U character of the donors in  $\text{CdF}_2$ .

### Introduction

In and then Ga donors in  $\text{CdF}_2$  crystals were first fully characterised bistable donors in semiconductors [1-4]. Recent theoretical computations by Song et al. [5] confirmed the basic feature of the early model of bistable donors in  $\text{CdF}_2$ , namely the one electron character of both localised and delocalized states, the existence of symmetric large lattice relaxation (the lattice collapses onto the In or Ga positively charged core upon the defect photoionization) and the vibronic nature of the barrier separating the two bound states of the donor: deeper - localised and shallower - hydrogenic, effective mass state. In case of In, the theory reproduces well the energy levels and the barrier, while for the deeper Ga, the barrier height is underestimated. Although a standard one-electron defect model of these donors explains well most of the experimental data, it cannot reconcile for the lack of the ESR signal for the donor in the ground localized state. Only upon illumination the ESR signal appears and it is unambiguously related to the effective mass shallower bound metastable state of the donor [6]. Such a behavior is similar to that observed for the DX centers in III-V and II-VI compounds [7] and could serve as hint for the negative U character of the donors in highly ionic  $\text{CdF}_2$ . Another hint for the negative-U character comes from a close to bimolecular character of the decay of the photoinduced hydrogenic state of In and Ga [8]. Each of these results could, however have been interpreted without invoking a two-electron character of the ground state of the bistable donors in  $\text{CdF}_2$  crystals (see Ref. 9 for a thorough discussion of the problem of testing the sign of U in case of standard DX donors in GaAs-based compounds). Due to a different type of bonding, it is highly unlikely that similar bond-breaking mechanism to that found in III-V and II-VI semiconductors may be applicable there, if indeed a negative sign of U for these donors was confirmed.

One of the measurements that could provide more direct evidence for the sign of U is photomagnetisation. If the ground state of the donor is a singlet ( $S=0$ ) two electron state, then a photoconversion of this state to a pair of hydrogenic one-electron bound states causes appearance of two  $\frac{1}{2}$  spins, that could be detected by a sensitive magnetometer as an additional paramagnetic contribution to the "dark" magnetisation of the crystal. This idea was first applied to DX centers in AlGaAs and resulted in notable controversy of results reported by two groups. First Khachaturian et al. showed that photoinduced magnetisation data could be well reconciled by a one electron model [10], but later on this measurement was repeated on thicker samples in a more conventional experimental setup with quite opposite result, namely that there is large metastable additional paramagnetic signal after light illumination and its magnitude agrees well with the number of photogenerated occupied shallow donor states [11]. The later results agrees with a widely accepted

Chadi and Chang negative-U model of the DX centres in AlGaAs [7]. Reason of experimental controversy is not clear, but indicates that great care must be taken before final conclusion on a sign of U is reached.

Following suggestion by one of us (JML), the measurement of photoinduced magnetisation on  $\text{CdF}_2:\text{In}$  crystals was done by St. Petersburg group [12]. Kazanski et. al. detected increase of magnetic susceptibility after illumination. Based upon this observation they concluded that In donors are negative-U systems. Independently of the St. Petersburg group we performed photomagnetisation experiment on In and Ga donors in  $\text{CdF}_2$  crystals and the results are presented there. The key difference is not only a sensitivity and type of our equipment (SQUID vs Faraday balance), but much broader temperature range (especially for temperatures below 5 K) and magnetic fields spanning a linear susceptibility range (St. Petersburg experiment) up to high magnetic field, at which a saturation of dark and photoinduced magnetisation could be seen. We shall show below, that measurement in the susceptibility limit (magnetisation is proportional to external magnetic field) is not sufficient to determine the sign of U and in fact may even lead to wrong conclusions about the mechanism causing the change of the crystal magnetisation after illumination by light. Both conditions (i.e. low temperatures and high magnetic fields) are essential for experimental discrimination between the two models of bistable donors in  $\text{CdF}_2$  crystals.

### Experimental procedure

$\text{CdF}_2$  bulk crystals doped with In or Ga were converted to a semiconductor state by annealing in Cd. vapours. Thermal processing causes outdiffusion of compensating interstitial fluorine ions. The liberated electrons are then captured by empty In or Ga positively charged donors. Largest thermal conversion (i.e. highest occupied donor concentration) was detected in Mn codoped crystals (0.2%). These crystals were used previously in experiments on electroluminescence [13].

Photoinduced magnetisation was measured in a commercial setup, in which the SQUID head detects magnetisation of the sample. Photoconversion was done by illumination by low-power multiline Ar laser. Stability and repeatability of the system is better than 1 ppb emu. It was essential for reliability of the conclusions, as the photoinduced signal is a difference between magnetic field scans done in darkness and after the illumination.

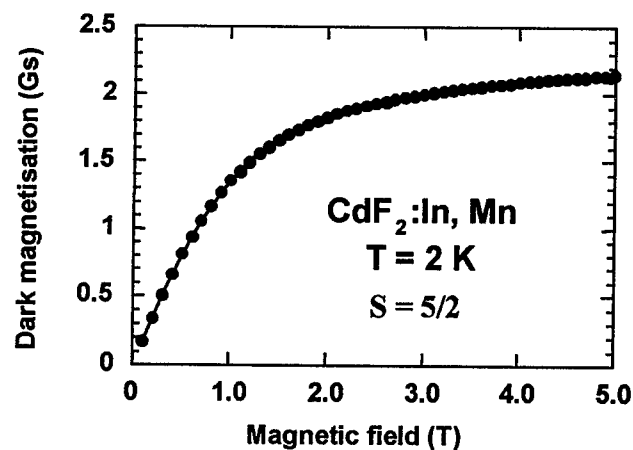


Fig. 1 Dark magnetisation of  $\text{CdF}_2:\text{In, Mn}$  crystals. Solid line is a fit to standard Brillouin function with  $S=5/2$

Dark magnetisation is dominated by background Mn signal. Its magnetic field dependence can be fitted with very high accuracy to a standard Brillouin function with spin  $S=5/2$ . As it is clear from Fig. 1 Mn-Mn clustering is insignificant, if any (concentration of Mn codopants is small enough and no preferential pairing occurs).

UV-VIS light from Ar laser causes increase of magnetisation. The effect is metastable at temperatures at which metastability of In or Ga donors has already been found [1-4] (below 80K for In and

below 200K for Ga). Photoinduced signal persists over several days, after which measurements were first repeated in the photoinduced, but frozen in state. Then after heating-cooling cycle the „dark” magnetisation of the crystal was measured. The value of photoinduced signal was the same within accuracy of the instrument.

At low magnetic fields photoinduced magnetisation follows the Curie law in a whole temperature range (2-100K). Qualitatively the increase of magnetic susceptibility (low-magnetic field effect) agrees with a hypothesis of a two-electron character of the relaxed ground state of the bistable donors in  $\text{CdF}_2$  crystals. However in all our samples Mn was additional dopant. It is plausible to assume that a ferromagnetic coupling occurs between spin 5/2 of Mn and spin 1/2 of the shallow donor (its extended wavefunction allows for overlap and exchange interaction with the localised Mn wavefunction). Such interaction produces spin molecule with effective spin  $S=3$  and thus effectively increases magnetic susceptibility, which is proportional to  $S(S+1)$ . It is thus clear, that without knowledge of exact number of photopopulated shallow donor states, the low magnetic field data alone are not enough to discriminate between the above two options. Kazanski et al. [12] determined concentration of active In shallow donor states by using a scaling based upon photoionization absorption [14] and concluded that whole additional magnetisation comes from photopopulated shallow donors, and thus the ground state of In donors is a two-electron state and forms the negative-U system. Unfortunately there is a certain drawback of this procedure, namely the scaling proposed in Ref. 14 has been done for different impurities and for donor concentration by at least one order of magnitude smaller. Both shape of the absorption (at high donor concentration only the high energy tail of the shallow states absorption can be measured) and likely the oscillator strength (effect of the wavefunction overlap and the influence of random internal electric fields) may change with the concentration (especially when approaching the Mott transition). This has not yet been quantified for shallow donors in  $\text{CdF}_2$  crystals. At the early stage of our study we did the same scaling, and like in case of Kazanski et al. [12] reasonable agreement between concentration deduced from magnetic susceptibility and shallow donor absorption was obtained. However, the concentration was in  $10^{19} \text{ cm}^{-3}$  range, suspiciously high for  $\text{CdF}_2$ . This is why we decided to extend our measurements to lower temperatures (down to 2K) and higher magnetic fields (5T) to go beyond susceptibility limit. Even if there is a ferromagnetic coupling between Mn ions and shallow donors, the high magnetic field limit (saturation) provides most precise measure of the number of all contributed spins. Therefore, if the system was a positive U, then after initial increase photoinduced magnetisation should drop to zero (there are no extra spins generated). If the system was negative U, then the photoinduced magnetisation should saturate and its value is a sum of contribution from all shallow donors, thus permitting independent calibration of the donor concentration. From our measurements we found that for the magnetic fields above 1 T saturation of magnetic response builds up. It is most clearly seen at lowest temperatures (see Fig3). Analysis of the whole magnetic field range allows separation of the contribution of shallow donors and spin-spin coupling between Mn and shallow donors, as well as the determination of the shallow donors concentration. It is more than a factor of 3 smaller than obtained by the optical scaling used by Kazanski et al. [12]. and thus makes procedure used in previous works (at least for the highest donor concentrations) not reliable for quantitative analysis of magnetisation data.

#### Mn - shallow donor spin-spin interaction

At low magnetic fields magnetisation of the system with spin  $S$  is proportional to  $S(S+1)$ . In our crystals there are intentionally introduced Mn impurities. As the spin of the  $d^5$  shell is 5/2, Mn dominates „dark” magnetisation of the sample. Light transforms bistable donors (In or Ga) from a localised to hydrogenic - delocalized state with spin 1/2. Depending on the sign of  $U$ , ground state is a singlet with  $S=0$  ( $U<0$ , two electron ground state) or a doublet with spin  $S=1/2$  ( $U>0$ , one electron state). If there is effective spin-spin interaction between background Mn and shallow donors (interaction with deep states is highly unlikely, as there is no indication of any donor-Mn pairing), then a spin molecule is formed with effective spin being a sum of Mn spins and that of the shallow donor that interacts with Mn. Most likely such interaction is ferromagnetic [15], hence effective spin is  $S=3$  in case of just one Mn ion interacting with shallow donor. Bohr radius of shallow donors in  $\text{CdF}_2$  is about 0.8 nm, so for a given concentration of Mn (0,2%), simple pairs should dominate. In table 1, the spin dependent prefactor is given for the photoinduced magnetic susceptibility. It is



assumed that within each shallow donor orbit there is effectively one Mn  $d^5$  shell (a real situation in our samples, as it will be shown below). For the  $U < 0$  model two cases are considered. One (more likely, that both electrons form a singlet  $S=0$  state, and second, less likely, that both spins add to form a triplet state with  $S=1$ ). It is clear from the table, that presence of Mn ions (or other background spins) interacting with photopopulated donors dramatically affects the value of susceptibility, and one must be very cautious in using susceptibility data alone. The effect is even more dramatic if the number of interacting Mn ions is larger (magnetic polaron) [15].

Photoinduced susceptibility	$U > 0$	$U < 0$	
		$S_{loc} = 0$	$S_{loc} = 1$
no Mn-shallow donor spin-spin interaction	0	3/4	- 1/4
with Mn-shallow donor spin-spin interaction	10/4	13/4	11/4

#### Final results

For relatively small concentration of Mn ions, we may assume that within orbit of the shallow donor there is either one Mn ion or none. If we denote the fraction of donors interacting with Mn as  $f$ , then for the  $U < 0$  case with a singlet deep state ( $S_{loc}=0$ ) the photoinduced magnetisation per unit volume in Bohr magneton units equals

$$\Delta M = [(1-f)(1/2 B_{1/2}) + f(3B_3) - f(5/2 B_{5/2})] N_d \quad (1)$$

where  $B_j$  - the Brillouin function and  $N_d$  - concentration of shallow donors. Experimental data can be linearised by noting that

$$\Delta M/B_{1/2} = 1/2 N_d + f N_d (3B_3 - 5/2 B_{5/2} - 1/2 B_{1/2})/B_{1/2} \quad (2)$$

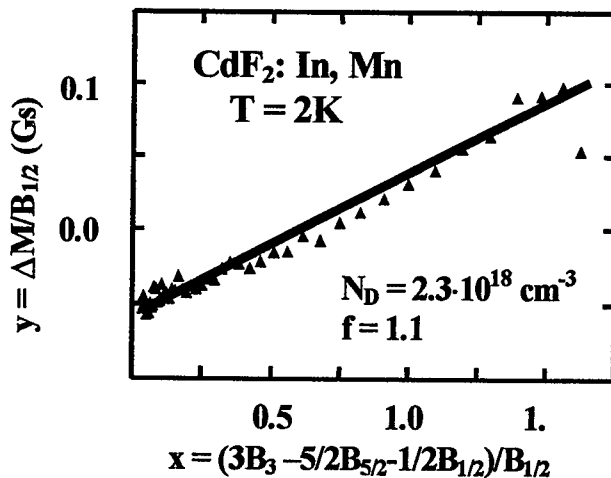


Fig.2 Photoinduced magnetisation plotted in a way allowing determination of the shallow donor concentration  $N_D$  and the average number  $f$  of Mn ions interacting with shallow donors.

The Brillouin functions depend only on  $T$  and  $H$ , so we may define conveniently the x-axis as  $x = (3B_3 - 5/2 B_{5/2} - 1/2 B_{1/2})/B_{1/2}$ . Dividing measured photoinduced magnetisation  $\Delta M$  by the Brillouin function  $B_{1/2}$ , the following linear relationship is expected:

$$y = 1/2 N_d + f N_d x \quad (3)$$

with the y coordinate being just  $\Delta M/B_{1/2}$ . Such plot is shown in Fig.2. It spans magnetic fields up to 5T. The point at highest x value corresponds to smallest magnetic field, at which the error is largest. Apparently the filling factor  $f$  is close to unity, thus validating considerations summarised in Table above.

Donor concentration obtained from the fit equals  $N_d = 2.3 \cdot 10^{18} \text{ cm}^{-3}$ . It is interesting to note that this value is almost 3 times smaller than obtained from the infrared absorption scaling [14] used by Kazanski et al. [12] and the value obtained from the low field susceptibility by assuming that it comes from shallow donors ( $S=1/2$ ) only.

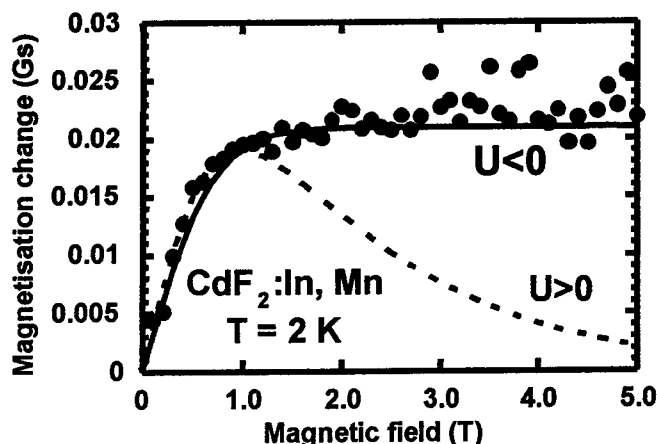


Fig.3 Photoinduced persistent magnetisation in  $\text{CdF}_2:\text{In, Mn}$  crystals measured at  $T=2\text{K}$ . Solid line is a fit to  $U<0$  model of bistable donors, while the dotted line for  $U>0$  case.

**direct proof that indeed In in  $\text{CdF}_2$  crystals is the negative-U system, like DX centres in III-V compounds.** Similar results (although more noisy, due to smaller concentration) were obtained for Ga, which thus is likely similar negative U centre.

The fit in Fig.2 showed that with a good approximation we can assume that „within” orbit of the electron bound at the shallow hydrogenic state there is only ions Mn interacting with it. Therefore we could model the experimental data by plotting magnetisation as the difference between standard magnetisation of  $N_d V$  ( $V$  is the sample volume) spin molecules (Mn and shallow donor) and the same number of Mn ions, that participate in the formation of the spin molecules.

$$\Delta M = 2\mu_B[(3B_3) - (5/2 B_{5/2})] N_d V \quad (4)$$

As it is clear from Fig.3, the fit is very good in a whole magnetic field range. We also plotted as a dashed line, the photoinduced magnetisation that would be expected if the system was a positive U (i.e. both deep and shallow states being one electron states). In such a case after initial rise reflecting formation of a spin molecule (Mn-donor), magnetisation drops to zero, when all spin become aligned by the magnetic field, as there are no extra spins liberated by light.

More advanced theoretical treatment must include fluctuations of distances between Mn and shallow donors, i.e. change of the exchange energy with distance. At higher temperatures, more distant pairs are being spin decoupled by thermal fluctuations, thus slightly changing the shape of the theoretical  $\Delta M(H)$  dependence for small and medium fields. We are now in the process of performing such analysis [16]. For temperatures above 5K, the difference between both cases becomes visible only at much larger fields. From this plot it is evident again that the low field and high temperature data are not sufficient to distinguish between the two cases if only some background spins are present. It is possible, that discrepancies between earliest data on DX centres in AlGaAs [10,11] may have the same source. Khachaturian et al. [10] used standard thin epitaxial layers on GaAs substrate, while Katsumoto et al. [11] did measurements on much thicker samples, but without substrate.

The raw data are shown in Fig.3. It is clear that above 1 T photoinduced magnetisation saturates. It must be remembered that it is the difference between the two sets of data (dark and after illumination). Each of them show slightly smaller saturation effect (see Fig.1). Additional magnetisation is just a contribution from electrons occupying shallow donors (i.e. proportional to the number of donors and their spin  $S=1/2$ ). It is a most direct evidence, that indeed extra spins are photoliberated and thus in the initial state spin pairing had to occur. **This constitutes the first**

**Acknowledgment**

We would like to acknowledge stimulating conversations with Yuri Semenov and Z. Wilamowski on the problem of spin-spin interactions between Mn and shallow donors. This work was supported in part by the contract no 8 T11B 017 09 from the Polish State Research Committee.

**References**

- [1] U. Piekara, J. M. Langer, B. Krukowska-Fulde, *Solid State Commun.* **23**, 583 (1977)
- [2] J. E. Dmochowski, J. M. Langer, Z. Kalinski, and W. Jantsch, *Phys. Rev. Lett.*, **56**, 1735 (1986)
- [3] J. E. Dmochowski, W. Jantsch, D. Dobosz, and J. M. Langer, *Acta Phys. Polon.* **A73**, 247 (1988).
- [4] J. M. Langer in *Lecture Notes in Physics* (Springer, New York), **122**, 123 (1980); *J. Phys. Soc. Jpn. Suppl.* **49A**, 207 (1980); *Radiat. Effects*, **72**, 55 (1983)
- [5] Y. Cai and K. S. Song, *J. Phys.: Condens. Matter*, **7**, 2275 (1995); C. Fu and S. Song, *J. Phys.: Condens. Matter*, **9**, 3575 (1997).
- [6] Z. Wilamowski, J. Dmochowski and W. Jantsch, this conference and earlier references cited therein.
- [7] P.M. Mooney, W. Wilkening, U. Kaufmann and T.F. Kuech, *Phys. Rev.B.* **39**, 5554 (1989); P. M. Mooney, *J. Appl. Phys.* **67**, R1 (1990)
- [8] A. S. Scheulin, A. I. Ryskin, K. Swiatek and J. M. Langer, *Physics Lett. A* **222**, 107 (1966).
- [9] J. M. Langer, L. Dobaczewski, J. Dmochowski, W. Jantsch and G. Brunthaler, in *Physics of DX Centers in GaAs Alloys*, ed. by J. Bourgoin, *Solid State Phenomena Vol. 10*, (Sci-Tech Publications, Vaduz, 1990), p. 233
- [10] K.A. Khachaturyan, D.D. Awschalom, J.R. Rozen and E.R. Weber, *Phys. Rev. Lett.* **63**, 1311 (1989)
- [11] S. Katsumoto, N. Matsunaga, Y. Yoshida, K. Sugiyama, and S. Kobayashi, *Jpn. J. Appl. Phys.* **29** L1572 (1990).
- [12] S. A. Kazanskii, A. I. Ryskin, V. V. Romanov, *Appl. Phys. Lett.* **70** (1997)
- [13] T. Langer, B. Krukowska-Fulde, J. M. Langer, *Appl. Phys. Lett.*, **34**, 216 (1979).
- [14] J. M. Langer, T. Langer, G. L. Pearson, B. Krukowska-Fulde, and U. Piekara, *phys. stat. sol. (b)* **66**, 537 (1974).
- [15] T. Wojtowicz, S. Kolesnik, I. Miotkowski, and J. K. Furdyna, *Phys. Rev. Lett.*, **70**, 2317 (1993) and references cited therein
- [16] Y. G. Semenov, J. M. Langer (1997), to be published, see also Y. G. Semenov and V. A. Stepanovich, *Semicond. Sci. Technology*, **7**, 364 (1992).

## EVIDENCE OF METASTABLE DEEP ACCEPTORS IN AgGaS<sub>2</sub> FROM TIME-RESOLVED EMISSION

I-H Choi<sup>1</sup> and P. Y. Yu<sup>2</sup>

<sup>1</sup>Physics Department, Chung-Ang University, Seoul, Korea

<sup>2</sup>Department of Physics, University of California and  
Materials Sciences Division, Lawrence Berkeley National Laboratory,  
Berkeley, CA 94720, USA

**Key words:** chalcopyrite semiconductors, time resolved photoluminescence, deep acceptors, metastability

**Abstract.** Time dependent decay of shallow-donor-to-deep-acceptor pair emission from the chalcopyrite semiconductors AgGaS<sub>2</sub> under constant laser illumination is reported. These photo-induced decays are well described by single exponents with time constants between 60 and 140 s dependent on the excitation laser intensity at 3.4 K. The dependence of the decay time on sample temperature is activated with a barrier height estimated to be ~2 meV. A model is proposed to explain the observed photo-quenching effects based on the existence of a metastable excited state of the deep acceptors involved.

### Introduction

While a number of defects in semiconductors such as GaAs and related alloys have been shown to exhibit the phenomenon of metastability, this has not been true for the I-III-VI<sub>2</sub> semiconductors with the chalcopyrite structure. The chalcopyrite semiconductors can be considered as "cousins" of the zincblende II-VI semiconductors[1]. They share the same difficulty in doping their larger bandgap (>2 eV) members p-type. It has been proposed that one reason for this behavior in the II-VI compounds is due to the existence of deep acceptors. In particular Park and Chadi [2] have proposed deep acceptors (labeled as AX centers) which exhibit large lattice displacements and metastability similar to the deep donor DX centers in GaAlAs[3]. However, the difficulty in fabricating pn-junctions makes it so far impossible to investigate deep centers in large bandgap II-VI or chalcopyrite semiconductors with conventional techniques such as Deep Level Transient Spectroscopies[4]. This difficulty does not preclude the possibility of using optical techniques to study deep centers in these materials. In the chalcopyrite semiconductors it is often found that their emission spectra are dominated by donor-acceptor pair recombination peaks[5]. In this paper we report the observation of quenching under constant laser illumination of this pair recombination in AgGaS<sub>2</sub> containing deep acceptors[6,7]. We attribute this quenching to the optical excitation of the deep acceptors to an optically-inactive metastable excited state. We propose a model to explain our results and compare it with the well-studied DX centers.

### Experimental Details and Results

The AgGaS<sub>2</sub> bulk single crystals used in this experiment were grown by the horizontal Bridgman method using a tubular two-zone furnace. Most of the crystals are not intentionally doped. Details of the crystal growth process have been described before [6] and will not be repeated here. The as-grown crystals, even when undoped, typically show variations in color from one end to the other as a result of defect concentration fluctuations. Metastability is found to occur in lighter color samples presumably because the concentration of defects are lower in these samples. The samples were cooled by a variable temperature optical refrigerator and the photoluminescence spectra were excited by the 442.0 nm line of a 30 mW cw He-Cd laser. To minimize heating effects the size of the focal spot on the sample is typically about 450 μm.

The photoluminescence (PL) spectra of AgGaS<sub>2</sub> bulk single crystals have been studied by many groups already (see Ref.[5] and references therein). Typically one finds that the PL spectrum is dominated by a strong "green emission peak" (labeled as B in Ref. [6,7]) below the band gap and

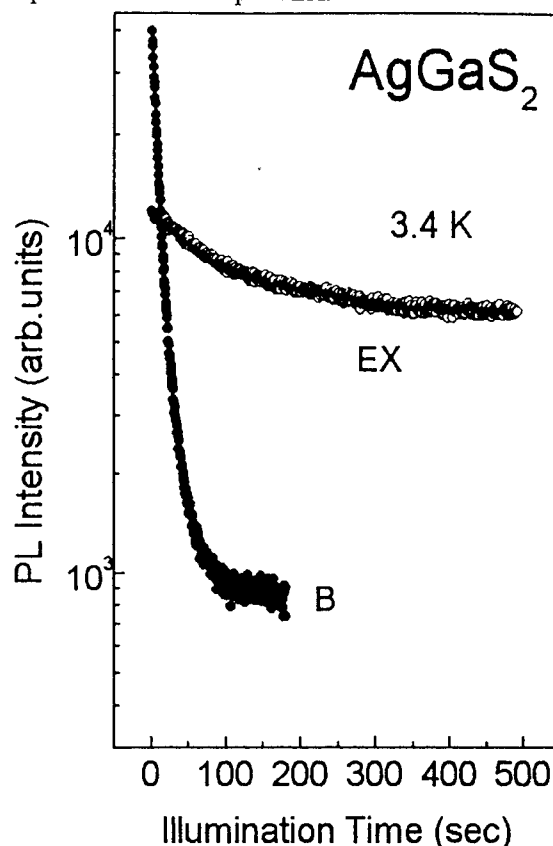
centered around 2.50 eV. This peak is usually identified with donor-acceptor pair recombination. In some samples a weak structure may also be observed at 2.70 eV and is attributed to emission from free excitons (labeled as EX in Ref.[6]). In some of our samples we found that the PL intensity of the peak B decreases continuously as a function of time under constant laser illumination. In Fig.1 we compare the time dependence of the peak B with that of peak EX.

While the intensity of the EX peak decreases by less than a factor of two the peak B decreases by a factor of more than 50 in about 10 minutes. We have verified that this is not caused by laser induced heating since in some samples the peak B remains constant under even higher intensity laser illumination. Although the time dependence in both types of samples are quite different, they show, however, quite similar temperature dependence. The decay of peak B intensity  $I$  with time  $t$  can be fitted with a single exponential :

$$I(t) = I(\infty) + I(0)e^{-t/\tau} \quad (1)$$

where  $\tau$  is the decay time constant. When the sample is left in the dark the peak B recovers completely in about 15 minutes.

**Figure 1.** The time decay of the peak B compared with the exciton peak EX



Based on the decay information on B one can obtain an emission spectrum segment at time  $t \sim 0$  in the following way : the sample is exposed to laser light for about 10 s while the spectrometer is scanned at a fast rate determined by the magnitude of the signal and then left in the dark for 15 minute to recover before another scan. To average out the change in intensity during the laser exposure, each segment of the spectrum is measured twice, once by scanning to higher photon energy and once in the reverse direction. By combining these 'averaged' segments the spectrum (a) shown in Fig. 2. is obtained. The spectrum (b) in the same figure shows the emission curve measured after the sample has been exposed to the laser for about 15 minute. This exposure is sufficient to quench the peak B so that the exciton peak becomes very prominent and well resolved. The decay time  $\tau$  was found to be roughly linearly dependent on laser power over the limited range of power available (see Fig. 3). Finally,  $\tau$  decreases as the sample temperature is increase. We have attempted to fit this temperature dependence (see Figure 4) with the following expression :

$$\tau(T) = \frac{\tau_0}{(1 + \alpha e^{-E_a/kT})} \quad (2)$$

where the three parameters  $\tau_0$ ,  $\alpha$  and  $E_a$  are treated as adjustable and  $k$  is the Boltzmann constant. The solid curve in Fig. 4 is obtained with  $\tau_0$  (the decay time at  $T=0$ ) = 57.4 s;  $\alpha=1.27$  and the activation energy  $E_a \sim 2$  meV.

**Figure 2.** The low temperature emission spectra of our AgGaS<sub>2</sub> sample measured under two different conditions: (a) was measured after the sample has been exposed to laser for less than 10 s while (b) was measured after about 15 minutes of exposure.

### Model

The peak B has already been studied by several groups [5] and has been identified with the radiative recombination of a donor with an acceptor. An activation energy of about 27 meV has been deduced from the temperature dependence of its intensity [6]. This has been attributed to the binding energy of a shallow donor. On the other hand its pressure dependence has been found to be larger than that of the bandgap[7]. Based on this observation it has been suggested that the acceptor involved in peak B is a deep acceptor[8]. Thus it is reasonable to assume that the photo-induced quenching of peak B is due to the optical excitation of the deep acceptors into a metastable excited state which is not optically active.

We propose the following model to explain the observed time decay of the peak B. Before the sample was exposed to the radiation there are no neutral acceptors because a typical AgGaS<sub>2</sub> sample is compensated and n-type. The laser excites free electrons and holes via absorption. These carriers are trapped at donors and acceptors before recombination. Thus under steady illumination neutral acceptor are continuously formed.

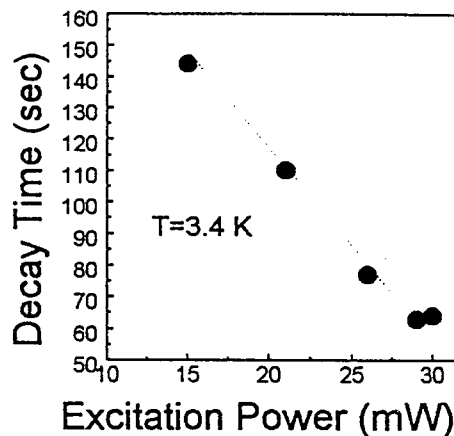
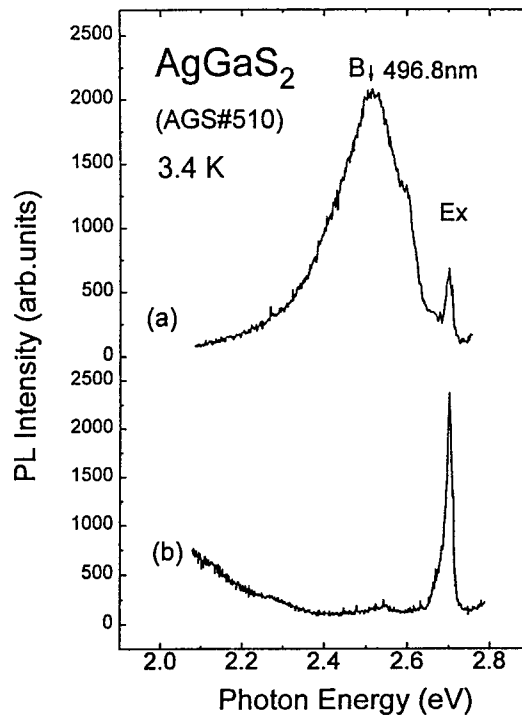


**Figure 3.** The dependence of the decay time  $\tau$  on the laser power.

This picture of bimolecular recombination is consistent with the laser power dependence of the initial intensity  $I(0)$  of peak B which was found to be quadratic. We suggest that the neutral acceptors (represented as  $A^0$ ) can further be excited into states (denoted as  $A^*$ ) which are displaced in configuration space from the  $A^0$  state. This model is shown schematically in Fig. 5. As a result of the lattice displacement the  $A^*$  excited states cannot participate in donor-acceptor pair recombination. Furthermore, they are metastable since there is now a barrier they have to overcome in order to return to the optically active ground state. From the temperature dependence of  $\tau$  we deduced a value of about 2 meV for the thermal capture barrier  $E_a$  while from the recovery time of

the sample in the dark we estimated the time of emission ( $\tau_{em}$ ) out of the  $A^*$  states at low temperature to be of the order of  $10^3$  s.

**Figure 4.** The dependence of the decay time  $\tau$  on sample temperature. The solid curve is a fit of the data points with Eq. (2).

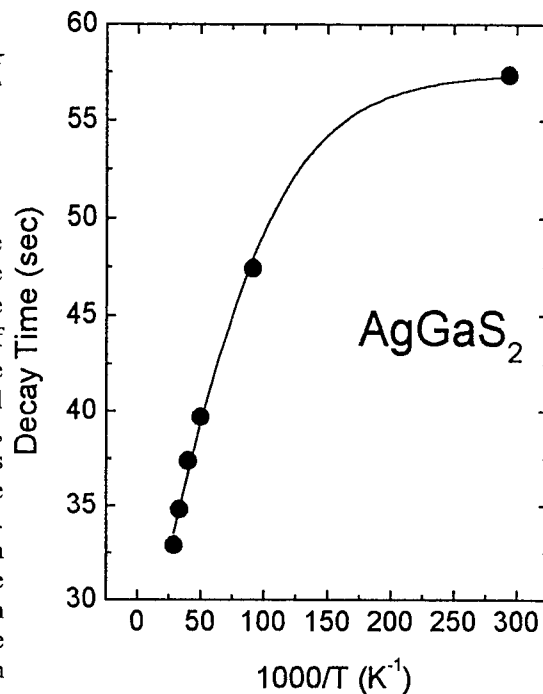
### Discussions

Within our model the photo-quenching of the peak B under constant illumination can be understood if  $\tau_{em}$  is much longer than the corresponding time of optical capture ( $\tau_{opt}$ ). If we assumed, for simplicity, that  $\tau_{em}$  is infinite and the laser is intense enough to convert all the acceptors to the neutral  $A^0$  state at  $t=0$ , then under constant illumination the acceptors will be continuously converted from  $A^0$  to the  $A^*$  state until all of them are in the  $A^*$  state. Since the  $A^*$  state cannot participate in radiative recombination with the donors the intensity of the donor-acceptor pair emission will decrease to zero with time. Thus from the observed decay time of the peak B one can deduce  $\tau_{opt}$ . In case  $\tau_{em}$  is finite the steady

state intensity  $I(\infty)$  is not zero and is proportional to the ratio  $\tau_{opt}/\tau_{em}$ . In this model we have assumed that the acceptors cannot be optically excited out of their metastable state. As a result  $\tau_{opt}$  and hence  $\tau$  should be inversely proportional to the laser intensity. The range of laser power available to us is unfortunately too small to verify this relation. We could not determine the decay time when the laser power was less than 8 mW. The reason is twofold. For low laser powers the emission intensity becomes too weak to be detected. Also as  $\tau_{opt}$  becomes comparable to  $\tau_{em}$  at low laser power, the photoluminescence intensity exhibits negligible time dependence.

Our model can explain why the photo-quenching effect is not observable in some samples. The incident laser excites  $A^0$  via capture of free holes while at the same time these optically-active  $A^0$  states are depleted by excitation into the metastable  $A^*$  states. In order to see the quenching effect the laser intensity must be high enough to generate enough holes at  $t=0$  to *convert all the acceptors into the neutral state*. If this not the case then the depleted neutral acceptors  $A^0$  can always be replaced via the capture of free holes by the remaining reservoir of  $A^-$  acceptors. Thus the availability of samples with low enough acceptor concentrations is crucial to the success of this experiment.

At this point there is not enough data to make a more definitive identification of the nature of the metastable  $A^*$  state of the acceptors nor to specify its charge state. While one is tempted to attribute this  $A^*$  state to a negative U center like the DX center; one finds many significant differences between these deep centers and the now familiar DX centers. For example, the relaxed  $DX^-$  state is the ground state while the unrelaxed free electron in the conduction band is metastable. We note, however, that in the present case the ground  $A^0$  state is unrelaxed and only the excited state is relaxed. The emission and capture barriers height in these deep acceptors are smaller than those found in DX centers by about two orders of magnitude. Finally, the quenching of the pair emission does not seem to be accompanied by the appearance of new peaks nor in the enhancement of the

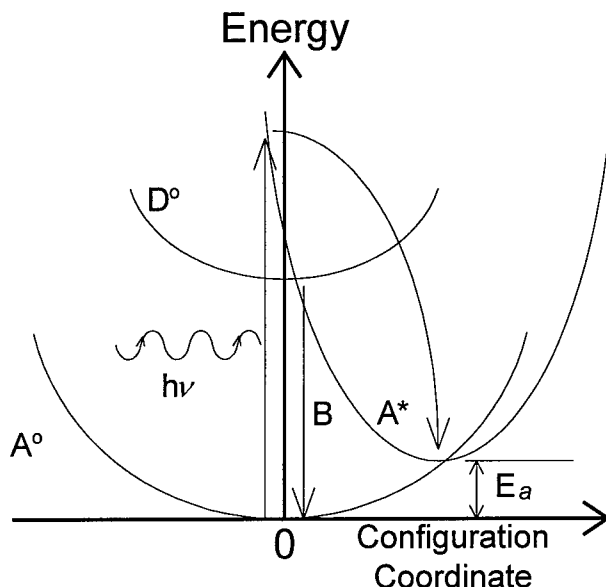


exciton emission. Thus these deep acceptors acts as an efficient channel for non-radiative recombination.

### Conclusions

In summary, we have discovered that deep acceptors in the chalcopyrite semiconductor  $\text{AgGaS}_2$  exhibit the phenomenon of photo-induced quenching in their photoluminescence. We interpret this

**Figure 5.** A schematical configuration coordinate diagram proposed to explain the photo-quenching of the donor-acceptor pair emission peak B.



result in terms of the optical excitation of the neutral acceptors into an optically-inactive metastable excited state. The thermal capture barrier height and the emission time of this metastable state have been deduced from our results.

**Acknowledgments:** The part of this work performed in Korea was supported by the Chung-Ang University Research Grants in 1997. The work at Berkeley was supported by the Director, Office of Energy Research, Office of Basic Energy Sciences, Materials Sciences Division, of the US Department of Energy under Contract No. DE-AC03-76SF00098. IHC also acknowledges a fellowship from the Korea Research Foundation (non-directed research fund).

### References

1. J. E. Jaffe and A. Zunger, *Phys. Rev. B* **29**, 1882 (1984).
2. C. H. Park and D. J. Chadi, *Phys. Rev. Lett.* **75**, 1134 (1995).
3. For a review, see P. M. Mooney, *J. Appl. Phys.* **67**, R1 (1990).
4. See, for example, articles in *Deep Centers in Semiconductor, A State of the Art Approach*, ed. by S. T. Pantelides (Gordon and Breach, New York, 1986).
5. P. W. Yu and Y. S. Park, *J. Appl. Phys.* **45**, 823 (1974); J. P. Aicardi, J. P. Leyris and A. Poure, *J. Appl. Phys.* **53**, 1690 (1982).
6. In-Hwan Choi and P. Y. Yu, *J. Phys. and Chem. Solids* **57**, 1695 (1996).
7. In-Hwan Choi and P. Y. Yu, *Physica Status Solidi (b)* **198**, 251 (1996).
8. In-Hwan Choi and P. Y. Yu, *Phys. Rev. B* **55**, 9642 (1997).



## A POSITRON LIFETIME STUDY OF LATTICE DEFECTS IN CHALCOPYRITE SEMICONDUCTORS

M. Sherif Al-Kothb<sup>1,\*</sup>, Werner Puff<sup>1</sup>, and G. Bischof<sup>2</sup>

<sup>1</sup> Institut für Technische Physik, Technische Universität Graz, Petersgasse 16, A-8010 Graz, Austria

<sup>2</sup> Institut für Materialphysik, Universität Wien, A-1090 Wien, Austria.

**Keywords:** Chalcopyrite Semiconductors, Positron Lifetime.

**Abstract:** This paper reports results of positron lifetime, Doppler-broadening, photoluminescence, and X-ray investigations to study the fundamental nature of point defects in CuInS<sub>2</sub>, CuInSe<sub>2</sub>, AgInSe<sub>2</sub>, AgInS<sub>2</sub> and AgGaS<sub>2</sub> semiconductors and, for the first time, provides direct evidence of the charge state of the defect configuration. The I-III-VI<sub>2</sub> (I = Cu, Ag, III = In, Ga and VI = S, Se) bulk crystals were grown using a direct fusion technique followed by slow directional solidification. The whole growing process took about 14 days ensuring crystals of very high quality. The Rietveld method for structure refinement was used to study the synthesised samples. Positron states and annihilation rates are also calculated. The calculations are based on the generalized gradient approximation (GGA) for the electron-positron correlation effects. It improves the predictive power of positron lifetime calculations over those based on the local density approximation (LDA).

### Introduction

The ternary chalcopyrite compounds I-III-VI<sub>2</sub> (I = Ag, Cu III = Al, Ga, In VI = S, Se, Te) are direct energy gap semiconductors. These compounds show interesting opto-electrical properties which can be applied in various fields, such as photovoltaics (CuInSe<sub>2</sub>) electro-luminescent devices (CuInS<sub>2</sub>) and non linear optics (AgInSe<sub>2</sub> and AgGaS<sub>2</sub>) [1]. Most of these materials are not very well characterized. Point defects play a crucial role for the optical and electrical properties. The behaviour of these defects under different conditions and especially their microscopic identification are of great importance for opto-electronic devices. Very important are the deep levels in the gap induced by defects. The band gap of the I-III-VI<sub>2</sub> compounds are substantially smaller than those of II-VI compounds and are strongly influenced by the local structure, such as chemical order and bond length through p-d hybridizations in the valence band [2].

The crystal structure of the chalcopyrite belongs to the nonsymmorphic space group  $\bar{I}42d$  (eight atoms per primitive unit cell). It is an isoelectronic analogue of the II-VI binary compound semiconductors, in that the atoms II are substituted alternately by a group-I and a group-III atom [3]. This substitution leads to a doubling of the Zinc-blende (with space group  $F\bar{4}3m$ ) unit cell along the tetragonal c-axis [for example the Zn atoms (valence 2) in ZnSe are replaced by Cu (valence 1) and In (valence 3) atoms in CuInSe<sub>2</sub>]. Each anion is coordinated by two group I and two group III cations, whereas each cation is tetrahedrally surrounded by four group VI anions. The chalcopyrite crystals show some interesting structural anomalies in comparison to their binary analogous [4]. First, there are two cation sublattices rather than one, leading to the existence of two pairs of unequal bond length  $R_{I-VI} \neq R_{III-VI}$ . Second, the unit cell is tetragonally distorted with a distortion parameter  $\eta = c/2a$ , differing from 1 by as much as 12 % [5]. Third, the anions are displaced from the ideal tetrahedral sites by an amount  $x_{VI} \neq 1/4$ .

A wide variety of techniques have been employed to investigate the intrinsic (vacancies, interstitials, and grain boundaries) and extrinsic (e.g., oxygen impurities) defects in chalcopyrite compounds using photoluminescence, deep-level transient spectroscopy, atomic processing microscope, cathodoluminescence and photoacoustic spectroscopy [6]. Recently, positron

annihilation spectroscopy has proved to be a valuable tool in studying atomic size defects and their interactions in semiconductors. Most of the theoretical and experimental positron work has focused on Si, III-V and II-VI compounds [7,8]. Until now, to our knowledge, ternary systems like CuInSe<sub>2</sub>, CuInS<sub>2</sub>, AgInSe<sub>2</sub>, AgInS<sub>2</sub>, and AgGaS<sub>2</sub> are not investigated by this method.

### Crystal Growth and Experimental Procedure

Bulk Crystals were prepared by melting a mixture of the constituent elements (purity 99.999%). The charge was about 9 gm which was loaded into a cylindrical quartz ampoule of 18 mm diameter and 12 cm length. The ampoule was sealed under vacuum of 10<sup>-6</sup> Torr and then heated in a vertical furnace. The detailed thermal treatment will be described elsewhere [9]. The whole growing process took about 14 days to ensure crystals of highest quality. The grown ingot had a length of about 2 cm.

This ingot was cut into several disks, and the two faces of each disk were polished for energy dispersive X-ray (EDAX) analysis. The chemical composition of each disk was checked at several positions using a Philips 505 scanning electron microscope (SEM) equipped with an EDAX DX4 system comprising a Si(Li) detector. The quantification analysis was calibrated with high pure constituent elements as standards. It was found that the disk composition was homogeneous.

Powder diffraction data were collected with an automatic step-scan Siemens D-501 powder diffraction system. CuK<sub>α</sub> radiation was utilised. The divergence slits located in the incident beam were selected to ensure complete illumination of the specimen surface at 12° (2θ). The range of observation was 10° ≤ 2θ ≤ 120° with a step width of 0.02°. The counting time per step was 20 s. At the end of the data collection the stability of the intensity of the incident beam was checked by recording the first lines of the pattern. The error of 2θ was tested with single crystal silicon as a calibration sample. For the chalcopyrite structure the atomic positions with the atomic local symmetries for I-III-VI<sub>2</sub> are as follows (International Table for X-Ray Crystallography, 1983):

4	I	a	$\frac{1}{4}$	(0 0 0)	(0 1/2 1/4)
4	III	b	$\frac{1}{4}$	(0 0 1/2)	(0 1/4 3/4)
8	VI	d	2	(x 1/4 1/8)	( $\bar{x}$ 3/4 1/8) (3/4 x 7/8) (1/4 $\bar{x}$ 7/8)

The structure refinements have been done with the Rietveld profile program DBW3.2S [10]. The complete set of results for the best fit are given in Table 1, for more details see Ref. [11]. All of the samples showed a chalcopyrite structure without inclusions of any other binary or ternary second phases. Photoluminescence spectra (PL) of CuInSe<sub>2</sub> were obtained at temperatures between 5 K and 40 K by using a 514 nm Ar laser with 100 mW incident power. The signal was detected by a Ge detector.

**Table 1.** Compositions and crystallographic parameters of the compounds

Sample	I : III : VI Atom %	a (Å)	c (Å)	x
CuInS <sub>2</sub>	24.84 : 24.34 : 50.82	5.5219(2)	11.1330(1)	0.2298(2)
CuInSe <sub>2</sub>	25.31 : 25.72 : 48.97	5.7878(1)	11.6189(2)	0.2341(1)
AgInS <sub>2</sub>	25.61 : 25.13 : 49.26	5.8718(1)	11.2152(3)	0.2501(3)
AgInSe <sub>2</sub>	24.90 : 24.79 : 50.31	6.1041(1)	11.7075(3)	0.2566(5)
AgGaS <sub>2</sub>	24.75 : 25.09 : 50.16	5.7571(2)	10.3028(4)	0.2907(3)

For the positron lifetime and Doppler-broadening experiments two disks of each sample were used. Positron lifetime measurements were carried out with a fast-fast lifetime spectrometer with a time resolution of 190 ps (full width at half maximum, FWHM). The lifetime spectra were repeated four times, each spectrum containing 5×10<sup>6</sup> counts. After source corrections (to take into account

annihilations in the source supporting foil and the surface of the samples) the lifetime spectra were analysed with two exponential decay components [12]. The positron experiments were done in the temperature range from 10 K to room temperature. Doppler-broadening of the annihilation radiation line was recorded by a Ge detector with an energy resolution of 1.18 keV. The shape of the 511 keV annihilation line was characterised by the conventional  $S$  parameter. Doppler spectra were repeated ten times (each containing  $2.5 \times 10^6$  counts in the 511 keV energy range).

### Model calculations

The positron annihilation rate  $\lambda$ , which is the inverse of the positron lifetime, is proportional to the electron density at the site of the annihilation and can be calculated for the positron state  $\psi_+(\vec{r})$  as

$$\lambda = \pi r_0^2 c \int d\vec{r} |\psi_+(\vec{r})|^2 n_-(\vec{r}) \gamma(\vec{r}) \quad (1)$$

where  $r_0$  is the classical electron radius,  $c$  the speed of light,  $n_-$  the electron density and  $\gamma$  the enhancement factor of the electron density at the positron. It takes into account the electron-positron correlation effects. As far as only the positron annihilation rates are considered a non-self-consistent electron density is sufficient. This ensues from the fact that the positron lifetime is determined by the integral over the product of positron and electron densities. The positron density relaxes following electron charge transfer and therefore has the tendency to conserve the value of the overlap integral [13]. This property of the positron annihilation rate enables an efficient and practical method (superimposed atom method [14, 15]) to calculate positron states. It is based on the approximation of the host electron density by the superposition of free atoms. The positron annihilation characteristics were calculated for perfect CuInSe<sub>2</sub> and AgInSe<sub>2</sub>. The enhancement factor  $\gamma$  is calculated within the generalized gradient approximation (GGA) [16] scheme. A supercell geometry with periodic boundary conditions is used. The size of the supercell for the chalcopyrite structure studied is 64 atomic sites. In the case of ideal vacancies, one site is left unoccupied and the neighbouring ions are not allowed to relax from their ideal lattice positions. The differences in the electronic structure between the different charge states are not taken into account in the atomic-superposition method. However, it has been shown that the dependence of the positron lifetime on the charge state is quite small if the ionic relaxation is omitted (see Ref. 17). By sampling over two  $k$ -points ( $\Gamma$ -point and the corner points of the Brillouin zone) the dependence of the positron lifetimes in vacancies on the supercell size could be reduced [18].

### Results and Discussion

The calculated positron lifetimes are given in Table 2. According to the macroscopic cavity model the single vacancy is regarded as a macroscopic cavity of volume  $V_v = 4\pi/3 r_w^3$ , where  $r_w$  is the effective Wigner-Seitz radius of the missing atom [19,20]. Therefore, the volume of  $V_{Se}$  is equal to  $22.36 \text{ \AA}^3$  in both CuInSe<sub>2</sub> and AgInSe<sub>2</sub>. But, due to the different electronic environments the annihilation characteristics of the trapped positrons are different for CuInSe<sub>2</sub> and AgInSe<sub>2</sub>. In Figure 1 the calculated wave functions for a free positron and a positron trapped in a selenium vacancy for CuInSe<sub>2</sub> are shown. Measurements in the temperature range between 10 – 300 K did not show any remarkable changes in the positron parameters [21]. Figure 2 shows the measured PL spectrum of CuInSe<sub>2</sub>. The transitions at 0.937 eV and 0.918 eV are assigned to  $V_{Se} - Cu_{In}$  and  $V_{Se} - V_{Cu}$ , respectively, as suggested in [22]. The emission intensity decreases very rapidly with temperature. From the PL results there is evidence that the sample contains Selenium vacancies.

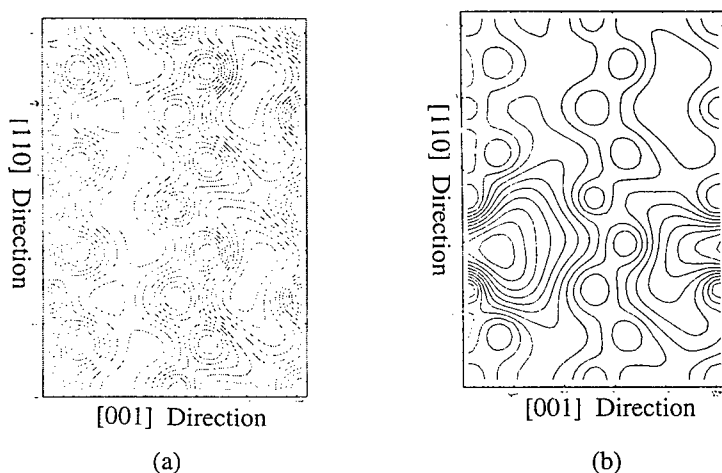


Figure 1. Positron wave function for CuInSe<sub>2</sub> (a) bulk (b) V<sub>Se</sub>

**Table 2.** Calculated positron lifetimes in bulk and the vacancy sites for CuInSe<sub>2</sub> and AgInSe<sub>2</sub>.  $\lambda_c$  is annihilation rate with core electrons,  $\lambda_v$  with valance electrons.

Sample	$\tau_b$ (ps)	V <sub>Se</sub> (ps)	$\lambda_c$ (ns <sup>-1</sup> )	$\lambda_v$ (ns <sup>-1</sup> )
CuInSe <sub>2</sub>	261.7	289.2	0.683	3.138
AgInSe <sub>2</sub>	286.3	315.2	0.683	2.811

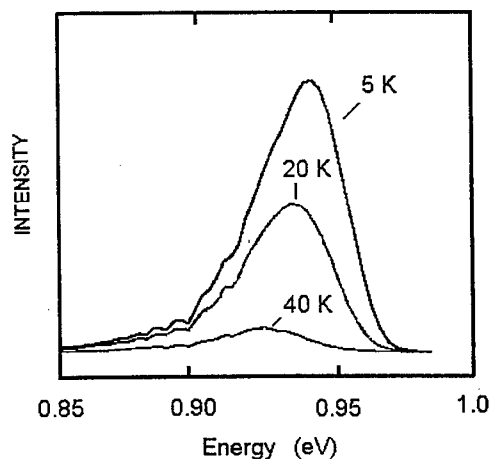


Figure 2. Photoluminescence spectra of CuInSe<sub>2</sub> for different temperatures

Groenink and Janse [23] have calculated the defect chemistry of a ternary compound of I-III-VI<sub>2</sub> type. According to their intrinsic defect model the ternary compounds are dominated by an acceptor-donor majority defect pair. The conditions for the existence of such a pair can be described by two parameters, called nonmolecularity  $\Delta m$  and nonstoichiometry  $\Delta s$ , as defined as

$$\Delta m = \frac{[I]}{[III]} - 1 \quad \text{and} \quad \Delta s = \frac{2 [VI]}{[I] + 3 [III]} - 1 \quad (2)$$

where [I], [III] and [VI] represent the total concentration of group I, III and VI atoms in the crystal, respectively. Among the lattice defects, some of them are more probable and stable than others. In Table 3 the values of  $\Delta m$  and  $\Delta s$  for different defects are summarised. The group VI element vacancies, for example, have a rather small energy of formation [24] and probably play an important role in the n-conductivity. On the other hand, the cationic sites act as negative charges and will be able to trap one (for  $V_{Cu}$ ) or several (for  $V_{In}$ ) holes [24].

**Table 3.** Composition conditions for the various defects [23].

Defect	$\Delta m$	$\Delta s$
$V_{VI}$ and antisite	$\geq 0$	$< 0$
$V_{III}$ and $VI_i$	$> 0$	$> 0$
$V_I$	$< 0$	$< 0$

In Table 4 the deduced defects together with the experimental positron lifetimes and intensities are shown. The ratio  $\tau_2/\tau_b$  is in the range 1.10 – 1.16 showing that the defects are of monovacancy-type [25]. The bulk lifetime is related to the volume of unit cell (Table 1) the vacancy lifetime, however, to the volume of cavity. The charge density surrounding the cavity is controlled by the anion displacement. The charge along the I-VI bond is generally more polarised towards the anion site than that along the III-VI bond [3,4]. The valence-electron contribution can thus explain most of the changes in the positron lifetime within the Cu-based and Ag-based compounds. The reduced electron density increases the positron lifetime in a vacancy. On the other hand, the anion displacement act on the S parameter, as can be seen Table 4.

**Table 4.** Decompositions of the lifetime spectra at 300 K and deduced defects

Sample	$\tau_1$ (ps)	$\tau_2$ (ps)	$I_2$ (%)	$\tau_b$ (ps)	S	Defect	Cavity volume ( $\text{\AA}^3$ )
CuInS <sub>2</sub>	168 (1)	289 (2)	87	264	0.4676 (2)	$V_{In}$	36.77
CuInSe <sub>2</sub>	160 (4)	294 (5)	87	265	0.4776 (6)	$V_{Se}$	22.36
AgGaS <sub>2</sub>	140 (1)	303 (2)	89	269	0.4646 (1)	$V_{Ag}$	44.11
AgInS <sub>2</sub>	186 (2)	276 (3)	68	238	0.4559 (2)	$V_S$	17.77
AgInSe <sub>2</sub>	203 (3)	323 (1)	77	284	0.4788 (2)	$V_{Se}$	22.36

## Conclusions

The intrinsic defect model, together with the positron lifetime measurements and theoretical calculations give evidence that in CuInSe<sub>2</sub> and AgInSe<sub>2</sub> the observed defects are selenium vacancies, in CuInS<sub>2</sub> indium vacancies, in AgGaS<sub>2</sub> silver vacancies and in AgInS<sub>2</sub> sulphur vacancies. Positron lifetime measurements in the temperature range between 10 and 300 K for CuInSe<sub>2</sub> and AgInSe<sub>2</sub> did not show any remarkable changes in the positron annihilation parameters showing that the vacancies are in the neutral charge state. It turns out that the defect lifetime component is related to the volume of the cavity.

### Acknowledgments

The authors would like to thank Dr. Sahar M. El-Khouly for advising in sample preparation, Dr. P. Poelt for carrying out the EDAX measurements, Dr. F. Mautner for X-ray investigations, and Dr. W. Heiss for the PL measurements.

### References

- \* On leave from Physics Department, Faculty of Science, Ain Shams University, Cairo, Egypt.
- 1. C. Schwab, Jpn. J. Appl. Phys. **19** (Suppl. **19-3**), 59 (1980).
- 2. K. Takarabe, K. Kawai, S. Minomura, T. Irie and M. Taniguchi, J. Appl. Phys. **71**, 441 (1992).
- 3. U. Kaufmann and J. Schneider, Festkörperprobleme **XIV**, 229 (1974).
- 4. J. E. Jaffe and A. Zunger, Phys. Rev. B **28**, 5822 (1983).
- 5. J. E. Jaffe and A. Zunger, Phys. Rev. B **29**, 1882 (1984).
- 6. L. L. Kazmerski, Jpn. J. Appl. Phys. **32** (Suppl. **32-3**), 25 (1993).
- 7. Dupasquier and A.P. Mills jr, Positron Spectroscopy of Solids (Amsterdam: IOS Press) (1995).
- 8. Y.-J. He, B.-S. Cao, and Y.C. Jean, Positron Annihilation, (Zürich: Trans Tech Publications) (1995).
- 9. M. Sherif Al-Kotb, W. Puff, to be published.
- 10. R. A. Young, A. Sakthivel, T. S. Moss and C. O. Paiva-Santos, J. Appl. Cryst. **28**, 366 (1995).
- 11. M. Sherif Al-kotb, W. Puff and R. Resel, to be published.
- 12. W. Puff, Computer Phys. Comm. **30**, 359 (1983).
- 13. M. Alatalo, B. Barbiellini, M. Hakala, H. Kauppinen, T. Korhonen, M. J. Puska, K. Saarinen, P. Hautojärvi, and R. M. Nieminen, Phys. Rev. B **54**, 2397 (1996).
- 14. K. Saarinen, P. Hautojärvi, and R. M. Nieminen, Phys. Rev. B **54**, 2397 (1996).
- 15. Barbiellini, M. J. Puska, T. Torsti and R. M. Nieminen, Phys. Rev. B **51**, 7341 (1995).
- 16. M. Hakala, *Masters Thesis*, Helsinki University of Technology (1996).
- 17. M. J. Puska, Phys. Status Solidi a **102**, 11 (1983).
- 18. M. J. Puska and R. M. Nieminen, J. Phys. F: Metal Phys. **13**, 333 (1983).
- 19. J. C. Phillips and J. A. Van Vechten, Phys Rev. Lett. **30**, 220(1973).
- 20. J. A. Van Vechten in Handbook of Semiconductors (ed. T. S. Moss), **3**, 1 (1980).
- 21. M. Sherif Al-Kotb, W. Puff and M. Mohsen, Mater. Sci. Forum (in press).
- 22. G. Dagan, F. Abou-Elfotouh, D. Dunlavy, R. J. Matson and D. Cahen, Chem. Mater. **2**, 286 (1990), and references cited in.
- 23. J. A. Groenink and P. H. Janse, Z. Phys. Chem. **110**, 17. (1978).
- 24. G. Messé, J. Appl. Phys. **68**, 2206 (1990).
- 25. S. Dannefaer, in Defects Control in Semiconductors, (ed. K. Sumino, North Holland), (1990).

## Magneto-optical characterization of $\text{CuIn}(\text{Ga})\text{Se}_2$

B.K. Meyer<sup>1</sup>, Mt. Wagner<sup>2</sup>, I. Dirnstorfer<sup>1</sup>, D.M. Hofmann<sup>1</sup>, F. Karg<sup>3</sup>,

<sup>1</sup> I. Physikalisches Institut, Justus-Liebig-Universität, Heinrich-Buff-Ring 16, D-35392 Gießen, Germany

<sup>2</sup> Department of Physics and Measurement Technology, Linköping University, S-581 83 Linköping, Sweden

<sup>3</sup> Siemens Solar GmbH, Postfach 460705, D-80807 München, Germany

Keywords: photovoltaic,  $\text{CuIn}(\text{Ga})\text{Se}_2$ , magneto-optic

### Abstract

We report on absorption and luminescence experiments under applied magnetic fields on Cu- and In-rich polycrystalline  $\text{CuIn}(\text{Ga})\text{Se}_2$  thin films. Making use of the selection rules of the absorbed polarized light we are able to identify the free exciton transition. We study its behavior as a function of the Cu/(In+Ga)-ratio (stoichiometry) and as a function of temperature to obtain the room temperature excitonic band gap. The two prominent donor acceptor pair transitions in Cu-rich films can clearly be distinguished by monitoring the degree of polarized emission in a magnetic field.

### 1. Introduction

Thin film solar cells made of  $\text{CuInSe}_2$  absorbers show efficiencies above 10 % when the Cu/In ratio is around 0.91, i.e. far away from stoichiometry. Stoichiometric and slightly Cu-rich

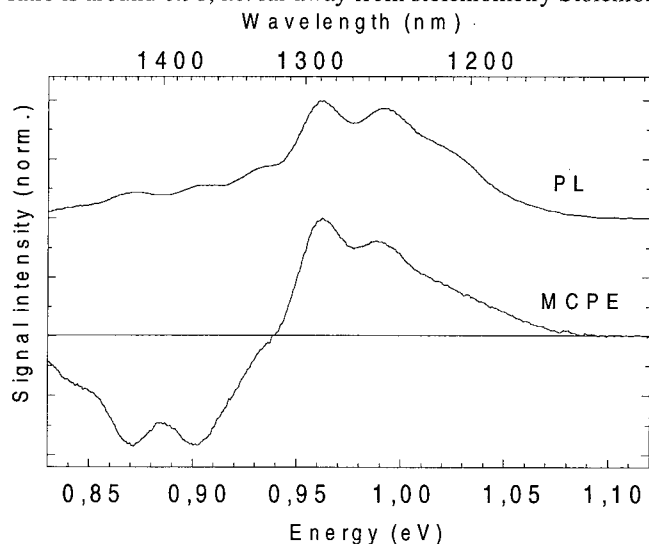


Fig.1. PL and MCPE-spectra of a nearly stoichiometric sample at 1.6 K and  $B=3$  T. All PL lines appear also in the MCPE-spectra, but the two transitions lowest in energy have an inverted sign.

polycrystalline layers produced in the rapid thermal processing technique [1] show pronounced donor acceptor pair recombination, however, almost no traces of free or impurity bound exciton radiative recombinations. In In-rich films rather broad single recombination lines are observable [4]. An important aspect is whether these rather large deviations from the nominal Cu/In ratio of 1 are accompanied by disorder, band tailing, secondary phases etc. and how much the intrinsic properties of  $\text{CuInSe}_2$  i.e. the band gap energy or exciton binding energies are changed. The absence of radiative excitonic recombinations made it necessary to use absorption experiments in the

presence of an external magnetic field. In this work MCD (magnetic circular dichroism) and MCPE (magnetic circular polarization of the emission) experiments were carried out.

## II. Experimental

Our setup consists of a helium bath cryostat with a superconducting magnet. Maximum magnetic field is 4 T and the coils are arranged in a way as to permit optical access along the magnetic field direction. By pumping on the sample chamber temperatures down to 1.6 K can be achieved. For photoluminescence (PL) excitation and the MCPE experiments we used the 488 nm line of an Ar<sup>+</sup>-laser, the light source in optical absorption and in the MCD experiments was a halogen lamp in connection with a SPEX 0.2 m monochromator. The same monochromator was also used for scanning the luminescence intensity in PL and MCPE. The signals were detected with a liquid nitrogen cooled Germanium detector (model North Coast).

## III. Experimental results

### A. Photoluminescence and magnetic circular polarized emission

In a magnetic field the spin substates of e.g. a defect level split and radiative transitions along the magnetic field axis are then sensitive to the polarization of the light. In the experimental technique of Magnetic Circular Polarization of the Emission (MCPE) one measures the difference in

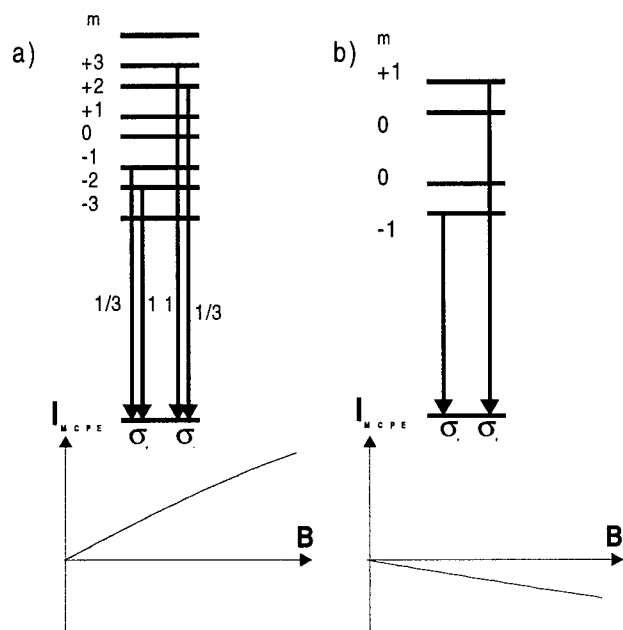


**Fig.2.** Magnetic sublevels of the combined donor-acceptor-state in a magnetic field when a) an effective mass acceptor with  $J=3/2$  and b) a semi-deep acceptor with  $J=1/2$  is assumed. The dependence of the MCPE-signals on the magnetic field is shown in the lower part.

We assume the shallower one is effective-mass like and the other one semi-deep. With this assumption the different signs in MCPE can be explained as follows:

the luminescence intensity of right- and left-circularly polarized light. For that purpose a quartz polarizer is inserted into the light beam which is modulated with a frequency of 50 kHz and which alternatively transmits right- and left-circularly polarized photons.

In fig. 1 is shown a typical PL spectrum of Cu-rich CuIn(Ga)Se<sub>2</sub> thin films together with the MCPE-signal recorded at a magnetic field of 3 T. It is apparent that all the PL lines also appear in the MCPE spectrum. But a striking feature of the MCPE curve is that the signals of the two transitions lowest in energy have an inverted sign compared to the two high energy lines. Both lines at 0.96 eV and at 0.90 eV are due to donor-acceptor-Pair (DAP) transitions, each followed by phonon replicas [2]. Our MCPE results now confirm that two different acceptors are indeed involved in these two transitions.

We assume the shallower one is



Consider first the case of an effective-mass acceptor. After photo-excitation the electrons are captured at the donors and the holes at the acceptors. The ground state of the donor (occupied by one electron) has  $J=S=1/2$  whereas the hole at the acceptor has  $J=S=3/2$ . The magnetic sublevels of the combined donor-acceptor-state in a magnetic field are shown in fig. 2.a. After recombination of the carriers the total angular momentum is zero. The allowed radiative transitions ( $\Delta m_j = \pm 1$ ) are indicated in fig. 2.a as arrows together with the relative transition probabilities [3]. To calculate the MCPE intensity one has to know the population probabilities on the different sublevels which we assume follows a Boltzmann distribution. For the holes the highest lying level is most strongly populated, for the electrons it is the lowest lying one. The calculated MCPE intensity is then

$$I_{MCPE} = N_e N_h \frac{3\exp(g_e X) + \exp(g_h X) - 3\exp(3g_h X) - \exp((g_e + g_h)X)}{3(1 + \exp(g_e X))(1 + \exp(g_h X) + \exp(2g_h X) + \exp(3g_h X))}$$

where  $N_e$  and  $N_h$  are the total number of electrons and holes in the donor- and acceptor-levels respectively,  $g_e$  and  $g_h$  their g-factors (which are unknown) and  $X = \mu_B B/kT$ .  $B$  is the magnetic field strength,  $T$  the temperature,  $k$  is the Boltzmann constant and  $\mu_B$  is the Bohr magneton. The resulting dependence of the MCPE intensity on the magnetic field is shown in the lower part of fig. 2.

Now consider the case when the involved acceptor is semi-deep. Then the orbital angular momentum of the hole is quenched and the total angular momentum in the ground state is  $J=S=1/2$ . In that case the splitting scheme of the combined donor-acceptor-state is simpler (fig. 2.b). Again assuming a Boltzmann distribution in the sublevels the calculated MCPE intensity is

$$I_{MCPE} = N'_e N'_h \left[ \frac{1}{(1 + \exp(g_e X))(1 + \exp(-g_h X))} - \frac{1}{(1 + \exp(-g_e X))(1 + \exp(g_h X))} \right]$$

Using the same parameters as above the magnetic field dependence of the signal looks as shown in fig. 2. The sign of the MCPE in the latter case is opposite to the one obtained for an effective-mass type acceptor.

### B. Absorption and magnetic circular dichroism

The method of the Magnetic Circular Dichroism of the Absorption (MCD) is closely related to the method of MCPE described above. The basic setup is that of an absorption measurement. In addition a magnetic field parallel to the light beam is applied. Again the modulated quartz polarizer is inserted into the beam, and the difference in absorption of left- and right-circularly polarized light is measured. The strength of the MCD is defined as

$$I_{MCD} = (T_r - T_l) / (T_r + T_l)$$

where  $T_r$  and  $T_l$  are the transmitted intensities of right- and left-circularly polarized light, respectively.

In an applied magnetic field the spin 1 state splits into the three sublevels according to the different magnetic quantum numbers  $m_j$ . Absorption of left- and right-circularly polarized photons occurs now at slightly different energies. The point where the MCD signal is zero between the two extrema gives the energetic position of the involved excited state.

In fig. 3. the MCD signal at  $B=2$  T of a slightly In-rich  $\text{Cu(In,Ga)Se}_2$  thin film is shown together

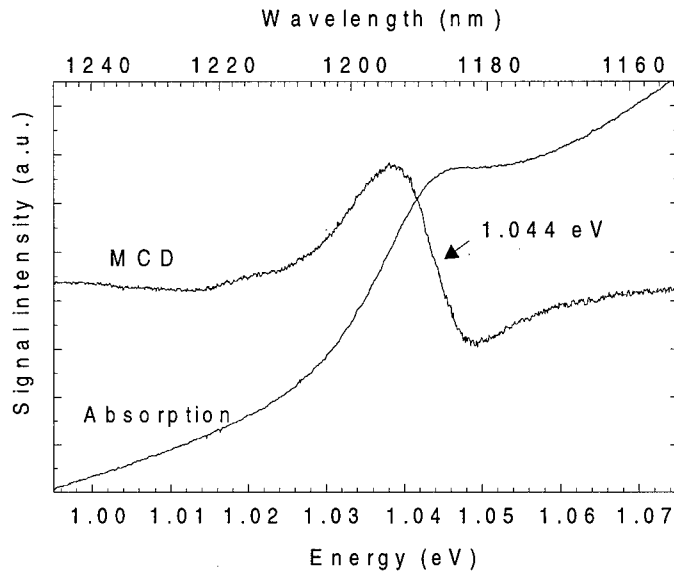


Fig. 3. Absorption and MCD-spectra of a slightly In-rich sample at 1.8 K. The free exciton at 1.044 eV can be detected as a relatively broad peak in absorption and as a derivative structure in MCD which is much better pronounced.

constant for which we took 13.6 [6]. Inserting the parameters we get  $E_B \sim 6$  meV and  $E_{gap} \sim 1.050$  eV at low temperatures. As can be seen in fig. 4, the excitonic band gap increases slightly up to 100 K and afterwards shrinks up to RT with a slope of 7 meV/ 100 K. The RT band gap of

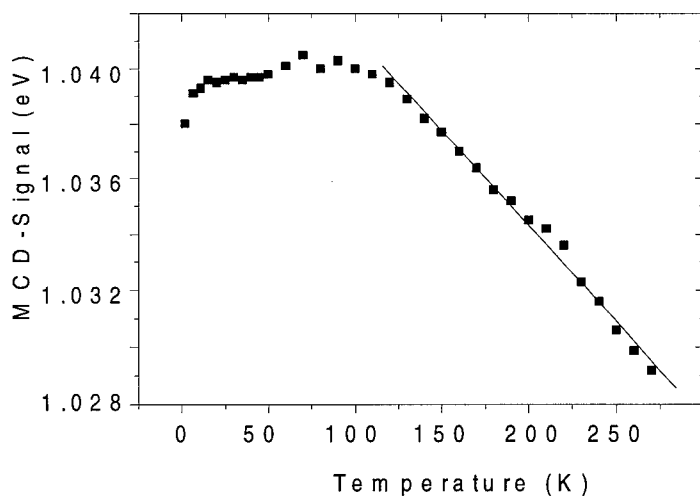


Fig.4. Dependence of the excitonic energy determined with MCD on the temperature. Above 100 K the excitonic band gap decreases with a slope of 7 meV/100 K.

with the absorption curve. The free exciton structure is visible already in absorption, but it is not very well resolved. In contrast the MCD signal which is not influenced by the background absorption is very pronounced. The energetic position of the free exciton can be determined very precisely to be 1.044 eV.

At low temperatures the band gap can be calculated by adding the binding energy of the free exciton to its energetic position. The binding energy  $E_B$  is found to be

$$E_B = 13.6 \cdot \frac{\mu}{\epsilon^2} \text{ eV}$$

where  $\mu$  is the exciton mass and  $\epsilon$  the dielectric constant for which we took 13.6 [6]. Inserting the parameters we get  $E_B \sim 6$  meV and  $E_{gap} \sim 1.050$  eV at low temperatures. As can be seen in fig. 4, the excitonic band gap increases slightly up to 100 K and afterwards shrinks up to RT with a slope of 7 meV/ 100 K. The RT band gap of  $\text{CuInSe}_2$  can be estimated to be 1.035 eV.

The optical properties of  $\text{CuIn(Ga)Se}_2$  thin films change drastically when the layers are grown with an increasing excess of indium. As has been reported before photoluminescence (PL) detects relatively sharp and well resolved lines for Cu-rich layers and only one very broad band for In-rich films [4]. Correspondingly the absorption edges become more and more smeared out as one turns from the Cu-rich to the In-rich side. We performed MCD measurements on sam-

ples with varying Cu/(In+Ga)-ratios and within experimental error obtained for all films the same MCD signal and spectral dependence.

#### IV. Conclusion

We studied the free exciton properties in Cu- and In-rich polycrystalline CuIn(Ga)Se<sub>2</sub> thin films with the use of the magnetic circular dichroism of absorption. Its energetic position at 1.044 eV at low temperatures does not depend on the stoichiometry of the films. Above 100 K the excitonic band gap decreases with a slope of 7 meV/100 K and allows for an estimate of the room temperature band gap of CuInSe<sub>2</sub>. It is 1.035 eV. The two dominant donor acceptor pair transitions in Cu-rich CuInSe<sub>2</sub> films are studied by the magnetic circular polarized emission technique. They differ in the sign of polarization, which can be explained under the assumption that the shallower acceptor behaves effective-mass like ( $J=3/2$ ) whereas for the deeper one the orbital momentum of the hole is quenched ( $J=1/2$ ).

#### References

- [1] F. Karg, V. Probst, H. Harms, J. Rimmasch, W. Riedl, J. Kotschy, J. Holz, R. Treichler, O. Eibl, A. Mitwaisky and A. Kiendl, *proc. of 23<sup>rd</sup> IEEE*, 441 (1993)
- [2] Mt. Wagner, I. Dirnstorfer, D.M. Hofmann, M.D. Lampert, F. Karg and B.K. Meyer, to be published
- [3] D.G. Thomas, J.J. Hopfield and W.M. Augustynaik, *Phys. Rev.* 140, A 202 (1965)
- [4] I. Dirnstorfer, Mt. Wagner, D.M. Hofmann, M.D. Lampert, F. Karg and B.K. Meyer, to be published
- [5] C. Lárez, C. Bellabarba and C. Rincón, *Appl. Phys. Lett.* 65(13), 1650 (1994)
- [6] A. Rockett and R.W. Birkmire, *J. Appl. Phys.*, 70(7), R81 (1991)

## DEFECTS SPECTROSCOPY IN $\beta$ -Ga<sub>2</sub>O<sub>3</sub>

**B.K. Meyer, U. Leib, A. Hofstaetter, C. Krummel\*, D. Kohl\***

**1. Physics Institute, Justus-Liebig University Giessen, 35392 Giessen, Germany**

**\*Applied Physics Institute, Justus-Liebig University Giessen, 35392 Giessen, Germany**

**Key words:**  $\beta$ -Ga<sub>2</sub>O<sub>3</sub>, magnetic resonance, vacancy, transition metals

We report on electron paramagnetic resonance (EPR) investigations of  $\beta$ -Ga<sub>2</sub>O<sub>3</sub> single crystals which behave under suitable preparation conditions insulating or conducting. We identify as trace impurities Iron, Chromium and Titanium in the 3+ charge states. The EPR of the shallow donor which in conducting crystals exhibits properties of electrons in the conduction band is studied in detail. Its linewidth is independent of temperature from 4.2 to room temperature. The resonance position depends however on temperature, but can be explained by a nuclear hyperfine interaction due to the Overhauser effect.

### Introduction

Gallium oxide  $\beta$ -Ga<sub>2</sub>O<sub>3</sub> is a wide band gap semiconductor with a band gap of 4.7 eV at room temperature [1]. It exhibits interesting intrinsic properties with applications in dielectrics, especially important is here the oxide layer on GaAs, and as gaseous sensors [2] where Ga<sub>2</sub>O<sub>3</sub> competes with ZnO and SnO<sub>2</sub>. Its conductivity has to be controlled in order to form metal (e.g. Pt) oxide semiconductor sensors. However, depending on growth conditions Gallium oxide can be an insulator or semiconductor. Growing under oxidizing conditions results in insulating crystals while crystals grown under reducing conditions are conducting. Its n-type conduction is thought to be controlled by oxygen vacancies according to the earliest reports [3]. They should act as shallow donors with binding energies around 30 meV. There are reports of EPR on transition metal impurities [4-7].

Recently Gourier et al [8] demonstrated a bistable Overhauser effect on the conduction band spin resonance (CESR) of oxygen deficient Ga<sub>2</sub>O<sub>3</sub>. It is observable from 4.2 K up to room temperature. For these investigations free electron concentrations around  $10^{19}$  cm<sup>-3</sup> were necessary. Binet et al [9] studied by EPR and ENDOR Ti in the 3+ charge state. No CESR was seen in these Ti doped crystals and they explained this observation by the efficient trapping of electrons at Ti<sup>4+</sup>. In our investigations we were able to observe the shallow donor resonance as well as the CESR in crystals prepared under oxidizing resp. reducing conditions.

### Experimental

We used a BRUKER EPR spectrometer (ESP300E) at X-band frequencies equipped with a continuous flow cryostat (OXFORD) for the temperature range from 4.2 to 300 K. Fig.1. gives an overview of the EPR signals seen in an insulating crystal.

As trace impurities we identify iron and chromium in the 3+ charge states. In addition a slightly anisotropic signal is seen by EPR around  $g=1.95$  which shows partially resolved ligand hyperfine (lhf) structure. From ENDOR we can demonstrate that the lhf arises from next nearest neighbor

Gallium nuclei in distorted tetrahedral and octahedral coordination (the crystal structure is monoclinic C2/m). The defect with  $S=1/2$  has the same  $g$ -values as reported by Binet et al [9] for  $Ti^{3+}$ . Indeed the presence of Ti was confirmed by SIMS on our nominally undoped crystals. Ti resides in the Gallium sublattice.

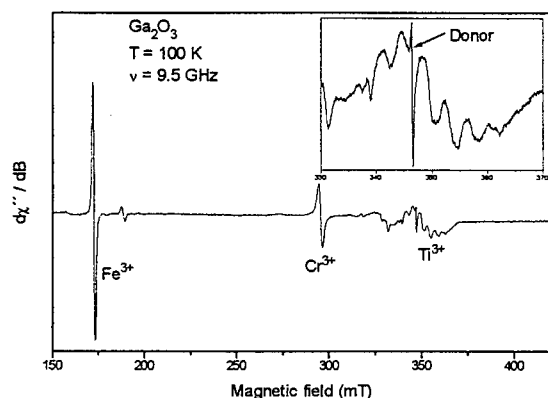


Fig. 1: EPR spectrum of a non conducting  $\beta$ - $Ga_2O_3$  crystal showing the presence of  $Fe^{3+}$ ,  $Cr^{3+}$  and  $Ti^{3+}$ . In the inset details of the  $Ti^{3+}$  and of the shallow donor signal are seen.

At low temperatures there is hardly any signal from the shallow donors nor from the electrons in the conduction band. The many line spectrum arises from  $Ti^{3+}$  and will not be discussed further. For more details see ref. [9]. However, at elevated temperatures one notes the appearance of a single Gaussian line (see Fig. 2.a) which is dominating at room temperature.

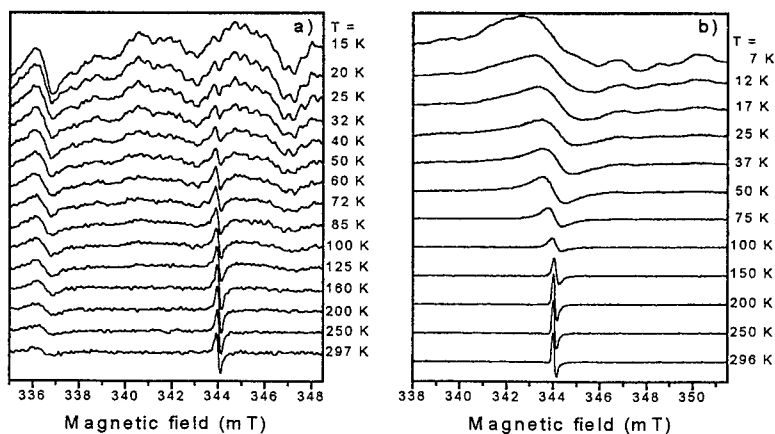


Fig. 2: Temperature dependence of the EPR (a) for a nonconducting and (b) for a conducting Gallium oxide crystal

Its intensity increase is thermally activated with two activation energies, at lower temperatures  $E_{a1}$  is  $\approx 1.8$  meV, between 100 and 300K the activation energy  $E_{a2}$  is  $\approx 7.3$  meV. One notes a slight shift

of the resonance position to high field values as the temperature is increased (see Fig.3). The line width is  $(2 \pm 0.4)$  G and shows no broadening over the complete temperature range. From the angular dependence one obtains the room temperature components of the g-tensor:  $g_x=1.9590$ ,  $g_y=1.9616$  and  $g_z=1.9635$  in agreement with Binet et al [9] which attribute this signal to the CESR, i.e. delocalized electrons.

The conducting crystals behaved completely different (see Fig.2.b). At low temperatures only an approx. 35 G broad feature is seen at the resonance position of the donor. This signal sharpens and at 100 K the line width has decreased already by a factor of 10. At room temperature the line width is 2 G, the line shows a pronounced asymmetry typically for a Dysonian indicating contributions from dispersion and absorption. By scaling the line shape according to the width of the line one finds that this Dysonian line shape exists from low to high temperatures. The integrated EPR intensity when correcting for the Boltzmann factor shows again thermally activated behavior however this time the intensity decreases from 4.2 K to approx. 50 K with an activation energy of  $\approx 1.3$  meV and from 50 K to room temperature with an activation energy of  $\approx 7.5$  meV.

The resonance position also depends on temperature as is shown in Fig.3. In this case the resonance position shifts from higher magnetic fields to lower magnetic fields. The anisotropy of the lines is identical over this temperature range within experimental error.

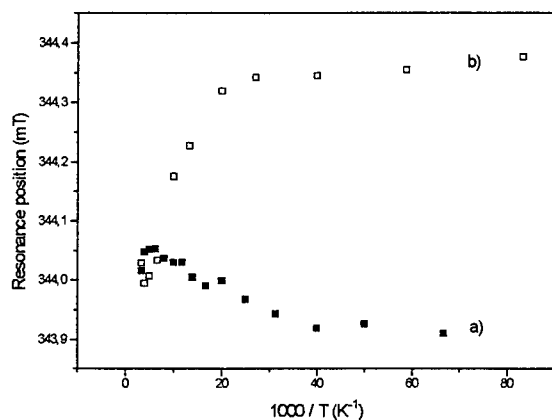


Fig.3: Dependence of the line position of the donor (a) and electron in conduction band (b) resonance on temperature

### Discussion

The crystal structure of  $\beta$ -Ga<sub>2</sub>O<sub>3</sub> is monoclinic with the space group C2/m and the lattice parameters  $a=12.23$  Å,  $b=3.04$  Å and  $c=5.8$  Å and  $\beta=103.7^\circ$  [9]. The Gallium atoms are tetrahedrally and octahedrally coordinated. In an extended Hueckel calculation Binet et al [9] concluded that the conduction band is strongly anisotropic and conduction electrons at the conduction band edge would be much more delocalized along **b** than perpendicular to this direction. Indeed the deviation of the donor g-value from the free electron value as well as its anisotropy can be understood from the bandstructure parameters. As, however, details of the valence as well as the conduction bands are hardly determined, we do not intend to go into a detailed **k**·**p** calculation procedure as has been done for other semiconductors [10]. We can compare with other wide bandgap semiconductors such as GaN and ZnO [11]. Both commonly

crystallize in the wurtzite structure and the valence band is splitted into light, heavy and spin orbit split hole states by a combined interaction of crystal field and spin orbit interaction. For both compounds the spin orbit splittings are small of the order of 5-10 meV. This will probably hold for  $\text{Ga}_2\text{O}_3$  too. Due to the axial symmetry in GaN and ZnO we have two components (parallel and perpendicular to the c-axis of the crystals) for the g-values of the donors, the anisotropy is small and the mean g-values are 1.95 and 1.96 for GaN and ZnO, respectively. The deviation from the free electron g-value of 2.0023 is explained within the **k-p** approach by a coupling of the valence band with the conduction band. The relevant parameters which enter are: band gap energy, spin orbit splitting energy and the interband matrix element. Certainly the band gap of  $\text{Ga}_2\text{O}_3$  is higher as compared to ZnO (3.3 eV at 4.2 K) and GaN (3.5 eV at 4.2 K) but one can nicely compare with  $\text{Al}_x\text{Ga}_{1-x}\text{N}$  alloys which span the band gap from 3.5 eV ( $x=0$ ) up to 6.2 eV ( $x=1$ ). There are now data available of EPR on the shallow donors in  $\text{Al}_x\text{Ga}_{1-x}\text{N}$  which demonstrate the shift from  $g=1.95$  (GaN) to  $g=1.96$  ( $\text{Al}_x\text{Ga}_{1-x}\text{N}$  with  $x=0.26$ ) [12]. For this composition the energy gap is around 4.3 eV thus not far away from Gallium oxide. Hence one can understand the g-value within the standard **k-p** approach, the lower crystal symmetry leads to the three components in the g-tensor instead of two for wurtzite ZnO and GaN.

The donor binding energy has been inferred from Hall effect measurements [3] but only an approximate value was given. From the temperature dependence of the Hall effect and the resistivity an activation energy of 0.02 to 0.03 eV was obtained [3]. This is the order of magnitude one would also calculate from an effective mass theory model. The binding energy in cubic symmetry neglecting anisotropies in the electron effective mass and the dielectric constant is

$$E_b = 13.58 m_e^* / \epsilon^2 \text{ in eV}$$

The parameters found [9] for  $\text{Ga}_2\text{O}_3$  are:  $m_e^* = 0.3 m_0$  and  $\epsilon=8.3$ . This gives for the binding energy a value of 58 meV in reasonable agreement with the Hall data where details about the electrical properties (compensated, uncompensated) were not specified. With such an energy depth one expects the semiconducting to metallic behavior (Mott transition) to occur for concentrations above  $10^{19} \text{ cm}^{-3}$  as evidenced from the CESR experiments in ref. [8]. In the case of low doping and/or partial compensation the EPR observation of the shallow donor depends on the position of the Fermi level. For the non conducting crystals the number of donors as measured by EPR was approx. a factor of 20 lower, thus in the mid  $10^{17} \text{ cm}^{-3}$  range. With a binding energy of 58 meV one expects that a substantial fraction of the donors will not be ionized at RT (having in mind that  $kT$  at room temperature is 26 meV) and the donor resonance should persist up to room temperature with a marginal decrease in intensity. The first item is observed, the second one not, since instead of a slight decrease a thermally activated increase is found.

The next point we address is the shift of the line position of the donor resonance in non conducting crystals. We noticed that the resonance position is temperature dependent (see Fig.3) and for clarity this effect is shown in Fig.4 on an expanded scale. The field difference between 4.2 K and RT is approx. 1.7 G and we attribute this shift to the Overhauser effect. It is given by

$$B_n = A/g^* \mu_B \langle I_z \rangle \quad (1)$$

where  $A$  is the isotropic Fermi contact interaction,  $g^*$  is the donor g-value,  $\mu_B$  is Bohr's Magnetron and  $\langle I_z \rangle$  is the ensemble average of the nuclear polarization for each nucleus.

$$\langle I_z \rangle = \hbar \gamma_n I(I+1)/3kT \quad (2)$$

The electron spin thus feels an effective field  $B_{\text{eff}}$

$$B_{\text{eff}} = B_0 + B_n \quad (3)$$

where  $B_0$  is the external magnetic field. The Gallium nuclei (nuclear spin  $I=3/2$ ) have together 100% abundance in contrast to the oxygen nuclei ( $I=0$ , 99.96 %) and the hyperfine interactions will almost completely be caused by Gallium nuclei.

The shift in resonance position as inferred from eq.2 is given by  $B/T$  and this is indeed observed as shown in Fig.4. The intercept at the magnetic field axis gives the resonance position in the absence of nuclear effects. We also note that the  $g$ -anisotropy is identical for low and high temperatures apart from the offset in  $B_n$ .

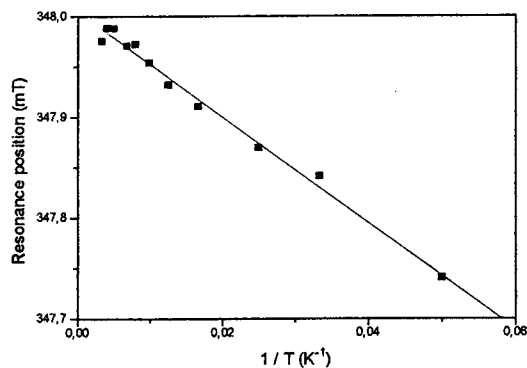


Fig.4: The resonance position of the shallow donor as a function of the inverse temperature showing the influence of the Overhauser effect.

The behavior of the donor/electron in conduction band resonance in conducting crystals is, however, puzzling. With increasing temperature the  $g$ -value tends towards the free electron  $g$ -value (see Fig.5). This behavior cannot be explained by the Overhauser effect. An explanation has to be searched by taking into account that EPR detects the carriers not at the bottom of the conduction band. Due to the high carrier concentration the Fermi level is in the conduction band and the electrons have excess kinetic energy  $E$ . The  $g$ -value will be energy dependent [13]

$$g^*(E) = g_0 + \beta E \quad (4)$$

where  $\beta$  is a constant to be determined from experiment. For the kinetic energy of the electrons one assumes a Maxwell Boltzmann distribution and one introduces an average  $g$ -factor [14]:

$$\langle g^* \rangle = \frac{\int_0^\infty g^*(E) D^{3D}(E) \exp(-E/k_B T) dE}{\int_0^\infty D^{3D}(E) \exp(-E/k_B T) dE} \quad (5) \quad \text{with} \quad D^{3D}(E) = \frac{1}{2\pi^2} \left( \frac{2m^*}{\hbar^2} \right)^{3/2} E^{1/2} \quad (6)$$

Our calculation shows that one obtains a linear dependence (see Fig.5) over a wide temperature range. The constant  $\beta$  is 0.11. This is a very reasonable value in view of the large electron effective mass. Further details will be published elsewhere [15]. Deviations at higher temperatures are at present not understood, whether the temperature dependent changes in the conduction and valence bands are responsible has to be clarified in future experiments.



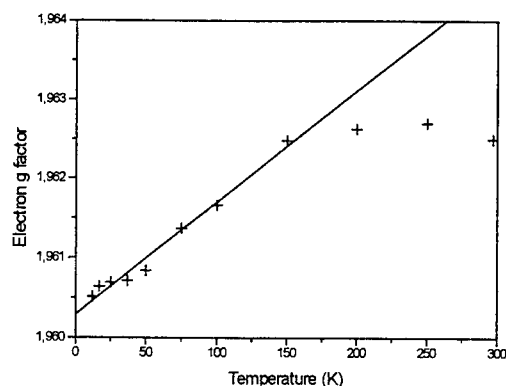


Fig.5: Temperature dependence of the g-factor of the electron in conduction band resonance. The drawn line is fit using eq.4.

### Conclusion

EPR shows the presence of shallow donors and electrons in the conduction band in  $\beta$ -Ga<sub>2</sub>O<sub>3</sub> depending whether the bulk crystals are non conducting or conducting. The properties of the shallow donor resonance are influenced by the Overhauser effect. Although the fundamental band structure parameters are not very well established by a comparison with other wide band gap semiconductors reasonable understanding can be achieved with respect to the shift of g-factor from the free electron value. In the conducting crystals the resonance position as a function of temperature is influenced by the kinetic energy of the carriers in the conduction band giving rise to an energy dependent g-factor.

### References

- [1] H.H. Tippins, Phys. Rev. 140, 316 (1965)
- [2] T. Hofmann, P. Schieberle, C. Krummel, A. Freiling, J. Bock, L. Heinert and D. Kohl, Sensors and Actuators, to be published
- [3] M.R. Lorenz, J.F. Woods and R.J. Gambino, J. Phys. Chem. Solids 28, 403 (1967)
- [4] F. Gesmundo and C. De Asmundis, J. Phys. Chem. Solids 34, 1757 (1973)
- [5] W. Gunsser and K. Rohwer, Phys. Stat. Sol. b 116, 275 (1983)
- [6] R. Büscher and G. Lehmann, Z. Naturforsch. 42a, 67 (1987)
- [7] G. Harms, Diploma thesis, Hamburg (1975)
- [8] D. Gourier, E. Aubay and J. Guglielmi, Phys. Rev. B50, 2941 (1994)
- [9] L. Binet, D. Gourier and C. Minot, J. Solid State Chemistry 113, 420 (1994)
- [10] C. Hermann and C. Weisbuch, Phys. Rev. B15, 816 (1977)
- [11] W.E. Carlos, J.A. Freitags Jr., M. Asif Kahn, D.T. Olson and J. N. Kuznia, Phys. Rev. B48, 17887 (1993)
- [12] W.E. Carlos, private communication and to be published
- [13] M.Y. Yang, R.J. Wagner, B. V. Shanabrook, J.R. Waterman and W.J. Moore, Phys. Rev. B47, 6807 (1993)
- [14] M. Oestreich, S. Hallstein, A.P. Heberle, K. Eberl, E. Bauser and W.W. Rühle, Phys. Rev. B53, 7911 (1996)
- [15] B.K. Meyer, A. Hofstaetter, C. Krummel and D. Kohl, to be published

## BISTABILITY OF OXYGEN VACANCY IN SILICON DIOXIDE

Atsushi Oshiyama  
Institute of Physics, University of Tsukuba  
Tennodai, Tsukuba 305, Japan

**Keywords :** SiO<sub>2</sub>, oxygen vacancy, bistability, negative-U, LDA

**Abstract.** I report total-energy electronic-structure calculations within the local density approximation in density functional theory performed for oxygen vacancy V in  $\alpha$ -quartz. I find (i) that the O vacancy has a variety of charge states from V<sup>++</sup> to V<sup>-</sup> depending on the location of the electron chemical potential in the energy gap, (ii) that for V<sup>0</sup> and V<sup>+</sup>, the O vacancy shows structural bistability, and (iii) that a set of charge states { V<sup>++</sup>, V<sup>+</sup>, V<sup>0</sup> } is an effective negative-U system which is accompanied by a charge-state dependent structural transformation.

### Introduction.

SiO<sub>2</sub> that is easily formed by Si oxidation is an important material in semiconductor technology, working as a high quality insulator in devices. With decreasing oxide thickness, however, degradation of the insulating properties has been observed and may be related to defects in SiO<sub>2</sub> [1]. More fundamentally, SiO<sub>2</sub> is a unique material with characteristics of covalency and ionicity: A Si atom is tetrahedrally bonded to nearest four O atoms ( sp<sup>3</sup> hybridization ) whereas electrons are distributed in vicinity of O atoms rather than Si atoms. This feature is common to most polymorphs of SiO<sub>2</sub> [2] and is preserved even in vitreous SiO<sub>2</sub> [3]. Properties of defects in this ambivalent material are certainly of interest.

A prototype intrinsic defect in SiO<sub>2</sub> is the E<sub>1</sub>' center that is observed by electron-spin-resonance and optical absorption measurements in  $\alpha$ -quartz upon irradiation [4, 5]. Based on cluster calculations, Fowler and his collaborators [6] proposed that the positively charged oxygen vacancy is the E<sub>1</sub>' center: The two Si atoms neighboring to the O vacancy are relaxed asymmetrically leaving a single electron in one of the dangling bonds. Subsequent cluster calculations [7] and a first-principle calculation [8] suggest that there is a structural bistability in oxygen vacancy: In one configuration the two Si atoms neighboring to the O vacancy are relaxed to be closer forming a bond ( a dimer configuration ) and in the other configuration one of the two Si is relaxed largely toward interstitial region forming a bond with another O atom ( a puckered configuration ). This bistability is corroborated by recent local spin density calculations performed for neutral and positively charged oxygen vacancy [9].

I here present total-energy electronic-structure calculations within the local density approximation (LDA) performed for oxygen vacancy in  $\alpha$ -quartz. It is found that the structural bistability exists for neutral and positively charged states but that for a doubly positively charged state the dimer configuration becomes *unstable* and thus spontaneously transforms to the puckered configuration. It is also found that the three charge states { V<sup>++</sup>, V<sup>+</sup>, V<sup>0</sup> } of the O vacancy constitute a *negative U* system in the sense that the

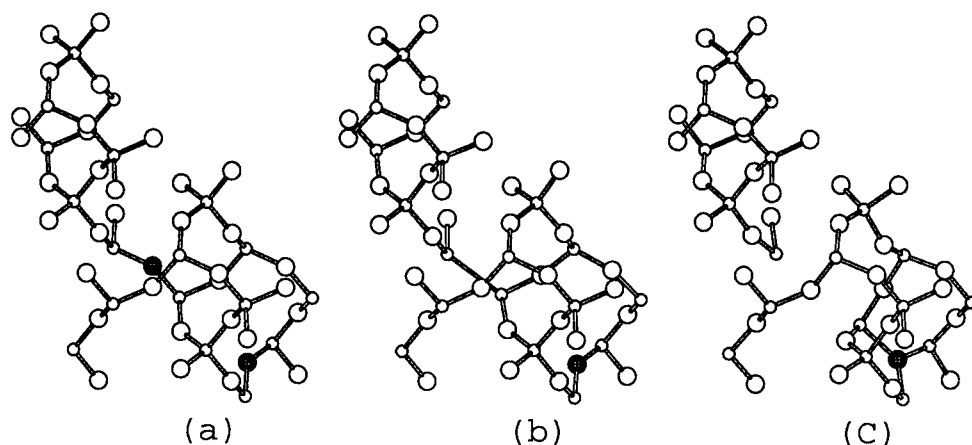


Figure 1: Stable dimer configuration and puckered configuration for the neutral O vacancy. Small and large circles represent Si and O atoms, respectively. (a) crystalline  $\alpha$ -quartz. A meshed circle in the central region represents an O atom which is removed to generate the O vacancy. Another meshed circle in right lower area is the back O atom. (b) the dimer configuration of the O vacancy. (c) the puckered configuration of the O vacancy.

positively charged state  $V^+$  is metastable for electron chemical potential at any position in the energy gap.

#### Calculation.

All calculations have been performed by use of norm-conserving pseudopotentials [10], LDA [11] for exchange correlation energy, and conjugate-gradient minimization technique as reported elsewhere [12]. The O pseudopotential used here has  $s$  nonlocality while the Si pseudopotential has  $s$  and  $p$  nonlocality. The plane-wave basis set with the energy cutoff of 60 Ry is necessary to reproduce structural properties of  $\alpha$ -quartz. The defect in an otherwise perfect crystal is simulated by a supercell model which contains 53 atoms plus a vacant site in a cell and is of triclinic symmetry. A special  $k$  point is used for integration over Brillouin zone. Geometry optimization has been performed for all atoms, and in the optimized geometries the remaining forces acting on the atoms are less than 0.005 Ry/ $\text{\AA}$ .

#### Dimer configuration vs puckered configuration.

Let us start with a neutral charge state. Fig.1(b) shows the stablest dimer configuration of the O vacancy. The neighboring 2 Si atoms are relaxed toward each other forming a bond. The Si-Si distance is 2.47  $\text{\AA}$ , 5% longer than the bulk distance in Si crystal. The calculated formation energy is 6.6 eV [13]. In this configuration, a deep level appears at 0.6 eV above the valence band top. This is a bonding state of the two dangling bonds of the neighboring Si atoms and accommodates 2 electrons, whereas the antibonding state

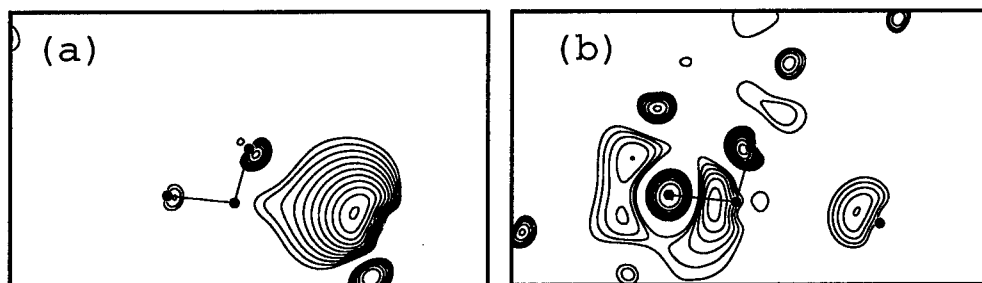


Figure 2: Contour plot of the squared wavefunctions of the deep-level states induced by the neutral O vacancy in the puckered configuration. Dots represent atoms on this plane: the displaced Si atom ( in central region ), the back O atom ( leftmost ), and another O atom. The rightmost dot represents the Si atom neighboring to the vacant site ( This atom is not on this plane, 0.09 Å off. ). (a) The deep-level state located at 3.0 eV above the valence band top. (b) The deep-level state at about 1.5 eV below the conduction band bottom.

is located in the conduction bands. ( In the present LDA calculations, the energy gap of  $\alpha$ -quartz is 6.0 eV, about 20 % narrower than the experimental gap so that the deep level position is of qualitative meaning. Yet the character of the level is well identified from analyses of its wavefunction).

The puckered configuration shown in Fig.1(c) is also stable. In the configuration one of the two Si atoms neighboring to the O vacancy undergoes large displacement along the direction reverse to the O vacancy and finally forms a bond with a back O atom. As a result of this relaxation, the Si recovers the fourfold coordination whereas the back O becomes threefold coordinated. This large displacement occurs only for the Si atom which is located to the long bond side [14] of the O vacancy in accordance with the previous calculations [8, 9]. The bond length between the Si and the back O is 1.90 Å, whereas the distance between the Si and the remaining Si near to the vacancy is 4.10 Å.

For the neutral charge state, The dimer configuration is lower by 3.1 eV in energy than the puckered configuration. In order to obtain the energy barrier between the two configurations, we calculate total energy variation as a function of the distance  $d$  of the two Si atoms which were bonded to the removed O atom. All the degrees of freedom except for  $d$  are relaxed to obtain the total energy at a fixed  $d$ . For the neutral charge state there is a barrier of 0.15 eV from the puckered configuration to the dimer configuration.

#### Electron states in puckered configuration.

Electron states in the puckered configuration is of interest. There are two deep states in the gap. One is located at 3.0 eV above the valence band top. This is a dangling bond state of the remaining Si atom near the O vacant site ( Fig.2(a) ). In the neutral vacancy the state is completely occupied by 2 electrons. The other state is located in upper half

of the gap, at about 1.5 eV below the conduction band bottom. This originates from a new bond between the displaced Si atom and the back O atom (Fig.2(b) ), Of note is its anti-bonding nature. The anti-bonding state of the usual Si-O bond constitutes the conduction band of  $\alpha$ -quartz. The back bond formed in the puckered configuration is not strong enough so that the anti-bonding state emerges in the gap. This state is empty in the neutral charge state.

### Structural transformation upon hole capture.

The relative stability is sensitive to the number of electrons accommodated in deep levels. It is indeed found that the puckered configuration is lower than the dimer configuration by 0.10 eV in energy for the positively charged state. A barrier of 0.56 eV exists for the transition from the puckered configuration to the dimer configuration. The reason for the change in the relative stability upon hole capture is electronic. In the neutral dimer configuration, 2 electrons are accommodated in the dimer bond, whereas in the positively charged state only one electron is available to form the dimer. For  $V^+$ , the distance  $d$  of the two Si atoms is indeed 3.03 Å almost identical to the bulk distance 3.04 Å. This weak bond renders the dimer configuration relatively unfavorable. On the other hand, the bond between the back O and the displaced Si in the puckered configuration is hardly affected upon hole capture ( the bonding state of this backbond is in the valence band ). In addition, in the positive puckered configuration the dangling bond of the Si atom left near to the vacancy site contains one electron instead of two in the neutral case. This renders the puckered configuration relatively favorable upon hole capture.

A drastic structural transformation occurs when an additional hole is captured. The dimer configuration becomes *unstable* for the doubly positive charge state. The puckered configuration is the only configuration which is stable. The bond length between the Si and the back O is 1.81 Å which is 5 % smaller than the value for the neutral puckered configuration. The dimer configuration spontaneously transforms to the puckered configuration upon capture of two holes.

**{  $V^{++}$ ,  $V^+$ ,  $V^0$  } as a negative-U system.**

Figure 3 shows the calculated formation energies for  $V^0$ ,  $V^+$ , and  $V^{++}$  as a function of electron chemical potential  $\mu$  ( or equivalently Fermi level ) in the energy gap of  $\alpha$ -quartz [15]. When  $\mu$  is larger than the valence band top  $\varepsilon_v$  plus 2.4 eV, the neutral dimer configuration is the stablest form of the O vacancy. When  $\mu$  is smaller than  $\varepsilon_v + 2.4$  eV, the doubly positive charge state with the puckered configuration is the stablest form. At any position of the chemical potential, the positively charged state is only metastable. In the doubly positive puckered configuration, the dangling bond state near the vacant site is empty so that the structure is stabilized. For  $V^+$ , an additional electron is accommodated in the dangling bond state, which causes the energy cost. When another electron is added to make  $V^0$ , the dimerization of the two Si atoms becomes effective so that the dimer structure is stabilized. The negative U character that I have found in the present calculations is therefore of covalent nature.

The negatively charged state is not possible for the dimer configuration since there is not

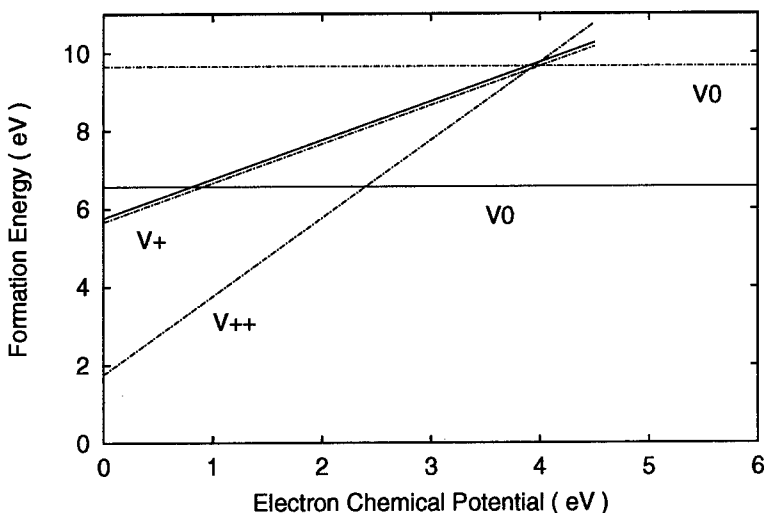


Figure 3: Formation energies of O vacancies for ++, +, and neutral charge states as a function of electron chemical potential in the energy gap measured from the valence band top. Solid lines are for the dimer configuration and dash-dotted lines for the puckered configuration.

a state in the energy gap which accommodates an additional electron. For the puckered configuration, however, a new state of the back-bond character emerges below the conduction band. It is indeed found that the negatively charged puckered configuration is stable. Yet this puckered configuration is metastable against the neutral dimer configuration plus an electron at the conduction-band bottom.

### Conclusion.

Total-energy electronic-structure calculations within LDA show that the oxygen vacancy in  $\alpha$ -quartz exhibits structural transformation upon hole capture. As a result of this,  $\{V^{++}, V^+, V^0\}$  becomes an effective negative-U system in which a covalent nature of the material plays an important role. This structural transformation and the subsequent variation in electron states may be related to degradation of insulating properties of  $\text{SiO}_2$ .

This work was supported in part by Japan Society for the Promotion of Science under Contract No. RFTF96P00203. Computations are carried out mostly on NEC-SX3 at Institute for Molecular Science in Okazaki.

### References

- [1] P. Olivo et al., IEEE Trans. Electron Devices **35**, 2259 (1988); R. Moazzami and C. Hu, IEDM Tech. Dig., (1992) p139; S. Takagi et al., IEDM Tech. Dig., (1996) p323; E. Rosenbaum and L. F. Register, IEEE Trans. Electron Devices **44**, 317 (1997).
- [2] R. J. Hemley et al., Nature **334**, 52 (1988).

- 
- [3] J. Sarntheim, A. Pasquarello, and R. Car, Phys. Rev. Lett. **74**, 4682 (1995) and references therein.
  - [4] C. M. Nelson and R. A. Weeks, J. Am. Ceram. Soc. **43**, 396 (1960); R. A. Weeks and C. M. Nelson, *ibid.* **43**, 399 (1960).
  - [5] R. H. Silsbee, J. Appl. Phys. **32**, 145 (1961).
  - [6] F. J. Feigl, W. B. Fowler, and K. L. Yip, Solid State Commun. **14**, 225 (1974); K. L. Yip and W. B. Fowler, Phys. Rev. B **11**, 2327 (1975).
  - [7] J. K. Rudra and W. B. Fowler, Phys. Rev. B **35**, 8223 (1987); K. C. Snyder and W. B. Fowler, Phys. Rev. B **48**, 13238 (1993).
  - [8] D. C. Allan and M. P. Teter, J. Am. Ceram. Soc. **73**, 3247 (1990).
  - [9] M. Boero, A. Pasquarello, J. Sarntheim, and R. Car, Phys. Rev. Lett. **78**, 887 (1997).
  - [10] N. Troullier and J. L. Martins, Phys. Rev. B **43**, 1993 (1991).
  - [11] D. M. Ceperley and B. J. Alder, Phys. Rev. Lett. **45**, 566 (1980).
  - [12] O. Sugino and A. Oshiyama, Phys. Rev. Lett. **68**, 1858 (1992); M. Saito, O. Sugino, and A. Oshiyama, Phys. Rev. B **46**, 2606 (1992); B. D. Yu and A. Oshiyama, Phys. Rev. Lett. **71**, 585 (1993).
  - [13] In generating a vacancy, an atom is removed from its lattice site and then brought to an atom-reservoir with some chemical potential. The O chemical potential in an O<sub>2</sub> molecule is adopted here as the chemical potential of the reservoir.
  - [14] There is a slight difference in length ( less than 0.01 Å) between the two types of Si-O bonds in  $\alpha$ -quartz. More importantly, local atomic arrangements ( e.g., distance to a back O atom ) in the long bond and the short bond sides differ significantly.
  - [15] In order to compare the formation energies of different charge states, Slater's transition state argument is used. Since the stable geometries for the V<sup>0</sup>, V<sup>+</sup> and V<sup>++</sup> are different to each other, there remains an ambiguity as to determine the occupancy levels. We have examined the deep level positions of a variety of geometries with +2, +1.5, +1, +0.5, 0 charged states, and found the ambiguity causes the error of the occupancy level less than 0.5 eV. The negative U character holds even with this numerical ambiguity.

## ENERGY TRANSFER PROCESSES AT ERBIUM IONS IN SILICON

J. Michel, J. Palm, T. Chen, X. Duan, E. Ouellette, S.H. Ahn, S.F. Nelson<sup>1</sup>,  
and L. C. Kimerling

Materials Processing Center, MIT, Cambridge, MA 02139

<sup>1</sup> Colby College, Waterville, ME 04901

**Key words:** erbium, photoluminescence, electroluminescence, excitation, light emitting devices

**Abstract.** Light emission from Er incorporated into Si is limited by deexcitation processes that reduce the emission efficiency significantly. We found a phonon mediated deexcitation process near room temperature by performing junction photocurrent spectroscopy (JPCS) on a Si:Er light emitting diode. We observed a photocurrent due to the optical excitation of the Er<sup>3+</sup> ion in Si. The energy transfer was found to be correlated to an Er-O donor complex.

### Introduction

As a potential light emitter for silicon based optoelectronic integrated circuits, Si:Er light emitting devices (LED) have attracted considerable attention. Room temperature emission at 1.54  $\mu\text{m}$  was reported in forward [1] and reverse [2] bias conditions, and the integration with CMOS devices has been demonstrated [3]. The challenge that remains is to overcome a significant decrease in emission intensity towards higher temperatures. At room temperature the emission intensity has decreased by about three orders of magnitude. This loss of intensity is due to non-radiative backtransfer mechanisms that deexcite the already excited Er 4f electron, responsible for the 1.54  $\mu\text{m}$  light emission.

The understanding of these loss processes is critical for the optimization of the emission efficiency of Si:Er based LEDs. At low temperatures an impurity Auger effect has been identified as responsible for the non-radiative backtransfer [4]. In this paper we will address the de-excitation mechanism that is active at temperatures above 150 K. The first part deals with the donor activity of Er complexes. In the second part we will show that the backtransfer is related to a charge transfer of the donor complex with additional phonon interaction.

### Donor Behavior of the Er-O Complex

Er implantation into Si and subsequent annealing introduces donor states [5,6]. It was not clear, however, if these donors are correlated to Er itself or to Er-ligand complexes. In order to determine the source for the donor behavior, we performed spreading resistance profiling (SRP) to compare the carrier profile with secondary ion mass spectroscopy (SIMS) profiles of the implanted Er. Fig. 1 shows the spreading resistance profiles of Er implanted at 4.5 MeV into *p*-type Czochralski(Cz) Si and annealed at 900°C for 30 min. *Er* labels a single Er implant, *Er/O* labels an additional O



implant, while O shows a reference sample implanted only with O. The spreading resistance profiles clearly show type conversion from *p* to *n* at 0.3  $\mu\text{m}$  and from *n* to *p* at 1.9  $\mu\text{m}$ , turning *n*-type where Er is implanted. A significant increase in donor concentration is observed for the O co-implanted sample.

To study the relationship between optically active Er and the donor activity, we implanted Er at 400 keV to achieve a shallow Er layer with peak concentration at 1500 Å. Additionally, O was implanted to match the Er implant. SIMS profiles showed that with increasing annealing temperature between 800 and 1000°C O diffuses out. The remaining [O], overlapping the Er profile, corresponds to the integrated carrier concentration, measured by SRP. The PL intensity for the differently annealed samples is shown in Fig. 2. We find a linear dependency between the integrated carrier concentration, measured by SRP and the Er PL intensity. This linear dependency shows that the donors are directly correlated to Er-O complexes. We will label this donor complex as  $[\text{Si:Er}^{3+}\text{-O}_x]^{0/+}$  indicating that the number of O atoms involved in this complex is unknown.

Hall effect data in Fig. 3 show two donor levels, a shallow donor level at 20 meV and a deep donor level at 160 meV that are related to Er/O complexes in implanted Cz-Si. Deep donor levels at about 160 meV were previously measured using DLTS for low concentrations of Er in Si [5,7].

### Junction Photocurrent Spectroscopy

For the junction photocurrent spectroscopy (JPCS) measurements we used mesa LED structures that were optimized for light emission. Er was implanted at 4.5 MeV to

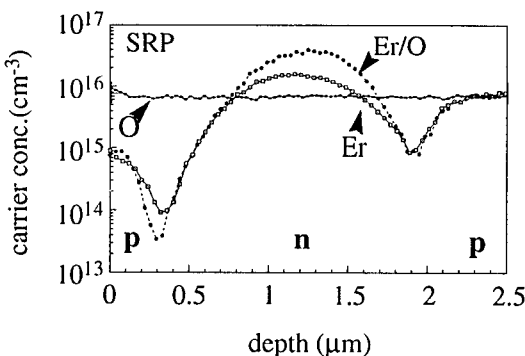


Figure 1 Carrier concentrations, measured by spreading resistance profiling, for Er and O implantations in Cz Si.

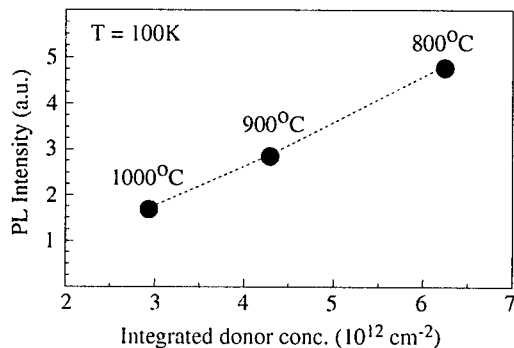


Figure 2 Er PL intensity as a function of integrated donor concentration. The annealing temperature for the samples is given.

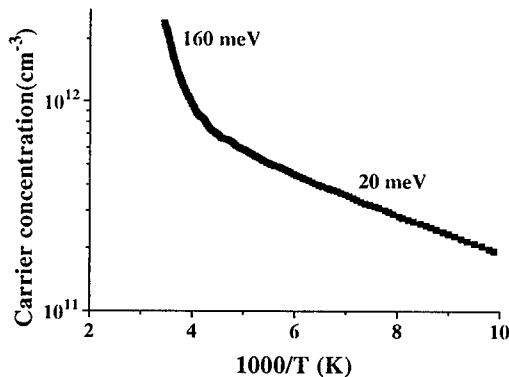
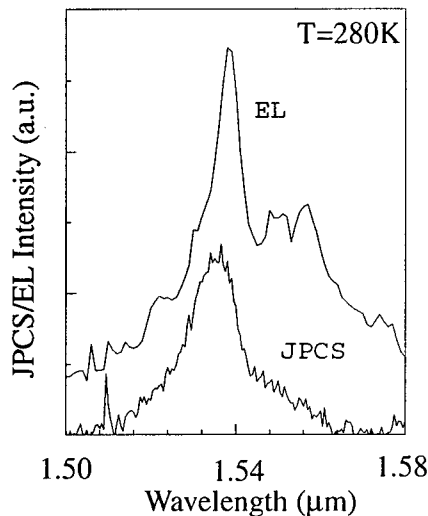
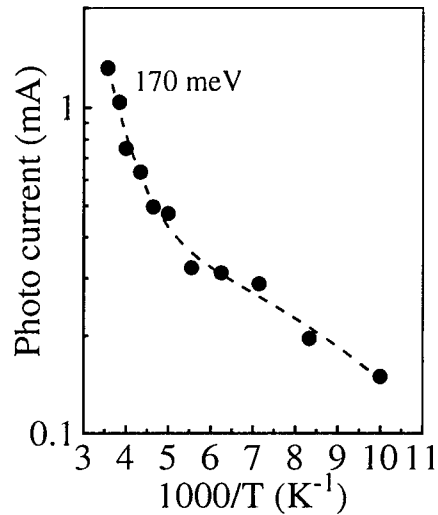


Figure 3 Hall Effect measurements of a mesa Si:Er LED. The Er implantation energy is 4.5 MeV, annealing temperature 900°C.



**Figure 4** Junction photocurrent spectroscopy on a Si:Er LED. The JPCS spectrum is compared to an EL spectrum of the same LED.



**Figure 5** Temperature dependence of the JPCS signal at 1.54  $\mu\text{m}$ . An exponential fit yields 170 meV activation energy above 220 K.

a peak depth of 1.35  $\mu\text{m}$ . O was coimplanted to match the Er implantation profile. For the JPCS experiment the white light of a quartz tungsten halogen source was dispersed through a 3/4 m grating spectrometer and focused on the LED front surface. A reverse bias was applied to the LED and the photocurrent was measured by a lock-in amplifier.

Near the band edge of Si the measured photocurrent is proportional to the absorption coefficient of Si and results from direct absorption of the photons and the generation of electron-hole pairs in the depletion region. The JPCS spectrum around 1.54  $\mu\text{m}$  is shown in Fig. 4. While a reference diode without Er implant does not show any photocurrent in this spectral region, an JPCS signal is observed for the Er doped LED. For comparison a spectrum of this LED in forward bias was measured to demonstrate the spectral coincidence of both signals. The only luminescence (EL/PL) signal observable above 1.2  $\mu\text{m}$  is due to  $\text{Er}^{3+}$  at 1.54  $\mu\text{m}$ . We conclude therefore that the JPCS signal at 1.54  $\mu\text{m}$  is correlated to  $\text{Er}^{3+}$ . The temperature dependence of the JPCS signal at 1.54  $\mu\text{m}$  is shown in Fig. 5. The signal could be measured between 100 and 270 K. Two thermally activated processes were observed. An exponential fit gives activation energies of 15 meV and 170 meV. The activation energy of 170 meV is correlated with a strong increase of the JPCS signal above 200 K.

The JPCS signal at 1.54  $\mu\text{m}$  is a direct evidence of an energy backtransfer process from the excited  $\text{Er}^{3+}$ . The first step in the experiment is the absorption of a 0.81 eV phonon by the Er 4f shell. We deduced the optical capture crosssection  $\sigma$  from the incident photon flux and the measured photocurrent. The value we obtained,  $\sigma = 10^{-22} \text{ cm}^2$ , is comparable to the Er 4f shell absorption in glass [8]. Instead of a radiative recombination process, the  $\text{Er}^{3+}$  ion then transfers the excitation energy to the electronic system of Si by generating an electron-hole pair, leaving the  $\text{Er}^{3+}$  in the

ground state ( $I = 15/2$ ).

This process can be explained by the configuration coordinate diagram in Fig. 6. As mentioned previously, we have to consider an Si:Er-O complex as the optically active donor. As indicated by the + sign, the donor is singly ionized. The direct optical absorption of a 0.81 eV photon excites the  $\text{Er}^{3+}$  from the  $I=15/2$  ground state to the  $I=13/2$  excited state as indicated in the labels of the parabolas. Because the probability for a radiative recombination is small because of the long radiative lifetime of 1 ms for  $\text{Er}^{3+}$ , a non-radiative backtransfer can occur. Assuming that an exciton is trapped at the defect state, relaxation of the 4f electron plus additional phonon energy can emit a hole into the valance band. Evidence of trapping of an exciton at the defect complex was demonstrated

as excitonic excitation is the dominant excitation process at low temperatures [4]. If the exciton is stable, reexcitation can occur. Once the hole is emitted, hole capture will not occur in the depletion region since there are no free holes available.

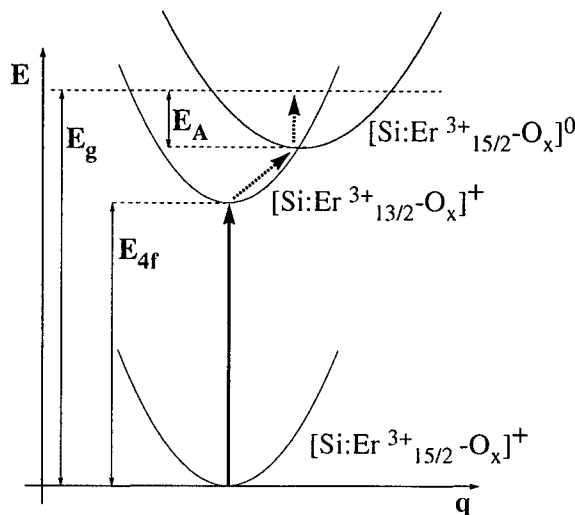


**Figure 6** Configuration coordinate diagram of the deexcitation path at temperatures above 200 K.

The deexcitation process, therefore, involves a charge transfer reaction from  $[\text{Si:Er}^{3+}\text{-O}_x]^+$  to  $[\text{Si:Er}^{3+}\text{-O}_x]^0$  at the associated donor level. Thermalization of the electron gives the measured photocurrent. A similar multi phonon model has been proposed by Taguchi et al. [9] for rare earth ions in InP. The phonon energy needed for the phonon mediated process in Si:Er is  $\Delta E = E_A - E_{4f} = 140$  meV for a trap state at  $E_A = E_c - 160$  meV. Local phonon modes due to Er-O bonds can participate in the process since Er and O are part of a defect complex. Compared to local vibrational modes of O in Si ( $\hbar\omega = 138$  meV) only one phonon is needed. Therefore a simple thermally activated behavior can be expected for the phonon absorption process.

Since the photocurrent is measured while applying a reverse bias, the JPCS experiment differs from an LED forward bias operation mode. The backtransfer through charge transfer can only occur if the donor level is empty. This condition is always fulfilled for Er in the depletion region or if the boron background doping exceeds the Er related donor concentration. In forward bias the donor level is always empty immediately after the excitation process. We expect to find a reduced backtransfer in highly doped n-type Si. Experiments are currently on the way.

## Conclusions

A second backtransfer process that reduces the emission efficiency for Si:Er LEDs ( $\lambda = 1.54 \mu\text{m}$ ) has been identified by JPCS as a phonon mediated process above 200 K. We observed a photocurrent by optically exciting the Er ions. The photocurrent is due to the emission of a hole after an exciton is trapped at the Er-O defect complex. Thermalization of the electron into the conduction band leads to the observed photocurrent.

## Acknowledgements

We acknowledge partial support by ARPA, Rome Laboratories, AFOSR, and SRC. J. Palm was supported by the Deutsche Forschungs Gemeinschaft.

## References

- [1] B. Zheng, J. Michel, F.Y.G. Ren, L.C. Kimerling, D.C. Jacobson and J.M. Poate, Appl. Phys. Lett. **64**, 2842 (1994)
- [2] G. Franzo, F. Priolo, S. Coffa, A. Polman, and A. Carnera, Appl. Phys. Lett. **64**, 2235 (1994)
- [3] J. Michel, B. Zheng, J. Palm, E. Ouillette, F. Gan, and L.C. Kimerling, (MRS, Pittsburg, PA, 1996) Vol. **422**, p. 317
- [4] J. Palm, F. Gan, B. Zheng, J. Michel, and L.C. Kimerling, Phys. Rev. **B 54**, 17603 (1996)
- [5] J.L. Benton, J. Michel, L.C. Kimerling, D.C. Jacobson, Y.-H. Xie, D.J. Eaglesham, E.A. Fitzgerald, and J.M. Poate, J. Appl. Phys. **70**, 2667 (1991)
- [6] F.P. Widdershoven, J.P.M. Naus, Mat. Sci. Eng. **B4**, 71 (1989)
- [7] S. Libertino, S. Coffa, G. Franzo, and F. Priolo, J. Appl. Phys. **78**, 3867 (1995)
- [8] W.J. Miniscalco, J. Lightwave Technol. **9**, 234 (1991)
- [9] A. Taguchi, K. Takahei, and Y. Horikoshi, J. Appl. Phys. **76**, 7288 (1994)

## ENERGY TRANSFER RATE BETWEEN ERBIUM 4f SHELL AND Si HOST

A. Taguchi, K. Takahei, M. Matsuoka,\* and S. Tohno\*  
NTT Basic Research Labs., Atsugi-shi, Kanagawa 243-01 Japan  
\*NTT Opto-electronics Labs., Tokai, Ibaraki 319-11, Japan

**Keywords:** Er, Si, energy transfer rate, luminescence decay time, time response

**Abstract.** We estimated the energy transfer rate between an erbium (Er) 4f shell and a Si host by analyzing the temperature dependence of the decay time of the Er 4f-shell luminescence and its time response at low temperature. We assumed that thermal quenching of the Er luminescence is due to an energy back-transfer mechanism and that the energy transfer is assisted by a non-radiative multiphonon process. Based on these assumptions, the energy transfer rate was estimated to be  $2 \times 10^8 \text{ s}^{-1}$  from the temperature dependence of the decay time. We also measured the time response of the luminescence after the pulsed host excitation and the energy transfer rate was estimated to be larger than  $1 \times 10^7 \text{ s}^{-1}$ . These results show that the energy transfer rate for Si:Er is not so small as  $10^4 \sim 10^6 \text{ s}^{-1}$  as had been suggested by several previous studies.

### I. Introduction

Erbium (Er) in Si has received much attention recently due to its potential use for Si-based optical devices using its very sharp and temperature-stable Er 4f-shell luminescence, which is caused by the Er intra-4f-shell transition from the first excited state of  $^4I_{13/2}$  to the ground state of  $^4I_{15/2}$ . In the early stages of the study of Si:Er, the Er 4f-shell luminescence intensity was weak [1], but it was found that the intensity could be enhanced by co-doping with other impurities [2]. Oxygen is the most commonly used co-dopant. Some groups reported that the Er luminescence intensity increases after host photo-excitation, and there is a time delay in the luminescence intensity peak after the host excitation [3]. Based on this observation, it was claimed that the energy transfer rate is rather small. The energy transfer rate between the Si host and the Er 4f shell is an important parameter that determines optical properties. If the energy transfer rate is low and it is intrinsic nature of the Er 4f-shell luminescence in Si, this material is not suitable for optical devices. The reported delay times are 30 and 100  $\mu\text{s}$ , suggesting a small energy transfer rate. However, time response of the detection system was not taken into account in the analysis in these previous studies. The detection system response plays a crucial role, as will be shown in this paper.

In this paper, we discuss the energy transfer rate of Er in Si based on the temperature dependence of the decay time and the time response of the Er 4f-shell photoluminescence (PL) for a Si:Er,O sample, which was grown by an ion beam epitaxial method [5]. From the temperature dependence of the 4f-shell PL decay time, the energy transfer rate can be estimated by assuming that a thermal quenching, which is the decrease in the PL decay time as temperature increases, is due to an energy back-transfer process and by assuming that the energy transfer is assisted by non-radiative multiphonon (NRMP) processes [4]. On the other hand, from the time response measurements, the energy transfer rate can be measured directly, the lower rate being limited by the measurement system response time. In the next section, we describe the sample and the experimental setups. In Sec. III, the excitation mechanism is explained. An equation expressing time response is deduced based on the excitation process. The experimentally obtained temperature dependence of the decay time will be shown and the energy transfer rate is estimated in Sec. IV. In Sec. V, the results of the time response measurements are shown and analyzed taking into account the time response of the detection system.

## II. Experimental conditions

The Si:Er,O samples used in this study have been grown by an ion beam epitaxial method. The details of the growth method and conditions have been reported [5]. A P-doped Si substrate was used and B was co-doped with Er and oxygen in the epitaxial layer. The epitaxial layer thickness was 500 nm. The sample shows Er 4*f*-shell luminescence dominantly from one type of Er-O complex center under the host excitation at 4 K [5].

To measure the Er 4*f*-shell photoluminescence (PL) spectrum, a He-Ne laser was used as an excitation source. The spectrum was analyzed by a 1.25-m monochrometer with a cooled Ge detector. To measure the time dependence of the PL intensity, a Nd YAG laser-pumped dye laser operating at 10 Hz was used as the excitation source. The pulse width of the excitation light was 5 ns and the wavelength was 680 nm. The luminescence was dispersed by a 0.5-m monochrometer with the spectrum resolution of about 10 nm. A fast-response photomultiplier operating at 1.5  $\mu\text{m}$  was used as an detector.

## III. Excitation mechanism

The Er 4*f*-shell luminescence has been observed by the host photo-excitation. This shows that there is an energy transfer from the photo-excited free carriers to the Er 4*f* shell. The excitation process, which is schematically drawn in Fig. 1, is widely accepted. The Er 4*f* shell is excited by a recombination of an electron-hole pair formed at the carrier trap level, which originated from the Er atom. As temperature increases, the luminescence decay time decreases (the thermal quenching). Assuming that the reverse process to the excitation process (the energy back-transfer process) is responsible for the thermal quenching and that NRMP assists the energy transfer, the temperature dependence of the decay time can be calculated by solving rate equations by using two parameters  $E_0$  and  $W_0$ . Here,  $E_0$  is the energy which has to be compensated for during the energy transfer.  $W_0$  is the transition matrix element which corresponds to the energy transfer rate discussed in this paper. The detailed energy transfer processes and calculations have been explained in Ref. 4. By fitting the calculated temperature dependence of the decay time to the experimentally obtained temperature dependence,  $W_0$  can be estimated.

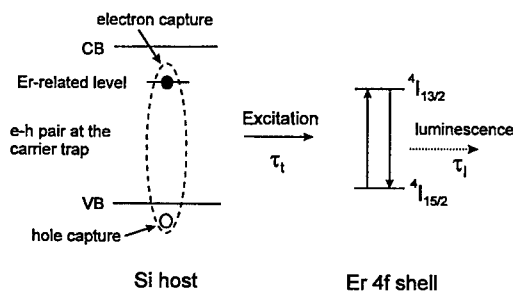


FIG. 1 Schematic picture of the excitation process.  $\tau_t$  is the energy transfer time and  $\tau_l$  is the decay time of the Er 4*f*-shell PL.

If the measurement system response time is sufficiently fast (although this is actually not the case), two possibilities may be considered as the origin of the reported luminescence delay after the host photo-excitation. One is that the energy transfer rate is high but the formation process of the electron-hole pair at the Er-related trap is slow. In this case, to explain the luminescence delay of several tens of  $\mu\text{s}$ , free carriers have to migrate in the host for several tens of  $\mu\text{s}$ . Such long carrier life time is not expected in samples doped with Er and oxygen, since the doped impurities produce deep levels that reduce the free carrier life time. The other possible reason is that the electron-hole pair formation process is fast but the energy transfer rate is small. In this case, we can estimate the time response of the Er 4*f*-shell luminescence by solving the rate

equations assuming that the electron-hole pair formation process is negligibly fast. The rate equations are

$$\begin{aligned}\frac{dN_{eh}}{dt} &= g - \tau_t^{-1}N_{eh}, \\ \frac{dN_{4f}}{dt} &= \tau_t^{-1}N_{eh} - \tau_l^{-1}N_{4f}.\end{aligned}$$

Here,  $N_{eh}$  and  $N_{4f}$  are the number of electron-hole pairs and the number of the Er 4f shells in the excited state, respectively.  $g$  is the generation rate of the electron-hole pair.  $\tau_t$  is the energy transfer time, which is the inverse of the energy transfer rate ( $\tau_t \equiv W_0^{-1}$ ).  $\tau_l$  is the radiative decay time of the excited Er 4f shell, that has been experimentally measured. Assuming that  $g=0$  after the pulsed excitation, the above coupled equations can easily be solved. The time dependence of  $N_{4f}$  is expressed by a bi-exponential form as follows,

$$N_{4f}(t) = C\{exp(-\tau_t^{-1}t) - exp(-\tau_l^{-1}t)\}. \quad (1)$$

$C$  is a time-independent constant. The Er 4f-shell luminescence intensity is proportional to the number of Er 4f shells in the excited state,  $N_{4f}$ . The second term on the right side of the equation expresses the decrease in the luminescence intensity with the time constant  $\tau_l$ . This term expresses the most frequently observed PL time decay. The first term on the right side of the equation, which varies with the time constant of  $\tau_t$ , expresses the increase in the luminescence intensity with time. Hence, if the energy transfer time  $\tau_t$  is large enough to be detected by the measurement system used, the luminescence delay should be observed. The time constant of the increase in the PL intensity corresponds to the inverse of the energy transfer rate.

#### IV. Temperature dependence of the decay time of the Er 4f-shell luminescence

Figure 2 shows a typical PL spectrum at 5 K for the Si:Er,O samples grown by the ion beam epitaxial method. A well resolved luminescence due to the Er intra-4f-shell transition can be seen at around 1540 nm. The Er PL comes from dominantly one type of luminescence center. The same luminescence center was reported in ion implanted samples [6]. A very sharp band-edge-related luminescence is also seen at 1135 nm. We measured the temperature dependence of the decay time of the Er 4f-shell PL to estimate the energy transfer rate. Figure 3 shows the PL time decay curve measured at 6 K. The PL intensity shows a clear single exponential decay, confirming that this luminescence mainly comes from one type of the Er luminescence center. In this time scale, the luminescence delay was not observed. The estimated decay time was 1.2 ms, which is almost the same as that previously reported [7].

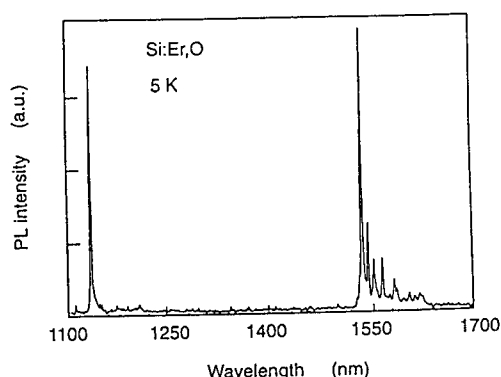


FIG. 2 Typical PL spectrum for Si:Er,O samples grown by the ion beam epitaxial method.

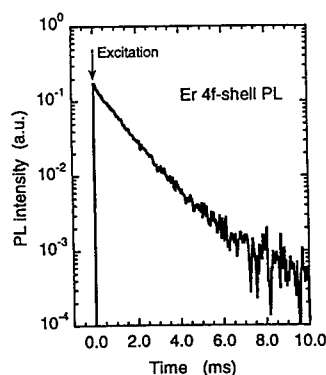


FIG. 3 Time decay of the Er 4f-shell photoluminescence at 6 K.

As temperature increases, the decay time decreases as shown in Fig. 4. Applying the fitting procedures explained in Ref. 4, the calculated temperature dependence of the decay time was fitted to the experimentally obtained temperature dependence, as shown by the solid line. In the calculations, values of 0.14 eV and  $2 \times 10^8 \text{ s}^{-1}$  were used as  $E_0$  and  $W_0$ , respectively. The estimated value of the energy transfer rate is too large to explain the previously reported luminescence delay of several tens of  $\mu\text{s}$ .

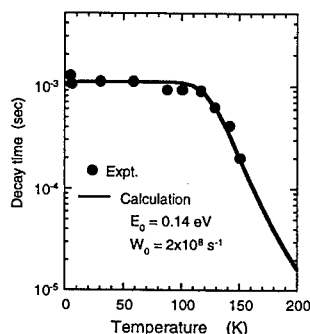


FIG. 4 Temperature dependence of the Er 4*f*-shell PL decay time. Filled circles are the experimental results. Solid line is obtained by assuming that  $E_0 = 0.14 \text{ eV}$  and  $W_0 = 2 \times 10^8 \text{ s}^{-1}$ .

### V. Time response of the Er 4*f*-shell luminescence

To investigate the PL time delay, we measured the time response of the PL for a much shorter time region than that shown in Fig. 3. The results are shown in Fig. 5. If we detect the luminescence at the wavelength of 1535 nm, where the strongest Er luminescence was observed, the PL intensity increases after the pulsed excitation and shows a peak at around 0.1  $\mu\text{s}$ , and after that, it becomes almost constant with a decay time of 1.2 ms. Contrary to the previous reports [7], we do not observe the luminescence delay in some tens of  $\mu\text{s}$  orders. The almost constant part in the figure is due to the Er 4*f*-shell PL. Therefore, the peak seen at approximately 0.1  $\mu\text{s}$  is due to some other luminescence. When we detect the luminescence at the wavelength of 1500 nm, at which the Er 4*f*-shell luminescence is not to be observed

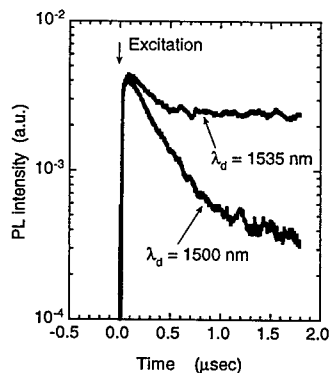


FIG. 5 PL-TD curves detected at the different wavelengths of 1535 and 1500 nm.

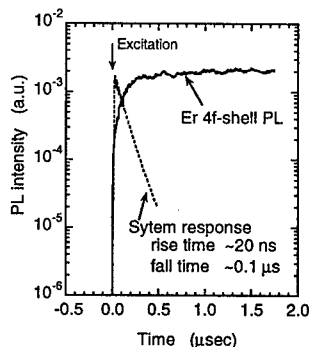


FIG. 6 Time response of the Er 4*f*-shell PL obtained by subtracting the background luminescence.



(Fig. 2), fast-decaying PL is still observed as shown in the figure. This luminescence shows a faster decay than the Er 4*f*-shell PL. Even when we detect the PL at 1400 nm, we still observe a similar fast decaying luminescence with a similar peak intensity. Therefore, the fast decaying part must be due to the background luminescence not related to Er, and the background luminescence is almost independent of the wavelength. To obtain the time dependence of the Er 4*f*-shell PL, we regarded the signal obtained by detecting the PL at 1500 nm is the background luminescence, and that signal was subtracted from the signal detected at the wavelength of 1535 nm. The results are shown in Fig. 6. The signal increases after the pulsed excitation. In the figure, a system response of the detection system is also shown. Here, we defined the system response as the time response of the bandedge-related luminescence for *n*-type InP, since the decay time of this luminescence is less than 10 ns, which is much smaller than the time scale discussed here.

It looks as if the time response of the Er 4*f*-shell PL shown in Fig. 6 can be explained by Eq.(1). However, this is the case when the response of a detecting system is much faster than the time scale of the observation. In such a case, the system response can be regarded as a  $\delta$ -function, and the time response of the observed signal will be expressed by Eq.(1). This condition is not fulfilled in the present case. The system rise time  $\tau_r$  is approximately 20 ns, and the fall time  $\tau_f$  is approximately 0.1  $\mu$ s. The rise time of the signal and the system fall time are both in the sub-micro second order. Therefore, to analyze the observed signal, the system response has to be taken into account. In the present detection system, the bandedge-related PL for *n*-type InP is much shorter than the system response time, but the Er 4*f*-shell PL decay time, 1.2 ms, is much longer than the system response times. So within such a relatively short time  $t_0$  after the pulsed excitation, some of the Er centers still emit light. Therefore, the observed signal at time  $t$  is the integration of the detection system output for all the light emitted before the time  $t$ . The system responds to the light emitted at time delay  $t_0$  after the pulsed excitation with a rise time of 20 ns and a fall time of 0.1  $\mu$ s. Assuming that the system time response to  $\delta$ -function input light is expressed by Eq.(1), the system time response for the light emitted at  $t_0$ ,  $I_s(t, t_0)$ , is expressed as,

$$I_s(t, t_0) = C'[\exp\{-\tau_r^{-1}(t - t_0)\} - \exp\{-\tau_f^{-1}(t - t_0)\}].$$

Then, the time response of the observed signal  $I_{ob}(t)$  for the Er 4*f*-shell PL is obtained by integrating the product of the time dependence of the Er 4*f*-shell PL intensity and the system response as follows,

$$I_{ob}(t) \propto \int_0^t N_{4f}(t_0) I_s(t - t_0) dt_0. \quad (2)$$

Due to this convolution, the system fall time causes an apparent rise time of the observed luminescence intensity. There are four time constants ( $\tau_r$ ,  $\tau_f$ ,  $\tau_l$ , and  $\tau_t$ ) in the equation, but the unknown parameter is only  $\tau_t$ .

Figure 7 compares the experimentally obtained time dependences of the Er 4*f*-shell PL (same as that shown in Fig. 6) and the ones calculated using Eq. (2) for several  $\tau_t$  values. When  $\tau_t$  is  $5 \times 10^{-7}$  s, which is larger than the system fall time  $\tau_f$ , the calculated curve is apparently lower than the experimentally obtained signal. As  $\tau_t$  decreases, the calculated signal becomes close to the experimental results. Although the curve calculated by using  $5 \times 10^{-8}$  s as  $\tau_t$  shows the best agreement with the experiments, the experimental results include experimental errors and the error due to the ambiguity in the background-luminescence subtraction. Moreover, when  $\tau_t$  is smaller than  $\tau_f$ , the calculated signal intensity is not sensitive to  $\tau_t$ . Therefore, the exact  $\tau_t$  value can not be determined, but it can be said that  $\tau_t$  is larger than about  $1 \times 10^{-7}$  s. Since  $\tau_t$  is the inverse of the energy transfer rate, this indicates that the energy transfer rate is larger than the  $1 \times 10^7$  s<sup>-1</sup>. This is consistent with the result obtained from the temperature dependence of the Er 4*f*-shell decay time, where the energy transfer rate of  $2 \times 10^8$  s<sup>-1</sup> was obtained.

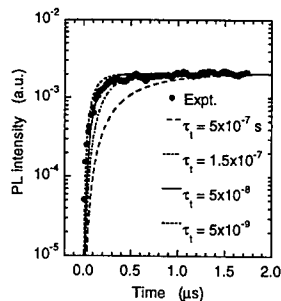


FIG. 7 Comparison between the experimentally obtained time dependence of the Er 4*f*-shell PL and the calculated temperature dependence using Eq. (2). The calculated curves for different  $\tau_t$  values of  $5 \times 10^{-7}$ ,  $1.5 \times 10^{-7}$ ,  $5 \times 10^{-8}$ , and  $5 \times 10^{-9}$  s are drawn.

## VI. Conclusion

We investigated the energy transfer rate between the Er 4*f* shell and Si host by measuring the temperature dependence of the decay time of the Er 4*f*-shell luminescence and its time response. From the temperature dependence of the decay time, the energy transfer rate was estimated to be  $2 \times 10^8 \text{ s}^{-1}$ . Although several groups reported a luminescence delay as large as some tens of  $\mu\text{s}$ , we did not observe such a luminescence delay. The previously observed delay must be due to some extrinsic effects. In the analysis of the time response of the luminescence, we found that the time response of the detection system is important. Detailed analysis of the observed signal taking into account the system response time showed that the energy transfer rate is larger than  $1 \times 10^7 \text{ s}^{-1}$ .

## Acknowledgments

The authors would like to thank Dr. Yoshiro Hirayama for his valuable discussion. They also would like to thank Dr. Naoshi Uesugi for his encouragement throughout this work.

## References

- [1] H. Ennen, J. Scheider, G. Pomrenke, and A. Axman, *Appl. Phys. Lett.*, **43** 943 (1983).
- [2] S. Coffa, F. Priolo, G. Franzó, V. Bellani, A. Carnera, and C. Spinella, *Phys. Rev. B*, **48** 11782 (1993); J. Michel, L. Benton, R. F. Ferrante, D. C. Jacobson, D. J. Eaglesham, E. A. Fitzgerald, Y. -H. Xie, J. M. Poate, and L. C. Kimering, *J. Appl. Phys.*, **70** 2762 (1991).
- [3] H. Przybylinska, G. Hendorfer, M. Bruckner, W. Jantsch, and L. Palmetschofer, *J. Alloys Compounds*, **225**, 555 (1995); J. H. Shin, G. N. van den Hoven, and A. Polman, *Appl. Phys. Lett.*, **67** 377 (1996); T. Gregorkiewicz, I. Tsimperidis, C. A. J. Ammerlaan, F. P. Widdershoven, and N. A. Sobolev, *MRS Symp. Proc.*, **422** 207 (1996).
- [4] A. Taguchi, K. Takahei and Y. Horikoshi, *J. Appl. Phys.*, **76** 7288 (1994).
- [5] M. Matsuoka and S. Tohno, *MRS Symp. Proc.*, **422** 3 (1996).
- [6] H. Przybylinska, W. Jantsch, Yu. Suprun-Bellevitch, M. Stepikhova, L. Palmetschofer, G. Hendorfer, A. Kozanecki, R. J. Wilson, B. J. Sealy, *Phys. Rev. B*, **54**, 2532 (1996).
- [7] S. Coffa, G. Franzó, F. Priolo, A. Polman, and R. Serna, *Phys. Rev. B*, **49** 16313 (1994); A. Palm, F. Gan, B. Zheng, J. Michel, and L. C. Kimering, *to be published in Phys. Rev. B*.

## PHOTOLUMINESCENCE STUDY OF ERBIUM IN SILICON WITH A FREE-ELECTRON LASER

I. Tsimperidis, T. Gregorkiewicz, H.H.P.Th. Bekman<sup>1</sup>, C.J.G.M. Langerak<sup>2</sup>,  
and C.A.J. Ammerlaan

Van der Waals-Zeeman Institute, University of Amsterdam,  
Valckenierstraat 65-67, NL-1018 XE Amsterdam, The Netherlands

<sup>1</sup>TNO Physics and Electronics Laboratory,  
Oude Waalsdorperweg 63, NL-2509 JG The Hague, The Netherlands

<sup>2</sup>FOM-Institute for Plasma Physics "Rijnhuizen",  
P.O. Box 1207, NL-3430 BE Nieuwegein, The Netherlands

**Keywords:** silicon, rare-earth doping, photoluminescence, free-electron laser

**Abstract** The influence of intense infrared (IR) radiation in the range 7–17  $\mu\text{m}$  on the photoluminescence (PL) of erbium in silicon has been investigated. To excite the PL a pulsed Nd:YAG laser operating in the visible with a wavelength of 532 nm has been used. The infrared beam was generated by a free-electron laser. In the experiment the intensity and decay kinetics of the low-temperature PL of Er-doped silicon were monitored as a function of the wavelength of the quenching beam and its delay with respect to the excitation pulse of the visible-light laser. The experiments show quenching of the PL by the IR pulse only at delays shorter than approximately 250  $\mu\text{s}$ . The result is interpreted as dissociation of the Er-related bound-exciton (BE) state whose effective lifetime is then estimated as approximately 100  $\mu\text{s}$ . A special quenching feature for  $\lambda \approx 12.5 \mu\text{m}$  is detected indicating a possible "back-transfer" mechanism involving the excited Er state. For still longer delay times a small transient increase of Er PL is observed.

### Introduction

The presence of an incompletely filled 4f shell distinguishes rare earth (RE) atoms from other elements. The spin-orbit interaction within this shell gives rise to a very characteristic splitting of the energy levels which can be experimentally observed in photoluminescence due to transitions between the (lowest) excited and the ground states. When placed within a solid the emissions can further be influenced by the local crystal field; this effect is, however, usually small due to screening of the 4f electron shell. Consequently, the PL spectrum of a RE dopant is very similar to that of a free atom, with rather narrow lines and a very limited dependence on the host crystal. Further, being due to internal atomic transitions, the emissions have a temperature-stable wavelength. These characteristic features make RE's very attractive for practical applications and they stimulated intensive investigations. In case of the erbium-in-silicon system the interest is fortified by potential applications as the sharp, atomic-like emission of Er coincides with the absorption minimum of glass fibers commonly used in telecommunications. Currently Er doping of silicon is among the most promising approaches to photonics of this basic electronic material.

However, the successful development of Er-based optical silicon devices requires high-efficiency emission at room temperature. In order to achieve that, mechanisms responsible for the excitation of the intrashell and its recombinations (both radiative and non-radiative) have to be thoroughly understood [1]. Here especially the energy transfer between the silicon host and the Er core appears complex, since the Er atom, which embedded in Si assumes an  $\text{Er}^{3+}$  charge state, most probably does not introduce any energy levels in the bandgap. Based on numerous experimental and theoretical studies [2] an energy transfer mechanism has been proposed which involves creation of an intermediate state when an exciton becomes bound to an Er ion by a local potential [3]. The properties of this state, such as its lifetime and generation and recombination paths, are crucial for the Er excitation process and govern the PL intensity. Following exciton localization the core excitation is then accomplished in an Auger process involving the nonradiative recombination of the bound

exciton with a simultaneous energy transfer to an electron localized in the 4f shell and compensation of (a possible) energy mismatch. The efficiency of this indirect energy transfer is additionally hampered by an alternative quenching of the BE system. A low PL intensity follows further from the fact that the internal 4f transitions are parity-forbidden and become only partially allowed due to crystal-field-induced mixing of states. Consequently, the radiative recombination time is long. The decay time is effectively shortened by an efficient nonradiative de-excitation channel competing with the radiative recombination. As a possible mechanism responsible for this quenching a nonradiative Auger process, involving conduction electrons, has been suggested. Due to the low probability of the radiative recombination the PL efficiency is additionally hampered by the so-called “back-transfer” process reversing the excitation by regeneration of the intermediate BE state.

In the current study we probe the PL mechanism of Er in Si with intense far-infrared radiation provided by a free-electron laser. In view of the complex character of the energy transfer mechanism one might expect that different stages of this process may be influenced. In particular, this novel approach could reveal information on the so-far experimentally inaccessible intermediate BE state and on the back-transfer process.

### Experimental conditions

The experiments were performed at the FOM Institute for Plasma Physics “Rijnhuizen”.

Two excitation sources have been used. The PL spectrum was generated by a pulsed Nd:YAG laser operating at  $\lambda=1064$  nm, with a pulse duration of approximately 7 ns and a repetition rate of 5 Hz. The pulse was passed through a second-harmonic generator; consequently the sample was exposed to the green laser beam of 532 nm. In the experiment the averaged excitation power level was kept below  $\approx 20$   $\mu$ W. In addition to this over-the-bandgap excitation the infrared probing beam has been applied. This was provided by the Free Electron Laser for Infrared Experiments (FELIX) at Rijnhuizen. The FELIX delivers so-called “macropulses” with a length of 5–10  $\mu$ s at a maximum repetition rate of 10 Hz. Each macropulse consists of a train of “micropulses” with a spacing that can be either 1 or 40 ns (1 GHz or 25 MHz operation mode). In the study a 40 ns micropulse-spacing was used with the macropulse length of approximately 7  $\mu$ s and a micropulse width of 1.7 ps. It is estimated that the energy in each micropulse is 1.7  $\mu$ J. The sample was mounted inside a variable temperature cryostat operated within a 4–40 K range and with a stability of  $\pm 0.1$  K. In the infrared beam a cut-off 7.2  $\mu$ m filter has been used in order to block the shorter wavelengths present due to the generation of higher harmonics. Both laser beams were coincident on the sample. The emerging PL was collected from the laser-irradiated surface and passed through a band pass filter centered for  $\lambda=1548.8$  nm and with a bandwidth of 20 nm. The PL has been detected by a germanium detector. The signals were then amplified and analyzed by a digital oscilloscope. The experimentally detected response of the system was 5  $\mu$ s on the rising slope and 75  $\mu$ s for the decay time. We note that in a chosen experimental configuration the measured signal corresponds to the total emission integrated over the filtering range. Therefore the information contained in the form of the spectrum, e.g., individual spectral lines, is not accessible. The decision to use the band-pass filter rather than a monochromator was necessary in order to achieve a satisfactory signal-to-noise ratio.

The sample used in the experiment was prepared from  $\langle 100 \rangle$ -oriented, n-type, phosphorus-doped float-zoned silicon, with a donor concentration of approximately  $6 \times 10^{15}$   $\text{cm}^{-3}$  and a room-temperature resistivity between 0.7 and 0.9  $\Omega\text{cm}$ . It has been implanted with  $\text{Er}^{2+}$  ions to a dose of  $10^{13}$   $\text{cm}^{-2}$  with an energy of 1100 keV. The implantation has been performed at a temperature of approximately 500  $^{\circ}\text{C}$ ; no further heat-treatment has been given.

### Experimental results and discussion

#### A. Preliminaries

In the past the PL of the Si:Er system has been intensively investigated. In order to study the de-excitation mechanism the decay characteristics as well as the temperature quenching of the PL intensity and decay time are usually investigated [3,4]. The results reveal that the temperature dependencies are governed by a set of activation energies; their particular values appear to be different in FZ- and Cz-grown Si. These differences are especially evident for the quenching processes which become important at an elevated temperature and are characterized by activation energies in the 100–150 meV range. For the identification of the particular mechanism responsible for this process two

possibilities are currently considered: the ionization of an electron at the Er-related trap [5], and the already mentioned back-transfer process. Regardless of the actual mechanism it is evident that this activation energy value contains information on a most characteristic step in the energy transfer mechanism between the silicon crystal and the Er core. Unfortunately, in the temperature range where this quenching process is important the PL intensity is already very low and, consequently, this informative parameter is poorly determined. In the current experiment the IR pulse provides the possibility to induce the back-transfer process at low temperature, i.e., for high intensity of the PL emission.

Preliminary to the current experiments the temperature dependence of the PL intensity of the sample has been measured. It was found to be controlled by two activation energies:  $E_1 \approx 15$  meV and  $E_2 \approx 110$  meV [6]. Also the decay time was investigated and no significant change in the temperature range up to 70 K was found. In the present study we start by measuring the time development of an Er PL signal upon a single pulse of the Nd:YAG laser, as depicted in Fig.1. The points represent experimental data averaged over 100 excitation pulses. The solid line represents a computer fit according to the formula

$$I_{PL}(t) = A [\exp(-t/\tau_R) - \exp(-t/\tau_{TR})], \quad (1)$$

which can be derived from the set of rate equations for the excitation model where the existence of an intermediate BE state is assumed [2]. In the formula  $\tau_R$  and  $\tau_{TR}$  correspond to the Er radiative recombination time constant and the excitation transfer time between the intermediate BE state and the Er core, respectively.  $A$  is a proportionality constant. As can be seen, a good agreement with  $\tau_{TR} = 45 \mu s$  and  $\tau_R = 580 \mu s$  can be obtained for almost the entire time window used in the depicted measurement. The discrepancy appearing for  $t > 600 \mu s$  is due to a slower decaying component whose existence is not incorporated in the rate equation set from Ref.[2], and which could be due to a different species of Er-related PL centers [7]. We conclude that in the investigated sample the effective lifetime of the intermediate state responsible for the excitation of the Er core has a relatively high value, similar to those found for excitons bound to isoelectronic centers.

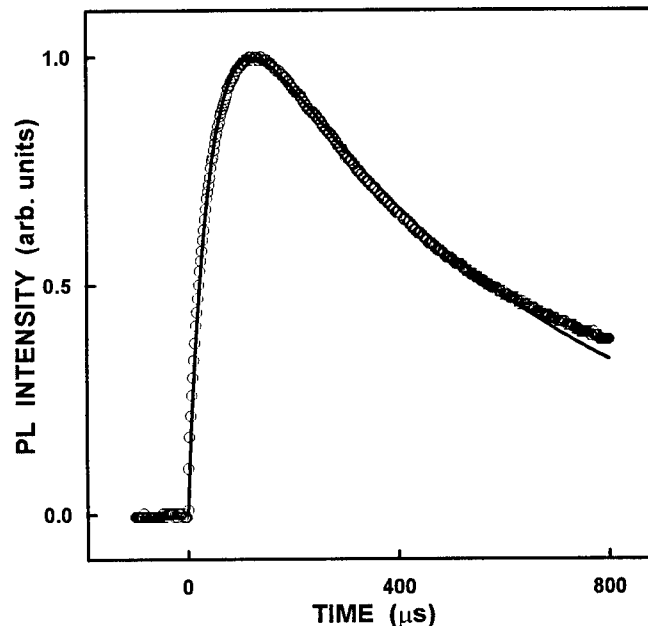


**Figure 1:** The time development of the Er PL signal generated by the Nd:YAG laser pulse. The experimental points were fitted according to Eq.(1) with  $\tau_{TR} = 45 \mu s$  and  $\tau_R = 580 \mu s$ .

#### B. Effect of the IR beam - quenching of Er PL

Upon application of the infrared beam the intensity of the Nd:YAG-excited PL changes. This is illustrated in Fig.2. The broken line corresponds to the original PL signal, while the solid ones,

labeled A, B, C, and D, show the effect of the free-electron laser pulse ( $\lambda=9.5 \mu\text{m}$ ) which is fired 10, 50, 100, and 200  $\mu\text{s}$  after the Nd:YAG pulse, respectively. As can be seen, the intensity of the signal quenches, with the effect becoming smaller as the time difference between the two pulses increases. For longer delay times,  $\Delta t > 50 \mu\text{s}$ , the form of the signal indicates that upon the IR pulse the excitation of Er is terminated immediately and only the decay takes place. For still larger delays,  $\Delta t > 250 \mu\text{s}$ , no influence of the IR beam on the PL signal can be observed.

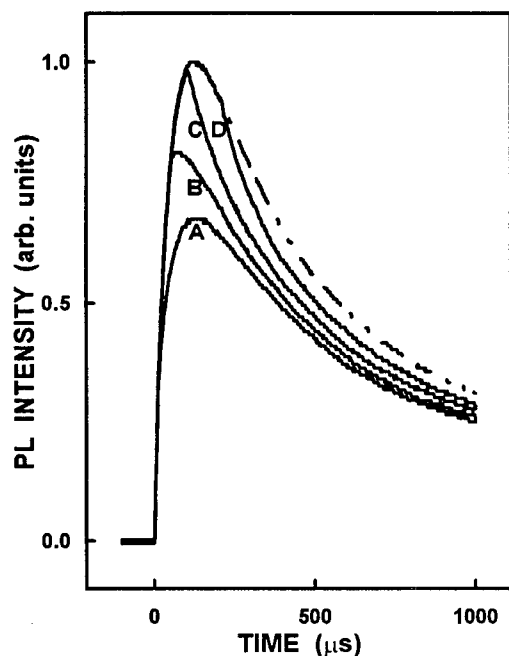


**Figure 2:** Quenching of the Er PL signal (broken curve) with the  $\lambda=9.5 \mu\text{m}$  FELIX pulse. Curves A, B, C, and D correspond to delay times of 10, 50, 100, and 200  $\mu\text{s}$ , respectively.

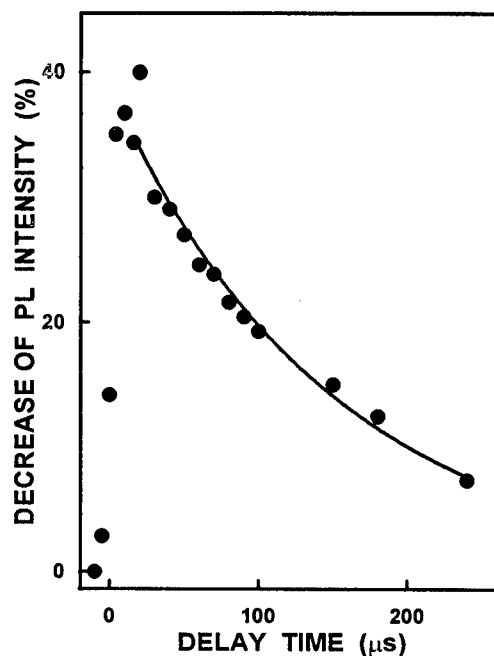


**Figure 3:** Dependence of the quenching effect on the delay time for  $\lambda=9.5 \mu\text{m}$ . The solid line has been fitted as a single-exponential decay yielding a time constant  $\tau_{TR} \approx 100 \mu\text{s}$ .

The results depicted in Fig.2 are readily understood if we assume that the infrared beam affects not the excited Er state but the transient BE state intermediating Er excitation; the effect diminishes as the concentration of these centers decreases and the excitation is transferred to Er. In such an interpretation the difference between the undisturbed signal (broken curve) and curves A through D corresponds to the number of Er atoms whose excitation is prevented by the IR pulse. If we assume that the total PL is proportional to the number of intermediate BE centers available at the beginning of the excitation, then the magnitude of the quenching effect for different delay times will monitor the actual number of these centers. In Fig.3 the magnitude of the FELIX-induced quench is plotted versus the delay time between both laser pulses. As can be seen, the quenching effect has a sharp onset and reaches its maximum for  $\Delta t \approx 10 \mu\text{s}$ , which corresponds to the situation when the Nd:YAG is fired immediately following the FELIX (macro) pulse, which has approximately 7  $\mu\text{s}$  duration. In this case the IR pulse quenches the Er-related photoluminescence to approximately 60% of its total intensity. For longer delays the effect gradually ceases to exist, in agreement with Fig.2, and can no longer be detected for  $\Delta t > 250 \mu\text{s}$ . If we assume, as outlined before, that the quenching effect is proportional to the number of intermediate BE states available at the moment of the pulse, then the lifetime of these centers can be estimated from Fig.3. A satisfactory computer fit can be obtained for  $\tau \approx 100 \mu\text{s}$ . The factor 2 difference between this effective lifetime value of the intermediate BE state and that estimated from the form of the PL signal, Fig.1, is most probably indicative of the approximations used in developing the quantitative description of the energy transfer process expressed by Eq.1. In any case we note that, according to the assumed energy transfer model, the

effective lifetime of the intermediate BE state should depend on relaxation paths alternative to Er excitation (e.g. nonradiative energy transfer to the conduction band) and, as such, could be strongly time-dependent, following the development of conduction electron concentration, see, e.g., Ref.2.

### C. A special quenching feature for $\lambda \approx 12.5 \mu\text{m}$

The quenching effect of the Er-related BE state outlined in the preceding section has been investigated as a function of the wavelength of the IR laser beam. The experiments were performed for various delay times. For a short delay of  $\Delta t = 5 \mu\text{s}$  (maximum quench) no significant differences were found, except for a general lowering of the effect for  $\lambda > 16 \mu\text{m}$ , presumably due to water absorption in air. However, for  $\Delta t = 50 \mu\text{s}$  an additional feature around the wavelength  $\lambda \approx 12.5 \mu\text{m}$  was detected: following the IR pulse the PL signal remained stable for approximately 30-40  $\mu\text{s}$  before starting to decrease, as observed for other wavelengths. This resulted in a somewhat smaller quench monitored as total integrated PL signal. The effect is depicted in Fig.4, where the PL signal remaining after the FELIX pulse is plotted - a local maximum centered around  $\lambda = 12.5 \mu\text{m}$  can be concluded. For still longer delay times the  $\lambda = 12.5 \mu\text{m}$  feature gradually disappears, as does also the total quenching effect.

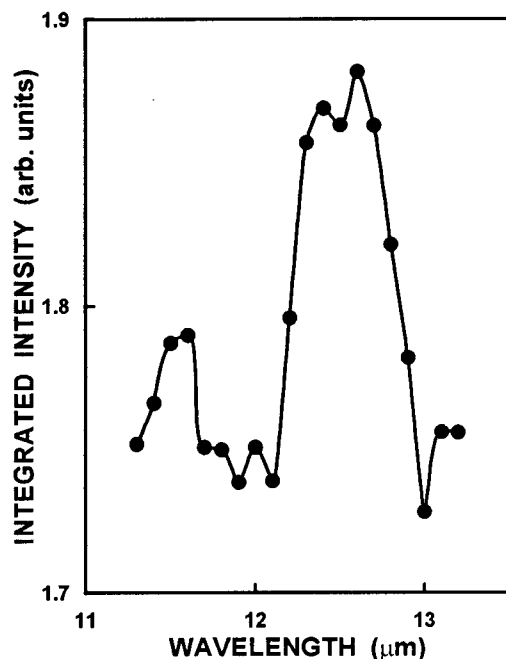


**Figure 4:** Quenching effect as observed for the delay time  $\Delta t = 50 \mu\text{s}$ . A reduced quenching for  $\lambda \approx 12.5 \mu\text{m}$  can be noted.

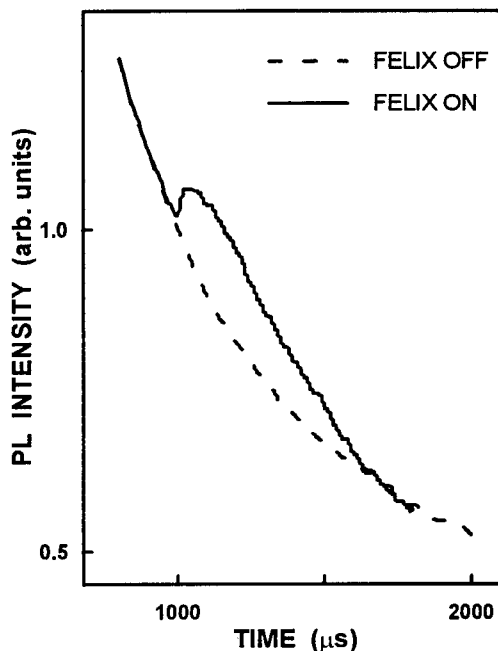


**Figure 5:** An increase of the PL signal by the IR pulse observed for large delay times;  $\Delta t = 1 \text{ ms}$ ,  $\lambda = 9.6 \mu\text{m}$ .

While the experimental finding reported here is a matter of current investigation and requires further confirmation, it is certainly tempting to relate it to the back-transfer process outlined in the introductory section. In case that this process would be induced, one might expect that part of the energy of the IR beam would now be absorbed by excited Er atoms converting them back into the intermediate BE state. This could lead to an additional excitation of Er after termination of the IR pulse, thus generating an effect of "delayed PL". Taking into account the available detector decay time, such a feature could result in a smaller recorded quench of the total signal. If the observed effect would indeed be related to the back-transfer mechanism then it could take place only when a considerable concentration of excited Er would become available; this could explain why it is not observed immediately following the Nd:YAG pulse ( $\Delta t = 5 \mu\text{s}$ ). We note further that no quenching can be observed for  $\Delta t > 250 \mu\text{s}$ . To this end we recall that recent theoretical work [4] suggests

that the back-transfer process requires participation of an electron in the conduction band; in our experiment conduction electrons are present immediately after the excitation, or, alternatively, they can be generated by the IR pulse due to the dissociation of the intermediate Er-related BE state. In the latter case the back-transfer process could not be observed after decay of the BE state, in agreement with the experiment. Finally, we point out that the photon energy for which the described special quenching feature takes place is very similar to one of the activation energies as determined from the temperature dependence of the PL intensity for the same sample [7].

#### D. Enhancement of PL intensity for long delay times

For long delay times between the two pulses,  $\Delta t \geq 800 \mu\text{s}$ , a different effect has been observed. This is illustrated in Fig.5. As can be seen, the IR pulse applied when the intensity of PL has already decayed to below 50% causes a transient increase of PL; following that, the signal continues to decay with, possibly, a somewhat shorter time constant. The enhancement effect, clearly observed here, needs to be further investigated in more detail. Its origin is at present unclear, as no such feature has been predicted by the existing models of Er-related energy transfer mechanisms.

As mentioned before, it has been suggested in the past that within the PL of Er in silicon two components can be separated with different decay time constants [6]. According to that interpretation, after a delay of more than  $800 \mu\text{s}$  the PL would be dominated by a “slow” species giving a long-lasting, weak emission. An effect as depicted in Fig.5 could take place if the IR laser pulse would be capable of converting the slow-decaying species into the fast ones. At this moment, however, such a mechanism remains purely speculative and it is evident that more research is required.

#### Conclusions

In the performed study the influence of an intense IR illumination on intensity and decay characteristics of the PL signal generated by a visible laser pulse in Er-doped silicon has been investigated. The quenching of the PL signal was concluded. This effect has been related to the dissociation of the Er-related BE state rather than to the decrease of the concentration of the excited Er centers. A special quenching feature was found for  $\lambda = 12.5 \mu\text{m}$ ; this could be a manifestation of the back-transfer process converting excited Er centers into the BE state intermediating the energy transfer to the 4f shell. If confirmed, the observed effect would indicate that conduction electrons are required for the back-transfer process. Investigations currently on the way will further elucidate the reported issues [8].

#### Acknowledgements

We gratefully acknowledge the support by the *Stichting voor Fundamenteel Onderzoek der Materie* (FOM) in providing the required beam time on FELIX and highly appreciate the skillful assistance by the FELIX staff, in particular Dr A.F.G. van der Meer. This work was supported in part under the TMR program of the European Community. The sample used in the study was kindly provided by Dr F.P. Widdershoven of Philips Research Laboratory, Eindhoven, The Netherlands.

#### References

1. T. Gregorkiewicz, I. Tsimperidis, C.A.J. Ammerlaan, F.P. Widdershoven, and N.A. Sobolev, in *Rare Earth Doped Semiconductors II*, ed. S. Coffa, A. Polman, and R.N. Schwartz, Materials Research Society Symposia Proceedings, Vol.442, p.207-218, (MRS, Pittsburgh, 1996).
2. J. Palm, F. Gan, B. Zheng, J. Michel, and L.C. Kimerling, *Phys. Rev. B* **54**, 17603 (1996).
3. I.N. Yassievich and L.C. Kimerling, *Semicond. Sci. Technol.* **8**, 718 (1993).
4. M.S. Bresler, O.B. Gusev, B.P. Zakharchenya, and I.N. Yassievich, *Solid State Physics* **38**, 813 (1996), (*Fizika Tverdogo Tela* **38**, 1474 (1996)).
5. F. Priolo, G. Franzò, S. Coffa, A. Polman, S. Libertino, R. Barklie, and D. Carey, *J. Appl. Phys.* **78**, 3874 (1995).
6. D. T. Xuan Thao, T. Gregorkiewicz, C.A.J. Ammerlaan, F.P. Widdershoven, and N.A. Sobolev - to be published.
7. S. Coffa, G. Franzò, F. Priolo, A. Polman, and R. Serna, *Phys. Rev. B* **49**, 16313 (1994).
8. I. Tsimperidis, T. Gregorkiewicz, H.H.P.Th. Bekman, C.J.G.M. Langerak, and C.A.J. Ammerlaan - to be published.



## DIRECT EVIDENCE FOR STABILITY OF TETRAHEDRAL INTERSTITIAL Er IN Si UP TO 900°C

U. Wahl, J.G. Correia<sup>1</sup>, G. Langouche, J.G. Marques<sup>2</sup>,  
A. Vantomme, and the ISOLDE collaboration<sup>1</sup>

Instituut voor Kern- en Stralingsfysica, University of Leuven, Celestijnenlaan 200 D,  
B-3001 Leuven, Belgium, email: ulrich.wahl@fys.kuleuven.ac.be

<sup>1</sup> CERN-PPE, CH-1211 Genève 23, Switzerland

<sup>2</sup> CFNUL, Av. Prof. Gama Pinto 2, P-1699 Lisboa Codex, Portugal

**Keywords:** Si, Er, rare earth doping, lattice location, ion implantation

### Abstract

Conversion electron emission channeling from the isotope  $^{167m}\text{Er}$  (2.28 s), which is the decay product of radioactive  $^{167}\text{Tm}$  (9.25 d), offers a means of monitoring the lattice sites of Er in single crystals. We have used this method to determine the lattice location of  $^{167m}\text{Er}$  in Si directly following room temperature implantation of  $^{167}\text{Tm}$ , after subsequent annealing steps, and also in situ during annealing up to 900°C. Following the recovery of implantation damage around 600°C, about 90% of Er occupies near-tetrahedral interstitial sites in both FZ and CZ Si. While in FZ Si  $^{167m}\text{Er}$  was found to be stable on these sites even at 900°C, the tetrahedral Er fraction in CZ Si decreased considerably after annealing for 10 min at 800°C and above.

### Introduction

Despite an impressive success in manufacturing light-emitting diodes from Er-doped Si [1-3], the microscopic structure and detailed luminescence mechanisms of Er in Si are still a matter of debate. This includes in particular the lattice sites of Er and the role of possible light element ligands such as C, N, O or F which were found to intensify the luminescence yield [4]. Theoretical investigations [5] predict that tetrahedral interstitial (T) sites are the most stable sites for all oxidation states of isolated Er atoms in Si, while substitutional (S) and hexagonal interstitial (H) sites should be metastable. Direct lattice location using the Rutherford backscattering (RBS) channeling technique, however, only suggested Er on S [6] or H [7,8] sites. Photoluminescence (PL) spectroscopy studies have identified a number of Er defects with different symmetry properties in Si [9,10]. The most intense PL yield resulted from two centers having cubic and axial symmetry, respectively. The cubic center occurred in both float-zone (FZ) and Czochralski (CZ) Si and was attributed to tetrahedral interstitial Er, while the center with axial symmetry was characteristic to CZ Si and ascribed to Er-O complexes [10]. Possible explanations for several other PL centers of lower symmetry, observed mainly in Si annealed at lower temperatures (600°C), were Er on H sites [9], Er paired with implantation-induced defects [10], and recently also Er on S sites [11]. Different atomic surroundings of Er in FZ Si and CZ Si were clearly revealed by studying its extended X-ray absorption fine structure (EXAFS) [12,13]. In FZ Si and 600°C-annealed CZ Si, EXAFS observed Er surrounded by 6-12 Si atoms at distances around 3.0 Å. This can be explained by the majority of Er in  $\text{Er}_3\text{Si}_5$  or  $\text{ErSi}_2$  silicide phases, where 10, respectively 12, nearest neighbour (NN) Si atoms are at 2.99 Å. However, isolated Er on T sites with 4 NN at 2.35 Å and 6 next-nearest neighbours (NNN) at 2.72 Å, or on H sites (6 NN at 2.25 Å, 8 NNN at 3.53 Å) cannot be ruled out taking into account possible relaxations of surrounding Si atoms, while Er on S sites (4 NN at 2.35 Å, 12 NNN at 3.84 Å) seems less probable. In contrast to this, Er in O-implanted or CZ Si annealed to 900°C was characterized by  $\text{Er}_2\text{O}_3$ -like surroundings with 5-6 nearest O neighbours at distances around 1.5-2.5 Å. We report on direct lattice location of Er in Si using the emission channeling technique [14], which makes use of the fact that charged particles emitted from radioactive isotopes in a single crystal experience channeling or blocking effects along crystallographic axes and planes. This leads to an

anisotropic emission yield from the crystal surface, which depends in a characteristic way on the occupied lattice sites of the probe atoms. Previously [15], we have already applied this method to study Er in CZ Si. In the present contribution we focus on results in FZ Si and compare both types of Si.

### Experiment

For lattice location of Er we monitored the angular-dependent emission yield of the combined intensity of 150, 199 and 206 keV conversion electrons emitted from the nucleus  $^{167m}\text{Er}$  ( $t_{1/2}=2.28$  s). This isomeric state is populated as a result of the decay of radioactive  $^{167}\text{Tm}$  ( $t_{1/2}=9.25$  d). The isotope  $^{167}\text{Tm}$  was produced at the ISOLDE facility [16] at CERN. We investigated four different samples,  $p\text{-Si:B FZ}$  (10 k $\Omega\text{cm}$ ,  $\langle 111 \rangle$  surface orientation, implanted dose  $4.8 \times 10^{13} \text{ cm}^{-2}$ ),  $n\text{-Si:P FZ}$

( $>4$  k $\Omega\text{cm}$ ,  $\langle 111 \rangle$ ,  $5.1 \times 10^{13} \text{ cm}^{-2}$ ),  $p\text{-Si:B CZ}$  ( $\langle 100 \rangle$ , 5-14  $\Omega\text{cm}$ ,  $4.4 \times 10^{13} \text{ cm}^{-2}$ ) and  $n\text{-Si:P CZ}$  ( $\langle 100 \rangle$ , 1-10  $\Omega\text{cm}$ ,  $3.5 \times 10^{13} \text{ cm}^{-2}$ ). All samples were initially dipped into HF to remove native oxide layers. Following 60 keV room temperature implantation of  $^{167}\text{Tm}$ , the  $n\text{-Si CZ}$  crystal was annealed in an external vacuum furnace at  $<10^{-5}$  mbar, while thermal treatment of all other samples took place in the channeling setup at  $<10^{-6}$  mbar by means of a W filament for radiative heating up to 900°C. The conversion electron emission yield as a function of the angle from different crystallographic directions was measured using a position-sensitive Si "pad" detector [17], consisting of  $22 \times 22$  pads (or pixels) of  $1.3 \times 1.3 \text{ mm}^2$  size and mounted at a distance of 285 mm from the sample.

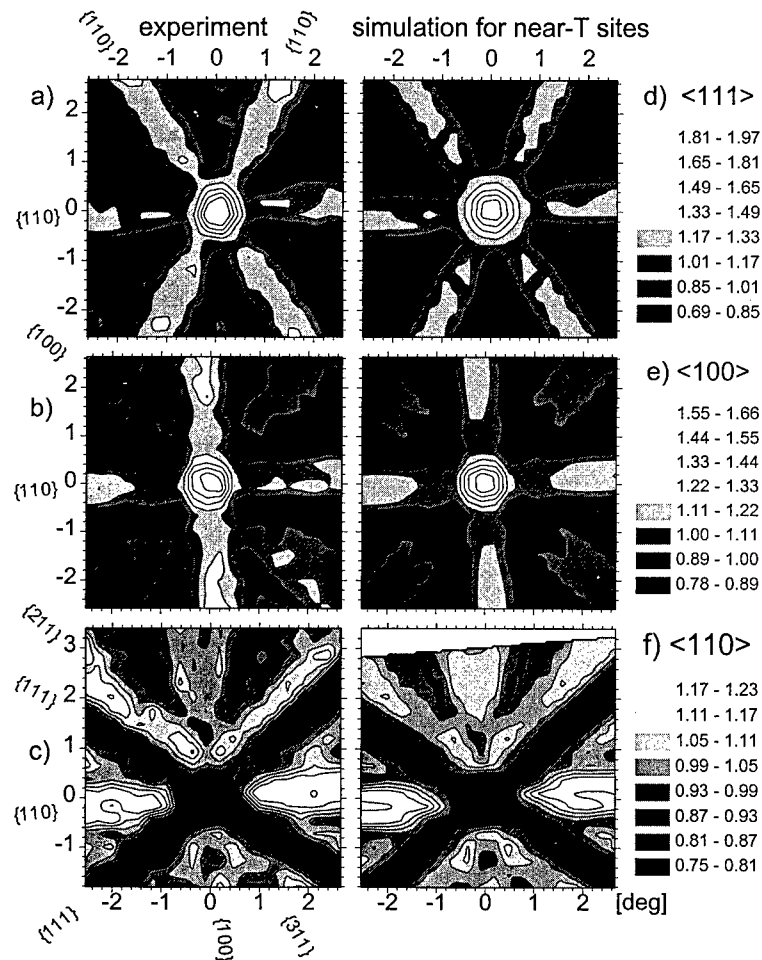


**Fig. 1.** a), b), c): channeling patterns from  $^{167m}\text{Er}$  in  $n\text{-Si FZ}$  annealed at 600°C for 10 min. Normalized electron emission yields in the vicinity of  $\langle 111 \rangle$ ,  $\langle 100 \rangle$  and  $\langle 110 \rangle$  directions are shown. d), e), f): best fits of simulated patterns to the experimental yields, corresponding to 94%, 99% and 95% of emitter atoms on sites which are displaced by 0.43 Å from the T site.

## Results and Discussion

Figures 1a, 1b and 1c show the normalized emission yield of conversion electrons from  $^{167\text{m}}\text{Er}$ , measured at 20°C after annealing the *n*-Si FZ crystal at 600°C for 10 min. Clearly visible are channeling effects along axial  $\langle 100 \rangle$  and  $\langle 111 \rangle$  and planar  $\{110\}$ ,  $\{100\}$  and  $\{211\}$ , while axial  $\langle 110 \rangle$  and planar  $\{111\}$  and  $\{311\}$  directions all show yields close to or below unity. The combination of these patterns provides direct evidence that the majority of  $^{167\text{m}}\text{Er}$  occupies sites close to the tetrahedral interstitial position. The T sites are perfectly aligned with  $\langle 100 \rangle$ ,  $\langle 111 \rangle$ ,  $\{110\}$ ,  $\{100\}$  and  $\{211\}$  lattice directions, leading to channeling of electrons emitted from these sites, but they are off the  $\langle 110 \rangle$  atomic axes and  $\{111\}$  and  $\{311\}$  atomic planes, causing yield minima along these directions. In order to extract more specific information, the experimental patterns are compared to theoretical emission yields for a variety of different lattice sites. The basic principles of computer simulations of electron emission channeling are discussed in Ref. [14]. More detailed information on calculations for  $^{167\text{m}}\text{Er}$  in Si and on the fitting procedures for comparison of theoretical and experimental patterns were given in Ref. [15]. Note that the fitting procedures are only slightly modified versions of those used already for alpha emission channeling [18].

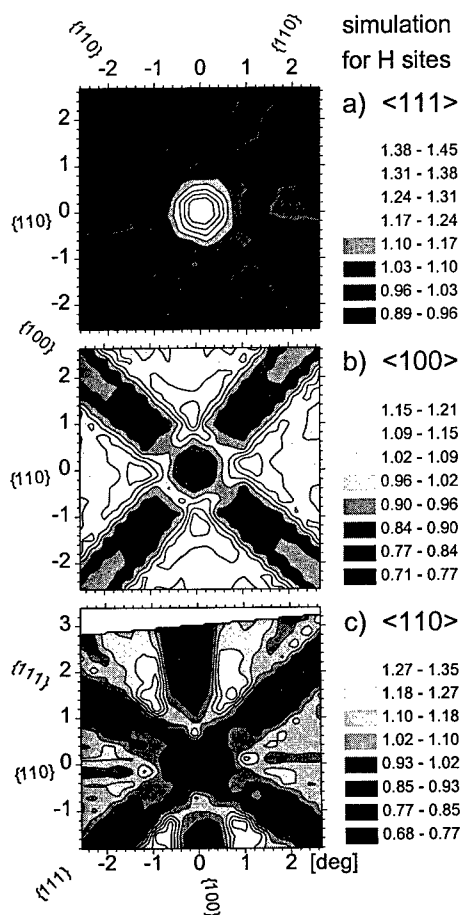


**Fig. 2.** Calculated patterns for 100% of  $^{167\text{m}}\text{Er}$  on H sites, choosing the same orientation and angular resolution as used in the fits in Fig. 1.

The experimental data shown in Fig. 1 can be well described by assuming only one type of Er lattice site and a small so-called "random" fraction, the latter responsible for an isotropic electron emission yield. Under these assumptions, best fit results are obtained for nearly 100% of emitter atoms on sites which are 0.43(8) Å displaced from the tetrahedral interstitial T site. Note that ideal T sites would yield much more pronounced  $\langle 111 \rangle$  and  $\langle 100 \rangle$  channeling effects. Therefore ideal T sites cannot satisfactorily fit the experimental patterns, leading to a >30% increase in the chi square value. However, the fit quality is not particularly sensitive to the direction of the displacement, and displacements along  $\langle 111 \rangle$  and  $\langle 100 \rangle$  give similar results. Allowing for contributions from more than one site does not significantly improve fit quality, while comparable chi square values can usually be obtained for several combinations of lattice sites in the range  $d \approx 0.0\text{--}0.6$  Å from the T sites. This behaviour is not astonishing since in case of small displacements the channeling effect mainly senses the projected mean displacement of the emitter atoms. On the other hand, significant Er fractions on sites further away from T sites can be ruled out, since these exhibit entirely different emission patterns. This is illustrated for the case of H sites in Fig. 2, where characteristic changes compared to T sites are the emission minima along  $\langle 100 \rangle$  and  $\{100\}$  directions. This is due to the fact that H sites are located off all atomic  $\langle 100 \rangle$  axes and  $\{100\}$  planes. Note that the  $\langle 111 \rangle$  and  $\langle 100 \rangle$  patterns of bond center (BC) and anti-bonding (AB) sites are completely identical to H sites. If existing at all, the Er fraction on substitutional sites must also be small. Only the

$\langle 110 \rangle$  pattern (Fig. 1c) allows to discriminate between S and T sites. Slight improvements in  $\langle 110 \rangle$  fit quality indicated possible fractions of up to 5% on S sites, however, this value is close to the statistical limit of the data.

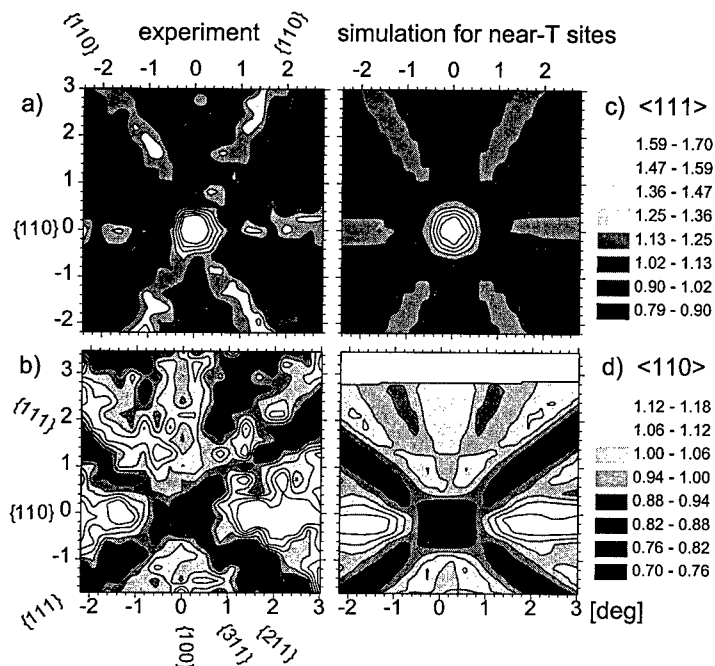


**Fig. 3.** a), b):  $\langle 111 \rangle$  and  $\langle 110 \rangle$  channeling patterns from  $^{167\text{m}}\text{Er}$  in  $n$ -Si FZ measured at 900°C. c), d): best fits of simulated patterns to the experimental yields, corresponding to 95% and 87% of emitter atoms on near-T sites.

channeling patterns while keeping the  $n$ -Si FZ sample at 600°C and 900°C, we obtained essentially the same results as at room temperature (Figs. 3 and 4). This gives direct evidence that Er is stable on the near-T sites up to 900°C, at least during the 2.28 s time window of the half life of the isomeric state.

Figure 4 displays the Er fractions on near-T sites following isochronal annealing steps of both FZ and CZ Si. Electron emission channeling effects were already clearly visible directly after room temperature implantation. The channeling patterns could be well fitted by assuming 20-25% of Er on near-T sites and the others contributing with an isotropic emission yield. Isotropic emission yields are characteristic for probe atoms on sites of very low crystal symmetry or in amorphous surroundings. Since the  $^{167}\text{Tm}/^{167}\text{Er}$  probes end up in highly defective crystalline surroundings, we believe that in the as-implanted state the fraction of probe atoms which are located near tetrahedral interstitial positions with only short-range order preserved, is much higher than 20-25%. Upon annealing to 600°C, electron emission channeling effects increased markedly. We attribute this to the well-known solid phase epitaxial regrowth of implanted Si in the temperature range 550-600°C (see, e.g., Ref. [19]). As a result, the quality of the crystal lattice is restored to a large extent, and our measurements show that subsequently more than 90% of  $^{167}\text{Er}$  emitter atoms are located on near-T sites. For annealing above 800°C, the fraction on near-T sites dropped markedly in CZ Si. However, this decrease was not compensated by an increase of other specific lattice sites but was

We can not a priori exclude that the observed  $^{167\text{m}}\text{Er}$  lattice sites are already completely determined by the chemical nature of the parent Tm. The influence of the electron capture decay of  $^{167}\text{Tm}$  is hard to predict. The  $^{167}\text{Er}$  nucleus receives a recoil energy of 0.7 to 0.9 eV due to neutrino emission, and the initial electronic configuration of Er contains a hole in the K shell. Both thermalization of nuclear recoil and electronic deexcitation via X-ray emission are finished when the conversion electrons are emitted, but could have produced metastable configurations. We have therefore chosen to directly monitor the thermal stability of near-tetrahedral  $^{167\text{m}}\text{Er}$  by increasing the measuring temperature.

Recording emission

rather due to the occupancy of random sites. In contrast, even prolonged annealing at 900°C for 2h could not reduce the near-T fraction in FZ Si by more than 10%.

Comparing with RBS studies reported in the literature, our results correspond with the near-T sites assigned to Yb in Si [20,21], Er in GaAs [22,23] and Er in highly doped AlGaAs [23], but differ from the H sites reported for Er in 600°C-annealed CZ Si [8,9], S sites for Er in unspecified Si [7], and S sites for Er in low-doped AlGaAs [23]. Possible reasons for the discrepancy in the case of CZ Si could be the higher Er doses applied in the RBS experiments combined with hot implantation at 350°C, or the influence of nuclear decay in our experiments. However, since the RBS data shown in Refs. [8,9] closely resemble those in Refs. [22,23], we suggest that the interpretation as H sites is questionable and the authors of [8,9] also observed near-T sites.

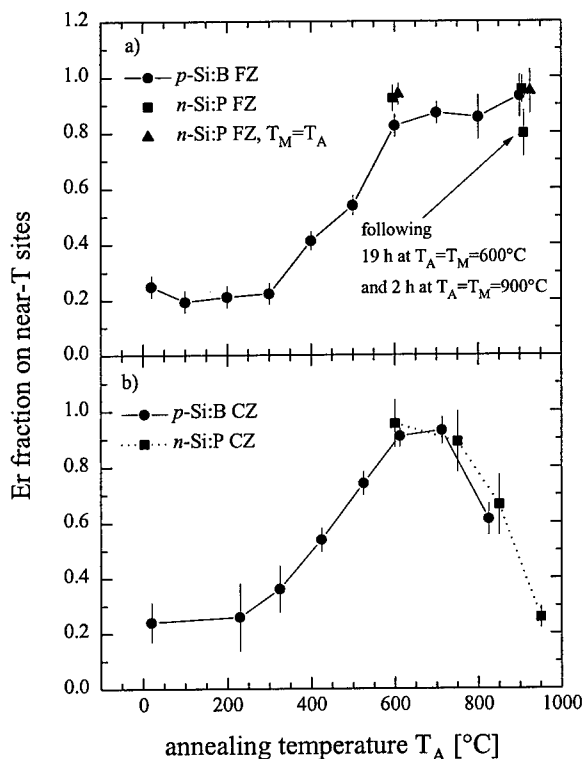


**Fig. 4.** Isochronal annealing sequences (10 min) for the fraction of  $^{167m}\text{Er}$  on near-T sites in FZ and CZ Si. All measurements were done at room temperature, except for those marked  $T_M=T_A$ , where measuring and annealing temperature were identical.

precipitation nuclei for additional oxygen supplied by the bulk and the remaining rare earths, forming disordered  $\text{Er}_2\text{O}_3$ -like precipitates.

### Conclusions

Our experiments give direct evidence that Er can be incorporated close to tetrahedral interstitial sites in Si, as was already suggested by the existence of a cubic PL center [9,10] and is in accordance with theoretical predictions [5]. However, we observed either static displacements of 0.43(8) Å from ideal T sites for all Er atoms, or, equally possible, the existence of several different Er lattice sites in the range 0-0.6 Å from the T sites. Our interpretation is that there exists a mixture of

What could be the reasons for the decrease in the near-T Er fraction in CZ Si? The Tm/Er concentration reaches a maximum of  $2 \times 10^{19} \text{ cm}^{-3}$  in the peak of the implantation cascade, which is about a factor of 20 or more higher than the usual O concentrations in CZ Si. From the diffusivity of O ( $D=0.13 \text{ cm}^2 \text{ s}^{-1} \exp[-2.53 \text{ eV/kT}]$  [24]) one estimates migration lengths of 110 Å within 10 min at 600°C and 8100 Å at 900°C. Therefore, a few simple O-Tm and O-Er pairs might already form at moderate annealing temperatures. Complexes where all Tm/Er atoms are saturated with multiple oxygen atoms, however, would require prolonged annealing since the additional oxygen has to be supplied by the bulk of the sample. At 900°C the diffusivity of Er ( $D \approx 10^{-15} \text{ cm}^2 \text{ s}^{-1}$  [1]) also plays a role, giving mean diffusion lengths of 190 Å within 10 min. The parent Tm probably acts similar to Er. The following scenario is compatible with both our observations in CZ Si and the EXAFS results of Refs. [12,13]. Some Er atoms capture oxygen already around 600°C, probably still residing on near-T sites. Upon further annealing to 900°C these centers act as pre-

Er on ideal T sites and some displaced Er paired with nearby vacancies or other defects. In contrast to FZ Si, where near-T Er shows a remarkable thermal stability even at 900°C, the near-T fraction of  $^{167m}\text{Er}$  in CZ Si decreases considerably for 10 min annealing at 800°C and above. We therefore suggest that segregation of Er and O into small disordered rare earth oxide precipitates accompanies the increase in luminescence yield which is usually observed for Er-doped CZ Si annealed at 900°C.

### Acknowledgments

We thank H. Hofsäss for the permission to use his electron channeling simulation code "Manybeam". J.G.M. and J.G.C. acknowledge JNICT (Portugal) for grants under the Praxis XXI program, A.V. the post-doctoral research program of the Fund for Scientific Research, Flanders (FWO).

### References

- [1] F.Y.G. Ren, J. Michel, Q. Sun-Paduan, B. Zheng, H. Kitagawa, D. C. Jacobson, J. M. Poate and L. C. Kimerling, *Mat. Res. Soc. Symp. Proc.* **301**, 87 (1993).
- [2] G. Franzo, F. Priolo, S. Coffa, A. Polman and A. Camera, *Appl. Phys. Lett.* **64**, 2235 (1994).
- [3] B. Zheng, J. Michel, F.Y.G. Ren, L.C. Kimerling, D. C. Jacobson and J. M. Poate, *Appl. Phys. Lett.* **64**, 2842 (1994).
- [4] J. Michel, J.L. Benton, R.F. Ferrante, D.C. Jacobson, D.J. Eaglesham, E.A. Fitzgerald, Y.H. Xie, J.M. Poate and L.C. Kimerling, *J. Appl. Phys.* **70**, 2672 (1991).
- [5] M. Needels, M. Schlüter and M. Lannoo, *Phys. Rev. B* **47**, 15533 (1993).
- [6] Y. S. Tang, Z. Jingping, K. C. Heasman and B. J. Sealy, *Sol. State Comm.* **72**, 991 (1989).
- [7] A. Kozanecki, R. Wilson, B. J. Sealy, J. Kaczanowski, and L. Nowicki, *Appl. Phys. Lett.* **67**, 1847 (1995).
- [8] A. Kozanecki, J. Kaczanowski, R. Wilson and B. J. Sealy, *Nucl. Instr. Meth. B* **118**, 709 (1996).
- [9] Y.S. Tang, K.C. Heasman, W.P. Gillin, and B.J. Sealy, *Appl. Phys. Lett.* **55**, 432 (1989).
- [10] H. Przybylinska, W. Jantsch, Y. Suprun-Belevitch, M. Stephikhova, L. Palmetshofer, G. Hendorfer, A. Kozanecki, R. J. Wilson and B. J. Sealy, *Phys. Rev. B* **54**, 2532 (1996).
- [11] S.Y. Ren and J.D. Dow, *J. Appl. Phys.* **81**, 1877 (1997).
- [12] D.L. Adler, D.C. Jacobson, D.J. Eaglesham, M.A. Marcus, J.L. Benton, J.M. Poate and P.H. Citrin, *Appl. Phys. Lett.* **61**, 2181 (1993).
- [13] A. Terrasi, G. Franzo, S. Coffa, F. Priolo, F. D'Acapito and S. Mobilio, *Appl. Phys. Lett.* **70**, 1712 (1997).
- [14] H. Hofsäss and G. Lindner, *Phys. Rep.* **201**, 123 (1991).
- [15] U. Wahl, J.G. Correia, J. De Wachter, G. Langouche, J.G. Marques, R. Moons, A. Vantomme, and the ISOLDE collaboration, *Mat. Res. Soc. Symp. Proc.* **469** (1997), in press.
- [16] E. Kugler, D. Fiander, B. Jonson, H. Haas, A. Przewloka, H.L. Ravn, D.J. Simon, K. Zimmer and the ISOLDE collaboration, *Nucl. Instr. Meth. B* **70**, 41 (1992).
- [17] P. Weilhammer, E. Nygård, W. Dulinski, A. Czermak, F. Djama, S. Gadomski, S. Roe, A. Rudge, F. Schopper and J. Strobel, *Nucl. Instr. Meth. A* **383**, 89 (1996).
- [18] U. Wahl, S.G. Jahn, M. Restle, C. Ronning, H. Quintel, K. Bharuth-Ram, H. Hofsäss, and the ISOLDE collaboration, *Nucl. Instr. Meth. B* **118**, 76 (1996).
- [19] E. Rimini, *Ion Implantation: Basics to Device Fabrication*, Kluwer, Boston, 1995, p 173 ff.
- [20] J.U. Andersen, O. Andreassen, J.A. Davies and E. Uggerhøj, *Radiat. Effects* **7**, 25 (1971).
- [21] F. H. Eisen and E. Uggerhøj, *Radiat. Effects* **12**, 233 (1972).
- [22] J. Nakata, M. Taniguchi and K. Takahei, *Appl. Phys. Lett.* **61**, 2665 (1992).
- [23] E. Alves, M.F. da Silva, A.A. Melo, J.C. Soares, G.N. van den Hoven, A. Polman, K.R. Evans and C.R. Jones, *Mat. Res. Soc. Symp. Proc.* **301**, 175 (1993).
- [24] Landolt-Börnstein, *Numerical Data and Functional Relationships in Science and Technology*, Vol. 22b, edited by M. Schulz (Springer, Berlin, 1989).

## PHOTO- AND ELECTROLUMINESCENCE OF ERBIUM-DOPED SILICON

S. Lanzerstorfer<sup>1</sup>, M. Stepikhova<sup>1,2</sup>, J. Hartung<sup>3</sup>, C. Skierbiszewski<sup>4</sup> and W. Jantsch<sup>1</sup>

<sup>1</sup>Institut für Halbleiterphysik, Johannes Kepler Universität, 4040 Linz, AUSTRIA

<sup>2</sup>Permanent address: State University, 603600 Nizhny Novgorod, RUSSIA

<sup>3</sup>Centre for Electronic Materials and Dept. of Electrical Engineering and Electronics, UMIST, PO Box 88, Manchester M60 1QD, UK

<sup>4</sup>High Pressure Research Center, Polish Academy of Sciences, 01-142 Warsaw, Poland

**Keywords:** erbium, silicon, electroluminescence, excitation mechanism, rise time, decay time

**Abstract.** We investigate Er implanted light emitting diodes operating under forward bias and we discuss the mechanisms responsible for the luminescence quenching. The Er-related photo- and electroluminescence intensity exhibit qualitatively the same temperature dependence as the decay time of the 1.54  $\mu\text{m}$  emission. Both the rise time and the decay time of the Er luminescence decrease with increasing driving current. The rise time drops to a minimum value, whereas the decay is accelerated with increasing current. Depleting the space charge region of the diode between the forward bias pulses gives no change in decay time. This demonstrates, that an Auger process via free carriers cannot account for the de-excitation process at the present carrier concentrations. We ascribe the temperature quenching to a thermally activated energy back-transfer via a deep level in the gap. Our results indicate, that the 1.54  $\mu\text{m}$  emission at room temperature is due to dislocation related luminescence.

### Introduction

Optical transitions within the 4f shell of rare earth dopants in semiconductors and other luminescent materials can be utilized for a variety of applications like photon up-conversion, optical amplification and lasers. Er in its trivalent charge state shows luminescence at 1.54  $\mu\text{m}$  which is an important wavelength in optical communication due to minimum losses in fibers. The emission wavelength of this intra 4f ( $^4\text{I}_{13/2} \rightarrow ^4\text{I}_{15/2}$ ) transition is nearly host- and temperature independent. Especially Er doped Si has attracted considerable interest for the last decade and great efforts were undertaken to increase the photo- (PL) and the electroluminescence (EL) yield [1-3]. The incorporation of Er in Si circumvents the indirect bandgap of Si and it offers the benefit of a temperature stable infrared light source compatible with Si technology. Co-doping with light elements (mainly oxygen) high Er concentrations and specific annealing procedures are required to achieve intense luminescence [4, 5]. Only non-equilibrium methods like ion implantation and molecular beam epitaxy (MBE) provide Er concentrations far beyond the solubility limit [6, 7]. The main obstacle in obtaining practical devices of Er doped Si is the temperature induced quenching of the luminescence well below 200 K. Therefore it is necessary to understand which mechanisms govern the excitation and the radiative and non-radiative de-excitation of the  $\text{Er}^{3+}$  ion, respectively. The excitation of PL, which is similar to EL in forward bias, occurs via an energy transfer from localized excitons to the Er 4f shell. Competing processes to the radiative de-excitation are back-transfer to a level in the gap and Auger recombination including free carriers, demonstrated in literature [8, 9]. In contrast to recent investigations [10], we used large area diodes to observe the luminescence yield and decay time behavior under a low current density excitation.

### Experimental

A single crystal (100) oriented p-type (boron doped) float zone silicon wafer with a resistivity of 20  $\Omega\text{cm}$  was implanted with Er, O and P at room temperature. To obtain a homogeneous doping profile Er was implanted with two energies, 300 keV and 80 keV and doses of  $7 \cdot 10^{12} \text{ cm}^{-2}$  and

$3 \cdot 10^{12} \text{ cm}^{-2}$ , respectively. O and P were coimplanted choosing such parameters that the projected range coincided with the 120 nm deep Er profile. The O dose was adjusted to obtain a concentration ten times higher than the Er concentration. Since the donor efficiency of Er in the presence of O is only 20% [11], P was implanted with a dose of  $1.5 \cdot 10^{12} \text{ cm}^{-2}$  in order to obtain a steeper p/n-junction. For comparison a p-type Czochralski silicon wafer with the same resistivity was implanted with  $8 \cdot 10^{13} \text{ cm}^{-2}$  Er. After implantation the samples were annealed at 900 °C for 30 min in a nitrogen ambient. The diode fabrication was completed by evaporation of 800 Å thick Au contacts. The light output was taken from the polished backside of the sample through a 30 μm spaced grating contact which ensures a fairly homogeneous electric field distribution within the 4x4 mm<sup>2</sup> sized samples. PL and EL measurements were performed by the use of a Bomem DA8 Fourier transform spectrometer. The samples were mounted on a cold finger of a continuous He flow cryostat placed in a vacuum chamber at the back port of the spectrometer. A liquid nitrogen cooled Ge detector was used to detect the light emitted from the samples. An InGaAs detector with a Peltier cooler and a 1.54 μm bandpass filter with a full width at half maximum of 15 nm were used for time resolved measurements recorded by an averaging Tektronix storage oscilloscope. The overall system response time was 20 μs.

### Results and discussion

EL spectra measured on a forward biased diode under cw-conditions are shown in Fig. 1a. We obtain a series of sharp lines characteristic for Er intra-4f transitions. Those from the center with cubic symmetry are labeled „C“, whereas line „D“ has been ascribed to a complex of Er and implantation defects [12, 13]. Increasing the current density affects only the intensity, but no additional lines appear. The background around 1.54 μm increases linearly with current density, whereas the Er related luminescence tends to saturate at relatively low current densities (s. Fig. 1b). Equivalent spectra are obtained in PL indicating that the same centers are excited, either optically or electrically.

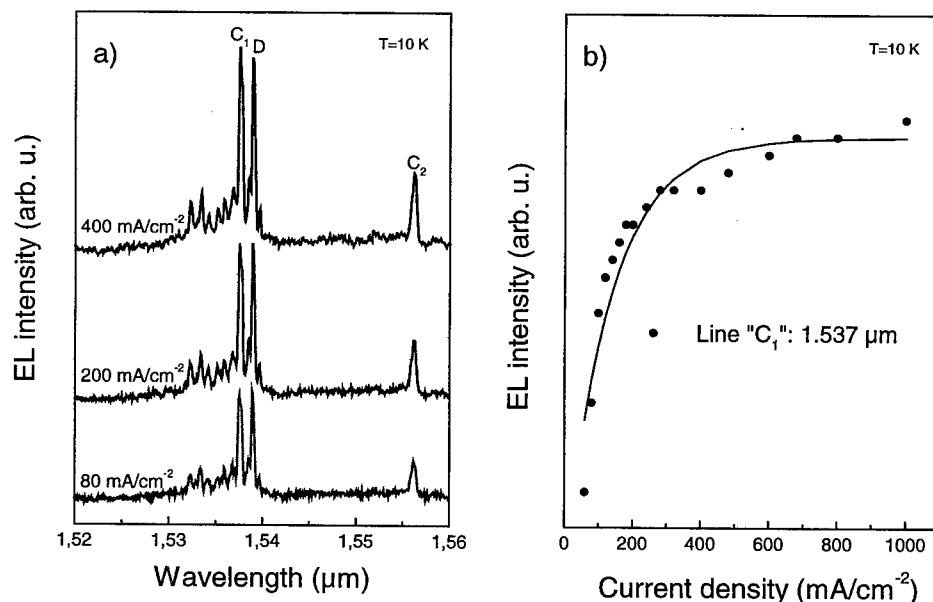


**Fig.1a)** EL spectra obtained at T=10 K with increasing current densities below saturation. The emission is caused by Er ions with cubic surrounding („C“) and by complexes of Er and implantation defects (D). **b)** Dependence of the C<sub>1</sub>-line intensity at 1.537 μm on current density at a constant temperature (10 K).



Figure 1b shows the dependence of the EL intensity of the 1.537  $\mu\text{m}$  line on current density. Below  $100 \text{ mA/cm}^2$  a linear increase of EL intensity is observed, while saturation occurs beyond  $400 \text{ mA/cm}^2$  at low temperatures. The solid line represents a fit applying a saturation law with  $120 \text{ mA/cm}^2$  as  $1/e$  value. At elevated temperatures this saturation threshold is shifted to higher current densities. The temperature quenching of the EL intensity in Fig. 2 is governed by three regimes. Below 20 K the intensity remains constant. At intermediate temperatures between 20 K and 100 K the EL yield starts to decrease with an activation energy of 10 meV. At temperatures higher than 100 K an efficient quenching mechanism reduces the EL intensity with a much higher activation energy of 70 meV which is responsible for vanishing EL at room temperature. As also depicted in Fig. 2 the temperature dependence of the EL intensity is nearly identical with the one of the decay time.

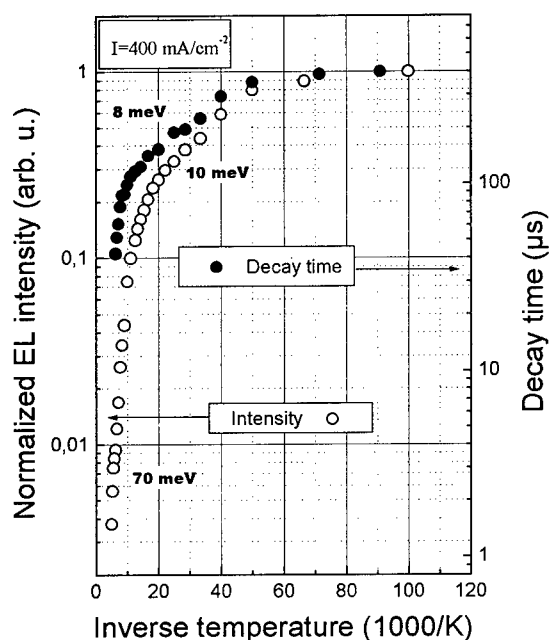


Fig. 2) Arrhenius plot of the EL intensity and the decay time of the 1.537  $\mu\text{m}$  line. The decay time is observed down to 40  $\mu\text{s}$ , which is twice the system response time.

in the luminescence quenching is ascribed to the exciton binding energy at a deep level localized in the vicinity of the Er ion where a subsequent energy transfer to the 4f shell can occur. Thermally released bound excitons and their non-radiative recombination without energy transfer could account for the different activation energies of luminescence- and decay time quenching. We relate the 90 meV quenching mechanism to contributions of both exciton dissociation and non-radiative de-excitation of the Er ion. The defect to which the exciton is bound serves as a co-activator for the Er excitation [13] and thus it can support also the energy back-transfer from the 4f shell including phonons to a carrier bound at this deep level, still populated at high temperatures. Since this activation energy does not depend on current density below saturation, we rule out an Auger process involving free carriers in this regime for our samples. However, an impurity Auger mechanism can be responsible for the de-excitation after back-transfer to this trap level.

The dependence of the EL intensity on current density (Fig. 1b) is similar to the behavior of the excitation probability, which is proportional to the inverse rise time, as revealed in Fig. 3a. Below the saturation regime the inverse rise time increases linearly with current density, whereas under

saturation the rise time drops to a minimum value of 80  $\mu\text{s}$  at the highest applied current density of 1 A/cm<sup>2</sup>. In the linear regime, the slope is proportional to the excitation cross section calculated to be  $\sigma = 2.5 \cdot 10^{-15} \text{ cm}^2$ , which demonstrates a relatively efficient excitation of the Er ions at low temperatures as compared with the cross section for direct optical excitation in the order of about  $5 \cdot 10^{-21} \text{ cm}^2$  [14]. An extrapolation of the rise time towards zero current gives a value of 270  $\mu\text{s}$ , which is about a quarter of the extrapolated decay time (see Fig. 3b) at the same temperature.

As shown in Fig. 3b, the decay time of the excited Er ions develops in a completely different way. Increasing the current density into the saturation regime results in a rapid drop of decay time indicating that a fast non-radiative mechanism becomes dominant at high current densities. The decay time in this region can be fitted using a quadratic dependence on the carrier concentration, as shown by the dotted line in Fig. 3b, which is characteristic for an Auger process involving free carriers. The relatively sharp onset of de-excitation via an Auger process and the coincidence with the saturation current density reveals

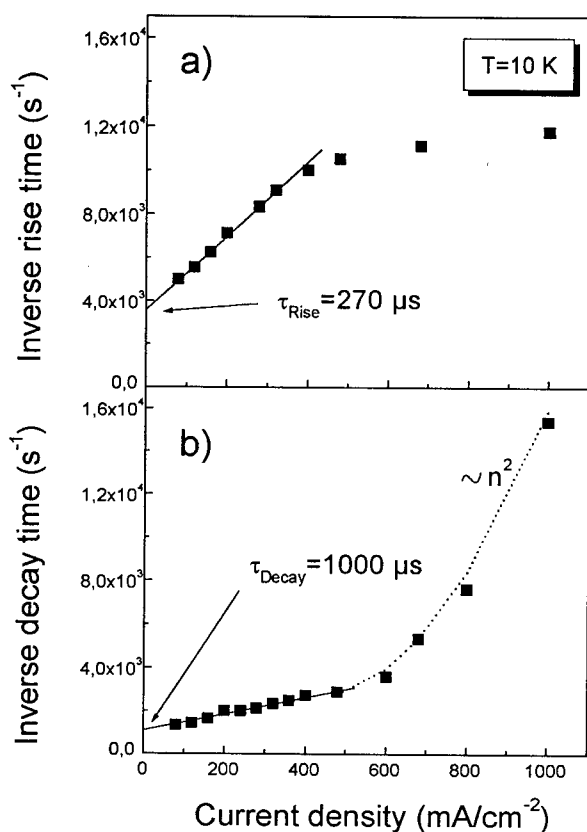


**Fig. 3a)** Dependence of the inverse rise time of the EL signal on current density in forward bias. **b)** Inverse decay time as a function of current density. Note the onset of non radiative de-excitation exceeding 600 mA/cm<sup>2</sup>.

a strong correlation between the excess carrier concentration and the quenching efficiency. In the low current density regime, there is no indication of Auger de-excitation mechanism in our samples. To strengthen this conclusion we investigated the EL decay time under different bias conditions with a current density below saturation. Fig. 4 shows the EL response excited by a 1 ms pulse in forward direction. The solid line represents the EL response without reverse bias between the forward biased pulses. Open circles give data for a reverse bias corresponding to 400 mA/cm<sup>2</sup>, which is well below the onset of decay time quenching. There is no influence of reverse bias, neither on rise time nor on the EL intensity nor on the decay time. This again indicates the absence of a free carrier Auger process below saturation conditions.

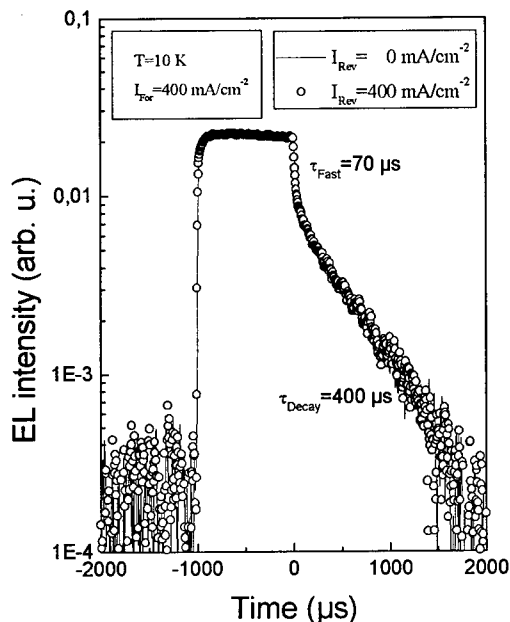


Fig. 4) EL response during applying a 1 ms pulse in forward direction. The solid line corresponds to zero bias, open circles represent the yield of the negative biased diode.

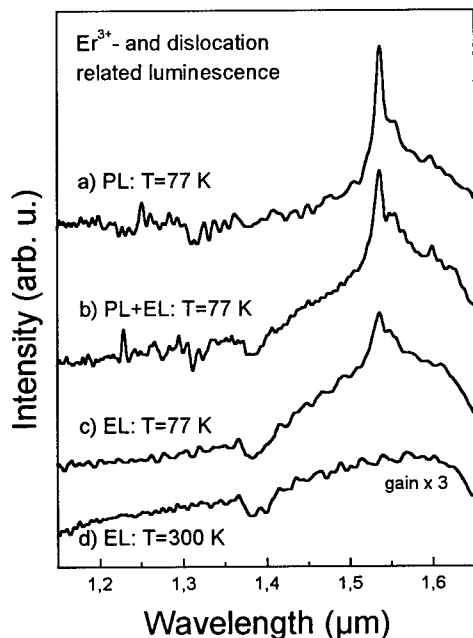


Fig. 5a) PL spectrum of the heavily doped sample at 77 K. b) Spectrum obtained applying photo- and electro excitation simultaneously. EL spectrum at the same temperature (c) and at room temperature (d)

As exemplified in Fig. 4, at low temperatures a fast initial decay of EL intensity is followed by a slow decay. Increasing the current density in forward bias results not only in a decrease of decay time (Fig. 3b), but this fast initial decay becomes more pronounced, too. In contrast to the slow decay time, the fast decay time of 70  $\mu\text{s}$  is not affected by increasing the current density at 10 K. Increasing the temperature to 100 K shortens the fast decay time, however, to the detector limit of 20  $\mu\text{s}$ . The portion of the EL yield which decays with this fast component grows linearly with the applied current density. These findings indicate that the fast de-excitation mechanism, which does not show saturation, is caused by centers without any direct correlation to Er. A comparison of the spectra obtained at current densities just below and well above saturation threshold reveals an unchanged Er related emission superimposed on a background, which grows linearly with increasing current density. Therefore we assume that the initial decay corresponds rather to dislocation related luminescence, which is always present as some background, than to Er.

Figure 5 shows spectra of the CZ sample implanted with a ten times higher Er dose ( $8 \cdot 10^{13} \text{ cm}^{-2}$ ). No sharp distinct lines occur as a consequence of substantial broadening due to heavy Er implantation. There is a weak background at 77 K in the range between 1.4  $\mu\text{m}$  and 1.7  $\mu\text{m}$  in the PL spectrum (trace a) caused by defect related luminescence. After applying also a current simultaneously to the photo-excitation (trace b), this background increases in magnitude and spectral extension. Exciting solely electrically (trace c) results mainly in this broad band luminescence rather than in Er related emission indicating an efficient energy transfer to centers responsible for the background luminescence.

The shape of the background and its spectral evolution with increasing temperature to higher energies resemble that of the so-called D1 dislocation line [15]. The dip around 1.4  $\mu\text{m}$  is an experimental artifact due to the setup used. Increasing the temperature to 300 K the Er luminescence vanishes as shown in trace d, whereas the dislocation related luminescence is still visible.

### Conclusions

The temperature quenching of the EL yield is related to the decay time. Below 20 K, both the EL yield and the decay time remain constant. Between 20 K and 100 K quenching of the EL intensity occurs with an activation energy of 10 meV corresponding to the exciton binding energy at a deep level. This possibly Er-, O-related level acts as a gateway for Er excitation and, at temperatures above 100 K, also for the de-excitation via an energy back transfer. Below saturation a direct Auger de-excitation of Er can be ruled out for our samples. However, at high current densities the free carrier Auger process becomes important as confirmed by the dependence of the decay time on current density. The time evolution of the EL transient shows a fast and a slow decay. The slow decay is Er related, whereas the fast initial decay could be caused by broad band dislocation luminescence.

### Acknowledgments

Work supported by the *Gesellschaft für Mikroelektronik*, and the *Fonds zur Förderung der Wissenschaftlichen Forschung*, Vienna.

### References

1. H. Ennen, J. Schneider, G. Pomrenke, and A. Axmann, *Appl. Phys. Lett.* **43**, 943 (1983)
2. H. Ennen, G. Pomrenke, A. Axmann, K. Eisele, W. Haydl and J. Schneider, *Appl. Phys. Lett.* **46**, 381 (1985)
3. F. Priolo, G. Franzò, S. Coffa, A. Polman, S. Libertino, R. Barklie, and D. Carey, *J. Appl. Phys.* **78**, 6 (1995)
4. Y.S. Tang, K.C. Heasman, W.P. Gillin and B.J. Sealy, *Appl. Phys. Lett.* **67**, 432 (1989)
5. Michel, J.L. Benton, R.F. Ferrante, D.C. Jacobson, D.J. Eaglesham, E.A. Fitzgerald, Y.-H. Xie, J.M. Poate, and L.C. Kimerling, *J. Appl. Phys.* **70**, 5 (1991)
6. J. Michel, L.C. Kimerling, J.L. Benton, D.J. Eaglesham, E.A. Fitzgerald, D.C. Jacobson, J.M. Poate, Y.-H. Xie, and R.F. Ferrante, *Mat. Science Forum* **83-87**, 653 (1992)
7. B. Zheng, J. Michel, F.Y.G. Ren, L.C. Kimerling, D.C. Jacobson, and J.M. Poate, *Appl. Phys. Lett.* **64**, 21 (1994)
8. J. Stimmer, A. Reittinger, J.F. Nützel, H. Holzbrecher, Ch. Buchal, and G. Abstreiter, *Appl. Phys. Lett.* **68**, 23 (1996)
9. J. Palm, F. Gan, B. Zheng, J. Michel, and L.C. Kimerling, *Phys. Rev. B* **54**, 17603 (1996)
10. P. G. Kik, M. J. A. de Dood, K. Kikoin, and A. Polman, *Appl. Phys. Lett.* **70**, 1721 (1997)
11. F. Priolo, S. Coffa, G. Franzò, and A. Polman, *Mat. Res. Soc. Symp. Proc.* **422**, 305 (1996)
12. L. Palmetshofer, Yu. Suprun-Belevich, and M. Stepikhova, *Nuclear Instruments and Methods in Physics Research B* **11362** (1997)
13. H. Przybylinska, W. Jantsch, Yu. Suprun-Belevitch, M. Stepikhova, L. Palmetshofer, G. Hendorfer, A. Kozanecki, R.J. Wilson, and B.J. Sealy, *Phys. Rev. B* **54**, 2532 (1996)
14. W. Jantsch, H. Przybylinska, C. Skierbiszewski, S. Lanzerstorfer, and L. Palmetshofer, *Mat. Res. Soc. Symp. Proc.* **422**, 101 (1996)
15. S. A. Payne, L. L. Chase, L. K. Smith, W. L. Kway, and W. F. Krupke, *IEEE J. Quantum Electr.* **28** (11) 2619 (1992)
16. E. Ö. Sveinbörnsson and J. Weber, *Appl. Phys. Lett.* **69**, 2686 (1996)

## DONOR CENTERS IN Er-IMPLANTED SILICON

V.V. Emtsev, B.A. Andreev<sup>1</sup>, D.S. Poloskin, N.A. Sobolev, and E.I. Shek

Ioffe Physicotechnical Institute, Russian Academy of Sciences, 194021 St.Petersburg, Russia

<sup>1</sup>Institute of Chemistry of High-Purity Substances, Russian Academy of Sciences,  
603600 Nizhnyi Novgorod, Russia

**Keywords:** silicon, erbium impurity, electrical measurements

**Abstract.** Donor centers formed in Czochralski-grown silicon after erbium implantation and subsequent annealing at 700° and 900°C were studied. Two kinds of centers are produced at 700°C: shallow oxygen-related donors with ionization energies between ~0.03 eV and ~0.04 eV and deeper erbium-related centers. Modifications of donor centers at 900°C lead to the appearance of donor states at  $E_C-0.15$  eV in large concentrations. These centers are thought to be involved in the erbium-related luminescence. Heat treatment of Er-implanted Cz-Si at 450°C doesn't produce any pronounced effect on the erbium-related centers. By contrast, it has a marked effect on the oxygen-related shallow donors.

### Introduction

A lot of information on the electrical and optical properties of Er-related centers in crystalline Si has been collected over the last six years; see for instance [1-6]. Active interest in this impurity has been generated by a luminescence band at 1.54  $\mu\text{m}$  associated with the erbium. This opens new ways for important technical applications [7].

Although the excitation and deexcitation mechanisms of  $\text{Er}^{3+}$  are known in general terms (see for instance [6, 8]), some essential details, among them the relevant energy states, require elucidation. Very recently, measurements of the temperature dependence of the erbium luminescence intensity and lifetime in Si after Er and N co-implantation made it possible to identify the energy levels involved in excitation and deexcitation of the erbium. For Si after co-implantation of Er and O, donor levels at  $E_C-0.15$  eV are claimed to be important in the luminescence process [3], even though their concentration was found to be very low. The purpose of this work is to provide detailed information on donor centers formed in Czochralski-grown Si after Er implantation and subsequent annealing at 700° and 900°C.

### Experimental

Wafers of carbon-lean Czochralski-grown silicon (Cz-Si) doped with boron ( $\rho \approx 50 \Omega\text{-cm}$  and  $7.5 \Omega\text{-cm}$ ) were used. Samples with low (a few  $10^{17} \text{ cm}^{-3}$ ) and high ( $\sim 1 \cdot 10^{18} \text{ cm}^{-3}$ ) oxygen contents were subjected to Er-implantation. The implantation dose of Er ions of 1.2 MeV ranged from  $1 \cdot 10^{11} \text{ cm}^{-2}$  to  $1 \cdot 10^{13} \text{ cm}^{-2}$ . In some cases we also used co-implantation of O ions of 0.17 MeV. All samples were then annealed in two steps at 700° and 900°C for 30 min in a chlorine-containing atmosphere. After the annealing the implanted layers of about 0.5  $\mu\text{m}$  in thickness become n-type. Some samples prepared in this way were subjected to additional heat treatment at 450°C to trigger oxygen aggregation processes in this "classical" temperature region. Though this heat treatment doesn't produce effects on the erbium luminescence [9], it is interesting to take a look at the formation of oxygen-related centers in Cz-Si:Er.

Hall effect measurements were taken by means of the Van der Pauw technique over the temperature range of 20 K to 300 K. The data obtained were analyzed with the use of relevant electroneutrality equations [10-12]. Infrared photoconductivity spectra were

recorded at low temperatures, 4 K to 20 K, by a contactless method in the 200-800  $\text{cm}^{-1}$  range using a Bruker IFS-113v Fourier transform spectrometer.

## Results and Discussion

### Annealing of Cz-Si:Er at $T=700^\circ\text{C}$

Shallow donor centers appear in the Si:Er at a dose of  $5 \cdot 10^{11} \text{cm}^{-2}$  (Fig. 1); with decreasing

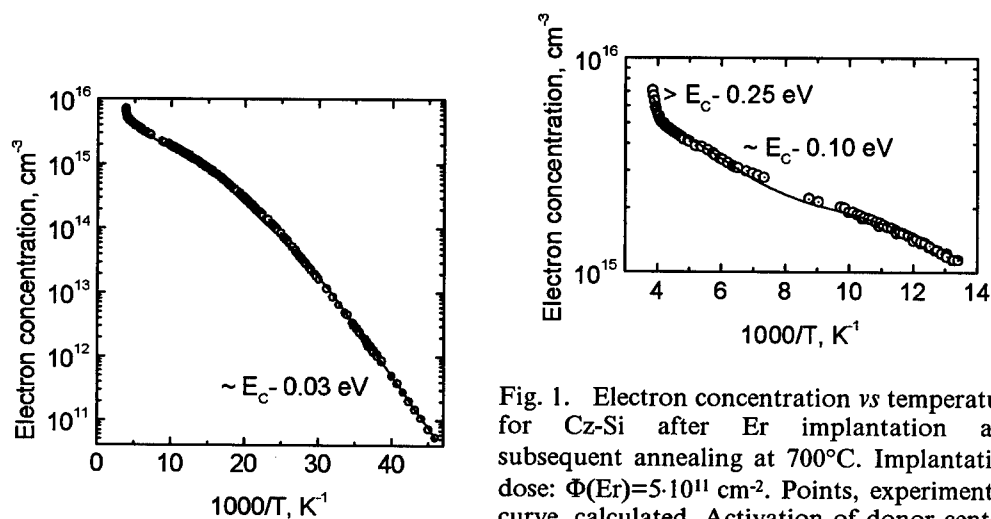


Fig. 1. Electron concentration vs temperature for Cz-Si after Er implantation and subsequent annealing at  $700^\circ\text{C}$ . Implantation dose:  $\Phi(\text{Er})=5 \cdot 10^{11} \text{cm}^{-2}$ . Points, experimental; curve, calculated. Activation of donor centers at  $\sim E_C - 0.10 \text{ eV}$  is shown on the expanded scale.

dose  $\Phi(\text{Er})$  down to  $1 \cdot 10^{11} \text{cm}^{-2}$  there is no shallow donor state, except for residual phosphorus in a concentration of  $7 \cdot 10^{13} \text{cm}^{-3}$  for the samples with higher resistivity before the implantation. Analysis of the  $n(T)$  curve revealed that a three level model including donor states at  $\sim E_C - 0.03 \text{ eV}$ ,  $E_C - 0.046 \text{ eV}$ , and  $E_C - 0.10 \text{ eV}$  provides a good description of the experimental points; see Fig. 1. As is seen, the  $n(T)$  curve over the temperature range of 100 K to 200 K shows only the presence of donors at  $\sim E_C - 0.10 \text{ eV}$ . A new step on the curve at  $T > 250 \text{ K}$  points to deeper donor states at  $\geq E_C - 0.2 \text{ eV}$  in considerable concentrations. It means that there is no trace of donor levels at  $E_C - 0.15 \text{ eV}$  which are believed [3] to be important for the characteristic luminescence of  $\text{Er}^{3+}$ .

The  $n(T)$  curves for higher implantation doses are shown in Fig. 2. Again, we did not detect the presence of donor centers at  $E_C - 0.15 \text{ eV}$  for Cz-Si:Er at a dose  $1 \cdot 10^{12} \text{cm}^{-2}$ . The distribution of the observed donor states vs their ionization energies is given in Fig. 3 over the dose range of  $5 \cdot 10^{11} \text{cm}^{-2}$  to  $1 \cdot 10^{13} \text{cm}^{-2}$ . With increasing the dose of Er ions the total concentration of all donors at  $E_d < E_C - 0.2 \text{ eV}$  also increases, roughly speaking, linearly with the dose up to  $\Phi(\text{Er})=1 \cdot 10^{13} \text{cm}^{-2}$ ; see Fig. 4. At higher doses the curve in Fig. 4 deviates from this linearity likely due to the high concentration of radiation-induced defects resulting in high densities of extended structural defects upon the annealing [13].

There are many similarities between the shallow donor states formed in Cz-Si:Er and Cz-Si due to thermal treatment over the temperature range of  $600^\circ\text{C}$  to  $700^\circ\text{C}$  [7]; similar thermal donors have been formed in Cz-Si doped with Mg by means of nuclear transmutation reactions; see also [14]. It appears that there is one family of oxygen-related donor states within the energy interval between  $\sim E_C - 0.03 \text{ eV}$  and  $\sim E_C - 0.04 \text{ eV}$ , the gravity center always being at the higher energy; see Fig. 3. Some differences in their behaviour (higher thermal stability and production rates) are assumed to be related to the fact that they are formed in

the presence of intrinsic defects available in abundance. These lattice defects can act as nucleation sites for the growing of oxygen aggregates and may be incorporated into their electrically active cores.

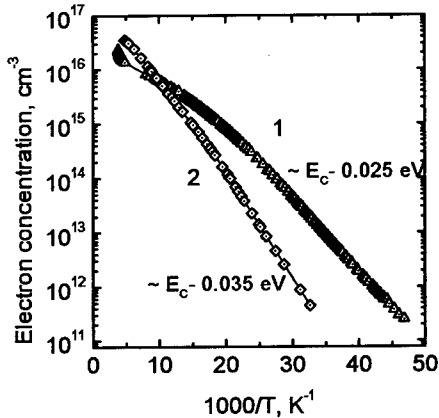


Fig. 2. Electron concentration vs temperature for Cz-Si after implantation and subsequent annealing at 700°C. Implantation dose:  $\Phi(\text{Er})=1 \cdot 10^{12} \text{ cm}^{-2}$ , curve 1;  $\Phi(\text{Er})=1 \cdot 10^{13} \text{ cm}^{-2}$  and  $\Phi(\text{O})=1 \cdot 10^{14} \text{ cm}^{-2}$ , curve 2. Points, experimental; curves, calculated.

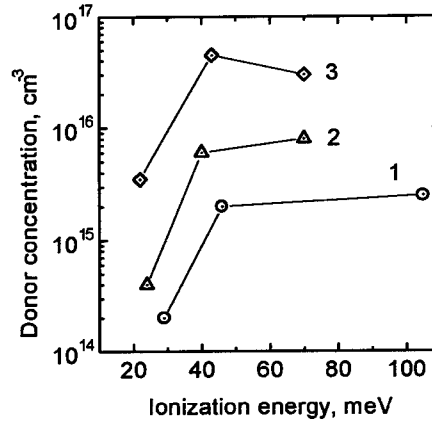


Fig. 3. Concentration of donor centers vs ionization energy for Cz-Si after implantation and subsequent annealing at 700°C. Implantation dose:  $\Phi(\text{Er})=5 \cdot 10^{11} \text{ cm}^{-2}$ , curve 1;  $\Phi(\text{Er})=1 \cdot 10^{12} \text{ cm}^{-2}$ , curve 2;  $\Phi(\text{Er})=1 \cdot 10^{13} \text{ cm}^{-2}$  and  $\Phi(\text{O})=1 \cdot 10^{14} \text{ cm}^{-2}$ , curve 3.

By contrast, for donor centers at  $\sim E_c - 0.07 \text{ eV}$  and at  $\sim E_c - 0.10 \text{ eV}$  we have not found any similarity to the oxygen-related thermal donors formed in Cz-Si at  $T \geq 600^\circ\text{C}$ . First, they are well characterized by the single ionization energy. Second, there are not other donor states down to  $\sim E_c - 0.16 \text{ eV}$ . This enables us to suggest that both centers are erbium-related.

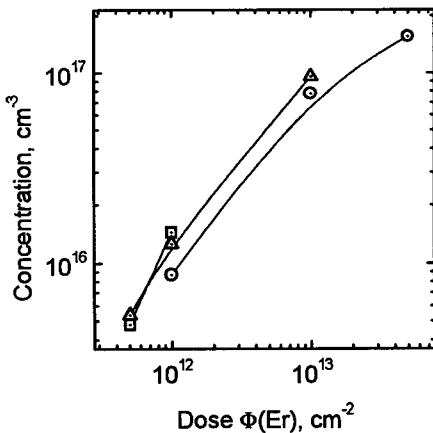


Fig. 4. Total concentration of donors at  $E_d < E_c - 0.2 \text{ eV}$  vs implantation dose of Er for Cz-Si. Post-implantation annealing at 700°C. Samples: Cz-Si with oxygen contents of  $1 \cdot 10^{18} \text{ cm}^{-3}$  (squares); Cz-Si with oxygen contents of about  $7 \cdot 10^{17} \text{ cm}^{-3}$  (circles); Cz-Si with oxygen contents in the low  $10^{17} \text{ cm}^{-3}$  (triangles) after co-implantation of oxygen ions at  $\Phi(\text{O})=10\Phi(\text{Er})$ .

Summing up, the donor centers formed in Cz-Si:Er at 700°C (Fig. 3) fall into two groups: oxygen-related shallow thermal donors whose energy states occupy the energy interval from  $\sim E_c - 0.03 \text{ eV}$  and  $\sim E_c - 0.04 \text{ eV}$  to erbium-related centers at  $\sim E_c - 0.10 \text{ eV}$  and  $\sim E_c - 0.07 \text{ eV}$ . No trace of donor states at  $E_c - 0.15 \text{ eV}$  has been found.

### Annealing of Cz-Si:Er at $T=900^\circ\text{C}$

By way of illustration, we plotted in Fig. 5 the  $n(T)$  curves for two samples. Let us first discuss the oxygen-related shallow donor centers with  $E_d \leq E_C - 0.05$  eV. For the samples with

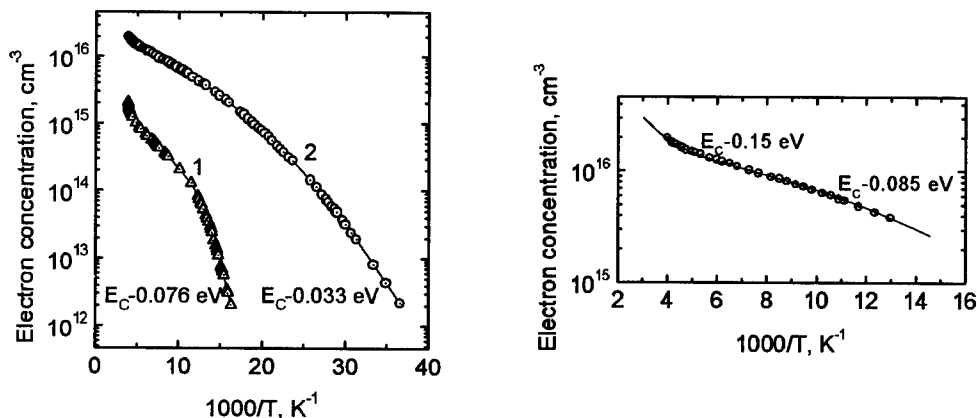


Fig. 5. Electron concentration vs temperature for Cz-Si after Er implantation and subsequent annealing at  $900^\circ\text{C}$ . Implantation dose:  $\Phi(\text{Er}) = 5 \cdot 10^{11} \text{ cm}^{-2}$ , curve 1;  $\Phi(\text{Er}) = 1 \cdot 10^{12} \text{ cm}^{-2}$ , curve 2. Points, experimental; curves, calculated. Activation of donor centers at  $E_C - 0.15$  eV for Cz-Si at  $\Phi(\text{Er}) = 1 \cdot 10^{12} \text{ cm}^{-2}$  is shown on the expanded scale.

low Er concentration, they disappeared after the annealing (curve 1 in Fig. 5). For the samples, with high Er concentrations, they even show an increase of about 20 per cent in their total concentration as compared to that found after annealing at  $T=700^\circ\text{C}$ . However, the most important result of the annealing is the appearance of donor states at  $E_C - 0.15$  eV; see Fig. 5. These donors are well separated from the nearest shallower donor states, by  $\sim 7$  kT, and they are well characterized by the single ionization energy. Their concentration is large, up to  $\sim 1.5 \cdot 10^{16} \text{ cm}^{-3}$ .

In a recent study of DLTS spectra taken on epitaxial Si co-implanted with Er and O [2], the development of a peak showing an activation energy of 0.15 eV was also observed. However, this peak has not been found in Er doped Cz-Si which has the same content of oxygen as that in the co-implanted sample. In stark contrast, we observed the formation of donors at  $E_C - 0.15$  eV in implanted Cz-Si with Er only. Further, a maximum trap concentration was estimated in [2] to be of order of  $\sim 10^{13} \text{ cm}^{-3}$ . Our electrical measurements give direct evidence that the concentration of the relevant donors is much higher, at least by two orders of magnitude. Anyway, the ratio of the concentration of donor centers at  $E_C - 0.15$  eV to the total concentration of Er in the implanted layers is about several tenths, in contrast to  $\sim 2 \cdot 10^{-3}$  quoted in [2]. At present there is no plausible explanation for the observed differences.

### Heat Treatment of Cz-Si:Er at $T=450^\circ\text{C}$

Figure 6 displays two curves of  $n(T)$  for a Cz-Si:Er sample first annealed at  $700^\circ\text{C}$  and then heat-treated at  $450^\circ\text{C}$ . After the heat treatment at  $450^\circ\text{C}$  we observed that the substrates were still of p-type, though high resistive due to compensation of the boron by Thermal Double Donors (TDD). The presence of TDD in the substrates was evidenced by IR spectroscopy under bandgap illumination. Besides, the spectroscopic data made it possible to estimate the total concentration of TDD in the substrates as a reference using the optical cross-sections of the  $2p_o$ -transitions of the neutral TDD given in [15].



As is seen from Fig. 6, the heat treatment at 450°C gives rise to the formation of thermal donors in the implanted layers. The total concentration of TDD can be estimated from the electrical data. Analysis showed that their production rate in the implanted layers is enhanced at least by a factor of 1.5. The enhanced formation of TDD was evidenced even for Cz-Si with low contents of oxygen, a few  $10^{17} \text{ cm}^{-3}$ . Most likely, this behaviour is associated with damage-related defects remaining in Cz-Si annealed at 700°C; cf [1].

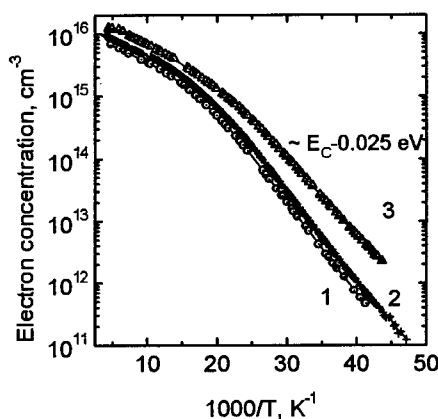


Fig. 6. Electron concentration vs temperature for Cz-Si after Er implantation and subsequent annealing at 700°C (curve 1). Implantation dose:  $\Phi(\text{Er})=1 \cdot 10^{12} \text{ cm}^{-2}$  and  $\Phi(\text{O})=1 \cdot 10^{13} \text{ cm}^{-2}$ . Heat treatment at 450°C for 10 hrs (curve 2) and 20 hrs (curve 3). Points, experimental; curves, calculated.

Together with the enhanced formation of TDD, a pronounced increase in the concentration of shallow donor states already existing in the Si after annealing at 700°C, from  $\sim 5 \cdot 10^{15} \text{ cm}^{-3}$  to  $\sim 7 \cdot 10^{15} \text{ cm}^{-3}$ , was observed as a result of the heat treatment at 450°C for 20 hours. This provides additional support for our suggestion that this family of shallow donors is oxygen-related. By contrast, we could not trace any change in the concentration of erbium-related donor centers at  $\sim E_C - 0.07 \text{ eV}$  and, therefore, they are not involved in the oxygen aggregation processes taking place at 450°C.

### Conclusions

The present work has provided detailed information on the formation and modification processes of donor centers at  $E_d \leq E_C - 0.2 \text{ eV}$  in Er-implanted Cz-Si subjected to annealing at 700°C and 900°C. The general picture includes two kinds of donors making their appearance following the 700°C annealing: a family of oxygen-related shallow donor states stretching from  $\sim E_C - 0.03 \text{ eV}$  to  $\sim E_C - 0.04 \text{ eV}$  and Er-related centers at  $\sim E_C - 0.07 \text{ eV}$ ; the latter ones become slightly deeper at low implantation doses. The fate of the oxygen-related shallow donors after the 900°C annealing, survive or disappear, turned out to be dose-dependent, too. The most important consequence of such a high-temperature annealing is the formation of donor centers at  $E_C - 0.15 \text{ eV}$  in appreciable concentrations comparable to the total concentration of Er in the implanted layers. The role of these Er-related donor states in excitation and deexcitation of the erbium may be of practical importance.

Additional heat treatment of Er-implanted Cz-Si at 450°C produces pronounced effects on the oxygen-related shallow donors formed at higher temperatures but the erbium-related centers are not involved in oxygen aggregation processes.

### Acknowledgments

The expert assistance of Mr. E.O.Parshin is highly appreciated. This work was partly supported by the International Science and Technology Center ( grant 168 ) and INTAS-RFBR (grant 95-0531).

**References**

1. J.L. Benton, J. Michel, L.C. Kimerling, D.C. Jacobson, Y.H. Xie, D.J. Eaglesham, E.A. Fitzgerald, and J.M. Poate, *J. Appl. Phys.* **70**, 2667 (1991).
2. S. Libertino, S. Coffa, G. Franzó, and F. Priolo, *J. Appl. Phys.* **78**, 3867 (1995).
3. F. Priolo, G. Franzó, S. Coffa, A. Polman, S. Libertino, R. Barklie, and D. Carey, *J. Appl. Phys.* **78**, 3874 (1995).
4. H. Przybylinska, W. Jantsch, Yu. Suprun-Bellevitch, M. Stepikova, L. Palmetshofer, G. Hendorfer, A. Kazanecki, R.J. Wilson, and B.J. Sealy, *Phys. Rev. B* **54**, 2532 (1996).
5. I. de Maat-Gersdorf, T. Gregorkiewicz, C.A.J. Ammerlaan, and N.A. Sobolev, *Semicond. Sci. Technol.* **10**, 666 (1995).
6. P.G. Kik, M.J.A. de Dood, K. Kikoin, and A. Polman, *Appl. Phys. Lett.* **70**, 1721 (1997).
7. L.C. Kimerling, *Light-Emitting Diodes: Research, Manufacturing, and Applications*, ed. E.F. Schubert, *Proc. SPIE* **3002**, pp. 192-197 (1997).
8. M.S. Bresler, O.B. Gusev, B.P. Zakharchenya, and I.N. Yassievich, *Fiz. Tverd. Tela* **38**, 1474 (1996) [*Phys. of the Solid State (AIP)* **38**, 813 (1996)].
9. J. Michel, L.J. Benton, R.F. Ferraute, D.C. Jacobson, D.J. Eaglesham, E.A. Fitzgerald, Y.-H. Xie, J.M. Poate, and L.C. Kimerling, *J. Appl. Phys.* **70**, 2672 (1991).
10. J. S. Blakemore, *Semiconductor Statistics* (New York: Pergamon Press) (1962).
11. H.J. Hoffmann, *Appl. Phys. (Springer) A* **33**, 47 (1984).
12. V.V. Emtsev, G.A. Oganessian, and K. Schmalz in *Solid State Phenomena*, Vols **47-48**, eds H. Richter, M. Kittler, and C. Claeys (Switzerland: Scitec Publications) pp. 259-266 (1996).
13. R.N. Kyutt and N.A. Sobolev, *Fiz. Tverd. Tela* **39**, 853 (1997) [*Phys. of the Solid State, (AIP)* **39**, 759 (1997)].
14. N.A. Sobolev, V.V. Emtsev, D.S. Poloskin, and E.I. Shek in *Shallow-Level Centers in Semiconductors*, eds C.A.J. Ammerlaan and B. Pajot (Singapore-New Jersey-London-Hong Kong: World Scientific), pp. 291-296 (1997).
15. P. Wagner in *MRS Symp. Proc.*, Vol. **59**, eds J.C. Mikkelsen, Jr., S.J. Pearton, J.W. Corbett, and S.J. Pennycook (Pittsburgh, Pennsylvania: MRS) pp. 125-137 (1986).

## STRUCTURAL DEFECTS AND PHOTOLUMINESCENCE IN DISLOCATION-RICH ERBIUM-DOPED SILICON

V.I.Vdovin, N.A.Sobolev<sup>1</sup>, E.M.Emel'yanov<sup>1</sup>, O.B.Gusev<sup>1</sup>, E.I.Shek<sup>1</sup> and T.G.Yugova

Institute for Chemical Problems of Microelectronics, B.Tolmachevsky per. 5,  
Moscow 109017, Russia

<sup>1</sup>Ioffe Physicotechnical Institute, Polytechnicheskaya 26, St.Petersburg 194021, Russia

**Keywords:** silicon, erbium implantation, structural defects, photoluminescence.

**Abstract.** Structural defects and optical features of p-type Cz-Si after implantation of erbium with 0.8-2.0 MeV energies and  $1 \times 10^{13} \text{ cm}^{-2}$  dose and coimplantation of oxygen with 0.1-0.25 MeV energies and  $1 \times 10^{14} \text{ cm}^{-2}$  dose followed by annealing at 1100 °C for 0.5-3.0 hrs in chlorine-containing atmosphere have been studied by transmission electron microscopy, optical microscopy in combination with selective chemical etching, and photoluminescence. The defects found are Frank loops, perfect prismatic dislocation loops and pure edge dislocations, distributed over the layer of about 1  $\mu\text{m}$  depth. Frank loop density and size vary over  $5 \times 10^7 - 2 \times 10^6 \text{ cm}^{-2}$  and 0.4-10.0  $\mu\text{m}$  ranges, respectively, depending on the implantation and annealing conditions. In all the samples, small perfect dislocation loops are of the same size of 0.1-0.5  $\mu\text{m}$  but their density strongly depends on the implantation conditions. Pure edge dislocations result from large perfect loops at their interaction and form three-dimensional network. Dislocation density in the network depends on the implantation and annealing conditions and varies from  $2 \times 10^6$  to  $8 \times 10^7 \text{ cm}^{-2}$ . Strong D1 and D2 bands dominate in the photoluminescence spectra. A correlation between intensity of D1/D2-bands and edge dislocation density has been found. The D1 and D2 bands are attributed to the dislocation nodes arising at the edge dislocation crossings in the three-dimensional dislocation networks.

### Introduction.

Fabrication of the light-emitting structures with wavelength of 1.54  $\mu\text{m}$  is of great interest for application in optoelectronics. One of the ways to produce such structures involves the doping silicon with erbium, which results in occurrence of intra-4f shell transitions of rare-earth ion [1]. The fabrication of structures with luminescence caused by the presence of dislocations in material can be considered as another possible way. Formerly the dislocation related luminescence (D-bands) has been observed in plastically deformed silicon [2-5] and relaxed epitaxial SiGe layers [6,7]. Recently D-bands have been observed in photoluminescence (PL) spectra of silicon doped with erbium and annealed at 1100 °C [8-11]. An assumption has been advanced that these bands are related to the dislocations, too. In this paper, a study of the structural defects arising in such material has been carried out and an analysis of the PL behavior with regard to certain defects has been performed.

### Experimental.

For formation of Si:Er, Er ions were implanted at 0.8-2.0 MeV energies and  $1 \times 10^{13} \text{ cm}^{-2}$  dose in p-type Cz-Si(001) with a resistivity of 1-20  $\Omega\text{cm}$ . Coimplantation of oxygen ions with 0.1-0.25 MeV energies and  $1 \times 10^{14} \text{ cm}^{-2}$  dose was also performed. Postimplantation annealing at 1100 °C for 0.5-3.0 hrs was carried out in chlorine-containing atmosphere. A study of the structural defects were carried out by transmission electron microscopy (TEM) on the cross-sectional and plan-view samples, by optical microscopy with Nomarski interference contrast in combination with selective chemical etching on the oblique sections, and photoluminescence. PL was excited by a mechanically chopped Ar laser beam. The radiation emitted was collected by a lens, dispersed by a 0.75 m monochromator and registered by an nitrogen-cooled Ge detector. The sample temperature was 1.8 K. Luminescence spectra were recorded using a lock-in amplifier.

## Results and Discussion.

### Influence of implantation conditions.

Investigations were carried out on the samples with single and multiple implantation of erbium as well as with coimplantation of oxygen. The annealing of the samples was performed at identical conditions for 0.5 h. The implantation conditions and structural and optical findings for these samples are given in Table 1.

**Structural defects.** The chemical etch patterns revealed on the oblique sections show straight segments typical for stacking faults and small etch pits. Three types of the defects were observed by TEM: i) Frank loops, ii) perfect prismatic dislocation loops, iii) pure edge dislocations (Fig. 1, a). Frank loops are the interstitial dislocation loops on  $\{111\}$  planes with Burgers vector  $b=a/3\langle 111 \rangle$ . Perfect prismatic dislocation loops are the interstitial loops with Burgers vector  $b=a/2\langle 110 \rangle$  and lie mainly on  $\{110\}$  planes. Pure edge dislocations (Fig. 1, b-c; dislocation contrast disappears under  $\langle 220 \rangle$  diffraction) arise as a segment between two touching large perfect loops [12]. Multiple interaction of such perfect loops leads to the formation of three-dimensional network with high density of the edge dislocations. The study of defect contrast shows that all of them are free from erbium precipitates. The study of the wafer cross-sections shows that structural defects are localized over the layer of about 1  $\mu\text{m}$  depth (Fig. 2). Frank loops of small and middle sizes are distributed over the whole implanted layer. Large Frank loops extend through the whole layer in such a way that their growth downward stops when they reach a bottom of the implanted layer and their further propagation proceeds along this layer. Dislocation network consists of complex-shaped meshes and extends through the whole layer. Small perfect loops locate mainly in the upper half of the layer.

After implantation of erbium with 1.2 MeV ion energy and thermal annealing (sample A), large Frank loops ( $>1 \mu\text{m}$ ) are formed with density of  $2 \times 10^7 \text{ cm}^{-2}$ . The small Frank loops (0.4–0.8  $\mu\text{m}$ ) was not observed in this structure. Coimplantation of oxygen (sample B) leads to increasing the total density of Frank loops (see Table 1). However sizes and density ( $1.5 \times 10^7 \text{ cm}^{-2}$ ) of large Frank loops slightly decrease, the fraction of small Frank loops is about 40%. The multiple erbium implantation (sample C) also leads to increasing the total Frank loop density, but the fraction of small loops reaches about 80%. In this case, the sizes and density of large loops ( $7 \times 10^6 \text{ cm}^{-2}$ ) decrease to a high extent.

Table 1. Conditions of implantation, structural and photoluminescence features of silicon annealed at 1100 °C for 0.5 h.

Sample	Energy, MeV	Frank loops		Small perfect loop density, $\text{cm}^{-2}$	Dislocation density, $\text{cm}^{-2}$	PL intensity,	
		Size, $\mu\text{m}$	Density, $\text{cm}^{-2}$			D1 arb. un.	D2 un.
A	Er: 1.2	1.1-4.0	$2 \times 10^7$	$2 \times 10^6$	$4 \times 10^7$	272	462
B	Er: 1.2 O: 0.17	0.7-3.0	$2.5 \times 10^7$	$4 \times 10^6$	$8 \times 10^7$	327	516
C	Er: 2.0; 1.6 1.2; 0.8	0.4-1.9	$4 \times 10^7$	$7 \times 10^7$	$8 \times 10^7$	186	144

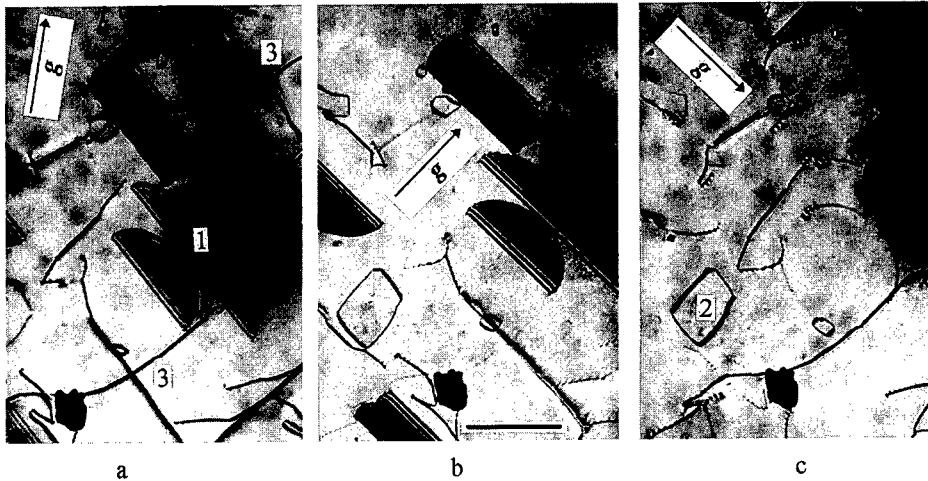


Fig. 1. Plan-view TEM images of structural defects in sample B at the same area in different reflections: a)  $g = \langle 400 \rangle$ ; b,c)  $g = \langle 220 \rangle$ : (1 - Frank loops; 2 - perfect dislocation loops; 3 - pure edge dislocations). Marker represents 1  $\mu\text{m}$ .

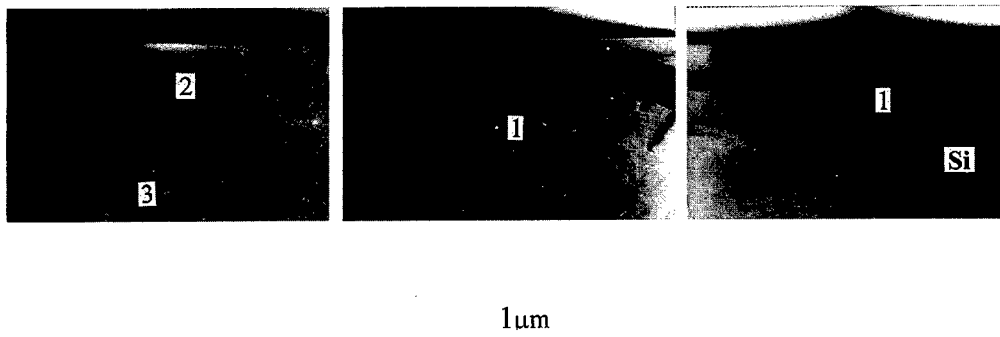


Fig. 2. Cross-sectional TEM images for the sample B: various areas along the implanted layer (1 - Frank loops; 2 - perfect dislocation loops; 3 - three-dimensional dislocation network).

In all the samples, small perfect dislocation loops have the same size 0.1-0.5  $\mu\text{m}$  but their density varies - it is about 2 times higher for coimplantation of oxygen (sample B) and is more than one order of magnitude higher for multiple implantation of erbium (sample C) than that for single implantation of erbium (sample A). The dislocation density estimated from TEM plan-view images varies insignificantly in range  $(4-8) \times 10^7 \text{ cm}^{-2}$ . However, the character of the dislocation network changes noticeably. In samples A and B, dislocation structure is similar and characterized, along with the other defects, by the presence of a lot of straight segments of pure edge dislocations forming large meshes in the three-dimensional network. In sample C, such dislocations are rare because perfect dislocation loops are not too large to form well-developed dislocation network while they are numerous.

As can be seen from Table 1, the density of small perfect loops is significantly less than dislocation density. In this case, the small etch pits revealed at the surface of oblique sections can be attributed to the dislocation etch pits. For these samples, the density of small etch pits is registered to be practically similar about  $(3-5) \times 10^7 \text{ cm}^{-2}$  and these values are in a good agreement with data estimated from

TEM images (Table 1). Notice that, until defect density is less than  $10^8 \text{ cm}^{-2}$ , the data obtained with optical microscope are more reliable due to more statistic of account of revealed defects as well as to taking account of the inhomogeneity of their distribution over the sample surface.

**Photoluminescence.** From all these samples, intensive D1- and D2-bands (Fig. 3) with strictly fixed wavelengths at 1525 nm (0.8196 eV) and 1417 nm (0.875 eV), respectively, were observed. The intensity of D1- and D2-bands was found to increase on the same value (Table 1) in the sample B with coimplantation of oxygen in comparison with initial silicon implanted with erbium (sample A). In the sample C with multiple implantation of erbium, a decreasing intensity of the both bands was registered in comparison with the sample A. It is noteworthy that the decreasing intensity of D2-band has occurred much more sharply.

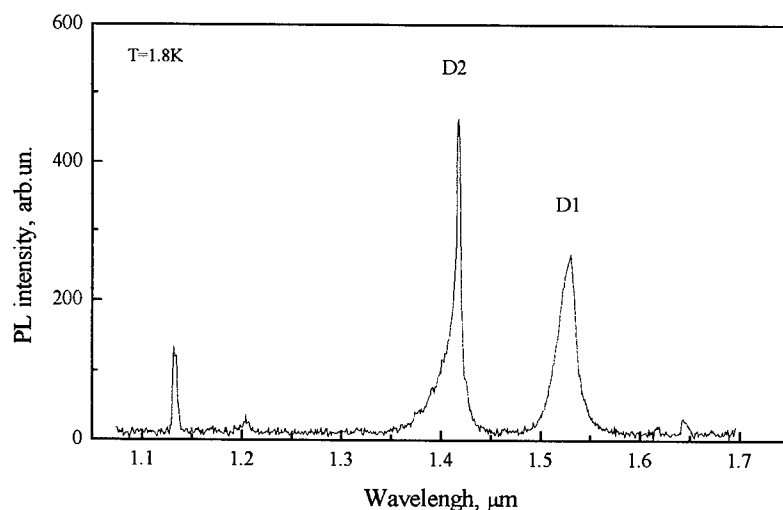


Fig. 3. PL spectrum for sample A.

#### Influence of annealing conditions.

To study regularities of defect structure formation during the postimplantation annealing and to clarify a relationship between D1/D2-bands and certain defects, a study has been carried out of the samples with single implantation of erbium with 1.0 MeV energy and annealed at the identical conditions for 0.5, 1.0 and 3.0 hrs. The size and density of Frank loops as well as dislocation density were estimated from chemical etch patterns. Obtained results indicate that there is a well-defined tendency in the defect structure alteration as annealing time increases. Frank loop density (Fig. 4, a, curve 1) gradually decreases over about an order of magnitude. Simultaneously their sizes increase from 0.4 to 10.0  $\mu\text{m}$ . In all the samples of this set, the density of small perfect loops is practically the same and much below than the dislocation density. The dislocation density gradually changes in the range  $(2-4) \times 10^7 \text{ cm}^{-2}$  (Fig. 4, a, curve 2). The TEM study of the plan-view specimens shows that practically all dislocations in the network are the pure edge dislocations. The intensity of D1- and D2-bands as function of annealing time is shown in Fig. 4, c.

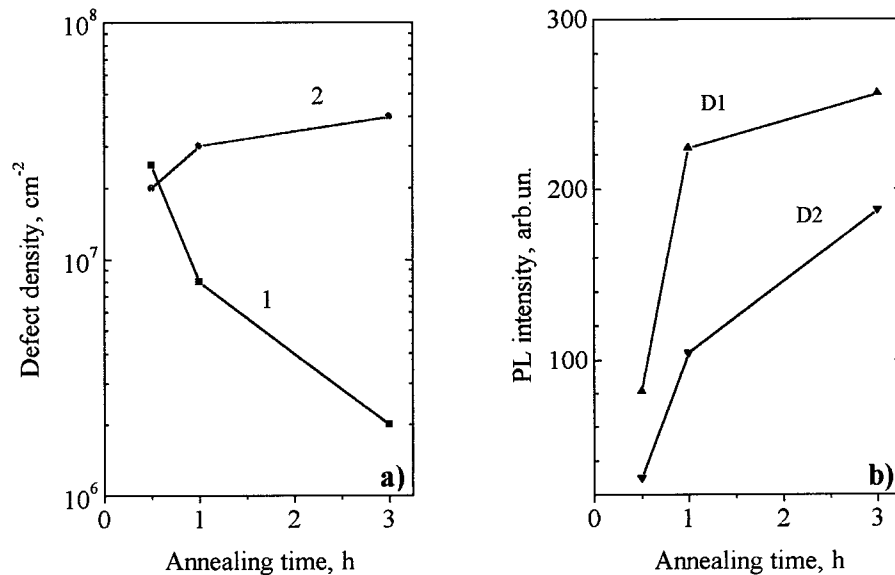


Fig. 4. Defect density (a) and photoluminescence intensity (b) as functions of annealing time: 1 - Frank loops; 2 - pure edge dislocations.

As seen in Fig. 4, there is a correlation between intensity of D1/D2-bands and the density of pure edge dislocations. This conclusion is confirmed by data obtained on the samples with different implantation conditions, in which strong D1/D2-bands were registered for A and B samples with high density of edge dislocations whereas much lower intensity of both bands was registered for C sample where poor developed network with low number of edge dislocations has been observed. However, as it follows from an analysis of the appropriate curves shown in Fig. 4, the intensity of D1/D2-bands changes distinctly stronger than the edge dislocation density. It is likely that this discrepancy can be connected with observed difference in the sizes of meshes in the dislocation network. Thus it allows us to suggest that appearance of D1/D2-bands in PL spectra is related to the dislocation nodes arising at the crossings of edge dislocations rather than to the dislocations themselves. The similar idea has been advanced in Refs. [5,7] where another type of dislocation ensembles in plastically deformed silicon or relaxed epitaxial SiGe/Si structures have been studied.

In conclusion, we have demonstrated that implantation of high-energy erbium ions with  $1 \times 10^{13} \text{ cm}^{-2}$  dose followed by annealing at  $1100^\circ \text{C}$  in chlorine-containing atmosphere leads to the formation of complex ensemble of structural defects in p-type Cz-Si and to appearance of the intensive dislocation related PL. The D1 and D2 bands in PL spectra are attributed to the dislocation nodes arising at the edge dislocation crossings in the three-dimensional dislocation network.

#### Acknowledgements.

This work was supported, in part, by Russian Foundation for Basic Research (Grant 96-02-18608), International Science and Technology Center (Grant #168), and INTAS-RFBR (Grant 95-0531).

**References.**

1. J.Michel, J.L.Benton, R.F.Ferrante, D.C.Jacobson, D.J.Eaglesham, E.A.Fitzgerald, Y.-H.Xie, J.M.Poate and L.C.Kimerling, *J.Appl.Phys.* **70**, 2672 (1991).
2. N.A.Drozdov, A.A.Patrin, V.D.Tkachev, *Sov. Phys. JETP Lett.* **23**, 597 (1976).
3. R.Sauer, J.Weber, and J.Stolz, *Appl. Phys.* **A36**, 1 (1985).
4. V.V.Kveder, E.A.Steinman and H.G.Grimmeiss, *J. Appl. Phys.* **78**, 446 (1995).
5. T.Sekiguchi and K.Sumino, *Mater. Sci. Forum* **196-201**, 1201 (1995).
6. V.Higgs, E.C. Lightowlers and S. Tajbakhsh, *Appl. Phys. Lett.* **61**, 1087 (1992).
7. T.Sekiguchi, K.Sumino, Z.J.Radzimski and G.A.Rozgonyi, *Mat. Sci. Eng.* **B42**, 141 (1996).
8. N.A.Sobolev, M.S.Bresler, O.B.Gusev, M.I.Makoviishuk, E.O.Parshin and E.I.Shek, *Semicond.* **28**, 1100 (1994).
9. N.A.Sobolev, O.V.Alexandrov, M.S.Bresler, O.B.Gusev, E.I.Shek, M.I.Makoviishuk and E.O.Parshin, *Mater. Sci. Forum* **196-201**, 597 (1995).
10. T.Gregorkiewicz, I.Tsimperidis, C.A.J.Ammerlaan, F.P.Widdershoven, and N.A.Sobolev, *Mat. Res. Soc. Proc.* **422**, 207 (1996).
11. G.Davies (private communication).
12. S.Mader and A.F.Michel, *Phys. Stat. Sol. (a)*, **33**, 793 (1976).



## INFLUENCE OF FABRICATION CONDITIONS ON PROPERTIES OF Si:Er LIGHT-EMITTING STRUCTURES

N.A. Sobolev, A.M.Emel'yanov<sup>1</sup>, Yu.A.Nikolaev, K.F.Shtel'makh<sup>1</sup>, Yu.A.Kudryavtsev,  
V.I.Sakharov, I.T.Serenkov, M.I.Makovijchuk<sup>2</sup>, and E.O.Parshin<sup>2</sup>

Ioffe Physicotechnical Institute, St.Petersburg 194021, Russia

<sup>1</sup>St.Petersburg State Technical University, Department of Experimental Physics,  
St.Petersburg 195251, Russia

<sup>2</sup>Institute of Microelectronics, Yaroslavl' 150007, Russia

**Keywords :** silicon, erbium, luminescence, defects

**Abstract.** Secondary ion mass spectroscopy, Rutherford back scattering, photo- and electroluminescence have been used to characterize the structural and optical properties of silicon after erbium and oxygen ion co-implantation at different doses followed by annealing. Boron and phosphorus implantation, subsequent annealing, metal contact evaporation and chemical etching of a mesa-like edge counter have been performed to fabricate the crystalline Si-based light-emitting structures. The Er<sup>3+</sup>-related electroluminescence at ~ 1.54  $\mu\text{m}$  excited due to impact ionization in avalanche regime has been observed in the 80÷300 K temperature range.

### Introduction.

Er<sup>3+</sup> ions exhibit a sharp and temperature-independent luminescence peak at ~ 1.54  $\mu\text{m}$  as a result of internal 4f-shell atomic transitions. In the silicon host, the ions can be excited both optically and electrically. Therefore, erbium-doped silicon may be a potential material for the fabrication of optoelectronic devices.

Photoluminescence (PL) and electroluminescence (EL) of erbium-doped silicon at liquid nitrogen temperature were first reported in 1983 and 1985 by Ennen et al. [1,2]. Michel et al. [3] observed erbium-related PL at room temperature for the first time in 1991. Since that time, much effort has been made to reveal the luminescence mechanisms and to achieve efficient room-temperature EL in the Si:Er system [4]. Yassievich and Kimerling [5] showed that the Auger recombination of excess carriers at an Er-related level localized in the forbidden gap and the impact excitation by high energy ('hot') carriers were the most effective mechanisms of excitation for the f-electron system of threefold ionized rare earth ions in silicon. During 1993-1996, room temperature EL was observed in Si:Er diodes fabricated by the ion implantation [6,7], solid phase epitaxy [8,9], and molecular beam epitaxy [10] techniques. EL was found to occur under both forward [6-10] and reverse bias [8-10]. Various experiments [11-15] have unambiguously established that the excitation of an Er core during PL or injection EL is associated with the Auger recombination of an exciton bound to an Er-related defect. An appreciable decrease in the PL and injection EL intensities by two or three orders of magnitude was observed with temperature increasing from 77 to 300 K [3,4]. At the same time, the temperature-related quenching of the EL in reverse biased diodes was strongly reduced [8-10]. In this case, luminescence was excited by hot carriers generated during the tunnel (Zener) breakdown. It was reasonable to suggest that Er<sup>3+</sup> ions could also be excited by hot carriers generated during the p-n junction avalanche breakdown. In this paper, we describe the fabrication and characterization of erbium-oxygen-doped silicon avalanching light-emitting diodes (LEDs) operating at room temperature.

### Experimental.

The starting wafers of phosphorus-doped <100> and <111> Cz silicon (5-20  $\Omega\text{ cm}$ ) were used as substrates. To increase the Er-related luminescence intensity, we used a conventional procedure of erbium and oxygen ion co-implantation [3,11,14]. Erbium ions were implanted at two energies of 2.0 and 1.6 MeV and doses from  $1 \times 10^{13}$  to  $1 \times 10^{14}\text{ cm}^{-2}$ . Oxygen co-implantation with two energies

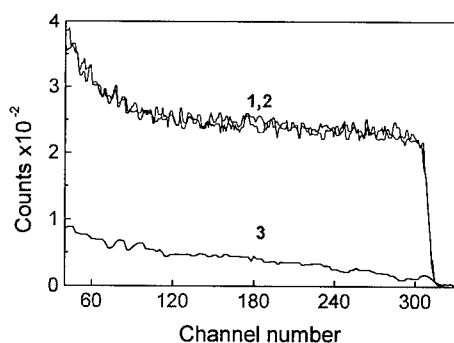


Fig.1. Random (1) and channeling (2,3) RBS spectra for the <100> samples before (1,2) and after (1,3) annealing at 620°C/1h+900°C/0.5h.

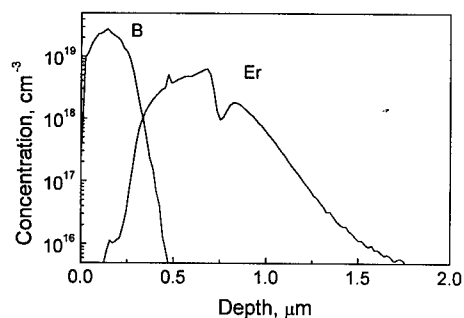


Fig.2. SIMS profiles of erbium and boron in the <100> LED.

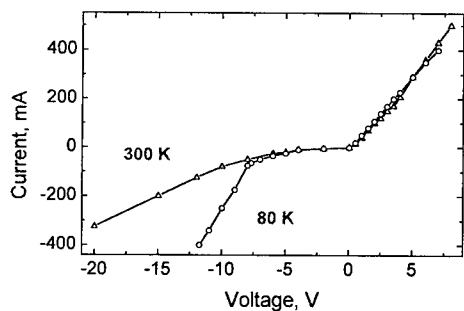


Fig.3. Current-voltage characteristics of the <100> sample at various temperatures .

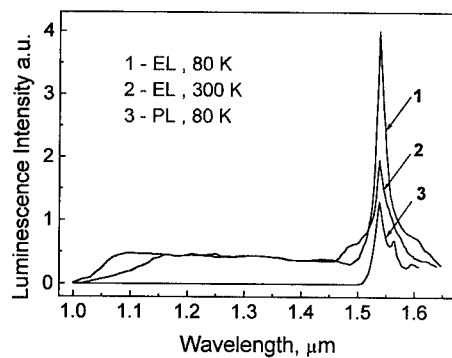


Fig.4. Electro- and photoluminescence spectra of the <100> sample at various temperatures. The electroluminescence spectra were taken under breakdown conditions at a drive current of 150 mA. A resolution is 6 nm.

0.28 and 0.22 MeV and doses from  $1 \times 10^{14}$  to  $1 \times 10^{15} \text{ cm}^{-2}$  was designed to specially overlap the erbium implant. Heat treatment of  $620^\circ\text{C}/1 \text{ h} + 900^\circ\text{C}/0.5 \text{ h}$  in a chlorine-containing atmosphere was carried out to remove the implantation damage and to activate the electrically and optically active erbium-related centers [8,9,11,14]. The chlorine-containing atmosphere was an oxygen flow with addition of trichloroethylene which concentration was 0.5 mole % [14]. The implantation and subsequent annealing led to the formation of  $n^+$  type erbium-related near-surface regions with a donor concentration of  $\sim 8 \times 10^{16}$  to  $\sim 6 \times 10^{17} \text{ cm}^{-3}$ . The  $p^+-n^+$  junctions were produced by 40 keV boron implantation at a dose of  $5 \times 10^{15} \text{ cm}^{-2}$  into the front side of the wafer. The back side was implanted with phosphorus at 80 keV energy and  $1 \times 10^{15} \text{ cm}^{-2}$  dose. High-dose boron and phosphorus implantation and subsequent annealing at  $900^\circ\text{C}/0.5 \text{ h}$  in the same chlorine-containing medium provided an effective low-doped n-region modulation with the charge carriers in the structures under the forward bias conditions. All the ion implantation were performed at room temperature. Metal contacts were prepared by aluminum sputtering. Silicon mesa-like structures were formed by chemical etching in the CP4 solution. After that the diodes were scribed and mounted on headers. The resulting devices have an operating area from 3 to  $7 \text{ mm}^2$ . Secondary ion mass spectroscopy (SIMS), Rutherford back scattering (RBS), current-voltage, capacitance-voltage, PL and EL techniques were used to study the properties of Si:Er:O. EL was measured by applying the voltage in both the reverse and forward bias. A square pulse excitation with the duty cycle 1:5 at 30 Hz was used. PL was excited by a mechanically chopped beam from 75 mW halogen lamp. The radiation emitted from a LED was collected by a lens, dispersed by a 0.75 m monochromator and registered by an InGaAs detector at room temperature. The sample temperature was varied from 80 to 300 K. Luminescence spectra were recorded using a lock-in amplifier.

### Results and Discussion.

RBS of protons with an energy of 234 keV has shown that the erbium implantation at a dose of  $1 \times 10^{13} \text{ cm}^{-2}$  does not lead to amorphization of silicon. An increase of the implantation dose is accompanied by the formation of an amorphous layer separating the bulk layer and a thin monocrystalline surface layer. At an implantation dose of  $1 \times 10^{14} \text{ cm}^{-2}$  the monocrystalline surface layer is completely amorphized. Figure 1 shows the random (curve 1) and aligned (curves 2) RBS spectra of the  $\langle 100 \rangle$  silicon after implantation at doses of  $1 \times 10^{14} \text{ Er/cm}^2$  and  $1 \times 10^{15} \text{ O/cm}^2$ . Subsequent annealing at  $620^\circ\text{C}$  induces the solid phase epitaxial recrystallization of this layer. Further thermal treatment of single crystal Si:Er:O structures at  $900^\circ\text{C}$  permitted a reduction in the structural defect concentration and provided the formation of electrically and optically active Er-related centers. The minimum channeling yield (see Fig.1, curves 1 and 3), which is the ratio between the backscattered intensity of the channeled and random sample orientation, was  $< 3\%$ , indicating 'high quality' material.

Let us consider the properties of these  $\langle 100 \rangle$  structures in detail. The SIMS concentration profiles of Er and B impurities in the LED are shown in Fig.2. The  $p^+-n^+$  junction depth was determined by a beveling and staining technique to be equal to  $0.35 \mu\text{m}$ .

The current-voltage (I-V) characteristics of the LED are shown in Fig. 3 for both 80 and 300 K. The operating area is  $6.4 \text{ mm}^2$ . Under the reverse bias, the breakdown voltage increases with temperature. An analysis of the reverse I-V curves demonstrates that the  $p^+-n^+$  junction breakdown essentially represents an avalanche breakdown.

Figure 4 shows the EL spectra of the sample biased in the reverse direction at 80 and 300 K. The drive current is 150 mA for both spectra. A sharp luminescence line at  $1.537 \mu\text{m}$  is produced at both operating temperatures. No line shift of the peak wavelength with temperature is observed, consistent with the  $\text{Er}^{3+}$  intra-4f shell transition. Only a weak broadening is observed with increasing temperature. The full width at half maximum (FWHM) increases from 20 nm at 80 K to

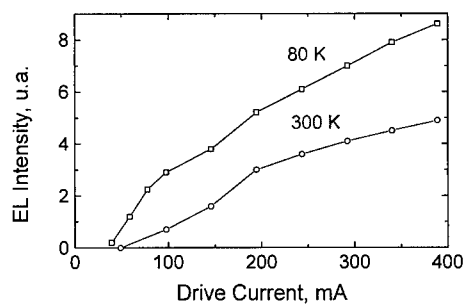


Fig.5. Electroluminescence intensity as a function of reverse current at various temperatures for the <100> sample.

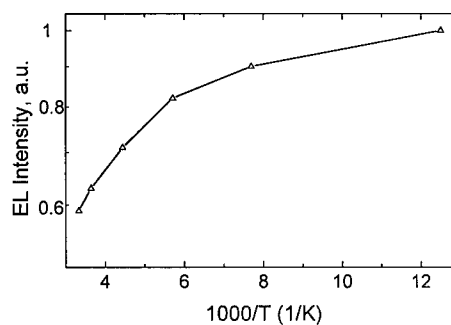


Fig.6. Temperature dependence of electroluminescence intensity at a current of 300 mA for the <100> sample.

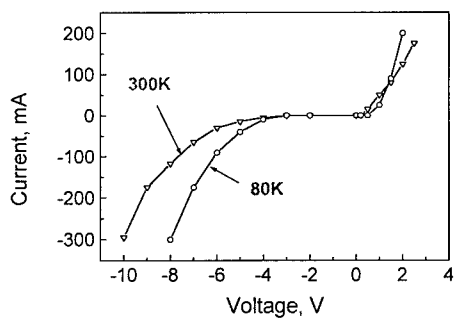


Fig.7. Current-voltage characteristics of the <111> sample at various temperatures.

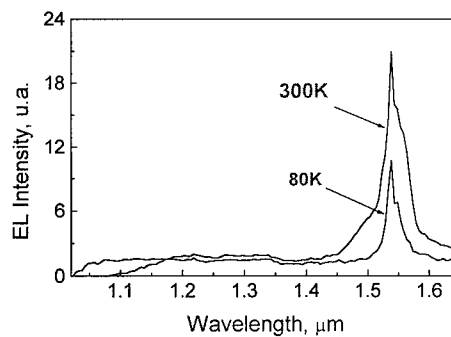


Fig.8. Electroluminescence spectra of the <111> sample at various temperatures. The spectra were taken at a drive current of 200 mA. A resolution is 6 nm.

28 nm at 300 K. The FWHM at 300 K in the avalanching diodes is comparable to that (33 nm) in tunneling diodes [10]. One can see that there is a relatively weak continuous background starting at  $\sim 1.01 \mu\text{m}$ . No luminescence related to the Si band gap (free or bound exciton) was detected.

The PL spectrum for the same diode at 80 K is shown in Fig. 4 (curve 3). Two additional Er-related maxima (at 1.564 and 1.595  $\mu\text{m}$ ) are observed, and there is no exciton-related luminescence.

The dependencies of the  $\text{Er}^{3+}$ -related EL intensity on the drive reverse current for 80 and 300 K are plotted in Fig. 5 with a threshold current of 40–50 mA. In the same current range, an EL signal of a continuous background appears (see Fig. 4) which increases with increasing current. This radiation is related to intraband transitions of energetic carriers in the carrier multiplication region [16]. The obtained experimental data permit a suggestion that the Er-related EL in the reverse biased LEDs discussed occurs due to impact ionization in high enough electric fields.

The temperature dependence of the Er-related EL intensity at a constant reverse drive current of 300 mA is shown in Fig. 6. The EL yield decreases only by a factor of 1.7 from 80 to 300 K. Such a low temperature decrease under the reverse bias in the avalanche breakdown conditions is very similar to the quenching observed in [8–10] under the Zener breakdown conditions. The Er-related EL intensity at the forward drive current of 300 mA decreased more than one order of magnitude with the temperature increase from 80 to 300 K.

Co-implantation of erbium and oxygen at lower doses ( $1 \times 10^{13} \text{ Er/cm}^2$  and  $1 \times 10^{14} \text{ O/cm}^2$ ) also allows us to fabricate avalanching light-emitting structures operating at room temperature. However, a decrease of the total erbium concentration, followed by decreasing concentrations of electrically and optically active centers, results in an increase of the avalanche breakdown voltage and a decrease of the EL intensity at the same reverse current density.

Co-implantation of erbium and oxygen at doses of  $1 \times 10^{14} \text{ Er/cm}^2$  and  $1 \times 10^{15} \text{ O/cm}^2$  in the  $\langle 111 \rangle$  samples leads to a decrease of the breakdown voltage (see Figs. 3 and 7) and an increase of the EL intensity at room temperature. Figure 8 shows some EL spectra for the diode at 80 and 300 K. Two peculiarities seen in Fig. 8 may be pointed out as compared with Fig. 4. Firstly, the room temperature EL intensity is higher than that at 80 K. This ratio is valid until a drive current of 400 mA (the operating area is 3.2  $\text{mm}^2$ ). Secondly, the ratio between the Er-related EL intensity and background EL intensity increases in the  $\langle 111 \rangle$  sample as compared with that in the  $\langle 100 \rangle$  sample (see Fig. 4). It may be associated with a change of contributions of the avalanche and tunnel mechanisms to carrier generation as a result of variations of the electrically active center concentration.

## Conclusion.

Room-temperature Er-related EL in the erbium-oxygen-co-doped single crystal silicon p-n diodes has been observed. Effects of the ion implantation doses and substrate orientation on the properties of Si:Er:O avalanching light-emitting structures has been studied. The present results are the indication that impact ionization occurring due to p-n junction avalanche breakdown can be used to excite  $\text{Er}^{3+}$ -related luminescence.

## Acknowledgements.

We wish to thank A.V.Shestakov and R.V.Tarakanova for technical assistance. This work was made possible by financial support from the International Science and Technology Center (grant # 168) and Civilian Research and Development Foundation (grant # 235).

**References.**

1. H. Ennen, J. Schneider, G. Pomrenke, and A. Axmann, *Appl. Phys. Lett.* **43**, 943 (1983).
2. H. Ennen, G. Pomrenke, A. Axmann, K. Eisele, W. Haudl, and J. Schneider, *Appl. Phys. Lett.* **46**, 381 (1985).
3. J. Michel, J. L. Benton, R. F. Ferrante, D. C. Jacobson, D. J. Eaglesham, E. A. Fitzgerald, Y. H. Xie, J. M. Poate, and L. C. Kimerling, *J. Appl. Phys.* **70**, 2672 (1991).
4. Rare Earth Doped Semiconductors II, *MRS Symp. Proc.* **422** (1996).
5. I. N. Yassievich and L. C. Kimerling, *Semicond. Sci. Technol.* **8**, 718 (1993).
6. F. Y. G. Ren, J. Michel, Q. Sun-Paduano, B. Zheng, H. Kitagawa, D. S. Jacobson, J. M. Poate, and L. C. Kimerling, *MRS Symp. Proc.* **301**, 87 (1993).
7. B. Zheng, J. Michel, F. Y. G. Ren, L. C. Kimerling, D. C. Jacobson, and J. M. Poate, *Appl. Phys. Lett.* **64**, 2842 (1994).
8. G. Franzo, F. Priolo, S. Coffa, and A. Carnera, *Appl. Phys. Lett.* **64**, 2235 (1994).
9. S. Coffa, F. Priolo, G. Franzo, A. Polman, S. Libertino, M. Saggio, and A. Carnera, *Nucl. Instrum. Meth. B* **106**, 386 (1995).
10. J. Stimmer, A. Reitinger, J. F. Nutzel, G. Abstreiter, H. Holzbrecher, and Ch. Buchal, *Appl. Phys. Lett.* **68**, 3290 (1996).
11. S. Coffa, F. Priolo, G. Franzo, V. Bellani, A. Carnera, and S. Spinella, *Phys. Rev. B* **48**, 11782 (1993).
12. J. Michel, J. Palm, F. Gan, F. Y. G. Ren, B. Zheng, S. T. Dunham, and L. C. Kimerling, *Mater. Sci. Forum* **196-201**, 585 (1995).
13. I. Tsimperidis, T. Gregorkiewicz, and C. A. J. Ammerlaan, *Mater. Sci. Forum* **196-201**, 591 (1995).
14. N. A. Sobolev, O. V. Alexandrov, M. S. Bresler, O. B. Gusev, E. I. Shek, M. I. Makovijchuk, and E. O. Parshin, *Mater. Sci. Forum* **196-201**, 597 (1995).
15. J. H. Shin, G. N. van den Hoven, and A. Polman, *Appl. Phys. Lett.* **67**, 377 (1995).
16. A. G. Chynoweth and K. G. McKay, *Phys. Rev.* **102**, 369 (1956).

## HIGH TEMPERATURE LUMINESCENCE DUE TO Er IN POROUS Si

M. Stepikhova<sup>1,2</sup>, W. Jantsch<sup>1</sup>, G. Kocher<sup>1</sup>,  
M. Schoisswohl<sup>3</sup>, J.L. Cantin<sup>3</sup>, H.J. von Bardeleben<sup>3</sup>

<sup>1</sup> Institut für Halbleiterphysik, Johannes-Kepler-Universität, A-4040 Linz, AUSTRIA

<sup>2</sup> Permanent Address: State University, 603600 Nizhni Novgorod, RUSSIA

<sup>3</sup> Universites de Paris 6&7, 75251 Paris Cedex 05, FRANCE

**Keywords :** erbium centers, porous silicon, PLE spectroscopy

**Abstract.** Porous Si layers electrolytically doped with Er show a sharp and intense Er<sup>3+</sup> related photoluminescence spectrum at 4.2 K after annealing at 1000°C for 10 s in an N<sub>2</sub>/O<sub>2</sub> atmosphere. The spectrum consists of one line centered at 1.548 μm and a line at least three times broader centered at 1.539 μm. The latter one reveals very stable temperature behavior: it decreases only by about a factor of 6 when the temperature is increased from 4.2 K to 300 K. Photoluminescence excitation spectroscopy performed for the <sup>4</sup>I<sub>9/2</sub> and <sup>4</sup>I<sub>11/2</sub> Er spin-orbit multiplets, indicates two types of optically active Er centers located (i) in porous nanograins and (ii) in an amorphous, glass-like matrix. We demonstrate that the efficient room temperature Er-luminescence seen in porous Si originates from Er ions incorporated in a glass-like environment.

### Introduction

Recently, Er doped materials are widely studied in context with the interest in temperature stable light emitters for optical communication systems. The intra-4f-shell transition between the two lowest spin-orbit levels of Er<sup>3+</sup> ions, namely <sup>4</sup>I<sub>13/2</sub> → <sup>4</sup>I<sub>15/2</sub>, occurs at 1.54 μm, a wavelength close to that with minimum loss in silica based optical fibers.

Being possibly compatible to silicon technology, porous Si (po-Si) was suggested as one of the promising host materials for Er doping. Owing to the enlarged energy bandgap of the porous nanograins (1.8...2 eV, as reported) a weaker temperature quenching of PL was predicted for this material in agreement with the empirical Favenne rule [1]. Furthermore, spatial confinement of photocarriers in silicon nanograins near the incorporated Er was supposed to result in very efficient excitation of Er<sup>3+</sup> ions and also in a stable temperature dependence [2-4]. The enormous surface area of porous Si and the small distance between the Er and surface oxygen atoms were considered to allow for easy oxygen acquisition and therefore the improved activation of Er ions.

Erbium has been incorporated in po-Si either by ion implantation before [4] and after [3,5,6] etching the pores, by electrochemical deposition [2], or by diffusion from spin-on films [7]. In most cases room-temperature photoluminescence (PL) was reported, and as a common feature, broad spectra were obtained with a full width at half maximum (FWHM) of about 7 ÷ 11 nm at ~18 K. The spectra reported were centered, depending on preparation conditions, at 1.535 ÷ 1.538 μm [2,3,5,6,8]. To our knowledge only Taskin *et al.* [4] observed sharp atomic-like PL spectra in po-Si corresponding to Er ions in sites with cubic and axial symmetry identified earlier in single crystal bulk Si [9]. These lines exhibit strong quenching at temperatures above 150 K, together with the visible PL in the porous host. So far, little is known about the location and the microscopic structure of the optically active and especially the temperature stable erbium centers in porous silicon.

In this paper we report results of the photoluminescence excitation spectroscopy (PLE), which enable us to identify two kinds of optically active Er centers in porous Si. We show that the efficient room temperature luminescence originates, most likely, from Er ions incorporated in an amorphous glass-like matrix.

## Experimental

Po-Si layers were produced by anodic etching of p-type silicon wafers ( $10\ \Omega\text{-cm}$ ) in a diluted HF ( $\text{HF}/\text{C}_2\text{H}_5\text{OH}/\text{H}_2\text{O}$ ) solution. The thickness of the studied porous layers was  $2\ \mu\text{m}$  and the porosity about 70%. The po-Si layers have been doped with Er by an electrolytical method using  $\text{ErCl}_3$  dissolved in ethanol. The concentration of Er atoms in the layers was estimated to be 10% of the total charge introduced in the electrolytical process, namely about  $4.4 \cdot 10^{18}\ \text{cm}^{-3}$ . The samples were subjected to isochronal rapid thermal annealing (RTA) at  $1000^\circ\text{C}$  for 10 s in  $\text{N}_2/\text{O}_2$  (20%) atmosphere. The same samples prepared in pure  $\text{N}_2$  flow show only weak and broad luminescence associated with dislocations. Annealing in  $\text{N}_2$  at a temperature of  $900^\circ\text{C}$  for 30 min and two stage annealing at  $600^\circ\text{C}$  for 30 min and at  $900^\circ\text{C}$  for 15 s (the procedures reported as most efficient for the activation of Er centers in implanted CZ-Si [10]) did not result in intense Er- luminescence in po-Si layers either.

For comparison, we investigate also: (i) p-type monocrystalline CZ-Si implanted with Er at an energy of 2 MeV and a dose of  $3 \cdot 10^{13}\ \text{cm}^{-2}$ , annealed at  $900^\circ\text{C}$  in  $\text{N}_2$  for 30 min; (ii) silica glass - a slice of optical fiber preform material with a composition of the Er doped core of  $\text{SiO}_2 + \text{Al}_2\text{O}_3 + \text{C}_{\text{Er}}^{3+}$  where erbium concentration  $\text{C}_{\text{Er}}^{3+} \approx (1 \div 2) \cdot 10^3\ \text{ppm}$ ; and (iii) a sample of fluorozirconate (ZBLAN) glass doped with 1 mol.% of  $\text{Er}^{3+}$ .

The photoluminescence measurements were performed by illuminating the samples with the 514.5 nm Ar-ion laser line and an excitation power density below  $1\ \text{W}\cdot\text{cm}^{-2}$ . The luminescence signal was registered by a grating spectrometer and a liquid nitrogen cooled Ge detector for the infrared ( $\geq 1\ \mu\text{m}$ ) range, while a photomultiplier tube was used for measurements in the visible range. The spectral resolution was varied from 10 to  $40\ \text{\AA}$ . For the excitation spectroscopy, a Ti : sapphire laser was tuned over two wavelength ranges of 740 - 860 nm and 950 - 1020 nm. A constant power density of  $0.7\ \text{W}\cdot\text{cm}^{-2}$  was maintained at all wavelengths.

## Results and discussion

Figure 1 shows low temperature (4.2 K) PL spectra of Er doped po-Si obtained in samples annealed at  $1000^\circ\text{C}$  for 10 s in  $\text{N}_2/\text{O}_2$  (20%) atmosphere. The visible PL spectrum originates from the host

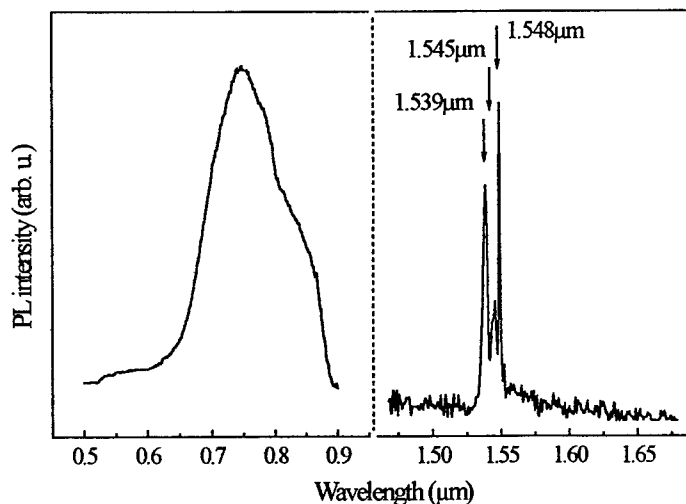


Fig. 1: Low temperature photoluminescence spectra of electrolytically Er doped porous Si. The spectrum on the left represents the visible PL originating from the host porous layer, on the right-hand side - an infrared Er related PL spectrum.

porous layers. In our samples the visible band covers in the wavelength region of 650 - 900 nm with an intensity maximum at about 750 nm. The spectrum on the right-hand side of Fig. 1 represents the infrared luminescence measured under excitation at a wavelength of 514.5 nm. In the  $1.54\ \mu\text{m}$  region two intense, sharply peaked lines are detected at wavelengths of  $1.548\ \mu\text{m}$ ,  $1.539\ \mu\text{m}$ , respectively, and a weaker one at  $1.545\ \mu\text{m}$ . The FWHM of the strongest peak was determined to be 1.2 nm at 4.2 K (limited by the resolution of the detection



system). An at least a three times broader PL line occurs at  $1.539\mu\text{m}$  with a FWHM of  $3.6\text{ nm}$ . Relatively long radiative lifetimes of  $4\text{ ms}$  and  $2.8\text{ ms}$  are obtained at  $4.2\text{ K}$  for the PL lines at  $1.538\text{ }\mu\text{m}$  and  $1.549\text{ }\mu\text{m}$ , respectively. These values are characteristic for parity forbidden intrashell transitions of Er but they exceed those obtained for Er centers in crystal bulk Si ( $\sim 1\text{--}1.6\text{ ms}$ ) considerably [11]. The chemical etching in a typical etch-solution for Si shows, that the  $1.54\text{ }\mu\text{m}$  PL originates from the Er centers incorporated in the near-surface porous layer of about  $1\text{ }\mu\text{m}$  thickness: after removing a layer of this thickness we did not obtain any signal in  $1.54\text{ }\mu\text{m}$  wavelength region. In Er doped po-Si, both the visible emission from the porous host and the infrared  $\text{Er}^{3+}$ -emission around  $1.54\text{ }\mu\text{m}$  were observed up to room temperature. The temperature dependent PL spectra are shown in Fig. 2. The different behavior of the main  $1.539\text{ }\mu\text{m}$  and  $1.548\text{ }\mu\text{m}$  PL lines clearly demonstrates that they originate from different Er centers. The emission at  $1.539\text{ }\mu\text{m}$  is most stable at high temperature. In the insert in Fig. 2 we compare the temperature dependencies of this emission

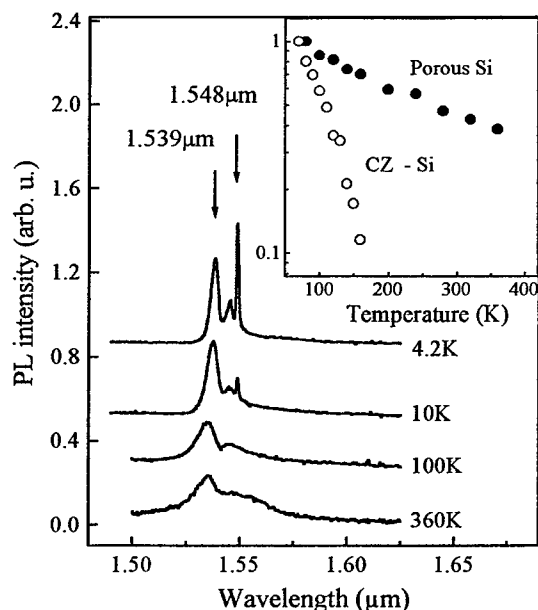


Fig. 2: Temperature evolution of the PL spectrum of Er doped po-Si. The insert shows the temperature dependence of the  $1.539\text{ }\mu\text{m}$  emission line compared with that measured for the cubic Er center in CZ-Si. The spectra at  $100\text{ K}$  and  $360\text{ K}$  are magnified by a factor 2 and 4, respectively.

intrashell excitation of Er ions apparently becomes possible due the enlarged energy bandgap of po-Si. In contrast to po-Si, no resonances are observed in the PLE spectra of Er implanted monocrystalline bulk Si in the wavelength range of  $740\text{--}860\text{ nm}$ : the PL of Er ions excited in bulk Si through electron-hole pair recombination in the host shows only insignificant changes of intensity with increasing excitation wavelength.

Figure 3 shows PLE spectra obtained for both the  $1.539\text{ }\mu\text{m}$  and  $1.548\text{ }\mu\text{m}$  Er PL lines observed in po-Si. The excitation energies were chosen close to the energies of the  $^4\text{I}_{15/2} \rightarrow ^4\text{I}_{9/2}$  and  $^4\text{I}_{15/2} \rightarrow ^4\text{I}_{11/2}$  intra-4f shell transitions of the  $\text{Er}^{3+}$  ions, namely in the wavelength ranges centered at  $810\text{ nm}$  and  $980\text{ nm}$ . Sharp atomic-like features are observed in the PLE spectra detected at the emission wavelength of  $1.548\text{ }\mu\text{m}$  due to the crystal field splitting of the  $^4\text{I}_{9/2}$  and  $^4\text{I}_{11/2}$  states. Five peaks with energetic distances of  $112.7\text{ cm}^{-1}$ ,  $76.2\text{ cm}^{-1}$ ,  $65.1\text{ cm}^{-1}$ ,  $28.2\text{ cm}^{-1}$  for  $^4\text{I}_{9/2}$  level and six peaks with

line with that measured for the cubic Er center in CZ-Si. The PL of the Er center in po-Si, comparable in intensity at  $4.2\text{ K}$ , shows weak quenching at elevated temperatures in contrast to the Er luminescence in crystal bulk Si, which dies away completely at about  $180\text{ K}$ : the photoemission of the Er center in po-Si at  $1.539\text{ }\mu\text{m}$  decreases only by a factor of about 8 between  $4.2\text{ K}$  and  $360\text{ K}$ .

The emission at  $1.548\text{ }\mu\text{m}$ , belonging to the other Er center in po-Si, drops very rapidly with increasing temperature: it is not observable above  $60\text{ K}$ . This low temperature quenching is caused rather by non-radiative recombination processes due to surface defects activated by temperature than by suppression of the excitation mechanism for the Er center, since we observe the same temperature behavior also under direct intrashell excitation of Er centers at the wavelengths  $804.4\text{ nm}$  and  $966.2\text{ nm}$  (see below).

In order to investigate the lattice position and the crystal field symmetry of Er centers in po-Si we performed PLE measurements. The direct

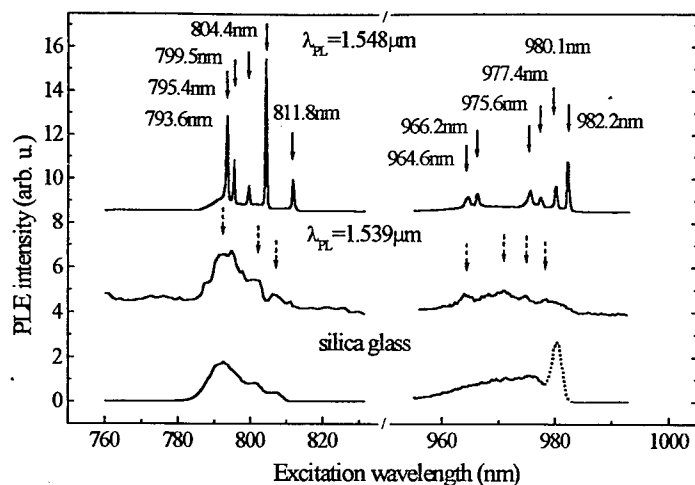


Fig. 3: PLE spectra of the  $\text{Er}^{3+}$  centers in po-Si (top and middle trace) and silica glass (bottom). Solid and dashed arrows indicate  ${}^4\text{I}_{15/2} - {}^4\text{I}_{9/2}$  and  ${}^4\text{I}_{15/2} - {}^4\text{I}_{11/2}$  transitions related to the different Er centers in po-Si. The curves in the middle are magnified by the factor 10.

Figure 3 shows also the PLE spectra of the Er center with emission at 1.539  $\mu\text{m}$  in po-Si and, for comparison, spectra measured in silica glass. We obtain practically identical (with exception of the

dashed peak caused by ytterbium contaminations in the silica glass) broad PL spectra for both samples with some features of po-Si spectra indicated with dashed arrows. The PLE transitions of  ${}^4\text{I}_{9/2}$  Er state in po-Si are situated very close to those observed in silica glass at wavelengths of 792.4 nm, 801.4 nm and 807.5 nm. In po-Si, the PLE intensity of this center is weaker by a factor of 10, though. We assign this center thus to an Er center in a glass-like  $\text{SiO}_2$  phase formed on the porous surface during the annealing process. This speculation is supported by the observed temperature behavior of the 1.539  $\mu\text{m}$  emission line (Fig. 4). At elevated temperature, when the sharp spectra of po-Si have faded away, the emission spectra of po-Si and silica glass are qualitatively alike as seen in Fig. 4a,b. The continuous broadening of the spectra with temperature up to values of 100 - 300  $\text{cm}^{-1}$ , which are comparable to the energy spread of one Er manifold, is representative for predominantly inhomogeneously broadened spectra of centers in a amorphous glass - like structures. Such behavior could be explained in terms of thermal

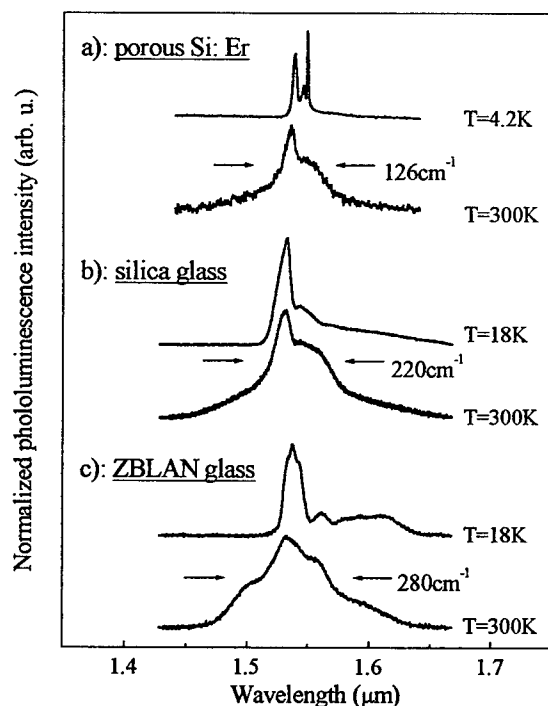


Fig. 4: Normalized PL spectra of the Er doped po-Si as compared with those observed in glass materials at low (4.2K) and high (300K) temperatures.

population of higher energy Stark levels of the  $^4I_{13/2}$  manifolds for strongly overlapping spectra due to different Er sites [12,13]. In contrast, for PL spectra of Er centers in crystal structures with well defined crystal field symmetry it was reported that the energy and the linewidth of the  $Er^{3+}$ - related emission does not depend on temperature up to 300 K [14,15]. Because of the weak electron-phonon coupling of the 4f states, only negligible thermal broadening was suggested and observed for each Stark level in manifold - of the order of  $10\text{ cm}^{-1}$  [12,15] and as a consequence so-called "hot PL lines" [9] are clearly detectable in the Er spectra at elevated temperature.

We propose that this amorphous glass-like phase consists of an  $SiO_2$  layer and is created on the anomalously sensitive po-Si surface during annealing in oxygen-containing atmosphere, although

another possible nature of this amorphous phase - an a-Si:O:H phase on the surface can not be excluded.

The crystalline environment of the  $1.548\text{ }\mu\text{m}$  Er center is clearly evidenced from the excitation spectroscopy measurements. This center corresponds to Er ions incorporated in a matrix with lower than cubic crystal field symmetry and relatively wide energy bandgap, namely in porous silicon nanograins. To determine the splitting of the ground  $^4I_{15/2}$  multiplet of Er ions we performed photoluminescence measurements under direct intra- 4f shell excitation at wavelengths corresponding to the maxima of the PLE spectra shown in Fig.3. These measurements allowed to distinguish the levels of the same Er state which have by one order of magnitude smaller intensity. Actually the multiplet structure of this Er center incorporated in porous nanograins consists of the lines at  $1.545\text{ }\mu\text{m}$ ,  $1.548\text{ }\mu\text{m}$ ;  $1.555\text{ }\mu\text{m}$ ; and  $1.565\text{ }\mu\text{m}$ . The exact line positions and correlation of the line intensities for this center are comparable to those seen in crystalline Si and III-V compound semiconductors [14,16,17]. The number of observed

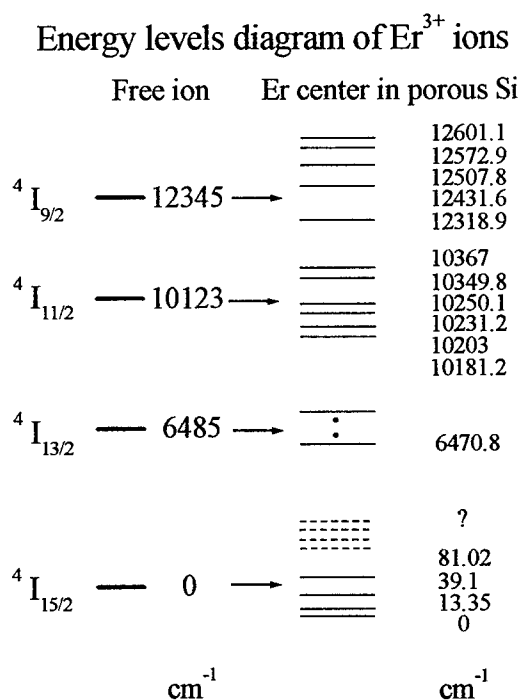


Fig. 5: Energy level diagram for Er centers in porous nanograins

excitation lines excludes cubic symmetry of the center as proposed in the literature [14,16]. We attribute only this type of spectrum to Er diffused into the po-Si. The energy levels of the  $^4I_{9/2}$ ,  $^4I_{11/2}$  and  $^4I_{15/2}$  multiplets determined from the excitation spectroscopy measurements for Er centers in porous nanograins are summarized in Fig. 5.

## Conclusions

Efficient low- and high-temperature infrared photoluminescence is obtained from po-Si, which was electrochemically doped with Er and annealed at  $1000^\circ\text{C}$  for 10s in  $N_2/O_2$  atmosphere. Two kinds of optically active Er centers were identified in these structures from the photoluminescence excitation spectroscopy for the  $^4I_{9/2}$  and  $^4I_{11/2}$  Er spin-orbit multiplets observed for the first time in po-Si: (i) centers, located in porous nanograins and (ii) centers in an amorphous, glass-like matrix. The resonant PLE spectra for the center in the crystalline part of the po-Si infers the splitting of the Er multiplets in a crystal field with lower than cubic symmetry. Analysing results of the PLE spectroscopy and temperature dependence of PL for both type centers we show that the efficient

room temperature Er-luminescence seen in porous Si originates from Er ions incorporated in a glass-like environment. The multiplet structure of the Er centers in porous Si is presented.

**Acknowledgements :** We would like to thank H. Przybylinska, Institute of Physics, Polish Academy of Sciences for many stimulating discussions and also I.A. Grishin, Nizhni Novgorod State University for fabricating and providing the glass samples. One of us (M. Stepikhova) acknowledges support from the Johannes-Kepler Universität Linz during her stay in Linz. This work was supported by the *Gesellschaft für Mikroelektronik*, Vienna and the *Fonds zur Förderung der Wissenschaftlichen Forschung*, Austria

## References

1. P.N. Favenec, H.L' Haridon, D. Moutonnet, M. Salvi, and M. Gauneau, *Mat. Res. Soc. Symp. Proc.* **301**, 181 (1993)
2. T.Kimura, A. Yokoi, H. Horiguchi, R. Saito, T Ikoma, and A. Sato, *Appl. Phys. Lett.* **65**, 983 (1994)
3. F. Namavar, F. Lu, C.H. Perry, A. Cremins, N. M. Kalkhoran, R.A. Soref, *J. Appl. Phys.* **77**, 4813 (1995)
4. T. Taskin, S. Gardelis, J.H. Evans, B. Hamilton and A.R. Peaker, *Electr. Lett.*, Vol. 31, No 24, 2132 (1995)
5. J.H. Shin, G.N. van den Hoven, and A. Polman, *Appl. Phys. Lett* **66**, 2379 (1995)
6. R. White, X. Wu, U. Hömmerich, F. Namavar, A.M. Cremins-Costa, *Mat. Res. Soc. Symp. Proc.* **422**, 137 (1996)
7. A.M. Dorofeev, N.V. Gaponenko, V.P. Bondarenko, E.E. Bachilo, N.M. Kazuchits, A.A. Leshok, G.N. Troyanova, N.N. Vorosov, V.E. Borisenko, H. Gnaser, W. Bock, P. Becker and H. Oechsner, *J. Appl. Phys.* **77**, 2679 (1995)
8. X. Zhao, S. Komuro, S. Maruyama, H. Isshiki, Y. Aoyagi and T. Sugano, *Mat. Res. Soc. Symp. Proc.* **422**, 143 (1996)
9. H. Przybylinska, W. Jantsch, Yu. Suprun-Belevitch, M. Stepikhova, L. Palmetshofer, G. Hendorfer, A. Kozanecki, R.J. Wilson, B.J. Sealy, *Phys. Rev. B.* **54**, 2532 (1996)
10. J. Michel, J. L.Benton, R.F. Ferrante, D.C. Jacobson, D.J. Eaglesham, E.A. Fitzgerald, Y.H. Xie, J.M. Poate, and L.C. Kimerling, *J. Appl. Phys.* **70**, 2672 (1991)
11. W. Jantsch, H. Przybylinska, Yu. Suprun-Belevich, M. Stepikhova, G. Hendorfer and L. Palmetshofer, *Mat. Science Forum* **196-201**, 609 (1995)
12. S. Zemon, G. Lambert, L.J. Andrews, W.J. Miniscalco, B.T. Hall, T. Wei, R.C. Folweiler, *J. Appl. Phys.* **69**, 6799 (1991)
13. T. Tsuneoka, K. Kojima & S. Bojja, *Phys. Cem. Glasses* **37**, 97 (1996)
14. X. Zhao, K. Hirakawa, and T. Ikoma, *Appl. Phys. Lett.* **54**, 712 (1989)
15. H. Ennen, J. Wagner, H.D. Müller, R.S. Smith, *J. Appl. Phys.* **61**, 4877 (1987)
16. F. Bantien, E. Bauser, and J. Weber, *J. Appl. Phys.* **61**, 2803 (1987)
17. A. Majima, S. Uekusa, K. Ootake, K. Abe and M. Kumagai, *Mat. Res. Soc. Symp. Proc.* **301**, 107 (1993)

## ELECTRON PARAMAGNETIC RESONANCE OF ERBIUM IN BULK SILICON CARBIDE CRYSTALS

P.G. Baranov, I.V. Ilyin and E.N. Mokhov

A.F. Ioffe Physico-Technical Institute, Politechnicheskaya 26, 194021 St. Petersburg, Russia

**Keywords:** silicon carbide, rare-earth impurities, electron paramagnetic resonance

We report the first EPR observation of rare-earth impurities in erbium doped bulk 6H-SiC crystals, grown by the sublimation sandwich-method. Two lines for axial  $\text{Er}^{3+}$  centre with crystalline  $c$ -axis being the axis of the  $g$  tensor, which seem to arise from different lattice sites in 6H-SiC and three  $\text{Er}^{3+}$  centres with same nearly orthorhombic symmetries, attributed to different lattice sites have been observed. A direct identification of erbium ions has been established by the presence of hyperfine interaction with  $^{167}\text{Er}$  nuclei. The principal  $g$  values of the axial and orthorhombic  $\text{Er}^{3+}$  centres were found. The average  $g$  values suggest that the parent cubic ground state may have  $\Gamma_7$  representation for both centres. Presumably, erbium substitute for silicon in a regular environment for axial centre. The orthorhombic  $\text{Er}^{3+}$  seems to include another defect at carbon position along with  $\text{Er}^{3+}$  ion at silicon site. The EPR spectrum of the excited state of  $\text{Er}^{3+}$  in 6H-SiC seems to be observed at higher temperature. The trace amounts of the other rare-earth elements, in particular  $\text{Dy}^{3+}$ , had probably been present in EPR spectra.

### Introduction

Rare-earth doped semiconductors attract an increasing interest due to their possible applications in light emitting diodes or diode lasers. The most promising property of these materials is the possibility of excitation of narrow temperature-independent luminescence. Since the luminescence is due to an intra-4f shell transition, the influence of the crystal field of host lattice is weak and this luminescence was found to be fairly independent on the host materials. Erbium doped semiconductors have attracted particular attention because the  $\text{Er}^{3+}$  intra-4f-shell transition  $^4I_{13/2} \rightarrow ^4I_{15/2}$  at 1.54  $\mu\text{m}$  matches the minimum in the absorption of silica-based fiber-optic communication systems. A number of papers have been published on the photoluminescence properties of rare-earth elements in III-V compounds [1] and silicon [2]. The techniques used to incorporate these elements were ion implantation, liquid-phase epitaxy, molecular-beam epitaxy. At present, the main obstacle for applications is the low luminescence yield, particularly at room temperature. The quenching of the emission intensity decreases with increasing energy gap of the semiconductor host. This trend is particularly important for the devices' aspects of Si:Er, since it seems to imply a basic principle suggesting that Si:Er will not give a reasonable yield at room temperature [3]. In Ref. 4 intense erbium-1.54- $\mu\text{m}$  photoluminescence was observed in ion-implanted SiC crystal which is wide-band gap semiconductor. The maximum penetration of the erbium was about 0.3  $\mu\text{m}$ .

Electron paramagnetic resonance (EPR) has proven to be an extremely powerful tool for the study of defects in semiconductors. The reason for this is that the EPR spectra usually contain highly detailed microscopic information about the structure of the defects, details that often cannot be obtained in any other way. However, ionic implantation produces a very thin layer and EPR measuring of such a layer has always been a big problem. The second problem is that the defects in the layer produced by ionic implantation, on the one hand, and in as-grown bulk material, on the other, as a rule, differ structurally. What is more, the impurities which could be introduced by ionic

implantation could often not be doped in the process of the crystal growth. In recent paper [5] EPR spectrum from erbium/oxygen complex ( $\text{Er}^{3+}$  surrounded by six O atoms) with a structure similar to that of the orthorhombic site of  $\text{Er}_2\text{O}_3$  embedded with well-defined orientations within the Si lattice. A 2  $\mu\text{m}$ -thick O-rich layer was produced by using the solid phase epitaxial regrowth of an amorphous layer produced by Er implantation. The hyperfine structure could not be observed above the noise level in Ref. 5 and the possibility of Er-pairs must not be ruled out.

We report here the first EPR results for rare-earth impurities in silicon carbide crystals grown by the sublimation sandwich method. Preliminary results have been published elsewhere [6].

### Experimental results

The samples were erbium doped bulk 6H-SiC crystals which were grown by the sublimation sandwich-method [7] in vacuum at temperatures 1850-1900<sup>o</sup> C. The source of the impurity was metallic erbium which was directly placed inside the tantalum container. As-grown crystals were of *n*-type, owing to nitrogen donors. The using of the container from the tantalum material allowed to decrease the concentration of nitrogen donors up to  $\sim 10^{16} \text{ cm}^{-3}$  level.

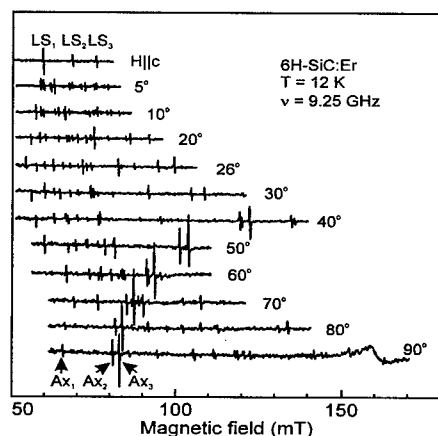


Fig. 1. X-band EPR spectrum of  $\text{Er}^{3+}$  ions in 6H-SiC: Er crystal in some orientations of crystal under rotation in plane near to the  $\{11\bar{2}0\}$  plane. In orientations  $H \parallel c$  and  $H \perp c$  the positions of low symmetry (LS) and axial symmetry (Ax) centres are indicated..

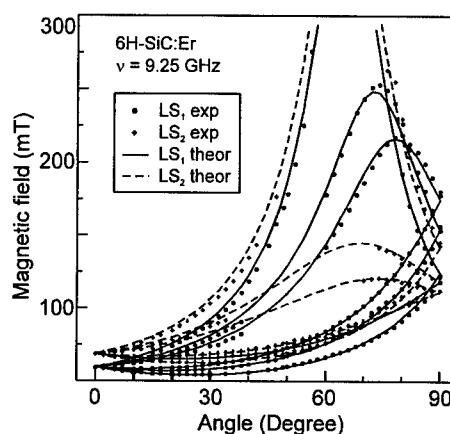


Fig. 2. The measured (circles) and calculated (lines) angular dependencies of line positions of  $\text{Er}^{3+}$  ions for  $\text{LS}_1$  and  $\text{LS}_2$  centres in 6H-SiC obtained at 9.25 GHz with the field rotated in the  $\{11\bar{2}0\}$  plane

The EPR spectra were studied in the temperature range 4.5-300 K using an X-band (9.3 GHz) spectrometer. The samples were oriented for rotation in the  $\{11\bar{2}0\}$  plane. The samples had the shape of a platelet ( $3 \times 4 \text{ mm}^2$ ) with the face perpendicular to the hexagonal axis (*c*-axis) and the thickness was about 1 mm.

The observed EPR spectra in an Er doped 6H-SiC crystal were composed of many lines whose positions varied with orientation in the region of magnetic field from 50 mT to 800 mT. The EPR spectra of, at least, three types of centres having qualitatively different orientation dependencies have been observed.

### Low symmetry $Er^{3+}$ centres

Figure 1 shows the low-field part of X-band EPR spectra observed in a Er doped 6H-SiC crystal at 12 K for magnetic field at different angles  $\theta$  with respect to the  $c$ -axis. In principal, it can be resolved into three sets of sharp lines, designated  $LS_1$ ,  $LS_2$  and  $LS_3$  (LS - low symmetry) in Fig. 1. The peak-to-peak linewidths of the lines are  $\sim 0.1$  mT. The signals labelled by  $LS_1$ ,  $LS_2$  and  $LS_3$  belong to different centres as the ratio of the intensities of these signals is sample and temperature sensitive. We believe, that these spectra can be attributed to three different lattice positions. 6H-SiC has over-all hexagonal symmetry and for 6H-SiC there are a hexagonal-like and two cubic-like crystallographic inequivalent lattice sites, when the first- and second-nearest neighbours are considered.

The simplification of the spectrum occurred with  $H \parallel c$ . The spectrum of every lattice position shows the typical orthorhombic symmetry. The similarity of the EPR spectra's orientation dependencies implies that all centres have the same symmetries. Quantitative differences have only been observed in the spin Hamiltonian parameters and in decay temperatures of the different  $LS_1$ ,  $LS_2$  and  $LS_3$  EPR signals. There are six sites that are magnetically inequivalent; these coalesce into four in the  $\{11\bar{2}0\}$  plane. The spectra of these sites share a common point when the magnetic field is along the  $c$ -axis. As the field direction changes in the  $\{11\bar{2}0\}$  plane, the lines split as one can see in Fig. 1.

A direct identification of erbium ions has been established by the presence of hyperfine (hf) interaction with  $^{167}\text{Er}$  nuclei. Erbium has only one stable odd isotope,  $^{167}\text{Er}$  (natural abundance 22.8%), having nuclear spin  $I=7/2$  and one normally expects a spectrum consisting of one intense main line and eight equally intense weak satellite lines. Their intensity, as a fraction of the main line, is expected to be about 3% only and the hyperfine structure could not be observed for all orientations. The separations between the lines are about 80 G for  $H \parallel c$ . The hyperfine structure is difficult to analyse as orientations with the magnetic field exactly parallel to the  $c$ -axis were not obtained.

Each of the spectra  $LS_1$ ,  $LS_2$  and  $LS_3$  can be fitted to the spin Hamiltonian

$$H = \mu_B \mathbf{B} \cdot \mathbf{g} \cdot \mathbf{S} + \mathbf{S} \cdot \mathbf{A} \cdot \mathbf{I} \quad (1)$$

with  $S=1/2$  and  $I=7/2$  which is the spin of the  $^{167}\text{Er}$  nucleus,  $\mu_B$  is the Bohr magneton and  $\mathbf{g}$  is the  $\mathbf{g}$  tensor. The first term is the interaction of the electron spin with the external magnetic field, the second term in Eq. (1) describes the hyperfine interaction of the electron spin with  $^{167}\text{Er}$  nuclei and  $\mathbf{A}$  is the corresponding tensor (this term is zero for even Er isotopes). The local  $z$ -axis coincides with one of the six directions Si-C, which is not coincide with  $c$ -axis,  $x$  and  $y$  axes are in a plane perpendicular to the  $z$  axis and  $x$  axis lies in one of the  $\{11\bar{2}0\}$  planes. The principal  $\mathbf{g}$  values for  $LS_1$  spectra are  $g_{1x}=12.2$ ,  $g_{1y}=3.35$ ,  $g_{1z}=1.5$ ; for  $LS_2$   $\mathbf{g}$  tensor has the magnitudes which are closely related to the  $LS_1$   $\mathbf{g}$  values: for  $LS_2$  they are  $g_{2x}=10.6$ ,  $g_{2y}=6.16$ ,  $g_{2z}=1.26$ . For  $LS_3$  the relative values of the  $\mathbf{g}$ -factors differ from that of the  $LS_1$  centre and our estimation gives:  $g_{3x}=9.6$ ,  $g_{3y}=7.52$ ,  $g_{3z}=1.45$ .

The measured and calculated angular dependencies of EPR line positions of  $Er^{3+}$  ions (only for  $LS_1$  and  $LS_2$ ) obtained at 9.25 GHz are plotted as open circles and solid lines ( $LS_1$ ), crosses and dashed lines ( $LS_2$ ) respectively, in Fig. 2. It should be noted that a slight misalignment ( $7^\circ$ ) of the sample occurred so that the magnetic field was not wholly in the  $\{11\bar{2}0\}$  plane. This small misalignment has been taken into account in the analysis and did not affect the conclusions. The defect coordinate system for orthorhombic centres is tilted by small angle of  $\sim 5^\circ$  around  $y$  axis.

The intensities of the EPR lines were strongly temperature dependent and the spectra were unobservable above 30 K.

#### Axial centres

In addition to the EPR spectrum of the orthorhombic  $\text{Er}^{3+}$  centres we observed EPR lines in the region from 100 mT to 600 mT which clearly show axial symmetry with crystalline  $c$ -axis being the axis of the  $g$  tensor. The part of these spectra is shown in Fig. 1. One can see three lines

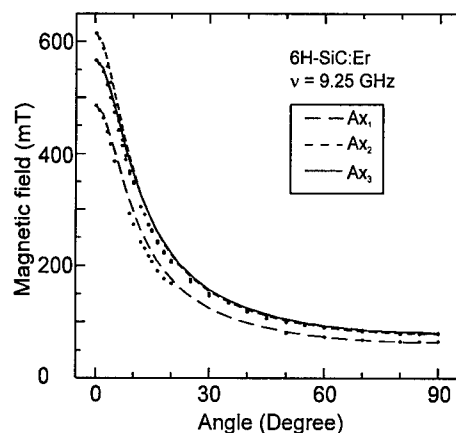


Fig. 3. The measured (circles) and calculated (lines) angular dependencies of line positions of  $\text{Er}^{3+}$  ions for axial centres in 6H-SiC obtained at 9.25 GHz with the field rotated in the  $\{11\bar{2}0\}$  plane.

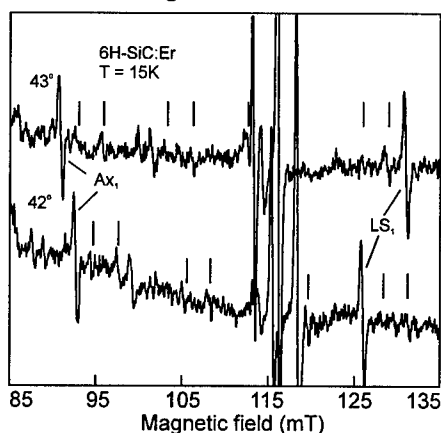


Fig. 4. Part of the EPR spectra observed in 6H-SiC:Er for two orientations of the crystal in the magnetic field. The two strong lines near 115 mT belong to the  $\text{Ax}_2$  and  $\text{Ax}_3$  centres. The lines, which belong to the hf structures of these signals are labelled by vertical marks. Only parts of the hf structures are shown.

labelled as  $\text{Ax}_1$ ,  $\text{Ax}_2$  and  $\text{Ax}_3$ . The EPR spectra can be described by the spin Hamiltonian of Eq. (1) with axial symmetry. The principal  $g$  values for  $\text{Ax}_1$  centre are  $g_{\parallel}=1.359$ ,  $g_{\perp}=10.251$ ; for  $\text{Ax}_2$  centre  $g_{\parallel}=1.073$ ,  $g_{\perp}=8.284$  and for  $\text{Ax}_3$  centre  $g_{\parallel}=1.164$ ,  $g_{\perp}=8.071$  where the parallel axis coincides with the  $c$ -axis of the crystal. Clearly, the relative intensities of all the EPR spectra depended strongly on the temperature in the experiments. These temperature dependencies of the EPR spectra intensities for two axial  $\text{Er}^{3+}$  centres  $\text{Ax}_2$  and  $\text{Ax}_3$  in  $H \parallel c$  orientation are shown as an inset in Fig. 1. The measured and calculated angular dependencies of EPR line positions of  $\text{Er}^{3+}$  ions obtained at 9.25 GHz are plotted as circles and lines, respectively, in Fig. 3. The hyperfine structures from  $^{167}\text{Er}$  have also been observed for  $\text{Ax}_2$  and  $\text{Ax}_3$  axial centres. Figure 4 shows a part of the EPR spectra observed in 6H-SiC:Er for two orientations of the crystal in the applied magnetic field. Two strong lines near 115 mT belong to the  $\text{Ax}_2$  and  $\text{Ax}_3$  centres. The lines, which arise from the hf interaction with the  $^{167}\text{Er}$  nuclei are labelled by the vertical marks. On the Fig. 4 only parts of the hf structures are shown, however it proves that the central  $\text{Ax}_2$  and  $\text{Ax}_3$  lines and the signals which we attribute to their hf structures move in coincidence in the narrow region of the angular dependency.



In addition to the spectra above, an EPR line in the region 800 mT which seems to show axial symmetry with  $g_{\parallel}=0.776$  was also observed. This spectrum is presented in Fig. 5. A striking feature in this observation is a large variation of the signal intensity with the orientation of the applied magnetic field. This seems to be a result of the highly anisotropic  $g$ -values, and it led to difficulties in following the line over the angles larger than  $10^\circ$ . This spectrum seems also to belong  $\text{Er}^{3+}$  although the hyperfine structure associated with the  $^{167}\text{Er}$  isotope could not be clearly observed above the noise level. The relative intensity of the EPR line depended strongly on the temperature in the experiments. This dependence is shown as an inset in Fig. 3.

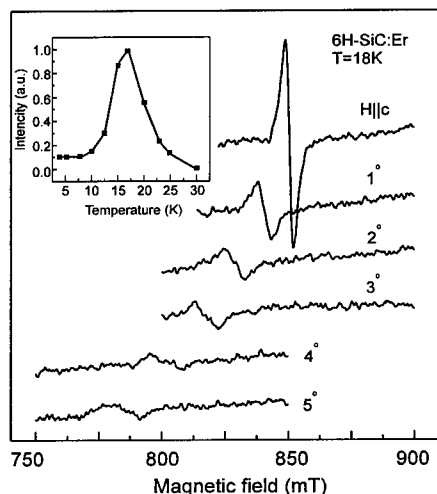


Fig. 5. EPR spectra observed in 6H-SiC:Er crystal for some orientations of the sample Rotation in the plane near to  $\{11\bar{2}0\}$ , at 9.25 GHz. The temperature dependency of the signal intensity is shown in the inset.

The new EPR lines can probably be attributed to the first excited state of the  $\text{Er}^{3+}$  ions much as it was observed in  $\text{Y}_3\text{Al}_5\text{O}_{12}:\text{Er}$  crystal [8]. By assuming that this dependence is exponential, one obtains the energy of the first excited state of erbium in 6H-SiC amounting to  $\sim 15 \text{ cm}^{-1}$  (one reasoned that the energy of the ground state must be zero).

The nature of  $\text{Ax}_1$  centre is not clear up to now, however there is some evidence which indicates that this spectrum belongs to  $\text{Dy}^{3+}$  ions.

Several other resonance lines have been noted in every Er-doped SiC sample so far examined, but these lines have not yet been identified. These resonance lines (noted as  $\text{Ax}_4$  and  $\text{Ax}_5$ ) exhibit axial symmetry with following  $g$ -factors: for  $\text{Ax}_4$ :  $g_{\parallel}=2.92$ ,  $g_{\perp}=7.69$ ; for  $\text{Ax}_5$ :  $g_{\parallel}=4.32$ ,  $g_{\perp}=7.22$ . The trace amounts of the other rare-earth elements had probably been present as impurities in the erbium starting material. Analogous result was observed in  $\text{Y}_3\text{Al}_5\text{O}_{12}:\text{Er}$  crystal in which in addition to the EPR spectra of the  $\text{Er}^{3+}$  centres the signals of trace impurities of other rare-earth elements as  $\text{Nd}^{3+}$  and  $\text{Yb}^{3+}$  were observed [9].

### Discussion

The resonances are attributed to  $\text{Er}^{3+}$  as erbium is not expected to attain any other valence under normal conditions. Besides,  $\text{Er}^{2+}$  valence state can be ruled out since for a non-Kramers' ion a different spin Hamiltonian to that shown in Eq. (1) would have to be used. The electronic configuration of  $\text{Er}^{3+}$  is  $4f^7$  with a free-ion ground state of  $^4I_{15/2}$ . The sixteenfold ground-state degeneracy will be split by crystal field into a number of quartet and doublet Stark levels, for example, an electric field of  $T_d$  symmetry splits this state into three  $\Gamma_8$  quartets and two doublets,  $\Gamma_6$  and  $\Gamma_7$ . According to the Ref. 10, the ground state is either  $\Gamma_6$  or  $\Gamma_7$  and it depends on the ratio of the fourth to sixth order crystal field terms. The isotropic  $g$  values for  $\text{Er}^{3+}$  ion was found to be  $g(\Gamma_6) = 6.772$  and  $g(\Gamma_7) = 5.975$ .

The average  $g$  values  $\langle g \rangle$  defined by  $\langle g \rangle = (g_{\parallel} + 2g_{\perp})/3$  for  $\text{Ax}_2$  and  $\text{Ax}_3$  axial centres will be 5.88 and 5.77, respectively; for orthorhombic centres  $\langle g \rangle = (g_x + g_y + g_z)/3$  will be 5.68 ( $\text{LS}_1$ ), 6.0 ( $\text{LS}_2$ ) and 6.17

(LS<sub>3</sub>). The average  $g$  values can be compared with the isotropic cubic  $g$  factor but one should assume that the axial (and orthorhombic) field is small compared to the cubic field. This suggests that the parent cubic ground state may have  $\Gamma_7$  representation for axial and orthorhombic  $\text{Er}^{3+}$  centres. The  $\Gamma_7$   $g$  value should be corrected for covalent bonding and the reduction may be due to covalency. The average  $g$  value for  $\text{Ax}_1$  axial center is  $\langle g \rangle = 7.29$  and it fits very well for  $\Gamma_6$  ground state of  $\text{Dy}^{3+}$  ion which is  $g(\Gamma_6) = 7.56$  [11]. The average  $g$ -values for  $\text{Ax}_4$  and  $\text{Ax}_5$  are 6.1 and 6.25 respectively. Since these average  $g$ -values can fit for  $\text{Dy}^{3+}$  as well as  $\text{Er}^{3+}$ , we cannot now identify these centres.

Comparison of the ionic radii of rare-earth ions with the silicon and carbon radii leads one to expect that rare-earth impurities would occur substitutionally for silicon in SiC. Presumably, erbium substitutes for silicon and lies in a regular environment for axial centre. The orthorhombic  $\text{Er}^{3+}$  has a more complicated structure and it seems to include another defect at carbon position along with  $\text{Er}^{3+}$  ion.  $\text{Er}^{3+}$  ion is substitutionally incorporated probably in association with nearest oxygen atom or carbon vacancy such that the lines joining them to the  $\text{Er}^{3+}$  ion are one of the Si-C directions which do not coincide with  $c$ -axis for hexagonal and cubic-like sites. In addition, the EPR spectrum of the excited state of  $\text{Er}^{3+}$  in 6H-SiC seems to be observed at higher temperature.

*Acknowledgements* - This work was partially supported by VW foundation under Grant No. I/70958, under NOW Grant No 047.005.12.96 and by Russian Foundation for Basic Research under Grant No. 96-02-16927.

## References

1. V.F. Masterov, Semiconductors **27**, 791-801 (1993) [Fiz. Tekh. Poluprovodn. **27**, 1435-1452 (1993)], and references therein.
2. J. Michel, J.L. Benton, R.F. Ferrante, D.C. Jacobson, D.J. Eaglesham, E.A. Fitzgerald, Y.-H. Xie, J.M. Poate, and L.C. Kimerling, J. Appl. Phys. **70**, 2672 (1991).
3. W. Jantsch and H. Przybylinska, 23rd International Conference on the Physics of Semiconductors, Berlin, July 21-26, 1996, ed. M. Scheffler and R. Zimmermann, World Scientific, Singapore-New Jersey-London-Hong-Kong, 3025-3032.
4. W.J. Choyke, R.P. Devaty, L.L. Clemen, M. Yoganathan, G. Pensl, and Ch. Haessler, Appl. Phys. Lett., **65**, 1668-1670 (1994).
5. J.D. Carey, J.F. Donegan, and R.C. Barklie, F. Priolo, G. Franzo and S. Coffa, Appl. Phys. Lett. **69**, 3854 (1996).
6. P.G. Baranov, I.V. Ilyin and E.N. Mokhov, Sol. St. Comm., to be published in 1997.
7. Yu.A. Vodakov, E.N. Mokhov, M.G. Ramm & A.D. Roenkov, Krist. und Techn. **5**, 729 (1979).
8. G.R. Asatryan, P.G. Baranov, V.I. Zhekov, T.M. Murina, A.M. Prokhorov, and V.A. Khramtsov, Sov. Phys. Solid State **33**, 559 (1991) [Fiz. Tverd. Tela (Leningrad) **33**, 976 (1989)].
9. P.G. Baranov, V.I. Zhekov, T.M. Murina, A.M. Prokhorov, and V.A. Khramtsov, Sov. Phys. Solid State **29**, 723 (1987) [Fiz. Tverd. Tela (Leningrad) **29**, 1261 (1987)].
10. K.R. Lea, M.J.M. Leask, and W.P. Wolf, J. Phys. Chem. Solids **23**, 1381 (1962)],
11. R.K. Watts and W.C. Holton, Phys. Rev. **173**, 417 (1968).

## 1.54 $\mu\text{m}$ LUMINESCENCE IN Er AND Er+O IMPLANTED 6H SiC

A. Kozanecki<sup>1</sup>, W. Jantsch<sup>2</sup>, S. Lanzerstorfer<sup>2</sup>, B. J. Sealy<sup>3</sup>, S. Jackson<sup>3</sup>

<sup>1</sup>Institute of Physics, Polish Academy of Sciences, Al. Lotnikow 32/46, 02-668 Warsaw, POLAND

<sup>2</sup>Institut für Halbleiterphysik, Johannes Kepler Universität, A-4040 Linz, AUSTRIA

<sup>3</sup>Surrey Centre for Research in Ion Beam Applications, University of Surrey, Guildford, Surrey, GU2 5XH, UK

**Keywords:** erbium centres, silicon carbide, Fourier-transform spectroscopy

**Abstract.** Photoluminescence (PL) due to the  $^4I_{13/2} - ^4I_{15/2}$  transitions of  $\text{Er}^{3+}$  in 6H SiC implanted with Er and Er+O ions is studied by means of high resolution Fourier-transform spectroscopy. It is shown that coimplantation of 6H SiC:Er with O ions does not introduce new PL transitions and causes only some redistribution of the intensity of lines existing already in SiC:Er samples. The temperature dependence of the individual PL lines have been measured. It is suggested that the migration of the excitation energy between different Er centres takes place. It is also found that transitions from a higher lying sublevel in the  $^4I_{13/2}$  multiplet are activated at temperatures above 50 K. The emission from all Er centres is quenched above 100 K with a characteristic energy of 60 meV, which probably corresponds to the binding energy of excitons at Er centres. It is shown that the  $\text{Er}^{3+}$  emission decays with a lifetime of 5.2 msec at 6 K.

### Introduction.

Optoelectronic materials doped with Er atoms are receiving widespread attention due to their possible impact on optical telecommunication. Erbium in its trivalent state exhibits luminescence around 1.54  $\mu\text{m}$  originating in electronic transitions between the two lowest spin-orbit levels, namely  $^4I_{13/2}$  and  $^4I_{15/2}$ , of  $\text{Er}^{3+}$  ions. This wavelength corresponds to minimum absorption and low dispersion of silica-based fibers. Semiconductors doped with Er offer prospects of very stable, temperature insensitive laser diodes and optical amplifiers. The major obstacle to reach this goal, however, is the still unsolved problem of efficient temperature quenching of the  $\text{Er}^{3+}$  emission. While many Er-doped semiconductors have been studied to date, only few show emission around 1.54  $\mu\text{m}$  at 300 K. Favenec *et al.* [1], Neuhaufen and Wessels [2], and Kozanecki [3] showed that quenching of the  $4f-4f$  photoluminescence (PL) of rare earth ions in semiconducting hosts is closely related to the width of the band gap, and becomes more effective with the decrease of the energy gap. Attempts to increase the emission efficiency at 300 K in most common semiconductors, as Si and GaAs, by codoping with oxygen have been quite successful [4-6]. Further progress is needed, however, as the emission intensity from Er-doped light emitting diodes is still too low for practical applications.

All these observations indicate that wide band gap semiconductors, like SiC, GaN, AlN, *etc.* are more promising for obtaining efficient emission at room temperature. This suggestion seems to be confirmed by recent studies of Er implanted SiC by Choyke *et al.* [7], who showed that the integrated PL intensity of  $\text{Er}^{3+}$  in the wavelength range of 1.49  $\mu\text{m}$  to 1.64  $\mu\text{m}$  in different SiC polytypes is almost constant up to about 400 K. Later on, the same group [8] found that the emission intensity and the quenching temperature of the  $\text{Er}^{3+}$  PL depend in a complex way on the concentration of nitrogen donors. On one hand the PL intensity increases with the N-donor concentration, whereas on the other hand the quenching temperature goes rapidly down for the donor concentration higher than  $5 \cdot 10^{17} \text{ cm}^{-3}$ .

Our preliminary low resolution measurements [9] performed on Er and Er+O implanted 6H SiC showed that there is no significant difference in the PL spectra of  $\text{Er}^{3+}$  in samples implanted solely

with Er and intentionally codoped with oxygen. This observation might indicate that residual oxygen is involved in any case in the atomic structure of Er-centres emitting at 1.54  $\mu\text{m}$ . As Fourier PL spectroscopy allowed to distinguish between the isolated and O-related Er centers in Si [10], we expected that at high resolution it also would be possible in the case of 6H SiC.

In this paper we present the results of a study of the  $4f-4f$  emission of  $\text{Er}^{3+}$  ions in Er and Er+O implanted 6H SiC by means of high resolution Fourier-transform PL spectroscopy. First results of decay time measurements of the  $\text{Er}^{3+}$  emission are also presented.

### Experimental.

Samples of 6H SiC single crystals (Cree Research Inc.) doped with N-donors to a concentration of  $8 \cdot 10^{17} \text{ cm}^{-3}$  were implanted at room temperature with 800 keV Er ions. The Er ion doses were  $10^{13}$  -  $2 \cdot 10^{15} \text{ cm}^{-2}$ . Some samples were implanted with 1 MeV Er ions ( $8 \cdot 10^{13} \text{ cm}^{-2}$ ) at 350°C to avoid amorphization. Oxygen was implanted at an energy of 125 keV to produce an O-impurity profile overlapping that of erbium. Oxygen implantation was done at room temperature as well as at 350°C, and doses were  $3 \cdot 10^{14}$  -  $5 \cdot 10^{15} \text{ cm}^{-2}$ .

The implanted samples were subsequently annealed at 1500°C in an argon gas flow for half an hour. After annealing the surface of the samples was covered with a black deposit that indicates that some carbon pseudomorphs were formed due to losses of Si from the surface. This deposit could be easily removed by a simple mechanical cleaning procedure.

Photoluminescence was excited with the 365 nm line of an Ar laser at 40 mW power. PL measurements were performed with a Bomem DA8 Fourier-transform spectrometer and the PL signal was detected with a liquid nitrogen cooled Ge detector. The spectral resolution was  $0.5 \text{ cm}^{-1}$ . The temperature dependence of both the Er PL intensity and its decay time were studied to follow quenching of the  $4f-4f$  emission.

Samples were also analysed using Rutherford backscattering and channeling spectroscopy to control the recrystallization of the implanted layers and the redistribution of the Er profile as a result of high temperature annealing. The detailed results of RBS measurements will be published elsewhere [11].

### Results.

At high resolution, many of the PL lines observed with conventional PL spectroscopy were resolved into fine structures resulting in more than 15 sharp lines at 6K. As the local site symmetries in 6H SiC are possibly lower than  $C_{3v}$  (no substitutional fraction of Er has been found with channeling

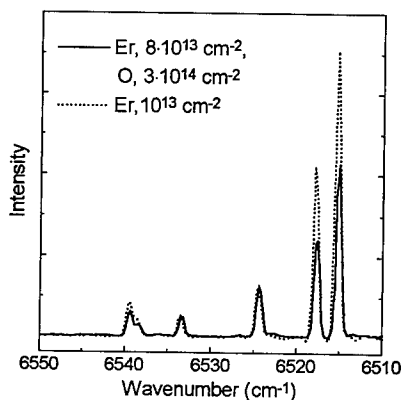


Fig. 1. Comparison of the high resolution PL spectra for 6H SiC:Er and SiC:Er+O.

[11]), the  $^4I_{15/2}$  multiplet has eight crystal field split energy sublevels. There is thus more than one type of Er centers in our samples. As it was mentioned above in low resolution PL measurements we could not find a difference in the  $4f-4f$  spectra of  $\text{Er}^{3+}$  in Er and Er+O implanted 6H SiC. In Fig. 1, high resolution Fourier-transform PL spectra of  $\text{Er}^{3+}$  are presented for samples with and without intentional O-codoping. We found that the number of lines as well as their positions are the same in all samples under study, independent of implant conditions. However, as it can be seen in Fig. 1, the intensities of some lines remain constant in the spectra of both samples and this difference holds at all measurement temperatures. Altogether we have found eight lines whose relative intensities in O-implanted samples are higher in comparison with the other lines. It can be concluded that O-codoping influences at least one

Er-centre. No new emissions that could be related to the formation of specific Er+O centres were observed even for an O implant dose of  $5 \cdot 10^{15} \text{ cm}^{-2}$ . Therefore, as the overall pattern of lines is the same in all samples we conclude that oxygen is always involved in different proportions in the formation of Er centers emitting at  $1.54 \text{ }\mu\text{m}$ .

In Fig.2, the PL spectra measured at selected temperatures are presented for a sample implanted with a dose of  $10^{13} \text{ cm}^{-2}$  of Er<sup>+</sup> ions. As can be seen, at elevated temperatures the intensity of the PL lines changes and, in particular, approximately 20 new hot lines appear. It seems that the appearance of hot lines occurs on the expense of transitions that dominate the emission at 6 K, *i.e.*, the lines at  $6515.3 \text{ cm}^{-1}$  ( $1.5348 \text{ }\mu\text{m}$ ) and  $6517.9 \text{ cm}^{-1}$ . On the basis of the temperature evolution of line intensities we can distinguish at least three groups of lines which behave in some characteristic way. First of all, there is a group of lines dominant at 6 K whose intensities always decrease with the increasing temperature. The second group is observed on the low energy side of the dominant line ( $6515.3 \text{ cm}^{-1}$ ). Here at least three intense hot lines appear already at 16 K. None of them is observed at 1.4 K [10] even the most intense one at  $6475.7 \text{ cm}^{-1}$ . New lines rise also on the high energy side of the dominant  $6515.5 \text{ cm}^{-1}$  line at 16 K (Fig.2). The highest energy transitions begin to increase fast in intensity at temperatures exceeding 50 K, suggesting that they may originate in the excited level of the  $^4\text{I}_{13/2}$  multiplet.

An analysis of the temperature dependence of the intensities of all the individual lines has been performed, and in Fig.3 the temperature evolution of the selected lines representative for each group is presented. First of all it can be seen that the increase of the intensity of hot lines takes place on the expense of transitions dominant at 6 K. We estimate that within the temperature range of 6 - 35 K the dominant lines decrease with a characteristic energy of 1-2 meV, while the intensity of hot lines increases with the same activation energy.

In the temperature range of 50 - 60 K a dramatic redistribution of the intensities is

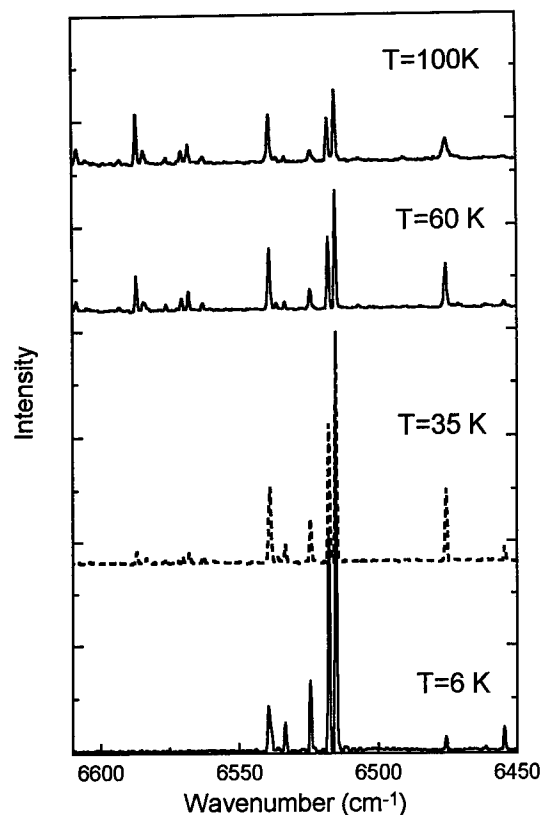


Fig.2. Temperature evolution of the PL spectra for 6H SiC implanted with  $10^{13} \text{ cm}^{-2}$  of Er ions.

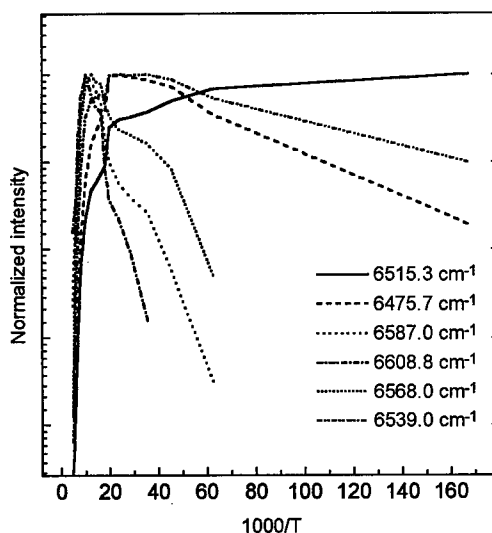


Fig.3. Normalized intensity of some PL lines of Er<sup>3+</sup> ions versus reciprocal temperature

observed (Fig.3). The decrease as well as the increase of the intensities proceed with the same characteristic energy of 13 meV. With respect to this behavior we suggest that at temperatures exceeding 50 K transitions from an excited sublevel in the  $^4I_{13/2}$  multiplet take place on the expense of transition from the lowest lying sublevel in the  $^4I_{13/2}$  manifold.

At temperatures above 100 K all the observed PL lines decrease in intensity in a similar way (Fig.3). The decay energy of 60 meV has been calculated from the exponential part of the temperature dependence. It seems that the same process is responsible for quenching of the 4f-4f emission of  $Er^{3+}$  ions independent of their exact chemical environment.

We have also evaluated the temperature evolution of the integrated  $Er^{3+}$  PL intensity, following the suggestion of Choyke *et al.* [7] about its impressive stability up to 400 K. We have found, however, that the integrated intensity stays more or less constant up to approximately 100 K and then it begins to decrease with an energy of 35 meV. At 200 K the integrated intensity is by a factor of 4 lower than at 6 K. Further increase in temperature up to 300 K results in a slow intensity decrease by 20% in comparison with 200 K.

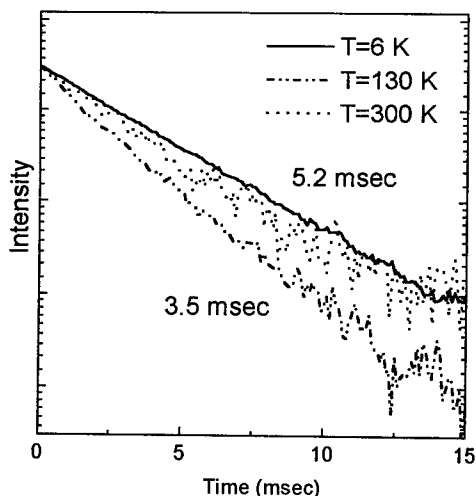


Fig.4. Time decay of the 1.54  $\mu m$  luminescence of  $Er^{3+}$  ions at different temperatures.

We have also performed the time resolved PL measurements of the 4f-4f emission. A 15 nm band pass filter for 1.54  $\mu m$  was used to select the most intense part of the emission. The results of measurements are presented in Fig.4. At 6 K the time decay curve can be described with a single exponential function. The characteristic decay time of 5.2 msec has been evaluated. We have found that the decay time changes only slightly up to 70 K and then it begins to decrease reaching its minimum of 3.5 msec at 130 K. However, beginning from 150 K the decay time begins to rise again, stabilizing at 4.3 msec at 190 K.

As a band pass filter was used we checked the temperature evolution of this part of the spectrum and we found that the intensity changes follow the character of the integrated spectrum rather than that of individual lines, *i.e.* the characteristic decay energy is about 35 meV.

### Discussion.

The close similarity of the high resolution spectra of  $Er^{3+}$  in samples implanted solely with Er and doubly implanted with Er and oxygen may suggest that oxygen is most probably involved in all Er-centres. As it was mentioned above we could not find any new transitions due to oxygen codoping even for oxygen doses as high as  $5 \cdot 10^{15} \text{ cm}^{-2}$ . On the other hand, however, the existence of very sharp lines, whose width is limited only by the resolution of the spectrometer, indicates that Er atoms are located in regular crystalline and chemical environment. Apparently, there exists a variety of centres, but their structure is the same in all 6H SiC samples implanted with Er. A careful comparison of our high resolution spectra with those presented by Yoganathan *et al.* [8] shows that in spite of different annealing condition the centres in these materials are the same.

As it was mentioned at temperatures exceeding 6 K about 20 hot lines appear in the spectra around 1.54  $\mu m$  of  $Er^{3+}$  in 6H SiC. Unfortunately, we could not establish a characteristic pattern of energy differences between the PL lines that would allow us to determine a unique energy level scheme of the excited  $^4I_{13/2}$  multiplet. Therefore, we conclude that there are several Er centres in our samples differing only slightly in their binding energies for charge carriers or excitons, which most probably participate in the excitation process of the 4f shell. Therefore, it seems to us that the characteristic

energies of 1-3 meV of excitation and de-excitation of particular PL transitions in the temperature range of 6 - 40 K are associated rather with the migration of the excitation energy from one Er center to another than with transitions from the excited sublevels in the  $^4I_{13/2}$  multiplet. On the other hand, we believe that at temperatures exceeding 50 K we observe a transition from a higher lying sublevel in the  $^4I_{13/2}$  manifold. The characteristic energy of 13 meV evaluated by us agrees reasonably well with that (14 meV) estimated by Yoganathan *et al.* [8] for the highest lying level in the  $^4I_{13/2}$  state.

The constant integrated intensity of PL that holds up to approximately 100 K indicates that the redistribution of a constant part of the excitation energy is maintained within the Er centre system, and excitation of one centre or sublevel takes place on the expense of other transition in Er centres. However, at temperatures above 100 K all the Er-related transitions decay in a similar way, with a characteristic energy of approximately 60 meV. We suggest that similarly to the situation found *i.e.* in InP:Yb [12] the quenching process proceeds via back transfer of energy to the exciton (or to charge carriers). Thus a value of 60 meV would be an approximate binding energy of excitons or of charge carriers to Er centres.

Unfortunately, the decay time measurements do not clarify a picture of relaxation process, as neither in the temperature range (80 - 130 K) at which a decrease of the time constant is observed nor its behavior at temperatures above 150 K are correlated with the behavior of the individual lines. Results of these measurements, similarly as results obtained for the integrated intensity suffer from a strong contribution of the broad background which rises with the increasing temperature. The contribution of this background exceeds the sum of contributions from all the PL lines by far pointing out to the necessity to measure the decay time for individual transitions separately.

### Conclusions.

The results of high resolution Fourier-transform photoluminescence spectroscopy presented in this work show that there is no substantial difference between the PL spectra of SiC:Er and SiC:Er+O. It suggests that all Er-centres might involve oxygen atoms. An analysis of the temperature evolution of individual lines indicates that at temperatures below 20 K some Er centres are activated as a result of the migration of the excitation energy among different Er centres. Transitions from a higher lying energy sublevel in the  $^4I_{13/2}$  multiplet, located about 13 meV above the lowest energy level are operative at temperatures above 50 K. The Er emission is quenched above 100 K with a characteristic energy of 60 meV. It seems that the quenching of the  $^4I_{13/2} - ^4I_{15/2}$  PL is due to the back transfer of the excitation energy of the 4f shell to excitons bound at Er centres. Thus an energy of 60 meV may reflect the binding energy of excitons at Er centres. It is shown that the  $Er^{3+}$  emission decays with a lifetime of 5.2 msec at 6 - 80 K, and then it decreases reaching its minimum value of 3.5 msec at 130 K. Its further temperature evolution, however, does not seem to be correlated with the intensity decrease of the individual PL transitions.

**Acknowledgements.** This work has been supported in part by the Committee for Scientific Research of Poland (grant No. PB 1027 /T11 /96 /10) and in Austria by the "Gesellschaft für Mikroelektronik". One of us (AK) thanks the support by the "Österreichischer Akademischer Austauschdienst" during 2 stays in Linz.

### References.

1. P.N. Favennec, H. L'Haridon, D. Moutonnet, M. Salvi, and M. Gauneau in "Rare Earth Doped Semiconductors II", ed. by S. Coffa, A. Polman, R.N. Schwartz, (Mater. Res. Soc. Symp. Proc. vol. 422, Pittsburgh, PA, 1996), p 181.
2. A.J. Neuhaufen and B.W. Wessels, Appl. Phys. Lett. **60**, 2657 (1992).
3. A. Kozanecki, Acta Phys. Polon. **A90**, 73 (1996).
4. J. Michel, L.C. Kimerling, J.L. Benton, D.J. Eaglesham, E.A. Fitzgerald, D.C. Jacobson, J.M. Poate, Y.H. Xie, and R.F. Ferrante, Mater. Sci. Forum, **83-87**, 653 (1992).

5. S. Coffa, F. Priolo, G. Frenzo, V. Bellani, A. Carnera and C. Spinella, *Phys. Rev.* **B48**, 11872 (1992).
6. K. Takahei and A. Taguchi, *J. Appl. Phys.* **77**, 1735 (1995).
7. W. J. Choyke, R. P. Devaty, L.L. Clemen, M. Yoganathan, G. Pensl, and Ch. Hassler, *Appl. Phys. Lett.* **66**, 562 (1995).
8. M. Yoganathan, W. Choyke, R.P. Devaty, G. Pensl, and J.A. Edmond in "Rare Earth Doped Semiconductors II", ed. by S. Coffa, A. Polman, R.N. Schwartz, (*Mater. Res. Soc. Symp. Proc.* vol. **422**, Pittsburgh, PA, 1996), p. 339.
9. A. Kozanecki, W. Jantsch, W. Heiss, G. Prechtel, B.J. Sealy, and C. Jeynes, *Acta Phys. Polon.*, to be published.
10. H. Przybylinska, W. Jantsch, Yu. Suprun-Belevitch, M. Stepikhova, L. Palmetshofer, G. Hendorfer, A. Kozanecki, R. J. Wilson, and B. J. Sealy, *Phys.Rev.* **B54**, 2532 (1996).
11. A. Kozanecki, C. Jeynes and B.J. Sealy, *Nucl. Instr. Meth. B*, to be published.
12. A. Taguchi, H. Nakagome and K. Takahei, *J. Appl. Phys.* **70**, 5604 (1991).



## ERBIUM RELATED DEFECTS IN GALLIUM ARSENIDE

A R Peaker, F Coppinger<sup>1</sup>, H Efeoglu, J H Evans-Freeman, D K Maude<sup>1</sup>  
J-C Portal<sup>1</sup>, P Rutter, K E Singer, A Scholes and A C Wright<sup>2</sup>

Centre for Electronic Materials, University of Manchester Institute of Science and  
Technology, PO Box 88, Manchester, M60 1QD, UK

<sup>1</sup> CNRS.SNCI, 25 ave Martyrs, BP 166, 38042 Grenoble Cedex 9, France

<sup>2</sup> Advanced Materials Lab, North East Wales Institute, Connah's Quay,  
Clwyd, CH5 4BR, Wales, UK

**Keywords :** erbium, silicon, gallium arsenide, defects, quantum dots, luminescence, DLTS

**Abstract:** This paper reviews our recent experimental work on erbium incorporated into gallium arsenide during MBE growth. The electrical behaviour of the erbium is considered in relation to its interaction with intentionally added dopants (silicon, selenium and beryllium) and the effect of the erbium on the deep state population is discussed. At higher concentrations the morphology of phase separation is considered and results are presented showing the controlled precipitation of erbium arsenide as quantum structures. The magnetic properties of these dots and wires are reported.

### Introduction

We have studied the behaviour of erbium in gallium arsenide and silicon over the concentration range  $10^{15} \text{ cm}^{-3}$  to  $10^{21} \text{ cm}^{-3}$ . In this paper the work on gallium arsenide is presented but comparisons are made with the silicon work which will be published in detail elsewhere. In order to interpret the behaviour of the erbium related defects and link it to previously published work, three regimes are considered. At low concentrations the behaviour is dominated by complexes formed as a result of the reaction of the erbium with impurities in the semiconductor host. At higher concentrations the behaviour is much more dependent on the interactions of erbium with the host itself and at very high concentrations precipitation, or phase separation, occurs in which the properties are dominated by the presence of erbium arsenide in the gallium arsenide host or erbium silicide in silicon.

The emission wavelength of erbium (and other rare earths) is almost independent of the host because of the strong screening due to the outer electron shells, in the case of erbium the 5s and 5p shells. However, subtle changes in the optical absorption and emission spectra are attributable to crystal field splitting from the host lattice. Information on the siting symmetry can be derived from an analysis of these splittings provided the erbium siting is limited to one or two structural locations. In other cases the complexity and broadening of the lines contribute to reduced confidence in the interpretation. In an insulating host, the luminescence efficiency can be very high but when the rare earths are incorporated into semiconductors, mechanisms come into effect which compete with the overall luminescence process, generally resulting in a reduction in the overall luminescent efficiency. This is particularly marked for semiconductors with "non-wide" bandgaps (eg, Si and GaAs) at temperatures  $>100\text{K}$ . In recent years effort has been directed towards the electrical excitation of rare earths in semiconductors and hence on understanding the electrical states of the rare earths in various semiconductors. This contrasts with the majority of earlier studies which have focused on optical excitation (which is now the basis for fibre lasers, fluorescent tube phosphors and electron beam/hot electron excitation which is used in the cathodo luminescent materials).

In the case of direct electrical excitation (and unfortunately de-excitation in the “non-wide” semiconductors) the interaction of the rare earth with the lattice is an issue of much greater importance. This is because we become concerned with carrier capture mechanisms associated with the ion and hence with the electronic states within the bandgap associated with the rare earth. Although various publications contain self-consistent results, it is not possible to generalise in a way which embraces the majority of the literature on the subject. A truly major problem is that measurements which give us more direct structural information (Rutherford Backscattering, Spin Resonance Techniques, etc) have by necessity been conducted with rather high concentrations whereas techniques which give us direct electrical information (eg, DLTS) have, again by necessity, been conducted with rather low concentrations. In this paper we present measurements which have been conducted over a considerable range of concentrations. These results are interpreted by considering three regimes of concentration as indicated below.

1. Very dilute systems. Here the electrical (and to some extent the optical) properties of the erbium are dependent on the impurities in the semiconductor host. The detailed behaviour is due to the chemical affinity of the erbium for the relatively mobile impurities present and the complexes that are formed. In the case of float zone or epitaxial silicon for this regime to be operative the erbium concentration must be less than  $10^{16} \text{ cm}^{-3}$  but is much higher in GaAs. Intentionally added impurities (eg, shallow dopants in III-Vs or oxygen in silicon) may be involved in such complexing.
2. “Native” regime. Here the role of complexes is less significant and the behaviour is defined principally by the interaction of erbium with the host semiconductor and intrinsic defects. In general the crystal field split luminescence bands indicate high symmetry and the electrical properties are more reproducible. This regime is easily identifiable in silicon but is difficult to achieve in III-Vs.
3. Precipitated or phase separated systems. This regime occurs at high erbium concentrations, ie,  $[\text{Er}] \geq 10^{18} \text{ cm}^{-3}$  in near equilibrium growth but at much higher concentrations ( $\geq 5 \times 10^{19} \text{ cm}^{-3}$ ) in grossly non-equilibrium systems (eg, ion implanted with controlled solid phase re-growth). We have used this regime in GaAs MBE to produce three dimensional arrays of self-organised quantum dots (10-20 Å diameter) and quantum wires.

### **Erbium**

Erbium is quite a large atom and does not fit well into either the silicon or gallium arsenide lattices. It is a very reactive element and there is a strong driving force to produce the  $3^+$  ion [1]. In consequence, it is not particularly mobile in the host lattice. Diffusivity and solubility are low [2], resulting in accumulation at growth interfaces, notably during solid phase re-growth in amorphised silicon [3] and during molecular beam epitaxy of both silicon, silicon-germanium [4] and gallium arsenide [5]. Its chemical and physical properties make it tedious to purify by conventional techniques and so it is not unusual for rather impure erbium to be used as a dopant source. In ion implanted material this is irrelevant due to the mass separation inherent in the implantation process but in solid source MBE growth the layers are often contaminated with unwanted impurities originating from the erbium (eg, copper). This has been a source of much confusion in some early DLTS measurements.

### Electrical Behaviour of Erbium in Dilute Gallium Arsenide Solution

When a source of erbium is turned on during the MBE growth of doped gallium arsenide, a reduction in the carrier concentration of the grown layer occurs. In this work, this has been observed for the dopants silicon, selenium (n-type) and beryllium (p-type). Figure 1 provides a summary of the "carrier loss" as a function of erbium concentration.

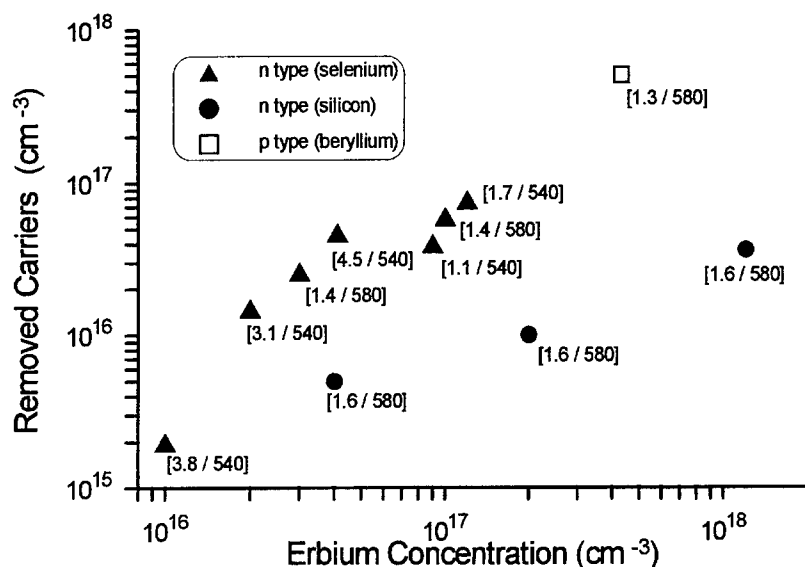


Figure 1. The reduction in carrier concentrations observed in MBE GaAs (using the shallow dopants indicated) when erbium is incorporated during growth. The figures in brackets adjacent to each point show the V/III ratio and the substrate temperature during growth.

The erbium concentration was measured by SIMS using reliable concentration standards. The error on individual measurements is  $\pm 20\%$ . The carrier loss is measured by CV techniques and is a quite precise measure ( $\pm 5\%$ ) in most cases. It is apparent that there is a general trend of increasing erbium concentration causing increasing carrier loss, but it is also apparent that the carrier loss is species dependant being lower for silicon than for the other dopants. It is interesting to note that when erbium is added to undoped material ( $\sim 10^{14} \text{ cm}^{-3}$  p-type background) there is a small increase in hole concentration.

The samples shown in Figure 1 were not all produced under identical growth conditions, the V/III ratio and growth temperature being marked adjacent to each data point. Although these parameters affect other aspects of the sample characterisation, the effect in relation to carrier loss is small compared to those resulting from changes in the erbium concentration.

In some of the samples SIMS measurements of the selenium have been conducted to determine the concentration of the intentionally added shallow donors. This was done to check on the possibility that the decrease in carrier concentration in the presence of erbium was associated with the incorporation mechanism during MBE growth. Although these measurements are not very precise, all the evidence we have indicates that the expected chemical concentration was incorporated into the lattice irrespective of whether the erbium is present or not. Consequently, in general terms, there are two mechanisms which could

account for the removal of carriers. One is that the erbium produces compensating centres. As compensation is observed for both n- and p-type dopants, these centres would have to be deep, and both donor-like and acceptor-like species would have to be present. Such behaviour is, of course, well known in gallium arsenide in relation to intrinsic defects used to grow semi-insulating material. The other possibility is that the erbium complexes with the shallow donor or acceptor producing an electrically inactive complex or states sufficiently deep to remain un-ionised at room temperature. Inspection of Figure 1 indicates that chemical complexing is more likely. It is quite evident that in the case of silicon doped material, far fewer carriers are removed. This is best explained in relation to the lower chemical affinity between the erbium and the silicon as compared to the selenium or beryllium cases. The differences cannot be explained on the basis of siting. Although the silicon donor occupies the gallium site while the selenium donor occupies the arsenic site, the beryllium acceptor (which shows almost identically removed carrier behaviour to the selenium), occupies the gallium site. Simplistic arguments in relation to competition for sites would also suggest that as the  $\text{Er}^{3+}$  is more likely to occupy a gallium site, the effects in relation to the silicon should be more pronounced ..... exactly the opposite to the effect which is observed.

Further evidence for the chemical complexing hypothesis is provided by a study of the crystal field split luminescence. Unfortunately the analysis of the erbium luminescence in our gallium arsenide is not as elegant as that which is possible for silicon. Even in the case of a moderate erbium concentration in undoped gallium arsenide, we do not see crystal field splitting which can be interpreted in terms of a unique siting of the erbium. This is consistent with most previous work on MBE, MOCVD and annealed LPE material, but a few groups have reported simple spectra indicative of a unique siting of erbium in material grown at low temperatures [6]. As we add dopants to the lattice, the crystal field splitting becomes more complex (indicating multiple siteings rather than a lowering of the symmetry of a single site) and the spectral lines broaden. This can only be interpreted as changes in the local environment of the erbium and although other possibilities exist, the most likely explanation is complexing of the shallow dopant with the erbium.

We are left with two key questions: are the erbium complexes electrically active in the sense that they introduce states into the bandgap and is the erbium ion itself still in the optically active  $3^+$  state? We have addressed both these issues and have preliminary results on the  $\text{Er}^{3+}$  concentration and detailed results on the deep state population.

We have attempted to measure the  $\text{Er}^{3+}$  concentration by observing the quasi-saturation of the luminescence under increasing excitation density. This technique has been used to determine the concentration of the ZnO iso-valent complex which is the well known red luminescence centre in gallium phosphide [7]. The luminescence efficiency is measured as a function of excitation density. The efficiency shows a peak at the point when the centres taking part in the radiative recombination process are following an excitation and emission cycle at the maximum rate possible. If the decay rate of the radiative emission and the excitation time of the centre are known along with the absolute value of the radiative power emitted within the crystal, the number of radiative centres can be calculated. The determination of the absolute value of the internal emission power is essential for the calculation and is difficult to measure precisely.

So far only four samples have been measured using this technique and all are selenium doped. The measurements were done at 20K to try to avoid the complications of any back-transfer processes. For the case of the sample shown in the bottom left of Figure 1, most of the erbium is optically active. Our calculation for the number of  $\text{Er}^{3+}$  centres is  $6 \times 10^{15} \text{ cm}^{-3}$  ( $[\text{Er}] = 10^{16} \text{ cm}^{-3}$ ). For the samples with higher erbium concentration but associated with substantial carrier removal, a concentration of  $\text{Er}^{3+}$  centres active in the radiative recombination process does not appear to increase significantly above  $10^{16} \text{ cm}^{-3}$ . There are, however, two complications which make this simplistic interpretation at best preliminary. Firstly it is an unfortunate coincidence that the low doped erbium sample had a much higher V/III ratio than the others measured. Although the V/III ratio does not appear to be significant in the carrier removal rate (Figure 1), it may well effect the luminescence properties. We hope to report on a more detailed study of the  $\text{Er}^{3+}$  concentration in both gallium arsenide and silicon in the near future.

#### Deep States in Erbium-doped Gallium Arsenide

There is a very substantial literature on deep states in gallium arsenide [8] and although very little of this is associated with rare earths, it is evident that there are many states associated with intrinsic defects. It is known that the introduction of erbium into gallium arsenide causes some lattice dilation [9] and irrespective of any other effects this would be expected to change the native defect population. DLTS measurements have been carried out previously on erbium doped gallium arsenide by researchers at Wright-Patterson on both MBE [10] and ion-implanted [11] material. A hole trap located at 35 meV above the valence band was found in MBE material doped with low erbium concentrations ( $5 \times 10^{16} \text{ cm}^{-3}$ ) and attributed to an iso-valent level resulting from erbium on the gallium site. In addition, a hole trap located at 360 meV above the valence band was observed to be present in optically active MBE material and also in ion implanted samples that had high erbium concentrations ( $\text{Er} > 10^{17} \text{ cm}^{-3}$ ). This level was attributed to interstitial erbium that has formed an optically active complex.

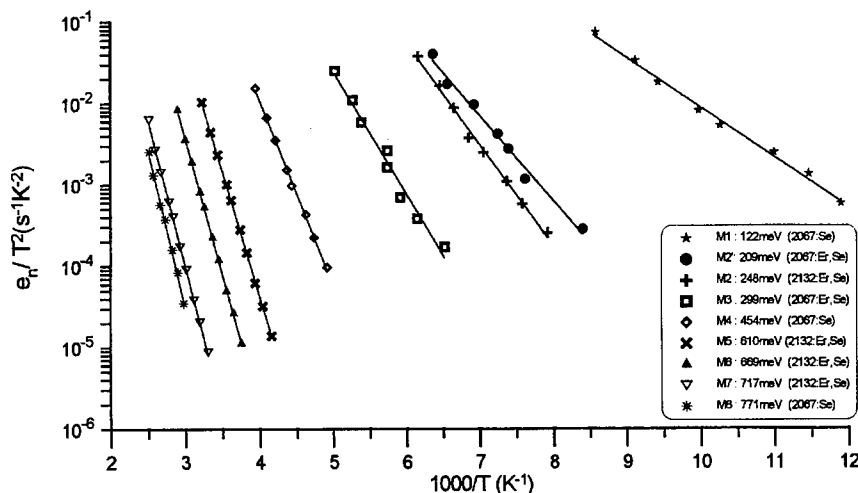


Figure 2. Arrhenius plot of the nine deep states observed in the upper half of the bandgap of n-type GaAs:Er. Of these states, M1, M2', M2, M3, M4, M5 and M7 are observed to scale linearly with the erbium concentration.

In our work we have used both admittance spectroscopy and DLTS techniques to study the deep level population. We have not been able to confirm the presence of the hole trap at 35 meV but do see a state at 350 meV above the valence band which could be the same as that observed in the previously referenced work. It is, however, important to note that the concentration of this state is four orders of magnitude lower than the erbium concentration.

Looking at the upper half of the bandgap, higher concentrations of deep states are observed. Seven of these deep states scale almost linearly with erbium concentration in the range,  $6 \times 10^{16} \text{ cm}^{-3} < [\text{Er}] < 10^{18} \text{ cm}^{-3}$ . However, over this range the maximum deep state concentration is approximately three orders less than the erbium concentration.

A close examination of the data related to Figure 2 reveals that these states have almost identical properties to the M-levels first observed by Lang [12] and later characterised by Blood et al [13]. We have conducted detailed measurements, not only of the emission characteristics, but also of the directly measured majority and minority carrier cross sections whenever this has been possible. We have also changed the V/III ratio and observed the concentration changes of these defects expected from the reports in the previous references. As there was no possibility of any erbium being incorporated into the MBE layers studied in the Lang or Blood work, one can only assume that none of these states is directly associated with the erbium despite the strong concentration dependence. Our conclusion is that the formation of the M-states results from intrinsic defect reactions driven primarily by strain associated with the erbium.

If we sum all the concentrations of deep states observed in any one sample and compare it with the number of carriers removed, there is no case in which the deep state concentration is more than a third of the observed “compensation”. As we have examined both halves of the bandgap and also used admittance spectroscopy to probe the near band regions (which are difficult to see in conventional DLTS), we can state categorically that the carrier removal process associated with erbium in gallium arsenide is not due to a simple compensation mechanism. In combination with the evidence presented previously in this paper, it seems that the dominant carrier removal method is complexing between the erbium and the shallow donors or acceptors. Equally significantly there are no shallow or deep states present in the sort of concentrations in which the erbium donor or erbium acceptor complexes must exist and therefore it must be also assumed that these complexes are electrically inactive.

### **The High Concentration Regime**

The apparent solid solubility of erbium in gallium arsenide at 580°C in  $7 \times 10^{17} \text{ cm}^{-3}$  [5]. This is measured in MBE growth conditions. There is evidence that the “true” or equilibrium solid solubility is much less than this. Above an erbium concentration of  $10^{18} \text{ cm}^{-3}$ , a phase of erbium arsenide separates. The separated phase, which has a rock salt structure, incorporates in a fashion which is coherent with the host lattice. There is a 1.6% mismatch between the lattices in the  $\langle 100 \rangle$  direction but a marked difference in the relaxed Ga-As and Er-As bond lengths (0.24nm and 0.28nm respectively) therefore the Er and Ga atoms are located along the  $\langle 100 \rangle$  atomic rows in positions accommodating the strain. The form of the precipitates can be varied controllably by adjusting the growth conditions, most importantly the growth temperature and V/III ratios. The dominant mechanism determining the morphology is the transport of the relevant species along the growth interface. Figure 3 shows a case where the growth conditions have been adjusted so that the dominant

morphology is spherical precipitates of ErAs. The size of the precipitates can be varied by changing the temperature of the substrate during growth. Figure 4 shows the relationship between growth temperature and the diameter of the precipitated sphere. The morphology of these defects is not restricted to a spherical form. By manipulating the V-III ratio during growth it is possible to move the energetic balance at the growth interface into a situation where the growth of columns perpendicular to the growth interface is favoured, so producing quantum wires.



Figure 3. Erbium arsenide precipitates shown in dark field TEM using the  $\{002\}$  reflection.

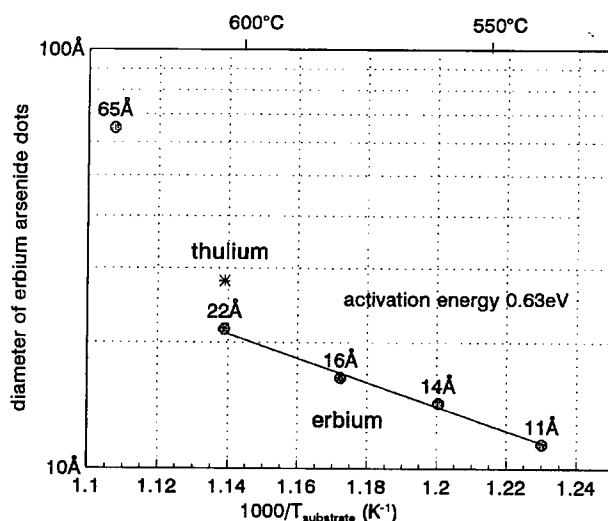


Figure 4. The size of the spherical precipitates of erbium arsenides in a gallium arsenide matrix as a function of substrate temperature during MBE growth. Measurements of precipitate size were made using a two beam dark field TEM technique which used the  $\{002\}$  and  $\{004\}$  beams.

Bulk erbium arsenide is a semi-metal and, as in the case of silicon, the formation of such precipitates reduces the minority carrier lifetime in the gallium arsenide into the pico second region and kills any luminescence. Our original objective in studying these systems was to

create self organised quantum dots. Calculations indicated that the confinement of the erbium arsenide dot in the gallium arsenide lattice would separate the bands of the semi-metal so creating a narrow gap semiconductor. Indications so far are that this does not happen but it has been found that the erbium dots have interesting magnetic properties.

Recently [14], we have used the mesoscopic electrical properties of self organised ErAs precipitates in a GaAs matrix as described above to observe macroscopic quantum tunnelling (MQT). A statistical analysis of Two Level Fluctuations (TLF) appearing in the resistance through the GaAs/ErAs layer (vertical transport) was used to measure the small magnetisation of the isolated anti-ferromagnetic ErAs clusters, which in the cases studied containing ~1000 atoms. The TLF in the resistance arises because of the coherent nature of the transport through the device. The resistance of the sample is sensitive to the scattering from a single cluster, which depends on the orientation of the magnetic moment of the cluster. If the orientation of the cluster is continuously switching between two possible orientations then this leads to a TLF in the resistance. Using this technique it is possible to measure extremely small magnetic moments, ie, of the order of ten electronic spins. At low temperature a saturation of the switching rate was observed and attributed to MQT. A report of a detailed study of these observations will be submitted for publication elsewhere [15].

#### References

- [1] Ch Delerue, M Lannoo, *Phys Rev Lett*, vol.67, p.3006 (1991)
- [2] Z Xinwei, K Hirakawa and T Ikoma, *Appl Phys Lett*, vol.54, p.712 (1989)
- [3] D J Eaglesham, J Michel, E A Fitzgerald, D C Jacobson, J M Poate, J L Bouton, A Polman, Y-H Xie and L C Kimmerling, *Appl Phys Lett*, vol.58, p.2797 (1991)
- [4] H Efeoglu, J H Evans, T E Jackman, B Hamilton, D C Houghton, J M Langer, A R Peaker, D D Perovic, I Poole, H Ravel, P Hemment and C W Chan, *Semicond Sci Technol*, vol.8, p.236 (1993)
- [5] I Poole, K E Singer, A R Peaker and A C Wright, *J Crystal Growth*, vol.121, p.121 (1992)
- [6] H Ennen, J Wagner, H Muller and R S Smith, *J Appl Phys*, vol.61, p.4877 (1987)
- [7] A R Peaker, S Fisk and A Mottram, *Electronics Letts*, vol.5, p.186, (1969)
- [8] A R Peaker, "Deep Defects States", in *Properties of GaAs 3rd Edition*, IEE, INSPEC, London, (1996)
- [9] I Poole, H Efeoglu, K E Singer and A R Peaker, *J Crystal Growth*, vol.127, p.703 (1993)
- [10] D W Elsaesser, J E Colon, Y K Yeo, R L Hengehold, K R Evans and J S Soloman, *J Crystal Growth*, vol.127, p.707 (1993)
- [11] J E Colon, D W Elsaesser, Y K Yeo, R L Hengehold and G S Pomrenke, *Mats Sci Forum*, vol.83-87, p.6271 (1992)
- [12] D V Lang, A Y Cho, A C Gossard, M Ilegems and W Wigmann, *J Appl Phys*, vol.47, p.2558 (1976)
- [13] P Blood and J J Harris, *J Appl Phys*, vol.50, p.993 (1984)
- [14] F Coppinger, J Genoe, D K Maude, Ulf Gennser, J C Portal, K E Singer, P Rutter, T Taskin, A R Peaker and A C Wright, *Phys Rev Lett*, vol.75, p.3513 (1995)
- [15] F Coppinger, J Genoe, D K Maude, X. Kleber, L.B. Rigal, Ulf Gennser, J C Portal, K E Singer, P Rutter, T Taskin, A R Peaker and A C Wright, 'Magnetic Characterization of Self Organised ErAs Clusters Using Telegraph Noise Spectroscopy' submitted to *Phys Rev B*



## ELECTRON SPIN RESONANCE OF Er-Oxygen COMPLEXES IN GaAs

T. Ishiyama, E. Katayama, K. Takahei<sup>1, 2</sup>, A. Taguchi<sup>1</sup> and K. Murakami

Institute of Materials Science, University of Tsukuba

1-1-1 Tennoudai, Tsukuba, Ibaraki 305, Japan

<sup>1</sup>NTT Basic Research Laboratories

3-1 Morinosato-Wakamiya, Atsugi, Kanagawa 243-01, Japan

**Keywords :** erbium, GaAs, oxygen, ESR, anisotropic g-tensor

**Abstract.** We have performed electron spin resonance (ESR) measurements on Er-doped GaAs grown with oxygen codoping by metalorganic chemical vapor deposition. Only an isotropic ESR signal with an effective g-value,  $g = 5.95$ , which had been already reported, was observed in Er-doped GaAs without oxygen codoping. In the Er-doped GaAs with oxygen codoping, anisotropic ESR signals originated from four kinds of Er-O centers were newly observed in addition to the isotropic signal. Anisotropic g-tensors were obtained by analyzing the angular dependence of ESR signals for three Er-O centers. One of them exhibits monoclinic  $C_{1h}$  symmetry and the others exhibit orthorhombic  $C_{2v}$  symmetry.

### I. Introduction

Semiconductors doped with rare-earth impurities exhibit sharp and temperature-stable luminescence. Therefore, these have been widely studied because of their possible applications to new optical devices. Er-doped semiconductors such as GaAs and Si have attracted particular attention, because the wavelength of the luminescence due to the  $^4I_{13/2} \rightarrow ^4I_{15/2}$  intra-4f-shell transition of  $Er^{3+}$  ions is in the  $1.5 \mu m$  region being the minimum in the absorption of silica-based optical fibers. It was recently shown that Er-doped GaAs grown with oxygen codoping by metalorganic chemical vapor deposition (MOCVD) exhibits sharp and simple photoluminescence (PL) lines from one kind of Er center, when the GaAs host is photoexcited by a photon energy exceeding the bandgap of GaAs [1]. The analysis by PL and photoluminescence excitation (PLE) spectroscopy revealed that there are many kinds of Er centers having different atomic configurations in Er-doped GaAs grown with oxygen codoping by MOCVD, although its host-excited PL spectrum is dominated by the luminescence of one kind of Er center [2, 3]. Knowledge of the atomic configurations of rare-earth impurities in host semiconductors is very important for fabricating efficient injection-type light emitting devices, but it has not been clarified. The electron spin resonance (ESR) is a good technique of understanding the atomic configurations of impurities in semiconductors. An isotropic ESR signal with an effective g-value of about 6 has been observed in GaAs implanted with Er [4] and in melt-grown GaAs crystals doped with Er [5]. This ESR signal is originated from  $Er^{3+}$  center under cubic symmetry. ESR signals originated from  $Er^{3+}$  center under monoclinic symmetry were recently observed in Si implanted with Er and oxygen [6].

In this study, ESR measurements were performed on Er-doped GaAs grown with oxygen codoping by MOCVD. An ESR signal with the effective g-value,  $g = 5.95$ , originated from  $Er^{3+}$  center under cubic symmetry was observed in both Er-doped GaAs without oxygen codoping and with oxygen codoping. In addition to this ESR signal, anisotropic ESR signals originated from

<sup>2</sup> Present address: Anritsu Corp., 1800 Onna, Atsugi, Kanagawa 243, Japan

four kinds of Er-O complexes were newly observed in Er-doped GaAs with oxygen codoping. Details of these complexes are described.

## II. Experimental Procedures

The samples used in this study were grown at 500°C on (100)-oriented undoped GaAs substrates by MOCVD. Sources were tri-ethyl gallium (TEG), arsine and tris-iso-propyl-cyclopentadienyl-Er. The thickness of the grown epitaxial layers were in the range of 2 to 3  $\mu\text{m}$ . Doping concentration profiles of Er and oxygen were measured by secondary-ion mass spectrometry (SIMS). Er concentrations were almost constant in each sample and the concentration ranged from  $1.8 \times 10^{17}$  to  $6.0 \times 10^{18}/\text{cm}^3$  among the samples used here. Oxygen concentrations of the samples with oxygen codoping were two or three times higher than the Er concentrations. Oxygen is unintentionally incorporated into the epitaxial layer without oxygen codoping at a level of  $2.5 \times 10^{17}/\text{cm}^3$ , and the oxygen concentration was much lower than those of the samples with oxygen codoping. ESR measurements were performed at 4.2 K with an X-band (9.05 GHz) spectrometer. The relative ESR intensity was obtained by using an ESR signal of  $\text{Mn}^{2+}$  in MgO measured simultaneously. The magnetic field was swept from 500 to 13500 G. The effective g-value obtained in this range of the magnetic field corresponds to 0.5 to 16.

## III. Experimental Results and Discussion

Isotropic ESR spectra of an  $\text{Er}^{3+}$  center of cubic symmetry are shown in Figure 1(a) and 1(b) for the samples with oxygen codoping ( $[\text{Er}] = 2.5 \times 10^{17}/\text{cm}^3$ ,  $[\text{O}] = 7.0 \times 10^{17}/\text{cm}^3$ ) and without oxygen codoping ( $[\text{Er}] = 2.5 \times 10^{17}/\text{cm}^3$ ,  $[\text{O}] = 2.5 \times 10^{17}/\text{cm}^3$ ) respectively. The effective g-value of these signals are  $g = 5.95$ . This g-value is comparable to previously reported values of 5.947 for GaAs implanted with Er [4] and 5.921 for melt-grown GaAs crystals doped with Er [5]. The relative ESR intensity in the sample with oxygen codoping decreases to a third of that in the sample without oxygen codoping.

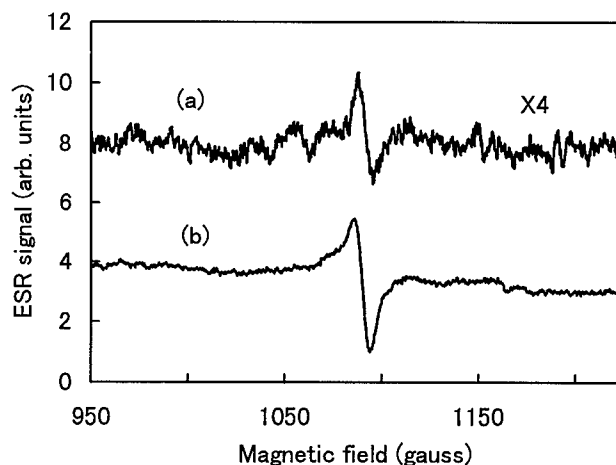


Fig. 1. The ESR signals of  $\text{Er}^{3+}$  center of cubic symmetry for the samples with oxygen codoping (a) and without oxygen codoping (b) at 4K. Microwave power was 0.8 mW.

In addition to this signal, stronger ESR signals were observed only in the samples with oxygen codoping, as shown in Fig. 2. They can be classified into three centers (A, B and C). They

originate from  $\text{Er}^{3+}$  in Er-O complexes. The hyperfine lines of the B center due to  $^{167}\text{Er}$  ( $I = 7/2$ , natural abundance 22.8%) are also shown in Fig. 3. As well as the B center, the A and C centers also showed the hyperfine structures. The relative ESR intensities of A, B and C are about two orders of magnitude higher than that of the signal with  $g = 5.95$ .

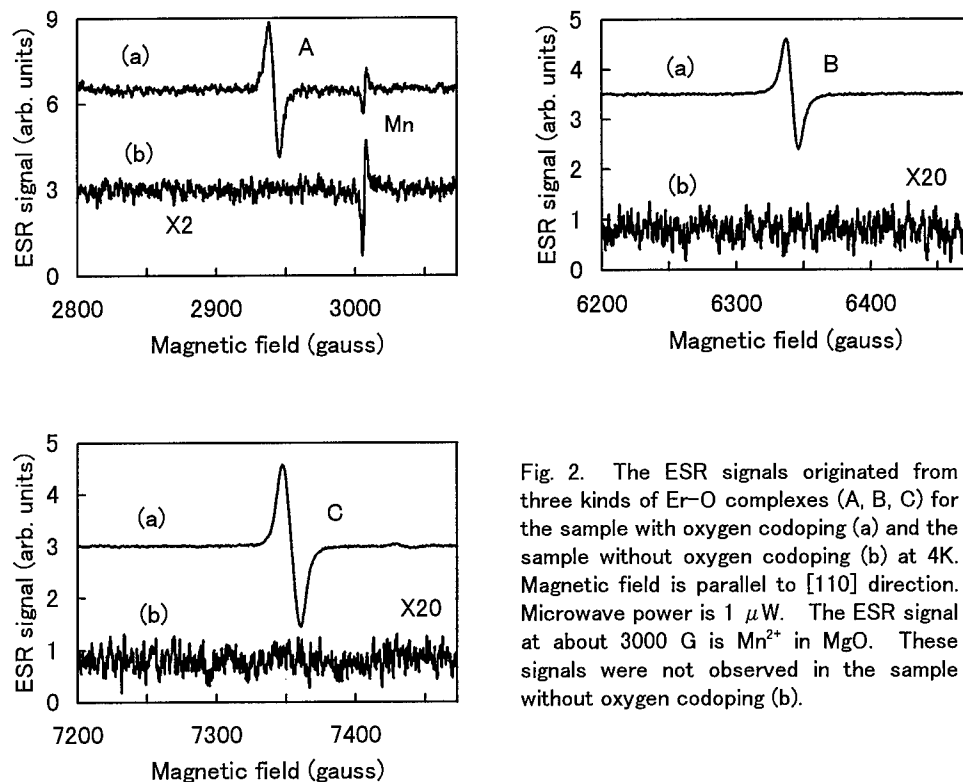


Fig. 2. The ESR signals originated from three kinds of Er-O complexes (A, B, C) for the sample with oxygen codoping (a) and the sample without oxygen codoping (b) at 4K. Magnetic field is parallel to  $[110]$  direction. Microwave power is  $1 \mu\text{W}$ . The ESR signal at about 3000 G is  $\text{Mn}^{2+}$  in  $\text{MgO}$ . These signals were not observed in the sample without oxygen codoping (b).

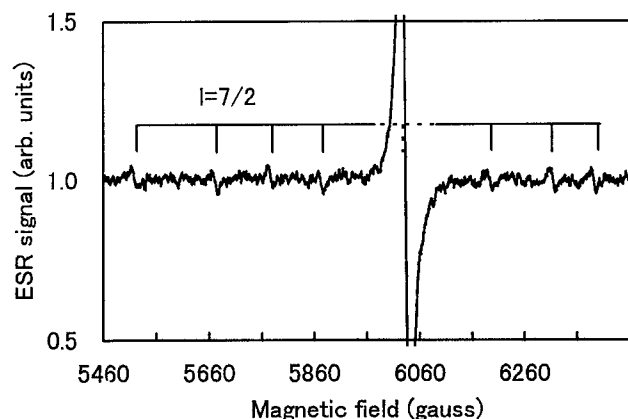


Fig. 3. The hyperfine lines for the B center due to  $^{167}\text{Er}$  ( $I = 7/2$ ) at 4K. The magnetic field is approximately parallel to  $[001]$  (grown direction). The Er and oxygen concentrations in the sample are  $[\text{Er}] = 1.4 \times 10^{18}/\text{cm}^3$  and  $[\text{O}] = 4.5 \times 10^{18}/\text{cm}^3$ .

These ESR signals indicate the angular dependence between the crystal direction and magnetic field. This angular dependence is shown in Fig. 4, with calculated curves. The simulation was

performed by using the effective spin Hamiltonian with effective spin  $S = 1/2$ , as Equation (1).

$$H = \mu_B \mathbf{B} \cdot \mathbf{g} \cdot \mathbf{S} \quad (1)$$

The principal  $g$  values ( $g_A$ ,  $g_B$  and  $g_C$ ) for the A, B, and C centers are  $g_{A1} = 0$ ,  $g_{A2} = 1.84$ ,  $g_{A3} = 2.85$  and  $g_{B1} = 0$ ,  $g_{B2} = 1.08$ ,  $g_{B3} = 1.25$  and  $g_{C1} = 0$ ,  $g_{C2} = 0.97$ ,  $g_{C3} = 1.12$ . The 1-axis is along a  $\langle 110 \rangle$  direction and both the 2- and 3-axis lie in the plane perpendicular to the 1-axis. The 2-axis is along a  $\langle 100 \rangle$  direction and the 3-axis is along a  $\langle 110 \rangle$  direction. But, the  $g_{A2}$ -axis is tilted by an angle  $\theta$  of  $30^\circ$  from a  $\langle 100 \rangle$  direction to nearest  $\langle 111 \rangle$  direction in the plane perpendicular to the 1-axis. Consequently, the  $g$ -tensor of the A center exhibits monoclinic symmetry  $C_{1h}$  and those of B and C centers exhibit orthorhombic  $C_{2v}$  symmetry. These anisotropic  $g$ -tensors suggest that oxygen atoms adjacent to  $\text{Er}^{3+}$  influence the crystal field around Er.

These Er-O complexes (A, B and C) have twelve equivalent atomic configurations for Er under  $C_{1h}$  symmetry (A center) and six equivalent atomic configurations for Er under  $C_{2v}$  symmetry (B and C centers), respectively. In general, when the magnetic field is rotated in the  $(110)$  plane, ESR lines corresponding to these configurations reduce to seven for the A center and four for B and C centers. However, the ESR spectra observed for each Er center (A, B and C) showed only two lines as shown in Fig. 4; i. e., the lines for the atomic configurations with the 2-axis along  $[001]$  direction being the growth direction were not observed. These experimental results show that the atomic configurations with the 2-axis along the growth direction is produced much less than those with the 2-axis along  $[100]$  and  $[010]$  directions perpendicular to the growth direction. This suggests that the preferential alignment of Er-O complexes occurs during the MOCVD.

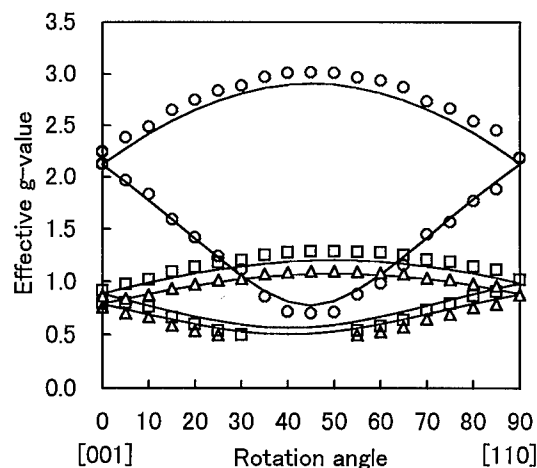


Fig. 4. The angular dependence of the ESR signals for centers A ( $\circ$ ), B ( $\square$ ) and C ( $\triangle$ ). As simulation, the calculated curves (—) are also shown. The magnetic field is rotated in the  $(110)$  plane from  $[001]$  (growth direction) to  $[110]$ .

It was reported that there are many kinds of Er centers having different atomic configurations in Er-doped GaAs grown with oxygen codoping by MOCVD, while the Er center exhibiting luminescence under host photo-excitation (which we denote as a luminescent Er-2O center) is thought to correspond to Er at the Ga sublattice with two adjacent oxygen atoms and of  $C_{2v}$  symmetry [2, 3, 8]. Recently, the extended X-ray absorption fine structure (EXAFS) measurement on Er-doped GaAs grown with oxygen codoping by MOCVD indicated that an Er atom at the Ga sublattice is coordinated with two As atoms and two oxygen atoms, but no clear signals for the second-nearest-neighbor sites were observed [9]. These reports suggest that most of Er centers are coordinated with two As atoms and two oxygen atoms, but they have various configurations of

the second-nearest-neighbors in Er-doped GaAs with oxygen codoping. It is expected that those Er centers are of orthorhombic  $C_{2v}$  symmetry or a symmetry close to it. This is consistent with the B and C centers of  $C_{2v}$  symmetry. It is probable that the A center of  $C_{1h}$  symmetry originates from Er having a different nearest neighbor-atomic configuration.

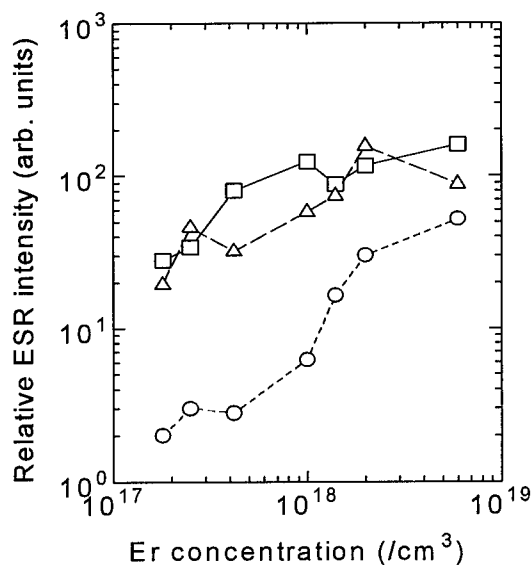


Fig. 5. The Er concentration dependence of the relative ESR intensities for A (○), B (□) and C (△) at 4K. Microwave power is  $1 \mu\text{W}$ .

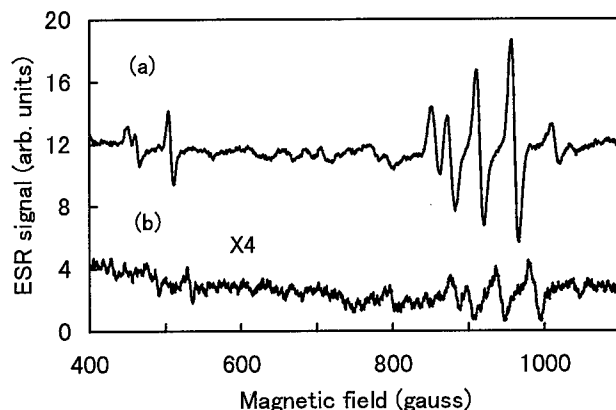


Fig. 6. The ESR signals of a center different from A, B and C centers in the samples with oxygen codoping at 4K. Magnetic field is parallel to  $[110]$  direction. Microwave power is  $0.8\text{mW}$ . The Er and oxygen concentrations are  $[\text{Er}] = 1.4 \times 10^{18}/\text{cm}^3$ ,  $[\text{O}] = 4.5 \times 10^{18}/\text{cm}^3$  for (a) and  $[\text{Er}] = 2.5 \times 10^{17}/\text{cm}^3$ ,  $[\text{O}] = 7.0 \times 10^{17}/\text{cm}^3$  for (b).

The Er concentration dependence of the relative ESR intensities of A, B and C centers are

shown in Fig. 5. The intensity of the A center increases with Er concentration, while those of B and C centers are saturated above  $[\text{Er}] \sim 10^{18}/\text{cm}^3$ . The PL and PLE measurements indicated that the increment of PL intensity of the luminescent Er-2O center is small, as compared with that of Er concentration and other Er centers, which do not exhibit luminescence under host photo-excitation, increase with increasing Er concentration in the same region of Er concentration as in Fig. 5 [2]. The former tendency is consistent with the Er concentration dependence of the relative ESR intensities for B and C centers and the latter is consistent with that for the A center. Only the relative ESR intensity of the B center decreased under the illumination with 632-nm laser and the decrement was approximately 30 percent, while A and C centers showed no changes in the intensity. This suggests that Er 4f-shell of the B center is excited under host photo-excitation. The PL spectrum from one kind of Er center under host photo-excitation was also observed in Er-doped GaAs grown by molecular-beam epitaxy (MBE) [10]. This Er center was different from the luminescent Er-2O center in the sample grown with oxygen codoping by MOCVD and the PL intensity of this center was very weak compared to the luminescent Er-2O center [1]. As in this report, there are a few kinds of Er centers exhibiting luminescence under host photo-excitation in the sample with oxygen codoping. From the experimental results (anisotropic g-tensor, the Er concentration dependence of the relative ESR intensity and the change in the intensity under the illumination), it is likely that the B center is one of the luminescent centers.

ESR signals of a center different from A, B and C centers were also observed in lower magnetic fields for the samples with oxygen codoping, as shown in Fig. 6. These were definitely observed above  $[\text{Er}] \geq 10^{18}/\text{cm}^3$ . The ESR intensity of these signals increases with Er concentration, and the intensity is one order of magnitude lower than the intensities of A, B and C centers. The magnetic field at which these signals are observed is in the same region at which the ESR signals were observed in Si implanted with Er and oxygen [6].

#### IV. Conclusions

The ESR measurements were performed for Er doped GaAs grown with oxygen codoping by MOCVD. The ESR signal for Er of cubic symmetry was observed in the samples with oxygen codoping and without oxygen codoping. In addition to this signal, the ESR signals originating from four kinds of Er centers adjacent to oxygen atoms were observed only in the samples with oxygen codoping. One of these centers is of monoclinic  $C_{1h}$  symmetry and two of these are of orthorhombic  $C_{2v}$  symmetry. This is consistent with the atomic configuration (Er atom are adjacent to two oxygen atoms) which had been already reported. The relative ESR intensities of these three Er centers were two orders of magnitude higher than that with  $g = 5.95$ . The fourth center was clearly observed above  $[\text{Er}] \geq 10^{18}/\text{cm}^3$  and the intensity was one order of magnitude lower than the other three Er centers.

#### References

- [1] K. Takahei and A. Taguchi, *J. Appl. Phys.* **74**, 1979 (1993).
- [2] K. Takahei and A. Taguchi, *J. Appl. Phys.* **77**, 1735 (1995).
- [3] K. Takahei and A. Taguchi, *J. Appl. Phys.* **78**, 5614 (1995).
- [4] P. B. Klein, F. G. Moor and H. B. Dietrich, *Appl. Phys. Lett.* **58**, 502 (1991).
- [5] M. Baeumler, J. Schneider, F. Kohl and E. Tomzing, *J. Phys. C: Solid State Phys.* **20**, L963 (1987).
- [6] J. D. Carey, J. F. Donegan, R. C. Barklie, F. Priolo, G. Franzo and S. Coffa, *Appl. Phys. Lett.* **69**, 3845 (1996).
- [7] A. Abragam and B. Bleaney, *Electron Paramagnetic Resonance of Transition Ions* (Clarendon, Oxford, 1970).
- [8] K. Takahei, A. Taguchi, Y. Horikoshi and J. Nakata, *J. Appl. Phys.* **76**, 4332 (1994).
- [9] H. Ofuchi, T. Kubo, M. Matsumoto, M. Tabuchi, Y. Takeda and K. Takahei, *Extended Abstracts (44<sup>th</sup> Spring Meeting, 1997), Jap. Soc. Appl. Phys. and Related Societies*, **28p-V-12**, in Japanese.
- [10] H. Ennen, J. Wagner, H. D. Muller and R. S. Smith, *J. Appl. Phys.* **61**, 4877 (1987).

## Er CENTERS IN GaAs STUDIED BY OPTICAL SPECTROSCOPY UNDER HYDROSTATIC PRESSURE

R.A. Hogg<sup>†</sup>, A. Taguchi, K. Takahei,  
 NTT Basic Research Laboratories, 3-1 Morinosato Wakamiya,  
 Atsugi-shi, Kanagawa, 243-01, Japan.

<sup>†</sup> present address: University of Tokyo, Institute for Industrial Science,  
 7-22-1 Roppongi, Minato-ku, Tokyo, 106, Japan.

**Keywords :** GaAs, Er, O, photoluminescence, hydrostatic pressure, impurity level.

**Abstract.** A study of Er related luminescence in GaAs:Er,O as a function of temperature and hydrostatic pressure is reported. At elevated pressure, new Er related luminescence is observed, and its appearance is well explained by the entry of Er-related trap levels into the band-gap. The impurity levels within the band-gap formed by different types of Er centers indicates that it is the constituents of the Er complex which determine its electrical character and its resulting optical efficiency.

### Introduction.

The host-excited photoluminescence (HEPL) spectra of MOCVD grown GaAs co-doped with Er and O is dominated by sharp transition lines in the 1.5 $\mu$ m spectral region [1,2]. Transitions of the Er<sup>3+</sup> ion in this region are due to the intra-4f-shell transition  $^4I_{13/2} \rightarrow ^4I_{15/2}$ . Resonant excitation of the Er 4f-shell confirmed that the HEPL transitions are due to only one type of Er center [3]. Many different types of Er centers have been observed by direct excitation of the Er ion, the different configurations of these complexes giving rise to different crystal-field-splittings of the intra-4f-shell transitions. These different crystal-field-splittings result in absorptive transitions of well defined energy, allowing the selective excitation of different types of Er centers. As one type of Er center exhibited a site-selective photoluminescence (SSPL) spectra identical to that obtained by HEPL, the dominant HEPL luminescence was attributed to this Er center. Further work has shown that this complex consists of an Er ion at the Ga sublattice, associated with two O atoms [4].

The temperature dependence of the  $^4I_{13/2} \rightarrow ^4I_{15/2}$  transitions is of major importance if Er doped material systems are to be of practical use. The excitation mechanism we assume is similar to that which has been successfully applied to the (de)excitation of Yb ions in InP [5], and is shown schematically in Fig 1. Following the absorption of an above-band-gap photon, a carrier (in this case we assume an electron) is captured by a trap level associated with the Er center. Subsequent Coulomb attraction then forms an exciton, the non-radiative recombination of which results in the excitation of the Er 4f-shell. The mismatch in energy between the bound exciton and the intra-4f-shell transition energy is given up as phonons.

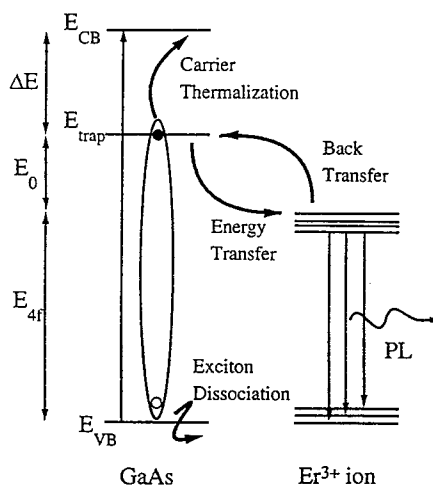


**Figure 1:** Schematic of the excitation mechanism assumed. In this case, an electron trap level is assumed.

Possible mechanisms which could de-excite (energy back transfer - the opposite of excitation) or result in a reduced excitation efficiency (for example carrier thermalisation) are also shown. All these processes are expected to reduce PL intensity, while only de-excitation of the Er ion will result in a change in the lifetime of the  $^4I_{13/2} \rightarrow ^4I_{15/2}$  transition.

The reason for only one type of Er center exhibiting a strong energy transfer between the Er ion and excited carriers in the host semiconductor requires further consideration. The application of hydrostatic pressure is a powerful tool in the study of condensed matter as the energy bands and impurity levels of a semiconductor are very sensitive to inter-atomic distance and so their relative positions may be “tuned” by the application of pressure, allowing fundamental studies of electronic structure. In a previous paper we reported an optical spectroscopic study of the Er-related luminescence of GaAs:Er,O under hydrostatic pressure [6]. At least two new sets of intra-4f-shell transitions which are due to Er centers, were observed at elevated pressures. In the present paper we report a study of the effects of temperature and pressure on the PL spectra, and discuss the reason for the appearance of luminescence from Er centers which are silent by HEPL at ambient pressure.

### Experimental.

The sample described in this study was grown by low-pressure MOCVD at 500° C on a (001)-oriented undoped GaAs substrate as detailed previously [1,2]. The Er concentration for this sample was  $5 \times 10^{17} \text{ cm}^{-3}$  as measured by secondary ion mass spectrometry. 2.2  $\mu\text{m}$  of GaAs:Er,O was deposited. The sample was mechanically thinned to  $\sim 30 \mu\text{m}$  and cut to size  $\sim 120 \times 120 \mu\text{m}^2$ . Hydrostatic pressure was applied in a miniature diamond anvil cell [7] with argon as the pressure transmitting medium. The shift of the R1 and R2 lines of a ruby chip were used as the pressure sensor, which gave an accuracy of  $\pm 0.5$  kbar. The ratio of the intensities of the R1 and R2 lines provides a measure of temperature [8], which enabled us to ensure there was negligible heating of the sample due to the excitation light. For measurements of HEPL intensity as a function of temperature a constant pressure (within the accuracy of the ruby pressure sensor) was maintained within the cell. Measurements were taken under only increasing pressure so as to ensure non-hydrostatic effects were avoided. HEPL was excited with the 514.5 nm line of an Ar-ion laser which was introduced through the top of the diamond anvil cell via an optic-fiber. This excited both sample and ruby chip simultaneously, allowing the excitation optics to be undisturbed as pressure was increased. This ensured a constant excitation power ( $\sim 10 \text{ W/cm}^2$ ) on the sample to facilitate accurate measurements of HEPL intensity as a function of pressure. Luminescence transmitted through the substrate of the sample was collected from the bottom of the diamond anvil cell via a 45° prism. Suitable filters were used to cut out stray excitation light and luminescence from the ruby. The luminescence was dispersed using a 1.25 m single spectrometer providing a resolution of 0.4 nm (0.2 meV), and was detected using a liquid nitrogen cooled Ge-detector. The excitation light was chopped and the signal recovered by standard lock-in techniques.

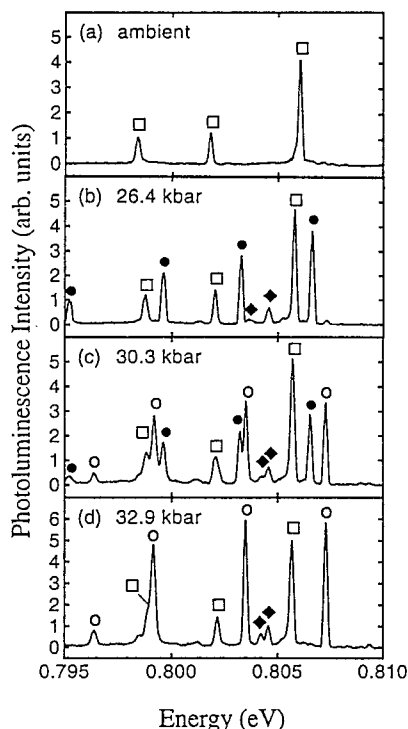
### Results and Discussion.

Figure 2 shows typical HEPL spectra obtained at: (a) ambient pressure, and elevated pressures of (b) 26.4 kbar, (c) 30.3 kbar, (d) 32.9 kbar. The spectra were obtained at 5K. The different types of Er centers present within the sample are identified by a number, and symbols are used in the PL spectra to identify the center to which the luminescence is attributed. At ambient pressure, “center 9” is the only center which is observed by HEPL. As the  $^4I_{13/2} \rightarrow ^4I_{15/2}$  peak positions are relatively insensitive to pressure, the new luminescence transitions observed in Figs. 2(b-d) are identified as being due to other types of Er centers by comparison of the HEPL spectra obtained at high pressure with SSPL spectra obtained for each different type of center at ambient pressure [9]. Such a comparison has revealed that most of the new features may be attributed to “center 11”



and "center 2". In addition, center 11 has been shown to exhibit a change in atomic configuration at ~30 kbar. At low pressures (<25 kbar) only configuration 11<sup>A</sup> is stable. As pressure is further increased (25~30 kbar) both configurations 11<sup>A</sup> and 11<sup>B</sup> are stable resulting in two sets of crystal-field-split transitions. At even higher pressure only configuration 11<sup>B</sup> is stable. The reason for this change in configuration for center 11 is not understood. However, a change in site for a second-nearest-neighbour of the Er ion has been proposed [10].

The effect of pressure on the band-structure of GaAs is shown schematically in Fig. 3. The predicted positions of the conduction-band minima are shown with respect to the  $\Gamma$  valence-band maximum. Typical experimentally obtained values for the pressure coefficient in meV/kbar (change in energy as a function of pressure) of the  $\Gamma$ , X, and L conduction-band minima with respect to the  $\Gamma$  valence-band maximum are marked [11,12]. A trap level may be considered to be a superposition of conduction-band and/or valence-band wavefunctions from the  $\Gamma$ , X, and/or L points of the Brillouin zone. As the deformation potential for the valence-band is about  $1/10^{\text{th}}$  of that of the conduction band [13], the pressure coefficient of the valence-band is expected to be much smaller than the conduction-band. For this reason the valence band is usually considered stationary. The optical properties are related to the relative proportions of the special point wavefunctions ( $\Gamma$ , X, L). The pressure coefficient of the impurity level will be determined by an average of the pressure coefficients of the special points taking into account the number of valleys at the special points. For example, a deep donor level made up of wavefunctions from throughout the Brillouin zone, like the DX center, has a pressure coefficient of ~5 meV/kbar [14]. A hydrogenic state made up of  $\Gamma$ -like wavefunctions, like an exciton bound to a donor, will have a pressure coefficient equal to the  $\Gamma$  band-gap ~10.7 meV/kbar. Furthermore, the luminescence intensity in the region of the  $\Gamma$ /X crossover will depend upon the nature of the impurity level wavefunction. For example, a level which is made up of wavefunctions from throughout the Brillouin zone will be insensitive to the  $\Gamma$ /X crossover. Luminescence from hydrogenic states made up mainly of  $\Gamma$ -like wavefunctions will be drastically reduced when the material becomes indirect. The pressure at which the  $\Gamma$ /X crossover takes place in GaAs (~41 kbar) is marked in Fig. 3, although due to inter-valley mixing this reduction is observed from ~30 kbar [11].



**Figure 2:** HEPL spectra obtained at (a) ambient pressure, (b) 26.4 kbar, (c) 30.3 kbar, (d) 32.9 kbar. Transitions are marked to identify which center they are attributed to: "□" center 9, "◆" center 2, "●" center 11<sup>A</sup>, "○" center 11<sup>B</sup>.

A possible reason for the appearance of luminescence from Er centers as pressure is increased is that the impurity level associated with the center enters the band-gap. Previous work has shown the appearance of luminescence from excitons bound to the N isoelectronic trap in GaAs as pressure is applied [15]. The N-related level was shown to be in resonance with the conduction

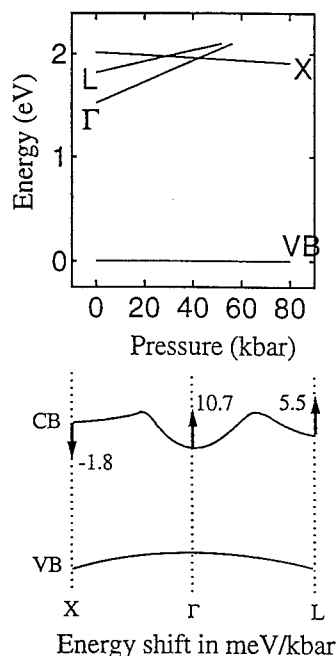


**Figure 3:** Schematic diagram of the effect of pressure on the band-structure of GaAs [13,14].

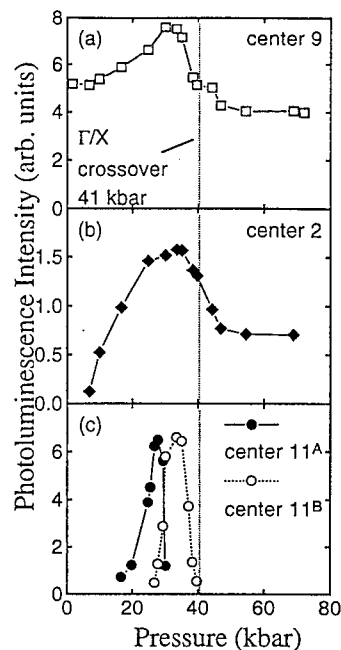


**Figure 4:** Plot of integrated HEPL intensities for (a) center 9, (b) center 2, (c) centers 11<sup>A</sup> and 11<sup>B</sup>. The pressure at which the band-structure of GaAs changes from direct to indirect is also marked.

band at ambient pressure, but entered the band-gap at elevated pressure. The appearance of an Er-center-related level within the band-gap would allow excitation of the Er ion via the mechanism discussed previously. In such a case, the depth of the level from the band-edges would be expected to increase with increasing pressure. Figure 4 shows a plot of integrated PL intensity of the highest energy transition for each center observed by HEPL as a function of pressure. For centers 2 and 11<sup>A</sup> a gradual increase in PL intensity as pressure is increased is observed. This is consistent with the impurity level entering the band-gap

as the probability of carrier capture (and hence PL intensity) is expected to increase with increasing depth.

By measuring the effect of temperature on the  $^4I_{13/2} \rightarrow ^4I_{15}$  transition lifetime an activation energy of  $\sim 300$  meV was extracted from an Arrhenius plot [16]. An Arrhenius plot of the PL intensity at ambient pressure yields a similar energy  $\sim 340$  meV. As a change in lifetime is only expected for a de-excitation of the excited ion, then, for center 9 at ambient pressure the dominant mechanism for thermal quenching is back-transfer. The activation energy obtained from a measure of PL intensity is a measure of the back-transfer energy mismatch, i.e.  $E_0 \sim 300$  meV. As the luminescence energy of the Er 4f-shell,  $E_{4f}$ , is  $\sim 800$  meV, the depth of the impurity level,  $\Delta E$ , is calculated to be  $\sim 400$  meV (refer to Fig. 1 where the impurity level is assumed to be an electron trap). At a range of pressures the activation energy obtained from Arrhenius plots of PL intensity was roughly constant with a value of  $375 \pm 50$  meV. This indicates that the value of  $E_0$  remains constant under the application of pressure for center 9.

The relative dominance of the quenching processes is expected to depend upon the relative sizes of  $\Delta E$  and  $E_0$ . In the case of an impurity level entering the band-gap,  $\Delta E$  should be much smaller than  $E_0$  ( $\Delta E \sim$  a few meV,  $E_0 \sim 900$  meV). Carrier thermalisation may therefore be expected to dominate the thermal quenching of luminescence in the case of impurity levels entering the band-gap. Activation energies extracted from Arrhenius plots of integrated PL intensity for centers 2

and 11 are shown in Table 1. The continuous increase in the activation energy and the small value of activation energy for centers 2 and 11<sup>A</sup> confirm that the appearance of luminescence is due to impurity levels entering the band-gap. The activation energies obtained for centers 2 and 11 therefore provide a measure of the impurity level depth  $\Delta E$ , in contrast to the activation energies obtained for center 9 which provide a measure of the back-transfer energy  $E_0$ .

Pressure (kbar)	Center 2 (meV)	Pressure (kbar)	Center 11 <sup>A</sup> (meV)	Center 11 <sup>B</sup> (meV)
9.9	4	22.6	35	
22.5	10	24.1	45	
33.5	15	27.2	55	65
54.1	18	30.3	80	72
72.2	25	32.9		75
		36.0		67

**Table 1:** Experimentally determined impurity level depths from the band-minima measured at various pressures for centers 2, 11<sup>A</sup>, and 11<sup>B</sup>.

Considering the insensitivity of the PL intensity of center 9 to the  $\Gamma/X$  crossover (Fig. 4(a)) the impurity level wavefunction is best described as being made up of many points from throughout the Brillouin zone, i.e. not just from wavefunctions from one of the special points. Although the results of the temperature dependence of the PL intensity indicates that  $E_0$  is constant at all pressures  $\sim 375 \pm 50$  meV, the precise nature of the wavefunction (i.e. whether it is made up of conduction-band or valence-band wavefunctions) cannot be deduced. In this paper we shall discuss this center no further.

For center 2 also, an insensitivity to the  $\Gamma/X$  crossover is observed in Fig 4(b). this indicates that the associated level is made up of a wide range of points throughout the Brillouin zone. Should the impurity level be an electron trap then the very small change in  $\Delta E$  would indicate that the impurity level was made mainly from  $\Gamma$ -like states. This would result in a drastic reduction in PL intensity as the GaAs band-gap is made indirect, which is not the case. Furthermore, the gradual increase in trap depth,  $\Delta E$ , regardless of the  $\Gamma/X$  crossover is inconsistent with it being made up of conduction-band wavefunctions. If it were made up of valence-band wavefunctions then the observed properties can be explained. The impurity level must be made up of a wide range of valence-band states (explaining the insensitivity to the  $\Gamma/X$  crossover). The gradual increase in  $\Delta E$  regardless of  $\Gamma/X$  crossover, and the small value of this increase (the valence-band states show a much small change in energy than the conduction-band states) are also well explained. We therefore attribute center 2 to a level which is resonant with the valence-band at ambient pressure. Figure 5 (a) shows a schematic of the behaviour of center 2 as determined by these measurements.

For center 11<sup>A</sup> the change of  $\Delta E$  with pressure indicates a pressure coefficient of  $\sim 5$  meV/kbar. This value is rather too large to be attributed to valence-band states (due to the differences in deformation potentials), so we therefore attribute center 11 to be a level which is resonant with the conduction-band at ambient pressure.

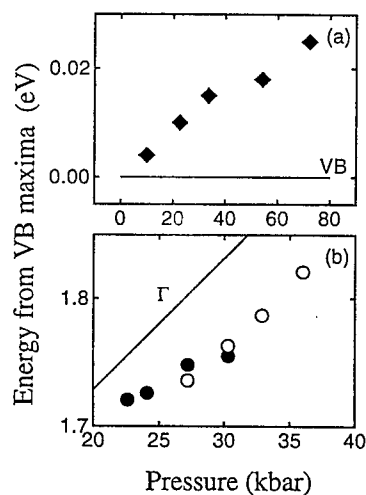


**Figure 5:** Schematic diagram of the band-structure and impurity level positions as determined in this work for (a) center 2, and (b) centers 11<sup>A</sup> and 11<sup>B</sup>.

For center 11<sup>B</sup> the value of  $\Delta E$  is almost independent of pressure. As the trap level remains at a constant energy below the  $\Gamma$  band-gap, the impurity level wavefunction appears to be made up of mainly  $\Gamma$ -like wavefunctions. This is confirmed by the disappearance of luminescence at the  $\Gamma/X$  crossover. The change in band-structure from direct to indirect results in the  $\Gamma$ -like electron wavefunction being unable to efficiently capture the electrons lying at the X minima, resulting in a small recombination rate with a  $\Gamma$ -like hole. Figure 5 (b) shows a schematic of the behaviour of center 11 as determined by these measurements.

### Conclusions.

Er related luminescence in GaAs:Er,O has been studied as a function of temperature and hydrostatic pressure. The appearance of luminescence is well explained by the entry of Er-related impurity levels into the band-gap, thus allowing the energy transfer to take place. The formation of various energy levels by different types of Er centers indicates that it is the constituents of the Er complex which determine its electrical character. The requirement of an impurity level being within the band-gap for efficient energy transfer between the host and the rare-earth 4f-shell is also highlighted.

### References.

1. K. Takahei, and A. Taguchi, *J. Appl. Phys.* **74**, 1979, (1993).
2. K. Takahei, and A. Taguchi, *Jpn. J. appl. Phys.* **33**, 709, (1994).
3. K. Takahei, and A. Taguchi, *J. Appl. Phys.* **77**, 1735, (1995).
4. K. Takahei, A. Taguchi, Y. Horikoshi, and J. Nakata, *J. Appl. Phys.* **76**, 4332, (1994).
5. A. Taguchi, K. Takahei, and Y. Horikoshi, *J. Appl. Phys.* **76**, 7288, (1994).
6. K. Takarabe, T. Mizushima, S. Minomura, R.A. Hogg, A. Taguchi, K. Takahei, Accepted for publication in *Appl. Phys. Letts.*
7. D.J. Dunstan, and W. Scherrer, *Rev. Sci. Instrum.* **59**, 627, (1988).
8. B. A. Weinstein, *Rev. Sci. Instrum.* **57**, 910, (1986).
9. K. Takahei, A. Taguchi and R.A. Hogg, Accepted for publication in *J. Appl. Phys.*
10. R.A. Hogg, K. Takahei, A. Taguchi, K. Takarabe, T. Mizushima, S. Minomura, Accepted for publication in *J. Appl. Phys.*
11. D.J. Welford, and J.A. Bradley, *Sol. Stat. Comm.* **53**, 1069, (1985).
12. K.J. Chang, S. Froyen, M.L. Cohen, *Sol. Stat. Comm.* **50**, 105, (1984).
13. S. Adachi, "Physical properties of III-V semiconductor compounds". Published by John Wiley and sons.
14. D.J. Chadi, and K.J. Chang, *Phys. Rev. Lett.* **61**, 873, (1988).
15. D.J. Welford, J.A. Bradley, K. Fry, and J. Thompson, *Proceedings of 17<sup>th</sup> International Conference on the Physics of Semiconductors*, page 627.
16. A. Taguchi, and K. Takahei, *J. Appl. Phys.* **79**, 4330, (1996).

## EXAFS MEASUREMENT ON LOCAL STRUCTURE AROUND ERBIUM ATOMS DOPED IN GaAs WITH OXYGEN CO-DOPING

M. Tabuchi, H. Ofuchi, T. Kubo, K. Takahei\*, and Y. Takeda  
Department of Materials Science and Engineering,  
Nagoya University, Furo-cho, Chikusa-ku, Nagoya 464-01, Japan  
\*NTT Basic Research Laboratories, 3-1 Morinosato-Wakamiya,  
Atsugi, Kanagawa 243-01, Japan<sup>1</sup>

**Key Words:** EXAFS, erbium, oxygen, co-doping, local-structure, GaAs

**Abstract.** Er doped GaAs sample with O co-doping was investigated by fluorescence EXAFS (extended X-ray absorption fine structure) in order to study the local structure around the Er atoms. The bond lengths of Er-O and Er-As were obtained to be 2.14Å and 2.79Å, respectively. The coordination numbers of both O atoms and As atoms were approximately two. Although the ordinal structure of Er oxide is cubic bixbyite structure Er<sub>2</sub>O<sub>3</sub>, the local structure around Er atoms in the sample is not considered to be similar to the Er<sub>2</sub>O<sub>3</sub> structure. Because the measured bond length of 2.14Å is not close to the Er-O bond length of 2.27Å in cubic bixbyite structure Er<sub>2</sub>O<sub>3</sub>. By the EXAFS measurement using [010], [110] and [110] polarized X-ray, we could not determine that either Er or O atoms adsorbed at first on GaAs (001) surface.

### Introduction.

Er-doped semiconductors are important for optical communication systems since one of the prominent luminescent peaks of Er at 1.5μm is in the minimum absorption region of silica based optical fibers. The origin of the luminescence is intra-4f-shell transition of Er<sup>3+</sup>. The wavelength of the luminescence from intra-4f-shell transition is stable regardless of host semiconductors and temperature. III-V semiconductors are useful as the host semiconductors for Er-doping because advanced growth techniques are available. Recently, the Er atoms doped in GaAs with O co-doping showed high efficient photoluminescence[1, 2, 3], and the local structure around the Er atoms attracts a strong interest because photoluminescence excitation measurement revealed that Er formed many types of luminescent centers. In this work, Er doped GaAs samples with O co-doping were investigated by fluorescence EXAFS (extended X-ray absorption fine structure) in order to study the local structure around the Er atoms. The EXAFS measurement is a powerful technique to investigate a local structure around a specific element[4, 5, 6]. Furthermore, polarized X-ray from synchrotron radiation source was used for the EXAFS measurement in order to investigate the direction of the atoms located around Er.

### Experimental.

The sample was grown by OMVPE (organometallic vapor phase epitaxy) at 500°C on undoped GaAs (001) substrate. The concentration of the Er atoms in the sample was measured as  $4.0 \times 10^{18} \text{cm}^{-3}$  by SIMS. The EXAFS measurement was conducted using synchrotron radiation at beam line BL12C of the Photon Factory in the National Laboratory for High Energy Physics at Tsukuba. Er L<sub>III</sub>-edge EXAFS was measured at 100K using polarized X-ray to [010], [110] or [110] direction. Using the polarized X-ray, the position of the O atoms around the Er atoms could be identified if most of the O atoms occupy the same sites.

## Results.

### A. Local structure around Er atoms.

Figure 1 shows the measured EXAFS  $k^3\chi(k)$  spectrum (background subtracted and normalized) with [010] polarized X-ray. Results with [110] and  $[1\bar{1}0]$  polarized X-ray will be discussed later. The obtained spectrum was analyzed by comparing it with theoretically calculated spectra assuming several local structures around the Er atoms. For example, spectra of (a) Er atoms forming cubic bixbyite structure  $\text{Er}_2\text{O}_3$ , (b) Er atoms on Ga site with two O atoms and two As atoms on the nearest As sites (Er-2O structure), (c) Er atoms forming rocksalt structure ErAs, (d) Er atoms on Ga site with no O atoms on nearest sites as shown in Fig. 2 were calculated using FEFF6 program[7, 8, 9].

Figure 3 shows the calculated spectra with the model structures as shown in Fig. 2. From these spectra, the model in which Er atoms are on Ga site and some of the neighbor As atoms are substituted by O was decided to be most probable because only Er-2O model among these models well represented the positions and shapes of the first several major peaks observed at around  $k = 3.5, 5.2, 6.6$ , and  $7.2$ , although the peak positions are shifted by the phase factor.

The measured  $k^3\chi(k)$  spectrum was Fourier transformed into  $R$ -space as shown in Fig. 4. Theoretically calculated spectra were also Fourier transformed as shown in Fig. 5. The region of the Fourier transformation was from  $3.0$  to  $10.0 \text{ \AA}^{-1}$ . The shapes of the first two peaks in Fig. 4

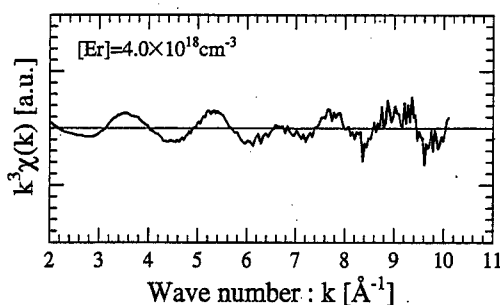


Fig. 1 Measured EXAFS spectrum for Er-doped GaAs with O co-doping.

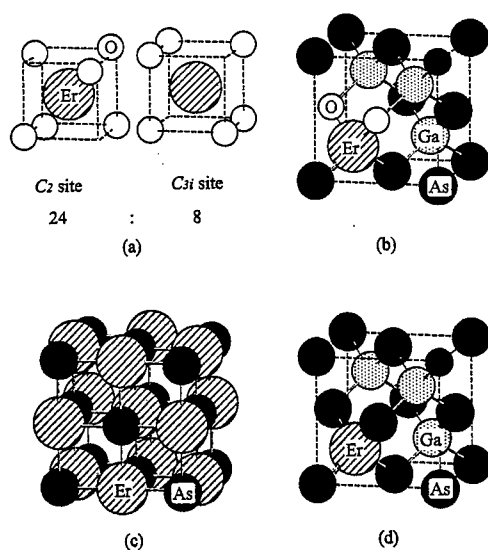


Fig. 2 Schematically shown atom locations around Er atoms for (a)  $\text{Er}_2\text{O}_3$ , (b) Er-2O, (c), rocksalt ErAs, and (d) Er on Ga site models.

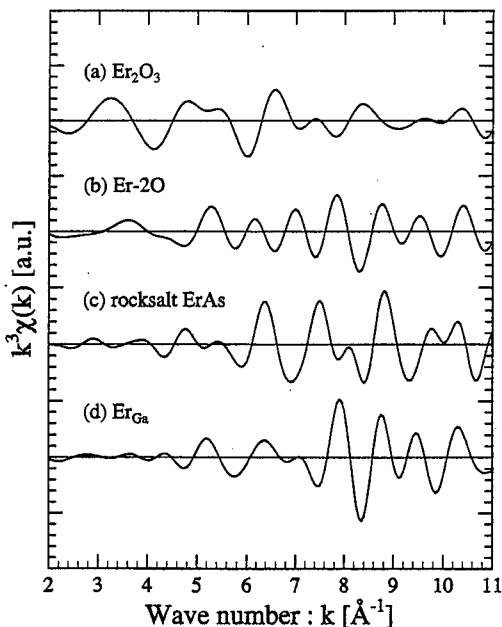


Fig. 3 Theoretically calculated EXAFS spectra assuming four types of local structures around Er atoms in GaAs.

agreed with (b) in Fig. 5. In the Fourier transformed spectrum, two near neighbor peaks were observed at about 1.7 Å and 2.3 Å which corresponded to O and As, respectively. These two peaks were cut out and were Fourier transformed into  $k$ -space. Parameter fitting was conducted in  $k$ -space as shown in Fig. 6. Bond lengths of Er-O ( $r_{\text{Er-O}}$ ) and Er-As ( $r_{\text{Er-As}}$ ), coordination numbers of O atoms ( $N_{\text{O}}$ ) and As atoms ( $N_{\text{As}}$ ) around the Er atom, and Debye-Waller factors about the Er-O bond ( $\sigma_{\text{Er-O}}$ ) and Er-As bond ( $\sigma_{\text{Er-As}}$ ) were chosen as fitting parameters. The bond lengths of Er-O and Er-As were obtained to be 2.14 Å and 2.79 Å, respectively. The coordination numbers of both O atoms and As atoms were approximately two. Although the ordinal structure of Er oxide is cubic bixbyite structure  $\text{Er}_2\text{O}_3$ , the local structure around Er atoms in the sample is not considered to be similar to the  $\text{Er}_2\text{O}_3$  structure. It is because the measured bond length of 2.14 Å is not close to the Er-O bond length of 2.27 Å in cubic bixbyite structure  $\text{Er}_2\text{O}_3$ .

As shown in Fig. 7, if two As atoms and two O atoms locate on tetrahedral As sites in GaAs and the Er-O bond length is 2.14 Å, the Er-As bond length must be 2.82 Å. This value is close to the obtained value, 2.79 Å. Therefore we concluded that most of the Er atoms doped in GaAs with O co-doping constructed Er-2O structure even in the sample where many types of luminescent centers were observed. This result suggests that the difference of the luminescent centers are due to the difference of the configurations of atoms further than 2nd near-neighbors around the Er atoms.

### B. Occupation sites of O atoms.

We conducted the EXAFS measurement using [010], [110] and  $[\bar{1}\bar{1}0]$  polarized X-ray. Figure 8 shows the measured spectra with polarized X-ray. Figure 9-(a) shows the relationship between polarized X-ray direction and atomic sites. Er and O atoms were supplied to the growing GaAs (001) surface. If O atoms absorbed on the As sites and then Er atoms absorbed on the Ga sites

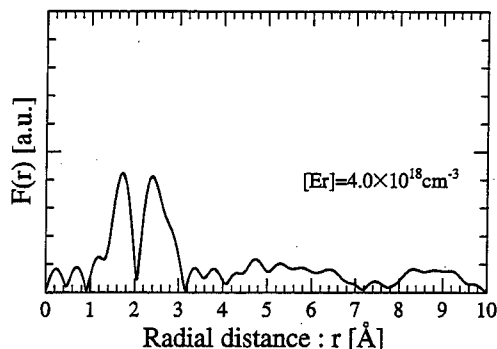


Fig. 4 Fourier transformed EXAFS spectrum.

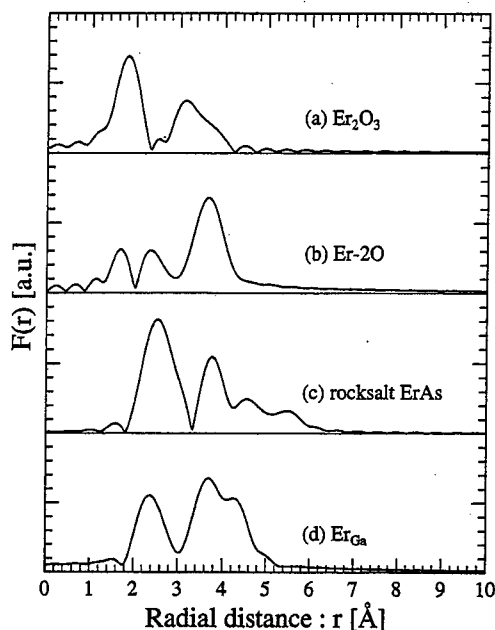


Fig. 5 Fourier transformed theoretically calculated EXAFS spectra.

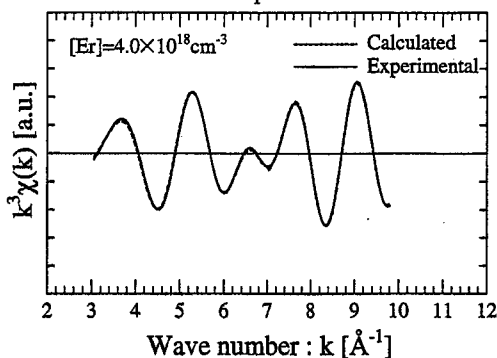


Fig. 6 Parameter fitting in  $k$ -space.

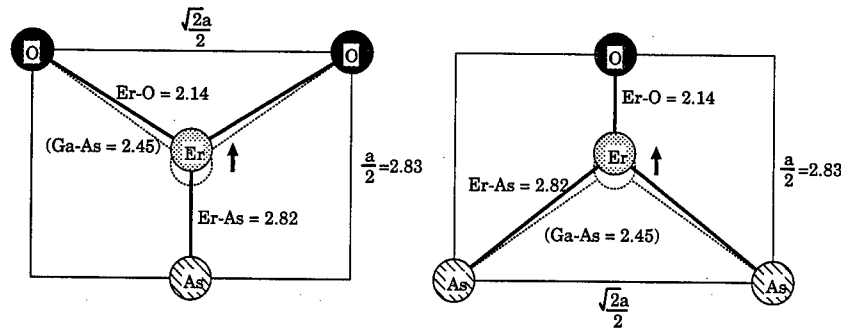


Fig. 7 Position of Er atoms in GaAs lattice.

which are next to the O atoms on As sites, the O atoms must be located in  $[1\bar{1}\bar{1}]$  or  $[\bar{1}11]$  direction from Er atoms (Fig. 9-(b)). Those O atoms cannot be detected using the X-ray polarized to  $[110]$  direction. On the other hand, if Er atoms absorbed on Ga sites and then O atoms absorbed on As sites which are next to the Er atoms on Ga sites, the O atoms must be located in  $[111]$  or  $[\bar{1}\bar{1}1]$  direction from Er atoms (Fig. 9-(c)). Those O atoms cannot be detected using the X-ray polarized to  $[1\bar{1}0]$  direction. Using the X-ray polarized to  $[010]$  direction, the O atoms on both of the sites are observed equally. Therefore, these two positions should be distinguished by comparing the two spectra measured using  $[110]$  and  $[1\bar{1}0]$  polarized X-ray. If O atoms are observed using the X-ray polarized to  $[110]$  direction, it means that the O atoms are above the Er atoms like Fig. 9-(c). On the other hand, if O atoms are observed using the X-ray polarized  $[1\bar{1}0]$  direction, it means that the O atoms are beneath the Er atoms as shown in Fig. 9-(b). However, as shown in Fig. 8, the measured spectra were very similar and the results of the analysis for all of the spectra were almost the same. The results of the parameter fitting are listed in Table I. This result suggests that the probability of O atoms located over or under the Er atoms is almost equal. In other words, It was not determined whether Er or O atoms were adsorbed at first on GaAs (001) surface.

### Conclusions.

Er doped GaAs samples with O co-doping were investigated by fluorescence EXAFS in order to study the local structure around the Er atoms. The bond lengths of Er-O and Er-As were obtained to be 2.14 Å and 2.79 Å, respectively. The coordination numbers of both O atoms and As atoms were approximately two. Although the ordinal structure of Er oxide is cubic bixbyite structure  $\text{Er}_2\text{O}_3$ , the local structure around Er atoms is not considered to be similar to the  $\text{Er}_2\text{O}_3$  structure. It is because, the measured bond length of 2.14 Å is not close to the Er-O bond length of 2.27 Å in cubic bixbyite structure  $\text{Er}_2\text{O}_3$ . By the EXAFS measurement using  $[110]$  and  $[1\bar{1}0]$  polarized X-ray, we could not determine whether Er or O atoms adsorbed at first on GaAs (001) surface.

Table 1: Results of the parameter fitting. Symbols are defined in manuscript.

Polarized Direction	$r_{\text{Er-O}}$ [Å]	$N_{\text{O}}$	$\sigma_{\text{Er-O}}$	$r_{\text{Er-As}}$ [Å]	$N_{\text{As}}$	$\sigma_{\text{Er-As}}$	R. Factor
$[010]$	2.140	2.44	0.100	2.789	2.00	0.095	0.016
$[110]$	2.133	2.09	0.079	2.791	1.71	0.087	0.048
$[1\bar{1}0]$	2.138	2.18	0.088	2.804	1.60	0.082	0.038



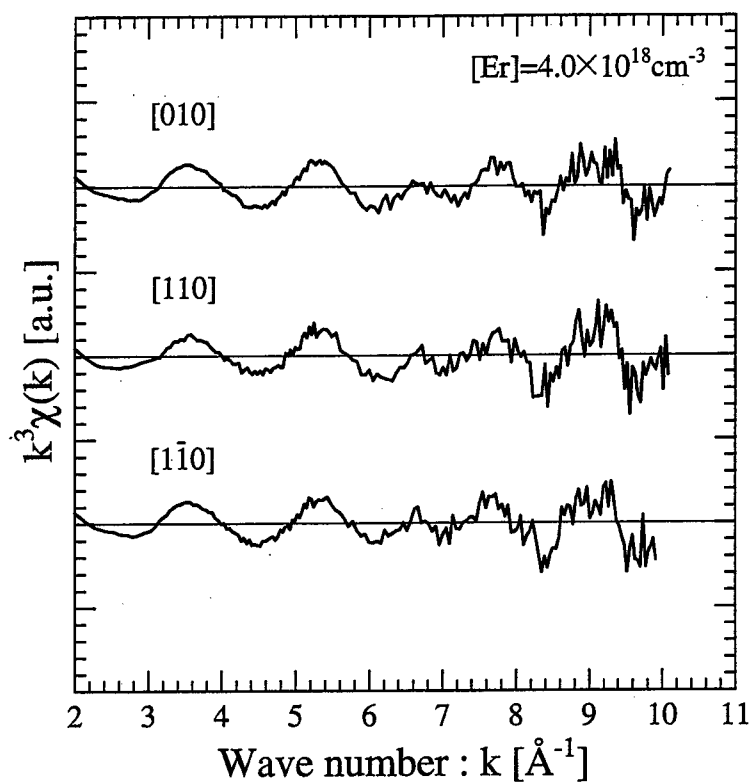


Fig. 8 Measured EXAFS spectra with  $[110]$ ,  $[1\bar{1}0]$  and  $[010]$  polarized X-ray. The spectrum measured with  $[010]$  polarized X-ray is the same as that shown in Fig. 1.

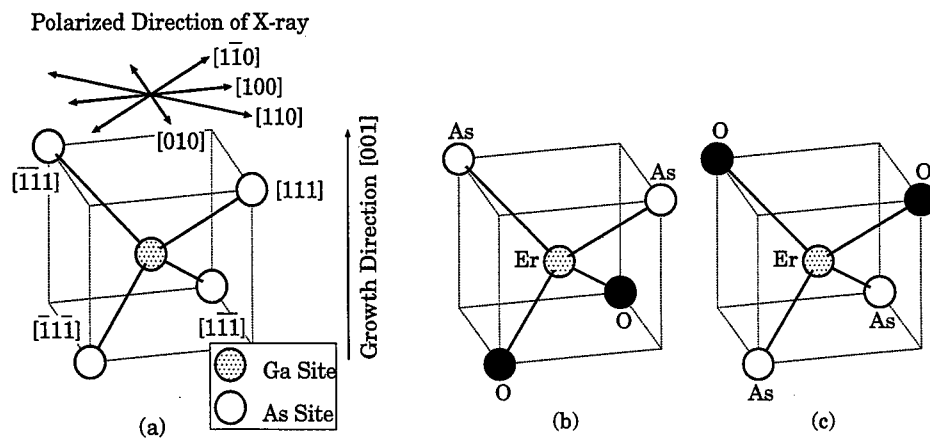


Fig. 9 X-ray polarized directions used for the EXAFS measurement.

**Acknowledgments.**

This work was performed as part of a project (Project No. 95G221) accepted by the Photon Factory Program Advisory Committee, supported in part by the Grant-in-Aid Scientific Research (A)(1) No. 07555100 from the Ministry of Education, Science and Culture.

**References.**

- [1] K. Takahei, and A. Taguchi, *J. Appl. Phys.*, **77**, 1735 (1995).
- [2] K. Takahei, A. Taguchi and Y. Horikoshi, *J. Appl. Phys.* **76**, 4332 (1994).
- [3] K. Takahei, and A. Tabuchi, *J. Appl. Phys.*, **74**, 1979 (1993).
- [4] J.B. Boyce and J.C. Mikkelsen, Jr., *J. Cryst. Growth*, **98**, p.37 (1989).
- [5] H. Oyanagi, T. Matsushita, H. Tanoue, T. Ishiguro, and K. Kohara, *Jpn. J. Appl. Phys.*, **24**, p.610 (1985).
- [6] Y. Takeda, H. Oyanagi, and A. Sasaki, *J. Appl. Phys.*, **68**, p.4513 (1990).
- [7] J.J. Rehr and R.C. Albers, *Phys. Rev.*, **B41** 8139 (1990).
- [8] J.J. Rehr, S.I. Zabinsky, and R.C. Albers, *Phys. Rev.*, **69** 3397 (1991).
- [9] J. Mustre de Leon, J.J. Rehr, S.I. Zabinsky and R.C. Albers, *Phys. Rev. Lett.*, **B44** 4146 (1991).

## LUMINESCENCE AND ANNEALING STUDIES OF Er-IMPLANTED GaN WITH AND WITHOUT OXYGEN CO-DOPING

E. Silkowski, Y. K. Yeo, R. L. Hengehold, and L. R. Everitt  
Department of Engineering Physics, Air Force Institute of Technology  
Wright-Patterson AFB, OH 45433, USA

**Keywords:** gallium nitride, erbium, ion implantation, photoluminescence.

**Abstract.** Strong rare-earth (RE) 4f-emissions from erbium ion-implanted GaN have been observed through photoluminescence (PL) measurements. PL measurements were also performed as a function of excitation laser wavelength from an Ar<sup>+</sup>-ion laser ranging from above (351.1 nm) and below (514.5 nm) bandgap energy at the sample temperatures ranging from 2 to 300 K. The results of PL measurements of Er-implanted GaN showed two well-resolved 4f-transitions of the Er<sup>3+</sup> center, the <sup>4</sup>I<sub>13/2</sub>→<sup>4</sup>I<sub>15/2</sub> at ~1.54 μm and the <sup>4</sup>I<sub>11/2</sub>→<sup>4</sup>I<sub>15/2</sub> at ~1.00 μm from the crystal-field split manifolds along with numerous 'hot' lines. An energy level model requiring at least two non-cubic Er<sup>3+</sup>-centers is proposed, which accounts for the majority of the observed luminescence peaks. Oxygen co-implantation with Er was found to enhance the ~1.54 μm peaks, and to lower the optimal annealing temperature from 1000 to 800 °C. The formation of Er-O complexes was thought to be responsible.

### Introduction.

Oxygen co-doping has been reported to enhance Er emissions in other semiconductors [1,2]. Several groups have now reported room temperature Er<sup>3+</sup> luminescence at 1.54 μm from GaN co-implanted with Er and oxygen [3,4]. Previous studies with low temperature PL performed on Er implanted GaN revealed strong luminescence emissions from crystal-field split intra-4f shell transitions associated with Er<sup>3+</sup> after annealing at temperatures greater than 700 °C [5]. An optimal annealing temperature of 1000 °C was found to produce the strongest photoluminescence signal for GaN implanted with Er alone [5]. In contrast to our results, Wilson *et al.* [3] reported that the ~1.54 μm luminescence signal from GaN co-implanted with Er and oxygen was strongest with annealing temperature of 700 °C. This paper reports the results of PL studies on Er-implanted GaN both with and without oxygen co-implantation.

### Experiment.

GaN grown on sapphire by MOCVD was implanted with Er at an ion energy of 1150 keV, with doses of  $1 \times 10^{13}$  and  $5 \times 10^{13}$  cm<sup>-2</sup> at room temperature. Annealing was performed in a conventional tube furnace by the proximity cap method at temperatures ranging from 700 to 1000 °C for 90 min under an atmosphere of flowing NH<sub>3</sub>. To study the effects of oxygen co-implantation of GaN, a set of samples was co-implanted with oxygen at an energy of 135 keV and a dose of  $5.0 \times 10^{14}$  cm<sup>-2</sup>. These parameters were chosen in order to place the oxygen concentration peak at the same depth as the implanted Er concentration peak. Oxygen co-implanted GaN:Er samples were annealed under conditions identical to those used for the GaN:Er.

Photoluminescence was performed using an Ar<sup>+</sup> laser, a 3/4-meter spectrometer, and a liquid nitrogen cooled Ge detector. The temperature of the sample could be varied from 2 to 300 K by placing the sample in a temperature controlled optical cryostat. The spectra were not corrected for system response. Photoluminescence excitation of GaN:Er was performed using the available discrete lines of the Ar<sup>+</sup> ion laser. All wavelengths were below the low temperature GaN bandgap at ~3.5 eV with the exception of the multiline UV excitation between 351.1 and 363.8 nm.

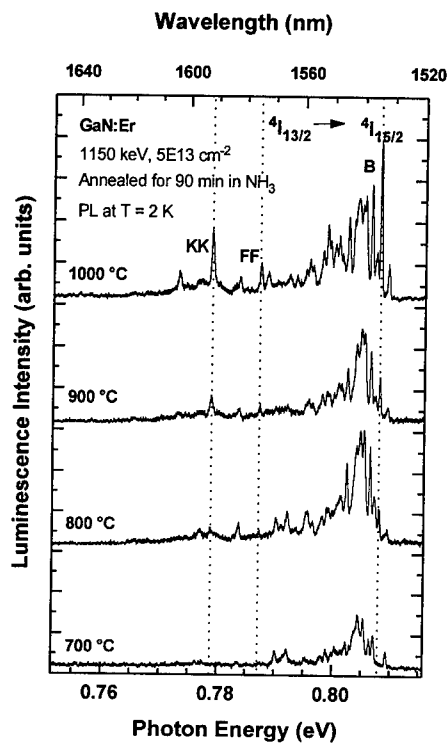


Fig. 1. Annealing temperature dependent low temperature photoluminescence of  $\text{Er}^{3+}$  centers in GaN implanted with Er alone.

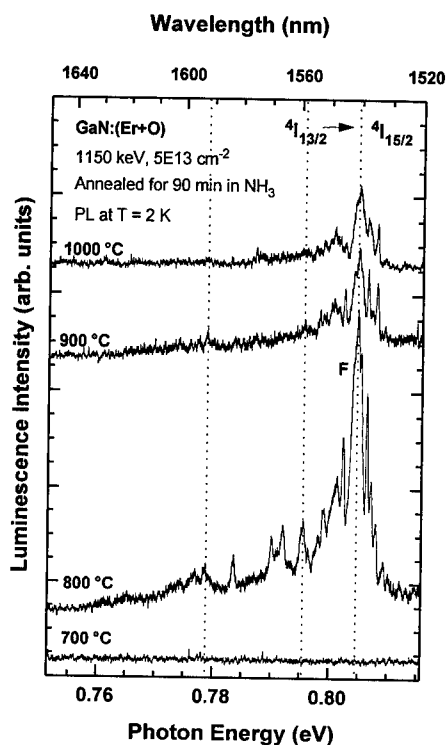


Fig. 2. Annealing temperature dependent low temperature photoluminescence of  $\text{Er}^{3+}$  centers in GaN co-implanted with Er and oxygen.

### Results and Discussion.

Annealing studies were performed on Er-implanted GaN without and with oxygen co-implantation to determine the optimal annealing temperature for activation of the  $\text{Er}^{3+}$  intra-4f shell luminescence. Figure 1 shows the PL peaks observed at 2 K for the  $^4I_{13/2} \rightarrow ^4I_{15/2}$  4f-transitions of the  $\text{Er}^{3+}$  center at  $\sim 1.54 \mu\text{m}$  from the crystal-field split manifolds for the GaN implanted with Er alone. Er ions were implanted at room temperature at an energy of 1150 keV with a dose of  $5 \times 10^{13} \text{ cm}^{-2}$ . Photoluminescence spectra were excited by the 514.5 nm line from an  $\text{Ar}^+$  ion laser. The 700 °C annealed sample showed very weak  $\text{Er}^{3+}$  luminescence, and the luminescence signal increased in intensity as annealing temperature was increased from 700 to 1000 °C. Identical annealing temperature dependence behavior was also observed for the  $^4I_{11/2} \rightarrow ^4I_{15/2}$  manifold at  $\sim 1.00 \mu\text{m}$ . As shown in Fig. 1, 1000 °C was the optimal annealing temperature for all manifolds of  $\text{Er}^{3+}$ . Numerous lines of  $\text{Er}^{3+}$ -related signals were observed, and observations about the energetic location of these lines gave valuable clues as to their origin. The observed number of  $\text{Er}^{3+}$  PL peaks due to crystal-field splittings was indicative of the existence of non-cubic site occupancy by  $\text{Er}^{3+}$ . Furthermore, the GaN:Er had numerous peaks which changed in relative intensity as annealing temperature was increased. Each group of several lines showed the same consistent trend of increasing intensity with annealing temperature. For example, these peaks were labeled as B, FF, and KK in Fig. 1. The underlying cause for the changes in relative intensities among the various luminescence peaks as annealing temperature was increased cannot be determined with absolute certainty from the data in hand. However, it was clear that some change must have occurred in the nature of the  $\text{Er}^{3+}$  luminescence centers as annealing temperature was increased. This change could indicate that a different type of Er luminescent center was formed at high annealing temperature.

Figure 2 shows the PL peaks observed at 2 K for the  $^4I_{13/2} \rightarrow ^4I_{15/2}$  4f-transitions of the  $\text{Er}^{3+}$  center at  $\sim 1.54 \mu\text{m}$  from the crystal-field split manifolds for the GaN co-implanted with Er and oxygen. Er ions were implanted at room temperature at an energy of 1150 keV with a dose of  $5 \times 10^{13} \text{ cm}^{-2}$ , and oxygen ions were implanted at room temperature at an energy of 135 keV with a dose of  $5 \times 10^{14} \text{ cm}^{-2}$ . Photoluminescence spectra were excited by the 514.5 nm line of an  $\text{Ar}^+$  ion laser. In contrast to the results of GaN:Er, 800 °C was the optimal annealing temperature for these oxygen co-doped samples. The  $^4I_{11/2} \rightarrow ^4I_{15/2}$  transitions also showed this same optimal annealing temperature of 800 °C. The most intense peak for the oxygen co-implanted GaN:Er was the peak labeled F in Fig. 2, which reached maximum intensity for samples annealed at 800 °C. This peak was also observed in GaN:Er. As the annealing temperature was increased above the 800 °C, the luminescence signal decreased in intensity. The differing optimal annealing temperature between GaN:Er and GaN:(Er+O) samples suggests that the Er luminescence centers may have been modified by oxygen co-implantation. The  $\text{Er}^{3+}$  luminescence intensity of the optimally annealed GaN:(Er+O) was about four times larger than that of the optimally annealed GaN:Er. This enhancement was similar to that found in a GaAs host [1]. However, the  $^4I_{11/2} \rightarrow ^4I_{15/2}$  transitions at  $\sim 1.0 \mu\text{m}$  showed no enhancement with oxygen co-implantation. The peak locations were nearly identical for the Er-implanted GaN with or without oxygen co-implantation. However, the relative intensities of the various  $^4I_{13/2} \rightarrow ^4I_{15/2}$  lines for the Er and oxygen co-implanted GaN remained about constant with annealing temperature in contrast to the results of GaN:Er. There were no lines which grew in relative intensity as was the case for GaN implanted with Er alone [5]. These data supported the conclusion that at least two different Er centers may be responsible for the observed  $\sim 1.54 \mu\text{m}$  luminescence.

Sample temperature dependent PL for the GaN implanted with Er alone at an energy of 1150 keV with a dose of  $5 \times 10^{13} \text{ cm}^{-2}$  was also carried out, and the results are plotted in Figs. 3 and 4 for the  $^4I_{13/2} \rightarrow ^4I_{15/2}$  and  $^4I_{11/2} \rightarrow ^4I_{15/2}$  transitions, respectively. PL spectra were excited by the 514.5 nm line from an  $\text{Ar}^+$  ion laser. As shown in Fig. 3, the  $^4I_{13/2} \rightarrow ^4I_{15/2}$  luminescence of  $\text{Er}^{3+}$  at  $\sim 1.54 \mu\text{m}$  remained strong as sample temperature was raised to room temperature. The integrated intensity of the entire manifold of lines only dropped by less than 50% as sample temperature was increased from 2 to 300 K. These results were similar to findings by others for oxygen co-implanted GaN:Er [3,4]. Only a few new, higher energy 'hot' lines also appeared in this manifold above 0.81 eV as temperature was increased. In contrast, for the  $^4I_{11/2} \rightarrow ^4I_{15/2}$  manifold as depicted in Fig. 4, several 'hot' lines were observed as sample temperature was increased to 25 K, but the luminescence was almost completely quenched by 175 K. The six lines labeled a, c, d, f, h, and j were present at a sample temperature of 2 K. As sample temperature was increased, at least five new lines labeled b, e, g, i, and k appeared with increasing relative intensity. Under a shift of +4.45 meV, the lines a, d, h, and j fell almost exactly on the positions of b, e, i, and k, respectively. The c line became almost coincident with the position of the d line after the shift. Thus, due to overlap, no corresponding 'hot' line could be observed for the c peak. According to observations of all the peak positions, the data strongly fit a model wherein the low temperature lines originated from the lowest energy crystal-field split level within the  $^4I_{11/2}$  manifold and terminated to the various crystal-field split energy levels of  $^4I_{15/2}$ . Furthermore, the 'hot' lines all originated from a common, higher lying energy level within the  $^4I_{11/2}$  manifold, and terminated upon the corresponding energy level within the  $^4I_{15/2}$  manifold. Thus, the energy spacing of the crystal-field split levels involved could be determined. The observed lines allowed only six of a maximum eight expected energy levels [6] for non-cubic symmetry to be mapped for the  $^4I_{15/2}$  manifold, and only two of a maximum of six levels could be mapped for the  $^4I_{11/2}$  manifold.

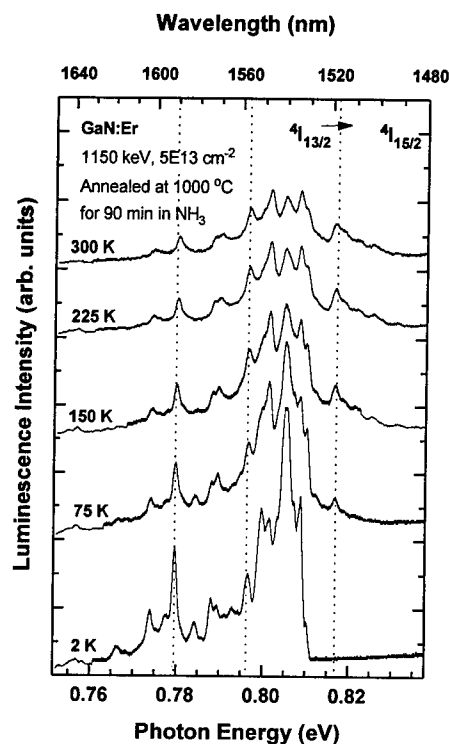


Fig. 3. Sample temperature dependent photoluminescence of  $\text{Er}^{3+}$  for the 4f-transitions of  $^4I_{13/2} \rightarrow ^4I_{15/2}$ .

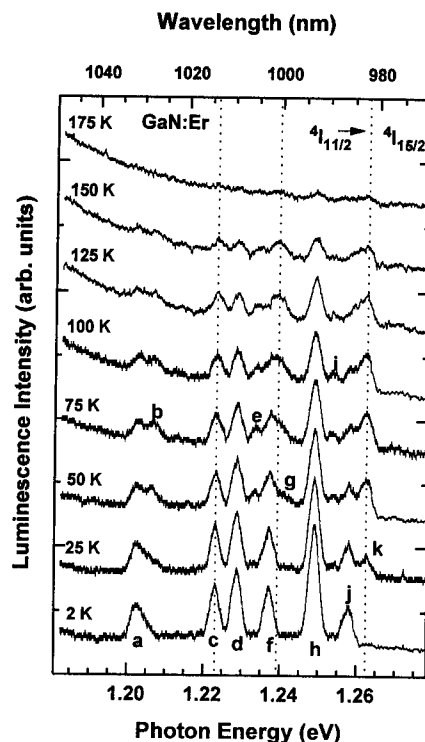


Fig. 4. Sample temperature dependent photoluminescence of  $\text{Er}^{3+}$  for the 4f-transitions of  $^4I_{11/2} \rightarrow ^4I_{15/2}$ .

Limited comparisons of Er dose dependence PL studies were also made for the GaN implanted with Er alone at two different doses of  $1 \times 10^{13}$  and  $5 \times 10^{13} \text{ cm}^{-2}$ . Both Er doses showed identical manifolds of lines and nearly identical annealing behavior with temperature including the relative intensities of the luminescence peaks. Thus, it could be concluded that no differentiation in the luminescence centers occurred due to dose within the limited range examined. The only change observed between the two doses was a change in the total intensity of the Er-related luminescence. The intensity of the strongest peak in each manifold was between three and five times larger in the higher dose samples. Allowing for the inherent uncertainty in measuring relative intensities between samples, and since the difference in dose was a factor of five, the evidence demonstrated that the doses selected have not exceeded the solubility limit of Er in GaN.

Selective photoluminescence excitation of GaN:Er was performed using the several available different wavelength lines of the  $\text{Ar}^+$  laser, and the results of luminescence are shown in Figs. 5 and 6 for the  $^4I_{11/2} \rightarrow ^4I_{15/2}$  and  $^4I_{13/2} \rightarrow ^4I_{15/2}$  transitions, respectively. Er ions were implanted at room temperature at an energy of 1150 keV with a dose of  $5 \times 10^{13} \text{ cm}^{-2}$ . A laser power level of 50 mW was used since this power level was obtainable for all laser lines. All wavelengths were below the low temperature GaN bandgap at  $\sim 3.5 \text{ eV}$  with the exception of the multiline UV excitation between 351.1 and 363.8 nm (3.408–3.531 eV). Both manifolds of transitions were observed for each excitation wavelength. Lower resolution was necessary since the laser power levels were lower. As shown in Fig. 5, it was apparent that all of the same lines of the  $^4I_{11/2} \rightarrow ^4I_{15/2}$  transition

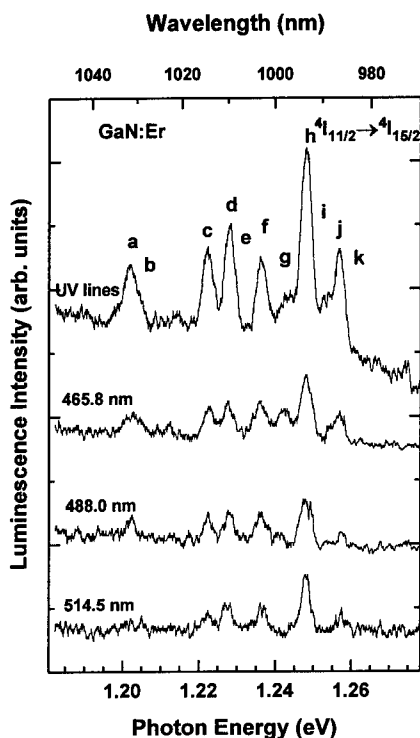


Fig. 5. Selective excitation luminescence spectra excited with various laser wavelengths taken at 2K for the  $^4I_{11/2} \rightarrow ^4I_{15/2}$  transition of  $Er^{3+}$  centers in GaN implanted with Er alone.

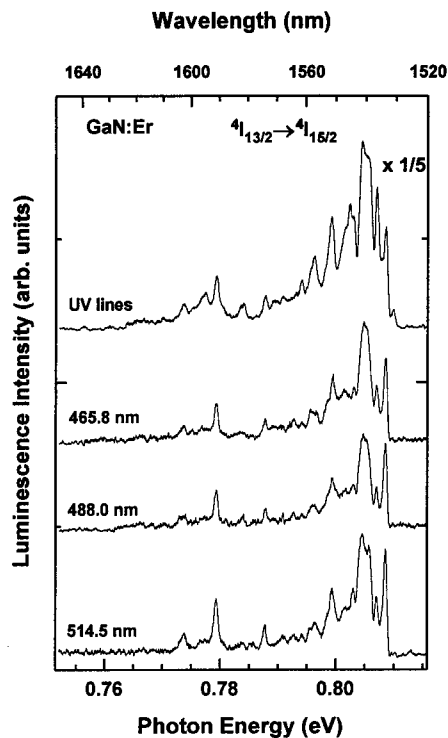


Fig. 6. Selective excitation luminescence spectra excited with various laser wavelengths taken at 2K for the  $^4I_{13/2} \rightarrow ^4I_{15/2}$  transition of  $Er^{3+}$  centers in GaN implanted with Er alone.

were observed for the various line excitations as with the longest wavelength of 514.5 nm excitation, with the exception of the k line. All of the previously observed 'hot' lines labeled b, e, g, and i were apparent in the UV excited sample even at low temperatures. This may indicate that some change in the energy transfer to these lines occurred. It was also notable that the total intensity of the luminescence did not change substantially with the change in excitation wavelength except for the case of UV excitation. As shown in Fig. 6, the integrated intensity of the  $^4I_{13/2} \rightarrow ^4I_{15/2}$  transitions at  $\sim 1.54 \mu m$  showed no appreciable changes as the excitation photon wavelength decreased from 514.5 to 465.8 nm. However, it should be noted that the intensities of the PL signal after exciting with UV wavelength changed by a factor of more than 5 from that of the 514.5 nm.

### Conclusion.

Well resolved  $Er^{3+}$  crystal-field split intra-4f shell emissions were observed by low temperature PL from Er implanted GaN both with and without oxygen co-doping. The strongest  $Er^{3+}$  luminescence was observed from the  $^4I_{13/2} \rightarrow ^4I_{15/2}$  transitions at  $\sim 1.54 \mu m$ , and the  $^4I_{11/2} \rightarrow ^4I_{15/2}$  transitions at  $\sim 1.0 \mu m$  were also observed. Optimum annealing temperatures were found to be 1000 and 800 °C for GaN:Er and GaN:(Er+O) samples, respectively. 'Hot' lines were observed for all manifolds. Higher dose resulted in greater PL intensity with identical luminescence peaks. The data on annealing temperature dependence, energetic spacings, 'hot' lines, and laser excitation wavelength dependence all support the conclusion of at least two, non-cubic Er luminescence centers in GaN:Er. Different luminescence centers seem to dominate in Er implanted GaN with and without oxygen co-implantation. One proposed mechanism for an enhanced Er luminescence for co-

implanted GaAs with Er and oxygen was an interaction between oxygen and erbium to form a complex luminescent center [1].

**References.**

1. J. E. Colon, D. W. Elsaesser, Y. K. Yeo, R. L. Hengehold, and G. S. Pomrenke, *Appl. Phys. Lett.* **63**, 216 (1993).
2. J. Michel, J. L. Benton, R. F. Ferrante, D. C. Jacobson, D. J. Eaglesham, E. A. Fitzgerald, Y.-H. Xie, J. M. Poate, and L. C. Kimerling, *J. Appl. Phys.* **70**, 2672 (1991).
3. R. G. Wilson, R. N. Schwartz, C. R. Abernathy, S. J. Pearton, N. Newman, M. Rubin, T. Fu, and J. M. Zavada, *Appl. Phys. Lett.* **65**, 992 (1994).
4. C. H. Qiu, M. W. Leksono, J. I. Pankove, J. T. Torvik, R. J. Feuerstein, and F. Namavar, *Appl. Phys. Lett.* **66**, 562 (1995).
5. E. Silkowski, Y. K. Yeo, R. L. Hengehold, B. Goldenberg, and G. S. Pomrenke, *Mat Res Soc Proc.* **422**, 69 (1996).
6. U. Walter, *J Phys Chem Solids.* **45**, 401 (1984).



## Er-LUMINESCENCE IN MBE-GROWN AlGaAs

O.B.Gusev, E.K. Lindmark<sup>1</sup>, J.P. Prineas<sup>1</sup>, M.S.Bresler, G.Khitrova<sup>1</sup>, H.M.Gibbs<sup>1</sup>,  
I.N.Yassievich, B.P.Zakharchenya, and V.F. Masterov<sup>2</sup>

A F Ioffe Physico-Technical Institute, Politekhnikeskaya 26, 194021 St.Petersburg, Russia

<sup>1</sup>Optical Sciences Center, University of Arizona, Tucson, AZ 85721, U.S.A.

<sup>2</sup>St Petersburg Technical University, 195251 St Petersburg, Russia

**Key words :** erbium, AlGaAs, photoluminescence, temperature quenching

**Abstract.** Er-doped AlGaAs samples were grown by the MBE technique with concentrations of Er in the range  $10^{18}$ -  $2 \times 10^{19}$  cm<sup>-3</sup>. Photoluminescence (PL) of Er<sup>3+</sup> ions and Er-induced defects was studied at liquid helium and higher temperatures. From high resolution PL spectra the existence of three types of Er centers is deduced which differ by positions of fine structure lines, PL lifetimes, and temperature dependence. Our results indicate that these centers are accompanied by the appearance of three types of carrier traps with binding energies of 20, 50 and about 400 meV, respectively. Our experiments show evidence that carriers captured into these traps control the Auger excitation of Er ions assisted by multiphonon emission of local phonons. Temperature quenching of erbium luminescence is controlled by depopulation of defect states in the case of Auger excitation via the most shallow hole trap (20 meV) and by competition of multiphonon nonradiative capture with the Auger transitions in the case of the deepest defect (400 meV). Besides erbium luminescence at 1.54  $\mu$ m, we have observed luminescence of erbium ions from upper excited states at 0.82 and 0.98  $\mu$ m which demonstrates the possibility to realize a three-level scheme of light emission.

### Introduction.

Recently there has been an outburst of interest in photoluminescence (PL) from erbium inserted into semiconductor matrices (see [1] and references therein). This attention is caused by the well known application of rare earths (RE) in laser active media and hopes to use semiconductors to achieve electrical pumping of RE centers instead of familiar optical pumping. Erbium is especially promising since it emits light with 1.54  $\mu$ m wavelength corresponding to an absorption minimum of silica glass optical fibers. The emission at 1.54  $\mu$ m wavelength arises from internal transitions in the 4f-shell of Er<sup>3+</sup> from the first excited <sup>4</sup>I<sub>13/2</sub> to the ground <sup>4</sup>I<sub>15/2</sub> state.

In this paper we present results of detailed studies of Er-doped AlGaAs grown by MBE.. We have shown that doping of quantum structures with erbium leads to the formation of three defect levels in the AlGaAs bandgap and that charge carriers localized on these levels determine the processes of excitation of erbium ions. We have actually succeeded in exciting erbium ions via high excited states; this favors the development of lasers on radiative transitions in the f-shell of erbium ions inserted into semiconductor structures.

### Experimental procedure.

The erbium-doped structures were grown by MBE at ~600°C on GaAs substrates. (For details see [2]). Using SIMS data, and PL measurements, we have shown that the introduction of erbium in GaAs/AlGaAs quantum well structures in the process of growth by MBE leads to efficient diffusion of Er and interdiffusion of Ga and Al. In the limit of high

concentrations of erbium inserted during MBE growth we have observed the degradation of the quantum structure and practically a homogeneous distribution of erbium, gallium, and aluminum throughout the bulk of the sample. However, due to interaction of aluminum and erbium erbium prefers to have aluminum rather than gallium surrounding and all the spectra of erbium luminescence observed by us are characteristic of AlGaAs but not of GaAs [2]. The Er concentrations measured by secondary ion mass spectroscopy (SIMS) were  $9 \times 10^{18} \text{ cm}^{-3}$  and  $2.2 \times 10^{19} \text{ cm}^{-3}$  for Er21, Er23, respectively. Two samples were prepared as Er-doped  $\text{Al}_x\text{Ga}_{1-x}\text{As}$  layers with  $x=0.3$  (Er29) and  $x=0.5$  (Er40). They had Er concentrations of  $9 \times 10^{18} \text{ cm}^{-3}$  and  $5 \times 10^{18} \text{ cm}^{-3}$ , respectively. In what follows we would refer to all our samples as Er-doped AlGaAs.

PL spectra were measured at liquid helium and higher temperatures. The spectra were analyzed with an 822 mm double grating spectrometer and detected by a nitrogen-cooled germanium photodetector. Excitation was by the 488 nm line of an argon cw laser with pumping power up to 40 mW. PL lifetimes were determined by a phase shift method in which a phase sensitive detector is used to measure the phase difference between two signals (PL and pumping light). Temperature dependencies of intensities of different spectral lines were studied.

#### Experimental results.

All the spectra of erbium photoluminescence in the 1.54  $\mu\text{m}$  band observed consisted of some ten lines. The interpretation of such spectra is usually not straightforward. However, having compared the spectra of Er21 measured at  $T = 5 \text{ K}$  and  $T = 40 \text{ K}$  (Fig. 1) we have observed a sharp difference in the behaviour of the lines intensities. We have selected three series of these lines (a, b, and c) according to their temperature quenching. The measurements of the lifetime of erbium ions in the excited states have demonstrated that the lifetime corresponding to the a line was about 0.5 ms while those for b and c lines only 0.05-0.07 ms. Besides the differences in temperature dependence and lifetimes, the a, b, c series of lines differ also by the linewidths which is less than 7  $\text{\AA}$  in the a series and 15  $\text{\AA}$  in the b and c series. In addition, the ratio of the line intensities within each series is constant and independent of the concentration of erbium inserted into the GaAs Qws. Thus, from the temperature quenching, lifetimes, and linewidths of erbium PL, and the ratios of line intensities in each series we have concluded that the introduction of erbium in AlGaAs leads to the formation of three groups of erbium centers. We propose that the existence of these centers is accompanied by the appearance of three defect levels in the semiconductor bandgap involved in Auger excitation of erbium ions. We have labeled these defect levels as Da, Db, and Dc (Fig. 2). It follows from the temperature dependence that Da is a deep level while Db and Dc are shallow levels.

It is known that the introduction of erbium into a GaAs semiconductor matrix induces an impurity potential in the crystal lattice [3]. The isovalent impurity potential leads to shear deformation of the lattice resulting in the splitting of the degenerate GaAs valence band. As a result the induced potential attracts holes. This is presumably the origin of the shallow hole traps with binding energy of 35 meV in GaAs induced by the introduction of erbium. If erbium concentration exceeds  $5 \times 10^{17} \text{ cm}^{-3}$  (the limiting solubility of erbium in GaAs), erbium begins to occupy the interstitial positions which leads to the formation of deep defect hole trap with an energy of 350 meV [3,4,5].

We assume that similar hole traps should be formed also in AlGaAs on the introduction of erbium, and their binding energies should be close to those observed in GaAs. In fact, we have found two lines of defect luminescence in the 640-680 nm range at high pumping rates when the intrinsic erbium PL tends to saturation (Fig. 2).

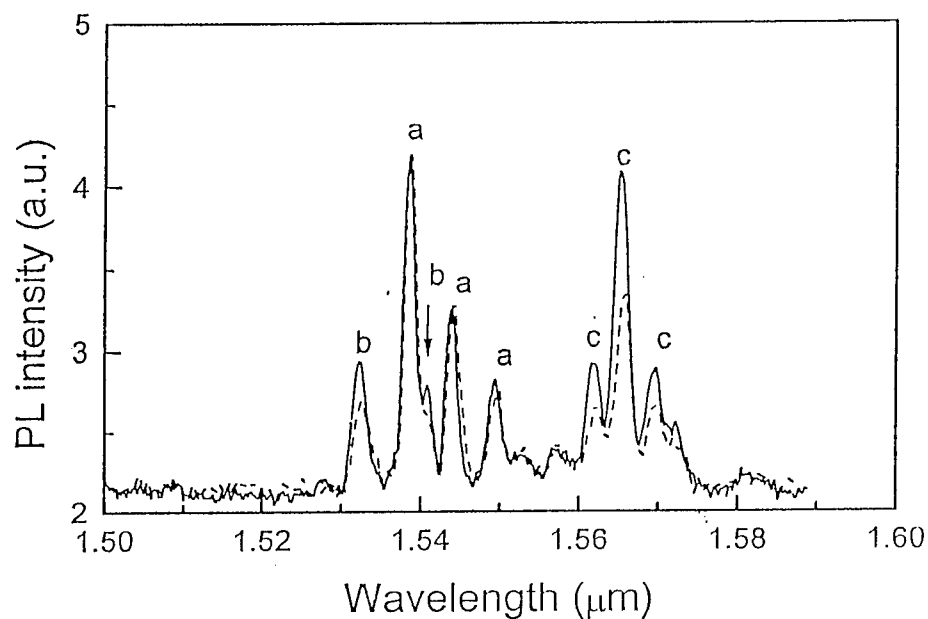


Fig. 1. High resolution PL spectrum of Er21 at  $T = 5\text{ K}$  (full line) and  $T = 40\text{ K}$  (dashed line) demonstrating three series of lines a, b, c.

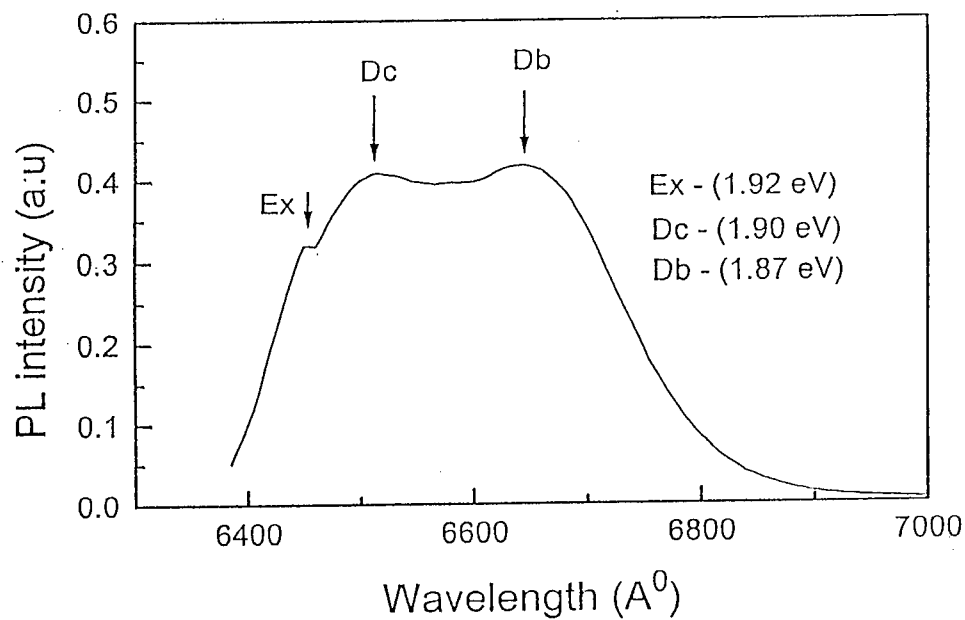


Fig. 2. PL spectrum of Er23 demonstrating the presence of shallow defect states in Er-doped AlGaAs.  $T = 10.5\text{ K}$ .

In the spectrum of Fig. 2 we can see two fairly wide lines with the maxima at  $Db = 1.87$  eV and  $Dc = 1.90$  eV and a narrow exciton line at  $E_x = 1.92$  eV. Reasoning similar to the GaAs case leads to the assumption that erbium ions in AlGaAs in the substitutional positions induce two shallow defect levels with binding energies of 20 and 50 meV (calculated from the differences in the positions of the exciton line  $E_x$  and the defect PL lines  $Db$  and  $Dc$ ). The existence of two types of shallow traps in AlGaAs instead of only one in GaAs is probably due to the different surroundings of erbium ions in the AlGaAs matrix. It should be noted that we cannot ascribe these defect states unambiguously to hole traps. This point actually needs further study.

The results of studies of temperature quenching of the  $Db$  and  $Dc$  defect lines and  $b$ ,  $c$ , and  $a$  erbium series demonstrate that the quenching of the defect  $Dc$  line is significantly stronger than that of  $Db$  line. The activation energy 65 meV found from the temperature dependence of the  $Db$  line is in fair agreement with the binding energy of the  $Db$  level deduced from the photoluminescence data:  $1.92 - 1.87 = 0.05$  eV. The temperature quenching of the erbium PL  $c$  line occurs with the activation energy of 25 meV corresponding to the binding energy of the  $Dc$  level found from the PL data:  $1.92 - 1.90 = 0.02$  eV. Thus, the quenching of erbium PL connected with the most shallow trap  $Dc$  is controlled by depopulation of this state with the temperature rise. The temperature quenching of the  $b$  and  $a$  lines of erbium PL is weaker than that of the  $c$  line. The effective drop of the line  $a$  intensity starts only at about 50 K for Er23 and above  $\sim 100$  K for Er29 (AlGaAs). The line  $a$  can be observed up to room temperature (Fig.3). Note, that the temperature quenching of the  $b$  and  $a$  lines occurs earlier than we would expect from depopulation of the corresponding defect levels.

It should be noted that the position of the exciton line at  $E_x = 1.92$  eV corresponds to the composition of the alloy  $Al_xGa_{1-x}As$  with  $x = 0.32$ . However, the average composition of  $Al_xGa_{1-x}As$  which would be obtained as a result of complete levelling of gallium and aluminum concentrations over the QW region due to cations interdiffusion could not exceed  $x = 0.25$ . This difference indicates that there exist erbium-containing clusters enriched by aluminum.

In the PL spectrum for Er23 measured in the 800-1800 nm range we have seen distinctly a series of narrow lines at the wavelengths 820, 980 and 1550 nm which corresponds to transitions of the  $Er^{3+}$  ion from three lowest excited states:  $^4I_{9/2} \rightarrow ^4I_{15/2}$  (1.49 eV),  $^4I_{11/2} \rightarrow ^4I_{13/2}$  (1.26 eV) and  $^4I_{13/2} \rightarrow ^4I_{15/2}$  (0.81 eV). Besides the PL band at 640 - 690 nm determined by the transitions to the shallow defect traps  $Db$  and  $Dc$  and the exciton line discussed above a wide PL band is observed around 1000 nm. We believe that it is caused by optical transitions to deep hole states  $Da$ . The observation of a wide band evidences probably the existence of strong electron-phonon interaction for the deep state. Thus, we have actually found three types of erbium-induced traps in AlGaAs and PL from the upper excited states  $^4I_{9/2}$  and  $^4I_{11/2}$  of the  $Er^{3+}$  ions.

#### Discussion of the excitation mechanism.

Based on our experimental results, we propose the following model of excitation of the erbium ion 4f-shell. The pumping radiation generates electron-hole pairs in the erbium-containing AlGaAs region. Holes are quickly captured by the hole traps  $Dc$ ,  $Db$ , and  $Da$  induced by erbium at the cation sites and interstitials (Fig. 4). Recombination of a free electron and a hole captured by the trap can be radiative (i.e. defect PL that was observed by us at high pumping rates), nonradiative multiphonon capture of a free electron, or Auger capture of an electron with excitation of the 4f-shell of an erbium ion (Auger excitation). In the latter case the main part of the recombination energy is transferred to the erbium ion to excite the f-shell via Coulomb interaction.

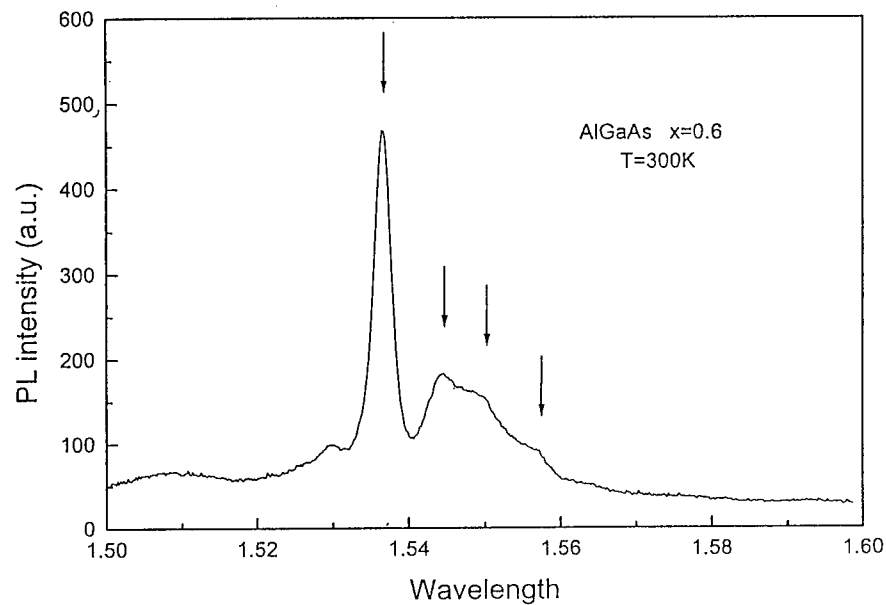


Fig. 3. High resolution spectrum of Er40 at  $T = 300$  K.

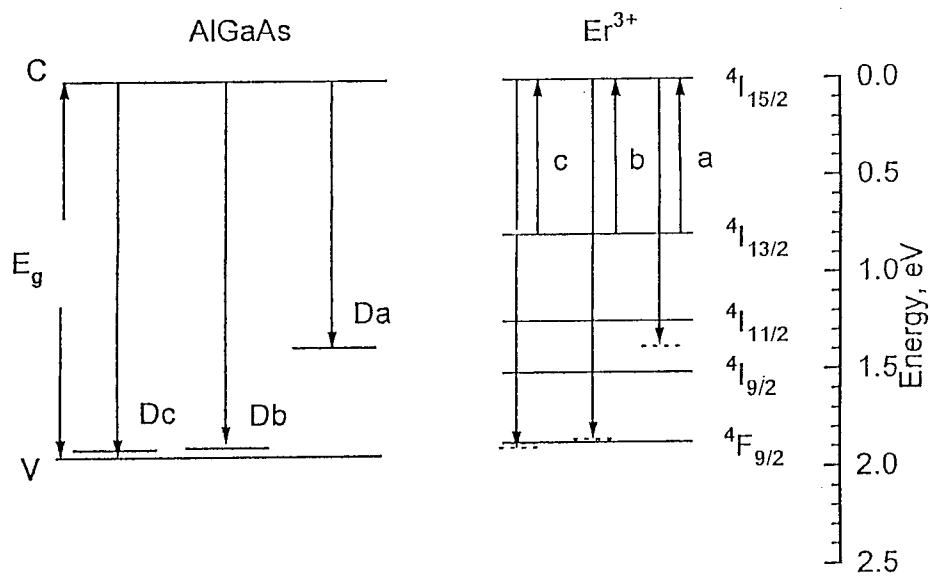


Fig. 4. Energy level diagrams and scheme of transitions for Auger excitation of erbium ions via Da, Db, and Dc defect centers. For comparison of defect and f-f transition energies the positive direction of the energy axis for  $\text{Er}^{3+}$  ions is reversed.

In Fig. 4 a possible diagram of Auger excitation of erbium ions via deep Da and shallow Db and Dc local states is presented. Since the energies of defect PL connected with the shallow traps (Db and Dc lines) are close to the energy of  $^4F_{9/2} \rightarrow ^4I_{15/2}$  transition it is reasonable to propose that the excitation occurs via the  $^4F_{9/2}$  level. For excitation via the deep trap Da we can expect excitation via  $^4I_{11/2}$  and  $^4I_{13/2}$  levels. This assumption is confirmed by observation of erbium PL corresponding to the  $^4I_{9/2} \rightarrow ^4I_{15/2}$  and  $^4I_{11/2} \rightarrow ^4I_{15/2}$  transitions.

In the case of excitation of erbium via shallow traps the temperature quenching of erbium PL could be controlled by the thermal depopulation of shallow defect levels. We have actually observed this situation for the c line of erbium PL. In the case of excitation via deep defects Da the temperature quenching is no more determined by the thermal depopulation of the Da level but is controlled by a competition between the Auger-excitation and multiphonon nonradiative capture, i.e. by the ratio of their probabilities. We have calculated the temperature dependence of this ratio and compared it to the temperature quenching of the erbium PL a line at  $1.54 \mu\text{m}$  for Er29. A good agreement was obtained demonstrating that our assumption is sound. This point explains also why the increase in Al content (x) in  $\text{Al}_x\text{Ga}_{1-x}\text{As}$  leads to a weaker temperature quenching of the a line for Er40: the rise of the energy gap with x (and the corresponding increase in the energy of defect level) increases the height of the energy barrier for the multiphonon transition and reduces its importance as compared to the Auger process.

### Conclusions.

In conclusion, we have demonstrated that 1. Erbium impurity forms three types of hole traps in the bandgap of AlGaAs (one of them being deep with the binding energy about 400 meV and two shallow ones with the energies of 25 and 50 meV). 2. Excitation of the f-shell of erbium ions is determined by an Auger process with participation of holes captured by the traps accompanied by release of excess energy transferred to local phonons. 3. The temperature quenching of erbium PL excited via shallow traps is caused by a thermal depopulation of the defect levels. The temperature quenching of erbium PL excited via deep trap is due to an increase of probability of multiphonon thermally activated capture of free electrons competing with the Auger excitation process. 4. Erbium PL on the  $1.54 \mu\text{m}$  linewidth excited via the deep trap can be observed up to room temperature. 5. The observation of erbium PL corresponding to the transitions from the  $^4I_{9/2}$  and  $^4I_{11/2}$  levels indicates that three-level excitation scheme for the PL on  $1.54 \mu\text{m}$  can be realized in erbium-doped AlGaAs.

This work was partially supported by AFOSR (F49620-94-1-0390), DARPA (DAAH04-95-1-0612), NSF Lightwave Technology (ECS9421517) and International Programs, the Russian Foundation of Basic Research (grant 95-02-04163-a), by INTAS-RFBR 95-0531 grant and by Russian Ministry of Science (grant 97-1036).

### References.

- [1] Rare Earth Doped Semiconductors, edited by G.S. Pomrenke et al. (Materials Research Society, Pittsburgh, 1993); Rare Earth Doped Semiconductors II, edited by A. Polman et al. (Materials Research Society, Pittsburgh, 1996)
- [2] M.S.Bresler et al., this conference.
- [3] D.W.Elsaesser, Y.K.Yeo, R.L.Hengehold, K.R.Evans, and F.L.Pedrotti, J. Appl. Phys. **77**, 3921 (1995)
- [4] J.E.Colon, D.W.Elsaesser, Y.K.Yeo, R.L.Hengehold, and G.S.Pomrenke, ref.1, p.251
- [5] A.Taguchi and T. Ohno, Mater. Sci. Forum **196-201**, 627 (1995).

## CRYSTAL-FIELD TRANSITIONS OF Nd<sup>3+</sup> AND Er<sup>3+</sup> IN PEROVSKITE-TYPE CRYSTALS

M. Dietrich, P. Thurian, I. Loa, S. Gronemeyer, A. P. Litvinchuk, and C. Thomsen  
Institut für Festkörperphysik, Technische Universität Berlin,  
Hardenbergstr. 36, 10623 Berlin, GERMANY

**Keywords:** rare earth, erbium, neodymium, perovskites, photoluminescence, Raman effect

**Abstract :** We report on a study on Nd<sup>3+</sup> and Er<sup>3+</sup> in Nd<sub>2</sub>Ba(Zn,Cu)O<sub>5</sub>, Er<sub>2</sub>BaNiO<sub>5</sub> and Er<sub>2</sub>BaCuO<sub>5</sub> by means of photoluminescence, absorption, and Raman spectroscopy in magnetic fields up to 15 T. Crystal-field levels of Nd<sup>3+</sup> and Er<sup>3+</sup> were determined in the range 0–30000 cm<sup>-1</sup> applying the optical techniques mentioned above at different temperatures. For the Er<sub>2</sub>Ba(Ni,Cu)O<sub>5</sub> material, the <sup>4</sup>I<sub>13/2</sub>–<sup>4</sup>I<sub>15/2</sub> transition with the well known 1.54 μm luminescence is strongest. The photoluminescence of the Nd<sub>2</sub>Ba(Zn,Cu)O<sub>5</sub> compound is dominated by the emission from the <sup>4</sup>F<sub>3/2</sub> state to the <sup>4</sup>I<sub>15/2</sub>, <sup>4</sup>I<sub>13/2</sub>, <sup>4</sup>I<sub>11/2</sub> and <sup>4</sup>I<sub>9/2</sub> multiplet. However, more zero-phonon lines (ZPLs) were observed for Nd<sub>2</sub>Ba(Zn,Cu)O<sub>5</sub> than expected in the simple crystal-field picture. This indicates that either other phases are present in the crystal or that the rare-earth is also incorporated on other sites.

### Introduction

The crystal-field levels of the 4f electrons of rare-earth ions introduced as dopants into a solid matrix have been studied extensively. Their electronic wavefunctions are strongly localized, but nevertheless influenced by the electric and magnetic order in the host crystal. Their study in high-T<sub>c</sub> superconductors, where the rare-earth ion is a part of the crystallographic unit cell, has become of increasing interest [1]. The aim of this paper is to study compounds which have a crystal structure and composition similar to that of high-T<sub>c</sub> superconductors and determine the properties of the rare-earth element and its environment.

Compounds like R<sub>2</sub>BaMO<sub>5</sub> (R=rare-earth element, M=Cu, Ni, Zn) crystallize in four different structures depending on the rare-earth ionic radius and the transition metal M. The group Er<sub>2</sub>BaMO<sub>5</sub> is orthorhombic with space groups *Pnma* (for M=Cu) and *Immm* (for M=Ni). The second family Nd<sub>2</sub>BaMO<sub>5</sub> (M denotes Cu and Zn) is tetragonal, the space group is *I4/mcm* (for M=Zn) and *P4/mbm* (for M=Cu). The latter structures contain R-O layers separated by slabs consisting of isolated MO<sub>4</sub>/MO<sub>5</sub> tetrahedral/orthorhombic units except for Er<sub>2</sub>BaNiO<sub>5</sub> containing chains of NiO<sub>6</sub> flattened octahedra. Ba atoms are arranged between the octahedra [1]-[4]. Most of the components with the composition R<sub>2</sub>BaCuO<sub>5</sub> have an orthorhombic structure described by the space group *Pbnm* [2]. Er<sub>2</sub>BaCuO<sub>5</sub> has *Pnma* structure and is the so called *green phase*. Er is incorporated at two crystal sites of Er<sub>2</sub>BaCuO<sub>5</sub> with a environment of seven oxygen atoms. There are two sets of Er states with all degeneracies lifted due to the crystal sites [4]. All of these components are insulators.

In this study we focus on Raman and photoluminescence (PL) spectra of these perovskites in external magnetic fields (0-15 T). In addition, Fourier-transform spectroscopy (FTIR) was used to investigate the <sup>4</sup>F-ground multiplet of Nd<sub>2</sub>BaMO<sub>5</sub>.

### Experiments

The samples were polycrystalline pellets obtained by solid-state reactions. In connection with PL, crystal-field Raman scattering is a powerful tool to obtain information on the crystal-field levels. The combination of these experimental methods allows the determination of the crystal-field levels of the rare-earth elements as well as the phonon energies of the host compounds. We measured Raman and PL spectra at different temperatures in the range 1.5–20 K in magnetic fields of 0–15 T. For that we used a split-coil magnet based on a superconducting NbSn-coil in Faraday configuration. The split-coil magnet was prepared for Raman scattering by using a special optics to focus the laser beam down to a spot diameter of  $\sim 10\mu\text{m}$  and for collection of the scattered light. The Raman spectra were taken at various excitation energies of an  $\text{Ar}^+/\text{Kr}^+$ -Laser. The spectra were recorded with a triple-grating Raman-spectrometer (Dilor XY800). PL spectra were detected with a cooled Ge-photodiode.

### Results and discussion

$\text{Er}_2\text{Ba}(\text{Cu},\text{Ni})\text{O}_5$  has a complex crystal-structure. Phonon frequencies of  $\text{Er}_2\text{BaNiO}_5$  were previously measured by de Andrés *et al.* [4]. Raman data for  $\text{Er}_2\text{BaCuO}_5$  have not been published so far, but comparable phonon energies can be found in  $\text{Ho}_2\text{BaCuO}_5$  [5]. All investigated Raman spectra of  $\text{Er}_2\text{Ba}(\text{Cu},\text{Ni})\text{O}_5$  show a large number of intense lines in the range up to  $1000\text{ cm}^{-1}$ . Due to the use of various laser lines, Er-PL and Raman lines can be distinguished. Furthermore, two different types of Raman-lines were observed, namely phonons as well as crystal-field related peaks. In order to separate between these two different scattering processes, a magnetic field can be applied. Crystal-field Raman transitions show the characteristic Zeeman splitting of ground and excited state of the rare-earth element, whereas no Zeeman effect is observed for the phonon peaks in the Raman-spectrum. In the PL spectra, many of the 4f transitions within the rare-earth elements are observed. Because of the weak phonon coupling of the rare-earth elements, only crystal-field transitions without phonon sidebands can be seen in PL spectra.

In Fig. 1 the Raman spectra for  $\text{Er}_2\text{BaNiO}_5$  for two laser lines are shown. Because of the superposition of PL and Raman-lines in the spectra, Raman measurements were performed at three different laser wavelengths (488, 501 and 514 nm). At laser wavelengths of 488 and 514 nm phonons and Raman-crystal-field transitions are superimposed by strong PL of higher crystal-field states which is not the case for excitation at 501 nm. At  $21139\text{ cm}^{-1}$  a resonant PL could be observed with 514 nm excitation. Comparing all Raman spectra, the phonon and Raman-crystal-field lines of  $\text{Er}^{3+}$  in  $\text{Er}_2\text{BaNiO}_5$  could be determined. The intensity of the five observed crystal-field Raman peaks is very weak compared to the phonon peaks. Only four phonons could be identified. Thus, we could not verify all of the results of Ref. [4]. Possibly, some PL-peaks were misinterpreted as phonons. Finally, we observe a slightly different phonon energy for the  $A_g$  mode at  $548\text{ cm}^{-1}$  instead of  $539\text{ cm}^{-1}$  [4]. Together with the PL experiments the crystal-field levels within the  $^4I_{15/2}$  ground state could be identified (Table 1). The PL measurements for  $\text{Er}_2\text{BaNiO}_5$  show only three peaks at 6389, 6460 and  $6473\text{ cm}^{-1}$  (Figure 2). The peak at  $6460\text{ cm}^{-1}$  has the highest intensity. The two high-energy peaks split with increasing magnetic field whereas the one at  $6389\text{ cm}^{-1}$  broadens and vanishes. Therefore, there are two excited states 13 and  $84\text{ cm}^{-1}$  above the lowest state in the  $^4I_{15/2}$  multiplet. For a classification of the transitions see table 1.



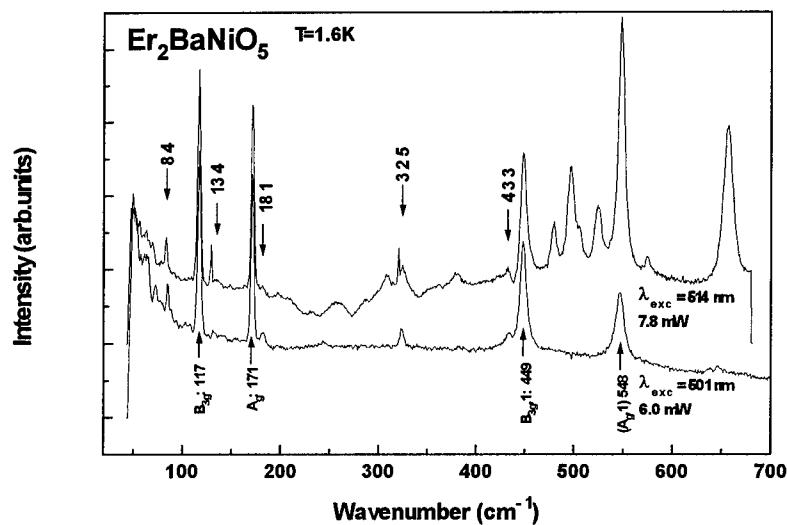


**Figure 1:** Raman spectra of  $\text{Er}_2\text{BaNiO}_5$  excited at 501 and 514 nm. The energy of the crystal-field levels are labeled on top by their frequency, the phonon energies and their symmetries are given below the curve. Other peaks are due to the superposition of Er-luminescence.

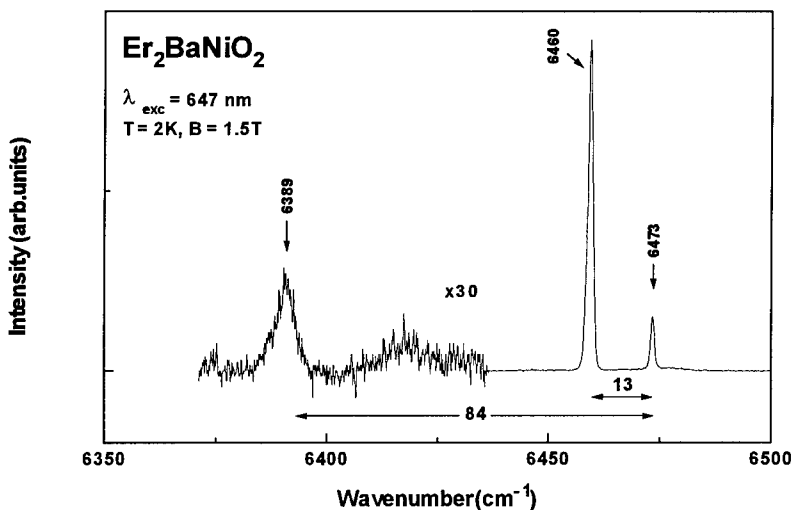


**Figure 2:** PL spectra of  $^4I_{15/2}$  crystal-field levels in  $\text{Er}_2\text{BaNiO}_5$ , excited with the 647 nm laser line of  $\text{Kr}^+$  at a temperature of 2 K and a magnetic field of 1.5 T. The two low-energy emissions corresponds to excited states of the  $^4I_{15/2}$  ground state multiplet at 13 and  $84\text{cm}^{-1}$ , respectively.

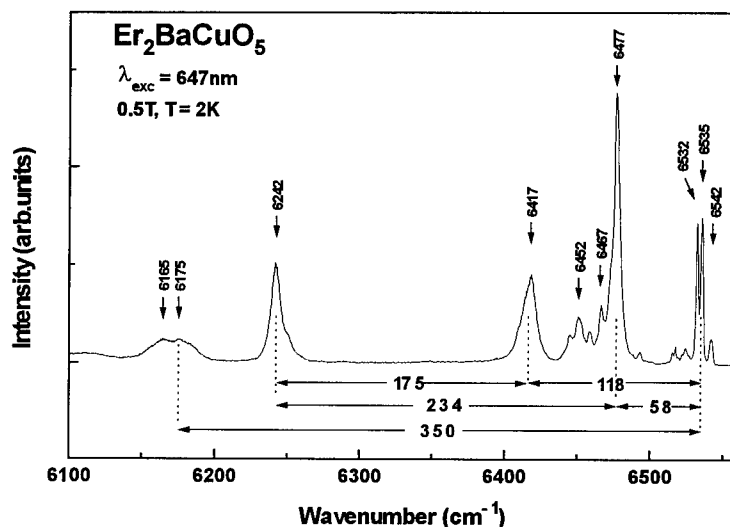


**Figure 3:** PL spectra of  $\text{Er}_2\text{BaCuO}_5$  excited with the 647 nm laser line of  $\text{Kr}^+$  at a temperature of 2 K in a magnetic field of 0.5 T. The low-energy emissions corresponds to excited states of the two  $^4\text{I}_{15/2}$  ground state multiplets.

Due to the two crystal sites of Er in  $\text{Er}_2\text{BaCuO}_5$ , the Raman spectra are much more complex than those of the nickelates. Based on a comparison with the phonon energies of  $\text{Ho}_2\text{BaCuO}_5$  and  $\text{Y}_2\text{BaCuO}_5$  most peaks could be identified as atomic vibrations (Cu, O(1), O(2)). Due to a similar atomic radius and weight and equal symmetry of the host crystals, this transfer of Raman data between  $\text{Ho}_2\text{BaCuO}_5$  and  $\text{Er}_2\text{BaCuO}_5$  within the bounds of error of  $\pm 4 \text{ cm}^{-1}$  is permissible [5]. Crystal-field lines are identified by line splittings and broadenings in a magnetic field or in comparison with the PL spectra. The PL spectra of  $\text{Er}_2\text{BaCuO}_5$  show peak structures in a range between 6100 and 6550  $\text{cm}^{-1}$  (see Fig. 3). About 20 peaks can be seen easily. All of them are broadened or split in a magnetic field. Eight of the expected sixteen crystal-field levels of the  $^4\text{I}_{15/2}$  multiplets could be determined. However, a reliable assignment of the observed crystal-field transitions to the crystal site is not possible up to now. For  $\text{Er}_2\text{BaNiO}_5$  five crystal-field levels could be identified. Overall,  $\text{Er}^{3+}$  shows a more intensive PL in the cuprate than in the nickelate.

For  $\text{Nd}^{3+}$  in  $\text{Nd}_2\text{BaZnO}_5$  a calculation of the crystal-field transitions exists [6]. Therefore, we expect transitions to the  $^4\text{I}$ -groundstates in the spectral range of 0-7000  $\text{cm}^{-1}$ . Crystal-field transitions of  $\text{Nd}_2\text{BaCuO}_5$  can be expected in the same range because of a similar environment of the  $\text{Nd}^{3+}$ . Raman data were published by M. V. Abrashev *et al.* [2]. We performed Raman scattering and PL measurements in various magnetic fields and Fourier spectroscopy on  $\text{Nd}_2\text{Ba}(\text{Zn,Cu})\text{O}_5$ . In figure 4 a PL spectrum of  $\text{Nd}_2\text{BaZnO}_5$  is shown. The  $^4\text{F}_{3/2} \rightarrow ^4\text{I}_{11/2}$  transition was chosen as an example. Similar PL spectra were detected for the  $^4\text{F}_{3/2} \rightarrow ^4\text{I}_{9/2}$ ,  $^4\text{I}_{13/2}$ ,  $^4\text{I}_{15/2}$  transitions, respectively. About 14 peaks are observed (Fig. 4). The classification is similar to

that of the Er compounds. Here, the thermal excitation of the  $^4F_{3/2}$  doublet can be seen in the thermalization of lines of the  $^4I_{11/2}$ -multiplet with an energy difference of  $60\text{ cm}^{-1}$  (1 and 2, 7 and 8, 11 and 12). All crystal-field levels of  $\text{Nd}^{3+}$  in  $\text{Nd}_2\text{BaZnO}_5$  could be identified, and most of  $\text{Nd}_2\text{BaCuO}_5$  [3].

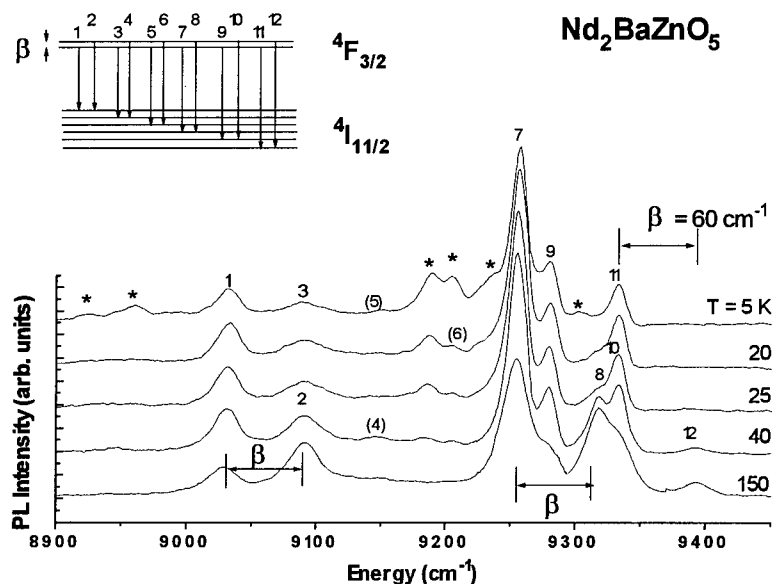


**Figure 4:** PL spectra of  $\text{Nd}_2\text{BaZnO}_5$  measured at various temperatures between 5 and 150 K. The spectral range corresponds to transitions from  $^4F_{3/2}$  to  $^4I_{11/2}$ . Odd numbers denote the transitions from the lower  $^4F_{3/2}$  level to the  $^4I_{11/2}$  multiplet, those from the upper level are marked with even numbers. As shown in the inset,  $\beta = 60\text{ cm}^{-1}$  is the gap of the  $^4F_{3/2}$  doublet.

Excellent agreement of the measured energy levels with the calculations is obtained. Additional lines are observed in  $\text{Nd}_2\text{BaZnO}_5$ , compared to the crystal-field calculations. This is a hint for another phase present in the host crystal or another crystal site at which the rare-earth is also incorporated. Investigations on monocrystalline samples of different phases should clarify this point.

### Summary

The optical properties of the perovskite crystals investigated here are dominated by the rare-earth element in the unit cell of the host crystal. For  $\text{Er}_2\text{BaNiO}_5$  five crystal-field levels of the  $\text{Er}^{3+}$  ( $^4I_{15/2}$ ) ground state multiplet were identified, whereas for  $\text{Nd}_2\text{BaZnO}_5$  all crystal-field states have been determined. The observed crystal-field levels of  $\text{Nd}_2\text{BaZnO}_5$  are in excellent agreement with finestructure calculations of Taibi *et al.* [6]. A proper group theoretical classification of crystal-field lines is not possible without polarized PL measurements on single crystals.

Nd <sub>2</sub> BaZnO <sub>5</sub>			Er <sub>2</sub> BaNiO <sub>5</sub>				
CF	Expt. (cm <sup>-1</sup> )	Calc. (cm <sup>-1</sup> )	Raman 488 nm	Raman 501 nm	Raman 514 nm	PL	CF PL Phonons
<sup>4</sup> I <sub>9/2</sub>	0	-5	0	0	0	0	CF
	65	70				13	CF
	216	243					
	288	336	84	84	84	84	CF
	455	493	118	118	118		B <sub>3g</sub>
<sup>4</sup> I <sub>11/2</sub>	1928	1916	134	134	134		CF
	1985	2026	153				PL
	2007	2038	171	171	171		A <sub>g</sub>
	2117	2148	218				PL
	2170	2204	238				PL
	2233	2254			259		PL
<sup>4</sup> I <sub>13/2</sub>	3865	3848	290				PL
	3928	3973	307		308		B <sub>2g</sub> /B <sub>3g</sub> 2 ?
	3942	3987	324	325	325		CF
	4050	4102			381		PL
	4133	4133	394				PL
	4200	4209	?	433	433		CF
	4220	4263	440				PL
<sup>4</sup> I <sub>15/2</sub>	5719	5779	448	449	449		B <sub>3g</sub> 1
	5785	5911	463				PL
	5840	5972			479		PL
	5895	6076			497		PL
		6232			524		PL
	6100	6310	547	548	548		A <sub>g</sub> 1 ?
	6284	6366			576		PL
	6361	6429	637				PL
				645			PL
					657		PL

**Table 1:** Classification of the <sup>4</sup>I<sub>15/2</sub>-crystal-field levels (CF), phonons and photoluminescence (PL) of Er<sub>2</sub>BaNiO<sub>5</sub> and <sup>4</sup>I-CF levels of Nd<sub>2</sub>BaZnO<sub>5</sub>. 6 of 8 multiplets of the <sup>4</sup>I<sub>15/2</sub> multiplet have been identified for Er<sub>2</sub>BaNiO<sub>5</sub>. For the PL emissions, energy differences to the highest energy ZPL are given. All energies are given in cm<sup>-1</sup>.

#### References

- [1] A. de Andres, S. Tabaoda, J. C. Martinez, M. Dietrich, A. P. Litvinchuk, and C. Thomsen, Phys. Rev B 55, 3568 (1997)
- [2] M. V. Abrashev, G. A. Zlateva, M. N. Iliev, M. Gyulmezov Phys. Rev. B 49, 11783 (1994)
- [3] B. Dareys, P. Thurian, M. Dietrich, M. V. Abrashev, A. P. Litvinchuk, C. Thomsen Phys. Rev B 55, 6871 (1997)
- [4] A. de Andres, S. Tabaoda, J. L. Martínez, A. Salinas, J. Hernández, R. Sáez-Puche Phys. Rev B 47, 14898 (1993)
- [5] M. V. Abrashev, M. N. Iliev Phys. Rev. B 45, 8046 (1992)
- [6] M. Taibi, J. Aride, E. Antic-Fidancev, M. Lemaitre-Blaise, P. Porcher Phys. Stat. Sol. (a) 115, 523 (1989)

## EXCITATION AND DE-EXCITATION OF ERBIUM IONS IN SEMICONDUCTOR MATRICES

I.N.Yassievich, M.S.Bresler, O.B.Gusev, and G.Khitrova<sup>1</sup>

A F Ioffe Physico-Technical Institute, Politekhnikeskaya 26, 194021 St.Petersburg, Russia

<sup>1</sup>Optical Sciences Center, University of Arizona, Tucson, AZ 85721, U.S.A.

**Key words :** erbium ions, excitation of photoluminescence, semiconductor matrices

**Abstract.** We have considered defect-related Auger excitation and de-excitation of erbium ions in semiconductor matrices assisted by multiphonon transitions. The results are applied to explanation of temperature quenching of erbium luminescence in AlGaAs and amorphous silicon.

### Introduction.

Rare earths (RE) are extensively used as dopants in laser active media. The hopes to use semiconductors to achieve electrical pumping of RE centers inserted in semiconductor matrices attracted much attention to these materials (see [1] and references therein). Erbium is especially promising among RE since it emits light with 1.54  $\mu\text{m}$  wavelength corresponding to an absorption minimum of silica glass optical fibers. On introduction of erbium into semiconductor matrices, three of its electrons are spent on formation of valence bonds, therefore the erbium ion occurs in a three-valent  $\text{Er}^{3+}$  state with the ground  $4f^{11}(^4I_{15/2})$  state. The emission at 1.54  $\mu\text{m}$  wavelength arises from internal transitions in the 4f-shell of  $\text{Er}^{3+}$  from the first excited  $^4I_{13/2}$  to the ground  $^4I_{15/2}$  state. We should like to stress that the energy levels of the f-states of RE ion are located well below the valence band edge of the semiconductor (by  $\sim 10$  eV). Since the average radius of the incompletely populated 4f-shell is small, strong screening of the f-orbitals occurs by the outer populated electronic shells with  $5s^25p^6$  configuration. This results in a comparatively weak effect of the crystalline field of the semiconductor matrix on the f-f transitions leading to a relative independence of the position of the erbium PL lines on the pumping intensity, temperature, and nature of the matrix.

There is a strong evidence that erbium ions in semiconductor matrices are excited not by direct absorption of pumping light but via interaction with the charge carriers. The energy transfer from them to the f-electrons is produced by Coulomb interaction. In principle, there are following possible ways of electronic excitation of the f-states: impact excitation by mobile carriers, or various Auger processes: for example, Auger excitation in the recombination process of band electron-hole pairs or excitons, and an Auger process in which the electron (or hole) is captured in a localized state in the forbidden gap. The excess energy released in electron transitions is transferred to the phonon system and/or to a third particle (electron or hole). It was shown that impact excitation was responsible for electroluminescence in Er-doped silicon diodes biased in the reverse direction [2]. The probability of impact excitation of erbium ions was calculated in [3]. There exists an evidence that exciton mechanism is important for erbium ions in crystalline silicon [4].

Here we consider Auger excitation and de-excitation processes assisted by multiphonon transitions. The carriers captured by defects play an important role in this case since electron-phonon coupling is stronger for localized states than for free carriers. We shall treat this problem by the example of Er-doped AlGaAs and amorphous silicon. We shall demonstrate

that the temperature quenching of erbium luminescence can be explained by competition of Auger excitation and multiphonon nonradiative processes.

#### Auger excitation and de-excitation of erbium ions in AlGaAs.

Based on experimental results on erbium photoluminescence in AlGaAs [5], the following model of excitation of the erbium ion 4f-shell was suggested. The pumping radiation generates electron-hole pairs in the erbium-containing AlGaAs region. Holes are quickly captured by the hole traps Dc, Db, and Da induced by erbium at the cation sites and interstitials. Recombination of a free electron and a hole captured by the trap can be radiative, nonradiative multiphonon capture of a free electron, or Auger capture of an electron with excitation of the 4f-shell of an erbium ion (Auger excitation). In the latter case the main part of the recombination energy is transferred to the erbium ion to excite the f-shell via Coulomb interaction. The corresponding transitions are shown in the configuration coordinate diagram of Fig. 1a (processes 1, 2, and 3). In this diagram adiabatic potentials of the unpopulated defect (lower parabola) and that of the system formed by the defect with a captured hole and a free electron in the conduction band (upper parabola) are shown. The dotted line indicates the adiabatic potential for the intermediate (virtual) state of the Auger excitation process when the transition in the electron system has already occurred but the lattice has not yet readjusted. For each of the transitions (1, 2, and 3) the unpopulated defect occurs at first at the excited vibrational level and the transition from this level to the equilibrium vibrational state proceeds by emission of local phonons. Since emission of local phonons is a fast process, the total probability of the transition is determined by the first stage of the process.

The probability of the radiation process (process 1) is only slightly temperature dependent. The main contribution into the temperature dependence of the probabilities of the processes 2 and 3 occurs because of the existence of energy barriers  $\epsilon_{yb}$  and  $\epsilon_{yb}$  which control multiphonon processes determining the readjustment of adiabatic potentials. Such readjustment occurs by thermally activated tunneling of the defect in the configuration space. The temperature dependence of the probability of the thermally activated tunneling involved in the multiphonon nonradiative capture (process 2 in Fig. 1a) is given by the expression:

$$W_2 = W_2^0 \exp(-\varphi_2) \quad (1)$$

$$\varphi_2 = \left\{ \frac{\theta}{2} + \ln \frac{1 + \sqrt{1 + \xi^2}}{\xi} - \sqrt{1 + \xi^2} + \xi \cosh\left(\frac{\xi}{2}\right) \right\} \frac{\epsilon_T}{\hbar \omega_p} \quad (1a)$$

$$\theta = \frac{\hbar \omega_p}{k_B T} \quad (1b)$$

$$\xi = \frac{\Delta \epsilon}{\epsilon_T \operatorname{sh}(\theta/2)} \quad (1c)$$

Here  $\Delta \epsilon = \epsilon_T - \epsilon_L$  is the difference of energies of thermal excitation and defect luminescence,  $\hbar \omega_p$  the energy of local phonon,  $k_B$  the Boltzmann constant, and  $W_2^0$  is assumed to be constant. For the temperature dependence of the Auger excitation we shall obtain correspondingly:

$$W_3 = W_3^0 \exp(-\varphi_3) \quad (2)$$

where  $\varphi_3$  is determined by the expression (1a) where we should replace  $\epsilon_T$  by  $\epsilon_T - \epsilon_{ff}$  and the same procedure we should apply to the formula (1c) for  $\xi$ . The energy  $\epsilon_{ff}$  corresponds to the excitation energy of f-f transition in the erbium ion.

The height of the barrier for the readjustment of adiabatic potentials assisting the Auger excitation process

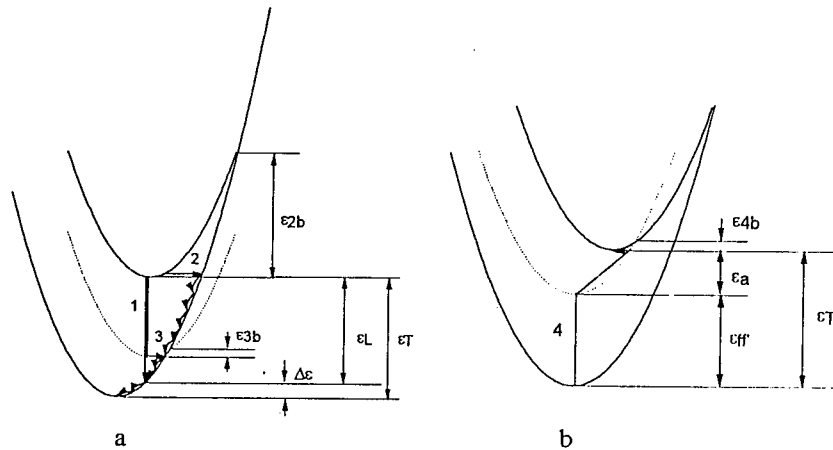


Fig. 1. Configuration-coordinate diagram demonstrating excitation (a) and de-excitation (b) of erbium ions in AlGaAs. The lower parabola corresponds to the adiabatic potential of unpopulated defect. The upper parabola corresponds to the adiabatic potential of a system formed by the defect with a captured hole and a free electron in the conduction band. The intermediate line indicates the adiabatic potential for the intermediate state of the Auger process when the transition in the electron system has already occurred but the lattice has not yet readjusted. In Fig. (a) process 1 is a radiative capture of an electron by the defect, process 2 is a multiphonon nonradiative capture, process 3 is an Auger excitation of erbium ion. Here  $\epsilon_L$  is the luminescence energy of radiative transition,  $\epsilon_T$  is the energy of thermal ionization,  $\Delta\epsilon = \epsilon_T - \epsilon_L$ ,  $\epsilon_{2b}$  and  $\epsilon_{3b}$  are the energy barriers for readjustment of adiabatic potentials in the case of multiphonon capture and Auger excitation, respectively. In Fig. (b)  $\epsilon_{ff}$  is the excitation energy of f-f transition in the erbium ion,  $\epsilon_a$  is the activation energy for the de-excitation process,  $\epsilon_{4b}$  is the energy barrier for readjustment of adiabatic potentials in the case of de-excitation process.

$$\epsilon_{3b} = \frac{(\epsilon_T - \epsilon_{ff} - \Delta\epsilon)^2}{4\Delta\epsilon} = \frac{(\epsilon_L - \epsilon_{ff})^2}{4\Delta\epsilon} \quad (3)$$

is higher, the larger is the difference between the energy of the f-f transition and that of the defect PL  $\epsilon_L$  (see Fig. 1a). Therefore, the probability of the Auger excitation increases on the approach of the energy of defect PL to the excitation energy of the f-f transition (resonance condition).

In the wide-gap AlGaAs alloy the excitation process proceeds via upper states. In this case the reverse process of de-excitation of erbium ions from the lowest excited state  $^4I_{11/2}$ , the initial state of 1.54  $\mu\text{m}$  radiative transition, should be negligible. However, de-excitation processes from the upper excited state to which the f-electron is excited in the Auger process can be important. The corresponding probability increases drastically for resonance conditions. In Fig. 1b the diagram of de-excitation process is shown. The dotted line indicates the adiabatic potential of the virtual state when the electron transition has already occurred but the lattice has not yet readjusted. The de-excitation process consists in a transition of an f-electron of the erbium ion from the excited to the ground state and a simultaneous generation of an electron-hole pair: a free electron appears in the conduction band while the hole is localized on the defect. If the energy of pair generation exceeds the

energy of the f-f transition (see Fig. 1b) the energy deficit is compensated by the lattice playing the role of a thermostat. Thus, the de-excitation process is characterized by an activation energy  $\varepsilon_a = \varepsilon_T - \varepsilon_{ff'}$ . The temperature dependence of the de-excitation process would be determined by this activation energy and also by thermally activated tunneling under the corresponding barrier with the height  $\varepsilon_{4b} = \varepsilon_{3b} = \varepsilon_T - \varepsilon_{ff'}$  controlling the readjustment of the adiabatic potentials (Fig. 1b). As a result the temperature dependence of de-excitation probability will be given by the formula

$$W_4 = W_4^0 \exp\left(-\frac{\varepsilon_T - \varepsilon_{ff'}}{k_B T} - \varphi_3\right) \quad (4)$$

where  $W_4^0$  is again assumed to be independent of the temperature. We can see that realization of the resonance condition favorable for the excitation process also enhances de-excitation.

In the case of excitation of erbium via shallow traps the temperature quenching of erbium PL could be also controlled by the thermal depopulation of shallow defect levels. In the case of excitation via deep defects Da the temperature quenching is no more determined by the thermal depopulation of the Da level. We assumed that in this case the temperature quenching of erbium PL is controlled by a competition between the Auger-excitation and multiphonon nonradiative capture, i.e. by the ratio  $W_3 / W_2$ . In Fig. 2 a comparison is done between the ratio  $W_3 / W_2$  calculated from the formulae (1, 2) and experimental data on the temperature quenching of the erbium PL a line at 1.54  $\mu\text{m}$  (points). In the calculations we assumed that excitation occurs to the  $^4I_{11/2}$  state (with the transition energy  $\varepsilon_{ff'} = 1.26$  eV). For the energy of local phonon we used the value  $\hbar\omega_p = 45$  meV which is close to the energy of optical phonon in AlGaAs. The energies  $\varepsilon_T$  and  $\Delta\varepsilon$  were used as fitting parameters. The best fit was obtained for  $\varepsilon_T = 1.5$  eV and  $\Delta\varepsilon = 0.2$  eV (Fig. 2).

Analysis of eqs.(1) shows that the probability of the multiphonon process decreases with the rise of the thermal energy  $\varepsilon_T$ . This result can be easily seen from the configuration diagram (Fig. 1a). On the rise of  $\varepsilon_T$  the height of the potential barrier for multiphonon transitions

$$\varepsilon_{2b} = \frac{(\varepsilon_T - \Delta\varepsilon)^2}{4\Delta\varepsilon} \quad (5)$$

increases. This means that the temperature quenching of erbium PL induced by an excitation via deep defect level will be reduced on increase of the width of the bandgap. The weakening of the temperature quenching of erbium PL for the semiconductors on increase of the bandgap is known. However, up to now no explanation of this fact was proposed.

#### **Erbium ions in amorphous silicon.**

Recently strong photo- and electroluminescence were observed at room temperature in erbium-doped amorphous hydrogenated silicon, a-Si:H(Er) [6]. Experimental results [6] show that introduction of erbium into amorphous hydrogenated silicon, a-Si:H(Er), leads to rupture of the silicon bonds and formation of D-defects in concentration on the order of  $10^{18}$   $\text{cm}^{-3}$ . Basing on experimental results obtained, a defect-related Auger excitation (DRAE) mechanism was suggested in which a  $D^0 + e \rightarrow D^-$  transition for a dangling-bond D-defect is accompanied by an excitation of f-electron of erbium ion from  $^4I_{15/2}$  to  $^4I_{13/2}$  state. In amorphous matrix the mobile carriers excited into conduction or valence band are fastly thermalized into band tails, therefore, their capture by defects occurs from localized rather than extended electronic states. We have calculated the probability of the DRAE process which is given by



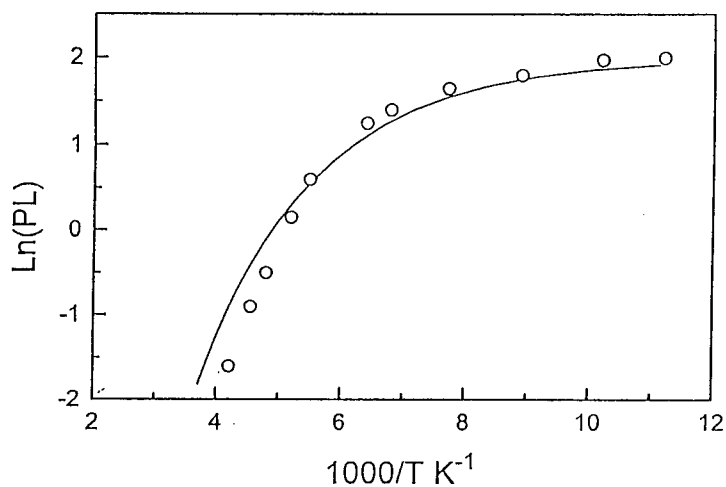


Fig. 2. A comparison of temperature dependence of intensity of erbium luminescence in AlGaAs with theoretically calculated ratio  $W_3/W_2$  of probabilities of the Auger excitation and multiphonon capture.

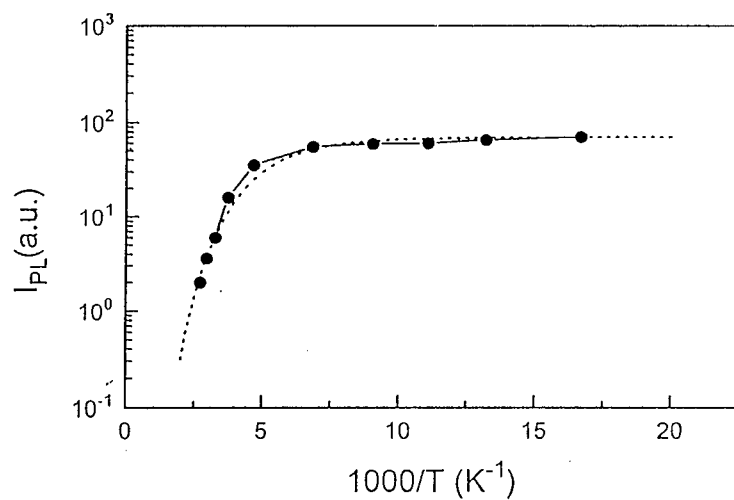


Fig. 3. A comparison of temperature dependence of intensity of erbium luminescence in amorphous silicon with theoretically calculated ratio  $W_3/W_2$  of probabilities of the Auger excitation and multiphonon capture.

$$w_A(R_0) = \frac{8\sqrt{2\pi}}{27} \frac{e^4 d_{ff}^2}{\epsilon_\infty^2 (\kappa a)^4 \hbar \sqrt{\Delta \epsilon k_B T}} \exp(-\epsilon_{ac} / k_B T) \exp\left(-\frac{2R_0}{a}\right) \quad (6)$$

where  $d_{ff}$  denote dipole moments of transitions in the f-shell of erbium ion,  $\kappa^{-1}$  the localization radius of the electron on a defect,  $a$  the localization radius of a state in the conduction band tail,  $\omega_p$  the local phonon frequency,  $R_0$  the distance between the electron in the bandtail and the D center and  $\epsilon_\infty$  the high frequency dielectric constant. As the activation barrier  $\epsilon_{ac}$  for the DRAE process is small, we have written Eq.(6) for the case when multiphonon process occurs via activation. Calculation shows that the DRAE process is more effective than the radiative electron capture by a factor of 7. In our calculations we used the following parameters:  $\epsilon_{opt} = 1.05$  eV,  $\epsilon_l = 0.85$  eV and  $\hbar\omega_p \approx 50$  meV. The temperature dependence of the ratio  $W_3/W_2$  is compared in Fig. 3 with the temperature dependence of the intensity of erbium luminescence. From the similarity of both curves we conjecture that temperature quenching of the erbium luminescence is controlled by the competition of Auger excitation and multiphonon nonradiative capture of electrons by  $D^0$  defects.

### Conclusions.

In conclusion, we have calculated the probability of defect-related Auger excitation and de-excitation of erbium ions for AlGaAs and amorphous silicon assisted by multiphonon transitions. We have demonstrated that the temperature quenching of erbium luminescence in these materials is controlled by competition of Auger excitation and multiphonon nonradiative capture.

This work was partially supported by AFOSR (F49620-94-1-0390), DARPA (DAAH04-95-1-0612), NSF Lightwave Technology (ECS9421517) and International Programs, the Russian Foundation of Basic Research (grant 95-02-04163-a), by INTAS-RFBR 95-0531 grant and by Russian Ministry of Science (grant 97-1036).

### References.

- [1] Rare Earth Doped Semiconductors, edited by G.S. Pomrenke et al. (Materials Research Society, Pittsburgh, 1993); Rare Earth Doped Semiconductors II, edited by A. Polman et al. (Materials Research Society, Pittsburgh, 1996).
- [2] G.Franzo, F.Priolo, S.Coffa, A.Polman, and A.Carnera, Appl. Phys. Lett. **64**, 2235 (1994).
- [3] I.N.Yassievich and L.C.Kimerling, Semicond. Sci. Technol. **8**, 718 (1993).
- [4] M.S.Bresler, O.B.Gusev, B.P.Zakharchenya, and I.N.Yassievich, Phys. Solid State **38**, 813 (1996).
- [5] O.B.Gusev et al., this conference and J. Appl. Phys. (accepted for publication).
- [6] M.S.Bresler et al., Appl. Phys. Lett. **67**, 3599 (1995); O.B.Gusev et al., Appl. Phys. Lett. **70**, 240 (1997); W.Fuhs et al. Phys. Rev. (accepted for publication).

## MECHANISM OF GENERATION OF $f$ - $f$ RADIATION IN SEMICONDUCTOR HETEROSTRUCTURES

G. G. ZEGRYA\*, V. F. MASTEROV\*\*

\*A.F.Ioffe Physical-Technical Institute of Russian Academy of Sciences,

26 Polytekhnicheskaya St., St.Petersburg 194021, Russia

\*\*St.Petersburg State Technical University,

29 Polytekhnicheskaya St., St.Petersburg 194251, Russia

**Keywords:**  $\text{Er}^{3+}$ -doped quantum wells, Auger excitation, laser

### Abstract.

A mechanism is proposed by which inverse distribution of  $\text{Er}^{3+}$   $f$ -electrons can be created in semiconductors with quantum wells. It is shown that, if the electrons are localized in quantum wells, the Coulomb excitation of  $\text{Er}^{3+}$   $f$ -electrons by electrons of the semiconductor has resonant nature. The double Coulomb excitation of  $f$ -electrons,  $I_{15/2} \rightarrow I_{11/2}$  and  $I_{15/2} \rightarrow I_{13/2}$ , produces electron population inversion for the  $I_{13/2}$  level. A possibility is demonstrated of developing a laser with wavelength  $\lambda = 1.54 \mu\text{m}$  based on  $I_{13/2} \rightarrow I_{15/2}$  transitions.

### Introduction.

Recently much interest has aroused in studying the impurity photoluminescence of rare earth (RE) elements in semiconductors [1, 2]. Attention is attracted to the greatest extent by investigations of  $\text{Er}^{3+}$  luminescence in the semiconductors  $\text{A}_3\text{B}_5$  and Si, aimed at designing a laser with the wavelength  $\lambda = 1.54 \mu\text{m}$  (the transition  $^4I_{13/2} \rightarrow ^4I_{15/2}$ ) [3-6]. However, the mechanism by which population inversion is created for  $f$ -electrons and stimulated emission occurs still remains unclear.

The Auger recombination is known to be a primary mechanism of  $f$ - $f$  luminescence excitation in a forward-biased  $p$ - $n$  junction, while under reverse bias the key role is played by impact excitation of the  $f$ -shell. Despite certain advantages of the impact excitation mechanism (here, in particular, is meant the possibility of exciting transitions from the ground state into various excited states at a sufficient energy of hot carriers, with no need to have electron and hole levels localized at the RE center and having an energy separation in resonance with the  $f$ - $f$  transition), it seems highly improbable that a laser could be developed on the basis of a reverse-biased  $p$ - $n$  structure. The primary reason for the lack of lasers based on  $f$ - $f$  transitions and utilizing the above-listed ways of excitation is, in the first place, the impossibility of creating a population inversion for carriers on the  $f$ -level of  $\text{Er}^{3+} - I_{13/2}$ . As is known, population inversion can be created for carriers on the  $I_2$  level in a three-level system ( $I_1, I_2, I_3$ ) provided that the lifetime of a carrier on level  $I_3$  is much shorter than that on the  $I_2$  level. In the case of  $\text{Er}^{3+}$  the lifetime of a carrier on the level  $I_{11/2}$  is of the same order as that on the level  $I_{13/2}$ , despite the fact that here we have a three-level system ( $4I_{15/2}, 4I_{13/2}, 4I_{11/2}$ ). Therefore, in exciting  $\text{Er}^{3+}$  by the above conventional way we can only equalize the occupancies of the ground ( $I_{15/2}$ ) and excited ( $I_{13/2}$ ) states.

The aim of this paper is to put forward a possible mechanism by which population inversion can be created for  $f$ -electrons in  $\text{Er}^{3+}$  ions placed in a heterostructure with quantum wells (QWs). We are going to consider simultaneous Coulomb (Auger) excitation of the transitions

$^4I_{15/2} \rightarrow ^4I_{11/2}$  and  $^4I_{15/2} \rightarrow ^4I_{13/2}$  in a forward-biased  $p$ - $n$  junction.

#### Double Coulombd excitation of $\text{Er}^{3+}$ $f$ -electrons in QWs

The essence of the new approach described here is as follows. Consider an  $\text{Er}^{3+}$ -doped heterostructure with QWs of two types having different effective forbidden gap widths:  $E_{g1}^{eff} = 1.24$  eV and  $E_{g2}^{eff} = 0.8$  eV (Fig. 1). Erbium is distributed both over the region of QWs and over that of barriers. However, according to recent experimental studies [7], in strained structures  $\text{Er}^{3+}$  is commonly located at the interface. Two types of QWs were chosen so as it would be possible to excite simultaneously the transitions  $I_{15/2} - I_{11/2}$  (excitation energy  $E_{1f}^{ex} = 1.24$  eV  $\equiv E_{g1}^{eff}$ ) and  $I_{15/2} - I_{13/2}$  (excitation energy  $E_{2f}^{ex} = 0.8$  eV  $\equiv E_{g2}^{eff}$ ). Nonequilibrium electrons and holes are produced in the QWs by injection. Recombining, the electron-hole pairs may excite an  $f$ -electron of the impurity center via Coulomb interaction (Auger excitation). In the process, the electrons and holes, localized in the wide gap QW ( $E_{g1}^{eff}$ ), excite via the Auger process the transition  $I_{15/2} - I_{11/2}$ , and electron-hole pairs, localized in the narrow gap well ( $E_{g2}^{eff}$ ), Auger-excite the transition  $I_{15/2} - I_{13/2}$  (see Fig. 1). It is of fundamental importance that: (1) such an excitation has resonant nature, being, therefore, temperature insensitive; (2) the excited levels  $^4I_{11/2}$  and  $^4I_{13/2}$  are populated simultaneously. The transitions of additional electrons from the  $^4I_{11/2}$  level to  $^4I_{13/2}$  make the latter (i.e., the level  $^4I_{13/2}$ ) more populated than the level  $^4I_{15/2}$ , giving rise to population inversion for the level  $^4I_{13/2}$  with respect to the ground state  $^4I_{15/2}$ . Of significance here is the part played by QWs in creating population inversion for  $f$ -electrons.

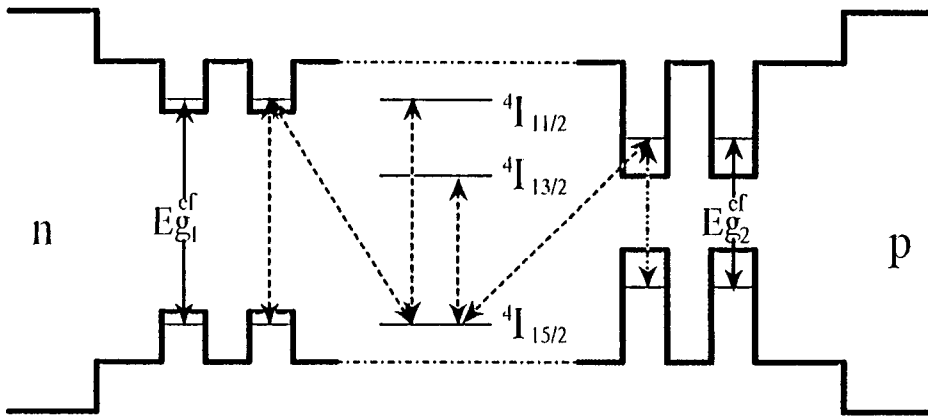


Fig.1 Double Coulomb excitation of  $f$ -electrons.  $I_{15/2} \rightarrow I_{11/2}$  and  $I_{15/2} \rightarrow I_{13/2}$ , by Auger process. Arrows show the possible quantum transition under Auger excitation.

As shown in our previous works (see [8, 9]), Coulomb excitation of  $f$ -electrons by an electron-hole pair localized in a QW is more effective than a similar excitation in the bulk semiconductor: (i) varying the QW width  $a$ , one can always select an effective  $E_g^{eff}(a)$  value, such that it be equal to the energy of Auger excitation of  $f$ -electrons,  $E_{ex}^f$  (resonant Coulomb excitation of  $f$ -electron); (ii) owing to the localization of the electron in a direction perpendicular to the QW, the overlap integral  $I_{ch}$ , entering into the rate of Coulomb excitation of  $f$ -electron, increases; (iii) the existence of a heteroboundary also increases the overlap integral for the transition of an electron from the initial to the excited state in an impurity center [8, 9]. This follows from the fact that the presence of a heteroboundary reduces the symmetry of the intracrystalline field. As a result, states of other parity are added to  $f$ -states, which in the end allows dipole

f-f transitions previously forbidden for parity reasons [10, 11].

We now proceed to a qualitative and quantitative investigation of the mechanism of Coulomb Auger excitation of *f*-electrons in  $\text{Er}^{3+}$ . Here a simultaneous excitation of the transitions  $^4I_{15/2} \rightarrow ^4I_{11/2}$  and  $^4I_{15/2} \rightarrow ^4I_{13/2}$  is concerned. It will be shown below that in calculating the Auger excitation rate there is no need to use an explicit expression for the wave function of *f*-electrons localized on an impurity center. It suffices to know the dipole matrix element for the optical transition between the ground state and an excited state in such a center. The wave functions of carriers in the QW will be calculated in the framework of Kane's model [8, 9].

The rate of Coulomb excitation (Auger excitation) of an *f*-electron by an electron-hole pair in a QW can be calculated in terms of the perturbation theory to a first order in electron-electron interaction:

$$G = \frac{2\pi}{\hbar} N_I \sum_{1,2,3,4} |M|^2 \delta(E_1 + E_3 - E_2 - E_4) f_3^c f_4^h. \quad (1)$$

Here  $N_I$  is the 3D concentration of *f*-electrons in the  $\text{Er}^{3+}$  center;  $f_3^c$  and  $f_3^h$  are the Fermi distribution functions for electrons and holes in a QW;  $E_1, E_3$  are the initial, and  $E_2, E_4$  the final states of electrons in the center and the well, respectively, with the hole state "4" considered as final state "3" for an electron. The matrix element of Coulomb interaction between an electron localized in the impurity center "1" and an electron from the QW "3" can be expressed as follows:

$$M = \frac{4\pi e^2}{\kappa_0} \int \frac{d^3 q}{(2\pi)^3} \frac{1}{q^2} I_{12}(q) I_{34}(-q), \quad (2)$$

where

$$\begin{aligned} I_{12}(q) &= \int \psi_{1c}^*(\mathbf{r}) \psi_{2c}(\mathbf{r}) e^{i\mathbf{q}\mathbf{r}} d^3 r, \\ I_{34}(-q) &= \int \psi_{3c}^*(\mathbf{r}') \psi_{4h}(\mathbf{r}') e^{-i\mathbf{q}\mathbf{r}'} d^3 r', \end{aligned} \quad (3)$$

$q$  is the momentum transferred in the Coulomb interaction of the electrons;  $\kappa_0$  is the permittivity of the medium; and  $\psi_i(\mathbf{r})$  are the wave functions of the particles, calculated in terms of multiband Kane's model [8, 9]. Note that the quantity  $I_{12}(q)$  is proportional to the overlap integral of electron states in the impurity center. Similarly,  $I_{34}(q)$  is proportional to the overlap integral of electrons and holes recombining in QWs.

Resonance *f*-electron excitation occurs in those cases when the energy separation of electron and hole size-quantization levels  $E_g^{ef} = E_g + E_{0c} + E_{0h}$  (where  $E_{0c}$  and  $E_{0h}$  are the energies of ground size-quantization levels of holes and electrons) is exactly the same as that of the ground and excited states of an *f*-electron  $E_{ex}^f$  (Fig. 1). This mechanism of Coulomb excitation of *f*-electrons possesses a remarkable property: it provides a means to control the condition of resonance by varying the QW width  $a$  and composition,  $E_g^{ef}$  depending on  $a$  through  $E_{0c}$  and  $E_{0h}$ .

The wave functions of electrons and holes in the QW are a superposition of band states of *s*- and *p*-type:  $\Psi(\mathbf{r}) = u(\mathbf{r})|s\rangle + \mathbf{v}(\mathbf{r})|\mathbf{p}\rangle$ , where  $u(\mathbf{r})$  and  $\mathbf{v}(\mathbf{r})$  are smooth envelopes of Bloch functions, found from Kane's equations [8, 9]. The overlap integral for electrons and holes in the QW  $I_{34}$  can be expressed in terms of  $u$  and  $\mathbf{v}$  by

$$I_{34} = (2\pi)^2 \delta(\mathbf{q}_4 - \mathbf{q}_2 - \mathbf{q}) \int_{-\infty}^{+\infty} (u_3^* u_4 + \mathbf{v}_3^* \mathbf{v}_4) e^{i\mathbf{q}x} dx, \quad (4)$$

where  $\mathbf{q}_3$  and  $\mathbf{q}_4$  are the momenta of electron and hole in the QW plane. Using Kane's equations [8, 9], we get

$$u_3^* u_4 + v_3^* v_4 = \frac{1}{E_4 - E_3} \text{div } \mathbf{S}_{34}, \quad (5)$$

where:

$$\mathbf{S}_{34} = i\gamma (u_3^* v_4 + u_4 v_3^*),$$

$\gamma$  is Kane's matrix element. Substituting (4) and (5) in (2) and integrating with respect to  $q_x$ , we obtain

$$M = -i \frac{2\pi}{\kappa_0} \frac{e^2}{E_g^{eff}} \left\{ \frac{\mathbf{q}_{34}}{|\mathbf{q}_{34}|} \mathbf{d}_{12}^{\parallel} \int e^{-|x||\mathbf{q}_{34}|} \text{div } \mathbf{S}_{34} dx + i d_{12}^x \int \text{sign } x e^{-|x||\mathbf{d}_{34}|} \text{div } \mathbf{S}_{34} dx \right\}, \quad (6)$$

where  $\mathbf{d}_{12} = (d_{12}^x, \mathbf{d}_{12}^{\parallel})$ ,  $\mathbf{q}_{34} = \mathbf{q}_3 - \mathbf{q}_4$ ,  $\mathbf{v}_4 = (v_4^x, v_4^{\parallel})$ ,  $\text{sign } x = 1$  for  $x > 0$  and  $\text{sign } x = -1$  for  $x < 0$ ,  $\mathbf{d}_{12} = \int d^3r \Psi_1^*(\mathbf{r}) \mathbf{r} \Psi_2(\mathbf{r})$  is proportional to the dipole matrix element for the transition of an  $f$ -electron from the ground state "1" into the excited state "2" in the  $\text{Er}^{3+}$  impurity center. In deriving (6) we kept used the following approximation:  $I_{12}(q) \approx i q \mathbf{d}_{12}$ . This is justified since  $q r \approx q_T / \kappa = (T/E_{ex}^f)^{1/2} \ll 1$ , where  $q_T = (2m_c T / \hbar^2)^{1/2}$  is the thermal momentum of electron,  $\kappa^{-1} = (2m_c E_{ex}^f / \hbar^2)^{-1/2}$  is the characteristic length of  $f$ -electron localization on the impurity center,  $m_c$  is the electron effective mass. Performing integration with respect to  $x$  in (6), we get for the squared modulus of the matrix element

$$|M|^2 = \left( \frac{4\pi e^2}{\kappa_0} \right)^2 |\mathbf{d}_{12}|^2 \frac{\gamma^2}{(E_g^{eff})^2} \left| \mathcal{L} \left( \frac{a}{2} \right) \right|^2, \quad (7)$$

where :

$$\mathcal{L} \left( \frac{a}{2} \right) \approx -\frac{i}{(8a)^{1/2}} \left( \frac{du_3^*}{dx} \right)_{x=\frac{a}{2}} \frac{k_{4x}}{k_{4x}^2 + (\mathbf{q}_3 - \mathbf{q}_4)^2},$$

$$\left( \frac{du_3^*}{dx} \right)_{x=\frac{a}{2}} \approx -\frac{\pi}{a} \left( \frac{2}{a} \right)^{1/2},$$

$k_{4x}$  is the heavy hole wave vector component in the direction perpendicular to the heteroboundary,  $a$  is the QW width. As follows from (7), the matrix element for the Coulomb excitation of  $f$ -electrons depends on the QW width  $a$  via the overlap integral  $I_{34}$ , with  $|M|^2 \propto a^{-4}$ . Such a dependence of  $|M|^2$  on the QW width follows from the fact that, according to (7),  $I_{34} \propto (du_3/dx) v_4$ ;  $v_4 \propto a^{-1/2}$ ,  $(du_3/dx) \propto a^{-3/2}$ . Consequently,  $I_{34} \propto a^{-2}$ . Further, we substitute the expression (7) derived for the matrix element into (1). Performing summation over initial and final states of the particles, we obtain the rate of Auger excitation of  $f$ -electron

$$G = 8\pi \frac{E_B}{\hbar} \left( \frac{E_{0c}}{T} \right)^2 \frac{m_c}{m_h} \lambda_{E_g}^2 |\mathbf{d}_{12}|^2 N_I n p \exp(-\delta\epsilon/T). \quad (8)$$

Here  $E_B = m_c e^4 / 2\hbar^2 \kappa_0^2$  is the Bohr energy of electron-electron interaction,  $n$  and  $p$  are the two-dimensional concentrations of electrons and holes,  $m_h$  is the effective mass of heavy holes,  $\lambda_{E_g} = \hbar / (2m_c E_g^{ef})^{1/2}$ ,  $\delta\epsilon = E_{ex}^f - E_g^{ef} > 0$ ,  $E_{0c} = \hbar^2 \pi^2 / (2m_c a^2)$ . Since the  $E_g^{ef}$  value can be controlled by varying the QW width  $a$  and composition, the true resonance can be approached ( $\delta\epsilon \rightarrow 0$ ). Here we set :  $\delta\epsilon \ll T$ , so that:  $\exp(\delta\epsilon/T) \simeq 1$ .

### Discussion.

The inverse time of Coulomb excitation of  $f$ -electron  $1/\tau = G/N_I$  is proportional to the quantity  $d_{12}$ . In addition,  $1/\tau$  strongly depends on the QW width,  $1/\tau \propto a^{-4}$ . It should be noted that expression (8) can be used to evaluate the Coulomb excitation of the two transitions

$^4I_{15/2} \rightarrow ^4I_{11/2}$  and  $^4I_{15/2} \rightarrow ^4I_{13/2}$ . For both of these the frequency of Coulomb excitation of  $f$ -electrons  $\tau^{-1} \sim 10^9 - 10^{10} \text{ s}^{-1}$ . To evaluate  $\tau^{-1}$ , we used the following parameters for the QW based on InGaAsP/InP:  $m_c = 0.04m_0$ ,  $m_h = 0.4m_0$ ,  $a = 70 \text{ \AA}$ ,  $E_g^{ef} = 0.8 \text{ eV}$ ,  $n = p = 10^{12} \text{ cm}^{-2}$ ,  $d_{12} = 10^{-7} \text{ cm}$ . The characteristic time of spontaneous radiative recombination of  $f$ -electrons in  $\text{Er}^{3+}$ ,  $\tau_f \sim 10^{-3} - 10^{-4} \text{ s}$ , is by many orders of magnitude longer than the time of their Coulomb excitation  $\tau$ , i.e.,  $\tau_f \gg \tau$ . Consequently, the given mechanism of Coulomb excitation of  $f$ -electrons is rather efficient. Even in the case when the  $\text{Er}^{3+}$  concentration  $N_I$  exceeds the concentration of electron-hole pairs by several orders of magnitude, all erbium ions will be excited. Apparently, for the  $I_{15/2} \rightarrow I_{11/2}$  transition to be excited, heterostructures should be used with barrier height exceeding 1.3 eV.

The InP/In<sub>x</sub>Ga<sub>1-x</sub>As<sub>y</sub>P<sub>1-y</sub>/InP heterostructure is the most suitable for creating population inversion for  $f$ -electrons by the above method. A resonator can be easily fabricated in such a structure. For In<sub>x</sub>Ga<sub>1-x</sub>As<sub>y</sub>P<sub>1-y</sub> QWs, the compositions  $x$  and  $y$  are selected so that, at a given QW width  $a$ ,  $E_{g1}^{ef} = 1.24 \text{ eV}$  for one pair of  $x$  and  $y$  values and  $E_{g2}^{ef} = 0.8 \text{ eV}$  for the other.

It should be noted that high erbium concentrations  $N \geq 10^{19} \text{ cm}^{-3}$  cause heteroboundary smearing in perfect superlattices of the type AlGaAs/GaAs [12]. Therefore, strained InP/InGaAsP structures should be used, as noted in Ref. 7. The optimal lasing structure must contain several QWs with  $E_{g1}^{ef} = 1.24 \text{ eV}$  and several wells with  $E_{g2}^{ef} = 0.8 \text{ eV}$ . The QWs with  $E_{g2}^{ef}$  must be arranged symmetrically about the middle of the waveguide (the  $X$ -axis) (see Fig. 1). Such an arrangement of QWs corresponds to the maximum gain  $g_f$  for the  $f$ -radiation.

In order for the  $f$ -radiation not to be absorbed in a QW with  $E_{g2}^{ef} = 0.8 \text{ eV}$ , one should create a concentration of electrons and holes such that the coefficient of intraband absorption  $\alpha_i$  be less than the losses associated with the mirrors  $1/L \ln(1/R)$ , where  $L$  is the resonator length, and  $R$  is the reflection coefficient by power. This means that in a QW with  $E_{g2}^{ef} = 0.8 \text{ eV}$ , the carrier concentration should be close to the transparency threshold ( $n_{tr} \sim 10^{12} \text{ cm}^{-3}$ ). At these electron and hole concentrations, the Auger excitation of  $f$ -levels,  $I_{11/2}$  and  $I_{13/2}$ , is so strong that it corresponds to a high gain for  $f$ -radiation  $g_f > 1/L \ln(1/R)$ . This means that, as soon as the condition  $g_f = 1/L \ln(1/R) + \alpha_i$  starts to be fulfilled, generation of  $f$ -radiation is initiated very abruptly. It is significant that, if the inversion threshold is achieved in a QW with  $E_{g2}^{ef} = 0.8 \text{ eV}$ , this suppresses practically entirely inverse Auger excitation of electrons in the QW by  $f$ -electrons. The estimates show that in the steady generation regime the characteristic time of stimulated  $f$ -transitions  $\tau \sim 10^{-7} \div 10^{-8} \text{ s}$ , with an expected radiation power of such a laser of about 100 mW, and a threshold current density  $J_{th} \sim 200 \text{ A/cm}^2$ . In estimating  $J_{th}$ , we used the above-listed parameters of an InGaAsP/InP structure. The  $J_{th}$  value is proportional to the inversion threshold, and for a structure with four QWs the main contribution to  $J_{th}$  comes from the currents of radiative and Auger recombination:  $J_{th} = eBn_{th}^2 + eC_A n_{th}^3$ , where  $B$  is the coefficient of radiative recombination, and  $C_A$  is the coefficient of Auger recombination. For our QWs:  $B = 1.2 \cdot 10^{-4} \text{ cm}^2/\text{s}$ ,  $C_A = 2 \cdot 10^{-16} \text{ cm}^4/\text{s}$ .

Note in conclusion that we have proposed an efficient mechanism by which population inversion can be created for  $f$ -electrons in  $\text{Er}^{3+}$ -ion-doped heterostructures with QWs. In these heterostructures the laser generation of  $f$ -radiation with wavelength  $\lambda = 1.54 \mu\text{m}$  is possible. Since the  $f$ -electrons being excited by resonance mechanism, the radiation intensity practically temperature insensitive.

The work was supported by AFOSR and INTAS.

## References.

- [1] Rare-Earth Doped Semiconductors. MRS Proc., v. 301, ed. by G. Pomrenke, P. Klein, D. Langer (1993).

- [2] Rare-Earth Doped Semiconductors. MRS Proc., v. 422, ed. by A. Polman, S. Coffa, R. N. Schwartz (1996).
- [3] S. J. Chang, K. Takahei, Appl. Phys. Lett. **65**, 433 (1994).
- [4] G. Franzo, F. Priolo, S. Coffa, A. Polman, A. Carnero, Appl. Phys. Lett. **64**, 2235 (1994).
- [5] B. Zheng, J. Michel, F. Y. G. Ren, L. C. Kimerling, D. C. Jacobson, J. M. Poate, Appl. Phys. Lett. **64**, 2842 (1994).
- [6] T. Kimura, A. Yokoi, Y. Nichida, R. Saito, S. Yugo, Appl. Phys. Lett. **67**, 2687 (1987).
- [7] H. M. Gibbs, G. Khitrova, L. G. Gerchikov, V. F. Masterov, T. R. Stepanova, N. N. Faleev (to be published)
- [8] G. G. Zegrya, V. F. Masterov, Semiconductors **29**, 989 (1995).
- [9] G. G. Zegrya, V. F. Masterov, Proc. SPIE **2706**, 235 (1996).
- [10] G.S. Ofelt, J. Chem. Phys., **37**, 511 (1962)
- [11] B.R. Judd, Phys. Rev, **127**, 750 (1962)
- [12] O. B. Gusev, B. Ya. Ber, M. S. Bresler, I. N. Yassievich, B. P. Zakharchenya, V. F. Masterov, E. K. Lindmark, J. P. Prineas, H. M. Gibbs, G. Khitrova, Appl. Phys. Lett. (in print).



## INFRARED INDUCED EMISSION FROM SILICON QUANTUM WIRES

N.T. Bagraev, E.I. Chaikina, W. Gehlhoff<sup>1</sup>, L.E. Klyachkin,  
I.I. Markov, and A.M. Malyarenko

A.F. Ioffe Physico-Technical Institute, St.Petersburg, 194021, Russia  
<sup>1</sup>Technische Universität Berlin, Institut für Festkörperphysik,  
Hardenbergstr. 36, D-10623 Berlin, Germany

**Keywords:** silicon quantum wires, lasing oscillations, impurity dipoles

**Abstract.** We present the first findings of the infrared induced emission from the silicon quantum wires, which is due to the formation of a correlation gap in the DOS of degenerate hole gas. The quantum wires of this art are created by electrostatic confining potential inside ultra-shallow p<sup>+</sup>n junctions which are realized using controlled surface injection of self-interstitials and vacancies in the process of non-equilibrium boron diffusion.

### 1. Introduction

Properties of excitonic insulators harnessed in semiconductor crystals are known to be difficult to study as a consequence of many obstacles posed by the decay of three dimensional charge correlations [1,2]. Excitonic insulators can be stabilized in two- and one-dimensional systems because of the enhancement of Kohn screening singularities and exciton binding energies [3]. So far, the two-dimensional excitonic instability has been predicted for dangling bonds at dislocations [4] and semiconductor surfaces [3]. As a result of strong charge/spin correlations, a narrow metallic band of one-electron dangling bonds is likely to be split into two subbands forming a gap in the density of states (DOS) of the two-dimensional electron/hole gas. Such a 'freezing' of two-dimensional charge correlations should be suppressed under external electric fields, which ought to stimulate the infrared emission due to the annihilation of the excitons localized at dangling bonds or shallow impurities. Therefore, ultra-shallow silicon p<sup>+</sup>n junctions, which contain a two-dimensional degenerate hole gas, being analogues of semiconductor surfaces, represent the best candidate for the observation of the radiative annihilation of low-dimensional excitonic correlations localized at shallow centres, a spectral study of which was a goal of the present work.

### 2. Experimentals

The diffusion experiments involving boron were performed from the gas phase into 350 µm thick n-type Si (100) wafers. The working and back sides of the wafers were previously oxidized using a thermal oxidation process. Windows corresponding to the geometry for the Hall effect measurements were then opened up on the working side of the platelets by photolithography. The parameters varied in the course of the short time diffusion of boron were the oxide overlayer thickness, diffusion temperature (800°C-1100°C) and Cl levels in the gas phase. Diffusion profiles measured using the SIMS technique reveal the depths to be in the range from 5 nm to 30 nm (Figs. 1a and b).

The impurity diffusion in semiconductors is known to be accelerated when there are excess fluxes of self-interstitials (the kick-out diffusion mechanism) or vacancies (the dissociative vacancy diffusion mechanism) which are generated by the oxidized surface [5]. The use of thin SiO<sub>2</sub> layers combined with high diffusion temperatures leads to a sharp intensification of the kick-out diffusion mechanism (curves 1 and 2 in Fig. 1a), while thick SiO<sub>2</sub> layers and low diffusion temperature, in contrast, stimulate the dissociative vacancy diffusion mechanism and increase the dopant concentration (curves 3 and 4 in Fig. 1a). The p<sup>+</sup>n junctions are seen to be anomalously shallow at the diffusion temperature of 900°C which provides the parity between the kick-out and dissociative vacancy diffusion mechanisms.

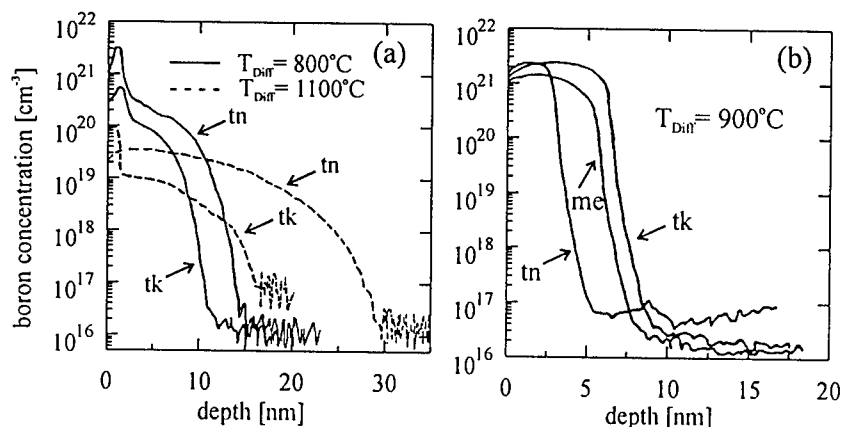


Fig. 1: SIMS data for the ultra-shallow  $p^+$ -diffusion profiles obtained for the boron dopant at diffusion temperatures of 1100°C and 800°C (a) and 900°C (b) in n-type silicon (100)-wafers with oxide overlayers of different thickness characterized by thin (tn), medium (me) and thick (tk).

The ultra-shallow diffusion profiles obtained were studied using cyclotron resonance (CR) and quantized conductance (QC) techniques. The CR measurements were carried out at 3.8 K with an X-band (9.1-9.5 GHz) EPR spectrometer[6]. The CR quenching brought about the deflection of the magnetic field from the normal to the diffusion profile plane reveals the anisotropy of both electron/hole effective mass in silicon bulk and Landau level scheme in heavily doped quantum wells spontaneously formed inside the ultra-shallow diffusion profile during non-equilibrium diffusion process [6].

The CR findings and current-voltage (CV) characteristics measured at different angles between the  $p^+n$  junctions plane and the bias voltage show that the  $p^+$ -diffusion profiles obtained at 900°C consist of self-assembly longitudinal quantum wells (LQW) (Fig. 2a), whereas the diffusion profiles at 1100°C and 800°C contain lateral quantum wells (LaQW) (Fig. 2b) oriented respectively along the  $\langle 111 \rangle$  and  $\langle 100 \rangle$  crystallographic directions. Besides, the quantized conductance measurements at different angles obtained at high temperature (77 K and 300 K) (Figs. 3a and b) has revealed the quantum wires induced inside self-assembly quantum wells by a strong electrostatic confining potential [7] due to impurity charge correlations.

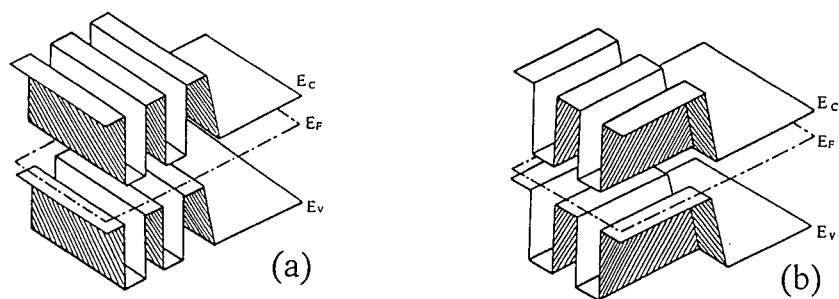


Fig. 2: Three dimensional diagram of the one-electron band scheme of an ultra-shallow  $p^+n$  junction which is a system of LQW (a) and LaQW (b)

Temperature dependencies of the thermal friction coefficient (Fig. 4) [8] as well as the forward and reverse CV characteristics [8] demonstrate the formation of a correlation gap in the DOS of the de-

generate hole gas in the crystallographically oriented quantum wires (Fig. 5). The dispersion in the energy of a correlation gap is dependent on local fluctuations in the dopant distribution along a quantum wire thereby determining a regime of both longitudinal and lateral quantum wires from a strongly correlated metal to weak localization [8]. The results obtained can be explained in the framework of the model for a quantum wire due to the charge correlations created by the elastic reconstruction of a shallow boron acceptor as a result of negative-U reaction:  $2B^0 \rightarrow B^+ + B^-$ , which is accompanied by the formation of the  $C_{3v}$  symmetry dipole ( $B^+ - B^-$ ) centres that cause the correlation gap in the DOS of the degenerate hole gas (Fig. 5).

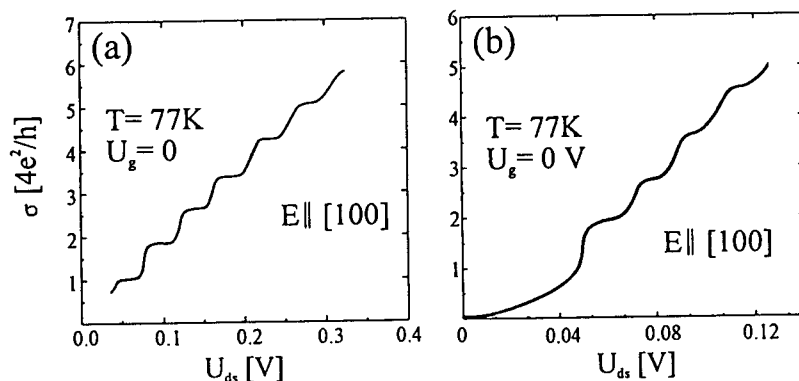


Fig. 3: The quantized conductance (QC) at 77 K vs crystallographically-oriented voltage applied along longitudinal (a) and lateral (b) self-assembly quantum wells.

The fluctuations of the correlation gap value represent the places of the creation of isolated quantum dots under the gate voltage. The generation of similar quantum wires with isolated quantum dots using external electric fields could be responsible for the infrared emission induced by the injection of non-equilibrium carriers (Fig. 5).

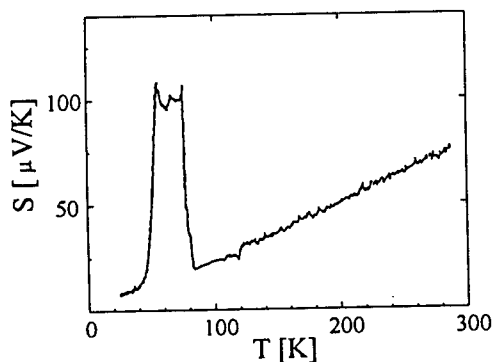


Fig. 4: Temperature dependence of the thermo-emf (Seebeck coefficient) due to the isolated quantum wire with the single fluctuation of the correlation gap, which was obtained in  $p^+$ -diffusion profile at 900°C and a thin oxide overlayer.

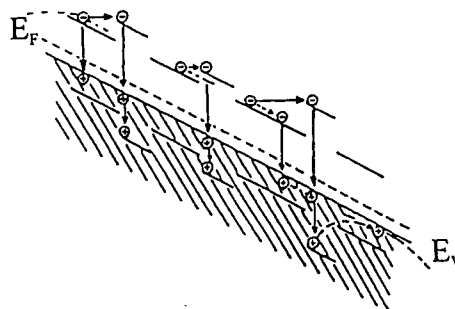


Fig. 5: One-electron band scheme for a quantum wire with a correlation gap under the passage of a longitudinal current along the ultra-shallow  $p^+$ -diffusion profile.

Using a ST-50 double monochromator and infrared photorecorders based on cooled InSb, the high power infrared (IR) emission was found, for the first time, under forward (Fig. 6a) and reverse (Fig. 6b) voltage applied to ultra-shallow silicon  $p^+n$  junctions (Figs. 1a and b) as well as under the pas-

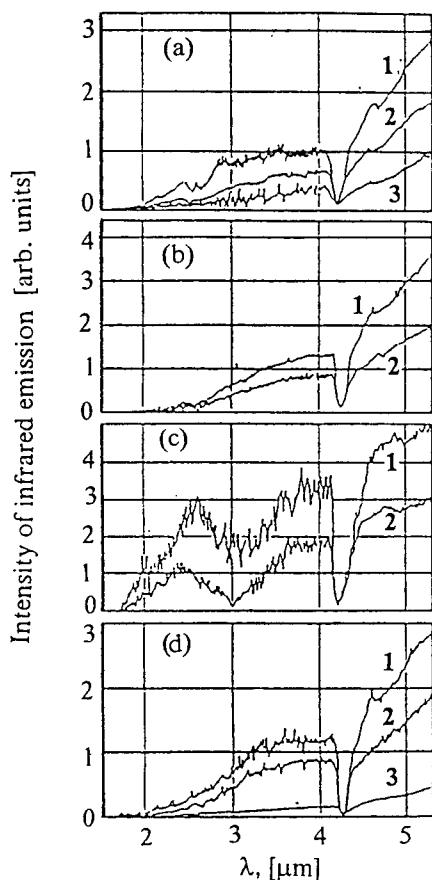


Fig. 6: The spectrum of the infrared emission from the ultra-shallow silicon  $p$ - $n$  junctions under forward (a) and reverse (b,c,d) voltage at 300 K (a,b,d) and 77 K (c).

The depth of the ultra-shallow  $p^+$ -diffusion profile corresponds to the following curves in Fig. 1b: (d) to curve tk and (a,b,c) to the curves tk, me, tn, respectively.

The power of infrared emission at the different current value are: (a) 100  $\text{mW}\cdot\text{mm}^{-2}$ , 200 mA (curve 1); 60  $\text{mW}\cdot\text{mm}^{-2}$ , 150 mA (curve 2); 30  $\text{mW}\cdot\text{mm}^{-2}$ , 100 mA (curve 3). (b) 55  $\text{mW}\cdot\text{mm}^{-2}$ , 60 mA (curve 1); 40  $\text{mW}\cdot\text{mm}^{-2}$ , 30 mA (curve 2). (c) 25  $\text{mW}\cdot\text{mm}^{-2}$ , 150 mA (curve 1); 15  $\text{mW}\cdot\text{mm}^{-2}$ , 130 mA (curve 2). (d) 270  $\text{mW}\cdot\text{mm}^{-2}$ , 30 mA (curve 1); 180  $\text{mW}\cdot\text{mm}^{-2}$ , 30 mA (curve 2); 40  $\text{mW}\cdot\text{mm}^{-2}$ , 30 mA (curve 3).

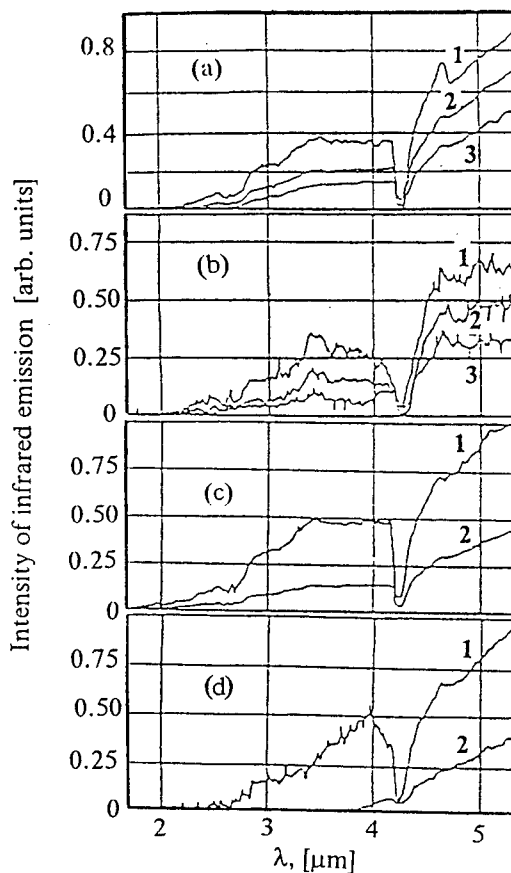
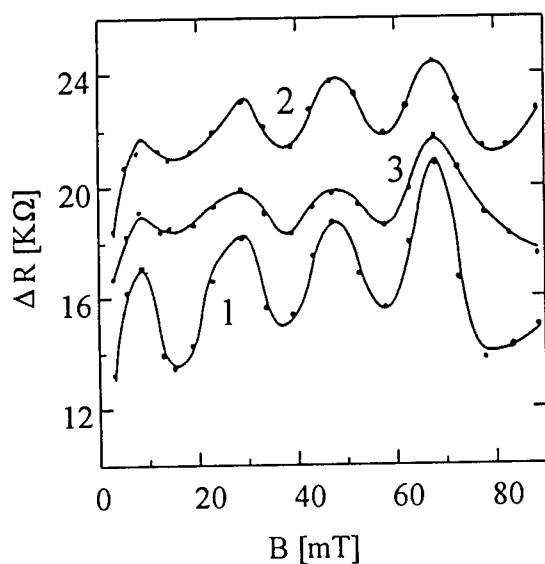


Fig. 7: The spectrum of the infrared emission from the ultra-shallow silicon  $p^+n$  junctions under the passage of a longitudinal current along the ultra-shallow  $p^+$ -diffusion profile at 300 K (a,c,d) and 77 K (b).

The depth of the ultra-shallow  $p^+$ -diffusion profile in (a,b,c,d) corresponds to the following curves in Fig. 1a: curves 2 (a,b,c) and 1(c) to the 800°C-curves tn and tk, respectively; curves 1(d) and 2(d) to the 1000°C-curves tn and tk, respectively. The power of the infrared emission at the different current value are: (a) 900  $\text{mW}\cdot\text{mm}^{-2}$ , 100 mA (curve 1); 680  $\text{mW}\cdot\text{mm}^{-2}$ , 50 mA (curve 2); 450  $\text{mW}\cdot\text{mm}^{-2}$ , 35 mA (curve 3). (b) 100  $\text{mW}\cdot\text{mm}^{-2}$ , 250 mA (curve 1); 80  $\text{mW}\cdot\text{mm}^{-2}$ , 200 mA (curve 2); 45  $\text{mW}\cdot\text{mm}^{-2}$ , 160 mA (curve 3). (c) 1600  $\text{mW}\cdot\text{mm}^{-2}$ , 50 mA (curve 1); 680  $\text{mW}\cdot\text{mm}^{-2}$ , 50 mA (curve 2). (d) 360  $\text{mW}\cdot\text{mm}^{-2}$ , 150 mA (curve 1); 90  $\text{mW}\cdot\text{mm}^{-2}$ , 150 mA (curve 2).

sage of a longitudinal current along the  $p^+$ -diffusion profiles (Fig. 7). The emission intensity is seen to increase with increasing current and with decreasing the depth of the ultra-shallow  $p^+$ -diffusion profile (Figs. 6 and 7). Moreover, the emission ability of the ultra-shallow  $p^+$ -n junctions is lower at 77 K than at 300 K. A dip in the emission spectra at  $\lambda = 4.27 \mu\text{m}$  corresponds to the IR absorption due to the natural abundance of  $\text{CO}_2$  in the atmosphere. The power of the IR emission has been found to demonstrate the threshold character on reverse/longitudinal current and decrease sharply when the depth of the ultra-shallow  $p^+$ -diffusion profile exceeds 20 nm [8,9]. These two facts indicate the important role low-dimensional charge correlations in the generation of the IR emission from the ultra-shallow silicon  $p^+$ -n junctions. Therefore, the results obtained can be explained in the framework of the model for a quantum wire due to strong charge correlations, which were identified using CR and QC techniques (Fig. 5).

The infrared emission results obtained represent the basis toward the infrared silicon lasers in which both electrons/holes and photons are fully quantized. The dipole impurity microcavity that is the length of the quantum wire restricted by two isolated quantum dots is shown to produce the lasing oscillations at the wavelengths determined by a correlation gap value, which coincide with the resonance wavelength of the microcavity. The dimension of the microcavity ( $d$ ) has been found to reveal from the period of the Aharonov-Bohm-like magnetoconductance oscillations ( $\Delta B$ ) [10] in the external magnetic field perpendicular to the self-assembly QW plane:  $\hbar/2e = \Delta B \cdot S$ , where  $S = \pi d^2/4$ ;  $d/2n \approx \lambda$ , ( $n=1,2,3,\dots$ ); and  $\lambda$  is the resonance wavelength of the microcavity (Fig. 8).



from the period of the Aharonov-Bohm-like magnetoconductance oscillations ( $\Delta B$ ) [10] in the external magnetic field perpendicular to the self-assembly QW plane:  $\hbar/2e = \Delta B \cdot S$ , where  $S = \pi d^2/4$ ;  $d/2n \approx \lambda$ , ( $n=1,2,3,\dots$ ); and  $\lambda$  is the resonance wavelength of the microcavity (Fig. 8).

Fig. 8: The Aharonov-Bohm-like magnetoconductance oscillations observed in the ultra-shallow silicon  $p^+$ -n junctions under the electrical field applied along the self-assembly LQW. The periodicity of the oscillations is determined by the relationship  $\Delta\Phi = \hbar/2e$ ;  $\hbar/2e = \Delta B \cdot S$ ;  $\lambda \approx d \approx (2\hbar/\pi e \Delta B)^{1/2}$  is the wavelength of the infrared emission, which coincides with the dimension of the microcavity ( $d$ ).

$U_{ds}$ : 1 - 0.18V; 2 - 0.29V; 3 - 0.35V.

The value of the resonance wavelength ( $\lambda \approx 3591 \text{ nm}$ ) that is obtained from the magnetoconductance measurements is in a good agreement with the data of the dynamic spectrum narrowing found with studying the same structure that identifies the fabrication of the microcavity inside the Si quantum wire in which both holes and photons are fully quantized (Figs. 9).

The threshold character of the irradiative power and dynamic spectrum narrowing found at 3591 nm, 3744 nm, 3969 nm, 4457 nm and 4881 nm as a function of the current that traverses the quantum wire due to strong charge correlations are evidence of light stimulated emission from silicon nanostructures (Figs. 9 and 10).

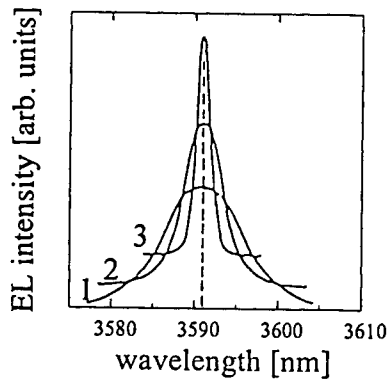


Fig. 9: The electroluminescence spectra recorded at 300 K under the passage of a longitudinal current along the ultra-shallow silicon  $p^+$ -diffusion profile obtained at the diffusion temperature of 900°C in the n-type silicon (100)-wafer with a thin oxide layer. 1 - 30 mA, 2 - 50 mA, 3 - 70 mA.

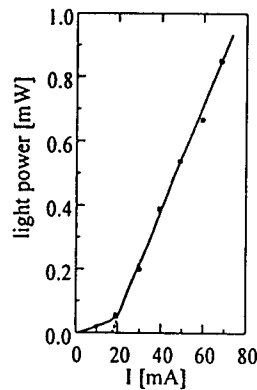


Fig. 10: The dependence of the radiative power on the longitudinal current along the ultra-shallow silicon  $p^+$ -diffusion profile obtained at the diffusion temperature of 900°C in the n-type silicon (100)-wafer with a thin oxide layer.  $T=300\text{K}$ ,  $\lambda=3591\text{ nm}$ .  $I_{th} = 18\text{ mA}$ .

### 3. Summary

The generation of the silicon quantum wires with isolated quantum dots using external electric fields applied along the self-assembly diffusion quantum wells has been found to be responsible for the infrared emission in the range 1-10  $\mu\text{m}$ , which is induced by the injection of non-equilibrium carriers into quantum wire systems. The dipole impurity microcavity that is a length of quantum wire restricted by two isolated quantum dots has been shown to produce the lasing oscillations at the wavelengths determined by a correlation gap value, which coincide with the resonance wavelength of the microcavity. The threshold character of the irradiative power and dynamic spectrum narrowing that has been found as a function of the current traversed the quantum wire with isolated quantum dots are evidence of the light induced emission from silicon nanostructures. These results represent the basis toward the infrared silicon lasers in which both electrons/holes and photons are fully quantized.

### References

1. N.F. Mott, *Phil.Mag.*, **6**, 287 (1961).
2. B.I. Halperin, T.M.Rice, *Solid State Phys.*, **21**, 115 (1968).
3. E. Tosatti, P.W. Anderson, *Solid State Commun.*, **14**, 773 (1994).
4. V.V. Kveder, *Defect and Diffusion Forum*, **103-105**, 431 (1993).
5. N.T. Bagraev, L.E.Klyachkin and V.L.Sukhanov, *Defect and Diffusion Forum*, **103-105**, 20 (1993).
6. W. Gehlhoff, N.T. Bagraev and L.E. Klyachkin, *Solid State Phenomena*, **47-48**, 589 (1995).
7. N.T. Bagraev, L.E. Klyachkin and A.M. Malyarenko, *Int.Symp. Nanostructures 95*, St. Petersburg, Abstracts, 280 (1995).
8. N.T. Bagraev, E.V. Vladimirovskaya, V.E. Gasumyants, V.I. Kaidanov, L.E. Klyachkin, V.V. Kveder, A.M. Malyarenko, E.I. Chaikina and A.I. Shalynin, *Semiconductors*, **29**, 1112 (1995).
9. N.T. Bagraev, L.E. Klyachkin and E.I. Chaikina, *JETP Lett.*, **58**, 598 (1993).
10. T. Ando, *Proc. of the ICPS-23*, ed. by M. Scheffler and R.Zimmermann, (Singapore:World-Scientific) pp. 59-68 (1996)

## ACCEPTOR STATES IN BORON DOPED SiGe QUANTUM WELLS

K.Schmalz\*, M.S.Kagan, I.V.Altukhov, K.A.Korolev, D.V.Orlov, V.P.Sinis,  
S.G.Tomas\*\*, K.L.Wang\*\*, and I.N.Yassievich\*\*\*

Institute of Radioengineering and Electronics of RAS, 11, Mokhovaya, 103907 Moscow,  
RUSSIA.

\* Institute for Semiconductor Physics, Walter-Korsing str., 2, 15230 Frankfurt (Oder),  
Germany

\*\* University of California, 66-147KK Engineering IV, Los Angeles, CA 90095, USA

\*\*\* A.F.Ioffe Physico-Technical Institute of RAS, 26, Politekhnikeskaya, 194021  
St.Petersburg, RUSSIA

**Keywords:** *SiGe* quantum wells, transport properties, acceptor states

### Abstract.

The temperature dependences of lateral conductivity and hole mobility in *SiGe* quantum well structures selectively doped with boron are presented. The boron  $A^+$  centers are found to exist and determine the low-temperature conductivity. The activation energy of conductivity at higher temperatures is shown to be determined by the energy distance between strain-split boron  $A^0$  centers. The model of two-stage excitation of free holes including the thermal activation of holes from the ground to split-off state and next tunneling into the valence band is proposed. The binding energy of  $A^+$  centers and the energy splitting of boron ground states by strain are found.

### Introduction.

Selectively doped *SiGe* quantum well structures (QWs) are of great interest for study of acceptor states which are degenerate in bulk material and should be split in two-dimensional (2D) systems due to space quantization and/or strain. The energy positions of ground and excited states of an acceptor can be controlled in a wide range by alloy composition, QW width, doping level and space position of an acceptor center. In this report, the binding energies of 2D positively charged ( $A^+$ ) acceptor states and strain-splitting energy of neutral ( $A^0$ ) states in boron doped *SiGe* QWs for structures with the same QW width and doping level and different alloy composition are determined. So-called  $A^+$  states (acceptors binding an additional hole) [1,2] are of specific interest as they should exist in *SiGe* QWs in thermal equilibrium in contrast to bulk material where they can appear only due to excitation, e.g., by light. Similar  $D^-$  states of donors have been investigated in GaAs/GaAlAs structures [3,4].

### Experiment.

The *p*-type *Si/SiGe/Si* QWs MBE-grown pseudomorphically on the *n*-type *Si* substrate and selectively doped with boron were used for conductivity and magnetoconductivity measurements at the temperatures of 4 up to 300 K. The *SiGe* layer of 20 nm thickness was sandwiched between undoped *Si* buffer (130 nm wide) and cap (60 nm) layers. The *SiGe* QW was uniformly doped with boron; the *B* concentration was of  $3 \cdot 10^{17} \text{ cm}^{-3}$ . The content of *Ge*, *x*, in *SiGe* alloy was 0.1 and 0.15, respectively. Two boron delta layers with *B* concentration of  $2 \cdot 10^{11} \text{ cm}^{-2}$  positioned within the buffer and cap layers on the distance of 30 nm from each QW interface were used to obtain  $A^+$  centers inside the QW. The buffer delta layer should also supply holes to form the *p-n* junction between the *p*-layers and the *n*-substrate. This hole concentration  $N_{pn}$  was calculated by the expression:  $N_{pn} = (\kappa N_d \Phi / 2\pi e^2)^{1/2}$ ,  $\kappa$  is the dielectric constant,  $N_d$  is the donor concentration in the substrate,  $\Phi$  is the initial difference of Fermi energies in *n*- and *p*-regions ( $\Phi \approx 1 \text{ eV}$ ), taking into account the total depopulation of donors in space charge region. From the measurements of donor-bound exciton luminescence, we have  $N_d \approx 2 \cdot 10^{14} \text{ cm}^{-3}$  for the QWs with  $x=0.1$  and  $N_d \approx 5 \cdot 10^{14} \text{ cm}^{-3}$

for  $x=0.15$ . (We are indebted to A.S.Kaminskiy for obtaining this data.) So, we get that the concentration in the buffer delta layer is diminished by  $N_{pn} \approx 5 \cdot 10^{10} \text{ cm}^{-2}$  and  $8.5 \cdot 10^{10} \text{ cm}^{-2}$  for above structures.

The contacts were deposited on the  $p$ -type side of structures so that the  $p$ - $n$  junction prevented from a current along the substrate.

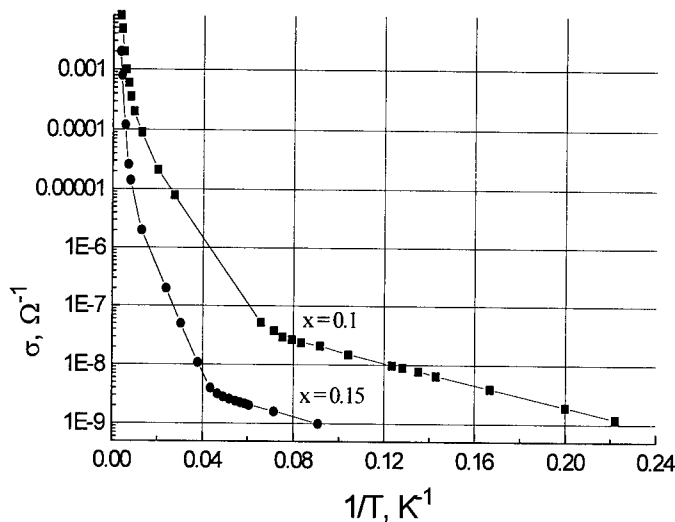


Fig.1. Temperature dependence of conductivity.

conductivity,  $H$  is the magnetic field,  $c$  is the light velocity). The temperature dependence of  $\mu$  is shown in Fig.2. The maximum in the  $\mu(T)$  dependence points at the change of scattering mechanism. Note the comparatively high mobility values.

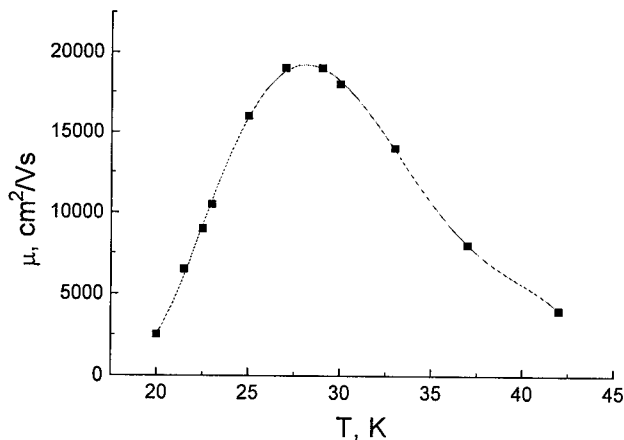


Fig.2. Temperature dependence of hole mobility for  $x=0.1$ .

Figure 1 shows, in  $\log-1/T$  scale, the temperature dependence of conductivity along the  $\text{SiGe}$  layer for the samples with 0.1 and 0.15 Ge content,  $x$ . One can see two activation-law regions in the curves. The low-temperature activation energy is approximately 2 meV and practically coincides for the samples with different Ge content. The activation energy at higher temperatures ( $T \geq 20 \text{ K}$ ) is of  $12 \pm 1 \text{ meV}$  for  $x=0.1$  and  $19 \pm 1 \text{ meV}$  for  $x=0.15$ . The hole mobility,  $\mu$ , was determined from the measurements of transverse magnetoconductivity by means of the expression  $\Delta\sigma/\sigma = (\mu H/c)^2$  ( $\sigma$  is the

#### Discussion.

There are two possible explanations of the observed exponential temperature dependence of conductivity. First, the low-temperature activation energy ( $\approx 2 \text{ meV}$ ) can be due to the thermally activated hopping conductivity. In dependence on the Fermi level ( $\epsilon_F$ ) position, the hopping can be over neutral ( $A^0$ ) boron states if  $\epsilon_F \approx \epsilon^0$ ,  $\epsilon^0$  is the  $A^0$  binding energy, or positively charged  $A^+$  states if  $\epsilon_F \approx \epsilon^+$ , it is  $A^+$  centers binding energy. The main argument against the hopping is the

low conductivity observed. Really, at the given doping level in QW,  $3 \cdot 10^{17} \text{ cm}^{-3}$ , the mean distance



between impurities ( $\approx 8$  nm) is of the order of the effective Bohr radius of impurity, which can be estimated by the expression  $a_B \approx \hbar/\sqrt{2m\epsilon_B}$ . Using linear interpolation of *GeSi* parameters between *Si* and *Ge*, we get  $a_B \approx 2.5$  nm for  $A^0$  and  $\approx 10$  nm for  $A^+$  states [5]. Because of strong overlapping impurity states, the specific (on square) conductivity value can not be less than 1 - 10 kOhm (see, f.i., [6] for references). It is several orders of magnitude more than the experimental values.

The second possible origin of 2 meV activation energy can be the thermal hole emission from  $A^+$  states. The calculation of the  $A^+$  binding energy [6] gives just  $\epsilon^+ \approx 2$  meV, being weakly dependent on *Ge* content in *SiGe* alloy. The necessary condition for conductivity due to thermal activation of  $A^+$  centers is the Fermi level to be near  $\epsilon^+$  at low temperatures. Let's now discuss this possibility for our samples. Shown in Fig.3 is the schematic view of the valence band potential profile of the QW structures investigated. Due to charged *B*-delta layers, two barrier regions with linear potential distribution should appear outside of QW. To find the Fermi level position and then the temperature

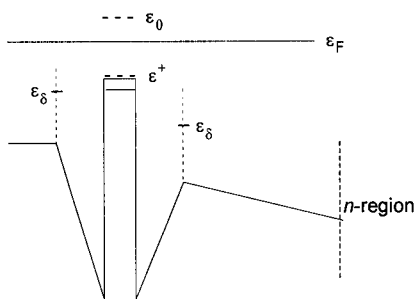


Fig.3. Schematic view of *SiGe* QW valence band structure.

dependence of free hole concentration we used the following set of equations:

$$\begin{aligned} N_{1,2} &= N_\delta \{1 + \exp[-(\epsilon_\delta - \epsilon_{1,2})/kT]\}^{-1}, \\ N - N^- - N^+ &= N \{1 + \exp[-(\epsilon_0 - \epsilon_F)/kT]\}^{-1}, \\ N^+ &= N \{1 + \exp[-(\epsilon^+ - \epsilon_F)/kT]\}^{-1}, \\ \epsilon_1 &= \epsilon_F - \Delta + (4\pi e^2 d/\kappa) [N_1 - (N_2 - N_{pn}) + N^+ - N + p], \\ \epsilon_2 &= \epsilon_F - \Delta + (4\pi e^2 d/\kappa) [-N_1 + (N_2 - N_{pn}) - N^+ + N - p], \\ N_1 + N_2 + N &= N^+ + p. \end{aligned}$$

Here  $N_{1,2}$  are the concentrations of empty (negatively charged) *B* centers in the cap and buffer  $\delta$ -layers, respectively,  $N_\delta$  and  $N$  is the *B* concentration in  $\delta$ -layers and in *SiGe* QW,  $N^+$  and  $N^-$  are the concentrations of positively and negatively charged *B* centers in the QW,  $p = N_v \exp(\epsilon_F/kT)$  is the free hole concentration and  $N_v$  is the density of states in the QW,  $\epsilon_\delta$ ,  $\epsilon_0$ , and  $\epsilon^+$  are the binding energies of *B* centers in *Si*, and boron- $A^0$  and  $A^+$  centers in the *SiGe* QW,  $\Delta$  is the valence

band offset,  $d=30$  nm is the distance between the  $\delta$ -layers and QW interfaces,  $\kappa$  is the dielectric constant. The QW top energy was taken for zero. The calculated temperature dependence of hole

concentration  $p$  for  $x=0.1$  and for different  $\delta$ -layer doping level is presented in Fig.4. The main feature of curves is the absence of a free hole density saturation at the temperatures of depopulation of the  $A^+$  level which should exist at similar conditions in the bulk material. The reason for such a behavior is the absence of local charge neutrality and "horizontal" redistribution of carriers between the QW and  $\delta$ -layers with changing temperature.

The values of the binding energies of  $A^0$  and  $A^+$  centers,  $\epsilon_0$  and  $\epsilon^+$ , was varied to fit the experimental curve. The

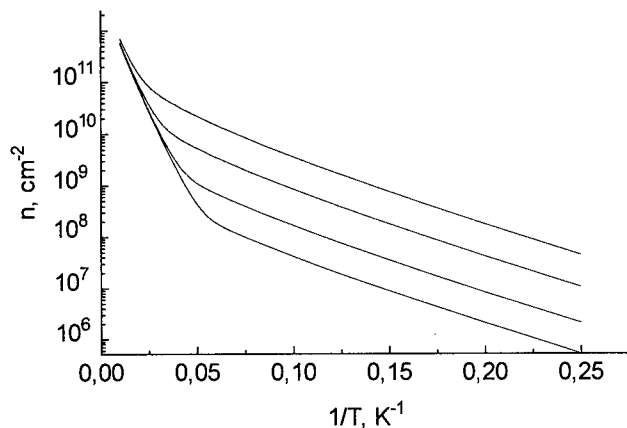


Fig.4. Calculated temperature dependence of hole concentration in QW at various  $\delta$ -layer doping level.

parameters for the best fit are the following:  $\epsilon_0 = 24$  meV and 36 meV for  $x=0.1$  and  $x=0.15$ , respectively,  $\epsilon^+ = 2$  meV and  $N_\delta = 10^9 \text{ cm}^{-2}$  for both structures. Thus the low-temperature activation energy is the binding energy of the boron  $A^+$  centers in QW. However, the extra hole concentration supplied into QW turns out to be two orders less than the doping level of  $\delta$ -layers. The only reason for this seems to be  $Si$  surface states which can accumulate almost all holes from the  $\delta$ -layers.

The origin of activation energy at higher temperatures is not so obvious. It should be one half of boron- $A^0$  binding energy because the Fermi level lies between the valence band edge and the  $B^0$  ground state as it is filled. So, the observed high-temperature activation energies, 12 and 18 meV, correspond to 24 and 36 meV  $B^0$  binding energies. These values are, however, quite surprising. Indeed, the binding energy of shallow impurity should decrease with increasing both  $Ge$  content and strain, it is quite the contrary to the experiment. Moreover, the value of  $\epsilon_0 = 24$  meV seems not to be real for  $x=0.1$ .

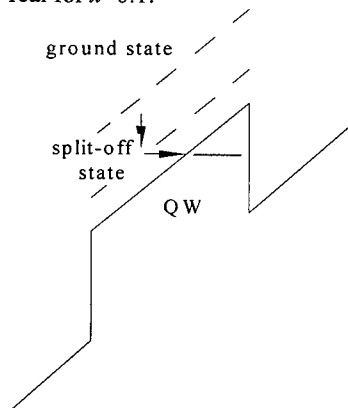


Fig.5. Scheme of conductivity activation by tunneling.

The only energy which could agree with the above values of  $\epsilon_0$  is the energy difference between acceptor levels split by strain. Indeed, the splitting energy of the ground acceptor state found by means of linear interpolation between  $Si$  and  $Ge$  is  $\approx 15$  and 25 meV for  $x=0.1$  and  $x=0.15$ , respectively. This is close to the experimental activation energies. (Note that the estimation of the energies by interpolation is very approximate.) The splitting energy can be as the activation one only if holes can pass from the split-off state into the valence band without activation, that is by tunneling. It is impossible in the scheme of flat bands. On the other hand, we have seen from the experiment that almost all holes from the  $\delta$ -layers accumulate in the surface states making the surface charged. So, the potential across the structure should appear inclining the valence bands. The scheme of potential distribution for this case is shown in Fig.5. One can see from this scheme that the conductivity in this case can be controlled by

two-stage process: first, the thermal activation of holes from the ground to split-off state takes place and then hole tunneling into free hole band creates the conductivity. To estimate the possible potential drop across the structure, let's remember an empirical law that for most homeopolar semiconductors the Fermi energy is fixed on the surface near 1/3 of the energy gap from the valence band. It is  $\approx 0.4$  eV for  $Si$ . The QW width is 5 times less than the structure width. So, the potential drop on the QW is of  $\approx 80$  meV. Of course, this estimation is too rough but it shows that the proposed model can be real. Thus, the arguments for the model are (i) the increasing activation energy of conductivity with  $Ge$  content, (ii) small additional hole concentration supplied from  $\delta$ -layers into the QW, and (iii) charging the surface and arising the potential drop across the QW, as a consequence.

### Summary.

The experimental data presented give evidence for existence of  $A^+$  centers in  $B$  doped  $SiGe$  QW structures in thermal equilibrium. The thermal emission of holes from these centers determines the conductivity along the QW at low temperatures. At higher temperatures, the conductivity is shown to be due to thermal activation of holes from the ground to strain-split  $B$  states following by hole tunneling into the QW valence band. The tunneling is made possible due to a potential drop across the QW which arise due to hole capture at surface states of the  $Si$  cap layer making the surface charged. Note that in structures with doping profile and level investigated, it is possible to find the energy splitting of acceptor levels by strain from temperature dependence of conductivity.

This work was supported in part by Grants No 96-02-17352 and 97-02-16820 from RFBR, No 97-10-55 from Russian Ministry of Science and Technology and Volkswagen Stiftung Grant.

---

**References.**

1. E.M.Gershenzon, Yu.P.Ladyzhenskii, and A.P.Mel'nikov, JETP Lett., **14**, 380 (1971)
2. E.E.Godik, Yu.A.Kuritsyn, and V.P.Sinis, JETP Lett., **14**, 377 (1971).
3. S.Huant, S.P.Najda, and B.Etienne, Phys.Rev.Lett., **65**, 1486 (1990).
4. D.M.Larsen, S.Y.McCann, Phys.Rev.B, **46**, 3966 (1992).
5. K.Schmalz, I.N.Yassievich, K.L.Wang, and S.G.Tomas, Phys.Rev.B (1997), in print
5. B.I.Shklovskii and A.L.Efros, Electronic Properties of Doped Semiconductors, Springer, Heidelberg (1984)
6. I.N.Yassievich, K.Schmalz, M.A.Odnobludov, and M.S.Kagan, Proc. 7th Int.Conf. on Modulated Semicond. Structures, 152, Spain (1995)

## COULOMB INTERACTION BETWEEN CARRIERS LOCALIZED IN InAs/GaAs QUANTUM DOTS AND ON POINT DEFECTS

M.M.Sobolev, A.R.Kovsh, V.M.Ustinov, A.Yu.Egorov, A.E.Zhukov, M.V.Maximov and  
N.N.Ledentsov

A.F.Ioffe Physical Technical Institute, 194021 St. Petersburg, Russia

**Key words:** quantum dots, defects, DLTS

**Abstract.** In this work we report on the deep level transient spectroscopy (DLTS) and capacitance-voltage (C-V) studies of InAs/GaAs vertically coupled quantum dot structures inserted in an active region of laser diode. We found that DLTS spectra are changed dramatically for isochronous annealing temperatures below and above 245K and for cooling conditions: bias voltages  $V_b=0$  or of filling pulse voltages  $V_f>0$ . They are bound up with manifestation of the effect of Coulomb interaction between carriers captured in quantum dots and on point defects located in regions close to the dots, and dipoles are formed after annealing below 245K at  $V_f>0$  and in the absence its after annealing above 245K. It has been observed that in the dipoles the carriers from deep levels can tunnel into quantum dots from which they were previously thermally evaporated.

### Introduction.

Studies of quantum confined low dimensional systems are of considerable interest from the point of view of fundamental physics and for technological applications, since they can be treated as artificial trap with unique the possibilities to tailor their electrical and optical properties [1-3]. A remarkable progress in this area has been achieved recently with direct growth methods involving self-organization phenomena. [1]. The first injection laser with low current density and high temperature stability based on InAs and InGaAs quantum dots in GaAs matrix was demonstrated at A.F.Ioffe Institute [2]. The typical lateral size of the dots is smaller than 20 nm, providing a strong confinement in three dimensions. Additionally, the formation of new type of QDs structures i.e. vertically coupled QDs via tunneling suitable for fabrication of cascade laser was also demonstrated. At the same time the specific growth conditions of the QDs (deposition at low temperature) must stimulate the generation of the point defects in the vicinity of QDs due to a local stoichiometry variation during the growth of a heteroepitaxial layer [4-5]. They acts as capture and nonradiative recombination centers. Near room temperature, the thermal emission of the carriers from quantum dots and the point defects retrapping by the defects causes a decrease of the quantum efficiency of the radiative recombination and finally degradation of the lasers.

Defects with deep levels in low dimensional structures have, on the other hand, exciting application as new tools for structure engineering. Among the latter tunable band discontinuities using doping interface dipoles, interaction phenomena between deep levels and minibands would add a powerful degree of freedom in the design of materials and may lead to the development of new devices [6-7]. A new use of quantum dots in wavelength-domain-multiplication memory using spectral-hole burning was proposed [8]. A system with such a capability could be used to read and write data using an optical signal, based on the quantum dots bleaching effect and will be suitable for application to high-density memory. Also, current instabilities in low dimensional heterostructures are of great interest due to the possibility of multi-stage switching, and bistable behavior [9-10].

In this work we report on the deep level transient spectroscopy (DLTS) and capacitance-voltage (C-V) studies of InAs/GaAs vertically coupled quantum dot (VECOD) structures inserted in an active region of laser diode. We find that in DLTS spectra besides, clear signal due to localization of carriers in quantum dots. Additionally, signal due to deep traps was revealed in the region spatially coincident with quantum dots. We observed a manifestation of the effect Coulomb interaction between carriers localized in quantum dots and on point defects, and bistable dipoles formation. We also report on the first detection of the effect tunneling of the carriers between states of the VECOD and point defects.

### Experimental

The structures were grown in a Riber 32P molecular beam epitaxy system on  $n^+$ -GaAs  $\langle 100 \rangle$  Si-doped substrates. To form the vertically coupled quantum dots array, the QD sheets of 5Å InAs and 50Å GaAs spacers were successively deposited six times. QD active region was inserted into the center of  $p^0$  GaAs layer of GaAs- $Al_xGa_{1-x}$ As double heterostructure laser diode. The dots have a well-developed pyramid-like shape with base sides along  $[100]$  and  $[010]$  directions. The vertically coupled quantum dots are separated by a several-monolayer-thick GaAs layer. DLTS spectra and C-V measurements were carried out on laser diodes by BIO-RAD DL4600 spectrometer. The capacitance was measured on a Boonton-72B bridge operating at a frequency of 1 MHz. The sensitivity of this apparatus is  $\Delta C/C_0 \approx 10^{-4}$ .

### Results

The apparent carrier concentration profiles (ACCP) of the InAs/GaAs vertically coupled quantum dot (VECOD) laser structure obtained from 1 MHz C-V measurements are shown in Fig.1. These measurements show that at zero base the space-charge region of the studied sample takes up the optical confinement layer, including QD active region, and the sample is of very little leakage current. C-V measurements were carried out by applying the forward bias to the sample for determining the apparent carrier concentration profile of the structure in the QD active region and the waveguide. It can be seen from Fig.1 that in center of the waveguide the peak related with an accumulation of the carriers is observed. Since the region involving VECOD was manifested when

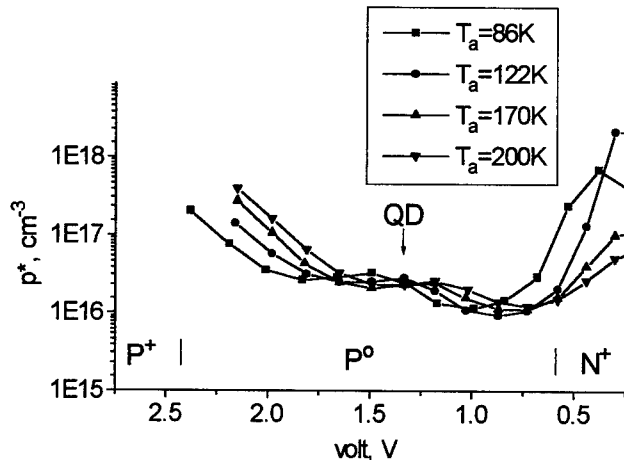


Figure 1 The apparent carrier concentration profiles of the InAs/GaAs vertically coupled quantum dot (VECOD) laser structure obtained from 1 Mhz C-V measurements.

applying the forward bias to the sample, this is caused to modify DLTS measurements. We apply different combinations of bias voltages  $V_b$  and of filling pulse voltages  $V_f$  to perform the DLTS study of the regions below, coincident, and above the layer with VECODs. To vary the occupation of the dots and defects with deep levels and in accord with the result of the C-V measurements, the filling pulse ( $V_f$ ) was applied in the forward bias. Its magnitude varied from 1.7 up to 0.95 V. The filling pulse duration was 5 $\mu$ s. The DLTS signals was detected when the voltage applied in the forward bias. The detection bias ( $V_b$ ) varied from 0.9 to 1.6V and always  $V_b < V_f$ . The capacitance of the sample was easily compensated at the DLTS measurements. This clearly demonstrated that the forward current was insignificant and did not lead to dramatic change the capacitance of the sample. All the DLTS measurements were performed under dark condition, unless specially indicated. Before each scan, the sample was isochronously annealing for 1.0 min. at a fixed temperature  $T_0$ . This temperature varied from 240 to 300K. The sample then was cooled to the  $T=80$ K in two regimes: with applied forward bias  $V_f$  and  $V_b=0$ . DLTS measurements made during the warm up cycle before 300K. We found that DLTS spectra are changed dramatically for isochronous annealing

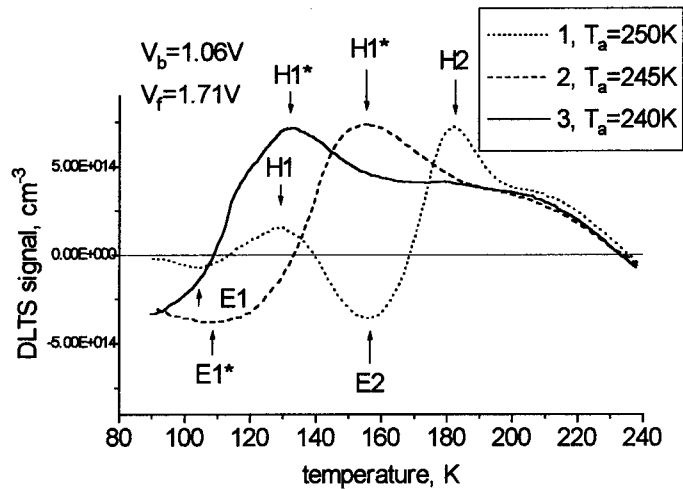


Figure 2. DLTS spectra of InAs/GaAs vertically coupled quantum dot structures at the various isochronous annealing temperatures  $T_a$  and preliminary cooling conditions  $V_f > 0$ .

temperatures below and above 245 K and for cooling conditions  $V_f > 0$  or  $V_b = 0$  (Fig.2). The thermal activation energies ( $E_a$ ) and the capture cross sections ( $\sigma_{n,p}$ ) of levels observed in DLTS spectra were determined from Arrhenius plots (Table). The emission rate of the carrier is given by

$$e_{n,p} = A \sigma_{n,p} T^{3/2} \exp(-E_a/kT) \quad (1)$$

where  $A$  is a constant independent of temperature,  $k$  is Boltzmann's constant.

After annealing at  $T_a > 245$  K, apart H2, H3 and E2, E3 levels, E1 electron and H1 hole levels were observed (Table). The DLTS measurements showed unusual properties of the H1 level ( $T_a > 245$  K) at varying  $V_b$  (Fig.3) and of the H1\* level ( $T_a < 245$  K) at varying  $V_f$  (Fig.4). The position of the H1 peak in DLTS spectra was shifted to the regions of the low temperatures. To the contrary, the amplitude and shape of the peak were unchanged. This peak was emerged at  $V_b = 1.0$  V and disappeared at  $V_b = 1.3$  V. The thermal activation energy of the H1 level was 194 meV at  $V_b = 1.07$  V. In the beginning a sharp decrease of the amount  $E_a$  to 132 meV and then slow increases were happened with increase of the  $V_b$  up to 185 meV at  $V_b = 1.30$  V. In that case the increase  $V_b$  was corresponded to decreasing of p-n junction-induced electric field. When varying  $V_f$  the H1 peak was appeared at  $V_f > 1.4$  V and was saturated at  $V_f = 1.7$  V. These changes were accorded with localization of the peak of the apparent carrier concentration profiles (Fig.1). Furthermore, other deep traps (H2, H3) have been revealed in the region spatially coincident with QDs. At increasing  $V_b$  the H2, H3 peaks disappeared and the broad E3 peak was emerged. The amplitude of the H2, H3 peaks did not depend on amount of filling pulse. After annealing at  $T_a < 245$  K the peaks, related to E1, E2, H1 and H2 levels, disappeared and other broader E1\* and H1\* peaks appeared (Fig.4). The position of the H1\* peak in DLTS spectra depended on values of  $V_f$ , annealing temperature  $T_a$ , cooling conditions ( $V_f > 0$  or  $V_b = 0$ ) (Fig.4) and optical illumination. The thermal activation energy of the H1\* level also varied from 132 to 199 meV with  $V_f$  and  $T_a$ . After illumination and cooling at  $V_f > 0$ , when the carriers from QDs photoexcited, peak is shifted towards the position measured at  $V_f = 0$ . The amplitude H1\* and H2\* peaks were decreased at increasing of the  $V_b$  and they has disappeared at  $V_b = 1.30$  V that also verified a spatial localization the H1\* and H2\* levels. The thermal activation energies of the E1 and E1\* levels were coincident and equaled 110 meV.

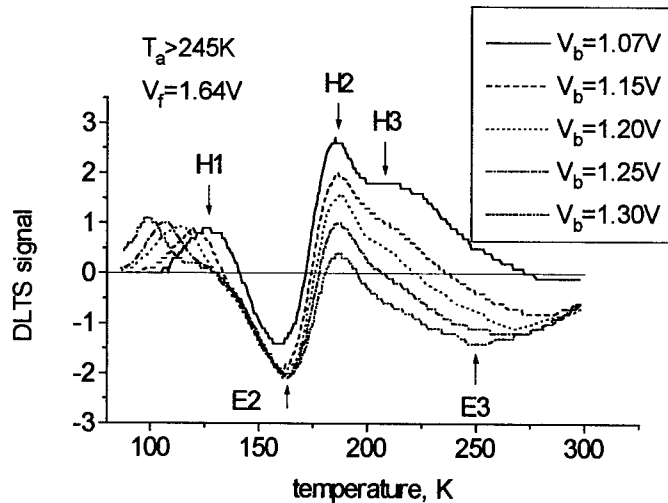


Figure 3. DLTS spectra of InAs/GaAs vertically coupled quantum dot structures at the various  $V_b$  and after annealing at  $T_a > 245\text{K}$  and preliminary cooling conditions  $V_b = 0$ .

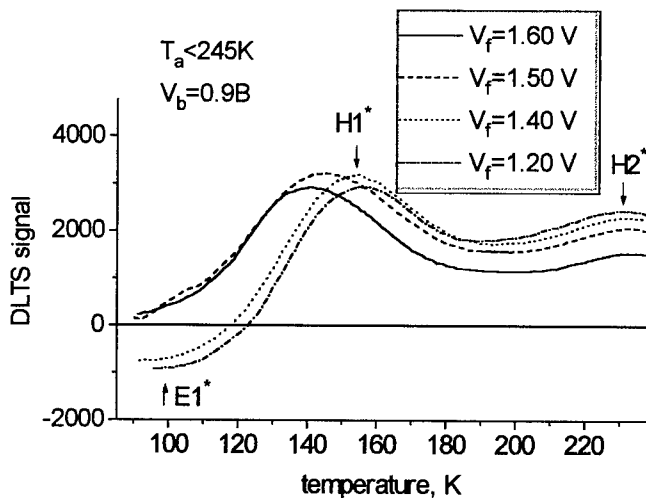


Figure 4. DLTS spectra of InAs/GaAs vertically coupled quantum dot structures at the variable  $V_f$  and after annealing at  $T_a < 245\text{K}$  and preliminary cooling conditions  $V_f > 0$ .

#### Discussion.

The results of the DLTS investigation (Fig.2-4 and Table 1) allows to associate H2, H3, H2\* and E2, E3 levels with that well known for GaAs. Our investigations showed that the point defects forming at low temperature GaAs growth during multiple InAs-GaAs deposition cycles were like those forming in GaAs under Ga-rich condition. Among them is HL5 [11] defect with energies 390 meV and well known for GaAs EL14 [12]. Also it is quite possible that in this GaAs a antisite double acceptor  $\text{Ga}_{\text{As}}$  with ionization energies 77 and 230 meV from the valence-band edge is generated[13].

The behavior of H1 and H1\* levels depending on condition of the isochronous annealing (annealing temperature also varying  $V_b$  and  $V_f$ ) can not be understood as to one of the defect, including a metastable defect. The position of the peak in DLTS spectra for this defect may depend on annealing temperature  $T_a$  and cooling conditions ( $V_f > 0$  or  $V_b = 0$ ), but it must not depend on values of filling pulse voltages  $V_f$ . In paper [15] S.Forrest and O.K.Kim observed dependence of the

Table

Deep level No.	Energy, meV	Cross section, cm <sup>2</sup>	Identification and origin
$T_a > T_{ac}$			
E1	111	$1.7 \times 10^{-17}$	
E2	235	$1.3 \times 10^{-14}$	EL14(Ni)[12]
E3	426	$4.2 \times 10^{-16}$	NiGa [14]
H1	194	$2.5 \times 10^{-16}$	
H2	390	$1.8 \times 10^{-13}$	HL5 [11]
H3	420	$1.6 \times 10^{-14}$	HL4(Cu)[11]
$T_a < T_{ac}$			
E1*	110	$5.2 \times 10^{-16}$	
H1*	194	$2.5 \times 10^{-18}$	
H2*	420	$1.6 \times 10^{-14}$	HL4(Cu)[11]

acceptor did not yet trap holes and has a negative charge. The density of Ga<sub>As</sub> and H2 defects as well as holes trapped in QDs coincided and were equal  $\approx 10^{11} \text{ cm}^{-2}$ . The electrostatic potential caused by these dipoles is superimposed to the QD potential barriers caused by conduction and valence band discontinuities. This may result in change the energy of the carrier emissions from QDs in the band. For their return capture in QDs the carriers must overcome potential barrier. Varying the magnitude of the  $T_a$  and  $V_f$  we change occupation QDs and height of the potential barriers. The carriers from deep levels can tunnel into quantum dots from which they were previously thermally evaporated. This effect is responsible for the appearance of the broad band in DLTS spectra that replaces the EL14 and HL5 levels. At cooling under  $V_b=0$  the carriers are absent in the bands and the dipoles did not form. At annealing temperatures  $T_a > 245 \text{ K}$  ( $V_b=0$  or  $V_f > 0$ ) QDs the carriers are evaporated from QDs and dipoles can not be formed. In this sense, the observed shift of the energy is connected with an effect of lowering of the potential barrier for carrier emission from VECODs and with tunneling through its due to p-n junction-induced electric field. The energies of the E1 and E1\* are coincident and equal 110meV.

### Conclusions.

We found that can be obtained two different DLTS spectra having peaks associated with QDs depending on the isochronous annealing temperatures one below on above 245K. At annealing temperatures  $T_a > 245 \text{ K}$  and cooling conditions  $V_f > 0$  we detected E1, E2, H1 and H2 levels. At annealing temperatures  $T_a < 245 \text{ K}$  and cooling conditions  $V_f > 0$  they disappear and appear E1\* and H1\* levels. Our results allowed us to conclude that H1, E1 as well as H1\*, E1\* levels are related with the same VECOD. In the first case QDs are not occupied and Coulomb interaction lack. In the second case QDs are occupied by the carriers, and Coulomb interaction between the charged QDs and deep centers located in regions close to QDs takes place and dipoles are formed. In these dipoles the carriers from deep levels can tunnel into quantum dots from which they were previously thermally evaporated.

apparent band discontinuity at heterointerface from the temperature. F.Capasso et al [6] reported the change of band discontinuity associated with interface dipole consists of ultrathin ( $\leq 50 \text{ \AA}$ ) ionized donor and acceptor sheets within a few tens of angstroms from the heterointerface. The electrostatic potential of this dipole is added to or subtracted from the dipole potential of the discontinuity. Since the separation between the charge sheets is the order of magnitude or smaller than the carrier de Broglie wavelength, electrons crossing the interface "see" a new band discontinuity. In such a manner the changing in DLTS spectra of our H1\* level, which occur at annealing at  $T_a < 245 \text{ K}$  and cooling at  $V_f > 0$ , is likely to be associate with formed dipoles, which came about from Coulomb interaction carrier captured in QDs and deep centers. The defects of the double acceptor Ga<sub>As</sub> with ionization energies of the levels that are smaller than the energy of the H1\* level are located in the region spatially coincident with QDs. It is possible temperature region where deep



**References**

- [1] N.Kirstaedter, N.N.Ledentsov, M.Grundmann, D.Bimberg,V.M.Ustinov, S.S.Ruvimov, M.V.Maximov, P.S.Kop'ev, Zh.I.Alferov, *Electron Lett.*, **30**, 1416, (1994).
- [2] V.M.Ustinov, A.Yu.Egorov, A.R.Kovsh, A.E.Zhukov, M.V.Maximov, A.F.Tsatsul'nikov, N.Yu.Gordeev, S.V.Zaitsev, Yu.M.Shernyakov, N.A.Bert, P.S.Kop'ev, Zh.I.Alferov, N.N.Ledentsov, J.Bimberg, A.O.Kosogov\*, P.Werner, U.Gosele, *Proc. 9 Int. Conf. On MBE*, Aug. 5-9, 1996, Malibu, USA, *Abstract Book*, p.3.1. (to be published in *Journal of Crystal Growth*, **175**, (1997).
- [3] S.Anand, N.Carlsson, M-Epistol, L.Samuelson, W. Seifert, *Appl. Phys. Lett.* **67**, 3016 (1995).
- [4] M.M.Sobolev, A.V.Gittsovich, M.I.Papentsev, I.V.Kochnev, B.S.Yavich, *Sov.Phys.Semicond.*, **26**, 985 (1992).
- [5] M.M.Sobolev, A.V.Gittsovich, S.G.Konnikov, I.V.Kochnev, B.S.Yavich, *MaterialsSci.Forum*, **143-147**, 1547, (1994).
- [6] F.Capasso, F.Beltram. *Mat.Res.Soc.Symp.Proc.*,**104**, 47, (1988).
- [7] M.Schmeits, *J.Appl.Phys.*, **80**, 941 (1996).
- [8] K.Imamura, S.Sugiyama, Y.Nakata, Sh.Muto, N.Yokoyama, *Jpn J.Appl.Phys.*, **34**, L1445, (1995).
- [9] R.Cingolani, R.Rinaldi, M.De Vittorio, L.Vasanelli, U.Marti, F.K.Reinhart, *J.Appl.Phys.*, **80**, 936 (1996).
- [10] K.Natori, N.Sano, *superlat. and Microstruct.*, **20**, (1996).
- [11] A.Mitonneau, G.M.Martin, A.Mircea. *Electron.Lett.*, **13**, 666 (1977).
- [12] L. Samuelsson, P.Omling, H.Titze, and H.G.Grimmeis. *J.Cryst.Growth*, **55**, 164 (1981).
- [13] Ph. Won Yu, W.C.Mitchel, M.G.Mier, S.S.Li, W.L.Wang. *Appl. Phys.Lett.*, **41**, 532 (1982).
- [14] D.L.Partin, J.W.Chen, A.G.Milnes, L.F.Vassamillet. *J.Appl.Phys*, **50**, 6845 (1979).
- [15] S.R.Forrest, O.K.Kim. *J.Appl.Phys.*, **53**, 5738 (1982).

## INFLUENCE OF ERBIUM DOPING ON STRUCTURE AND OPTICAL PROPERTIES OF THE InGaAs/GaAs SUPERLATTICES

L.G.Gerchikov\*, V.F.Masterov\* T.R.Stepanova\*, H.Gibbs\*\*, G.Khitrova\*\* and  
N.N.Faleev\*\*\*

\*St.Petersburg State Technical University, 195251 St.Petersburg, Russia

\*\*University of Arizona, Optical Science Center, Arizona, USA

\*\*\*Physico-Technical Institute of the RAS, 194021 St.Petersburg, Russia

**Key Words:** erbium, superlattice, optical spectrum, energy level.

**Abstract.** The  $\text{In}_x\text{Ga}_{1-x}\text{As}/\text{GaAs}$  structures at  $x = 0.1 - 0.2$  doped with erbium have been prepared by MBE method. The Er concentration is equal to  $(2-3)10^{19} \text{ cm}^{-3}$ . The SIMS measurements have shown that maximum of the erbium concentration takes place at the heterobounders. Accordingly to the X-ray studies doped structures are more perfective than undoped ones and a density of misfit dislocations is less in structures doped with erbium than in undoped superlattices. The spectra of optical absorption of these structures have been investigated, and their energy diagrams have been calculated. The Er related emission at wavelength about  $1.54 \mu\text{m}$  was observed in the  $\text{InGaAs}/\text{GaAs}:\text{Er}$  structures at helium temperatures.

### Introduction.

It is well known [1] that the most of impurities in the  $\text{AlGaAs}/\text{GaAs}$  structures distort a heteroboundary. This effect was also observed in the  $\text{AlGaAs}/\text{GaAs}:\text{Er}$  structure [2] at erbium concentration about  $10^{19} \text{ cm}^{-3}$ . At the same time the size quantization of the electron and hole energies can lead to increasing of efficiency of rare-earth related emission in these structures [3]. There are two important processes in this case. First, the carrier localization in a direction perpendicular to the heteroboundary increases the electron - hole overlap integrals. Second, the Auger excitation of an impurity center is of a resonance character without participation of additional energy levels localized on the impurity center. Besides, there are a lot of localized carriers in a quantum well to which the surplus of energy can be transfer at nonresonance Auger process of excitation of the intrashell f-f emission.

It is common knowledge that the  $\text{In}_x\text{Ga}_{1-x}\text{As}/\text{GaAs}$  structures are strain structures, and it is not possible to prepare them at  $x > 0.2$  due to the large difference in lattice parameters of GaAs ( $a = 0.56325 \text{ nm}$ ) and InAs ( $a = 0.60583 \text{ nm}$ ), and as consequence, it is a difficult task to form narrow quantum wells with relatively large electron quantum-size energy. At the same time this energy takes important role in an efficiency of Auger excitation f - f transitions in rare-earth ions, as it is shown in article [3].

In this paper it is shown that in the strain  $\text{InGaAs}/\text{GaAs}$  structures doped with erbium the heterobounders are more perfective than undoped structures. The Er related emission in the structures was observed at excitation by photons with an energy more than the GaAs bandgap, and at the difference between the quantum-size electron and hole energy level larger the energy of the  $I_{1/2} \Rightarrow I_{11/2}$  transition in the  $\text{Er}^{3+}$  ion.

### Experimental Details.

The undoped structures  $\text{In}_x\text{Ga}_{1-x}\text{As}/\text{GaAs}$  (samples 22, 27) with  $x \approx 0.2$  and the same structures doped with erbium (samples 23,30) have been prepared by MBE method. The maximal Er concentration in the sample 23 is about  $3 \cdot 10^{19} \text{ cm}^{-3}$  and in the sample 30 it is about  $2 \cdot 10^{19} \text{ cm}^{-3}$ . The structures of the samples 22, 23 are illustrated schematically in Fig.1a,b. The erbium doping of sample 23 was achieved by Er introduction into GaAs barriers close to heteroboundaries as it is

shown in Fig. 1b. The quantum wells in the structures 27 and 30 were formed by alternating of 1.4 InAs monolayer and 7 GaAs monolayers (see Fig. 1c) of general width about 12 nm. The width of GaAs barriers was equal to 25 nm. Erbium doping of the structure 30 was achieved by Er introduction into quantum wells.

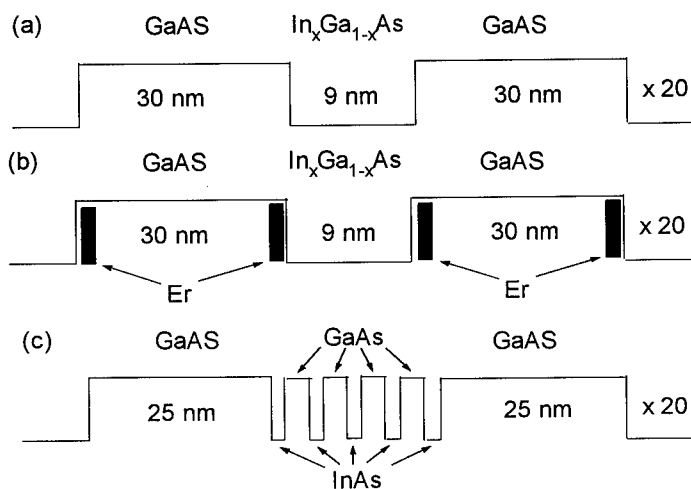


Fig. 1. Schemes of heterostructures, sample 22 (a), sample 23 (b) and samples 27, 30 (c).

The lattice parameters for GaAs and InAs are 0.565325 nm and 0.60583 nm, respectively. That is why structures InGaAs/GaAs:Er are strain structures. The indium concentration in quantum wells was chosen equal to 0.15 and width of wells equal to 10 nm in order to obtain a difference in energy between quantum-size levels of electron and hole equal to 1.24 eV ( $\lambda = 1\mu\text{m}$ ). The energy corresponds to intrashell transition  $^4I_{15/2} \rightarrow ^4I_{11/2}$  in  $\text{Er}^{3+}$  ion. The Er related emission corresponding to  $^4I_{13/2} \rightarrow ^4I_{15/2}$  has been observed.

The surface of these structures was covered by 10 nm cap layer of gallium arsenide. Characterization of the fabricated structures was done by SIMS technique with the resolution of 5 nm and with X-ray spectrometer. The absorption spectra of the structures were measured at liquid helium, liquid nitrogen, and room temperature. The spectra were analyzed with a double grating spectrometer and detected by a nitrogen-cooled germanium photodetector.

### Results.

The distributions of Ga, In and Er atoms in samples 23 and 30 were obtained by the SIMS. It should be noted that the maximum of Er concentration ( $3 \cdot 10^{19} \text{cm}^{-3}$  in sample 23 and  $2 \cdot 10^{19} \text{cm}^{-3}$  in sample 30) in both cases takes place on heteroboundaries. The same result was obtained for other ten structures InGaAs/GaAs doped with erbium. The indium concentration in quantum wells is about 0.1 - 0.15 in different samples. Besides, in contrary to AlGaAs/GaAs:Er structures [2] the InGaAs/GaAs superlattice is well formed at Er concentration above  $10^{19} \text{cm}^{-3}$ . Accordingly to the SIMS data quantum wells in samples 27 and 30 are formed by InGaAs compound with small difference of the indium concentration: 14% and 15% correspondingly.

The X-ray studies of the sample 22 show that in this case the superlattice period is equal to  $33.5 \pm 0.5$  nm and the average composition in quantum wells corresponds to  $x \approx 0.155 \pm 0.005$ . These results correlate well with the SIMS data. The density of misfit dislocations in this sample is equal to  $3 \cdot 10^8 \text{cm}^{-2}$ . The misfit parameter in direction parallel to substrate plane  $(\Delta a/a)_p$  is equal to 4.6% ( $a$  is lattice parameter for GaAs,  $\Delta a$  is the difference between lattice parameters for InGaAs and GaAs).

Using the values of elastic moduli from [10], we obtain the average misfit parameter  $\langle \Delta a/a \rangle = 2.3$ . The width of wells is equal to 10 nm. Accordingly to X-ray measurement the structure of superlattice in sample 23 is more perfective than in sample 22! The density of misfit dislocations in this sample is less than or equal to  $1.2 \times 10^8 \text{ cm}^{-2}$  at misfit parameter  $\langle \Delta a/a \rangle = 2.35\%$ . The average composition in quantum wells corresponds to  $x \approx 0.15$  and period of superlattice is  $36.5 \pm 0.5 \text{ nm}$ , width of the well is about 11 nm, and width of the GaAs barrier is about 25.5 nm. So, the Er doping increases a quantum well width. Also, the X-ray studies of the samples 27 and 30 show that the structure of superlattice doped with erbium is more perfective than the structure without erbium. Specifically, the density of misfit dislocation in sample 27 is about  $3.5 \times 10^8 \text{ cm}^{-2}$  and less than or equal to  $1.10^8 \text{ cm}^{-2}$  in sample 30. Besides, the intensity of diffraction peaks in sample 30 is larger and their width is less than in sample 27, by other words, the structure InGaAs/GaAs:Er is more perfective than that is one without erbium. The average misfit parameters for these structures obtained from X-ray data are equal to 0.3% and 0.4% correspondingly.

The X-ray study of samples 27, 30 shows the absent of the interfaces separating the InAs and GaAs layers in quantum wells. Accordingly to the X-ray data the quantum wells are formed by the homogenius InGaAs compounds. Also, it should be noted that width of quantum wells in Er doped structures are somewhat wider than in undoped ones. The periods of superlattice in samples 27 and 30 are equal to 28 and 31 nm correspondingly, and the width of the wells - 10.2 nm and 11.2nm.

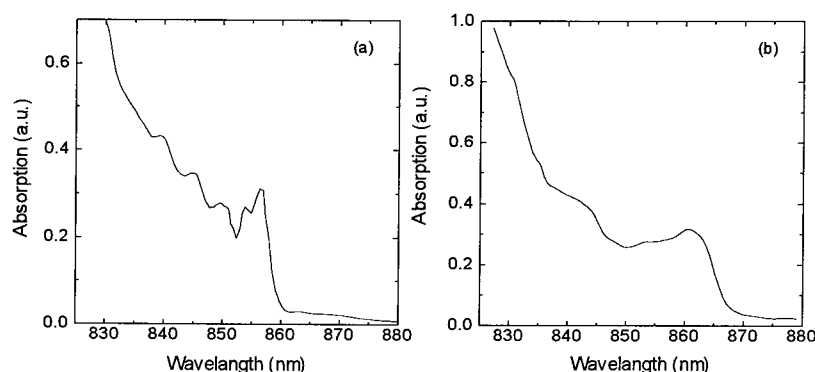


Fig. 2. Absorption spectra of samples 27 (a) and 30 (b) at  $T=4\text{K}$ .

The spectra of optical absorption of samples 22 and 23 at  $T=77\text{K}$  are different in spite of the fact that the parameters of superlattices are practically equal. Moreover, as noted above, the structure 23 is more perfective than structure 22. Just the same, the sharp band of absorption at wavelength about  $1 \mu\text{m}$  transition was observed in the spectrum of the sample 22 and it has smaller intensity in the spectrum of sample 23. On the other hand, the absorption spectrum of undoped structure 27 contains the sharp band at wavelength near to  $0.92 \mu\text{m}$  ( $1.35 \text{ eV}$ ) at  $T=294\text{K}$  and  $0.86 \mu\text{m}$  ( $1.45 \text{ eV}$ ) at  $T=4\text{K}$ , as it is shown in Fig.2a. It should be noted there is a fine structure in the absorption spectra at  $T = 4\text{K}$ . The same spectrum for sample 30 are presented in Fig.2b. As can be seen from these spectra an absorption band has moved to region of large wavelengths. The exciton peak in this case is much broader than in spectrum of the sample 27 and the fine structure disappears. Besides, there is shift of absorption spectra of Er doped samples to longwave side. For example, in Fig.6 the PL spectrum for sample 30 is presented. In this spectrum there is the sharp line at  $\lambda = 1.54 \mu\text{m}$  corresponding to  $^4I_{13/2} \rightarrow ^4I_{15/2}$  transition in  $\text{Er}^{3+}$  ion.

### Discussion.

The main result of structure studies is that the strain structures InGaAs/GaAs doped with erbium are more perfective than those structures without impurity. The maximum of Er concentration takes place on the interfaces in direction to a substrate. We assume that the Er ions for crystallization process move to interface by field of elastic strains; the general energy of heteroboundary caused by misfit strains therewith slows down. As a result of this, the structure InGaAs/GaAs doped with erbium is more perfective than the same structure without erbium. The same picture have been observed at any method of Er doping of structures InGaAs/GaAs. The  $\text{Er}^{3+}$  ions placed near strain interface should have a low symmetry electrical crystalline field that decreases a time of forbidden f-f transitions and consequently, it increases an emission efficiency due to strong mixing ground state and excited states of  $\text{Er}^{3+}$  ion accordingly to the Judd - Ofelt mechanism [5,6].

As it has been shown previously [3], an excitation of rare-earth related emission in quantum well is more effective than in bulk material. It is well known that energy the transfer from lattice to Er ion at its photoexcitation is accounted for by the Auger recombination electron-hole pair localized on the rare-earth center. The standard Auger recombination process is a threshold process; this is consequence of the laws of energy and momentum conservation. The threshold for the Auger recombination process is removed by the presence of a heteroboundary. If an impurity center is placed near the heteroboundary or in a quantum well, then the rate of excitation of the impurity center by Auger mechanism increases due to several reasons. First, the restrictions imposed on the electron-electron coupling by the energy and momentum conservation laws are removed. Second, the electron-hole overlap integral increases, and the characteristic distance, at which the heteroboundary starts to have a large effect, is determined by the characteristic decay scale  $k^{-1}$  of the wave function of the impurity center [7]

$$r \propto k^{-1} = \hbar / \sqrt{2m_e E_{\text{ex}}^f}, \quad (1)$$

where  $m_e$  is the effective mass of an electron, and  $E_{\text{ex}}^f$  is the excitation energy of f-shell.

It should be noted that high efficiency of the Er related emission in quantum well can be obtained at a resonance excitation only, when the difference of energies of electron and hole quantum-size levels is exactly equal to an energy of the transition of the Er ion from the ground state to an excited state. It may be the  $^4I_{13/2}$  state as well as the  $^4I_{11/2}$  state or any other excited state. However, there is strong difference between an energy of the  $^4I_{15/2} \rightarrow ^4I_{11/2}$  transition for  $\text{Er}^{3+}$  ion ( $E_{\text{ef}} = 1.24$  eV) and the energy separating electron and hole quantum-size levels obtained from absorption spectra of samples 27 and 30 ( $E_{\text{eh}} > 1.4$  eV). That is why there is nonresonance Auger excitation in this case.

We have calculated the energy-band spectrum for the samples 27 and 30, using method proposed in the paper [8]. We determine the values of the heterolayers band gaps and the band offsets taking into account the deformation effects according to [9]. We take the following values of deformation potentials  $a_c = -5.08$  eV and  $a_v = 1.00$  eV for InAs, and  $a_c = -7.17$  eV and  $a_v = 1.16$  eV for GaAs from [9];  $b = -1.8$  eV,  $d = -3.6$  eV for InAs, and  $b = -1.7$  eV,  $d = -4.5$  eV for GaAs from [10].

As was pointed out above, accordingly to results of the X-ray investigations in both samples the quantum wells are formed by homogeneous InGaAs compounds with close indium contents but have different width. Namely, the width of well is equal to 10.2 nm for sample 27 and 12.2 for sample 30; content of indium  $x = 0.14$  and  $x = 0.15$ , for samples 27 and 30 correspondingly. We have used these X-ray data for structure parameters of the samples to calculate the energy diagrams. Since the indium concentrations are close in both samples and the difference of their energy spectra is connected mostly with the difference of quantum well width we show in Fig.3 the electron and the hole energy quantum levels as a function of the quantum well width, A. For sample 27 ( $A=10.2\text{nm}$ )

there are one electron miniband with edge energy at 1.425 eV (here and further we measured energies from the top of valence band of InGaAs), four heavy hole levels at energies -0.003, -0.012, -0.026, -0.044 eV. These results allow to explain the absorption spectrum of the sample 27 shown in Fig.2a. Really, there are four absorption bands in spectrum of this sample at  $\lambda = 860, 852, 847,$  and  $842$  nm, which are attributable to the transitions from the heavy hole levels to electron miniband. The sharp line in absorption spectrum of the sample at  $T = 4$  K (Fig.2a) is attributable to excitonic transition, but the nature of double peak is not understood. The energy difference between positions of the four absorption bands correlate well with energy difference between heavy hole levels.

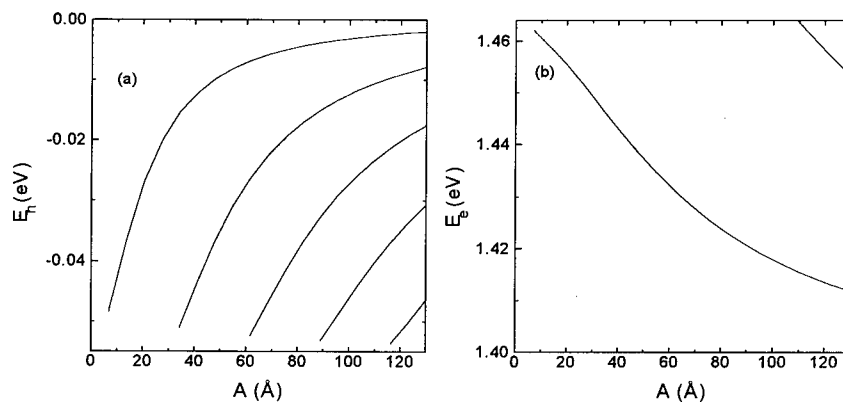


Fig. 3. Energies of hole (a) and electron (b) levels in QW as a function QW width A.

The width of quantum well of sample 30 is larger than in sample 27. This is why there are two electron minibands with edge energies 1.413 and 1.457 eV, as it is presented in Fig.3b. These data allow to explain two wide absorption bands at 1.425 and 1.462 eV in spectrum shown in Fig.2b as transitions from quantum-size hole levels to electron minibands. The hole energy spectrum does not change considerably and turns out to be equal to -0.002, -0.009, -0.020, -0.034, -0.051 eV. One additional hole level appears.

The large width of an excitonic line in the spectrum of the sample 30 may be explained by the disruption of the exciton by the charged  $\text{Er}^{3+}$  ions. The broadening of the absorption bands in the spectrum of the sample 30 may be caused by unresolved fine structure which is attributed to the transitions from different hole quantum size levels. This effect due to fluctuations of interface electric field due to high concentration of the  $\text{Er}^{3+}$  ions in interface. The late influence on an energy of electron moving along the InGaAs layer.

The energy excess at nonresonant Auger excitation of rare-earth related emission should be transferred to a third body. As it was shown in [11], the Auger process, where the energy excess is transferred to localized carriers, is the most effective excitation process. The rate of Auger recombination in this case is proportional to carrier concentration. That is why the additional doping of quantum well by shallow impurities is needed for the increasing of efficiency of f-f luminescence. Accordingly to the work [3] the ratio of the Auger-excitation rate of an impurity center in a quantum well to the Auger-excitation rate of same center in an uniform semiconductor is

$$G^{\text{QW}}/G = (np/NPa^2)(E_{0c}/kT)(m_h/m_c)^{1/2}, \quad (2)$$

where  $n$  and  $p$  are two-dimensional electron and hole concentrations;  $N$  and  $P$  are volume concentrations of electrons and hole respectively;  $a$  is the quantum well width;  $E_{0c}$  is the electron quantum-size energy. This ratio is large for narrow quantum wells, for which  $E_{0c} \gg kT$ . Only at this condition the f-f luminescence excitation process is more efficient in a quantum well than in the bulk materials. This result was obtained for resonance transfer of an energy to rare-earth ion due to the Auger process, not matter what transition to first or to second excited state of an impurity ion takes place. Besides, the Auger process rate increases with the decreasing of width of the quantum well due to the increasing of the overlap integral value.

### Conclusions.

The results presented in this work show that the high Er concentration can be obtained in strain quantum-size structures. Accordingly to X-ray data of structural investigations the Er doped InGaAs/GaAs structures are more perfective than undoped ones. The reason is that Er ions in process of growth of the structure are localized at heteroboundary decreasing its energy. That is why it is possible to prepare narrow wells  $\text{In}_x\text{Ga}_{1-x}\text{As}$  with  $x > 0.2$ , resulting in increasing of energy of an electron quantum-size level and in turn an efficiency of f-f emission is increased also.

Another way of decreasing of the quantum well width and increasing Auger recombination rate is using compound AlInAs for barrier [12]. In this case a quantum well with depth more than or equal to 0.8 eV and misfit parameter  $\Delta a = 0.05 - 0.1\%$  can be prepared, as it is shown by our calculations. In any case it is needed to increase a depth and to decrease a width of a quantum well for increasing of efficiency of f-f emission from superlattices doped with rare-earth elements. The longest time at high-rate Auger process is time of the spontaneous forbidden f-f transition which is equal to 0.1 - 1mc. That is why it is needed to obtain induced radiation.

We are grateful to Prof.M.S.Bresler and Dr.O.B.Gusev, who put at our disposal a PL spectra of the samples 27 and 30. This work is supported by the AFOSR (grant F 499620-94-1-0390) and INTAS (grant RFBR 95-0531).

### References.

- 1.D.G.Deppe and N.Holonyak. J.Appl.Phys. **64**, R93 (1988)
- 2.O.B.Gusev, B.Ya.Ber, M.S.Bresler, et al. (to be published)
- 3.G.G.Zegrya, V.F.Masterov. Semiconductors **29** (10), 989-996, 1995
- 4.X.G.He, M.Erdtmann, R.Williams, S.Kim, and M.Rozeghi. Appl.Phys.Lett. **65**(22), 2812, 1994
- 5.B.R.Judd. Phys.Rev. **127**, 750, 1962
- 6.G.S.Ofelt. J.Chem.Phys. **37**, 511, 1962
- 7.A.A.Pakhomov, I.N.Yassievich. Semiconductors **27**, 270, 1993
- 8.L.G.Gerchikov, G.V.Roznov, A.V.Subashiev. Sov.Phys. JETP, **74**, 77, 1992
- 9.C.G.Van de Walle. Phys.Rev. B **39**, 1871, 1989
- 10.Landolt-Bornstein Zahlenwerte und Funktionen aus Naturwissenschaften und Technik. Semiconductors, Springer-Verlag Berlin, Heidelberg, New York 1982
- 11.V.F.Masterov, and L.G.Gerchikov. MRS Proceedings, Rare-Earth Doped Semiconductors, ed. A.Polman, S.Coffa, and R.N.Schwartz, v.422, 227-238,1996
- 12.A.M.Cohen, S.R.Aladim, and G.E.Marques. Surface Science, **267**, 464-469, 1992

## DEFECT FORMATION DURING LASER INDUCED INTERMIXING OF GaAs/AlGaAs MULTIPLE-QUANTUM-WELL STRUCTURES

Nguyen Hong Ky

Institute of Applied Optics, Swiss Federal Institute of Technology,  
CH-1015 Lausanne, Switzerland

**Key words:** GaAs/AlGaAs, laser induced disordering,  $\text{Si}_{\text{Ga}}$ - $\text{Ga}_{\text{As}}$  complex, cathodoluminescence.

**Abstract.** Low-temperature cathodoluminescence and secondary electron imaging modes of a scanning electron microscope are used to study the formation of point defects during laser induced disordering of GaAs/Al<sub>0.45</sub>Ga<sub>0.55</sub>As multiple-quantum-well structures. Micron-sized melted regions where the GaAs/AlGaAs multilayered structure is totally disordered are observed under the irradiated surface. The cathodoluminescence spectra of the melted region are dominated by a broad emission band at 1.47 eV. This emission band is believed to be due to the recombination of a  $\text{Si}_{\text{Ga}}$  donor - column III antisite acceptor complex. The luminescence spectra obtained for the 8  $\mu\text{m}$  wide transition regions adjacent to the melted region show a broadening and a blue shift of the emission peak associated with excitons confined in the quantum wells. This indicates a partial disordering of the multilayered structure. In addition, the column III antisite related emission band and an emission band due to the transition of free electrons to Si acceptor level in the quantum wells are seen in the luminescence spectra of the partially disordered region. Our results demonstrate that column III antisites are the main intrinsic point defects generated during laser irradiation induced disordering of GaAs/AlGaAs multilayered structures. The  $\text{Si}_{\text{Ga}}$  - column III antisite complex is formed at high concentration in the melted region. The mechanism responsible for the disordering of multilayered structure around the melted region is discussed on the basis of the diffusion of  $\text{Si}_{\text{Ga}}$  - column III antisite complex.

### Introduction.

Impurity-induced disordering (IID) is a planar process to alter the effective energy gap and the refractive index in selective regions of multilayered structures [1], [2]. The disordering occurs when an impurity diffuses into the multilayered structure during annealing at a high temperature of hundreds °C. A localized disordering of GaAs/AlGaAs multilayered structures has also been produced by laser irradiation without annealing [3], [4]. Material processing techniques using high-power lasers are intensively developed for the fabrication of micro- and optoelectronic devices because of the following advantages [5], [6]: i) the heat treatment can be localized in a very small region, whereas the remainder of the material is at room temperature; ii) it is possible to perform the heat treatment in selective regions of a non-uniform structure by choosing appropriate wavelengths of the laser; iii) the intense thermal energy is applied to the annealed region during a limited time, this prevents the formation of defects and reduces the contamination problem; and iv) it is possible to work under the atmospheric condition. Moreover, laser induced disordering (LID) is an impurity-free technique that can be used to obtain intermixed alloys without introducing free-carrier populations into the material. In spite of these advantages, LID process has not been sufficiently investigated. The works concerning LID-related defects has not been reported so far. In this study, we concentrate on the defect formation during LID process. The laser irradiated samples are investigated by cathodoluminescence (CL) and secondary electron (SE) imaging modes of a scanning electron microscope (SEM). The LID regions of the multilayered structure are observed in the SE images. A detailed analysis of the CL spectra taken at different regions of the structure permits to obtain useful information about the defect formation and to understand the physical mechanism occurring during the LID process.

### Experiment.

To study the LID process, we use a GaAs/Al<sub>0.45</sub>Ga<sub>0.55</sub>As multiple-quantum-well (MQW) structure grown by molecular beam epitaxy (MBE) on (001)-oriented Si-doped GaAs ( $n \approx 2 \times 10^{18} \text{ cm}^{-3}$ ) substrates. The structure consists of the following undoped layers: a 0.4  $\mu\text{m}$  thick GaAs buffer layer, a MQW region with 30 GaAs wells separated by Al<sub>0.45</sub>Ga<sub>0.55</sub>As barriers, and a 0.1  $\mu\text{m}$  thick GaAs cap layer. The thickness of the wells and the barriers is  $100 \pm 4$  and  $200 \pm 5$  Å, respectively. The free surface of the GaAs/AlGaAs multilayered samples is selectively irradiated with a scanned Ti:sapphire laser beam. The laser wavelength is 700 nm. The spot size is fixed at about 2.6-3  $\mu\text{m}$ . The power level of the cw laser beam is between 250 and 1000 mW. The sample mounted on a computer-controlled translation table is moved in the plane perpendicular to the laser beam. The scanning speed



is varied in the 0.01-0.1 mm/s range to produce annealing lines on the free surface of sample. The (100) free surface and the (110) cleaved surface of the irradiated sample are investigated with a Cambridge 360 SEM. A primary electron beam at an acceleration voltage of 10 kV is used for both CL and SE imaging modes. The radius of the excitation volume is about 0.2  $\mu\text{m}$ . In the SE mode, the secondary electrons are received by a positively biased collector placed near the sample. The CL signal is focused into the entrance slit of a 32 cm focal length monochromator by an elliptical mirror system. A cooled Si avalanche photodiode is used as detector. The measurement temperature is 25 K.

### Results and discussion.

Figure 1 shows a SE image of the cross section of a LID line formed by laser irradiation at a scanning speed of 0.01 mm/s and an incident power of about 1 W. Due to the Gaussian intensity distribution in the laser beam, an important fraction of the incident power concentrates within the sample region below the laser spot, where the material is melted. The melted region with 1.3  $\mu\text{m}$  depth and 2.9  $\mu\text{m}$  width includes the MQW layers, the GaAs buffer layer, and a portion of the substrate. In this region, the incident power of the laser beam is absorbed and converted into the thermal energy, the material is melted and then recrystallized. The MQW structure is totally disordered and becomes a solid solution. The smoothness of the melted region indicates that it appears nearly homogeneous. A fraction of the thermal energy is dispersed in the 8  $\mu\text{m}$  wide transition regions adjacent to the melted region. The dispersed energy causes damages within a 0.3  $\mu\text{m}$  thick layer below the free surface of the sample. In Fig. 2 we present a CL image taken on the free surface of the sample, around a LID line. The bright regions of the CL image correspond to the CL signal recorded at the photon energy of 1.539 eV. The 1.539 eV emission is associated with the radiative recombination of  $n=1$  electron-heavy hole excitons confined in the wells of the GaAs/ $\text{Al}_{0.45}\text{Ga}_{0.55}\text{As}$  MQW structure [7]. The 1.539 eV CL signal is not detected within a 20  $\mu\text{m}$  wide stripe including the LID line and the regions adjacent to it. This indicates that the underlying MQW structure is disordered. The CL image taken from the region around the cross section of the LID line on the (110) cleaved surface (Fig. 3) also shows the disordering of the MQW structure in the melted region and the 8  $\mu\text{m}$  wide transition regions adjacent to it. Hence, after laser irradiation, the MQW structure consists of three regions: a) the region outside the 20  $\mu\text{m}$  wide dark stripe, where the MQW structure is intact (ordered); b) the 2.9  $\mu\text{m}$  wide melted region at the center of the dark stripe; and c) the transition region within the dark stripe, where the material is not melted but the MQW structure is partially disordered.



Figure 1: SE photograph of the cross section of a LID line.

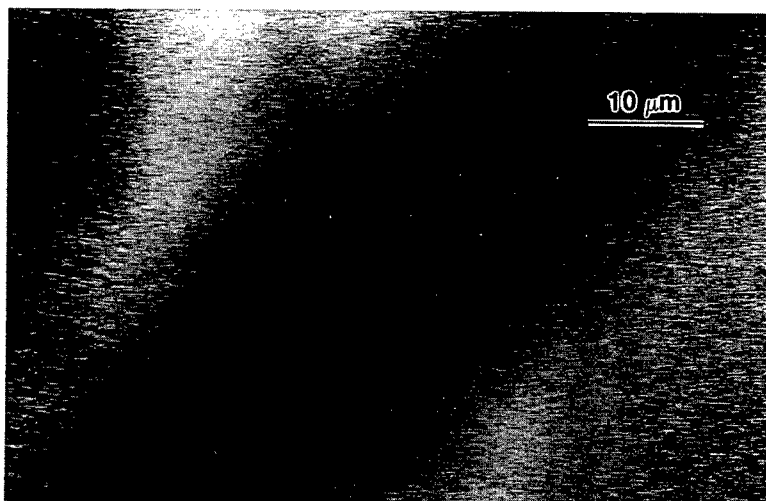


Figure 2: 25 K CL image of the region around a LID line on the (100) free surface of the sample. The image is recorded at the photon energy of 1.539 eV.

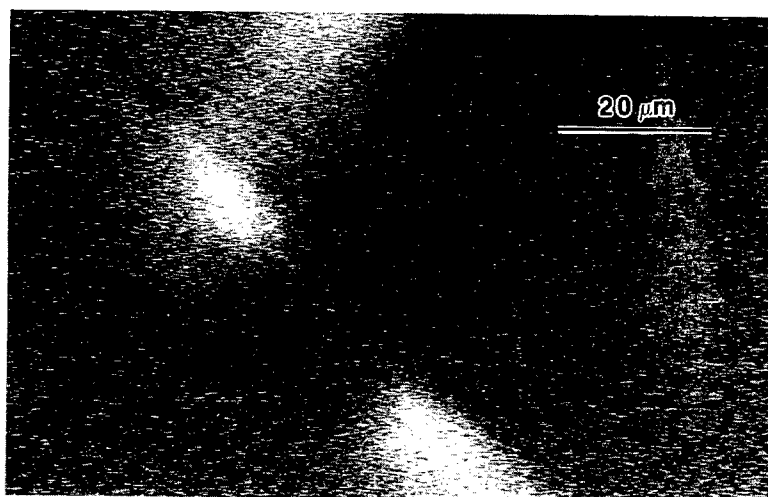


Figure 3: 25 K CL image of the region around the cross section of a LID line on the (110) cleaved surface. The image is recorded at the photon energy of 1.539 eV.

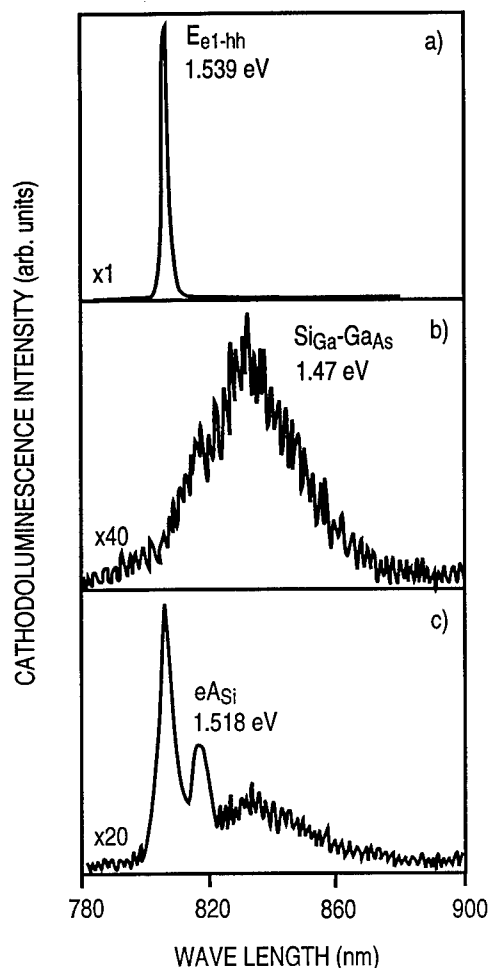


Figure 4: 25 K CL spectra taken on the (100) free surface of the sample: a) in the ordered region, b) in the melted region, and c) in the transition region.

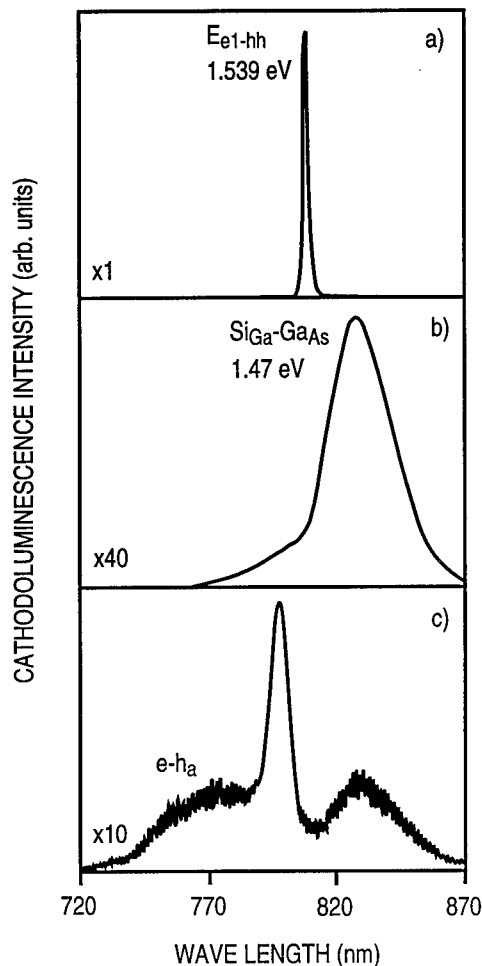


Figure 5: 25 K CL spectra taken on the (110) cleaved surface: a) in the ordered region, b) in the melted region, and c) in the transition region.

25 K CL spectra taken in different regions of the (100) free surface are shown in Fig. 4. The CL spectrum of the as-grown MQW structure (Fig. 4a) shows an intense and narrow peak ( $E_{e1-hh}$ ) at 1.539 eV due to the radiative recombination of  $n=1$  electron-heavy hole excitons. In the CL spectrum of the melted region (Fig. 4b) the  $E_{e1-hh}$  emission line disappears completely, indicating that the MQW structure is totally disordered. A broad emission band centered at about 1.47 eV dominates the spectrum. The Gaussian lineshape and the large bandwidth of the 1.47 eV emission are typical for the radiative recombination of a donor - deep acceptor complex [8]. The 1.47 eV emission band has been reported for laser-irradiated AlGaAs multilayered structures [9], where it only appears if the structures are doped with Si or Ge. The 1.47 eV emission band has also been observed in the photoluminescence (PL) spectra of Si-doped  $Al_{0.3}Ga_{0.7}As$  epitaxial layer grown by MBE [10]. The PL intensity of this emission band increases after annealing the  $Al_{0.3}Ga_{0.7}As$  sample in vacuum (As-poor condition), whereas annealing in As-rich condition results in a reduction of its intensity. In [10], we suggested that the 1.47 eV emission band could be due to a donor-to-acceptor pair transition of a  $Si_{Ga}$  - column III antisite complex. To simplify the text, the column III antisites will be written as  $Ga_{As}$ , but it should be borne in mind that column III antisites in AlGaAs include  $Ga_{As}$  and  $Al_{As}$ . For

our laser-irradiated sample, the material in the melted region is converted into an  $\text{Al}_x\text{Ga}_{1-x}\text{As}$  solid solution with  $x \approx 0.2$ . Since the melted region develops into the Si-doped GaAs substrate, Si atoms present in the substrate dissolve into the melt, and the AlGaAs melted region is doped with Si. During melting, volatile As atoms can diffuse to the sample surface and evaporate from the sample. As a consequence, As vacancies ( $V_{\text{As}}$ ) can be generated at high concentration in this region. This enhances the occupation of As sites by column III atoms [8]. Theoretical calculations of the formation energy of point defects in GaAs [11], [12] have predicted that the formation of  $\text{Ga}_{\text{As}}$  is energetically favorable in Ga-rich n-type GaAs. Hence, a high concentration of  $\text{Ga}_{\text{As}}$  is expected in the melted region. Since  $\text{Ga}_{\text{As}}$  is a deep acceptor, it can form complex with  $\text{Si}_{\text{Ga}}$  donor. We believe that the 1.47 eV emission band ( $\text{Si}_{\text{Ga}}\text{-Ga}_{\text{As}}$ ) observed in the spectrum of the melted region is due to the recombination of a  $\text{Si}_{\text{Ga}}\text{-Ga}_{\text{As}}$  complex. The domination of the  $\text{Si}_{\text{Ga}}\text{-Ga}_{\text{As}}$  emission band in the spectrum indicates a high concentration of  $\text{Si}_{\text{Ga}}\text{-Ga}_{\text{As}}$  complex in the melted region. In the spectrum of the transition region (Fig. 4c), the  $E_{\text{e1-hh}}$  emission line remains but its intensity decreases by a factor of 20 and its linewidth is broadened. The intensity decrease could be related with the formation of hole traps in the wells. The linewidth broadening may be due to the interdiffusion of column III atoms at the well-barrier interfaces [2]. On the other hand, the linewidth broadening may also be originated from an increase in Si donor concentration in the wells [13]. The  $\text{Si}_{\text{Ga}}\text{-Ga}_{\text{As}}$  emission band is also seen in Fig. 4c. Its intensity is strongly reduced as compared with that of the melted region (Fig. 4b). In addition, its peak position shifts to 1.48 eV. The peak shift of the  $\text{Si}_{\text{Ga}}\text{-Ga}_{\text{As}}$  emission band is observed in Fig. 4c because the  $\text{Si}_{\text{Ga}}\text{-Ga}_{\text{As}}$  complexes are confined in the intact or partially disordered quantum wells of the transition region. Using the  $\text{Si}_{\text{Ga}}\text{-Ga}_{\text{As}}$  emission peak position determined from Fig. 4c, the  $\text{Ga}_{\text{As}}$  energy level is estimated to be at 67 meV above the heavy-hole energy band in the quantum well. This  $\text{Ga}_{\text{As}}$  energy level value is in good agreement with that reported for GaAs [8]. A new emission band appears on the spectrum at 1.518 eV. This emission band ( $\text{eAs}_i$ ) is believed to be related with the band-to- $\text{Si}_{\text{As}}$  acceptor transition in the quantum wells. In the transition region, the dispersed thermal energy is not enough to melt the material, but  $V_{\text{As}}$  are generated. The  $V_{\text{As}}$  in the quantum wells can be occupied by Si atoms that diffuse from the melt into this region.

The 25 K CL spectra taken in different regions on the (110) cleaved surface (Fig. 5) confirm above observations. The CL spectra of the ordered (Fig. 5a) and melted (Fig. 5b) regions are similar to those taken on the free surface. Some differences between the spectrum of the transition region taken on the (110) cleaved surface (Fig. 5c) and that taken on the free surface (Fig. 4c) are found. The absence of the  $\text{eAs}_i$  emission band in Fig. 5c indicates that the transfer of Si atoms from Ga sites to As sites occurs mostly near the free surface where  $V_{\text{As}}$  are generated at high concentration. The disordering of MQW structure in the transition region is clearly shown in Fig. 5c. A blue shift of up to 14 meV and a broadening are observed for the  $E_{\text{e1-hh}}$  emission line. A high-energy emission ( $\text{e-h}_a$ ) covers a large spectral region between the  $E_{\text{e1-hh}}$  emission line and 1.64 eV. The interdiffusion of Ga and Al atoms at the barrier-well interface modifies the well shape. Initially finite square GaAs wells become rounded AlGaAs wells and the barrier potential is reduced. The electron subbands move upward whereas the hole subbands move down, causing an increase in the electron-hole transition energy [2]. As a consequence, a blue shift of the excitonic peak is seen in the CL spectrum. The observation of the broad  $\text{e-h}_a$  emission band on the high-energy side of the  $E_{\text{e1-hh}}$  emission line indicates that the disordering levels of the wells in the transition region are different. The disordering seems to be laterally non-uniform. The column-III interdiffusion decreases with increasing distance from the melted region. Fig. 5c shows a disordering effect stronger than that of Fig. 4c because the CL spectrum of Fig. 5c is measured at a point nearer to the melted region than that of Fig. 4c. The  $\text{Si}_{\text{Ga}}\text{-Ga}_{\text{As}}$  emission band in Fig. 5c is also more intense than in Fig. 4c. The observed correlation between the disordering level and the intensity of  $\text{Si}_{\text{Ga}}\text{-Ga}_{\text{As}}$  emission band indicates that the diffusion of  $\text{Si}_{\text{Ga}}\text{-Ga}_{\text{As}}$  complex may play an important role in the disordering process. We suggest that  $\text{Si}_{\text{Ga}}\text{-Ga}_{\text{As}}$  complex and  $\text{Si}_{\text{Ga}}\text{-Al}_{\text{As}}$  complex diffuse laterally from the melted region into the transition region by alternately exchanging sites with  $V_{\text{As}}$ :



The diffusion process described by Eq. (1) is favorable in the transition region where  $V_{\text{As}}$  is abundant. In addition, the  $V_{\text{As}}$  concentration gradient between the free surface and the bulk is a driving force for the diffusion of these complexes in the direction perpendicular to the layer interface. The Al-Ga interdiffusion mediated by the diffusion of  $\text{Si}_{\text{Ga}}\text{-Ga}_{\text{As}}$  complex and  $\text{Si}_{\text{Ga}}\text{-Al}_{\text{As}}$  complex results in the disordering of the MQW structure in the transition region.

**Conclusion.**

The formation of point defects during LID process in GaAs/Al<sub>0.45</sub>Ga<sub>0.55</sub>As MQW structures has been investigated by CL and SE imaging modes of a SEM. The scanning laser irradiation produces a micron-sized melted line where the GaAs/AlGaAs MQW structure is totally disordered and partially disordered regions adjacent to the melted line. The domination of Si<sub>Ga</sub>-Ga<sub>As</sub> emission band in the CL spectra of the melted region indicates that column-III antisites are the main intrinsic point defects generated during LID process. The Si<sub>Ga</sub>-Ga<sub>As</sub> complex is formed at high concentration in the melted region. The diffusion of Si<sub>Ga</sub>-Ga<sub>As</sub> complex is suggested to be responsible for the disordering of multilayered structure in the region around the melted line.

**Acknowledgments.**

The author wish to thank F. Morier-Genoud for the growth of MQW structures, D. Araújo and J. D. Ganière for SEM observations, and F. K. Reinhart for his continuous support.

**References.**

1. D. G. Deppe and N. Holonyak Jr., *J. Appl. Phys.* **69**, R93 (1988).
2. Nguyen Hong Ky, J. D. Ganière, M. Gailhanou, B. Blanchard, L. Pavesi, G. Burri, D. Araújo, and F. K. Reinhart, *J. Appl. Phys.* **73**, 3769 (1993).
3. J. E. Epler, R. D. Burnham, R. L. Thornton, T. L. Paoli, and M. C. Bashaw, *Appl. Phys. Lett.* **49**, 1447 (1986).
4. J. Ralston, A. L. Moretti, R. K. Jain, and F. A. Chambers, *Appl. Phys. Lett.* **50**, 1817 (1987).
5. R. P. Salathé, in "Optique intégrée, 27<sup>e</sup> cours de perfectionnement de l'Association Vaudoise des chercheurs en physique", eds. P. Fasan and J. D. Ganière (Lausanne: EPFL), p. 268 (1985).
6. J. L. Boulnois, "Le laser-principes et techniques d'application" (Paris: Technique et documentation), p. 107 (1990).
7. Nguyen Hong Ky, J. D. Ganière, M. Gailhanou, F. Morier-Genoud, D. Martin, and F. K. Reinhart, *Phys. Rev. B* **46**, 6947 (1992).
8. Nguyen Hong Ky, and F. K. Reinhart, to be published.
9. R. P. Salathé, H. H. Gilgen, Th. Binkert, F. K. Reinhart, and R. A. Logan, *J. Appl. Phys.* **53**, 3769 (1982).
10. L. Pavesi, Nguyen Hong Ky, J. D. Ganière, F. K. Reinhart, N. Baba-Ali, I. Harrison, B. Tuck, and M. Hennini, *J. Appl. Phys.* **71**, 2225 (1992).
11. G. A. Baraff, and M. Schlüter, *Phys. Rev. Lett.* **55**, 1327 (1985).
12. H. Seong, and L. J. Lewis, *Phys. Rev. B* **52**, 5675 (1995).
13. Nguyen Hong Ky, J. D. Ganière, F. K. Reinhart, and B. Blanchard, *J. Appl. Phys.* **79**, 4009 (1996).

## **LOCALIZED EPITAXY FOR VERTICAL CAVITY SURFACE EMITTING LASER APPLICATIONS**

**M. Erdtmann, S. Kim, and M. Razeghi**

**Center for Quantum Devices, Northwestern University, Evanston, IL 60208 USA**

**Keywords:** VCSEL, Al-free, distributed Bragg reflector, localized epitaxy, misfit dislocation.

**Abstract.** VCSELs have emerged as an important device for several key applications. Nearly all VCSELs reported contain Al, which easily oxidizes and degrades the device. As of yet, very little effort has been put into Al-free VCSELs. We demonstrate an Al-free GaInP/GaAs DBR with a reflectivity of 0.989 near 0.98  $\mu\text{m}$ . We also show the benefits of localized epitaxy for the growth of mismatched epilayers, which can cut down on the effects of dislocations. These are two pieces to the puzzle of producing longer-wavelength ( $> 1 \mu\text{m}$ ) Al-free VCSELs on GaAs substrates.

### **Introduction.**

Because they emit normal to the surface and are readily fabricated into two-dimensional arrays, vertical cavity surface emitting lasers (VCSELs) are ideally suited as light sources for optical fiber communication, digital printing and scanning, and optical disk storage. [1] Other advantages VCSELs possess over edge-emitting lasers are ease of fabrication and testing, circular beam output, and low-bias, low-threshold operation. [2]

Superb results have been obtained from VCSELs with oxidized apertures, including record wall-plug efficiency [3] and threshold current [4]. However, the distributed Bragg reflector (DBR) mirrors in these laser structures are made from different compositions of  $\text{Al}_x\text{Ga}_{1-x}\text{As}$ . The lifetime and reliability of these lasers is an issue since they do contain Al, which oxidize easily and degrade much more rapidly than Al-free lasers. [5] This has already been demonstrated in edge-emitting lasers. [6,7]

For Al-free VCSELs, [8] the DBRs are created from GaInP and GaAs. [9,10] The active region, for emission wavelengths longer than 0.87  $\mu\text{m}$ , is made from GaInAs quantum wells sandwiched between GaAs barriers; as the emission wavelength increases, the In content in GaInAs increases, which adds to the strain in the layer. This paper discusses both these topics and offers some of our experimental results.

### **Al-free distributed Bragg reflectors.**

Thus there is motivation for producing Al-free VCSELs with alternative materials in the DBRs. For emission wavelength over 1  $\mu\text{m}$ , two possible substrates that can be used are InP and GaAs. GaAs is the better choice because it is cheaper, more widely available, and has better thermal and mechanical properties than InP. Also, the refractive index difference between the two alternating materials on InP substrates is very small, making growth of DBRs on this substrate impractical.

However, the growth of GaInP/GaAs DBRs on GaAs substrates is feasible, though challenging because, for the same reflectivity, approximately twice as many periods are needed in a GaInP/GaAs DBR than in a AlAs/GaAs DBR due to the smaller refractive index difference of GaInP/GaAs. Nevertheless, we have grown a 36-period GaInP/GaAs DBR with a reflectivity of 0.989 at a wavelength near 0.98  $\mu\text{m}$ . To satisfy the quarter-wavelength requirement of a DBR, the each GaAs layer thickness is 69 nm, and each GaInP thickness is 76 nm. The measured and calculated reflectivity is shown in Fig. 1; there is very good agreement between the two.

The high resolution x-ray diffraction spectrum, pictured in Fig. 2, reveals over 25 orders of satellite peaks, indicating the excellent crystalline and interfacial quality of this structure. All growths were performed in a low-pressure metalorganic chemical vapor deposition reactor with triethylgallium and trimethylindium as our Ga and In sources and arsine and phosphine as our As and P sources, respectively.

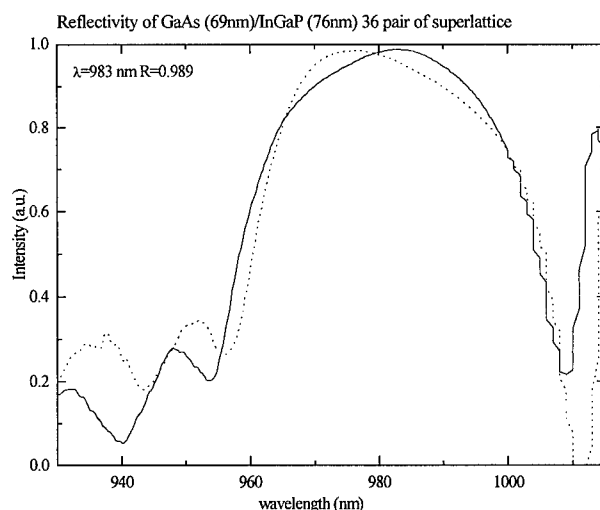


Fig. 1. The measured (solid line) and calculated (dashed line) reflectivity of the 36 period GaInP/GaAs DBR.

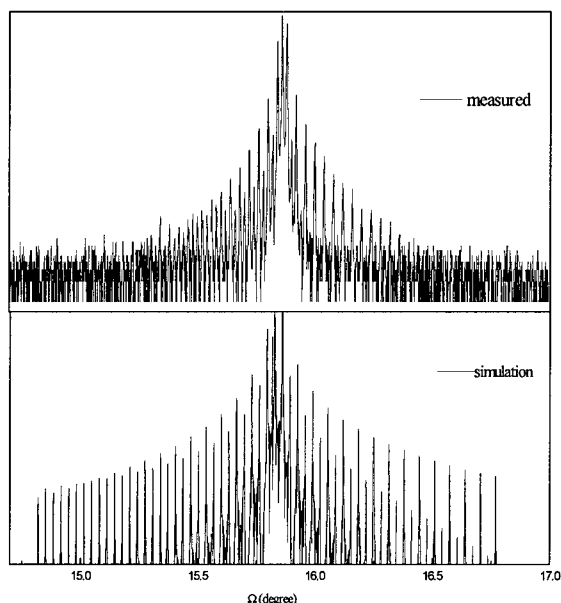


Fig. 2. The high resolution x-ray diffraction (top) and simulation (bottom) spectra of the 36 period GaInP/GaAs DBR.

#### Localized epitaxy.

A bigger challenge for GaAs-based devices is the push to longer wavelength emission. The ultimate for GaAs-based VCSELs is operation at 1.3  $\mu\text{m}$  and 1.55  $\mu\text{m}$ , the two wavelengths most suitable for transmission over silica optical fibers. This is accomplished with GaInAs active layers, which have lattice mismatches of up to 5% to the substrate, depending on the quantum well thickness. For thicknesses of these layers above the critical thickness, this leads to the formation of misfit dislocations, [11,12] which kill device performance. Therefore, to create these long-wavelength devices, a method must be used to reduce or eliminate the number of dislocations present in the strained layers.

This can be accomplished with localized epitaxy, where growing on a reduced area decreases not only the spreading of dislocations but the formation of them as well. [13,14] We have taken advantage of this by patterning GaAs substrates with mesas of one of two sizes—16 x 16  $\mu\text{m}$  or 400 x 400  $\mu\text{m}$ —then depositing mismatched GaInP on top. The GaAs substrates, which have a surface normal of [001] with a 2° misorientation toward the  $[\bar{1}10]$  direction, were initially patterned with photoresist then selectively etched with electron cyclotron resonance enhanced reactive ion etching in a  $\text{BCl}_3/\text{Ar}$  environment to a depth of 1.5  $\mu\text{m}$ . The remaining photoresist was removed and the surface was cleaned. The next step is the epitaxy, where 0.5  $\mu\text{m}$  of GaInP with a mismatch of +0.30% was deposited.



Figure 3 shows a scanning electron microscopy (SEM) micrograph of the  $16 \times 16 \mu\text{m}$  mesas after etching but before regrowth. Both the surface and sidewalls are very smooth. Figure 4 is a picture of the same sample after epitaxy of the GaInP. The mesa surface has maintained its smoothness, but the sidewalls are considerably rougher.

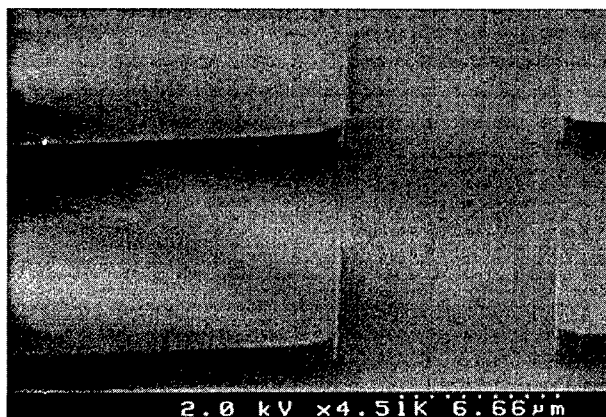


Fig. 3. An SEM micrograph of the  $16 \times 16 \mu\text{m}$  mesa sample after patterning but before epitaxy.

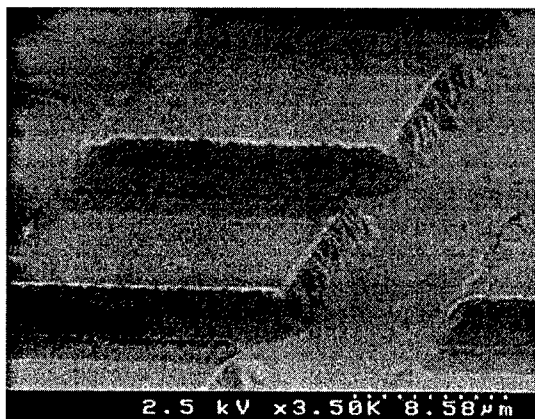


Fig. 4. An SEM micrograph of the same sample shown in Fig. 3 after GaInP deposition.

Figure 5 is a topophotoluminescence (TPL) image of the  $400 \times 400 \mu\text{m}$  mesa sample, grown side-by-side with the  $16 \times 16 \mu\text{m}$  one. This examination technique can readily reveal surface and sub-surface blemishes like point defects and dark-line defects that cannot be detected with an ordinary optical microscope. With the mismatch of the GaInP epilayer (+0.30%), many misfit dislocations are expected and indeed observed in the figure. On an ordinary planar substrate, these misfit dislocations would propagate unheeded until it reaches a free edge, namely, the edge of the substrate. However, as seen in the mesa below,  $60^\circ$  misfit dislocations that nucleate on the mesa surface terminate at the mesa edge. This phenomenon overtly shows the advantage of growing on patterned substrates: nucleation sources that depend on surface area, such as threading dislocations and dislocation multiplication, are sharply reduced.

Better results can therefore be achieved with a smaller mesa size. Figure 6 shows the TPL image taken from the  $16 \times 16 \mu\text{m}$  mesa sample, and no misfit dislocations on the mesa surfaces are observed. However, they do appear in the trenches between the mesas, and run unheeded since there is no barrier to stop them in the trenches. This should not affect the epilayers on the mesa since the dislocations can not interact through the mesa edge.



Fig. 5. A TPL image of the  $400 \times 400 \mu\text{m}$  mesa sample revealing the termination of misfit dislocations at the mesa edge.

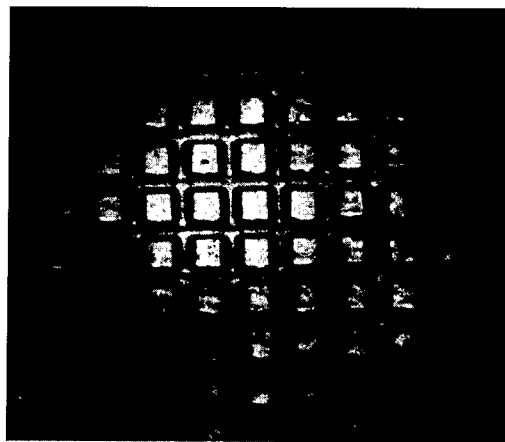


Fig. 6. A TPL image of the  $16 \times 16 \mu\text{m}$  mesa sample showing no dislocations on the mesas but in the trenches running the length of the image.

This method is practical for any material system, and is very well-suited for epitaxy of longer-wavelength laser structures on GaAs substrates. Al-free VCSELs are one such device, as are Al-free buried ridge VCSELs, which have the active region selectively etched before epitaxy of the top DBR.

### Conclusion.

We have grown a 36-period Al-free GaInP/GaAs DBR with a reflectivity of 0.989 at a wavelength of 0.983  $\mu\text{m}$ . We have also performed localized epitaxy of mismatched GaInP on patterned GaAs substrates and shown a reduction in the spreading of misfit dislocations, or in the case of the 16 x 16  $\mu\text{m}$  mesa sample, a complete elimination from the mesa surfaces. These techniques can be used for the epitaxy of Al-free VCSEL structures for wavelengths of 0.98  $\mu\text{m}$  and longer, which are potentially more reliable than Al-containing ones.

### References.

1. S. E. Swirhun, R. P. Bryan, W. S. Fu, W. E. Quinn, J. L. Jewell, and G. R. Olbright, in *Vertical-Cavity Surface-Emitting Laser Arrays*, Jack L. Jewell, ed., *Proc. SPIE* **2147**, 74 (1994).
2. J. A. Lehman, R. A. Morgan, M. K. Hibbs-Brenner, and D. Carlson, *Electron. Lett.* **31**, 1251 (1995).
3. K. L. Lear, K. D. Choquette, R. P. Schneider, Jr., S. P. Kilcoyne, and K. M. Geib, *Electron. Lett.* **31**, 208 (1995).
4. D. L. Huffaker, L. A. Graham, H. Deng, and D. G. Deppe, *IEEE Photon. Technol. Lett.* **8**, 974 (1996).
5. I. Eliashevich, J. Diaz, H. Yi, L. Wang, and M. Razeghi, *Appl. Phys. Lett.* **66**, 3087 (1995).
6. M. Razeghi, H. Yi, J. Diaz, S. Kim, and M. Erdtmann, in *In-Plane Semiconductor Lasers: from Ultraviolet to Midinfrared*, H. K. Choi and P. S. Zory, eds., *Proc. SPIE* **3001**, 243 (1997).
7. M. Razeghi, *Nature* **369**, 631 (1994).
8. K. Shinoda, K. Hiramoto, M. Sagawa, and K. Uomi, *Jpn. J. Appl. Phys. 2B* **35**, 4660 (1996).
9. K. Shinoda, K. Hiramoto, K. Uomi, and T. Tsuchiya, *Jpn. J. Appl. Phys. 2B* **34**, 1253 (1995).
10. B. Saint-Cricq, A. Rudra, J. D. Gainère, and M. Illegems, *Electron. Lett.* **29**, 1854 (1993).
11. J. W. Matthews and A. E. Blakeslee, *J. Cryst. Growth* **27**, 118 (1974).
12. R. People and J. C. Bean, *Appl. Phys. Lett.* **47**, 322 (1985).
13. A. Madhukar, *Thin Solid Films* **231**, 8 (1993).
14. E. A. Fitzgerald, Y. H. Xie, D. Brasen, M. L. Green, J. Michel, P. E. Freeland, and B. E. Weir, *J. Electron. Mater.* **19**, 949 (1990).

**The long wavelength luminescence observation from the self-organized InGaAs quantum dots grown on (100) GaAs substrate by metalorganic chemical vapor deposition.**

S. Kim, M. Erdtmann and M. Razeghi

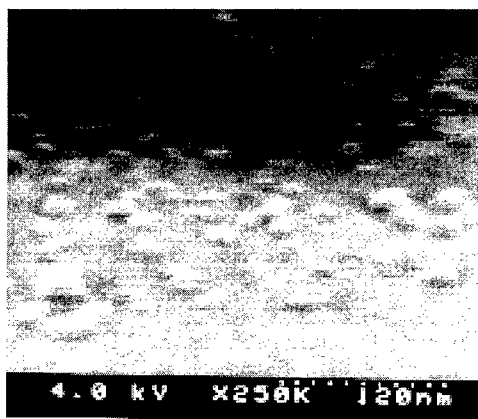
*Center for Quantum Devices, Department of Electrical and Computer engineering, Northwestern University, Evanston, IL 60208, USA*

**Abstract**

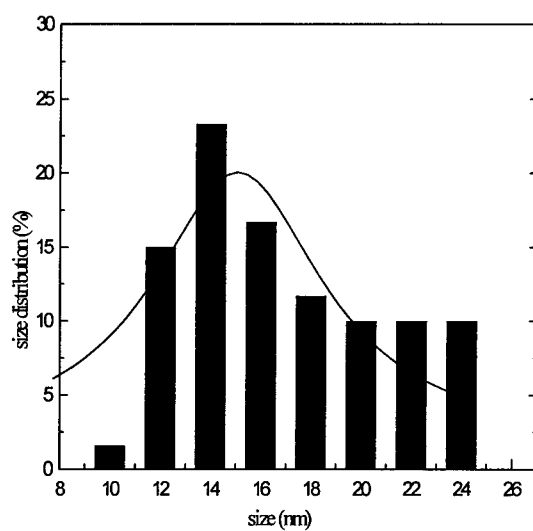
The self-organized InGaAs quantum dots with uniform size distribution were realized on (100) GaAs by metalorganic chemical vapor deposition (MOCVD). We demonstrated double stacked InGaAs dot structure constructed on InGaP matrix for the first time. Strong luminescence of 1.37  $\mu\text{m}$  peak wavelength from the dots, which is longest wavelength ever reported, was observed at room temperature. The temperature dependence of integrated luminescence intensity shows that the internal quantum efficiencies is very high.

The growth and fabrication of the nanostructure for optoelectronic devices have been receiving great interest recently not only because quantum dots can improve the laser performance drastically such as lower threshold current density, higher gain and higher temperature stability, but because fundamental physical phenomena are remained to be understood.<sup>1,2</sup> Recently self-organized growth technique has proven to be very successful in realizing a highly ordered array for InGaAs/GaAs, InAs/GaAs quantum dots without forming any defects.<sup>3-6</sup> Room temperature operation of InGaAs/GaAs and InAs/GaAs single and multilayer quantum dot lasers has been already reported.<sup>7-10</sup> However, majority of the previously reported dot structures were constructed on GaAs which made it difficult for determining the In composition of the InGaAs dots. Also it is hard to drag the luminescence at longer wavelength above 1.2  $\mu\text{m}$ . In this letter, we demonstrated the very long wavelength luminescence from the InGaAs dots assembled on the InGaP surface. The temperature dependence (77K ~ 300K) of the photoluminescence was measured. It shows the enhanced radiative efficiency comparable to the quantum well structure.

The double stacked InGaAs dot structures for this work were grown by MOCVD on (100) GaAs substrate at growth temperature of 480°C. Trimethylindium (TMIn), Triethylgallium (TEGa) Arsine( $\text{AsH}_3$ ) and Phosphine( $\text{PH}_3$ ) were used as the precursors. After the growth of GaAs buffer layer, lattice matched InGaP epilayer is deposited with 0.2  $\mu\text{m}$  thickness. The 10ML of  $\text{In}_x\text{Ga}_{1-x}\text{As}$  were deposited on the InGaP surface with growth rate of 0.6 ML/S. The dot formation was clearly observed using scanning electron microscope as shown in figure1. For double stacked structure, the InGaAs dots were



(a)



(b)

Figure 1. High resolution scanning electron microscope of an InGaAs dots on InGaP surface (a), and its Gaussian distribution of the dot size (b).

separated by the 300Å InGaP layer and finally InGaP layer were deposited as the carrier confinement. During forming of InGaAs dots, two different V/III ratios were used which are indicated as QD1 and QD2. For QD2, the V/III flow ratio is reduced to 200 from 450 for QD1. As a reference the separate confinement quantum well structure by inserting the 500Å thickness of GaAs between InGaP and InGaAs were grown at the same time. The well thickness is 28 Å and it didn't show any islands on the surface.

The formation of InGaAs dots on InGaP surface are shown in figure 1 (a). The sizes of dots were measured randomly. Most of dots are distributed from 12 nm and 23 nm in diameter. A few of large islands exceeding 500 Å due to the coarsening of the several dots are observed at the same time. The size distribution was fitted as Gaussian function centered at 16 nm given in figure 1(b). The average areal dot density for this small size dot is  $1 \times 10^{11} \text{ cm}^{-2}$ .

Photoluminescence was measured with varying the temperature from 77K to 300K at whole range by the Fourier transform PL system with 488 nm  $\text{Ar}^+$  laser. The strong and sharp luminescence emitting wavelength of 1.37  $\mu\text{m}$  from the InGaAs double stacked dots (QD1) was observed at room temperature given in figure 2. This peak wavelength is longest emitting wavelength from the epilayer grown on GaAs ever reported. The FWHM of the spectrum is 50meV at room temperature, which is not broadened with varying the temperature. But the broad peak at 77K is due to the size fluctuation.<sup>11</sup>

The effect of the fluctuation of dot sizes on the luminescence spectrum were clearly observed in the QD2 which were grown with lower V/III ratio. It has been analyzed more precisely in figure 3. The three different sharp peaks at 77K were

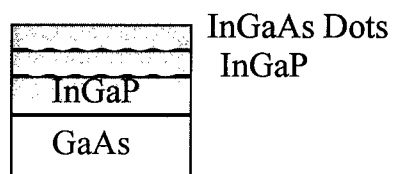


Figure 2 (a)

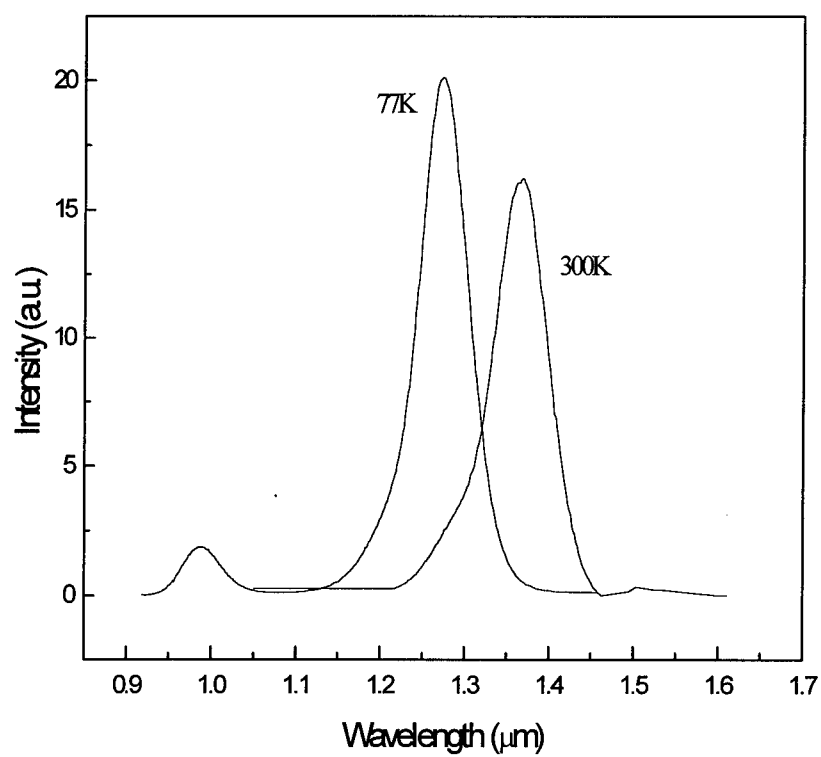


Figure 2. The double stacked dot structure (a), and the photoluminescence spectra of QD1 at 77K and 300K (b).



separated at 1.254eV, and 0.995eV, 0.953eV. The intensity of the peak at 1.254eV is rapidly dropped with increasing temperature and disappeared above 150K. However, the intensity and the lineshape of the peak 2 follow as the main peak1 with varying the temperature. The peak 2 may come from different size of the dot ensemble deviated from the peak1. The temperature dependence of the peak energy of peak1 and peak2 is clearly decomposed as given in figure 3 (b).

The optical transition energy from E1-HH1 of InGaAs/InGaP dots were estimated from <sup>12</sup>,

$$E(E1-HH1) = \frac{\hbar^2 \pi^2}{2 R^2} \left( \frac{1}{m_e} + \frac{1}{m_h} \right) - \frac{1.8 e^2}{\epsilon R} \quad (1)$$

$m_e$  is the electron effective mass,  $m_h$  is heavy hole effective mass, and  $R$  is the radius of the spherical dots. Because the effective mass of  $\text{In}_x\text{Ga}_{1-x}\text{As}$  is varied with the  $x$  composition, first we need to determine the In composition for calculation. It was determined using the *as grown* quantum well structure. From the photoluminescence measurement, the PL peak energy was found at 1.008 eV. Because we know the well thickness, the composition was easily found nearly at  $x=0.6$  from the calculation of the transition energy for the single quantum well with 28 Å well thickness. Using this  $x$  composition at 0.6, the approximate transition energy is derived as 0.93 eV from the equation (1), assuming the dots are spherical with radius of 80Å which is measured as shown above. This value has good agreement with the PL peak energy (0.905eV) observed from our dot structures. This implies also the In composition of the InGaAs dots formed on InGaP surface is more uniform comparable to be grown on GaAs from the calculation.

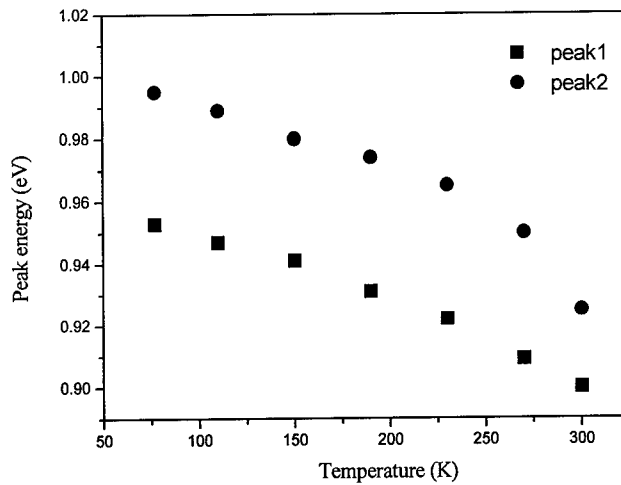
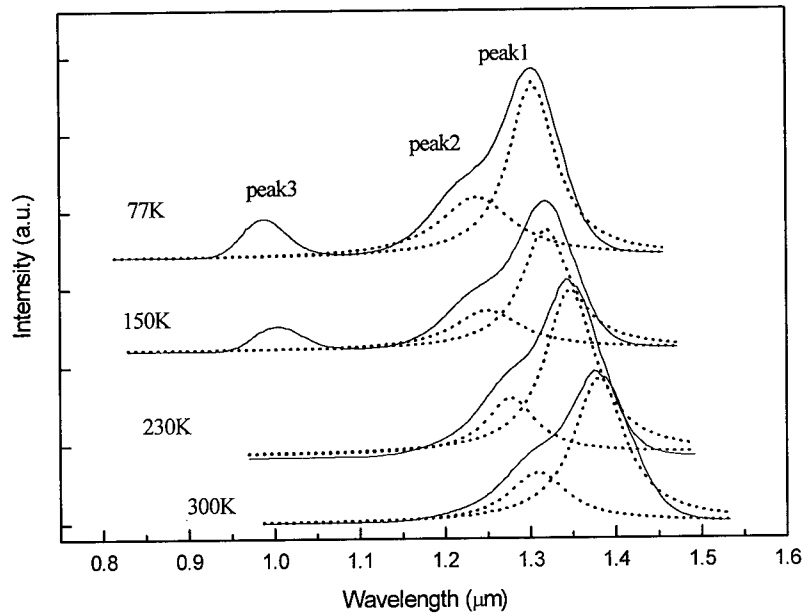


Figure 3. (a) The temperature dependence of photoluminescence spectra from QD2. The peaks are resolved with Gaussian distribution. (b) The temperature dependence of the peak energy for separated peaks.

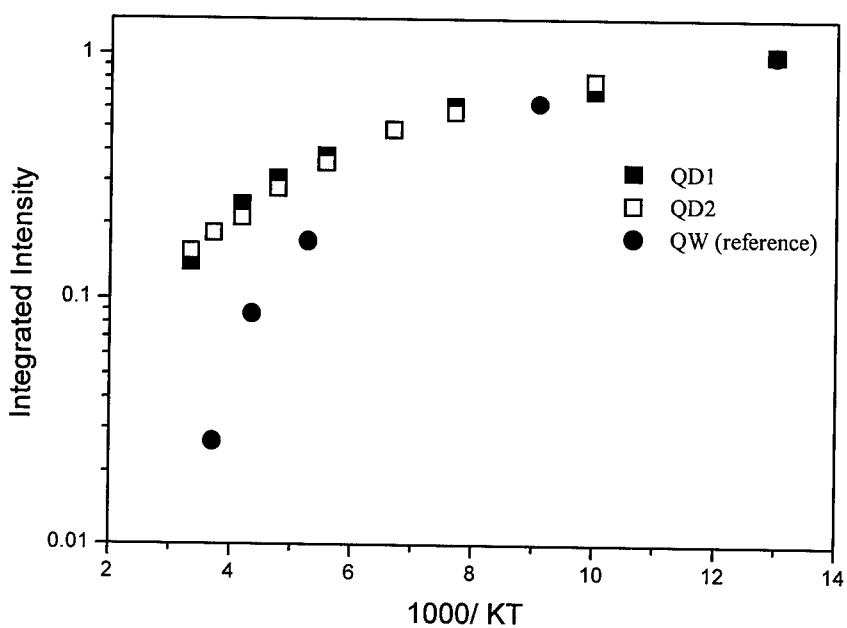


Figure 4. The temperature dependence of the integrated intensity of QD structures and QW structure.

In figure 4, the temperature dependence of integrated intensity from 77K to 300K is shown for QD structures and QW structure as reference. The radiative efficiency is increased compared to the quantum well as shown in this figure. This is due to the reduction of the non-radiative recombination for dot structure compared to the QW structure. Apparently QW structure suffer from the misfit dislocation and defects caused from the large lattice mismatch as 3.8 % between well and barrier. This explains the drastic dropping of the integrated luminescence intensities as increasing temperature for QW structure. The intensities of the QDs are dependent on temperature as  $I(T) \sim I(0) e^{-E_a/kT}$  fitted as a curve above 150K. The activation energy is 3 times lower than QW structure.

In conclusion, we successfully grew self-organized InGaAs double stacked quantum dot structures on (100) GaAs substrate by metal organic chemical deposition. The dots were constructed on InGaP surface with areal dot density of  $1 \times 10^{11} \text{cm}^{-2}$ . The strong photoluminescence from E1-H11 optical transition was observed at 1.37  $\mu\text{m}$ . The temperature dependence of the integrated intensity reveals the enhanced radiative efficiency by a factor of 3.

#### Reference

1. Y. Arakawa and H. Sakaki, *Appl. Phys. Lett.* **40**, 939 (1982)
2. M. Asada, Y. Miyamoto, and Y. Suematsu, *IEEE. J. Quantum. Electron.* QE-**22**, 1915 (1986)

3. D. Leonard, M. Krishnamurthy, C. Reaves, S. Denbaars, and P. Petroff, Appl. Phys. Lett. **63**, 3203 (1993)
4. J. Pamulapaiti, P. Bhattacharya, J. Singh, P. Berger, C. Snyder, B. Orr and R. Tober, J. Electron. Mater. **25**, 479 (1995)
5. L. Goldstein, F. Glas, J. Marzin, M. Charasse, and G. LeRoux, Appl. Phys. Lett. **47**, 1099 (1985)
6. D. Leonard, S. Fafard, K. Pond, Y. Zhang, J. Mertz, and P. Petroff, J. Vac. Sci. Technol. **B12**, 2516 (1994)
7. R. Mirin, A. Cossard, and J. Bowers, Electron Lett. **32**, 1732 (1996)
8. Q. Xie, A. Kalburge, P. Chen, and A. Mudhukar, IEEE photo. Technol. Lett. **8**, 965 (1996)
9. K. Kamath, J. Phillips, H. Jiang, J. Singh, and P. Bhattacharya, Appl. Phys. Lett. **70**, 2952 (1997)
10. F. Heinrichsdorff, M. H. Mao, N. Kirstaedter, A. Krost, D. Bimberg, A.O. Kosogov, P. Werner, Appl. Phys. Lett. **71**, 22 (1997)
11. M. Grundmann, V.N. Ledentsov, O. Stier, D. Bimberg, V.M. Ustinov, P.S. Kopèv, and Zh.I. Alferov, Appl. Phys. Lett. **68**, 979 (1996)
12. Ulrike Woggan *Optical properties of semiconductor quantum dots*, Springer, pp48-52

## DEEP HOLE TRAPS IN Be - DOPED $\text{Al}_{0.5}\text{Ga}_{0.5}\text{As}$ MBE LAYERS

J. Szatkowski, E. Płaczek-Popko, K. Sierański, O.P. Hansen<sup>1</sup>  
Institute of Physics, Technical University of Wrocław,  
Wybrzeże Wyspiańskiego 27, 50-370 Wrocław, Poland.  
<sup>1</sup>Oersted Laboratory, University of Copenhagen, Universitetsparken 5,  
DK-2100 Copenhagen, Denmark.

**Keywords:** AlGaAs, defects, DLTS.

**Abstract:** Deep hole states in p-type  $\text{Al}_{0.5}\text{Ga}_{0.5}\text{As}$  grown by MBE have been studied by the deep-level transient spectroscopy (DLTS) method. The as grown and  $\text{He}^{++}$ -ion irradiated samples have been investigated.

In the as-grown samples five hole traps labelled by us as H0 to H4 were detected. For the traps H1, H3 and H4 thermal activation energies obtained from Arrhenius plots were equal to:  $E_{T1} = 0.15$  eV,  $E_{T3} = 0.4$  eV and  $E_{T4} = 0.46$  eV. Hole emission from H2 trap has been found to be electric field dependent. The electric field dependence has been explained in the terms of the Frenkel-Poole mechanism.

$\text{He}^{++}$ -ion bombardment of samples introduced a new deep trap with activation energy scattered among samples within 0.62 eV to 0.77 eV range.

### INTRODUCTION

Heavily doped p type  $\text{Al}_x\text{Ga}_{1-x}\text{As}$  has been used both as an active element in many devices and as a constituent of lattice matched heterostructures. Molecular beam epitaxy (MBE) has been extensively applied for growing GaAs/  $\text{Al}_x\text{Ga}_{1-x}\text{As}$  heterostructures. At present beryllium is a preferable dopant in MBE-grown  $\text{Al}_x\text{Ga}_{1-x}\text{As}$  as it is nearly an effective mass like acceptor of a sharp incorporation profile [1]. However, Be behaves not only as a shallow acceptor level but it may introduce some deep levels, especially for higher Al contents [2,3]. In [2] the photoluminescence from highly Be-doped  $\text{Al}_x\text{Ga}_{1-x}\text{As}$  grown by MBE was studied and the experimental results have been attributed to the existence of deep levels associated with interstitial Be. In [3] the results of photoluminescence measurements on highly Be-doped  $\text{Al}_x\text{Ga}_{1-x}\text{As}$  have been explained in the terms of dopant-defect complexes, the so-called self-activated centers. Using secondary ion mass spectroscopy [4], it has been found that in Be-doped  $\text{Al}_{0.6}\text{Ga}_{0.4}\text{As}$  grown by MBE the presence of oxygen results in formation of stable Be - O complexes. In [5] MBE AlAs  $p^+-n$  junctions grown on GaAs have been studied by DLTS and the incorporation of Be was found to give rise to two hole traps.

The presence of defect levels within a heterostructure is the factor limiting performance of semiconductor devices and this is the main reason for investigating properties of these levels. Apparently an established picture of deep hole traps in  $\text{Al}_{1-x}\text{Ga}_x\text{As}$  does not exist. A number of parameters, such as: growth method, Al fraction, type of acceptor dopants, and sample configurations seem to play a role for the hole trap formation. The best of systematics is related to hole traps caused by transition metal impurities, e.g. Fe and Cu. It has been found that the position of the energy levels of such impurities according to vacuum level is constant, in isovalent semiconducting compounds, so the energetic positions of such traps can be used as common reference level [6,7]. Thus in  $\text{Al}_{1-x}\text{Ga}_x\text{As}$  the activation energies of the traps depend on the aluminium fraction in the same way as does the energy of the top of the valence band.

The defect centers in p type  $\text{Al}_x\text{Ga}_{1-x}\text{As}$  have been studied so far mainly by photoluminescence and electrical transport measurements. We have recently presented a preliminary report on DLTS measurements of hole traps in Be-doped  $\text{Al}_{0.5}\text{Ga}_{0.5}\text{As}$  grown by MBE [8]. In present paper we have added some new results on electric field enhanced emission rate followed by deeper theoretical analysis of it and compared our results (for  $x=0.5$ ) with results obtained by other authors for different Al content. We have shown also preliminary observations of  $\text{He}^{++}$  ion irradiated samples. We expect that the results on irradiated samples would mark the traps connected with vacancies.

### RESULTS AND DISCUSSION

The wafer of  $1\mu\text{m}$  thickness from which the samples were made was grown on a semi-insulating [001] GaAs substrate in a Varian Gen II MBE-machine, dedicated to Ga, Al, and As, with Si and Be as the dopants. The sample configuration was that of Schottky diodes with ohmic contact made to  $\text{p}^+$  GaAs [8]. Thermal evaporation of Au/Zn/Au followed by alloying was used for the ohmic contact, and Al/Ti/Au for the Schottky contact. Leads were attached by silver paint.

The measurements made on our samples were following : C-V measurements, standard DLTS and electric field dependence of emission rate. DLTS measurements were performed within 80K-300K temperature range using DLS-82E system manufactured by Semitrap Hungary. This system is based on a 1 MHz capacitance bridge meter and a lock-in integrator. All studied samples have shown the same DLTS behaviour.

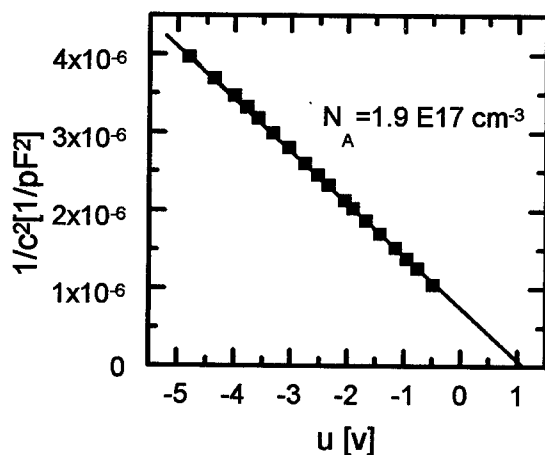


Fig.1.  $C^{-2} - V$  dependence for an exemplary sample.

### C-V MEASUREMENTS

The samples showed a linear  $C^{-2} - V$  dependence, as it can be seen in Fig.1 for an exemplary sample, with shallow net acceptor concentration  $N_A = (2.0 \pm 0.1) \times 10^{17} \text{ cm}^{-3}$  and built-in voltage  $U_B = (1.1 \pm 0.1) \text{ V}$ ; the  $\pm$  indicating the spread among the samples. A reverse voltage up to  $-5\text{V}$  was applied. From these numbers we have estimated the depletion width to be about  $200 \text{ nm}$  at a reverse bias of  $-5\text{V}$ ; comfortably less than  $1 \mu\text{m}$  thickness of the  $\text{Al}_{0.5}\text{Ga}_{0.5}\text{As}$  layer.

### STANDARD DLTS

The standard DLTS measurements were carried out for different reverse voltage  $U_R$  ranging from  $-3.5\text{V}$  to  $-5 \text{ V}$ . Different duration time of filling pulses were used. Five dominant levels, labelled by us as H0 to H4 were detected in all of our samples. A representative DLTS spectrum is shown in Fig.2.

Properties of the H0 trap were not investigated as the temperature position of its DLTS peak was beyond our experimental range, i.e. below  $77\text{K}$ .

The dynamic process of capture and emission of holes by deep traps can be described in terms of a capture cross section,  $\sigma_p$ , and emission rate,  $e_p$ . The hole emission rates are related to capture cross section by detailed balance equation :

$$e_p = \sigma_p v_{th} N_v \exp\left(-\frac{E_T}{kT}\right) \quad (1)$$

where  $v_{th}$  is a thermal velocity of holes,  $N_v$  is an effective density of states at valence band edge and  $E_T$  is activation energy for transient emission. In our DLS-82E system the DLTS signal peak takes place at temperature where lock-in frequency,  $f$ , is related to emission rate by relation  $e_p = 2.17f$ . From Arrhenius plot i.e. the plot of experimentally obtained emission rates divided by square temperature ( $e_p/T^2$ ) versus reciprocal temperature ( $1/T$ ) activation energy and capture cross section of a trap can be determined.

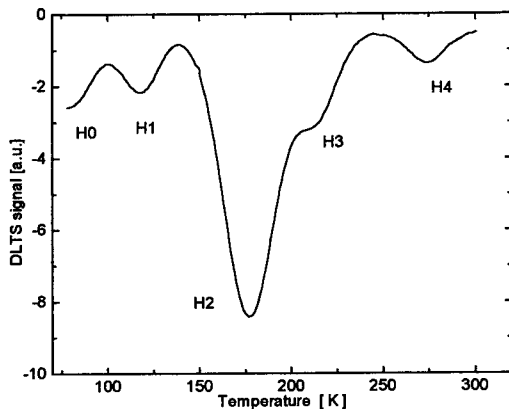


Fig.2. Exemplary DLTS temperature scan for Be doped  $\text{Al}_{0.5}\text{Ga}_{0.5}\text{As}$ -Al/Ti/Au Schottky contact (taken at  $f=699$  Hz and for  $5\mu\text{s}$  filing pulse).

Arrhenius plots for H1, H2, H3 and H4 traps are shown in Fig.3. For H2 trap apparently the Arrhenius plots for high field (H2 - H)  $4.5 \cdot 10^5$  V/cm and low field (H2 - L)  $1.8 \cdot 10^5$  V/cm are presented.

Activation energy  $E_T$  and capture cross section  $\sigma_p$  calculated from the Arrhenius plots are given in Table I. For H2 trap, from the Arrhenius plots, we obtained energy activation equal to 0.22 eV for high field and 0.26 eV for low field.

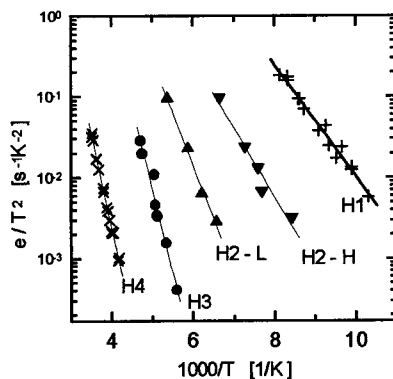


Fig.3. Arrhenius plots for the traps H1, H2, H3 and H4. The straight lines are the best least square fit to the experimental data.

In all samples the traps concentrations are of the order of  $10^{14} \text{ cm}^{-3}$ . Concentration of H1 is decreasing slightly towards the junction depth (from  $5 \cdot 10^{14} \text{ cm}^{-3}$  to  $2 \cdot 10^{14} \text{ cm}^{-3}$ ) whereas for the trap H4 it remains nearly constant (about  $2 \cdot 10^{14} \text{ cm}^{-3}$ ) within whole junction region.

The profile for H3 trap was not measured as it was very difficult to extract the value of DLTS signal related to this trap from the total DLTS signal; however qualitative comparison of corresponding DLTS signal (cf. Fig.2) let us evaluate that its concentration is of the order of  $10^{13} \text{ cm}^{-3}$ .



trap	Energy activation [eV]	$\sigma_p$ [cm <sup>2</sup> ]
H1	0.15	$5 \cdot 10^{-17}$
H3	0.40	$3 \cdot 10^{-14}$
H4	0.46	$6 \cdot 10^{-16}$

Table I. Activation energy  $E_T$  and capture cross section  $\sigma_p$  for H1, H3, H4 traps.

### ELECTRIC FIELD DEPENDENCE OF THE EMISSION RATE FOR H2 TRAP

In order to study the influence of electric field on the emission rate we applied the double correlation DLTS method (DDLTS) introduced by Lefevre and Schulz [9]. In our DLS-82E system this method corresponds to the differential DLTS technique [10]. These measurements were performed by using two filling pulses of the same widths and different heights,  $U_1$  and  $U_2$ . The value of reverse bias  $U_R$  and  $\Delta U = U_1 - U_2$  was kept constant and chosen in such a way that the  $\Delta U < U_1, U_2$  condition was fulfilled. This way the DLTS signal came from a thin slice of the depletion region, ensuring the near uniformity of the electric field. The value of electric field was varied by changing the value of  $U_1$  voltage within  $|U_R| > U_1 > 0$  voltage range. For each fixed value of  $U_1$ , isothermal DLTS scans i.e. DLTS signal at constant temperature as a function of a lock-in frequency  $f$  were taken. This way we obtained emission rate versus electric field intensity dependence. Results are shown in Figure 4. The emission rates obey following relationship (solid lines in Fig.4):

$$e_p = e_{p0} \exp[\alpha F^{1/2} / kT] \quad (2)$$

where  $F$  is the electric-field intensity. The value of  $\alpha$  obtained from Fig.4. is equal to  $2.3 \pm 0.1 \cdot 10^{-4} ((\text{eV})^2 \text{cm/V})^{1/2}$  at both temperatures. The dependence of emission rate on a square root of electric field intensity described by Eq.(2) can be interpreted as the consequence of the Poole-Frenkel effect. According to the theory of that effect the theoretical value of  $\alpha$  for  $\text{Al}_{0.5}\text{Ga}_{0.5}\text{As}$   $\alpha = 2.2 \cdot 10^{-4} ((\text{eV})^2 \text{cm/V})^{1/2}$  [11]. The experimental value of  $\alpha$  agrees excellently with the theoretical one. Combining Eq.(1) and Eq.(2) one could expect that the trap activation energy  $E_T$  depends on the electric - field intensity  $F$  according to the equation:

$$E_T(F) = E_{T0} - \alpha F^{1/2} \quad (3)$$

where  $E_{T0}$  is the activation energy in the bulk (i.e. far away from the space-charge region). With the help of above equation and experimentally obtained value of  $\alpha = 2.3 \cdot 10^{-4} ((\text{eV})^2 \text{cm/V})^{1/2}$  we calculated for the trap H2  $E_{T0} = 0.37 \text{ eV}$ .

The electric field dependence of emission rate indicates that carrier emission from the trap has to be accompanied by acquiring a net charge by the defect, i.e. the H2 trap has to be charged upon a hole emission and neutral upon a hole capture. According to our DLTS measurements emission from the trap H2 in the bulk i.e.  $D^0 \rightarrow D^+ + h^+$  transition requires energy  $E_{T0} = 0.37 \text{ eV}$ .

### IRRADIATED SAMPLES

We have obtained some preliminary results on samples irradiated with  $\text{He}^{++}$  -ions of 500keV. In Fig.5 we present the DLTS scan both for irradiated and non-irradiated sample. In 77K - 300 temperature range we observe four traps. For all traps DLTS signal is much higher (about one order) then for non-irradiated sample. Two of them (H3 and H4) have the same energy activation. The origin of the first DLTS peak in irradiated samples is not clear.

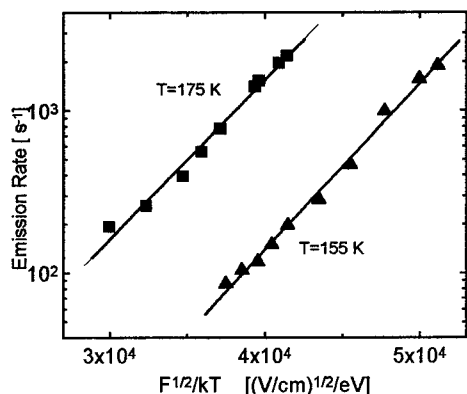


Fig.4. Emission rate determined from isothermal DLTS analysis for the trap H2 versus square root of electric field intensity divided by  $kT$  product at two temperatures.

New trap labelled by us as H5 appears on the temperature scan. Its activation energy is evaluated as equal to 0.62 eV - 0.77 eV for different samples. According to above result we can make a hypothesis that the traps H3 and H4 are related to native defects in  $\text{Al}_x\text{Ga}_{1-x}\text{As}$ .

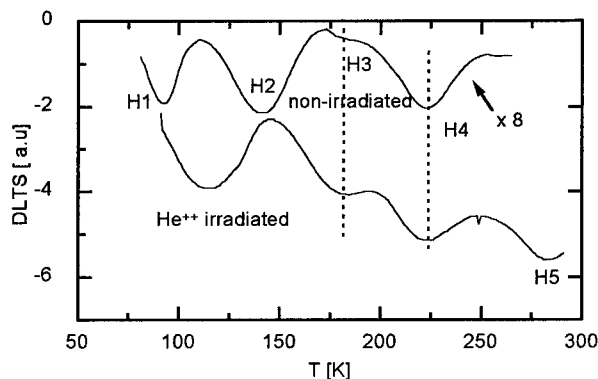


Fig.5. Exemplary DLTS scan of  $\text{He}^{++}$  irradiated sample (taken at  $f=5\text{Hz}$  and for 1ms filing pulse) as compared to the non irradiated one.

### CHEMICAL TRENDS

Up to date the results concerning hole traps in  $\text{Al}_x\text{Ga}_{1-x}\text{As}$  are obtained mostly for n type materials. All the most important results are collected in [12]. In Fig.6 we have compared our results ( $x=0.5$ ) with the results obtained by other authors for different Al content [5,12,13,14]. In the figure the trap energies are referred with respect to the valence band edge after taking into account valence band shift with Al content [15,16]. Zero energy in the figure was taken at the energy of the GaAs valence band top. Due to the uncertainty of their origin, deep levels are labelled by their activation energy. For our H2 traps we draw the energy in the bulk.

### CONCLUSIONS

In the paper we have presented systematic study of deep levels in Be doped  $\text{Al}_{0.5}\text{Ga}_{0.5}\text{As}$  by DLTS measurements. The DLTS measurements reveal the presence of five hole traps. Properties of four traps have been determined. From the measurements of electric field dependence of emission rate we established that emission from one level (H2) is strongly electric field dependent. This dependence was explained in terms of Poole-Frenkel effect, resulting in significant

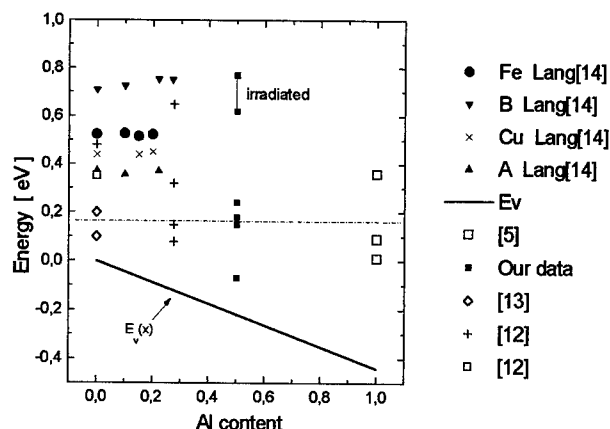


Fig.6. Trap energies in  $\text{Al}_x\text{Ga}_{1-x}\text{As}$  as referred with respect to the valence band edge versus Al content, after taking into account valence band shift with Al content  $x$  (solid line is  $E_v = f(x)$  taken from [15,16]). Dashed line is only eye-guide. Vertical line means spread among the data for energy activation for H5 for different samples.

shift of the activation energy with electric field (from 0.22 eV for field intensity  $4.5 \cdot 10^5$  V/cm to 0.37 eV for zero field). Preliminary results for irradiated samples show existence of another trap of energy activation from 0.62 eV to 0.77 eV (for different samples).

**Acknowledgements.** MBE-growth and sample processing was made by C.B. Soerensen at the III-V Nano-Lab in Copenhagen.

## References

1. Ilegems, J. Appl. Phys. **48**, 1278-1287 (1977)
2. M. Morita, K. Kobayashi, T. Suzuki, Y. Okano Jpn. J. Appl. Phys. **28** (1989) 553.
3. J. Ogawa, K. Tamamura, K. Akimoto, and Y. Mori, J. Appl. Phys. **63**, 2765 (1988)
4. N. Chand, A. S. Jordan, and S. N. G. Chu, Appl. Phys. Lett. **59**, 3270 (1991)
5. P. Krispin and R. Hey, Materials Science Forum **143-147**, 359 (1994)
6. L. J. Sham in „Physics of low dimensional semiconductor structures” ed. P. Butcher, N. H. March, M. P. Tosi (Plenum Press 1993) Chap. 1., p. 13.
7. K. W. Nauka in „Imperfections in III / V materials” edited by E. R. Weber, vol. 38 of *Semiconductors and semimetals* edited by R. K. Willardson and A. C. Beer (Academic Press), p. 343-396 (1993)
8. J. Szatkowski, E. Płaczek-Popko, K. Sierański, and O. P. Hansen in „Proc. of the International Conference on Advanced Devices and Mikrosystems”, Smolenice, October 20-24, 1996 p. 69-72
9. H. Lefevre, M. Schulz Appl. Phys. **12**, 45 (1977).
10. G. Ferenczi, P. Krispin, M. Somogyi J. Appl. Phys. **54**, 3902 (1983).
11. J. Frenkel, Phys. Rev. **54**, 647 (1938).
12. A. R. Peaker and F. Saleemi in „Properties of Aluminium Gallium Arsenide” edited by S. Adachi (EMIS Datareview Series No. 7, INSPEC 1993), p. 269-277 (1993)
13. S. Kalem and G. E. Stillman, Jpn. J. Appl. Phys. **33**, 6086 (1994)
14. D. V. Lang, R. A. Logan, and L. C. Kimerling in „Physics of Semiconductors, Proc. of the 13<sup>th</sup> International Conference, Rome, August 30-September 3, 1976.” ed. F. G. Fumi p. 615-618
15. T. Forchhammer, E. Veje and P. Tidemand-Petersson, Phys. Rev. B **52**, 14693 (1995)

## NANOTUBES AND PINHOLES IN GaN AND THEIR FORMATION MECHANISM

**Z. Liliental-Weber, Y. Chen,\* S. Ruvimov, and J. Washburn**  
Lawrence Berkeley National Laboratory 62/203, Berkeley, CA 94720, USA  
\* Hewlett Packard, Palo Alto, CA, USA

### Introduction

GaN has been recognized as a wide-bandgap, high temperature semiconductor material that has important applications in both short-wavelength optoelectronic and high power/high frequency devices [1]. Because of lack of lattice matched substrates GaN is grown mostly on  $\text{Al}_2\text{O}_3$  or SiC with about 14% or 3.5 % lattice mismatch, respectively. This lattice and also the thermal mismatch between the layer and the substrate leads to three dimensional growth and a high density of defects. These defects are mainly dislocations located at small-angle grain boundaries. However, there are other defects e.g. inversion domains (IDs) and nanotubes which appear as straight lines in cross-section transmission electron micrographs (TEM) are also visible in plan-view [2-6]. In plan-view they have a perfect or slightly elongated hexagonal shape. Another defect which looks similar in plan-view micrographs is a pinhole. This suggests that some defects that have been assumed to be "nano-tubes" may not be.

The nanopipes and pinholes appear to have the same origin [3,7]. Both start with a V-shape cone-like feature faceted on  $(10\bar{1}1)$  low energy polar planes, and both are empty inside. Their presence is not limited to a particular growth method or substrate. Furthermore, in GaN there are inversion domains which look very similar to nanotubes, they are elongated along the c-axis and they are faceted on  $(1\bar{1}00)$  planes, but are filled with material having opposite polarity compared to the surrounding matrix. They can be easily distinguished by convergent beam electron diffraction (CBED).

It is not clear at this point how a nanotube forms. From the study of SiC one could conclude that nanotubes are empty core screw dislocations following the Frank model [8], who suggested that a screw dislocation of large Burgers vector might have an empty core. The open-core, therefore, should represent an equilibrium between the extra surface free energy and the decrease in lattice strain energy. According to Frank's model the radius of the hole is proportional to the square of the Burgers vector, e.g.  $r = \mu b^2 / 8\pi^2 \gamma$ , where  $r$  is the radius of empty core,  $b$  is the Burgers vector of the dislocation,  $\mu$  is the shear modulus,  $\gamma$  is the specific surface energy. The present TEM observations show that although some of the empty holes are associated with dislocations [3,9] the radii of the holes have values ranging from a minimum at about 10 nm. From the Frank equation it can be estimated that the Burgers vector  $b$  corresponding to an empty hole of 10 nm should be about 4 nm, which is an order of magnitude larger than the Burgers vectors observed in these experiments. Therefore, the Frank equilibrium model can not explain the presence of these empty holes if one takes  $\gamma/\mu \sim 5 \times 10^{-2} \text{ nm}$  based on constants for metals. In recently published data for

SiC  $1.1 \times 10^{-3}$  to  $1.6 \times 10^{-3}$  nm were used [10]. These data did agree with  $3.3 \times 10^{-3}$  nm empirically obtained by Sunagawa [11], but do not agree with values obtained by Tanaka [12]. Theoretical estimation of surface energy  $\gamma$  for the  $(1\bar{1}00)$  and  $(11\bar{2}0)$  in SiC and experimentally measured values of  $\mu$  would give values of  $\gamma/\mu$  ranging from  $1.8 \times 10^{-2}$  to  $2.8 \times 10^{-2}$  nm [13]. Since elastic constants in GaN are not well established the validity of the empty core screw dislocation model is questionable. In this paper a different possible explanation will be provided for the formation of “hollow” type defects based on the observation of strong growth rate hierarchy in GaN for nonpolar and polar growth directions and formation of facets on slow growth  $(10\bar{1}1)$  planes, especially when growth steps may be poisoned by foreign atoms such as oxygen, other impurities or dopants such as: Al, In, Mg or Si.

### Experimental data and discussion

(Fig. 1a) shows a typical example of a nanotube in plan-view TEM faceted on  $(1\bar{1}00)$  planes. The lattice planes visible on this micrograph could be seen only with large image defocus suggesting a large depth along the c-axis. Some contrast “disturbance” in the central part of this image is coming either from a dislocation attached to this hole or from some foreign particle. The sample outside the nanotube is much too thick for lattice imaging. Burgers circuits around such a “particle” in many cases does not show an image displacement, meaning that if there is a dislocation associated with the hole it is a pure screw dislocation. However, there are similar micrographs [14] which clearly show an image displacement which establishes the presence of an edge dislocation. (Fig. 1b) shows an example of two nanotubes formed above each other along a screw dislocation. Both these nail-like tubes shown on (Fig. 1b) are closed on the top along c-planes, however, in the same sample others extend all the way to the sample surface. These tubes all start with the V-shape feature on  $(10\bar{1}1)$  polar planes, similar to the pinhole shown in the subsurface area of the sample (Fig. 1c). Many nanotubes were found to be formed on the top of dislocation half loops formed above a GaN buffer grown either on SiC or sapphire (Fig. 1d). A much higher density of nanotubes were observed on the top of the buffer layer grown on sapphire suggesting that oxygen outdiffusion from the substrate may play a significant role [7]. Similar observations were provided by another group [6]. It was noticed that these tubes were attached not only to straight dislocations along the c axis but were also attached to the “arching” dislocations. Since heteroepitaxial layers of GaN always have a high density of dislocations, it is difficult to determine if dislocations are always associated with the nucleation of these “hollow” defects or if they are attracted to the holes later so as to reduce line energy.

Clear evidence of attraction of a dislocation to the wall of a pinhole was observed in a homoepitaxial layer (Fig. 2). This figure shows two dislocations attracted to an inversion domain and a pinhole. This inversion domain and the dislocations were independently originated at the substrate interface but with subsequent growth they terminated on the facet of the pinhole. The dislocations then bend toward the hole during further layer growth to shorten their length and, therefore, reduce the total free energy of the system. Diffraction contrast used for the characterization of these

dislocations showed that they were of different types, the lower dislocation closer to the inversion domain had a near screw character, while the upper one was lying at a larger angle to its Burgers vector. This observation clearly shows that dislocations did not originate this pinhole but were later attracted to it.

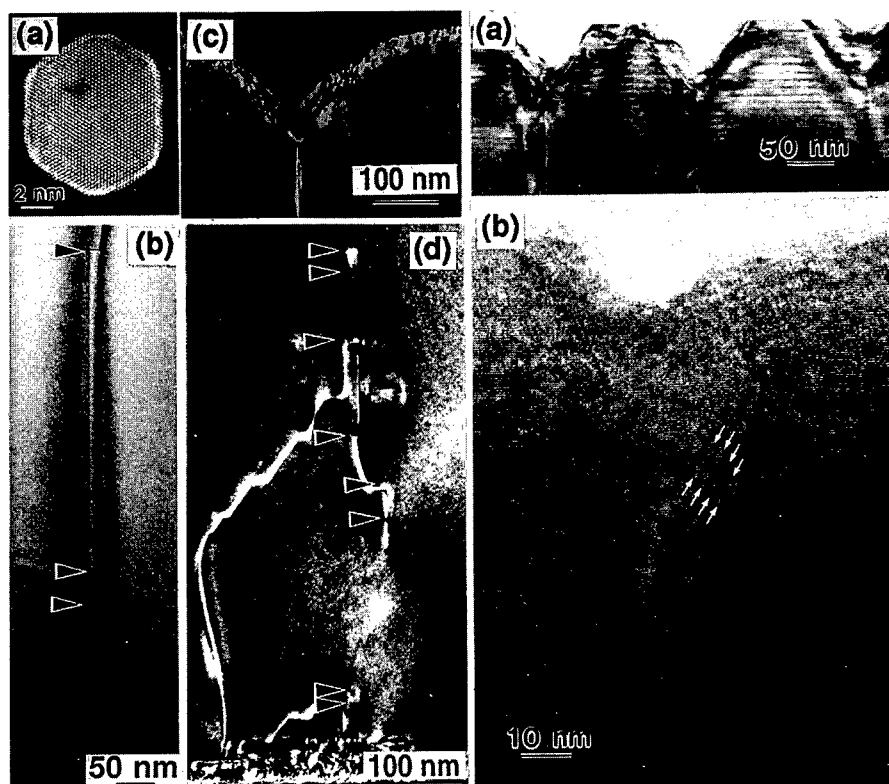


Fig. 1. (a) Plan-view TEM micrograph of a nanotube in GaN; (b) Cross-section micrograph showing two nanotubes along the growth direction aligned with a screw dislocation; (c) Cross-section micrograph showing a dislocation in oxygen rich GaN (with mixed edge-screw character) attached to a pinhole; (d) Nanotubes formed above a GaN buffer layer grown on sapphire attached to a dislocation half-loop.

Fig. 3. (a) Pinholes formed in InGaN/GaN; (b) High resolution image of MQW's across a pinhole. Note growth of QW on  $(10\bar{1}1)$  planes with different thickness (marked by arrows) than along the c-direction.

From a careful study of the contrast on Fig. 2a one can also distinguish three grains of GaN which were formed at the interface (with the inversion domain in the center-see Fig.2b- a schematic drawing). From the contrast difference within the islands (II and III on Fig. 2a) and above them, observed on the two sides of the

inversion domain it can be seen that the layer growth on top of the islands proceeded in two directions: along the  $c$ -axis and along faceted walls of the islands inclined to the  $c$  axis. These faceted island walls were parallel to  $(10\bar{1}1)$  polar planes. By measuring the layer thickness  $t_2$  on the top of the islands along the  $c$ -axis and on the sides of the  $(10\bar{1}1)$  facets  $t_1$  one can estimate that the growth rate on these polar planes was about 2 to 2.5 times slower in comparison to the growth on the  $c$ -plane. Bulk GaN platelets, are very thin in the  $c$  direction compared to their length and width [15]. Measurement of these GaN plate dimensions shows that growth in the non-polar directions can be up to 50-100 times faster than in the polar  $c$ -direction. The details of these studies are described elsewhere [3,7]. Therefore, growth on  $(10\bar{1}1)$  is the slowest and any growth surface indentation results in  $(10\bar{1}1)$  facets that tend to stabilize the hollow indentation allowing it to increase in size during further growth.

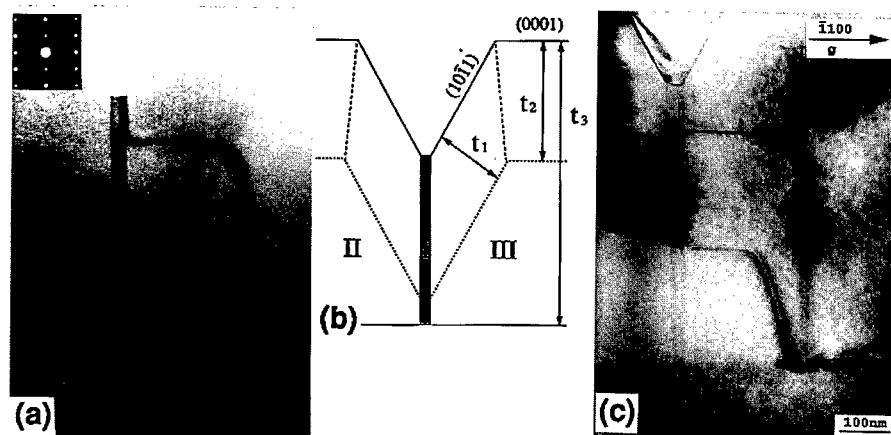


Fig. 2. (a) Cross-section of a homoepitaxial GaN layer grown in B polarity (direction N to Ga along the  $c$ -axis) on bulk GaN. Two dislocations and an inversion domain are associated with a pinhole, only the lower part of the sample is shown; (b) Schematic drawing of fig. (a) extended to the sample surface. Measurements from the full image show that the height of the inversion domain (I) is about half that of the surrounding layer  $t_3$ , showing different growth rates for the two opposite polar growth directions. Two subgrains (marked in b as II and III) are growing on the two sides of the inversion domain. Growth proceeds on these grains with thickness  $t_2$  along the  $c$ -axis and  $t_1$  perpendicular to the  $(10\bar{1}1)$  facets; (c) The same image taken with a different diffraction condition. Note the contrast disappearance from the inversion domain and that the dislocations and the inversion domain start from two different defects present at the interface.

Our studies show that impurities such as oxygen lead to increased numbers of hollow defects. It was observed that the density of nanotubes increased by a factor of about 3 (from  $1 \times 10^7$  to  $2.7 \times 10^7 \text{ cm}^{-2}$ ) when oxygen concentration changes from  $5 \times 10^{17}$  to  $4 \times 10^{18} \text{ cm}^{-3}$ , and the number of pinholes changes by almost one order of

magnitude from  $6 \times 10^6$  to  $4 \times 10^7 \text{ cm}^{-2}$ . The diameter of nanotubes is changing only slightly from (3-10) nm to (6-12) nm, and the diameter of pinholes changes from about 100 nm to (300-1800) nm, whereas the density of dislocations remains almost constant ( $1.8 \times 10^9$  to  $2 \times 10^9 \text{ cm}^{-2}$ ). This lack of correlation between density of dislocations and numbers of "hollow" defects was also observed in Si doped GaN, where a change of Si concentration from  $9 \times 10^{16}$  to  $1 \times 10^{19} \text{ cm}^{-3}$  lead to a decrease of dislocation density from  $1 \times 10^{10}$  to  $3 \times 10^9 \text{ cm}^{-2}$ , whereas density of "hollow defects" increased from  $1 \times 10^6$  to  $7 \times 10^7 \text{ cm}^{-2}$ .

An even more drastic increase in the formation of pinholes was observed when GaInN/GaN quantum wells (QWs) are grown (Fig. 3a). For 20% of In and a thickness of 20 periods of QWs the first pinholes started to appear on the second well and their density increases at higher wells. This pinhole formation interrupts the QWs and growth proceeds on separate mesas also leading to different thickness of QWs due to decreasing growth area. Growth with much smaller rate (Fig. 3b) on the facets of pinholes is observed, as previously discussed. This pinhole formation and the change of thickness of QW periods, as well as growth on the facet walls is detrimental for the device application.

It was interesting to observe that nanotubes formed within the layer below the QWs did not propagate through the QWs. They were all converted into pinholes. This shows that it is rather unlikely that a nanotube is just an empty core screw dislocation. All the observations taken together suggest that it is rather an empty space formed due to incorporation of foreign atoms that poison growth steps on  $\{10\bar{1}0\}$  nonpolar planes.

## Conclusions

In conclusion, it has been suggested that the origin of pinholes and nanotubes in epitaxial polar materials may be related to growth kinetics on particular crystallographic planes, and impurity poisoning of growth steps. Two types of related "hollow" defects (pinholes and nanotubes) have been identified in GaN samples. Formation of a nanotube appears to require nucleation of a pinhole. Pinhole formation results from slow growth rate on polar  $\{10\bar{1}1\}$  planes resulting in the observed V-shape feature, with about  $60^\circ$  between the arms, in good agreement with the angle between two  $\{10\bar{1}1\}$  planes. The pinhole walls remain on  $\{10\bar{1}1\}$  polar planes but evolution of some of these pinholes with  $\{10\bar{1}1\}$  facets into long nano-tubes requires that the  $\{10\bar{1}1\}$  facets become  $\{10\bar{1}0\}$  facets parallel to the growth direction. Development of some pinholes into nanotubes appears to depend on impurity attraction to these hollows which can stabilize their growth as tubes along the growth direction. When the impurity is depleted a closing of a nanotube is expected due to the normally high growth rate on  $\{10\bar{1}0\}$ . Closing of a nanotube, as observed experimentally, is similar to growth on the side edges of a bulk platelet. The diameter of nanotubes change with an increase of impurity concentration. For some cases pinholes do not evolve into nanotubes but rather continue to grow larger and larger. This was observed experimentally when In was added during the growth of quantum wells. Accumulation of In at QW interfaces (formation of dislocation loops) would suggest that strain might be one of the factors influencing formation of pinholes. However, the formation of pinholes in strain free



homoepitaxial layers and as well in the samples with increased oxygen where no change of the lattice parameter was observed suggest, that strain is not a necessary condition for formation of a pinhole. The experimental observations suggest that impurities or dopant elements play a major role in the nucleation of pinholes and in their development into nanotubes. Elimination of these defects may be possible with sufficient impurity reduction. Inversion domains, however, which appear similar to nanotubes, particularly in plan-view but are filled with material of opposite polarity probably do not depend on the presence of impurities or dopant atoms. They are usually formed at the substrate/GaN layer interface either at a surface step or dislocation loop.

### Acknowledgments

This work was supported by the U.S. Department of Energy under the Contract No. DE-AC03-76SF00098. The use of the facility at the National Center for Electron Microscopy at the LBNL is greatly appreciated. The authors want to thank W. Swider for the excellent sample preparation and photographic work, J.W. Yang for the samples with MQWs and Drs. K. Pakula and J. Baranowski for the GaN homoepitaxial layers.

### References:

1. S. Nakamura, M. Senoth, S. Nagahama, N. Iwasa, T. Matsushita, H. Kiyuku, and Y. Sugimoto, *Jpn. J. Appl. Phys.* **35**, L74 (1996).
2. Z. Liliental-Weber, H. Sohn, N. Newman, and J. Washburn, *J. Vac. Sci. Technol B* **13** (4), 1578 (1995).
3. Z. Liliental-Weber, Y. Chen, S. Ruvimov, and J. Washburn, *Mater. Res. Soc. Symp.* **449**, 417 (1997).
4. L.T. Romano, J.E. Northrup, , and M. O'Keefe, *Appl. Phys. Lett.*, **69**, 2394 (1996).
5. J.L. Rouviere, M. Arlery, R. Niebuhr, K.H. Bachem, and O. Briot, *Internet J. Nitride Semiconduct.* **1**, 227 (1997).
6. P. Vennegues, B. Beaumont, M. Vaille, and P. Gilbard, *Appl. Phys. Lett.* **69**, 2434 (1997).
7. Z. Liliental-Weber, Y. Chen, S. Ruvimov, and J. Washburn-unpublished
8. F.C. Frank, *Acta Cryst.* **4**, 497 (1951)
9. W. Qian, M. Skowronski, and G.S. Rohrer, *Mat. Res. Soc. Mat.* **423**, 475 (1996).
10. W. Si, M. Dudley, R. Glass, V. Tsvetkov, and C. Carter, Jr, *J. of Electronic Materials* **26**, 128 (1997).
11. I. Sunagawa and P. Bennema, *J. Cryst. Growth* **53**, 490 (1981).
12. H. Tanaka, Y. Uemura and Y. Inomata, *J. Cryst. Growth* **53**, 630 (1981).
13. B. Daudin, J.L. Rouviere, and M. Arlery, *Appl. Phys. Lett.* **69**, 2480 (1996).
14. Z. Liliental-Weber, S. Ruvimov, Ch. Kisielowski, Y. Chen, W. Swider, J. Washburn, N. Newman, A. Gassmann, X. Liu, L. Schloss, E.R. Weber, I. Grzegory, M. Bockowski, J. Jun, T. Suski, K. Pakula, J. Baranowski, S. Porowski, H. Amano , and I. Akasaki, *Mat. Res. Soc.Symp. Proc.*, vol. **395**, 351 (1996).
15. Z. Liliental-Weber, C. Kisielowski, S. Ruvimov, Y. Chen, J. Washburn, I. Grzegory, M. Bockowski, J. Jun, and S. Porowski, *J. Electr. Mat.* vol. **25**, 1545 (1996).

## DEFECT-RELATED RECOMBINATION PROCESSES IN LOW-DIMENSIONAL STRUCTURES OF ZnCdSe/ZnSe, CdTe/CdMnTe AND GaAs/AlGaAs

M. Godlewski\*, D. Hommel\*\*, T. Wojtowicz\*, G. Karczewski\*, J. Kossut\*, K. Regiński\*\*\*,  
M. Bugajski\*\*\*, J.P. Bergman\*\*\*\* and B. Monemar\*\*\*\*

\*Inst. Phys., Polish Acad. Sci., 02-668 Warsaw, Al. Lotników 32/46, POLAND

\*\*Inst. Solid State Phys., Bremen Univ., D-28334 Bremen, GERMANY

\*\*\*Inst. Electron Technol., 02-668 Warsaw, Al. Lotników 32/46, POLAND

\*\*\*\*Dept. Phys. & Meas. Technol., Linköping Univ., S-581 83 Linköping, SWEDEN

**Keywords:** defects in heterostructures, II-VI and III-V semiconductors, bound excitons

**Abstract.** The two-line structure of the photoluminescence (PL) emission from quantum wells (QWs) of nominally undoped II-VI and III-V semiconductors is often related to a simultaneous observation of free and bound (typically neutral donor bound) excitons. In this work we discuss defect-related recombination processes in doped and undoped quantum well structures of II-VI and III-V semiconductors. We show that trapping of free excitons by donor impurities is relatively inefficient in typical quantum well structures, which show at low temperature PL emission of either localized (by potential fluctuations) or quasi-localized excitons. Bound excitons are preferentially formed in such structures under excitation conditions which generates free electrons and holes.

### Introduction

A two-line photoluminescence (PL) spectrum from a given quantum well (QW) is often observed in nominally undoped QW structures of II-VI and III-V semiconductors [1]. Such a PL structure is, in most of the cases, related to a simultaneous observation of free (FE) and neutral donor bound (DBE) excitons [1]. In this work we discuss the properties of DBEs in QW structures of CdTe/CdMnTe, ZnCdSe/ZnSe and GaAs/AlGaAs. Mechanisms of the DBE formation are discussed and are compared to those observed in bulk samples.

### Excitonic processes in heterostructures of II-VI and III-V semiconductors

In bulk samples of II-VI and III-V semiconductors the DBE exciton is formed by either a subsequent trapping of an electron and then a hole, or by trapping of a free exciton (FE). The latter process is enhanced in bulk samples by the polaritonic process, which limits the radiative decay rate of FEs. If the process of FE trapping is efficient, the decay time ( $\tau_{dec}$ ) of the FE PL should depend on the concentration of donor species ( $N_D$ ), which may be described by a simple equation:  $\tau_{dec} = \tau_{rad} (1 + c_{trap} \tau_{rad} N_D)^{-1}$ , where  $\tau_{rad}$  is the radiative decay time of the FE, and  $c_{trap}$  is the trapping rate of the FE by a neutral donor. Thus, with an increasing donor concentration a shorter decay time of the FE PL should be observed.

We have verified this dependence by studying the PL emission of a unique two QW (16 monolayer (ML) and 30 ML wide) CdTe/CdMnTe structure  $\delta$ -doped with In in the middle of the QWs, with the doping level varying in four steps within the length of the sample. The so-called wedge QW structures contained an undoped region, with some inadvertent contamination, a lightly doped ( $0.03$  of  $N_d^{max}$ ) region, a moderately doped ( $0.1$  of  $N_d^{max}$ ) region and a relatively heavily doped region, with the doping level  $N_d^{max} \sim 10^{12} \text{ cm}^{-2}$ . For such structures we could study the properties of FE and

DBE excitons at different doping levels moving the excitation spot within the length of the same sample.

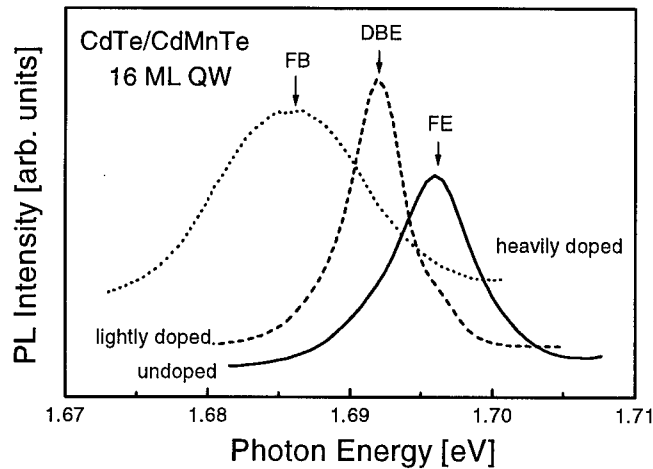


Figure 1: 2 K PL spectra from the  $\delta$ -doped 16 ML wide CdTe QW in the wedge CdTe/CdMnTe structure. The PL was measured at three spots with different doping level.

In Fig. 1 we show the PL spectrum measured for the 16 ML wide QW at three different spots. For the undoped region of the QW a single-line PL spectrum is observed, due to the FE emission. Already for the weakly doped region of the structure the DBE PL becomes dominant. These two emissions are replaced by the broad free-to-bound (donor - free hole) PL in the heavily doped region of the structure. The PL kinetics of the FE and DBE emissions was measured by moving the excitation spot within the length of the sample (the  $z$  direction in figure 2). The results of this experiment are shown in Fig. 2 for the 16 ML and 30 ML wide QWs, respectively.

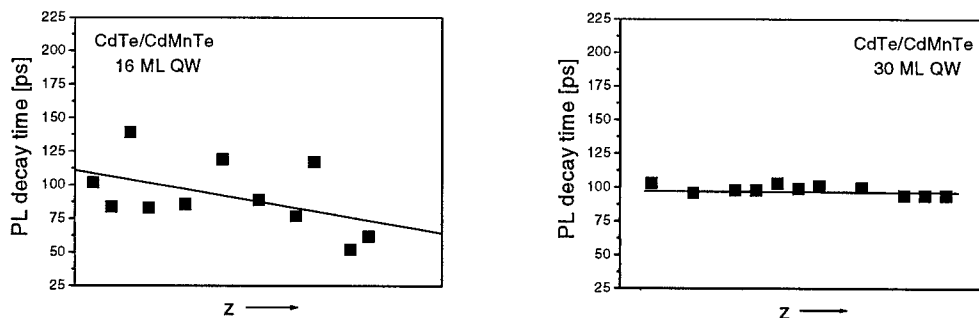


Figure 2: Dependence of the decay time of the FE emission in 16 ML (left) and 30 ML (right) QWs in the doped wedge CdTe/CdMnTe structure. The doping level varies within the length of the sample in the  $z$  direction.

The decay time of the DBEs in these structures is fast, of the order 150 ps. The FE decay is comparable, or slightly shorter. Fig. 2 shows that for the 16 ML wide QW the PL decay time of FEs

shortens in the doped regions of the structure. (The scatter in the corresponding data in Fig. 2 is due to a weak FE PL peak in the doped samples, which makes the evaluation of the corresponding decay times less accurate). For the 30 ML wide QW the PL decay time of FEs is practically constant, i.e., it does not depend on the doping level. This means that for the same sample and for the same doping level the FE PL from the narrower QW shows the expected dependence on the doping, whereas the PL from the broader QW is doping independent.

To explain this puzzling observation we performed detailed PL kinetics investigations. We observed an important difference in exciton properties for the 16 ML and 30 ML wide QWs. For the narrower QW the excitons behaved as they were not localized even at 2 K, but for the 30 ML wide QW excitons were localized at low temperature. A similar situation we found in several structures studied by us separately [2]. The above result suggests that exciton localization may be responsible for the observed weak link between FE and DBE excitons in the 30 ML wide QW. In fact, if the localization of the FE can occur before it can be trapped by donor impurities present in the QW plane the two excitonic emissions (FE and DBE excitons) can decouple.

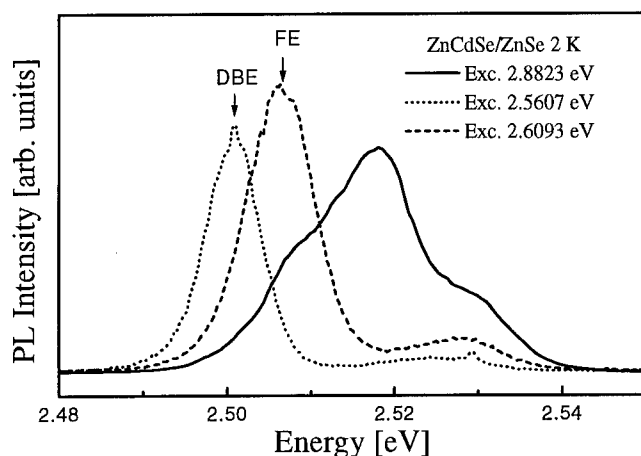


Figure 3: PL spectrum of the two-QW (8 nm and 14 nm wide) ZnCdSe/ZnSe heterostructure measured at three different excitation conditions indicated in the figure. The two lower energy peaks (2.50 eV - 2.51 eV) are associated with the 14 nm QW, while the peaks in the region 2.52 eV - 2.53 eV relate to the 8 nm QW. The full curve (—) is obtained under nonresonant excitation.

We verified the above suggestion on the influence of exciton localization on the FE-to-DBE transfer link by performing PL investigations of several CdTe/CdMnTe, ZnCdSe/ZnSe and GaAs/AlGaAs heterostructures. In Fig. 3 we show the PL spectrum observed for a two-well ZnCdSe/ZnSe heterostructure with 8 nm and 14 nm wide ZnCdSe (12 % of Cd) QWs. By selecting proper excitation conditions we could excite either the FE or the DBE PL from the 14 nm wide QW. For this QW excitons were localized at 2 K, the temperature at which the PL spectrum shown in Fig. 3 was taken. The fact that the resonant excitation (into the light hole (LH) FE peak) of the FE results only in the FE emission confirmed our suggestion that FE and DBE excitons can decouple in QW structures with relatively rough interfaces.

Previous PL kinetics investigations of similar ZnCdSe/ZnSe structures showed that excitons start to delocalize at about 40 - 50 K [3]. We performed PL excitation measurements to verify whether

exciton delocalization will result in an efficient FE-to-DBE transfer link. In Fig. 4 we show the PL spectrum for two excitation conditions measured at 20 K and 50 K. The 20 K spectrum shows separate PL emissions of FE and DBE excitons for two different excitation conditions, i.e., the results are identical with those taken at 2 K. However, at a further increased temperature (50 K in Fig. 4) the DBE emission can be observed under resonant excitation of the FE excitons. Delocalized excitons can now be trapped by neutral donor species, i.e., the FE-to-DBE transfer link is re-established by exciton delocalization.

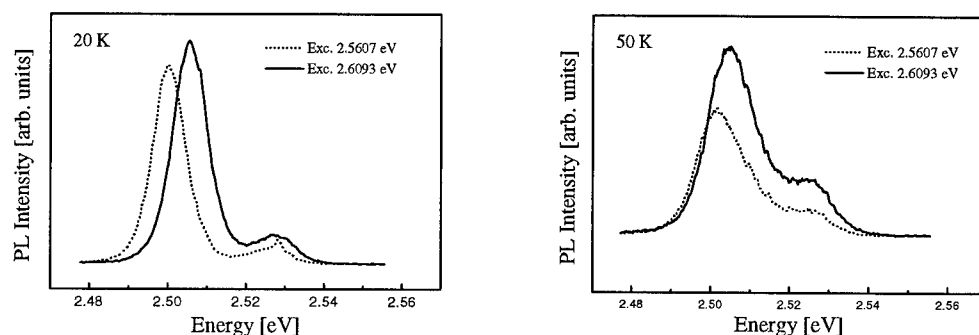


Figure 4: PL spectra observed at 20 K (left) and 50 K (right) of the ZnCdSe/ZnSe QW structure with 8nm and 14 nm wide QWs, measured at two different excitation conditions.

Similar results were also obtained for GaAs/AlGaAs heterostructures, even though only quasi-localized excitons were observed there at low temperature. In Fig. 5 we show the PL emission from a 25 ML wide GaAs QW, from a sample showing the appearance of QW regions with a width different by 1 ML from the nominal [4]. Similarly to the results obtained for the II-VI heterostructures, we observed either FE or DBE emission under different excitation conditions (Fig. 5). The latter emission partly overlaps with a free-to-bound (FB) transition at the low energy wing.

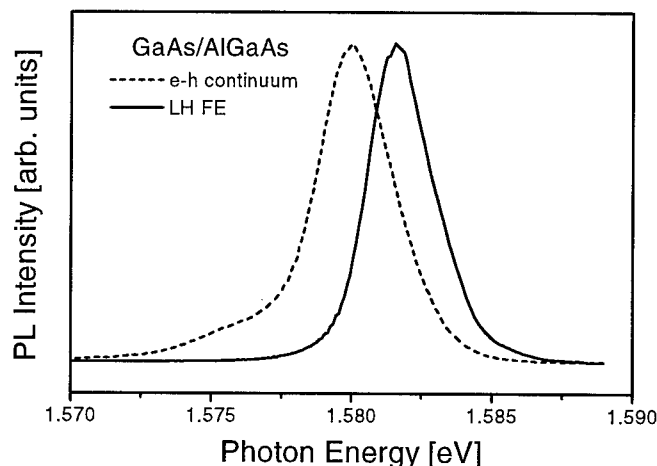


Figure 5: 2 K PL emission from a 25 ML wide QW in the GaAs/AlGaAs structure, measured at two different excitation conditions. The solid line represents FE PL from the 25 ML wide QW regions. The broken line shows DBE and FB (at the low energy wing) emissions observed under excitation into the continuum of e-h states.

The relevant question, which should now be answered, is what are the excitation conditions under which either FE or DBE emission can be observed separately. We already mentioned that the FE emission is observed under resonant excitation conditions into heavy (HH) or LH hole FE states. The conditions for the preferential observation of the DBE emission remained unknown in previous work, however. We measured PL excitation spectra for the II-VI and III-V heterostructures studied in this work, to clear this point. In Fig. 6 we show the PL excitation spectrum measured for the GaAs/AlGaAs structure discussed above. The excitation spectrum shown in Fig. 6 was obtained for the detection set at the two partly overlapping PL emissions of FE and DBE excitons from the 25 ML wide QW regions. Two sharp structures, due to the resonant excitation into the HH peaks of the FE in the 24 ML and the 25 ML QW regions, were observed indicating an efficient inter-QW exciton migration [4]. At lower energy a broad PL excitation peak is observed related to the excitation into the continuum of electron-hole states. This peak was observed only for the detection set at either the DBE or the FB PL. For the detection set at the peak of the FE PL only HH and LH peaks due to FEs in the 24 ML and the 25 ML wide QW regions were observed in the low energy part of the excitation spectrum.

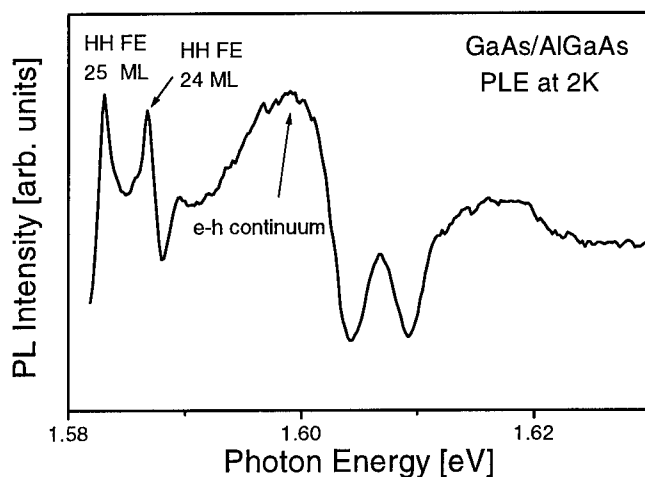


Figure 6: PL excitation spectrum of the QW PL emission from the 25 ML wide QW regions measured for the GaAs/AlGaAs structure. The spectrum was measured by setting the detection at the partly overlapping PL emissions of FE and DBE excitons in the 25 ML wide QW regions (Fig. 5).

These PL excitation studies confirmed our suggestion on a very weak FE-to-DBE transfer link in the heterostructures with relatively rough interfaces. The PL excitation spectrum shown in Fig. 6 demonstrates also another difference between excitonic emissions in bulk samples and in QW structures. We observed (also for the II-VI heterostructures) that excitation creating free electrons and holes preferentially results in DBE formation. Only a weak FE emission is observed under such excitation conditions. The separate DBE emissions, shown in Figs. 3-5 above, were excited under such conditions.

Concluding this point we show that the FE and DBE formation mechanisms in QW structures are different from those known in bulk samples. Due to exciton localization the transfer link between

FE and DBE excitons is inefficient at low temperatures. In turn, excitation of free carriers results mostly in formation of DBE and not FE excitons. This point is rather important. In several cases nonresonant excitation conditions are used in PL studies of QW structures. If free carriers are generated under such conditions we can observe a very enhanced DBE emission even for nominally undoped QWs. We may thus incorrectly conclude on a heavy contamination.

Another condition for the enhanced DBE emission was observed by us for the GaAs/AlGaAs heterostructure having QW islands with the width varying by 1 ML from the nominal width. If the islands are small, as compared to a typical diffusion distance for the FE excitons, excitons generated in QW regions of a smaller width will escape to the QW regions of the nominal thickness and will recombine there. Then only a weak, if any, PL from the narrower QW regions is expected. However, if they are trapped at donor impurities before they can migrate to the wider QW regions, the DBE PL from the QW islands can be observed. This is why the PL emission from the islands can be dominated by the DBE emission (Fig. 7).

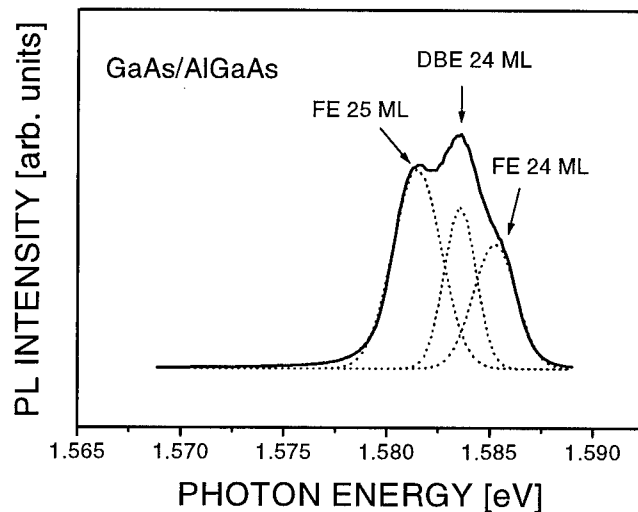


Figure 7: PL spectrum of the GaAs/AlGaAs heterostructure measured at 2 K and for excitation resonant into HH peak of FE excitons in the 24 ML wide QW islands.

#### Acknowledgements:

This work was partly financed by grant numbers: 8T 11B 014 11 and 8T 11B 027 11 of KBN

#### References:

1. M. Godlewski, J.P. Bergman, B. Monemar, B. Koziarska, A. Suchocki, G. Karczewski, T. Wojtowicz, J. Kossut, A. Waag and D. Hommel, *Mat. Sci. Forum* **196-201**, 455 (1995).
2. M. Godlewski, J.P. Bergman and B. Monemar, *Lithuanian Physics Journal* **35**, 563 (1995).
3. M. Godlewski, J.P. Bergman, B. Monemar, E. Kurtz and D. Hommel, *J. Cryst. Growth* **159**, 533 (1996).
4. M. Godlewski, P.O. Holtz, J.P. Bergman, B. Monemar, K. Reginski, M. Bugajski, E.M. Goldys and T.L. Tansley, *Semicond. Sci. Technol.* (in press)

## STUDY OF HOLE TRAPS IN p-TYPE ZnSe and ZnSSe EPILAYERS BY DLTS AND ADMITTANCE SPECTROSCOPY

I.S. Hauksson, D. Seghier, H.P. Gislason, K.A. Prior<sup>1</sup> and B.C. Cavenett<sup>1</sup>

Science Institute, University of Iceland, Dunhagi 3, IS-107 Reykjavík, Iceland

<sup>1</sup> Department of Physics, Heriot-Watt University, Edinburgh EH14 4AS, Great Britain

**Abstract.** We studied nitrogen doped ZnSe and ZnSSe epilayers grown on p-GaAs substrates by MBE using deep-level transient spectroscopy and admittance spectroscopy. Three major hole traps T1-T3 were observed with energy levels at 0.11, 0.46, and 0.56 eV from the valence band. Similar energy levels were observed in ZnSSe:N except that T1 was at 0.12 eV from the valence band. We attribute T1 to a nitrogen acceptor which controls the p-type conduction in the materials. A crude estimation of the 0.11 eV trap concentration obtained from the data shows correlation with the free carrier concentration due to nitrogen. The two remaining levels may originate from the nitrogen doping process.

**Keywords:** II-VI, ZnSe, ZnSSe, p-type, MBE, DLTS, Admittance, Nitrogen

### Introduction

In the effort of making blue-light emitting devices using II-VI large band gap materials it is well known that the doping of ZnSe epilayers by nitrogen causes difficulties in obtaining good p-type conductivity due to a compensation effect [1]. The highest concentration of electrically active acceptors obtained in N-doped p-type ZnSe is limited to about  $10^{18} \text{ cm}^{-3}$  in samples grown by molecular beam epitaxy (MBE) [2,3]. Photoluminescence measurements have shown a creation of new deep donors due to nitrogen complexes in such samples [4] as nitrogen is introduced. So far, optical methods have mainly been used to study the nitrogen level which is responsible for the p-type conductivity in ZnSe epilayers. Reports on electrical measurements on nitrogen doped ZnSe are few and energy levels introduced by nitrogen in the band gap have not been measured directly by electrical method. A binding energy of a nitrogen acceptor of about 110 meV has been determined from photoluminescence by many groups. In this work, we report on hole traps present in N-doped ZnSe and ZnSSe grown by MBE which were measured by deep-level transient spectroscopy (DLTS) and admittance spectroscopy (AS). In particular the acceptor level related to nitrogen was investigated. We finally discuss the series resistance usually encountered in this kind of material and its effect on the capacitance measurements.

### Experimental Details

The ZnSe and ZnSSe samples were grown by MBE on GaAs substrates. For p-type doping, a nitrogen plasma source was used and the RF plasma power was changed between samples to have different incorporation of nitrogen. The ZnSe:N epilayers with thickness of 1  $\mu\text{m}$  were grown without GaAs buffer layer onto p<sup>+</sup>-type GaAs (100) substrates at a growth temperature of 250 - 300 °C. The growth rate was 0.5  $\mu\text{m/h}$ . The ZnSSe:N layers were grown under similar conditions with 20 nm thick ZnSe:N buffer layer onto GaAs substrate. The sulphur content was 6 - 8% and the epilayers are therefore lattice matched to the GaAs substrate. The DLTS measurements were performed using 1 MHz Boonton B72 capacitance meter and an Innovance D20 DLTS signal processor. Schottky diodes with diameter 1 mm were made by evaporating Au onto the ZnSe epilayer and ohmic contacts by evaporating Au-Zn alloy or using In-Ga onto the GaAs substrate. The acceptor concentration ( $N_A - N_D$ ) determined from capacitance-voltage (C-V) in the studied samples ranges between  $2 \times 10^{16}$  and  $5 \times 10^{17} \text{ cm}^{-3}$ .



The equivalent electrical circuit of the resulting structure consists of two barriers: a Schottky barrier diode (SD) formed at the Au/p-ZnSe junction, and an isotype p-ZnSe/p-GaAs heterojunction (HJ). Because of a large valence band discontinuity in the HJ ( $> 1$  eV) there is a depletion region on the wide band-gap side, i.e., in the ZnSe layer. The same analysis is valid for ZnSSe/GaAs structures. Current-voltage characteristics taken at low as well as room temperature systematically show the back to back diode behavior typical of structures of this kind. Consequently, it is difficult to estimate the series resistance ( $R_s$ ) of the samples. However, due to the low hole mobility in ZnSe [5] and defects due to the mismatch in the heterointerface, a high  $R_s$  is generally expected. If the leakage current is reasonably low the junction conductance  $G$  can be neglected, and the measured capacitance  $C_m$  is related to the depletion region capacitance  $C$  as:  $C_m = C/[1 + (\omega R_s C)^2]$ , where  $\omega$  is the pulsation of the ac test signal. Broniatowski et al. [6] showed that if  $(\omega R_s C)^2 > 1$  the amplitude of the DLTS peak is reduced, and finally the capacitance transient may exhibit a sign reversal. In our samples, a capacitance of about 250 pF was measured. Hence, if  $R_s$  is larger than about 500  $\Omega$ , which is quite likely in these samples, the effects on the DLTS observations are not negligible. When  $(\omega R_s C)^2$  is small  $C_m$  can be close to  $C$ . A practical way to fulfill this condition is to measure  $C_m$  at low  $\omega$ , because the other parameters are characteristic of the sample. In our DLTS set-up the capacitance meter works at a fixed frequency  $f = 1$  MHz, thus it was necessary to confirm these measurements by AS studies at different frequencies.

## Results

Figure 1 (a) shows representative DLTS spectra measured from a nitrogen doped ZnSe epilayer. In the measurement a reverse bias of  $V_r = 5$  V, a carrier filling pulse of 3 V and a DLTS rate window of  $\tau = 2 \times 10^{-4}$  s were used. There are three dominant peaks in the DLTS spectrum labeled T1, T2 and T3 from the lowest to the highest temperature, respectively. It is clear from the spectra that all of them originate from hole traps. The trap apparent activation energy  $E_t$  and the apparent hole capture cross section  $\sigma_{p\infty}$  calculated from the equation of detailed balance and shown in Table 1. Close values were measured for the ZnSSe samples. For T1 scattered values of  $E_t$  ranging from some 94 to 130 meV were obtained.

	$E_t$	$\sigma_{p\infty}$
T2	0.46 eV	$1 \times 10^{-15} \text{ cm}^2$
T3	0.56 eV	$3 \times 10^{-15} \text{ cm}^2$

Table 1. DLTS results for ZnSe epilayers.

The capacitance transient at low temperature at which this peak is observed is not purely exponential, as can be seen in Fig. 2. This non-exponential behavior seems to be a characteristic of this peak since it is observed in all samples. A typical capacitance transient is composed of an initial rapid decay followed by a subsequent long transient. This behavior may explain the range of  $E_t$  values observed for this trap. Since the calculation of  $E_t$  from DLTS analysis supposes that the capacitance transient varies exponentially with time, apparent  $E_t$  values which may be erroneous are measured when this condition is not well satisfied. There are several possible reasons for a capacitance transient to be non exponential: (i) an electric-field dependence of the trapped charge emission, (ii) the presence of several energy levels with similar emission rates, and (iii) trap density of the same order as that of the free carriers. Possibility (i) can be checked by performing DLTS at different values of reverse bias at the same rate window. In case of an electric-field dependence of the trap emission a temperature shift of the DLTS peak should be observed. For T1 no such shift did occur, indicating that the emission from T1 is not field dependent. To check condition (ii) we repeated DLTS under different conditions in order to separate peaks in the case there are more than one trap, but always observed a single peak, which indicates the presence of only one trap.

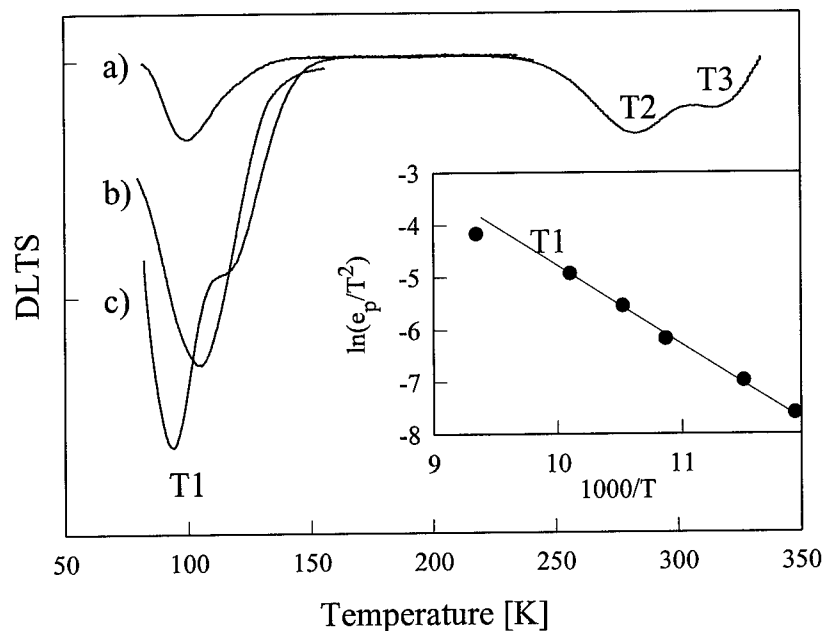


Figure 1: DLTS signal from a Au/p-ZnSe:N junction from three samples: a) #490, b) #519 and c) #522. The inset shows an Arrhenius plot for trap T1.

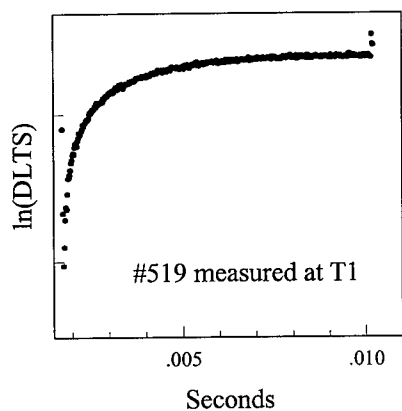


Figure 2: DLTS transient recorded at the T1 trap showing the non-exponential behavior.

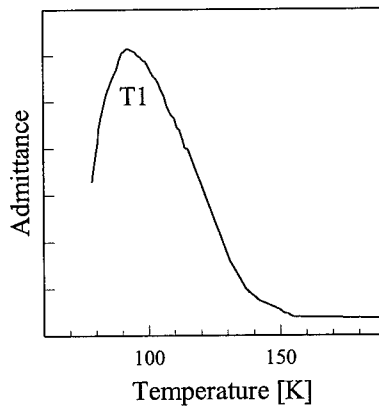


Figure 3: Conductance vs temperature for the N-doped ZnSe sample.  $f = 10$  KHz.

However, the possibility of several traps with too close emission rates to be separated in the DLTS spectrum cannot be completely excluded. Due to the strong signal observed for peak T1, it is very likely that the non-exponential behavior also arises from the high concentration of the trap.

Furthermore, fitting of data showed that the second portion of the capacitance decay may well be approximated by an exponential curve. Wang et al. [7] showed that the problem of a trap with a high concentration is then equivalent to that of low concentration when  $t \gg 1/e_n$ , where  $t$  is the time and  $e_n$  is the trap emission rate. Then the corresponding part of the transient must be exponential with the true emission rate. This result fits our data for T1 well. Therefore, exploiting only this tail of the transient, we deduced the values of  $E_t$  and  $\sigma_{p\infty}$  for T1 shown in Table 2.

	$E_t$	$\sigma_{p\infty}$
ZnSe	112 meV	$2 \times 10^{-18} \text{ cm}^2$
ZnSSe	125 meV	$4 \times 10^{-19} \text{ cm}^2$

Table 2. DLTS results for the trap T1.

At low temperature the capacitance increases with a long time constant when the filling pulse is applied, sometimes accompanied with a sign reversal of the subsequent transient. This is most likely caused by a high value of  $R_s$ . Therefore, when using the DLTS peak height to calculate the trap concentration, erroneous values may result since the presence of  $R_s$  tends to reduce the peak height. For these reasons the concentration of T1 estimated from DLTS to about  $10^{16} \text{ cm}^{-3}$  has to be regarded a lower limit for the trap concentration.

Due to the departure from the conventional DLTS conditions, it is interesting to check the reliability of the results, especially in the low-temperature range of the spectra. Admittance spectroscopy provides some improvements to conventional DLTS: (i) it is possible to overcome problems arising from  $R_s$  by measuring the sample admittance at lower frequencies, and (ii) it is convenient to investigate levels with a high concentration [8]. Figure 3 shows the temperature dependence of the conductance of a ZnSe sample measured at 10 KHz. A clear peak is observed at low temperature. It is due to a hole trap since only majority carrier traps are observed in AS. The Arrhenius plot of this peak fits well to the DLTS data for T1. Hence, we conclude that they are identical.

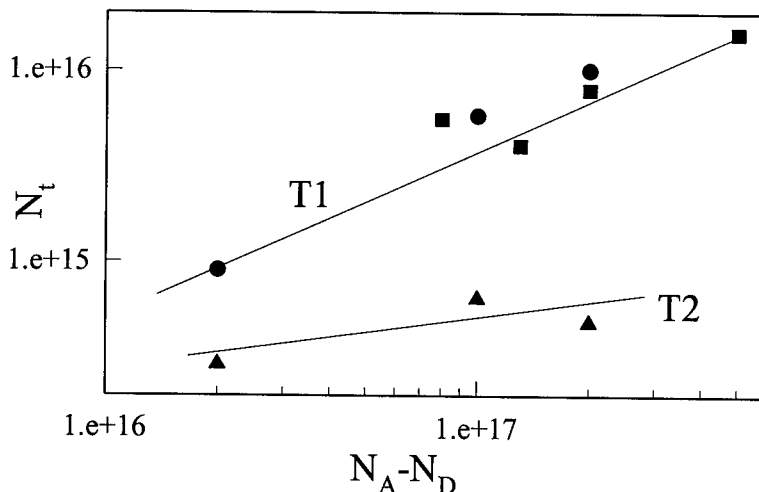


Figure 4: The variation of the concentration of T1 and T2 estimated from DLTS versus the free hole concentration. Data are obtained from both ZnSe:N and ZnSSe:N.

The origin of the T1 peak is further demonstrated by the three different curves shown in Fig. 1, obtained from three different samples, #490, #519, and #522, having similar doping levels. The level of incorporated nitrogen can be estimated from photoluminescence measurements of the donor-acceptor pair (DAP) emission [4] where increasing nitrogen incorporation results in a shift from shallow DAP to deep DAP emission. Sample #490 showed only a shallow DAP emission while sample #519 and #522 showed a deep DAP emission, demonstrating more nitrogen incorporation. We have obtained a crude estimation of the concentration of T1 from the DLTS peak height in several samples with doping levels ranging from  $3 \times 10^{16}$  to  $5 \times 10^{17} \text{ cm}^{-3}$ . The samples were measured under same reverse bias, carrier filling pulse and DLTS rate window as shown in Fig. 1. The variation of the estimated concentration of T1 versus the free carrier concentration  $p$  of the corresponding sample is shown in Fig. 4. The trend clearly shows that the concentration of T1 is increasing with  $p$ . Measurements for T2 do not show such a strong correlation, supporting that T1 peak is due to nitrogen acceptor.

### Discussions

In some samples the capacitance versus temperature spectra measured at different frequencies present at low temperature a structure which is composed of at least two slopes. Also the corresponding conductance spectra present rather a broad peak in the same range of temperature. This behavior may confirm the hypothesis that there are two levels close in energy with similar concentrations.

An acceptor level at around  $E_v + 0.11 \text{ eV}$  has been observed in photoluminescence and attributed to nitrogen. We ascribe T1 to the same acceptor level for reasons of its ionization energy and its correlation with the free carrier concentration in the samples. Indeed, T1 due to its high concentration is considerably influencing the hole carrier density in the material. In case there are two energy levels with similar activation energies, as discussed above, this could mean that nitrogen acceptor atoms are present in slightly different configurations in the host material. It is difficult to speculate about this point since even in normal conditions of DLTS it is not convenient to investigate a high concentration energy level.

Hole traps with activation energies similar to T2 and T3 have also been reported in the literature [11,12]. It has been suggested that these traps involve nitrogen impurities. The fact that the density of these traps is significant, even comparable to trap T1 leads us to suggest that they are related to the nitrogen doping process. At this point we are not able to speculate on their origin without further studies.

### Conclusions

In summary, nitrogen-doped p-type ZnSe and ZnSSe epilayers grown by MBE were investigated using standard DLTS and admittance spectroscopy measurements. Three major hole traps are observed. The low-temperature level with an apparent activation energy of 0.11 eV in ZnSe and 0.12 eV in ZnSSe is attributed to a nitrogen acceptor. This is the first report of observation of the nitrogen level in p-type ZnSe epilayer observed by DLTS. The remaining two (at  $E_v + 0.46 \text{ eV}$  and  $E_v + 0.56 \text{ eV}$ ) may originate from the nitrogen doping process.

This research was supported by the Icelandic Research Council and the University research fund.

### References

1. I.S. Hauksson, J. Simpson, S.Y. Wang, K.A. Prior and B.C. Cavenett. *Appl. Phys. Lett.* **61**, 2208 (1992).
2. R.M. Park, M.B. Troffer, C.M. Rouleau, J.D. DePuydt, and M.A. Haase, *Appl. Phys. Lett.* **57**, 2127 (1990).
3. J. Qiu, H. Cheng, J.M. DePuydt, and M.A. Haase, *J. Cryst. Growth* **127**, 279 (1993).

4. I.S. Hauksson, S.Y. Wang, J. Simpson, K.A. Prior, B.C. Cavenett, W. Liu and B.J. Skromme, *Phys. Rev. B* **52**, 17184 (1995).
5. Hazufiro Ohkawa, Akira Ueno, and Tsuneo Mitsuyu, *Jpn. J. Appl. Phys.* **30**, 3873 (1991).
6. A. Broniatowski, A. Blossé, P.C. Srivastava, and J.C. Bourgoin, *J. Appl. Phys.* **54**, 2907 (1983).
7. Alex C. Wang, and C.T. Sah, *J. Appl. Phys.* **55**, 565 (1984).
8. G. Vincent, A. Chantre, and D. Bois, *J. Appl. Phys.* **50**, 5484 (1979).
9. W.B. Leigh and B.W. Wessels, *J. Appl. Phys.* **55**, 1614 (1984).
10. P.A. Fisher, E. Ho, J.L. House, G.S. Petrich, and L.A. Kolodziecki, *Mat. Res. Soc. Symp. Proc.* **340**, 451 (1994).
11. B. Hu, G. Karczewski, H. Luo, N. Samarth, and J.K. Furdyna, *Appl. Phys. Lett.* **63**, 358 (1993).
12. H. Goto, T. Tanoi, M. Takemura, and T. Ido, *Jpn. J. Appl. Phys.* **34**, L827 (1995).

## AUGER-TYPE NONRADIATIVE RECOMBINATION PROCESSES IN BULK AND IN QUANTUM WELL STRUCTURES OF II-VI SEMICONDUCTORS CONTAINING TRANSITION METAL IONS

M. Godlewski\*, M. Surma\*, A. J. Zakrzewski\*, T. Wojtowicz\*, G. Karczewski\*, J. Kossut\*  
 J.P. Bergman\*\* and B. Monemar\*\*

\*Inst. Phys. Polish Acad. Sci., Al. Lotników 32/46, 02-668 Warsaw, Poland

\*\*Dept. Phys. & Meas. Technol., Linköping Univ., S-581 83 Linköping, Sweden

**Keywords:** Auger process, photoluminescence, nonradiative recombination, transition metal ions

**Abstract.** Two new Auger-type processes, related to transition metal impurities in II-VI compounds, are identified from the studies of photoluminescence and magnetic resonance spectroscopy of doped bulk ZnSe crystals and CdTe-based quantum well structures containing chromium. It is shown, that for bulk ZnSe crystals the two-center Auger process enhances capture rates of free electrons by iron  $\text{Fe}^{3+}$  ions. For quantum well structures containing chromium excitonic Auger effect is a dominant mechanism of nonradiative recombination.

### Introduction

Transition metal (TM) impurities such as iron, chromium or nickel are known to be efficient centers of nonradiative recombination in wide band gap II-VI compounds [1]. We have shown [2] that for ZnS and ZnSe bulk crystals the so-called bypassing process is responsible for high efficiency of the

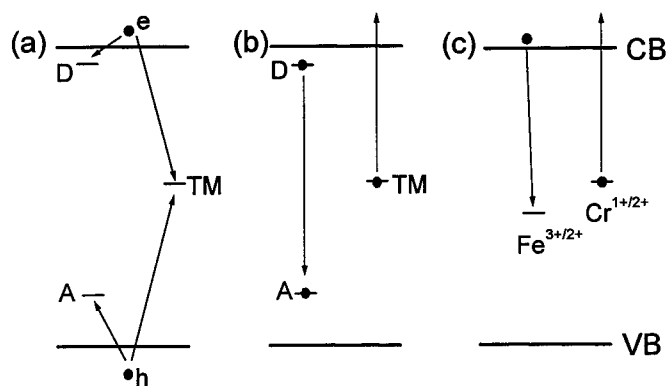


Figure 1: Model of TM-related nonradiative recombination processes in bulk ZnS and ZnSe crystals. Visible DAP recombination is deactivated by either (a) electron (e) - hole (h) trapping via a TM ion, instead of by donor (D) and acceptor (A) centers active in radiative recombination, or (b) by Auger-type energy transfer process from recombining DAP to TM ion, which is ionized in a consequence of the transfer. In (c) we show the model of two-center Auger process discussed in the text.

deactivation of the visible photoluminescence (PL) by TM ions. By the bypassing process (Fig. 1 (a)) we mean here a recombination of free electrons and holes via TM ion and not via centers active in radiative recombination transitions, e.g. in donor-acceptor pair (DAP) transitions resulting in visible PL of ZnS and ZnSe. Our previous PL excitation studies shown that electron/hole capture by Fe and Cr ions is mostly a nonradiative process. Majority of the excess capture energy is dissipated without radiative emission. For Fe ion in ZnS only an infrared  $^5T_2 - ^5E$  emission of  $Fe^{2+}$  was observed following electron capture by  $Fe^{3+}$  ions [3]. It was assumed, thus, that capture process results in energy dissipation by emission of optical phonons. Even though, the quantum yield of the process, which requires a dissipation of a large (1-2 eV) energy via multi-phonon emission, is expected to be very small, a very efficient bypassing process was observed [2]. In this paper we discuss a new type of the Auger effect related to iron and chromium ions, which is an "additional" channel for the energy dissipation during the capture process. This process enhances the overall efficiency of the bypassing mechanism and may explain, otherwise puzzling, high efficiency of this process in ZnS and ZnSe.

In addition to the bypassing process, the three-center Auger-type process (shown in Fig. 1 (b)) was also observed [2]. In this process the energy of recombining DAP is transferred to a nearby TM ion and is used for TM ionization. However, for bulk ZnS and ZnSe samples this process is by far less efficient than the bypassing process. In this work, we discuss TM-related recombination processes in quantum wells (QW) containing chromium ions. We show that the Auger-type energy transfer process, analogue of the one in Fig. 1 (b), is responsible for nonradiative recombination of excitons in QW structures.

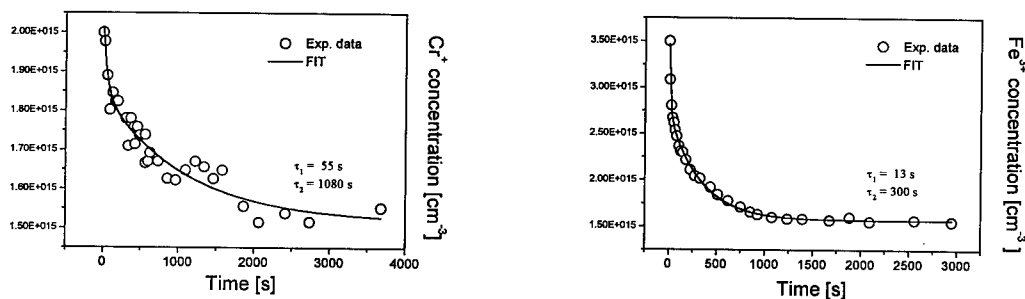


Figure 2: Decay kinetics of the photo-generated ESR signals of  $Cr^{3+}$  (left) and  $Fe^{3+}$  (right).

### Two-center Auger effect in ZnSe bulk crystals

We performed light induced electron spin resonance (ESR) and photoluminescence (PL) investigations of bulk ZnSe crystals. These crystals were intentionally doped with iron, to the concentration varying from  $10^{17}$  to  $4 \times 10^{18} \text{ cm}^{-3}$ , and contained manganese, chromium and copper ions as unintentional impurities. In the ESR study we observed before illumination the ESR signal of  $Mn^{2+}$  ions. Under illumination with 2.3 eV photon energy and at low temperature (below about 100 K) the ESR signals of  $Fe^{3+}$  and  $Cr^{3+}$  were photo-generated. Both these photo-generated signals decayed slowly after turning off the light. Spectral dependencies of the ESR signals excitation and photo-quenching were studied, but will not be discussed here. Instead we will analyse the kinetics of the decay of the ESR signals observed after turning off the light. The measured kinetics, shown in

Fig. 2, can be described by a two exponential function:  $\exp(-t/\tau_1) + \exp(t/\tau_2)$ , suggesting the existence of two relaxation mechanisms. The slow component of the decay, which is not purely exponential, we observed in several cases. This component of the decay was related to tunneling transitions of the type: hole on acceptor -  $\text{Cr}^+$  ion or electron on donor -  $\text{Fe}^{3+}$  ion. We believe that similar processes describe the slow component of the decay of ESR signals in the present study.

The temperature dependence of the fast component of the decay time was measured. Both for Cr and Fe ions the  $\tau_1$  time exhibits an activation behaviour, with the activation energy about 8 meV for both ESR signals. The same activation energy was found from the temperature dependence of the visible DAP emissions (green and red) observed by us in the PL studies and was explained by a thermal ionization of shallow donors, which are active in radiative DAP recombination. Thus, we also relate the fast component of the decay of ESR signals to a thermal ionization of shallow donors.

The  $\text{Fe}^{3+}$  ESR signal should be quenched, once shallow donors are thermally ionized. This is due to efficient electron trapping by  $\text{Fe}^{3+}$  centers (bypassing process). However, the  $\text{Cr}^+$  ESR signal should be enhanced under such conditions. This we observed for intentionally Cr doped crystals [4].  $\text{Cr}^{2+}$  ions relatively efficiently trap electrons thermally ionized to conduction band (CB) [4] and in consequence the  $\text{Cr}^+$  ESR signal rises as long as electrons are induced to the CB. This is followed by a slow decay of the ESR  $\text{Cr}^+$  signal, which is due to the mentioned above  $\text{Cr}^+ \rightarrow$  acceptor tunneling. Instead, we observe a decrease of the ESR signal with the kinetics of the decrease which reflects the kinetics of the decay of the  $\text{Fe}^{3+}$  ESR signal. To explain these experimental data we propose a new mechanism - a two-center Auger recombination, in which  $\text{Cr}^+$  ions are ionized as a consequence of transfer of the excess energy of electron capture by  $\text{Fe}^{3+}$  ions. In fact, this mechanism (shown in Fig. 1 (c)) leads to a simultaneous decay of both  $\text{Cr}^+$  and  $\text{Fe}^{3+}$  populations and its temperature dependence is controlled by a thermal activation of electrons from shallow donors to the CB. Based on the present experimental results we propose that the Auger process, of the type described above, is responsible for a high efficiency of the bypassing process for TM ions.

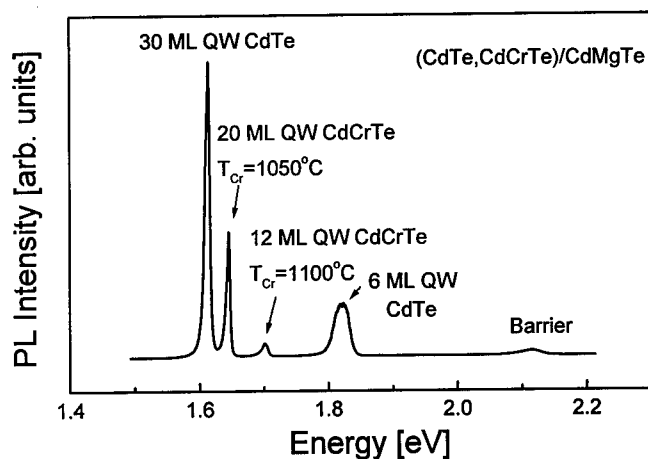


Figure 3: 2 K PL spectrum of the multiple  $(\text{CdTe,CdCrTe})/\text{CdMgTe}$  QW structure containing two CdTe QWs and two Cr containing CdCrTe QWs.



### Nonradiative recombination in (CdTe,CdCrTe)/CdMgTe heterostructures

For bulk II-VI samples the bypassing process is responsible for deactivation of PL emission by TM ions. The present study suggests that a high efficiency of this process may be explained by the Auger-type mechanism of carrier trapping by TM ions. The relevant nonradiative processes in TM doped QW structures remained unknown, so far. Below we discuss such processes in QWs containing Cr ions. The (CdTe,CdCrTe)/CdMgTe heterostructure studied was grown by molecular beam epitaxy and was a multiple QW structure consisting of two CdTe QWs (30 monolayers (ML) and 6 ML wide) and two CdCrTe QWs (20 ML wide, grown at 1050 °C Cr cell temperature, and 12 ML wide, grown at 1110 °C Cr cell temperature). The resulting concentration of chromium in the latter two QWs remains unknown, but it was increasing with an increase of the Cr cell temperature. QWs were separated by CdMgTe barriers.

In Fig. 3 we show the PL spectrum of the (CdTe,CdCrTe)/CdMgTe heterostructure studied. Free excitonic emission is observed from each of the QWs. However, intensity of this emission is strongly reduced for QWs containing Cr ions.

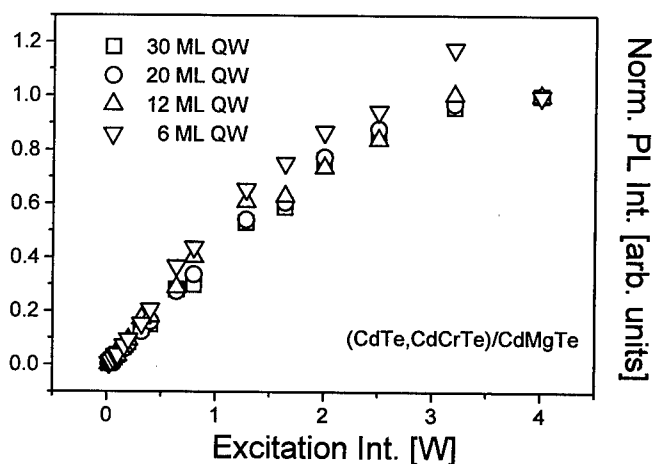


Figure 4: Dependence of the intensity of the QW PL in (CdTe,CdCrTe)/CdMgTe heterostructure on excitation intensity. PL intensity from different QWs is normalized to be equal at the highest excitation intensity.

Dependence of the PL intensity on excitation intensity was measured (see Fig. 4). Up to relatively high excitation intensities PL rises linearly and then saturates and starts to decrease. The latter we relate to the sample heating expected for high excitation intensities and focussed light used by us.

PL kinetics was measured under a 2 ps long pulsed excitation. The results of PL kinetics experiments are shown in Fig. 5. We observed a dramatic shortening of the PL decay times from 490 ps (30 ML wide) and 320 ps (6 ML wide) for the CdTe QWs to 200 ps (20 ML wide) and 75 ps (12 ML wide) for the CdCrTe QWs. The shortest PL decay time was observed for the QW with the highest Cr contents.

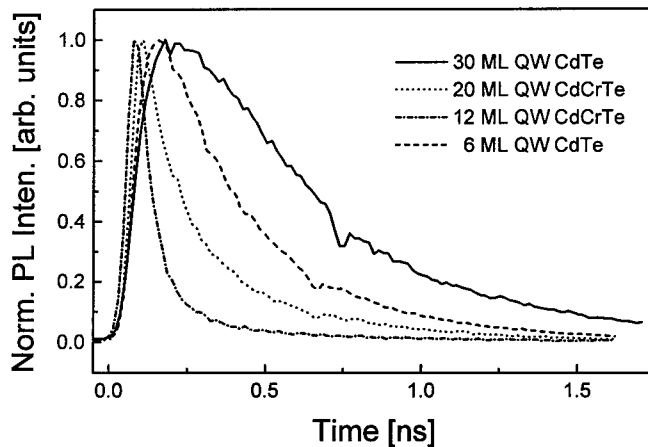


Figure 5: PL kinetics measured at 2 K for CdTe and CdCrTe QWs in the (CdTe,CdCrTe)/CdMgTe heterostructure studied.

The experimental results described above indicate a strong deactivation of the PL from QWs containing Cr. The obvious question is what is the nature of the quenching mechanism of the excitonic emissions. Based on the analogy of the results obtained for the bulk samples, we considered the bypassing process (Fig. 1(a)) and the Auger process (the analogue of the one shown in Fig. 1 (b)) as the processes responsible for the PL quenching. For the bypassing process the photo-generated free electrons and holes in a QW are trapped by chromium ions and thus they do not form free excitons. For the Auger process, excitons are efficiently formed but later on they decay nonradiatively, due to the energy transfer to Cr ions, which are ionized in the process.

To get a deeper insight into the problem we solved a set of kinetic equations describing rise and decay of the PL emission either in the absence or in the presence of chromium ions. These kinetic equations were solved under some simplifying assumptions. We have assumed that chromium related processes are the only channels of nonradiative recombination and only two processes mentioned above (the bypassing process and the Auger process) are efficient. We have also assumed that the absorption coefficients for the ionization transitions of chromium are small compared to coefficient of free carrier generation in QWs. Solution of the kinetic equations is given in the Table.

Recombination process	PL intensity	PL decay time
FE transition	$\tau_R I \alpha$	$\tau_R$
Bypassing process	$(c_X \tau_R / c_{Cr}^n \sqrt{c_{Cr}^p}) (I \alpha)^{3/2} / N_{Cr}$	$\tau_R$
Auger process	$\tau_R (1 + c_A \tau_R N_{Cr})^{-1} I \alpha$	$\tau_R (1 + c_A \tau_R N_{Cr})^{-1}$

Where:  $I$  - light intensity,  $\tau_R$  - radiative decay time of excitons,  $c_X$  - exciton formation rate,  $N_{Cr}$  - chromium concentration,  $c_A$  - Auger transfer rate,  $c_{Cr}^{n,p}$  - capture rates of electrons (n) and holes (p) by Cr ions

Solving the kinetic equations (see Table) we have found that it is possible to distinguish experimentally between two types of chromium-related nonradiative recombination processes. In the case of the efficient bypassing process the PL intensity is reduced, but the PL decay time remains unchanged. Whereas, in the case of the dominant Auger effect we expect both the reduction of the PL intensity and the shortening of the PL decay time. Moreover, the analysis of the kinetic equations yields the next difference between the Auger and the bypassing processes. For the Auger type transition we expect linear dependence of the PL intensity vs. excitation intensity ( $I$ ). For the bypassing process this dependence is super-linear, i.e., it varies as  $I^{3/2}$ .

The present experimental results indicate that the excitonic Auger effect is efficient chromium-related PL quenching mechanism. The bypassing process, dominant in the bulk samples, is here less important. To get a "rough" estimation of the efficiency of the Auger transition we employed Inokuti - Hiramaya theory of the resonant energy transfer [5]. Treating the chromium concentration  $N_{Cr}$  and the critical transfer radius  $R_0$  as the fitting parameters we obtained that  $N_{Cr} \sim 10^{19} \text{ cm}^{-3}$  and that  $R_0 \sim 20\text{-}30 \text{ \AA}$ . Such value of the critical transfer radius means that the Auger process is efficient only if one or more of Cr ions is located within the Bohr radius of the exciton. It remains to be checked if the low efficiency of the Cr-related bypassing process can be explained by a relatively low efficiency of free exciton formation under excitation of free e-h pairs in QW structures with rough interfaces [6] or in fact is due to enhanced role of the Auger processes in low dimensional structures.

Concluding, we show here that the Auger-type processes play a crucial role in nonradiative recombination processes in both bulk and QW structures of II-VI semiconductors doped with TM ions. These processes are shown to be especially efficient in QW structures containing chromium, where they are responsible for the quenching of excitonic recombination transitions.

#### Acknowledgements:

This work was partly financed by the grants no. 2 P03B 018 13 and 8T 11B 014 11 of the KBN

#### References:

1. M. Tabei, S. Shionoya and H. Ohmatsu, *Jpn. J. Appl. Phys.* **14**, 240 (1976).
2. M. Godlewski, M. Surma and A.J. Zakrzewski, *J. Appl. Spectr.* **62**, 72 (1995).
3. M. Godlewski and M. Skowronski, *Phys. Rev.* **B32**, 4007 (1985).
4. M. Godlewski, *Physica Statuts Solidi (a)* **90**, 11 (1985).
5. M. Inokuti and F. Hiramaya, *J. Chem. Phys.* **43**, 1978 (1965).
6. M. Godlewski, P.O. Holtz, J.P. Bergman, B. Monemar, K. Reginski, M. Bugajski, E.M. Goldys and T.L. Tansley, *Semicond. Sci. and Technol.* (in press).

## SPIN-DEPENDENT PROCESSES IN SELF-ASSEMBLY IMPURITY QUANTUM WIRES

N.T. Bagraev, W. Gehlhoff<sup>1</sup>, L.E. Klyachkin, A.M. Malyarenko,  
and A. Näser<sup>1</sup>

A.F. Ioffe Physico-Technical Institute, St.Petersburg, Russia  
<sup>1</sup>Institut für Festkörperphysik, Technische Universität Berlin,  
Hardenbergstr. 36, D-10623 Berlin, Germany

**Keywords:** self-assembly silicon nanostructures, spin-dependent localization

**Abstract.** We present the first findings of the quantized conductance, EPR-EDEPR and NMR techniques which reveal the spin-dependent confinement and quantization phenomena in the silicon quantum wires created by electrostatically ordering of the self-assembly dipole boron ( $B^+-B^-$ ) centres. These  $C_{3v}$  symmetry dipole impurity centres are regularly arranged along the edges of self-assembly longitudinal and lateral quantum wells (LQW and LaQW) which are naturally formed in the  $p^+$ -diffusion profile inside ultra-shallow silicon  $n^+-p^+-p$  and  $n^+-p^+-n$  structures. A negative magneto-resistance that is evidence of the spin-dependent weak localization in self-assembly quantum wells at low electric fields is studied. The presence of natural quantum-size contacts inside self-assembly quantum wells is exhibited using the quantized conductance technique in weak magnetic fields.

### 1. Introduction.

Dopant diffusion in silicon is known to be controllable by adjusting the fluxes of self-interstitials and vacancies emerging from monocrystalline surface, which stimulate the kick-out and dissociative vacancy diffusion mechanism, respectively [1]. By varying the parameters of the surface oxide layer, the Cl levels in the gas phase and diffusion temperature, it was possible to define the criteria leading to parity between these two mechanisms. The deceleration of the diffusion process thus achieved has permitted, for the first time, the fabrication of ultra-shallow  $n^+-p^+-n$  transistor structures with quantum well (QW)  $p^+$ -base diffusion profile, the depth of which could be controlled using the SIMS technique over 5 nm-30 nm. The cyclotron resonance investigations and current-voltage (CV) measurements at different angles between the diffusion profile plane and the bias voltage show that the  $p^+$ -diffusion profiles obtained under parity between two diffusion mechanisms consist predominantly of self-assembly longitudinal quantum wells (SLQW), whereas self-assembly lateral quantum wells (SLaQW) oriented along the  $\langle 111 \rangle$  and  $\langle 100 \rangle$  crystallographic axes dominate in the  $p^+$ -diffusion profile realized respectively by the kick-out and dissociative vacancy diffusion mechanism [2].

The present work reports on studies of the spin-dependent weak localization in SQW obtained inside ultra-shallow silicon  $n^+-p^+-p$  and  $n^+-p^+-n$  structures. The quantized conductance technique reveals the dynamic quantum wires due to the electrostatically ordered dipole ( $B^+-B^-$ )-centres which are arranged along the edges of SQW. Finally, natural quantum-size contacts inside SQW are exhibited by the negative magnetic resistance measurements in weak magnetic fields.

### 2. Preparation of ultra-shallow silicon $n^+-p^+-p$ and $n^+-p^+-n$ structures.

Short-time diffusion of boron and phosphorus has been performed at 900°C and 1100°C, respectively, from gas phase into  $p$ - and  $n$ -type Si(100) wafers (Figs. 1 a and b). The working and back sides of the wafers were previously oxidized using the thermal oxidation process. Impurity doping was done on the working side of the wafers after covering the oxide overlayer with mask and performing the subsequent photolithography. The additional use of a high Cl level in the gas phase leads to homogeneous distribution of boron inside the  $p^+$ -base diffusion profile in the  $n$ -type Si(100) wafer (Fig. 1b).

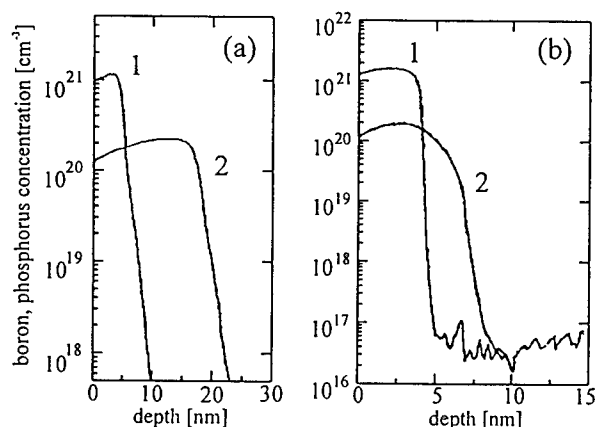


Fig. 1: Ultra-shallow SIMS diffusion profiles obtained during subsequent diffusion of (1) boron and (2) phosphorus dopants at diffusion temperature of 900°C and 1100°C, respectively, in (a) p-type Si (100) wafer with  $N(B)=3.5 \cdot 10^{14} \text{ cm}^{-3}$  and thick oxide overlayer and in (b) n-type Si(100) wafer with  $N(P)=2 \cdot 10^{14} \text{ cm}^{-3}$  and thin oxide overlayer.

### 3. Results and Discussion.

#### 3.1. Self-assembly dipole boron ( $B^+-B^-$ ) centres.

The cyclotron resonance studies show that the  $p^+$ -diffusion profile obtained in the p-type Si wafer with a thick oxide layer consists of both SLQW and SLaQW, whereas the presence of a thin oxide layer and high Cl level causes predominantly the formation of SLQW inside the  $p^+$ -diffusion profile obtained in the n-type Si wafer [2]. Thermo-emf and tunneling CV measurements demonstrate that reconstructed centres of dopants at the edges of self-assembly quantum wells represent the  $C_{3v}$  symmetry dipole defects of the ( $B^+-B^-$ )-type, which are ordered by an applied external electric field (Fig. 2) [3]. Therefore, the field associated to the dipole centre's ordering seems to be taken into account

in order to present the spin-splitting of both the valence and conduction bands for spin-flip single-particle excitation studies. This spin splitting caused by the impurity dipole ordering can be revealed by the EPR (Fig. 3) and weak localization (Fig. 4) studies.

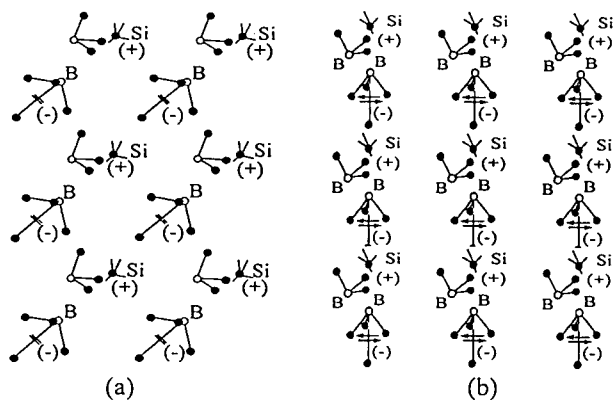


Fig. 2: Model for an elastic reconstruction of a shallow acceptor, which is accompanied by the formation of the  $C_{3v}$  dipole ( $B^+-B^-$ )-centres as a result of the negative-U reaction:  $2B^0 \rightarrow B^+ + B^-$  (a)  $E=0$ ; (b)  $E \parallel [001]$ .

The dipole ( $B^+ + B^-$ ) model of the charge correlations in SLQW and SLaQW allows to account for a strong angular dependent new EPR-line (Fig. 3), the observation of which in the X-band and low temperatures depends on cooling conditions and demonstrates pyroelectric behavior of heavily doped  $p^+$ -diffusion profiles. This EPR line clearly exhibits metastable behavior. No signals are observed if the  $p^+n$  junction is cooled down without external magnetic field. Angular rotation patterns are measured only after cooling down in the external magnetic field and the amplitude of the signals as well as the resonance fields are dependent on its value and crystallographic orientation. With increasing temperature, the line observed changes its magnetic resonance field position and disappears at 27 K

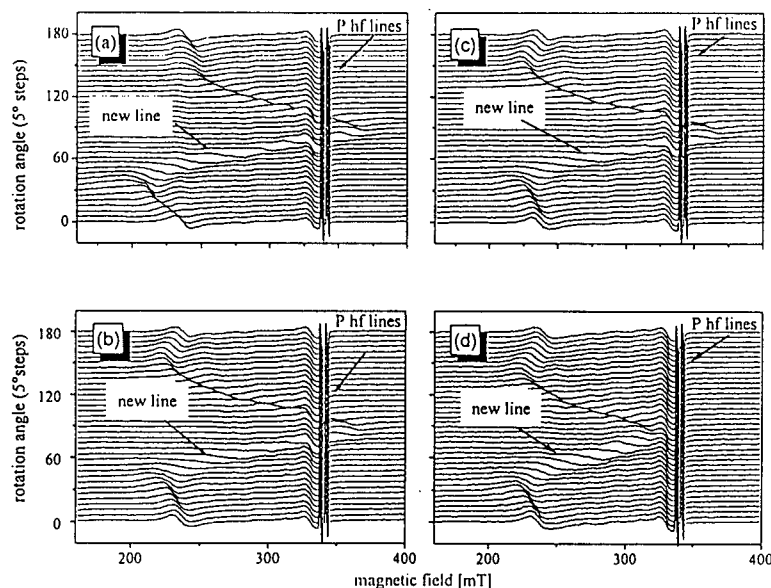


Fig. 3: New EPR line obtained for the ultra-shallow  $p^+$ -diffusion profile consisting of SLaQW after cooling down in an external magnetic field  $B_{ext}$  applied in different crystallographic directions.  $B_{ext} \parallel \langle 110 \rangle$  (a),  $\parallel \langle 112 \rangle$  (b),  $\parallel \langle 111 \rangle$  (c,d). The  $p^+$ -diffusion profile was prepared in n-type Si(100) wafer at 1100°C without previous oxidation. Rotation of the magnetic field in {110}-plane perpendicular to a {100}-interface ( $0^\circ$ ,  $180^\circ = B_{ext} \parallel \text{interface}$ ,  $90^\circ = B_{ext} \perp \text{interface}$ ),  $\nu = 9.45$  GHz,  $T = 14$  K (a,b,c) and  $T = 21$  K (d).

which is the temperature for the thermal ionization of phosphorus donor centers in the n-type region of the  $p^+n$  junction. The EPR signal is really persistent in the temperature interval from 3.8 K to 27 K as a function of the magnetic field value during cooling down process. These new line effects may be explained in the framework of the dynamic magnetic moment which is induced by the exchange interaction of the trigonal ( $B^+-B^-$ )-dipoles through the phosphorus donor centres close to the  $p^+$ -diffusion profile. The principal orientation of the impurity dipole axis is determined by the reconstruction of dopants along the  $\langle 111 \rangle$  crystallographic axis.

### 3.2. Spin-dependent weak localization.

A weak localization effect is due to the interferences along a closed coherent path between two propagating waves  $\Psi_+(R)$  and  $\Psi_-(R)$ , one being the time-reversed of the other increase the back scattering probability by a factor of 2 because these waves come back in phase. As a result, the conductivity along SQW is decreased: this effect is known as a weak localization (Fig. 4 a). The correction  $\Delta\sigma_{WL}$  to the conductivity can be obtained using classical description of diffusion (the inelastic length  $L_\phi$  is

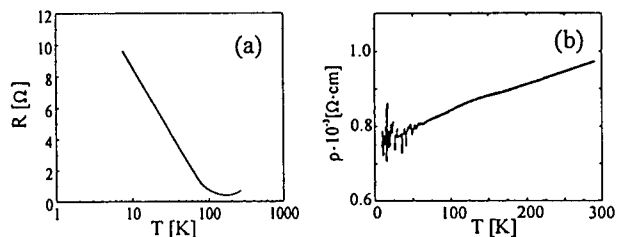


Fig. 4: Temperature dependencies of the resistivity of the  $p^+$ -diffusion profile consisting of SQW, which was prepared at 900°C in p-type Si (100) wafer with  $N(B) = 3.5 \cdot 10^{14} \text{ cm}^{-3}$  and thick oxide overlayer (see Fig. 1 a, curve 1); (a) low electric field; (b) strong electric field.

The correction  $\Delta\sigma_{WL}$  to the conductivity can be obtained using classical description of diffusion (the inelastic length  $L_\phi$  is

supposed to be much larger than the mean free path  $l_e$ ):

$$\Delta\sigma_{WL} = -(4e^2/h) \cdot \log(L_\phi/l_e) \quad (1)$$

When a transverse magnetic field is applied, the time-reversal invariance is broken. The phase of the two waves around a closed loop is modified in the same way as in the Aharonov-Bohm experiment, i.e. by  $\pm 2\pi\Phi/\Phi_0 = S/(l_B)^2$  (where  $\Phi = BS$  is the enclosed flux,  $\Phi_0 = h/2e$  is the flux quantum, and  $l_B = (h/eB)^{1/2}$  is the magnetic length). The backscattering is reduced, because the loops with the area larger than  $(l_B)^2$  are added classically in average. A negative magnetoresistance is observed (Fig. 5a).

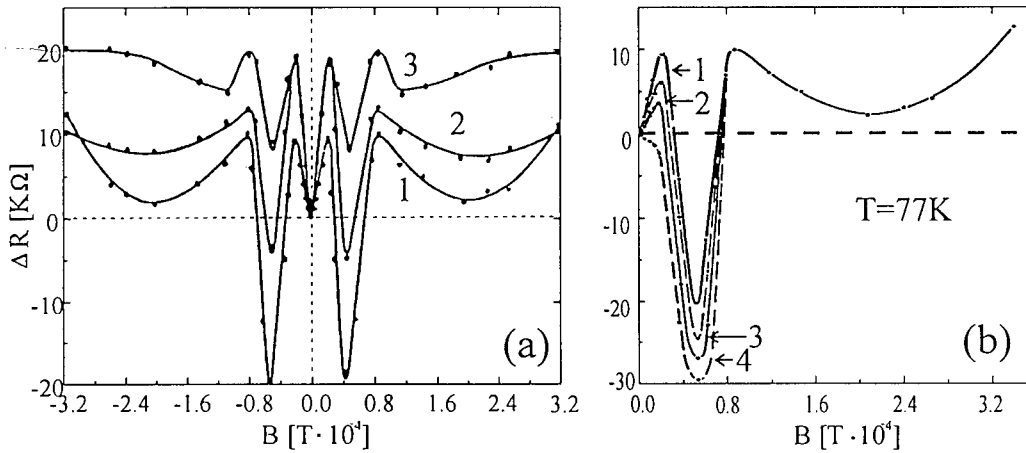


Fig. 5: The variations of the resistance at  $T=77$  K with an magnetic field  $B$  applied to the 2D hole gas in SQW inside ultra-shallow  $p^+$ -diffusion profile (see Fig. 1a, curve 1) under the application of the external electric field along the SQW plane (a) and different NMR saturation conditions of the  $^{29}\text{Si}$  nuclei determined by the strength of the microwave field  $H_1$  (b). (a) 1 -  $U=0.07$  V; 2 -  $0.13$  V; 3 -  $0.22$  V.; (b)  $U=0.07$  V,  $H_0=0.02$  mT;  $f_0'=545$  Hz;  $H_1$ : (1):  $0$  mT, (2):  $0.4 \cdot 10^{-5}$  mT, (3):  $1 \cdot 10^{-5}$  mT, (4):  $5 \cdot 10^{-5}$  mT.

But, if the spin influence will be taken into account, the probability of the return to the origin is a sum of the probabilities calculated for each component of the spinor  $\psi = (\psi_\uparrow, \psi_\downarrow)$ . The value obtained is lower than the classical return probability. Thus, if there is some spin-orbit coupling which rotates the spin components, the backscattering is reduced instead of being increased. This is related to the fact that upon a rotation by  $2\pi$  the radial part comes out in phase, whereas the spin part comes out with a phase shift by  $\pi$ . The product is phase shifted by an odd multiple of  $\pi$ . The conductivity is therefore enhanced if compared to the result of a calculation which neglects the coherence effects. The phenomenon is the weak antilocalization in the weakest magnetic fields (Fig. 5a) [4]. The  $C_{3v}$  symmetry dipole centres could also give an additional contribution to this effect by the influence on the spin-splitting value in both the valence and conduction band. Besides, spin nuclear polarization can be induced in the weak localization regime as a result of the hyperfine interaction between  $^{29}\text{Si}$  nuclei with  $I=1/2$  (natural abundance 4.7%) and the holes in quantum wells, which decreases additionally the mobility of holes. The experimental test on the contribution of this effect to the antilocalization phenomenon represents the magnetoresistance measurements under the nuclear magnetic resonance (NMR) saturation of the  $^{29}\text{Si}$  nuclei, which demonstrate the positive/negative transformation of its value in weak magnetic fields (Fig. 5b). The electrically-detected NMR of the  $^{29}\text{Si}$  nuclei verify the nuclear spin polarization by the corresponding shift of the resonance frequency  $\Delta f = f_0' - f_0$  which is determined through the resonance condition with the nuclear magnetic field values  $(H_0' - H_0)$ , where  $H_0' = H_0 + H_L + H_{H1}$  and  $H_0$  is the external magnetic field,  $H_L = 0.0176$  mT is the local field of the  $^{29}\text{Si}$  nuclei and  $H_{H1}$  is the hole field on neighbour lattice nuclei. The observed shift of the NMR frequency of  $\Delta f = 385$  Hz ( $H_0 = 0.02$  mT) in these measurements seems to be due to the electrically- induced polarization of the  $^{29}\text{Si}$  nuclei.

### 3.3. Dynamic quantum wires.

The logarithmic temperature dependence of resistivity has revealed a weak localization regime of two-dimensional hole gas (Fig. 4a), which is transformed in the quantum wire system under the voltage applied along both self-assembly SLQW and SLaQW (Fig. 4b). Thermo-emf and tunneling CV

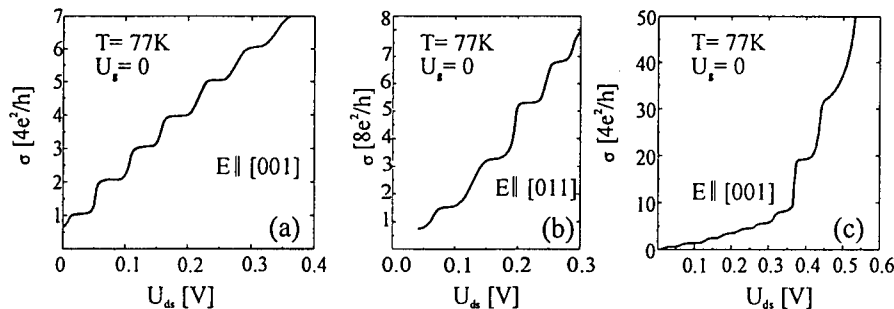


Fig.6: The quantized conductance (QC) at 77 K vs crystallographically-oriented drain-source voltage applied along the [001] (a,c) and [011] (b) crystallographic axes in the SQW plane inside ultra-shallow  $p^+$ -diffusion profile (see Fig. 1a, curve 1).

measurements demonstrate that these quantum wires seem to be created by the electrostatic confinement potential of self-assembly dipole ( $B^+B^-$ )-centres which cause a correlation gap in the density of states of the hole gas in SQW [3]. The quantized conductance measurements for different crystallographic directions has revealed dynamic quantum wires with semitransparent redouts that contribute to the process of hole's backscattering (Fig. 6). The relation  $\Delta E \cdot \Delta \tau \sim \hbar$  is found to be carried out, thereby confirming the number of redouts that take part in the backscattering of holes: where  $\Delta E = e\Delta U$ ,  $\Delta U$  is the period of the current step in Figs. 6a and b;  $\Delta \tau = 2l/v$ ,  $l$  is the distance between two semitransparent redouts, which is equal the width of the quantum wire and corresponds to the distance between two neighbour impurity dipoles. The valley's effect on the quantized conductance is also exhibited (Fig. 6b) that is in a good agreement with the prediction by the Landauer formula. The quantized conductance technique has also identified new near-edge resonances that appear in the  $I(V)$  dependence and are due to the hole scattering on single iron-related centres because of the interaction between the d-levels and minibands in quantum wires (see Fig. 6c).

### 3.4. Natural quantum-size contacts

SLQW obtained in the  $p^+$ -diffusion profile with homogeneous dopant distribution (Fig. 1b) are found to be exhibited only single fluctuations in the correlation gap value [3]. Therefore, the dynamic quan-

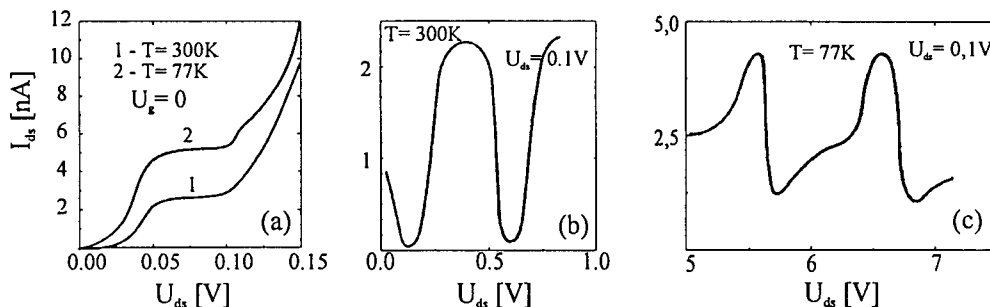


Fig.7: A single plateau in the drain-source  $I_{ds}$ - $U_g$  characteristics (a) and gate-voltage  $I_{ds}$ - $U_g$  characteristics (b,c) of the quantum wire in SLQW inside the ultra-shallow  $p^+$ -diffusion profile (see Fig. 1 b, curve 1), which reveal the single hole (curve 1 in (a), (b)) and Cooper pair (curve 2 in (a), (c)) tunnelling through the natural quantum-size contact by the positive ( $U_g > 0$ ) (c) gate voltage applied to the QW  $n^+p^-n$  silicon transistor structure in the field-effect regime.



tum wires induced electrostatically in such SQW are of great interest as a basis of single hole transistor structures [3]. The double step in the current plateau and corresponding changes in the period of current oscillation vs the gate voltage demonstrate that the single fluctuation in a correlation gap value can be present as the Josephson's quantum-size contacts which seem to be responsible for the hole pair tunnelling at 77 K and single-hole tunnelling process at 300 K ( $e=C \cdot \Delta U_g$ ;  $2e=C \cdot 2\Delta U_g$ ) (Fig. 7). This model has been shown to be confirmed by the temperature dependence of the resistance of the QW  $p^+$ -diffusion profile, which is due to the thermal excitation of single holes and allow to determine the correlation gap value as  $\Delta \approx 44$  meV ( $R \sim R_0 \cdot \exp(-\Delta/kT + \Delta/kT_c)$ ).

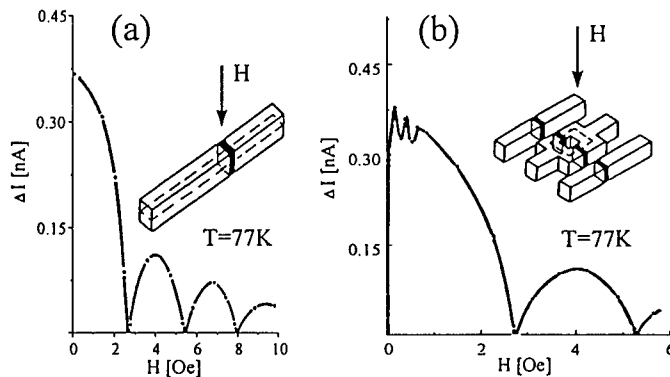


Fig. 8: The current variations with the magnetic field applied to the Si quantum wire containing a natural quantum-size contact (a) and parallel natural quantum-size contacts (b). The insert depicts the quantum wire with single (a) and two parallel (b) quantum-size contacts.  $E \parallel [001]$ ;  $U_{ds} = 0.11$  V;  $T=77$  K.

The presence of the natural quantum-size contacts in the Si dipole quantum wires is demonstrated to induce the sinusoidally varying quenching at applied external magnetic field:

$$I \sim I_0 \cdot \sin(\pi\Phi/\Phi_0) / (\pi\Phi/\Phi_0), \quad (2)$$

where  $\Phi_0 = h/2e$ ;  $\Phi = \Delta B \cdot S$ ;  $S \approx d(d+\lambda)$ ;  $d$  is the width of the quantum wire (see Fig. 8a). The parallel quantum-size contacts are also formed inside quantum wires during impurity dipole ordering, which are responsible for the current enhancement in a weak magnetic field as a result of the natural SQUID structure creation (see Fig. 8b):

$$I_{\max} = 2I_0 \cdot |\cos(\pi\Phi/\Phi_0)| \quad (3)$$

Finally, the temperature and magnetic field dependencies of the magnetic susceptibility show a strong diamagnetism as a correlation gap arises, which confirm additionally hole pair tunneling mechanism [3].

#### 4. Summary

Spin-dependent confinement and natural quantum-size contacts have been shown to be revealed in dynamic silicon quantum wires created by electrostatically ordering dipole boron ( $B^+-B^-$ )-centres. These  $C_{3v}$  symmetry dipole impurity centres have been found to be arranged along the edges of self-assembly quantum wells that are exhibited in a weak localization regime.

#### References

1. N.T. Bagraev, L.E. Klyachkin, V.L. Sukhanov, Defect and Diffusion Forum 103-105, 201 (1993).
2. W. Gehlhoff, N.T. Bagraev, L.E. Klyachkin, Materials Science Forum 196-201, 467 (1995).
3. N.T. Bagraev, L.E. Klyachkin, A.M. Malyarenko, W. Gehlhoff, Proc. of the ICPS-23, ed. by M. Scheffler and P. Zimmermann (Singapore: World Scientific) p.1241 (1996)
4. G. Bergmann, Phys. Rep. 107, 1 (1984)

## COMPARISON BETWEEN AS-GROWN AND ANNEALED QUANTUM DOTS MORPHOLOGY

J. C. Ferrer<sup>1,2</sup>, F. Peiró<sup>1</sup>, A. Cornet<sup>1</sup>, J. R. Morante<sup>1</sup>, T. Utzmeier<sup>3</sup>, G. Armelles<sup>3</sup>,  
F. Briones<sup>3</sup>

<sup>1</sup>EME, Enginyeria i Materials Electrònics, Dept. Física Aplicada i Electrònica,  
Universitat de Barcelona, Diagonal 645-647, E-08028, Barcelona, Spain.

<sup>2</sup>Serveis Científico-Tècnics, Universitat de Barcelona, Lluís Solé i Sabarís 1-3, E-08028  
Barcelona, Spain.

<sup>3</sup>CNM, "Instituto de Microelectrónica de Madrid", Isaac Newton 8, Parque Tecnológico  
de Madrid, E-28760 Tres Cantos, Madrid, Spain.

**Keywords:** Quantum dots, InSb, ALMBE

**Abstract.** InSb self-assembled islands have been grown by epitaxial deposition on InP substrates, and the effect of an annealing process has been studied. Transmission electron microscopy and atomic force microscopy observations have been performed before and after annealing the InSb islands in order to assess the effects on the dot morphology and on their distribution on the wafer surface. Measurements of high-energy electron diffraction during the growth indicate a three-dimensional growth beyond the onset of 1.1 InSb monolayer deposition, obtaining InSb islands. It has been confirmed that the annealing process after the InSb deposition improves the dots quality. Whereas as-grown islands have a relatively inhomogeneous shape, the annealed sample has a uniform distribution of well defined dots. Dots are slightly elongated along the [110] direction. In both cases the substrate surface has developed an anisotropic undulation parallel to dot elongation direction. Raman measurements show a more intense peak in the annealed dot spectra confirming the formation of better quality islands.

### Introduction

Self-organisation processes of atomic species on substrate surfaces have become a promising method to obtain low dimensional structures such as quantum dots or wires. The capability of obtaining these nanostructures, exhibiting the properties of carrier confinement, without the need of additional technological processes, often inducing size limitations, make them a promising way to fabricate optoelectronic devices [1]. The most usual method to achieve good quality quantum dots is based on the three-dimensional growth of III-V materials when deposited on mismatched substrates. In low mismatched systems, thick layers are grown before the three-dimensional growth takes place due to the lower energy related to strain or, in most cases, an assortment of defects originated at the interface relaxes the layer allowing it to grow in a two-dimensional mode. Conversely, higher lattice mismatch leads to an earlier transition from layer by layer to island growth, or to a direct three-dimensional growth. Some studies have been reported devoted to the growth of quantum dots based on several

combinations of III-V materials such as InAs, InAlAs, InGaAs or InP on GaAs [2-5] with low lattice mismatch. Recently the studies have been extended to systems with a higher lattice mismatch such as InSb on GaAs [6-8] or InSb on InP [9].

In the present work, the effects of the annealing on InSb dots grown by atomic layer molecular beam epitaxy (ALMBE) on InP substrates are studied, paying special attention to changes in dot size, surface density, relaxation state and optical properties before and after the annealing.

### Experimental

An amount of InSb equivalent to 2.8 monolayers (ML's) was deposited by ALMBE on two pieces of a semi-insulating (001)InP substrate at a temperature of 410°C, maintaining the group V element pulsed to enhance the surface migration. Previous to InSb deposition, InP oxide was desorbed at 490°C and a 500 ML thick InP buffer layer was grown. In order to know the growth evolution and assess if the InSb follows a Stransky-Krastanov or a Volmer-Weber growth mode, i.e. initial layer by layer growth followed by a three-dimensional growth or directly island formation, high-energy electron diffraction measurements during the deposition were performed, indicating a transition from two-dimensional to three-dimensional growth mode in the onset of the 1.1 ML's. A sample was annealed at 440°C during 500 s to evaluate the effects of this process.

In order to compare the morphology and distribution of the dots over the substrate surface, transmission electron microscopy (TEM) and atomic force microscopy (AFM) measurements were performed with a Philips CM-30 Electron Microscope operating at 300 KV and a Nanoscope III Multimode AFM Digital Instruments operating in tapping mode, respectively. Samples for electron microscopy were prepared in cross section configuration by conventional methods of mechanical polishing and final Ar<sup>+</sup> ion mill, in a cooled stage, until perforation. Raman measurements were also performed to assess the influence of the annealing on the dot quality.

### Results.

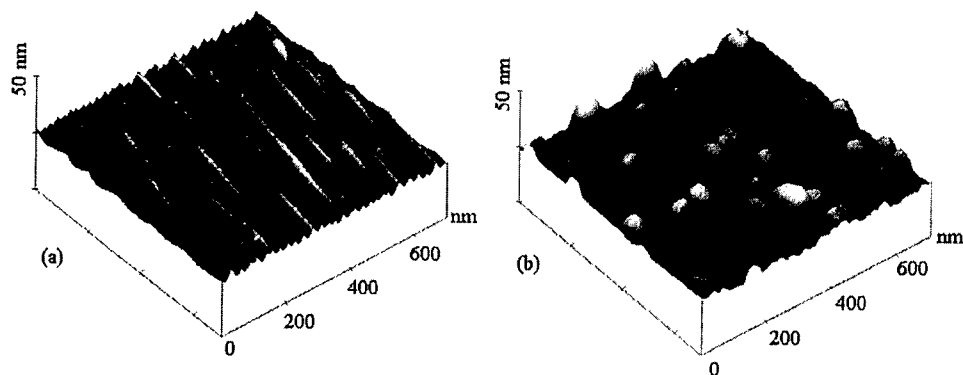


Figure 1. AFM images of the as-grown sample (a) where it is difficult to distinguish InSb island from InP substrate, and the annealed sample (b) where well defined quantum dots can be observed. In both cases a highly directional undulation is found at the substrate surface

AFM results show meaningful differences between the as-grown and the annealed samples as can be observed in fig. 1. In the former case it is difficult to distinguish the dots from the substrate surface: the surface has developed an anisotropic wavy-like surface, which has been previously observed in similar samples [9], that makes very difficult the identification of the islands which are flat and without clear facets limiting the structures. On the contrary, well defined InSb islands are found in the annealed sample, with an acceptable regular distribution over the surface and homogeneous sizes.

Notice that the dots are slightly elongated in the direction [110] parallel to the hillocks and valleys of the substrate surface, which conserve the undulation after the annealing. Measurements based on AFM images provide a result for the dots density of  $7.4 \cdot 10^9 \text{ cm}^{-2}$ , a mean height of 10 nm, mean size of 50 nm for the [110] direction and 33 nm for the [110] direction.

AFM results are confirmed by TEM observations. Moreover we can obtain further information about the structure of as-grown dots. Observing the fig. 2a we can realise why we could not distinguish the dots in the AFM images: it is clear from this image that the height and length of the dots are comparable to that of the substrate undulations. This image also shows the presence of three-dimensional defects inside the InSb structure, i.e. the dot is composed by several disorientated crystals separated by plane boundaries indicated by arrows in fig. 2a. On the other hand, annealed dots (fig. 2b) have better crystal quality. They are faceted by a (001) top plane and {111} lateral sides, with a shape that allows to distinguish it perfectly from the undulations. Moreover no extended defects are found inside the InSb, that appears as a single crystal. Notice, nevertheless, that an array of misfit dislocations is placed at the dot/substrate interface,



Figure 2. High resolution TEM [110] images of an as-grown dot (a) and annealed dot (b). In the former case some defects can be found inside the InSb island. Observe the faceting of the dot in the later case.

which relaxes the strain induced by the large lattice mismatch (10.4%). Some mechanisms

have been proposed to explain the nucleation of such array based on the generation of dislocations as dot growth proceeds [12].

These morphological differences affect the optical properties of dots as can be checked in the Raman spectra of both types of samples (fig.3). A more intense peak is found for the annealed sample due to the better quality of the islands.

From the presented results it seems that the growth follows a Stransky-Krastanov mode because, as the RHEED results indicate, a transition from two-dimensional to three-dimensional mode is produced when the equivalent amount of 1.1 ML InSb is deposited. Despite this fact, there is no evidence, from high resolution TEM images, of the existence of a wetting layer connecting the dots. Moreover calculations based on the size and density of annealed dots, show that there is not enough material after island formation to have a remaining wetting layer. Thus, the final configuration is similar to that obtained following a Wobler-Weber growth mode (direct three-dimensional growth of islands). This behaviour could be explained taking into account that the energy related to the strain in the growth of InSb on InP is high. Calculations based on the Van der Merwe model show that the critical

thickness below which an InSb layer may be grown coherently on an InP substrate is a 10% of the thickness corresponding just to a monolayer. Thus it is likely that the energy related to the initial single monolayer of InSb monitored by RHEED is too high and that it could be in a metastable state, achieved thanks to the controlled kinetics of the growth during the ALMBE process.

It is clear from AFM and TEM images that a regular distribution of dots with a truncated pyramidal shape is thermodynamically preferred after the annealing, i.e. it is a configuration which minimises the energy, but it is necessary to introduce the annealing process to enhance the atom kinetics that allows the atomic species to have an increased diffusivity over the surface, and reach a state in which the InSb is developing bigger islands. Instead, in the paper of Kosogov et al. [2] the effects of the annealing of capped InAs quantum dots on GaAs are reported, finding an increment on dots size but no change in shape. In our case, the absence of a cap

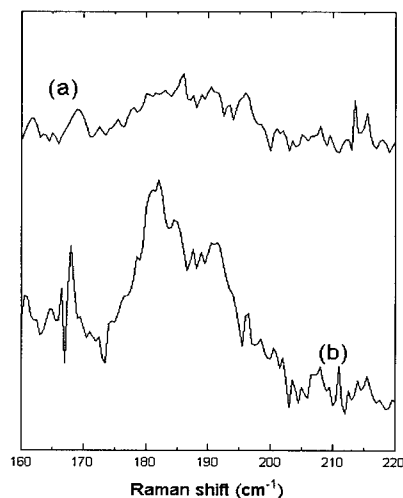


Figure 3. Raman spectra of both as-grown (a) and annealed (b) samples. An intense peak is found for the later case due to the better quality of InSb islands.

layer could lead to an enhancement of surface diffusion and to the formation of truncated pyramidal dots with low-index facets, {111} for lateral sides and a (001) top plane. Another consequence of the annealing is the better crystalline quality, reducing the amount of defects inside dots.

The last point to be commented on is the origin of the surface undulation. It could be already observed before the annealing, and this process does not introduce qualitative changes in the

rugosity morphology. Thus the substrate roughness should have been produced (i) during the InP buffer layer growth as it may happen depending on the deposition technological parameters in homoepitaxial growth [11,12], or (ii) during the InSb deposition. In the later case, the ripples would be the result of strain fields of elongated dots. The dot elongation [9] could be explained following the paper of Tersoff et al. [13]. In this paper it is shown that for sufficient atomic diffusion on the surface, islands tend to grow with a square shape until a critical size is reached. Beyond this limit, they become enlarged to minimize the total energy.

### Conclusions

In summary, the effects of an annealing treatment on the morphology and optical properties of quantum dots have been studied. Although there is island formation before the annealing, the improvement in dot quality after this process has been demonstrated, obtaining regularly distributed dots with truncated pyramidal shape and homogeneous sizes. On the other hand, thermal treatment also affects the optical properties, since more intense peaks appear in Raman spectra for the annealed sample.

### References

- [1] D.Bimberg, N.N.Ledentsov, M.Grundmann, N.Kirstaedter, O.G.Schmidt, M.H.Mao, V.M.Ustinov, A.Yu.Egorov, A.E.Zhukov, P.S.Kop'ev, Zh.I.Alferov, S.S.Ruminov, U.Gösele and J.Heydenreich, *Phys. Status Solidi* **194**, 159 (1996).
- [2] A.O.Kosogov, P.Werner, U.Gösele, N.N.Ledenstov, D.Bimberg, V.M.Ustinov, A.Yu.Egorov, E.Zhukov, P.S.Kop'ev and N.A.Bert, *Appl. Phys. Lett.* **69**, 3072, (1996)
- [3] D.Leonard, M.Krishnamurthy, S.Fafard, J.L.Merz and P.M.Petroff, *J. Vac. Sci. Technol. B* **12**, 1063 (1994).
- [4] K.Tillmann, D.Gerthsen, P.Pfundstein, A.Förster and K.Urban, *J. Appl. Phys.* **78**, 3824 (1995)
- [5] M.Sopanen, H.Lipsanen and J.Ahopelto, *Appl. Phys. Lett.* **67**, 3768 (1995)
- [6] Brian R.Bennett, R.Magno and B.V.Shanabrook, *Appl. Phys. Lett.* **68**, 505 (1996)
- [7] B.R.Bennett, P.M.Thibado, M.E.Twigg, E.R.Glaser and R.Magno, *J. Vac. Sci. Technol. B* **14**, 2195 (1996)
- [8] X.Zhang, A.E.Staton-Bevan, D.W.Pashley, S.D.Parker, R.Droopad, R.L.Williams, R.C.Newman, *J.Appl.Phys* **67**, 800 (1990)
- [9] J.C.Ferrer, F.Peiró, A.Cornet, J.R.Morante, T.Utzmeier, G.Armelles, F.Briones, *Appl. Phys. Lett.* **69**, 3887 (1996)
- [10] G.W.Smith, A.J.Pidduck, C.R.Whitehouse, J.L.Glasper, A.M.Keir and C.Pickering, *Appl. Phys. Lett.* **59**, 3282 (1991)
- [11] F.Briones, D.Golmayo, L.Gonzalez and J.L.de Miguel, *Jpn. J. Appl. Phys.* **24**, L478 (1985)
- [12] Y.Chen, X.W.Lin, Z.Liliental-Weber, J.Washburn, J.F.Klem and J.Y.Tsao, *Appl. Phys. Lett.* **68**, 111 (1996)
- [13] J.Tersoff, R.M.Tromp, *Phys.Rev.Lett.* **70**, 2782 (1993)

## EPR STUDIES OF MAGNETIC SUPERLATTICES

Z. Wilamowski<sup>1,2</sup>, G. Springholz<sup>1</sup> and W. Jantsch<sup>1</sup>

<sup>1</sup>Institut für Halbleiterphysik, Johannes Kepler Universität, A-4040 Linz, AUSTRIA

<sup>2</sup>Institute of Physics of the PAS, Al. Lotnikow 32/46, PL 02-668 Warsaw, POLAND

**Key words:** Interdiffusion, Strain, Superlattices, Magnetic Anisotropy

### Abstract.

Magnetic resonance techniques constitute a powerful tool for the investigation of the properties of thin magnetic layers and superlattices (SL's). In this paper we present results where the EPR of isolated paramagnetic centers, that of pairs and that of strongly interacting spins is used for the investigation of the spatial distribution of strain, dipole fields and of magnetic ions, *i.e.*, for interdiffusion in SL's. In particular, we study SL's of the type PbTe/EuTe and CdTe/MnTe.

### Introduction.

Recent progress in molecular beam epitaxy and in characterization techniques allows to grow thin films also of magnetic materials with monolayer (ML) control in combination with layers of diamagnetic semiconductors [1]. This kind of combination allows to control electronic and magnetic properties and to "design" the interaction between carriers and magnetic ions [2]. A range of new devices can be envisioned to result from such structures, *e.g.*, by combining magnetic memories and logic circuits. In order to study such interactions, multilayer structures or superlattices of magnetic and diamagnetic layers are grown and studied as a first step since they provide sufficient sensitivity in many experimental techniques which require some minimum number of layers or particles. Superlattices (SL) also allow to investigate the influence of geometrical order and strain as compared to alloys.

The investigation of magnetic properties in low dimensions has received considerable attention recently also because of basic interest in the influence of dimensionality *e.g.* on magnetic structure and phase transitions[3,4]. For such investigations, the perfection of the interfaces is much more critical than for the electronic properties of low d systems since the relevant magnetic interactions are of shorter range, extending mostly only to the interatomic distances or second nearest neighbours. Therefore analytical tools are needed to investigate the interface properties on a monolayer scale for which no standard method exists at present.

Magnetic resonance experiments permit the investigation of numerous details as known already from three dimensional (3d) crystals like the chemical identity of paramagnetic centers, their configuration in the lattice, their electronic properties and details of the wavefunction of bound carriers. In SL's, there are various signals observed in EPR with peculiarities due to the 2d situation which can be used to learn about the magnetic properties in low dimensions but also to characterize the perfection of the SL. In particular, CdTe/MnTe and PbTe/EuTe SL's have been investigated with respect to the antiferromagnetic phase transition which occurs on cooling below the Néel temperature [4,5]. The phase transition manifests itself in EPR by a critical broadening of the paramagnetic signal which consists of a single broad line. Below the Néel temperature an antiferromagnetic resonance is seen.

In this paper, we restrict ourselves to the investigation of three types of EPR signals due to:

- I. isolated magnetic ions, which appear in the diamagnetic layers due to diffusion,
- II. pairs of magnetic ions, which appear there if the concentration is higher,
- III. strongly interacting spins in the paramagnetic phase of the magnetic layers.

These different spectra allow us to evaluate a number properties of the SL. In particular, the relative amplitudes depend on the details of the SL structure and on the degree of interdiffusion of the layers which are a few monolayers thick only.

## 2.0 Experiment: I. Spectra of isolated magnetic ions.

Most of the information derived from EPR of isolated magnetic ions is contained in the fine- (FS), and the hyperfine- (HFS) structure of the spectra. The HFS reflects the chemical nature of the magnetic centers and it is not affected by the reduced dimension. The FS, however, is sensitive to the local distribution of strain, exchange and magnetic fields.

Usually, FS and HFS can be resolved only if the concentration of magnetic ions is less than 1%. If the FS is resolved, deviations from the cubic symmetry manifest themselves by a finite  $D$  parameter in the FS part of the Spin Hamiltonian,  $D \cdot S_z^2$ , which vanishes for cubic symmetry. This term can be used to detect small strain as it has been demonstrated already in 3d layers of HgSe:Fe [6] and PbTe:Mn [5], where strain in relaxed layers results from different thermal expansion coefficients of the GaAs substrate and the HgSe layer and the fact that the strain relaxation is a thermally activated process that stops below some temperature [6].

For EuTe/PbTe superlattices, we observe the well resolved FS and HFS due to isolated Eu in the PbTe wells. Like in the case of PbTe:Mn and HgSe:Fe, the FS splitting shows deviations from the angular dependence expected for cubic surrounding. The values for the  $D$  parameter which is thus evaluated, vary from sample to sample. They have values of up to 1 mT. The  $g$ -factor, in contrast, does not show any measurable anisotropy - the latter is much smaller than expected because of shape anisotropy. The linewidth of the different SHF lines is bigger for the outer parts of the spectrum. This feature results from the fluctuation of the  $D$  parameter as shown in Fig.1.

For MnTe/CdTe SL's, we are not able to detect the FS satellite lines because of excessive broadening. Nevertheless we detect the narrow central FS lines since broadening *e.g.* due to strain does not occur for them. As a consequence HFS is well resolved in these samples.

## II. Pairs of magnetic ions.

Pairs of magnetic ions give completely different spectra as compared to the isolated ions. For pairs, the HFS corresponds to the coupling of the paramagnetic moments to two equivalent nuclear spins, whereas the FS reflects the symmetry of the pair, determined by the anisotropic coupling between the two interacting electronic spins. Pair spectra can be resolved for  $x > 0.5\%$ , for which the probability

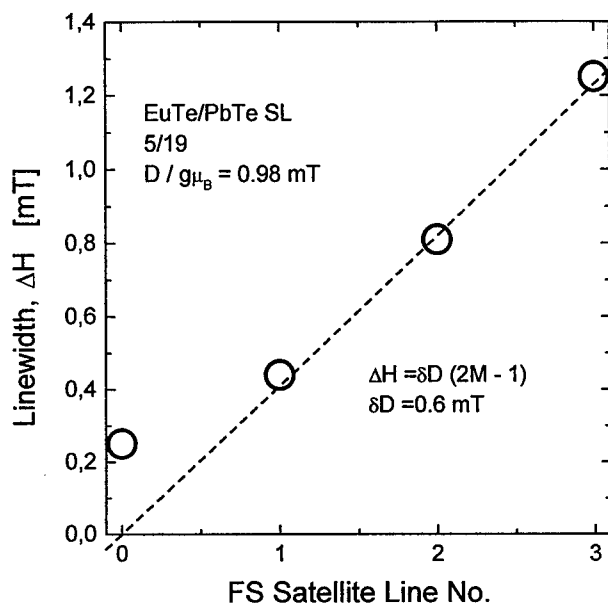


Fig.1: Linewidth of different FS lines of an EuTe/PbTe superlattice with a ML ratio of 5/19 and a total of 100 periods. The FS lines are characterized by the magnetic quantum number  $M$ , that changes to  $M-1$  during the transition. The satellite number is defined as  $(2M-1)/2$  which is proportional to the FS line shift as described by  $D$ .



for finding pairs becomes appreciable. For  $x > 3\%$ , however, bigger clusters occur which prevents the resolution of the individual parts of the spectra and a single broad line without any resolvable structure is seen.

Mn pairs in 3d layers of CdTe were analysed and a singlet ground state ( $S^* = 0$ ) is found. EPR is seen thus only of two excited states: the triplet state ( $S^* = 1$ ) located at  $2J = k_B T_p$  with  $T_p = 14$  K, and a quintet ( $S^* = 2$ ) at 6J. All 11 HFS lines are seen corresponding to the 11 possible relative orientations of the two nuclear spins ( $I = 5/2$ ). The angular dependence of the fine structure reflects the  $D_{2d}$  symmetry of the pair. The fine structure covers a range of 0.6T.

Eu pairs in the PbTe layers of EuTe/PbTe superlattices are observed for a wide thickness range of the diamagnetic PbTe layers (3..30 monolayers (ML)). The FS spreads over a range of 0.2 T. As compared to Mn pairs in CdTe, the main difference comes from the ferromagnetic coupling of the two Eu ions. The ground state is thus 15 fold degenerate ( $S^* = 7$ ) and 14 FS lines result for each of the 6 non-equivalent orientations of the Eu pairs. The complexity of the resulting FS prevents an unequivocal assignment of the Spin-Hamilton parameters but the amplitude of these spectra provides a tool to investigate diffusion of Eu into the PbTe wells.

### III. EPR of strongly interacting spins.

For concentrations of magnetic ions of a few percent only a single broad EPR line is seen. In that case the microscopic contributions to magnetic anisotropy are averaged and the only resulting anisotropy is that of the mean g-factor. So far, we have investigated three types of superlattices: MnTe/CdTe,  $\text{Cd}_x\text{Mn}_{1-x}\text{Te}/\text{CdTe}$  and EuTe/PbTe and data for EuTe are given in Fig. 2. In Fig. 2 we plot the inverse anisotropy field  $H_A$  defined below as a function of temperature. This presentation was chosen to demonstrate the Curie behaviour.

As we discuss below this g-factor anisotropy originates mainly from the magnetic dipole field and it depends on the diffusion profile in the SL.

#### 3. Magnetic dipole anisotropy

Anisotropy results from two effects namely the crystal field due to electrostatic interaction with neighbours and the dipole field due to other magnetic moments in the sample. If the total dipole field acting on a chosen spin depends on the magnetization direction then the resonance field for given frequency depends also on the direction of the external field. The difference of the dipole field for two characteristic directions (in the present case in-plane and perpendicular) is called the anisotropy field,  $H_A$ . In SL's, there are three contributions to the anisotropy of the dipole field, namely: (i) shape anisotropy, (ii) the mean anisotropy of individual monolayers and (iii) microscopic fluctuations.

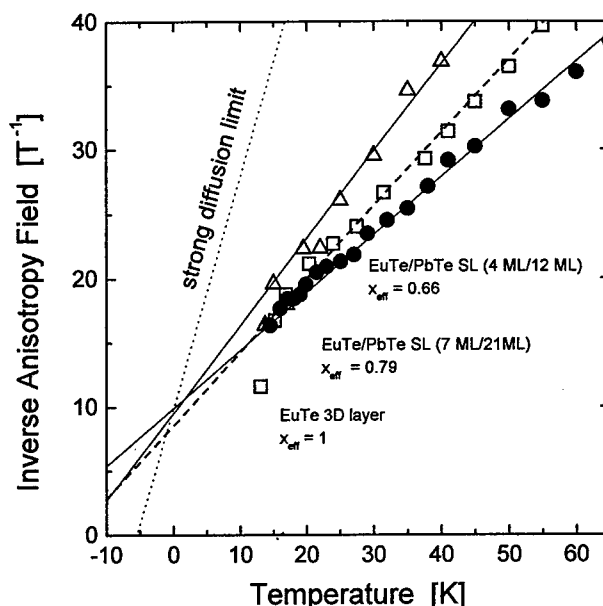


Fig.2: g-factor anisotropy, presented by the inverse anisotropy field, for two EuTe/PbTe superlattices (100 periods, thickness ratio: 4/12 (triangles) and 7/21 (squares), respectively) as a function of temperature. Values are given also for a homogeneous 3d EuTe layer (dots). The dotted line gives the limit of complete interdiffusion.

The shape anisotropy (i) is determined by the macroscopic shape of the sample. For a layered structure, where the sample thickness is much smaller than the in-plane dimensions, the difference in the demagnetisation factors is 1 and the shape anisotropy is given by:

$$H_A^S = M = \langle x \rangle g \mu_B \langle S \rangle / V_0 \quad (1)$$

where  $M$  is sample magnetisation,  $\langle x \rangle$  is mean composition of magnetic ions with a magnetic moment  $g \mu_B \langle S \rangle$ , and  $V_0$  is the volume of the elementary cell.

The shape anisotropy field is effective for all three types of EPR (isolated impurity (I), pairs (II), and strongly coupled spins (III)) in the same manner. In the paramagnetic phase, shape anisotropy is important if the mean composition of the magnetic phase exceeds a few %.

As shown by our numerical simulation of the dipole field distribution in a SL the anisotropy field of each monolayer is different. This individual layer anisotropy (ii) is evaluated by the summation of all magnetic moments within a sphere of mesoscopic dimension. The result is determined by the magnetic composition of the layer under consideration,  $x_i$ , the mean composition of the structure,  $\langle x \rangle$ , and that of the nearest neighbouring ML's,  $x_{i\pm 1}$ . Thus, in SL's we have to treat a profile of this field which is directly related to the composition profile. For a smooth composition profile the individual layer anisotropy becomes simply proportional to the difference between the layer composition  $x_i$  and the mean composition of the structure  $\langle x \rangle$ . As a result, the total dipole anisotropy field contributions due to shape and the individual layer is well approximated by:

$$H_A^i = x_i g \mu_B \langle S \rangle / V_0 \quad (2)$$

The same expression holds for a thin disk with a composition  $x_i$ . Within the diamagnetic wells, the two contributions due to individual layer anisotropy and that due to shape are found to cancel each other. So, the anisotropy field acting on the magnetic impurities (type I) which diffuse into the semi-conducting well is negligible. The resonance frequency of impurities and the  $g$ -anisotropy in an ultrathin diamagnetic well is thus not affected by the neighbouring magnetic layers as we have observed in PbTe:Eu in 2d and in isolated Mn in CdTe in 2d.

Spins located in the vicinity of an interface are additionally affected by the surface anisotropy which is also of magnetic dipole nature. For a sharp interface the surface anisotropy is:

$$H_{SA}^i = \delta x_i g \mu_B \langle S \rangle \quad (3)$$

where  $\delta \ll 1$  and it depends on the type of crystallographic plane. For (100) in simple cubic lattices, we obtain  $\delta = 0.07827$ .

When the magnetic anisotropy of the type (III) is measured, each layer has a different contribution to the mean anisotropy of the coupled spin system. The magnetic anisotropy averaged over all ML's is proportional to the square of the layer composition (since each contribution is weighted by the number of resonating spins in the layer). Considering also the effect of the surface anisotropy we obtain the following expression for the total magnetic anisotropy of the type (III) spectra:

$$H_A = \left( 1 + \frac{\delta}{m_p \langle x \rangle} \right) \left( x_{\text{eff}} - \langle x \rangle \right) \frac{g \mu_B \langle S \rangle}{V_0} + \langle x \rangle \frac{g \mu_B \langle S \rangle}{V_0} \quad (4)$$

where  $m_p$  is the SL period (this term reflects the number interfaces per mean layer), and the effective layer composition is the mean value of the square of composition of the individual layers and:

$$x_{\text{eff}} = \sum_i x_i^2 / \sum_i x_i \quad (5)$$

The second term in Eq. (4) stands for the shape anisotropy.

The experimental data for the anisotropy field in Fig.2 show clearly that samples with the same average concentration  $\langle x \rangle$  and the same shape show quite different slope. From these data  $x_{\text{eff}}$  is evaluated as single parameter.

**Fluctuations of the local dipole field** are caused by the stochastic distribution of magnetic impurities in the vicinity of resonating spins. Their effect is well known as the dipole broadening of the resonance linewidth. The contribution to the second moment of the resonance line decreases with the 6<sup>th</sup> power of distance, so the broadening of the line width is proportional to the mean concentration of magnetic moments, where the averaging should be done within the close vicinity only. In short period SL's, however, where the distance between the centre of the well and layers of high  $x_i$  is a few ML's only, the magnetic layers affect dipole fluctuations in the diamagnetic well.

The resulting so-called dipole-dipole broadening affects every type of resonance. But the broadening increases with the local concentration of magnetic ions. It is smallest for type (I) but it dominates the fluctuation of D. The broadening is strongest for type (III).

Another characteristic feature of the dipole-dipole broadening is its different influence on the central line and on the satellite lines. In fact, this type of coupling is described by a term of the form  $S_i D S_j$  in the spin Hamiltonian and thus lines with a big  $M$  are more strongly affected. Therefore dipole-dipole coupling leads to a splitting describable by a contribution to  $D$ , but not to a mean field which would cause a  $g$ -shift.

#### 4. Crystal field and pseudo-dipole coupling

The distribution of the Coulomb potential and the hybridisation of the magnetic shells with the ligand orbitals modify the magnetic properties of the magnetic ions via spin orbit coupling, an effect generally called the crystal field effect (CF). A non-cubic CF leads to anisotropies of the  $g$ -factor and the  $D$  parameter of individual ions (I). If the neighbours are magnetic ions, an additional pseudo-dipole contribution due to the anisotropic part of exchange interaction has to be included.

A strain of layers is expected generally in every 2D structure. The experimental data of isolated impurities in diamagnetic wells show, however, that the total effect of strain is relatively weak. Moreover, surprisingly, the strain effects for rare earth- and transition metal ions are of the same order of magnitude in spite of quite different localization. The  $D$ -anisotropy does not exceed a few mT in both types of ions. Also the anisotropy of the  $g$ -factor of isolated spins is very weak, it is below the experimental error, *i.e.* smaller than  $10^{-4}$  in the cases investigated. Formally this  $g$ -factor anisotropy contributes to the total magnetic anisotropy of type (III) spectra. But since this type of  $g$ -factor anisotropy is by orders of magnitude smaller as compared to that originating from magnetic dipole coupling, it can be neglected when analysing the mean  $g$ -factor anisotropy of type (III) spectra.

Much stronger effects result from the strain caused by the stochastic occupation of neighbouring sites by different, magnetic or nonmagnetic ions. This effect is much stronger than that of the mean strain in the layer. This effect is directly monitored by the fine structure of magnetic pairs (II) (of the order 200 mT) which is by two orders of magnitude bigger than the  $D$  anisotropy of individual ions (1 mT). In that case we are not able to distinguish experimentally the CF and pseudo-dipole effects.

Anyway, the coupling is strong, and of short range. Thus, if the fine structure is not resolved, *i.e.*, for type (III) systems, it plays a basic role for the linewidth contributing to the total second moment of the line. But because of the short interaction range of the discussed effects, they are well averaged and do not contribute substantially to the  $g$ -factor anisotropy. For very sharp profiles they lead to a new contribution to the surface anisotropy.

#### 5. Diffusion in SL's

The magnetic interactions discussed above are rather complex and the analysis of magnetic resonances allows to evaluate these interactions. Much more direct conclusions can be drawn concerning the spatial distribution of the magnetic ions. We have at least three independent tools, basing on the EPR studies to evaluate the real profile of SL,  $x(i)$ : (1) the evaluation of  $x_{\text{eff}}$  from the type (III) spectra, (2)

measurement of the amplitude of type (I) and (3) of type (II) spectra.

(1)  $x_{\text{eff}}$  depends on the profile  $x(i)$ . For very sharp profile,  $x(i) = 0$  or  $1$ , and  $x_{\text{eff}} = 1$ . Then, according to Eq.(4), the anisotropy of the SL is (with the correction of surface anisotropy of interfaces) equal to that of a solid magnetic layer. When diffusion takes place, the anisotropy field decreases. For a full diffusion, when  $x(i) = \langle x \rangle$  and  $x_{\text{eff}} = \langle x \rangle$  and only shape anisotropy is observed. Thus for a layer with a mean composition  $\langle x \rangle = 0.25$ , as presented in Fig. 2, the anisotropy decreases by a factor 4 when diffusion takes place. For an intermediate degree of diffusion one can easily compare the observed  $x_{\text{eff}}$  with a mathematical model of the diffusion. For the data presented in the Fig. 2, we evaluated the thickness of interlayer,  $\sigma$ , assuming a Gaussian profile. In particular, for the 7ML/21ML sample, with  $x_{\text{eff}} = 0.79$  we have  $\sigma = 0.9$  ML. For thicker EuTe layers in the as-grown SL the interface thickness,  $\sigma = 0.5$  ML. It increases with decreasing thickness. For 4 ML,  $x_{\text{eff}} = 0.66$  and  $\sigma = 1.1$  ML. After sample annealing  $\sigma$  increases.

(2) We observe the EPR signal of isolated impurities in semiconducting wells in structures of the highest quality. With increasing diffusion its amplitude increases and then it decreases again. The experimentally observed amplitude allows to evaluate the degree of diffusion. For a 6/18 SL, e.g., this spectrum is expected to vanish for an interdiffusion corresponding to  $x_{\text{eff}} = 0.65$  or  $\sigma = 2$  ML.

(3) The signal of pairs appears when the local composition is within a small range of  $0.005 < x < 0.02$ . Its amplitude can be also evaluated to estimate interface diffusion.

These 3 methods are complementary and lead to similar results. Depending on the structure the accuracy of each method is different. Method (2) is effective for a weak interdiffusion, method (3) for intermediate and (1) for strongest diffusion.

### Conclusions

We investigate inter-diffusion in EuTe/PbTe SL's. We analyse the amplitude of EPR spectra of isolated Eu impurities and of Eu-Eu pairs. The observation of spectra of isolated impurities is possible if the local concentration of diffused impurities is lower than 1% in the well. Since we are able to observe such spectra in SL's with a width of the diamagnetic wells of a few monolayers only we conclude that these SL's are characterised by very weak diffusion and an almost rectangular shape of the concentration profile  $x(z)$ , which cannot be effectively evaluated by X-ray analysis.

For a quantitative evaluation of strain from the measured  $D$  parameter a calibration procedure is needed using another method like high resolution X-ray diffraction since the theoretical description of the  $D$  parameter is rather complex.

**Acknowledgments.** Work supported by the *Committee for Scientific Research*, Poland, grant 2 P03B 191 08 and by the *Fonds zur Förderung der Wissenschaftlichen Forschung*, and the *Österreichischer Akademischer Austauschdienst*, Austria.

### References.

- [1] G. Springholz, N. Frank, and G. Bauer, Appl. Phys. Lett. **64** 2970 (1994) and: G. Springholz, Material Science Forum **182-184**, 573 (1995) ed. by H. Heinrich and J.B. Mullin (Trans Tech Publications, Switzerland 1995)
- [2] S.A. Crooker, D.A. Tulchinsky, J. Levy, D.D. Awschalom, R. Garcia, and N. Samarth, Phys. Rev. Lett. **75**, 505 (1995)
- [3] T. M. Giebultowicz, Mat. Sci. Forum **182-184**, 579 (1995)
- [4] Z. Wilamowski, W. Jantsch, M. Ludwig, G. Springholz, Proc. XXIII. Int. Conf. Phys. Semicond., Berlin July 21-26, 1996 in: *The Physics of Semiconductors*, Ed. by M. Scheffler and R. Zimmermann, (World Scientific 1996) p 2415
- [5] Z. Wilamowski, W. Jantsch, G. Springholz, Material Science Forum **182-184**, 669 and 677 (1995) ed. by H. Heinrich and J.B. Mullin (Trans Tech Publications, Switzerland 1995)
- [6] G. Hendorfer, W. Jantsch, W. Helzel, J. Li, Z. Wilamowski, T. Widmer, D. Schikora, K. Lischka, Materials Science Forum **196-201**, 561 (1995) ed. by M. Suezawa and H. Katayama-Yoshida (Trans Tech Publications, Switzerland 1995)

## Er DIFFUSION AND Er-INDUCED Ga-Al INTERDIFFUSION IN GaAs/AlGaAs QUANTUM STRUCTURES

M.S. Bresler, B.Ya. Ber, O.B. Gusev, E.K. Lindmark<sup>1</sup>, J.P. Prineas<sup>1</sup>, H.M. Gibbs<sup>1</sup>,  
G. Khitrova<sup>1</sup>, V.F. Masterov<sup>2</sup>, I.N. Yassievich, and B.P. Zakharchenya  
A. F. Ioffe Physico-Technical Institute, Politekhnikeskaya 26,  
194021 St. Petersburg, Russia

<sup>1</sup> Optical Sciences Center, University of Arizona, Tucson, AZ 85721, U.S.A.

<sup>2</sup> Technical University, Politekhnikeskaya 29, St. Petersburg, Russia

**Key words :** erbium, GaAs/AlGaAs quantum structures, interdiffusion

**Abstract.** It is shown that the introduction of erbium in GaAs/AlGaAs quantum well structures in the process of growth by MBE leads to efficient interdiffusion of Ga and Al and diffusion of Er due to impurity-enhanced formation of cation vacancies. A mechanism of cation vacancies formation is proposed based on local strain induced by introduction of erbium. We have demonstrated also that erbium interacts with aluminum in arsenides. This interaction can be responsible for the formation of Er-containing Al-enriched clusters.

### Introduction.

Recently there has been much interest in rare-earth doped semiconductors motivated by the need for effective electrically-excited light sources emitting at 1.54- $\mu\text{m}$ , the wavelength of minimum absorption in silica glass optical fibers [1]. One suggestion is to seek a resonance between a quantum-well (QW) transition and a rare-earth-ion transition [2]. In the process of studying GaAs:Er/AlGaAs QWs seeking such a resonance at  $\approx 800\text{-nm}$  we have discovered extremely effective interdiffusion of Ga and Al and diffusion of Er in the case of MBE growth. The phenomena of impurity-induced layer disordering [3] are well known in the technology of quantum structures and have been extensively studied [4]. However, impurity-induced interdiffusion was observed mainly in the case of electrically active impurities (donors or acceptors) and is connected with Fermi-level dependence of formation of lattice vacancies or interstitials in the semiconductor crystal lattice [4]. Our results point to formation of cation vacancies induced by internal strain arising from introduction of large erbium ions on the sites of smaller gallium (or aluminum) ions.

### Experimental.

The erbium-doped structures were grown by MBE at  $\sim 600^\circ\text{C}$  on GaAs substrates. The structures we label Er20 to Er23 were grown on a  $625\text{-}\mu\text{m}$  GaAs substrate, and consist of an  $\text{Al}_x\text{Ga}_{1-x}\text{As}$  etch stop layer  $0.6\text{-}\mu\text{m}$  thick with  $x = 0.3$ , then 50 quantum wells of  $10\text{-nm}$  GaAs:Er well and  $21\text{-nm}$  AlGaAs barriers with the Er source temperature  $450^\circ\text{C}$  (and shutter closed),  $900^\circ\text{C}$ ,  $870^\circ\text{C}$ , and  $930^\circ\text{C}$  respectively. (Variation of temperature of erbium source permits to change erbium concentration). In all the samples there were also  $0.9\text{-nm}$  AlAs spikes at each end of the barriers separating the GaAs:Er and AlGaAs. On top of the 50 QWs there was another identical  $0.6\text{-}\mu\text{m}$  AlGaAs window to symmetrize the strain. Finally about  $7\text{-nm}$  of GaAs was grown on top to prevent the AlGaAs from oxidizing. The structure Er26 consisted of  $8\text{-nm}$  GaAs:Er ( $900^\circ\text{C}$ ) layers separated by  $22\text{-nm}$  of GaAs repeated 50 times with  $300\text{-nm}$  of GaAs on top. Er25 and Er34 are like Er20 except that they have no AlAs spikes and Er25 has Er ( $900^\circ\text{C}$ ) in the GaAs well only and Er34 in the AlGaAs barrier only. The Er concentrations in  $10^{18}\text{cm}^{-3}$ , measured by secondary ion mass spectroscopy (SIMS) with  $5\text{-nm}$  resolution, were  $<0.1$ , 9, 22, 7, 4, and 6 for samples Er 20, 21, 23, 25, 26, and 34, respectively. The dependence of erbium concentration on temperature of the source during growth (deduced from our measurements) can be described by the formula

$$N_{\text{Er}} = N \exp(-E_b / kT) \quad (1)$$

where  $N = 2.85 \times 10^{34} \text{ cm}^{-3}$  and  $E_b = 3.6 \text{ eV}$  which corresponds nicely to the activation energy  $E_b = 3.3 \text{ eV}$  of erbium evaporation from the metal source.

Photoluminescence (PL) spectra of the structures were measured at liquid helium temperature, analyzed with a double grating spectrometer, and detected by a nitrogen-cooled germanium photodetector. Excitation was done by an argon cw laser with pump powers up to 100 mW.

### Results.

The SIMS profile for the Er26 sample (GaAs:Er) showed a concentration of  $4 \times 10^{18} \text{ cm}^{-3}$  completely independent of position, contrary to opening and closing of the Er shutter during growth. It is clear that no erbium layers exist in the structure, but complete leveling of erbium concentration occurred indicating a high diffusion coefficient of erbium in bulk GaAs grown by MBE method in contrast to the case of introduction of erbium by diffusion. In Fig.1 the SIMS profiles are presented for three samples in order of increasing erbium concentration. While for Er20 (no Er) distinct QWs are seen in the SIMS picture, for Er21 they are less pronounced, and in Er23 QWs are no longer seen with our SIMS resolution. In Er23 ( $N_{\text{Er}} = 2.2 \times 10^{19} \text{ cm}^{-3}$ ) no SIMS modulation is seen for either Ga, Al or Er. Thus, the interdiffusion of gallium and aluminum and diffusion of erbium depends directly on the concentration of erbium ions.

The phenomena of interdiffusion resulting in impurity-induced layer disordering observed by us resemble closely those described for electrically active impurities (donors and acceptors) in GaAs/AlGaAs structures [4]. However, it is believed that the predominant position of  $\text{Er}^{3+}$  ions in the crystal lattice of a III-V semiconductor is the substitutional cation position [5]; in this case, erbium behaves as an isovalent impurity, i.e. it does not supply (or trap) an additional charge. Therefore we cannot expect that the concentration of erbium ions will influence directly the Fermi level position of the semiconductor, and the explanation of high diffusion coefficients discussed in [4] cannot be applied to our results. It should be noted that in our case impurity-induced layer disordering due to interdiffusion of Ga and Al is observed at a temperature (substrate) lower by 100-200 K compared to the studies described in [4].

We have observed also that there exists interaction between erbium and aluminum ions which makes erbium to prefer Al rather than Ga environment. The evidence on Er and Al interaction comes from the PL spectra of Fig. 2. Even though Er was introduced only into GaAs layers in structures Er21 and Er23, the Er PL spectra at  $1.54\text{-}\mu\text{m}$  are characteristic of AlGaAs [6] which are much more complex than that of Er in GaAs. This clearly indicates Al-Er interaction.

### Discussion.

Our results can be explained if we take into account internal strain induced in the crystal lattice when we insert an erbium ion on the site of a group III cation. Since the dimension of an erbium ion is larger than those of gallium and aluminum, the introduction of an erbium ion leads to local strain around it and excess elastic energy is acquired by the crystal lattice of the erbium-doped semiconductor. This internal strain can be removed by formation of additional vacancies (compared to equilibrium) and the concentration of them can be estimated from energy conservation arguments.

Let us estimate the number of vacancies which can arise in the situation when erbium occupies the substitutional position. Though we do not know the covalent radius of erbium, the ionic radius (and atomic radius) is about 10 percent greater than that of a group III cation, so we can conclude that the deformation of erbium's surroundings would be of the order of  $3\Delta R/R_0 \approx 0.3$  where  $\Delta R$  is the change in the radius of the cation and  $R_0$  the radius of

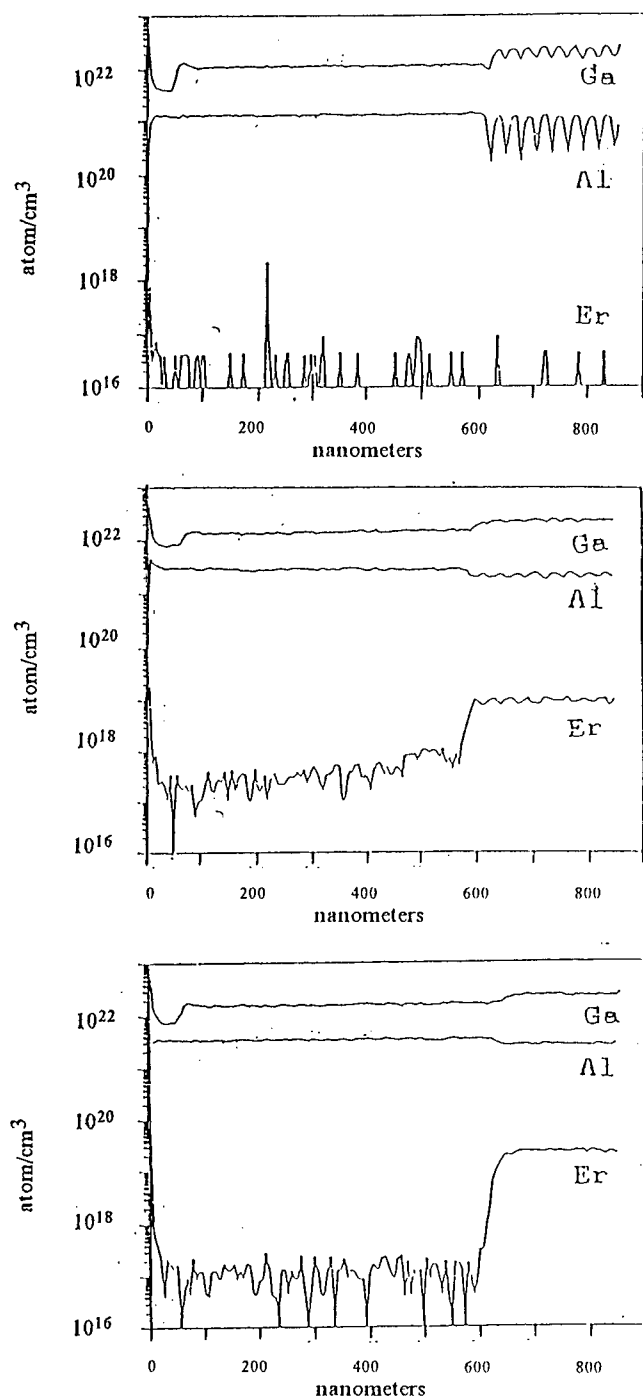


Fig. 1. SIMS profiles for Er20, Er21, and Er23 samples.

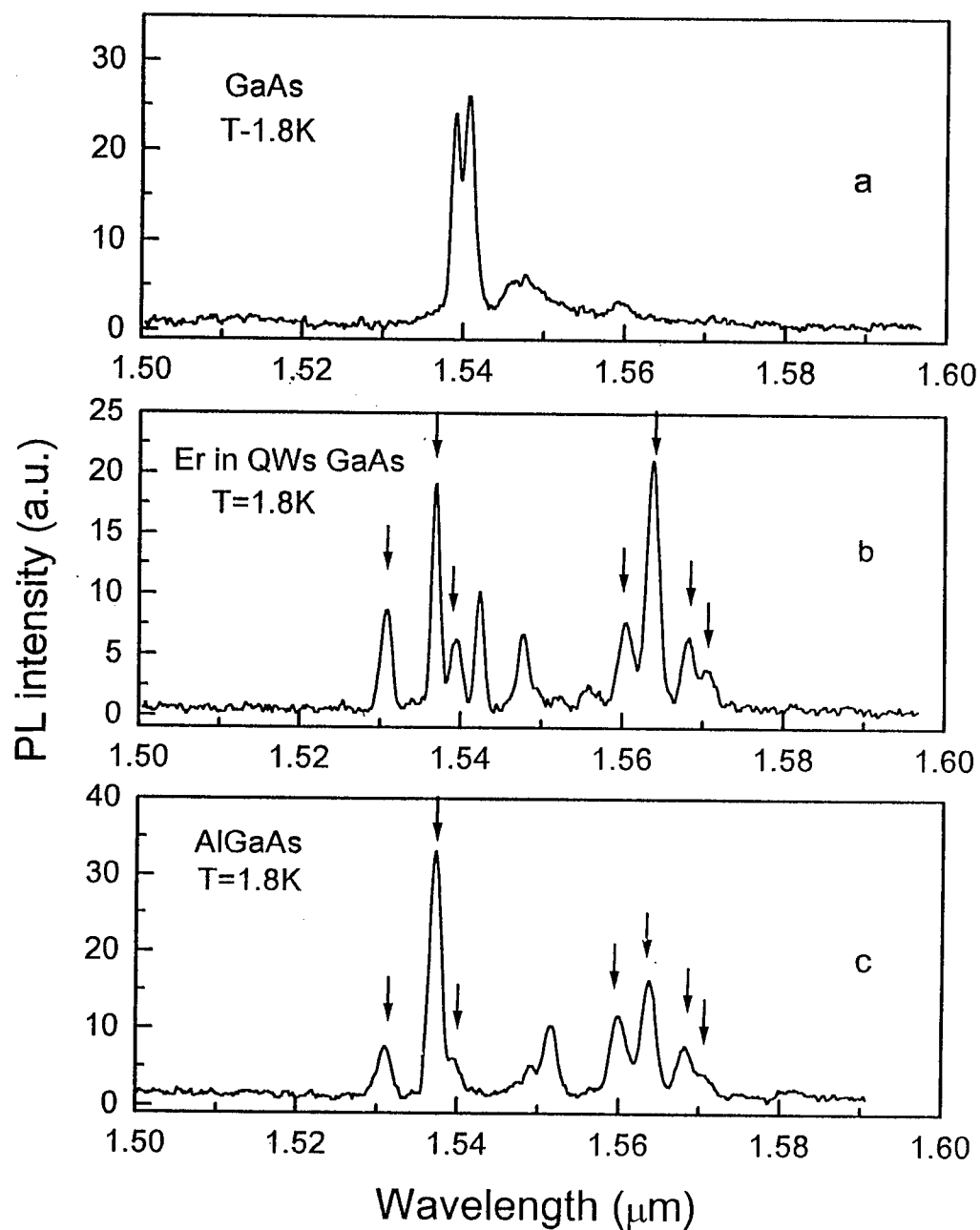


Fig. 2. PL spectra of Er26, Er21, and Er29. The notations a, b, and c refer to series of spectral lines with the same temperature dependence and lifetime.



the cation. For corresponding elastic energy per cubic centimeter we can write an order-of-magnitude estimate

$$U = \frac{2\pi}{3} c \left( \frac{3\Delta R}{R_0} \right)^2 (R_0^3 N_{Er}) \quad (2)$$

where  $c$  is the elastic constant and  $N_{Er}$  the concentration of erbium ions. Releasing the internal strain in the lattice formation of vacancies is energy advantageous. If we assume that the elastic energy accumulated will be entirely spent on formation of vacancies we shall get an estimate of vacancies concentration

$$[V_{III}] = U / E_v \quad (3)$$

where  $E_v$  is the cohesion energy of GaAs semiconductor which determines the energy of vacancy formation. If we take for  $c$  the value of  $10^{12}$  erg/cm<sup>3</sup>,  $\Delta R/R_0 \approx 0.1$ ,  $R_0 \approx 10^{-8}$  cm,  $N_{Er} = 10^{18}$  cm<sup>-3</sup>,  $E_v = 1.6$  eV we shall obtain  $[V_{III}] = 7.3 \times 10^{16}$  cm<sup>-3</sup>. It is well known that in an As-rich atmosphere effective generation of cation vacancies occurs in GaAs and AlGaAs [4]. Since the growth of structures by MBE technique is performed just in these conditions, we conclude that the introduction of erbium would result in the formation of the density of cation vacancies calculated above. Now we should compare the concentration obtained above with the equilibrium concentration of cation vacancies at the substrate growth temperature ( $\approx 627^\circ\text{C}$ )

$$[V_{III}] = N_0 \exp(-E_v / kT) \quad (4)$$

where  $N_0 = 1.1 \times 10^{22}$  cm<sup>-3</sup> is the total number of cation sites per cubic centimeter and  $E_v = 1.6$  eV is the cohesion energy of GaAs semiconductor determining the energy of vacancy formation. Thus, the equilibrium value of vacancies concentration is  $[V_{III}] = 1.2 \times 10^{13}$  cm<sup>-3</sup>, and the introduction of erbium significantly increases the concentration of cation vacancies. It should be mentioned that the diffusion coefficient is small when erbium is introduced into GaAs by diffusion because the radius of the erbium ion is larger than the gallium radius. The diffusion coefficient of impurities depends also on the concentration of cation or anion vacancies, but since the concentration of vacancies in the equilibrium condition is constant at constant temperature, it is the size of the impurity atom that determines the diffusion rate. The situation is different in the case when the vacancies are created in the process of growth, and this is what happens in the MBE growth of Er-doped GaAs/AlGaAs structures. As shown in [7] in the case of Al<sub>0.5</sub>Ga<sub>0.5</sub>As prepared by MBE for concentrations up to  $10^{18}$  cm<sup>-3</sup>, 88 percent of erbium ions occupy substitutional positions (the cation site). For higher erbium concentration the fraction of erbium ions in interstitial positions increases, and for  $N_{Er} = 5 \times 10^{19}$  cm<sup>-3</sup> only 30 percent of erbium is in substitutional positions. (Still we can expect that the deformation induced by an erbium ion in the interstitial position is even larger).

As shown in [4], the diffusion coefficient of cations in GaAs (or AlGaAs) can be written in the form

$$D_{III} = f D_{III}^0 [V_{III}] \quad (5)$$

where  $f$  is the factor taking account of the crystal structure and the concentration of Column III lattice sites,  $D_{III}^0$  is the diffusion coefficient of cations corresponding to the jump to the adjacent cation site being on the order of  $\omega a^2 \exp(-E_b/T)$  ( $\omega$  is the frequency of vibrations of the ion,  $a$  the lattice constant, and  $E_b$  the energy barrier between two adjacent cation sites). Since  $[V_{III}]$  is proportional to  $N_{Er}$ , the diffusion coefficient is strongly enhanced by the presence of erbium ions. This result relates both to diffusion of gallium or aluminum and to diffusion of erbium. Our estimates of the erbium diffusion coefficient, derived from the characteristic length of the erbium profile in Fig.1 and the time of growth of the

corresponding layer, give the value of  $D_{Er} \sim 10^{-15} \text{ cm}^2/\text{s}$  which is very high for the temperature of 627°C.

The tendency of erbium to have aluminum surrounding is probably due to their chemical interaction since it is known that there exist several intermetallic compounds of erbium with aluminum [8]. On these grounds we can expect the formation of different erbium-aluminum complexes in our samples.

### Conclusions.

In conclusion, we have shown that the introduction of erbium in GaAs/AlGaAs quantum structures leads to efficient interdiffusion of Ga and Al and Er diffusion due to impurity-enhanced formation of cation vacancies. A mechanism of cation vacancies formation is proposed based on local strain induced by introduction of erbium. We have demonstrated also that erbium interacts with aluminum in arsenides. This interaction can be responsible for formation of Er-containing Al-enriched clusters.

This work was partially supported by AFOSR (F49620-94-1-0390), DARPA (DAAH04-95-1-0612), NSF Lightwave Technology (ECS9421517), by INTAS-RFBR 95-0531 grant, by the Russian Foundation of Basic Research (grant 95-02-04163-a), and by Russian Ministry of Science (grant 97-1036). We are indebted to R.Sh. Malkovich who attracted our attention to the phenomenon of impurity-induced layer disordering in GaAs/AlGaAs structures.

### References.

- [1] Rare Earth Doped Semiconductors, edited by G.S. Pomrenke, P.B. Klein, and D.W. Langer (Materials Research Society, Pittsburgh, 1993); Rare Earth Doped Semiconductors II, edited by S.Coffa, A.Polman, and R.N.Schwartz (Materials Research Society, Pittsburgh, 1996).
- [2] G.G. Zegrya and V.F. Masterov, in Tenth Feofilov Symposium on Spectroscopy of Crystals Activated by Rare-Earth and Transitional-Metal Ions, edited by A.I. Ryskin and V.F. Masterov, SPIE Proceedings, **2706** (1996), pp. 235-240.
- [3] W.D. Laidig, N. Holonyak, M.D. Camras, K. Hess, J.J. Coleman, P.D. Dapkus, and J. Bardeen, Appl. Phys. Lett. **38**, 776 (1981).
- [4] D.G. Deppe and N. Holonyak, J. Appl. Phys. **64**, R93 (1988).
- [5] A. Taguchi and T. Ohno, Mater. Sci. Forum **196-201**, 627 (1995).
- [6] T. Zhang, J. Sun, N.V. Edwards, D.E. Moxey, R.M. Kolbas, and P.J. Caldwell, in ref. 1, pp. 257-262. One series of our PL lines is still detectable at 300K.
- [7] E. Alves, M.F. Da Silva, A.A. Melo, J.C. Soares, G.N. van den Hoven, A. Polman, K.R. Evans, and C.R. Jones, in ref. 1, pp. 175-180.
- [8] W.E.Wallace, Rare Earth Intermetallics (Academic Press, N.Y., 1973), p.34, p.58.

## GROUND AND EXCITED STATES OF $D^-$ CENTRES IN SEMICONDUCTOR QUANTUM DOTS

B. Szafran, J. Adamowski, and B. Stébé<sup>1</sup>

Faculty of Physics and Nuclear Techniques, Technical University (AGH),  
30-059 Kraków, Poland

<sup>1</sup>Institut de Physique et d'Electronique, Université de Metz,  
57078 Metz, France

**Keywords:**  $D^-$  donor centre, quantum dot.

**Abstract.** Energy spectrum of negatively charged donor centres ( $D^-$ ) in spherical semiconductor quantum dots (QDs) has been calculated in the framework of effective-mass approximation by the variational method. We have studied the on-centre donor impurity in the single isolated QD embedded in a passivating medium. The confinement potential for electrons has been assumed to be the spherically symmetric potential well of the depth  $V_0$  and radius  $R$ . We have considered the ground state ( $1^1S$ ) and the excited states ( $1^1P$ ,  $1^3P$ ,  $1^1D$ ,  $1^3D$ ,  $2^1S$ ,  $2^3S$ ) of the  $D^-$  donor centre. The ground state of the  $D^-$  centre in the QD is always bound like in the bulk crystal. We have shown that the  $D^-$  excited states can also be bound if the effective QD capacity,  $C = V_0 R^2$ , exceeds a certain critical value. The critical values of  $C$  have been determined for each considered state. We have also discussed the properties of energy spectra of the two-electron system in the QD with and without the donor impurity. For the  $D^-$  in GaAs QD, the calculated  $1^1S \rightarrow 1^1P$  transition energy exceeds 100 meV for the QD with the radius of about 5 nm. The estimated electron penetration into the barrier region and the average electron-electron and electron-donor separations lead to the conclusion that the binding of the  $D^-$  excited states results from the strong confinement of electrons within the QD.

### 1. Introduction

A  $D^-$  donor centre in a semiconductor is a solid-state analogue of the  $H^-$  hydrogen ion. In bulk crystals, the hydrogen-like  $D^-$  centre possesses only one bound state like the  $H^-$  ion. The  $D^-$  centres were also observed in semiconductor multiple quantum-well (MQW) structures [1, 2], in which electrons are subjected to the confinement potential in the growth direction. The three-dimensional confinement of electrons has been obtained in recently fabricated [3] quantum dots (QDs). Such QDs are prepared, e.g., by a colloidal chemical synthesis [3], which allows one to obtain nearly spherical nanocrystals with narrow size distribution embedded in organic material. In particular, the GaAs nanocrystals were obtained by this method [4]. The QDs produced by an MBE technique can have a disk-like shape [5]. A possible observation of the  $D^-$  centres in the disk-like QDs was discussed by Ashoori *et al.* [5]. In MQW structures in an external magnetic field, transitions to the excited states of the  $D^-$  centre were identified [6, 7]. These excited states correspond to the similar excited states observed for the  $H^-$  ion in the magnetic field. However, the following question appears: can the three-dimensional confinement potential of the QD lead to a formation of bound excited states of the  $D^-$  centre without an additional external field? The present paper provides a solution to this problem. We study the  $D^-$  centre in a spherical QD assuming the confinement potential in the form of potential well of finite depth. The present treatment is well suited to the nanocrystals of spherical shape embedded in a passivating medium.

### 2. Theory

We consider the single isolated QD of spherical shape embedded in a dielectric matrix. The effective-mass approximation is applied to a description of electrons. Due to the large band

gap of the surrounding material, the electrons are subjected to a confinement potential, which is assumed to be the spherically symmetric potential well, i.e.

$$V(r) = \begin{cases} 0 & \text{for } r < R, \\ V_0 & \text{for } r \geq R, \end{cases} \quad (1)$$

where  $R$  is the radius of the QD. This means that the potential barrier for electrons is formed in the surrounding medium and the potential well – in the QD region. Because of the confinement the energy bands of the QD nanocrystal are replaced by discrete energy levels, which are associated with the bound states of the electron in potential well (1).

Let us consider the negatively charged two-electron ( $D^-$ ) donor centre in the QD. We assume that the positively charged donor impurity (Coulomb centre) is located in the centre of the QD. The  $D^-$  centre consists of two electrons, which interact between themselves and with the positive donor centre via the Coulomb interactions, which are screened by the static dielectric constant. We neglect the difference of the electron effective band masses and dielectric constants between the QD region and the surrounding medium.

The eigenvalue problem for the  $D^-$  centre is solved by the variational method with the trial wave function proposed in the form

$$\Psi_{\pm}^L(\vec{r}_1, \vec{r}_2) = \sum_{mnp} c_{mnp}^L (1 \pm P_{12}) \varphi_{mnp}^L(\vec{r}_1, \vec{r}_2), \quad (2)$$

where

$$\varphi_{mnp}^L(\vec{r}_1, \vec{r}_2) = \exp[-\alpha(r_1 + r_2)] r_1^m r_2^n r_{12}^p \chi^L(r_1, \theta_1), \quad (3)$$

are the basis wave functions. In Eqs. (2) and (3),  $L$  is the quantum number of the total angular momentum,  $P_{12}$  is the operator of permutation of electron indices ( $1 \rightleftharpoons 2$ ), the signs  $+$  and  $-$  correspond to the spin-singlet and spin-triplet states, respectively,  $c_{mnp}^L$  and  $\alpha$  are the variational parameters,  $r_j = |\vec{r}_j|$  ( $j = 1, 2$ ),  $r_{12} = |\vec{r}_1 - \vec{r}_2|$ , and  $\theta_1 = \angle(\vec{r}_1, 0z)$ . We consider the states with  $L = 0, 1$ , and  $2$ , i.e.,  $S$ ,  $P$ , and  $D$ , for which we take on

$$\chi^S(r, \theta) = 1, \quad (4)$$

$$\chi^P(r, \theta) = r \cos \theta, \quad (5)$$

and

$$\chi^D(r, \theta) = r^2(3 \cos^2 \theta - 1), \quad (6)$$

respectively. We have calculated the energy levels of the  $D^-$  centre in the QD for the ground state ( $1^1S$ ) and the following excited states:  $1^1P$ ,  $1^3P$ ,  $1^1D$ ,  $1^3D$ ,  $2^1S$ ,  $2^3S$ . For the  $S$  states, the applied variational wave function has included 66 basis elements, while for the  $P$  and  $D$  states – 78 elements. The electron-electron correlation, i.e. the terms dependent on  $r_{12}$ , has been taken in account only for the  $S$  states, since this correlation plays a minor role for the  $P$  and  $D$  states.

In order to answer the question if the given quantum state of the  $D^-$  centre does form the stable bound state, we have calculated binding energies for the considered states. We define the binding energy of the  $\nu$ th quantum state of the  $D^-$  as the difference between the energy of the continuum threshold and the energy of the given  $\nu$ th state. The continuum threshold corresponds to the lowest energy of the system, which consists of the one electron bound to the Coulomb centre and forming the  $D^0$  donor centre inside the QD and the second – liberated to the barrier region. Taking into account the fact that the lowest energy of the liberated electron corresponds to the conduction-band minimum of the barrier material, i.e.,  $V_0$ , and denoting by  $E_0^0$  the ground-state energy of the  $D^0$  centre and by  $E_\nu^-$  the energy of the  $\nu$ th state of the  $D^-$  centre, we calculate the binding energy of the  $\nu$ th state of the  $D^-$  by the formula

$$W_\nu = E_0^0 + V_0 - E_\nu^- . \quad (7)$$

The ground-state energy  $E_0^0$  of the  $D^0$  donor centre has also been calculated by the variational method with the help of the trial wave function expanded in the Slater basis. We have checked that this approach reproduces the analytical results [8].

### 3. Results

The calculated energy levels  $E_\nu^-$  for the considered states of the  $D^-$  centre are displayed in Fig. 1(a) as functions of the QD radius for the potential-well depth  $V_0 = 5R_D$ , where  $R_D$  is the donor rydberg. The continuum-threshold energy, i.e.,  $E_0^0 + V_0$ , is also shown in Fig. 1(a).

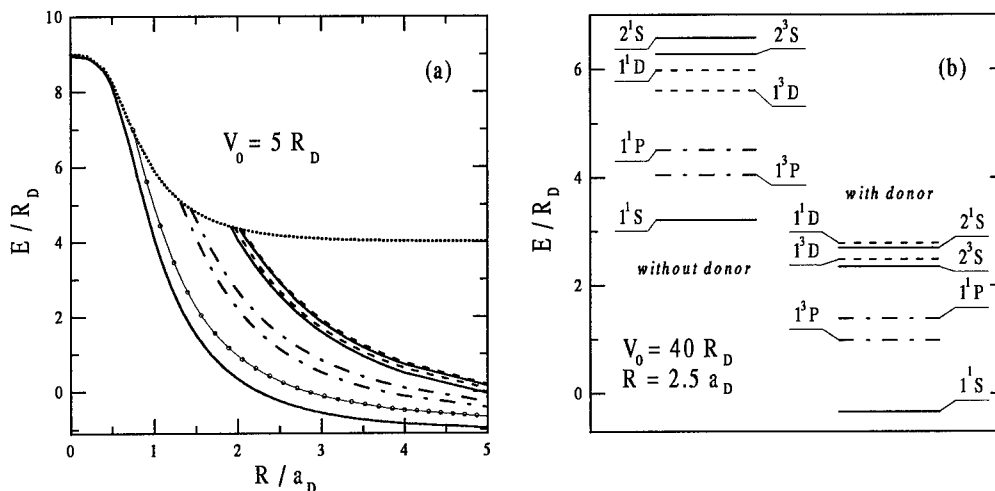


Figure 1: (a) Energy levels of the  $D^-$  centre as functions of the QD radius. Solid curves show the  $1^1S$ ,  $2^3S$ , and  $2^1S$  levels with the increasing energy, respectively, dash-dotted (dashed) –  $1^3P$  and  $1^1P$  ( $1^3D$  and  $1^1D$ ) levels (lower curve – triplet, upper – singlet). Dotted curve corresponds to the continuum threshold and solid curve with open circles – the sum of the ground-states energies of  $D^0$  centre and electron in QD. Donor rydberg ( $R_D$ ) is the unit of energy and donor Bohr radius ( $a_D$ ) is the unit of length. (b) Energy levels of two-electron systems in the QD with the on-centre donor (right side) and without the donor (left side) for  $V_0 = 40R_D$  and  $R = 2.5a_D$ .

We see that – like in the bulk crystal – the ground state of the  $D^-$  centre is always bound (the corresponding curve lies below the continuum threshold for all values of  $R$ ). Moreover, the results of Fig. 1(a) show that the excited states of the  $D^-$  centre are bound if the QD radius is large enough. Among them, first the  $1P$  states become bound, and next – the  $2S$  and  $1D$  states. For each  $L$ , the triplet state always possesses the lower energy than the corresponding singlet state. This property reminds the similar energy-level order for the triplet and singlet states of the helium atom. However, the sequence of the  $2S$  and  $1D$  energy levels is different in comparison to that of He atom, which results from the combined influence of the donor impurity center and confining potential of the QD. The order of the  $D^-$  energy levels is shown in Fig. 1(b). Moreover, Fig. 1(b) shows a comparison between the calculated two-electron spectra for the spherical QD with and without the donor impurity centre. Neglecting the spin splitting, we can see that the energy-level order of the two-electron system without the donor center is the same as that for one-electron states in the spherical potential well. The presence of the positive donor center changes this order by shifting the  $2S$  energy levels downwards with respect to the  $1D$  levels, which results from the non-zero electron probability density for the  $S$  states at the Coulomb centre. These conclusions are based on the results of the variational calculations, which provide the upper bounds to the energy levels. However, due to the flexibility of the

applied trial wave function, the obtained order of the energy levels can be regarded to be correct.

The curve with open circles in Fig. 1(a) corresponds to the sum of the ground-state energies of the  $D^0$  centre and the electron in the spherical QD. On the contrary to Ref. [9], we argue that this energy does not correspond to any two-electron system confined within the single isolated QD. Instead, it is related to the system, which consists of the one electron bound in the  $D^0$  ground state inside the one QD and the second – confined within the another QD in the potential-well state of the lowest energy.

We mention that the energy levels of the two-electron system in the spherical QD without the donor center [Fig. 1(b)] lie below the continuum threshold appropriate for this electron pair. Therefore, the corresponding quantum states of the electron pair are bound. The properties of these states have been discussed in Ref. [10].

It is well-known that the one-electron states in spherical potential well (1) are bound if the effective capacity defined as

$$C = V_0 R^2 \quad (8)$$

is sufficiently large. The binding two-electron  $D^-$  excited states is also determined by the effective capacity of the QD given by Eq. (8). The larger value of  $C$ , the more quantum states of the  $D^-$  are bound. We have numerically estimated the critical values of  $C$  for several states of the  $D^-$  centre. The results are listed in Table 1. If the effective capacity of the QD exceeds the value quoted in Table 1, the given quantum state of the  $D^-$  center becomes bound.

$1^3P$	$1^1P$	$2^3S$	$2^1S$	$1^3D$	$1^1D$
9.08	10.21	19.82	21.02	20.63	21.18

Table 1: Critical values of the effective capacity [Eq. (8)] determining the binding of the excited states of the  $D^-$  centre in the QD. The donor rydberg  $R_D$  is the unit of energy, the donor Bohr radius  $a_D$  is the unit of length.

We have calculated the  $1^1S \rightarrow 1^1P$  and  $1^1P \rightarrow 1^1D$  transition energies for the  $D^-$  center being located in the QD GaAs nanocrystal embedded in  $\text{Al}_x\text{Ga}_{1-x}\text{As}$  matrix with  $x = 0.2$ , which corresponds to  $V_0 = 212$  meV. The results are displayed in Fig. 2(a), which as well shows the  $1s \rightarrow 1p$  and  $1p \rightarrow 1d$  transition energies for the  $D^0$  donor centre and the binding energies for the  $1^1S$  and  $1^1P$  states of the  $D^-$  centre.

We see that with decreasing QD radius the transition energies increase reaching the maximum values at about 5 nm. The maximum value of the  $1^1S \rightarrow 1^1P$  transition energy exceeds 100 meV. These maxima are reached at that value of  $R$ , at which the state of higher energy becomes unbound, i.e., its energy is equal to the continuum-threshold energy. The binding energies of the  $D^-$  states are monotonically increasing functions of the QD radius and for  $R \rightarrow \infty$  tend to the binding energy, which corresponds to the single bound state of the  $D^-$  centre in the bulk crystal, i.e.,  $V_0 + 0.0555R_D$ . We notice that the values of the transition energies between the corresponding states of the  $D^0$  and  $D^-$  donor centres are close to each other. It may therefore happen that the radiative transitions between the  $D^-$  states are masked by those between the  $D^0$  states.

In order to find a physical interpretation for the obtained formation of the excited states of the  $D^-$  centre, we have studied the spatial distribution of electrons. Fig. 2(b) shows a measure of the two-electron probability density in the barrier region for the  $1^1S$  and  $2^1S$  states of the  $D^-$  centre as functions of the QD radius. It is visible that a degree of the electron penetration into the barrier region drops off very rapidly and becomes negligible for the QDs of the radius of about one donor Bohr radius. This result gives an *a posteriori* justification for the neglected change in the effective band mass and dielectric constant.

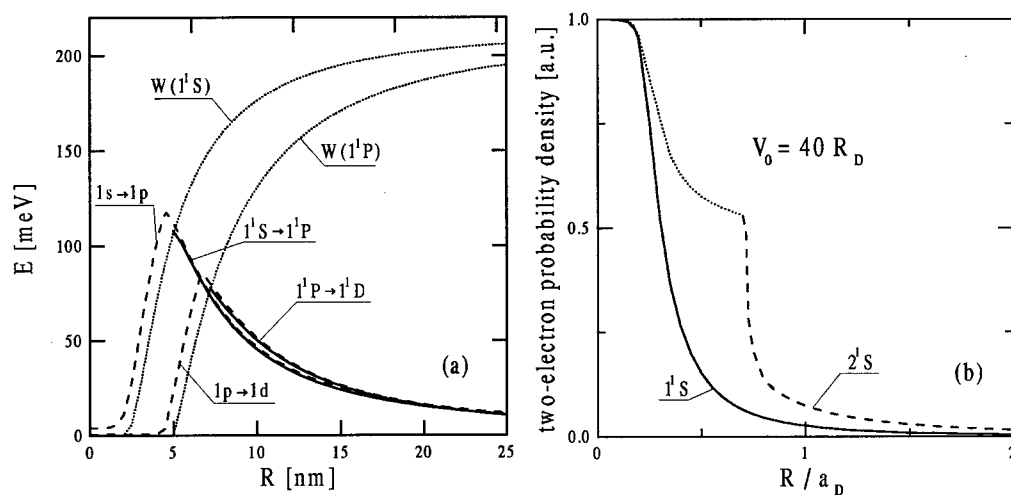


Figure 2: (a) Transition and binding energies for the donor centres in the GaAs QD with  $V_0 = 212$  meV as functions of QD radius. Solid curves show the  $1^1S \rightarrow 1^1P$  and  $1^1P \rightarrow 1^1D$  transition energies for the  $D^-$  centre, dashed –  $1s \rightarrow 1p$  and  $1p \rightarrow 1d$  transition energies for the  $D^0$  centre, and dotted –  $1^1S$  and  $1^1P$  binding energies for the  $D^-$  centre. (b) Two-electron probability density in the barrier region as a function of the QD radius for the  $1^1S$  (solid curve) and  $2^1S$  (dashed curve)  $D^-$  states for  $V_0 = 40 R_D$ . Dotted part of the curve corresponds to the unbound  $2^1S$  state.

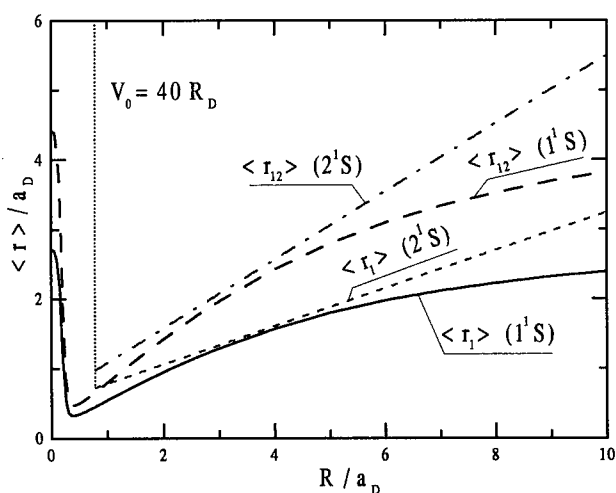


Figure 3: Average electron-donor ( $\langle r_1 \rangle$ ) and electron-electron ( $\langle r_{12} \rangle$ ) distances as functions of the QD radius for the  $1^1S$  and  $2^1S$  states of the  $D^-$ . Dotted line corresponds to the delocalized unbound  $2^1S$  states.  $a_D$  is the donor Bohr radius.

Fig. 3 displays the calculated expectation values of the electron-electron and electron-donor separations for the  $1^1S$  and  $2^1S$  states. The behaviour of these interparticle distances for the excited  $2^1S$  state clearly points out the delocalization of electrons in the unbound state (vertical dotted line) and their localization in the bound states. We have checked (see also Fig. 3) that for all the considered excited states the size of the  $D^-$  donor centre increases almost linearly with the QD radius, but is always smaller than this radius. This allows us for the interpretation of the binding of the  $D^-$  excited states as resulting from the confinement of electrons within the QD.

#### 4. Conclusions

The results of the present paper show that several quantum states can be bound for the  $D^-$  centre in the spherical quantum dot. We have calculated the energy levels associated with the states  $1^1S$ ,  $2^1S$ ,  $2^3S$ ,  $1^1P$ ,  $1^3P$ ,  $1^1D$ , and  $1^3D$ , and shown that the excited states are bound if the effective capacity of the QD is sufficiently large. The critical values of the effective QD capacity have been determined for the formation of the subsequent bound excited states of the  $D^-$  centre. A nature of binding of  $D^-$  excited states has also been studied. This binding mainly results from the QD confinement potential, which leads to the strong localization of electrons within the QD potential-well region with only a small possible penetration of electrons into the barrier region. We have discussed the spatial distribution of electrons, which expresses the electron confinement, and calculated the transition energies between the low-energy states of  $D^0$  and  $D^-$  centres in the QD. For the GaAs QDs, the transition energies can exceed 100 meV, which means that an experimental evidence of these states should be possible in spectroscopic measurements.

#### Acknowledgments

This work has been performed in the framework of the French-Polish scientific cooperation and is partially supported by the Polish State Scientific Committee (KBN). We are grateful to Dr. S. Bednarek for fruitful discussions.

#### References

- [1] S. Huant, S.P. Najda, and B. Etienne, *Phys. Rev. Lett.* **65**, 1486 (1990).
- [2] E.R. Mueller, D.M. Larsen, J. Waldman, and W.D. Goodhue, *Phys. Rev. Lett.* **68**, 2204 (1992).
- [3] A.P. Alivisatos, *Science* **271**, 933 (1996).
- [4] M.A. Olshavsky, A.N. Goldstein, and A.P. Alivisatos, *J. Am. Chem. Soc.* **112**, 9438 (1990).
- [5] R.C. Ashoori, H.L. Stormer, J.S. Weiner, L.N. Pfeiffer, K.W. Baldwin, and K.W. West, *Physica B* **189**, 117 (1993).
- [6] E.R. Mueller, D.M. Larsen, W.D. Goodhue, and J. Waldman, *Phys. Rev. B* **51**, 2326 (1995).
- [7] A.B. Dzyubenko, A. Mandray, S. Huant, A.Yu. Sivachenko, and B. Etienne, *Phys. Rev. B* **50**, 4687 (1994).
- [8] R. Buczko and F. Bassani, *Phys. Rev. B* **54**, 2667 (1996).
- [9] C. Büsser and C.R. Proetto, *J. Phys.: Condens. Matter* **8**, L131 (1996).
- [10] B. Szafran, J. Adamowski, S. Bednarek, and B. Stébé, *Mol. Phys. Reports* – in print.



## ELECTRON SPIN RESONANCE FEATURES OF THE $P_{b1}$ INTERFACE DEFECT IN THERMAL (100)Si/SiO<sub>2</sub>

A. Stesmans and V. V. Afanas'ev

Department of Physics, University of Leuven, 3001 Leuven, Belgium

**Keywords:** Si/SiO<sub>2</sub> structure; interface defects; point defects; electron spin resonance

### Abstract

K-band electron spin resonance (ESR) study of high-temperature processed thermal (100)Si/SiO<sub>2</sub> structures exhibiting predominantly the  $P_{b1}$  signal has allowed improved ESR characterisation of this defect. The results affirm the  $P_{b1}$  point symmetry as monoclinic-I, the  $g$  matrix being characterized by the principal values  $g_1=2.0058$ ,  $g_2=2.00735$ , and  $g_3=2.0022 \pm 0.0001$ , where the  $g_2$  direction is at an angle of  $3 \pm 1^\circ$  (towards the interface) with a  $\langle 111 \rangle$  direction at  $35.3^\circ$  with the interface plane. The presence of a field angle dependent broadening in the linewidth is unveiled, ascribed to a strain induced spread  $\sigma_{g\perp}$ , about 2-3 times less than typical for  $P_b$  in (111)Si/SiO<sub>2</sub>. The significance of these results in combination with previously attained salient experimental facts is addressed as to the atomic nature of  $P_{b1}$ .

### Introduction

The thermal growth of the Si/SiO<sub>2</sub> structure is known to be attendant with the natural incorporation of coordination defects at the Si/SiO<sub>2</sub> interface as a result of network-lattice mismatch.[1] Over the recent decades, these have been the subject of intense research, undoubtedly mainly driven by their early recognized adverse electrical effect as current degrading and charge trapping centers in Si-based devices. This has evoked ceaseless electrical characterization. However, as to atomic identification, the key information so far came from electron spin resonance (ESR) investigations [2-5].

As detected by ESR, it has become a common practice to refer to the group of Si/SiO<sub>2</sub> interface defects globally as  $P_b$  centers, their appearance being dependent on the Si substrate surface orientation.[2] At the (111)Si/SiO<sub>2</sub> interface, ESR has so far detected only one type of defect, specifically called  $P_b$ . It has been convincingly identified as the interfacial  $\circ\text{Si} \equiv \text{Si}_3$  defect,[1] that is, a dangling  $sp^3_{[111]}$ -like hybrid on an interfacial Si atom trivalently backbonded to three Si atoms in the substrate. Importantly, only the variant with the unpaired hybrid perpendicular to the (111) interface is observed in standard thermal (111)Si/SiO<sub>2</sub>. The center exhibits  $C_{3v}$  ([111] axial) symmetry with principal  $g$  values of  $g_{\parallel}=2.0014$  and of  $g_{\perp}=2.0086$ , where the  $\parallel$  sign refers to the applied magnetic field  $\mathbf{B} \parallel [111]$ .

At the (100)Si/SiO<sub>2</sub> interface, by contrast, ESR has isolated two spectroscopically different types of defects, called  $P_{b0}$  and  $P_{b1}$ . [2] While both were initially also pictured as interfacial single dangling Si-bond type of defects, their atomic identity is still cryptic, the more so for  $P_{b1}$ . Because of the much similar ESR characteristics,  $P_{b0}$  (like  $P_b$ ) was also assigned to  $\circ\text{Si} \equiv \text{Si}_3$ , as illustrated in Fig. 1. As compared to the  $P_b$  model, noteworthy is that the defected Si atom was now suggested situating more on sub-interface plane (second) level, the unpaired orbital facing an O atom, i.e., the  $\text{Si}_3 \equiv \text{Si} \cdot \text{O} = \text{Si}_2$  model. So,  $P_{b0}$  was basically seen as the (100) equivalent of  $P_b$  except for the fact that it was placed at a crystallographically differently oriented interface, which could evoke some marginal differences. For one, within an idealised view of near perfect interface Si crystallography, the unpaired orbital, pictured as pointing into a microvoid, is at an angle of  $90^\circ$  and  $35.3^\circ$  with respect to the (111) and (100) interface, respectively. Over the many years since its observation, this initial assignment is still under debate [6,7,8].

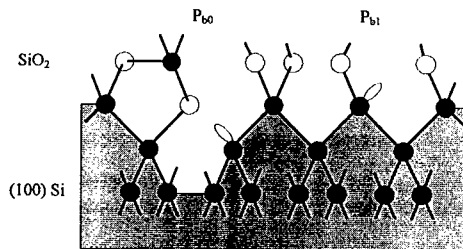


FIG. 1: Initially advanced structural models for  $P_{b0}$  and  $P_{b1}$  defects at the thermal (100)Si/SiO<sub>2</sub> interface (after Ref. [2]).

The  $P_{b1}$  defect in turn with the  $g$  matrix clearly not axial [2,9,10] (Table I) was modelled [2] as an interfacial  $^{\circ}\text{Si} \equiv \text{Si}_2\text{O}$  entity, (see Fig. 1) the center thus suggested to be of different chemical structure than  $P_{b0}$ . However, this assignment was subsequently countered both experimentally and theoretically.

There was the experimental ESR observation [11] under the orientation  $\mathbf{B} \parallel [100]$  (the interface normal) on 51.26%  $^{17}\text{O}$  enriched (100)Si/SiO<sub>2</sub>, reporting that the enrichment only led to a broadening of  $\sim 3.5$  G of the single Zeeman line; no  $^{17}\text{O}$ -induced hyperfine (hf) structure was observed, against what might generally be expected with an O atom in a first neighbor position of the defected Si. Another experimental dispute arose from the observation of interface defect passivation by moisture (H) upon pulling Si/SiO<sub>2</sub> (800 °C; O<sub>2</sub>+4% HCl) structures from a conventional open furnace into room ambient.[8] From the apparent identical behavior,  $P_{b1}$  was concluded similar to  $P_{b0}$ , while  $P_{b0}$  would be fundamentally (chemically) different, even suggesting the latter not to be a simple dangling Si bond. This conclusion, however, was recently countered [12] by extensive analysis of the passivation kinetics of all three defects in molecular H<sub>2</sub>. Close values of the activation energy for passivation were found, i.e.,  $1.53 \pm 0.04$ ,  $1.57 \pm 0.04$ , and  $1.51 \pm 0.04$  eV for  $P_{b0}$ ,  $P_{b1}$ , and  $P_b$ , respectively, giving little basis for preferably identifying  $P_b$  with either  $P_{b0}$  or  $P_{b1}$ . Rather, with the faithful  $^{\circ}\text{Si} \equiv \text{Si}_3$  model for  $P_b$  as backdrop, these results would indicate  $^{\circ}\text{Si} \equiv$  to be the core of all three defects. A strong opposition for the model came from theory. [13] Using a combination of *ab initio* and semiempirical molecular orbital techniques, extensive calculations were carried out on five model clusters for the  $P_{b1}$  defect, including Poindexter's  $^{\circ}\text{Si} \equiv \text{Si}_2\text{O}$  model. The model was concluded incorrect based on calculated electrical band gap level structure incompatible with experiment and effective correlation energy considerations. Interestingly, closest to experimental results regarding the electrical level position was found the model of an unpaired Si bond on a strained reconstructed Si dimer, called SB1, i.e.,  $\text{Si}_2=\text{Si}^{\circ}-\text{Si} \equiv \text{Si}_2\text{O}$ , where the long hyphen represents a strained bond. The model, however, was also discarded as it predicted a central  $^{29}\text{Si}$  hf interaction only about half the experimental value; in a single experiment on standard (100)Si/SiO<sub>2</sub>, Brower observed for  $\mathbf{B} \parallel [100]$  an hf splitting  $A_{[100]}(P_{b1}) \sim 157$  G, about 40 G larger than for  $P_b$ . [11] Except for a cautious suggestion that rather than  $^{\circ}\text{Si} \equiv \text{Si}_2\text{O}$ , the  $^{\circ}\text{Si} \equiv \text{Si}_3$   $P_{b0}$  model of Poindexter could be a good candidate for  $P_{b1}$ , the  $P_{b1}$  defects was essentially left unmodelled.

This leaves the atomic structure still obscure, mainly because ESR analysis has so far failed to provide an as convincing set of data as for  $P_b$ . Reasons for this are the inherently smaller defect density ( $\sim 3$  times) in (100)Si/SiO<sub>2</sub> and spectral overlap [2]. Particularly in the case of  $P_{b1}$ , this has obstructed an accurate  $g$  matrix and hyperfine interaction evaluation. The present work regards to the former part. During recent extended analysis of intrinsic interface defect generation as a function of oxidation conditions, fabrication parameters could be delineated predominantly leading to  $P_{b1}$  incorporation ( $[P_{b1}]/[P_{b0}] > 10$ ). This has allowed accurate  $P_{b1}$  signal characterization, among others the  $g$  matrix (symmetry). The element of inclusiveness inherent to inferring ESR parameters from entangled weak  $P_{b0}$  and  $P_{b1}$  spectra has thus been alleviated.

TABLE I: Compilation of the principal  $g$  matrix values (in notation after Ref. [14]) of the  $P_{b1}$  interface defect in (100)Si/SiO<sub>2</sub>; [100] is taken as the interface normal.

Reference	$g_1$	$g_1$ orientation	$g_2$	$g_2$ orientation	$g_3$
[2] <sup>a</sup> $\Delta g = \pm 0.001$	2.0052	$\langle 011 \rangle$	2.0081 <sup>b</sup>	approx. $\parallel \langle 111 \rangle$	2.0012
[9] <sup>a</sup> $\Delta g = \pm 0.0003$	2.0058	$[0 \bar{1} 1]$	2.0084	$[1 \bar{1} \bar{1}]$	2.0020
[10] <sup>a</sup> $\Delta g = \pm 0.0003$	2.0058	$[0 \bar{1} 1]$	2.0069	$[1 \bar{1} \bar{1}]^c$	2.0029
This work $\Delta g = \pm 0.0001$	2.00577	$[0 \bar{1} 1]$	2.00735	$\angle [1 \bar{1} \bar{1}], g_2 = 3 \pm 1^\circ$	2.0022

<sup>a</sup> Extracted from overlapping  $P_{b0}$  and  $P_{b1}$  spectra

<sup>b</sup> See remark in Ref. [9]

<sup>c</sup> Taking into account exchange in  $g_2, g_3$  labels

### Experimental

Slices of 2x9 mm<sup>2</sup> main face were cut from commercial two-side polished Cz-grown (001) Si wafers (p type;  $\sim 10 \Omega\text{cm}$ ) about 80  $\mu\text{m}$  thick; their 9-mm edge was a (011) direction (see Fig. 3). After appropriate cleaning, including a 10-min treatment in Piranha etch, various sets of (100) slices were oxidized at  $\sim 970^\circ\text{C}$  (1.1 atm O<sub>2</sub>; 99.9996%; oxide thickness  $\sim 38\text{--}130 \text{ nm}$ ). To maximize  $P_{b1}$  production, some were submitted to a postoxidation anneal at high temperature. All thermal steps were terminated by slow cooling ( $\sim 20 \text{ min}$ ) to room temperature in unaltered ambient. The thermal treatments were carried out in a laboratory set up He-leak tight to better than  $10^{-10} \text{ Torr l/s}$ . Details of the thermal facility can be found elsewhere [4,5].

ESR observations were carried out at 4.3 K using a K-band ( $\sim 20.2 \text{ GHz}$ ) spectrometer routinely driven in the adiabatic slow passage absorption mode. Usually, first derivative absorption signals were detected by employing  $\sim 100 \text{ kHz}$  modulation of  $\mathbf{B}$ , with the modulation field amplitude ( $\sim 0.25 \text{ G}$ ) and incident microwave power  $P_\mu$  reduced to linear signal response levels and spectra were averaged over 10–20 traces. However, the  $P_{b1}$  signal was found extremely saturable, imposing reduction of  $P_\mu$  to below 20 pW, thus impairing the signal-to-noise ratio. Fortunately, it turned out that significant improvement could be attained by recouring to the second harmonic out-of-phase detection mode ( $\sim 75 \text{ kHz}$  field modulation;  $P_\mu \sim 0.3 \mu\text{W}$ ). The rapid passage effects for this kind of spectrometer settings gave undifferentiated absorptionlike peaks. For signal improvement, typically about 20 slices were stacked.

Accurate  $g$  value determination is a major aim in this work, attained using a micro-sized Si:P powder standard of  $g_{\text{Si:P}}(4.2 \text{ K}) = 1.99869 \pm 0.00002$ , attached to the Si sample stack and recorded in the same trace. The consistency between  $g$  readings on the first and second harmonic detected signals were carefully checked for some high symmetry (least complicated ESR spectra)  $\mathbf{B}$  directions.  $\mathbf{B}$  was rotated in the (011) plane with  $\phi_B$ , the angle of  $\mathbf{B}$  with the [100] interface normal, varying from  $0 \rightarrow 90^\circ$  (see Fig. 2).

### Experimental results and interpretation

Figure 3 presents a major  $P_{b1}$  result obtained on samples with  $[P_{b1}]/[P_{b0}] \geq 10$  in the second harmonic detection mode. It shows the angular dependence of the  $P_{b1}$   $g$  value for  $\mathbf{B}$  in the (011) plane. Three branches are observed with relative intensity (from top to bottom in Fig. 3) of 1:2.3 ( $\pm 0.2$ ):1, as deduced from fitting Lorentzian shapes. For the particular crystal plane scanned, such 3-branch pattern (as well recognized initially [2]) can only be fitted with monoclinic type-I symmetry [14], with the added restriction that only part (3 out of 7) of the

branches are experimentally observed. Not all crystallographically equivalent defect orientations occur. The relative branch intensity 1:2:1 of the model (cf. Fig. 3) complies with experiment. The optimized fitting (solid curves in Fig. 6) give the principal  $g$  values tabulated in Table I, with the  $g_2$  ( $=2.00735$ ) direction at an angle of  $3 \pm 1^\circ$  with  $[111]$  towards  $[011]$ . The  $g$  values are compared in Table I with previous values obtained through disentangling interfering  $P_{b0}$  and  $P_{b1}$  spectra. The tensor orientation is sketched in Fig. 2. While consolidating, these results refine the initial assignment [2].

A next interesting observation is that the  $P_{b1}$  linewidth, as  $P_b$ , is also found to exhibit some field anisotropy –unnoticed previously [2,10]. The width at half height  $B$  of the absorption peak (second harmonic detection) is found to increase from  $4.0 \pm 0.3$  G for  $\mathbf{B} \parallel [211]$  (approximately  $g_3$  direction) to  $6.3 \pm 0.9$  G for  $\mathbf{B} \parallel [111]$  (approximately  $g_2$  direction). Assuming that this angle dependent broadening for  $P_{b1}$ , like for  $P_b$ , also results from a spread in  $g_\perp$  [15], the  $\sigma_{g\perp}$  value may be inferred using the approximation

$$\Delta B^G = 1.18(2hf g_\perp / g^3 \beta) \sigma_{g\perp} \sin^2(\Theta) \quad (1)$$

for the Gaussian part  $\Delta B^G$  of the broadening, where  $h$  represents Planck's constant,  $\beta$  the Bohr magneton,  $f$  the microwave frequency, and  $\Theta$  the angle of  $\mathbf{B}$  with the minimum linewidth direction (in this case, the  $g_2$  direction). This resulted in  $\sigma_{g\perp} = 0.00035 \pm 0.00005$ , which may be compared with  $\sigma_{g\perp} \sim 0.0008$  of the axially symmetric  $P_b$  in standard bulk (111)Si/SiO<sub>2</sub>. It needs to be remarked that for  $P_{b1}$ , in contrast with  $P_{b0}$ ,  $\Delta B$  of the 2nd harmonic absorption-like signal is observed, instead of the generally quoted  $\Delta B_{pp}$ . Without knowledge of the correct line shape (and spectroscopic passage effects) the conversion of  $\Delta B$  to  $\Delta B_{pp}$  is not straightforward. However, for  $\mathbf{B} \parallel (100)$  face normal, the value  $\Delta B_{pp}(\parallel [100]) = 3.3 \pm 0.2$  G was measured directly, which may be compared with  $\Delta B = 4.7 \pm 0.3$  G.

The  $P_{b1}$  defect configuration, albeit weaker than  $P_b$ , thus appears also sensitive to local strain variations present in interfacial layers. Accordingly, it also testifies to the interfacial character of the defect.

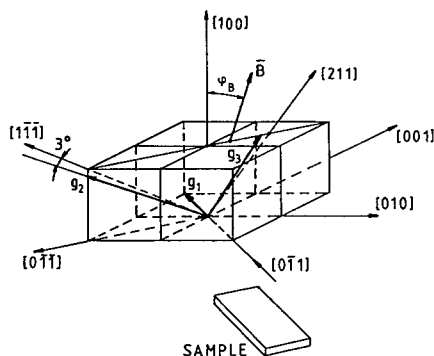


FIG. 2: Schematic drawing of the inferred  $P_{b1}$   $g$  dyadic orientation within the cubic Si lattice for one of the four interface restricted equivalent defect orientations at the (100)Si/SiO<sub>2</sub> interface. Also shown is the applied sample geometry.

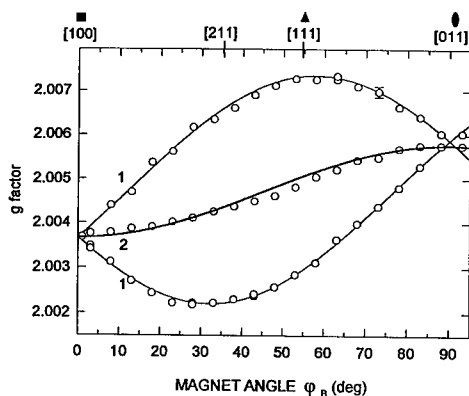


FIG. 3: Rotation pattern of the  $P_{b1}$   $g$  value in bulk thermal (100)Si/SiO<sub>2</sub> (970°C; 1.1 atm O<sub>2</sub>) for  $\mathbf{B}$  rotating in the (011) plane. The curves represent the theoretical fit for monoclinic-I point symmetry. The added numbers indicate the relative intensities of the branches.

### Discussion

The unknown atomic structure of the  $P_{b1}$  center is still of key interest, particularly in view of its presumed pervasive activity as a degrading electrical interface defect in technological applications. As addressing such issue should be guided by the salient experimental facts thus far established (apparently mainly by ESR), it might be useful to compile those considered most essential. (1)  $P_{b1}$ , like  $P_b$  and  $P_{b0}$ , was also concluded operating as a deep amphoteric trap with two electrical levels in the Si bandgap [16]. (2) Recent ESR studies on the interface-hydrogen interaction kinetics unveiled all three defects,  $P_b$ ,  $P_{b0}$ , and  $P_{b1}$ , to exhibit very similar values of the activation energy for passivation, i.e.,  $1.51 \pm 0.04$ ,  $1.51 \pm 0.04$ , and  $1.57 \pm 0.04$  eV, respectively [12]. With  $P_b$  reliably identified as  $Si_3 \equiv Si_\circ$ , this result strongly suggests that  $P_{b1}$  also constitutes basically an unpaired Si hybrid on an interfacial defect Si. (3) Hyperfine doublets, due to the unpaired spin-defect  $^{29}Si$  nucleus interaction, were observed for all three defects in standard bulk Si/SiO<sub>2</sub> [3,5,7,11]. For  $B \parallel (100)$  interface normal, the  $P_{b1}$  hf splitting is  $\sim 40$  G larger than for  $P_b$ . (4) Studies on  $^{17}O$  enriched Si/SiO<sub>2</sub> of  $P_b$ ,  $P_{b0}$ , and  $P_{b1}$  indicate that oxygen is not an immediate part of either defect [11,17]. (5) The  $P_{b1}$  linewidth depends on magnet angle, though significantly weaker than  $P_b$ . When referring to the stress origin of this effect, it indicates the  $P_{b1}$  defect, on average, to reside in a more regular (less strained) interfacial environment. (6) The  $g$  dyadic data learn that  $P_{b1}$  is an interface-restricted monoclinic-I type defect, with the lowest principal  $g$  value axis  $g_3$  at  $3 \pm 1^\circ$  with  $\langle 211 \rangle$ , and largest principal  $g$  value axis  $g_2$  at  $3^\circ$  with  $\langle 111 \rangle$ . The linewidth is smallest for  $B$  along the  $g_3$  axis (7). The  $P_{b1}$  defect appears more saturable than  $P_{b0}$  ( $P_b$ ).

As to the  $P_{b1}$  atomic structure, the total of these salient facts are seen complying with a provisional model picturing  $P_{b1}$  as an unpaired Si bond on a defect Si atom backbonded to three Si atoms in the bulk, located, in average, sub-interface plane, i.e, somewhat deeper into the Si substrate than  $P_{b0}$ . Final conclusive modelling, within ESR context, must await data on the full  $^{29}Si$  and  $^{17}O$  hf and shf structure backed up by theory. In light of the complexity of the ESR spectrum and typical interface defects encountered in standard (100)Si/SiO<sub>2</sub>, this might turn out a tough goal for state-of-the-art classical ESR. It likely has to come from more exquisite spectroscopy such as electron-nuclear double resonance.

### Concluding remarks

The element of inclusiveness inherent to inferring ESR parameters from entangled  $P_{b0}$  and  $P_{b1}$  spectra has been alleviated through measurements on conventional thermal (100)Si/SiO<sub>2</sub> structures almost solely exhibiting the  $P_{b1}$  signal in the second harmonic detection mode. This has allowed accurate  $g$  dyadic and linewidth-vs-magnet angle calibration.

For  $P_{b1}$ , the results include: (1) an accurate  $g$  matrix determination confirming the monoclinic-I point symmetry with the  $g_2$  axis (admittedly about the unpaired Si hybrid direction) at  $3 \pm 1^\circ$  (towards the interface plane) with one of the  $\langle 111 \rangle$  directions at  $35.3^\circ$  with the interface. Only the four crystallographic defect orientations (ESR) equivalent through the 4 [100] face symmetry occur; (2) The  $g$  shift is largest along the  $g_2$  axis ( $\sim \langle 111 \rangle$ ). (3) In contrast with previous belief, the existence of a line broadening component due to a statistical spread in  $\sigma_g$  has been demonstrated;  $\sigma_{g\perp}$  is 2-3 times smaller than for  $P_b$ .

As to a  $P_{b1}$  atomic working model, the salient ESR facts appear reconcilable with a dangling Si orbital, possibly facing a desymmetrising foreign atom, and located slightly sub-interface plane.

### References

- 1 For a review, see e.g. E. H. Poindexter and P. Caplan, Prog. Surf. Sci. **14**, 211 (1983); R. Helms and E. H. Poindexter, Rep. Prog. Phys. **57**, 791 (1994)

- 
2. E. H. Poindexter, P. Caplan, B. Deal, and R. Razouk, *J. Appl. Phys.* **52**, 879 (1981)
  3. K. Brower, *Appl. Phys. Lett.* **43**, 1111 (1983)
  4. G. Van Gorp and A. Stesmans, *Phys. Rev. B* **45**, 4344 (1992)
  5. A. Stesmans, *Phys. Rev. B* **48**, 2418 (1993)
  6. F. C. Rong, J. F. Harvey, E. H. Poindexter, and G. J. Gerardi, *Appl. Phys. Lett.* **63**, 920 (1993)
  7. J. W. Gabrys, P. M. Lenahan, and W. Weber, *Microelectr. Eng.* **22**, 273 (1993)
  8. J. Stathis and L. Dori, *Appl. Phys. Lett.* **58**, 1641 (1991)
  9. A. Stesmans, J. Braet, J. Witters, and R. F. Dekeersmaecker, *Surf. Sci.* **141**, 255 (1984)
  10. J. L. Cantin, M. Schoisswohl, H. J. von Bardeleben, N. H. Zoubir, and M. Vergnat, *Phys. Rev. B* **52**, R11 599 (1995)
  11. K. L. Brower, *Z. Phys. Chem. Neue Folge* **151**, 177 (1987)
  12. A. Stesmans, *Appl. Phys. Lett.* **68**, 2723 (1996); 2076 (1996)
  13. A. H. Edwards, in *The Physics and Chemistry of SiO<sub>2</sub> and the SiO<sub>2</sub> interface*, edited by C. R. Helms and B. E. Deal (Plenum, New York, 1988), p. 271
  14. See, e.g., C. A. J. Ammerlaan, in *Landolt-Börnstein Numerical Data and Functional relationships in Science and Technology*, Vol 22, Edited by O. Madelung and M. Schulz (Springer, Berlin, 1987), p. 365
  15. K. L. Brower, *Phys. Rev. B* **38**, 9657 (1988)
  16. G. J. Gerardi, E. H. Poindexter, P. J. Caplan, and N. M. Johnson, *Appl. Phys. Lett.* **49**, 349 (1986)
  17. A. Stesmans and K. Vanheusden, *Phys. Rev. B* **44**, 11353 (1991); J. H. Stathis, S. Rigo, and I. Trimaille, *Solid State Commun.* **79**, 119 (1991)

## SILICON SURFACE DEFECTS: THE ROLES OF PASSIVATION AND SURFACE CONTAMINATION

Anand J. Reddy, Tracey A. Burr, Julia K. Chan,  
 Gerd J. Norga\*, Jürgen Michel, and Lionel C. Kimerling  
 Department of Materials Science and Engineering  
 Massachusetts Institute of Technology  
 Cambridge, MA 02139, USA  
 \*Interuniversity Microelectronics Centre  
 B 3001 Leuven, Belgium

**Keywords:** surface defect, passivation, dangling bond, lifetime, native oxidation

**Abstract.** We show that the degree of surface passivation of a silicon wafer is easily detected by monitoring the surface recombination velocity. Dangling surface bonds and chemisorbed metals introduce deep states in the gap that act as recombination centers for minority carriers. This method is sensitive to  $10^{-7}$  ML ( $10^8 \text{ cm}^{-2}$ ) surface defect concentrations. A brief survey of applications to metal deposition, oxidation, and halogen passivation will be given.

### Introduction

The production of clean silicon surfaces is essential for the fabrication of electron devices. The detrimental effects of metals in silicon are quite well documented. In charge storage based devices, metals can decorate extended defects and lead to junction shorting, while in CMOS, interfacial metals can lead to a drop in gate oxide integrity (GOI) [1]. The chemisorption of oxygen on the silicon surface is known to be detrimental to certain fabrication process steps, such as epitaxial layer growth and metal film deposition [2].

Passivation of the silicon surface is essential to prevent contamination by physisorption and chemisorption. A bare silicon surface is highly reactive, and therefore easily attracts oxygen, metal ions, and small particles that lead to surface contamination. Immersion in hydrofluoric acid (HF) solutions is a common method for producing a hydrogen-terminated surface. We have investigated defects formed on the hydrogen-terminated surface due to deposition of metals from solution and attack by oxygen during exposure to air. Some of our results are summarized in Table 1. Since HF is a serious health and safety hazard, we have also been investigating halogen passivation as a benign alternative to hydrogen passivation.

Defect	Surface coverage ( $\text{cm}^{-2}$ )	SRV ( $\text{cm/s}$ )	$\sigma$ ( $\text{cm}^2$ )
Au atom	$2 \times 10^{11}$	20	$10^{-17} \text{ cm}^2$
Cu atom	$3 \times 10^{10}$	30	$9 \times 10^{-17} \text{ cm}^2$
Cu cluster	$2.5 \times 10^{12}$	40	$2 \times 10^{-14} \text{ cm}^2$
H atom	$1 \times 10^{15}$ (1ML)	0.25	—

**Table 1:** Capture cross-sections for selected defects.

## Experimental

We have developed a lifetime measurement system, Radio-Frequency Photoconductance Decay (RF-PCD), that affords high sensitivity to midgap surface states. Minority carriers are injected using a strobe light while an RF wave is used to probe the wafer conductivity. A 60 MHz wave incident upon the wafer is reflected due the screening of free carriers. As the injected carriers recombine, the reflected wave intensity correspondingly decays.

In general, the minority carrier lifetime has contributions from both bulk and surface recombination centers. Recombination at the surface is characterized by the surface recombination velocity (SRV), which is defined by

$$S = N_s \sigma v_{th}, \quad (1)$$

where  $N_s$  is the density of surface states,  $\sigma$  is the minority carrier capture cross-section, and  $v_{th}$  is the carrier thermal velocity.

As surface conditions vary, there are three distinct regimes of measured lifetime. For very high SRV, carrier recombination is limited only by the time required for carriers to reach the wafer surface, so  $\tau_{meas} = \frac{d^2}{\pi^2 D}$ , where  $D$  is the minority carrier diffusion constant. In the limit of very low SRV, bulk recombination is the dominant mechanism and  $\tau_{meas} = \tau_{bulk}$ . For surfaces with defect concentrations between these two extremes, the measured lifetime varies with SRV as

$$\tau_{meas} = \frac{d}{2S}. \quad (2)$$

Only in this regime can lifetime be used to probe surface defects. To increase the range of sensitivity to surface defects, only wafers with high bulk lifetimes ( $> 1$  ms) are used.

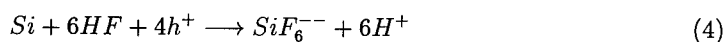
Since this technique is sensitive to very low levels of surface states, care must be taken to prepare very clean surfaces. Our standard cleaning procedure consists of: 2 minutes in dilute (1:100) HF, 4 minutes in a 4:1  $H_2SO_4:H_2O_2$  (Piranha) bath at 90°C, followed by another 2 minutes in dilute HF. The purpose of the first step is to remove any native oxide present on the surface. The Piranha step then grows a 2-3 nm thick chemical oxide, which traps any contaminants present on the silicon surface. The final dilute HF step removes this oxide and the contaminants trapped in it. To limit the degree of metal contamination, only Ashland Gigabit<sup>TM</sup> chemicals (specified to  $< 1$  part per billion of each heavy metal) and 18M $\Omega$ -cm de-ionized water (DI) are used for all cleaning procedures.

## Metal Related Surface Defects

Metal ions dissolved in acidic solutions may deposit on the silicon surface via an electrochemical reduction process:



The electrons required for this reaction are supplied by corrosion of the silicon substrate, which in HF solutions proceeds as:



Previous work [3] has correlated the deposition tendencies of metals with their reduction potentials. More electropositive metals, like Fe and V, are observed to remain in solution while Au and Cu are seen to reduce on the silicon surface.

To study the influence of Au-related states on surface recombination, wafers were cleaned with the standard MIT sequence before immersion in dilute HF contaminated with 12.5 ppb Au.



The wafers were then transferred to a bath of 49% HF for lifetime measurement. In the case where ion diffusion to the wafer surface is the rate limiting step of the deposition process, the surface concentration of Au should be:

$$N_{Au}(t) = 2D^{\frac{1}{2}}C\pi^{-\frac{1}{2}}t^{\frac{1}{2}} \quad (5)$$

where  $D$  is the liquid state diffusion constant and  $C$  is the  $Au^{+++}$  concentration in the solution bulk. Figure 1 shows the reciprocal lifetime plotted against (immersion time) $^{\frac{1}{2}}$ . The strong  $t^{\frac{1}{2}}$  dependence is consistent with the diffusion-limited model proposed above. Using a literature value of  $D=9.7 \times 10^{-6} \text{ cm}^2/\text{s}$  for  $Au(CN)_4^-$ , the capture cross-section is calculated as  $\sigma = d/2(N_{Au}\tau v_{th}) = 10^{-17} \text{ cm}^2$ .

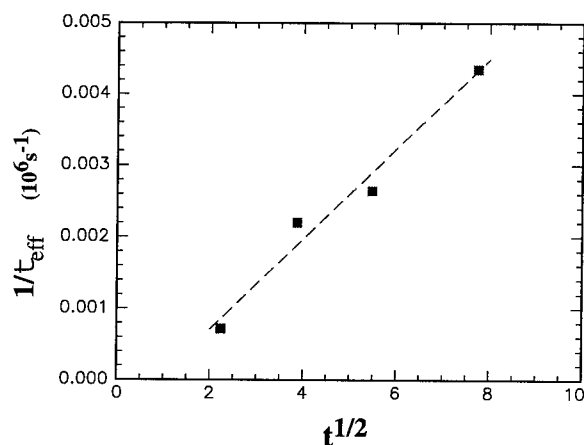


**Figure 1:** Inverse lifetime plotted versus (time) $^{\frac{1}{2}}$ . The  $t^{\frac{1}{2}}$  dependence supports the model of diffusion-limited deposition.

Surface states related to Cu have also been studied. In the low coverage range ( $<5 \times 10^{11} \text{ cm}^{-2}$ ), Cu is observed to deposit atom-by-atom. As the surface coverage increases, the formation of Cu clusters on the surface becomes possible. Thus this high coverage regime allows for a second deposition mechanism in which the Cu ions deposit directly onto pre-existing Cu clusters using  $e^-$  supplied by silicon corrosion [4].

Since Cu deposition is known to occur more slowly from concentrated HF solutions than from dilute HF [5], low surface coverage samples were obtained by immersing clean n- and p-type wafers in 10% and 49% HF solutions containing 30 ppb  $Cu^{++}$ . Lifetime measurements were performed in 49% HF. The wafers were then analyzed by TXRF for an accurate determination of the surface coverage. The calculated cross-sections are  $\sigma_n \approx 6 \times 10^{-17} \text{ cm}^2$  for electrons in p-type material and  $\sigma_p \approx 9 \times 10^{-17} \text{ cm}^2$  for holes in n-type.

Wafers with high Cu coverage were prepared by immersing clean n- and p-type wafers in a 1:100 HF bath contaminated with 400 ppb  $Cu^{++}$  for 5 minutes. Precipitate size distributions, prepared using Atomic Force Microscopy (AFM), are shown in Fig. 2. Although precipitate morphologies are quite different, with n-type showing smaller but more numerous clusters than p-type, the minority carrier capture cross-section per cluster,  $\sigma = 2 \times 10^{-14} \text{ cm}^{-2}$  is roughly the same for both materials.

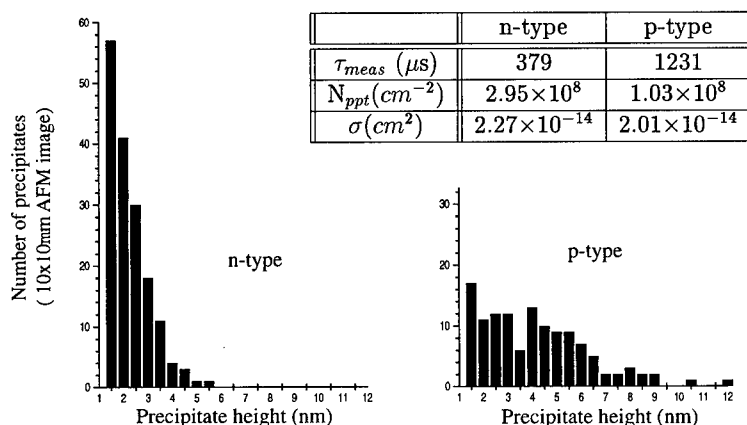


**Figure 2:** Precipitate size distributions for wafers immersed for 5 minutes in 1:100 HF containing 400 ppb  $Cu^{++}$ .

### Initial Stages of Native Oxide Growth

Numerous studies have been performed on the initial stages of silicon oxidation, using a variety of techniques like Fourier Transform Infrared Spectroscopy (FTIR) [6], X-ray Photoelectron Spectroscopy (XPS) [7], and High Resolution Electron Energy Loss Spectroscopy (HREELS) [8]. Unfortunately, many of these techniques suffer from low sensitivity and can't observe any surface activity within the first 30 minutes of air exposure. The high sensitivity of RF-PCD makes it useful for studying these initial stages of the oxidation process.

Experiments to study the reactivity of H-terminated silicon surfaces under different ambients have been performed. An n-type silicon wafer was cleaned and immersed in 49% HF for lifetime measurement. The HF solution and wafer were then placed in a glovebox which was purged with  $N_2$ . The wafer was subsequently removed from the HF and its lifetime was monitored continuously.

Figure 3a shows a wafer that has been taken directly from a 49% HF solutions into a  $N_2$  environment. At 1250s, the flow gas was switched from  $N_2$  to dry  $O_2$ . The immediate decrease in the measured lifetime indicates that  $O_2$  is reacting with the surface. Figure 3b shows similar data for dry  $N_2$  and  $N_2$  that was bubbled through DI water. The lifetime remains high, indicating that no degradation is occurring as a result of the increased water content. Together, these sets of data implicate  $O_2$  and not  $H_2O$  as the major reactive agent in the initial stage of the native oxidation of silicon.

Oxygen is initially thought to insert in Si-Si backbonds [8]. This insertion strains the lattice and leads to the formation of dangling bonds in the near surface region. Assuming a capture cross-section  $\sigma = 10^{-16} cm^2$  for a dangling bond, and assuming that full monolayer surface coverage is achieved after 20 days, we can extrapolate from our data that the Si/native oxide interface will contain  $\approx 8 \times 10^{13}$  dangling bonds /  $cm^2$ . This areal density translates to the formation of a dangling bond with the insertion of roughly each 10 oxygen atoms.

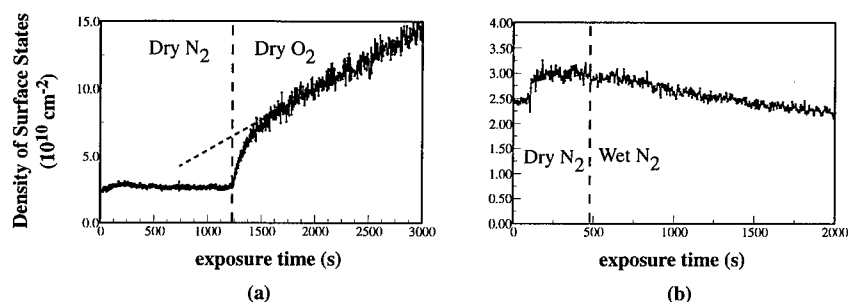


**Figure 3:** Number of surface states versus time for a wafer (a) contained under nitrogen and then exposed to dry  $\text{O}_2$ , and (b) contained under dry  $\text{N}_2$  and then exposed to  $\text{N}_2$  which had been bubbled through DI water.

### Surface Passivation by Halogens

Hydrogen passivation of the silicon surface is known to make it less reactive and thus limit the potential for contamination by physisorption and chemisorption of foreign species. Such passivation, though, is rarely perfect, as there is usually some equilibrium concentration of dangling bonds remaining on the surface. Subsequent immersion of these surfaces in halogen/alcohol solutions is thought to passivate these remaining dangling bonds and further reduce the reactivity of the surface.

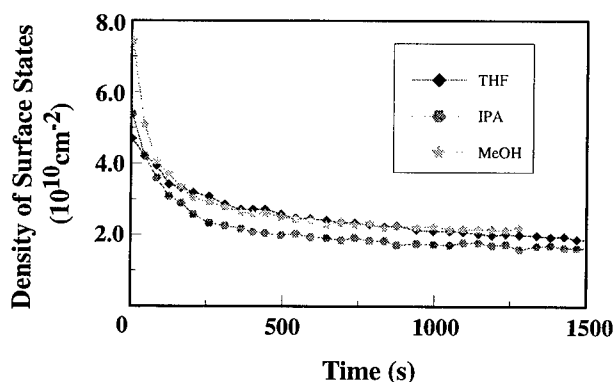


**Figure 4:** Density of surface states versus time for wafers immersed in various iodine/alcohol solutions following treatment with 1:100 dilute HF. The similarity of the curves indicates that solvent polarity is not a significant factor in the passivation process.

To determine the efficacy of halogen surface passivation, wafers were given the standard MIT clean and then immersed in halogen/methanol solutions. By monitoring the surface recombination lifetime it was determined that iodine is a more effective electronic passivant than bromine as it leaves fewer trap states on the surface at an order of magnitude lower solution

concentration. In addition, the role of the solvent in the passivation mechanism was investigated using iodine containing solutions of methanol, isopropyl alcohol (IPA) and tetrahydrofuran (THF). The number of surface states, calculated from  $\tau^{-1}$  assuming  $\sigma = 10^{16} \text{cm}^{-2}$ , is plotted as a function of time in Fig. 4. All curves obey first order reaction kinetics with roughly the same time constant and yield similar degrees of surface passivation for long immersion times. THF is a polar aprotic solvent and as such cannot participate in dissociation and addition to the silicon surface. This property provides strong evidence that iodine is the passivating species and that the mechanism of passivation involves the reaction of unpassivated sites with monatomic halide radicals. Also consistent with this mechanism, the effectiveness of halide passivation correlates inversely with halogen bond strength and the passivation rate remains constant regardless of solvent polarity.

### Conclusions

We have detected surface defect states caused by the adsorption of Au and Cu ions from solution. Au deposition occurs atom by atom. Cu deposition occurs atom by atom in the low coverage regime ( $< 5 \times 10^{11} \text{cm}^{-2}$ ) and forms metallic clusters for higher coverages.

We have observed that degradation of the H-passivated silicon surface begins immediately upon exposure to  $\text{O}_2$ . Wet  $\text{N}_2$  results in no surface states, implicating  $\text{O}_2$  as the dominant reactive species in the native oxidation of silicon. Under the assumption that dangling bonds with  $\sigma = 10^{-16} \text{cm}^{-2}$  are the observed defects, we calculate that 1 dangling bond is formed for every 10 O atoms inserted in the silicon lattice.

We have shown that halogen-containing solutions can passivate the silicon surface. The uniformity of the results for different solvents provides strong evidence that the passivating agent is the halogen and that the passivation reaction involves monatomic halide radicals.

### References

- [1] W. B. Henley, L. Jastrzebski, N. F. Haddad, *Mat. Res. Soc. Symp. Proc.* Vol. 315, 299 (1993).
- [2] M. Morita, T. Ohmi, *Jpn. J. Appl. Phys.* **33**, 370 (1994).
- [3] G. J. Norga, K. A. Black, M. R. Black, J. Michel, and L.C. Kimerling, in *Proc. of the 4th Int'l Symp. on Cleaning Technology in Semiconductor Device Manufacturing*.
- [4] G. J. Norga, "Chemistry and Physics of Metallic Impurities on Crystalline Silicon Surfaces", Ph.D. Thesis, Materials Science and Engineering, MIT (June 1996).
- [5] L. A. Nagahara, T. Ohmori, K. Hashimoto, A. Fujishima, *J. Vac. Sci. Tech. A* **11**, 763 (1993).
- [6] T. Miura, M. Niwano, D. Shoji, and N. Miyamoto, *Appl. Surf. Sci.* **100**, 454 (1996).
- [7] D. Gräf, M. Grundner, and R. Schulz, *J. Appl. Phys.* **68**, 5155 (1990).
- [8] H. Ikeda, K. Hotta, S. Furuta, S. Zaima, and Y. Yasuda, *Jpn. J. Appl. Phys.* **35** Pt. 1, 1070 (1996).

## HEAT-TREATMENT INDUCED MODIFICATIONS OF POROUS SILICON

S. Dannefaer, C. Wiebe and D. Kerr  
Department of Physics  
University of Winnipeg  
Winnipeg, MB, Canada R3B 2E9

**Keywords:** Porous silicon, positron annihilation

**Abstract.** Positron lifetime spectroscopy was used to investigate a porous silicon film subjected to heat treatments in argon atmosphere. After annealings between 300 and 500°C the mass of the film increased by 17% due to oxygen uptake. Vacancy clusters in the silicon oxide layer covering the nano-crystallites increased their concentration by a factor of 3. Above 900°C significant structural changes of the film took place as manifested by growth in the size of vacancy clusters.

### Introduction.

Nanocrystalline semiconductors are being investigated extensively in part because of their novel physical properties but also because of the technological interest in nano-sized devices. Porous silicon is a nanocrystalline material whose surface area per unit volume is very large ( $\sim 100\text{m}^2/\text{cm}^3$ ) so that surface properties play an important role in determining its characteristics. These surface properties, in turn, are strongly dependent on the preparation of the material and its subsequent treatment.

Porous silicon is produced by the anodization of crystalline silicon in a hydrofluoric acid solution following which infrared spectroscopy indicates an abundance of Si-H bonds on the internal surfaces (i.e. the pore walls); these measurements also show that the hydrogen is completely removed in a brief annealing at  $\sim 400^\circ\text{C}$  in vacuum [1]. Simple aging in air inevitably results in the formation of an oxide layer on the surfaces.

Positron annihilation offers the possibility of investigating a number of important aspects of the material since some positrons will sample the silicon oxide where they may be trapped by vacancy-like defects while others escape from the crystallite and form positronium in the pores or on the pore walls. The lifetime of those positrons which are trapped depends upon, among other things, the open volume of the defect; those positrons forming positronium produce either parapositronium which undergoes rapid (125 ps) self annihilation, or orthopositronium from which annihilation normally occurs by the so-called pick-off process with a lifetime strongly dependent on the surface condition of the pores.

### Experimental.

The porous silicon layer was produced by the anodization of p-type crystalline silicon in a solution of 50% hydrofluoric acid in ethanol (4:1) for 22 min. at a current density of  $57\text{ mA}/\text{cm}^2$ . The resulting layer was  $94\text{ }\mu\text{m}$  thick and had a gravimetrically determined porosity of 69%.

Heat treatments were done in a pure argon atmosphere in order to minimize atmospheric oxidation at high temperature. With this procedure, however, air adsorbed on the pore surface may still contribute to oxidation.

Positron lifetime measurements were performed using a lifetime spectrometer with a time resolution of 200 ps. The positron source consisted of 15  $\mu\text{Ci}$  of  $^{22}\text{NaCl}$  deposited very uniformly over a small area on 0.8  $\mu\text{m}$  thick aluminum foil resulting in a very small source contribution (2% intensity with a lifetime of 250 ps). Further details of data acquisition and analysis procedures may be found in Ref. [2].

### Results and discussion.

The thickness of the porous silicon layer is not sufficient to stop all the positrons incident upon it (in fact it stops only about one-third) so the rest annihilate in the crystalline silicon backing with a characteristic lifetime of 217 ps. The intensity of this component,  $I_{217}$ , which is a direct measure of the fraction of positrons penetrating the porous layer, is readily determined from the lifetime spectrum. This makes possible an estimation of the mass of the porous layer since the fraction is given by

$$I_{217} = \exp(-t \cdot \alpha), \quad (1)$$

where  $t$  is the thickness of the layer and  $\alpha$  is

$$\alpha = 17.6\rho/E^{1.47}[\text{cm}^{-1}], \quad (2)$$

where  $\rho$  is the density of the layer (in  $\text{g}/\text{cm}^3$ ) and  $E$  is the maximum energy of the positrons (in MeV). Thus, a change in the mass (per unit area) of the layer will be reflected in a change in  $I_{217}$ . Fig. 1 shows the fraction of positrons passing through the porous layer as a function of heat treatment temperature and Table 1 shows the corresponding calculated relative changes in mass of the layer at selected temperatures.

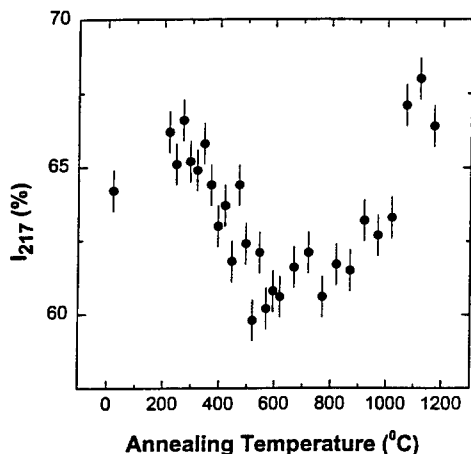


FIG. 1. The percentage of positrons,  $I_{217}$ , transmitted through the porous layer as a function of annealing temperature.

The decrease in mass between 20 and 200°C is probably due to the desorption of adsorbed gases. The 17% increase between 300 and 500°C most likely arises from the incorporation of oxygen to form

Table I. Relative change in layer mass as a function of heat treatment temperature.

Temp. (°C)	20	200	250	300	400	450	500	550
$\Delta m/m_o$ (%)	0	-5.8	-5.8	-5.8	2.0	7.7	11.3	11.3

silicon oxide replacing the hydrogen which effuses in this temperature range. Oxygen uptake under similar circumstances (heat treatments in an inert atmosphere) was also observed by Möller et al. [3] by means of infrared spectroscopy. As suggested above, the source of the oxygen is most likely the air adsorbed on the pore walls. Thus, the number of oxygen atoms involved is nearly 34% of the number of silicon atoms in the porous layers. If each oxygen atom satisfies two dangling bonds left by the effusion of hydrogen, the original hydrogen uptake during the formation of the porous silicon would be  $\sim 68\%$  of the number of silicon atoms, but this is undoubtedly an overestimate.

To adequately describe the lifetime spectra, five lifetimes,  $\tau_1$  to  $\tau_5$ , with associated intensities,  $I_1$  to  $I_5$ , were required. The longest lifetime,  $\tau_5$ , was obtained from a measurement using a coarse time calibration (100 ps/channel). This value was then fixed in the analysis of a lifetime spectrum measured with a finer time calibration (25 ps/channel) yielding the remaining components. The two shortest components,  $\tau_1$  and  $\tau_2$ , relate to parapositronium annihilation and the annihilation of positrons in the silicon substrate. The remaining three components are relevant to the porous layer and their lifetimes and intensities are shown in Figures 2 and 3. In Fig. 3 the intensities are normalized to the fraction of positrons annihilating in the porous layer. The intensity,  $I_1$ , of the parapositronium component, which is not shown, constitutes the balance to 100%.

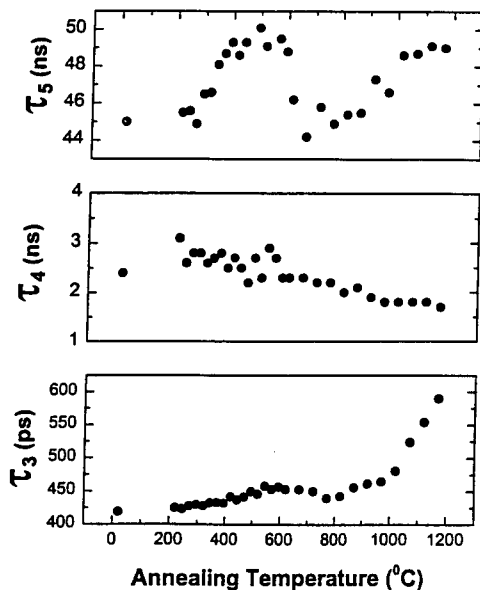


FIG. 2. Porous layer positron lifetimes as a function of annealing temperature.

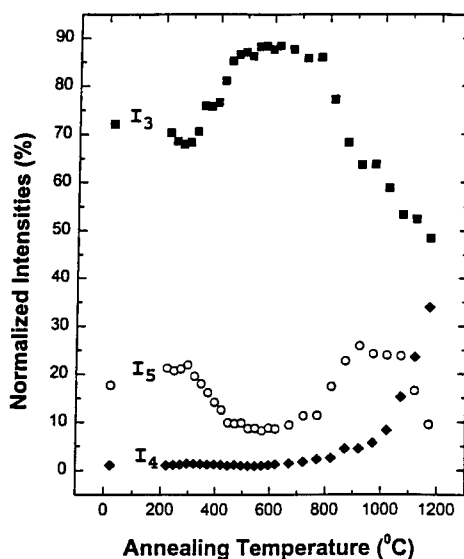


FIG. 3. Intensities of the lifetime components for the porous layer normalized to the fraction of positrons annihilating in the layer.

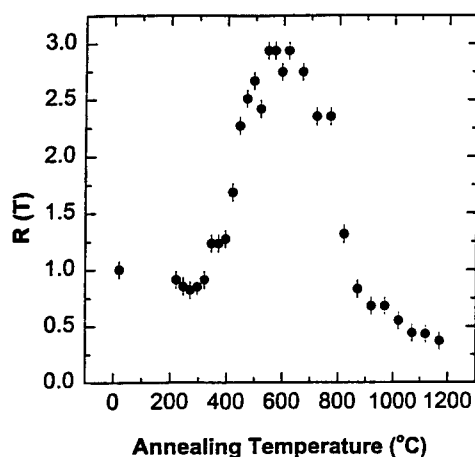


FIG. 4. Relative vacancy cluster concentration as a function of annealing temperature.

The lifetime  $\tau_3$  is attributed to vacancy clusters in the silicon oxide since the lifetime of  $\sim 450$  ps is substantially larger than for crystalline  $\text{SiO}_2$  (235 ps). Above  $900^\circ\text{C}$  there is substantial increase in cluster size (as indicated by the increase in  $\tau_3$ ), suggesting vacancy migration around  $900^\circ\text{C}$ . From the intensity of this lifetime component (see Fig. 3) the relative change in cluster concentration can be calculated, with results shown in Fig. 4. From this figure it is clear that the vacancy cluster concentration increases significantly during the oxygen uptake to  $500^\circ\text{C}$  as discussed above. Subsequently, relaxation takes place gradually up to  $\sim 900^\circ\text{C}$ , restoring the content of vacancies to the original level. Above this temperature further reduction to about one-third of the original value takes place, likely due to va-

cancy migration. The above suggests that the silicon oxide is heavily defected up to  $\sim 600^\circ\text{C}$ , but heat treatment above  $\sim 900^\circ\text{C}$  can significantly reduce the defect content. It is also at such high temperatures that good quality  $\text{SiO}_2$  must be grown on crystalline Si, an observation which points to the detrimental influence from vacancies. We also note that grown-in vacancies in single crystalline  $\text{SiO}_2$  undergo significant reduction in concentration and clustering around  $1000^\circ\text{C}$ .

The  $\tau_4$  component in Fig. 2 is attributed to positronium trapped at surface defects, the amount of which increases dramatically above  $1000^\circ\text{C}$  from  $\sim 3\%$  to  $35\%$  (see Fig. 3). The last lifetime,  $\tau_5$ , arises from positronium in the pores. This positronium interacts only weakly with the pore walls (as deduced from its large lifetime value in contrast to  $\tau_4$ ). Noteworthy is the sharp decrease around  $600^\circ\text{C}$  which suggests a stronger interaction possibly arising from a structural change in the surface of the silicon oxide. The intensity of the  $\tau_5$  component decreases above  $\sim 1000^\circ\text{C}$  while the intensity of the surface related  $\tau_4$  increases markedly. This indicates that surface traps are generated, thus increasing  $I_4$  at the expense of  $I_5$ .

### Conclusion.

Porous silicon undergoes several changes upon heat treatment. Hydrogen effusion (up to  $500^\circ\text{C}$ ) results in oxygen uptake (34% atomic), and a three-fold increase in vacancy cluster concentration in the silicon oxide. This increase is removed gradually above  $600^\circ\text{C}$  dropping below the original concentration only above  $\sim 900^\circ\text{C}$ . Above this temperature significant structural changes take place in the silicon oxide layer, reducing the vacancy content but at the same time increasing the "activity" of surface traps.



**References**

1. S. Gardelis and B. Hamilton. *J. Appl. Phys.* **76**, 5327 (1994).
2. S. Dannefaer, D. Kerr, D. Craigen, T. Bretagnon, T. Taliercio and A. Foucaran. *J. Appl. Phys.* **79**, 9110 (1996).
3. F. Möller, M. Ben Chorin and F. Koch. *Thin Solid Films* **255**, 16 (1995).

## LUMINESCENCE DUE TO ELECTRON-HOLE CONDENSATION IN SILICON-ON-INSULATOR AND ITS APPLICATION TO DEFECT AND INTERFACE CHARACTERIZATION

M. Tajima, S. Ibuka<sup>1</sup> and M. Warashina

Institute of Space and Astronautical Science, Yoshinodai, Sagamihara 229, Japan

<sup>1</sup>Science University of Tokyo, Kagurazaka, Shinjuku 162, Japan

**Keywords:** photoluminescence, silicon, silicon-on-insulator, electron-hole liquid, exciton

**Abstract.** Photoluminescence of silicon-on-insulator (SOI) wafers was investigated using ultraviolet (UV) light as an excitation source. A characteristic emission band appeared at liquid helium temperature with a shape similar to the electron-hole liquid signal. The band was observable over a wide temperature range up to room temperature with systematic peak shift and broadening. The spectral shape analysis of the band indicates that the emission occurs as a result of the recombination of photoexcited electrons and holes in their condensed phase. The condensation is realized, since UV light is absorbed predominantly in the SOI layer and the SOI structure prevents the photoexcited carriers from diffusing into the substrate. This was confirmed by the spectral dependence on the excitation intensity and the SOI layer thickness. We showed that the characteristic emission is sensitive to the microdefects and the interfacial quality, suggesting its applicability to the characterization of SOI wafers.

### Introduction.

A silicon-on-insulator (SOI) appears to be one of the most promising structures for a next generation device. Various techniques have recently been reported for producing high quality ultrathin SOI layers, such as separation by implanted oxygen (SIMOX) [1] and bond and etch-back SOI (BESOI) [2]. The thickness of the state-of-the-art SOI layers is a mere 100 nm, and characterization of such ultrathin SOI layers has so far been quite difficult.

We reported in an earlier paper [3] that a characteristic luminescence appeared in the SOI wafers under ultraviolet (UV) light excitation at 4.2 K, which we assumed is ascribable to electron-hole liquid (EHL) on the basis of its spectral similarity. In this report we investigate the dependence of the characteristic luminescence on the temperature, the excitation intensity and the sample properties. Since this luminescence is observable above the critical temperature of EHL and has a spectral shape similar to EHL, we refer to it hereafter "condensate" emission. We show that condensate emission is due to the radiative recombination of electrons and holes in their condensed phase. We demonstrate the applicability of the luminescence to the characterization of defects and interfaces in SOI wafers.

### Experimental procedures.

**Sample preparations.** Samples used for the present measurement were SIMOX and BESOI wafers. The SIMOX wafers were prepared by an oxygen implantation at a low dose condition of  $4 \times 10^{17} \text{ cm}^{-2}$ . The wafers were annealed to remove the implantation damage and to control the thickness of the SOI layer [1], SOI thickness ( $t_{\text{SOI}}$ ) was varied at 54, 75, 180, and 320 nm. Resistivity of the SOI layers was 20-30  $\Omega \cdot \text{cm}$  (boron-doped, *p*-type). The BESOI wafers with a 100 nm thick SOI layer were prepared by the plasma assisted chemical etching technique. The wafers were annealed to remove damages induced by the plasma etching and were covered with an oxide layer during annealing. Both SIMOX and BESOI wafers had the identical structure of substrate / buried oxide layer / SOI layer / surface oxide layer. For comparison we measured the samples whose oxide and SOI layers were removed by HF and alkaline solutions, respectively. The thickness and the resistivity of the SOI layer were nearly the same in the SIMOX and BESOI wafers. As a result, the essential features of the luminescence were the same between the two wafers. We will show the

results on the SIMOX wafers in this report. Detailed comparison between the two wafers is now being made.

**Photoluminescence measurements.** Photoluminescence (PL) spectra from the samples were taken at 4.2 - 295 K using UV light excitation from an Ar ion laser operated at 351 and 364 nm. Visible light excitation with a Kr ion laser operated at 647 nm was also used for comparison. The penetration depth of the UV and visible light in Si crystals is about 50 and 5000 nm, respectively [4]. The incident power and beam size on the sample surface were about 50 mW and 3 mm, respectively. The incident power was varied by three orders of magnitude to investigate the excitation intensity dependence. PL from the samples was analyzed with a grating monochromator ( $f = 0.67$  m,  $F = 4.7$ ) and detected by a photomultiplier (Hamamatsu R5509-41).

## Results and discussion

**Characteristic PL in SOI.** We compared the PL spectra from the following three types of samples at 4.2 K under both UV and visible light excitation: (a) the as-received SIMOX wafer (substrate /  $\text{SiO}_2$  / Si /  $\text{SiO}_2$ ), (b) the wafer without surface oxide layer (substrate /  $\text{SiO}_2$  / Si), and (c) the substrate. When the samples were excited by the visible light, the light penetrated deep into the substrate. Therefore, the emission came out predominantly from the substrate in all the samples; there was no substantial difference in the PL spectra among the samples. The PL spectra were identical with that shown in Fig. 1(c) explained later.

In contrast, a drastic change occurred under the UV light excitation: Figures 1(a), (b) and (c) are the PL spectra of samples (a), (b) and (c) of the SIMOX wafer with  $t_{\text{SOI}} = 75$  nm, respectively. The spectrum from sample (c) consists of free exciton (FE), boron bound exciton ( $B^1$ ), and boron bound multiple exciton complex ( $B^2$ ,  $B^3$ ) lines [5]. The subscript TO in the label denotes the transverse-optical-phonon sideband. This spectrum is generally observed in boron-doped Si crystals with a resistivity of about  $20 \Omega \cdot \text{cm}$ . Condensate emission appeared in sample (a), and disappeared in (b): The emission appeared if and only if the SOI layer was sandwiched by oxide layers. The spectral shape of condensate emission at 4.2 K was the same as that of EHL observed in conventional Si wafers under very high excitation intensity condition [6,7].

We believe that condensate emission originates from the electron-hole condensation in the SOI layer. The UV light can excite only the SOI layer because of the shallow penetration depth, and the excited carriers are confined within this layer by the presence of the diffusion barrier. If the SOI layer is sandwiched by the oxide layers, the recombination velocity at the interfaces becomes very low. This makes the density of electrons and holes extremely high even under a weak excitation condition.

The characteristic shape of condensate emission also supports this idea. Spectral shape of the radiative recombination of electrons and holes in

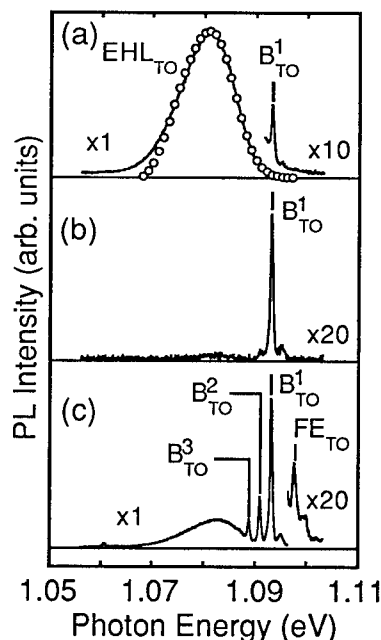


Fig. 1. PL spectra of SIMOX wafers ( $t_{\text{SOI}} = 75$  nm) at 4.2 K under UV light excitation. (a) as-received wafer, (b) wafer without surface oxide layer, and (c) substrate. Symbol "x10" denotes relative amplitude factor. Open circles indicates calculated spectral shape with  $n = 3.0 \times 10^{18} \text{ cm}^{-3}$  and  $T = 12$  K.

their condensed phase is given by the following equation [6,7]:

$$I(h\nu) = A \int_0^{h\nu - E_{\text{onset}}} D_e(E) D_h(h\nu - E_{\text{onset}} - E) f(E, F_e, T) f(h\nu - E_{\text{onset}} - E, F_h, T) dE \quad (1)$$

where  $D_e$  and  $D_h$  are densities of states of electron and hole, respectively,  $F_e$  and  $F_h$  are the respective quasi-Fermi energy,  $f$ 's are the respective Fermi functions,  $h\nu$  is the energy of emitted photon, and  $E_{\text{onset}}$  is the onset energy of condensate emission. Since the observed emission is the TO-phonon sideband,  $E_{\text{onset}}$  is equal to the effective bandgap energy for the condensed electrons and holes minus TO phonon energy. The values of  $F_e$  and  $F_h$  are determined by the carrier concentration ( $n$ ) and temperature ( $T$ ). The spectral shape of condensate emission was fitted by Eq. (1), taking  $n$ ,  $T$  and  $E_{\text{onset}}$  as adjustable parameters. Details of the curve fitting procedure will be described in a separate paper [8]. The best fit result is shown by open circles in Fig. 1(a), where  $T = 12$  K and  $n = 3.0 \times 10^{18} \text{ cm}^{-3}$ . There was close agreement between the calculated and observed spectra. The obtained  $n$  value coincides with the theoretical carrier density in EHL [6,7]. The discrepancy between the fitted  $T$  value and the measurement temperature is due to the local heating of the sample and to the difference between the carrier temperature and the lattice temperature. The estimated carrier temperature is lower than the critical temperature for EHL ( $\approx 25$  K). These results confirm for us that condensate emission at 4.2 K originates from EHL.

**Temperature dependence.** Electron-hole condensation should occur in the SOI layer under the UV light excitation regardless of the sample temperature, while EHL cannot exist above the critical temperature. It is, therefore, interesting to investigate the temperature dependence of condensate emission from the SOI layer. Figure 2 shows the PL spectra of the same sample as Fig. 1(a) at temperatures between 12 and 293 K; solid and broken lines were taken under the UV and visible light

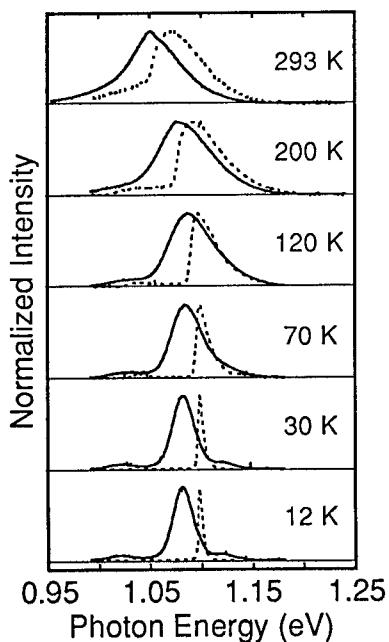


Fig. 2. Temperature dependence of PL spectra of SIMOX wafer ( $t_{\text{SOI}} = 75$  nm). Solid and broken lines are spectra taken under UV and visible light excitation, respectively

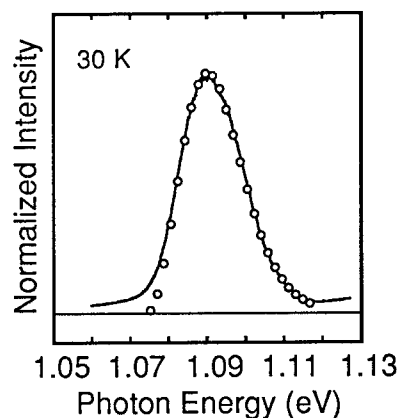


Fig. 3. PL spectrum of SIMOX wafers ( $t_{\text{SOI}} = 75$  nm) at 30 K under UV light excitation. Open circles indicates calculated spectral shape with  $n = 3.0 \times 10^{18} \text{ cm}^{-3}$  and  $T = 45$  K.

excitations, respectively. Condensate emission was observable above the critical temperature under the UV light excitation and, surprisingly, remained up to room temperature. The nearly symmetric shape of condensate emission is in marked contrast to the Boltzmann-shape of the FE line observed from the substrate under the visible light excitation.

Electron-hole condensation above the critical temperature leads to the formation of electron-hole plasma (EHP) [9]. The spectral shape of the EHP emission is also given by Eq. (1). The shape of the spectrum at 30 K fitted well with Eq. (1), as shown by open circles in Fig. 3. The adjustable parameters in the fitting procedure were  $T = 45$  K and  $n = 3.0 \times 10^{18} \text{ cm}^{-3}$ . It is reasonable that the present spectrum at 30 K is fitted well by the same  $n$  value as that at 4.2 K, since the excitation condition is nearly the same. The difference in the temperature between the fitting parameter (45 K) and the measured value (30 K), which is larger than that for the spectrum at 4.2 K, is possibly due to the error in temperature measurement because of the heat-conduction-type sample holder of the temperature-variable cryostat. A good agreement between the observed and calculated spectra leads us to suggest that condensate emission above the critical temperature originates from EHP. This is further investigated in the following section.

**Excitation intensity dependence.** According to the phase diagram of electron-hole condensation in Si, FE's are dissociated into EHP when the density of FE reaches the Mott criterion [9]. The density of electrons and holes in the EHP increases with the excitation intensity, resulting in the broadening and red-shift of the emission band. This contrasts remarkably with the EHL emission below the critical temperature, which shows neither broadening nor red-shift. We examined the excitation intensity dependence of condensate emission to check whether or not the emission is really due to EHP.

The PL spectra of the SIMOX wafer with  $t_{\text{SOI}} = 75$  nm at 30 K are shown in Fig. 4 as a function of the excitation intensity. At the lowest excitation intensity a typical FE luminescence appeared with

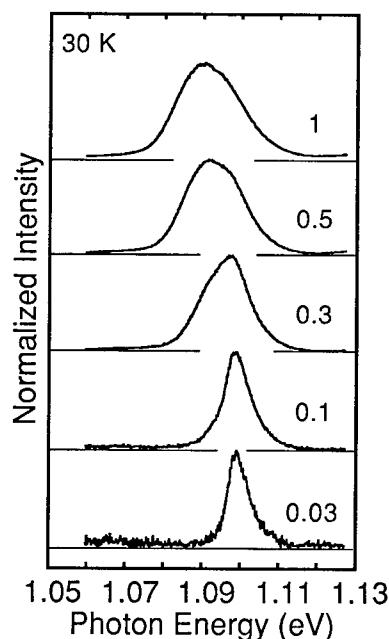


Fig. 4. Excitation intensity dependence of condensate emission from SIMOX wafer ( $t_{\text{SOI}} = 180$  nm) at 30 K under UV light excitation. Numbers adjacent to the spectra indicate relative excitation intensities.

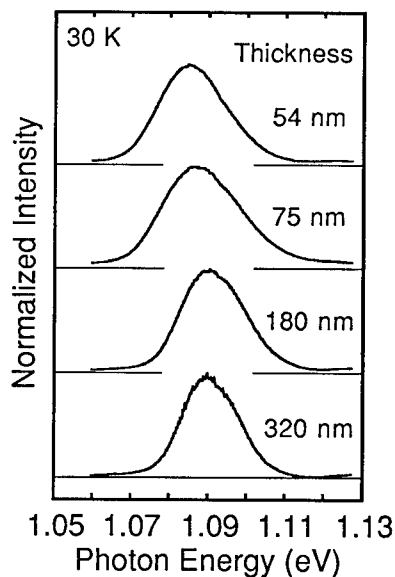


Fig. 5. Effect of SOI thickness on EHP luminescence from SIMOX wafer at 30 K.

the Boltzmann shape. The spectral shape changed gradually with the excitation intensity: The peak shifted toward the low energy side and the halfwidth broadened. This change agrees with that expected for the FE-EHP transition mentioned above, which confirms the idea that condensate emission above the critical temperature originates from EHP.

**Sample dependence.** In the preceding sections we have shown the characteristics of condensate emission. Those characteristics were commonly observed in the SOI samples with a surface oxide layer. Now we will show variations of this emission, depending on the sample properties.

Figure 5 shows the effect of the thickness of the SOI layer in SIMOX wafers on the EHP luminescence at 30 K. As the thickness decreased, the peak position of the EHP emission shifted to the low energy side and its halfwidth broadened. This tendency is substantially the same as the excitation intensity dependence (Fig. 4), where the smaller thickness corresponds to the higher excitation intensity. This is explained by the fact that the volume in which EHP is confined decreases with decrease in SOI thickness, resulting in an increase of the plasma density.

Sample dependent variation was also found in the excitation intensity dependence of the condensate emission at 16 K. Two typical excitation intensity dependences are shown in Fig. 6. Since the temperature of 16 K is lower than the critical temperature for the EHL formation, we can expect the coexistence of FE and EHL [9]. As expected, both FE and EHL were observed in the first type of dependence (Fig. 6(a)). The EHL emission appeared even under the weakest excitation intensity condition and dominated the spectra under higher excitation. However, the EHL emission was not observed under the weak excitation condition in the second type dependence, as shown in Fig. 6(b). Instead, the evolution of the EHP-like emission was recognized by increasing the excitation intensity. A similar spectral change was observed in bulk Si and was interpreted by a modified phase diagram for FE, EHP and EHL [10]. We measured four samples: Two samples showed the first type dependence and the others showed the second type. We have not yet identified the difference in

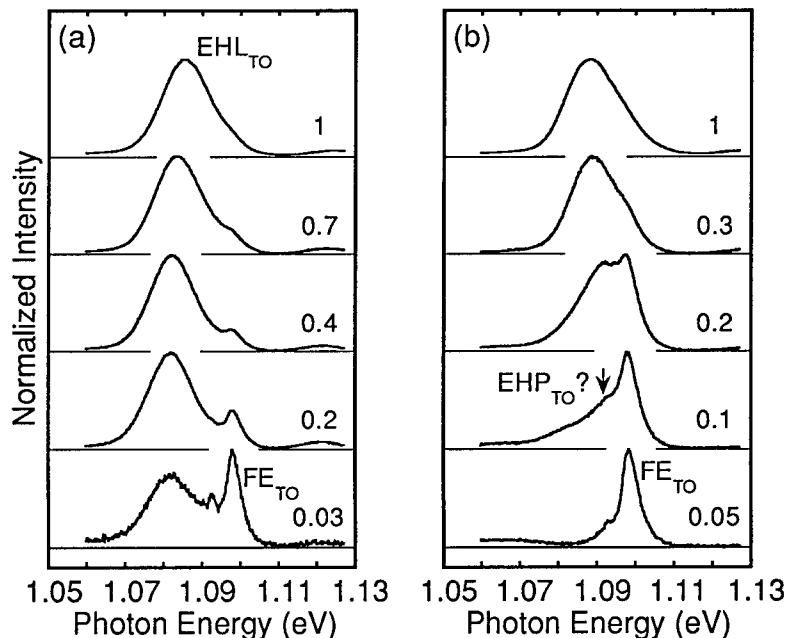


Fig. 6. Two types of excitation intensity dependence of condensate emission from SIMOX wafers at 16 K under UV light excitation. EHL emission appears at low excitation intensity in the first type (a), while evolution of EHP with excitation intensity is recognized in the second type (b).

properties between these two sample groups.

We speculate that microdefects and interfacial irregularities act as the nucleation centers for EHL. Thus, the density of the microdefects and/or the degree of the interfacial irregularities are higher in the samples showing the first type dependence than in those showing the second type. Further analysis on the sample dependent variation of condensate emission should allow us to characterize microdefects in the SOI layer and the interfacial quality.

### Conclusion.

We have investigated condensate luminescence from SOI wafers excited by UV light in the temperature range between 4.2 and 295 K. The spectral shape of the emission at 4.2 K and that at 30 K were fitted well by the theoretical calculation for electrons and holes recombining from their condensed phase with the adjustable parameter of the carrier concentration being  $3.0 \times 10^{18} \text{ cm}^{-3}$ . This value is equal to the reported critical carrier concentration for EHL. Condensate emission showed red-shift and spectral broadening with increasing excitation intensity and with decrease in SOI layer thickness. These confirm the idea that the photoexcited carriers are confined in the SOI layer and reach their condensed phase. We demonstrated the applicability of the condensate emission to characterization of the microdefects and the interfacial quality of SOI wafers.

### Acknowledgments.

The authors would like to thank E. Otsuka of Fukui University of Technology and H. Nakata of Osaka University for valuable comments and discussions on EHL and EHP, and M. Saito and J. Jablonski of Komatsu Electronic Metals Co., Ltd. for the preparation of SIMOX wafers. This work was partly supported by the Japan Society for the Promotion of Science.

### References.

1. S. Nakashima, T. Katayama, Y. Miyamura, A. Matsuzaki, M. Kataoka, D. Ebi, M. Imai, K. Izumi and N. Ohwada, *J. Electrochem. Soc.* **143**, 244 (1996).
2. T. Abe, M. Nakano and T. Itoh in "Silicon-on-Insulator Technology and Devices" ed. D. N. Schmidt (Pennington, NJ: The Electrochemical Society) pp. 61-71 (1990).
3. M. Tajima, S. Ibuka, H. Aga and T. Abe, *Appl. Phys. Lett.* **70**, 231 (1997). We used the term "electron-hole droplet (EHD)" to specify the condensed phase of electrons and holes in Ref. [3]. To be accurate, EHD means a certain volume in which the liquid phase of electron-hole condensation is confined. In the present paper we consider it appropriate to use the term "electron-hole liquid (EHL)" to specify the condensed phase.
4. W. C. Dash and R. Newman, *Phys. Rev.* **99**, 1151 (1955).
5. M. L. W. Thewalt, *Can. J. Phys.* **55**, 1463 (1977).
6. Ya. Pokrovskii, *Phys. Status Solidi (a)* **11**, 385 (1972).
7. R. B. Hammond, T. C. McGill and J. W. Mayer, *Phys. Rev. B* **13**, 3566 (1976).
8. S. Ibuka, M. Tajima, M. Saito, J. Jablonski, M. Warashina and K. Nagasaka, in preparation.
9. J. Shah, M. Combescot and A. H. Dayem, *Phys. Rev. Lett.* **38**, 1497 (1977).
10. L. M. Smith and J. P. Wolfe, *Phys. Rev. Lett.* **57**, 2314 (1986).

## DEEP ELECTRONIC STATES AT THE INVERTED AlAs/GaAs INTERFACE UNDER DIFFERENT GROWTH MODES

P. Krispin, R. Hey, H. Kostial, and K. H. Ploog

Paul-Drude-Institut für Festkörperelektronik, Hausvogteiplatz 5-7, D-10117 Berlin, Germany

**Keywords:** AlAs growth modes, GaAs-on-AlAs interface, intrinsic deep-level defects

**Abstract.** At the GaAs-on-AlAs interface grown by molecular beam epitaxy (MBE), deep electronic states are observed by deep-level transient spectroscopy and capacitance-voltage measurements. It is shown that the generation of two electron traps at this AlAs/GaAs interface is related to the growth mode of the AlAs layer. For the two-dimensional growth modes, the trap concentrations are lowest. We attribute the deep levels to intrinsic defects, which are steadily formed during growth on the AlAs surface. The defects are incorporated into the AlAs layer close to the interface. When AlAs is grown in the pseudo-two-dimensional mode at the rather low temperature of 550 °C, the total charge density at the GaAs-on-AlAs interface can be minimized.

### Introduction

The properties of the  $\text{Al}_x\text{Ga}_{1-x}\text{As}/\text{GaAs}$  interface have significant consequences for the characteristics of heterojunction-based semiconductor structures. It is well established that the electronic properties of the inverted (GaAs on  $\text{Al}_x\text{Ga}_{1-x}\text{As}$ ) interface are inferior to those of the normal ( $\text{Al}_x\text{Ga}_{1-x}\text{As}$  on GaAs) interface. The origin for this asymmetry has not been fully understood yet. One reason might be the interface roughness induced by the lower Al mobility on the  $\text{Al}_x\text{Ga}_{1-x}\text{As}$  surface during MBE growth [1]. Furthermore, interface charges can arise from the segregation of ambient impurities [2-4]. It has been demonstrated for example that oxygen can accumulate at the inverted interface [2,4]. In Si-doped isotype heterojunctions, however, such an accumulation of oxygen has not been observed [5]. Using deep-level transient spectroscopy (DLTS) [6], we have recently found a series of electron traps, which appear at the Si-doped inverted  $\text{Al}_x\text{Ga}_{1-x}\text{As}/\text{GaAs}$  interface [7]. Their occurrence on the  $\text{Al}_x\text{Ga}_{1-x}\text{As}$  side of the heterojunction is characteristic for the inverted interface in the entire composition range.

In order to study the mechanism, by which these interfacial defect states are formed, we have examined GaAs-on-AlAs interfaces grown under different conditions. It is known that three-dimensional (3D) growth of AlAs occurs in a *forbidden window* between 600 and 680 °C [8,9]. This growth mode identified by the formation of facets results in a rough surface [9,10]. The 2D mode at temperatures above 680 °C leads to a smooth AlAs surface. In addition, a re-entrant pseudo-2D mode can be realized with sufficiently high  $\text{As}_4$  flux at temperatures below 600 °C, as indicated by oscillations of reflection high-energy electron diffraction (RHEED) intensities [8,9]. The pseudo-2D growth mode also provides an AlAs surface without facets. Since there is no similar peculiarity for GaAs, the inverted interface between GaAs and AlAs should reflect the distinct AlAs growth modes. We show that the generation of two electron traps at the inverted AlAs/GaAs interface is related to the AlAs growth mode. The deep levels probably originate from native point defects, which are formed on the growing AlAs surface and hold back at the inverted interface. The total density of interfacial charges is lowest, when the AlAs layer is grown in the pseudo-2D mode.

### Experimental

Isotype AlAs/GaAs heterojunctions were grown by conventional MBE on n-type GaAs(001) substrates without growth interruption. The growth rate was 0.4  $\mu\text{m}/\text{h}$  for both the GaAs and the AlAs layers. Si was used as dopant. The temperature of the Si cell was kept constant during growth of the heterojunction and resulted in an electron density of about  $1 \times 10^{17} \text{ cm}^{-3}$ . The 2D, 3D, and



pseudo-2D modes of AlAs growth were, respectively, realized at temperatures of 680, 610, and 550 °C with similar As<sub>4</sub> fluxes. 2D (including pseudo-2D) and 3D growth of the AlAs layer were verified by the observation of straight and chevron-shaped RHEED features, respectively. Only for the 2D and the pseudo-2D modes, persistent oscillations of the RHEED intensity were observed. The heterostructures consisted of 240 nm AlAs embedded in GaAs. The thickness of the top GaAs layer was about 200 nm. Vacuum-deposited Al dots on the GaAs top layer were applied as Schottky contacts for the electrical measurements.

In order to determine the depth profile of the free carrier concentration, the capacitance  $C$  was measured as a function of the applied bias voltage  $V$  (C-V method) [11]. The apparent free electron concentration  $N_{C-V}$  at the edge of the space-charge layer was obtained from the expression

$$N_{C-V}(W) = \frac{2}{A^2 q \epsilon \epsilon_0} \left[ \frac{d}{dV} \left( \frac{1}{C^2} \right) \right]^{-1}, \quad (1)$$

where  $A$  denotes the contact area,  $\epsilon \epsilon_0$  the dielectric constant, and  $q$  the elementary charge. The depth  $W$  was calculated from the depletion capacitance  $C$  using  $W(V) = \epsilon \epsilon_0 A / C(V)$ . By applying the dc bias in reverse direction, the space charge layer edge below the contact could be shifted across the inverted AlAs/GaAs interface.

The deep levels at the inverted AlAs/GaAs interface were investigated by a particular capacitance method based on the release of carriers from interface states [12] and by the DLTS technique [6]. During the measurement the conductance in parallel to the capacitance was controlled to verify that the loss factor of the diode is always less than 0.1. The effective thermal activation energy  $E_{th}$  of the electronic states was determined from the temperature dependence of the emission rate  $e_n$  for electrons from the deep level into the conduction band according to  $e_n = \sigma_n v_{th} N_C \exp(-E_{th}/kT)$  [6], where  $\sigma_n$  denotes the capture cross section of the deep level for electrons at high temperature,  $v_{th}$  the thermal velocity of electrons in the conduction band, and  $N_C$  the effective density of states of the conduction band.

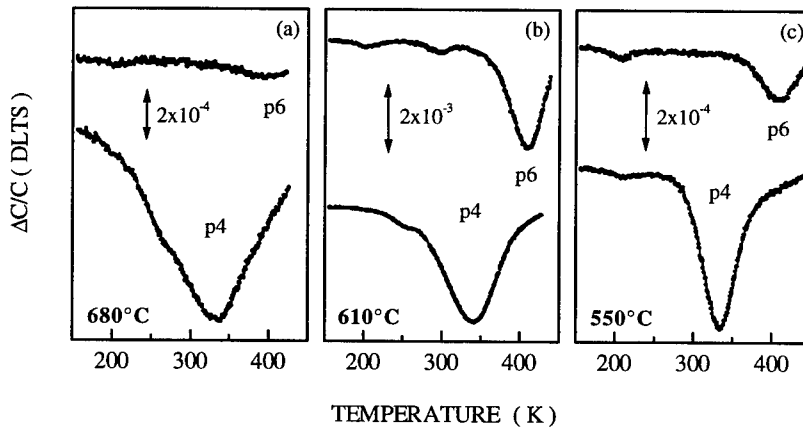


**Fig. 1.** Deep-level spectra (emission rate 90 s<sup>-1</sup>, filling pulse width 0.1 ms) for Si-doped inverted AlAs/GaAs interfaces grown at (a) 680, (b) 610, and (c) 550 °C. The resolution of the DLTS signals  $\Delta C/C$  is indicated. Filling pulses of 0.5 V and 1 V were applied for the spectra of the levels p4 and p6, respectively. The DLTS curves are offset for clarity.

### Results and discussion

Using the DLTS technique, interface traps can be distinguished from bulk states, since the DLTS peak height for spatially confined states becomes highest, when the Fermi level crosses the particular interfacial level at a specific bias value. From our studies on AlAs/GaAs heterostructures it can be deduced that the Si-doped GaAs and AlAs layers were practically free of electron traps (cf. also Ref. 7). A series of deep levels was, however, found at the inverted AlAs/GaAs interface [7]. In the following, we concentrate on the interfacial levels p4 at 0.60 eV and p6 at 0.95 eV below the AlAs conduction band edge [7].

For the AlAs/GaAs heterojunctions grown at 680, 610, and 550 °C with similar  $\text{As}_4$  fluxes, typical spectra of the DLTS signal  $\Delta C/C$  are shown in Figs. 1(a), 1(b), and 1(c), respectively. The deep-level spectra in Fig. 1 were measured at biases, where the responses of the levels p4 and p6 are maximal. In spite of the interface roughness, which is especially produced by the 3D growth of the AlAs layer, discrete levels are clearly indicated in Fig. 1. The interface seems to be reasonably perfect on an atomic scale. It is seen in Fig. 1 that the maximum peak height for both electron traps is strongly related to the AlAs growth mode and, in particular, by about one order of magnitude higher, if the interface is formed after 3D growth of the AlAs layer (Fig. 1(b)). The interfaces grown under 2D and pseudo-2D mode conditions for the AlAs layer (Figs. 1(a) and 1(c)) exhibit about the same contents of the interfacial levels p4 and p6. Since their concentrations are minimized for both the 2D and the pseudo-2D growth modes, it is suggested that both traps are associated with imperfect processes on the AlAs surface during growth.

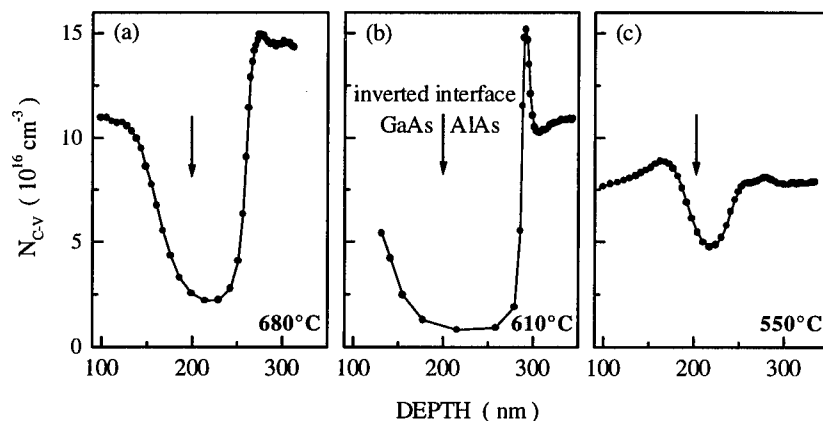


**Fig. 2.** Depth profiles of the apparent electron concentration  $N_{C,V}$  (measured at 300 K and 100 kHz) for Si-doped inverted AlAs/GaAs interfaces grown at (a) 680, (b) 610, and (c) 550 °C. The positions of the inverted AlAs/GaAs interfaces are indicated by arrows. Note the same horizontal and vertical scales in (a), (b), and (c).

For the heterointerfaces grown at 680, 610, and 550 °C, the depth profiles of the apparent electron concentration  $N_{C,V}$  are displayed in Figs. 2(a), 2(b), and 2(c), respectively. The positions of the inverted interface are indicated. The depth profiles differ remarkably from each other. Note the identical scaling in Figs. 2(a) - 2(c). The interfaces grown at 680 and 610 °C show a large carrier deficit of about  $1 \times 10^{12} \text{ cm}^{-2}$ , which is due to a high concentration of electron traps at the inverted interface. When AlAs is grown in the pseudo-2D mode at 550 °C, electrons are accumulated on the GaAs side of the inverted AlAs/GaAs interface (cf. Fig. 2(c)), because the total density of electron traps is drastically reduced to a level of about  $4 \times 10^{10} \text{ cm}^{-2}$ .

The bumps in the  $N_{C-V}$  vs depth profiles just below 300 nm originate from additional capacitance contributions of discrete electronic levels at the interface [11,12]. The release of captured electrons from interface levels, which at sufficiently high reverse biases gives rise to the apparent carrier enhancement, can be employed for a spectroscopy of spatially confined traps (release spectroscopy). Applying the model of Ikeda et al. [12], the energy distribution of the interface state density  $N_{is}(E_t)$  is calculated from

$$N_{is} = \left( \frac{N_{C-V} - I}{N_D} \right) \frac{\epsilon \epsilon_0 W(V)}{q^2 W_i (W(V) - W_i)} \quad \text{and} \quad (2a)$$

$$E_{Fn} - E_t = \frac{q^2 N_D}{2 \epsilon \epsilon_0} (W(V) - W_i)^2, \quad (2b)$$

where  $N_D$  denotes the doping density,  $W_i$  the location of the interface, and  $E_{Fn}$  the position of the bulk Fermi level. The level position  $E_t$  may differ from the thermal activation energy  $E_{th}$  due to a thermally activated capture process [6,11]. In contrast to the DLTS method, the release spectroscopy is not affected by the filling process. Actual numbers of interfacial traps per unit area can be therefore directly determined.

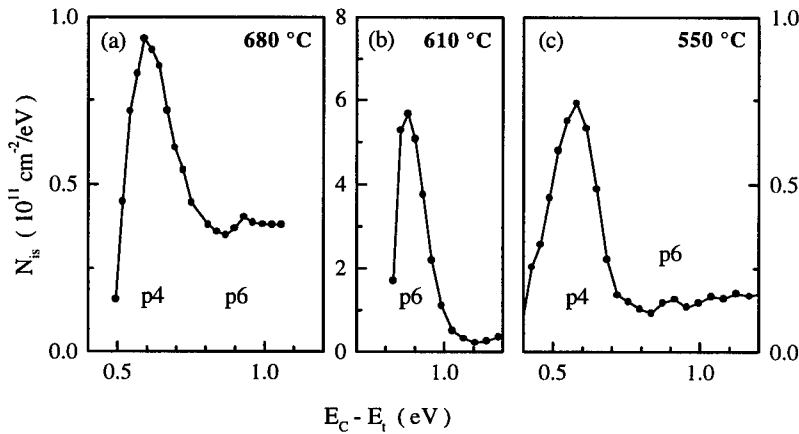


**Fig. 3.** Energy distributions of the state density  $N_{is}$  at the inverted AlAs/GaAs interface (release spectra) as obtained by Eq. (2) from C-V measurements on the samples studied in Fig. 2.  $E_C$  is the AlAs conduction band edge. Note the same energy scaling.

For the GaAs-on-AlAs interfaces studied in Fig. 2, release spectra are depicted in Fig. 3. In accordance with the DLTS result for the electron traps p4 and p6, signals of discrete levels are found at energies of about 0.6 and 0.9 eV. Since the peaks in Fig. 3 originate exclusively from spatially confined electronic states, the interfacial character of the DLTS levels p4 and p6 is confirmed by the release spectra. The largest contribution ( $5.7 \times 10^{11} \text{ cm}^{-2}/\text{eV}$ ) is observed for the level p6 at the AlAs/GaAs interface grown at 610 °C. The area below the p6 signal in Fig. 3(b) corresponds to an interface state density of about  $6.5 \times 10^{10} \text{ cm}^{-2}$ . Unfortunately, the release of electrons from shallower traps cannot be observed at that interface, since the electrons are immediately captured by the deeper level p6. For the heterojunctions grown at 680 and 550 °C, contributions of both levels are found (Figs. 3(a) and 3(c)), because the density of the interfacial level p6 is strongly reduced and by far lower than that of the trap p4.

**Table I.** Characteristic data for the electron traps p4 and p6 as well as the total carrier deficit at the GaAs-on-AlAs interfaces studied: The capacitance contributions  $\Delta C/C$  were obtained from DLTS measurements. The actual interface state densities  $N_i$  were determined from release spectra. The total carrier deficit was measured by the C-V method. The AlAs layers were grown in different modes with similar  $\text{As}_4$  fluxes.

AlAs growth	Electron trap p4		Electron trap p6		Carrier deficit (cm <sup>-2</sup> ) (C-V)
	$\Delta C/C$ (DLTS)	$N_i(\text{cm}^{-2})$ (Release)	$\Delta C/C$ (DLTS)	$N_i(\text{cm}^{-2})$ (Release)	
<b>2D mode at 680 °C</b>	$7.5 \times 10^{-4}$	$2.0 \times 10^{10}$	$7.0 \times 10^{-5}$	$\leq 2 \times 10^9$	$8.5 \times 10^{11}$
<b>3D mode at 610 °C</b>	$3.3 \times 10^{-3}$	-	$3.0 \times 10^{-3}$	$6.5 \times 10^{10}$	$1.5 \times 10^{12}$
<b>Pseudo-2D mode at 550 °C</b>	$4.0 \times 10^{-4}$	$1.5 \times 10^{10}$	$1.2 \times 10^{-4}$	$\leq 2 \times 10^9$	$4.0 \times 10^{10}$

Characteristic data of the GaAs-on-AlAs interfaces, which were realized with different AlAs growth modes, are compiled in Table I. The 2D mode at 680 °C as well as the pseudo-2D mode at 550 °C lead to reduced densities of about  $2 \times 10^{10} \text{ cm}^{-2}$  and below  $2 \times 10^9 \text{ cm}^{-2}$  for the traps p4 and p6, respectively. DLTS and release spectra demonstrate that there is practically no difference between both growth modes as far as the interfacial traps p4 and p6 are concerned. The total carrier deficit, however, is minimized exclusively by the pseudo-2D growth mode at 550 °C. In this case, the interface charge of the trap p4 becomes comparable to the total carrier deficit at the inverted AlAs/GaAs interface (cf. Table I). The remaining charge difference is likely due to traps in the lower half of the AlAs band gap.

The levels p4 and p6 are probably associated with intrinsic defects on the growing AlAs surface, because their formation is largely suppressed by the nearly perfect growth in the 2D mode at higher temperature as well as in the pseudo-2D mode at lower temperature. Oxygen might be neglected as the origin of both interfacial levels, since a pile-up of oxygen was never observed at Si-doped inverted interfaces [5]. Moreover, the levels p4 and p6 were not detected in the AlAs layer, although impurity atoms were certainly incorporated into AlAs. An intrinsic origin seems also to be indicated by the compositional dependence of the levels p4 and p6 in  $\text{Al}_x\text{Ga}_{1-x}\text{As}$  [7].

### Conclusions

The electronic properties of the inverted AlAs/GaAs interface can be optimized, when the AlAs layer is grown in the pseudo-2D mode at comparatively low temperatures. Because the total density of interface charges becomes sufficiently low under this condition, we achieve the accumulation of free electrons on the GaAs side of the inverted interface. The electron traps p4 and p6 at the GaAs-on-AlAs interface are related to the AlAs growth mode and likely due to intrinsic defects which are continuously formed on the AlAs surface during growth. The defects are incorporated into the last AlAs sheet, when GaAs is grown on top. The optimization of the growth kinetics on the AlAs surface can be therefore investigated via the electronic states at the inverted AlAs/GaAs interface.

Our results on interfacial traps are in accordance with the observation that the photoluminescence of  $\text{Al}_x\text{Ga}_{1-x}\text{As}/\text{GaAs}$  structures is improved at higher as well as at lower growth temperatures [13,14]. One reason for the higher electron mobilities achieved in inverted  $\text{Al}_x\text{Ga}_{1-x}\text{As}/\text{GaAs}$  heterojunctions

with growth temperatures below 600 °C [15-18] and above 680 °C [1] could be the lower density of interfacial defects under pseudo-2D and 2D growth mode conditions, respectively.

#### Acknowledgment

The authors would like to thank H. T. Grahn for a critical reading of the manuscript. The technical assistance of M. Hōricke with the sample growth is gratefully acknowledged.

#### References

- [1] H. Morkoç, T. J. Drummond, R. Fischer, and A. Y. Cho, *J. Appl. Phys.* **53**, 3321 (1982).
- [2] T. Achnich, G. Burri, M. A. Py, and M. Ilegems, *Appl. Phys. Lett.* **50**, 1730 (1987).
- [3] R. S. Miller, W. T. Tsang, and O. Munteanu, *Appl. Phys. Lett.* **41**, 374 (1982).
- [4] N. Chand, S. N. G. Chu, and M. Geva, *Appl. Phys. Lett.* **59**, 2874 (1991).
- [5] N. Chand, E. A. Fitzgerald, and M. Geva, *Appl. Phys. Lett.* **61**, 2893 (1992).
- [6] D. V. Lang, *J. Appl. Phys.* **45**, 3014 (1974); *ibid.* **45**, 3023 (1974).
- [7] P. Krispin, R. Hey, and H. Kostial, *J. Appl. Phys.* **77**, 5773 (1995).
- [8] A. M. Dabiran, S. K. Nair, H. D. He, K. M. Chen, and P. I. Cohen, *Surf. Sci.* **298**, 384 (1993) and references therein.
- [9] A. M. Dabiran and P. I. Cohen, *J. Cryst. Growth* **150**, 23 (1995).
- [10] R. Mirin, M. Krishnamurthy, J. Ibbetson, A. Gossard, J. English, and P. Petroff, *Materials Research Soc. Symposium Proc.* **312**, 273 (1993).
- [11] P. Blood and J. W. Orton, *The Electrical Characterization of Semiconductors: Majority Carriers and Electron States* (Academic, London, 1992).
- [12] E. Ikeda, H. Hasegawa, S. Ohtsuka, and H. Ohno, *Jpn. J. Appl. Phys.* **27**, 180 (1988).
- [13] W. T. Tsang, F. K. Reinhart, and J. A. Ditzenberger, *Appl. Phys. Lett.* **36**, 118 (1980).
- [14] N. Chand, T. D. Harris, S. N. G. Chu, E. E. Becker, A. M. Sergent, M. Schnoes, and D. V. Lang, *J. Cryst. Growth* **111**, 20 (1991).
- [15] U. Meirav, M. Heiblum, and F. Stern, *Appl. Phys. Lett.* **52**, 1268 (1988).
- [16] T. Sajoto, M. Santos, J. J. Heremans, M. Shayegan, M. Heiblum, M. V. Weckwerth, and U. Meirav, *Appl. Phys. Lett.* **54**, 840 (1989).
- [17] D. Kim, A. Madhukar, K.-Z. Hu, and W. Chen, *Appl. Phys. Lett.* **56**, 1874 (1990).
- [18] T. Saku, Y. Horikoshi, and S. Tarucha, *Jpn. J. Appl. Phys.* **33**, 4837 (1994).

## TEM-STUDY OF FRANK PARTIAL DISLOCATIONS IN ZnSe/GaAs(001) CAUSED BY SUBSTRATE-PREPARATION

**H. Preis<sup>\*</sup>, T. Frey<sup>1</sup>, T. Reisinger and W. Gebhardt**

**Institut für Festkörperphysik, Universität Regensburg, 93040 Regensburg, Germany**

**<sup>1</sup>Universität-GH Paderborn, Warburger Str. 100, 33095 Paderborn, Germany**

**<sup>\*</sup>Corresponding author: Tel.: +49 941/943-2066; Fax.: +49 941/943-4226; e-mail: Herbert.Preis@physik.uni-regensburg.de**

**Keywords:** ZnSe, GaAs, MBE, TEM, RHEED, QMS, Frank partial dislocations, hydrogen

### Abstract

A detailed study is presented about the formation of Frank partial dislocations (FPDs) in ZnSe/GaAs (001) grown by molecular beam epitaxy (MBE). The investigations were carried out by transmission electron microscopy (TEM), reflection high energy electron diffraction (RHEED) and quadrupole mass spectrometry (QMS).

The GaAs-substrates are pretreated in two steps: a wet chemical etching and a subsequent treatment with a hydrogen(H)-plasma in the growth chamber. Plan-view-TEM micrographs reveal a strong dependence of the FPD density on the time of chemical etching as well as on the substrate temperature during H-plasma etching. Without further precautions the RHEED pattern show thus a (2x1)-reconstruction. However, if the H-plasma treatment proceeds under Zn-stabilised conditions the (2x1)-reconstruction disappears and the generation of FPDs in the growing layer is reduced. Since the (2x1)-reconstruction results from the formation of a Ga<sub>2</sub>Se<sub>3</sub>-layer at the interface, it is suggested that the presence of Zn-atoms suppresses the formation of Ga-Se-bonds. Small amounts of H<sub>2</sub>Se act as a Se-source and lead to the formation of Ga<sub>2</sub>Se<sub>3</sub> observed in QM-spectra during plasma activation. The H<sub>2</sub>Se-partial pressure can be drastically reduced by cooling the cryoshields in the growth-chamber with liquid nitrogen. After optimizing the substrate preparation on the line described we succeeded in a reduction of the Frank defect density to  $6 \cdot 10^6 \text{ cm}^{-2}$ .

### Introduction

Since the first blue emitting laser structure based on ZnSe was realized [1] degradation limits its lifetime and therefore the potential application as a device. The main reason of degradation seems to be the nucleation of stacking faults in the ZnSe/GaAs interface region. This nucleation occurs during the initial stages of growth which are often 3-dimensional and are correlated with the formation of a Ga<sub>2</sub>Se<sub>3</sub>-interlayer [2]. Dark line defects which develop from these dislocations reduce the luminescence efficiency [3]. In the present work the nucleation of dislocations at the interface is studied during the initial growth especially in its dependence on substrate preparation. Much work has been done to optimize the initial growth of ZnSe on GaAs buffer layers varying the surface stoichiometry of the layer during the growth start [4]. Furthermore the influence of GaAs-surface termination before growth [5] and the growth mode (MBE or ALE) as a function of several growth parameters were studied [6]. In all these investigations a GaAs-buffer layer is grown which needs a separate III-V MBE-chamber with a UHV transport system in order to avoid an oxidation of the GaAs-surface prior the II-VI growth. We have studied how far growth optimization is possible without a GaAs buffer.

Ga<sub>2</sub>O<sub>3</sub> formed during wet etching of the substrate can be desorbed thermally at 580°C, a process which leads to As-deficiency correlated with a high FPD density in the subsequently grown II-VI-layer [7]. In contrast, the use of atomic hydrogen for desoxidation the substrate temperature can be lowered to about 350°C. At this moderate temperature a removal of Ga<sub>2</sub>O<sub>3</sub> [8] as well as an As-rich ((2x4)-reconstruction) surface is observed [9] but also As-deficiency is discussed [10]. The authors of ref. [8] suggest that atomic H reduces Ga<sub>2</sub>O<sub>3</sub> to Ga<sub>2</sub>O, which is a volatile oxide and desorbs at 350°C. Yu et al. [11] estimated a minimal defect density less than  $10^4 \text{ cm}^{-2}$  in ZnSe grown directly

on hydrogen cleaned GaAs-substrates. The authors used optical fluorescence microscopy and related their results with extended stacking faults which act as nonradiative recombination centers. The samples of Yu et al. were grown to a layer thicknesses of  $2\mu\text{m}$ , which greatly reduced the density of extended stacking faults. In a preceding publication of our group plan-view TEM investigations of dislocation reactions has been carried out [12]. It was found that extended stacking faults initially formed annihilate within a thickness range of 300 to 900 nm. On the other hand threading segments of dislocations are found after strain relaxation with a density of  $10^8\text{cm}^{-2}$  [12]. In this work we investigate the wetchemical and H-plasma preparation of the substrate and its influence on the density of Frank partial dislocations (FPDs). These were directly observed in 50-60nm thick ZnSe/GaAs samples by plan-view TEM. Furthermore the partial pressure of Se was recorded by QM-spectra taken during H-plasma treatment.

### Experimental setup

The ZnSe-samples were grown in a custom designed elemental source (6N-materials, BN-crucibles) MBE-chamber at a background pressure of  $2\cdot 10^{-9}$  mbar. The substrate temperature during growth was  $310^\circ\text{C}$  and the growth rate about  $200\text{nm/h}$ . The layers were grown on GaAs(001). Before the growth starts the substrates were pretreated in a two step wetchemical procedure: the adsorbates were removed with a KOH(15%)-solution for 5 minutes, followed by etching in a  $\text{NH}_3(25\%):\text{H}_2\text{O}_2(30%):\text{H}_2\text{O}=5\text{ml}:1\text{ml}:1\text{ml}$ -solution for 2 minutes. After each step the substrate was rinsed three times in  $18.2\text{ M}\Omega\text{cm}$ -water. The GaAs-substrates thus prepared are covered with a 1 nm thick  $\text{Ga}_2\text{O}_3$ -layer [13], which is subsequently desoxidized with atomic hydrogen from a RF-plasma source in the growth chamber (MPD 21, Oxford Applied Research). We obtained stable H-plasma-conditions at a RF-power of 300W and a hydrogen flow of 3 sccm. The applied RHEED-system (Staib Co.) for in-situ observation of surface reconstructions contains a 35 kV electron gun, beam-deflection and -rocking unit, fluorescence screen, CCD-camera, PC and evaluation software. We used 10 kV accelerating voltage, an incident angle of  $1.5\text{--}1.8^\circ$  and the azimuth of the two  $\langle 110 \rangle$ -directions. The MBE-chamber is equipped with a QMS (QMA150 with SEV, Balzers) to analyze the residual gas composition during the H-plasma treatment. For plan-view TEM investigation the samples were cut into  $1\times 3\text{ mm}^2$  pieces with a diamond wire saw and bonded with the layer side onto a metal supporting. While an acetone soluble wax protects the epilayers the substrate side is mechanically thinned to a thickness of  $70\mu\text{m}$  with a disc grinder and subsequently to  $20\mu\text{m}$  with a dimple grinder (Gatan). After polishing we reach electron transparency by chemical etching with a solution of  $\text{NaOH}(1\text{mol/l}):\text{H}_2\text{O}_2(30\%)=43:7$ . The TEM-investigations were carried out with a Philips CM 30 equipped with a TWIN-lens and a point resolution of  $0.23\text{ nm}$ . The evaluation of the FPD-density used several plan-view micrographs obtained from different sample areas with a magnification of 10500 showing an area of  $10\times 7\mu\text{m}^2$ .

### Results

Prior to this study the H-plasma preparation was optimized in an earlier investigation using PL. Best results were obtained with 3 sccm hydrogen flow, a RF-power of 300W and 15 minutes exposure at a substrate temperature  $T_s = 350^\circ\text{C}$ . Before the initial growth of ZnSe  $T_s$  was lowered to  $310^\circ\text{C}$  and the substrate exposed to a Zn-flux for one minute. The growth started with the opening of the Se-shutter.

In the first step of this study only the growth temperature was varied whereas all other parameters were kept constant. No change in the FPD-density was observed. Only the shape of the dislocations changed with  $T_s$ .

Subsequently  $T_s$  was varied during H-plasma desoxidation keeping the treatment time constant. In order to minimize the influence of a possible temperature variation between the plasma treatment and initial growth we changed  $T_s$  continuously within the last 5 minutes of plasma desoxidation with the help of a ramp driven PID-control unit. The resulting density of FPDs was evaluated from plan-view TEM images and plotted versus  $T_s$  as shown in Fig. 1. A minimal density of  $2.4 \cdot 10^7$  is found for  $T_s = 350^\circ\text{C}$ . Lower as well as higher temperatures lead to an increase of the defect density.

One reason for the creation of FPDs on a Se-terminated GaAs surface is 3-dimensional initial growth combined with the formation of a  $\text{Ga}_2\text{Se}_3$ -interlayer [2].

Fig. 2 shows a plan-view TEM image of a ZnSe-layer grown on a Se-terminated GaAs. We evaluated a FPD-density of  $7.5 \cdot 10^8 \text{ cm}^{-2}$ . Therefore the Se and  $\text{H}_2\text{Se}$  partial pressure was recorded especially during H-plasma exposure of the sample.

The QM-spectra taken during H-supply and plasma treatment in the growth chamber are plotted in Fig. 3. The partial pressure of the Se-isotopes including their hydrides increases slightly (factor 8) under  $\text{H}_2$ -flow and drastically (factor 60) with ignition of the plasma. Obviously atomic hydrogen reacts with Se adsorbed on the metal surfaces inside the growth chamber to  $\text{H}_2\text{Se}$ . This effect, however, can be strongly inhibited when  $\text{H}_2\text{Se}$  condensates

at the cooled  $\text{LN}_2$ -shield. The cryogenic reduction lowers the Se partial pressure by a factor 20. The respective QMS-spectra between 0-90 amu are shown in Fig. 3. The results allow an estimation of the total residual Se pressure  $p_{\text{Se}} \approx 5 \cdot 10^{-7} \text{ mbar}$ .

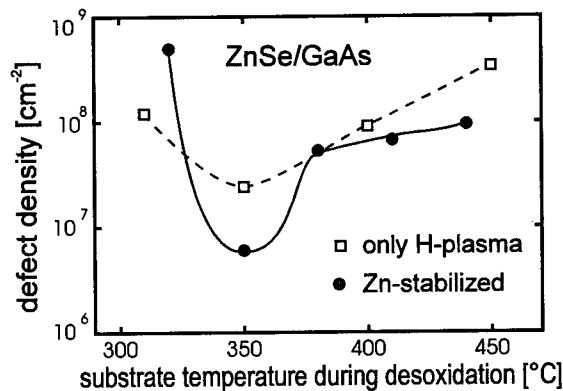


Fig. 1: The density of Frank partial dislocations depends on the temperature during H-plasma treatment. Additional Zn-supply reduces the defect density at  $350^\circ\text{C}$  and alters the temperature dependence.

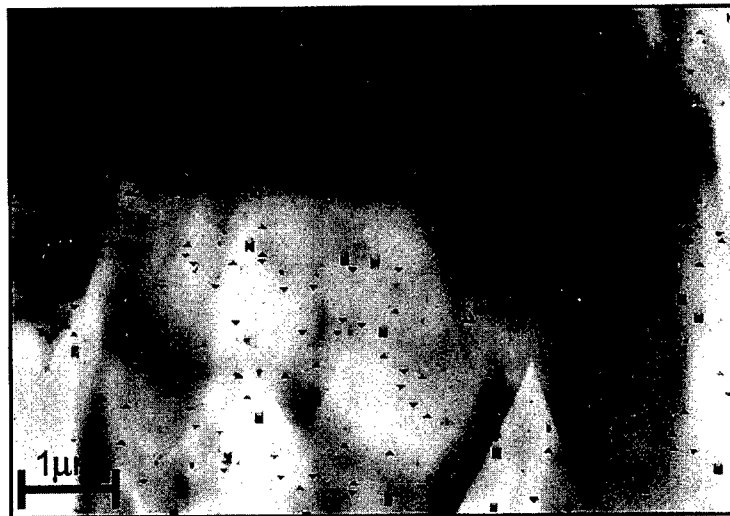


Fig. 2: Plan-view TEM image of ZnSe-layer on a Se-pretreated GaAs-substrate shows a FPD density of  $7.5 \cdot 10^8 \text{ cm}^{-2}$ .



The presence of Se during desoxidation and the formation of  $\text{Ga}_2\text{Se}_3$  [4] stimulated further experiments in which Zn is supplied during the whole time of plasma treatment. This procedure changes the (2x1)- into a (1x1)-surface reconstruction. The results of the respective TEM-investigations are also shown in Fig. 1. The optimum temperature is found again to be  $350^\circ\text{C}$ , below this temperature the density of Frank partial dislocations increases drastically whereas at higher temperatures only a smooth rise of FPD density is observed.

In the last step we changed the wet etching time from 1 to 5 minutes but kept the parameters of optimized preparation, mentioned above, constant. Note that the standard etching time is usually 2 min. The FPD density versus etching time is plotted in Fig. 4: The optimal time is indeed found to be 2 min., shorter as well as longer etching times lead to an increase of the density of FPDs.

### Discussion

The experiments show that an optimal set of parameters exists for substrate preparation. The plasma treatment of the samples depends on  $T_s$ . Above an optimum temperature of  $T_s = 350^\circ\text{C}$   $\text{Ga}_2\text{Se}_3$  is formed [2] giving rise to the formation of FPDs whereas below  $350^\circ\text{C}$  the removal of residual  $\text{Ga}_2\text{O}_3$  is incomplete and leads also to an increase of FPD density. However, an additional Zn-supply leads to a further defect reduction at  $350^\circ\text{C}$  and a smaller rise to higher temperatures possibly induced by a suppression of Ga-Se-bonds. The drastic rise of FPD density below  $350^\circ\text{C}$  is related to a different kind of dislocations which is seen in the two weak-beam TEM-images in Fig. 5. The most noticeable features are an arrangements of stacking faults (1), threading segments of perfect dislocations (2) and Shockley pair dislocations (3). In the nucleation center of these dislocation arrangements, especially type (1), we observe Moiré-pattern in high magnified weak beam images (not shown here) which can be related to the formation of nanocrystals. The increase of the FPD-density after treating the sample beyond the optimum time of chemical etching can be interpreted as follows: Residual structural defects from wafer preparation and polishing survive under short time etching, whereas during too long etching periods precipitates are formed because the etching solution saturates.

It is interesting that all deviations from optimal treatment, with one exception (s. Fig. 5), lead to the same kind of triangular shaped stacking faults which are related with FPDs as seen in Fig. 2. This suggests that there is no single reason for the FPD formation. An As-terminated (2x4)-

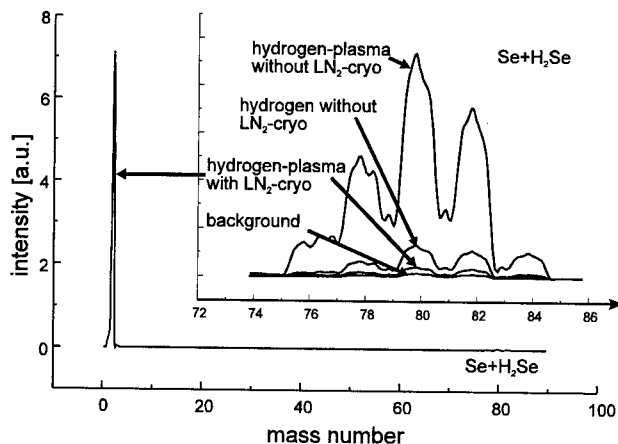


Fig. 3: QMS-analysis during H-plasma-treatment. The insertion illustrates the behaviour of  $\text{Se} + \text{H}_2\text{Se}$  dependent on  $\text{H}_2$ -supply, plasma activity and  $\text{LN}_2$ -cryo-cooling.

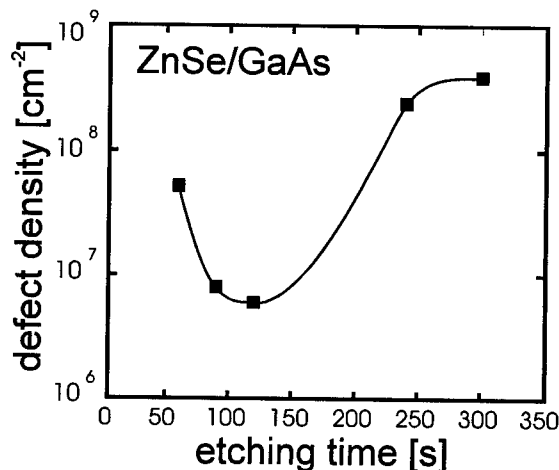


Fig. 4: The density of FPDs is strongly dependent on the time of the wet chemical etching procedure.

reconstructed GaAs-surface was proposed to achieve FPD densities lower than  $10^4 \text{cm}^{-2}$  [6]. If, however, the GaAs-substrate is desoxidized with atomic hydrogen a residual Se partial pressure leads always to a compensation of the surface As-deficiency [10] and a formation of a  $\text{Ga}_2\text{Se}_3$  layer which acts as a source of FPD formation.

### Conclusions

We have studied the density of Frank partial dislocations depending on various parameters of substrate preparation. A strong dependence on the substrate temperature  $T_s$  during

H-plasma treatment is observed. The optimum temperature is found to be  $350^\circ\text{C}$ . A further reduction of FPDs at  $350^\circ\text{C}$  to a minimum of  $6 \cdot 10^6 \text{cm}^{-2}$  was observed when Zn was supplied during desoxidation. We also found that the time of chemical etching affects the defect density and must be optimized. QMS-investigations revealed a background partial pressure of Se including  $\text{H}_2\text{Se}$  during H-plasma treatment in the range of  $10^{-7}$  mbar. This background is the main limiting factor in obtaining low defect densities.

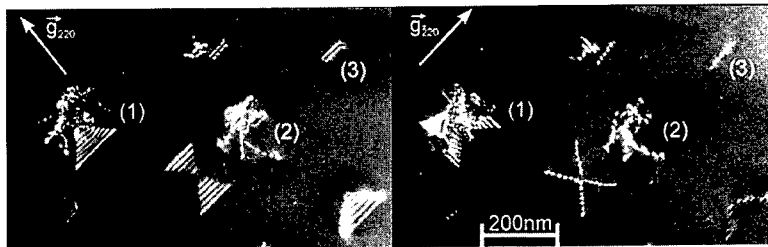


**Fig. 5:** Weak beam TEM-images of ZnSe on H-plasma treated GaAs at  $320^\circ\text{C}$  under Zn-supply. The same sample position is shown with two different (220)-reflections.

### References

1. M. Haase, J. Qui, J. DePuydt, and H. Cheng, Appl. Phys. Lett. **59**, 1272 (1991).
2. S. Guha, H. Munekata, and L. L. Chang, J. Appl. Phys. **73** (5) 2294 (1993).
3. S. Guha, J. M. DePuydt, J. Qiu, G. E. Hofler, M. A. Haase, B. J. Wu, and H. Cheng, Appl. Phys. Lett. **63** (22), 3023 (1993)
4. L. H. Kuo, K. Kimura, S. Miwa, T. Yasuda, and T. Yao, Appl. Phys. Lett. **69** (10), 1408 (1996)
5. W. Spahn, H. R. Ress, K. Schüll, M. Ehinger, D. Hommel, G. Landwehr, J. Cryst. Growth **159**, 761 (1996)
6. C. C. Chu, T. B. Ng, J. Han, G. C. Hua, and R. L. Gunshor, Appl. Phys. Lett. **69** (5), 602 (1996)
7. L. H. Kuo, L. Salamanca-Riba, Appl. Phys. Lett. **67** (22), 3298 (1995)
8. M. Yamada, Y. Ide, and K. Tone, Jpn. J. Appl. Phys. **31**, pp. L1157 part 2 (1992)
9. S. V. Hattangady, R. A. Rudder, M. J. Mantini, G. G. Fountain, J. B. Posthill, J. Appl. Phys. **68** (3) 1233 (1990)
10. M. Kuball, D. T. Wang, N. Esser, M. Cardona, and J. Zegenhagen, Phys. Rev. **B 52**, no. 23, 16337 (1995)
11. Zhonghai Yu, S. L. Buczkowski, N. C. Giles, and T. H. Myers, Appl Phys. Lett. **69** (1), 82 (1996)
12. A. Rosenauer, T. Reisinger, F. Franzen, G. Schütz, B. Hahn, K. Wolf, J. Zweck, and W. Gebhardt J. Appl. Phys. **79** (8), 4124 (1996)
13. C. M. Wilmsen, *Physics and Chemistry of III-V Semiconductor Interfaces*, Plenum Press, London, 1985
14. S. Guha, H. Munekata, F. K. LeGoues, and L. L. Chang, Appl. Phys. Lett. **60** (26) 3220 (1992)

## DEFECT FORMATION AND ELECTRONIC TRANSPORT AT $\text{Al}_x\text{Ga}_{1-x}\text{N}/\text{GaN}$ INTERFACES

L. Hsu<sup>1</sup>, W. Walukiewicz<sup>2</sup>, and E. E. Haller<sup>2,3</sup>

<sup>1</sup>Physics Dept., Univ. of California, Berkeley, Berkeley, CA 94720 USA

<sup>2</sup>Materials Science Div., Lawrence Berkeley Nat'l Lab, Berkeley, CA 94720 USA

<sup>3</sup>MSME Dept., Univ. of California, Berkeley, Berkeley, CA 94720 USA

**Keywords:** heterostructure, modulation doping, two-dimensional electron gas, GaN

**Abstract.** We have calculated the effects of charged defects located near a  $\text{Al}_x\text{Ga}_{1-x}\text{N}/\text{GaN}$  heterointerface on the transport properties of the two dimensional electron gas confined at the interface and also determined the distribution of those defects taking into consideration the dependence of the formation energy on the Fermi level. In addition, we have investigated the effects of hydrostatic pressure on such modulation doped heterostructures and find that pressure can be used to make the determination of the properties of the two dimensional electron gas easier by eliminating parallel three dimensional conduction paths.

### Introduction.

Because of its large bandgap, tunable from 3.4 to 6.2 eV, and high saturation drift velocities for electrons,  $\text{Al}_x\text{Ga}_{1-x}\text{N}$  is ideally suited for high power, high temperature electronic and opto-electronic devices. Much recent research has confirmed the possibility of creating a two-dimensional electron gas (2 DEG) at a  $\text{Al}_x\text{Ga}_{1-x}\text{N}/\text{GaN}$  heterointerface with low temperature mobilities greater than 7000  $\text{cm}^2/\text{V s}$  and sheet carrier concentrations of roughly  $5 \times 10^{12} \text{ cm}^{-2}$  [1, 2]. In addition, the fabrication of high electron mobility transistors (HEMTs) and heterostructure field effect transistors (HFETs) with operation frequencies in the GHz range has demonstrated the potential for developing devices for high power microwave applications [3,4].

However, despite experimental progress in optimizing the parameters of such heterostructures, very little is known regarding the impurities which give rise to the 2 DEG. In particular, it is far from clear whether the 2 DEG electrons in currently grown structures originate from shallow hydrogenic impurities or from resonant donors in the  $\text{Al}_x\text{Ga}_{1-x}\text{N}$ . In a previous paper, we have described the characteristics of standard  $\text{Al}_x\text{Ga}_{1-x}\text{N}/\text{GaN}$  modulation doped heterostructures (MDHs) in which shallow donors such as Si provided the 2 DEG in the GaN well [5]. Here, we will discuss heterostructures in which the source of 2D conduction electrons are resonant donors which are responsible for n-type conductivity in nominally undoped  $\text{AlGaIn}$ . It has been shown recently that resonant donor defects which are formed in low temperature grown InP can be used to fabricate modulation defect doped InGaAs/InP heterostructures [6,7].

### Electron transport.

The mobility and transport characteristics of defect-doped  $\text{Al}_x\text{Ga}_{1-x}\text{N}/\text{GaN}$  MDHs are largely the same as those which are doped with shallow impurities with a few important differences. In contrast to MDHs doped with shallow impurities, the Fermi level of defect doped structures lies within the conduction band of the  $\text{Al}_x\text{Ga}_{1-x}\text{N}$  barrier (Fig. 1). This increase of the Fermi energy relative to impurity doped MDHs allows a more efficient transfer of electrons from the barrier into the well, especially at higher remote doping concentrations for which the Fermi energy can be more than 100 meV above the  $\text{Al}_x\text{Ga}_{1-x}\text{N}$  conduction band in regions far from the interface. This difference is illustrated in Fig. 2, in which the 2 DEG concentration is plotted as a function of the remote doping concentration for

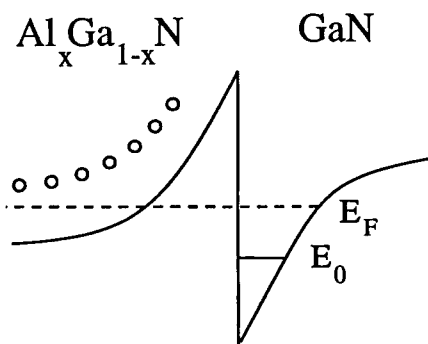


Figure 1. Schematic representation of a  $\text{Al}_x\text{Ga}_{1-x}\text{N}/\text{GaN}$  heterostructure, showing resonant donors, lowest electric subband, and Fermi level.

structures with and without a 200Å spacer of undoped  $\text{Al}_x\text{Ga}_{1-x}\text{N}$ . All numbers have been calculated assuming an Al fraction (x) of 15%. The 2 DEG concentration was calculated from the electrostatic equilibrium equation

$$V_0 - \frac{4\pi e^2}{\epsilon_s} N_s d - \frac{4\pi e^2}{2\epsilon_s} \frac{N_s^2}{N_i} = E_0 + \frac{\pi \hbar^2}{m^*} N_s - E_F' \quad (1)$$

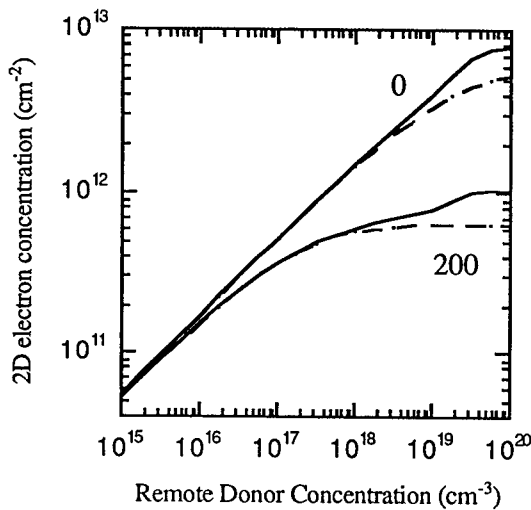


Figure 2. 2D electron concentration plotted as a function of remote doping concentration for heterostructures with no (0) and a 200Å (200) spacer. The solid lines are for defect doped structures and the dashed lines are for standard MDHs.

where  $V_0$  is the conduction band offset,  $N_s$  the 2 DEG concentration,  $N_i$  the  $\text{Al}_x\text{Ga}_{1-x}\text{N}$  defect concentration,  $d$  the spacer width, and  $E_F'$  is the Fermi level in the  $\text{Al}_x\text{Ga}_{1-x}\text{N}$  barrier. The kink in the graph for the structure with a spacer occurs at the point where the Fermi energy in the  $\text{AlGaIn}$  barrier reaches the resonant defect level and becomes pinned there. The defect level was estimated to be 475 meV above the GaN conduction band edge based on experimentally measured reductions in the carrier concentration of  $\text{Al}_x\text{Ga}_{1-x}\text{N}$  samples as a function of Al fraction [8,9,10,11].

Figures 3a and 3b show the dependence of the low temperature 2 DEG mobilities on the concentration of defects in the  $\text{Al}_x\text{Ga}_{1-x}\text{N}$  barrier as calculated by the method used in [12]. As the sheet carrier concentration is increased, ionized impurity scattering from impurities in the GaN becomes much less effective in reducing the carrier mobility due to the decreased scattering cross section of screened Coulomb potentials at high electron energies. On the other hand, scattering due to interactions

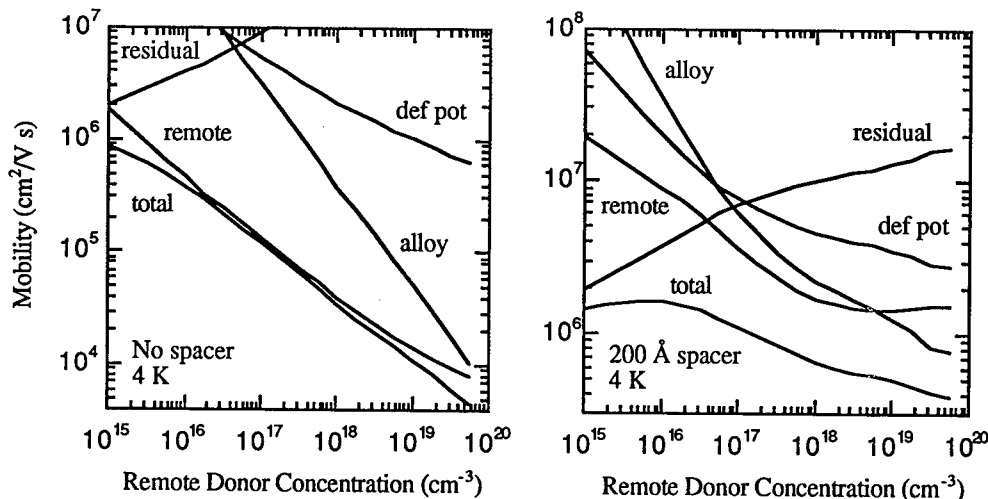


Figure 3a/3b. 2D electron mobilities plotted as a function of remote doping concentration. Also shown are the component mobilities due to alloy disorder scattering, deformation potential scattering, and scattering from remote and residual (background) donors.

with the remote donors increases because of the increasing concentration of these Coulomb centers. In addition, alloy disorder scattering becomes much more effective at limiting the mobility at high electron densities due to increased penetration of the electronic wavefunctions into the  $\text{Al}_x\text{Ga}_{1-x}\text{N}$ . Typical low temperature mobilities from several thousand up to a couple million  $\text{cm}^2/\text{Vs}$  in structures with a spacer are predicted by our calculations. Obtaining the highest mobilities, however, requires that the concentration of ionized impurities and defects in the GaN be kept very low ( $< 10^{14} \text{ cm}^{-3}$ ).

#### Defect distribution.

In calculating the mobilities shown in Figs. 3a and 3b, it was assumed that the defect concentration was uniform throughout the  $\text{Al}_x\text{Ga}_{1-x}\text{N}$  barrier. This would be the case if the  $\text{Al}_x\text{Ga}_{1-x}\text{N}$  layer were grown first. However, in all heterostructures grown so far, the GaN well is grown first and a doped  $\text{Al}_x\text{Ga}_{1-x}\text{N}$  layer is grown on top of it. In such a case, one must take into consideration the fact that as the  $\text{Al}_x\text{Ga}_{1-x}\text{N}$  barrier is grown, the electrons from these donor defects are transferred into the GaN well. This transfer of electrons to lower energy levels results in a decrease of the formation energy of the defects.

The concentration of singly charged resonant defects is given by [13]

$$N_D = N_{\text{sites}} \exp\left(\frac{-E_f}{k_B T}\right) \quad (2)$$

where  $N_{\text{sites}}$  is the concentration of possible defect sites in the crystal lattice and  $E_f$  is the defect formation energy. For positively charged (ionized) donor defects,

$$E_f = E_f^0 + E_F \quad (3)$$

where  $E_f^0$  is the formation energy for neutral defects and  $E_F$  is the Fermi energy in the GaN well relative to the  $E_d(0/+)$  charge transition state. In pure GaN,

$$E_d(0/+) = E_C + 0.475 \text{ eV} \quad (4)$$

However, for the heterostructures that we consider here,

$$E_d(0/+) = E_C + 0.475 - \Delta E \quad (5)$$

where  $\Delta E$  is the conduction band offset between the  $\text{Al}_x\text{Ga}_{1-x}\text{N}$  and GaN.

To calculate the concentration of defects from Eq. (2), one must know  $E_f^0$ . The value of this parameter can be estimated from the experimentally measured carrier concentration in nominally undoped, isolated  $\text{Al}_x\text{Ga}_{1-x}\text{N}$  layers, in which the electrons are assumed to originate from these resonant defects. The formation energy given in Eq. (3) can then be written as

$$E_f = E_f^0 + E_C + E_F - E_C \quad (6)$$

where  $E_C$  is the energy of the conduction band edge. Substituting (6) into Eq. (2), we find

$$N_D = N_{\text{sites}} \frac{N_C}{n} \exp\left(\frac{-E_f^0 + E_C}{k_B T}\right) \quad (7)$$

where  $N_C$  is the conduction band density of states and  $n$  is the electron concentration. If these resonant defects are the dominant donors, then  $n = N_{\text{def}}$  and we obtain

$$E_f^0 + E_C = k_B T \ln\left(\frac{N_{\text{sites}} N_C}{N_{\text{def}}^2}\right) \quad (8)$$

The concentration of the donor defects depends on the growth conditions and the Al content. We have performed model calculations assuming that for  $\text{Al}_{0.15}\text{Ga}_{0.85}\text{N}$  grown at a temperature of 1373 K, the defect concentration is roughly  $10^{17} \text{ cm}^{-3}$  [2]. Equation (8) then gives  $E_f^0 + E_c \approx 2.18 \text{ eV}$  for the formation energy of the charged defects when the Fermi energy is at the conduction band edge.

To see how the formation energy and defect concentrations vary in a real heterostructure, we consider the case when  $\text{Al}_{0.15}\text{Ga}_{0.85}\text{N}$  is grown on a pure GaN layer. Because the formation energy of these native defects depends on the Fermi energy a greater concentration of defects is expected to be found close to the interface. When the first few atomic layers of  $\text{Al}_x\text{Ga}_{1-x}\text{N}$  are grown on top of the GaN layer, the Fermi energy in the structure is well below the conduction band of the GaN due to the high growth temperature. The formation of defects in the  $\text{Al}_x\text{Ga}_{1-x}\text{N}$  at this point is aided by the fact that these donor centers can transfer their electrons to the GaN, gaining an amount of energy equal to the difference between the Fermi levels in the  $\text{Al}_x\text{Ga}_{1-x}\text{N}$  and the GaN. This results in a substantial lowering of the formation energy for charged defects. As more layers of  $\text{Al}_x\text{Ga}_{1-x}\text{N}$  are grown, more electrons continue to be transferred to the GaN well and the Fermi energy increases, decreasing the amount of energy gained by the transfer process and causing the defect formation energy to increase. Thus, the concentration of defects incorporated into the  $\text{Al}_x\text{Ga}_{1-x}\text{N}$  also decreases.

Based on the above considerations, the variation of the charged defect formation energy and the concentration of incorporated defects is shown as a function of the distance from the  $\text{Al}_x\text{Ga}_{1-x}\text{N}/\text{GaN}$  interface in Fig. 4. As can be seen, the concentration of defects at the interface is enhanced by more than an order of magnitude. While this concentration of defects near the interface aids in the transfer of charge from the  $\text{Al}_x\text{Ga}_{1-x}\text{N}$  barrier to the GaN well, it also has the effect of degrading the overall 2 DEG mobility. As can be seen from Figs.

3a and 3b, ionized impurity scattering from remote donors is often the dominant mechanism limiting the two-dimensional mobility, especially in structures with no spacer. By putting the majority of the ionized remote donors closer to the interface, the Coulomb interactions between the donors and the carriers is enhanced, causing a greater amount of carrier scattering. Although a similar effect may be expected in heterostructures doped with hydrogenic impurities, the result is much less dramatic as the formation energy of such extrinsic defects is affected much less by the location of the Fermi level.

#### Hydrostatic pressure.

One significant disadvantage of defect doped structures relative to those doped with hydrogenic impurities is that they are themselves highly conductive, even at low temperatures, since the carriers do not freeze out. As a consequence, if the barrier layer is grown too thick, a low mobility parallel conduction path may be formed. This additional conduction path may lead to misleading Hall effect concentration and mobility measurements as the conductivities of the two types of electrons will be mixed together. One possibility for separating the two contributions is by the application of large

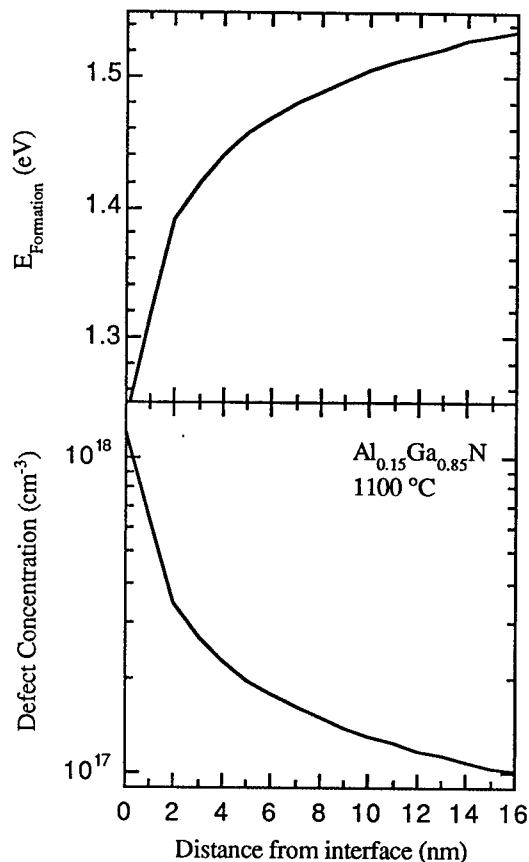


Figure 4. Formation energy (top) and concentration of defects incorporated in the  $\text{Al}_{0.15}\text{Ga}_{0.85}\text{N}$  barrier layer (bottom) as a function of distance from the interface.

hydrostatic pressures. When hydrostatic pressure is applied to GaN or  $\text{Al}_x\text{Ga}_{1-x}\text{N}$ , the conduction band shifts upwards in energy. On the other hand, since the defects are highly localized, their energy remains constant. This difference in behaviors makes it possible to "freeze out" any three-dimensional electrons in the  $\text{Al}_x\text{Ga}_{1-x}\text{N}$  barrier by pushing it into the forbidden gap. The concentration of two dimensional electrons in the GaN well remains relatively unchanged, as the charge transfer is governed by the actual defect concentration, which remains unchanged, and more weakly on the Fermi energy, which does not change much at low temperatures. Figure 5 shows the change in electron concentration on both sides of the interface as a function of pressure. This effect has been seen in InGaAs/InP heterostructures [7].

For the Al fraction for which Fig. 5 was calculated, a substantial amount of pressure ( $\sim 40$  kbar) is required to "freeze out" the unwanted conduction. However, in order to see this effect at lower pressure, a higher Al fraction could be used to bring the defect energy closer to the  $\text{Al}_x\text{Ga}_{1-x}\text{N}$  conduction band.

### Conclusion.

We have performed calculations to determine the distribution of donor defects at the interface of  $\text{Al}_x\text{Ga}_{1-x}\text{N}/\text{GaN}$  heterostructures. Due to the dependence of the formation energy of the defects on the Fermi level, we find that the defect concentration near the interface may be enhanced by more than an order of magnitude as compared to the defect concentration in isolated  $\text{Al}_x\text{Ga}_{1-x}\text{N}$  layers grown under the same conditions. Although this leads to a more efficient transfer of electrons to the GaN well, the increased concentration of defects near the interface also leads to a degradation of the 2 DEG mobility due to the closer proximity of the charged defect centers. This problem could be eliminated by first growing the  $\text{Al}_x\text{Ga}_{1-x}\text{N}$  barrier before the pure GaN layer.

Another feature of modulation doped heterostructures doped with resonant donor defects which is not found in those doped with shallow hydrogenic donors is the possible presence of an alternate conduction path in the barrier layer. As the wavefunctions of the carriers in the barrier are three dimensional in nature and have much lower mobilities than the 2 DEG, the overall effect of the additional conduction path is to increase the concentration and decrease the mobility of the electrons as calculated from Hall effect measurements. However, hydrostatic pressure can be applied to "freeze out" the undesirable three dimensional conduction path.

### Acknowledgments.

This work has been supported in by the Director, Office of Energy Research, Office of Basic Energy Sciences, Materials Science Division of the U. S. Department of Energy under contract number DE-AC03-76SF00098 and by US NSF grant DMR-94 17763.

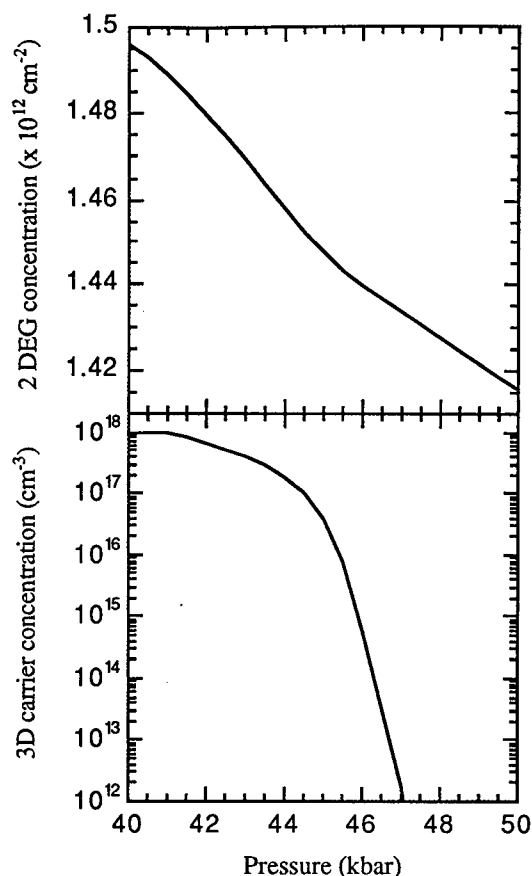


Figure 5. Plot of carrier concentration in the GaN well (top) and the AlGaIn barrier (bottom) as a function of pressure.

---

**References.**

1. M. Shur, B. Gelmont, and M. Asif Khan, *J. Electronic Mat.* **25**, 777 (1996).
2. J. M. Redwing, M. A. Tischler, J. S. Flynn, S. Elhamri, M. Ahoujja, R. S. Newrock, and W. C. Mitchel, *Appl. Phys. Lett.* **69**, 963 (1996).
3. M. Asif Khan, A. Bhattarai, J. N. Kuznia, and D. T. Olson, *Appl. Phys. Lett.* **63**, 1214 (1993).
4. M. Asif Khan, J. N. Kuznia, D. T. Olson, W. J. Schaff, J. W. Burm, and M. S. Shur, *Appl. Phys. Lett.* **65**, 1121 (1994).
5. L. Hsu and W. Walukiewicz, *Phys. Rev. B* **56**, 1520 (1997).
6. W. M. Chen, I. A. Buyanova, A. V. Buyanov, T. Lundstrom, W. G. Bi, and C. W. Tu, *Phys. Rev. Lett.* **77**, 2734 (1996).
7. D. Wasik, L. Dmowski, J. Lusakowski, L. Hsu, W. Walukiewicz, W. G. Bi and C. W. Tu, [see elsewhere in these conference proceedings].
8. M. Asif Khan, R. A. Skogman, R. G. Schulze, and M. Gershenson, *Appl. Phys. Lett.* **43**, 492 (1983).
9. S. Yoshida, S. Misawa, and S. Gonda, *J. Appl. Phys.* **53**, 6844 (1982).
10. X. Zhang, P. Kung, A. Saxler, D. Walker, T. C. Wang, and M. Razeghi, *Appl. Phys. Lett.* **67**, 1745 (1995).
11. Y. Koide, H. Itoh, N. Sawaki, I. Akasaki, et al., *J. Electrochem. Soc.* **133**, 1956 (1986).
12. W. Walukiewicz, H. E. Ruda, J. Lagowski, and H. C. Gatos, *Phys. Rev. B* **30**, 4571 (1984).
13. W. Walukiewicz, *Phys. Rev. B* **50**, 5221 (1994).



## CHARACTERIZATION OF THE RELAXATION BY MISFIT DISLOCATIONS CONFINED AT THE INTERFACE OF GaN / Al<sub>2</sub>O<sub>3</sub>(0001) STUDIED BY TEM

S. Kaiser \*, H. Preis \*, O. Ambacher \*\* and W. Gebhardt \*

\* Institut für Festkörperphysik, Universität Regensburg, 93040 Regensburg, Germany

\*\* Walter Schottky Institut, Technische Universität München, 85748 Garching, Germany

Keywords: GaN, Al<sub>2</sub>O<sub>3</sub>, TEM, HRTEM, relaxation, misfit dislocations, confinement, MBE

### ABSTRACT

A transmission electron microscopy (TEM) investigation of the relaxation process by misfit dislocations confined at the interface of the highly mismatched system GaN / Al<sub>2</sub>O<sub>3</sub>(0001) has been carried out.

Wurtzite type GaN was grown epitaxially by plasma induced molecular beam epitaxy (PIMBE) on the (0001) basal plane of Al<sub>2</sub>O<sub>3</sub>. We determined the orientation between epilayer and substrate by selected area electron diffraction (SAED). The diffraction images show that the  $\langle 11\bar{2}0 \rangle$ -direction in GaN is parallel to the  $\langle 10\bar{1}0 \rangle$ -direction in Al<sub>2</sub>O<sub>3</sub> whereas the [0001]-direction is the same in both materials. In this orientation a high lattice mismatch of  $f = -13.9\%$  appears and therefore the critical thickness of dislocation formation is reached when the first monolayer of GaN is grown. An expected interfacial relaxation process is observed and characterized by the results of high resolution transmission electron microscopy (HRTEM) which reveals a relaxation process with misfit dislocations confined at the interface:

HRTEM images show  $\{11\bar{2}0\}_{\text{Al}_2\text{O}_3}$ -lattice fringes terminating at the interface in regular intervals of about 8 lattice spacings, whereas no bending of the (0001) lattice planes is obtained in the interface region. Thus misfit dislocations have Burgers vectors parallel to the (0001)-interface plane, and therefore the extension of these dislocations into the GaN-layer is obviously suppressed.

The quantitative evaluation of the HRTEM images shows the effectiveness of the observed relaxation process by confined misfit dislocations: in this work a degree of relaxation  $\delta = (-11.8 \pm 1.1)\%$  was measured. A residual strain of  $\epsilon_r = (-2.1 \pm 1.1)\%$  causes a typical threading dislocation density of  $10^{10} \text{ cm}^{-2}$  in the GaN epilayer as reported by many authors.

### INTRODUCTION

GaN has received much attention recently as a semiconductor which is applicable for optical devices including light emitting diodes and lasers in the blue, violet and near ultraviolet spectral range. There is as well the possibility to develop electronic devices operating at high temperatures, high frequencies and high power. To guarantee a satisfying operation of GaN a suitable substrate material for the epitaxial growth is required. Many publications [1-4] show that growth of the wurtzite type GaN on the (0001) basal plane of Al<sub>2</sub>O<sub>3</sub> seems to be well-suited. However, the difference of lattice constants of  $a_{\text{Al}_2\text{O}_3} = 0.4758 \text{ nm}$  [4] and  $a_{\text{GaN}} = 0.3189 \text{ nm}$  [5] causes a high lattice misfit of  $f = -13.9\%$  between epilayer and substrate. This is expected to prevent an epitaxial growth with low dislocation densities ( $10^{10} \text{ cm}^{-2}$ ) in the GaN layer as reported in many works [1, 6-8] since the critical thickness of defect generation is already reached when the first monolayer of GaN is grown.

In this paper we will show that a relaxation process takes place at the interface between GaN and Al<sub>2</sub>O<sub>3</sub> that suppresses largely the extension of dislocations into the GaN layer. We report on transmission electron microscopy (TEM) investigations of the relaxation process. High resolution transmission electron microscopy (HRTEM) allows a quantitative evaluation of the strain reduction by the formation of dislocations. Finally, the residual strain in the GaN layer is estimated. We will

show that its relaxation by non-confined dislocations would generate a density of threading dislocations in the order of  $10^{10}$ - $10^{11}\text{cm}^{-2}$ .

### EXPERIMENTAL DETAILS

Epitaxial GaN films were grown on  $\text{Al}_2\text{O}_3(0001)$  substrates without buffer layer by plasma induced molecular beam epitaxy (PIMBE) using a conventional gallium effusion cell and a r.f.-plasma atomic radical source for nitrogen. The inductively coupled plasma power was 400W and the pressure in the MBE chamber during growth was  $4 \cdot 10^{-5}$  mbar. The gallium flux and the substrate temperature during growth including the initial stage were fixed at  $8 \cdot 10^{14}\text{cm}^{-2}\text{s}^{-1}$  and  $810^\circ\text{C}$ , resulting in a growth rate of  $0.6\text{ }\mu\text{m/h}$  [9]. The investigated samples have a GaN layer thickness of  $1\text{ }\mu\text{m}$ .

For TEM investigations cross sectional samples were prepared in a conventional sandwich technique. The specimens were thinned mechanically to a thickness of about  $20\text{ }\mu\text{m}$ .  $\text{Ar}^+$  and  $\text{Xe}^+$  ion milling was applied as a final stage of thinning. All TEM observations were carried out with a Philips CM30 electron microscope (EM) operated at an accelerating voltage of 300 kV.



**Fig.1:** HRTEM image of the GaN/ $\text{Al}_2\text{O}_3(0001)$  interface (IF) region. Insert: Corresponding selected area electron diffraction (SAED) pattern with  $\langle 1\bar{2}10 \rangle_{\text{GaN}}$  - and  $\langle 1\bar{1}00 \rangle_{\text{Al}_2\text{O}_3}$  -beam incidence. The white arrow marks the (0000) reflection.

### EXPERIMENTAL RESULTS

Figure 1 shows a HRTEM image of the GaN/ $\text{Al}_2\text{O}_3(0001)$  interface region. This sample reveals a typical threading dislocation density of  $10^{10}$ - $10^{11}\text{cm}^{-2}$  in the GaN epilayer which was estimated by cross sectional view. We determined the orientation between GaN and  $\text{Al}_2\text{O}_3$  by selected area electron diffraction (SAED) (Fig.1) with the well-known result [10] that the  $\langle 10\bar{1}0 \rangle$ -direction in GaN is parallel to the  $\langle 11\bar{2}0 \rangle$ -direction in  $\text{Al}_2\text{O}_3$ . The  $[0001]$ -directions are parallel in layer and substrate.

Figure 2a shows a part of a HRTEM image of the GaN/ $\text{Al}_2\text{O}_3(0001)$  interface region. In order to facilitate the visualization of lattice planes in epilayer and substrate Fourier filtering is applied. The digitized HRTEM image is Fourier transformed and only selected areas are used for the reconstruction of the image. Figure 2b shows the (0001) lattice planes of  $\text{Al}_2\text{O}_3$  and GaN running parallel to the interface. Note that no lattice plane terminates. The image reconstruction with Fourier

coefficients corresponding to the perpendicular direction (Fig. 2c) leads to  $\{11\bar{2}0\}$  lattice planes in  $\text{Al}_2\text{O}_3$  and  $\{10\bar{1}0\}$  lattice planes in GaN. Figure 2c shows regularly distributed  $\{11\bar{2}0\}_{\text{Al}_2\text{O}_3}$  lattice fringes terminating at the interface. A statistic of the distribution evaluated from a 120 nm wide region is depicted in Fig. 3. The average distance between two terminating fringes is  $n = 8.3 \pm 0.7$   $\text{Al}_2\text{O}_3$  lattice spacings.

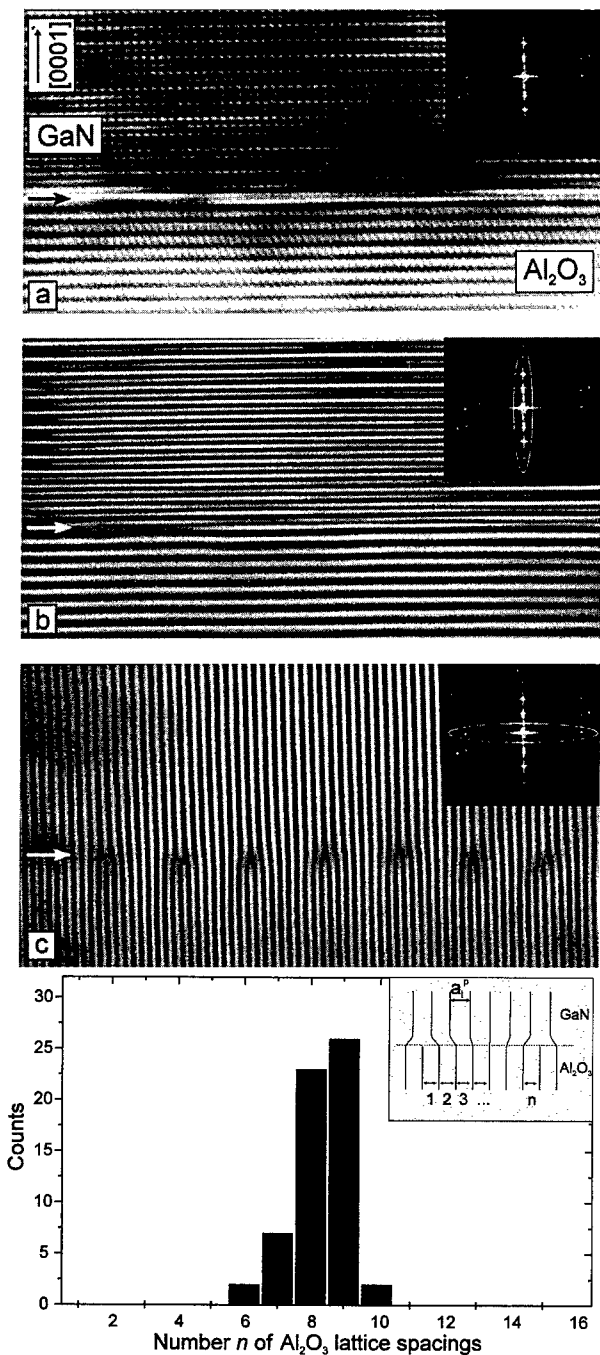


**Fig. 2:** (2a) HRTEM image of the GaN/Al<sub>2</sub>O<sub>3</sub> interface region in  $\{1210\}_{\text{GaN}}$  and  $\{1100\}_{\text{Al}_2\text{O}_3}$ -projection. The insert shows the intensity plot of the corresponding Fourier transformed image. The Fourier filtered image (2b) visualize the (0001) lattice planes of GaN and Al<sub>2</sub>O<sub>3</sub> without any recognizable plane bending or termination in the interface region. (2c) Image after Fourier filtering of the perpendicular direction. At the interface some  $\{11\bar{2}0\}_{\text{Al}_2\text{O}_3}$  fringes are terminating in regular intervals. In the inserts of (2b) and (2c) the selected area of the Fourier transformed image is marked which is used for the subsequent reconstruction.

**Fig. 3:** Statistical distribution of the number  $n$  of Al<sub>2</sub>O<sub>3</sub> lattice spacings between two terminating substrate fringes (see insert). About 500  $\{11\bar{2}0\}_{\text{Al}_2\text{O}_3}$  fringes were counted which cover almost 120nm.

## DISCUSSION

The analysis of the observed relaxation process which takes place at the interface GaN/Al<sub>2</sub>O<sub>3</sub> starts with the Fourier filtered HRTEM images (Fig. 2). Figure 2b contains no terminating (0001)<sub>GaN</sub> lattice plane or any recognisable lattice bending. Therefore, we conclude that misfit dislocations in the interface region have a vanishing component of their Burgers vector  $\vec{b}$  perpendicular to the interface GaN/Al<sub>2</sub>O<sub>3</sub>. Figure 2c shows {10 $\bar{1}$ 0}<sub>GaN</sub> - and {11 $\bar{2}$ 0}<sub>Al<sub>2</sub>O<sub>3</sub></sub> lattice fringes and reveals a regular distribution of terminating substrate fringes at the interface. In comparison with the obtained lattice spacing in the substrate material we detect in the epilayer larger distances (Fig. 2c). In order to explain the distances appearing in Fig. 2c we have to discuss the (0001) projection of the Al<sub>2</sub>O<sub>3</sub> and the GaN crystal (Fig. 4). Figure 4 shows the projection of the (0001) plane of GaN (Fig. 4a) and Al<sub>2</sub>O<sub>3</sub> (Fig. 4b) which have a hexagonal symmetry in both cases. Note that the <10 $\bar{1}$ 0> -direction in GaN is parallel to the <11 $\bar{2}$ 0> -direction in Al<sub>2</sub>O<sub>3</sub> whereas the electron beam direction is the same. Thus the beam incidence in Fig. 4 corresponds to that of Fig. 1 and the (0001) projections of the crystals (Fig. 4) show the obtained orientation relationship after growth. Presuming a bulk lattice constant  $a_{\text{GaN}} = 0.3189\text{nm}$  we would expect in the GaN layer lattice spacings in the Fourier filtered HRTEM image of  $a_l = 0.2762\text{nm}$  (Fig. 4a). Using  $a_{\text{Al}_2\text{O}_3} = 0.4758\text{nm}$  we obtain lattice spacings  $a_s = 0.2379\text{nm}$  (Fig. 4b) in the substrate material. The difference between  $a_l$  and  $a_s$  causes the well-known lattice misfit

$$f = \frac{a_s - a_l}{a_l} = -13.87\% \quad (1)$$

at room temperature and therefore a compressive strain ( $f < 0$ ) in the GaN layer.

In the case of a pseudomorphic growth the observed lattice spacings in layer and substrate would be identical. Furthermore the number of {10 $\bar{1}$ 0}<sub>GaN</sub> lattice fringes is expected to be the same as the number of {11 $\bar{2}$ 0}<sub>Al<sub>2</sub>O<sub>3</sub></sub> lattice fringes. The plastic relaxation of GaN by the formation of misfit dislocations provides a partially relaxed lattice spacing  $a_l^p$  in the layer (Fig. 3, insert), which is larger than  $a_s$  and which leads to a termination of {11 $\bar{2}$ 0}<sub>Al<sub>2</sub>O<sub>3</sub></sub> lattice fringes at the interface.

In Fig. 2c the terminating substrate fringes are regularly distributed and are a clear indication of a relaxation by misfit dislocations in the investigated samples. The corresponding Burgers vectors  $\vec{b}$  are parallel to the interface plane because no perpendicular component can be detected (Fig. 2b). Thus the (0001) interface plane acts as corresponding glide plane and suppresses the extension of these misfit dislocations into the GaN layer [11]. Therefore, this relaxation process works by confined misfit dislocations and does not contribute to the defect density of  $10^{10}$ - $10^{11}\text{cm}^{-2}$  estimated for the GaN epilayer.

We determine the degree of relaxation caused by the formation of confined misfit dislocations by establishing a relation between the lattice misfit  $f$  and the number  $n$  of lattice spacings between two terminating {11 $\bar{2}$ 0} substrate fringes. After relaxation the GaN layer adopts a partially relaxed lattice distance  $a_l^p$  and the lattice misfit  $f$  (Eq. (1)) can now be subdivided in a relaxed part  $\delta$  and a residual strain  $\epsilon_r$

$$f = \delta + \epsilon_r = \underbrace{\frac{a_s - a_l^p}{a_l}}_{\delta} + \underbrace{\frac{a_l^p - a_l}{a_l}}_{\epsilon_r} \quad (2)$$

Assuming that from  $n$  substrate planes one is terminating at the interface, we have

$$n(a_l^p - a_s) = a_l^p \quad (3)$$

for  $a_l > a_s$ . With the help of Eq. (2) and (3) we obtain in the case of a compressive strain ( $f < 0$ )

$$\delta = \frac{f+1}{1-n} \quad \text{and} \quad \epsilon_r = \frac{f \cdot n + 1}{n-1} \quad (4)$$

Using the result  $n = 8.3 \pm 0.7$  from the evaluation of the HRTEM images we obtain with Eq. (4)

$$\delta = (-11.80 \pm 1.14)\%$$

$$\epsilon_r = (-2.07 \pm 1.14)\%$$

As a result we may conclude that the large lattice mismatch of  $f = -13.9\%$  is mainly compensated by misfit dislocations confined at the interface. A much smaller residual strain of  $\epsilon_r = (-2.1 \pm 1.1)\%$  seems to be responsible for the threading dislocation density of  $10^{10}$ - $10^{11} \text{ cm}^{-2}$  in the GaN epilayer.

As one possibility we assume the following process for the generation of non-confined misfit dislocations: During the initial growth process of the first monolayers only confined misfit dislocations are generated before the entire substrate is covered with GaN. We expect that these dislocations originate at island borders and then start to glide beneath the islands. The occurrence of islands or of a rough surface during the initial growth can be expected in most highly mismatched heterostructures. The confined dislocations lead to a relaxation of a large part of the misfit and a comparatively minor strain of  $-2.1\%$  remains.

Here we have to notice that the GaN epilayers were grown at a substrate temperature of  $T = 810^\circ\text{C}$ . With linear thermal expansion coefficients perpendicular to the c-axis  $\alpha_{\perp}^{\text{GaN}} = 5.6 \cdot 10^{-6}/^\circ\text{C}$  [12] and  $\alpha_{\perp}^{\text{Al}_2\text{O}_3} = 7.3 \cdot 10^{-6}/^\circ\text{C}$  [12] we calculate a lattice misfit  $f = -13.75\%$  at  $T = 810^\circ\text{C}$ . Cooling of the sample from growth temperature down to room temperature thus causes a layer strain of  $-0.11\%$ , which was also measured by XRD in the investigated samples, but which is a negligibly small contribution compared to the residual strain  $\epsilon_r = -2.1\%$ .

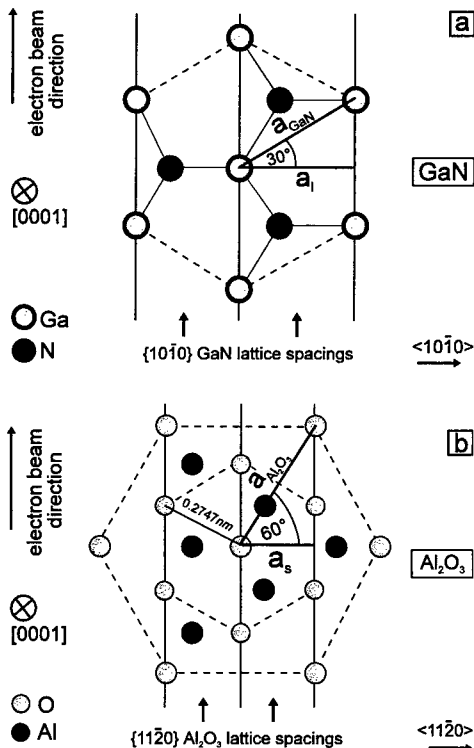


**Fig. 4:** (0001) projection of GaN (4a) and Al<sub>2</sub>O<sub>3</sub> (4b). Both show a hexagonal symmetry with their lattice constants  $a_{\text{GaN}}$  and  $a_{\text{Al}_2\text{O}_3}$ . The crystal orientation is equivalent to that obtained from SAED after growth. The electron beam direction is the same in (4a) and (4b). Therefore, in HRTEM images the lattice spacing  $a_1$  in GaN (4a) and  $a_s$  in Al<sub>2</sub>O<sub>3</sub> (4b) would be observed.

With proceeding layer growth the strain energy of the layer increases until it is sufficient to generate misfit dislocations in a second stage. However, misfit dislocations with glide planes parallel to the interface plane are now less effective because they do not contribute to strain relaxation below the growth surface and eventually the surface is just too smooth. Therefore secondary glide planes perpendicular to the interface plane are activated. The corresponding dislocation lines possess threading segments running parallel to the growth direction and contribute to the defect density in the epilayer. This is frequently observed in TEM [13].

### CONCLUSION

TEM was used to investigate the epitaxial growth of wurtzite type GaN on the (0001) basal plane of  $\text{Al}_2\text{O}_3$  substrates by PIMBE. In the obtained in-plane orientation a high lattice misfit of  $f = -13.9\%$  appears, which makes an interfacial relaxation process necessary. HRTEM images reveal, after Fourier filtering,  $\{1\bar{1}20\}_{\text{Al}_2\text{O}_3}$  lattice fringes terminating at the interface between GaN and  $\text{Al}_2\text{O}_3(0001)$ . We have shown that the Burgers vectors of the misfit dislocations are parallel to the (0001) interface plane. Glide is therefore limited to the (0001) planes and therefore these misfit dislocations are confined at the interface. This interfacial relaxation process is very effective and the extension of dislocations into the GaN layer is suppressed.

The quantitative evaluation of the Fourier filtered HRTEM images reveals an average value of  $n = 8.3 \pm 0.7$   $\text{Al}_2\text{O}_3$  lattice spacings between two terminating  $\{1\bar{1}20\}_{\text{Al}_2\text{O}_3}$  fringes. Therefore a large portion  $\delta = (-11.8 \pm 1.1)\%$  of the high mismatch  $f = -13.9\%$  is compensated by dislocations confined at the interface. The relaxation process allows an epitaxial growth of GaN on the (0001) basal plane of  $\text{Al}_2\text{O}_3$  with a dislocation density of about  $10^{10}$ - $10^{11} \text{ cm}^{-2}$  in the GaN epilayer which we suppose to be caused by the residual strain of  $\epsilon_r = (-2.1 \pm 1.1)\%$ .

### ACKNOWLEDGEMENT

This work is supported by "Bayerischer Forschungsverbund Optoelektronik".

### REFERENCES

1. M. Koike, S. Yamasaki, S. Nagai, N. Koide and S. Asami; H. Amano and J. Akasaki; Appl. Phys. Lett. **68**(10), 1403 (1996).
2. S. Nakamura, M. Senoh, S. Nagahama, N. Iwasa, T. Yamada, T. Matsushita, Y. Sugimoto and H. Kiyoku; Appl. Phys. Lett. **70**(7), 868 (1997).
3. K. Das and D.K. Ferry; Solid State Electron. **19**, 851 (1976).
4. H. Morkoc, S. Strite, G.B. Gao, M.E. Lin, B. Sverdlov and M. Burns; J. Appl. Phys. **76**(3), 1363 (1994).
5. M. Leszczynski, H. Teisseyre, T. Suski, I. Grzegory, M. Bockowski, J. Jun and S. Porowski; K. Pakula and J.M. Baranowski; C.T. Foxon and T.S. Cheng; Appl. Phys. Lett. **69**(1), 73 (1996).
6. R.C. Powell, N.-E. Lee and J.E. Greene; Appl. Phys. Lett. **60**(20), 2505 (1993).
7. S.D. Lester, F.A. Ponce, M.G. Craford and D.A. Steigerwald; Appl. Phys. Lett. **66**, 1249 (1995).
8. W. Qian, M. Skowronsk, M. DeGraef, K. Doverspike, L.B. Rowland and D.K. Gaskill; Appl. Phys. Lett. **66**, 1252 (1995).
9. H. Angerer, O. Ambacher, R. Dimitrov, T. Metzger, W. Rieger and M. Stutzmann; MRS Internet J. of Nitride Semiconductors Research **1**, 15 (1996).
10. T. Lei and K.F. Ludwig Jr.; T.D. Moustakas; J. Appl. Phys. **74**(7), 4430 (1993).
11. A. Rosenauer, H. Stanzl, K. Wolf, S. Bauer, M. Kastner, M. Grün and W. Gebhardt; Materials Science Forum, **143-147**, 567 (1994).
12. K. Ito, K. Hiramatsu, H. Amano and I. Akasaki; J. of Crystal Growth **104**, 533 (1990).
13. N.-E. Lee, R.C. Powell, Y.-W. Kim and J.E. Greene; J. Vac. Sci. Technol. A **13**(5), 2293 (1995).

## FORMATION KINETICS OF THE AL-RELATED SHALLOW THERMAL DONORS: A PROBE FOR OXYGEN DIFFUSION IN SILICON

P. Kaczor<sup>1</sup>, L. Dobaczewski<sup>1</sup>, T. Gregorkiewicz<sup>2</sup>, C. A. J. Ammerlaan<sup>2</sup>

<sup>1</sup>Institute of Physics, Polish Academy of Sciences

Al. Lotników 32/46, 02-668 Warsaw, Poland

<sup>2</sup>Van der Waals-Zeeman Institute, University of Amsterdam

Valckenierstraat 65-67, 1018 XE Amsterdam

**Keywords:** Shallow thermal donors, oxygen diffusion in silicon, defect reactions

**Abstract.** In this paper we investigate in detail the formation kinetics of the new type of shallow thermal donors, the K-donors, found in Al-doped silicon. A modeling of this kinetics in terms of diffusion controlled chemical reactions of oxygen and aluminum provides a new insight into the problem of oxygen diffusion in silicon at annealing temperatures of about 450 °C.

### Introduction.

Thermal donors (TD) in silicon belong, since their discovery in the 1950's [1], to the most intriguing and most studied defect systems in solids. There has been a lot of information gathered during the 40 years of research: the multi-species character of the TD has been evidenced by the IR-absorption measurements and ENDOR and magnetic circular dichroism measurements demonstrated the  $C_{2v}$  symmetry of TD and probable constituting elements (oxygen, Si-interstitials) of the defect core [2].

However, no definite undisputed model of TD structure exists at present, because other main problems related to the thermal donors, that of generation kinetics of the TD and the oxygen diffusion at TD annealing temperatures (350-500 °C) still lack a consistent explanation [2]. The activation energy of isolated oxygen diffusion has been estimated to be of the order of 2.5 eV over a wide temperature range [3]. This does not seem to account for the oxygen agglomeration data at TD annealing temperatures - the diffusion of oxygen atoms creating thermal donors should have activation energy of about 1.8 eV, i.e. the diffusion coefficient at 470 °C should be more than 2 orders of magnitude higher than the diffusivity of isolated oxygen [2].

Even less is known about other defects, which, similarly to the TD, are generated during oxygen agglomeration: the shallow thermal donors (STD). They were observed for the first time in the mid eighties by photo-thermal ionization spectroscopy [4]. The binding energies of these single shallow donors are about 30 meV below the conduction band, while the TD double donors have binding energies of the order of 60 meV and 150 meV in  $TD^0/TD^+$  and  $TD^+/TD^{++}$  charge states, respectively. Recent comparative studies carried out with infrared absorption and ENDOR techniques tentatively related the STD to the NL10 defect and showed that their generation does not depend on co-dopant species but only on the initial Fermi level position [5].

Infrared transitions attributed tentatively to a new member of the STD-family, called the K-donor, have been found recently in the Al-doped silicon [6]. The defect is generated simultaneously, though with different kinetics, with other shallow thermal donors. It has a very similar binding energy, but, contrary to other shallow thermal donors, it exhibits a metastable behaviour. The K-donor was believed to contain aluminium as it has been found only in Al-doped samples [6].

In this paper we present results of the generation kinetics of the oxygen agglomeration related centers in Si. The creation process of the K-donors, the STD and TD can be linked to a more general problem of oxygen diffusion in silicon at TD-annealing temperatures. Several models of possible generation mechanisms based on the second order, diffusion controlled reaction kinetics have been proposed and their results compared to the experimental data. It seems that the investigation of thermal donor formation in terms of a nonlinear reaction-diffusion process can provide a new insight into the still unsolved problem of the oxygen diffusion and precipitation at 450 °C.

### Experimental results and models of the thermal donor generation kinetics .

The generation kinetics of the thermal donors was measured in boron ( $N_A - N_d = 1 \cdot 10^{16} \text{ cm}^{-3}$ ) and aluminium ( $N_A - N_d = 4 \cdot 10^{15} \text{ cm}^{-3}$ ) doped Cz-Si samples (WASO-grade) at 470 °C in the nitrogen atmosphere. The initial oxygen concentration was  $N_{ox} = 1 \cdot 10^{18} \text{ cm}^{-3}$  and the samples undergone an oxygen dispersion treatment at 1350 °C. By means of the FTIR spectrometer (Bomem DA3) infrared absorption bands of the TD, STD and K-donors were measured at the resolution of  $1 \text{ cm}^{-1}$ . The relative concentration of the generated species was drawn from the strength of the IR-bands.

Of several TD absorption bands observed some could be attributed to that already identified in [7] and [8]. Some of them were not reported in literature. They were all named according to the nomenclature of ref. [7]. A total of 10 different TD species (from TD<sub>5</sub> to TD<sub>15</sub>) could be resolved and their kinetics monitored during several annealing steps at 470 °C (the details of the IR spectra and the identification of different species can be found in [5]). The several STD absorption lines, were more difficult to resolve in the absorption experiment due to their low absorption strength but the kinetics of the deepest of them (the F, G and the K absorption bands) could be monitored in sufficient detail for B- as well as for Al-doped Si samples.

The absorption of the K-donors exhibits metastable behaviour. A photo-excitation experiment [6] showed that the metastability of this defect is very similar to that found for DX centres in AlGaAs.

The generation kinetics of each species approximately follows (at its beginning) the power law  $n(t_{\text{anneal}}) \sim t_{\text{anneal}}^p$  where  $n$  is the TD concentration and  $t_{\text{anneal}}$  is the annealing time (Fig. 1). The power  $p$  for all TD<sup>0</sup> and STD species ranges from 1.3 to 1.7 for the Al-doped samples and from 1.5 to 2.3 for the B-doped samples. The power  $p$  does not show any dependence on the thermal donor number. It seems that a constant (average) value of  $p$  is characteristic for all the thermal donors observed. The deviation from this value is being due to the fact that it was impossible to estimate the exact “starting point” of the generation kinetics for all different TD’s and thus to estimate exactly the “initial slope” power  $p$  of each kinetics curve. The average power  $p_{av}$  seems to be somewhat higher for the B-doped samples ( $p_{av} = 1.8$ ) than for the Al-doped samples ( $p_{av} = 1.5$ ) but this again can be explained with different conditions of the “initial slope” measurements for both types of samples. For B-doped samples (higher doping level, shallower acceptor) the absorption bands could be observed at the very initial stage of the agglomeration (apparently larger slope). For the Al-doped sample (lower doping level, deeper acceptor) the “first” absorption bands resolved could only be measured for a later (than for B-doped samples) agglomeration stage. The power  $p$  for the shallow thermal donors has been found to be approx. 1 for both types of samples.

The K-donors kinetics differ markedly from those of the other donors: they have the “initial slope” power  $p = 0.6$  and exhibit a pronounced saturation behaviour in contrary to the generation kinetics curves of the TD and STD where the saturation behaviour could be only tentatively (because of possible errors of the absorption coefficient measurement) attributed to a few species for both types of samples (Fig. 1).

There have been several attempts to model the generation kinetics of TD-related centers [9] [10]. One general assumption of all these models was that the annealing time dependence of the TD generation is a process of stepwise

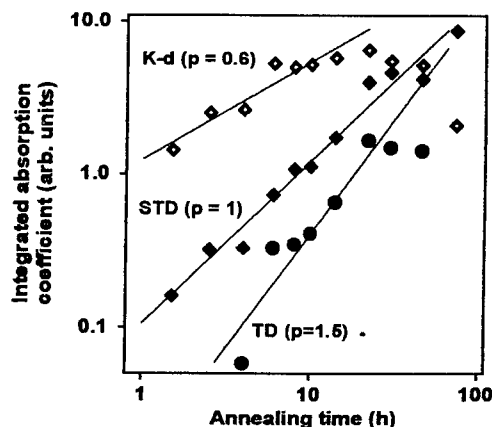


Fig. 1 The generation kinetics of the K-donors (K-d), shallow thermal donors (STD) and thermal donors (TD). The data presented are „as measured” with no further scaling. The two points (for highest annealing times) of the K-donor and STD curve and one for the TD curve are quite unreliable because of the measurement below the 5% transmission limit. The apparent saturation for the TD curve could thus be an artefact.



agglomeration of single oxygen atoms on seed centres which should be the "first" thermal donors. Thus, each of the species observed in the absorption experiment (TD1, TD2 etc.) would "contain" a different number of agglomerated oxygen atoms. Each of the reactions was assumed to be diffusion limited and to follow a second order kinetics. The rate coefficients were constant of the type:  $k = 4\pi DR$  where  $D$  - sum of diffusion coefficients of reacting species (usually a multiple of the oxygen diffusion coefficient  $D_{ox}$ ),  $R$  - "interaction radius" - the distance from the seed within which an irreversible agglomeration of the single oxygen atom takes place. In some of these models [9] the order of the kinetics was reduced by assumption that the oxygen concentration ( $N_{ox}$ ) was much larger than the TD concentration and therefore constant during the agglomeration process. The task was to solve a system of coupled differential equations - each of them describing the growth process of a single TD-species.

Such a mathematical procedure (even without the assumption of  $N_{ox} = \text{const}$ ) is not able to describe the time dependence of the TD annealing kinetics observed in our annealing experiment. A simple numerical test - solving of 10 coupled equations - showed that the initial slopes of the generation kinetics *do* depend strongly on the "sequence number" of the TD-species. Secondly, assuming an initial oxygen concentration of  $1 \cdot 10^{18} \text{ cm}^{-3}$ , a dimer seed,  $D = D_{ox} = 5 \cdot 10^{-19} \text{ cm}^2/\text{s}$  (a  $470^\circ \text{C}$  extrapolation of higher temperature diffusion data) and  $R = R_{ox} \sim 5 \text{ \AA}$ , the yield of already the fifth TD-species would have been under the sensitivity limit of any spectrometer ( $N_{TD5} < 10^{12} \text{ cm}^{-3}$ ) thus the TD6 - TD15 species would not be accessible for the observation. Increasing of the rate constant (i.e.  $D_{ox}$  or  $R_{ox}$ ) helps to improve the yield but the strong dependence of  $p$  on the TD sequence number remains. A further improvement, especially when large interaction radii are assumed, can be achieved

by introduction of the time dependent reaction rate [11]:  $k = 4\pi DR \left( 1 + \frac{R}{\sqrt{\pi Dt}} \right)$ .

The dependence of the "initial slope" powers on the TD sequence number is less striking but still present. Eventually, it seems that for implementing the above model to the description of the TD generation kinetics a diffusion coefficient of oxygen or an "interaction radius"  $R_{ox}$  (or both) are needed which are much higher than "reasonable" values of  $D_{ox} \sim 5 \cdot 10^{-19} \text{ cm}^2/\text{s}$  and  $R_{ox} \sim 5 \text{ \AA}$ . The result however is still not satisfactory.

Instead of modelling a complex process consisting of several consecutive reactions one can attempt to investigate the K-donor kinetics only. It seems that it is quite distinct from the other TD's and STD's generation processes: the annealing curve is markedly different from that of the other defects ( $p = 0.6$ !) and the K-donor is observed only in Al-doped samples which strongly suggest that the K-donor must be an oxygen-aluminium complex.

We tested four relatively simple reaction schemes based on two assumptions: a) the K-donor generation is independent of the TD and STD generation, b) the Al-atoms act as quasi-immobile seed-centers for fast diffusing oxygen atoms: the diffusivity of aluminium in silicon at the TD-annealing temperature is three to five orders of magnitude lower than that of oxygen [12].

The reaction schemes for 1 or 2 agglomerating oxygens are as follows: a)  $\text{Al} + \text{O} \rightarrow \text{K-donor}$ , b)  $\text{Al} + 2\text{O} \rightarrow \text{K-donor}$ , c)  $\text{Al} + \text{O} \rightarrow \text{Intermediate}$ ,  $\text{Intermediate} + \text{O} \rightarrow \text{K-donor}$ , d)  $\text{O} + \text{O} \rightarrow \text{O}_2$ ,  $\text{O}_2 +$

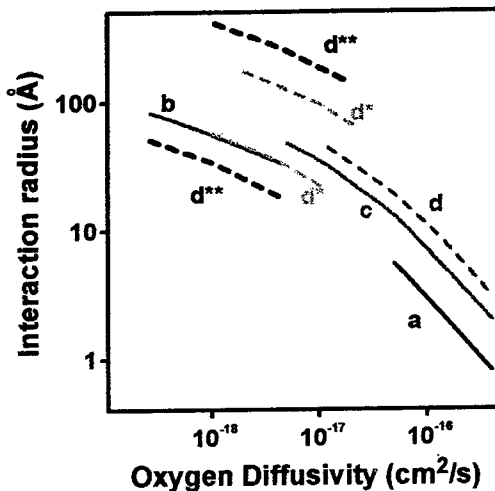


Fig. 2. The interaction radius  $R$  vs the diffusivity  $D$  for various K-donor generation mechanisms (explanation of the symbols can be found in text).

Al  $\rightarrow$  K-donor. Each of the schemes is described by a set of first order nonlinear differential equations with rate coefficients as in [11]. The annealing time dependence of the K-donor concentration -  $n_K(t_{\text{anneal}})$  - for all above the reaction schemes depends on only 2 parameters -  $R_{\text{ox}}$ ,  $D_{\text{ox}}$  of the single oxygen atom. For the solution of the scheme d) a simplifying assumption was made: the reaction rate of the molecule formation is by a constant factor  $f$  smaller than the rate for the K-donor formation reaction. In this way, the model of fast diffusing ( $D_{\text{O}_2} > D_{\text{ox}}$ ) oxygen molecule [13] could be tested.

Each theoretical  $n_K(t_{\text{anneal}})$  dependence was fitted to the experimental K-donor generation kinetics and values of  $R_{\text{ox}}$  and  $D_{\text{ox}}$  have been obtained. A comparable fit quality has been obtained for different  $R_{\text{ox}}-D_{\text{ox}}$  pairs for each agglomeration mechanism. Therefore, not a single  $(R, D)$ -pair but a  $R$  vs  $D$  curve connecting values of diffusivity and interaction radius could be estimated for the particular mechanism. The results obtained from the best fit to the experimental K-donor annealing kinetics for the particular agglomeration mechanism are displayed in Fig. 2.

As one can see, for any considered model, it is not possible to obtain an interaction radius of the order of the lattice constant of silicon ( $R \sim 5 \text{ \AA}$ ) without assuming very high diffusivities of the isolated oxygen. On the other hand, if one assumes oxygen diffusivities to be of the order of that estimated from Ref. [3] the interaction radius becomes large and the reaction mechanism has to involve two consecutive reactions.

Even the model of fast diffusing oxygen molecules does not provide a sufficient improvement. The  $R(D)$ -curves for this mechanism have been estimated at three different ratios  $f$  of the K-donor formation rate to the oxygen molecule formation rate (Fig. 2). In the case when this ratio is larger than 1 a pair of curves is obtained. The  $R_{\text{O}_2}(D_{\text{O}_2})$ -curve representing the K-donor formation (the Al +  $\text{O}_2$  reaction) is shifted up with respect to the one for the oxygen-molecule formation  $R_{\text{ox}}(D_{\text{ox}})$  (curves labeled d\* at  $f = 6$  and d\*\* at  $f = 32$  in Fig. 2). For  $f = 1$ ,  $R_{\text{O}_2}(D_{\text{O}_2}) = R_{\text{ox}}(D_{\text{ox}})$  (curve d) and the mechanism of "fast diffusing  $\text{O}_2$  molecule" is comparable to the subsequent addition of oxygen atoms to the seed. As the ratio  $f$  increases, the diffusion coefficient of oxygen -  $D_{\text{ox}}$  can be "reduced" to the value of Ref. [3] but, on the other hand, the interaction radii  $R_{\text{ox}}$  - for the molecule formation and  $R_{\text{O}_2}$  - for the Al +  $\text{O}_2$  reaction remain as high ( $\sim 70 \text{ \AA}$ ) as for other, simpler mechanisms or grow rapidly to a completely unrealistic  $R_{\text{O}_2} \sim 300 \text{ \AA}$ , respectively.

If one assumes that the diffusivity of oxygen is of the order of  $D_{\text{ox}} \sim 5 \cdot 10^{-19} \text{ cm}^2/\text{s}$ , a very high interaction radius for all considered reaction mechanisms is obtained. A simple Coulomb attraction of the reacting species (if they were of the opposite sign and Al is certainly a negatively charged acceptor at  $470^\circ\text{C}$ , when the K-donor is generated) could be the "interaction" of which the "radius" has to be estimated only if it overcame the mean energy of the species ( $kT$  value at  $470^\circ\text{C} \approx 64 \text{ meV}$ ). In this case however the interaction radius not larger than  $20 \text{ \AA}$  would be sufficient and a diffusivity of the order of  $3 \cdot 10^{-17} \text{ cm}^2/\text{s}$  will be required (Fig. 2).

All the mechanisms considered above for the TD as well as for the K-donor (regarded as an aluminium-oxygen complex) formation are based on one common general assumption: the formation process consists of a series of consecutive reactions in which single diffusing oxygen atoms (or oxygen molecules) are trapped by seed centres - oxygen atoms or dimers in case of the TD-formation or an Al-atom in the case of the K donor generation. The mechanisms require an oxygen diffusivity being two orders of magnitude higher than the value

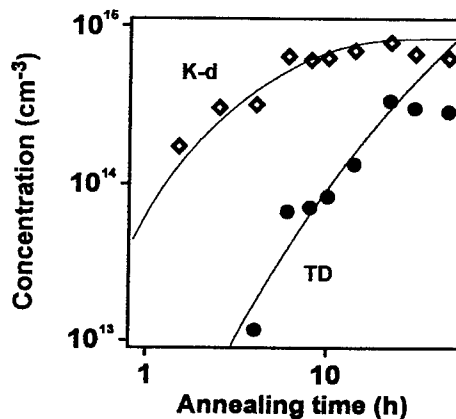
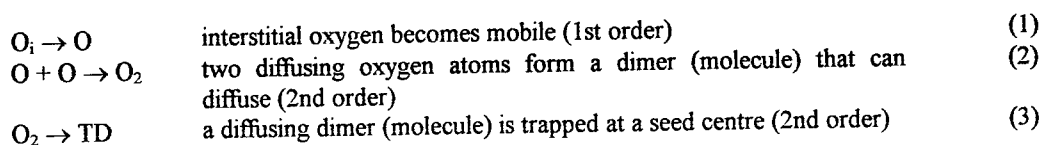


Fig. 3. A simulation of the K-donor and TD generation during dimer creation and concurrent dimer trapping reactions.

expected from direct oxygen diffusion measurements [3] at temperatures higher and lower than 470 °C. This seems to be consistent with several indirect estimates of  $D_{\text{ox}}$  at TD formation temperatures [2].

However, we can propose an other simple mechanism which models basic features of the measured TD and K-donor kinetics and *does not* require either an oxygen diffusivity value higher than that estimated according to ref. [3] or a high value of "interaction radius". It consists of the following three reactions:



Following rate parameters have been chosen: for the reaction (1) a constant rate is assumed, sufficiently high to provide a constant concentration (equal to the initial oxygen concentration) of diffusing oxygen atoms throughout the entire duration of the reaction time (that all oxygen atoms present in the sample can diffuse was implicit also in the mechanisms discussed above). For the reactions (2) and (3) time dependent reaction rates [11] have been assumed. The reaction (3) represents in fact several *concurrent* trapping reactions (8 in our simulation). The diffusivity  $D$  in (2) and (3) has been put equal to the oxygen diffusivity value of  $5 \cdot 10^{-19} \text{ cm}^2/\text{s}$  for simplicity, although a *lower* diffusivity for the dimer would not essentially limit the efficiency of the entire process. The radius  $R$  was chosen to be  $1.5 \text{ \AA}$  for both reactions. The concentration of the seed centres is  $1.5 \cdot 10^{20} \text{ cm}^{-3}$  (!). The numerical solution of the differential equation set for reactions (1)–(3) are displayed in Fig. 3 versus the experimental data of the K-donor and TD kinetics. The experimental points are not any more in arbitrary units but were scaled to give „reasonable“ concentration values of the K-donors and the particular TD species. This scaling is of course somewhat arbitrary as there is no direct relation of the TD-absorption coefficient and TD-concentration. The criterion was that the lowest concentration values correspond to the detectivity limit of the spectrometer setup used and the relations of Fig. 2 are conserved. One sees that the simulation remarkably well corresponds to the experiment. The only (quickly) saturating annealing curve is that of the K-donor kinetics. The TD generation curve is far from saturation.

The model was proven to work well simulating the *entire* kinetics of oxygen agglomeration i.e. for several TD and STD species and the K-donor simultaneously. A fit to the scaled experimental data could be obtained by retaining the  $R$  and  $D$  values given above and varying only the seed center concentration. The value of this concentration determines the particular value of the „initial slope“ power  $p$ . The seed centre concentration was found to be approximately of the order of  $1 \cdot 10^{20} \text{ cm}^{-3}$  for all TD species and of the order of  $5 \cdot 10^{18} \text{ cm}^{-3}$  for the STD. Similar results were obtained also for three different scalings of the experimental data.

A very interesting property of the model has also been found: the concentration of all the TD-related centres goes below the  $10^{12} \text{ cm}^{-3}$  as the initial oxygen concentration becomes lower than  $O_i \sim 1 \cdot 10^{16} \text{ cm}^{-3}$ . This agrees well with the experimental finding that the TD's are observed only at higher oxygen concentrations [2].

## Discussion

In a previous paper [14] it was argued that a physical reason for the very high oxygen diffusivity at TD annealing temperatures found for models based on the *consecutive* agglomeration of oxygen atoms might be expected due to the metastable behaviour of the "early" TD and the K-donors. The metastability mechanism of the K-donors and TD are similar and both remind of the metastable behaviour of the so called DX-centres in AlGaAs [15]. The DX-type metastability found for the K-donors and TD defects are signs that this defect may be a very good candidate for an intermediate diffusion step (saddle point) in the diffusion process of oxygen at the TD annealing temperatures. By

an analogy, the DX centre configuration in GaAs:Si has been found to be a low energy saddle point for the vacancy-mediated Si diffusion in GaAs [16], for which a substantial lowering of the migration barrier is expected.

Now, it seems that a powerful alternative explanation can be proposed - the model of *concurrent trapping* reactions. The high oxygen diffusivity would no longer be needed. Instead, a high concentration of trapping centres would be welcome. This can be easily provided by the silicon atoms themselves - they are present in sufficient quantity in the Si-sample. According to a recent theoretical model [17] of the TD centre structure two oxygen atoms and one Si interstitial build the core of the TD-species. One could imagine that the moving oxygen dimer (the dimer diffusivity can be of the order of the oxygen diffusivity or lower !) becoming trapped by the silicon atom pushes it out of the substitutional into the interstitial position and the lattice relaxation involved stabilizes this configuration immobilizing the dimer. The immobilized dimer would be the thermal donor centre. Each centre would form nearly the same way independently from the others. The "initial slope" power would thus be the same for each thermal donor and would not depend on the TD "sequence number". The differences in binding energy observed for the TD-species would then have its origin in the different central cell structure of each thermal donor being due to unavoidable slight variations in the centre short range potential and symmetry after the (trapping) relaxation of the three atom complex.

The K-donor in turn would then represent a dimer "loosely" bound to the silicon lattice (or aluminum) atoms. The "loose" bond would then be responsible for large relaxation phenomena observed for the K-donors.

This work is supported in part by the European Community grant N° CIPA-CT94-0172.

## References

1. S. Fuller, J. A. Ditzenberger, N. B. Hannay, E. Buehler, *Phys. Rev.* **96**, 833 (1954).
2. J. Michel and L. C. Kimmerling in *Semiconductors and Semimetals Vol. 42*, eds. R. K. Willardson, A. C. Beer, W. R. Weber, vol. ed. F. Shimura, p. 251 (Academic Press, 1994).
3. Stavola, J. R. Patel, L. C. Kimmerling, and P. E. Freeland, *Appl. Phys. Lett.* **42**, 73 (1983).
4. A. Griffin, H. Navarro, J. Weber, L. Genzel, J. T. Borenstein, J. W. Corbett, and L. C. Snyder, *J. Phys. C* **19**, L579 (1986).
5. P. Kaczor, K. Kopalko, M. Godlewski, and T. Gregorkiewicz, *Acta Phys. Pol.* **82**, 677 (1992).
6. P. Kaczor, K. Kopalko, M. Godlewski, and T. Gregorkiewicz, *Proc. of the 17th Intern. Conf. on Defects in Semiconductors, Gmunden, Austria, 1993*, ed. by H. Heinrich and W. Jantsch, *Mat. Sci. Forum* **117-120**, (Trans Tech Publications, Switzerland 1994), p. 1185.
7. P. Wagner, J. Hage *Appl. Phys. A* **49**, 123 (1989).
8. W. Götz, G. Pensl, and W. Zulehner *Phys. Rev. B* **46**, 4312 (1992).
9. M. Suezawa and K. Sumino, *phys. stat. sol. (a)* **82**, 235 (1984); K. Wada, *Phys. Rev. B* **30**, 5884 (1984).
10. D. Mathiot, *Appl. Phys. Lett.* **51**, 904 (1987).
11. M. Smoluchowski, *Zeitschrift f. Phys. Chem.* **92**, 129 (1917).
12. Landoldt-Börnstein, Numerical Data and Functional Relationships in Science and Technology New Series Group **III** Vol. **22b**, Semiconductors, Impurities and Defects in Group IV Elements and III-V Compounds pp. 230-249 (1989).
13. U. Gösele, K.-Y. Ahn, B. P. R. Marioton, T. Y. Tan, S.-T. Lee, *Appl. Phys. A* **48**, 219 (1989).
14. P. Kaczor, L. Dobaczewski *Proc. of the 7th International Conference on Shallow Level Centres in Semiconductors, Amsterdam, The Netherlands 1996*, ed. C. A. J. Ammerlaan and B. Pajot, (World Scientific, Singapore 1997), p. 197.
15. J. E. Dmochowski, L. Dobaczewski, J. M. Langer, W. Jantsch, *Phys. Rev. B* **40**, 9671 (1989).
16. J. Dąbrowski, J. E. Northrup, *Phys. Rev. B* **49**, 14 286 (1994).
17. P. Deak, L. C. Snyder, J. W. Corbett *Phys. Rev. B* **45**, 11612 (1992).

## DIFFUSION AND PRECIPITATION OF OXYGEN IN SILICON DOPED WITH GERMANIUM

L.I.Khirunenko, V.I.Shakhovtsov , V.V.Shumov

Institute of Physics of the National Academy of Sciences of Ukraine ,  
Pr.Nauki 46, 252650, Kiev-22, UKRAINE

**Keywords:** silicon, germanium, oxygen, thermal donor, relative oxygen loss

**Abstract.** A nonmonotonic dependence of rate of oxygen loss on germanium content during isothermal ( $T=450^{\circ}\text{C}$ ) annealing of  $\text{Si}<\text{Ge}>$  has been found. A possible mechanism of germanium doping influence on the formation process of low-temperature thermal donors in silicon is proposed.

### Introduction.

Oxygen precipitation in silicon is strongly affected by the presence of impurities such as C, Ge and N. The doping of silicon with germanium is known to decrease of formation efficiency of low-temperature ( $T=450^{\circ}\text{C}$ ) thermal donors (TD) [1-4]. However, the mechanism of this effect is still not clear. New data on the influence of the doping of Si with germanium on the rates of loss and precipitation of oxygen during heat treatment at  $450^{\circ}\text{C}$  are discussed in present paper.

### Experimental.

The samples of n-type Cz Si  $<\text{Ge}>$  with resistivity about  $25\Omega\cdot\text{cm}$  were used for investigations. The germanium concentration was  $N_{\text{Ge}}=10^{18}\text{-}10^{20}\text{ cm}^{-3}$ . The concentrations of oxygen and carbon measured by IR absorption were  $N_{\text{O}}=(0.8\text{-}1)\cdot 10^{18}\text{ cm}^{-3}$  and  $N_{\text{C}}\leq 10^{16}\text{ cm}^{-3}$ , respectively. Heat treatment up to  $t = 550$  hours was performed at  $T=450^{\circ}\pm 5^{\circ}\text{C}$  in the air atmosphere. Chemical etching of samples in HF was carried out before measurements. IR Fourier transform spectroscopy and Hall effect measurements were used for investigations.

### Results and Discussion.

The dependence of relative oxygen loss  $\eta(t) = 1 - N_{\text{O}}(t)/N_{\text{O}}(0)$  on thermal treatment duration and concentration of Ge which were obtained in our investigations is shown in Fig.1. It is seen that the values of  $\eta(t)$  in samples with  $N_{\text{Ge}} < 5\cdot 10^{19}\text{ cm}^{-3}$  are larger than those in undoped Si at any thermal treatment duration while at higher germanium concentrations values of  $\eta(t)$  are smaller than those in Si. In Fig.2 (curve a) the dependence of  $\eta(t)$  on germanium concentration in Si  $<\text{Ge}>$  at thermal treatment duration  $t = 250$  hours is illustrated. At  $N_{\text{Ge}} \approx 3\cdot 10^{19}\text{ cm}^{-3}$  a well pronounced maximum is seen. The same behavior of  $\eta(t)$  on  $N_{\text{Ge}}$  was observed for time of annealing up to 550 hours.

The dependence of TD concentrati on germanium content after 550 hours of annealing is demonstrated in Fig.3 (curve a). As it is seen unlike behavior of  $\eta(t)$  this dependence is monotonic.

The process of oxygen precipitation in Si is known to occur by successive trapping and releasing of interstitial oxygen atoms by oxygen-related clusters of various sizes. This process may be described by quasi-chemical combined equations [5,6]. The trapping probability of interstitial oxygen atom by oxygen-related cluster is described then by next expression [5,6]:

$$k_i = 4\pi \cdot D \cdot r_c^i, \quad (1)$$

where  $D$  is the diffusion coefficient of interstitial oxygen,  $r_c^i$  is the capture radius of  $O$  atom by cluster  $O_i$  which contains  $i$  oxygen atoms.

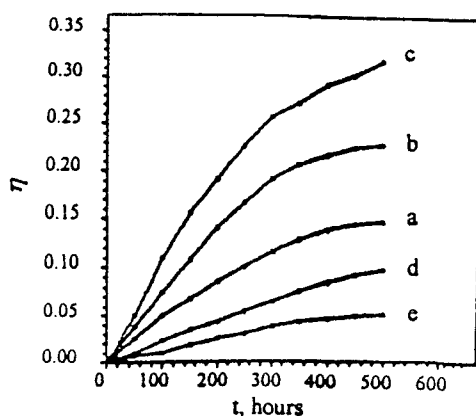


Figure 1. The annealing time dependence of relative oxygen loss in Si<Ge>.  
 $N_{Ge}, \text{cm}^{-3}$ : a - 0; b -  $3 \cdot 10^{18}$ ; c -  $2.6 \cdot 10^{19}$ ; d -  $5.3 \cdot 10^{19}$ ; e -  $1 \cdot 10^{20}$

As it was reported earlier [7,8], the doping with *Ge* appears to increase the diffusion coefficient  $D$  of interstitial oxygen in *Si*. In accordance with (1) the formation efficiency of TD would have to be increased in *Si<Ge>* in this case. However, existing experimental data [1-4] provide an evidence that both formation efficiency and maximum concentration of TD in *Si<Ge>* are smaller than those in *Si*. So the decrease of values of  $k_i$  in *Si<Ge>* may be caused by a decrease of capture radius  $r_c^i$  of oxygen atoms by TD embryos  $O_i$  in the fields of internal elastic strains created by germanium atoms [4].

The TD core is known to produce considerable strain in the lattice, and strain relief to be a driving force for oxygen atom trapping [10]. An average strain that is produced by *Ge* atoms in *Si<Ge>* can influence on the strain relief near TD embryo and thus can change the value of capture radius of an oxygen atom. In accordance with [11] the value of capture radius is defined by:

$$\frac{1}{r_c} = \int_{r_0}^{\infty} \frac{\exp\{\varphi(r)/kT\}}{r^2} \cdot dr, \quad (2)$$

where  $\varphi(r)$  is the strain interaction potential between an O atom and TD core,  $r_0$  is the minimum distance between them and  $k$  is Boltzmann's constant.

It was shown recently [9] that elastic strain fields which are formed in *Si<Ge>* appears to decrease the potential barrier height for diffusion of interstitial oxygen. At low germanium concentration ( $N_{Ge} \leq 1 \cdot 10^{20} \text{cm}^{-3}$ ) the value of average change of potential barrier height may be approximated by the expression [9]:

$$\delta E_a \approx -\gamma \cdot n \quad (3)$$

where  $\gamma$  is a constant and  $n$  is the concentration of *Ge*.

In accordance with (2,3) the expression for capture radius may be transformed to:

$$r_c \approx r_c^0 \cdot \exp\{\delta E_a / kT\} \quad (4)$$

where  $r_c^0$  is the capture radius of oxygen atoms by TD embryos in undoped Si, which is calculated from (2) - (3) at  $x=0$ . Taking into consideration the change of potential barrier height for interstitial oxygen diffusion, the capture radius  $r_c^i$  and size  $r_i$  of TD embryo, expression (1) may be written as:

$$k_i \approx k_i^0 \left( 1 - \frac{r_i}{r_c^i} \cdot \exp\{-\delta E_a / kT\} \right) \quad (5)$$

where  $k_i^0$  is the value of  $k_i$  in undoped Si. An analysis of the obtained expression shows that the probability of interstitial oxygen trapping by  $O_i$  cluster is decreased monotonically as germanium

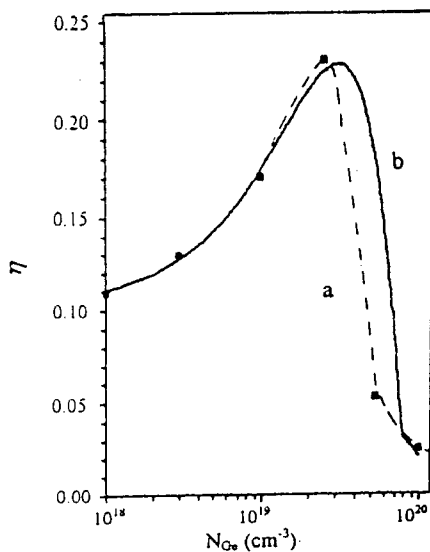


Figure 2. Relative oxygen loss resulting from annealing of Si<Ge> after  $t=250$  hours.  
a - experimental, b - theoretical

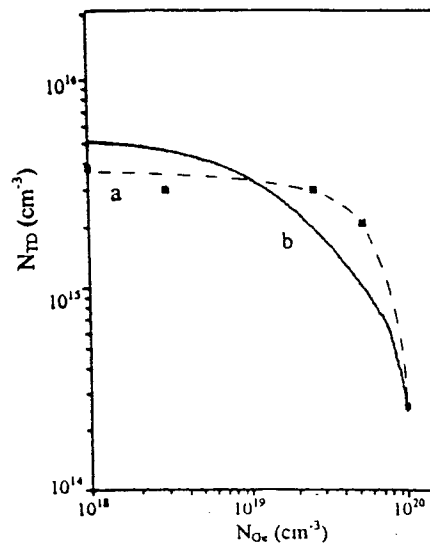


Figure 3. The dependence of TD concentrations on germanium content in Si after 550 hours of annealing.  
a - experimental, b - theoretical

concentration is increased. That would have to lead to a monotonic decrease both relative oxygen loss and TD concentration during heat treatments. However, as it was mentioned above a nonmonotonic dependence of  $\eta$  ( $i$ ) on germanium concentration was observed.

Earlier [12] the appearance of new type (new embryos) of TD in Si<Ge> in comparison with Si was reported. In view of this process the quasi-chemical combined equations [5,6] may be altered to:

$$\begin{aligned} \frac{dO_1}{dt} &= 2b_2O_2 + b_2O_2 + b_0O_1 - k_0 \left( N - \sum_{i=1}^M O_i \right) O_1 - (2k_1O_1 + k_1O_1) + \\ &+ \sum_{i=2}^{M-1} ((b_{i+1}O_{i+1} + b_{i+1}O_{i+1}) - (k_iO_i + k_iO_i)O_i) \\ \frac{dO_i}{dt} &= b_2O_2 - b_0O_1 + k_0 \left( N - \sum_{i=1}^M O_i \right) O_i - k_1O_1O_i \end{aligned}$$

$$\begin{aligned}
\frac{dO_n}{dt} &= k_{n-1}O_{n-1}O_1 - b_nO_n + b_{n+1}O_{n+1} - k_nO_nO_1, \\
\frac{dO'_n}{dt} &= k'_{n-1}O'_{n-1}O_1 - b'_nO'_n + b'_{n+1}O'_{n+1} - k'_nO'_nO_1 \\
\frac{dO_M}{dt} &= k_{M-1}O_{M-1}O_1 - b_MO_M \\
\frac{dO'_M}{dt} &= k'_{M-1}O'_{M-1}O_1 - b'_MO'_M
\end{aligned} \quad (6)$$

where  $n = 2 \dots M-1$ ;  $M$  is the maximum number of oxygen atoms in cluster considered;  $N'$  is the concentration of additional centers for oxygen precipitation;  $O_i$  is the concentration of oxygen cluster which contains  $i$  oxygen atoms;  $O'_i$  is the concentration of additional oxygen-related clusters which include  $i$  oxygen atoms;  $k_0'$  and  $b_0'$  are the probabilities of trapping and releasing of O atom to the additional precipitation center, respectively and  $k_i$ ,  $k'_i$ ,  $b_i$ ,  $b'_i$  are the probabilities of trapping and releasing of an O atom to  $O_i$  and  $O'_i$  clusters, respectively.

The theoretical dependence of  $\eta(t)$  value on germanium concentration was obtained by numerical integration of (6). The results for  $T=450^\circ\text{C}$  and  $t = 250$  hours are shown in Fig.1 (curve  $b$ ). The assumptions made were that the temperature dependence of diffusion coefficient is defined by expression [6]  $D_0 = 0.13 \exp(-2.53eV/kT) \text{ cm}^2\text{s}^{-1}$ ; the decay probability of oxygen-related clusters were  $(b_i = b'_0 = b'_i = 5 \cdot 10^{-7} \text{ s}^{-1})$ , oxygen atoms are distributed homogeneously in initial time with the concentration  $1 \cdot 10^{18} \text{ cm}^{-3}$ ; the values  $k_i$  and  $k'_i$  are the same for all clusters which contain up to  $M=10$  oxygen atoms and defined by expression (5). The assumed values of  $r_i \cong a = 2.35 \text{ \AA}$ ,  $r_c^i \cong 4.5 \text{ \AA}$ ,  $r_c \cong 3.5 \text{ \AA}$ ,  $\gamma = 4 \cdot 10^{-22} \text{ eV} \cdot \text{cm}^3$  agree reasonably with those used in other work [6,13]. As it is seen from Fig.2 conformity of theoretical dependence with experimental data ( $a$  and  $b$  curves) is observed.

Using quasi-chemical combined equations (6) the dependence of TD concentration on germanium content in Si was calculated. In Fig.3 the theoretical and experimental dependences are illustrated for heat treatment duration  $t=550$  hours. To obtain a theoretical value of TD concentration was used the total concentration of oxygen-related clusters which contain  $n \geq 3$  oxygen atoms was used. As it is seen from Fig.3 the satisfactory conformity for theoretical and experimental dependences is also observed. The absence of the pronounced maximum observed experimentally may be explained by supposing that the majority of oxygen loss during the heat treatment results in formation of oxygen-related clusters which contain less of atoms than those in the core of the smallest TD. The qualitative conformity between experimental and calculated dependences is in good correlation with proposed theoretical model of germanium doping influence on the TDs formation processes in Si.

#### Acknowledgements

This work was supported by the Science and Technology Centre in Ukraine (project N351).

#### References.

1. D.I.Brinkevich, N.I.Gorbacheva, V.V.Petrov, V.D.Tkachev, B.M.Turovskij and V.V.Chernyi, Doklady Akademii Nauk BSSR 30, 308 (1986).
2. Y.M.Babitskij, N.I.Gorbacheva, P.M.Grinstein, M.A.Ilin, V.P.Kuznetsov, M.G.Milvidskij and B.M.Turovskij, Fizika i Tekhnika Poluprovodnikov 22, 307 (1988).
3. D.N.Korljakov, Neorganicheskie materialy 27, 1333 (1991).



- 
4. D.I.Brinkevich, V.P.Markevich, L.I.Murin and V.V.Petrov, *Fizika i Tekhnika Poluprovodnikov* **26**, 682 (1992).
  5. T.Y.Tan, R.Kleinhenz and C.P.Shneider, *Mat. Res. Symp. Proc.* **59**, 195 (1986).
  6. S.A.McQuaid, M.J.Binns, C.A.Londos, J.H.Tucker, A.R.Brown and R.C.Newman, *J.Appl. Phys.* **77**, 1427 (1995).
  7. A.K.Tipping, R.C.Newman, D.C.Newton and J.H.Tucker, *Material Science Forum* **10-12**, 887 (1986).
  8. V.M.Babich, N.P.Baran, K.I.Zotov, V.L.Kirica and V.B.Kovalchuk, *Fizika i Tekhnika Poluprovodnikov* **29**, 58 (1995).
  9. L.I.Khirunenکو, V.I.Shakhovtsov and V.V.Shumov, *Fizika i Tekhnika Poluprovodnikov* (in press).
  10. G.D.Watkins, in "Early Stages of Oxygen Precipitation in Silicon" ed. R.Jones (Dordrecht / Boston / London: Kluwer Academic Publishers) pp.1-18 (1996).
  11. V.L.Vinetskij and I.I.Yaskovets, in: "Physical Processes in Defect Crystals" ( Kiev: Institute of Physics of the Academy of Sciences of Ukraine) pp. 76-110 (1990).
  12. T.V.Kritskaja, L.I.Khirunenکو, V.I.Shakhovtsov and V.I.Yashnik, *Fizika i Tekhnika Poluprovodnikov* **22**, 1129 (1990).
  13. M.Lannoo and J.Bourgoin in "Point Defects in Semiconductors. Theoretical aspects". (Berlin-Heidelberg-New York, Springer Verlag) p. 246 (1981).

## THE INFLUENCE OF ISOVALENT DOPING ON DIFFUSION OF INTERSTITIAL OXYGEN IN SILICON

L.I.Khirunenکو, Yu.V.Pomozov, V.I.Shakhovtsov, V.V.Shumov

Institute of Physics of the National Academy of Sciences of Ukraine

**Keywords:** silicon, isovalent impurities, elastic stresses, elastic continuum, potential barrier height.

**Abstract.** The doping of silicon with isovalent impurities is shown to change the potential barrier height for interstitial oxygen diffusion. The value and sign of this change are defined with the sign of deformation which arises in *Si* at doping with isovalent impurity and its concentration.

### Introduction.

The doping with isovalent impurities (IVI) was found to influence essentially on the processes of the diffusion and precipitation of interstitial oxygen in *Si* at heat treatment [1-3]. But the nature of this influence is still not completely understood up to now. The different and sometimes contrary points of view on this effect exist. Some authors have noted the increase of the activation energy for oxygen diffusion *Si* doped with *Ge* [1], other pointed out enhanced diffusion of oxygen in *Si*<*Ge*> [2,3], as others - delayed one [4]. But it is known to exist the correlative ditribution of *Ge* and oxygen atoms in *Si* [5,6].

The influence of internal elastic stresses produced in *Si* by IVI atoms on interstitial oxygen diffusivity is considered in this work.

### Results and Discussion.

In accordance with [7] the diffusion of interstitial oxygen occurs by successive jumps from one *Si-Si* bond to another in direction [110]. At that *O* atom breaks a bond with *Si*(1) atom and forms a new bond with *Si*(3) atom (Fig.1). During the jump the distance *O-Si*(2) undergoes an insignificant changes. Then one can consider the jump as a motion between *Si*(1) and *Si*(3) atoms. Let *d* - the *Si*(1) - *Si*(3) distance,  $\phi(r)$  - potential energy of *O-Si*(1) interaction (model potential),  $\phi(d-r)$  - potential energy of interaction *O-Si*(3), *r*<sub>0</sub> - equilibrium *O-Si*(1) distance corresponding to the minimum value of  $\phi(r)$ . The potential  $\phi(r)$  must be satisfied with following condition:

$$\lim_{r \rightarrow \infty} \phi(r) = \text{const} \quad (1)$$

Having assumed condition (1) the resulting potential may be written as the sum:

$$\Phi(r) = \phi(r) + \phi(d-r) \quad (2)$$

Such a summary potential creates a potential barrier for motion of *O* atom between *Si*(1) and *Si*(3) atoms. The height of this barrier is:

$$E_a = \Phi(d/2) - \Phi(r_0) \quad (3)$$

If the chain [110] of *Si* atoms includes an IVI atom then there are changes of interatomic distances because of difference of covalent radii of IVI and *Si* atoms. Let the change of distance between *Si*(1)

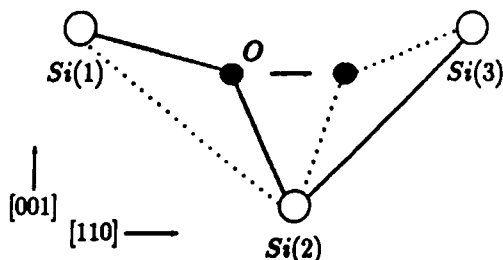


Figure 1. Diffusion of interstitial oxygen in silicon.

and  $Si(3)$  atom is  $\Delta d$ . Using (2) and (3) the change of potential barrier height may be expressed as:

$$\Delta E_a = 2 \cdot \{ \phi(d/2 + \Delta d/2) \} - \{ \phi(d + \Delta d - r_0) - \phi(d - r_0) \} \approx \{ \phi'(d/2) - \phi'(d - r_0) \} \cdot \Delta d, \quad (4)$$

where  $\phi'(r)$  is a derivative of function  $\phi(r)$ . Since  $r_0 < d/2$  for potential  $\phi(r)$  then taking into consideration (1) the next expressions seem to be correct (Fig. 2):

$$\phi'(d/2) > 0, \quad \phi'(d - r_0) > 0, \quad \phi'(d/2) > \phi'(d - r_0) \quad (5)$$

Then the term before  $\Delta d$  in (4) is positive that is the sign of value of change of potential barrier height  $\Delta E_a$  is defined by the sign of value of interatomic distance change.

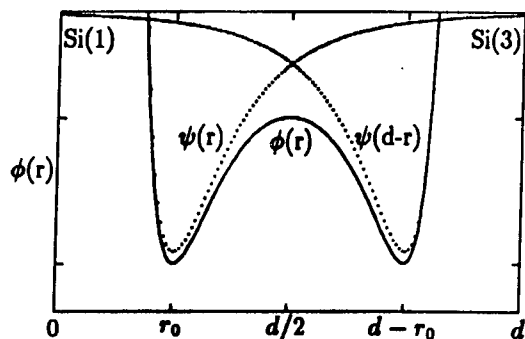


Figure 2. Potential barrier for diffusion of interstitial oxygen in silicon.

The change of interatomic distances produced by IVI atoms in  $Si$  may be described in an approach of elastic continuum. In this approach an IVI atom acts as a point source of deformation which produces the shift of lattice atoms [8,9]:

$$\vec{u}(\vec{r}) = A \cdot \frac{\vec{r}}{r^3}, \quad (6)$$

where  $\vec{u}(\vec{r})$  is the shift of the lattice atom from equilibrium position,  $r$  - distance of a lattice atom from point source of deformation,  $A$  - deformation charge of an IVI atom (volume change of crystal

equilibrium positions are radial directed. We are interested only the influence of IVI on possibilities of oxygen motion "to" *Ge* atom. Thus we shall consider further only the changes of interatomic distance in radial directions. The relative change of interatomic distance in radial direction is described by strain tensor component  $u_{rr}$  [10]:

$$u_{rr} \approx \frac{\Delta d(r)}{d} = - \frac{2 \cdot A}{r^3} \quad (7)$$

Using (4) and (7) we obtain finally:

$$\Delta E_a(r) = - \frac{\beta}{r^3}, \quad (8)$$

where 
$$\beta \approx 2 \cdot d \cdot A \cdot \{ \phi'(d/2) - \phi'(d-r_0) \} = \text{const} \quad (9)$$

Thus the doping of silicon with IVI may lead to the change of potential barrier height for diffusion of interstitial oxygen. The sign of value of this change is determined by the sign of deformation charge of IVI atom. For instance, in case of *Ge* ( $A_{Ge} = 1.2 \cdot 10^{-25} \text{ cm}^3$ ) and *Sn* ( $A_{Sn} = 8 \cdot 10^{-25} \text{ cm}^3$ ) the deformation charges are positive and in the case of carbon ( $A_C = -16.5 \cdot 10^{-25} \text{ cm}^3$ ) - negative. In the first case the enhanced oxygen diffusion [2,3] and in the second - delayed one should be observed.

At high IVI concentration the overlap of their elastic strain fields may occurs. In (8) we didn't considered this case. The uniform distribution of point sources of deformation (6) is well known to lead to the uniform dilatation [8]. The mean value of this dilatation is [8]:

$$\langle u \rangle = 24 \pi \cdot \frac{(1-2\nu)}{(1+\nu)} \cdot A \cdot n \quad (10)$$

where  $n$  - number of point sources of deformation per volume unit,  $\nu$  - Poisson's constant. The change of potential barrier height for oxygen diffusion due to uniform dilatation (10) may be expressed then as:

$$\Delta E_a = \frac{1}{3} \cdot d \cdot \langle u \rangle \cdot \{ \phi'(d/2) - \phi'(d-r_0) \} = -\gamma \cdot n \quad (11)$$

where

$$\gamma = 8 \pi \cdot d \cdot A \cdot \frac{(1-2\nu)}{(1+\nu)} \cdot \{ \phi'(d/2) - \phi'(d-r_0) \} = \text{const} \quad (12)$$

Thus the additional change of potential barrier height due to influence of strain fields of neighbouring IVI atoms leads to the change of diffusivity of oxygen on a constant term  $\exp(-\Delta E_a/kT)$  which is determined by IVI concentration.

It should be noted that various IVI influence in a different extent on the oxygen diffusion in Si. The equality of the summary deformations which are produced by each IVI may be used as a criterion of comparison of their influence on oxygen diffusivity:  $n_i = n_j$ , where  $n_i$ ,  $n_j$ ,  $A_i$ ,  $A_j$  - the concentrations and deformation charges of the IVI of  $i$ - and  $j$ -types. Since  $A \propto \Delta V$  then the next correlation may be written:

$$\frac{n_i}{n_j} = \frac{|\Delta V_j|}{|\Delta V_i|} \quad (21)$$

The next ratios between concentrations of various IVI which should produce the equivalent deformation of crystal lattice may be obtained:

$$\frac{n_{Ge}}{n_C} \approx 8, \quad \frac{n_{Ge}}{n_{Sn}} \approx 4, \quad \frac{n_C}{n_{Sn}} \approx 0,5 \quad (22)$$

Thus the doping of Si with IVI may lead to change of the potential barrier height for oxygen diffusion.

#### Acknowledgements.

This work was supported by Ukrainian Science and Technology Center (project No.351).

#### References.

1. Yu.M.Babitskii, N.I.Gorbacheva, P.M.Grinshtein, M.G.Milvidskii, *Fizika i Tekhnika Poluprovodnikov* **24**, 1129 (1984).
2. A.K.Tipping, R.C.Newman, D.C.Newton, J.H.Tucker, *Mater. Sci. Forum* **10-12**, 887 (1986).
3. V.M.Babitch, N.P.Baran, K.I.Zotov, V.L.Kiritsa, V.B. Kovalchuk, *Fizika i Tekhnika Poluprovodnikov* **29**, 58 (1995).
4. D.N.Korliakov, *Neorganicheskie Materialy* **27**, 1333 (1991).
5. L.I.Khirunencko, V.I.Shakhovtsov, V.K.Shinkarenko, *Fizika i Tekhnika Poluprovodnikov* **20**, 2222 (1986).
6. H.Yamada-Kaneta, C.Kaneta, T.Ogawa, *Phys.Rev. B* **47**, 9338 (1993).
7. M.Ramamoorthy, S.T.Pantelides, *Phys.Rev. Lett.* **76**, 267 (1996).
8. J.D.Eshelby in "Solid State Physics" ed. F.Siitz and Turnbull (New York: Academic Press) **3**, 7 (1956).
9. A.M.Stoneham in "Theory of Defects in Solids" 1 (Moscow: MIR) p. 176 - 196 (1978)
10. L.D.Landau, E.M.Lifshits in "Theory of elasticity" (Moscow: Nauka) p.12 (1965).

## EPR EVIDENCE OF HYDROGEN-ENHANCED DIFFUSION OF ALUMINUM IN SILICON

Yu.V.Gorelkinskii, B.N.Mukashev and Kh.A.Abdullin

Physical-Technical Institute, Kazakstan Academy of Sciences, 480082 Almaty, Kazakstan

**Keywords :** silicon, aluminum pair, hydrogen, diffusion, interstitial, magnetic resonance.

**Abstract.** New EPR spectra labelled Si-AA15 and Si-AA16 have been observed in monocrystalline silicon Si:Al bombarded with protons at  $\sim 80$  K. Hyperfine structure of the spectra reveals unambiguously that two and a single aluminum atom are incorporated in the AA15 and AA16 defects, respectively. Observation of the Al-Al pair (AA15 defect) in samples containing deliberately added hydrogen is the evidence of low-temperature long-range migration (at least over a range of 100 lattice constants) of an aluminum atom. The migration occurring in the experiment at  $T \leq 200$  K can not be a normal or recombination-enhanced migration and apparently is an atomic process catalyzed by hydrogen. Tentative models including a  $\langle 011 \rangle$ -split Al-Al interstitial pair and  $\text{Al}_i + \text{H}$  interstitial pair for the AA15 and AA16 defect, respectively, have been discussed.

### Introduction.

Recently the phenomenon of hydrogen-enhanced impurity migration in silicon has been discovered [1-3]. The presence of hydrogen atoms in silicon leads to the enhancement of the diffusivity of interstitial oxygen. This enhancement was observed at  $T \sim 300^\circ\text{C}$  and detected using the measurements of the  $\text{O}_i$  reorientation rate, the rates of  $\text{O}_i$  loss from solution and the rate of thermal donors formation. Theoretical models [4,5] have been proposed to explain this phenomenon.

In this paper, we report the observation of low-temperature ( $< 200\text{K}$ ) enhanced migration of aluminum atoms in silicon doped with hydrogen. The conclusion about long-range aluminum migration results from the detection of a new EPR spectrum (labelled Si-AA15) which is clearly identified as a defect including an Al-Al pair. The migration of Al atom occurring in our experiment at  $T \leq 200$  K cannot be recombination-enhanced [6] or radiation-induced migration and apparently is a hydrogen catalyzed process. Detection of a second new EPR spectrum (Si-AA16) gives additional evidence that hydrogen enhances the migration of Al atom.

### Experiment

Samples with typical dimensions  $14 \times 1.1 \times 0.5 \text{ mm}^3$  (the long axis being  $\langle 110 \rangle$ ) were fabricated from floating-zone-grown silicon doped with  $5 \times 10^{16}$  aluminum/cm<sup>3</sup>. Hydrogen was incorporated either by proton implantation or by thermal annealing in the presence of hydrogen species. The implantation was carried out at a sample temperature of  $\sim 80$  K to a total dose of  $(1-5) \times 10^{15} \text{ H/cm}^2$  which corresponds to a concentration of  $(1-5) \cdot 10^{17} \text{ H/cm}^3$ . Second way of introducing of hydrogen into the samples was heating in the presence of water vapor. The "as-grown" samples were sealed in a quartz ampoule containing some mg of distilled water and heated to  $1200-1250^\circ\text{C}$  for 1/2 hr and then either allowed to cool to room temperature or quenched in water. After etching to remove all surface damage, these samples with hydrogen free control ones were irradiated at 80 K with 30 MeV protons. Because the proton range is far beyond the thickness of the sample, hydrogen implantation in the bulk of the sample was completely avoided in this case. After bombardment the samples without warm-up were installed into the cavity of a 37 GHz EPR spectrometer. The measurements were performed at 77 K in the absorption mode. The magnetic field could be rotated in an  $\{011\}$  plane of the sample. The control samples were sliced from the same silicon boule but irradiated with protons without the implantation or by  $\alpha$ -particles.

### Experimental Results

Bombardment of the samples at 80 K by protons produces the known EPR spectra of divacancy and Si-B2 [7-9]. New spectra labelled Si-AA15 and Si-AA16 (Fig. 1 a) grow upon thermal annealing at ~180-200 K of the hydrogen implanted samples as well as the samples which were heat treated in the presence of water vapor and are not observed in control samples. The increased hydrogen concentration contributes to the growth of the AA15 and AA16 spectra intensity. These spectra are characterized by the 11 groups (for AA15) and 6 groups (for AA16) of lines (Fig. 1 b), and thus correspondingly two and one nucleus with spin  $I=5/2$  are involved in the structure of the defects. These nuclei in used silicon samples are 100% abundant and can be  $^{27}\text{Al}$  isotopes only.

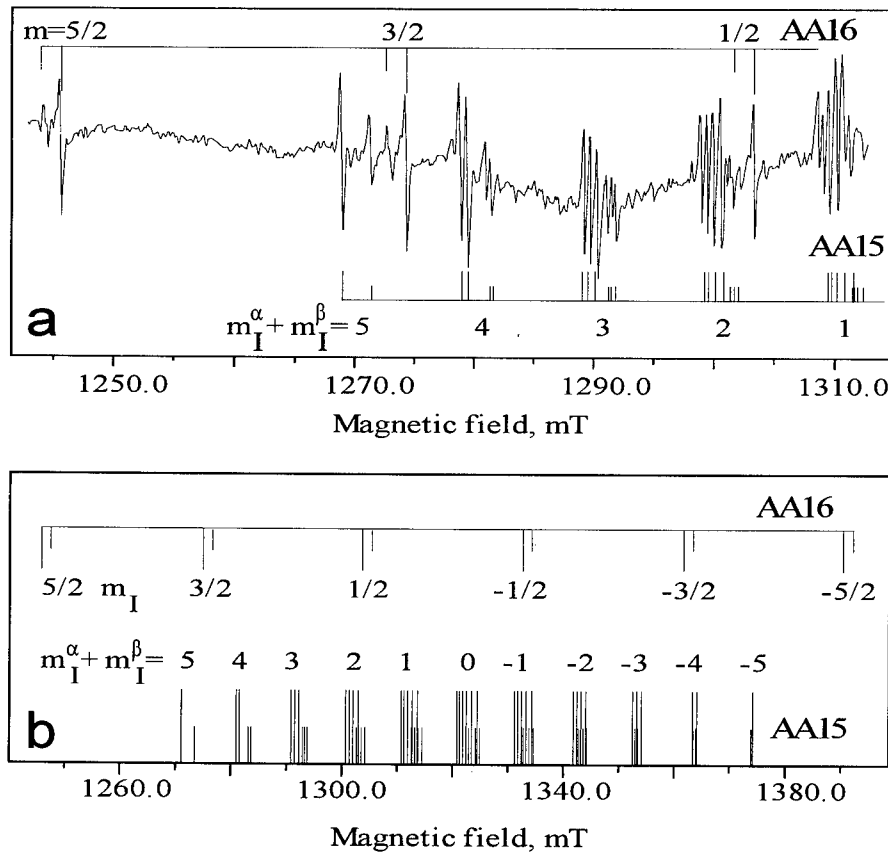


Fig 1. a) The low-field side of the Si-AA15 and Si-AA16 spectra at 77 K,  $\vec{H} \parallel \langle 001 \rangle$ . These spectra were observed after H-implantation of the FZ-Si(Al) sample at 80 K and annealing at 180 K for 10 min.

b) Computer fit of EPR lines positions,  $\vec{H} \parallel \langle 001 \rangle$ .

The AA15 spectrum can be described as arising from an anisotropic defect of  $C_{1h}$  symmetry with the spin Hamiltonian

$$H = \mu_B \vec{H} \vec{g} \vec{S} + \sum_{j=\alpha,\beta} \vec{S} \vec{A}_j \vec{I}_j \quad (1)$$

with  $S=1/2$ . The first term presents the electronic Zeeman interaction, the second term is the hyperfine interaction. The defect contains two Al nuclei (labelled  $\alpha$  and  $\beta$ ). The  $g$  and  $A$  values

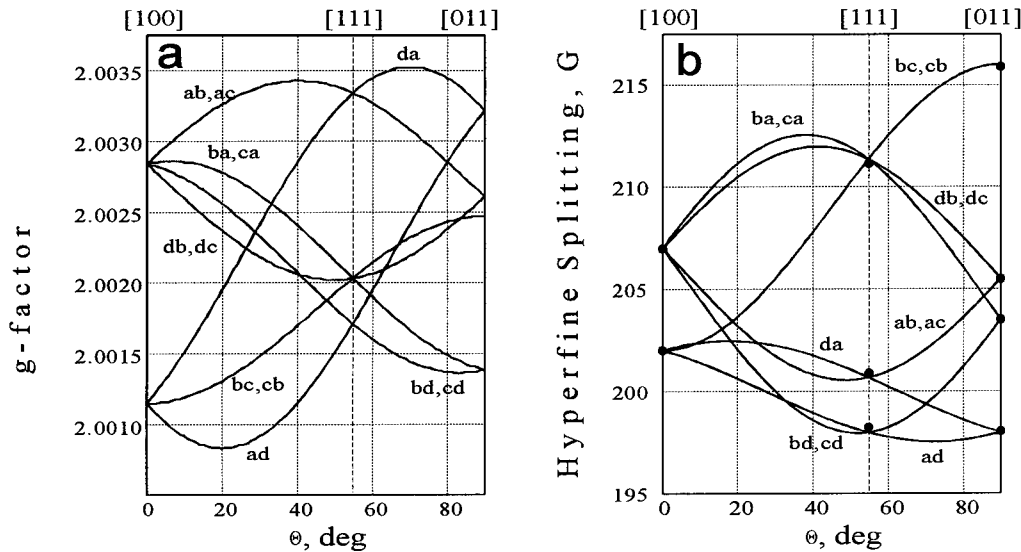


Fig. 2. The computed angular dependencies of the g-factors (a) and summary  $^{27}\text{Al}$  hf interaction (b) of the AA15 center (H in  $(0\bar{1}1)$  plane). The g- and A-constants from Table I were used

(Fig. 2) were determined from the angular dependence of the experimental spectrum using second order perturbation theory [10]. The principal values and axes of  $\vec{g}$ ,  $\vec{A}_\alpha$  and  $\vec{A}_\beta$  are given in Table 1 (with the relevant axes indicated in Fig. 3). We note that there is the deviation of  $\sim 0.3$  mT between calculated and experimental line positions when  $H \parallel \langle 111 \rangle$ . The discrepancy is likely to be a result of ignoring an anisotropic quadrupole interaction of Al nuclei. Although the AA15 spectrum is most prominent in intensity, its individual lines signal/noise ratio was insufficient for forbidden transition identification because the spectrum is split into 252 lines, for arbitrary direction of magnetic field in (011) plane.

Second spectrum, Si-AA16 ( $S=1/2$ ), has nearly isotropic g-tensor,  $\text{Tr } \vec{g} \approx 2.0030$ . Its  $^{27}\text{Al}$  hyperfine interaction is also nearly isotropic with weak trigonal distortion (Table 1). It is important to note that the width of individual lines of the AA16 spectrum depends slightly on direction of the magnetic field.

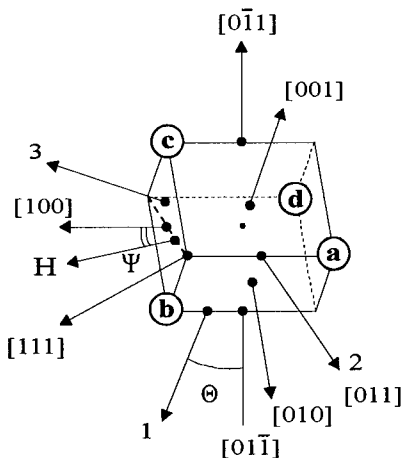


Fig. 3. Relevant principal axes for one of twelve equivalent orientations of the Si-AA15 defect in the lattice.



**Table I.** Principal values of g-tensor and  $^{27}\text{Al}$  hyperfine interaction A-tensors ( $^{27}\text{Al}_\alpha$  and  $^{27}\text{Al}_\beta$ ) for the Si-AA15 and Si-AA16 spectra (77 K) and molecular wave-function coefficients ( $\eta^2$  - the fraction of the total wave function at site,  $\alpha_j^2$  - from the isotropic part and  $\beta_j^2$  - from the anisotropic part of the hyperfine interaction).

EPR spectrum	g ( $\pm 0.0003$ )	A ( $\pm 3$ MHz)	$\alpha^2$	$\beta^2$	$\eta^2$
AA15	$g_1=2.0008$ $g_2=2.0025$ $g_3=2.0035$ $\Theta=70\pm 1^\circ$	$^{27}\text{Al}_\alpha$ $A_1=276.8$ $A_2=318.0$ $A_3=290.1$ $\Theta=20\pm 1^\circ$	0.35	0.65	0.18
		$^{27}\text{Al}_\beta$ $A_1=267.3$ $A_2=285.5$ $A_3=277.5$ $\Theta=33\pm 1^\circ$	0.57	0.43	0.10
AA16	$g=2.0035$	$^{27}\text{Al}$ $A_{  }=823$ $A_{\perp}=836$	0.80	0.20	0.29

Hyperfine interaction may be analyzed in terms of a one-electron wave function for the unpaired electron [11]. Using hyperfine parameters for 3s and 3p wave function of  $^{27}\text{Al}$ :  $|\psi_{3s}(0)|^2=20.4\times 10^{24}\text{cm}^{-3}$  and  $\langle r_{3p}^{-3} \rangle=8.95\times 10^{24}\text{cm}^{-3}$ , the observed hyperfine structure of the AA15 defect indicates that  $\sim 18\%$  and  $\sim 10\%$  of the unpaired spin wave function is located on the  $\alpha$  and  $\beta$  aluminum atoms and it has  $\sim 45\%$  3s and  $\sim 55\%$  3p character. The resolved  $^{29}\text{Si}$  hyperfine structure can also be seen whose intensity corresponds to  $\sim 4$ -6 neighboring sites accounting for only  $\sim 5\%$  of the wave function. The same analysis for the AA16 center indicates that about 30% of the resonant wave function localizes on the single aluminum atom, with mostly 3s-like character ( $\sim 80\%$ ), while the hyperfine interaction with  $^{27}\text{Al}$  nucleus in the case of isolated aluminum interstitial (EPR spectrum G18 [12]) is completely isotropic (100% 3s).

The AA15 spectrum is dominant one after 200 K annealing and its intensity does not change until 300 K annealing (Fig. 4). After 30-min annealing at room temperature the AA15 spectrum disappears. We note that the Si-G18 spectrum ( $\text{Al}_i$ ) [12] is not observed in both implanted and control samples immediately after 80 K irradiation but appears in all samples annealed at  $\sim 260$ -280 K and there is not revealed correlation of the AA15 and G18 spectra behavior. The second spectrum (AA16) disappears at 200-220 K. Narrow temperature region where the defect is observed by EPR may be the consequence of instability or mobility of the AA16 defect.

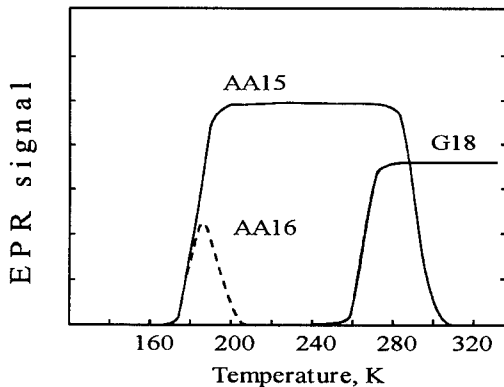


**Fig. 4.** Relative intensities of the AA15, AA16 and G18 EPR spectra vs temperature of annealing of FZ-Si(Al) sample implanted by protons at  $\sim 80$  K.

### Discussion

Formation of the AA15 defect including two aluminum atoms is a strong evidence of low-temperature long-range motion of Al atom, at least by a distance of  $\sim 100$  lattice constants. In the ordinary way the aluminum interstitials migrate at  $\sim 500$  K [12]. Recombination-enhanced migration may occur at room temperature [6] and cannot explain our result because it gives too long a recovery time at  $\sim 80$  K. Indeed, even though the  $\text{Al}_i$  recovery rate saturates under injection conditions of proton irradiation, the recovery will occur at 80 K with time constant  $\sim 10^{11}$  hours [6], while the observed time constant should not be more than the period of irradiation ( $\sim 1$  hour). We have to suppose that the aluminum atom migrates due to hydrogen-enhanced mechanism because the AA15 spectrum is not observed in control samples and grows when hydrogen concentration increases. Consequently, the presence of some radiation defect as well as hydrogen in the samples is required to create Al-Al pair (AA15 defect) and the diffusion takes place in the form of a certain radiation induced (Al+H) complex. This diffusion may occur in the process of irradiation at  $\sim 80$  K or annealing at  $T < 200$  K. Hydrogen role may be in the decrease of thermal barrier for migration of Al atom, much as the hydrogen has influence on the oxygen migration [1-3].

It is known that the hydrogen atom may be trapped by III group acceptors (B, Al, Ga) and passivate its electrical activity by forming of complexes  $(\text{B}_s+\text{H})$ ,  $(\text{Al}_s+\text{H})$  etc. [13,14]. But there is not any information concerning diffusion of these complexes. In our case the migration of (Al+H) complex takes place either by an interstitialcy or by a vacancy-controlled mechanism. But second way of diffusion is more proper for V group impurity (P, As, Sb). Therefore the rapidly diffusing species may be an  $(\text{Al}_i+\text{H})$  interstitial defect.

To create the  $(\text{Al}_i+\text{H})$  interstitial defect, it is necessary the presence of aluminum interstitial, which is produced by reaction of substitution:  $\text{Al}_s+\text{Si}_i \rightarrow \text{Al}_i+\text{Si}_s$  [12]. The Si-G18 spectrum ( $\text{Al}_i$ ) has, however, not been observed and consequently it may be concluded that most of the  $\text{Al}_i$  are involved in the  $(\text{Al}_i+\text{H})$  defects. These defects have to be mobile at temperature 200K or below to ensure forming of Al-Al pairs (AA15 complexes). The AA16 center is a suitable candidate as the  $(\text{Al}_i+\text{H})$  defect and an angular dependence of its linewidth may be a result of weak hyperfine interaction with proton. For the AA16 center about 30 % of the wave function appears to be accounted for on the Al atom. It is comparable to the case of  $\text{Al}_i$  tetrahedral interstitial ( $\sim 38$  %) [12]. The atomic orbitals are 20 % p character. This fact implies that the Al atom is slightly displaced from  $T_d$  site by some disturbance. Possible model for AA16 defect is shown in Fig. 5 a.

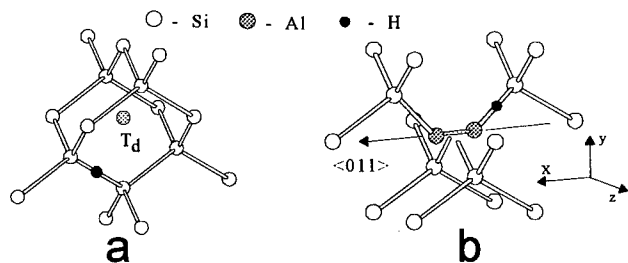


Fig. 5. Tentative model of  $(\text{Al-H})_i$  complex (Si-AA16) (a) and  $(\text{Al-Al})_i$   $\langle 110 \rangle$ -split interstitial (Si-AA15) (b).

In contrast to the case of known  $\text{Al}_i$ - $\text{Al}_s$  pairs (G19,G20) where the hyperfine parameters for  $\text{Al}_i$  and  $\text{Al}_s$  atoms diverged considerably, both Al atoms which are incorporated in the AA15 defect have similar hyperfine parameters. Hence both Al atoms are nearly equivalent and placed in interstitial positions which are equivalent in the perfect lattice. An additional slight distortion lowers the defect symmetry down to  $C_{1h}$  and results in non-equivalency of the atom positions. The distortion may be a consequence of the Jahn-Teller effect or presence of additional defect close to one of Al atom. This defect may be hydrogen atom.

As a result of interaction of mobile  $\text{Al}_i$  atom and substitutional  $\text{Al}_s$  atom, a  $\langle 110 \rangle$  - or  $\langle 100 \rangle$ -split interstitial distorted to  $\text{C}_{1h}$  may be formed. The interstitial atoms are situated in equivalent positions in the both these defects. But the  $\langle 110 \rangle$ -split interstitial seems to be more preferable. Indeed, the paramagnetic electron in the case of  $\langle 100 \rangle$ -split interstitial defect must be localized on two orbitals perpendicular to each other and having 3p character as in the case of carbon interstitial [15]. But the resonant wave function of AA15 defect has mainly 3s character, moreover the axes of  $\alpha$  and  $\beta$  orbitals are parallel. The model of Fig. 5b is best suited for the explanation of the experimental data. There are other models for the AA15 center, for example, model of vacancy with two nearest substitutional Al atoms or two  $\text{Al}_i$  atoms located nearly on two nearest hexagonal interstitial sites. But a probability of formation of defect involving two or more radiation defects is low.

We do not observe hyperfine interaction with hydrogen in the AA15 spectrum. Even if hydrogen is not involved in the structure of the center, we can assume that the AA15 pair is formed instead of the well known  $\text{Al}_i$ - $\text{Al}_s$  pair (G19, G20) owing to participation of H atom. Indeed, it is not to be expected that there is any substantial energy barrier for the  $\text{Al}_i$ - $\text{Al}_s$  pair forming because Coulomb attraction between  $\text{Al}_i^+$  and  $\text{Al}_s^-$ . This process of pairing should be slightly dependent on temperature and must be similar for both in case of  $\text{Al}_i$ - $\text{Al}_s$  defects appearance at  $\sim 500$  K [12] and in our case at  $T \sim 200$  K. Therefore the observed difference in Al-Al pairs structure may be a result of hydrogen influence on the kinetics of defect formation.

## References

1. R.C.Newman, 20th International Conference on the Physics of Semiconductors, **1**, ed. E.M.Anastassakis and J.D.Joannopoulos, World Scientific, Singapore, p.332 (1991).
2. R.Murray, *Physica B* **170**, 115 (1991).
3. R.C.Newman, *Materials Science and Engineering B* **36**, 1 (1996).
4. R.Jones, S.Öberg and A.Umerski, *Materials Science Forum* **83-87**, 551 (1992).
5. S.Estreicher, *Phys. Rev. B* **141**, 9886 (1990-I).
6. J.R.Troxell, A.P.Chatterjee, G.D.Watkins and L.C.Kimerling, *Phys. Rev. B* **19**, 5336 (1979).
7. H.Lutgemeier and K.Schnitzke, *Phys. Lett. A* **25**, 267 (1967).
8. D.F.Daly and K.A.Pickar, *Appl. Phys. Lett.* **15**, 267 (1969).
9. Yu.V.Gorelkinskii and N.N.Nevinnyi, *Physica B* **170**, 155 (1991).
10. E.L.Elkin and G.D.Watkins, *Phys. Rev.* **174**, 881 (1968).
11. G.D.Watkins and J.W.Corbett, *Phys. Rev.* **134**, A1359 (1964).
12. G.D.Watkins, *Materials Science Forum* **143-147**, 9 (1994); *Radiation Damage in Semiconductors*, p.94, (1964).
13. S.J.Pearson, J.W.Corbett and M.Stavola. *Hydrogen in Crystalline Semiconductors* (Springer-Verlag, Berlin Heidelberg 1992).
14. E.E.Haller: *Hydrogen in Crystalline Semiconductors*, in *Handbook on Semiconductors*, Vol. 3, ed. S.Mahajan (North Holland, Amsterdam 1994).
15. G.D.Watkins, K.L.Brower, *Phys. Rev. Lett.* **36**, 1329 (1976).

## SEGREGATION OF GOLD AT DISLOCATIONS CONFIRMED BY GOLD DIFFUSION INTO HIGHLY DISLOCATED SILICON

H. Bracht<sup>1,\*</sup>, A. Rodriguez Schachtrup<sup>1</sup>, and I. Yonenaga<sup>2</sup>

<sup>1</sup> Institut für Metallforschung, Universität Münster, Wilhelm-Klemm-Straße 10,  
 D-48149 Münster, Germany

<sup>2</sup> Institute for Materials Research, Tohoku University,  
 Katahira 2-1-1, Sendai 980, Japan

**Keywords :** silicon, gold, neutron-activation analysis, dislocations, segregation.

**Abstract.** We report on Au-diffusion experiments performed between 850°C and 1100°C into plastically deformed Si monocrystals, undoped and uniformly doped with a B concentration of  $3 \times 10^{19} \text{ cm}^{-3}$ . After indiffusion, Au profiles were monitored with neutron activation analysis (NAA) in conjunction with mechanical sectioning. The profiles show Au-diffusion to be faster in heavily B-doped Si than in undoped samples. Fitting of the experimental profiles which are accurately described with complementary error functions yields an effective diffusion coefficient  $D_{Au}^{eff}$  and a boundary concentration  $C_{Au}(x=0)$ . Data for  $D_{Au}^{eff}$  and  $C_{Au}(x=0)$  obtained for diffusion temperatures lower than 1000°C are considerably lower and higher, respectively, than expected from the extrapolation based on the high-temperature results. The unusual temperature dependence of  $D_{Au}^{eff}$  and  $C_{Au}(x=0)$  is explained taking into account segregation of Au at dislocations in addition to the kick-out diffusion mechanism which is the generally accepted process for Au diffusion in dislocation-free Si. The segregation of Au at dislocations is found to increase with decreasing temperature with an activation enthalpy of about -1.9 eV. From the influence of doping observed on Au diffusion into dislocated Si, we deduce that interstitial Au is positively charged in p-type Si and introduces a donor level at about 0.47 eV above the valence-band edge.

### Introduction.

Diffusion of Au into *dislocation-free* Si is known to be mainly mediated by the kick-out reaction [1]



This reaction accounts for the experimentally observed long-range transport of predominantly substitutionally dissolved  $\text{Au}_s$  by fast interstitial Au diffusion. A  $\text{Au}_i$  atom changes to the substitutional lattice site by displacing a  $\text{Si}_s$  lattice atom into the interstitial position thereby forming a Si self-interstitial  $I$ . Au-concentration profiles  $C_{Au}(x)$  in dislocation-free Si and more generally also Pt [2] and Zn [3] profiles are characterized by the concentration-dependent effective diffusion-coefficient ( $X \in \{\text{Au}, \text{Pt}, \text{Zn}\}$ )

$$D_X^{eff} = \frac{C_I^{eq} D_I}{C_X^{eq}} \left( \frac{C_X^{eq}}{C_X(x)} \right)^2 \quad (2)$$

Equation (2) holds for diffusion times which are sufficient to establish the equilibrium concentration  $C_{X_i}^{eq}$  of the interstitially dissolved foreign atoms. Data for the product  $C_I^{eq} D_I$  of the thermal equilibrium concentration and diffusivity of  $I$  which are deduced from  $D_X^{eff}$  are nowadays widely considered for modeling of self- and dopant-diffusion processes in Si.

For Au diffusion into *highly dislocated* Si, the kick-out model predicts a concentration-independent effective diffusion-coefficient given by [1]

\* currently at Lawrence Berkeley National Laboratory, One Cyclotron Road, MS 2-200, Berkeley, CA 94720 USA

$$D_{Au}^{eff} = \frac{C_{Au_i}^{eq} D_{Au_i}}{C_{Au}^{eq}} \quad (3)$$

This equation shows that the distribution of Au in dislocated Si is governed by  $C_{Au_i}^{eq} D_{Au_i}$ . However, upon more detailed inspection of Au profiles in highly dislocated Si, a deviation from the predicted diffusion behavior is observed. In the present paper we give experimental evidence that this deviation is caused by segregation of Au at dislocations. From the increase of Au segregation with decreasing temperature we deduce the fraction of Au trapped at dislocations. Comparison of Au profiles in undoped and extrinsically B-doped dislocated Si shows Au diffusion to be considerably faster under B-doping conditions. Analysis of this doping effect on diffusion yields information on the electrical properties of  $Au_i$  in Si.

### Experimental.

For our Au-diffusion experiments we used single-crystalline, plastically deformed undoped floating-zone Si and heavily B-doped ( $C_B = 3 \times 10^{19} \text{ cm}^{-3}$ ) crystals grown by the Czochralski method. Plastic deformation by compression was performed at  $870^\circ\text{C}$  on Si bars with  $[12\bar{3}]$ -longitudinal axis and  $(111)$  and  $(\bar{5}41)$  lateral surfaces and dimensions  $8 \times 8 \times 18 \text{ mm}^3$ . The resulting dislocation density is at least  $10^7 \text{ cm}^{-2}$  or higher, as estimated from etch pit counting. Slices of thicknesses ranging from 0.7 to 1.4 mm were cut parallel to the  $(111)$  surface. High-purity  $^{197}\text{Au}$  was evaporated on two opposite surfaces of mechano-chemically polished samples. Then the samples were sealed in evacuated quartz ampoules under vacuum. Diffusion was carried out in a three-zone resistance furnace. The temperature was monitored by a calibrated

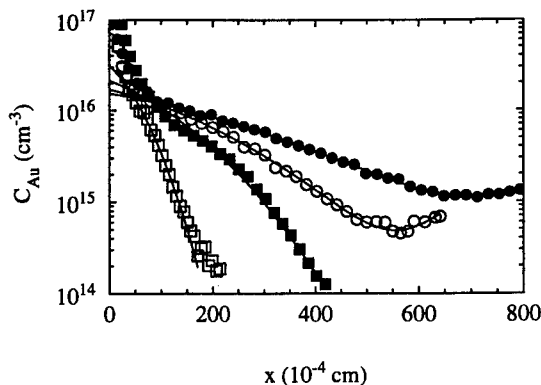


Figure 1: Concentration profiles of Au in highly dislocated undoped (open symbols) and B-doped (closed symbols,  $C_B = 3 \times 10^{19} \text{ cm}^{-3}$ ) Si samples after diffusion at  $900^\circ\text{C}$  for 3600 s (squares) and at  $1000^\circ\text{C}$  for 2220 s (circles). Solid lines represent best fits to experimental profiles based on appropriate error-function solutions.

Pt/PtRh thermocouple and controlled within  $\pm 2 \text{ K}$ . Au diffusion was stopped by plunging the ampoule in ethylene glycol at room temperature. After diffusion the samples were irradiated at the GKSS research center of Geesthacht with thermal neutrons resulting in neutron transmutation of  $^{197}\text{Au}$  to  $^{198}\text{Au}$ . After mechanical sectioning the activity of each section related to  $^{198}\text{Au}$  was recorded with a NaI-scintillation counter. The penetration depths were determined by weighing the samples. In order to transform activity profiles to Au-concentration profiles, Si samples saturated with Au at  $1200^\circ\text{C}$  were simultaneously neutron activated. Since the solubility of Au under intrinsic conditions is well known these samples were used for calibration.

### Results.

Diffusion profiles of Au in highly dislocated, virtually undoped and B-doped Si at  $1000^\circ\text{C}$  and  $900^\circ\text{C}$  are illustrated in Fig. 1. The profiles show that Au diffusion is enhanced in B-doped Si as compared to undoped samples. Solid lines represent results of successful fitting of Au concentration profiles which are based on complementary error-function (erfc) solutions taking into account in-diffusion of Au from two opposite surfaces. The strong increase of the Au concentration near the surface is probably caused by a slower Au diffusion along dislocations compared to bulk diffusion and/or a Si-Au alloy formed at the surface during annealing. Additional experiments are in progress to decide whether this part of the profile is diffusion limited

or not. The near surface regime was neglected for fitting of complementary error functions to the experimental Au profiles. Data obtained for  $D_{Au}^{eff}$  from Au profiles in undoped and B-doped Si are shown in Fig. 2. The errors in  $D_{Au}^{eff}$  resulting from the least-squares fit are about 5%. The solid line in Fig. 2 represents results for  $D_{Au}^{eff}$  given by [4]. This author has investigated Au-diffusion under intrinsic doping conditions in already Au-saturated dislocation-free Si. Analysis of these Au profiles also yields data for the effective diffusivity  $D_{Au}^{eff}$  which is characterized by Eq. (3).

$D_{Au}^{eff}$  values for intrinsic conditions given by [4] and the present work for temperatures at and above 1000°C are mutually consistent. However for  $T < 1000^\circ\text{C}$ ,  $D_{Au}^{eff}$  deduced from Au profiles in highly dislocated Si deviates from the results obtained from Au-isoconcentration diffusion experiments. Fig. 2 additionally illustrates that Au diffusion in heavily B-doped dislocated Si is higher than in undoped Si. The dashed line shows a calculated temperature dependence of  $D_{Au}^{eff}$  under intrinsic conditions if segregation of Au at dislocations is considered (see below).

The temperature dependence of the boundary concentration  $C_{Au}(x=0)$  is shown in Fig. 3 in comparison to Au-solubility data which were determined from neutron activation analysis (NAA) of virtually intrinsic dislocation-free, Au-saturated Si samples [5, 6]. The total errors in  $C_{Au}(x=0)$  are about 15% due to the limited accuracy of NAA for determining absolute Au concentrations. Within our experimental errors,  $C_{Au}(x=0)$  obtained for 1000°C and 1100°C in undoped and B-doped Si equals the Au solubility under intrinsic conditions. This weak doping dependence of  $C_{Au}^{eq}$  has been explained by substitutional  $Au_s$  which introduces both a donor and acceptor level in the Si band-gap even at high temperatures [7]. At temperatures lower than 1000°C, however, the boundary concentration even for the undoped samples clearly exceeds the expected Au solubility. In the following, this deviation is attributed to segregation of Au at dislocations.

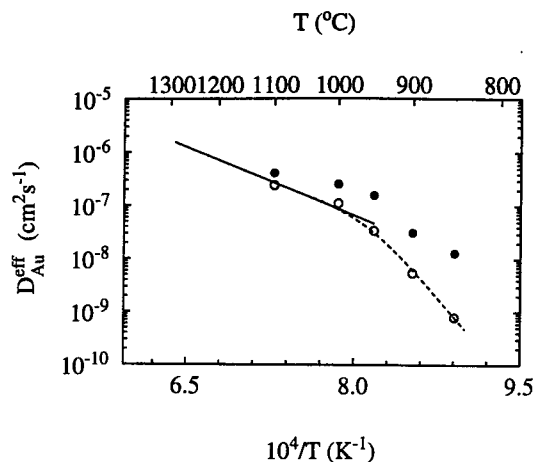


Figure 2: Temperature dependence of the effective diffusion coefficients of Au in highly dislocated, virtually undoped Si (○) and B-doped Si (●). The solid line represents the results obtained from Au-diffusion into dislocation-free Si performed under isoconcentration conditions [4]. The dashed line is obtained if the effect of trapping of Au at dislocations on  $D_{Au}^{eff}$  is taken into account.

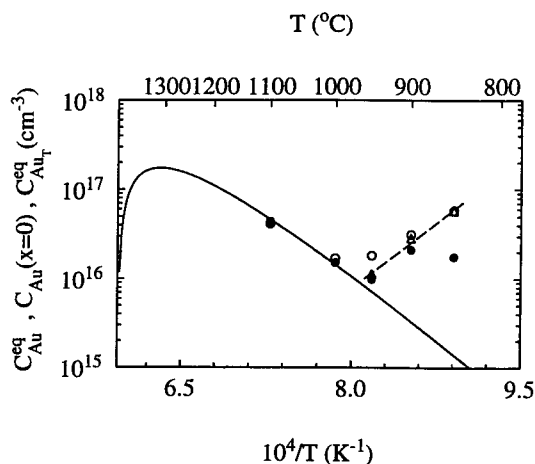
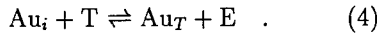


Figure 3: Temperature dependence of the Au-boundary concentration  $C_{Au}(x=0)$  after Au diffusion into highly dislocated, undoped (○) and B-doped (●) Si. The solid line represents Au solubility  $C_{Au}^{eq}$  in undoped dislocation-free Si which based on data given by [5, 6]. The dashed line shows the best fit of the concentration  $C_{AuT}^{eq}$  (Δ) of Au trapped at dislocations.

### Evidence of Au segregation.

Following Eq. (3), the product between  $C_{Au}^{eq}$  and  $D_{Au}^{eff}$  equals the transport capacity  $C_{Au_i}^{eq} D_{Au_i}$ . The boundary concentration  $C_{Au}(x=0)$  deduced from the Au profiles is considered to represent the total Au equilibrium concentration  $C_{Au}^{eq}$  under the present experimental conditions. The temperature dependence of the product  $C_{Au}(x=0)D_{Au}^{eff}$  is shown in Fig. 4. The solid line represents the best fit of our data  $C_{Au}(x=0)D_{Au}^{eff}$  for undoped Si. Our data are in remarkable agreement with the results obtained from the Au-isoconcentration diffusion analysis, although the values for  $D_{Au}^{eff}$  and  $C_{Au}(x=0)$  individually strongly deviate from the extrapolation based on the corresponding high temperature results (see Fig. 2 and 3). This finding is accurately explained taking into account in addition to reaction (1), a mechanism which describes the capture of  $Au_i$  at traps provided e.g. by dislocations



In reaction (4), T and  $Au_T$  denote an unoccupied and occupied trap, respectively, and E an empty interstitial site. Based on the partial differential-equation system for reaction (1) and (4), a single partial differential-equation

$$\frac{\partial C_{Au}}{\partial t} = D_{Au}^{eff} \frac{\partial^2 C_{Au}}{\partial x^2} \quad (5)$$

can be derived with an effective diffusion coefficient  $D_{Au}^{eff}$  [8]. For a moderate occupation of the traps,  $D_{Au}^{eff}$  is characterized by [8]

$$D_{Au}^{eff} = \frac{C_{Au_i}^{eq} D_{Au_i}}{C_{Au_s}^{eq} + C_{Au_i}^{eq} + C_{Au_T}^{eq}} = \frac{C_{Au_i}^{eq} D_{Au_i}}{C_{Au}^{eq}} \quad (6)$$

Equation (6) confirms that  $D_{Au}^{eff}$  decreases if Au is trapped at dislocations whereas the total Au concentration  $C_{Au}^{eq}$  increases such that the product  $C_{Au}^{eq} D_{Au}^{eff}$  is unaffected. The concentration  $C_{Au_T}^{eq}$  is given by the difference between the total Au concentration in highly dislocated Si and the Au-solubility data for dislocation-free Si given by [5, 6].  $C_{Au_T}^{eq}$  data so-obtained for undoped dislocated Si are illustrated in Fig. 3. The temperature dependence of  $C_{Au_T}^{eq}$  is accurately described by an Arrhenius law and shows Au segregation at dislocations to be an exothermic process with an activation enthalpy of  $H = -1.9$  eV and a pre-exponential factor of

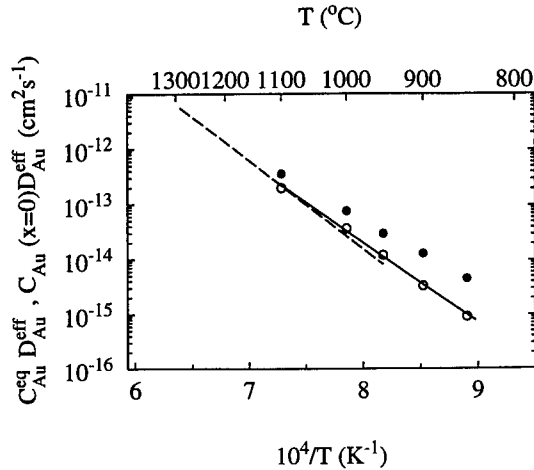


Figure 4: Temperature dependence of  $C_{Au}(x=0)D_{Au}^{eff}/C_0$  (Si atom density:  $C_0 = 5 \times 10^{22} \text{ cm}^{-3}$ ) deduced from Au profiles in virtually undoped (o) and B-doped (●) highly dislocated Si. The solid line shows the best fit of our experimental data (o) which is represented by  $C_{Au}(x=0)D_{Au}^{eff}/C_0 = 7.7 \times 10^{-3} \exp(-2.87 \text{ eV}/k_B T)$ . The dashed line shows the temperature dependence of  $C_{Au}^{eq} D_{Au}^{eff}$  which based on  $D_{Au}^{eff}$  data reported by [4] and Au-solubilities  $C_{Au}^{eq}$  given by [6].

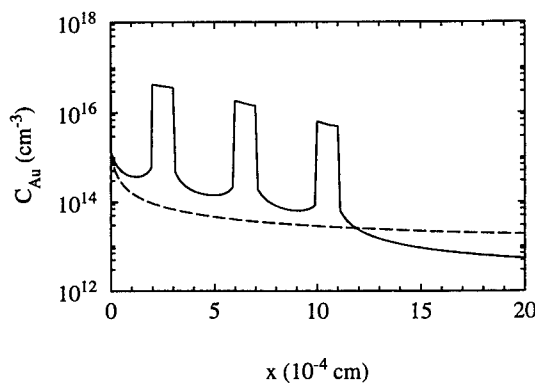


Figure 5: Calculated Au-concentration profile (solid line) in a heterostructure with alternating dislocation-free and highly dislocated layers compared to a Au profile in dislocation-free Si.

about  $1 \times 10^8 \text{ cm}^{-3}$ . Taking into account the temperature dependence determined for  $C_{AuT}^{eq}$ ,  $C_{Au_i}^{eq} D_{Au_i}$  and for the solubility of Au in dislocation-free Si [5, 6], the dashed line in Fig. 2 is obtained which accurately reproduces our  $D_{Au}^{eff}$  data. It should be noted that the total Au concentration in dislocated Si depends on the actual density of dislocations acting as trapping centers. This dislocation density of about  $10^8 \text{ dislocation/cm}^2$  is considered to be nearly constant in all undoped, plastically deformed Si samples as revealed by preferential etching. The B-doped dislocated Si samples, however, show larger variations in the dislocation density. Consequently, the amount of Au trapped at dislocations in the B-doped samples can not be described by a simple Arrhenius equation.

The increasing tendency of Au to segregate at dislocations with decreasing temperature could have potential application in the formation of microwires. Figure 5 shows a Au concentration profile obtained after a simulation of Au diffusion at  $850^\circ\text{C}$  for 60 s in a semiconductor heterostructure with alternating dislocation-free and highly dislocated layers ( $10^{10} \text{ disl./cm}^2$ ). For the calculation the segregation- and diffusion behavior of Au was considered, respectively, as it was deduced from the present work and previous investigations of Au diffusion into dislocation-free Si [5, 6]. Figure 5 illustrates that segregation of Au at dislocations causes an increase of the total Au concentration in the dislocated layer of about two orders of magnitude compared to the dislocation-free layers. We expect that segregation-controlled Au-diffusion profiles are formed in appropriately relaxed Si/Si<sub>1-x</sub>Ge<sub>x</sub>/Si/Si<sub>1-x</sub>Ge<sub>x</sub>/Si heterostructures.

#### Effect of doping on Au diffusion.

Figure 4 illustrates that the ratio of  $C_{Au_i}^{eq} D_{Au_i}$  for B-doped and undoped conditions increases with decreasing temperature. This enhancement of  $C_{Au_i}^{eq} D_{Au_i}$  under B-doping conditions confirms Au<sub>i</sub> to be positively charged in p-type Si, because the formation of interstitial Au<sub>i</sub> which may introduce a donor level  $E_{Au_i^{o/+}}$  in the Si band-gap becomes energetically more favored if the Fermi-level  $E_f$  lies below the donor level. The temperature dependence of the ratio of  $C_{Au_i}^{eq} D_{Au_i}$  for B-doped and undoped Si is shown in Fig. 6 together with the best fit of the doping effect on  $C_{Au_i}^{eq} D_{Au_i}$ . Fitting of our experimental data is based on the equation

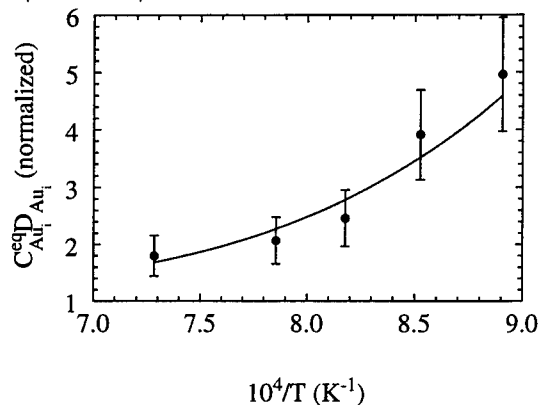


Figure 6: Temperature dependence of the transport capacity  $C_{Au_i}^{eq} D_{Au_i}$  in B-doped Si normalized by intrinsic conditions. The solid line shows the best fit of our experimental data.

$$\frac{C_{Au_i}^{eq} D_{Au_i}}{C_{Au_i}^{eq, in} D_{Au_i}^{in}} \approx \frac{C_{Au_i}^{eq}}{C_{Au_i}^{eq, in}} = \frac{1 + g_{Au_i} \frac{p}{p_{in}} \exp\left(\frac{E_{Au_i^{o/+}} - E_f^{in}}{k_B T}\right)}{1 + g_{Au_i} \exp\left(\frac{E_{Au_i^{o/+}} - E_f^{in}}{k_B T}\right)} \quad (7)$$

assuming that Au<sub>i</sub> introduces a single donor level in the Si band-gap and that doping mainly influences the equilibrium concentration  $C_{Au_i}^{eq}$  rather than the diffusion coefficient  $D_{Au_i}$ . The intrinsic carrier concentration  $p_{in}$  provided by Morin and Maita [9] was taken into account in Eq. (7) for the evaluation of  $E_{Au_i^{o/+}}$ . The free hole concentration  $p$  for the given B doping level was calculated using the neutrality equation. The Fermi-level  $E_f^{in} \approx E_g(T)/2$  under intrinsic conditions was considered using the expression for the shrinkage of the Si energy band-gap  $E_g(T)$  with increasing temperature given by Thurmond [10]. Assuming a degeneracy factor of  $g_{Au_i} = 0.5$  and that the energy level  $E_{Au_i^{o/+}}$  of the Au<sub>i</sub> donor remains fixed with respect to the valence band-edge as the energy gap shrinks with increasing temperature, the ionization



energy of neutral  $\text{Au}_i^0$  was determined to  $E_{\text{Au}_i^0/+} = (0.47 \pm 0.02)$  eV. The small standard deviation illustrates that the doping dependence of  $C_{\text{Au}_i}^{\text{eq}} D_{\text{Au}_i}$  is accurately described by Eq. 7. To the authors knowledge this is the first evidence of a donor level introduced by  $\text{Au}_i$  in Si. The  $\text{Au}_i$ -related ionization level can *not* be detected with common spectroscopic methods such as the infrared spectroscopy or deep-level transient spectroscopy. This is most likely due to the low  $\text{Au}_i$  concentration compared to the concentration of  $\text{Au}_s$  which introduces both a deep donor and acceptor level (see e.g. [11]). The concentration of  $\text{Au}_i$  in the Si samples becomes even less during cooling from high diffusion temperatures due to an expected fast outdiffusion of  $\text{Au}_i$ . However, Au diffusion in highly dislocated Si is mediated directly by the transport capacity  $C_{\text{Au}_i}^{\text{eq}} D_{\text{Au}_i}$ , although Au-concentration profiles mainly represent the distribution of  $\text{Au}_s$  and  $\text{Au}_T$ . This explains why the properties of  $\text{Au}_i$  are accessible by appropriate Au-diffusion experiments in highly dislocated Si.

### Conclusion.

Diffusion profiles of Au into undoped and B-doped highly dislocated Si are accurately described by the kick-out model and a mechanism which takes into account trapping of Au at dislocations. Au segregation increases with decreasing temperature as confirmed by Au profiles which show an enhanced boundary concentration and a simultaneously retarded effective Au-diffusion coefficient. From the temperature dependence of the concentration of Au trapped at dislocations in undoped Si, an activation enthalpy of  $-1.9$  eV was obtained assuming a constant dislocation density in all samples. Simulations performed on the basis of the observed segregation and diffusion behavior of Au in highly dislocated Si predict that Au-diffusion may be used to introduce microwires in appropriately designed semiconductor heterostructures.

The Au-diffusion enhancement observed in B-doped Si compared to undoped samples is attributed to a solubility enhancement of  $\text{Au}_i$ . Analyzing this effect of doping on  $C_{\text{Au}_i}^{\text{eq}} D_{\text{Au}_i}$  shows for the first time that  $\text{Au}_i$  introduces a single donor level in the Si energy band-gap which lies about 0.47 eV above the valence-band edge.

### Acknowledgement.

We thank Dr. W. Zulehner at Wacker Siltronic AG in Burghausen (Germany) for donating heavily B-doped silicon crystals and the GKSS research center of Geesthacht for neutron activation of the Au-diffused Si samples. Financial support by the 'Deutsche Forschungsgemeinschaft' is gratefully acknowledged.

### References.

- [1] U. Gösele, W. Frank and A. Seeger, *Applied Physics* **23**, 361 (1980).
- [2] S. Mantovani, F. Nava, S. Nobili and G. Ottaviani, *Phys. Rev. B* **33**, 5536 (1986).
- [3] H. Bracht, N.A. Stolwijk, H. Mehrer, *Phys. Rev. B* **52**, 16542 (1995).
- [4] B. Kühn, Doctoral Thesis, University of Stuttgart (1991).
- [5] N.A. Stolwijk, B. Schuster J. Hölzl, H. Mehrer and W. Frank, *Physica* **116B**, 335 (1983).
- [6] N.A. Stolwijk, J. Hölzl, W. Frank, E.R. Weber and H. Mehrer, *Appl. Phys. A* **39**, 37 (1986).
- [7] H. Bracht, *Defect and Diffusion Forum* **143-147**, 979 (1997).
- [8] A. Rodriguez Schachtrup, H. Bracht, I. Yonenaga and H. Mehrer, *Defect and Diffusion Forum* **143-147**, 1021 (1997).
- [9] F.J. Morin and J.P. Maita, *Phys. Rev.* **96**, 28 (1954).
- [10] C.D. Thurmond, *J. Electrochem. Soc.* **122**, 1133 (1975).
- [11] C.B. Collins, R.O. Carlson and C.J. Gallagher, *Phys. Rev.* **105**, 1168 (1957).

## ANNEALING OF LOW-TEMPERATURE SUBSTITUTIONAL GOLD IN SILICON: RING-DIFFUSION OF SUBSTITUTIONAL GOLD IN SILICON

Masami Morooka

Fukuoka Institute of Technology, Wajiro, Higashi-ku, Fukuoka 811-02, JAPAN

**Key words:** impurity diffusion, Si:Au, ring mechanism, substitutional impurity, gold in silicon.

**Abstract.** Annealing characteristics of low-temperature substitutional gold in silicon have been investigated by a special annealing method. Concentration profiles of substitutional gold and their decrease during the annealing were measured with an isothermal capacitance transient spectroscopy, ICTS, and resistivity. The concentration decreases uniformly kept intact with a flat profile and the average concentration decreases rapidly with the annealing time. The rapid decrease is caused by a homogeneous agglomeration of low-temperature substitutional gold via a ring-diffusion to an agglomeration center. Diffusion coefficient of the ring-diffusion was obtained as  $(10^{-5}-10^{-3})\exp(-(1.7\pm0.2)/kT)$  cm<sup>2</sup>/s from the initial concentration dependence of the time constant in the annealing. A tendency of out-diffusion profile near the specimen surface was observed, however, the observed diffusion length was larger than the length calculated from the diffusion coefficient. The average concentration obtained from resistivities is followed by a slow decreases after the first rapid one. The slow decrease may be caused by a diffusion of other impurities such as shallow or deep acceptors.

### Introduction.

Gold atoms in silicon occupy interstitial and substitutional sites, and substitutional gold exists in three states [1] due to the thermal condition: high-temperature substitutional gold in the condition of supersaturation above 850 °C or undersaturation, low-temperature substitutional gold in that of supersaturation below 850 °C, and agglomerates of substitutional gold as a fraction of annealed one. High-temperature substitutional gold diffuses via kick-out mechanism as confirmed by Gösele et al. [2]. Morooka et al. [1,3] proposed a ring mechanism for the diffusion of low-temperature substitutional gold. Therefore, gold atoms in silicon diffuse by intricate processes due to the state of substitutional gold depending on the condition of heat treatment. In addition them, the diffusion of high-temperature substitutional gold depends on silicon crystals such as specimen thickness and intrinsic defects [4].

A heat treatment for annealing experiment of high-temperature substitutional gold is shown in Fig. 1 and those of low-temperature substitutional gold is shown in Fig.2 [5], conceived with consideration of the existence of each substitutional gold. Gold atom diffuses as a high-temperature substitutional gold during indiffusion process in both heat treatment. Supersaturated substitutional gold diffuses also as a high-temperature substitutional gold in the subsequent heat treatment for continuous annealing as shown in Fig. 1. On the other hand, those diffuses as a low-temperature substitutional gold in the heat treatment for ordinary annealing as shown in Fig.2, because the gold-diffused specimen had been cooled to the room temperature before the annealing. In this work, annealing characteristics of low-temperature substitutional gold, namely the ring-diffusion of substitutional gold, has been investigated by the special annealing of supersaturated substitutional gold as show in Fig.2,

called as "ordinary annealing method".

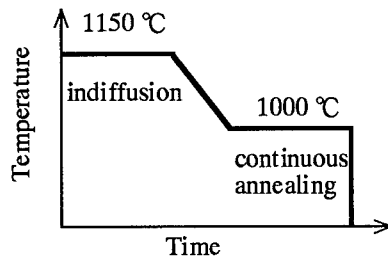


Fig.1 Heat treatment for annealing of high-temperature substitutional gold in silicon (kick-out mechanism)

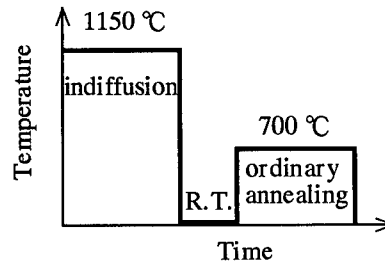


Fig.2 Heat treatment for annealing of low-temperature substitutional gold in silicon (ring-diffusion mechanism)

#### Experimental procedures and results.

Silicon specimens, in which gold had been diffused previously at 1000 °C - 1150 °C, was heat-treated again at 500 °C - 700 °C after rapid cooling to a room temperature, and the supersaturated low-temperature substitutional gold was reduced to a thermal equilibrium concentration by the annealing as shown in Fig. 2. An annealing-time dependence of the concentration of the substitutional gold was measured. The average concentration in a specimen is obtained from resistivities before and after the heat treatment, and the concentration profile was obtained briefly from ICTS signals measured by moving Schottky contact on an angle-lapped surface [6].

Concentration profiles after the annealing at 600 °C and 700 °C are shown in Figs. 3 and 4, respectively. Annealing time is indicated in the figures. Specimen thickness in the heat treatment was about 2.5 mm. The profile becomes flat within a short annealing-time in spite of an initial profile retained from an indiffusion profile with higher concentration near the surface. After that, the concentration decreases uniformly in the whole of specimen without relations to the distance from the surface, and the profile is still flat in spite of a considerable decrease of the concentration. The profile depends on annealing temperature and time in addition to the initial profile, and is independent of silicon crystal such as specimen thickness and intrinsic defects. A weak evidence of out-diffusion to the surface is recognized slightly near the specimen surface.

Annealing-time dependence of the average concentration in specimen, which is obtained by resistivity measurement, is shown in Fig. 5. The annealing characteristics show an first order reaction, and the concentration decreased rapidly with a short time-constant at the first phase of annealing. The time-constant depends on the initial concentration and it becomes smaller with larger initial concentration [3], which is a distinctive feature of the annealing via homogeneous nucleation [8]. The concentration in a low level region in Fig. 5, is much larger than those in Fig. 3. The difference between the concentrations will be discussed later.

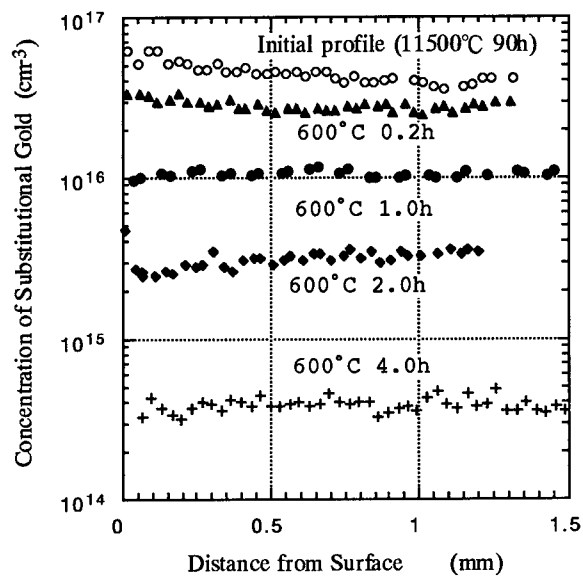


Fig.3 Concentration profiles of substitutional gold in the annealing of low-temperature substitutional gold in silicon at 600 °C.

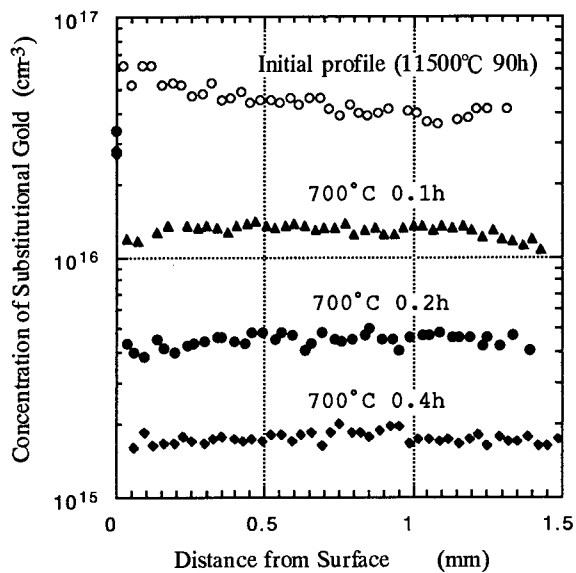


Fig.4 Concentration profiles of substitutional gold in the annealing of low-temperature substitutional gold in silicon at 700 °C.

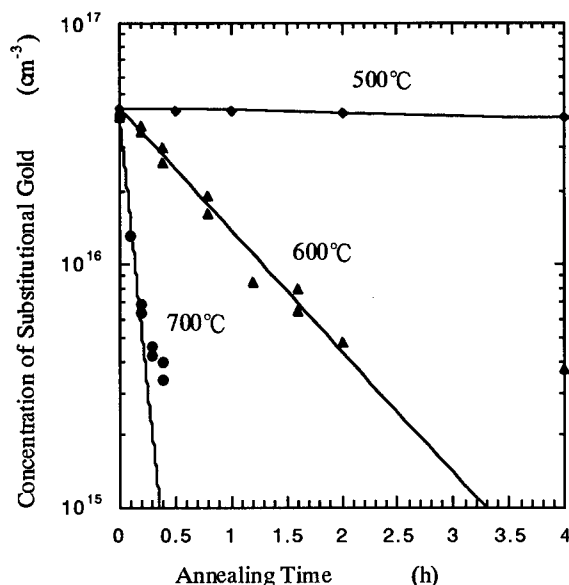


Fig.5 Decrease of substitutional gold concentration with annealing time, obtained by resistivity measurement.

### Discussion.

The rapid annealing is caused by a ring-diffusion of low-temperature substitutional gold accompanied by a homogeneous agglomeration [3], and the concentration of substitutional gold decreases uniformly resulting in a flat profile. A time constant  $\tau$  limited by a diffusion into spherical sinks, which are distributed randomly, is given by [7]

$$1/\tau = 4\pi r n D, \quad (1)$$

where  $D$  is the diffusion coefficient,  $r$  is the capture radius of nucleus and  $n$  is its concentration. Morooka et. al have obtained  $1/4\pi r D = 6.4 \times 10^{18} \text{ [cm}^{-3}\text{s]}$  at 600 °C,  $3.0 \times 10^{18} \text{ [cm}^{-3}\text{s]}$  at 650 °C and  $7.7 \times 10^{17} \text{ [cm}^{-3}\text{s]}$  at 700 °C from the dependence of  $\tau$  upon initial concentration of substitutional gold [3]. Temperature dependence of  $4\pi r D$  obtained from above values is shown in Fig. 6, and

$$4\pi r D = (10^{-11} - 10^{-9}) \exp(-(1.7 \pm 0.2)/kT) \quad [\text{cm}^3/\text{s}], \quad (2)$$

where  $k$  is Boltzmann's constant in eV/K and  $T$  is temperature. Assuming  $r = 1 \text{ nm}$  [3], the diffusion coefficient for ring-diffusion of substitutional gold is obtained,

$$D = (10^{-5} - 10^{-3}) \exp(-(1.7 \pm 0.2)/kT) \quad [\text{cm}^2/\text{s}]. \quad (3)$$

The activation energy for the ring-diffusion is from 1.5 eV to 1.9 eV. If the capture radius has a considerable activation energy, the activation energy for the diffusion should be subtracted by those for the capture radius from above values. If the capture radius is greater than 1 nm, the pre-exponential factor of Eq. (3) should be decreased in inverse proportion

to the radius. The diffusion coefficient is  $1.7 \times 10^{-11} \text{ cm}^2/\text{s}$  at  $700^\circ\text{C}$  in the largest case of Eq. (3), and the diffusion length is  $1.6 \times 10^{-4} \text{ cm}$  for the annealing time of 0.4 h. On the other hand, a tendency to an empirical out-diffusion with a diffusion length of several ten times larger than  $1.6 \times 10^{-4} \text{ cm}$  is observed in the experiments as shown in Fig. 4. The reason for the larger diffusion length than the theoretical one is not obvious now.

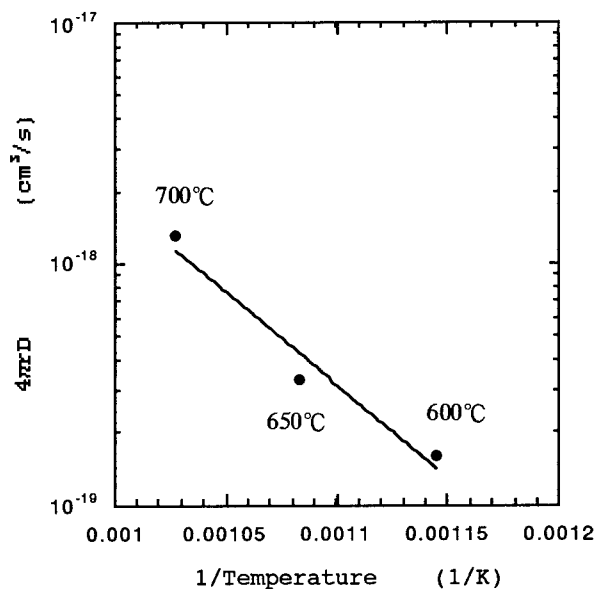


Fig.6 Temperature dependence of  $4 \pi r D$

The thermal equilibrium concentration of substitutional gold is estimated less than  $10^{15} \text{ cm}^{-3}$  at  $600^\circ\text{C}$  by an indiffusion experiment at the temperature, therefore, the concentration in Fig. 5 seems to decrease slowly with a long time-constant subsequent to the rapid decrease at the first phase. The gold concentration in Fig. 5 is obtained from resistivities before and after heat treatment. That is, the concentration is a quantity of free carrier concentration decreased by the heat treatment and includes other impurities in addition to substitutional gold. In evidence of them, the concentration of deep level of  $E_c - 0.54 \text{ eV}$ , which is the dominant acceptor level induced by substitutional gold, obtained from ICTS is  $4 \times 10^{14} \text{ cm}^{-3}$  after the annealing at  $600^\circ\text{C}$  4h as shown in Fig. 3 and the value is kept in an extension line of the rapid decrease in Fig. 5. The slow decrease of average concentration subsequent to the rapid decrease as shown in Fig. 5 will be caused by a diffusion of other impurity, which decreases the conduction electrons, such as shallow or deep acceptor. If an out-diffusion of substitutional gold to the specimen surface becomes to be effective in addition to the homogeneous agglomeration, the decrease of gold concentration should be accelerated and the concentration should be lower than the extension line in Fig. 5, because the diffusion to specimen surface and agglomeration center occurs simultaneously.

### Conclusions.

Annealing of low-temperature substitutional gold in silicon has been investigated. The

results are summarized as follows.

- 1) Diffusion coefficient of low-temperature substitutional gold, namely, that for ring-diffusion of substitutional gold is  $(10^{-5}-10^{-3})\exp(-(1.7\pm0.2)/kT)$  cm<sup>2</sup>/s.
- 2) Diffusion length for out-diffusion to specimen surface is larger than the length calculated using above diffusion coefficient.
- 3) At the second phase in the annealing, a slow diffusion of other impurity is effective for the decrease of free electrons in the n-type silicon.

#### References.

1. M. Morooka, H. Tomokage, H. Kitagawa and M. Yoshida: Jpn. J. Appl. Phys. **24** (1985) 133.
2. U. Gösele, W. Frank and A. Seeger: Appl. Phys. **23** (1980) 361.
3. M. Morooka, H. Tomokage and M. Yoshida: Jpn. J. Appl. Phys. **25** (1986) 1161.
4. M. Morooka: Jpn. J. Appl. Phys. **35** (1996) 2537.
5. M. Morooka, H. Kitagawa, H. Tomokage, S. Hirota and M. Yoshida: Jpn. J. Appl. Phys. **23** (1984) 124.
6. M. Morooka and F. Fukasako: Jpn. J. Appl. Phys. **35** (1996) 3686. An improved method for the detection limit will be submitted to Jpn. J. Appl. Phys.
7. A. C. Damask and G. J. Dienes: *Point Defects in Metals* (Gordon and Breach, New York, 1971) p.81.
8. D. Turnbull: *Solid State Physics* (Academic Press, New York, 1956), vol. III, p. 225.

## **RATE LIMITING MECHANISM OF TRANSITION METAL GETTERING IN MULTICRYSTALLINE SILICON**

**S.A. McHugo, A.C. Thompson, M. Imaizumi<sup>1</sup>, H. Hieslmair<sup>2</sup> and E.R. Weber<sup>2</sup>**

**Lawrence Berkeley National Laboratory, Advanced Light Source, Berkeley, CA 94720, USA**

**<sup>1</sup>Toyota Technological Institute, Nagoya 468, JAPAN**

**<sup>2</sup>Department of Materials Science, University of California at Berkeley, CA 94720, USA**

**keywords:** multicrystalline silicon, dislocations, transition metals, x-ray fluorescence, gettering

### **Abstract**

We have performed studies on multicrystalline silicon used for solar cells in the as-grown state and after a series of processing and gettering steps. The principal goal of this work is to determine the rate limiting step for metal impurity gettering from multicrystalline silicon with an emphasis on the release of impurities from structural defects. Synchrotron-based x-ray fluorescence mapping was used to monitor the release process. Copper and nickel impurities were found to reside primarily at dislocations in the as-grown state of the material. Short annealing treatments rapidly dissolved the impurity agglomerates. Based on these results and modeling of the dissolution process, copper and nickel is in the form of small agglomerates (<10nm) clustered together over micron-scale regions in the as-grown material. Aluminum gettering further disintegrated the agglomerates to below the sensitivity of the system, 2-5nm in radii. No significant barrier to release of copper or nickel from dislocations was observed.

### **Introduction**

Multicrystalline silicon (mc-silicon) is a very interesting material for terrestrial solar cells. Its low cost and respectable energy conversion efficiency (12-15%) makes it arguably the most cost competitive material for large-volume solar power generation. However, the efficiency of mc-silicon solar cells is severely degraded by regions of high minority carrier recombination which have been shown to largely possess dislocations and microdefects [1-3]. These structural defects are known to increase in recombination activity with transition metal decoration [4-9]. Therefore, frontside and/or backside segregation-type gettering of metal impurities from the mc-silicon bulk would be expected to greatly enhance solar cell performance as is observed in single crystal silicon [10-17]. Contrary to this rationale, experiments using these gettering treatments for mc-silicon have only improved regions of initially low recombination activity while little or no effect is observed on the initially high recombination regions and in turn only a slight improvement in overall cell performance is attained [2,3,14,18].

The gettering process can be described as a three step process of impurity release from its initial site, diffusion through the silicon matrix and capture into the gettering layer. Deep Level Transient Spectroscopy (DLTS) studies [3] have observed Fe in the highly dislocated regions of mc-silicon while still leaving the possibility of Cu, Ni and Co being present as well, due to the inability of DLTS to detect these impurities. All of these impurities diffuse rapidly in silicon [19], indicating the impurity diffusion from the initial site to the gettering layer occurs rapidly and would not limit the gettering process for a reasonably long gettering heat treatment. Measurements of metal impurity segregation coefficients for phosphorus and aluminum layers with respect to silicon [17,20], indicate one would expect a decrease of metal impurity concentration in the silicon on the order of  $10^{-4}$  to  $10^{-6}$ . This suggests the capture step is potent and does not limit the gettering process. The release of the impurities from their initial site is unstudied and may be responsible for the poor gettering of mc-silicon. Slow release may occur in mc-silicon but not in single crystal silicon due the presence of structural defects which stabilize the initial metal precipitates/agglomerates.



The goal of this research is to determine the mechanism by which gettering is ineffectual at improving high carrier recombination in mc-silicon. In the work presented here, we have analyzed metal impurity release from structural defects in mc-silicon after processing/gettering steps with the use of synchrotron-based x-ray fluorescence mapping and correlated structural defect analysis. Impurity release is compared to calculations of impurity diffusion from a precipitated state into the silicon matrix without any barrier to impurity release. We have been able to observe the dissolution process of Cu and Ni from dislocations as well as correlate the initial position of the impurities with specific structural defects.

### Experimental Procedure

Boron doped mc-silicon with a resistivity of 1.0 ohm-cm and an oxygen concentration of  $1-2 \times 10^{17}$  atoms/cm<sup>3</sup> was used. The 500 $\mu$ m thick wafers were formed by a casting method with subsequent cutting and etching to remove the damaged surface layer. Surface Photovoltage (SPV) apparatus was used to measure minority carrier diffusion length values over the as-grown mc-silicon wafer in order to locate high minority carrier recombination regions. These regions were rapid thermal annealed at 500°C for 30 seconds followed by a rapid quench to room temperature ( $\approx 1000$ K/s), to freeze in the kinetics of impurity release. This was followed by an Al gettering treatment at 800°C for 3 hours using a high purity 1 $\mu$ m Al layer on the sample backside. The frontside of the samples were analyzed using synchrotron-based x-ray fluorescence (XRF) mapping in order to determine metal impurity content and distribution at each step of the sample processing: in the as-grown state, following the RTA and lastly after the Al gettering treatment. Impurity mapping was performed on the same regions after each processing step by identifying fiducial marks on the sample surface. The XRF equipment generates 12.4 keV monochromatic radiation to excite elements in the sample with a spatial resolution of 1x1 $\mu$ m and a Si-Li detector to measure fluorescence x-rays from the sample, all in atmospheric conditions. System sensitivities are element specific but, for example, the system can detect a single Ni or Cu precipitate/agglomerate in silicon greater in radii than 2-5nm with a sampling depth on the order of 50 $\mu$ m. Impurity concentrations are quantified with the use of standard samples of known impurity concentrations. After Al gettering and XRF analysis, the diffusion length was measured with SPV and the samples were preferentially etched and analyzed with a scanning electron microscope to reveal structural defects.

### Results and Discussion

A minority carrier diffusion length ( $L_n$ ) map of the mc-silicon wafer is shown in Figure 1. The

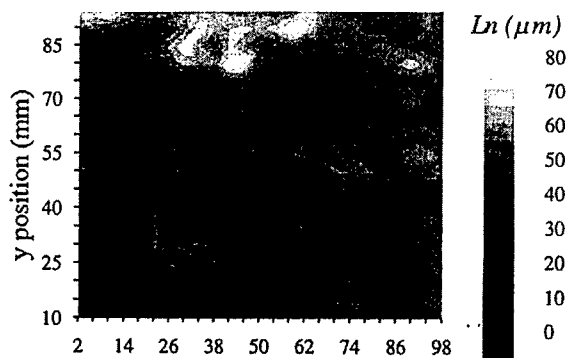
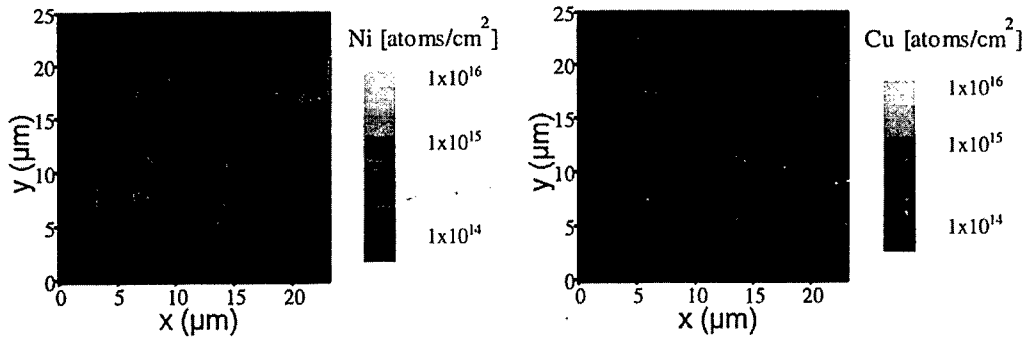


Figure 1: Minority carrier diffusion lengths ( $L_n$ ) across a multicrystalline silicon wafer.

material has a broad range of  $L_n$  values, from 10-80 $\mu$ m. These values are typical for a mc-silicon wafer and are not sufficient to make a high performance solar cell, further material improvement is required. A low diffusion length region with  $L_n=10\mu$ m was selected from the wafer and analyzed with XRF mapping. The XRF mapping revealed only Ni and Cu agglomerates. Maps of the impurity distributions are shown in Figures 2a&b. The Ni and Cu impurities are present at the same locations over regions spanning 2-5 $\mu$ m. Since the material was grown with a slow cooling rate and a concomitant low supersaturation of the impurities, the location of the Ni and



Figures 2a&b: Ni and Cu distributions in as-grown multicrystalline silicon as measured with x-ray fluorescence mapping. Deep black regions denote unscanned areas.

Cu are expected to be at the preferred precipitation sites. The sample was annealed at 500°C for 30 seconds with a rapid quench to room temperature in order to freeze in the kinetics of impurity dissolution. Based on diffusion data of Ni and Cu in silicon, [19], one would expect significant diffusion of both impurities for this anneal temperature and time. An XRF scan after the RTA treatment of the same region as in Figure 2, with some surrounding area, is shown in Figures 3a&b. Most impurity agglomerations

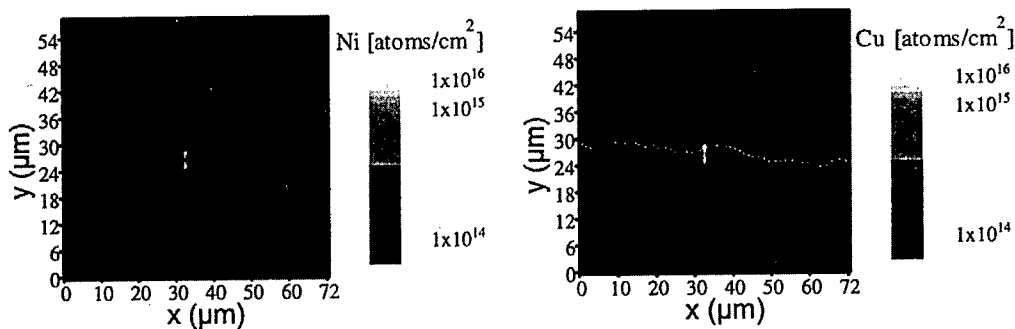


Figure 3a&b: Ni and Cu distributions in multicrystalline silicon after a 500°C-30 sec RTA quench. Only certain discrete agglomerations of impurities have remained from the as-grown state (Figure 2). Deep black regions denote unscanned areas.

have been dissolved. The few remaining positions with Ni and Cu at x,y (32,25-7)μm and to a lesser extent at (60,30)μm in Figures 3a&b correlate with peaks in Figures 2a&b at x,y (5,17)μm and (22,17.5)μm, respectively. It should be noted that the Ni and Cu agglomerates are no greater in size than the spatial resolution of the XRF system, 1 μm in diameter.

The initial size and distribution of the Ni and Cu precipitates can be calculated by using the data in Figures 2&3 and the theoretical models of precipitate dissolution which consider the dissolution process to be limited only by impurity diffusion from the precipitate [21,22]. It is important to note that no consideration of the surface reaction rate is considered in this model. For Ni and Cu, the theory provides a relatively simple formula for the maximum precipitate radius,  $R_{max}$ , which will not completely shrink for an anneal of time,  $t$ ,

$$R_{max} = \sqrt{2Dt \left[ \frac{C_i - C_m}{C_p - C_i} \right]} \quad (1)$$

where  $D$  is the impurity diffusivity in silicon,  $C_i$  is the impurity solubility in the silicon matrix at the dissolution temperature,  $C_m$  is the impurity concentration far from the precipitate and  $C_p$  is the metal

concentration in the precipitate. Equation 2 is in this simple form because of the large difference of impurity solubility between the precipitate and the silicon matrix.  $R_{\max}$  of  $\text{NiSi}_2$  and  $\text{Cu}_3\text{Si}$  precipitates for a  $500^\circ\text{C}$ -30 sec anneal are calculated to be 3 and 11nm, respectively. Any precipitates greater in size than this will not dissolve completely, e.g. a  $1\mu\text{m}$  diameter precipitate will be virtually unaffected by this anneal. Furthermore, this calculation taken in conjunction with the observed 2-5  $\mu\text{m}$  size of the Ni and Cu rich regions in the as-grown material (Figure 2) and the rapid dissolution of these impurity rich regions (Figure 3), suggests most of the as-grown impurities are in the form of nm-scale precipitates which are clustered over micron-scale regions of the material. The few impurity rich points remaining after the  $500^\circ\text{C}$  dissolution treatment, in Figure 3, were initially greater in size than 3-11 nm but now are at least  $\leq 1\mu\text{m}$ , the XRF spatial resolution.

The same sample was aluminum gettered for 3 hours at  $800^\circ\text{C}$  and analyzed with XRF over an even larger area than Figures 2&3. No Cu or Ni agglomerates were detected over this region. Calculations based on equation 1 indicate that  $\text{NiSi}_2$  and  $\text{Cu}_3\text{Si}$  precipitates with a diameter of  $<11.2\mu\text{m}$  and  $<23.2\mu\text{m}$ , respectively, should fully dissolve with the  $800^\circ\text{C}$ -3 hour treatment. Therefore, the precipitates in Figure 3, which are  $\leq 1\mu\text{m}$  in diameter, are expected to completely dissolve after the gettering treatment, as was experimentally observed. Considering the sensitivity of the XRF system, these results provide evidence that no Ni or Cu exists in this region clustered or precipitated at a diameter  $>2.5\text{nm}$ . Moreover, the  $800^\circ\text{C}$ -3 hour aluminum gettering treatment should be more than sufficient to decrease the Ni and Cu concentration throughout the silicon by many orders of magnitude considering simple diffusion of the impurities from the silicon matrix

into the aluminum layer which has a segregation coefficient of  $10^{-4}$  to  $10^{-6}$ . However, even with this rapid dissolution and sufficient diffusion/gettering times, the final minority carrier diffusion length was measured as  $52\mu\text{m}$ , only slightly higher than its initial value of  $10\mu\text{m}$  and significantly lower than required for a high performance solar cells. This low final diffusion length indicates a mechanism for minority carrier lifetime degradation remains in this region. Possible explanations for this residual degradation are discussed later.



Figure 4: SEM image of the XRF mapped regions (Figures 2&3) after etching. The white arrows locate Ni and Cu regions in the as-grown material. The black box indicates the area scanned with XRF after Al gettering.

A correlation between the Ni and Cu agglomerates of Figure 2 and the structural defects in the material was established with preferential etching and imaging with a scanning electron microscope. The results are shown in Figure 4 where the white arrows denote where the Ni and Cu was located in the as-grown material (Figure 2). The etch grooves are etched grain boundaries and the deep, black pits are etched dislocations. A strong

correlation is seen between the Ni and Cu rich regions and dislocations, with a single grain boundary possessing a small amount of Ni and Cu. The arrow farthest down and to the right points to a very shallow etch pit which is characteristic of a microdefect, e.g. a swirl defect or an oxygen precipitate. Considering the high concentration of impurities at this defect in the material's initial state, identification and investigation of this microdefect is desirable. Recent work has been carried out to identify microdefects in mc-silicon [23] with initial identifications showing predominantly single and multiple plate-like precipitates and a significantly lower concentration of spherical-like precipitates.

Since the material was cooled very slowly during growth, such that impurities were only slightly supersaturated during the cooling, the results of initial impurity distributions indicate dislocations are the preferred precipitation site in mc-silicon. In turn the dislocations would be expected to be the most thermodynamically-stable site for the impurity during dissolution. Even in this most stable configuration, the impurities quickly release from the dislocations and are fully removed with an Al gettering treatment, however, the minority carrier diffusion length of the material is not greatly enhanced. Considering the Al gettering treatment has more than sufficient thermal load for complete impurity diffusion from the dislocations to the Al layer and the segregation coefficient of the Al layer with respect to the silicon matrix is  $\approx 10^5$ , one would expect all released impurities to be completely gettered to the Al layer and, consequently, the minority carrier diffusion length would greatly increase. This is not observed, however, metal impurities may still be the dominant mechanism for this residual poor diffusion length. Two possible mechanisms are presented here: 1) the strain field of the structural defect may stabilize extremely small Ni and Cu clusters,  $<2\text{-}5\text{nm}$ , and 2) if one considers the structural defect as a completely different phase than the surrounding silicon matrix, this defect phase may possess a higher impurity solubility than the surrounding silicon. In the latter case the segregation-type gettering action of the Al backside layer will be severely retarded since the defect phase acts as a segregation-type gettering mechanism as well. Furthermore, both proposed mechanisms suggest once metal impurities interact with structural defects in silicon, complete impurity removal from the defect is an arduous task.

### Conclusions

Dislocations were found to be the preferred precipitation site for Ni and Cu impurities in multicrystalline silicon. Rapid thermal treatments rapidly released impurities from their initial state without any observable limitation other than simple diffusion in the silicon matrix. Gettering treatments dissolved the metal impurity precipitates below the sensitivity of these experiments ( $<2\text{-}5\text{nm}$ ), however, the gettering treatment does not greatly enhance minority carrier diffusion length values. This indicates metal impurities may remain either as very small precipitates/clusters or in a dissolved state within the phase of the dislocation.

### Acknowledgments

Thanks to Sumitomo SiTiX Corp. for providing the multicrystalline silicon for this work. Also, the illuminating conversations with H.A. Padmore are appreciated. This work was supported by the Director, Office of Energy Research, Office of Basic Energy Sciences, Materials Sciences Division, of the U.S. Department of Energy, under Contract No. DE-AC03-76SF00098.

### References

1. S. Pizzini, A. Sandrinelli, M. Beghi, D. Narducci, F. Allegretti, S. Torchio, G. Fabbri, G.P. Ottaviani, F. Demartin and A. Fusi, *J. Electrochem. Soc.* **135**, 155, 1988
2. B.L. Sopori, L. Jastrzebski, T. Tan, S. Narayanan in *Proc. of the 12th European Photovoltaic Solar Energy Conf.*, Netherlands, 1994, p. 1003
3. S.A. McHugo, H. Hieslmair and E.R. Weber, *Appl. Phys. A* **64**, 127, 1997
4. H. Alexander, C. Kisielowski-Kemmerich and E.R. Weber, *Physica* **116B**, 583, 1983
5. T.H. Wang, T.F. Ciszek and T. Schuyler, *Solar Cells* **24**, 135, 1988
6. C. Cabanel and J.Y. Laval, *J. Appl. Phys.* **67**, 1425, 1990.
7. M. Kittler, W. Seifert and V. Higgs, *Phys. Stat. Sol. (a)* **137**, 327, 1993
8. T.S. Fell, P.R. Wilshaw and M.D.d. Coteau, *Phys. Stat. Sol. (a)* **138**, 695, 1993
9. S.A. McHugo and W.D. Sawyer, *Appl. Phys. Lett.* **62**, 2519, 1993
10. L. Baldi, G. Cerofolini and G. Ferla, *J. Electrochem. Soc.* **127**, 164, 1980
11. R.D. Thompson and K.N. Tu, *Appl. Phys. Lett.* **41**, 440, 1982
12. J.S. Kang and D.K. Schroder, *J. Appl. Phys.* **65**, 2974, 1989

13. W. Schröter and R. Kühnapfel, *Appl. Phys. Lett.* **56**, 2207, 1990
14. M. Loghmarti, R. Stuck, J.C. Muller, D. Sayah and P. Siffert, *Appl. Phys. Lett.* **62**, 979, 1993
15. E.O. Sveinbjörnsson, O. Engström and U. Södervall, *J. Appl. Phys.* **73**, 7311, 1993
16. M. Apel, I. Hanke, R. Schindler and W. Schröter, *J. Appl. Phys.* **76**, 4432, 1994
17. S.M. Joshi, U.M. Gösele and T.Y. Tan, *J. Appl. Phys.* **77**, 3858, 1995
18. O. Porre, M. Stemmer and M. Pasquinelli, *Materials Science and Engineering*. **B24**, 188, 1994
19. E.R. Weber, *Appl. Phys. A*. **30**, 1, 1983
20. H. Hieslmair, S.A. McHugo and E.R. Weber in *Proc. of the 25th IEEE Photovoltaic Specialists Conf.*, Washington D.C. 1996, pg. 441
21. M.J. Whelan, *Metal Science Journal*. **3**, 95, 1969 .
22. H.B. Aaron and G.R. Kotler, *Metal. Trans.* **2**, 393, 1971
23. M. Werner, H.J. Möller and E. Wolf, to be published as part of the *Materials Research Society Spring 1997 meeting, Symposium E*

## **INTRINSIC POINT DEFECT ENGINEERING IN SILICON HIGH-VOLTAGE POWER DEVICE TECHNOLOGY**

**N.A. Sobolev**  
**Ioffe Physicotechnical Institute, St.Petersburg 194021, Russia**

**Keywords :** silicon, intrinsic point defects, defect formation

**Abstract.**  $\gamma$ -ray diffraction, chemical etching, DLTS, and temperature dependence of minority carrier lifetime have been used to study the processes of generation and relaxation of intrinsic point defects (IPDs) in high-voltage power devices technology. The role of IPDs in forming the structural and electrically active defects and the deep diffusion of aluminium have been demonstrated.

### **1. Introduction.**

The field of Intrinsic Point Defect Engineering started in the 70's. It is based on the idea that non-equilibrium intrinsic point defects (IPDs) take part in forming the structural defects and electrically active centers as well as in the diffusion of impurity atoms. Those ideas led to the development of different methods of gettering and passivation of defects in silicon devices.

Difficulties in studying the process of generation and relaxation of IPDs during the heat treatment are related to two factors. Firstly, vacancies and self-interstitials cannot be observed as free single defects. They can be studied only relying on the indirect data of structural defects, their electrically active centers and the diffusion of doping impurities. Secondly, due to a low concentration of these defects their nature cannot be investigated by such methods as the electron paramagnetic resonance, the optical absorption, etc.

The study the effects of IPDs on the formation of oxidation stacking faults and on the doping impurity diffusion provided a basis for the development of intrinsic point defect engineering in microelectronic device technology. The purpose of our work is to overview the results of our investigations on the influence of IPDs generated under high temperature annealing (characteristic of high-voltage power devices) on the behavior of structural defects in dislocation-free FZ-Si and neutron transmutation doped silicon (NTDS), on the formation of electrically active centers in high voltage p-n junctions and on the deep diffusion of aluminium in Si.

### **2. Experimental.**

Defect gettering and passivation techniques, developed for microelectronic devices, cannot be transferred to the technology of high-voltage power devices without conventional additional investigations, since the operating region for high-voltage power devices exceeds that for the microelectronic devices by several orders of magnitude. The operating region of a high-voltage device also is typically at sufficiently more depth from the device surface ( $\sim 100 \mu\text{m}$ ). The necessity of forming such deep p-n junctions requires rather long processes and higher temperatures. Besides, the silicon parameters used for manufacturing high-voltage devices differ a lot from those of silicon used in microelectronics. For manufacturing high-voltage devices, high purity dislocation-free n-type float zone Si (n-FZ-Si) is used. This contains concentrations of phosphorus and oxygen which on about two orders of magnitude lower than in the Czochralski silicon (Cz-Si) used in microelectronics.

The type and concentration of generated IPDs was controlled by changing the medium in which the heat treatment took place. Heat treatment in an oxidizing atmosphere results in the generation of self-interstitials; heat treatment in an inert atmosphere and in vacuum is accompanied by supersaturation of silicon with vacancies, while the heat treatment in the chlorine-containing

atmosphere (CCA) makes it possible to control the type of the dominating IPDs.  $\gamma$ -ray diffraction, chemical etching, DLTS, and temperature dependence of minority carrier lifetime were used to study the properties of defects and structures.

### 3. Results and Discussion.

#### 3.1. Influence of IPDs on the behavior of swirl-defects in dislocation-free FZ-Si.

The main type of structural defects in a high purity dislocation-free n-FZ-Si are swirl defects of the A type. High-resolution electron microscopy has showed that the A defects consist of dislocation loops, 1-5  $\mu\text{m}$  in size, of an interstitial type. These defects are formed as a result of the condensation of the excess interstitial atoms of silicon. To study the effect of an annealing atmosphere on the swirl defects within thick (1-5 mm)  $\langle 111 \rangle$  Si wafers with a lapped surface, we used selective etching and  $\gamma$ -ray diffraction techniques [1,2].

According to the data obtained by the selective etching method, annealing in CCA for 20-40 hours at 1100<sup>0</sup>-1250<sup>0</sup>C decreased the concentration of microdefects by the factor of 5 to 250. As the reduction took place, the dimensions of the etching pits on some samples were decreased by a factor of 2 or 3. The density of microdefects decreased with the increase of temperature and annealing time. The concentration of swirl defects after annealing in the air did not change or diminish even slightly, while the dimensions of the etching pits in practically all the samples increased by a factor of 2 to 4. The increase of the dimensions during annealing in the air may be related to Si supersaturation with self-interstitials. Whereas, the decrease of the concentration of swirl defects during annealing in the CCA evidences the generation of excess vacancies at the Si-SiO<sub>2</sub> interface.

Figure 1 shows the distributions of the integrated reflectivity  $R^{111}$  measured along the axis of the crystal growth (A) and the rocking curves (B, C) for the specimen before annealing in the chlorine-containing atmosphere (A1, B) and after the annealing, which lasted 40 hours at 1250<sup>0</sup>C (A2, C). The  $\gamma$ -ray diffraction for starting samples revealed the presence of fields of tensile strain conditioned by swirl defects. Annealing decreased both the integrated reflectivity and the half-width of the rocking curve compared to their values before annealing. This demonstrated the decrease of local stress in the bulk of the crystals, which is related to a decrease of the concentration of microdefects. The selective etching of the annealed crystal did not reveal a swirl pattern in the distribution of microdefects. The results show that annealing in the CCA makes it possible to diminish the concentration of as-grown microdefects with a swirl distribution within the thick silicon wafers.

#### 3.2. Influence of IPDs on the formation of structural defects during annealing of FZ-Si irradiated by thermal neutrons.

During the neutron transmutational doping of silicon, the crystals are irradiated by reactor neutrons with high doses. Simultaneously with the formation of doping atoms of phosphorus, radiation defects are created. We investigated structural defects in the FZ-Si crystals, irradiated by neutrons and annealed in different media, by the  $\gamma$ -ray diffraction technique in [2]. A diffuse scattering caused by the defect formation was observed in the near-surface region of some crystals. After annealing in the argon atmosphere for four hours at 850<sup>0</sup> C, the diffuse scattering increased at the angles larger than the Bragg angle (Fig. 2A). This was associated with the formation of structural defects of an interstitial type. The formation of interstitial structural defects under the same conditions was observed by X-ray topography by Lang (after the specimens were saturated with gold and copper) and by transmission electron microscopy, too [3]. The formation of the defects proves that at 850<sup>0</sup>C the mechanism of generating vacancies during annealing in argon is not effective.

After annealing in the CCA at 1050<sup>0</sup>C for four hours the diffuse scattering of  $\gamma$  rays was also discovered. As this took place, there was an increase of the diffuse scattering intensity at angles

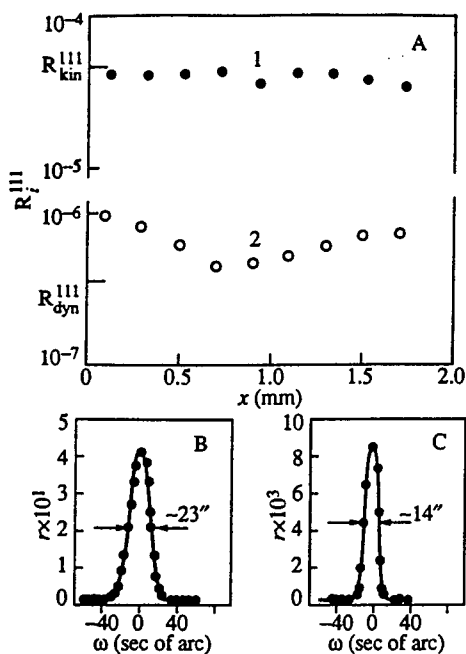


Fig. 1. Variations of the integrated reflectivity (A) and rocking curves (B, C) for (111) reflection for n-FZ-Si. (A) Before annealing (1); after annealing (2); (B) before annealing; (C) after annealing. The annealing is carried out in a chlorine-containing atmosphere ( $T=1250^\circ\text{C}$ ,  $t=40$  h, concentration of  $\text{CCl}_4=1.5$  mol.%).

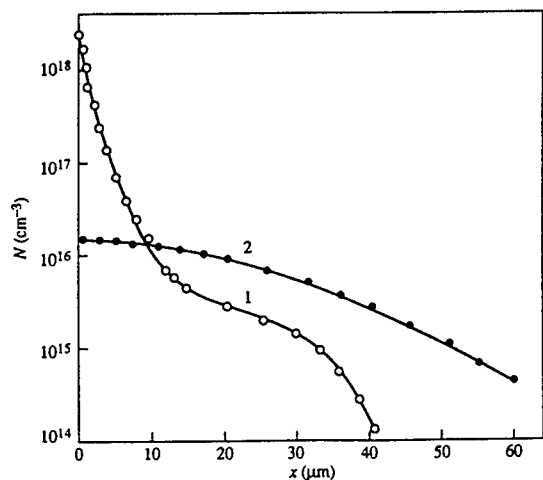


Fig. 3. Concentration profiles of Al in Si after diffusion ( $T=1250^\circ\text{C}$ ,  $t=16$  h) in nitrogen (1) and in oxygen (2). The points are the experimental data, and the curves are calculated.

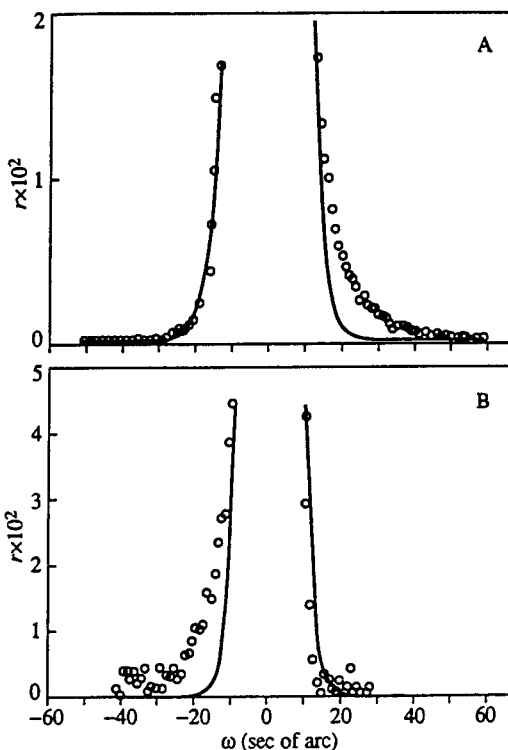


Fig. 2. Rocking curves for (111) reflection of FZ samples irradiated by thermal neutrons and annealed (A) in an argon flow and (B) in a chlorine-containing atmosphere. Solid lines correspond to fitting by the Gauss function.

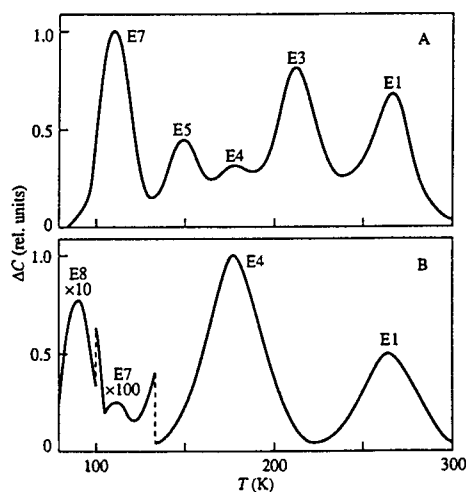


Fig. 4. DLTS spectra of samples after the diffusion of Al in Si (A) in nitrogen and (B) in oxygen ( $T=1250^\circ\text{C}$ ,  $t=16$  h). The emission rate of carriers from a level at the peak maximum was  $60 \text{ s}^{-1}$ .



smaller than the Bragg angle (Fig. 2B), which is related to the formation of the structural defects of a vacancy type. The investigation of the same crystal by diffuse X-ray scattering [4] confirmed the defect formation of a vacancy type in the near-surface region. The angular dependence of diffuse X-ray scattering indicated the presence of defects of different sizes. The shape of the diffuse peak revealed that the defects were not spherical clusters. The diffuse  $\gamma$ -ray and X-ray scattering made it possible for the first time to observe “directly” the formation of the structural vacancy defects related to the generation of vacancies during silicon annealing in a CCA. Thus it was established that the use of a CCA makes it possible to prevent the supersaturation of silicon with self-interstitials during postradiation annealing.

### 3.3. Influence of IPDs on the diffusion of aluminium in silicon.

The investigation of the effect of IPDs on the diffusion of impurity atoms allows one both to study the diffusion mechanism more thoroughly and to determine such important parameters of IPDs as the equilibrium diffusivity and the equilibrium concentration. We studied the diffusion of aluminium in silicon under conditions typical for high-voltage power device fabrication [5]. For the process to be conducted when the silicon was supersaturated with excess vacancies or self-interstitials, the diffusion was performed in nitrogen and in oxygen, respectively. The concentration profiles were determined by the differential conductivity technique.

The investigation of aluminium concentration profiles under diffusion at 1250 °C for 10 - 40 hours in different media has shown the following: (i) The concentration profiles after the diffusion in oxygen are described by the Gauss function. (ii) The concentration profiles after the diffusion in nitrogen have a nonclassical form and cannot be adequately described by the Gaussian curve. (iii) Under diffusion in nitrogen the surface concentration of aluminium is 1.5 to 2 orders of magnitude higher, and the depth of the p-n junction is 20%-30% smaller, than for diffusion taking place in an oxidizing medium.

Figure 3 shows the typical aluminium profiles after diffusion in inert and oxidizing media.

Experimental results can be qualitatively explained in the following way: Diffusion in nitrogen is accompanied by the generation of excess vacancies. Their interaction with the aluminium atoms can be described by following reaction



where  $Al_i$  and  $Al_s$  are the aluminium atoms in their interstitial and substitutional positions. That leads to an increase in the concentration of the electrically active aluminium atoms in the near-surface region. However, since the diffusion of aluminium in silicon takes place mostly according to the interstitialcy mechanism [6], the undersaturation of silicon by self-interstitials during the diffusion in nitrogen is accompanied by the decrease of the effective diffusivity and, accordingly, by the decrease of the p-n junction depth compared to the diffusion in oxygen.

We have also developed the numerical model for the diffusion of aluminium in silicon based on the participation of IPDs in the process. The analysis of the experimental results has shown that the thermodynamically equilibrium aluminium diffusivity is equal to  $2 \times 10^{-11} \text{ cm}^2/\text{s}$  and the self-interstitial diffusivity corresponds to values determined experimentally from boron diffusion in silicon [7].

### 3.4. Influence of IPDs on the formation of deep-level centers.

This section summarizes the results of work on deep-level center (DLC) formation which is related to the generation and relaxation of IPDs under the heat treatment of silicon crystals and structures with p-n junctions at high temperatures  $> 1000^\circ\text{C}$  [8,9]. To generate IPDs, wafers with polished surfaces were annealed, or aluminium has diffused into wafers with lapped surfaces in different media at  $1000^\circ\text{C}$ - $1250^\circ\text{C}$  for 1 to 16 hours.

Comparing the data for the samples after heat treatment in oxygen showed that two dominating deep levels E1 and E4 are formed with the following rates of thermal emission:  $e_1 = 1.6 \times 10^{-15} b T^2 \exp(-0.535/kT)$  and  $e_4 = 1.9 \times 10^{-17} b T^2 \exp(-0.277/kT)$ , where  $b = 6.6 \times 10^{21} \text{ cm}^{-2} \text{ s}^{-1} \text{ K}^{-2}$ ,  $T$  is the temperature in K,  $k$  is the Boltzmann constant,  $e$  was measured within the range  $10^{-2} - 10^3 \text{ s}^{-1}$ . Depending on the technological conditions, the concentrations of the centers were  $M4 = 10^{11} - 10^{12} \text{ cm}^{-3}$  and  $M1 = (0.6-0.9)M4$ .

The heat treatment of samples in an inert atmosphere or in a vacuum is accompanied by the formation of three DLCs with the following rates of thermal emission:

$e_3 = 1.2 \times 10^{-14} b T^2 \exp(-0.455/kT)$ ,  $e_5 = 4.0 \times 10^{-16} b T^2 \exp(-0.266/kT)$ ,  
 $e_7 = 1.1 \times 10^{-15} b T^2 \exp(-0.192/kT)$ . The concentration of the dominant center (E5 or E7) is typically within  $10^{12} - 10^{13} \text{ cm}^{-3}$ , depending on the technological conditions. The E3 center concentration is 10 to 50 times lower.

Some additional experiments were carried out to confirm the above hypothesis of the IPD role in forming the E1, E3-E5, and E7 centers. Simultaneous measurements by  $\gamma$ -ray diffraction and capacitance spectroscopy showed that the E1 and E4 centers dominated in the DLTS spectrum in those samples in which, according to the data of diffraction experiments, the formation of structural defects of an interstitial type was observed and the E3, E5, and E7 centers dominated in those samples where the structural defects of a vacancy type were revealed.

Figure 4 shows the DLTS spectra after aluminium diffusion in nitrogen (A) and oxygen (B) atmospheres. The aluminium impurity concentration profiles for the same samples are shown in Fig. 3. The comparison of the data proves that vacancies play a crucial role in the formation of E3, E5, and E7 centers, while interstitial silicon atoms play a similar role in the formation of E1 and E4 centers.

### 3.5. Influence of IPDs on the formation of recombination centers in p-n structures.

The DLCs and minority carrier lifetime parameters were measured in structures made by the diffusion of aluminium. The diffusion was performed at  $1250^\circ\text{C}$  first for 4 hours in a flow of argon and then for 4 to 32 hours in oxygen. The atmosphere was changed without switching off the furnace at the diffusion temperature [10]. Figure 5 gives the dependence of the total center concentration  $M$  of both vacancy and interstitial types on the duration of annealing in oxygen. These concentrations are normalized to the shallow donor concentration  $N$ . In the first stage (diffusion in argon), excess vacancies are mostly generated. If at that moment the sample is cooled to the room temperature, those excess vacancies lead to the formation of vacancy centers E3, E5, and E7. In the second stage (diffusion in oxygen), self-interstitials of Si are mostly generated, and their bimolecular recombination with the vacancies (which were formed in argon under diffusion) takes place. With an increase of duration in the second stage, the concentration of the excess vacancies decreases, while the concentration of self-interstitials increases. After some time the type of dominating IPDs and DLCs changes.

The dependence of lifetime on the duration of diffusion in oxygen is shown in Fig. 6. The maximum in this dependence can be explained in a similar way. The lifetime after diffusion in argon is determined by the vacancy recombination centers. The diffusion in oxygen is accompanied by the generation of the self-interstitials. The bimolecular recombination of the interstitials with the excess vacancies (which appears under the diffusion in oxygen) leads to a decrease in the concentration of the recombination centers and to a lifetime increase. With an increase in the duration of diffusion in oxygen, the type of dominating IPDs changes; and recombination centers of an interstitial type are formed. As their concentration increases, they begin to control the recombination process of nonequilibrium charge carriers; this leads to a drop in the lifetime.

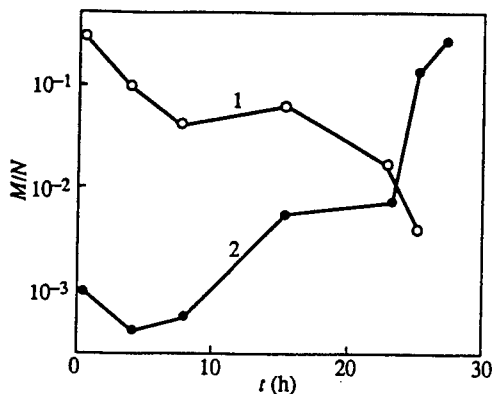


Fig. 5. Dependence of the total concentration of DLCs of the vacancy (1) and interstitial (2) types on the duration of annealing in an oxygen flow.

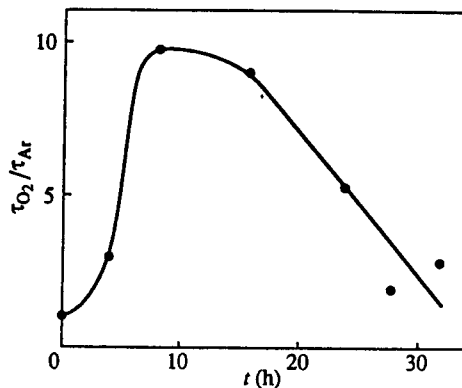


Fig. 6. Dependence of the minority carrier lifetime on the duration of annealing in an oxygen flow. Here  $\tau_{Ar}$  and  $\tau_{O_2}$  are the lifetimes measured after the diffusion of Al in the argon atmosphere and after the subsequent annealing in oxygen, respectively.

### Conclusion.

The significance of IPDs in defect formation in high-voltage power device technology has been demonstrated. The study of the behavior of structural defects, electrically active centers and the diffusion of aluminium makes it possible to investigate processes of generation and relaxation of IPDs and determine their parameters. The fundamentals of defect engineering in the technology of high-voltage power devices have been outlined.

### Acknowledgements.

The work was partly supported by the Russian Fund for Basic Research (Grant 96-02-17901).

### References.

1. N. A. Sobolev, E.I. Shek, S.I. Dudavskii, and A.A. Kravtsov, *Sov. Phys. Tech. Phys.* **30**, 842 (1985).
2. A.I. Kurbakov and N.A. Sobolev, *Mater. Sci. Eng.* **B22**, 149 (1994).
3. V.V. Vysotskaya, S.N. Gorin, I.M. Gres'kov, N.A. Sobolev, T.M. Tkacheva, E.I. Shek, *Inorg. Mater.* **24**, 302 (1988).
4. N.A. Sobolev, A.I. Kurbakov, R.N. Kyutt, E.E. Rubinova, A.E. Sokolov, and E.I. Shek, *Sov. Phys. Tv. Tela.* **34**, 1365 (1992).
5. B.N. Gresserov, N.A. Sobolev, Yu.V. Vyzhigin, V.V. Eliseev, and V.M. Likunova, *Sov. Phys. Semicond.* **25**, 488 (1991).
6. S. Mizuo, and H. Higuchi, *Jap. J. Appl. Phys.* **21**, 56 (1982).
7. H.-J. Gossmann, G.H. Gilmer, C.S. Rafferty, F.C. Unterwald, T. Boone, J.-M. Poate, H. S. Luftman, and W. Frank, *J. Appl. Phys.* **77**, 1948 (1995).
8. N.A. Sobolev, Yu.V. Vyzhigin, B.N. Gresserov, E.I. Shek, A.I. Kurbakov, E.E. Rubinova, and V.A. Trunov, *Diffus. Defect Data Sol. St. Data B. Sol. St. Phenomena* **19-20**, 169 (1991).
9. Yu.V. Vyzhigin, N.A. Sobolev, B.N. Gresserov, and E.I. Shek, *Sov. Phys. Semicond.* **25**, 799 (1991).
10. Yu.V. Vyzhigin, N.A. Sobolev, B.N. Gresserov, and E.I. Shek, *Sov. Phys. Semicond.* **26**, 1087 (1992).

## **INFLUENCE OF THE DISLOCATION LOOPS ON THE ANOMALOUS DIFFUSION OF Fe IMPLANTED INTO InP**

**C. Frigeri<sup>1</sup>, A. Carnera<sup>2</sup>, B. Fraboni<sup>2</sup>, A. Gasparotto<sup>2</sup>,  
F. Priolo<sup>3</sup>, A. Camporese<sup>4</sup> and G. Rossetto<sup>4</sup>**

<sup>1</sup> CNR-MASPEC Institute, via Chiavari 18/A, 43100 Parma, Italy

<sup>2</sup> INFN and University Physics Department, via Marzolo 8, 35131 Padova, Italy

<sup>3</sup> INFN and University Physics Department, C. so Italia 57, 95129 Catania, Italy

<sup>4</sup> CNR-ICTIMA Institute, C. so Stati Uniti 4, 35127 Padova, Italy

**Keywords:** InP, Fe implantation, Fe anomalous diffusion, dislocation loops.

**Abstract.** The influence of crystal defects formed upon annealing in determining the anomalous distribution of Fe implanted into InP has been studied by comparing samples submitted to single Fe implant and double Fe + P implant in the MeV energy range. It is shown that end of range dislocation loops, as well as interfaces of bands of defects, are preferential sites for gettering and accumulation of Fe.

### **Introduction**

The electrical characteristics of the layers obtained by ion implantation of semiconductor substrates are strongly dependent on the distribution of the implanted dopant. For both III-V compound semiconductors [1-4] and Si [5-8] an anomalous distribution of the implanted dopant was observed. For Si it has been shown recently [5-6] that the anomalous dopant diffusion can be affected by the end of range (EOR) dislocation loops, that form due to the preamorphization step of Si by a non-doping ion, like Ge [5-6, 10] or Si itself [8], which is done prior to the implantation of the dopant impurity to prevent dopant channeling. The EOR loops typically form when the implant dose exceeds the amorphization threshold [11]. Even the loops that form at the a/c interfaces of buried amorphous layers upon annealing can affect the dopant distribution in Si [9].

The anomalous diffusion of the dopant in InP, as well as in other III-V compounds, has mostly been studied by SIMS (Secondary Ion Mass Spectrometry) that is unable, however, to give information on the crystal defects. For Fe implanted InP, it has usually been explained as due to the interaction between the implanted species and excess intrinsic point defects, typically P interstitials, whose density is very high at the depths where Fe accumulation peaks were observed [1-3]. The calculated distribution of excess P and In interstitials of Christel and Gibbons [12] was generally used.

In order to clarify the relationship between anomalous diffusion and crystal defects associated with the implant and recovery processes in Fe implanted InP, we have studied samples submitted to single and double implant whose results are reported below. The single implant results have partially been discussed elsewhere [4, 13].

### **Experimental**

Two types of implanted InP samples were investigated: 1) InP crystals with a room temperature single implant of 2 MeV Fe ions at a dose of  $2 \cdot 10^{14} \text{ cm}^{-2}$ , i. e. above the

amorphization threshold [14]; and 2) InP crystals with double implant. The latter samples first received a 2 MeV Fe implantation at a dose of  $5 \cdot 10^{13} \text{ cm}^{-2}$  at 200 °C, followed by a room temperature implantation of P at 5 MeV with a fluence of either  $5 \cdot 10^{13} \text{ cm}^{-2}$  or  $2 \cdot 10^{14} \text{ cm}^{-2}$ . Annealing was performed at 650 and 750 °C for 1 or 1.5 hr in an MOCVD reactor under a controlled P atmosphere. Undoped (slightly n-type in the low  $10^{16} \text{ cm}^{-3}$  range) substrates were used. The depth distribution of the Fe dopant was measured by SIMS employing an oxygen primary beam. TEM, in the bright field and dark field modes, was used to determine the type and in-depth distribution of the defects. The cross sectional TEM specimens were thinned by mechanical polishing followed by Ar ions bombardment at liquid nitrogen temperature.

## Results

The as-implanted layer of the sample submitted to the single Fe implant was amorphous. Figure 1 a) is the TEM cross-sectional image of the annealed sample showing the in-depth distribution of defects that consists of a band of EOR dislocation loops formed at the position of the original a/c interface and slightly beyond it and of a band of twins due to the uncomplete recovery of the crystalline state from the amorphous state [15]. The twin band terminated with a tangled network of dislocations. The bottom interface of the twin band was located at a depth of ~1500 nm, whereas the depth range of the EOR loops was between ~1600 and 1800 nm. The majority of the EOR loops were faulted of the Frank type with  $\mathbf{b} = 1/3\langle 111 \rangle$ . The others were of the perfect type,  $\mathbf{b} = 1/2\langle 110 \rangle$ . All loops were extrinsic. They have undergone loop coarsening [10] as they increased in size and decreased in density by increasing the annealing temperature from 650 to 750 °C.

The typical SIMS spectra of the as-implanted and annealed samples for the InP substrate with single Fe implant are given in Fig. 1 b). The SIMS profiles show that after annealing Fe exhibits an anomalous distribution in that it shows accumulation peaks. For the annealing at 650°C there is a peak at a depth of 1500 nm that splits into two peaks at depths of 1500 and 1700 nm, respectively, for the annealing at 750 °C. For the latter annealing temperature another broad peak also appears at a depth around ~1000 nm.

Figures 2 a) and b) are the cross-sectional TEM images of the sample submitted to double implant with Fe (dose  $5 \cdot 10^{13} \text{ cm}^{-2}$ ) and P ( $2 \cdot 10^{14} \text{ cm}^{-2}$ ), before and after annealing, respectively. It has been seen preliminary by us that implantation of 2 MeV Fe at 200 °C in InP does not produce any crystal defect. The defects described in the following are thus only due to the implantation of P. The as-implanted sample contained a buried amorphous layer with the lower a/c interface at a depth of ~2800 nm. The maximum amorphization was reached close to such a/c interface, the top surface layer being nearly completely crystalline, as checked by selected area diffraction (Fig. 2 a). The top a/c interface was not well defined as the a/c transition was spread over a large distance. The annealed sample contained extrinsic EOR dislocation loops, of both Frank and perfect type, close to the position of the original a/c interface, i. e. in the depth range ~2750-2850 nm, and a band of extrinsic loops from the top surface down to a depth of ~2200 nm (Fig. 2 b). They are due to condensation of supersaturated intrinsic self-interstitials. At the bottom interface of this band small stacking fault tetrahedra were also detected in high density. Between this large band and the EOR loops large irregular dislocation loops were also seen (Fig. 2 b). Following Jones et al. [11] the latter loops should be shear type dislocation loops that have grown that large due to the shear associated with the misorientation of the two a/c interfaces of the buried amorphous layer when they met. Their location is close to the bottom a/c interface, which is consistent with the result that the higher degree of amorphization was detected very close to this a/c interface (Fig.

2a). The SIMS profiles of Fig. 3 show that after annealing there are Fe accumulation peaks at depths of  $\sim 2200$  and  $2750-2850$  nm, i. e. in correspondence of the bottom interface of the large band of loops and of the EOR loops region.

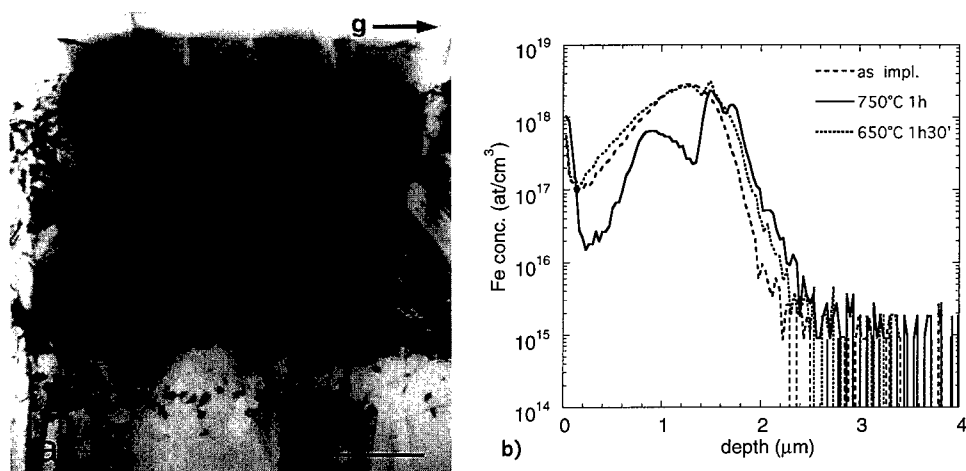


**Fig. 1** - InP substrate submitted to single Fe implant. a) Cross sectional TEM image of the annealed sample.  $g = [220]$ . Bar =  $0.5 \mu\text{m}$ . b) SIMS Fe profiles for the as-implanted and annealed samples.

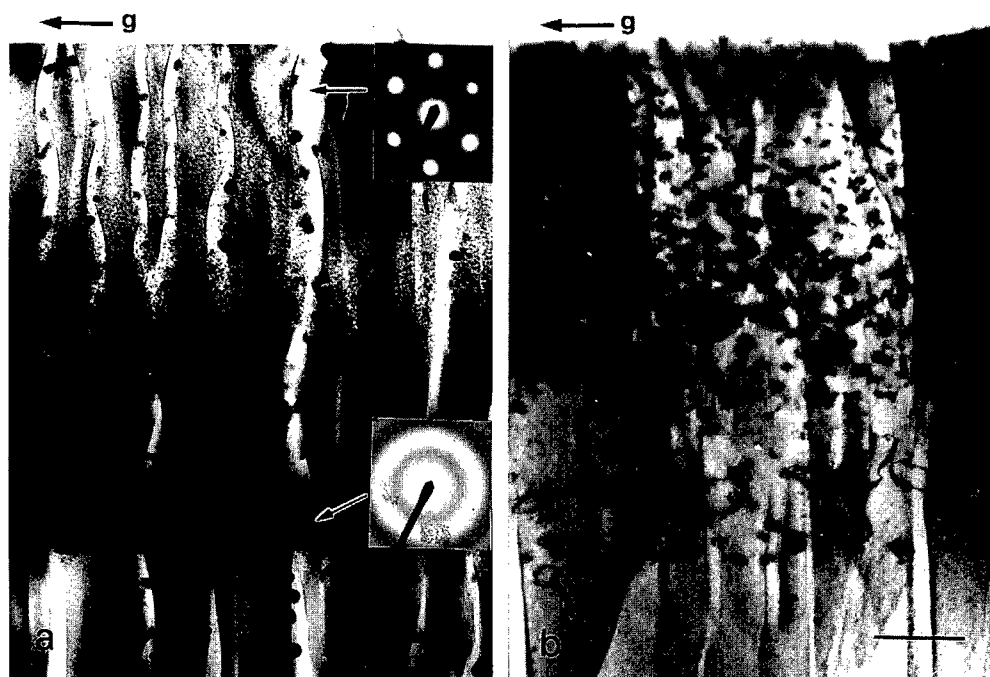


**Fig. 2** - Cross sectional TEM images of the InP substrate submitted to double implant with Fe (dose  $5 \cdot 10^{13} \text{ cm}^{-2}$ ) and P ( $2 \cdot 10^{14} \text{ cm}^{-2}$ ). a) As-implanted, b) annealed at  $750^\circ\text{C}$ .  $g = [220]$ . Bar =  $0.5 \mu\text{m}$ .

The InP sample submitted to double implant with the lower P dose (Fe at  $5 \cdot 10^{13} \text{ cm}^{-2}$  + P at  $5 \cdot 10^{13} \text{ cm}^{-2}$ ) was not amorphized. Its defect structure after annealing consists of a band of extrinsic loops, due to the condensation of supersaturated intrinsic interstitials, approximately centered around the projected range of the implanted P, as is typical for subthreshold doses [11] (Fig. 4 a). No EOR loop was detected. The Fe profiles before and after annealing at  $750^\circ \text{C}$  are given in Fig. 4 b). No significant anomalous Fe redistribution occurred after annealing.

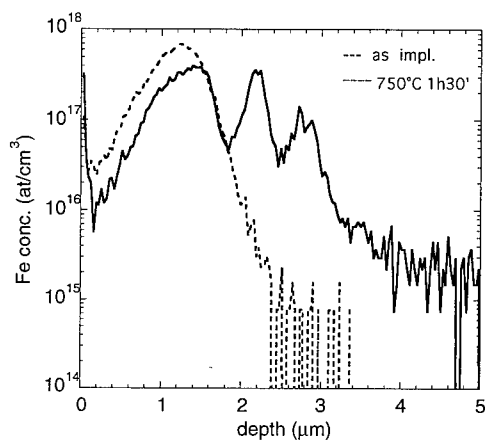


**Fig. 3** - SIMS Fe profiles for the as-implanted and annealed samples of the InP substrate submitted to double implant with Fe (dose  $5 \cdot 10^{13} \text{ cm}^{-2}$ ) and P ( $2 \cdot 10^{14} \text{ cm}^{-2}$ ).

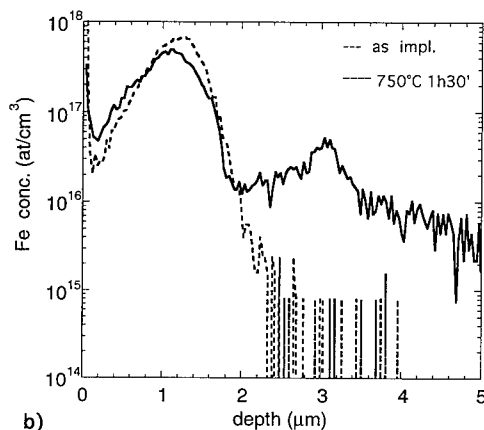


**Fig. 4** - InP substrate submitted to double implant with Fe (dose  $5 \cdot 10^{13} \text{ cm}^{-2}$ ) and P ( $5 \cdot 10^{13} \text{ cm}^{-2}$ ). a) Cross sectional TEM image of the annealed sample.  $g = [2\bar{2}0]$ . Bar = 0.5 μm. b) SIMS Fe profiles for the as-implanted and annealed samples.

## Discussion

For the sample submitted to single Fe implant, the striking correspondence between the depths of the Fe accumulation peaks and the positions of the twins band bottom

interface and of the region of EOR loops suggests that the anomalous diffusion of Fe is determined by its gettering at these extended defects. The trapping action of the EOR loops on the implanted dopant was recently shown by Claverie et al. for Si implanted with B [5-6] and has to be ascribed to the dopant gettering by the partial dislocations bordering the EOR loops and by the strain fields associated with the dislocations. Gettering by the tangled dislocations seen at the twin band bottom interface should be the cause for Fe trapping at this interface.

Based on SIMS analysis only, some authors suggested another explanation for the anomalous diffusion of Fe, or other transition elements, similar to that shown in our Fig. 1 b) [1-3]. Due to the fact the depths of the SIMS peaks roughly correspond to the values of  $0.8R_p$  and  $R_p + \Delta R_p$ ,  $R_p$  and  $\Delta R_p$  being the projected range and straggle of the Fe ions in InP, respectively, the dopant accumulation peak at  $R_p + \Delta R_p$  was ascribed to the interaction of Fe with excess P self-interstitials that should exist at such depth with the highest density, according to the calculations of Christel and Gibbons [12]. The values of  $R_p$ ,  $\Delta R_p$ ,  $0.8R_p$  and  $R_p + \Delta R_p$  in our case (2 MeV Fe ions) are given in Table I. The value of  $R_p + \Delta R_p$  is very close to the depth value of the EOR loops band.

The evolution of the Fe profile as a function of the annealing temperature, with the formation of two well separated peaks at 750 °C at depths of 1500 and 1700 nm, seems, however, to support our conclusion that the accumulation of Fe around  $R_p + \Delta R_p$  is due instead to gettering at crystal defects. If the two SIMS peaks at  $R_p + \Delta R_p$  had been due solely to the interaction of Fe with the recoil P interstitials, only one accumulation peak for Fe would have formed instead of two. The interaction between Fe and excess P interstitials [1-3] cannot explain the double peak structure of the accumulation of Fe at the depth around  $R_p + \Delta R_p$ .

Table I - Values of  $R_p$ ,  $\Delta R_p$ ,  $0.8R_p$  and  $R_p + \Delta R_p$  for 2 MeV Fe in InP

$R_p$ (nm)	$\Delta R_p$ (nm)	$0.8 R_p$ (nm)	$R_p + \Delta R_p$ (nm)
1260	350	1010	1610

It is very likely that the broad Fe peak at lower depth ( $\sim 0.8 R_p$ ) is only an apparent peak, its formation being due to the depletion of Fe at greater depths, because of the gettering at the twins band bottom interface and EOR loops, rather than to a real accumulation of Fe. Since at the depth of  $0.8 R_p$  the maximum implantation damage occurs [1-3, 10], this peak was ascribed to the trapping of Fe at such damage [1-3]. This hypothesis cannot be ruled out completely.

The double implant experiments conclusively show that the anomalous diffusion of Fe is affected by gettering at crystal defects, especially EOR loops. The distribution of the implanted Fe is the same as in the single implant experiments since 2 MeV Fe ions were used. The P implant at 5 MeV with the dose above the amorphization threshold created EOR loops much deeper than the original distribution of Fe (Figs. 2-3). The Fe peaks in the SIMS spectrum after annealing are again in correspondence of the EOR loops band and of the bottom interface of the large band of loops extending from the top surface to a depth of  $\sim 2200$  nm. The depths of the Fe peaks are  $2.22 R_p$  and  $1.75 R_p$ , respectively, with  $R_p$  the projected range of Fe at 2 MeV. This fact along with the absence of an Fe peak at the depth of  $R_p + \Delta R_p$ , where excess P interstitials due to Fe implantation at 2 MeV are expected to be present in high density [12], should rule out the possibility that Fe accumulation is due to the interaction with excess P interstitials. It might be the Fe peak at  $\sim 2200$  nm, i. e. at the bottom interface



of the large band of loops, is partially also due to Fe gettering at the stacking fault tetrahedra present at this interface. The absence of any significant Fe accumulation peak in the double implant sample with the lower dose of P ( $5 \cdot 10^{13} \text{ cm}^{-2}$ ), where EOR loops do not exist, confirms that the formation of anomalous Fe accumulation peaks is strongly affected mostly by the Fe gettering at crystal defects.

Very likely the Fe anomalous diffusion can also be determined by the enhanced Fe diffusivity in the EOR loops region, as suggested for Si [5-8]. The formation of the EOR loops and the continuous exchange of interstitials between them during the coarsening process is expected to help to maintain a supersaturation of self-interstitials in this region. Such interstitials may enhance the Fe diffusivity. The comparison between Fig. 3 and Fig. 4 b), showing that the amount of displaced Fe is greater in the double implant sample with the higher P dose (Fig. 3), which is expected to contain a higher density of self-interstitials, with respect to the sample with the lower P dose (Fig. 4 b), would support this conclusion. The increase of Fe diffusivity for increasing density of (In) self-interstitials may be possible if Fe diffuses by either a substitutional-interstitial kick-out reaction or an interstitialcy mechanism, as for both of them the diffusion coefficient increases for increasing density of intrinsic self-interstitials [16]. The former reaction is more likely to take place as it was found to be dominating for many substitutional p-type dopants in III-V compounds [16, 17].

## References

1. J. Vellanki, R. K. Nadella, M. P. Rao, O. W. Holland, D. S. Simmons and P. H. Chi, *J. Appl. Phys.* **73**, 1126 (1993).
2. H. Ullrich, A. Knecht, D. Bimberg, H. Krautle and W. Schlaak, *J. Appl. Phys.* **70**, 2604 (1991).
3. M. Gauneau, H. L'Haridon, A. Rupert and M. Salvi, *J. Appl. Phys.* **53**, 6823 (1982).
4. A. Carnera, B. Fraboni, A. Gasparotto, F. Priolo, A. Camporese, G. Rossetto, C. Frigeri and A. Cassa, *MRS Symp. Proc.* **396**, 829 (1996).
5. A. Claverie, C. Bonafos, A. Martinez and D. Alquier, *Solid State Phenomena* **47-48**, 195 (1996).
6. A. Claverie, L. Laânab, C. Bonafos, C. Bergaud, A. Martinez and D. Mathiot, *Nucl. Instr. and Meth.* **B96**, 202 (1995).
7. D. J. Eaglesham, P. A. Stolk, H.-J. Gossmann and J. M. Poate, *Appl. Phys. Lett.* **65**, 2305 (1994).
8. H. L. Meng, S. Prussin, M. E. Law and K. S. Jones, *J. Appl. Phys.* **73**, 955 (1993).
9. D. K. Sadana, J. Washburn and G. R. Booker, *Phil. Mag.* **B46**, 611 (1982).
10. C. D. Meekison, *Phil. Mag.* **A69**, 379 (1994).
11. K. S. Jones, S. Prussin and E. R. Weber, *Appl. Phys.* **A45**, 1 (1988).
12. L. A. Christel and J. F. Gibbons, *J. Appl. Phys.* **52**, 5050 (1981).
13. C. Frigeri, A. Carnera, B. Fraboni, A. Gasparotto, F. Priolo, A. Camporese and G. Rossetto, *Inst. Phys. Conf. Ser. (X Oxford Conf. on Microscopy Semiconducting Materials)*, in press (1997).
14. A. Carnera, A. Gasparotto, M. Tromby, M. Caldironi, S. Pellegrino, F. Vidimari, C. Bocchi and C. Frigeri, *J. Appl. Phys.* **76**, 5085 (1994).
15. C. Frigeri, A. Carnera, B. Fraboni, A. Gasparotto, A. Cassa, F. Priolo, A. Camporese and G. Rossetto, *Mater. Sci. Eng.* **B44**, 193 (1997).
16. U. M. Gösele and T. Y. Tan, in "Materials Science and Technology" ed. R. W. Cahn, P. Haasen and E. J. Kramer (New York: VCH) vol. 4, p. 197 (1991).
17. C. W. Farley and B. G. Streetman, *J. Electrochem. Soc.* **134**, 453 (1987).

## LITHIUM INDUCED VACANCY FORMATION AND ITS EFFECT ON THE DIFFUSIVITY OF LITHIUM IN GALLIUM ARSENIDE

H.P. Gislason, K. Leosson, H. Svavarsson, K. Saarinen<sup>1</sup> and A. Mari<sup>2</sup>  
Science Institute, University of Iceland, Dunhaga 3, 107 Reykjavik, Iceland

<sup>1</sup>Laboratory of Physics, Helsinki University of Technology,  
P.O. Box 1100, FIN-02015 HUT, Finland

<sup>2</sup>Laboratoire d'Optique des Solides, Case 80, Université Pierre et Marie Curie,  
4, Place Jussieu, F-75252 Paris cedex 05, France

**Keywords:** GaAs, vacancies, antisites, lithium, positron annihilation, diffusivity, local modes

**Abstract.** Diffusivity studies on Li in GaAs, where high concentrations of lithium have been introduced into undoped n-type starting material, reveal that diffusion of Li is trap-limited due to formation of complexes containing Li and native defects. The same defect complexes are found in Li-doped semi-insulating starting material and in p-type GaAs:Zn as well after passivation of the Zn acceptors. In partially Li-passivated Zn-doped starting material the Li is found predominantly in Li-Zn complexes which have a relatively low binding energy. In this case, the trapping effect is weak and the lithium exhibits high diffusivity. Using infrared absorption and positron lifetime measurements we investigate complexes of Li atoms and native defects which are formed in the Li-diffusion process. We observe significant  $V_{Ga}$  and  $Ga_{As}$  concentrations in the samples and demonstrate enhanced concentration of these native defects upon heat treatment. We show that Li also forms complexes with these native defects at low diffusion temperatures.

### Introduction

Lithium, like hydrogen, exhibits a strong tendency to form complexes with other impurities and native defects when migrating in crystals. In such cases, the diffusion kinetics are largely affected by the binding energy of the complexes in question. A 1.0-eV activation energy for diffusion of Li in GaAs, sometimes cited as intrinsic in the literature, e.g. [1, 2], was determined by Fuller and Wolfstirn [3] near the solubility limit of Li in GaAs,  $[Li] \approx 10^{19} \text{ cm}^{-3}$ . This value is evidently too high to represent the intrinsic diffusivity; lithium is found to diffuse readily even below room temperature and recent measurements yielded a 0.85 eV dissociation energy of Li-Zn complexes [4], defining an upper limit for the intrinsic migration energy of Li.

Fuller and Wolfstirn [3, 5] investigated in-diffusion of Li to the saturation limit in GaAs at 800 °C and a subsequent out-diffusion by heat treatment. Starting materials were undoped n-type GaAs, S-doped ( $\approx 10^{17} \text{ cm}^{-3}$ ) and Te doped ( $\approx 10^{18} \text{ cm}^{-3}$ ) GaAs. The authors suggested that Li was introduced as  $Li_i^+ Li_{Ga}^{2-}$  pairs during diffusion. While this simple model has not been verified by localised-vibrational-mode (LVM) experiments, Levy and Spitzer [6] reported LVM bands originating from five different Li-complexes, a donor, an acceptor and up to three neutral complexes in originally undoped GaAs after Li diffusion at high temperatures. All of these were attributed to two or more Li atoms associated with native defects of unknown origin.

This paper presents results of low-temperature reverse-bias and zero-bias annealing experiments on Li-rich undoped GaAs starting material and lightly Li-doped p-type GaAs. Charge density profiles are monitored during reverse-bias annealing, yielding dissociation energies of defect complexes. Similar measurements during zero-bias annealing give information about the activation energies for trap-limited diffusion in the different materials. In p-type GaAs:Zn with low Li concentration, the pairing interaction is weak enough to allow determination of the intrinsic diffusivity. Conversely, in the Li-rich samples we find that the lithium diffusion is strongly trap limited. LVM measurements indicate that the migration is governed by pairing interactions with native defects. Positron annihilation experiments, performed in order to identify these defects, reveal significantly enhanced  $V_{Ga}$  and  $Ga_{As}$  concentrations both in as-diffused samples and after heat treatment.

### Experimental

All starting materials were grown by the horizontal Bridgman method. For electrical measurements, nominally undoped GaAs ( $n_{300} = 1 \times 10^{16} \text{ cm}^{-3}$ ) and Zn-doped GaAs ( $p_{300} = 4 \times 10^{16} \text{ cm}^{-3}$ ) were used. Fourier transform infrared (FTIR) absorption measurements were carried out on several starting materials ranging from heavily Zn-doped p-type to nominally undoped n-type and semi-insulating starting

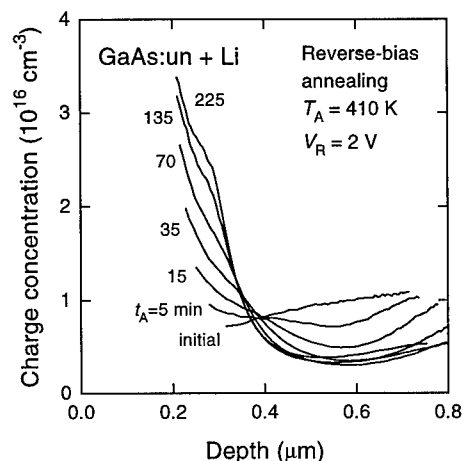


Fig. 1. Charge density profiles in Li-rich undoped GaAs during reverse-bias annealing at 410 K. Measurements were performed at 270 K after rapid cooling of the sample.

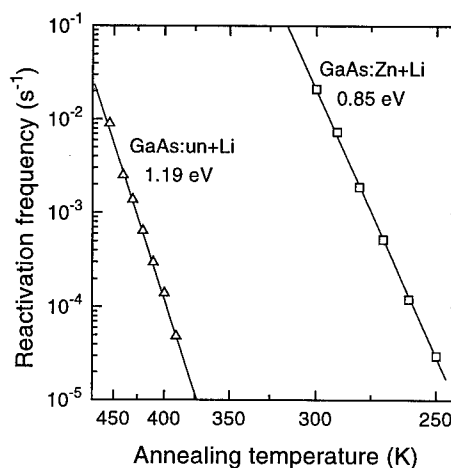


Fig. 2. Arrhenius plots of reactivation frequencies in Li-rich undoped GaAs and lightly Li-doped p-type GaAs:Zn materials. Activation energies are indicated in the figure.

materials. Li diffusions were made using open-tube diffusions as described elsewhere [7]. Schottky diodes were formed on p-type material by evaporating 1000 Å thick aluminium dots of diameter 1 mm on the sample surface. Gold dots of similar dimensions gave Schottky diodes on n-type material. Ohmic contacts were made by welding Zn- or Sn-coated gold wire to the surface of p- and n-type samples, respectively. Annealing experiments were carried out in vacuum using a Joule-Thompson refrigeration system.  $C(V)$  profiles were measured using a 1 MHz Boonton 72B differential capacitance meter. FTIR measurements were performed using DA3+ and DA8 Bomem interferometers equipped with a globar light source and mylar-Si beam splitters. The transmitted light was detected with a bolometer. Samples were cooled in a continuous-flow cryostat at 6 K. Positron lifetime measurements were performed and analysed at Helsinki University of Technology, as described in Ref. 8.

### Reverse-bias annealing

Reverse-bias annealing of Schottky diodes was carried out using the method of Zundel and Weber [9]. Samples from nominally undoped starting material which remained n-type after Li diffusion exhibited high thermal stability, and the charge density profiles were unchanged after reverse-bias annealing at temperatures up to 200 °C. We conclude that the compensating Li acceptor resides in stable configurations, either substituting for Ga or forming acceptor complexes of  $\text{Li}_{\text{Ga}}$ ,  $\text{Li}_i$  and native defects. In p-type starting material containing Li, however, significant charge transfer is observed after annealing under bias. This behaviour has been attributed to electric-field drift of  $\text{Li}^+$  [4].

Figure 1 shows charge concentration profiles measured in undoped GaAs starting material, converted to p-type by Li-diffusion at 500 °C for 20 hours. The Hall hole concentration at room temperature was  $2 \times 10^{15} \text{ cm}^{-3}$  and the Li concentration deduced from SIMS measurements of similar samples was around  $10^{17} \text{ cm}^{-3}$  [10]. Profiles were recorded after successive reverse-bias conditions followed by rapid cooling down to the measurement temperature. Annealing temperatures were in the range 390–455 K. After zero-bias annealing at 460 K for 30 minutes initial conditions were restored in the sample. The reactivation frequencies which describe the thermal dissociation of the passivated negative centres [9] are given in the Arrhenius plot in Fig. 2, from which the dissociation energy  $E_d = 1.19 \pm 0.03 \text{ eV}$  is deduced. Also shown are the reactivation frequencies measured in Li-passivated GaAs:Zn which give the much lower dissociation energy  $E_d = 0.85 \pm 0.02 \text{ eV}$ , attributed to the dissociation of Li-Zn complexes [4].

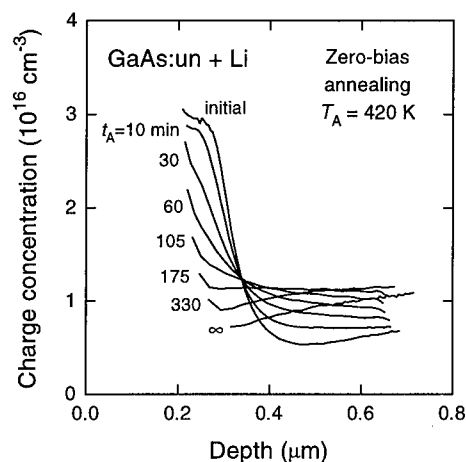


Fig. 3. Charge concentration profiles in Li-rich undoped GaAs material during zero-bias annealing. Initial curve was created under 2-V reverse bias at 420 K for 3 hours. Profiles were measured at 270 K after rapid cooling of the sample.

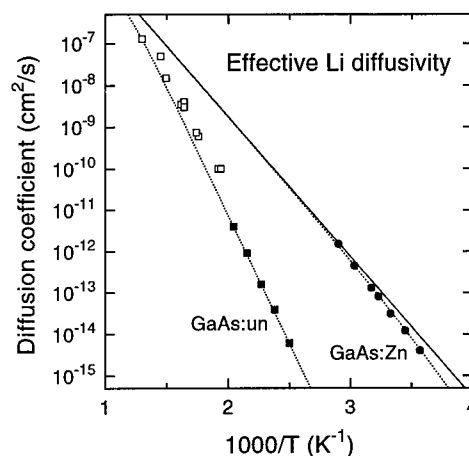


Fig. 4. Arrhenius plots showing effective diffusion coefficients of Li in Li-rich undoped GaAs and lightly Li-doped Zn-doped starting material. The solid line represents a calculation of the intrinsic diffusivity in the latter. Open squares are taken from Ref. 3. Dotted lines represent effective diffusivity [12].

### Zero-bias annealing

The charge density profile was monitored during zero-bias annealing at different temperatures. Figure 3 shows the restoration of the equilibrium profile after a step had been created in the charge density profile with prolonged reverse-bias annealing. The step disappears after several hours at 420 K as shown in the figure. The effective diffusivity of Li is determined from the zero-bias profiles as described in detail elsewhere [11]. Diffusion coefficients are shown on an Arrhenius plot in Fig. 4. Results of the high-temperature diffusion experiments of Fuller and Wolfstirn [3] are included in the figure. The activation energy for diffusion determined for the Li-rich undoped starting material is  $1.20 \pm 0.03$  eV. This value agrees with the complex dissociation energy derived from the reverse-bias annealing, indicating that in this material the diffusion behaviour is independent of the intrinsic diffusivity of Li and is governed by defect interactions. We note that the high-temperature diffusion data of Fuller and Wolfstirn agree fairly well with our measurements in strongly Li-doped samples. Exact agreement is not expected since the trapping process is predicted to depend on the concentration of Li and native defects in the material.

There is a frequently expressed concern that the strong electric field present in the depletion region of a junction affects the dissociation energy deduced from reverse-bias measurements. Dissociation energies determined from our reverse-bias and zero-bias annealing data agree to within error, and no significant high-field lowering of the complex dissociation energy takes place. It should be noted, however, that particularly low values of reverse bias, 1.5-2.0 V, were used in this work.

### The intrinsic diffusion coefficient

In the case of partially passivated Zn-doped starting material, an activation energy of  $0.75 \pm 0.02$  eV was determined from the diffusivity data of Fig. 4. This value deviates from the 0.85 eV dissociation energy measured in the Li-passivated GaAs:Zn, indicating that the diffusivity is not controlled exclusively by complex formation and dissociation. Given this and using the expression for the effective diffusivity from Zundel and Weber [12] we can calculate the intrinsic diffusivity  $D_i$ . The calculation yields  $D_i = D_o \exp(-E_m/kT)$  with  $E_m = 0.67 \pm 0.02$  eV, as illustrated by the solid line in Fig. 4 [11]. For details of the analysis see Leosson and Gislason [11]. In the Li-rich material it is clear from Fig. 4 that the impurity migration is controlled by the 1.20 eV complex dissociation energy. Using the effective diffusivity in the strong trapping limit, one obtains a good fit to the experimental data by assuming a concentration of trapping centres around  $4 \times 10^{15} \text{ cm}^{-3}$ . In this limit, the effective

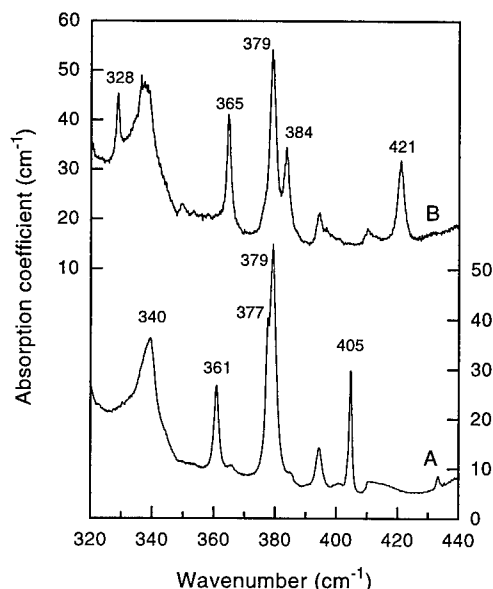


Fig. 5. FTIR absorption spectra of localised modes in GaAs. Curve A was measured in Li-diffused Zn-doped GaAs, but curve B in Li-diffused, undoped s.i. material.

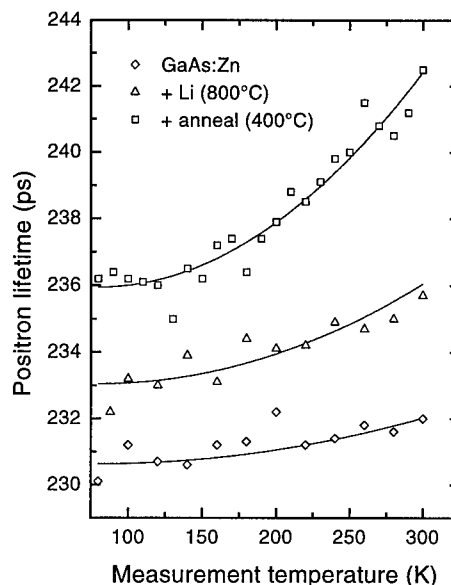


Fig. 6. Temperature variation of the positron lifetime in a GaAs:Zn reference sample, the same material after Li-diffusion at 800 °C and finally after a subsequent heating.

diffusivity is independent of  $D_i$  as pointed out above and no information about the intrinsic diffusivity in this temperature range can be obtained from the experimental data.

#### Native defects in strongly doped GaAs:Li

We now focus on the nature of the defects which are created by the diffusion of lithium into undoped, n-type, p-type and semi-insulating GaAs starting material. Curve A of Fig. 5 shows the Li-related LVM spectrum of GaAs:Zn co-doped with Li at 850 °C which gives a lithium concentration similar to the concentration of the Zn acceptor ( $p = 1.4 \times 10^{19} \text{ cm}^{-3}$ ). Under these conditions, the p-type samples are highly resistive through passivation of the Zn acceptors by Li [10]. The vibrational modes at 340, 361, 377 and 405  $\text{cm}^{-1}$  are attributed to neutral complexes of Li and Zn [10, 13]. As long as the Zn concentration exceeds that of Li, only these four peaks are present. Higher Li concentration makes the four Li-Zn peaks gradually disappear while five new LVM peaks appear, at 328, 365, 379, 384 and 421  $\text{cm}^{-1}$ . This LVM spectrum was previously observed by Levy and Spitzer [6] in originally undoped GaAs although relative peak intensities vary between samples. Weaker peaks appear as well but will be ignored here. Note that the 379  $\text{cm}^{-1}$  peak is already present in curve A, while the others are absent. In early work [6] the 379  $\text{cm}^{-1}$  peak (being strongest in p-type starting material) was assigned to a Li related donor complex. The same five peaks also appear after Li diffusion of n-type and semi-insulating starting materials. Curve B of Fig. 5 shows this spectrum in a semi-insulating starting material after Li-diffusion at 850 °C. On account of its relative strength in n-type starting material the 365  $\text{cm}^{-1}$  peak was attributed to an acceptor complex involving Li. The three remaining peaks were attributed to neutral defect complexes.

Heavy lithium doping of all GaAs starting materials makes the samples semi-insulating with a strong Li-related localised vibrational mode spectrum resembling curve B. The Hall mobility of free carriers always decreases in samples with the appearance of the five Li-related localised vibrational modes. Evidently, self-compensating Li-related donor and acceptor complexes are formed at high lithium doping levels, in agreement with the LVM results. These impurities act as effective scattering centres for the charge carriers when ionised, thereby reducing the free carrier mobility. Mixed isotope doping experiments suggest that all of the five above complexes, responsible for the Li-related absorption peaks in curve B, involve two or more Li atoms in addition to native defects of unknown origin [6].

Table I. Concentration of Ga vacancies and Ga antisite defects in different types of GaAs starting materials as determined by positron annihilation measurements.

Sample/ treatment	Li conc. [cm <sup>-3</sup> ]	Carrier conc. [cm <sup>-3</sup> ]	Vacancy conc. [cm <sup>-3</sup> ]	Negative ion conc. [cm <sup>-3</sup> ]
<b>A. High doping level</b>				
GaAs:Zn reference	none	p = 1 x 10 <sup>17</sup>	< 1 x 10 <sup>15</sup>	not detectable
Li: 800 °C	≈ 10 <sup>19</sup>	highly resistive	3.0 x 10 <sup>16</sup>	3.7 x 10 <sup>17</sup>
annealed 400 °C	≈ 10 <sup>16</sup>	p-type conducting	1.3 x 10 <sup>17</sup>	6.5 x 10 <sup>17</sup>
GaAs:Si	none	n = 2 x 10 <sup>16</sup>	< 2 x 10 <sup>16</sup>	< 2 x 10 <sup>17</sup>
Li: 800 °C	≈ 10 <sup>19</sup>	highly resistive	2.4 x 10 <sup>16</sup>	1.4 x 10 <sup>17</sup>
annealed 400 °C	≈ 10 <sup>16</sup>	p-type conducting	1.0 x 10 <sup>17</sup>	3.5 x 10 <sup>17</sup>
GaAs: undoped	none	semi-insulating	1.4 x 10 <sup>16</sup>	7.0 x 10 <sup>16</sup>
Li: 800 °C	≈ 10 <sup>19</sup>	highly resistive	1.4 x 10 <sup>16</sup>	7.0 x 10 <sup>16</sup>
annealed 400 °C	≈ 10 <sup>16</sup>	p-type conducting	2.2 x 10 <sup>16</sup>	1.0 x 10 <sup>17</sup>
<b>B. Low doping level</b>				
1 GaAs undoped	none	semi-insulating	1.2 x 10 <sup>16</sup>	5.0 x 10 <sup>16</sup>
2 Li 400 °C	2 x 10 <sup>15</sup>	semi-insulating	1.2 x 10 <sup>16</sup>	5.0 x 10 <sup>16</sup>
3 Li 400 °C/40 h	5 x 10 <sup>15</sup>	highly resistive	2.6 x 10 <sup>16</sup>	1.0 x 10 <sup>17</sup>
4 Li 500 °C/20 h	5 x 10 <sup>16</sup>	p = 1 x 10 <sup>16</sup>	0.8 x 10 <sup>16</sup>	2.5 x 10 <sup>16</sup>
5 #4 ann. 400 °C	2 x 10 <sup>16</sup>	p = 2 x 10 <sup>16</sup>	4.2 x 10 <sup>16</sup>	4.5 x 10 <sup>17</sup>

In order to identify the native defects in strongly Li-doped and heat-treated GaAs we performed positron lifetime measurements on different kinds of Li-diffused starting materials. We investigated strongly Li doped samples from n-type GaAs:Si, p-type GaAs:Zn and undoped semi-insulating GaAs starting materials on the one hand. On the other hand, we measured weakly Li doped semi-insulating starting material. Figure 6 shows the temperature variation of the positron lifetime in GaAs:Zn starting material, GaAs:Zn Li-diffused at 800 °C, and finally the latter sample annealed in As-saturated Ga melt at 400 °C. The latter two are typical of increased negative vacancy concentration since the average positron lifetime is longer than the one in as-grown samples. However, the decreased lifetime at low temperatures is indicative of negative ions which bind the positrons at temperatures below 150 K corresponding to a binding energy around 50 meV. Table I summarises the analysis of the positron lifetime measurements interpreted in terms of a defect containing a monovacancy and a negative ion containing no open volume. We suggest that the former is the  $V_{Ga}$  acceptor or an acceptor complex including a Ga vacancy and the latter the double  $Ga_{As}$  acceptor. The  $V_{Ga}$  acceptor complex may include the  $Ga_{As}$  acceptor, while the defect acting as a negative ion does not include vacancies. From the table we conclude that Li doping at 800 °C acts to increase the concentration of both  $V_{Ga}$  and  $Ga_{As}$ . It is obvious, however, that the Li concentration is not directly correlated to that of native defects. Instead the removal of lithium from the bulk enhances the latter. This is evident for all three starting materials in Table IA. Fuller and Wolfstirn observed that all Li-doped originally n-type samples showed p-type conductivity after heat treatment which removed the lithium [3, 5]. The undoped starting material exhibited  $10^{17} \text{ cm}^{-3} < p < 10^{18} \text{ cm}^{-3}$ , while the n-type starting materials showed similar values, which corresponds to a higher acceptor concentration. The acceptors were found to be readily removed from the undoped samples at 800 °C and suggested to be Ga vacancies. Similarly, we observe strongly enhanced p-type conductivity in all Li-diffused starting materials after heat treatment at 400 °C, with hole concentrations up to  $10^{18} \text{ cm}^{-3}$ . In p-type starting materials, in particular, the final hole concentration is not related to or limited by the original shallow doping.

#### Native defects in weakly doped GaAs:Li

Photoluminescence (PL) bands at 1.34 and 1.45 eV are observed after Li diffusion of n-type GaAs between 400 and 600 °C [14]. Both bands are present in Li-doped semi-insulating starting materials as well but the 1.34 eV band is usually weak. In an earlier communication [15] we reported sharp PL lines at 1.508 and 1.510 eV which appear in semi-insulating GaAs starting material at low lithium

Table II. Concentration of  $V_{Ga}$  and  $Ga_{As}$  in Li-doped semi-insulating GaAs listed in order of intensity of bound exciton lines at 1.508 and 1.510 eV relative to other spectral features in the samples.

Intensity of 1.508 and 1.510 eV bound exciton lines →					
Sample number	#1	#4	#2	#3	#5
BE line-intensity	no lines	no lines	weak	strong	very strong
Li concentration [cm <sup>-3</sup> ]	none	$5.0 \times 10^{16}$	$2.0 \times 10^{15}$	$5.0 \times 10^{15}$	$2.0 \times 10^{16}$
$V_{Ga}$ concentration [cm <sup>-3</sup> ]	$1.2 \times 10^{16}$	$0.8 \times 10^{16}$	$1.2 \times 10^{16}$	$2.2 \times 10^{16}$	$4.2 \times 10^{16}$
$Ga_{As}$ concentration [cm <sup>-3</sup> ]	$5.0 \times 10^{16}$	$2.5 \times 10^{16}$	$5.0 \times 10^{16}$	$1.0 \times 10^{17}$	$4.5 \times 10^{17}$

doping levels. The lithium diffusions were made at temperatures between 350 and 500 °C for periods of time ranging from a few hours to 40 h. The bound exciton lines were found to disappear for high lithium concentrations in the samples. PL bands with energies 1.34 and 1.45 eV have also been observed by Yu et al. after heat treatment of n-type samples at a much higher temperature than the Li diffusions, or 950 °C [16]. These authors assigned both PL bands to the two levels of an intrinsic  $V_{Ga}$ - $Ga_{As}$  double acceptor. This heat treatment also gave rise to a pair of sharp lines at 1.508 and 1.510 eV which the authors associated with the same acceptor levels [16]. It was concluded in Ref. 15 that the two pairs of bound exciton lines were identical. However, it was pointed out that the lines appear in lithium-diffused samples at much lower temperatures than after annealing in vacuum [16]. Also, the relative intensity of the BE lines is greater in Li-doped samples. Table IB summarises the results of positron lifetime measurements for the semi-insulating starting materials after Li-diffusion at moderate temperatures while Table II presents the same results in order of increasing intensity of the BE lines.

The bound-exciton line intensity is found to be correlated to the concentration of  $V_{Ga}$  and  $Ga_{As}$  but independent of the Li concentration. This is particularly obvious for samples #4 and #5. Figure 7, curve A, shows the PL spectrum of sample #4 (made from a semi-insulating starting material by Li-diffusion at 500 °C for 20 h) in which no bound exciton lines can be detected at 1.508 and 1.510 eV. Annealing of sample #4 at 400 °C for 2 hours, however, gives rise to strong BE lines as shown for sample #5 in Fig 7, curve B. The annealing strongly increases the concentration of  $V_{Ga}$  and in particular  $Ga_{As}$  while the Li concentration decreases as listed in Table II.

#### Model for the vacancy formation

Growth of GaAs under Ga-rich conditions is known to enhance the formation of arsenic vacancies,  $V_{As}$ . In samples containing a high concentration of  $V_{As}$  the  $V_{Ga}$ - $Ga_{As}$  pair is likely to be created by a single gallium atom hop into the arsenic vacancy,  $V_{As} \rightarrow V_{Ga} + Ga_{As}$ . Theoretical calculations by Baraff and Schlüter [17] suggest that its formation energy is positive in p-type crystals but negative in n-type crystals. Moreover, the binding energy of the  $V_{Ga}$ - $Ga_{As}$  pair is lower in n-type crystals than p-type [17]. Hence, the  $Ga_{As}$  antisite is expected to dominate over the  $V_{Ga}$  in Ga-rich ambience, at least when the Fermi level is mid-gap or higher. In p-type crystals, on the other hand, one might expect the  $V_{Ga}$ - $Ga_{As}$  pair to be stable. Significant concentrations of  $V_{Ga}$  and  $Ga_{As}$  are present in the samples after Li diffusion at 800 °C into different kinds of starting material and subsequent heat treatment at 400 °C.

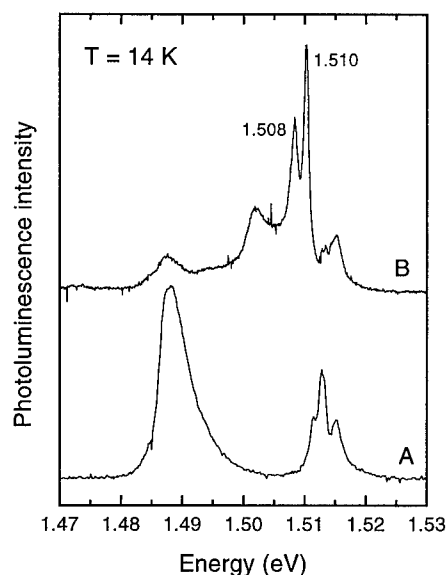


Fig. 7. PL spectra of semi-insulating GaAs starting material, Li-diffused at 500 °C, before (curve A) and after (curve B) heat treatment at 400 °C. BE lines at 1.508 eV and 1.510 eV appear after the latter.

From Table I we note that  $\text{Ga}_{\text{As}}$  is favoured in all of the starting materials under these conditions. The strongest  $\text{Ga}_{\text{As}}$  concentration is found in the p-type GaAs:Zn starting material, which might seem to contradict the above considerations. However, LVM measurements show that complexes of Li and native defects are not formed until full passivation of acceptors has taken place for Zn concentrations as high as  $10^{19} \text{ cm}^{-3}$ . Although the passivated complexes are not stable at 800 °C the material is semi-insulating by means of charge compensation when the Li diffusion promotes the formation of  $\text{Ga}_{\text{As}}$ . The  $\text{V}_{\text{Ga}}$  concentration is enhanced as well, in fact it always seems to follow the  $\text{Ga}_{\text{As}}$  concentration at a level around a decade lower. This type of correlation is not an artefact of the analysis, since it is not generally observed [8]. The above analogy with Ga-rich growth conditions is brought about by the fact that our Li diffusion is performed in a Ga melt, thus resembling LPE conditions. However, at the low and intermediate diffusion temperatures employed, the high activation energy for Ga self-diffusion in GaAs severely limits the concentration of  $\text{Ga}_i$  in the bulk. Instead, we propose the following sequence of events to explain our observations. The presence of Li in the Ga melt in the diffusion process ensures a large concentration of rapidly migrating positively charged  $\text{Li}_i^+$  donors in the GaAs bulk. It is well known that the formation energy of oppositely charged pairs is lower than that of isolated charged species, see e.g. [17]. In view of the well known tendency of  $\text{Li}_i^+$  to passivate acceptors in GaAs we suggest that the formation of passive complexes involving interstitial Li donors and  $\text{V}_{\text{Ga}}$  acceptors as well as Li donors and  $\text{Ga}_{\text{As}}$  acceptors is energetically favourable. We hesitate to postulate a similar enhancement of  $\text{V}_{\text{As}}$  donors through interaction with negative interstitial Li acceptors if they exist, since we have never observed signs of negatively charged mobile Li ions. However, the participation of the substitutional  $\text{Li}_{\text{Ga}}$  acceptor in the above complexes is by no means excluded. In fact, we suggest that combinations of  $\text{V}_{\text{Ga}}$ ,  $\text{Ga}_{\text{As}}$ ,  $\text{Li}_{\text{Ga}}$  and  $\text{Li}_i$  and perhaps other defects account for the five complexes of Li and native defects which give rise to the LVM spectra of curve B in Fig. 5.

Annealing at 400 °C releases the lithium from the defect complexes, leaving  $\text{V}_{\text{Ga}}$  and  $\text{Ga}_{\text{As}}$  in abundance in the lattice, isolated or as complex defects. These defects are detected in our positron measurements as enhanced negative vacancy and negative ion concentrations. The fact that we always observe a much lower  $\text{V}_{\text{Ga}}$  concentration than  $\text{Ga}_{\text{As}}$  concentration may be caused by the Ga vacancy being more unstable than the Ga antisite, as described by the reaction  $\text{V}_{\text{Ga}} \rightarrow \text{As}_{\text{Ga}} + \text{V}_{\text{As}}$  [17]. The presence of Li during heat treatment may be claimed to enhance the  $\text{V}_{\text{Ga}}$  and  $\text{Ga}_{\text{As}}$  concentrations from two points of view. First, heat treatment alone at 400 °C would not produce these defects. Second, heat treatment at 800 °C under Ga-rich conditions should, if anything, reduce the vacancy concentration. Therefore it is the presence of the ionised interstitial  $\text{Li}^+$  donors strongly interacting with the negatively charged  $\text{V}_{\text{Ga}}$  and  $\text{Ga}_{\text{As}}$  acceptors which stabilises these acceptors. We point out that reference samples annealed in Li-free Ga melt at 800 °C do not exhibit increased hole conductivity. For example, annealing of the semi-insulating starting material of Table IA neither produces p-type conductivity nor any signs of the LVM spectrum in curve B of Fig. 5. Most samples show increased vacancy and antisite concentrations already after the Li diffusion step alone, a fact which only illustrates that a fraction of the complexes avoids being neutralised by Li during the rapid quenching process.

Finally we emphasise the results from Table IB that Li diffusion at 400-500 °C also creates  $\text{V}_{\text{Ga}}$  and  $\text{Ga}_{\text{As}}$ . In this case we know that annealing alone neither gives the observed hole conductivity nor the bound exciton lines attributed by Yu et al. [16] to the  $\text{V}_{\text{Ga}}$ - $\text{Ga}_{\text{As}}$  pair. Our experiments do not contradict the excitons being bound to defects involving  $\text{V}_{\text{Ga}}$  or  $\text{Ga}_{\text{As}}$ . As pointed out earlier, however, we do not find it likely that the bound excitons both originate from the same double acceptor [15]. We also emphasise that sample #4 which shows hole conductivity already after the Li diffusion (presumably caused by the Li) also exhibits a reduction of both  $\text{V}_{\text{Ga}}$  and  $\text{Ga}_{\text{As}}$  concentrations. This supports the view that their formation is energetically less favourable in p-type samples.

## Conclusions

The intrinsic diffusion coefficient rarely characterises the migration of Li in GaAs due to its strong tendency to react with other defects. We have demonstrated that in highly Li-doped materials complexes containing several Li atoms are formed which strongly impede the migration of Li through the crystal. In our samples a fraction of the lithium can be released from such complexes after surmounting a dissociation energy of 1.20 eV, the majority of the Li atoms being more strongly bound. We have observed significant  $\text{V}_{\text{Ga}}$  and  $\text{Ga}_{\text{As}}$  concentration in samples containing these complexes and demonstrated enhanced concentration of these native defects upon heat treatment. We conclude that Li



forms complexes with these native defects in n-type and semi-insulating starting materials and in p-type GaAs:Zn material as well after complete passivation of the Zn acceptors.

In Li-passivated GaAs:Zn, FTIR measurements show that lithium is mainly paired with the Zn acceptors while at low doping levels there is only minimal indication of the association of Li with native defects. After complete passivation of the acceptors, however, complexes of Li and native defects are formed in a similar way as holds for other starting materials. The pairing interaction between Li and Zn is much weaker than that observed in Li-rich material and the original acceptor concentration is easily recovered in ion-drift measurements in the electric field of a Schottky diode. The activation energy for the effective diffusion coefficient is lower than the measured dissociation energy in this case, which illustrates that the pairing interaction is not limiting the diffusion kinetics. Values of the intrinsic diffusivity were determined from the effective diffusivity in this system. We maintain that this data gives the most accurate expression available in the literature for the intrinsic diffusion coefficient of interstitial lithium in GaAs.

#### Acknowledgements

The authors wish to thank B.H. Yang for some of the sample preparation. We are grateful to B. Clerjaud for discussions and C. Naud for assistance in the optical absorption measurements. This research was partially supported by the Icelandic Research Council and the University Research Fund.

#### References

1. S.M. Sze, in *Physics of Semiconductor Devices* (John Wiley & Sons, New York, 1981) p. 68
2. A.G. Milnes, *Advances in Electronics and Electron Physics* **61**, 63 (1983)
3. C.S. Fuller and K.B. Wolfstirn, *J. Appl. Phys.* **33**, 2507 (1962)
4. K. Leosson, B.H. Yang, and H.P. Gislason, *Materials Science Forum* **196-201**, 1395 (1995)
5. C.S. Fuller and K.B. Wolfstirn, *J. Appl. Phys.* **34**, 1914 (1963)
6. M.E. Levy and W.G. Spitzer, *J. Phys.* **C6**, 3223 (1973)
7. B.H. Yang, H.P. Gislason, and M. Linnarsson, *Phys. Rev.* **B48**, 12345 (1993)
8. P. Hautojärvi and C. Corbel, in *Positron Spectroscopy of Solids*, edited by A. Dupasquier and A.P. Mills (IOS Press, Amsterdam, 1995)
9. T. Zundel and J. Weber, *Phys. Rev.* **B39**, 13549 (1989)
10. H.P. Gislason, B.H. Yang, J. Petursson, and M. Linnarsson, *J. Appl. Phys.* **74**, 7275 (1993)
11. K. Leosson and H.P. Gislason, this conference.
12. T. Zundel and J. Weber, *Phys. Rev.* **B46**, 2071 (1992)
13. O.G. Lorimor and W.G. Spitzer, *J. Appl. Phys.* **38**, 3008 (1967)
14. B.H. Yang, T. Egilsson, S. Kristjansson, J. Petursson, and H.P. Gislason, *Materials Science Forum* **143-147**, 839 (1994)
15. H.P. Gislason and B.H. Yang, *Materials Science Forum* **196-201**, 201 (1995)
16. P.W. Yu, D.C. Look, and W. Ford, *J. Appl. Phys.* **62**, 2960 (1987)
17. G.A. Baraff and M. Schlüter, *Phys. Rev.* **B33**, 7346 (1986)
18. M. Bugajski, K.H. Ko, J. Lagowski, and H.C. Gatos, *J. Appl. Phys.* **65**, 596 (1988)

## AB-INITIO INVESTIGATIONS ON DIFFUSION OF HALOGEN ATOMS IN GaAs

Takahisa Ohno, Taizo Sasaki, and Akihito Taguchi\*

National Research Institute for Metals

I-2-1 Sengen, Tsukuba-shi, Ibaraki 305, Japan

\*NTT Basic Research Laboratories

3-1 Morinosato Wakamiya, Atsugi-shi, Kanagawa 243-01, Japan

**Keywords:** GaAs, halogen, chlorine, fluorine, diffusion, passivation, *ab-initio* calculations

**Abstract.** The properties of chlorine and fluorine atoms in GaAs, such as stable configurations, migration paths, charge-state effects, and interaction with dopant atoms are investigated using first-principles total-energy calculations. The stable charge state of an isolated halogen atom is determined as a function of the Fermi energy. We have found that the Cl and F atoms exhibit quite different behaviors. The Cl atom occupies preferentially the bond-center site of a Ga-As bond in the positive charge state, whereas the F atom tends to occupy the tetrahedral interstitial site in the negative charge state. In the Si-doped GaAs, the F atom passivates Si donors more effectively than the Cl atoms.

### I. Introduction

The reaction and diffusion of halogen atoms in the bulk semiconductor and the near-surface region is of great importance for various processes in device fabrication such as chemical etching of GaAs by chlorine [1]. Recently, the thermal degradation of AlInAs/GaInAs system is reported to be due to the diffusion of fluorine atoms from the surface into the Si-doped AlInAs layer [2]. It is suggested that the fluorine atoms diffusing into the AlInAs layer form complexes with the Si donor atoms and electronically passivate them [2]. It is noted that the thermal degradation is peculiar to the AlInAs ternary system.

A great deal of effort has been devoted to the behavior of hydrogen atoms in elemental [3,4] or compound semiconductors [5]. The features of stable configurations and charge states of H atoms are well understood. It is found that the doping condition of the bulk semiconductor has a profound effect on the behavior of H atoms. The H atom is likely to be in the positive charge state at the bond center site for p-type doping and in the negative charge state at the tetrahedral interstitial site in n-type materials. On the other hand, little is known about the properties of halogen atoms. In this paper, we present first-principles total-energy calculations for the properties of chlorine and fluorine atoms in the GaAs bulk, such as stable configurations, migration paths, charge-state effects, and interactions with Si donor atoms. It is found that the Cl and F atoms exhibit quite different behaviors.

### II. Calculation methods

The calculations are performed within the local density functional formalism [6] using the pseudopotential approximations. We employ the norm-conserving fully separable pseudopotentials for Ga, As, and Cl atoms [7], and use the ultrasoft one for F atom [8]. The pseudo wavefunctions are expanded in terms of a plane-wave basis set. The cutoff energy of the basis is 7.29 Ry for Cl and 20.25 Ry for F impurities. Four special *k* points are employed to sample the primitive Brillouin zone. The total energy functional is minimized with respect to both the plane-wave coefficients of the occupied orbitals and the ionic degrees of freedom by using the conjugate gradient technique [9].

An isolated Cl and F atoms in the bulk GaAs are modeled using the supercell geometry containing 32 and 16 GaAs units, respectively. The 64-atom supercell and the energy cutoff of 7.29 Ry for the Cl atom are sufficient to achieve the convergence of energy differences within 0.1 eV. Similar convergence is obtained for the F atom by the 32-atom supercell and the cutoff of 20.25 Ry. The total-energy calculations are performed for various positions of the halogen atom in the supercell, some of which are shown in Fig. 1. For each position, all surrounding Ga and As atoms are fully relaxed in order to find the minimum-energy configuration.

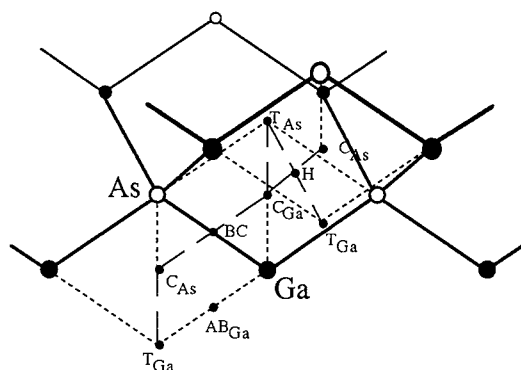


**Figure.1:** Relevant interstitial sites for a halogen atom in GaAs: BC the bond center site, T the tetrahedral site (the subscript Ga and As indicate the first-nearest-neighbor atom), H the hexagonal site, AB the antibonding site, C the site defined as the center of the rhombus formed by three adjacent atoms and the nearest T site.

### III. Results and discussions

#### Stable configurations.

Here, we examine the stable configurations of an isolated Cl atom in bulk GaAs, in the positive, neutral, and negative charge states. For the case of the negatively charged Cl ( $\text{Cl}^-$ ) atom, the lowest-energy position is the tetrahedral interstitial  $\text{T}_{\text{Ga}}$  site which has Ga atoms as the nearest neighbors. The equilibrium configuration of the  $\text{Cl}^-$  atom at the  $\text{T}_{\text{Ga}}$  site is shown in Fig. 2, together with the contour plot of the calculated valence charge density. The host lattice atoms relax little in the vicinity of the Cl atom at the  $\text{T}_{\text{Ga}}$  site. The Cl-related energy levels at the  $\text{T}_{\text{Ga}}$  site are buried deep in the GaAs valence band, and thus the Cl atom is inevitably negatively charged at the  $\text{T}_{\text{Ga}}$  site. The other tetrahedral  $\text{T}_{\text{As}}$  site surrounded by four nearest neighbor As atoms is 0.9 eV higher in energy, compared with the  $\text{T}_{\text{Ga}}$  site. This is because the  $\text{Cl}^-$  atom prefers to have the less electronegative Ga atoms as the nearest neighbors. The hexagonal (H) interstitial site is slightly lower in energy than the  $\text{T}_{\text{As}}$  site. It is noticeable that the bond center (BC) site is only 0.1 eV higher in energy than the  $\text{T}_{\text{Ga}}$  site.

The positively charged Cl ( $\text{Cl}^+$ ) atom prefers the region of high electron density in bulk GaAs and interacts strongly with the lattice atoms. The lowest-energy position for the  $\text{Cl}^+$  is the buckled bond center (BC) site, which bridges two neighboring Ga and As atoms. These Ga and As atoms have to move out over an appreciable distance, as shown in Fig. 3. The Ga-Cl and As-Cl bond lengths are 2.17 Å and 2.32 Å, respectively. The Ga-As distance is 4.08 Å, much longer than the Ga-As bond in bulk GaAs. The Ga-Cl-As bond is largely buckled with an angle of  $132^\circ$ . The Cl atom forms strong covalent bonds with the nearest neighbor Ga and As atoms. The Cl-related bonding states are buried deep in the GaAs valence band, and the antibonding states lie in the conduction band, which are empty. The Cl atom at the BC site behaves like a donor impurity in GaAs. The low-density region including the  $\text{T}_{\text{Ga}}$ ,  $\text{T}_{\text{As}}$ , and H sites is more than 1.8 eV higher in energy, compared with the BC site. The neutral Cl ( $\text{Cl}^0$ ) atom exhibits the features similar to the case of  $\text{Cl}^+$ , having the BC site as the lowest-energy position.

The stable configurations of a F atom in GaAs are considerably different from those of the Cl atom. There are two almost degenerated lowest-energy configurations for the negatively charged F-atom, that is, the  $\text{T}_{\text{Ga}}$  site and the antibonding  $\text{AB}_{\text{Ga}}$  site which has a Ga atom as a nearest neighbor. The  $\text{AB}_{\text{Ga}}$  site is not stable for the Cl atom. This arises from the difference between the Ga-Cl and Ga-F bond lengths. At the  $\text{AB}_{\text{Ga}}$  site, the Ga-F bond length is 1.87 Å and the Ga-As backbond is elongated to 2.74 Å. The  $\text{T}_{\text{As}}$  and H sites are about 0.9 eV higher in energy. The lowest-energy position of the positively charged  $\text{F}^+$  atom is the BC site, similar to the Cl atom. At the BC site, the Ga-F and As-F bond lengths are 1.79 Å and 1.87 Å, respectively. The angle of the Ga-F-As bond is  $178^\circ$ , which is compared with the Ga-Cl-As angle of  $132^\circ$  at the BC site. The F atom induces the formation of a three-center bond at the BC site, and an energy level appears in the band gap of GaAs. The  $\text{T}_{\text{Ga}}$  and  $\text{AB}_{\text{Ga}}$  sites are 0.4 eV higher in energy than the BC site. The  $\text{T}_{\text{As}}$  site is 1.3 eV unstable.

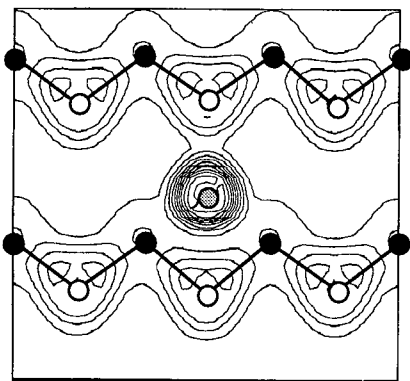


**Figure 2:** Contour plot of the calculated valence charge density in the (1-10) plane for the  $\text{Cl}^-$  atom at the  $\text{T}_{\text{Ga}}$  site in GaAs. Filled, open, and dotted circles denote Ga, As, and Cl atoms, respectively.

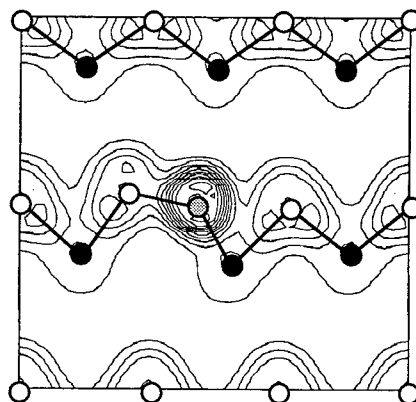


**Figure 3:** Contour plot of the calculated valence charge density in the (110) plane for the  $\text{Cl}^+$  atom at the bond center (BC) site.

#### Fermi-level dependence.

We determine the lowest energy state of the halogen atom in GaAs by calculating the relative energies of the different charge states. These relative energies depend on the position of the Fermi level, with which electrons are traded in order to alter the charge state of the halogen atom. Figure 4 presents the formation energy of the different charge states of Cl in GaAs as a function of the Fermi energy. When the Fermi level is situated at the top of the valence band, the lowest-energy state is the positively charged  $\text{Cl}^+$  in the BC site. At the bottom of the conduction band, on the other hand, there are two almost degenerated low-energy configurations, that is, the  $\text{T}_{\text{Ga}}$  and the BC sites. The BC site is only 0.10 eV higher in energy than the  $\text{T}_{\text{Ga}}$  site. It is shown in Fig. 4 that the Cl atom prefers the positive charge state at the BC site in almost the whole region of the Fermi level, in spite of its high electronegativity. The positive charge state of the Cl atom in GaAs is favored because the Cl atom forms strong bonding to the nearest neighbor Ga and As atoms. These strong bonding is not formed in the low-density region such as the  $\text{T}_{\text{Ga}}$  and the H sites.

The charge state of the F atom in GaAs quite differently depends on the Fermi-level position, in comparison with that of the Cl atom. The F atom prefers the negative charge state at the  $\text{T}_{\text{Ga}}$  or  $\text{AB}_{\text{Ga}}$  site, except for the Fermi level near the top of the valence band, as shown in Fig. 5. Near the top of the valence band, the F atom becomes to be located at the BC site in the positive charge state. It is of great interest that the Cl and F atoms are in the different charge states in bulk GaAs; Cl in the positive and F in the negative charge state. Furthermore, these charge-state properties of the Cl and F atoms are much different from those of the H atom in GaAs [5]. The H atom is in the positive charge state at the BC site for p-type doping and in the negative charge state at the T site for n-type doping. The crossover from the positive to the negative charge states occurs at the middle of the GaAs band gap.

We examine the possibility of F atoms pairing in GaAs. When two neutral F atoms are deposited near the same  $\text{T}_{\text{Ga}}$  site, the resultant F-F distance is 2.48 Å, which is much larger than the bond length of a  $\text{F}_2$  molecule of 1.42 Å. This indicates that the two F atoms do not bind to form a molecule. The pair composed of a F atom at the  $\text{AB}_{\text{Ga}}$  site and a F atom at the BC site, that is,  $\text{F}(\text{AB}_{\text{Ga}})\text{-Ga-F}(\text{BC})\text{-As}$ , is the most stable configuration of two F atoms. The  $\text{F}(\text{AB}_{\text{Ga}})\text{-Ga}$ ,  $\text{Ga-F}(\text{BC})$ , and  $\text{F}(\text{BC})\text{-As}$  bond lengths are, respectively, 1.84 Å, 1.86 Å, and 1.86 Å. This  $\text{F}(\text{AB}_{\text{Ga}})\text{-F}(\text{BC})$  pair is 1.0 eV lower in energy, compared with two isolated F atoms in the neutral charge state at the  $\text{T}_{\text{Ga}}$  site. It is seen from Fig. 5 that the F-F pair is more stable than the isolated F atoms in GaAs near the top of the valence band. The pairing behaviors of F atoms in GaAs also differs from those of H atoms in GaAs. The most stable pairing configuration of H atoms is a  $\text{H}_2$  molecule located at the  $\text{T}_{\text{Ga}}$  site [5].

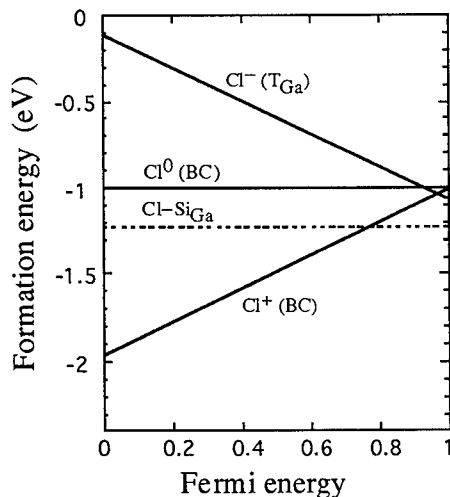


**Figure 4:** Formation energy of the different charge states of a Cl atom in GaAs as a function of the Fermi energy. The Cl atom is located at the most stable site in each charge state. The dotted line refers to the  $\text{Cl}-\text{Si}_{\text{Ga}}$  complex with a Si atom substituting for a Ga atom. The zero of the formation energy is the energy of a GaAs supercell and an isolated Cl atom in vacuum. The Fermi energy is measured from the top of the valence band, given in units of the energy gap  $E_g$  of GaAs.

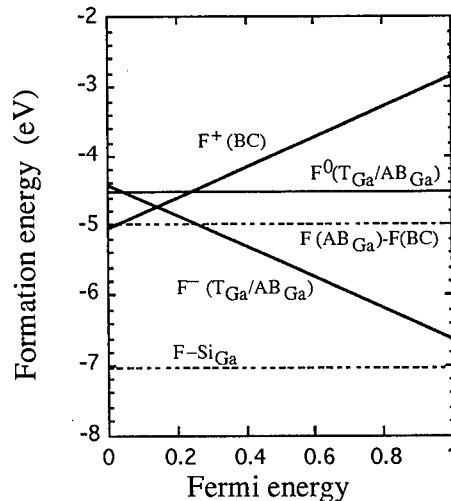


**Figure 5:** Formation energy of the different charge states of a F atom in GaAs as a function of the Fermi energy. The F atom is located at the most stable site in each charge state. The dotted lines refer to the  $\text{F}-\text{Si}_{\text{Ga}}$  complex with a Si atom substituting for a Ga atom and the  $\text{F} (\text{AB}_{\text{Ga}})-\text{F} (\text{BC})$  pair. The zero of the formation energy is the energy of a GaAs supercell and an isolated F atom in vacuum.

### Migration Path.

We now examine the migration processes of halogen atoms in GaAs. The Cl atom tends to occupy the BC site in the positive charge state and migrate through the high-density region in GaAs. As schematically shown in Fig. 6, when the Cl atom migrates from the left BC site to the right one in the high-density region, the nearest neighbor Ga atom needs to move from the right to the left. Although the process of Cl migration is rather complex in this way, we calculate the migration barrier by assuming that the Cl atom and the nearest neighbor Ga atom are on the vertical axis at the saddle point [Fig. 6(b)]. This simple procedure is known to work well in many systems [10]. The saddle point is very close to the  $\text{C}_{\text{Ga}}$  site, which is the center of two neighboring As atoms, with the Ga-Cl and As-Cl bond lengths being 2.13 Å and 2.56 Å, respectively. The migration barrier is calculated to be 0.7 eV. Via this migration path, the Cl atom at the BC site moves only around the nearest neighbor Ga atom, but does not diffuse through the crystal. The Cl atom needs to move around the Ga and As atoms alternately in order to migrate the whole crystal. The migration path around the nearest neighbor As atom has a barrier of 1.2 eV at the saddle point near the  $\text{C}_{\text{As}}$  site, which is the center of two neighboring Ga atoms. As a result, the energy barrier for the Cl migration through the whole crystal is 1.2 eV. Until the Fermi level reaches just below the bottom of the conduction band, the Cl atom exhibits the same migration properties. At the bottom of the conduction band, the Cl atom can diffuse through the lattice along a path connecting the  $\text{T}_{\text{Ga}}$  and BC sites, with an energy barrier of less than 0.4 eV. The migration barrier, on the other hand, is 0.9 eV along a path connecting the  $\text{T}_{\text{Ga}} - \text{H} - \text{T}_{\text{As}} - \text{H} - \text{T}_{\text{Ga}}$  sites in the low-density region.

The F atom prefers the  $T_{Ga}$  or  $AB_{Ga}$  site in the negative charge state and migrate through the low-density region. The migration along a path connecting the  $T_{Ga} - H - T_{As} - H - T_{Ga}$  sites is calculated to be as large as 0.9 eV, which is consistent with the low diffusivity of F atoms observed in GaAs [2]. The peculiar features of F atoms exhibiting high diffusivity in AlInAs is an open question to be solved.

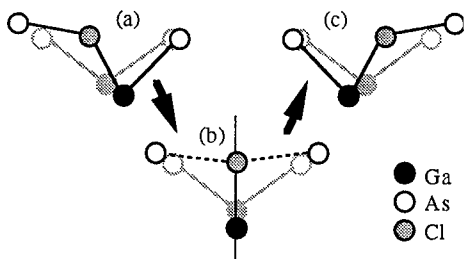


**Figure 6:** The geometry of the migration of  $Cl^+$  in a (110) plane: (a) the initial stable BC, (b) the saddle point, and (c) the final stable BC geometries. The shadow figures are the nominal positions of Ga and As atoms in the perfect crystal. Filled, open, and dotted circles denote Ga, As, and Cl atoms, respectively.

#### Donor Passivation.

Next we investigate the interaction of the halogen atom with a Si donor atom in GaAs. When Si substitutes for a Ga atom in bulk GaAs, a Si-related donor level is induced at the bottom of the conduction band. In this Si-doped GaAs, the minimum-energy configuration for the Cl atom is found near a  $T_{Ga}$  site with the substitutional Si atom as a nearest neighbor. Since the Cl-related energy level at the  $T_{Ga}$  site is much lower than the shallow donor level, the Cl atom behaves as an acceptor. The Cl atom electronically passivates the Si donor and the Cl-Si complex is neutral. This passivation is accompanied by an effective charge transfer from Si to Cl. The complex of the Cl atom at the  $T_{Ga}$  site and the neighboring Si donor atom is stable by only 0.2 eV against the dissociation into the isolated Cl atom at the BC site and the isolated Si atom. After the dissociation, the Si donor is not passivated since the Cl atom behaves like a donor at the BC site. The low dissociation energy of the Cl-Si complex indicates that the passivation of Si donors by Cl is not effective.

The F atom in the Si-doped GaAs is most likely to occupy the  $AB_{Si}$  site of the Si donor atom and form a neutral F-Si complex. The F-Si and As-Si bond lengths are, respectively, 1.73 Å and 2.66 Å. The dissociation energy of the F-Si complex is 2.5 eV, which is much larger than that of the Cl-Si complex. This implies that F atoms more effectively passivate Si donors in GaAs than Cl atoms. The H atom in Si does not bind to the donor atom and occupies the T site of a Si host atom adjacent to the donor [4], whereas the H atom in GaAs occupies the  $AB_{Si}$  site of the Si donor atom to form a bond with it [5]. The configuration for the F atom passivating donors in GaAs is similar to that of the H atom in GaAs.

#### Etching effects.

Finally, we make a comparison between Cl and F atoms in the context of etching. During etching of GaAs, the insertion of halogen atoms into Ga-As bonds is one of the most essential processes. As described above, the Cl atom prefers the BC site in almost the whole region of the Fermi level. This means that the Cl atom is likely to insert the Ga-As bond and disrupt the GaAs network, irrespective of the doping condition of the GaAs substrate. Thus, the GaAs etching rate by Cl atoms will depend slightly on the substrate doping. The F atom prefers the  $T_{Ga}$  site and does not insert the Ga-As bond, which indicates a low etching rate. The etching effect of F atoms, however, will exhibit a large dependence on the substrate doping as follows. The F atoms penetrating the GaAs network stay near the surface in a large concentration due to the large migration barrier. In heavily doped n-type GaAs, the high concentration of negatively charged F atoms near the surface induces a strong band bending and generates an inversion layer. Thus, the effective Fermi level near the surface drops to the top of the valence band, at which the F atom becomes to occupy the BC site and initiates the disruption of the GaAs network.

#### IV. Conclusions

We have theoretically investigated the properties of Cl and F atoms in GaAs, such as stable configurations, migration paths, charge-state effects, and interaction with dopant atoms, by using the first-principles total-energy calculation techniques. The stable charge state of an isolated halogen atom is determined as a function of the Fermi energy. It is found that the Cl and F atoms exhibit quite different behaviors. The Cl atom prefers the BC site in the positive charge state in spite of its high electronegativity, and migrates through the high-density region in GaAs. On the contrary, the F atom prefers the T<sub>Ga</sub> site in the negative charge state and diffuses through the low-density region. The migration barriers are fairly large for both Cl and F atoms. In the Si-doped GaAs, the F atoms passivate Si donors more effectively than the Cl atoms. Only a few experimental investigations of isolated halogen atoms in GaAs have been reported so far to allow a comparison with our calculated results. Our predictions regarding the charge state, migration path, and etching effect of Cl and F atoms provide useful information to understand technologically important halogen reactions.

#### References

1. W.T. Tsang, T.H. Chiu, and R.M. Kapre, *Appl. Phys. Lett.* **63**, 3500 (1993).
2. N. Hayafuji, Y. Yamamoto, N. Yoshida, T. Sonoda, S. Takamiya, and S. Mitsu, *Appl. Phys. Lett.* **66**, 863 (1995).
3. Hydrogen in Semiconductors, edited by J.I. Pankove and N.M. Johnson, *Semiconductors and Semimetals Vol.34* (Akademic, New York, 1991).
4. K.J.Chang and D.J.Chadi, *Phys. Rev. Lett.* **60**, 1422 (1988).
5. L. Pavesi and P.Giannozzi, *Phys. Rev. B***46**, 4621 (1992).
6. P. Hohenberg and W. Kohn, *Phys. Rev.* **136**, B864 (1964).
7. L. Kleinmann and D.M. Bylander, *Phys. Rev. Lett.* **48**, 1425 (1982).
8. D. Vanderbilt, *Phys. Rev. B***41**, 7892 (1990).
9. M.P. Teter, M.C. Payne, and D.C. Allan, *Phys. Rev. B***40**, 12255 (1989).
10. Z. Jiang and R.A. Brown, *Phys. Rev. Lett.* **74**, 2046 (1995).

## LOW TEMPERATURE INTRINSIC DIFFUSION COEFFICIENT OF LITHIUM IN GaAs

K. Leosson and H.P. Gislason

Science Institute, University of Iceland, Dunhagi 3, Reykjavik, Iceland IS-107

**Keywords:** GaAs, lithium, diffusion, defect complexes

**Abstract.** We have determined the intrinsic diffusivity of Li in GaAs in a low-temperature range (10–70°C). Li-migration was studied in weakly Li-doped *p*-type GaAs:Zn at a Schottky junction during zero-bias annealing. We describe a method used to evaluate the effective diffusion coefficient of a charged mobile defect species from space charge density profiles with an arbitrary initial charge distribution. Using data on effective diffusivity and Li-Zn complex dissociation frequency we derive an intrinsic diffusion coefficient for interstitial lithium in GaAs,  $D_i = 1 \times 10^{-2} \exp(-0.67 \text{ eV}/kT) \text{ cm}^2/\text{s}$ .

### Introduction

The influence of impurity trapping on low-temperature diffusion kinetics in semiconductors has been recognized for a long time. Specifically, early studies on lithium in GaAs indicated a non-Fickian, “dissociative” diffusion process. In this study, lithium migration was investigated in highly Li-doped samples in the temperature range 250–500°C. An effective diffusivity for the initial part of the diffusion process was quoted as  $5.3 \times 10^{-1} \exp(-1.0 \text{ eV}/kT) \text{ cm}^2/\text{s}$  [1]. Previously, the effect of Li-B pairing on lithium diffusion in silicon had been studied quantitatively, yielding kinetic parameters governing the pairing and dissociation of defect complexes in the material [2,3]. Recognizing the effect of impurity trapping, the true intrinsic diffusivity of Li in silicon was determined at temperatures and in samples where defect pairing was insignificant, giving  $D_i \approx 2.5 \times 10^{-3} \exp(-0.66 \text{ eV}/kT) \text{ cm}^2/\text{s}$  [4]. Similar work was not carried out for Li in GaAs and the effective diffusivity of Fuller and Wolfstirn has been quoted in the literature with intrinsic diffusion coefficients of impurities in GaAs [5,6].

Our previous studies [7] have indicated that the intrinsic diffusion coefficient of Li in GaAs samples exhibiting weak pairing interactions deviates significantly from the effective diffusivity proposed by Fuller and Wolfstirn. Wahl [8] has also studied the diffusion of implanted lithium to Ga vacancies introduced during the implantation process. In this study, numerical simulations indicated a migration energy around 0.6 eV. Activation energies in the range 0.5–0.7 eV are generally observed for interstitial diffusion [9]. The present paper describes measurements of the effective diffusivity of Li in Zn-doped GaAs. Li passivates Zn acceptors by forming Li-Zn complexes but the binding energy of these complexes is particularly low [10], allowing the true intrinsic diffusivity of Li to be derived.

### Experiment

The annealing experiments were performed on horizontal Bridgman Zn-doped GaAs ( $N_A \approx 10^{16} \text{ cm}^{-3}$ ), diffused with Li at 400°C for 8 hours as described elsewhere [11]. The sample was heat-treated to reduce the near-surface concentration of Li to approximately  $5 \times 10^{15} \text{ cm}^{-3}$ . It has been shown that at low concentrations, lithium forms complexes with Zn rather than with native defects [12]. Schottky diodes were formed by evaporating 1000 Å of aluminum on the sample surface. Charge density profiles were obtained using conventional capacitance-voltage [ $C(V)$ ] techniques, using a 1 MHz Boonton 72B capacitance meter. Thermal annealing was carried out under vacuum in an MMR Technologies Joule-Thompson refrigeration system using nitrogen gas and equipped with a wide-temperature-range thermal stage.



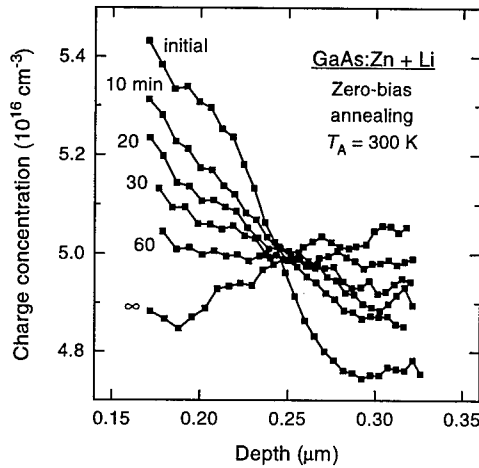


Figure 1: Space charge concentration profiles measured at 250 K after annealing at 300 K for the indicated annealing time. The initial concentration step was obtained after reverse-bias annealing at 330 K.

Measurements were carried out as follows. The sample was annealed at 60°C for several minutes with a 1.5-V reverse bias applied to the diode. The electric field in the depletion region of the biased diode drives out mobile  $\text{Li}^+$  and the temperature is sufficient to ensure complete reactivation of  $\text{Zn}^-$  acceptors in this region [10]. The space charge density was recorded after rapid cooling of the sample to 250 K. Without applying bias to the diode, the sample was then heated and maintained at the annealing temperature for a period of time. Charge density profiles were recorded regularly during annealing, after freezing the charge distribution by rapid cooling to the measurement temperature. Figure 1 shows charge density profiles recorded during zero-bias annealing at 300 K. The process was repeated for annealing temperatures in the range 280–345 K.

### Analysis

Assuming the simple case of one mobile defect species  $A$  and one non-migrating species  $B$  which may form a defect complex  $AB$ , the basic equation describing the diffusion of  $A$  in the material is

$$\frac{\partial C_A^f}{\partial t} = D_i \frac{\partial^2 C_A^f}{\partial x^2} - \frac{\partial C_{AB}}{\partial t}. \quad (1)$$

Here,  $C_X$  is the concentration of species  $X$  and superscripts  $f$  denote concentrations of free (unpaired) atoms.  $D_i$  is the intrinsic diffusivity of species  $A$  given by  $D_i = D_0 \exp(-E_m/kT)$  where  $E_m$  is the migration energy. Furthermore,

$$\frac{\partial C_{AB}}{\partial t} = \sigma C_A^f C_B^f - \nu C_{AB}, \quad (2)$$

where  $\sigma = 4\pi R D_i$  and  $\nu = \nu_0 \exp(-E_d/kT)$  are the capture coefficient and dissociation rate, respectively.  $R = q^2(4\pi\epsilon kT)^{-1}$  is the capture radius and  $E_d$  is the dissociation energy of the complexes  $AB$ . Under certain experimental conditions Eq. (1) simplifies to a conventional diffusion equation [13]

$$\frac{\partial C_A}{\partial t} = D_{\text{eff}} \frac{\partial^2 C_A}{\partial x^2}, \quad (3)$$

where  $D_{\text{eff}}$  is an effective diffusivity given by

$$D_{\text{eff}} = \frac{D_i}{1 + \sigma C_B / \nu} = \frac{D_i}{1 + \frac{4\pi R D_i C_B}{\nu}}. \quad (4)$$

The simplification of Eqs. (1) and (2) to Eq. (3) rests on two assumptions: (i) The reaction described by Eq. (2) must reach thermal equilibrium within a short time compared to typical diffusion times and (ii)  $C_A^f \ll C_{AB}$  [13].

In the low-temperature limit where trapping is strong, the effective diffusion coefficient approaches a trap-limited diffusion coefficient,  $D_t = \nu/4\pi RC_B$ , which is independent of the intrinsic diffusivity and has a thermal activation energy equal to  $E_d$ . At high temperature, the effective diffusivity equals the intrinsic diffusivity with an activation energy  $E_m$ . Since  $R$  does not change rapidly with temperature, we can define an approximate transition temperature where  $D_i \approx D_t$ :

$$T_{tr} \approx \frac{E_m - E_d}{k \ln(4\pi RC_B D_0 / \nu_0)}. \quad (5)$$

In the analysis of Zundel and Weber [13], the quality of the Si diodes and the relatively high dissociation energy of the H-B complex (1.28 eV) allowed the initial charge concentration profiles to be modeled as single step functions in a semi-infinite medium in the strong-trapping limit ( $T \ll T_{tr}$ ). In the temperature interval studied, assumptions (i) and (ii) were satisfied, allowing measured profiles to be compared with simple analytical solutions of Eq. (3). The present study differs from that of Zundel and Weber in two important respects; the low breakdown voltage of the diodes prevents us from treating the initial charge concentration as a single step function and, furthermore, the diffusion takes place in the transition regime  $T \approx T_{tr}$ . We have therefore carried out numerical simulations to verify the validity of the above approach under the present experimental conditions.

Equations (1) and (2) were solved numerically, using defect concentrations and temperatures corresponding to our experiments. The upper graph in Fig. 2 shows the calculated response of the system to a sharp initial concentration step after several annealing times. In the calculation we used the previously published expression for  $\nu$  [10] and  $D_i$  given below. The curves show  $C = C_B - C_A$  as a function of distance with  $C_B = 5 \times 10^{16} \text{ cm}^{-3}$  and initial conditions of  $C_A = 0$  for  $x < 0.48 \text{ } \mu\text{m}$  and  $C_A = 5 \times 10^{15} \text{ cm}^{-3}$  for  $x > 0.48 \text{ } \mu\text{m}$ . These curves correspond to charge density profiles in the simple case where defects  $A$  and  $B$  carry single and opposite charges. Dotted lines in the lower graph of Fig. 2 are derivatives of the concentration profiles.

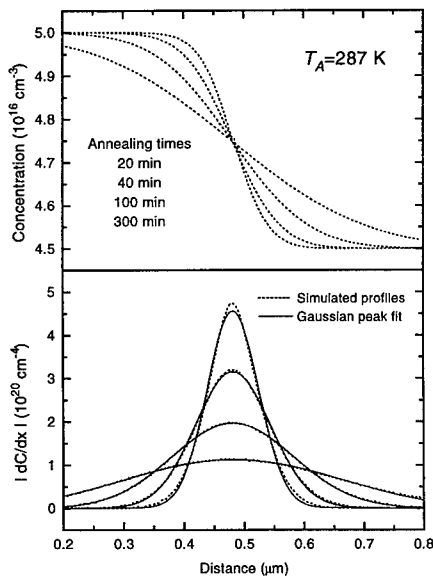


Figure 2: Numerically simulated diffusion profiles compared with theory.

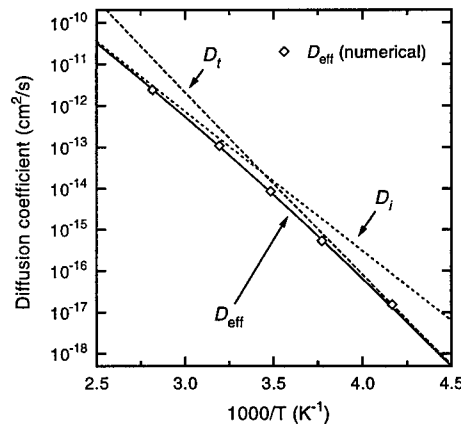


Figure 3: Effective diffusivity determined from numerical simulation. The intrinsic diffusivity  $D_i$  and the trap-limited diffusivity  $D_t$  corresponding to parameters used in the calculation are shown with dotted lines. The numerical simulation follows closely the effective diffusivity given by Eq. (4).

Analytically, the function  $dC/dx$  corresponding to an initial concentration step is a Gaussian peak centered at the initial step position. As shown in Fig. 2, the simulated profiles are well represented by Gaussian peaks. Analogous to Ref. 13 we introduce the annealing parameter  $s$  which equals the peak height and can be written as a function of the diffusion length  $L_d = \sqrt{4D_{\text{eff}}t}$ . If Eq. (3) holds, the reciprocal peak height  $1/s$  equals  $L_d\sqrt{\pi}/\Delta C$ , where  $\Delta C$  is the initial step height. We confirmed that a linear relationship between  $1/s$  and  $\sqrt{t}$  is rigorously satisfied, allowing us to determine  $D_{\text{eff}}$  from the simulated profiles. Figure 3 shows that effective diffusivities estimated from  $1/s$  data of simulated profiles are in excellent agreement with  $D_{\text{eff}}$  given by Eq. (4) in the transition interval between  $D_i$  and  $D_t$ . Calculations were also performed for high concentrations of the mobile species,  $C_A \approx C_B$ , using identical kinetic parameters. In this case, the diffusion behavior rigorously followed Eq. (3) in the high-temperature limit but deviated significantly from Fickian diffusion behavior at temperatures below the transition temperature  $T_{\text{tr}}$  given by Eq. (5).

### Results

The excellent agreement between numerical simulation and the approximate expressions (3) and (4) in the weak doping limit implies that diffusion in a weakly doped system should follow Eq. (3) for any initial charge distribution since any distribution can be regarded as a linear combination of step functions (or other functions for which Eq. (3) has analytical solutions). We therefore determined the effective diffusivity in our samples by comparing experimental profiles with solutions of the diffusion equation (3), using a combination of step functions to represent the initial conditions. For simplicity, we determine the maximum slope of the measured concentration profiles and compare with analytical values of the annealing parameter  $s$ , which is now understood to represent the maximum value of  $dC/dx$ . With our initial conditions, the peak does not remain centered at a fixed position and the reciprocal peak height does not vary linearly with  $\sqrt{t}$ . The theoretical variation in  $1/s$  with diffusion length is shown as a solid line in Fig. 4. Experimental data are scaled horizontally to fit the theoretical curve, giving values of  $D_{\text{eff}}$  for each temperature.

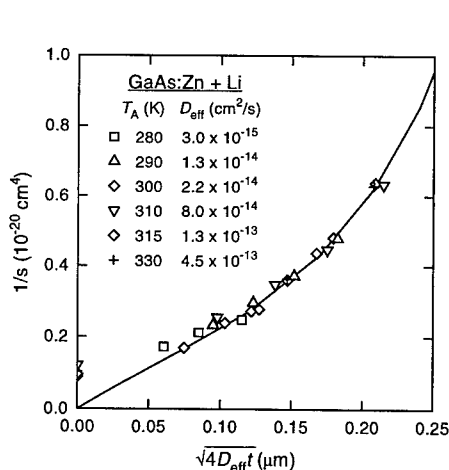


Figure 4: Reciprocal peak heights  $1/s$  determined from charge density profiles at different annealing temperatures. The effective diffusivities used to fit theoretical (solid line) and experimental (symbols) data are indicated.

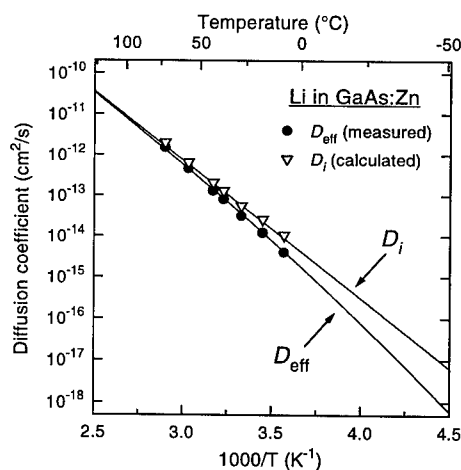


Figure 5: Effective diffusivity from Fig. 4 (solid circles) plotted against reciprocal annealing temperature and the intrinsic diffusivity of Li in GaAs derived from Eq. (4) and data on Li-Zn complex dissociation frequency [10] (open triangles).

Using values of  $\nu$  from Ref. 10 we calculate  $D_i$  from Eq. (4). It was verified that the complex dissociation in the present samples was governed by the previously published parameters [10]. Figure 5 shows the effective diffusivity derived from the experimental profiles and the corresponding values of  $D_i$ . A least-squares linear fit through the data gives the intrinsic diffusion coefficient for lithium in GaAs

$$D_i = 1 \times 10^{-2} \exp \left( \frac{-0.67 \pm 0.02 \text{ eV}}{kT} \right) \text{ cm}^2/\text{s}. \quad (6)$$

### Conclusions

We have determined the intrinsic diffusivity of Li in GaAs from data on effective diffusivity in a weakly trap-limited system. Excellent agreement was obtained between analytical expressions and numerical simulations of diffusion behavior. The 0.67 eV migration energy which we derive for  $\text{Li}^+$  in GaAs is consistent with an interstitial process and is close to the 0.6 eV estimate of Wahl [8]. It should be kept in mind that the intrinsic diffusivity rarely controls the diffusion behavior of reactive species and, in general, that macroscopic diffusion in III-V semiconductors is a complicated process, highly dependent on defect concentrations and crystal stoichiometry [9]. The high activation energy of the effective diffusion coefficient reported by Fuller and Wolfstirn [1] arises from interactions between Li and native defects as noted elsewhere [12] and the non-Fickian diffusion behavior can be attributed to the high Li concentration and the presence of several complexes with different dissociation energies.

### Acknowledgments

We thank Dr. B.H. Yang for carrying out the Li diffusion. The research was partially supported by the Icelandic Research Council and the University Research Fund.

### References

- [1] C.S. Fuller and K.B. Wolfstirn, J. Appl. Phys. **33**, 2507 (1962).
- [2] E.M. Pell, J. Appl. Phys. **31**, 291 (1960).
- [3] E.M. Pell, J. Appl. Phys. **32**, 1048 (1961).
- [4] E.M. Pell, Phys. Rev. **119**, 1014 (1960).
- [5] S.M. Sze, *Physics of Semiconductor Devices* (Wiley, New York, 1981), p. 68.
- [6] A.G. Milnes, Advances in Electronics and Electron Physics **61**, 63 (1983).
- [7] H.P. Gislason, T. Egilsson, K. Leosson, and B.H. Yang, Phys. Rev. B **51**, 9677 (1995).
- [8] U. Wahl, Phys. Rep. **280**, 145 (1997).
- [9] B. Tuck, *Atomic Diffusion in III-V Semiconductors* (Adam Hilger, Bristol, 1988).
- [10] K. Leosson, B.H. Yang, and H.P. Gislason, Mat. Sci. Forum, **196-201**, 1395 (1995).
- [11] H.P. Gislason, B.H. Yang, J. Petursson, and M. Linnarson, J. Appl. Phys. **74**, 7275 (1993).
- [12] H.P. Gislason *et al.*, this conference.
- [13] T. Zundel and J. Weber, Phys. Rev. B **46**, 2071 (1992).

## LOW TEMPERATURE IMPURITY DIFFUSION INTO LARGE-BAND-GAP SEMICONDUCTORS

N.T.Bagraev, A.A.Gippius<sup>1</sup>, L.E.Klyachkin, and A.M.Malyarenko,

A.F.Ioffe Physico-Technical Institute, St.Petersburg, 194021, Russia

<sup>1</sup>P.N.Lebedev Physical Institute, Moscow, 117924, Russia

**Keywords :** low temperature diffusion, diamond, 6H-SiC, electroluminescence

**Abstract.** Low temperature diffusion of boron and phosphorus has been performed for the first time into the monocrystalline diamond and 6H-SiC wafers through the controlled surface injection of vacancies. By varying the parameters of the surface oxide and polycrystalline silicon overlayer during the boron/phosphorus diffusion process, it was possible to obtain the planar quantum-size p<sup>+</sup>n and n<sup>+</sup>p junctions respectively in the 6H-SiC and diamond wafers as well as the 6H-SiC transistor structures. The first findings of the high temperature (77 K) quantized conductance and single-hole transistor operation are present, which identify the formation of self-assembly quantum wells inside ultra-shallow p<sup>+</sup>- and n<sup>+</sup>-diffusion profiles. These large-band-gap nanostructures are shown to cause the high electroluminescence efficiency of the diamond and 6H-SiC p-n junctions.

### 1. Introduction

Dopant diffusion in semiconductors is known to be amenable to control by adjusting the fluxes of self-interstitials and vacancies emerging from the monocrystalline surface. Use of thin oxide overlayers deposited on semiconductor wafers in combination with high diffusion temperatures has been found to result predominantly in the generation of self-interstitials by the oxidized surface, and hence, in increased rates of impurity diffusion by the kick-out mechanism [1], while the dissociative vacancy diffusion mechanism is associated with thick oxide or polycrystalline silicon overlayers and low diffusion temperatures [2]. Therefore, the present work was aimed at the realization of the diamond and 6H-SiC planar p-n junctions and transistor structures using thick oxide and polycrystalline silicon overlayers in combination with boron/phosphorus low temperature diffusion (<1000°C) which are responsible for the domination of the vacancy diffusion mechanisms.

### 2. Methods

The non-equilibrium diffusion experiments involving boron and phosphorus diffusion were performed from the gas phase at 1100°C and 900°C into p-type diamond as well as n-type 6H-SiC (0001) and epitaxial layers. The working and back side of the 6H-SiC wafers were previously oxidized using the pyrolysis of silane, whereas the diamond was covered by a thick polycrystalline silicon layer. The parameter that was varied in the course of the short-time diffusion was the oxide and polycrystalline silicon overlayer thickness. Diffusion profiles obtained were measured using the SIMS technique (Figs.1 a and b). The use of thick oxide and polycrystalline silicon overlayers has been found to lead to an increased depth for the p<sup>+</sup>-n and n<sup>+</sup>-p junctions up to 40 nm. This low temperature diffusion seems to result from the dissociative vacancy diffusion mechanism due to the excessive amount of the vacancies generated by the 6H-SiC-SiO<sub>2</sub> and C-poly Si interfaces.

### 3. Results

The forward I-V characteristics of the sample with thick oxide and polycrystalline silicon overlayers have exhibited the classical type of the SiC and diamond p-n junctions

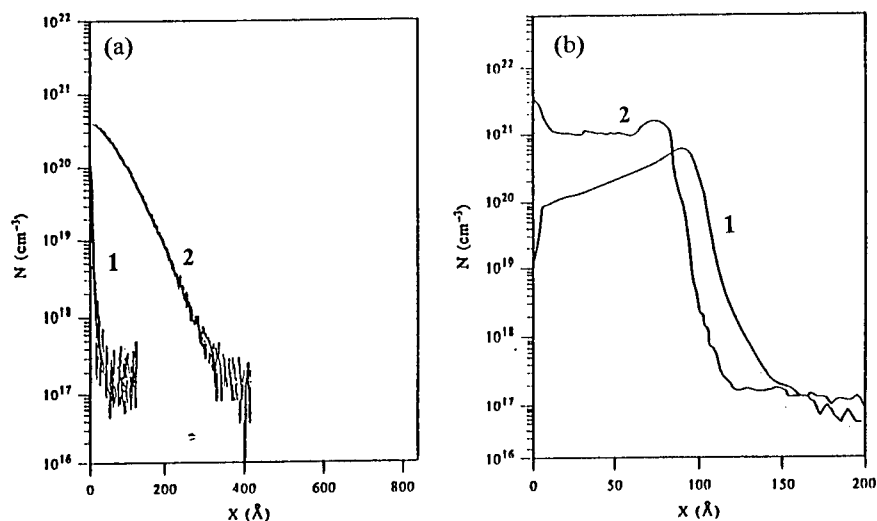


Fig.1. SIMS data for ultra-shallow 6H-SiC diffusion p-n junctions (a) and n-p-n transistor structure (b): (a) - diffusion of boron at  $900^\circ\text{C}$ , thin (1) and thick (2) oxide overlayer, respectively; (b) - diffusion of boron (1) at  $900^\circ\text{C}$  and phosphorus (2) at  $950^\circ\text{C}$ .

(Fig.2 and Fig.3). The behaviour of the I-V characteristics as a function of the oxide overlayer thickness has correlated with the diffusion profile depth obtained from the SIMS data with studying the 6H-SiC p<sup>+</sup>-n junctions (Figs.1 and 2). A quantum-well 6H-SiC n<sup>+</sup>-p<sup>+</sup>-n structure (Fig.1 b) has been demonstrated as a bipolar or field-effect transistor with the base of the quantum well type (5 nm, according to the SIMS data). The I-V characteristics of a such transistor reveal the occurrence of the conditions for both the emitter-base and base-collector tunneling which is responsible for the realization of the negative induced resistance due to avalanche current process [3].

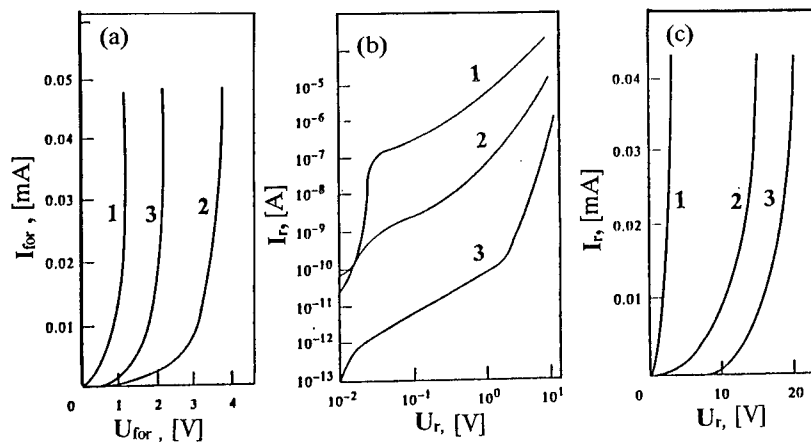


Fig.2. The forward (a) and reverse (b, c) I-V characteristics for the 6H-SiC planar p<sup>+</sup>-n junctions ( $0.8 \text{ mm}^2$ ) obtained using low temperature diffusion of boron ( $900^\circ\text{C}$ ) at thin (1), medium (2) and thick (3) oxide overlayer.

The crystallographically dependent quantized conductance obtained at 77 K with studying the 6H-SiC p<sup>+</sup>n junction has revealed the quantum wires that are formed as a result

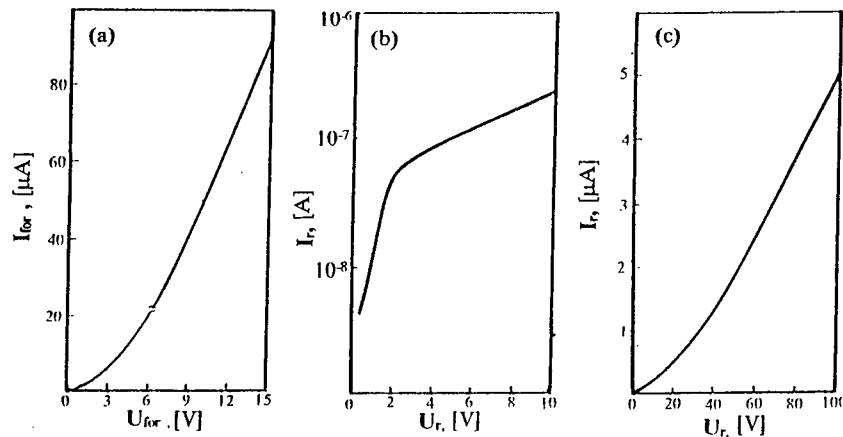


Fig.3. The forward (a) and reverse (b, c) I-V characteristics for the diamond planar n<sup>+</sup>-p junctions (10 mm<sup>2</sup>) obtained using low temperature diffusion of phosphorus (1100°C) at thick polycrystalline silicon overlayer.

of the electrostatic confining potential induced by strong charge correlations at the edges of the self-assembly quantum wells which are naturally formed inside the p<sup>+</sup> ultra-shallow diffusion profile (Figs.4 a and b). The tunnel character of the forward and reversal I-V characteristics demonstrates a correlation gap in the DOS of degenerate hole gas (Fig.4b), which seems to provide the weak localization regime in the crystallographically oriented quantum wires (Fig.4a,  $E \parallel [0001]$ ). The energy dispersion of a correlation gap is dependent on the local fluctuations in the dopant distribution along a quantum wire, which represent the places for the formation of dynamic quantum dots created by the applied voltage in the 6H-SiC n<sup>+</sup>-p<sup>+</sup>-n transistor structure.

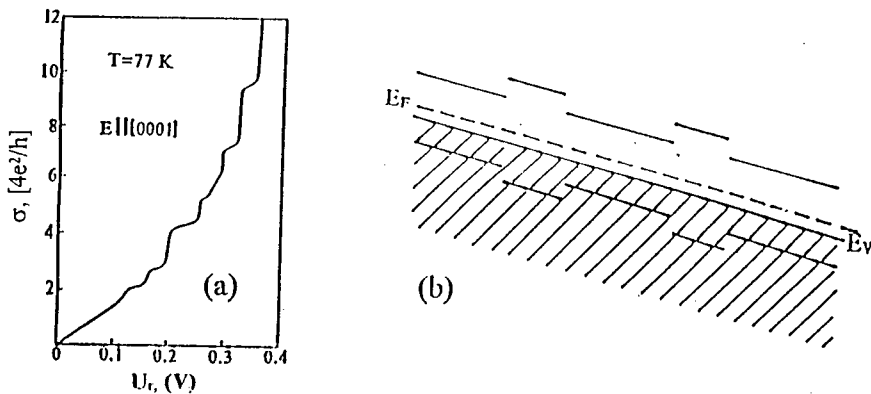


Fig.4. The quantized conductance as a function of reversal voltage in p<sup>+</sup>-n junctions (a) and one-electron band scheme for a quantum wire with a correlation gap in the weak localization regime under an applied voltage (b).

The nanotechnology suggested enables to obtain the ultra-shallow 6H-SiC p<sup>+</sup>n junctions and n<sup>+</sup>-p<sup>+</sup>-n transistor structures that represent the combinations of crystallographically oriented quantum wires and dynamic quantum dots with capacitances up

to  $10^{-19}$  F, which are enough to observe the charging effects of discrete holes at high temperatures (Fig.5a). The high temperature (77 K) 6H-SiC bipolar transistor structure which contains the dynamic quantum dot inside the isolated quantum wire reveals periodic current oscillations as a function of the applied voltage, evidence supporting operation of a single-hole transistor (Fig.5b).

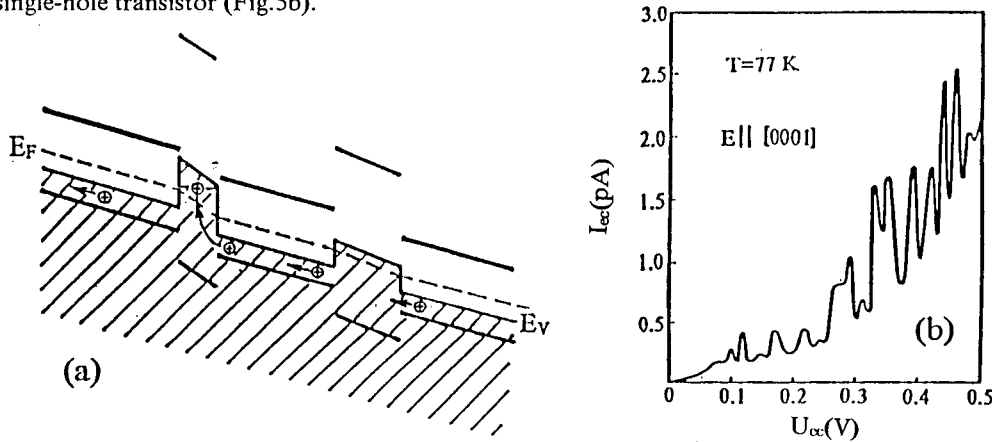


Fig.5. One-electron band scheme for the isolated quantum wire with dynamic quantum dot created by the applied voltage (a) and the reverse I-V characteristics which reveal the charging oscillations due to single hole tunnelling (b).

The creation of a correlation gap system in the DOS of degenerate hole gas has been found to result in the induced infrared emission under the strong electric field which ought to stimulate the electron/hole injection (Fig.6). The spectrum of infrared induced emission, which is due to the annihilation of the electrons and holes injected, reveals the degree of the correlation gap disordering. The power of the infrared emission can be enhanced as a result of the avalanche current process [3].

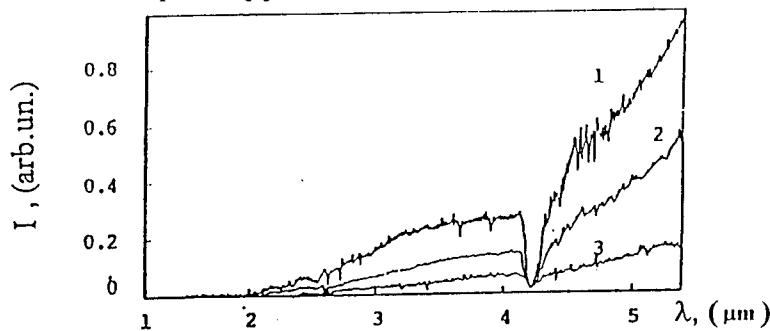


Fig.6. The spectrum of the induced infrared emission from the quantum-well 6H-SiC p-n junction under the electric field applied along the p-n junction plane at 300 K. The power of the infrared emission ( $\text{mW}/\text{mm}^2$ ): 1-90 (200 mA, 30 V), 2-45 (160 mA, 24 V), 3-15 (100 mA, 15 V). The drop in the emission spectrum at  $\lambda=4.27 \mu\text{m}$  corresponds to the absorption due to the natural contamination of  $\text{CO}_2$  in the atmosphere.

The self-assembly nanostructures obtained represent the basis toward the diamond and 6H-SiC light diodes in which both electrons/holes and photons are fully quantized. The self-assembly microcavity that is the length of the quantum wire restricted by two electrostatically-created quantum dots is found to produce the light emission at the wavelengths which coincide with the resonance wavelength of such self-assembly



microcavity. The high efficiency electroluminescence that seems to be due to the self-assembly nanostructure formation is observed with studying both the diamond and 6H-SiC p-n junctions, which is induced by the band-gap and band-shallow impurity level transitions (Fig. 7 a and b).

Figure 7c demonstrates also the electroluminescence spectra of the silicon p<sup>+</sup>n junction prepared using the same methods at the diffusion temperature of 800°C which contains self-assembly nanostructures, the dimensions of which were controlled using the STM technique and in a good agreement with the emission wavelength.

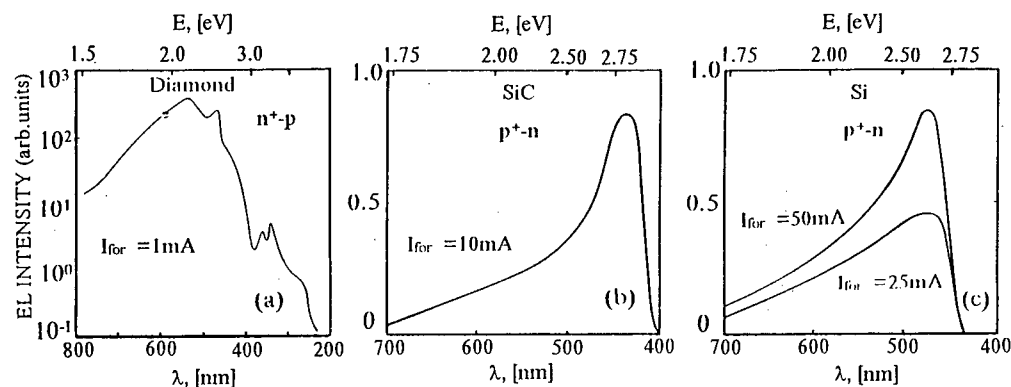


Fig. 7. The electroluminescence spectra of the diamond (a), 6H-SiC (b) and silicon (c) p-n junctions obtained using the low temperature boron (b,c) and phosphorus (a) diffusion.

#### 4. Summary

The use of thick oxide overlayers and polycrystalline layers has been demonstrated to make it possible the formation of both p<sup>+</sup>n and n<sup>+</sup>p junctions in the large-band-gap semiconductors. The I-V characteristics exhibit classical type of the 6H-SiC and diamond p-n junctions and reveal self-assembly quantum wells and crystallographically-oriented quantum wires inside both p<sup>+</sup>- and n<sup>+</sup>- ultra-shallow diffusion profiles. These large-band-gap nanostructures have been shown to cause the high efficiency electroluminescence of p-n junctions obtained, which is also exhibited with studying the self-assembly silicon nanostructures prepared using the same low temperature impurity diffusion.

#### References.

1. N.T.Bagraev, L.E.Klyachkin, V.L.Sukhanov, *Semicond.Sci.Technol.* **6** 577 (1991).
2. N.T.Bagraev, L.E.Klyachkin, V.L.Sukhanov, *Defect and Diffusion Forum* **103-105** 201 (1993).
3. N.T.Bagraev, L.E.Klyachkin, V.L.Sukhanov, *Sol.St.Electronics* **36** 1741 (1993).

## BACKGROUND DOPING EFFECTS ON Zn DIFFUSION IN GaAs/AlGaAs MULTIPLE-QUANTUM-WELL STRUCTURES

Nguyen Hong Ky

Institute of Applied Optics, Swiss Federal Institute of Technology,  
CH-1015 Lausanne, Switzerland

**Key words:** GaAs/AlGaAs, doping effect, column-III vacancies and interstitials, Zn diffusion.

**Abstract.** The effects of background n- and p-type doping on Zn diffusion in GaAs/AlGaAs multilayered structures are investigated by secondary-ion mass spectrometry and photoluminescence measurements. Zn diffusions are performed at 575 °C into Si-doped, Be doped, and Si/Be-codoped identical GaAs/Al<sub>0.2</sub>Ga<sub>0.8</sub>As multiple-quantum-well structures. The results obtained by secondary-ion mass spectrometry show that the Zn diffused region of all structures are disordered. The effective Zn diffusivity and the disordering rate are enhanced by Be doping and reduced by Si doping. Photoluminescence measurements give information about different point defects in the multilayered structures and the reactions of these defects during the diffusion process. Before Zn diffusion, the Si-doped structure contains a high concentration of column-III vacancies, whereas column-III interstitials may be the dominant defects in the Be-doped structure. After Zn diffusion, we observe a reduction of column-III vacancy concentration in the Si-doped sample and an increase in column-III interstitial concentration in the Be-doped sample. A model based on the "kick-out" mechanism of Zn diffusion is proposed to explain our observations. The incorporation of Zn into the crystal lattice during Zn diffusion results in a column-III interstitial supersaturation responsible for the Al-Ga interdiffusion. The effective Zn diffusivity and the disordering rate are controlled by the background donor or acceptor concentration in the structure and by the column-III interstitial concentration behind the Zn diffusion front. The effective Zn diffusivity and the disordering rate increase with increasing acceptor concentration, but they decrease with increasing donor concentration. Since column-III interstitials and column-III vacancies can mutually annihilate, the concentration of column-III interstitial and column-III vacancy in the Si-doped structures is reduced, leading to a retardation of Zn diffusion. On the contrary, the contribution of the column-III interstitial concentration in the Be-doped structure to the Zn-diffusion induced column-III interstitial supersaturation results in an enhancement of the Zn diffusivity.

### Introduction.

Impurity-induced disordering (IID) that permits alteration of the effective energy gap and the refractive index in selected regions of multilayered structures is an useful technique for fabrication of optoelectronic devices [1]. Since the multilayered structures consisting of p-doped, and n-doped regions are widely used for a variety of devices, it is very important to understand and to control the IID process in each of these regions [2]-[4]. Background doping effects have been observed for Si diffusion in Zn-doped GaAs bulk material [3] and for Zn diffusion in Si-doped multilayered structures [4]-[5]. In this paper, new results obtained by secondary-ion mass spectrometry (SIMS) and photoluminescence (PL) measurements are reported for Zn diffusion-induced disordering in Si-doped, Be-doped, and Si/Be-codoped identical GaAs/Al<sub>0.2</sub>Ga<sub>0.8</sub>As multiple-quantum-well (MQW) structures. This comparative study shows significant effects of background doping on the IID process. It permits to clarify the role of the Fermi level and that of the interactions between different defects in the IID process.

### Experiment.

Three GaAs/Al<sub>0.2</sub>Ga<sub>0.8</sub>As MQW structures (A, B, and C) are grown by molecular-beam epitaxy on (001)-oriented Si-doped GaAs ( $n \approx 2 \times 10^{18} \text{ cm}^{-3}$ ) substrates. The growth temperature is 620 °C. These MQW structures (Fig. 1a) consist of the following layers: i) a 0.1  $\mu\text{m}$  thick GaAs cap layer, ii) a MQW region with 29 GaAs wells separated by Al<sub>0.2</sub>Ga<sub>0.8</sub>As barriers, iii) a GaAs buffer layer, and iv) an AlAs marker. The well thickness is  $100 \pm 4 \text{ \AA}$ , whereas the barrier thickness is  $195 \pm 5 \text{ \AA}$ . Samples A and C are uniformly doped with Si ( $5 \times 10^{18} \text{ cm}^{-3}$ ) and Be ( $1 \times 10^{19} \text{ cm}^{-3}$ ), respectively. Sample B is uniformly doped with Si ( $5 \times 10^{18} \text{ cm}^{-3}$ ), but its 10 central well-barrier periods is codoped with Be ( $1 \times 10^{19} \text{ cm}^{-3}$ ). We diffuse Zn into the MQW samples at 575 °C for 4 h, using the sealed-ampoule technique [4]-[8] with 48 mg of ZnAs<sub>2</sub> source. PL measurements are performed at 77 K, using the 632.8 nm line of a He-Ne laser as excitation source and a Si photodiode as detector. The

excitation intensity of the laser beam is about  $10 \text{ W/cm}^2$ . The PL spectra are characterized for a probe region within  $0.5\text{--}0.7 \mu\text{m}$  below the sample surface. The SIMS profiles are obtained by a CAMECA IMS 300 system with a  $\text{Xe}^+$  primary-ion source at an acceleration voltage of  $9.5 \text{ kV}$ . A depth resolution smaller than  $1 \text{ nm}$  is achieved for SIMS measurements.

### Results and discussion.

Figure 1a shows a typical SIMS profile of Al concentration that is identical for all samples before Zn diffusion. After Zn diffusion, SIMS data reveals a Zn concentration profile and a change in the Al concentration profile of all samples (Figs. 1b-1d). The Zn concentration profile consists of a slowly decreasing high-concentration portion followed by a steep diffusion front. The surface Zn concentration is about  $1 \times 10^{20} \text{ cm}^{-3}$ . The depth of the Zn diffusion front decreases from sample A to sample C. This indicates the effect of background doping on the Zn diffusivity. In addition, the most gradual Zn diffusion front is observed for sample A, whereas the most abrupt Zn diffusion front is seen for sample C. The amplitude of Al signal oscillation in the region behind the Zn diffusion front is gradually reduced, indicating the disordering of MQW structures in this region. The diffused MQW

structures are composed of 3 regions: 1) an ordered region ahead of the Zn diffusion front, where the structure remains intact; 2) partially disordered and 3) totally disordered regions behind the diffusion front. We observe an out-diffusion of Al from the disordered MQW region into the GaAs cap layer. Hence, Al atoms are immobile in the undiffused region, whereas they become mobile in the Zn diffused region. This underlines the enhancement of Al-Ga interdiffusion by Zn diffusion. The Al out-diffusion depth in the GaAs cap layer seems to be independent of the background doping.

The PL spectrum of Be-doped sample A before Zn diffusion (Fig. 2,  $t=0\text{h}$ ) is dominated by the emission line at  $1.513 \text{ eV}$  ( $e\text{-A}_{\text{Be}}$ ) due to the transition of electrons from the  $n=1$  subband to Be acceptor level in the quantum wells [9]. The emission band due to the recombination of As vacancy-Be acceptor complex ( $\text{V}_{\text{As}}\text{-Be}$ ) is observed at  $1.34 \text{ eV}$  [7]–[10], indicating a high  $\text{V}_{\text{As}}$  concentration in sample A. The presence of high  $\text{V}_{\text{As}}$  concentration can result in single hops of column-III atoms forming column-III antisites ( $\text{III}_{\text{As}}$ ) and column-III vacancies ( $\text{V}_{\text{III}}$ ) [10]. This is confirmed by the observation of the  $\text{III}_{\text{As}}$ -related emission line at  $1.47 \text{ eV}$  [9], [10] and the emission band due to the recombination of residual donor- $\text{V}_{\text{III}}$  acceptor complex ( $\text{D-V}_{\text{III}}$ ) at about  $1.23 \text{ eV}$  [4]–[10]. On the other hand, sample A may contain column-III interstitials ( $\text{I}_{\text{III}}$ ) that can occupy  $\text{V}_{\text{As}}$  to form  $\text{III}_{\text{As}}$ . After Zn diffusion ( $t=4\text{h}$ ), the interdiffusion at the barrier-well interface modifies the well shape in the diffused region. Initially finite square GaAs wells become rounded AlGaAs wells and the barrier potential is reduced. The electron subbands move upward whereas the hole subbands move down, causing an increase in the electron-hole transition energy [4]–[6]. As a consequence, a blue shift of the  $e\text{-A}_{\text{Be}}$  emission line is expected for each quantum well. Since the disordering levels of the wells are different, we observe a broad emission band ( $e\text{-h}_a$ ) on the high-energy

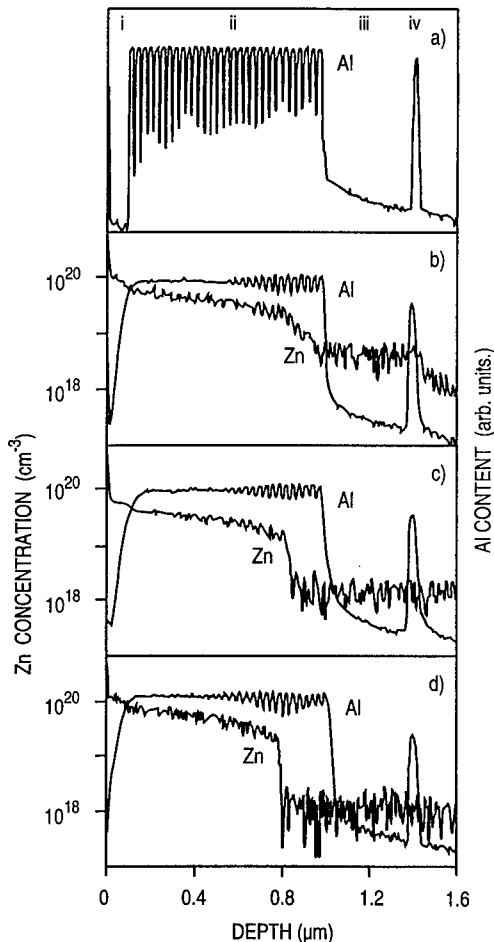


Figure 1: SIMS results: (a) Typical Al concentration profile in the MQW samples before Zn diffusion; (b), (c) and (d) Zn and Al concentration profiles in samples A, B, and C, respectively.

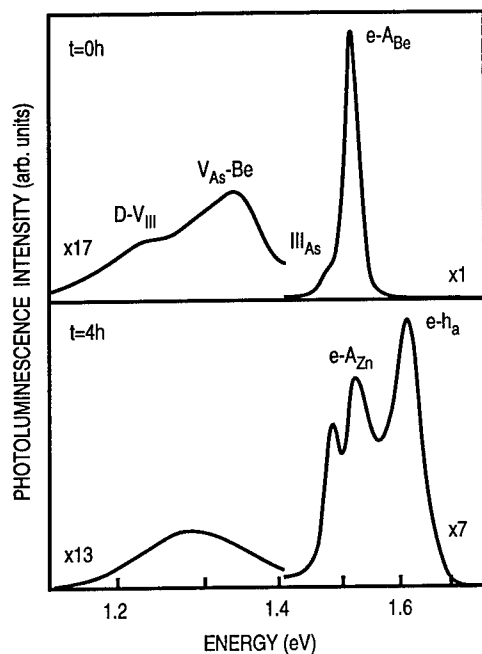


Figure 2: 77K PL spectra of sample A before and after Zn diffusion at 575 °C for 4 h.

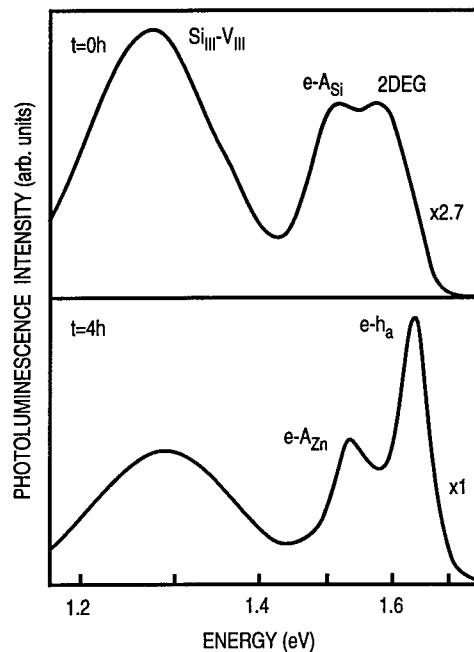


Figure 3: 77K PL spectra of sample C before and after Zn diffusion at 575 °C for 4 h.

side of the spectrum. The  $e-A_{Be}$  emission line is replaced by a new emission line at 1.509 eV ( $e-A_{Zn}$ ). The  $e-A_{Zn}$  emission line could be due to the recombination of electrons at the  $n=1$  subband with Zn acceptors in the quantum wells where a high Zn concentration is present but the disordering does not begin [4]-[6]. In particular, a significant decrease in intensity of the  $V_{As}-Be$  and  $D-V_{III}$  emission bands occurs simultaneously with an increase in intensity of the  $III_{As}$ -related emission line, indicating that the  $III_{III}$  concentration in the sample may increase during Zn diffusion. The increase in  $III_{III}$  concentration favors the  $V_{III}$  filling and the occupation of  $V_{As}$  by  $III_{III}$  to form  $III_{As}$ . In addition, a reduction of  $V_{As}$  concentration can be expected because Zn diffusion is carried out under As-rich condition.

For the Si-doped sample C, most of Si atoms occupy the column-III sites and act as donors. Electrons from the Si donors move into GaAs wells and a pseudo-two-dimensional electron gas (2DEG) is formed due to high concentration of the free carriers confined in the wells. The screening effect of the Coulomb interaction in the 2DEG results in the disappearance of the excitonic emission lines related with the MQW structures [4], [5]. Electrons in the 2DEG fill all of the confined states up to the Fermi level that locates above the lowest  $n=1$  electron quantized subband level in the well. All these electrons can participate in the recombination process. As a consequence, the excitonic emission line that usually dominates the PL spectrum of undoped MQW samples [11] is replaced by a broad emission band labeled 2DEG in the PL spectrum of sample C (Fig. 3,  $t=0h$ ). Since Si atoms incorporate also into As sites and act as acceptors, the emission line at 1.517 eV ( $e-A_{Si}$ ) is due to the transition of electrons in the 2DEG to the Si acceptor level in the wells. The emission band ( $Si_{III}-V_{III}$ ) due to the recombination of Si donor- $V_{III}$  complex dominates the PL spectrum because heavily Si-doped samples contain a high concentration of  $V_{III}$  [4], [5], [12]. After diffusion (Fig. 3,  $t=4h$ ), the  $e-A_{Zn}$  and  $e-h_a$  emission lines appear, indicating the incorporation of Zn in the wells and the disordering of the MQW structure. The intensity of the  $Si_{III}-V_{III}$  emission band is significantly reduced. This indicates a strong  $V_{III}$  filling effect in the Zn diffused region where column-III vacancies are filled by other defects generated during Zn diffusion process.

Since the uniformly Si-doped MQW structure in sample B has a central region codoped with Be, the PL spectrum taken on the sample surface before Zn diffusion (Fig. 4,  $t=0h$ ) exhibits the emission peaks similar to those observed in both samples A and C. The 2DEG and  $Si_{III}-V_{III}$  emission bands are related with the Si-doped quantum wells. The  $e-A_{Si}$  emission band observed for the Si-doped MQW

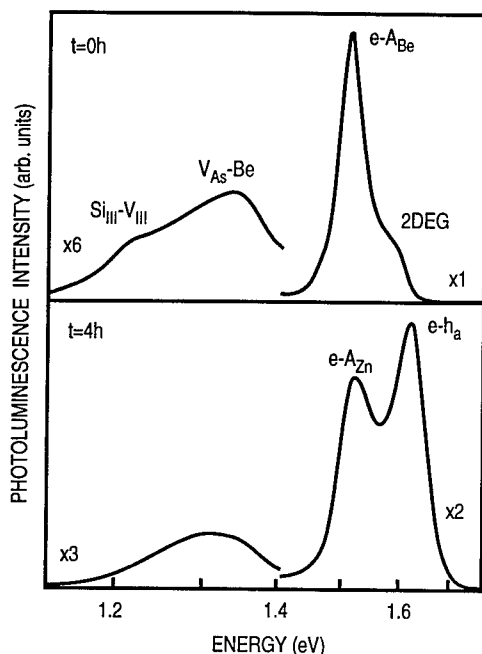


Figure 4: 77K PL spectra of sample B before and after Zn diffusion at 575 °C for 4 h.

and reduced by Si doping. In addition, the concentration of  $I_{III}$  and  $V_{III}$  that is controlled by the background doping plays an important role in the Zn diffusion and disordering process. In a III-V semiconductor, Zn diffusion is performed by the fast diffusion of interstitial Zn atoms ( $Zn_i^+$ ) and their change-over to occupy a substitutional column-III site ( $Zn_s^-$ ). The interchange between  $Zn_i^+$  and  $Zn_s^-$  can be described by the equation [4]-[6], [13]:



where  $h^+$  denotes a hole. The application of the law of mass action to Eq. (1) yields

$$\frac{p[Zn_s^-][I_{III}^+]}{[Zn_i^+]} = K_1 \quad (2)$$

where the square brackets denote the concentration,  $p$  is the hole concentration, and  $K_1$  is the equilibrium constant of Eq. (1). Equations (1) and (2) predict that Zn diffusion induces a supersaturation of  $I_{III}$  behind the Zn diffusion front. The excess  $I_{III}$  can be free to diffuse through the material causing the enhancement of Al-Ga interdiffusion. For Zn diffusion from a constant source into a Si-doped sample we can use the following electroneutrality condition [2], [4], [5]:

$$p = [Zn_s^-] - N_D + n \quad (3)$$

where  $N_D$  is the donor concentration, and  $n$  is the electron concentration. At the Zn diffusion temperature the intrinsic electron concentration,  $n_i$ , is of the order  $10^{15} \text{ cm}^{-3}$ . Since  $[Zn_s^-] > N_D$  and  $n_i \ll p$ , we obtain  $n \ll p$  and Eq. (3) can be approximated by

structure (Fig. 3,  $t=0$ ) may be hidden by the  $e-A_{Be}$  emission line. The  $e-A_{Be}$  emission line and the  $V_{As}-Be$  emission band are originated from the Be/Si codoped MQW region. The  $e-A_{Be}$  emission line due to the transition of electrons from  $n=1$  subband to Be energy level in the Be/Si codoped quantum wells dominates the spectrum. The presence of the  $V_{As}-Be$  emission band gives evidence for an abundance of  $V_{As}$  in the Be/Si codoped region. In spite of a high  $V_{As}$  concentration in the Be/Si codoped region, the  $III_{As}$  emission line seen in the spectrum of Be-doped sample A is not observed, indicating a lack of  $I_{III}$  in this region. A large amount of  $V_{III}$  may exist in the codoped region because of Si doping. The mutual annihilation of  $V_{III}$  and  $I_{III}$  could result in a low  $I_{III}$  concentration in this region. This is confirmed in the spectrum of sample B after Zn diffusion (Fig. 4,  $t=4h$ ) where a decrease in intensity of the  $V_{As}-Be$  and  $Si_{III}-V_{III}$  emission bands is observed, but the  $III_{As}$  emission line is absent. As Zn diffuses into the MQW structure and the disordering occurs, the  $e-A_{Zn}$  and  $e-h_a$  emission lines are present in the spectrum.

Our results show that Zn diffuses into both n- and p-doped samples where the disordering of MQW structure occurs behind the Zn diffusion front. The effective Zn diffusivity and the disordering rate are enhanced by Be doping

$$p \equiv [Zn_s^-] - N_D \quad (4)$$

Assuming that  $Zn_s^-$  are immobile, the Fick's second law for Zn diffusion can be written as

$$\frac{\partial [Zn_s]}{\partial t} \equiv \frac{\partial}{\partial x} \left( D_i \frac{\partial [Zn_i]}{\partial x} \right) \quad (5)$$

where  $D_i$  is the diffusivity of  $Zn_i$ . From Eqs. (2), (4) and (5) we obtain:

$$\frac{\partial [Zn_s]}{\partial t} \equiv \frac{\partial}{\partial x} \left( D_i K_I [I_{III}] (2[Zn_s] - N_D) \frac{\partial [Zn_s]}{\partial x} \right) \quad (6)$$

Equation (6) is the standard form of the Fick's second law of diffusion with the effective Zn diffusivity,  $D_{eff}$ , defined as

$$D_{eff} \equiv D_i K_I [I_{III}] (2[Zn_s] - N_D) \quad (7)$$

Using a similar procedure for the Be-doped sample, we obtain:

$$D_{eff} \equiv D_i K_I [I_{III}] (2[Zn_s] + N_A) \quad (8)$$

where  $N_A$  is the acceptor concentration. Equations (7) and (8) show that  $D_{eff}$  is controlled by  $N_A$ ,  $N_D$  and  $[I_{III}]$ . For sample A, the presence of  $N_A$  and additional  $[I_{III}]$  before Zn diffusion results in an enhancement of  $D_{eff}$ . An increase in  $[I_{III}]$  after Zn diffusion is observed by PL measurements. The  $D_{eff}$  value in sample C is determined by  $N_D$  and  $[I_{III}]$ . Since most of Si atoms act as donors,  $N_D$  increases with increasing [Si], leading to a reduction of  $D_{eff}$ . On the other hand,  $[I_{III}]$  can be significantly reduced by the  $V_{III}$  filling effect in which  $V_{III}$  recombines with  $I_{III}$  [4], [5]. During diffusion, the samples are principally surrounded by vapors of Zn and  $As_4$ . They have to move toward equilibrium with the surrounding  $As_4$  vapor by maintaining an equilibrium value of  $[V_{III}]$ . Excess  $V_{III}$  in sample C can participate in the  $V_{III}$  filling effect, resulting in a reduction of  $[I_{III}]$  and a retardation of Zn diffusion. In the Si/Be codoped region of sample B,  $N_A$  and  $N_D$  are compensated. The  $D_{eff}$  value of sample B is governed by the Si doping effect. However, this effect is reduced as compared with sample C because of the Si/Be codoped region. Equations (7) and (8) explain well our experimental observations.

## Conclusion.

Significant effects of background n- and p-type doping on Zn diffusion in GaAs/AlGaAs multilayered structures have been demonstrated. Si doping results in a retardation of Zn diffusion and disordering process, while Be doping enhances the Zn diffusivity and the disordering rate. The analysis of PL spectra measured on the surface of the Be-doped, Si-doped, and Si/Be codoped MQW samples before and after Zn diffusion reveals the important role of  $V_{III}$  and  $I_{III}$  in the Zn diffusion process. After Zn diffusion, a reduction of  $V_{III}$  concentration in the Si-doped sample and an increase in  $I_{III}$  concentration in the Be-doped sample are observed. Our model proposed on the basis of the "kick-out" mechanism of Zn diffusion indicates that the effective Zn diffusivity and the disordering rate are controlled by the  $I_{III}$  supersaturation behind the Zn diffusion front and the background donor or acceptor concentration of the sample. The high donor concentration and the annihilation of  $I_{III}$  by a large amount of  $V_{III}$  in the Si-doped structures lead to a retardation of Zn diffusion and disordering. On the contrary, the high acceptor concentration and the addition of  $I_{III}$  concentration originally present in the Be-doped structures to the Zn-diffusion induced  $I_{III}$  supersaturation results in an enhancement of the Zn diffusivity and the disordering rate.

**Acknowledgments.**

The author wish to thank F. Morier-Genoud and D. Martin for the growth of MQW samples, B. Blanchard for SIMS measurements, J. D. Ganière, and F. K. Reinhart for many fruitful discussions and their continuous support.

**References.**

1. D. G. Deppe and N. Holonyak Jr., *J. Appl. Phys.* **64**, R93 (1988) .
2. V. Swaminathan, N. Chand, M. Geva, P. J. Anthony and A. S. Jordan, *J. Appl. Phys.* **72**, 4648 (1992).
3. D. G. Deppe, N. Holonyak Jr., F. A. Kish and J. E. Baker, *Appl. Phys. Lett.* **50**, 998 (1987).
4. Nguyen Hong Ky, J. D. Ganière, F. K. Reinhart and B. Blanchard, *J. Appl. Phys.* **79**, 4009 (1996).
5. Nguyen Hong Ky, *Mater. Sci. Forum* **196-201**, 1643 (1995).
6. Nguyen Hong Ky, J. D. Ganière, M. Gailhanou, B. Blanchard, L. Pavesi, G. Burri, D. Araújo, and F. K. Reinhart, *J. Appl. Phys.* **73**, 3769 (1993).
7. Nguyen Hong Ky, L. Pavesi, D. Araújo, J. D. Ganière and F. K. Reinhart, *J. Appl. Phys.* **69**, 7585 (1991).
8. Nguyen Hong Ky, J. D. Ganière, F. K. Reinhart, B. Blanchard and J. C. Pfister, *J. Appl. Phys.* **74**, 5493 (1993).
9. Nguyen Hong Ky, in "IEEE Proc. Semiconducting and Insulating Mater. Conf., IEEE SIMC-9", ed. C. Fontaine (Piscataway: IEEE) pp.55-58 (1996).
10. Nguyen Hong Ky, and F. K. Reinhart, to be published.
11. Nguyen Hong Ky, J. D. Ganière, M. Gailhanou, F. Morier-Genoud, D. Martin, and F. K. Reinhart, *Phys. Rev. B* **46**, 6947 (1992).
12. L. Pavesi, Nguyen Hong Ky, J. D. Ganière, F. K. Reinhart, N. Baba-Ali, I. Harrison, B. Tuck, and M. Henini, *J. Appl. Phys.* **71**, 2225 (1992).
13. T. Y. Tan, U. Gösele and S. Yu, *Crit. Rev. Solid State Mater. Sci.* **17**, 47 (1991).

## AUTHOR INDEX

- Abdullin, K.A. .... 541, 1777  
 Abe, K. .... 185  
 Åberg, D. .... 367, 385  
 Abernathy, C.R. .... 1293  
 Ackermann, H. .... 763, 1389, 1395  
 Adamowski, J. .... 1287, 1707  
 Afanasjev, M.M. .... 559  
 Afanas'ev, V.V. .... 1713  
 Ahn, S.H. .... 429, 1485  
 Ahoujja, M. .... 1161  
 Aichele, N. .... 47  
 Avalos, V. .... 581  
 Al-Kotb, M.S. .... 1461  
 Alex, V. .... 241, 1009  
 Alt, H.Ch. .... 867  
 Altukhov, I.V. .... 71, 91, 1613  
 Alvarez, A. .... 825  
 Alves, E. .... 473  
 Ambacher, O. .... 1755  
 Amekura, H. .... 599  
 Ammerlaan, C.A.J. .... 373, 379, 491,  
     1497, 1761  
 Ammerlahn, D. .... 911  
 Andreev, B.A. .... 1515  
 Anthony, T.R. .... 757  
 Arai, N. .... 547, 535  
 Arlery, M. .... 1149  
 Armelles, G. .... 1689  
 Arnold, A. .... 703  
 Artacho, E. .... 41  
 Assali, L.V.C. .... 429, 893  
 Ashwin, M.J. .... 1, 379, 879, 283  
 Auret, F.D. .... 115, 133  
 Augustine, G. .... 691  
 Auret, F.D. .... 565, 1021, 1045  
 Avella, M. .... 825  
 Averbach, R.S. .... 1253  
 Bach, J.C. .... 97  
 Bagraev, N.T. .... 1607, 1683, 1833  
 Baierle, B.J. .... 11  
 Balakrishna, V. .... 691  
 Balogh, A.G. .... 733, 1419  
 Baran, M. .... 1449  
 Baranov, P.G. .... 697, 703, 1539, 1167  
 Baranowski, J.M. .... 1125  
 Baratta, G.A. .... 611  
 Barski, A. .... 1149  
 Barz, A. .... 109  
 Baur, J. .... 697  
 Baumann, H. .... 733, 1419  
 Bayerl, M.W. .... 963, 1309  
 Beaumont, B. .... 1155  
 Bechstedt, F. .... 653  
 Becla, P. .... 1247  
 Bécourt, N. .... 1211  
 Bednarek, S 1287  
 Beechinor, J.T. .... 1045  
 Beeman, J.W. .... 77  
 Bekman, H.P.Th. .... 1497  
 Bender, H. .... 341  
 Benz, K.W. .... 109  
 Ber, B.Ya. .... 1701  
 Bergman, J.P. .... 1125, 1149, 1665, 1677  
 Bethge, K. .... 867  
 Bharuth-Ram, K. .... 751, 763  
 Bi, W.G. .... 805, 813  
 Bieg, B. .... 1413  
 Bimberg, D. .... 831, 843, 911  
 Binns, M.J. .... 283, 379  
 Bischof, G. .... 1461  
 Bolay, H. .... 1093  
 Bonapasta, A.A. .... 855  
 Bollmann, J. .... 53, 473  
 Borgmann, Chr. .... 417



- 
- |                       |   |                     |                              |
|-----------------------|---|---------------------|------------------------------|
| Boudreau, M. ....     | 709                                       | Chadi, D.J. ....    | 1321                         |
| Bourgoin, J.C. ....   | 629, 929, 993, 997                        | Chaikina, E.I. .... | 1607                         |
| Bozdog, C. ....       | 1087                                      | Chan, J.K. ....     | 1719                         |
| Brandt, M.S. ....     | 963, 1309                                 | Chang, K.J. ....    | 1137                         |
| Bracht, H. ....       | 417, 1783                                 | Chaves, A.S. ....   | 1315                         |
| Bräunig, D. ....      | 53  | Chen, T. ....       | 1485                         |
| Brémond, G. ....      | 165                                       | Chen, W.M. ....     | 139, 685, 805                |
| Bresler, M.S. ....    | 1583, 1595, 1701                          | Chen, Y. ....       | 1659                         |
| Breuer, S.J. ....     | 35, 781                                   | Chirkova, E.G. .... | 71                           |
| Briddon, P.R. ....    | 35, 265, 277, 295, 391,<br>775, 781, 1203 | Choi, I.-H. ....    | 1455                         |
| Briones, F. ....      | 1689                                      | Chow, K.H. ....     | 179, 849                     |
| Broser, I. ....       | 1197                                      | Choyke, W.J. ....   | 1087                         |
| Brown, G.J. ....      | 1229                                      | Chung-rong Fu ....  | 1437                         |
| Brucato, J.R. ....    | 611                                       | Citrin, P.H. ....   | 879                          |
| Brunner, S. ....      | 1419                                      | Claeys, C. ....     | 121, 405, 1217               |
| Budde, M. ....        | 35, 391                                   | Clauws, P. ....     | 103, 405                     |
| Bugajski, M. ....     | 1665                                      | Clerjaud, B. ....   | 911                          |
| Burchard, A. ....     | 945, 1099, 1223, 1347                     | Coeck, M. ....      | 623                          |
| Burkard, M. ....      | 1093                                      | Compagnini, G. .... | 611                          |
| Burr, T.A. ....       | 1719                                      | Connell, S.H. ....  | 751                          |
| Butler, J.E. ....     | 751                                       | Coppinger, F. ....  | 1551                         |
| Buyanova, I.A. ....   | 139, 805                                  | Corbel, C. ....     | 879, 1033                    |
| Byberg, J.R. ....     | 515                                       | Corlatan, D. ....   | 1191                         |
| Caldas, M.J. ....     | 11  | Correia, J.G. ....  | 1223, 1503                   |
| Calvo-Barrio, L. .... | 727                                       | Cornet, A. ....     | 1211, 1689                   |
| Camporese, A. ....    | 1807                                      | Côte, D. ....       | 911                          |
| Canimoglu, A. ....    | 837                                       | Cox, S.F.J. ....    | 179, 849                     |
| Cantin, J.P. ....     | 1533                                      | Crean, G.M. ....    | 1045                         |
| Capizzi, M. ....      | 855                                       | Cunningham, J. .... | 787                          |
| Cardona, M. ....      | 757                                       | Dannefaer, S. ....  | 1725                         |
| Cardoso, S. ....      | 593                                       | Dadgar, A. ....     | 831, 843                     |
| Carlos, W.E. ....     | 1105                                      | Dalmer, M. ....     | 899                          |
| Carmo, M.C. ....      | 473                                       | Daly, S.E. ....     | 521                          |
| Carnera, A. ....      | 1807                                      | Damonte, L.C. ....  | 1235                         |
| Cavenett, B.C. ....   | 1383, 1671                                | Dannefaer, S. ....  | 581, 721                     |
| Caymax, M. ....       | 121                                       | Davidson, B.R. .... | 1                            |
|                       |   | Davies, G. ...      | 289, 411, 485, 571, 635, 769 |

- 
- |                              |                                    |                          |                 |
|------------------------------|------------------------------------|--------------------------|-----------------|
| Davis, E.A. ....             | 849                                | Erdtmann, M. ....        | 1637, 1643      |
| Davydov, V.Yu. ....          | 1143                               | Ehrhart, P. ....         | 1377            |
| Deák, P. ....                | 739                                | Esfandyari, J. ....      | 341             |
| Deenapanray, P.N.K. ....     | 565, 1045                          | Estle, T.L. ....         | 179, 849        |
| Dedek, U. ....               | 575                                | Estreicher, S.K. ....    | 171, 509, 605   |
| Degroote, S. ....            | 437                                | Evans-Freeman, J.H. .... | 1551            |
| Deicher, M. ....             | 473, 521, 945,<br>1099, 1223, 1347 | Everitt, L.R. ....       | 1577            |
| De Gryse, O. ....            | 405                                | Evwaraye, A.O. ....      | 691             |
| Deenapanray, P.N.K. ....     | 115, 133                           |                          |                 |
| Desnica, U.V. ....           | 1057, 1347                         | Faleev, N.N. ....        | 1625            |
| Desnica-Frankovic, I.D. .... | 1057, 1347                         | Falster, R. ....         | 283, 347, 379   |
| Dietrich, M. ....            | 1589                               | Fanciulli, M. ....       | 437             |
| Dirksen, R. ....             | 373                                | Farmer, J.W. ....        | 77              |
| Dirnstorfer, I. ....         | 1467                               | Fazzio, A. ....          | 975, 1275       |
| Dmochowski, J. ....          | 1443                               | Fedders, P.A. ....       | 171, 509        |
| Dmowski, L. ....             | 813                                | Fedoseyev, V.N. ....     | 437             |
| Dobaczewski, L. ....         | 337, 1241, 1761                    | Ferrer, J.C. ....        | 1211, 1689      |
| Dold, P. ....                | 109                                | Ferrero, J.L. ....       | 819, 1235       |
| Dombrowski, K.F. ....        | 109                                | Fijalkowski, P. ....     | 1413            |
| Domke, C. ....               | 885                                | Filz, T. ....            | 1341            |
| Don, D.T. ....               | 491                                | Flink, C. ....           | 449, 461, 467   |
| Dornberger, E. ....          | 341                                | Fogarassy, E. ....       | 47              |
| Dörnen, A. ....              | 697, 1093, 1401                    | Forkel-Wirth, D. ....    | 945, 1099, 1223 |
| Doyle, B.P. ....             | 751                                | Fornari, R. ....         | 825             |
| Dravin, V.A. ....            | 917                                | Fraboni, B. ....         | 1807            |
| Duan, X. ....                | 1485                               | França, E.J. ....        | 893             |
|                              |                                    | Franz, M. ....           | 109             |
| Ebert, Ph. ....              | 885                                | Frauenheim, Th. ....     | 739, 1203       |
| Efeoglu, H. ....             | 1551                               | Frehill, C.A. ....       | 521             |
| Egorov, A.Yu. ....           | 1619                               | Freitas, P.P. ....       | 1259            |
| Ehrhart, P. ....             | 503, 575, 1253                     | Frey, T. ....            | 1743            |
| Eisenmenger, W. ....         | 399                                | Friessnegg, T. ....      | 709, 721,       |
| Elsner, J. ....              | 1203                               | Frigeri, C. ....         | 1807            |
| Emel'yanov, A.M. ....        | 1527                               | Fukata, N. ....          | 203, 211, 235   |
| Emel'yov, E.M. ....          | 1521                               | Füllgrabe, M. ....       | 763, 1395       |
| Emtsev, V.V. ....            | 575, 1143, 1515                    | Fujii, A. ....           | 1217            |
| Era, K. ....                 | 1265                               | Fujimura, S. ....        | 203, 211, 235   |
|                              |                                    | Furthmüller, J. ....     | 653             |

- |   |                                 |   |                     |
|---|---------------------------------|---|---------------------|
| Gaber, A. ....                          | 1253                            | Grzegory, I. ....                           | 1125, 1149          |
| Gali, A. ....                           | 739                             | Gutierrez, R. ....                          | 739                 |
| Gall, S. ....                           | 53                              | Gusev, O.B. ....                            | 1583, 1595, 1701    |
| Gaspar, C. ....                         | 1155                            |   |                     |
| Gasparotto, A. ....                     | 1807                            | <b>Haase, D.</b> ....                       | 1093                |
| Gebauer, J. ....                        | 885, 905, 951                   | Hai, P.N. ....                              | 491                 |
| Gebhardt, W. ....                       | 1743, 1755                      | Hajdusianek, A. ....                        | 1413                |
| Gehlhoff, W. ....                       | 423, 1607, 1683                 | Halkias, G. ....                            | 1211                |
| Georgakilas, A. ....                    | 1211                            | Hall, G. ....                               | 671                 |
| Gerchikov, L.G. ....                    | 1625                            | Hallberg, T. ....                           | 361, 367, 385       |
| Gerrits, A.M. ....                      | 1241                            | Haller, E.E. . 47, 41, 77, 1099, 1247, 1749 |                     |
| Giannozzi, P. ....                      | 855                             | Hallin, C. ....                             | 685                 |
| Gibart, P. ....                         | 1155                            | Hamann, J. ....                             | 1341                |
| Gibbs, H.M. ....                        | 1583, 1625, 1701                | Hansen, J.L. ....                           | 97, 271             |
| Gill, K. ....                           | 671                             | Hansen, O.P. ....                           | 1653                |
| Gippius, A.A. ....                      | 917, 1833                       | Haneda, H. ....                             | 211                 |
| Gislason, H.P. ....                     | 1003, 1383, 1671,<br>1813, 1827 | Hansson, G.V. ....                          | 139                 |
| Göbel, C. ....                          | 861, 1173, 1179                 | Härle, V. ....                              | 1087                |
| Godlewski, M. ....                      | 1149, 1665, 1677                | Hartnett, S.J. ....                         | 1027                |
| Goldys, E.M. ....                       | 1149                            | Hartung, J. ....                            | 1509                |
| Gomes, H. ....                          | 793                             | Hässlein, H. ....                           | 53, 59              |
| Gommel, U. ....                         | 47                              | Hastings, J.L. ....                         | 509                 |
| Goncharuk, I.N. ....                    | 1143                            | Hauksson, I.S. ....                         | 1383                |
| Gonzalez, M.A. ....                     | 825                             | Hauksson, I.J. ....                         | 1671                |
| González-Varona, O. ....                | 727                             | Hautojärvi, P. ....                         | 879                 |
| Goodman, S.A. 115, 133, 565, 1021, 1045 |                                 | Hayashi, K. ....                            | 745                 |
| Gorelkinskii, Yu.V. ....                | 541, 1777                       | Hayama, K. ....                             | 121                 |
| Gorostiza, P. ....                      | 1211                            | Haynes, T.E. ....                           | 1057                |
| Göser, R. ....                          | 1069                            | Heemeier, M. ....                           | 763, 1395           |
| Goss, J. ....                           | 35, 295, 775, 781               | Heggie, M.I. ....                           | 1203                |
| Gower, J.E. ....                        | 289, 571                        | Heiser, T. ....                             | 461, 467            |
| Gracin, D. ....                         | 1057                            | Hengehold, R.L. ....                        | 1577                |
| Gräf, D. ....                           | 341                             | Henriques, R.T. ....                        | 331                 |
| Gregorkiewicz, T. ....                  | 373, 379, 491,<br>1761, 1497    | Henry, M.O. ....                            | 473, 521            |
| Gronemeyer, S. ....                     | 1589                            | Hernández, M.A. ....                        | 819                 |
| Grosche, E.G. ....                      | 1                               | Hey, R. ....                                | 1737                |
|   |                                 | Hieslmair, H. ....                          | 449, 461, 467, 1795 |
|   |                                 | Hirata, M. ....                             | 547, 553            |

- 
- |                            |                                    |                            |  |
|----------------------------|------------------------------------|----------------------------|--|
| Hitti, B. ....             | 179, 849                           | Janzén, E. ....            | 685  |
| Hobgood, H.McD. ....       | 691                                | Jeong, S. ....             | 951  |
| Hofmann, D.M. ....         | 1309, 1467                         | Johannesen, P. ....        | 515  |
| Hoffmann, L. ....          | 97, 1131, 1173, 1197               | Johnson, B.K. ....         | 347  |
| Hofsäss, H. ....           | 899                                | Jones, B.K. ....           | 933, 1039  |
| Hofstaetter, A. ....       | 1473                               | Jones, R. ....             | 35, 97, 265, 277, 295, 391, 775, 781, 1063, 1203 |
| Hogg, R.A. ....            | 1565                               | Jones, K.M. ....           | 191  |
| Hommel, D. ....            | 1395, 1665                         | Jyobe, F. ....             | 313  |
| Honda, T. ....             | 127                                | Jimenez, J. ....           | 825  |
| Hourahine, B. ....         | 277, 391                           |                            |  |
| Hsu, L. ....               | 813, 1749                          | Kaczmarczyk, G. ....       | 1173   |
| Hübner, C.G. ....          | 981                                | Kaczor, P. ....            | 1241, 1761                                       |
|                            |                                    | Kagan, M.S. ....           | 65, 71, 91, 1613                                 |
| Ibuka, S. ....             | 1731                               | Kageshima, H. ....         | 873  |
| Ichihashi, T. ....         | 553                                | Kaiblinger-Grujin, G. .... | 939  |
| Iijima, S. ....            | 553                                | Kaiser, S. ....            | 1755   |
| Ikarashi, T. ....          | 587                                | Kalinina, E.V. ....        | 1143   |
| Ikoma, T. ....             | 703                                | Kalinski, Z. ....          | 1241   |
| Ilyin, I.V. ....           | 1167, 1539                         | Kamińska, A. ....          | 1149   |
| Imaizumi, M. ....          | 1795                               | Kamiura, Y. ....           | 247, 313   |
| Iqbal, M.A. ....           | 933                                | Kamp, M. ....              | 1113   |
| Iqbal, M.Z. ....           | 485, 831, 843                      | Kanda, H. ....             | 769, 1265  |
| Ishibashi, A. ....         | 1329                               | Kaniewska, M. ....         | 319, 325   |
| Ishiga, N. ....            | 247                                | Kaniewski, J. ....         | 319, 325   |
| Ishioka, K. ....           | 203, 211, 235                      | Karatsu, T. ....           | 659  |
| Ishiyama, T. ....          | 1559                               | Karczewski, G. ....        | 1353, 1665, 1677                                 |
| ISOLDE Collaboration ..... | 437, 899, 945, 1099, 1223, 1503    | Karg, F. ....              | 1467   |
| Istratov, A.A. ....        | 449, 467, 1359                     | Kaschner, A. ....          | 1197   |
| Itoh, K.M. ....            | 47, 41, 77                         | Katajama, E. ....          | 1559   |
| Ittermann, B. ....         | 763, 1389, 1395                    | Katayama-Yoshida, H. ....  | 799, 1185  |
| Ivanda, M. ....            | 1057                               | Kaufmann, B. ....          | 697, 1401  |
| Ivanov, V.Yu. ....         | 1149                               | Kawasuso, A. ....          | 127  |
|                            |                                    | Kazakov, I.P. ....         | 917  |
| Jackson, S. ....           | 1545                               | Kelton, K.F. ....          | 347  |
| Janotti, A. ....           | 975                                | Kerr, D. ....              | 1725   |
| Jantsch, W. ....           | 1353, 1443, 1509, 1533, 1545, 1695 | Kervlishvili, P.D. ....    | 575  |
|                            |                                    | Khan, A. ....              | 831, 843   |

- 
- |                       |                        |                            |                                |
|-----------------------|------------------------|----------------------------|--------------------------------|
| Khirouni, K. ....     | 929                    | Koynov, S. ....            | 593                            |
| Khurunenko, L.I. .... | 41, 47, 1767, 1773     | Kozanecki, A. ....         | 1545                           |
| Khitrova, G. ....     | 1583, 1595, 1625, 1701 | Koziarska-Glinka, B. ....  | 1407, 1431                     |
| Kiefl, R.F. ....      | 849                    | Kozlovskii, V.V. ....      | 1143                           |
| Kiflawi, I. ....      | 769                    | Krambrock, K. ....         | 957, 1015, 1033,<br>1303, 1315 |
| Kikuchi, J. ....      | 203, 211, 235          | Krause, M. ....            | 911                            |
| Kim, K.S. ....        | 1229, 1637, 1643       | Krause-Rehberg, R. ....    | 885, 905, 951, 981             |
| Kim, Y. ....          | 1191                   | Kreissl, J. ....           | 1069, 1401                     |
| Kimerling, L.C. ....  | 429, 1485, 1719        | Kringhøj, P. ....          | 145                            |
| Kimoto, A. ....       | 185                    | Krispin, P. ....           | 1737                           |
| Kinoshita, T. ....    | 77                     | Kroll, F. ....             | 763, 1389, 1395                |
| Kishimoto, N. ....    | 599                    | Krüger, J. ....            | 467, 981, 1191                 |
| Kisielowski, C. ....  | 1191                   | Krummel, C. ....           | 1473                           |
| Kissinger, G. ....    | 341                    | Kubo, T. ....              | 1571                           |
| Kitajima, M. ....     | 203, 211, 235          | Kudou, T. ....             | 1217                           |
| Kitano, T. ....       | 587                    | Kudryavstev, Yu.A. ....    | 1527                           |
| Kleverman, M. ....    | 385, 455, 479, 497     | Kung, P. ....              | 1081, 1161, 1229               |
| Klockenbrink, R. .... | 1191                   | Kuno, T. ....              | 553                            |
| Klyachkin, L.E. ....  | 1607, 1683, 1833       | Kunzer, M. ....            | 697                            |
| Knopf, M.H.A. ....    | 473                    | Ky, N.H. ....              | 1631, 1839                     |
| Kohl, D. ....         | 1473                   |                            |                                |
| Köhne, L. ....        | 831                    | Laermans, C. ....          | 623                            |
| Köhne, L. ....        | 911                    | Laiho, R. ....             | 559                            |
| Kohn, H. ....         | 547                    | Laine, T. ....             | 879                            |
| Kohyama, M. ....      | 547                    | Lambert, U. ....           | 341                            |
| Konnov, V.M. ....     | 917                    | Landman, J.I. ....         | 923                            |
| Kono, K. ....         | 599                    | Landsberg, E.G. ....       | 65                             |
| Köpf, Ch. ....        | 939                    | Landwehr, G. ....          | 1395                           |
| Kornitzer, K. ....    | 1113                   | Lang, M. ....              | 423                            |
| Korolev, K.A. ....    | 71, 91, 1613           | Langer, J.M. ....          | 1431, 1449                     |
| Korona, K.P. ....     | 1125                   | Langerak, C.J.G.M. ....    | 1497                           |
| Koschnick, F.K. ....  | 1021, 1303, 1315       | Langouche, G. ....         | 437, 1503                      |
| Kosher, G. ....       | 1533                   | Lanzerstorfer, S. ....     | 1509, 1545                     |
| Kosina, H. ....       | 939                    | Larikova, T.V. ....        | 917                            |
| Kossut, J. ....       | 1665, 1677             | Larsen, A. Nylandsted .... | 83, 97, 145                    |
| Kostial, H. ....      | 1737                   | Laßmann, K. ....           | 47, 399, 417                   |
| Koto, K. ....         | 553                    | Lauer, St. ....            | 1341                           |
| Kovsh, A.R. ....      | 1619                   |                            |                                |

- 
- Lausmann, M. .... 905  
 Leary, P. .... 35, 97, 265,  
 Lebedev, A.A. .... 715  
 Ledentsov, N.N. .... 1619  
 Lee, Sun-Ghil .... 1137  
 Leib, U. .... 1473  
 Leigh, R.S. .... 1  
 Leipner, H.S. .... 981  
 Leitão, J.P. .... 473  
 Leitch, A.W.R. .... 241  
 Lemke, H. .... 301, 307  
 Leosson, K. .... 1813, 1827  
 Leroux, M. .... 1155  
 Lichti, R.L. .... 179, 849  
 Lieb, K.P. .... 763  
 Lightowlers, E.C. .... 259, 283, 289, 379,  
 411, 485, 521, 571, 617, 635  
 Liliental-Weber, Z. .... 1659  
 Linde, M. .... 1087  
 Lindmark, E.K. .... 1583, 1701  
 Lindström, J.L. ... 361, 367, 385, 391, 685  
 Lippold, G. .... 905  
 Litvinchuk, A.P. .... 1589  
 Loa, I. .... 1131, 1197, 1589  
 Loyko, N.N. .... 917  
 Lusakowski, J. .... 813  
 Luysberg, M. .... 951  
  
 Mabuchi, T. .... 547  
 Maçarico, F. .... 593  
 Machi, I.Z. .... 751  
 MacEvoy, B. .... 671  
 Maclear, R.D. .... 751  
 Madeiros, S.M. .... 957  
 Maeda, K. .... 313  
 Magerle, R. .... 473, 521, 945, 1099,  
 1223, 1347  
 Mai, F. .... 763, 1389, 1395  
  
 Maier, F. .... 47  
 Mainwood, A. .... 253, 787  
 Makovijchuk, M.I. .... 1527  
 Malik, A. .... 1425  
 Malyarenko, A.M. .... 1607, 1683, 1833  
 Mamor, M. .... 115, 133  
 Marbach, K. .... 763, 1389, 1395  
 Margaryan, M.A. .... 575  
 Mari, A. .... 1813  
 Marí, B. .... 819  
 Markevich, V.P. .... 217, 361, 367  
 Markov, I.I. .... 1607  
 Markvart, T. .... 665  
 Marques, J.G. .... 1503  
 Martins, R. .... 1425  
 Mascher, P. .... 709, 733, 1335, 1419  
 Mason, P.W. .... 1087  
 Masterov, V.F. ... 1583, 1601, 1625, 1701  
 Masterson, H.J. .... 1045  
 Matsuoka, M. .... 1491  
 Matsumoto, T. .... 703  
 Mattila, T. .... 1119  
 Maude, D.K. .... 1551  
 Maxim, P. .... 1131  
 Maximov, M.V. .... 1619  
 Mayer, M. .... 1113  
 McCluskey, M.D. .... 1247  
 McDonagh, C.J. .... 473  
 McGlynn, E. .... 521  
 McGuigan, K.G. .... 521  
 McHugo, S.A. .... 449, 461, 1795  
 McQuaid, S.A. .... 283, 347  
 Meier, P. .... 763, 1395  
 Mesli, A. .... 145  
 Metzner, H. .... 763  
 Meyer, B.K. .... 1467, 1473  
 Meyer, F. .... 165  
 Meyer, W.E. .... 115, 133, 565, 1045

- 
- |                     |                             |                        |   |
|---------------------|-----------------------------|------------------------|---|
| Michel, J. ....     | 429, 1485, 1719             | Navarro, F.J. ....     | 819, 1235   |
| Michelakis, K. .... | 1211                        | Nelson, S.F. ....      | 1485  |
| Mikucki, J. ....    | 813                         | Neugebauer, J. ....    | 19  |
| Miotkowski, I. .... | 1407                        | Newman, R.C. ....      | 1, 283, 379, 879                                    |
| Miró, J. ....       | 739                         | Ni, W.X. ....          | 139   |
| Mishin, V.I. ....   | 437                         | Nielsen, B. Bech ....  | 35, 97, 271, 391, 515                               |
| Mitchel, W.C. ....  | 691, 1081, 1161, 1229       | Nielsen, K. Bonde .... | 271, 337, 391, 515                                  |
| Mizuta, M. ....     | 1309                        | Nieminen, R.M. ....    | 969, 1119   |
| Mochizuki, Y. ....  | 1309                        | Niklas, J.R. ....      | 987   |
| Mohamed, El-M. .... | 647                         | Nikolaev, Yu.A. ....   | 1527  |
| Mokhov, E.N. ....   | 703, 1167, 1539             | Nilen, R.W.N. ....     | 751   |
| Molinari, E. ....   | 11                          | Nishimatsu, T. ....    | 799   |
| Monemar, B. ....    | 139, 1125, 1149, 1665, 1677 | Norga, G.J. ....       | 429, 1719   |
| Monteiro, T. ....   | 1155                        | Öberg, S. ....         | 35, 97, 265, 277, 295, 391,<br>775, 781, 1063, 1203 |
| Mooney, P.M. ....   | 151                         |                        |   |
| Morante, J.R. ....  | 727, 1211, 1689             | Odnoblyudov, M.A. .... | 71  |
| Morgado, E. ....    | 331, 1259                   | Ofuchi, H. ....        | 1571  |
| Morgan, C.G. ....   | 923                         | Ohashi, N. ....        | 1371  |
| Morooka, M. ....    | 1789                        | Ohkura, H. ....        | 1299  |
| Mota, R. ....       | 975, 1275                   | Ohmura, K. ....        | 1299  |
| Mukashev, B.N. .... | 223, 541, 1777              | Ohmura, Y. ....        | 185   |
| Mundbrod, M. ....   | 1113                        | Ohno, T. ....          | 1821  |
| Muñoz, V. ....      | 1235                        | Ohtaka, M. ....        | 185   |
| Murakami, K. ....   | 203, 211, 235, 1559         | Ohyama, H. ....        | 121, 1217   |
| Murin, L.I. ....    | 217, 361, 367               | Ohyama, S. ....        | 247   |
| Murtagh, M. ....    | 1045                        | Okada, N. ....         | 1299  |
| Müssig, H. ....     | 47                          | Okada, S. ....         | 127   |
| Muto, J. ....       | 77                          | Okushi, H. ....        | 745   |
| Myburg, G. ....     | 115, 565, 1045              | Olajos, J. ....        | 479   |
| Myers, S.M. ....    | 461                         | Oldekop, E. ....       | 1389  |
|                     |                             | Ono, A. ....           | 1265  |
| Nagle, J. ....      | 929                         | Orita, N. ....         | 799   |
| Nakagawa, S.T. .... | 641                         | Orlov, D.V. ....       | 91, 1613  |
| Nakamura, K.G. .... | 203, 211, 235               | Ornoch, L. ....        | 319, 325  |
| Nakanishi, H. ....  | 1051                        | Oshiyama, A. ....      | 1479  |
| Nakano, K. ....     | 1329                        | Ossicini, S. ....      | 11  |
| Nakashima, H. ....  | 429                         | Ostapenko, S. ....     | 197   |
| Näser, A. ....      | 423, 1683                   |                        |   |

- 
- |                          |                       |                         |                              |
|--------------------------|-----------------------|-------------------------|------------------------------|
| Ostheimer, V. ....       | 1341                  | Pomozov, Yu.V. ....     | 1773                         |
| Oullette, E. ....        | 1485                  | Ponder, M. ....         | 1407                         |
| Overhof, H. ....         | 677                   | Poortmans, J. ....      | 121                          |
| Ozhogin, V.I. ....       | 77                    | Porowski, S. ....       | 1125, 1149                   |
|                          |                       | Portal, J.-C. ....      | 1551                         |
| Pakula, K. ....          | 1125                  | Pöykkö, S. ....         | 969                          |
| Palm, J. ....            | 1485                  | Pozina, G. ....         | 139                          |
| Palmer, D.W. ....        | 837, 1027             | Prasad, A. ....         | 951                          |
| Panknin, D. ....         | 727                   | Pressel, K. ....        | 109, 1131                    |
| Papoulias, P. ....       | 923                   | Preis, H. ....          | 1755, 1743                   |
| Pajot, B. ....           | 41, 47                | Prineas, J.P. ....      | 1583, 1701                   |
| Parshin, E.O. ....       | 1527                  | Priolo, F. ....         | 1807                         |
| Partyka, P. ....         | 1253                  | Prior, K.A. ....        | 1383, 1671                   |
| Parveen, S. ....         | 831                   | Pritchard, R.E. ....    | 283, 379                     |
| Peaker, A.R. ....        | 1551                  | Prospero, A. ....       | 1099, 1223                   |
| Pearton, S.J. ....       | 1293                  | Provoost, R. ....       | 623                          |
| Peiró, F. ....           | 1211, 1689            | Przybylinska, H. ....   | 1087                         |
| Peka, P. ....            | 1401                  | Puff, W. ....           | 709, 733, 1419, 1461         |
| Pelzmann, A. ....        | 1113                  | Puska, M.J. ....        | 969                          |
| Pensl, G. ....           | 423                   |                         |                              |
| Pereira, E. ....         | 793, 1155             | Qurashi, U.S. ....      | 831                          |
| Pereira, L. ....         | 793                   | Qurashi, U.S. ....      | 843                          |
| Perel, V.I. ....         | 1281                  |                         |                              |
| Perenboom, J. ....       | 1241                  | Rahhal-Orabi, N. ....   | 923                          |
| Pérez-Rodríguez, A. .... | 727                   | Rauluszkiewicz, J. .... | 1431                         |
| Peters, D. ....          | 763, 1395             | Rasmussen, F. Berg .... | 373                          |
| Petersen, G.A. ....      | 461                   | Razeghi, M. ....        | 1081, 1161, 1229, 1637, 1643 |
| Petravic, M. ....        | 899                   | Reddy, A.J. ....        | 1719                         |
| Petzke, K. ....          | 861, 1179             | Reedy, R. ....          | 191                          |
| Pfeiffer, L.N. ....      | 879                   | Reginski, K. ....       | 1665                         |
| Pinheiro, M.V.B. ..      | 957, 1015, 1303, 1315 | Reinacher, N.M. ....    | 963                          |
| Piquini, P. ....         | 975, 1275             | Resende, A. ....        | 295                          |
| Placzek-Popko, E. ....   | 1413, 1653            | Reisinger, T. ....      | 1743                         |
| Platero, M.T. ....       | 429                   | Ridgway, M.C. ....      | 899                          |
| Ploog, K.H. ....         | 1737                  | Risse, M. ....          | 899                          |
| Pohl, U.W. ....          | 1401                  | Robbie, D.A. ....       | 1                            |
| Poloskin, D.S. ....      | 575, 1143, 1515       | Roberts, N. ....        | 1365                         |
| Poluektov, O.G. ....     | 703                   | Rocha, R. ....          | 1259                         |



- 
- |                               |                       |                         |                     |
|-------------------------------|-----------------------|-------------------------|---------------------|
| Rodriguez, F. ....            | 411, 635              | Schwarz, R. ....        | 593, 1259           |
| Rodriguez Schachtrup, A. .... | 1783                  | Schweizer, H. ....      | 1093                |
| Rossetto, G. ....             | 1807                  | Sealy, B.J. ....        | 1545                |
| Rossner, U. ....              | 1149                  | Seghier, D. ....        | 1383, 1671          |
| Rouvire, J.L. ....            | 1149                  | Segura, A. ....         | 1235                |
| Rubin, M. ....                | 1191                  | Sekiguchi, T. ....      | 319, 325, 745, 1371 |
| Rücker, H. ....               | 109                   | Selberherr, S. ....     | 939                 |
| Ruf, T. ....                  | 757                   | Sellschop, J.P.F. ....  | 751, 763            |
| Ruminov, S. ....              | 1659                  | Serpentini, M. ....     | 165                 |
| Rutter, P. ....               | 1551                  | Seghier, D. ....        | 1003                |
|                               |                       | Seitz, R. ....          | 1155                |
| Saarinen, K. ....             | 879, 1813             | Sekiguchi, T. ....      | 217                 |
| Sachse, J-U. ....             | 301, 307              | Selber, H.R. ....       | 1401                |
| Safanov, A.N. ....            | 259, 289, 521, 617    | Serenkov, I.T. ....     | 1527                |
| Sakharov, A.V. ....           | 1143                  | Shakhovtsov, V.I. ....  | 47, 1767, 1773      |
| Sakharov, V.I. ....           | 1527                  | Shek, E.I. ....         | 1515, 1521          |
| Samic, H. ....                | 997                   | Shinozuka, Y. ....      | 647, 659            |
| Sangster, M.J.L. ....         | 1                     | Shtel'makh, K.F. ....   | 1527                |
| Santana, J.M. ....            | 1039                  | Shum, Kai ....          | 151                 |
| Sanz, L.F. ....               | 825                   | Shumov, V.V. ....       | 1767, 1773          |
| Sasaki, T. ....               | 1821                  | Sieck, A. ....          | 739                 |
| Sauer, R. ....                | 757, 1113             | Siegle, H. ....         | 1197                |
| Saxler, A. ....               | 1081, 1161, 1229      | Sielemann, R. ....      | 53, 59              |
| Scherz, U. ....               | 861, 1075, 1173, 1179 | Sieranski, K. ....      | 1413, 1653          |
| Schick, J.T. ....             | 923                   | Silkowski, E. ....      | 1577                |
| Scholes, A. ....              | 1551                  | Silverans, R.E. ....    | 623                 |
| Scholtz, F. ....              | 1087, 1093            | Simoen, E. ....         | 121, 1217           |
| Schmalz, K. ....              | 71, 91, 1613          | Simpson, P.J. ....      | 709                 |
| Schmid, M. ....               | 1093                  | Sinis, V.P. ....        | 91, 71, 1613        |
| Schmidt, J. ....              | 703                   | Sionger, K.E. ....      | 1551                |
| Shmidt, N.M. ....             | 1143                  | Sitch, P.K. ....        | 1203                |
| Schneider, J. ....            | 697                   | Sittas, G. ....         | 769                 |
| Schoisswohl, M. ....          | 1533                  | Skierbiszewski, C. .... | 1353, 1509          |
| Scholz, F. ....               | 1087                  | Skorupa, W. ....        | 727                 |
| Schrepel, C. ....             | 861, 1075, 1173, 1179 | Slack, G.A. ....        | 1087                |
| Schroth, H. ....              | 417                   | Sleight, W. ....        | 1365                |
| Schulz, H.J. ....             | 1401                  | Sloan, T. ....          | 1039                |
| Schwab, C. ....               | 179, 849              | Smirnov, A.N. ....      | 1143                |

- 
- |                       |                                     |                       |                              |
|-----------------------|-------------------------------------|-----------------------|------------------------------|
| Smith, A.L. ....      | 429                                 | Sunaga, H. ....       | 1217                         |
| Smith, S.R. ....      | 691                                 | Surma, M. ....        | 1677                         |
| Soares, J.C. ....     | 593                                 | Suski, T. ....        | 1149                         |
| Sobolev, M.M. ....    | 1619                                | Svavarsson, H. ....   | 1813                         |
| Sobolev, N.A. ....    | 715, 917, 1515, 1521,<br>1527, 1801 | Svensson, B.G. ....   | 367, 385                     |
| Sohn, H. ....         | 951                                 | Svrcek, V. ....       | 1695                         |
| Solomon, J. ....      | 1081, 1161                          | Symko, M.I. ....      | 191                          |
| Son, N.T. ....        | 685                                 | Szafran, B. ....      | 1707                         |
| Song, K.S. ....       | 1437                                | Szatkowski, J. ....   | 1413, 1653                   |
| Song, C.Y. ....       | 1293                                | Szymczak, R. ....     | 1449                         |
| Sopori, B.L. ....     | 191, 527                            |                       |                              |
| Sörman, E. ....       | 685                                 | Tabuchi, M. ....      | 1571                         |
| Spaeth, J.-M. ....    | 1015, 1021, 1033, 1303,<br>1315     | Taguchi, A. .         | 873, 1491, 1559, 1565, 1821  |
| Specht, P. ....       | 951                                 | Tajima, M. ....       | 1731                         |
| Springhoz, G. ....    | 1695                                | Takahashi, T. ....    | 443                          |
| Stallinga, P. ....    | 515                                 | Takahei, K. ....      | 1491, 1559, 1565, 1571       |
| Stavola, M. ....      | 1293                                | Takami, Y. ....       | 121, 1217                    |
| Stébé, B. ....        | 1707                                | Takarabe, K. ....     | 1299                         |
| Stellmacher, M. ....  | 929                                 | Takeda, S. ....       | 535, 547, 553                |
| Stepanova, T.R. ....  | 1625                                | Takeda, Y. ....       | 1571                         |
| Stepikhova, M. ....   | 1509, 1533                          | Tanaka, M. ....       | 547                          |
| Sternschulte, H. .... | 757                                 | Tanderup, K. ....     | 391                          |
| Stesmans, A. ....     | 1713                                | Tansley, T.L. ....    | 1149                         |
| Stöckmann, H.-J. .... | 763, 1389, 1395                     | Terada, Y. ....       | 1371                         |
| Stoneham, A.M. ....   | 27                                  | Terashima, K. ....    | 587                          |
| Stötzler, A. ....     | 1099, 1223                          | Terauchi, M. ....     | 547                          |
| Strazzulla, G. ....   | 611                                 | Tessaro, G. ....      | 1335                         |
| Stutzmann, M. ....    | 963, 1309                           | Thieß, H. ....        | 763, 1395                    |
| Suchocki, A. ....     | 1407, 1431, 1449                    | Thompson, A.C. ....   | 1795                         |
| Suda, Y. ....         | 1265                                | Thomsen, C. ....      | 1131, 1197, 1589             |
| Sudhir, G.S. ....     | 1191                                | Thonke, K. ....       | 757, 1069, 1075, 1113        |
| Suezawa, M. ....      | 127, 217, 229, 443                  | Thurian, P. ....      | 1131, 1173, 1179, 1197, 1589 |
| Sumino, K. ....       | 159, 319                            | Tidlund, P. ....      | 455, 479                     |
| Sunaga, H. ....       | 121                                 | Tohno, S. ....        | 1491                         |
| Sumino, K. ....       | 325                                 | Tokmoldin, S.Zh. .... | 223                          |
| Sun, J.J. ....        | 1259                                | Tomas, S.G. ....      | 91, 1613                     |
|                       |                                     | Torres, V.J.B. ....   | 1063, 1275                   |
|                       |                                     | Trauwaert, M.-A. .... | 341                          |

Tsimperidis, I. ....	1497	Washburn, J. ....	1659
Tu, C.W. ....	805, 813	Wasik, D. ....	813
Tucker, J.H. ....	283, 379	Watanabe, M. ....	587
Uftring, S.J. ....	1087	Watkins, G.D. ....	1087
Uhrmacher, M. ....	763	Wauters, D. ....	403
Ulrici, W. ....	1069, 1075	Weber, Ch. ....	1021
Urban, K. ....	885	Weber, D. ....	1341
Ushakov, V.V. ....	917	Weber, E.R. ....	449, 461, 467, 951, 1191, 1795
Usher, D. ....	787	Weber, J. ....	241, 301, 307, 605, 1009
Usikov, A.S. ....	1143	Wehner, M. ....	899
Ustinov, V.M. ....	1619	Welker, G. ....	1389
Utzmeier, T. ....	1689	Wenisch, H. ....	1395
Van Bavel, A.-M. ....	437	Weyer, G. ....	437
Van de Walle, C.G. ....	19	Wichert, Th. ....	1341
Vanhellemont, J. ....	121, 341, 405, 1217	Wiebe, C. ....	1725
Vantomme, A. ....	437, 1503	Wiedemann, B. ....	867
Vdovin, V.I. ....	1521	Wietzke, K.-H. ....	1015, 1303, 1315
Vianden, R. ....	899	Wilamowski, A. ....	1353
Vieira, M. ....	593	Wilamowski, Z. ....	1443, 1695
Vlasenko, L.S. ....	559	Wimbauer, T. ....	963, 1309
Vlasenko, M.P. ....	559	Wirbeleit, F. ....	987
von Ammon, W. ....	341	Wirth, H. ....	727
von Bardeleben, H.J. ....	1533	Wisniewski, P. ....	1353
Vydyanath, H.R. ....	1161	Wojtowicz, T. ....	1407, 1665, 1677
Vyvenko, O.F. ....	1359	Wolf, H. ....	1341
Wada, K. ....	1051	Wright, A.C. ....	1551
Wagner, Mt. ....	1467	Wurster, C. ....	399
Wahl, S. ....	757	Yamada-Kaneta, H. ....	355
Wahl, U. ....	1503	Yamamoto, T. ....	1185
Walker, D. ....	1081, 1161, 1229	Yamasaki, J. ....	535
Walukiewicz, W. ....	77, 813, 1247, 1749	Yamashita, Y. ....	247, 313
Wang, K.L. ....	91, 1613	Yamaura, M. ....	185
Wang, R.-P. ....	1365	Yarykin, N. ....	301
Warashina, M. ....	1731	Yassievich, I.N. ....	71, 91, 1281, 1583, 1595, 1613, 1701
Warren Jr., W.W. ....	1365	Ye, S.-R. ....	1045

- 
- Yeo, Y.K. .... 1577  
Yonenaga, I. .... 127, 159, 1783  
Yu, P.Y. .... 1455  
Yugova, T.G. .... 1521  
  
Zafar, N. .... 831, 843  
Zaidi, M.A. .... 629  
Zakharchenya, B.P. .... 1583, 1701  
Zakrewski, A.J. .... 1677  
Zakrzewski, A. .... 1241  
Zazoui, M. .... 629  
Zegrya, G.G. .... 1601  
Zeitz, W.-D. .... 1389, 1395  
Zeller, F. .... 47, 399  
Zevenbergen, I.S. .... 379  
Zhang, X. .... 1081, 1161, 1229  
Zhao, S. .... 429  
Zhdanova, N.G. .... 65  
Zheng, J.-F. .... 1293  
Zhou, J.A. .... 1293  
Zhu, M.-X. .... 485  
Zhukov, A.E. .... 1619  
Zillgen, H. .... 503, 575, 1253, 1377  
Zistl, Ch. .... 53  
Zistl, Ch. .... 59  
Zuo, H.Y. .... 1149  
Zywietz, A. .... 653

## KEYWORD INDEX

- $\alpha$ -DLTS ..... 1039
- $\beta$ -Ga<sub>2</sub>O<sub>3</sub> ..... 1473
- $\beta$ -NMR ..... 1389
- $\beta$ -NMR ..... 763
- $\gamma$ -ray spectroscopy ..... 1223
- A-centre ..... 1341
- ab initio theory ..... 19, 35, 97, 235, 265, 277, 295, 547, 653, 739, 775, 781, 799, 1119, 1821
- absorption ..... 109, 229, 355, 379, 391
- ac electric field ..... 1281
- acceptors ..... 185, 703, 1033, 1125
- acceptor states ..... 91, 1613
- admittance spectroscopy ..... 691, 929, 1383, 1671
- Ag ..... 301, 485, 491
- Ag halides ..... 1437
- Al<sub>2</sub>O<sub>3</sub> ..... 1755
- AlAs ..... 1253
- AlAs growth ..... 1737
- AlGaAs ..... 1293 - 1320, 1583, 1653
- ALMBE ..... 1689
- AlN ..... 1087, 1119, 1131, 1173, 1259
- alloy hardening ..... 159
- AlSb ..... 1247
- Al pair in Si ..... 1777
- amorphous
  - ~ Si ..... 235, 331, 599, 963
  - ~ SiC ..... 709
  - ~ structures ..... 1057
- anharmonicity ..... 861
- annealing .... 127, 211, 361, 727, 787, 837
- antisite ..... 805, 945, 951, 957, 969, 981, 993, 1813
- As ..... 1179
  - ~ antisite ..... 1021
  - ~ interstitial ..... 923
  - ~ vacancy ..... 893
- athermal diffusion ..... 541
- atomic force microscopy ..... 1211
- Au ..... 295, 479, 1783, 1789
- Auger
  - ~ excitation ..... 1601
  - ~ process ..... 1677
- B** ..... 185, 691, 757, 763, 1389
- Be ..... 417, 1653
- band-offset ..... 165
- bias-annealing ..... 1051
- binding energy ..... 361
- bistability ..... 1479
- bistable donors ..... 1431
- blue emission ..... 1155
- BN ..... 1265, 1275
- boson peak ..... 1057
- bound
  - ~ excitons ..... 635, 757, 1665
  - ~ polaron ..... 1241
- Br ..... 899
- Bragg reflector ..... 1637
- C** (diamond) ..... 653, 745 - 804, 1833
  - ~ films ..... 793
  - ~ (impurity) ..... 97, 253, 259, 247, 565, 617, 861, 1293
  - ~ interstitial ..... 265
- C<sub>As</sub> ..... 1293
- capacitance ..... 1383
- cathodoluminescence ..... 745, 757, 1265, 1359, 1631
- cation vacancies ..... 1119, 1347
- Cd ..... 53, 423, 521, 1099, 1223
- CdF<sub>2</sub> ..... 1431 - 1455
- CdMnTe ..... 1407, 1413
- CdMnTeSe ..... 1407
- CdS ..... 1347, 1359
- CdTe ..... 1321, 1335, 1353
- CdTe/CdMnTe ..... 1665
- chalcopyrites ..... 1455, 1461, 1467
- charge state ..... 873
- charged defects ..... 1259
- Cl ..... 1821
- Co ..... 1069
- co-doping ..... 799, 1185, 1571
- compensated semiconductors ..... 77
- compensation ..... 879, 1039, 1321, 1341, 1347
- Cr ..... 697
- crystal growth ..... 159
- Cu ..... 461, 467, 587, 1003, 1347
- CuIn(Ga)Se<sub>2</sub> ..... 1467
- Cu related defects ..... 319
- Czochralski Si ..... 341, 399
- D**-lines ..... 151

- D- donor centre ..... 1707  
 dangling bonds ..... 197, 515  
 data storage ..... 1009  
 deep  
   ~ acceptors ..... 1299, 1455  
   ~ impurities ..... 1281  
   ~ levels ..... 121, 145, 325, 437, 497, 659, 715, 1137, 1217, 1353, 1737  
 defect  
   ~ clusters ..... 527, 535  
   ~ complexes ..... 831, 975, 1827  
   ~ engineering ..... 671  
   ~ formation ..... 1801  
   ~ modes ..... 1197  
   ~ reaction ..... 647, 659, 843, 1761  
   ~ symmetries ..... 1027  
 degradation ..... 1329  
 density-functional theory 861, 1179, 1203  
 deuterium ..... 417  
 diamond — see C  
 diffuse x-ray scattering ..... 1377  
 diffusion ..... 179, 211, 271, 283, 337, 347, 423, 849, 1293, 1761 - 1844  
 dislocation(s) ..... 151, 159, 313, 527, 981, 1359, 1783, 1795  
   ~ loops ..... 1807  
   ~ velocity ..... 159  
 dispersion ..... 933  
 divacancies ..... 671, 1321  
 DLOS ..... 1003  
 DLTS ..... 53, 115, 145, 151, 165, 247, 301, 319, 325, 423, 467, 565, 665, 715, 837, 843, 933, 1027, 1045, 1093, 1413, 1551, 1619, 1653, 1671  
 donor(s) ..... 1125, 1287, 1341  
   ~ -acceptor transitions 1113, 1149, 1191  
 Doppler broadening ..... 127  
 double acceptor ..... 417, 423  
 DX centres ..... 1247, 1353, 1359, 1407  
 dynamical relaxation ..... 641  
  
 E1-3 ..... 1027  
 E-centre ..... 83  
 EDMR ..... 957, 963, 1105, 1309  
 EELS ..... 547  
 EL2 . 929, 987, 993, 997 1003, 1009, 1015  
 electric-dipole spin resonance ..... 417  
 electrical measurements ..... 1515  
 electroluminescence ..... 1229, 1485, 1509, 1833  
  
 electron  
   ~ -beam metallization ..... 115  
   ~ correlation ..... 647  
   ~ -hole liquid ..... 1731  
   ~ irradiation ..... 1253, 1303  
   ~ mobility ..... 939  
   ~ irradiation ..... 127, 367, 503, 553, 685, 721, 1087, 1377, 1419  
 electronic structure ..... 975  
 emission channeling ..... 899  
 ENDOR ..... 987  
 energy transfer rate ..... 1491  
 epitaxial layer ..... 121  
 EPR ..... 331, 373, 379, 423, 443, 491, 515, 559, 697, 703, 987, 1033, 1069, 1105, 1167, 1401, 1473, 1539, 1559, 1713, 1777  
 equilibrium defects ..... 905  
 Er ..... 1485 - 1606, 1625, 1701  
 EXAFS ..... 1571  
 excitation mechanism ..... 1509  
 excited states ..... 27, 987, 993, 1437  
 exciton ..... 1731  
 extended defects ..... 319, 325, 547  
  
 F 1425, 1821  
 Fano resonance ..... 479, 571  
 fast diffusers ..... 1347  
 Fe ..... 325, 437, 443, 449, 455, 819, 825, 1807  
 Fe-acceptor pair ..... 429, 443  
 first-principles calculation — see ab initio  
 force constants ..... 1  
 formation energy ..... 873  
 Frank partial dislocations ..... 1743  
 free electron laser ..... 1497  
 Frenkel pairs ..... 503, 837  
 FTIR ..... 867, 1545  
  
 G complex ..... 295  
 g tensor ..... 1559  
 Ga ..... 1449  
 Ga vacancy ..... 905, 951  
 GaAs antisite ..... 945  
 GaAs ..... 1, 629, 849 - 1062, 1321, 1383, 1551 - 1576, 1743, 1813, 1821, 1827  
 GaAs/AlGaAs ..... 1665, 1839  
 GaAs/AlGaAs MQW ..... 1631  
 GaAs/AlGaAs quantum structures ... 1701

- GaN ..... 19, 1081 - 1210, 1321,  
 1577, 1659, 1749, 1755  
 GaP ..... 1, 1063 - 1080  
 gap modes ..... 1  
 GaS ..... 1235  
 gas desorption ..... 709  
 GaSb ..... 1241  
 GaSe ..... 1235  
 Ge (crystal) ..... 35 - 82, 97, 179  
 Ge (impurity) ..... 1315, 1767  
 gettering ..... 429, 461, 1795  
 glide velocity ..... 313  
 green luminescence ..... 1371  
 grown-in defects ..... 341  
 growth ..... 997  
   ~ induced alignment ..... 1293  
  
**H** 11, 19, 35, 391, 417, 515, 745, 751,  
 849, 855, 963, 1247, 1371, 1743, 1777  
   ~ impurity in Si ..... 171 - 340  
   ~ diffusion ..... 171, 191  
   ~ molecule ..... 203, 211, 235, 241,  
     277, 283  
   ~ passivation ..... 1223  
   ~ plasma ..... 313  
 Hall effect ..... 997  
 halogens ..... 1821  
 Ham's law ..... 449  
 He-plasma processing ..... 1045  
 HEMT ..... 805  
 heterojunction ..... 1383, 1425  
 heterostructure ..... 813, 1749  
 high pressure ..... 1197  
 high-voltage devices ..... 1801  
 homogeneity ..... 825  
 hole states ..... 479  
 hole traps ..... 151  
 HRTEM ..... 1755  
 hydrostatic pressure ..... 1565  
 hyperfine interaction ..... 491, 677  
 hysteresis ..... 1383  
  
 Ion implantation ..... 1389, 1395  
 implantation ..... 1057, 1093, 1099  
 impurity dipoles ..... 1607  
 In .... 53, 59, 455, 1341, 1347, 1431, 1449  
 InAlAs ..... 1211  
 InAs ..... 1223  
 InAs/GaAs quantum dots ..... 1619  
  
 infrared absorption ..... 355, 379, 391,  
   405, 611  
 InGaN ..... 1229  
 InGaAs ..... 805, 813, 1211, 1217  
 InGaAs quantum dots ..... 1643  
 injection-annealing ..... 1051  
 InP ..... 805 - 848, 1211, 1807  
 InSb ..... 1689  
 interband transition ..... 547  
 interdiffusion ..... 151, 1695, 1701  
 interface defects ..... 1259, 1383, 1713  
 interface states ..... 1737, 1755  
 interstitial atoms ..... 229, 503, 541, 781,  
   1253, 1377, 1777, 1839  
 ion  
   ~ channeling ..... 97  
   ~ etching ..... 133  
   ~ implantation ..... 271, 337, 587, 593,  
     611, 641, 727, 763, 1503, 1577,  
     1807  
 ionized impurity scattering ..... 77, 939  
 IR  
   ~ absorption ..... 997  
   ~ spectroscopy ..... 35, 41, 97, 103,  
     283, 455  
 irradiation ..... 1027, 1143  
 isoelectronic centre ..... 289  
 isotope effects ..... 41, 47, 635, 769, 1173  
 isovalent impurities ..... 1773  
 ITC ..... 1033  
  
 Jahn Teller effect ..... 653  
 JDOS ..... 547  
  
 Keating-Kane model ..... 1075  
  
 Laplace DLTS ..... 337  
 laser  
   ~ diode ..... 1329  
   ~ induced disorder ..... 1631  
 lasing oscillations ..... 1607  
 lattice  
   ~ location ..... 1503  
   ~ parameter ..... 1253, 1287  
   ~ relaxation ..... 659, 1431  
 LED ..... 1063, 1105, 1229, 1485  
 Li 411, 635, 1347, 1813, 1827  
 light-induced gratings ..... 1407  
 linewidths ..... 1, 355  
 local density approximation ..... 1479

- local vibrational modes ... 1, 41, 103, 109, 223, 253, 355, 361, 391, 617, 861, 867, 1075, 1173, 1179, 1247, 1813
- LT-GaAs ..... 951
- luminescence ..... 715, 917, 997, 1119, 1143, 1191, 1401, 1527, 1551, 1643  
~ decay time ..... 1491, 1509
- Madelung energy ..... 1185
- magnetic anisotropy ..... 1695
- magneto-optic ..... 1467
- magnetopolaron effect ..... 1241
- MBE 83, 139, 805, 957, 1671, 1743, 1755
- MCDA ..... 1303
- MCDA-EPR ..... 1021
- MESFET ..... 933
- metastability ..... 745, 969, 993, 1015, 1051, 1241, 1455
- metastable  
~ defects ..... 331, 647  
~ state ..... 217, 1443
- Mg ..... 19, 1155, 1229
- microcrystalline Si ..... 235, 593
- migration ..... 253
- misfit dislocation ..... 1637, 1755
- Mn ..... 1167
- mobility ..... 77
- MOCVD ..... 1081, 1125, 1293, 1643
- modulation doping ..... 1749
- molecular dynamics ..... 171, 509
- MOMBE ..... 1293
- multicrystalline Si ..... 1795
- multiphonon  
~ recombination ..... 659  
~ transition ..... 1281
- muonium ..... 179, 849
- N ..... 739, 867, 1395, 1671
- N-H complexes ..... 1063
- N-vacancy ..... 1275
- nanometer sized structures ..... 553, 641
- nanostructures ..... 1683
- nanotubes ..... 1659
- negative-U .. 873, 1407, 1443, 1449, 1479
- neodymium ..... 1589
- neutron  
~ -activation analysis ..... 1783  
~ irradiation ..... 623, 1235
- Ni ..... 325, 911, 1167
- NMR ..... 1365
- noble gases ..... 565, 593, 605
- noise ..... 933
- non-radiative  
~ centres ..... 139  
~ -radiative recombination ..... 1677
- n-type diamond ..... 799
- O (impurity) ..... 19, 41, 103, 271, 277, 283, 461, 565, 617, 739, 873, 1559, 1565, 1571, 1767, 1773  
~ diffusion in Si ..... 1761  
~ impurity in Si ..... 341 - 410  
~ dimer ..... 361, 367
- ODENDOR ..... 987
- ODEPR ..... 1303
- ODMR ..... 139, 685, 1015, 1033, 1087, 1105, 1309, 1315
- optical absorption ..... 1075
- order/disorder ..... 1057
- oxidation ..... 1719
- PAC 53, 59, 899, 1099, 1223, 1341, 1347
- particle detectors ..... 671
- passivation ..... 185, 191, 295, 411, 1063, 1371, 1719, 1821
- percolation ..... 65, 929
- perovskites ..... 1589
- persistent  
~ excited conductivity ..... 599  
~ photoconductivity ..... 1315
- phonon(s) ..... 109  
~ coupling ..... 41  
~ spectroscopy ..... 47, 399
- photoconductivity ..... 1003
- photocurrent ..... 825
- photoluminescence .... 109, 139, 151, 197, 259, 289, 473, 485, 521, 565, 587, 605, 617, 635, 825, 697, 1009, 1069, 1075, 1087, 1093, 1113, 1125, 1131, 1137, 1149, 1299, 1485, 1497, 1521, 1565, 1577, 1583, 1589, 1595, 1677, 1731
- photomagnetism ..... 1449
- photoquenching ..... 1003
- photothermal deflection spectroscopy 331
- photovoltaic ..... 1467
- PICTS ..... 1039
- PIN photodiodes ..... 1217
- plasma-induced defects ..... 1051
- plastic deformation ..... 975
- PLE spectroscopy ..... 1533



- porous Si ..... 11, 1533, 1725  
 positron annihilation ..... 127, 581, 709,  
     721, 733, 819, 879, 885, 905, 981,  
     1033, 1235, 1335, 1419, 1461, 1725,  
     1813  
 positronium ..... 709  
 post-growth annealing ..... 905  
 precipitates ..... 341, 347, 399, 405,  
     429, 449, 461, 929  
 pressure ..... 813  
 processing ..... 27  
 proton irradiation ..... 599, 733, 1021,  
     1419, 1431  
 pseudo donors ..... 497  
 Pt 473, 479  
  
**Quadrupole mass spectroscopy** ..... 1743  
**quantum**  
     ~ dots ... 1551, 1619, 1643, 1689, 1707  
     ~ interference effects ..... 65  
     ~ wells ..... 91, 1601, 1631, 1665  
     ~ wires ..... 1607  
  
**Radiation**  
     ~ damage ..... 121, 133, 411, 503 - 676,  
         787, 819, 1039, 1217  
     ~ effects ..... 831  
     ~ -induced defects ..... 843  
**Raman** ..... 109, 203, 211, 235, 241,  
     623, 727, 793, 1197, 1589  
 rare-earth elements ..... 917  
 reactive ion etching ..... 1045  
 recombination ..... 331, 629, 665  
     ~ -enhanced  
         ~ ~ diffusion ..... 443  
         ~ ~ reactions ..... 1329  
**RHEED** ..... 1743  
**ring**  
     ~ hexavacancy ..... 509  
     ~ mechanism ..... 1789  
  
**S** 1161  
 s-d coupling ..... 1443  
 scanning tunneling microscopy ..... 885  
 Schottky diodes ..... 115, 165, 1045  
 SDR ..... 957  
 segregation ..... 1783  
**self**  
     ~ assembly ..... 1683  
     ~ -compensation ..... 1185  
         ~ -interstitial ..... 35, 59, 229, 535, 541  
 shallow acceptor ..... 479, 575  
     ~ -deep transition ..... 1241  
     ~ donors ..... 497  
     ~ thermal donors ..... 379, 385, 1761  
 Si d-doping ..... 1299  
 Si (host) ..... 35, 103, 139, 145, 787,  
     1491 - 1532, 1767 - 1806  
 Si (impurity) ..... 781, 1229  
 Si — H impurity ..... 171 - 340  
 Si — metals ..... 411 - 502  
 Si — O impurity ..... 341 - 410  
 Si — radiation damage ..... 503 - 676  
 Si nanostructures ..... 1683  
 Si on insulator ..... 1731  
 Si quantum wires ..... 1607  
 Si/SiO<sub>2</sub> ..... 1713  
 SiC ..... 653, 677 - 744, 1539, 1545, 1833  
 SiGe ..... 83 - 164  
 SiGe quantum wells ..... 1613  
 SiGeC ..... 165  
 SIMS ..... 899, 997  
 SiO<sub>2</sub> ..... 1479  
 SnO films ..... 1425  
 solar cells ..... 527, 655, 629  
 space degradation ..... 629  
 spark source mass spectroscopy ..... 867  
 spin-dependent  
     ~ localization ..... 1683  
     ~ -dependent recombination ..... 559  
 spin relaxaton ..... 1443  
 Staebler-Wronski effect ..... 599  
 step-bunching ..... 1211  
 stimulated emission ..... 71  
 stoichiometric ..... 805  
**structural**  
     ~ change ..... 647  
     ~ defects ..... 1521  
 supercell approx ..... 1287  
 superlattice ..... 879, 1625, 1695  
**surface**  
     ~ defect ..... 1719  
     ~ reconstruction ..... 11  
  
**TEM** ..... 553, 1211, 1743, 1755  
**thermal**  
     ~ donor ..... 347, 367, 373, 379, 1767  
     ~ quenching ..... 139, 1583  
     ~ stability ..... 951  
 Thomas-Fermi model ..... 939

- 
- threading dislocations ..... 1203  
 time  
   ~ resolved spectroscopy ..... 1125, 1155, 1455  
   ~ response ..... 1491  
 total energy calculation ..... 535  
 transient ion drift ..... 461  
 transition metals ..... 145, 307, 677, 831, 893, 1131, 1173, 1401, 1473, 1677, 1795  
 transmutation doping ..... 945  
 transport  
   ~ phenomena ..... 65  
   ~ properties ..... 1613  
 triethylgallium ..... 1081  
 trimethylgallium ..... 1081  
 tunneling transport ..... 1259  
 two-dimensional electron gas ..... 1749  
  
 UHV ..... 553  
 ultrasound treatment ..... 197  
 uniaxial stress ..... 35, 71, 247, 455, 473, 485, 571, 635, 1027  
 UV photodetectors ..... 1425  
  
**V** ..... 1131  
 VGa-SiGa complexes ..... 885  
 vacancy ..... 19, 53, 59, 127, 503, 509, 515, 605, 653, 685, 721, 775, 981, 1253, 1321, 1377, 1473, 1813, 1839  
   ~ impurity complexes ..... 775  
 vertical cavity ..... 1637  
 Voids ..... 341  
 VPE ..... 997  
  
**W** ..... 165  
 water  
   ~ boiling ..... 185  
   ~ molecule ..... 277  
 wurtzite lattice ..... 1359  
  
 X-ray fluorescence ..... 1795  
  
 Zeeman effect . 455, 485, 697, 1131, 1401  
 Zn ..... 1839  
 ZnCdSe/ZnSe ..... 1665  
 ZnMgSSe ..... 1329  
 ZnO ..... 1371  
 ZnS ..... 1321, 1425  
  
 ZnSe ..... 1321, 1335, 1377, 1383, 1389, 1395, 1671, 1743  
 ZnSSe ..... 1671  
 ZnTe ..... 1321

# Materials Science Forum

ISSN 0255-5476

*As of January 1992 combined with Crystal Properties and Preparation*

## **Editors, Editorial and Advisory Board**

*see front inside cover*

## **Scope**

*Materials Science Forum* specializes in the rapid publication of international conference proceedings in every area of Materials Science, Solid State Physics and Chemistry. This permits such proceedings to be conveniently referenced, abstracted and read. It also guarantees that the proceedings are available in major libraries within two to three months of the close of the conference.

*Materials Science Forum* also publishes, on a regular basis, collections of research and review papers on topics of current interest. Abstracted in all of the major abstract media, and available in practically all of the major libraries which service materials research communities, *Materials Science Forum* offers both very rapid publication (within two months of acceptance of the manuscript) and high visibility.

## **Internet**

The table of contents of each volume is available on the World Wide Web at <http://www.ttp.ch/perdcs/msf.htm>.

## **Preview Service**

Trans Tech Publications' Preview Service offers automatic delivery of tables of contents via e-mail - several weeks before the actual release of the respective publication. This service is free of charge. For more information, please visit our home page or send an e-mail to [preview@ttp.ch](mailto:preview@ttp.ch) containing simply the word *help* as the message body.

## **Subscription Information**

*Materials Science Forum* is published in 30 volumes per year. In 1997, volumes 233-262 are scheduled to be published. The subscription rate is CHF 99.50 per volume (CHF 2985.00 per year).

## **Standing orders**

Standing Orders are available for the following topical areas of interest: Pt. A: Electronic and Electro-optic Materials; Pt. B: Metal Physics; Pt. C: Ceramic Materials and Glasses; Pt. D: Ionic Materials, Oxides; Pt. E: Corrosion and Oxidation; Pt. F: Surfaces, Interfaces and Thin Films; Pt. G: Crystal Growth and Crystal Structures.

Standing orders for one or more of these sections may be placed: the topics are not meant to be exclusive, i.e. a given volume can be assigned to two or more of these sections. Should a title be assigned to more than one section, the subscriber will receive the respective title only once. The price per volume is CHF 99.50.

 **Trans Tech Publications Ltd**  
Brandrain 6 • CH-8707 Uetikon-Zuerich • Switzerland  
Fax +41 (1) 922 10 33 • e-mail: [ttp@ttp.ch](mailto:ttp@ttp.ch)  
<http://www.ttp.ch>